

Sunday Afternoon, October 28, 2012

Biomaterials Plenary Session

Room: 23 - Session BP+AS-SuA

Biomaterials Plenary - Bioimaging: In Vacuo, In Vitro, In Vivo

Moderator: M.R. Alexander, University of Nottingham, UK

4:00pm **BP+AS-SuA1 NanoBio Imaging for New Biomedical Applications, D.W. Moon**, Korea Research Institute of Standards and Science **INVITED**

Surface and interface analysis techniques have been mainly developed to meet the demands on atomic scale characterization from semiconductor industries. KRIS has been trying to meet the surface and interface analysis challenges from semiconductor industries and furthermore to extend the application scope to biomedical areas. In this presentation, I'd like to report our recent activities of nanobio imaging for new biomedical applications such as 1) Coherent Anti-Stokes Raman Scattering (CARS) for atherosclerotic plaque imaging 2) Time-of-flight secondary ion mass spectrometry (TOF-SIMS) for mass imaging of collagen fibrils, atherosclerotic plaques, and cancer tissues and 3) Surface Plasmon Resonance Imaging Ellipsometry for cell adhesion, migration, and infiltration dynamics for HUVEC, CASMC, and T cells 4) TOF-medium energy ion scattering spectroscopy (TOF-MEIS) for nanothin films and nanoparticles such as CdSe/ZnS quantum dots and calcium hydroxyapatite nano-size biominerals. Future challenges of nanobio imaging for biomedical applications will be discussed.

4:40pm **BP+AS-SuA3 3-D View into Cells by X-ray Nano-Tomography, G. Schneider, P. Guttman, S. Werner, K. Henzler, S. Rehbein**, Helmholtz-Zentrum Berlin für Materialien und Energie GmbH, Germany **INVITED**

X-ray imaging offers a new 3-D view into cells. With its ability to penetrate whole hydrated cells it is ideally suited for pairing fluorescence light microscopy and nanoscale X-ray tomography. The HZB TXM at the undulator U41 provides a spectral resolution of 10.000 and a spatial resolution of 11 nm. For high resolution tomography, we adopted a tilt stage originally developed for electron tomography. The stage is able to tilt samples up to $\pm 80^\circ$. Such a large tilt of flat sample holders is impossible with TXM at bending magnet sources because they require a monochromator pinhole to be positioned close to the specimen. In our TXM, the holder geometry is no longer restricted to glass tubes. Conventional fluorescence images are diffraction-limited to ~ 200 nm, whereas current TXM achieve a ten-fold improvement in resolution. Since fluorescence and X-ray microscopy permit analysis of whole cells, it is possible to investigate the same cell in both microscopes by correlative microscopy. These correlative studies are ideally suited to X-ray microscopy because of its ability to image cells in 3D. In the talk, we present the cryo TXM and selected applications. In particular, we will show the internal structures of mammalian cells, i.e. plasma membrane, nuclear membrane, nuclear pores, nucleoli, endoplasmic reticulum, vesicles, lysosomes and mitochondria. It is now also possible to resolve internal organellar structures, such as mitochondrial cristae, the double nuclear membrane and lysosomal inclusions. In addition, we discuss ways towards 10 nm 3D imaging of cells. Keywords: X-ray microscopy, tomography, cell organelles, correlative microscopy

References

1. S. Rehbein, S. Heim, P. Guttman, S. Werner, G. Schneider, Phys. Rev. Lett. 103, (2009) 110801
2. G. Schneider, P. Guttman, S. Heim, S. Rehbein, F. Mueller, K. Nagashima, J.B. Heymann, W.G. Müller, J.G. McNally, Nature Methods 7 (2010), 985-987
3. P. Guttman, C. Bittencourt, S. Rehbein, P. Umek, X. Ke, G. Van Tendeloo, C. P. Ewels and G. Schneider, Nature Photonics 6 (2012), 25-29
4. G. Schneider, P. Guttman, S. Rehbein, S. Werner, R. Follath, J. Struct. Biol. 177 (2012), 212-223

5:20pm **BP+AS-SuA5 Nanoscopy with Focused Light, S.W. Hell**, Max-Planck-Institut für Biophysikalische Chemie, Germany **INVITED**

In STED microscopy¹, fluorescent features are switched off by the STED beam, which confines the fluorophores to the ground state everywhere in the focal region except at a subdiffraction area of extent. In RESOLFT microscopy,^{2,3} the principles of STED have been expanded to fluorescence

on-off-switching at low intensities I , by resorting to molecular switching mechanisms that entail low switching thresholds I_s . An I_s lower by many orders of magnitude is provided by reversibly switching the fluorophore to a long-lived dark (triplet) state² or between a long-lived 'fluorescence activated' and 'deactivated' state.^{2,5} These alternative switching mechanisms entail an I_s that is several orders of magnitude lower than in STED. In imaging applications, STED/RESOLFT enables fast recordings and the application to living cells, tissues, and even living animals.^{6,7}

Starting from the basic principles of nanoscopy we will discuss recent developments^{8,9} with particular attention to RESOLFT and the recent nanoscale imaging of the brain of living mice⁷ by STED.

1 Hell, S. W. & Wichmann, J. Breaking the diffraction resolution limit by stimulated-emission - stimulated-emission-depletion fluorescence microscopy, 780-782, doi:10.1364/OL.19.000780 (1994).

2 Hell, S. W. Toward fluorescence nanoscopy, 1347-1355 (2003).

3 Hell, S. W., Jakobs, S. & Kastrup, L. Imaging and writing at the nanoscale with focused visible light through saturable optical transitions, 859-860 (2003).

4 Hell, S. W. Far-Field Optical Nanoscopy, 1153-1158 (2007).

5 Hofmann, M., Eggeling, C., Jakobs, S. & Hell, S. W. Breaking the diffraction barrier in fluorescence microscopy at low light intensities by using reversibly photoswitchable proteins, 17565-17569 (2005).

6 Rankin, B. R. Nanoscopy in a Living Multicellular Organism Expressing GFP, L63 - L65 (2011).

7 Berning, S., Willig, K. I., Steffens, H., Dibaj, P. & Hell, S. W. Nanoscopy in a Living Mouse Brain, 551 (2012).

8 Grotjohann, T. Diffraction-unlimited all-optical imaging and writing with a photochromic GFP, 204-208 (2011).

9 Brakemann, T. A reversibly photoswitchable GFP-like protein with fluorescence excitation decoupled from switching, 942-947 (2011).

Monday Morning, October 29, 2012

Actinides and Rare Earths Focus Topic
Room: 6 - Session AC+MI+SS+TF-MoM

Electronic Structure and Spectroscopy of Actinides

Moderator: A.J. Nelson, Lawrence Livermore National Laboratory

9:00am **AC+MI+SS+TF-MoM3 Strong Correlations and the Electronic Structure of the Actinide Dioxides, R.L. Martin**, Los Alamos National Laboratory **INVITED**

The series of actinide dioxides (AnO_2 , $An=Pa, \dots Cm$) are difficult challenges for electronic structure theory. The early members of the series are Mott insulators, the band gap corresponding to f_7^2 transitions, while the later members, beginning with PuO_2 , are $O2p \rightarrow An5f$ charge transfer insulators. I will review recent experimental results (X-ray absorption, photoemission and optical band gaps) which now allow us to distinguish among several many-body approximations to their electronic structure, including the SIC, DFT+U, DMFT+U and hybrid DFT (HSE) approaches.

9:40am **AC+MI+SS+TF-MoM5 Synchrotron Radiation Studies of Actinide Compounds, S.M. Butorin**, Uppsala University, Sweden **INVITED**

Core-to-core resonant inelastic x-ray scattering (RIXS) and valence-to-core RIXS techniques are two complimentary ways for probing the electronic structure in actinide systems. Specific cuts of the core-to-core RIXS maps around $M\beta$ and L lines of actinides represent remarkably improved high-resolution x-ray absorption spectra of actinide $3d$ and $2p$ edges, respectively, as a result of limited lifetime broadening of core holes present in shallower levels in the final state of the spectroscopic process. That allows for more detailed studies of unoccupied states and better oxidation states assignments. In turn, the valence-to-core RIXS spectra are only limited by the instrumental resolution and provide information about actinide chemical bonding and interactions between valence electrons.

A comparison of experimental data with results of model calculations shows that the resonant spectra of actinide systems recorded at the actinide $M(3d)$ and $O(5d)$ thresholds which probe the $5f$ states can be interpreted using the many-body theory, such as the Anderson impurity model, while the data obtained at the $L3$ threshold and representing the $6d$ states of actinides can be described within a single-particle approach, such as LDA+ U (local density approximation with supplemented Coulomb interaction U) framework.

In course of discussion of the above statements, we present the RIXS data for a number of actinide systems with emphasis on the results contributing to understanding of the U-O and Pu-O phase diagrams, in particular data for UO_{2+x} , U_4O_9 , U_3O_8 and PuO_{2+x} . The influence of the Coulomb interaction between $5f$ electrons on the electronic structure of actinides is also discussed.

10:40am **AC+MI+SS+TF-MoM8 Quasiparticle Dynamics in Uranium Systems from Ultrafast Spectroscopies, T. Durakiewicz**, Los Alamos National Laboratory

Every time we add a new dimension to an experimental method, we open a window to novel, unexpected and fascinating phenomena. Here we show the results of our focused effort of adding time-domain to the powerful experimental techniques of Angle Resolved Photoelectron Spectroscopy (ARPES) and reflectivity. The novel tools are applied to actinides and help us understand the details of the electronic structure of the correlated f -electron materials.

In the hidden order system URu_2Si_2 we investigate the massive renormalization of the Fermi surface at specific k values. The application of time-resolved ARPES allowed a direct measurement of the momentum-resolved quasiparticle lifetime which was shown to increase by an order of magnitude at the hidden order transition. Time-resolved ARPES together with the ultrafast reflectivity results provided evidence for forming a multiple gap structure, including the hybridization gap, pseudogap and HO gap [1, 2].

Another actinide system of interest is a Mott insulator UO_2 , where we have investigated the complex dynamics of the Hubbard excitons. We have found that the dynamics can be divided into four distinct processes: instantaneous hop, picosecond lattice deformation, phonon emission and relaxation, and the slow relaxation related to the propagation of Hubbard excitons [3]. We

have also obtained the first direct measurement of Hubbard gap in $5f$ system [4].

The novel femtosecond pump-probe methods provide unique information about the dynamics of $5f$ quasiparticles, and open novel possibilities in addressing the long-standing questions about the role of near-Fermi level band renormalization in establishing the physical properties of correlated materials.

References

- [1] Physical Review B 84, 161101(Rapid Comm.) (2011)
- [2] Physical Review B 84, 161103(Rapid Comm.) (2011)
- [3] Physical Review Letters 106, 207402 (2011)
- [4] manuscript in preparation

11:00am **AC+MI+SS+TF-MoM9 Comparison of Spectroscopic Data with Cluster Calculations of Plutonium, Plutonium Dioxide and Uranium Dioxide, J.G. Tobin, S.W. Yu, B.W. Chung**, Lawrence Livermore National Laboratory, *M.V. Ryzhkov*, Russian Academy of Science-Ekaterinburg, *A. Mirmelstein*, Russian Federation Nuclear Center-Snezhinsk

Using spectroscopic data produced in the experimental investigations of bulk systems, including X-Ray Absorption Spectroscopy (XAS), Photoelectron Spectroscopy (PES) and Bremsstrahlung Isochromat Spectroscopy (BIS) [1-5], the theoretical results within for UO_2 [6], PuO_2 [6] and Pu [7] clusters have been evaluated. The calculations of the electronic structure of the clusters have been performed within the framework of the Relativistic Discrete-Variational Method (RDV). [6,7] The comparisons between the LLNL experimental data and the Russian calculations are quite favorable. The cluster calculations may represent a new and useful avenue to address unresolved questions within the field of actinide electron structure, particularly that of Pu . Observation of the changes in the Pu electronic structure as a function of size suggests interesting implications for bulk Pu electronic structure.

Acknowledgements

Lawrence Livermore National Laboratory is operated by Lawrence Livermore National Security, LLC, for the U.S. Department of Energy, National Nuclear Security Administration under Contract No. DE-AC52-07NA27344. JGT and SWY were supported by the DOE Office of Science, Office of Basic Energy Science, Division of Materials Science and Engineering. Work at the RAS and VNIITF was supported in part by Contract B590089 between LLNL and VNIITF. The Advanced Light Source (ALS) in Berkeley and the Stanford Synchrotron Radiation Laboratory are supported by the DOE Office of Science, Office of Basic Energy Science.

References

1. J.G. Tobin and S.-W. Yu, Phys. Rev. Lett, **107**, 167406 (2011).
2. S.-W. Yu, J. G. Tobin, J. C. Crowhurst, S. Sharma, J. K. Dewhurst, P. Olalde-Velasco, W. L. Yang, and W. J. Siekhaus, Phys. Rev. B **83**, 165102 (2011).
3. J.G. Tobin, B.W. Chung, R. K. Schulze, J. Terry, J. D. Farr, D. K. Shuh, K. Heinzelman, E. Rotenberg, G.D. Waddill, and G. Van der Laan, Phys. Rev. B **68**, 155109 (2003).
4. J.G. Tobin, P. Söderlind, A. Landa, K.T. Moore, A.J. Schwartz, B.W. Chung, M.A. Wall, J.M. Wills, R.G. Haire, and A.L. Kutepov, J. Phys. Cond. Matter **20**, 125204 (2008).
5. S.-W. Yu, J. G. Tobin, P. Olalde-Velasco, W. L. Yang, and W. J. Siekhaus, J. Vac. Sci. Tech. A. **30**, 011402 (2012).
6. M.V. Ryzhkov and A.Ya. Kupryazhkin, J. Nucl. Materials **384**, 226 (2009).
7. M.V. Ryzhkov, A. Mirmelstein, S.-W. Yu and J.G. Tobin, "Probing Actinide Electronic Structure through Pu Cluster Calculations," submitted to Phys. Rev. B, Feb 2012.

Quantitative Surface Chemical Analysis, Technique
Development, and Data Interpretation - Part 1

Moderator: J.A. Ohlhausen, Sandia National Laboratories,
S. Suzer, Bilkent University, Turkey

8:20am AS-MoM1 2012 AVS Albert Nerken Award Lecture:
Characterization of Thin-Film Nano-Structures by XPS, S. Tougaard*,
University of Southern Denmark
INVITED

This is a brief summary of the work that was involved in the development of the technique for quantitative XPS from analysis of the background of inelastically scattered electrons. About 30 years ago it became evident that these electrons must carry valuable information about the depth where the XPS electrons are excited. Theoretical modeling started and algorithms were developed. It was necessary to have an accurate description of the electron energy loss processes which at that time was not available. Theoretical calculations of inelastic cross sections based on a dielectric response description were done and a new experimental method to determine this from analysis of reflected electron energy loss spectra (REELS) was also developed.

To make these procedures for quantitative XPS analysis work in practice it is however not possible to use calculations valid only for specific sample compositions. Therefore an effort was made early on to find cross sections which can be used as an approximation for wide classes of materials and compositions. This resulted in the Universal cross sections which are now widely used and without which practical use of the formalism would have been very limited. The resulting XPS analysis technique was summarized in [1].

In the following years, much effort was then centered on applications to increasingly finer details of the morphology of nanostructures. This requires a careful data analysis since otherwise the uncertainty on the determined morphology may be large. Sometimes the detailed morphology is however not the most important issue for technological applications. Things like speed of analysis, robustness, and automation is often more important in industrial environments. It was therefore decided to develop a simpler algorithm which does not give as detailed information but which is very robust and therefore faster to use and less dependent on a meticulous analysis procedure. The resulting algorithm [2] has been shown to be very robust and therefore suitable for automation. It proved also effective in generating 3D images of nano-structures where automation is mandatory since thousands of spectra (one per pixel) must be analyzed.

Throughout, efforts were always exerted to test the validity of each step in the development of algorithms and procedures by designing and performing critical experiments. This is of utmost importance to ensure progress which does not lead to dead ends.

In this talk I will give an overview of the development of the technique and discuss some technological applications.

1. S. Tougaard, J. Vac. Sci. Technol. A14, 1415 (1996)
2. S. Tougaard, J. Vac. Sci. Technol. A23, 741 (2005)

9:00am AS-MoM3 Simulation of Electron Spectra for Surface Analysis (SESSA): (Hard) X-ray Photoelectron Spectra of Nanostructured Surfaces, W.S.M. Werner, W. Smekal, Vienna University of Technology, Austria, C.J. Powell, National Institute of Standards and Technology

The National Institute of Standards and Technology (NIST) Database for the Simulation of Electron Spectra for Surface Analysis (SESSA) [1,2] has been modified to allow a user to simulate XPS spectra of nanostructured surfaces, such as surfaces covered with rectangular islands, pyramids, spheres, layered spheres, etc. The effect of the nanomorphology of the surface on the emitted angular and energy distribution of photoelectrons is investigated. Comparison with simple models in the literature, which neglect several aspects of the physics of signal generation, such as elastic electron scattering, the dependence of the inelastic mean free path of the position of the electron in the specimen, the anisotropy of the photoelectric cross section, etc. gives good agreement when the same model assumptions are made in the simulations, but show significant deviations for more physically realistic simulations. The extent to which information on the nanomorphology can be extracted from the photoelectron angular/energy distribution is investigated, in particular the question is addressed whether the average size of nanostructures on a surface is accessible by means of

analysis of angular/energy photoelectron spectra. This is done for standard AlK α and Mg K α laboratory sources, but the possibility to gain additional information by increasing the photon energy to the hard x-ray regime is also examined.

1. <http://www.nist.gov/srd/nist100.cfm>.

2. W. Smekal, W. S. M. Werner, and C. J. Powell, Surf. Interface Anal. 37, 1059 (2005).

9:20am AS-MoM4 XPS Characterisation of InP Features Etched in Cl₂-Ar and Cl₂-H₂ Inductively Coupled Plasmas, C. Cardinaud, CNRS, France, R. Chanson, CNRS-IMN, France, S. Bouchoule, CNRS-LPN, France, A. Rhallabi, M.-C. Fernandez, Université de Nantes, France

High-aspect-ratio etching of InP-based heterostructures is a critical building block for photonic device fabrication. This study is focused on the chemical characterisation of the bottom and sidewall surfaces of InP ridge patterns etched with Cl₂-Ar and Cl₂-H₂ plasmas using a SiNx mask. Each sample contains five arrays combining various ridge widths (1.5 to 4 μ m) and space widths (5 to 16 μ m) plus four InP and mask open areas. Experiments are carried out in a Kratos-Axis-Ultra. The direction of analysis is vertical, i.e. normal to the sample surface, while the x-rays strike the surface with an angle of incidence $\alpha = 60^\circ$. The sample can be rotated in azimuth to align precisely the arrays, either parallel to or perpendicular to the plane defined by the x-source and the analyser. The first arrangement enables the analysis of the bottom (as well as the top of the ridge), whereas the second arrangement allows the analysis of the sidewall after tilting the sample. In this latter case two configurations are used. Taking advantage of the absorption of the x-rays by the InP ridges (1.8 μ m of InP absorbs 99% of AlK α under 60° of angle of incidence), the first configuration consists in tilting the sample opposite to the x-ray source until the bottom is totally screened. Simultaneously this brings the sidewall that is irradiated in the analyser line of sight. Tilting the sample towards the x-ray source to an angle $\theta = \text{atan}(\text{space width} / \text{ridge height})$ allows to shadow the bottom and observe photoelectrons coming from the sidewall (and the top of the ridges), in this case θ needs to be larger than α to obtain full irradiation of the sidewall that comes in the analyser line of sight.

For each array, the intensity of the In, P, N and Si core levels, normalised with respect to that measured on the mask and InP open spaces, are compared to the corresponding ratio calculated from the geometry of the array and the analysis arrangement or configuration. Modelling takes into account the contribution of the various surfaces (mask, InP) in the line of sight of the analyser, and the rate of irradiation according to the geometry of the array and the nature of the materials (InP ridge, mask) the x-rays pass through. This comparison points out the relation between the intensity emitted from the bottom and the aspect ratio of the array. A good agreement is obtained when including the analyser acceptance angle to the model. Concerning the sidewall the discrepancy between experiment and simulation corroborates the presence of a passivation layer. The presentation will discuss in detail the influence of the plasma chemistry on the quantitative composition of the sidewall and the bottom.

9:40am AS-MoM5 Simplified Extrinsic Background for XPS Data Fitting, A. Herrera-Gomez, UAM-Azcapotzalco and CINVESTAV-Queretaro, Mexico

In this presentation it is described a simplified form of the background for extrinsic scattering in the near-peak regime for X-Ray Photoelectron Spectroscopy (XPS) data peak-fitting. It directly accounts for the change on the slope of the background between the two sides of the core-level peak. With an approach similar to the employed for the Shirley background, it is proposed that the change on the background slope at energy E is proportional to the integrated signal above E . This functional form can be reproduced by assuming that the inelastic cross section is proportional to the energy loss. As for the Shirley background, and in contrast to the currently employed extrinsic background models, the background here introduced only employs one parameter. It has some extra advantages for XPS data peak fitting, such that its functional form is the same regardless of the core level, it account for the finiteness of the peak width in the generation of the background signal, it can be employed simultaneously with the intrinsic Shirley background, and last, but not least, it provides for good fits. Some implementations of the method are discussed.

10:00am AS-MoM6 Effective Attenuation Lengths for Photoelectrons in Thin Films of Silicon Oxynitride and Hafnium Oxynitride on Silicon, C.J. Powell, National Institute of Standards and Technology, W.S.M. Werner, W. Smekal, G. Tasneem, Vienna University of Technology, Austria
We have used the National Institute of Standards and Technology (NIST) Database for the Simulation of Electron Spectra for Surface Analysis (SESSA) [1,2] to simulate photoelectron intensities for thin films of SiO_{1.6}N_{0.4} and HfO_{1.9}N_{0.1} on silicon with excitation by Al K α X-rays. We considered Si 2p_{3/2} photoelectrons from SiO_{1.6}N_{0.4} and the substrate and Hf

* Albert Nerken Award Winner

4f_{7/2} photoelectrons from HfO_{1.9}N_{0.1}. The simulations were performed for ranges of film thicknesses and photoelectron emission angles and for two common configurations for X-ray photoelectron spectroscopy (XPS), the sample-tilting configuration and the Theta Probe configuration. We determined photoelectron effective attenuation lengths (EALs) by two methods, one by analyzing photoelectron intensities as a function of film thickness for each emission angle (Method 1) and the other by analyzing photoelectron intensities as a function of emission angle for each film thickness (Method 2). Our analyses were made with simple expressions that had been derived with the assumption that elastic-scattering effects were negligible. We found that EALs from both methods were systematically larger for the Theta Probe configuration, by amounts varying between 1 % and 5 %, than those for the sample-tilting configuration. These differences were attributed to anisotropy effects in the photoionization cross section that are expected to occur in the former configuration. Generally similar EALs were found by each method for each film material although larger EALs were found from Method 2 for film thicknesses less than 1.5 nm. SESSA is a useful tool for showing how elastic scattering of photoelectrons modifies EALs for particular materials, film thicknesses, and XPS configurations.

[1] <http://www.nist.gov/srd/nist100.cfm>.

[2] W. Smekal, W. S. M. Werner, and C. J. Powell, *Surf. Interface Anal.* 37, 1059 (2005).

10:40am **AS-MoM8 Valence Band XPS: A Valuable, but Underexploited, Tool for the Identification of Subtle Differences in Surface Chemistry**, *P.M.A. Sherwood*, Oklahoma State University
INVITED

Valence band X-ray photoelectron spectroscopy (XPS)¹ gives spectral features (peak positions and peak intensities) that arise from different physical principles than the core spectral region. This difference leads to the valence band region providing complimentary information to that of the core region. In many cases the valence band region can be used to detect subtle chemical differences that cannot be determined in core XPS studies. The value of using valence band XPS interpreted by calculation models will be demonstrated for various systems, and the use of core and valence band XPS for the study of buried interfaces will be discussed. Examples discussed will include the formation and study of thin (less than 100Å) oxide-free phosphate films, polymer films, composite surfaces, and the identification of different oxide films (including aluminum oxides) with similar chemical composition. Studies of shallow buried interfaces will be discussed. Recent work involving the preparation of hydroxyapatite films formed on metals which were coated with a thin oxide free film of metal etidronate will be reported. The metals studied were stainless steel and titanium. The key to adhesion of the hydroxyapatite films is the initial formation of a thin, oxide free, etidronate film on the metal. It was not found possible to prepare the hydroxyapatite films directly on the metal surfaces. Since hydroxyapatite is a key component of bone and teeth, it is likely that the coated metals will have desirable biocompatible properties, and that these treated metals may find applications in the production of medical implants.

¹P.M.A. Sherwood, "XPS Valence Bands", chapter in "Surface Analysis by Auger and X-ray Photoelectron

Spectroscopy" edited by D Briggs and J T Grant, SurfaceSpectra Ltd and IM Publications, Chapter 19, 531-555,

2003.

11:20am **AS-MoM10 Multitechnique Electron Spectroscopic Characterisation of Optoelectronic Devices**, *A.E. Wright, P. Mack, R.G. White, A. Bushell*, Thermo Fisher Scientific, UK

Optoelectronic devices, used for inter-conversion of light and electricity (e.g. photovoltaics and displays), depend upon careful optimisation of chemical, electronic and structural properties for efficient operation and useful operating lifetime.

Characterisation of such a device will typically identify the chemical bonding states, valence band positions, band gap and work function for each component. Lateral and depth resolution may be required to evaluate cell/pixel and multilayer structures.

Electron spectroscopic surface analysis techniques are ideal for the detailed analysis of the electronic structures of optoelectronic devices. Such techniques allow full quantitative characterisation of materials with chemical state and structural information. Surface specificity of spectroscopic information ensures that thin films can be analysed without interference from deeper parts of the sample. Multilayer structures may be studied with depth profiling techniques, and imaging functionality may be used to study cell or pixel structures.

The Thermo Scientific Escalab250Xi offers several such spectroscopic techniques, which have been employed in this study. X-ray Photoelectron

Spectroscopy (XPS) offers surface-sensitive, quantified chemical state analysis and imaging capabilities. Ultraviolet Photoelectron Spectroscopy (UPS) allows measurement of valence band positions. Reflected Electron Energy Loss Spectroscopy (REELS) yields information on the electronic band gap and hydrogen content of a material. These techniques are combined for a thorough characterisation of the electronic structure of optoelectronic devices.

11:40am **AS-MoM11 Chemically Resolved Electrical Characterisation of Working Devices by XPS**, *S. Suzer*, Bilkent University, Turkey

A noncontact chemical and electrical measurement technique of XPS is performed to investigate a CdS based Photoresistor and a Si-Diode during their operation. The main aim of the technique is to trace chemical and location specified surface potential variations as shifts of the XPS peak positions under operating conditions. For the Photoresistor Cd3d and for the Diode (p-n junction) Si2p peaks positions have been recorded, respectively. The variations in the Cd3d peak without and under photoillumination with 4 different lasers is extracted to yield the location dependent resistance values, which are represented; (i) two dimensionally for line scans, and (ii) three dimensionally for area measurements. In both cases one of the dimensions is the binding energy. For the Si p-n junction the variations in the Si2p peak position under normal and reverse bias are recorded to differentiate and identify the nature of the doping (p- or n-). The main advantage of the technique is its ability to assess element-specific surface electrical potentials of devices under operation based on the energy deviation of core level peaks in surface domains/structures. Detection of the variations in electrical potentials and especially their responses to the energy of the illuminating source *in operando*, is also shown to be capable of detecting, locating, and identifying the chemical nature of structural and other types of defects.

Biomaterial Interfaces

Room: 23 - Session BI-MoM

Surfaces to Control Cell Response

Moderator: A. Rosenhahn, Karlsruhe Institute of Technology, Germany

8:20am **BI-MoM1 Click Chemistry on Brominated Plasma Polymer Thin Films for Immobilizing and Patterning Biomolecules and Cells**, *B.W. Muir*, CSIRO Materials Science and Engineering, Australia, *R. Chen*, CSIRO Materials Science and Engineering and The University of Melbourne, Australia, *G.K. Such*, The University of Melbourne, Australia, *A. Postma*, *R.A. Evans*, *K.M. McLean*, CSIRO Materials Science and Engineering, Australia, *F. Caruso*, The University of Melbourne, Australia

The development of versatile and robust strategies for the surface modification of multiple classes of materials has proven challenging, with few generalized methods. Many available methods have limitation for widespread use due to the need for specific surface chemistries and/or laborious multistep procedures^[1]. A protocol to deposit brominated plasma polymer (Brpp) thin films on a variety of substrate surfaces (silicon wafers, glass, gold, Teflon) has been developed. These coatings are highly adherent and exhibit good stability in aqueous, biphasic and autoclaving conditions. The Brpp coating was found to be a useful platform for secondary reactions leading to surfaces with specific chemical properties. Following nucleophilic exchange, azide functionalized surfaces were developed and the copper catalysed azide alkyne cycloaddition (CuAAC) reaction^[2]; a paradigm of click chemistry, was successful in immobilizing various acetylenes. A particular highlight is the patterning of cells via selective surface functionalisation of PEG-alkyne using a photomask.^[3] This is the first known example of CuAAC reactions on pp thin films. A detailed physicochemical characterisation study of these films will also be presented.

[1] aH. Lee, S. M. Dellatore, W. M. Miller, P. B. Messersmith, *Science* 2007, 318, 426-430; bD. Y. Ryu, K. Shin, E. Drockenmuller, C. J. Hawker, T. P. Russell, *Science* 2005, 308, 236-239.

[2] R. A. Evans, *Australian Journal of Chemistry* 2007, 60, 384-395.

[3] Chen, R. T.; Marchesan, S.; Evans, R. A.; Styan, K. E.; Such, G. K.; Postma, A.; McLean, K. M.; Muir, B. W.*; Caruso, F., *Biomacromolecules* 2012, 13, (3), 889-895.

8:40am **BI-MoM2 Temperature-Induced Electrostatic Assembly of Poly (Ethylene Glycol) Co-Polymer for Non-Fouling Biomedical Applications: How Low Can You Go?**, R. Ogaki, O. Zoffmann Andersen, K. Kolind, D.C.E. Kraft, M. Foss, Aarhus University, Denmark

Development of long-term stable surfaces that resist bio-adhesion continues to stimulate the field of biomedical and biological research. While numerous strategies have been developed over the last several decades, the challenge remains in the creation of surfaces that can provide long-term 'zero' bio-adhesion from a variety of biological entities that spans lengths scales from biomolecules to cells. Although the physical and chemical properties of the resisting surface itself are important in achieving this ultimate goal, assessing the extent of bio-adhesion must be accompanied by detailed surface analysis via highly sensitive analytical techniques.

We have recently discovered that increasing the temperature alone during the assembly process of poly-L-lysine grafted poly (ethylene glycol) (PLL-g-PEG) results in the formation of highly dense PLL-g-PEG brush coating. The PLL-g-PEG surfaces prepared at various temperatures (20 to 80 °C) have been characterized by X-ray photoelectron spectroscopy (XPS). The PLL-g-PEG surfaces prepared at the 'standard' temperature of 20 °C are found to be comparable to the previously reported literatures. Interestingly, the surfaces prepared at 80°C have shown the highest surface grafted density of PLL-g-PEG, with ~ 4 times denser than those prepared at 20 °C.

The degree of cell and protein adhesions on these surfaces has been stringently determined using cell culture and serum/blood adsorption assays combined with XPS and time of flight secondary ion mass spectrometry (ToF-SIMS). The temperature-induced PLL-g-PEG surfaces have achieved 'zero' cell adhesions from three different types of mammalian cells for at least 36 days. In addition, XPS and ToF-SIMS analysis have confirmed near-zero protein adsorptions from 10% serum/MEM (at least 36 days), whole undiluted blood (at least 24 hrs) and undiluted serum (at least 24 hrs) with the surfaces being pre-incubated in high ionic strength buffer (2.4 M NaCl for 24 hrs).

The outcome of the rigorous bio-resistance tests presented here highlights the critical importance of processing temperature on the surface graft density of electrostatically driven PLL-g-PEG. The temperature induced assembly process can be effectively and easily implemented for a range of biomedical and biotechnological applications.

9:00am **BI-MoM3 Spatially and Temporally Coordinated Processes of Cells at Molecular to Cellular Scales**, J.P. Spatz, Max Planck Institute for Intelligent Systems & University of Heidelberg, Germany **INVITED**

Our approach to engineer cellular environments is based on self-organizing spatial positioning of single signaling molecules attached to synthetic extracellular matrices, which offers the highest spatial resolution with respect to the position of single signaling molecules. This approach allows tuning tissue with respect to its most relevant properties, i.e., viscoelasticity, peptide composition, nanotopography and spatial nanopatterning of signaling molecule. Such materials are defined as "nano-digital materials" since they enable the counting of individual signaling molecules, separated by a biologically inert background. Within these materials, the regulation of cellular responses is based on a biologically inert background which does not initiate any cell activation, which is then patterned with specific signaling molecules such as peptide ligands in well defined nanoscopic geometries. This approach is very powerful, since it enables the testing of cellular responses to individual, specific signaling molecules and their spatial ordering. Detailed consideration is also given to the fact that protein clusters such as those found at focal adhesion sites represent, to a large extent, hierarchically-organized cooperativity among various proteins. We found that integrin cluster have a functional packing density which is defined by an integrin-integrin spacing of approximately 68 nanometers. Such critical spacing values vary as matter of transmembrane receptor choice of interest. We have also developed methods which allows the light initiated activation of adhesion processes by switching the chemical composition of the extracellular matrix. This enabled us to identify the frequency of leader cell formation in collective cell migration as a matter of initial cell cluster pattern size and geometry. Moreover, "nano-digital supports" such as those described herein are clearly capable of involvement in such dynamic cellular processes as protein ordering at the cell's periphery which in turn leads to programming cell responses.

9:40am **BI-MoM5 Chemically Defined Synthetic Surfaces for Mesenchymal Stem Cell Expansion**, L. Meagher, H. Thissen, P. Pasic, R.A. Evans, S. Pereira, K. Tsang, V. Glattauer, K. Szyan, C.L. Be, D. Haylock, CSIRO Materials Science and Engineering, Australia

Interest in surface initiated polymerisation (SIP) for biomedical applications has increased rapidly recently, particularly the use of "living" free radical polymerisation mechanisms¹ as highly defined coating properties/architectures can be achieved. Here we demonstrate that advanced coatings can be produced using a surface immobilised macro-

chain transfer agent approach² and that such coatings can be used for the effective control of cell-surface interactions, an essential requirement in a broad range of applications in biomaterials and regenerative medicine. In the expansion of stem cells for therapeutic applications, fully synthetic, chemically defined materials are a requirement. Polymeric coatings which contain synthetic cell signalling molecules are key to ongoing progress in the generation of cells as therapies. Coating characterization was carried out using X-ray photoelectron spectroscopy (XPS) and colloid probe atomic force microscope (AFM). Cell culture studies were carried out using bone marrow derived human mesenchymal stem cells (hMSCs) using standard techniques. Differentiation of hMSCs was carried out using standard protocols in induction medias and the presence of characteristic cell surface markers was determined using flow cytometry. Substrate materials were silicon wafers or tissue culture polystyrene (TCPS).

In this study, we focus on a surface initiated Radical Addition-Fragmentation chain Transfer (RAFT) approach and present data demonstrating that dense polymer brushes can be prepared via surface immobilized macro-RAFT agents. The brush nature of the coatings was confirmed using a combination of XPS analysis and direct interaction force measurements with the AFM colloid probe technique. The properties of the coatings could be fine tuned using a variety of parameters such as the RAFT agent surface density, the polymerisation conditions, the monomer feed composition and the conjugation of cell attachment motifs such as cyclic peptides which interact with cell surface integrins. For example, the combination of a low cell adherent, low protein adsorbing polymer brush coating containing a conjugated peptide which interacted with $\alpha_5\beta_1$ integrins resulted in a surface which supported the expansion of hMSCs in a xeno-free, chemically defined, serum replacement media. In addition the expanded cells expressed cell surface markers typical of undifferentiated hMSCs and the expanded cells were able to differentiate along adipogenic, osteogenic and chondrogenic pathways.

¹ Edmond, S., Osborne, V.L. and Huck, W.T.S., Chem. Soc. Rev. 2004, 33, 14. ² Meagher, L., Thissen, H., Pasic, P., Evans, R.A. and Johnson, G., WO2008/019450.

10:00am **BI-MoM6 Binary Colloidal Crystal Structures Combined with Chemical Surface Modification to Achieve Superior Control Over Bointerfacial Interactions**, P. Koegler, Swinburne Univ. of Tech., Australia, P. Pasic, J. Gardiner, V. Glattauer, CSIRO Materials Science and Eng., Australia, A. Clayton, Swinburne Univ. of Tech., Australia, H. Thissen, CSIRO Materials Science and Eng., Australia, P. Kingshott, Swinburne Univ. of Tech., Australia

Bointerfacial interactions play a major role in the field of biomedical materials and regenerative medicine and are of tremendous importance to *in vivo* and *in vitro* applications. Cell-material interactions are mediated by surface parameters including the materials surface chemistry and topography. Colloidal lithography represents a promising tool to modify surface topographies at the nanoscale with precision and over large areas while at the same time not requiring complex instrumental set-ups or rigorous experimental conditions. The creation of nanostructured surfaces in this way can also be combined with sophisticated surface modification techniques such as polymer grafting techniques via functional groups (grafting-to) or initiating groups (grafting-from) on the particle surface. This platform, which provides control over surface chemistry and topography, offers great flexibility in regard to the design of advanced surface coatings. In the current study we have generated highly ordered binary colloidal crystal structures using surface functionalized particles. This approach allows precise control over particle size, spacing, and thus pattern morphology. In order to minimize undesired non-specific protein adsorption which can mediate cell attachment, graft polymer coatings were applied to particles using heterobifunctional poly(ethylene glycol) (PEG) to render the surfaces non-fouling. In addition, colloid crystal modified surfaces were modified with specific bioactive signals, such as the cyclic RGD peptide (cRGDfK) to promote cell attachment. Surface characterization was carried using scanning electron microscopy (SEM), atomic force microscopy (AFM) and X-ray photoelectron spectroscopy (XPS). Cell culture experiments were carried out using L929 mouse fibroblasts up to 24 hours. The unprecedented control over the surface chemistry and topography provided by this simple coating platform is of significant interest for the study of bointerfacial interactions and the development of new and improved biomedical devices.

11:20am **BI-MoM10 Influence of Ca²⁺ Binding to Titania on Platelet Activation Profiles**, S. Gupta, I. Reviakine, CIC biomaGUNE, Spain

Surface properties of implant materials are known to influence biological responses they elicit. However, complex processes operating at the interface remain poorly understood. To get an insight into these processes, we investigated the role played by surface ion equilibrium in defining interactions between an implant material (TiO₂) and components of blood (in this case, platelets), because blood is the first tissue that foreign

materials come into contact with when inserted into the body and because platelet response is crucial in defining the implant's fate.

Titanium is a widely used biomaterial. Its success is in part due to the favorable biocompatibility properties conferred by its oxide, TiO₂. We have previously shown that Ca²⁺-TiO₂ interactions affect the distribution of phospholipid phosphatidyl serine (PS) in model lipid membranes prepared on TiO₂. This allowed us to hypothesize that platelet activation will be affected by these interactions as well.

Platelets are anuclear cell fragments circulating in blood. Activated at wound sites, they aggregate and provide a catalytic surface for the formation of a fibrin-based clot that stops the bleeding. Recently, platelets have been recognized to participate in inflammation, wound healing, tissue regeneration, and immune responses. Activation of platelets by foreign surfaces is detrimental to blood-contacting implants but beneficial for osteoimplants. Upon activation, platelets expose on their surface and secrete a number of markers. These include PS, activated form of GPIIb-IIIa, and proteins CD62P and CD63 that are found in the membranes of the intracellular α - and dense granules of quiescent platelets. To assess the state of platelet activation on TiO₂, we assayed for the expression of these markers. In order to isolate a clear cause-and-effect relationship between Ca²⁺-TiO₂ interactions and platelet activation, we focused on purified platelets.

Our main finding is that the platelet activation profile on TiO₂ depends on the presence of Ca²⁺. Furthermore, in the absence of Ca²⁺, the α - and dense granule secretion is differentially regulated on titania. The differential granule secretion by platelets, as regulated by the surface properties, can be applied towards controlled release of molecules from platelets by nanoparticles or implants in drug delivery applications.

11:40am **BI-MoM11 Enhancing the Osseointegration of Titanium Dental Implants by Magnetron-Sputtered Strontium Containing Coatings**, *O.Z. Andersen*, Interdisciplinary Nanoscience Center (iNANO), Aarhus University, Denmark, *V. Offermanns*, Medizinische Universität Innsbruck, Universitätsklinik für Mund-, Kiefer- und Gesichtschirurgie, Austria, *M. Sillassen*, Interdisciplinary Nanoscience Center (iNANO), Aarhus University, Denmark, *D.C.E. Kraft*, Aarhus School of Dentistry, Denmark, *J. Böttiger*, *F. Besenbacher*, Interdisciplinary Nanoscience Center (iNANO), Aarhus University, Denmark, *F. Kloss*, Medizinische Universität Innsbruck, Universitätsklinik für Mund-, Kiefer- und Gesichtschirurgie, Austria, *M. Foss*, Interdisciplinary Nanoscience Center (iNANO), Aarhus University, Denmark

Introduction: Strontium (Sr) has been shown to have a beneficial influence on the subsequent remodelling of the bone structure in relation with implant osseointegration. Both decrease of the osteoclast driven bone resorption and enhancement of the osteoblast driven process of bone formation has been shown. Furthermore, Sr has proven to have an anti-inflammatory effect.

Methods: The coatings used in this study were either prepared on Ti implants (rods with diameter = 1.1 mm and length = 6 mm) or on silicon wafers. The Sr containing surface modifications were prepared by co-sputtering in a setup with a pure Ti and a sintered composite target. The samples were characterized using SEM, AFM, XPS and RBS. ICP-AES was used to investigate the amount of Sr released from the samples as a function of time. Human dental pulp stem cell (hDPSC) cultures were used to assess the *in vitro* cellular response: Cell attachment and proliferation was studied along with the cells ability to mineralize. Quantification of osteogenic expression markers and specific cytokines was performed via RT-PCR. Human blood derived monocyte cultures were carried out to investigate the *in vitro* differentiation of these into osteoclast-like cells in response to Sr. *In vivo* experiments were carried by inserting implants into the femur of Wistar rats and evaluation was done by assessing bone-to-implant contact and new bone volume.

Results: The amount of Sr incorporated in the surfaces was found to be between 0 and 8.7 at. %. The Sr release profile showed that the most Sr was released from samples incorporating 5.5 at. % Sr. In relation with the *in vitro* experiments, the hDPSC proliferation and mineralization was found to correlate with the surface Sr concentrations. Moreover, the Sr concentration also affected the differentiation of monocytes into osteoclast-like cells. In relation with the *in vivo* experiment it was found that the incorporation of Sr had a beneficial effect on implant osseointegration, where an increase in direct bone contact and in new bone volume was observed with an increasing Sr release.

Discussion: From the *in vitro* and *in vivo* Sr release experiments it was found that a more dense surface structure developed as the Sr concentration were increased. We therefore speculate that the peak in the Sr release around 5.5 at.% can be ascribed to an optimal correlation between the morphology and the amount of incorporated Sr. The results from the *in vitro* and *in vivo* models shows that the coating process we have developed for modifying implants is an interesting candidate in relation with shortening the healing period when inserting osseointegrating implants.

Spectroscopic Ellipsometry Focus Topic

Room: 19 - Session EL+TF+AS+EM+SS+PS+EN+NM-MoM

Spectroscopic Ellipsometry for Photovoltaics and Semiconductor Manufacturing

Moderator: M. Creatore, Eindhoven University of Technology, the Netherlands, H. Wormeester, MESA+ Institute for Nanotechnology, University of Twente, Enschede, The Netherlands

8:20am **EL+TF+AS+EM+SS+PS+EN+NM-MoM1 Multichannel Spectroscopic Ellipsometry: Applications in I-III-VI₂ Thin Film Photovoltaics**, *R.W. Collins*, *D. Attygalle*, *P. Aryal*, *P. Pradhan*, *N.J. Podraza*, University of Toledo, *V. Ranjan*, *S. Marsillac*, Old Dominion University

Multichannel spectroscopic ellipsometry (SE) has been applied successfully as an *in situ*, real time tool for optimizing, monitoring, and controlling multi-stage deposition processes in various thin film photovoltaics (PV) technologies. A particularly challenging process optimization problem involves the thermal co-evaporation of individual elements of Cu, In, Ga, and Se in a three-stage process, which has proven to produce high quality Cu(In_{1-x}Ga_x)Se₂ (CIGS) materials and high performance PV devices. This three-stage process provides a high level of flexibility in determining the phase, composition, and microstructure of the film, but also generates greater challenges in run-to-run reproducibility of the optimized process. Information extracted from real time SE measurements includes the evolution of the bulk layer and one or more surface layer thicknesses, as well as layer dielectric functions. The layer dielectric functions can be analyzed further to extract the phase and alloy compositions and the defect density or grain size, which can assist in understanding the fabrication process, in optimizing solar cells, and ultimately in monitoring and controlling the optimized process for improved reproducibility. In this study, the focus is on analysis of ellipsometric (ψ , Δ) spectra acquired by real time SE in order to characterize (i) the structural and compositional evolution in (In,Ga)₂Se₃ film growth from In, Ga, and Se fluxes in the first stage, (ii) the transition from Cu-poor to Cu-rich CIGS at the end of the second stage, which occurs under Cu and Se fluxes, and (iii) the transition from Cu-rich to the desired Cu-poor CIGS, which defines the end of the third and final stage, and occurs under a second application of In, Ga, and Se fluxes. After the transition from Cu-poor to Cu-rich material in the second stage, a Cu_{2-x}Se phase near the surface of the bulk layer is tracked. In the Cu-rich to Cu-poor transition, this Cu_{2-x}Se phase has fully reacted with In, Ga, and Se to form CIGS. Studies using a standard Mo substrate and 2 μ m thick CIGS for solar cells have also revealed features in the (ψ , Δ) spectra characteristic of the anticipated changes in the near surface phase composition as established by detailed modeling on thinner and smoother films. Although careful analysis of real time SE is expected to provide quantitative information on the surface properties and their evolution in this case of solar cells, control of the deposition has been successful simply by monitoring real time changes in the ellipsometric (ψ , Δ) spectra.

9:00am **EL+TF+AS+EM+SS+PS+EN+NM-MoM3 Contribution of Plasma Generated Nanoparticles to the Growth of Microcrystalline Silicon Deposited from SiF₄/H₂/Argon Gas Mixtures**, *J.-C. Dornstetter*, *S. Kasouit*, *J.-F. Besnier*, Total S.a, France, *P. Roca i Cabarrocas*, LPICM-CNRS, Ecole Polytechnique, France

Despite the low fabrication cost of thin film silicon solar modules, this type of technology remains non competitive in main stream markets because of the high BOS costs, due to the low energy conversion efficiency of this type of modules (~10%). We have recently shown that microcrystalline silicon films deposited using SiF₄/H₂/Argon RF capacitive plasmas have excellent structural and transport properties, compared to films deposited using conventional SiH₄/H₂ mixtures, allowing for a very good carrier collection, even for thick cells, and Voc values of 0.55 V, without device optimization, thus opening up the path for the realization of high performance solar cells. However, little is known so far about the growth mechanism of this type of materials and the reason for such interesting properties. Studies of silicon thin films deposition from SiF₄/H₂ mixes, under conditions different from ours, suggested that the growth is due to the deposition of SiF₂ radicals, followed by the abstraction of fluorine by hydrogen. Previous work within our group has also shown that deposition occurs only when particles are present in the plasma, and that growth starts from crystallites without any amorphous phase. We present here a systematic study of the growth of microcrystalline films, together with the composition of nanoparticles attracted by thermophoresis to cold traps located both on the walls of the plasma chamber and in the fore line as a function of deposition conditions.

The composition of the deposit on the traps is found to be amorphous at low power/ low hydrogen conditions and becomes crystalline when either of them increases. This correlates well with an increase in atomic hydrogen concentration in the plasma, as estimated by actinometry. The crystalline fraction of the deposited film was measured using in-situ ellipsometry and was found to correlate with the composition of the deposit on the cold traps. Deposition rate is drastically reduced when a water cooled trap is installed on the walls of the plasma chamber, and switches off at high H₂ flow rates. Under these conditions, TEM and AFM images, show that at the initial stages of the growth the film is constituted of sparse, hexagonal crystalline particles, having sizes on the order of few tens of nanometers. We interpret the data above as a result of plasma-generated nanocrystals being a significant contribution to the deposited film. This may explain the excellent electronic properties of the films, as the particles are formed in the bulk of the plasma region, free from energetic ions bombardment. We will correlate the structural properties and the film growth mechanisms to the properties of solar cells.

9:20am **EL+TF+AS+EM+SS+PS+EN+NM-MoM4 Multichannel Spectroscopic Ellipsometry for CdTe Photovoltaics: from Materials and Interfaces to Full-Scale Modules, P. Koirala, J. Chen, X. Tan, N.J. Podraza, The University of Toledo, S. Marsillac, Old Dominion University, R.W. Collins, The University of Toledo**

Real time spectroscopic ellipsometry (RTSE) has been implemented in studies of the evolution of the semiconductor structural and optical properties during sputter deposition of thin film polycrystalline CdS/CdTe solar cells on transparent conducting oxide (TCO) coated glass substrates. Analysis of the real time optical spectra collected during CdS/CdTe deposition requires an optical property database as a function of measurement temperature for all substrate components. These include not only soda lime glass, but also an SiO₂ layer and three different SnO₂ layers. We report optical functions parameterized versus temperature for the glass substrate and its overlayers starting from room temperature and ending at elevated temperature above which the semiconductor layers are deposited. In fact, such a database has additional applications for on-line, through-the-glass monitoring applications of coated glass at elevated temperature. In the RTSE studies, knowledge of the temperature dependent optical functions of the substrate components enables an accurate substrate temperature determination before the onset of deposition and is critical for accurate extraction of the semiconductor layer optical properties. We implement RTSE to study the filling process of the surface roughness modulations on the top-most SnO₂ substrate layer and modification of the optical properties of this layer. This modification is further studied post-deposition by infrared spectroscopic ellipsometry. In addition to providing information on interface formation to the substrate during film growth, RTSE also provides information on the bulk layer CdS growth, its surface roughness evolution, as well as overlying CdTe interface formation and bulk layer growth. Information from RTSE at a single point during solar cell stack deposition assists in the development of a model that can be used for mapping the completed cell stack properties, which can then be correlated with device performance. Independent non-uniformities in the layers over the full area of the cell stack enable optimization of cell performance combinatorially.

9:40am **EL+TF+AS+EM+SS+PS+EN+NM-MoM5 Determination of Electronic Band Gaps from Optical Spectra, R.A. Synowicki, J.A. Woollam Co., Inc.**

The band gap of a material E_g is defined theoretically as the lowest energy for electronic transition from the valence to conduction bands in a solid. For an ideal material free of defects this is the photon energy or wavelength where the optical properties change from transparent to absorbing. However, real materials contain defects which cause absorption to begin below the band gap (i.e. the Urbach Tail) making determination of the true band gap position difficult. For example, in a solar cell the measured absorption edge represents the onset of transitions first due to defects, then from band to band. Empirical methods used to determine the band gap in real materials with defects include the Tauc plot and the Mott-Davis plot. More theoretical mathematical dispersion models such as the Tauc-Lorentz, Cody-Lorentz, and Herzinger-Johs models have been developed which include an adjustable band gap parameter. The various plots and dispersion model methods will be discussed and applied to different materials measured optically via spectroscopic ellipsometry, intensity transmission, reflection, absorption, or a combination of these methods.

10:00am **EL+TF+AS+EM+SS+PS+EN+NM-MoM6 Optical Modeling of Plasma-Deposited ZnO: Extended Drude and its Physical Interpretation, H.C.M. Knoops, M.V. Ponomarev, J.W. Weber, N. Leick, B.W.H. van de Loo, Y.G. Melese, W.M.M. Kessels, M. Creatore, Eindhoven University of Technology, the Netherlands**

High-quality transparent conductive oxides such as ZnO are important due to their electrical and optical properties. To improve these properties the

responsible physical processes have to be understood. Traditionally, charge-carrier-scattering processes are investigated by combining morphology data and Hall measurements. This contribution discusses the extensive optical modeling of plasma-deposited ZnO and how its interpretation directly provides insight into the relevant charge-carrier-scattering processes at different length scales. The interpretation is generalized to the concept of frequency-dependent resistivity, which is used to explain the applicability of different Drude models.

Thin films (50-1000 nm) of Al-doped and undoped ZnO were deposited using an expanding thermal plasma MOCVD process.¹ Conditions of high pressure and high diethyl zinc flow allowed for dense films with low electrical resistivities (e.g., $4 \times 10^{-4} \Omega \text{ cm}$ at 300 nm). The films were analyzed with variable-angle spectroscopic ellipsometry (SE) (0.75 – 5.0 eV), FTIR reflection spectroscopy (0.04 – 0.86 eV), Four-point-probe (FPP), and Hall measurements.

The SE and FTIR data were combined and fitted with classical and extended Drude² models. The high intensity of the Drude in the FTIR range resulted in a high sensitivity with which the carrier concentration and mobility could even be determined for thin (~40 nm) undoped ZnO films. An extended Drude model was needed to correctly model the SE energy range, which was explained by the dominance of ionized impurity scattering and a reduction of this scattering for higher photon energies. The grain-boundary-scattering mobility could be determined by the difference between optical and Hall mobilities.³ When combined with FPP results, the effective mobility can be determined from these optical techniques without the use of Hall measurements. The optical response above the band gap was modeled by a PSEMI or Tauc-Lorentz oscillator model, where a broadening and shift of the transition was seen for increasing carrier concentration.⁴

These insights and a generalized view of electron scattering in ZnO at different length scales will be presented.

1. Ponomarev et al., *J. Appl. Phys.* **Submitted** (2012)
2. Ehrmann and Reineke-Koch, *Thin Solid Films* **519**, 1475 (2010)
3. Steinhäuser et al., *Appl. Phys. Lett.* **90**, 142107 (2007)
4. Fujiwara and Kondo, *Phys. Rev. B* **71**, 075109 (2005)

10:40am **EL+TF+AS+EM+SS+PS+EN+NM-MoM8 The Ellipsometric Response of Single-Crystal Silicon to Doping, H.G. Tompkins, Consultant**

The current wisdom is that for ellipsometry in the UV-vis-NIR spectral range, doping of single-crystal silicon can be ignored. We study the ellipsometric response of silicon doped with arsenic at various levels. We also studied the response after implant (before activation) and after the activation (anneal). We find that for samples implanted with 1E18 atoms/cm³, the single-crystal silicon was not amorphized. Implants of 2E19 atoms/cm³ and higher left an amorphous layer on the surface of the wafer the thickness of which was about the depth of the implant. Activation of the sample implanted with 2E19 atoms/cm³ returned the sample to single-crystal silicon and the ellipsometric response in the UV-vis-near IR is essentially that of undoped silicon. However, the response in the mid-IR is that the extinction coefficient is no longer zero. For samples implanted with 2.5E20 atoms/cm³ and greater, annealing did not return the UV-vis-near IR ellipsometric response to that of single-crystal silicon. Although this amount of other material (arsenic) is still less than about one tenth of one percent, our conjecture is that the microstructure simply could not be returned to that of a single crystal. As with the lower doped sample, the mid-IR spectral region showed significant increase in the extinction coefficient.

11:00am **EL+TF+AS+EM+SS+PS+EN+NM-MoM9 The Effect of Stress on the Optical Properties Semiconductor Films, A.C. Diebold, G.R. Muthinti, M. Medikonda, T.N. Adam, College of Nanoscale Science and Engineering, University at Albany, A. Reznicek, B. Doris, IBM Research at Albany Nanotech**

Here we review the impact of stress on the complex dielectric function of semiconductor films measured using spectroscopic ellipsometry. Two relevant examples of stressed semiconductor layers are pseudomorphic epitaxial layers fabricated during semiconductor manufacturing and strained silicon on insulator (sSOI) wafers. Stress is known to shift the energies of direct gap critical point transitions in semiconductors. The biaxial stress in pseudomorphic films grown on silicon wafers can be as high as that used during opto-elastic studies of bulk semiconductors. The amount of stress in un-relaxed, pseudomorphic films of Si_{1-x}Ge_x on Si (100) reaches 1 GPa for alloys with 20% Ge and is more than 3 GPa for films with > 50% Ge. The bi-axial stress in sSOI is typically ~1 GPa. An elastic theory approach for the effect of strain on the k^*p determined band structure and optical transition energy is well known. Both low shear stress and high shear stress approximations can apply to the shift in transition energy depending on the magnitude of the spin orbit splitting energy vs the magnitude of the shear

stress. Until recently it was difficult to obtain sets of samples that test both approximations. Here we discuss results from our recent study of pseudomorphic films of $\text{Si}_{1-x}\text{Ge}_x$ on Si (100) from $x = 0.05$ to 0.75 which covers both low and high shear regimes. We also present our recent study of the dielectric function of thinned sSOI which illustrates the impact of stress on the optical transitions for the Si layer on sSOI. All of these samples are examples of new materials being used in semiconductor research. The results of this study are directly transferred into cleanroom spectroscopic ellipsometry systems used for process control during manufacturing.

11:20am **EL+TF+AS+EM+SS+PS+EN+NM-MoM10 Numerical Ellipsometry: Spectroscopic n-k Plane Analysis of Thin Films Growing on Unknown Layered Substrates, F.K. Urban, D. Barton**, Florida International University

Spectroscopic ellipsometry measurements on thin films commonly make use of prior knowledge of the structure and optical properties of the underlying substrate. However, imprecision in substrate statistics propagates into the solution for the film of interest. Thus it is more accurate to have a method for solving for film properties which simultaneously obtains whatever is needed about the substrate. And it makes solutions possible whether or not book data or previous substrate solutions are available. In this work we apply Complex Analysis in the n-k plane to achieve solutions employing the well-known reflection equations. The method is carried out at each measured wavelength and does not necessitate an *a-priori* assumption of optical property dependencies on wavelength. The mean square error has been improved by many orders of magnitude, a selected limit of 10^{-14} as opposed to 1 to 30 or so for least squares. Thus the full accuracy of the ellipsometer is now available for more accurate measurements of film thickness and optical properties. The method requires six measurements during growth. The first is used to determine the relationship between R_p and R_s at the film-substrate interface. The following four are used to uniquely determine the values of R_p , R_s , and film n , k , and d . The final measurement confirms the unique solution. Suitability of the model is tested by comparing measurements at two of more wavelengths for self consistency. Results for n and k of the growing film are examined across the measurement spectrum in comparison with parameterizations in common use.

Electronic Materials and Processing

Room: 9 - Session EM+TF+OX+GR-MoM

High-k Dielectrics for MOSFETs I

Moderator: A.C. Kummel, University of California San Diego

8:20am **EM+TF+OX+GR-MoM1 Surface Preparation and Dielectric Growth for Graphene-based Devices, R.M. Wallace**, University of Texas at Dallas **INVITED**

In addition to interesting physics, numerous device applications are under investigation for graphene. Many of these devices require an interaction of graphene with dielectrics, and require a thorough understanding of the graphene/dielectric interface. As practical device applications require large area graphene, CVD methods have been employed to synthesize graphene and typically involve a wet chemical transfer process, which can leave residues that impact device behavior. This talk will review recent progress in the investigation of CVD graphene growth, transfer and dielectric growth processes with an emphasis on in-situ studies of the surfaces produced by these processes and the resultant electrical behavior. This work is supported by the NRI SWAN Center.

9:00am **EM+TF+OX+GR-MoM3 Antimonide-Based P-Channel MOSFET: Progress and Challenges, S. Oktyabrsky, A. Greene, S. Madiseti, P. Nagaiah, M. Yakimov, R. Moore, S. Novak, H. Bakhr, V. Tokranov**, University at Albany-SUNY **INVITED**

Development of p-type MOSFETs using new materials is an important goal to provide a further scaling of CMOS circuits. Although Ge is still considered as a main candidate for novel p-channels due to its superior bulk transport properties, recent progress in strained III-Sb channels and MOS technologies makes it a good competitor in particular for deeply scaled devices. The materials parameters affecting MOSFET's figures-of-merit are reviewed with the emphasis on strain in quantum wells (QWs), effective mass, density of states and mobility.

Progress in development of materials for III-Sb channels is reported. Optimization of MBE growth of metamorphic buffers and GaSb on lattice-mismatched GaAs substrates has resulted in "step-flow" growth mode of GaSb with monolayer-high steps on the surface, $\sim 10^7 \text{cm}^{-2}$ dislocation

density and bulk hole mobility $860 \text{cm}^2/\text{Vs}$. Optimization of strain in QWs provided the highest Hall mobility of $1020 \text{cm}^2/\text{Vs}$ at sheet hole density of $1.3 \times 10^{12}/\text{cm}^2$ obtained for $\text{In}_{0.36}\text{Ga}_{0.64}\text{Sb}$ with compressive strain of 1.8%. Hole mobility in QW channel was benchmarked against the thickness of top semiconductor AlGaSb barrier. The effect of interface-related scattering hole mobility in the channel was found to be significantly less than e.g. for n-InGaAs, that might be due to stronger localization of holes in QWs.

Two approaches to fabricate high-quality III-Sb/high-k interface were studied: all *in-situ* Al_2O_3 or HfO_2 gate oxides, and *ex-situ* atomic layer deposited (ALD) Al_2O_3 with InAs top semiconductor capping layer. Interface with *in-situ* MBE gate oxides was found to improve with *in-situ* deposited a-Si interface passivation layer (IPL). Interfaces with better thermal stability, reduced interface trap density and hysteresis were observed on both n- and p- type GaSb MOSCaps with the IPL. P-type MOSFETs with HfO_2 showed a maximum drain current of 23 mA/mm for a $3 \mu\text{m}$ gate length. Use of a-Si IPL has also resulted in a significant (over an order of magnitude) reduction of the hole density in QWs and corresponding negative flat band voltage shift and drop of mobility which becomes remote Coulomb scattering-limited. An interface with ALD Al_2O_3 was improved by a thin 2nm interface layer of InAs which was treated with HCl or $(\text{NH}_4)_2\text{S}$ immediately prior to ALD process. Optimized annealing further improved the C-V characteristics, reduced interface trap density down to $10^{12} \text{cm}^{-2}\text{eV}^{-1}$, leakage current and MOSFET subthreshold slope down to 200 mV/dec. Increasing annealing temperature to and above 450°C drastically degraded C-V characteristics due to low thermal budget of antimonides.

9:40am **EM+TF+OX+GR-MoM5 Interface Study of the Atomic Layer Deposited Al_2O_3 on $\text{Al}_{0.25}\text{Ga}_{0.75}\text{N}$, X. Qin, B. Brennan, H. Dong, R.M. Wallace**, The University of Texas at Dallas

Due to the high two-dimensional electron gas (2-DEG) density, AlGaIn/GaN high electron mobility transistors (HEMTs) are recognized as key devices for high power and low noise applications. However, the associated large gate leakage current degrades the performance of AlGaIn HEMTs. In order to solve this problem, MOS-HEMTs have been developed, in which the incorporation of a high-k gate dielectric layer can overcome the drawbacks.

In this work, the native and treated $\text{Al}_{0.25}\text{Ga}_{0.75}\text{N}$ surface chemical states and structure of were studied by x-ray photoelectron spectroscopy (XPS), ion scattering spectroscopy (ISS) and low energy electron diffraction. Different chemical treatment processes including $(\text{NH}_4)\text{OH}$, $(\text{NH}_4)_2\text{S}$ and HF were studied, followed by atomic layer deposition (ALD) Al_2O_3 layers on $\text{Al}_{0.25}\text{Ga}_{0.75}\text{N}$. The oxidation states of the $\text{Al}_{0.25}\text{Ga}_{0.75}\text{N}$ interface and Al_2O_3 deposition process were studied by in-situ XPS analysis. In addition, ex-situ atomic force microscopy (AFM) was used to observe the surface topography before and after the Al_2O_3 deposition. According to the XPS results, it is found that chemical treatments could remove the native Al_2O_3 but were not effective to eliminate the Ga oxide, and the growth rate of Al_2O_3 is low on the native and treated $\text{Al}_{0.25}\text{Ga}_{0.75}\text{N}$ samples. The AFM images show that there are many pin holes in the surface of $\text{Al}_{0.25}\text{Ga}_{0.75}\text{N}$. Studies of HfO_2 deposition will also be presented.

This work is supported by the AOARD under AFOSR Grant No. FA2386-11-1-4077

10:00am **EM+TF+OX+GR-MoM6 Ideal Monolayer Nitridation of Semiconductors using a Nitrogen Radical Generator, A.T. Lucero, J. Kim**, University of Texas at Dallas

Thin silicon nitride films have long been desirable for various applications. Suggested uses range from surface and interface passivation to ultra-thin dielectric layers. Traditional deposition techniques are low pressure chemical vapor deposition (LPCVD) and plasma enhanced chemical vapor deposition (PECVD). High quality LPCVD films require high processing temperatures, and PECVD exposes the substrate to damaging plasma and electric potentials. While both techniques are suitable for many applications, there are some instances where both processes are too harsh.

In this paper, we report the growth of silicon nitride using a remote nitrogen radical generator system. Growth temperatures range from room temperature to 400°C , and growth time is varied from two minutes to one hour. Film composition is analyzed using x-ray photoelectron spectroscopy (XPS) and morphology is checked using atomic force microscopy. Results indicate that surface nitrogen saturation can be reached at both low temperatures and short exposure times, and that the reaction is self limiting, terminating at one monolayer. Film thickness is approximately one Angstrom, as determined by XPS. Results for silicon and III-V passivation will be discussed.

We would like to thank Toshiba Mitsubishi-Electric Industrial Systems Corporation for providing the nitridation system used in this study.

11:00am **EM+TF+OX+GR-MoM9 Characterization of ALD Laminated Gate Dielectrics on GaN MOSCAPs**, *D. Wei, T. Hossain*, Kansas State University, *N. Nepal, N.Y. Garces*, Naval Research Laboratory, *H.M. Meyer III*, Oak Ridge National Laboratory, *C.R. Eddy, Jr.*, Naval Research Laboratory, *J.H. Edgar*, Kansas State University

To improve the efficiency of GaN based power electronic devices there is tremendous and growing interest in employing metal-insulator-semiconductor (MIS) transistors. As with all compound semiconductors, there is a significant challenge in forming an electronic quality dielectric-semiconductor interface. Thus, there is a need to better understand and improve the dielectric-semiconductor interface quality in order to improve the overall performance of the device.

This research focuses on the benefits and properties of Al₂O₃, TiO₂ and TiO₂-Al₂O₃ nanolaminated thin films deposited on GaN and GaOx/GaN by plasma-assisted atomic layer deposition (PA-ALD) for gate dielectric development. Correlations were sought between the films' structure, composition, and electrical properties. The gate dielectrics were approximately 15nm thick as determined by spectroscopic ellipsometry. The interface carbon concentration, as measured by x-ray photoelectron spectroscopy (XPS) depth profile, was lower for Al₂O₃/GaN than TiO₂/GaN, and the nanolaminated structure did not decrease the carbon concentration. However, carbon was not detected at the interface for the GaN samples pretreated by annealing in O₂ for 30 minutes at 800°C. Also, according to XPS, the Al₂O₃ films had a better coverage than TiO₂. The RMS roughness of TiO₂ and Al₂O₃ top layers were ~0.53nm and ~0.20nm respectively, as determined by atomic force microscopy. The dielectric constant of Al₂O₃ on GaOx/GaN was greatly increased compared to that of the TiO₂-Al₂O₃ and pure Al₂O₃ on GaN substrate. In addition, the Al₂O₃ deposited on the GaOx/GaN showing no hysteresis in capacitance-voltage (C-V) characteristics, which is corresponding with a negligible carbon concentration from the XPS depth profile. These results indicate the promising potential of plasma ALD deposited Al₂O₃ serving as the gate oxide on GaOx/GaN based MOS devices.

11:20am **EM+TF+OX+GR-MoM10 Passivation of Interfacial Defects in GaAs and Other III-Vs**, *J. Robertson*, Cambridge University, UK **INVITED**

It has always been harder to make FETs from GaAs than Si, because of 'Fermi level pinning' and the difficulty of passivating its surfaces. These issues were discussed by Spicer et al [1] in the 'unified defect model' and Hasegawa [2] is his 'Disorder Induced Gap states' model. Since 1997 it was possible to make inverted GaAs MOSFETs using the epitaxial Gadolinium gallium oxide [3]. The main impetus now is to use atomic layer deposition (ALD) to make scalable FETs [4], as recently achieved by Intel [5]. The obvious question is why (In)GaAs is much harder to passivate than Si. The early answer was its poor native oxide. But since the advent of good ALD HfO₂ or Al₂O₃ oxides on Si, this answer is deficient, as they should also work on GaAs [6]. The underlying reason for defects is not stress, it must be chemical. I show that it arises from the polar bonding of GaAs [7], and a driving force to keep the surface Fermi level in a gap. The electron counting rule of Pashley [8] that describes surface reconstructions is shown to be a variant of auto-compensation, and it works more generally [9]. It leads to a continuous generation of defects if it is not satisfied. So the answer is to deposit oxide layers that meet this rule, and also to break any surface reconstructions that may lead to As-As dimers [9]. Diffusion barriers are also crucial to a good passivant, on GaAs or on Ge .

1. W E Spicer, et al, J Vac Sci Technol 16 1422 (1979); Phys Rev Lett 44 420 (1980)
2. H Hasegawa, et al, J Vac Sci Technol B 5 1097 (1987)
3. M Hong et al, Science **283** 1897 (1997)
4. P D Ye et al, App Phys Lett 83 180 (2003)
5. M Radosavljevic, et al, Tech Digest IEDM (2009) p13.1
6. C Hinkle, et al, Curr Opin Solid State Mat Sci 15 188 (2011)
7. W Harrison, J Vac Sci Technol 16 1492 (1979)
8. M D Pashley, Phys Rev B **40** 10481 (1989)
9. J Robertson, L Lin, App Phys Letts 99 222906 (2011); **98** 082903 (2011)

Energy Frontiers Focus Topic
Room: 15 - Session EN+NS-MoM

Nanostructured Solar Cells

Moderator: M.S. Arnold, University of Wisconsin Madison

8:20am **EN+NS-MoM1 Doping Control for the Development of Silicon Quantum Dot Solar Cell**, *K.J. Kim, J.H. Park*, Korea Research Institute of Standards and Science (KRISS), Republic of Korea, *H.-J. Baek, H.H. Hwang*, University of Science and Technology (UST), Republic of Korea, *J.S. Jang*, Chungbuk National University (CBNU), Republic of Korea

Si quantum dots (QDs) imbedded in a SiO₂ matrix is a promising material for the next generation optoelectronic devices, such as solar cells and light emission diodes (LEDs). However, low conductivity of the Si quantum dot layer is a great hindrance for the performance of the Si QD-based optoelectronic devices. The effective doping of the Si QDs by semiconducting elements is one of the most important factors for the improvement of conductivity. High dielectric constant of the matrix material SiO₂ is an additional source of the low conductivity.

Active doping of B in Si nano structures and the effect of internal polycrystalline bridge layer were investigated by secondary ion mass spectroscopy (SIMS) depth profiling analyses. Phosphorous and boron doped-Si / SiO₂ multilayers on Si wafers were fabricated by ion beam sputtering deposition as a model structure for the study of the diffusion behavior of the dopants. The distributions of the dopants after annealing at high temperatures were analyzed by SIMS depth profiling analyses.

In this study, the diffusion behaviors of various dopants in silicon nanostructures will be discussed and the effects of the various parameters for the improvement of conversion efficiency in Si quantum dot solar cell will be introduced.

8:40am **EN+NS-MoM2 Photocarrier Generation in Si Quantum-dot Sensitized Solar Cells**, *G. Uchida, H. Seo, Y. Wang, K. Kamataki, N. Itagaki, K. Koga, M. Shiratani*, Kyushu University, Japan

The pressing need for massively scalable carbon-free energy sources has focused attention on both increasing the efficiency and decreasing the cost of solar cells. Quantum-dot (QD) solar cells employing multiple exciton generation (MEG) have attracted much attention as a candidate for the third generation solar cells, because MEG represents a promising route to increased solar conversion efficiencies up to about 44 % in single junction. Our interest has been concerned with QD sensitized solar cells using Si nanoparticles [1]. The main purpose of this study is to discuss the characteristic of the quantum yield in view of the MEG effect.

QD thin films composed of size-controlled Si nanoparticles were deposited using double multi-hollow discharge plasma chemical vapour deposition (CVD) of a SiH₄/H₂ and CH₄ or N₂ gas mixture [2]. Short-circuit current density of Si QD sensitized solar cells increases by a factor of 2.5 by irradiation of CH₄ or N₂ plasma to Si nanoparticle surface. We also have measured incident photon-to-current conversion efficiency (IPCE) in the near-ultraviolet range using quartz-glass plates as front panels of QD sensitized solar cells. IPCE gradually increases by light irradiation in a wavelength range less than 600 nm around optical band-gap (E_g) of Si nanoparticle films, and then steeply increases below 280 nm around 2E_g. This rapid increase of IPCE under the ultraviolet light incidence may be explained by the theoretically predicted MEG, the creation of two electron-hole pairs from one high-energy photon incidence, in Si nanoparticle QDs.

[1] G. Uchida, et al., Phys. Status Solidi C 8 (2011) 3021.

[2] G. Uchida, et al., Jpn. J. Appl. Phys. 51 (2011) 01AD01-1.

9:00am **EN+NS-MoM3 Quantum Dot Solar Cells with External Quantum Efficiency Exceeding 100% by Multiple Exciton Generation**, *J.M. Luther, M.C. Beard, A.J. Nozik, O.E. Semonin*, National Renewable Energy Laboratory **INVITED**

Traditional semiconductors used in photovoltaic devices produce one electron from each absorbed photon. On the other hand, new materials such as quantum dots, nanorods, carbon nanotubes and graphene can more efficiently convert high-energy photons into multiple electron-hole pairs through a process titled multiple exciton generation (MEG) provided that the energy of the photon is at least twice the bandgap of the absorber. This process has been shown to be more efficient in highly confined quantum dots than other forms of carrier multiplication (such as impact ionization) in bulk materials. Photovoltaic devices can benefit greatly from MEG by producing increased photocurrent from the multiple electrons and thus allowing a single junction solar cell to yield a theoretical maximum efficiency as high as 44% compared to 33% for bulk semiconductors. In this talk, we will present recent findings from incorporating PbSe quantum dots

(QDs) into semiconducting arrays that make up the absorber layer in prototype solar cells. In these devices, MEG is confirmed by demonstrating the first solar cell with external quantum efficiency (EQE) exceeding 100% for solar relevant photon energies. The EQE in our device reaches a maximum value of 114% at 380 nm and we have employed an optical model to determine that the PbSe QD layer produces as many as 1.3 electrons per photon (on average) for these photons. These findings are compared to ultrafast time resolved measurements of carrier quantum yields where we find reasonable agreement. We will also discuss future directions for materials designs that increase the quantum yield through more efficient MEG.

9:40am **EN+NS-MoM5 Quantum-Confined Nanocrystals as Building Blocks for Low-Cost Solution-Processed Multi-Junction Solar Cells**, T. Hanrath, J.W. Choi, W.N. Wenger, R.S. Hoffman, Cornell University

In light of recent advances in synthesis, characterization, and the emerging understanding of their size-dependent properties, there are many exciting opportunities for semiconductor nanomaterials to contribute to the development of next-generation energy conversion technologies. Semiconductor nanocrystal quantum dots are particularly attractive material candidates for the efficient capture of solar emission in inexpensive, thin film photovoltaic devices due to their large absorption cross sections, low-cost solution-phase processing and size-tunable energy gaps. The prospect of exploiting colloidal nanostructures for the creation of low-cost multi-junction solar cells has garnered immense scientific and technological interest. We recently demonstrated demonstrate solution-processed tandem solar cells created from nanocrystal quantum dots with size-tuned energy levels. Bringing this prospect to fruition requires the connection of absorber layers with cascaded energy gaps subject to stringent electrical and optical constraints. We show that interlayers composed of ZnO/Au/PEDOT provide appropriate carrier density and energy-level alignment to resolve this challenge. With such interlayers we have been able to create nanocrystal quantum dot tandem cells that exhibit IR sensitivity and a open circuit voltage approaching 1V. These advances provide guidelines for the design of an effective interlayer in tandem cell devices and suggest a promising future for solution-processed nanocrystal quantum dot solar cells.

10:00am **EN+NS-MoM6 Improvement of Carrier Transport in PbSe Quantum Dot-Embedded Polymeric Solar Cells Fabricated by a Laser Assisted Spray Process**, C. Hettiarachchi, D.M. Feliciano, D. Mukherjee, P. Mukherjee, S. Witanachchi, University of South Florida

PbSe quantum dots (QD) in the size range of 4-8 nm are promising candidates for solar energy harvesting as they exhibit multi-exciton generation with ultraviolet (UV) photon absorption. While generation of multi-excitons has been demonstrated, dissociation of excitons to enhance current densities has not been realized. One of the main bottlenecks has been the difficulty in removing the surfactants on QDs to form a clear interface between the QD and the polymer matrix. We have developed a Laser Assisted Spray (LAS) deposition technique to deposit uniform coatings of surfactant-free QDs on substrates. This technique involves the transient heating of aerosols containing PbSe QDs by a CO₂ laser-gas interaction to burn the organic surfactants. Transmission electron micrographs and absorption spectroscopy show, under optimum conditions, the particles remain as single crystals and maintain quantum confinement. Growth parameters are optimized by monitoring the degree of surfactant removal by studying the Fourier Transform Infrared (FTIR) spectra of coatings grown by LAS technique. Two-layer solar cell structures of PbSe/polymer that is sandwiched between ITO and Al electrodes have been fabricated. Comparison of the IV characteristics of these cells and cells fabricated by PbSe QDs with ligand-exchange will be presented.

10:40am **EN+NS-MoM8 Single and Multiple Exciton Dissociation in Colloidal Nanoheterostructures**, T. Lian, Emory University **INVITED**

The ability to control charge transfer dynamics to and from quantum dots (QDs) is essential to many QD-based devices, such as solar cells and light emitting diodes. Recent reports of multiple exciton generation (MEG) by one absorbed photon in some QDs offer an exciting new approach to improve the efficiency of QD-based solar cells and to design novel multi-electron/hole photocatalysts. Two major challenges remain. First, the efficiency of MEG process needs to be significantly improved for practical applications. Second, the utilization of multi-excitons requires ultrafast exciton dissociation to compete with the exciton-exciton annihilation process, which occurs on the 10s to 100s ps time scale. In this presentation we report a series of studies of exciton dissociation dynamics in QDs and nanorods by electron transfer to adsorbed electron acceptors. We show that excitons in CdX (X=S, Se, Te) and PbS QDs can be dissociated on the picosecond and faster timescales and multiple excitons (generated by multiple photons) per QD can be dissociated by electron transfer to adsorbed acceptors. We discuss approaches for optimizing the single and multiple exciton dissociation efficiencies by controlling the spatial

distributions of the electron and hole (i.e. wave-function engineering) in type II core/shell QDs and nanorods.

11:40am **EN+NS-MoM11 Intermediate Band Upconversion for Low-Cost, Solution Processed Photovoltaics**, J. Lewis, E.J.D. Klem, C.W. Gregory, G.B. Cunningham, S. Hall, D.S. Temple, RTI International

PV devices based on disordered semiconductors such as polymers, organic small molecules, and colloidal quantum dots have seen gradually improving performance in recent years, but are likely to be limited to efficiencies in the range of 10–15%. To increase efficiency further would require the use of tandem cells, which adds complexity and cost. Alternatively one can pursue devices such as intermediate band solar photovoltaics (IBPV) that can exceed the Shockley-Queisser efficiency limit. In an IBPV device mid-gap states are incorporated into a wider band-gap host, allowing infrared photons to contribute to the photocurrent of the device via sequential absorption of two photons. Ideally this occurs without compromising the open circuit voltage. We will present the first example of an IBPV solar cell using solution processed, low-cost disordered materials. We show that the nature of the defect states in Pb-salt quantum dots is uniquely suited to efficient upconversion at optical power densities that are relevant for unconcentrated solar illumination. This demonstration provides a path for a step-change in the efficiency of low-cost PV.

Graphene and Related Materials Focus Topic

Room: 13 - Session GR+EM+NS+PS+SS+TF-MoM

Graphene Growth

Moderator: M. Spencer, Cornell University, V.D. Wheeler, U.S. Naval Research Laboratory

8:20am **GR+EM+NS+PS+SS+TF-MoM1 Synthesis Ingredients**

Enabling Low Noise Epitaxial Graphene Applications, D.K. Gaskill, L.O. Nyakiti, V.D. Wheeler, U.S. Naval Research Lab, A. Nath, George Mason Univ., V.K. Nagareddy, Newcastle University, UK, R.L. Myers-Ward, N.Y. Garces, S.C. Hernández, S.G. Walton, U.S. Naval Research Lab, M.V. Rao, George Mason Univ., A.B. Horsfall, Newcastle Univ., UK, C.R. Eddy, Jr., U.S. Naval Research Lab, J.S. Moon, HRL Labs LLC

Sensors made from graphene flakes have demonstrated single molecule detection [Schedin *et al.*, Nat Mat **6**, 652 (2007)]; this ultra-sensitivity is likely due to the high crystalline quality of the graphene and the associated relative lack of defects that give rise to noise. The low noise nature of high quality graphene should also facilitate other applications, e.g., low-noise amplifiers. Combined with the unique ambipolar property of graphene field effect transistors (FETs), the low noise character of graphene would significantly advance the performance of frequency multipliers, mixers and high-speed radiometers. To exploit these applications, high quality, reproducible wafer-scale epitaxial graphene (EG) with minimal thickness variations and defects are essential requirements. Here, crucial graphene synthesis elements required to achieve the wafer-scale quality goal are described. Understanding the effect of substrate misorientation as well as hydrogen etch and Si sublimation conditions for graphene synthesis on the (0001) SiC surface is essential to achieve improved and reproducible wafer-scale graphene quality. For example, the impact of processing factors such as temperature control, laminar gas flow and substrate rotation on large area EG uniformity are described using examples created in an Aixtron SiC epitaxy reactor. In addition, managing SiC step formation on the nominal (0001) orientation is significant for achieving uniform EG thickness on terraces and to minimize additional growth at the step edges; this is illustrated using data from atomic force microscopy and scanning electron microscopy images in combination with Raman spectroscopy maps and x-ray photoelectron spectroscopy analysis. Managing step formation combined with optimal growth leads to the suppression of the Raman defect “D” band confirming minimal grain boundaries and defects, which are additional sources of electronic noise. Lastly, contactless Leighton resistivity maps of 75 mm wafers are used to illustrate the overall uniformity of optimally synthesized graphene as well as to show the resistance state-of-the-art, with individual wafers exhibiting about a ±3% relative variation. Examples of the impact of this synthesis approach on chemical sensors devices and FETs will be shown, each exhibiting 1/f noise behavior down to 1 Hz and possessing noise spectral densities similar to reports from exfoliated graphene. Hence, careful control of EG formation across the wafer results in improved quality which subsequently leads to the reduction or elimination of additional noise sources from graphene defects that would then adversely affect device performance.

8:40am **GR+EM+NS+PS+SS+TF-MoM2 Growth of Graphene by Catalytic Decomposition of Ethylene on Cu(100) and Cu(111) With and Without Oxygen Predosing.** *Z.R. Robinson, P. Tyagi, T. Mowll, C.A. Ventrice, Jr.*, University at Albany- SUNY, *K. Clark, A.-P. Li*, Oak Ridge National Laboratory

Graphene growth on Cu substrates has become one of the most promising techniques for the mass production of graphene, and therefore significant effort has been put into developing growth conditions that lead to large area, defect and grain boundary free graphene films. One key consideration is the influence that the underlying copper substrate has on the growth of the graphene. In order to study this, graphene growth on Cu(100) and Cu(111) was carried out in a UHV system. The samples were heated using an oxygen series button heater. The hydrocarbon pressure was measured using a capacitive manometer instead of an ion gauge, which could cause dissociation of the hydrocarbon molecules. Initially, it was found that annealing the crystals to 900 °C resulted in impurity segregation at the surface. Several cycles of sputtering at 600 °C were required to remove all bulk impurities so that the surface remained clean even after annealing to 900 °C. Initial attempts to grow graphene by annealing each crystal to temperatures as high as 900 °C in UHV, followed by backfilling the chamber with up to 5×10^{-3} torr of C_2H_4 did not result in graphene formation. It was found that by first backfilling the chamber with C_2H_4 and then raising the temperature from 25 °C to 800 °C, graphene growth could be achieved. A four-domain epitaxial overlayer is observed for the Cu(100) surface. Pre-dosing the Cu(100) with oxygen at 300 °C, which forms a saturation coverage of chemisorbed oxygen, was found to result in a 2-domain graphene overlayer using similar growth conditions. A study of the effect of oxygen pre-dosing on the growth of graphene on Cu(111) has been initiated.

9:00am **GR+EM+NS+PS+SS+TF-MoM3 Impact of Growth Parameters on Uniformity of Epitaxial Graphene.** *L.O. Nyakiti, V.D. Wheeler, R.L. Myers-Ward, J.C. Culbertson*, U.S. Naval Research Laboratory, *A. Nath, George Mason University, N.Y. Garcés*, U.S. Naval Research Laboratory, *J. Howe*, Oak Ridge National Laboratory, *C.R. Eddy, Jr., D.K. Gaskill*, U.S. Naval Research Laboratory

Epitaxial graphene (EG) offers a facile method for attaining large area graphene for device applications. Since wafer uniformity and thickness control is vital, a systematic study of the parameters affecting the EG growth process was performed and the optimal conditions for obtaining uniform morphology and high electronic quality were determined. EG was synthesized in a low pressure Ar flowing ambient on $8 \times 8 \text{ mm}^2$ 6H-SiC(0001) substrates that were offset 0.8° from the basal plane, using an Aixtron VP508 reactor. The samples were placed on a rotating ~ 100 mm diameter susceptor and excellent EG layer uniformity and run-to-run reproducibility were obtained. The investigation focused upon the critical synthesis parameters of temperature (T) (1520-1660°C) and time (t) (15-60 min), an *in-situ* H_2 etch conditions (1520-1600°C for 10-30min). Morphology, layer thickness, chemical analysis, and strain variations across the samples were characterized using electron microscopy, AFM, XPS and μ -Raman spectroscopy. Large-area van der Pauw Hall effect was performed to quantify the graphene mobility (μ), and carrier density. Results show that growth T and t had the most significant impact on EG electronic and morphological properties. For example, synthesis at 1660°C for 30min resulted in 4-8 monolayers (ML) and a step-bunched morphology with high concentration of wrinkles originating from the step-edge and pinned at the nearest terrace edge. Other morphological features were pits primarily located at the step edges having a depth ~ 20 nm and density $6.4 \times 10^6 \text{ cm}^{-2}$. In contrast, EG synthesis at 1520°C for 30min results in uniform ML coverage along the terrace width that is devoid of pits and wrinkles. Mobility was found to have a drastic dependence on graphene thickness. Under optimal conditions, 1-2 ML were obtained and μ as high as $1240 \text{ cm}^2 \text{ V}^{-1} \text{ s}^{-1}$ was achieved; in contrast, for EG with >2 ML $\mu \sim 550 \text{ cm}^2 \text{ V}^{-1} \text{ s}^{-1}$, presumably due to interlayer interaction and electronic screening. XPS C1s and Raman 2D spectra of EG grown on substrates after undergoing *in-situ* H_2 etch at different times did not show shifts in peak position/intensity suggesting lack of etch time dependence on EG electronic or structural quality. Yet etch conditions affect the final morphology, as EG synthesis performed after an *in-situ* H_2 etch at 1600°C resulted in step-bunched morphology with step heights 5-10nm, whereas, substrates etched at 1520°C had EG with step-heights 10-15nm. In addition other growth parameters investigated were found to be of secondary importance, including: Ar pressure, flow rates, and sample cool down conditions.

9:20am **GR+EM+NS+PS+SS+TF-MoM4 Uniform Epitaxial Growth of Charge Neutral Quasi-Free-Standing Monolayer Graphene on a 6H-SiC(0001) Surface by Combination of Metal Silicidation and Intercalation.** *H. Shin, I. Song, C.-Y. Park, J.R. Ahn*, Sungkyunkwan University, Republic of Korea

Intrinsic high mobility of graphene are much reduced in graphene devices by various factors. Two critical factors degrading mobility are uniformity in an atomic structure such as number of a layer and an interaction with a substrate. Recently Shuai-Hua Ji *et al.* reported quantitatively that conductivity is much reduced by one sixth when electrons pass through a boundary between monolayer and bilayer graphene at a step edge in comparison to conductivity of monolayer graphene. This suggests that uniformity of number of graphene layer is a more crucial factor than expected. In particular, in epitaxial graphene on SiC, the uniformity of number of layer is an intrinsic and serious problem because Si is more rapidly sublimated near a step edge in the formation of epitaxial graphene by thermal evaporation of Si and, subsequently, epitaxial graphene with different layers coexists intrinsically on a terrace. Another factor degrading mobility is an interaction between graphene and a substrate. In epitaxial graphene, the interaction was reduced by intercalation of metal or molecule such as H, F, and Au between graphene and a substrate, which results in quasi freestanding graphene. Various charge neutral quasi freestanding graphene has been reported, but the charge neutrality was found at an optimal coverage of an intercalated element and annealing temperature. This makes it difficult to achieve spatially homogeneous charge neutrality of quasi freestanding graphene, and a method with a broad range of coverage and temperature is demanded. We demonstrate that charge neutral quasi freestanding monolayer graphene can be grown uniformly without coexistence of a buffer layer and a bilayer graphene which limit mobility of epitaxial monolayer graphene. Because coexistence of two different phases is inevitable on a SiC surface, uniform monolayer graphene was produced based on two different phases, a Si-rich phase and a C-rich phase called a buffer. Pd was deposited on both the Si-rich and C-rich phases and annealed up to 900°C. The Si-rich phase produced Pd silicide and charge neutral quasi freestanding monolayer graphene was produced on the Pd silicide while, on the C-rich phase, Pd was intercalated between the buffer layer and SiC resulting in charge neutral quasi freestanding monolayer graphene, where the quasi freestanding monolayer graphene on two difference regions was connected atomically. The combination of Si silicidation and intercalation result in uniform charge neutral quasi freestanding uniform monolayer on a SiC surface, where the electronic and atomic structures were observed using angle-resolved photoemission spectroscopy and scanning tunneling microscopy.

9:40am **GR+EM+NS+PS+SS+TF-MoM5 Epitaxial Graphene on Ir(111) - A Playground for the Fabrication of Graphene Hybrid Materials.** *T.W. Michely*, Universität zu Köln, Germany **INVITED**

Carefully optimizing the growth of graphene on Ir(111) yields a virtually defect free, weakly bound epitaxial monolayer ranging from quantum dot sizes to macroscopic extension. In the talk I will show how this system can be used to construct new types of graphene based materials. Specifically, patterned adsorption of transition metals results in dense cluster arrays with exciting magnetic and catalytic properties. Intercalation underneath the graphene allows one to manipulate the properties of graphene itself, e.g. its ability to adsorb atoms and molecules as well as its magnetism.

10:40am **GR+EM+NS+PS+SS+TF-MoM8 Graphene Growth Studied with LEEM, PEEM, EELS, ARPES, MEIS, and STM.** *R.M. Tromp, J.B. Hannon, M.W. Copel, S.-H. Ji, F.M. Ross*, IBM T.J. Watson Research Center **INVITED**

We have studied the growth of graphene on a variety of substrates, including SiC (both Si and C terminated), polycrystalline Cu and Ni foils, as well as single-crystal Ni foils. Low Energy Electron Microscopy (LEEM) and Photo Electron Emission Microscopy (PEEM) offer the unique opportunity to follow the growth in real time, as it proceeds at high temperature, and in the presence of processing gases such as disilane (for growth on SiC) or ethylene (for growth on the metal substrates). Low Energy Electron Diffraction (LEED) allows us to determine crystallographic orientations as well as atomic structure of areas well below a micrometer in extent. Information on electronic structure can be obtained from the plasmon loss features using Electron Energy Loss Spectroscopy (EELS), or from Angle Resolved Photo Electron Spectroscopy (ARPES). These spectroscopic experiments are carried out in the LEEM/PEEM microscope using an in-line energy filter with which energy and angle resolved analysis of the electrons can be performed on selected areas. Finally, to obtain information on the layer-by-layer evolution of the graphene films, particularly on SiC, we have used isotope sensitive Medium Energy Ion Scattering (MEIS), to follow the growth by thermal decomposition of ^{12}C vs ^{13}C graphene monolayers from a three-bilayer thick Si^{13}C homoepitaxial film grown on a SiC substrate. Taken together, these

results provide a comprehensive view of the growth of graphene films. In this talk, we will review the most salient results of these studies, and their relevance to the use of graphene films for electronic applications. To address the latter, we will discuss the results of three-probe STM experiments in which we measured the excess resistivity of a graphene sheet as it crosses an atomic step of the underlying substrate.

11:20am **GR+EM+NS+PS+SS+TF-MoM10 Spatial Confinement of Epitaxy of Graphene on Microfabricated SiC to Suppress Thickness Variation**, *H. Fukidome, T. Ide, H. Handa*, RIEC, Tohoku Univ., Japan, *Y. Kawai*, Tohoku Univ., Japan, *F. Fromm*, Univ. Erlange-Nürnberg, Germany, *M. Kotsugi, T. Ohkouchi*, JASRI/SPring-8, Japan, *H. Miyashita*, Tohoku Univ., Japan, *Y. Enta*, Hirosaki Univ., Japan, *T. Kinoshita*, JASRI/SPring-8, Japan, *Th. Seyller*, Univ. Erlange-Nürnberg, Germany, *M. Suemitsu*, RIEC, Tohoku Univ., Japan

Epitaxial graphene on SiC (EG) is promising owing to a capability to produce high-quality film on a wafer scale [1]. One of the remaining issues is microscopic thickness variation of EG near surface steps, which induces variations in its electronic properties and device characteristics. To suppress the variation, spatial confinement of surface reactions is effective. The spatial confinement using substrate microfabrication, for instance homoepitaxy and sublimation on microfabricated Si substrates, can induce self-ordering of steps, and even produce step-free surfaces [2]. The spatial confinement is therefore anticipated effective to obtain EG without the thickness variation.

We have for this reason applied the spatial confinement to the epitaxy of graphene on 6H-SiC(0001). For the spatial confinement, 6H-SiC(0001) substrates were microfabricated by using electron beam lithography and fast atomic beam etching using sulfur hexafluoride [3, 4]. Epitaxial graphene on the microfabricated 6H-SiC(0001) substrates was obtained by annealing at 1923 K in Ar ambience [2]. It is verified by using low energy electron microscopy (LEEM) and photoemission electron microscopy (PEEM) that step-free SiC surface and EG without thickness variation can be formed on smaller patterns [4]. This result clearly demonstrate that the spatially confinement is effective for the epitaxy of graphene on SiC. Furthermore, Raman spectroscopy and LEEM reveals that the spatial confinement can suppress the fluctuations of the electronic properties, e.g. (unintentional) doping in EG [4].

In conclusion, we have demonstrated that the spatial confinement of EG is effective to control both structural and electronic properties. This novel technique can boost the development of electronic devices based on EG.

[References]

- [1] K. V. Emstev et al., *Nature Mater.* 8 (2009) 203.
- [2] Y. Homma et al., *Jpn. J. Appl. Phys.* 35 (1996) L241.
- [3] T. Ide et al., accepted for the publication in *Jpn. J. Appl. Phys.*
- [4] H. Fukidome et al., submitted.

11:40am **GR+EM+NS+PS+SS+TF-MoM11 Three-Dimensional Graphene Architecture Growth and Its Facile Transfer to Three-Dimensional Substrates**, *J.-H. Park*, Sungkyunkwan University, Republic of Korea, *H.-J. Shin, J.Y. Choi*, Samsung Advanced Institute of Technology, Republic of Korea, *J.R. Ahn*, Sungkyunkwan University, Republic of Korea

Recent development of large area graphene synthesis on metal layer by chemical vapor deposition (CVD) or epitaxial growth on silicon carbide (SiC) opened the possibility for applications such as transparent electrodes for ITO replacement. For instance, graphene has been demonstrated for use in a liquid crystal display (LCD) and/or organic light emitting diode (OLED) test cell as a bottom electrode. However, the actual device, e.g., an active-matrix (AM) LCD, operates by switching individual elements of a display, using a thin-film transistor (TFT) for each pixel. Here, the pixel electrode of a display should extend down to the transistor's source or drain, thereby making contact with a via hole, which demands that a three-dimensional (3D) architecture electrode be deposited on a flat surface as well as its side walls. Although large-area graphene growth can be applied for a wide range of applications, 3D graphene architecture growth has not been realized for actual devices due to the original limitation of planar graphene growth. Herein, we demonstrate for the first time 3D graphene architecture growth and its facile transfer to a planar and/or 3D substrate. To prevent agglomeration of nano-scale metal catalyst by the CVD process, we chose a SiC system. Graphene, a few layers thick, was epitaxially grown on a pre-patterned SiC substrate with nano-size thickness which was produced by photolithography and dry etching. Graphene on a vertical facet of the SiC pattern with a few-hundred nanometers in height was perfectly prepared using this approach, contrary to the CVD method. Furthermore, we suggest the use of a facile transfer method of graphene on SiC to a SiO₂ substrate using thermal release tape after hydrogen intercalation. In spite of the troublesome transfer issue of SiC, the geometry of the 3D graphene was

perfectly transferred onto the planar SiO₂ as well as the 3D SiO₂ structure. In other words, the 3D graphene architecture was maintained as a floating cap structure on planar SiO₂ and the vertical facet of the 3D SiO₂ structure was well covered. Moreover, the graphene bottom layer without a 3D cap and the inverted bowl structure in the 3D graphene architecture were selectively transferred by controlling intercalation and pressure. These approaches could provide a beneficial method for preparing a 3D graphene architecture as well as for modifying the ordered structure to be utilized in real devices.

MEMS and NEMS

Room: 10 - Session MN+AS-MoM

Characterization of Surfaces and Interfaces in MEMS and NEMS

Moderator: A.V. Sumant, Argonne National Laboratory

8:20am **MN+AS-MoM1 Probing Dynamical Surface and Interfacial Effects in High-Speed Nanoelectromechanical Systems (NEMS)**, *X.-L. Feng*, Case Western Reserve University **INVITED**

Nanoelectromechanical systems (NEMS), especially vibrating or resonant-mode NEMS based upon advanced materials and new nanostructures, are emerging as attractive candidates for many nanoscale sensing and signal transduction technologies. Understanding and controlling various surface and interfacial effects in NEMS are important for engineering NEMS toward such goals. In this talk, we focus on using high-speed NEMS themselves as highly sensitive transducers for probing dynamical surface effects and interfacial behavior in these devices.

First, the behavior of physisorbed thin layers on solid surfaces is both interesting for fundamental studies and important for technological applications. For many solid-state devices, ranging from conventional commodity transducers to emerging miniaturized sensors, surface contaminants and adsorbates can be critical for the device performance. Recent advances in NEMS, particularly their excellent sensitivities, make it possible and to probe surface adsorbates and their behavior in the new regime – where a small number of adatoms can cause a detectable frequency shift for a NEMS resonator with a high quality factor (*Q*); and random fluctuations in the sub-monolayer adsorbates may result in variations of the NEMS resonance. We experimentally measure the frequency noise induced by fluctuations of adsorbed xenon (Xe) atoms on the surface of a very high frequency (VHF, ~200MHz), high-*Q*, SiC NEMS resonator. The measured adsorption spectrum and phase noise suggest interesting kinetics of Xe atoms on the surface. We further examine contributions from both surface diffusion and adsorption-desorption. The combined measurements and analyses not only demonstrate that surface diffusion dominates the measured noise in the experimental regime, but also reveal new power laws of noise processes that may be important in various low-dimensional nanosystems.

Second, in NEMS devices with contacts and contact-mode operations, a lot of studies have to date yielded good intuitive understanding and empirical laws. For many new devices with genuinely nanoscale contacts, it has been highly desired but very challenging to understand these nanocontacts with greater details and with quantitative information. By combining experimental measurements and modeling, we explore the detailed electronic and nanomechanical characteristics in contact-mode NEMS with high-speed operations, with a focus on NEMS based on SiC nanowires and nanocantilevers.

9:00am **MN+AS-MoM3 Fabrication of Nanomechanical Switch Based on Ultrananocrystalline Diamond Nanowire**, *A.V. Sumant*, Argonne National Laboratory, *K.J. Pérez Quintero*, University of Puerto Rico, *D.A. Czaplowski*, Argonne National Laboratory

Fabrication of nanomechanical switches using various materials is being actively pursued over conventional solid state switch technology because of advantages of zero leakage current, ultra low power consumption and reasonable switching speeds reaching to 100 ns. Diamond is an ideal candidate material for nanomechanical switches due to high Young's modulus, moderate electrical conductivity when doped with boron or incorporated with nitrogen, high thermal conductivity and chemically inert nature. Recently, fabrication of nanomechanical switches in single crystal diamond has been demonstrated. However, batch fabrication of nanomechanical switches and their integration with complementary metal oxide semiconductor (CMOS) technology in bulk diamond is not feasible.

Ultrananocrystalline diamond (UNCD), originally developed at Argonne National Laboratory is an excellent candidate material for nanomechanical switches due to its high Young's modulus (comparable to single crystal

diamond), semi-metallic conductivity when doped with boron or incorporated with nitrogen and because it is the only diamond film that can be deposited at temperatures as low as 400 °C, at wafer scale, with demonstrated integration with CMOS electronics [1]. We have previously fabricated horizontally aligned N-incorporated UNCD nanowires by a top down approach using Electron Beam Lithography (EBL) patterning and Reactive Ion Etching (RIE) processes [2] with nanowire lengths of 50-100 μm and widths as small as 30 nm.

We demonstrate a fabrication of UNCD nanowire based switch with a movable source anchored at both ends. An immobile drain electrode is separated from the center of the source beam by a narrow gap. Two electrically connected gate electrodes are separated from the source by the gate gap, which is larger than the drain gap [3]. A UNCD layer was deposited on top of a sacrificial SiO₂ layer and covered with a SiO₂ layer that served as a hard mask for the RIE process. The UNCD layer represents the mechanical layer of the switch, the switch contacts and the gate electrodes. We aim to fabricate a reliable switch with fast switching times and low actuation voltages.

References:

- [1] Sumant *et al.* MRS Bulletin, 35, 281 (2010)
- [2] Wang *et al.* Nanotechnology, 23, 075301 (2012)
- [3] Czaplowski *et al.* Electronics Letters 45(11): 550 (2009)

9:20am **MN+AS-MoM4 Carbon Nanotube Templated MEMS: Three Dimensional Microstructures in Semiconductors, Ceramics, and Metals**, R.C. Davis, L. Barrett, R. Hansen, A. Konneker, D.D. Allred, B.D. Jensen, R. VanFleet, Brigham Young University

We discuss a materials breakthrough for MEMS. In contrast with conventional electromechanical devices, whose constituents are chosen from a vast range materials and alloys to optimize fabrication, performance and cost, MEMS have largely been made using the same materials and methods as those used in the silicon-based microelectronics industry. In order to make MEMS out of a much richer suite of materials, including metals, semiconductors, and ceramics, we have developed a process termed carbon nanotube templated microfabrication (CNT-M). In CNT-M we employ patterned, vertically aligned carbon nanotube forests as a three-dimensional microfabrication scaffold to create precise high-aspect-ratio (up to 200:1) microstructures. The "as grown" CNT forests are very low density (at 0.009 g/cc the forest is ~1% carbon and 99% air) and not useful as mechanical materials because they are extremely fragile, due to their low density and weak intratube bonding. However, when we replace the air spaces between tubes in the forest with a filler material by atomistic deposition, the infiltrated CNT framework becomes a robust microstructure consisting mostly of the filler material. Thus, by patterning the CNT microstructure and limiting the deposition of the filler material, CNT-M gives us control over structural features on both the nano and microscales (nanoscale porosity and microscale structure). We have used chemical vapor deposition to infiltrate the CNT framework with semiconductors (Si) and ceramics (SiO₂, SiN_x, and nanocrystalline carbon) for applications in microactuation, sensing, and chemical separations. But many potential MEMS applications would benefit from structures fabricated from functional metals. We now report on the fabrication of metal microstructures using the CNT-M process. We demonstrate the versatility of this fabrication approach by demonstrating both chemical vapor infiltration (making tungsten and molybdenum structures) and electrodeposition (making nickel structures) based metal CNT-M processes. These metals provide several desirable materials properties to high aspect ratio MEMS applications including high electrical and thermal conductivity, high melting temperatures, resistance to corrosion, low thermal expansion, high Young's modulus, hardness and yield strength. Electrical, mechanical, and structural characterization of the microfabricated metal structures will also be presented.

9:40am **MN+AS-MoM5 Filling through Silicon vias with a Carbon Nanotube/Copper Matrix**, M.B. Jordan, M. Rao, The University of Alabama, A.V. Sumant, R.S. Divan, Argonne National Laboratory, S.L. Burkett, The University of Alabama

The performance of through silicon vias (TSVs) depends on the material used to fill them. Copper and tungsten are two conventional metals used to fill TSVs. Recently carbon nanotubes (CNTs) have been considered as a filling material due to their superior material properties. CNT bundles can allow ballistic transport of electrons resulting in low resistivity and enabling them to carry a larger current density. CNT bundles also have a high Young's modulus, low coefficient of thermal expansion, and a high thermal conductivity. These properties make CNTs appealing for use as power delivery systems and as heat sinks. Protecting the CNTs after growth and making electrical contact to them remains a challenge. We have investigated a hybrid CNT/Cu TSV structure as a possible solution to these problems. Blind vias were formed using a cryogenic inductively coupled

plasma (ICP) etch process. A copper seed layer was sputtered on the via base and along the sidewalls. The vias were filled using a periodic reverse pulse electroplating technique to reduce voids in the high-aspect ratio structures. The center region of the copper filled vias were then etched by ion milling. The growth of CNT bundles in the center of the copper filled vias was done by thermal chemical vapor deposition (CVD). Electron-beam evaporated Fe serves as a catalyst for CNT growth.

Use of the Center for Nanoscale Materials at Argonne National Lab was supported by the U. S. Department of Energy, Office of Science, Office of Basic Energy Sciences, under Contract No. DE-AC02-06CH11357.

10:00am **MN+AS-MoM6 Optimization of STiGer Process used to Etch High Aspect Ratio Silicon Microstructures**, T. Tillocher, P. Lefaucheur, GREMI CNRS/Université d'Orléans, France, J. Ladroue, M. Boufnichel, ST Microelectronics, Tours, France, P. Ranson, R. Dussart, GREMI CNRS/Université d'Orléans, France

The STiGer process, which can be used in MEMS fabrication, is a time-multiplexed cryogenic process designed to etch deep anisotropic features in silicon: passivation and etching plasmas are cycled to get vertical structures. The passivation layer is a SiO_xF_y film which requires cryogenic substrate temperature conditions to grow. It desorbs and disappears when the substrate is heated back to room temperature. This is an advantage since no extra cleaning steps are required. Additionally, with the benefit of the periodic passivation cycles, this process is less sensitive to temperature or flow rate variations than standard cryoetching. This enhanced passivation helps to reduce undercut as well. Nevertheless, like in Bosch etching, the alternations induce a scalloping on the sidewalls.

We have already shown that trenches having critical aperture of about 0.8 μm can be etched with high aspect ratios (> 40). We have highlighted a defect called "extended scalloping", which is composed of anisotropic cavities developed on the feature sidewalls, just below the mask. It originates from ions scattered at the feature entrance that hit the top profile and remove locally the passivation layer. This defect is observed for aspect ratios higher than 10. Consequently, large structures, with openings larger than 100 μm , etched to a few hundred of μm show no extended scalloping.

We have proposed two methods that can help to reduce this defect. The first consists in adding a low oxygen flow in the etch cycle, favouring a low additional passivation. The second technique consists in gradually increasing the SF₆ flow, in the etching steps, during the first minutes of the recipe. Consequently, the process starts with a low etch rate and a more efficient passivation, which helps to limit the extended scalloping. These two techniques efficiently reduce the defects but the profiles tend to be always positive. It seems impossible to get at the same time vertical sidewalls and low defects.

We will present other ways to fix this problem. For example, we are currently investigating processes running at -50°C instead of usual cryogenic temperatures (-100°C). This aims to have a more conformal passivation layer, which may prevent the initiation of the extended scalloping. Additionally, this range of substrate temperatures is of interest since it can be reached with chillers and thus, liquid nitrogen is no longer required.

Finally, we will present our results on downscaled structures. We have designed a mask with e-beam lithography comprising 200 nm to 800 nm wide trenches. It is used to evaluate the performances of the STiGer process on submicron structures.

11:00am **MN+AS-MoM9 The Effect of Back-action Force for the Electron Tunneling Transduction in MEMS Measurement**, M.R. Kan, University of Alberta, Canada, Z. Diao, National Institute for Nanotechnology, NRC Canada, V.T.K. Sauer, M.R. Freeman, University of Alberta, Canada, W.K. Hiebert, National Institute for Nanotechnology, NRC Canada

Nano-electromechanical systems (NEMS) have exciting potential for fields ranging from quantum measurement science to ultrasensitive mass detection. For many of these applications, a key challenge is implementing a fast, reliable, low-noise technique for translating small mechanical motion to electronic signals. Electron tunneling transduction based on quantum tunneling is a promising technique to measure small displacements, because the tunneling current is so sensitive to the change in distance between the probing tip and the sample surface (one angstrom distance change causes 7 times tunneling current change). With frequency downmixing, the bandwidth limitation associated with the large RC time constant in the circuits can be overcome; very high frequencies may become accessible, fundamentally limited only by the tunneling rate I_T/e in the GHz range.

Using electron tunneling to sense nanomechanical motion comes with an inherent risk of back-action of the sensing probe (STM tip) on the mechanical device. The local tip-sample energy gradients introduce spring

forces that can produce sizable shifts in resonance frequencies and may also affect sample quality factors. Understanding these effects is important for reliable use of downmixed tunneling transduction. Controlling them will allow for novel methods of MEMS and NEMS tuning of both frequency and quality factor.

In this presentation, we will report our observation of back-action forces on MEMS devices during downmixed electron tunneling transduction. We explore differences in the magnitude of the back-action force for different flexural and torsional vibrational modes (with varying degrees of inherent stiffness). We also discuss the perturbation to device quality factors. Finally, the vibration of the back-action force as a function of tip-sample distance is investigated.

11:20am **MN+AS-MoM10 Electric-Stimulus-Responsive Pluronic Hydrogels as Actuators**, *L. Engel, I. Sokolov, O. Berkh, Tel Aviv University, Israel, K. Adesanya, E. Vanderleyden, P. Dubruel, Ghent University, Belgium, J. Shklovsky, I. Harari, Y. Shacham-Diamand, S. Krylov, Tel Aviv University, Israel*

Due to their unique mechanical and chemical characteristics, stimuli responsive hydrogels have garnered much interest in the field of biomedics. They perform dramatic volume transitions in response to external environmental stimuli such as pH and ionic strength of the solvent, temperature, and electrical field. Their soft elastomeric nature, serves to minimize mechanical and frictional irritation to the tissue bed, suggesting applications in artificial muscles and biomimetics, and their swelling capacity results in high permeabilities for certain drug molecules and metabolites making them ideal materials for drug delivery. Because the swelling rate of a hydrogel is inversely related to its size, MEMS offers a unique opportunity to exploit the capabilities of responsive hydrogels by minimizing actuator response time. While it is known that hydrogels with fixed charge groups deform when subjected to an externally applied electric field inside an electrolyte bath, the exact mechanism responsible for the deformation continues to be debated.

In this work, we have investigated the volume transformation of Pluronic based electroactive hydrogels immersed in a Krebs bathing solution under an applied electric field. The swelling characteristics of the crosslinked hydrogels were investigated and a model based on finite element analysis is proposed. Bias was applied via parallel Pt electrodes and the distance between the electrodes was varied as was the ionic concentration and pH of the solution inside the testing tank. The feasibility of using an array of interdigitated electrodes fabricated on a printed circuit board as a means of actuation hydrogel was demonstrated with the goal of downsizing the hydrogel electrical-stimulation system for the creation of MEMS electro-responsive hydrogel actuators.

11:40am **MN+AS-MoM11 CMOS MEMS Metal-based Tactile Sensors Development**, *Y.C. Lin, C.J. Hsieh, L.B. Wang, J.C. Liou, W.-C. Tian, National Taiwan University, Taiwan, Republic of China*

A CMOS MEMS tactile sensor using a pure metal-based structure by a special etchant (Silox Vapox III) to remove oxide sacrificial layers was developed. The tactile sensor was fabricated through a commercial 0.35mm 2 polysilicon and 4 metal CMOS technology followed by the self-developed post processes. In order to increase the effective gap between two electrodes, the tactile sensor used oxide as the sacrificial layer to replace the conventional metal sacrificial layer. Moreover, the CMOS MEMS-based tactile sensors provides the advantages such as lower cost, small size, compatible with the integrated circuits, and mass-production compared to other types of tactile sensors.

Two different capacitive-based tactile sensor designs, parallel-plate type and vertical-comb-drive type, were proposed in this work. A boss-structure was implemented to provide the uniformity of the membrane displacement during the device operation. The dynamic range of the sensor detection was targeted from 0 to 200 mmHg according to the human vessel pressure. The capacitance variation was measured and analyzed via an integrated circuit board, the arduino board, and an A/D IC, AD7746. The readout circuit module reduced the noise and improved the sensor accuracy to 4fF and the resolution down to 4 aF. The sensitivity of the parallel-plate type is measured to be 1.39 fF/mmHg which is suitable for the blood flow monitoring. More characterizations on the vertical-comb-drive type sensors will be presented.

Nanomanufacturing Science and Technology Focus Topic

Room: 16 - Session NM+AS+MS-MoM

Metrology and Environmental Issues in Nanomanufacturing

Moderator: N.A. Burnham, Worcester Polytechnic Institute, L.J. Gamble, University of Washington

8:20am **NM+AS+MS-MoM1 Nanomanufacturing – Beyond Silicon**, *J.A. Liddle, National Institute of Standards and Technology* **INVITED**

The fabrication of integrated circuits in silicon is the preeminent nanomanufacturing technology, and it occupies a very special niche in terms of functionality and value provided per unit area. As a consequence, it is economically viable to use very expensive fabrication processes to generate the required nanostructures. In addition, the degree of control over the manufacturing process that is required necessitates the use of complex and expensive metrology systems. In contrast the vast majority of other nanotechnology products cannot support the cost of comparably sophisticated manufacturing methods or the associated metrology schemes. In this talk I will give examples of how the complexity of the final product and its value dictate what type of nanomanufacturing approach is viable. In particular, I will describe the need for new metrology techniques that can provide nanoscale information, but do so at rates consistent with the high-volume manufacturing of low-cost products.

9:00am **NM+AS+MS-MoM3 Use of Mueller Matrix – Spectroscopic Ellipsometry for Scatterometry based Measurement of Critical Dimensions during Semiconductor Manufacturing**, *G.R. Muthinti, A.C. Diebold, University at Albany-SUNY, B. Peterson, Nanometrics Inc.*

Scatterometry is one of the most useful metrology methods for the characterization and control of critical dimensions (CD) during nanoelectronic manufacturing. Most Scatterometry is based on Spectroscopic Ellipsometry (SE) and Normal Incidence Reflectometry (NI) measurement and the simulation of the measured spectra through the Rigorous Coupled Wave Approximation. Evolution of better optical hardware and faster computing capabilities led to the development of Mueller Matrix (MM) based Scatterometry (MMS). Typically, spectroscopic ellipsometry based Scatterometry uses Ψ and D measured at each wavelength. In this presentation we discuss dimensional metrology using full Mueller Matrix (16 element) Scatterometry in the wavelength range of 245nm-1000nm measured using a dual rotating compensator spectroscopic ellipsometer. Unlike SE and NI, MM data provides complete information about the optical reflection and transmission of polarized light through a sample. The advantage of MMSE over traditional SE Scatterometry is its ability to measure samples that have anisotropic optical properties and depolarize light. We demonstrate this using a series of structures fabricated by e-beam lithography.

9:20am **NM+AS+MS-MoM4 Atomic Layer Deposition Monitored and Characterized by Joint *In Situ* Real-Time Spectroscopic Ellipsometry and Direct Surface Analysis**, *M. Junige, M. Geidel, M. Knaut, M. Albert, J.W. Bartha, Technische Universität Dresden, Germany*

Atomic layer deposition (ALD) is a special kind of chemical vapor deposition, which pulses at least two chemical reactants into a vacuum reactor alternately and separated by purging steps. ALD has emerged as a powerful technique for the conformal and uniform coating of complex three-dimensional structures, even on large-sized substrates. Accordingly, ALD has a high potential for application throughout the entire field of nanotechnology.[1]

Since ALD alters the physical and chemical properties of a surface during a material's deposition, these changes are observable by direct surface analysis techniques like photoelectron spectroscopy (PES) or scanning probe microscopy (SPM) and also by spectroscopic ellipsometry (SE). As previously described in the References [2] - [4], we acquired ellipsometric spectra *in situ* and in real-time and thus monitored the ALD processes at exactly the place and the time of a sample's modification. In addition, we conducted PES as well as SPM measurements without breaking a high vacuum after the ALD. This revealed, among others, the chemical composition as well as the roughness of a coated surface without alteration in air and so enabled the generation of appropriate optical models, which translate the ellipsometric spectra into rather descriptive quantities like a film thickness or a surface roughness.

In the present work, we will demonstrate the capability of joint *in-situ* real-time SE and direct surface analysis based on the ALD of two exemplary materials: tantalum nitride and ruthenium. In the linear homogeneous film

growth regime of both the ALD processes, the film thickness increment per cycle (also growth per cycle, GPC) was quantified and studied for varying process parameter sets. The initial ALD growth of TaN showed all the three possible growth modes according to Puurunen [5] depending on the starting substrate material. In the case of Ru, the ALD growth initiation indicated a substrate-inhibited island growth mode irrespective of the starting substrate.

[1] G. N. Parsons, S. M. George, and M. Knez, in *MRS Bulletin* **36**, 865 (2011).

[2] M. Junige, M. Geidel, M. Knaut, M. Albert, J. W. Bartha, in *IEEE 2011 Semiconductor Conference Dresden* (Dresden, 2011). – DOI: 10.1109/SCD.2011.6068739

[3] M. Knaut, M. Junige, M. Albert, J. W. Bartha, *J. Vac. Sci. Technol. A* **30**, 01A151 (2012).

[4] M. Geidel, M. Junige, M. Albert, J. W. Bartha: In-situ analysis on the initial growth of ultra-tin ruthenium films with atomic layer deposition, *Microelectron. Eng.* (manuscript submitted).

[5] R. L. Puurunen, *J. Appl. Phys.* **97**, 121301 (2005).

10:40am **NM+AS+MS-MoM8 Transformation of Engineered Nanomaterials in the Environment: Effects of Size, Shape and Morphology on Nanomaterial Toxicity**, *S. Obare*, Western Michigan University **INVITED**

Engineered nanomaterials (ENMs) are known to possess unique size and shape dependent chemical and physical properties. As a result of their properties, ENMs have been effective in several important applications including catalysis, sensor design, photonics, electronics, medicine, and the environmental remediation of toxic pollutants. Such properties and applications have led to an increase in the manufacture of ENMs and a rise in their presence in consumer products. The increase of ENMs in consumer products presents several opportunities and challenges, and necessitates a proactive study of their health and safety. An important and essential criterion toward a systematic study of the environmental safety of ENMs is the need to control their size, shape and morphology, and to produce them in high quantities. Synthetic procedures that produce gram-scale, well defined and monodisperse metallic nanoparticles with controlled size and shape, is not trivial and requires careful control of reaction conditions. This presentation will demonstrate our ability to develop new organic ligands that when used as stabilizers for metal nanoparticles, provide the ability to gain control of the particle size in one-step synthetic procedures. Monodisperse metallic nanoparticles were synthesized and characterized using spectroscopic, microscopic and x-ray techniques. The chemical composition, surface reactivity, solubility, and aggregation tendency of ENMs were studied under various environmental conditions. We will also discuss how ENMs interact with various components in the environment with an emphasis of their interaction with Gram-negative and Gram-positive bacteria. The results provide insights on the need for green manufacturing strategies of ENMs, their use and safe disposal practices.

11:20am **NM+AS+MS-MoM10 An Integrated Approach Toward Understanding the Environmental Fate, Transport, Toxicity and Occupational Health Hazards of Nanomaterials**, *V. Grassian*, University of Iowa **INVITED**

Nanoparticles, the primary building blocks of many nanomaterials, may become suspended in air or get into water systems, e.g. drinking water systems, ground water systems, estuaries and lakes etc. Therefore, manufactured nanoparticles can become a component of the air we breathe or the water we drink. One important issue in understanding the environmental fate, transport, toxicity and occupational health hazards of nanoparticles is in characterizing the nature and state of nanoparticles in air, water or in vivo. For the nanoparticles of interest in these studies, metals and metal oxides, it can be asked: (i) will metal oxide and metal nanoparticles be present in air or water as isolated particles or in the form of aggregates? (ii) will metal oxide and metal nanoparticles dissolve in aqueous solution or in vivo? and (iii) under what conditions will metal oxide and metal nanoparticles aggregate or dissolve? As the size regime will be very different depending on the state of the nanoparticles, as dissolved ions, isolated nanoparticles or nanoparticle aggregates, these questions are important to address as it impacts the size regime that needs to be considered or modeled in for example environmental transport or lung deposition models. Furthermore, the effect on biological systems including nanoparticle-biological interactions and toxicity will depend on the state of nanoparticles. In the studies discussed here, macroscopic and molecular-based probes that includes quantitative solution phase adsorption measurements, molecular based probes, light scattering and zeta-potential measurements to investigate the behavior of nanoparticles in aqueous suspensions. We have focused on several different metal and metal oxide nanoparticles including Fe, Ag, Zn, Cu, Ce and Ti. Some of our newest results which focus on aggregation and dissolution, including detailed size-dependent studies, in the presence and absence of organic acids will be

discussed. This research is beneficial as it significantly contributes to the growing database as to the potential environmental and health implications of nanoscience and nanotechnology and how nanomaterials will behave in the environment and impact human health.

Nanometer-scale Science and Technology
Room: 12 - Session NS-MoM

Nanoparticles and Quantum Structures

Moderator: G.S. Herman, Oregon State University

8:40am **NS-MoM2 Synthesis of Visible Light Emitting Self-assembled Ge Nanocrystals Embedded within a SiO₂ Matrix and Post-annealing Effects**, *A. Hernández-Hernández, F. De Moure-Flores, J.G. Quiñones-Galván*, CINVESTAV-IPN, Mexico, *L.A. Hernández-Hernández*, ESFM-IPN, Mexico, *J. Santoyo-Salazar, M. Meléndez-Lira*, CINVESTAV-IPN, Mexico

As-grown light emitting self-assembled Ge nanocrystals (Ge-NCs) embedded in a SiO₂ matrix were produced by a sequential deposition process of SiO₂/Ge/SiO₂ layers employing reactive radio frequency sputtering technique. Obtained Ge-NCs shown a crystallographic phase whose proportion, size, quality and specific orientation are determined by the oxygen partial pressure. Photoluminescence (PL) spectra indicate that the size distribution of Ge-NCs is reduced and centered at around 8 nm when higher oxygen partial pressure is employed; the formation of Ge-NCs is corroborated by transmission electron microscopy (TEM) measurements, their sizes are consistent with estimates from PL measurements. After vacuum annealing it is observed the elimination of an instable high pressure tetragonal phase of germanium present in as-grown samples. It is possible that this phase is related to the SiO₂ matrix stress on the Ge-NCs. In addition, the PL peaks shifted to higher energies indicating the formation of Ge-NCs probably from Ge dispersed within SiO₂ matrix. It was also found that the PL intensity increases drastically after annealing process. The strong size dependence of the PL spectra indicates that the observed PL originates from the recombination of electron-hole pairs confined in Ge-NCs.

† : partially funded by CONACyT-Mexico and ICYT-DF.

9:00am **NS-MoM3 A Single Atom Transistor**, *M.Y. Simmons*, University of New South Wales, Australia **INVITED**

Over the past decade we have developed a radical new strategy for the fabrication of atomic-scale devices in silicon [1]. Using this process we have demonstrated few electron, single crystal quantum dots [2], conducting nanoscale wires with widths down to ~1.5nm [3] and most recently a single atom transistor [4]. We will present atomic-scale images and electronic characteristics of these atomically precise devices and demonstrate the impact of strong vertical and lateral confinement on electron transport. We will also discuss the opportunities ahead for atomic-scale quantum computing architectures and some of the challenges to achieving truly atomically precise devices in all three spatial dimensions.

[1] F.J. Rueß et al., *Nano Letters* **4**, 1969 (2004).

[2] M. Fuchsle et al., *Nature Nanotechnology* **5**, 502 (2010).

[3] B. Weber et al., *Science* **335**, 64 (2012).

[4] M. Fuchsle et al., accepted for *Nature Nanotechnology* (2012).

9:40am **NS-MoM5 Transforming Luminescent Silicon Nanocrystals Into a Direct-Bandgap Semiconductor via Surface-Capping-Induced Strain**, *P. Hapala, P. Jelínek, K. Kusova, I. Pelant*, Institute of Physics of ASCR, Czech Republic

We report combined experimental and theoretical work pointing out the possibility to convert Silicon Nanoparticles (SiNcs) to a luminescing direct-band gap material via the concerted action of the quantum confinement and tensile force induced by proper surface passivation.

The transformation of silicon, originally a very poor light emitter due to indirect band gap, into a light-emitting medium is key challenge from the application point of view. One promising way to achieve this ultimate goal is through dramatic shrinkage in the size of the crystal down to nanoscale. The observation of an efficient room-temperature luminescence [1] from SiNcs initiated the debate about the nature of their band structure. The most common silicon-oxide-capped SiNcs maintain the indirect band gap showing long radiative lifetimes (>100 μs) [2].

Beside the size of the nanocrystal, a proper surface also plays an important role in the light emission process. Recently we have shown that SiNcs sized 2.5-3 nm with methyl-based surface passivating layer [3] exhibit luminescence properties (short radiative lifetime ~10 ns and enhanced

quantum yield ~20%) analogical to direct-band gap semiconductor. This property is further supported by single-crystal luminescence experiment giving emission pattern very similar to that observed in direct-band gap CdSe nanoparticles [4].

To understand the impact of surface passivation on the electronic structure of SiNcs we performed large-scale total energy DFT calculations including up to 1500 atoms and different functional surface groups (-H, -CH₃, -OH). Our calculations show that the presence of methyl group leads to significant elongation of the Si-Si distance in core region. Further we restore band structure of SiNc mapping real space molecular orbitals into the momentum space [6].

The resorted band structure clearly shows, that combination of tensile stress and the quantum confinement strongly modifies dispersion of the conduction band along the Γ -X direction, with significant lowering of the Γ 15 even as lifting the conduction minimum band Δ 1.

References

- [1] L. Canham, App. Phys. Lett. 57, 1046 (1990).
- [2] D. Kovalev et al, Phys. Rev. Lett. 81, 2803 (1998).
- [3] K. Kůsová et al ACS Nano, 4(8), 4495 (2010).
- [4] X. Wang et al Nature 459, 686 (2009).
- [5] K. K. Kůsová et al (submitted).
- [6] P. Hapala and P. Jelinek (ArXiv:cond-mat/1204.0421).

10:00am NS-MoM6 Plasma Synthesis and Hydrosilylation of Silicon Nanoparticles, S.L. Weeks, S. Agarwal, Colorado School of Mines, B. Macco, Eindhoven University of Technology, the Netherlands

Silicon nanoparticles (NPs) are of interest in a variety of optoelectronic applications due to the observation of multiple exciton generation, room temperature photoluminescence, size tunable band gap, and optical gain. Design of any device employing Si NPs requires control over both the size and interfacial passivation as these parameters dictate the electronic properties of the NPs. Our synthesis process employs a capacitively-coupled tubular Ar/SiH₄ plasma to produce H-terminated Si NPs. The surface composition and functionalization of the Si NPs was characterized via *in situ* attenuated total reflection Fourier transform infrared (ATR-FTIR) spectroscopy. Organic passivation of the H-terminated Si NPs was achieved through a two-stage gas-phase hydrosilylation process using 1-alkynes with different numbers of C atoms that led to surface coverages comparable to the thermodynamic limit for alkenyl monolayers on bulk H:Si(111) surfaces. The hydrosilylation reaction requires abstraction of a surface hydride to stabilize an intermediate surface radical formed upon absorption of the 1-alkyne. Injection of H₂ into the afterglow region of the synthesis plasma was employed to manipulate the surface hydride composition, which led to an increase in the relative fraction of SiH_x (x = 2, 3) species on the surface compared to SiH. The impact of these higher hydrides on the hydrosilylation reaction of 1-alkynes was investigated through *in situ* ATR-FTIR spectroscopy. Finally, using *in situ* photoluminescence measurements, we also determined the effect of the various hydrosilylation processes on the relative quantum yield from these Si NPs.

10:40am NS-MoM8 Exchange Bias in Pure and Core/Shell Structured γ -Fe₂O₃-based Nanoparticles, P. Lampen, H. Khurshid, M.H. Phan, H. Srikanth, University of South Florida

Iron oxide nanoparticles, Fe₃O₄ and γ -Fe₂O₃, are of great interest for applications in high-density magnetic recording media, sensor technology, and biomedicine. These systems are also excellent candidates for probing fundamental properties due to well-established synthesis methods that yield uniform, high quality particles with good control over size and shape. It has recently been shown by polarized small angle neutron scattering that Fe₃O₄ nanoparticles possess a chemically uniform, but magnetically distinct, core and canted-spin shell structure [1]. While many similarities exist in the magnetic and microstructural properties of γ -Fe₂O₃ and Fe₃O₄, the exchange bias that can be observed in nanoparticles of γ -Fe₂O₃ [2] is not present in similarly sized Fe₃O₄ [3]. Therefore, an investigation of the evolution of spin canting angle and shell thickness with temperature in γ -Fe₂O₃ is expected to yield valuable information about subtly altered spin geometries that can be correlated with the presence of exchange bias in this nanoparticle system.

In order to compare results for both chemically distinct and chemically uniform exchange-biased systems, we report the synthesis and characterization of γ -Fe₂O₃ and core/shell Fe/ γ -Fe₂O₃ nanoparticles. The particles used in the present study were synthesized by high temperature decomposition of iron organometallic compounds. X-ray diffraction and transmission electron microscopy techniques were used to study the structural and microstructural properties of the nanoparticles, which confirmed the presence of bcc iron and fcc γ -Fe₂O₃ in these particles. High-resolution TEM images evidenced monodisperse products with particle

diameters of 9 ± 0.8 nm in the pure γ -Fe₂O₃, while the core/shell particles showed 9.8 ± 0.7 nm Fe cores surrounded by a shell of γ -Fe₂O₃ with 2 ± 0.4 thickness. The DC magnetic properties of the samples were characterized using a vibrating sample magnetometer over a temperature range of 5-300 K, revealing a superparamagnetic behavior. Pronounced exchange bias of up to ~ 4100 Oe was confirmed in these particles using cooling fields of up to 5T. While the spin-glass-like phase associated with disordered surface spins in γ -Fe₂O₃ plays an important role as a fixed phase in both systems, providing the pinning force to the reversible spins, the frozen spins at the interface between Fe and γ -Fe₂O₃ are also shown to contribute to EB in the core/shell Fe/ γ -Fe₂O₃ nanoparticles.

11:00am NS-MoM9 Magnetic Polymer Nanocomposites with Tunable Microwave and RF Properties, K. Stojak, S. Chandra, H. Khurshid, S. Pal, C. Morales, J. Dewdney, J. Wang, T. Weller, M.H. Phan, H. Srikanth, University of South Florida

There has been much interest in magnetic polymer nanocomposites (MPNCs) recently due to potential applications for EMI shielding, tunable electromagnetic devices and flexible electronics. We report synthesis, structural, magnetic and RF characterization on MPNCs ranging from 30-80wt-% loadings of uniformly dispersed CoFe₂O₄ nanoparticles (~ 10 nm) in a high-temperature, thermosetting resin from the Rogers Corporation (RP). Nanoparticles were synthesized by thermal decomposition and structurally characterized by XRD and TEM. Magnetic properties were studied using a Quantum Design PPMS. MPNCs displayed characteristic features of superparamagnetism at room temperature and blocking at low temperature. A blocking temperature (T_B) of ~ 298 K was observed for all weight percentages. The saturation magnetization (M_S) was found to increase with increasing weight percentages of CoFe₂O₄, from 9.7 emu/g for 30wt-% to 28.5 emu/g for 80wt-%. A large value of coercivity (H_C), ~ 18.5 kOe, is observed at 10K and is not affected by various loadings of CoFe₂O₄. Microwave transmission/reflection studies were done using a linear microstrip resonator. Strong tunability in the microwave absorption was observed, particularly in the 80wt-% sample and the quality factor shows a strong enhancement with applied magnetic field. We extend our study to include nanoparticle-filled multi-walled carbon nanotubes (CNTs) synthesized by CVD. These high-aspect ratio magnetic nanostructures, with tunable anisotropy, are of particular interest in enhancing magnetic and microwave responses in existing MPNCs. The CNTs have an average diameter and length of 300nm and 2μ m, respectively and are partially filled with CoFe₂O₄ nanoparticles (~ 7 nm) [2]. When comparing the CoFe₂O₄ nanoparticles to the CoFe₂O₄-filled CNTs, T_B increases from 224K to 264K, and M_S increases from 36 emu/g to 37.1 emu/g. These results indicate that enclosing the nanoparticles within the CNTs enhances interparticle interactions, which is also independently confirmed with frequency-dependent AC susceptibility. This trend is also observed with NiFe₂O₄ and Fe₃O₄

nanoparticle fillers.

11:20am NS-MoM10 Factors Controlling Thermodynamic Properties at the Nanoscale: *Ab Initio* Study of Pt Nanoparticles, G. Shafai, M. Alcántara Ortigoza, T.S. Rahman, University of Central Florida

We analyze via density-functional-theory calculations how factors such as size, shape, and hydrogen passivation influence the bond lengths, vibrational density of states (VDOS), and thermodynamic quantities of 0.8-1.7 nm diameter Pt nanoparticles (NPs), whose shape was previously characterized via extended X-ray absorption fine structure spectroscopy (EXAFS) [1]. For a given shape, unsupported NPs display increasingly broader bond-length distributions with decreasing size. Since the VDOS is remarkably non-Debye-like (even for the largest NPs), the VDOS and the thermal properties are not correlated as they are in the bulk. Generally, the fundamental vibrational frequency of a NP is associated with the shape and decreases with increasing size, as in macroscopic systems. Not surprisingly, we find that the frequency of this fundamental mode largely characterizes the thermal properties. We demonstrate that the qualitative difference between the atomic mean-square-displacement and the corresponding mean bond-projected bond-length fluctuations should be taken into account when interpreting the Debye-Waller factor of NPs measured by X-ray (or neutron) scattering or EXAFS. We find that in H-passivated Pt NPs, H desorption with increasing temperature explains the appearance of negative thermal expansion.

This work was supported in part by DOE grant DE-FG02-07ER46354

[1] B. Roldán Cuenya, M. Alcántara Ortigoza, L. K. Ono, F. Behafarid, S. Mostafa, J. R. Croy, K. Paredis, G. Shafai, T. S. Rahman, L. Li, Z. Zhang, and J. C. Yang, PRB 84, 245438 (2011)

[2] G. S. Shafai, M. Alcántara Ortigoza, and T. S. Rahman, J. Phys.: Condens. Matter 24, 104026 (2012)

11:40am **NS-MoM11 Fabrication of Fe Doped Nano-engineered Matrix for Cholesterol Biosensor**, R.R. Pandey, C. Kant, CSIR-National Physical Laboratory, National Physical Laboratory, India, M. Dhayal, CSIR Centre for Cellular and Molecular Biology (CCMB), India, K.K. Saini, CSIR-National Physical Laboratory, National Physical Laboratory, India

In recent years, sol-gel chemistry has been a subject of intense investigations in the fields of chemical sensors and biosensors as it offers a cost effective route the fabrication of high surface area plate forms for sensitive biosensors. The inherent low temperature process of the technology, provide an attractive way for the immobilization of heat-sensitive biological entities (enzyme, protein, and antibody). This class of sol-gel silica (TiO₂) matrix possesses chemical inertness, non-toxic, physical rigidity, tunable porosity, high photochemical and thermal stability, and optical transparency.

Nanostructured nature of the metal-oxides films have been extensively reported, we have utilized this property of the material for effective enzyme adsorption per unit area to develop high sensitivity biosensors. We have further improved the matrix property to alter the surface properties (microstructure and charge transport) by Fe doping in the TiO₂ film. The modified matrix has been characterized by XRD, XPS, FTIR, SEM. The Fe³⁺ ion doped TiO₂ matrix successfully introduces redox property in the electrode and provides enhanced electron communication features. Sensing response obtained by the bioelectrocatalytic oxidation of cholesterol by cholesterol oxidase. Chox/ Fe³⁺ ion doped TiO₂/ITO electrode was studied using cyclic voltammetry (CV). These studies reveal that the Chox/ Fe³⁺ ion doped TiO₂/ITO bio-electrode exhibits improved biosensing response as compared to Chox/ Undoped TiO₂/ITO electrode. The results confirm promising application of the Fe³⁺ ion doped TiO₂ thin film matrix for the realization of efficient cholesterol biosensor.

Oxide Heterostructures-Interface Form & Function

Focus Topic

Room: 7 - Session OX+EM+MI+NS+TF-MoM

Structure-Property Relationships in Epitaxial Oxide Interfaces

Moderator: E.I. Altman, Yale University

8:20am **OX+EM+MI+NS+TF-MoM1 Role of Dual-laser Ablation in Controlling Mn Oxide Precipitation during the Epitaxial Growth of Mn Doped ZnO Thin Films with Higher Doping Concentrations**, D. Mukherjee, M. Hordagoda, R.H. Hyde, N. Bingham, H. Srikanth, P. Mukherjee, S. Witanachchi, University of South Florida

The low solubility of Mn (equilibrium limit of 13 %) and precipitation of Mn oxides at slightly higher Mn doping (> 4 %) have remained major obstacles in the growth of Mn doped ZnO (ZnO:Mn) thin films for potential spintronic applications. In this work, epitaxial ZnO:Mn thin films were deposited on c-cut Al₂O₃ (0001) substrates, with increasing Mn concentrations from 2 to 12 %, using the dual-laser ablation process. In this process, an excimer (KrF) laser and a CO₂ laser pulses are spatially and temporally overlapped onto the target surface. Initially the target is heated by the CO₂ laser to produce a transient molten layer, from which the slightly time-delayed KrF laser initiates the ablation. Ablation for a momentary liquid target not only results in a drastic reduction of particulates in the deposited films but also overcomes the problem of non-congruent ablation of the ZnO:Mn target, leading to stoichiometric film deposition. Moreover, the optimum coupling of the laser energies produces an ablation plume that has a broader angular distribution, compared to the plume generated by KrF pulse alone, as observed from the intensified-charge-coupled-detector (ICCD) images of the ablated plumes. This allows the deposition of uniform films over larger area. Further, the higher ionization of the ablated species as seen in the optical emission spectra (OES) of the dual-laser ablated plumes leads to enhanced gas phase reaction and better film morphology and crystallinity. X-ray diffraction studies revealed that the dual-laser deposited ZnO:Mn films were single crystalline with no secondary phase formation even at 12 % doping while single-laser deposited ZnO:Mn films showed secondary Mn oxide phases. Room temperature magnetic measurements showed ferromagnetism (FM) with enhanced saturation magnetization (M_s) values from 1.3 emu/cm³ for 2 % ZnO:Mn films to 2.9 emu/cm³ for 12 % ZnO:Mn films. In- and out-of-plane magnetization revealed absence of magnetic anisotropy. Further, temperature dependent Hall measurements showed a strong correlation between the effective carrier densities and the observed FM. All these measurements suggested a carrier mediated mechanism of FM in ZnO:Mn thin films. Using both the experimental data and theoretical analysis the FM in less conducting ZnO:Mn films was described by a bound magnetic polaron model whereas

that in highly conducting films was consistent with a carrier mediated interaction via RKKY exchange mechanism.

8:40am **OX+EM+MI+NS+TF-MoM2 Structural Characterization of Heterojunction n-ZnO/p-NiO Thin Films Epitaxially Deposited on (0002)Al₂O₃ Substrates**, Y.H. Kwon, Sungkyunkwan University, Republic of Korea, J.H. Lee, KAIST, Republic of Korea, S.H. Chun, Sungkyunkwan University, Republic of Korea, J.Y. Lee, KAIST, Republic of Korea, H.K. Cho, Sungkyunkwan University, Republic of Korea

Recently, oxide semiconductors with superior electrical properties have been considered as candidates to replace Si based electronics. Furthermore, their thermally and chemically stable characteristic is preferable for devices. Especially, among a lot of oxides, ZnO based semiconductors have been extensively investigated to apply in wide application such as thin film transistor and light emitting diode. ZnO is an intrinsic n-type semiconductor which characteristic comes from Zn interstitials and O vacancies. And band-gap and exciton binding energy are 3.37 eV and 60 meV, respectively, which is suitable for optical application operating in ultra-violet region. Therefore, p-n homojunction diode structure combined with n-ZnO and p-ZnO having well matched interface had been studied by a lot of researchers.[1] However, it was not reliable since p-type ZnO synthesized by doping of group V elements is unstable and return to the n-type by self-compensation.[2]

Therefore, p-n heterojunction diode composed of n-ZnO and stable p-type oxide such as Cu₂O and NiO was alternatively studied.[3] Among the p-type oxides, NiO with wide direct band-gap (3.7 eV) have been expected to apply in optical applications. And conductivity of NiO could be significantly controlled by Li⁺ doping. Furthermore, according to T. Dutta et. al., (111) plane of NiO could well matched with (0002) of ZnO by domain match epitaxy.[4]

In this study, heterojunction diode structure was fabricated with n-type ZnO and p-type NiO on [0002] oriented Al₂O₃ substrates. RF magnetron sputtering method was used for deposition of NiO and ZnO films. After the deposition of NiO films at 400°C in O₂ atmosphere, ZnO films were grown at 600°C and in Ar and O₂ mixed gas atmosphere. XRD result showed the NiO films were fabricated with high crystallinity and preferred orientation of [111]_{NiO}. And sixfold symmetry of (100)_{NiO} plane obtained by phi-scan indicates that the NiO films were bi-epitaxially grown on Al₂O₃ substrates. In addition, electrical properties of NiO showed relatively low resistivity (1.648 Ωcm) and high mobility (14.52 cm²/Vs) due to Li⁺ doping. Sixfold symmetry of (1-102)_{ZnO} observed at phi-scan result indicates that ZnO films were also epitaxially grown on [111] oriented NiO films.

REFERENCES

- [1] F. Zhuge, L. Zhu, Z. Ye, D. Ma, J. Lu, J. Huang, F. Wang, Z. Ji, S. Zhang, Applied Physics Letters, 87 (2005) 092103.
- [2] C. Park, S. Zhang, S.H. Wei, Physical Review B, 66 (2002) 073202.
- [3] H. Kawazoe, H. Yanagi, K. Ueda, H. Hosono, MRS Bulletin, 25 (2000) 28.
- [4] T. Dutta, P. Gupta, A. Gupta, J. Narayan, Journal of Applied Physics, 108 (2010) 083715.

9:00am **OX+EM+MI+NS+TF-MoM3 Manipulating the Electrostatic Boundary Conditions of Polar Interfaces**, Y. Hikita, SLAC National Accelerator Laboratory

INVITED

Transition metal oxides (TMO) offer various functionalities ranging from electronic devices to environmental catalysts [1, 2]. Often, the central part of such devices is the interface between different materials. In order to improve their device performance, control of charge transport across these interfaces is essential. Originally developed in semiconductor heterostructures, interface band alignment control is based on the interface electrostatic boundary conditions and is one of the most fundamental methods to tune the carrier transport across interfaces [3]. Given their strongly ionic nature and their accessibility to multiple valence states, the TMO interface should be more suitable than covalent semiconductors for manipulating interface band alignments. Here we focus on epitaxial metal-semiconductor Schottky interfaces between perovskite oxides to demonstrate the effectiveness of this technique. I will present two SrTiO₃ based perovskite Schottky junctions in which the interface energy barriers were modulated by interface dipoles controlled on the atomic scale [4]. Further, I will present the application of this technique in the form of an all-oxide hot electron transistor [5].

1. R. Ramesh and D. G. Schlom, MRS Bull. **33**, 1006 (2008).
2. J. Suntivich *et al.*, Science **334**, 1383 (2011).
3. F. Capasso *et al.*, Appl. Phys. Lett. **46**, 664 (1985).
4. Y. Hikita *et al.*, Phys. Rev. B **79**, 073101 (2009).
5. T. Yajima *et al.*, Nature Mater. **10**, 198 (2011).

11:20am **OX+EM+MI+NS+TF-MoM10 Strain-induced Oxygen Vacancy Ordering at SrTiO₃/La_{0.5}Sr_{0.5}CoO₃ Interfaces, and its Impact on Magnetic “Dead” Layers**, *S. Bose, M. Sharma, M. Torija*, University of Minnesota, *J. Gazquez, M. Varela*, Oak Ridge National Laboratory, *J. Schmitt, C. He*, University of Minnesota, *S. El-Khatib*, American University of Sharjah, United Arab Emirates, *M. Laver, J. Borchers*, NIST Center for Neutron Research, *C. Leighton*, University of Minnesota

The remarkable functionality and epitaxial compatibility of complex oxides provides many opportunities for new physics and applications in oxide heterostructures. Perovskite cobaltites provide an excellent example, being of interest for solid oxide fuel cells, oxygen separation membranes, catalysis, ferroelectric RAM, resistive switching memory, and oxide spintronics. However, the same delicate balance between phases that provides this diverse functionality also leads to a serious problem - the difficulty of maintaining desired properties close to the interface with other oxides. Although this problem is widespread, manifests itself in several ways, and could present a significant roadblock to the development of heterostructured devices for oxide electronics, there is no consensus as to its origin. In our work, using SrTiO₃(001)/La_{1-x}Sr_xCoO₃ as a model system, we have combined epitaxial growth via high pressure oxygen sputtering [1] with high resolution x-ray diffraction, atomic resolution scanning transmission electron microscopy (STEM) and electron energy loss spectroscopy (EELS), and detailed magnetic, transport, and neutron scattering measurements to determine the fundamental origin of the deterioration in interfacial transport and magnetism [2,3]. The effect is found to be due to nanoscopic magnetic phase separation in the near-interface region driven by a significant depletion in interfacial hole doping due to accumulation of O vacancies. This occurs due to a novel mechanism for accommodation of lattice mismatch with the substrate based on formation and long-range ordering of O vacancies [4]. This fundamental link between strain state and O vacancy formation and ordering is explored in detail in this presentation. We demonstrate that the O vacancy density, depth profile, and ordering vector can all be controlled via strain, leading to a potential mechanism to substantially improve interfacial properties.

UMN support from NSF and DOE (neutron scattering). ORNL support from DoE; UCM support from the European Research Council.

[1] Torija *et al*, *J. Appl. Phys.* **104** 023901 (2008); Sharma *et al*, *J. Vac. Sci. Technol.* **29** 051511 (2011).

[2] Torija *et al*, *Adv. Mater.* **23** 2711 (2011).

[3] Sharma *et al*, *Phys. Rev. B.*, **84** 024417 (2011). [4] Gazquez *et al*, *Nano. Lett.* **11** 973 (2011).

11:40am **OX+EM+MI+NS+TF-MoM11 Fabrication and Characterization of Titanium Oxide Films with Tunable Stiffness**, *K. Gottlieb-Vainshtein, O. Girshevitz, C.N. Sukenik*, Bar Ilan University, Israel, *D. Barlam, Ben Gurion University, Israel, E. Kalfon-Cohen, S.R. Cohen*, Weizmann Institute of Science, Israel

The design of surfaces with controlled stiffness is attractive for a variety of applications ranging from controlling cell growth to mechanical and electrical engineering design. Here, the creation of layered composites with tunable surface stiffness has been achieved by coating a soft PDMS polymer with a stiff film of amorphous titanium oxide with thickness varying from 2 to 50 nm. The oxide layer is smooth (6 nm rms roughness at 2 μm² image size), and crack-free. Air plasma treatment was used to form a silica surface layer on the soft polymer base to promote of adhesion of the titania overlayer. To gain insight into the mechanics of the layered structure, nanomechanical quantification has been performed using different experimental approaches, as well as modeling studies. The surface mechanical properties of the samples have been probed using both instrumented nanoindentation and atomic force microscopy—based nanomechanical characterization. These results have been compared to finite element analysis (FEA) simulations.

By fitting the FEA simulations with experimental curves it is shown that the hard titania film and softer PDMS substrate individually maintain their characteristic elastic moduli, while the stiffness of the vertical nanocomposite can be controllably modified by changing the thickness of the stiff layer. Liquid phase deposition of the oxide allows control of its thickness at the nm level. During an indentation cycle, the stiff layer transmits the stress to the underlying PDMS base by deformation of its overall shape, but only negligible compression of the film thickness.

This synthetic approach can be quite versatile, and can, in principle, be extended to different oxides and a wide range of thicknesses. It allows control of surface properties while maintaining bulk material properties. This exploratory work is a first step towards defining the range of surface stiffnesses that can be achieved in this way, as well as developing general methodologies for their characterization.

Plasma Science and Technology
Room: 24 - Session PS+EM-MoM

Atmospheric Plasma Processing and Micro Plasmas
Moderator: S.G. Walton, Naval Research Laboratory

8:20am **PS+EM-MoM1 Plasma Science and Applications in the Spatial Realm Below 1 mm: Recent Advances in Microcavity/Microchannel Plasmas**, *J.G. Eden*, University of Illinois at Urbana Champaign INVITED

The last decade has witnessed the rapid emergence of microcavity plasmas, a new subfield of plasma science and technology that pursues the fundamental physics and applications of low temperature, nonequilibrium plasma confined in at least one dimension to nominally < 1 mm. By melding plasma science with photolithography and other micro/nanofabrication techniques adapted from the integrated circuits and materials science communities, it has become possible to observe plasma behavior and realize electronic/photonic/chemical devices that were inaccessible previously. With all due respect to Captain Kirk, plasmas are now able “to go where no [plasma] has gone before.” This presentation will highlight recent advances in microcavity plasma science, such as the realization of plasma confined to < 3 μm. Interfacing a gas phase (e⁻ - ion) plasma with an e⁻ - h⁺ plasma in a semiconductor to yield an n⁺pn plasma bipolar junction transistor will be described. A new form of thin, flat lighting (“lighting tiles”) available in sheets as large as 900 cm² in area will be demonstrated, and massively-parallel plasmachemical processing of gases/vapors in arrays of microchannel plasmas will be described.

9:00am **PS+EM-MoM3 Development and Limitations of Microplasma Arrays on Silicon Operating in DC**, *R. Dussart, M. Kulsreshath, L. Schwaerle, V. Felix, P. Lefauchaux, O. Aubry, T. Tillocher, S. Sozias, GREMI - Polytech Orleans/CNRS, France, L.J. Overzet*, University of Texas at Dallas

Arrays of microreactors built from silicon wafers in clean room facilities were first proposed and developed about ten years ago by G. Eden's team [1]. They consist of Micro Hollow Cathode Discharges (MHCD) operating in parallel in DC or in AC. One of the remarkable properties of these MHCDs relies on the fact that they can operate in DC, in a stable regime at atmospheric pressure, without evolving to an arc regime [2]. Potential applications of these new technological devices are numerous and include different domains such as lighting, detection, local treatments, sensors, lab on chip, treatment and micromachining processing, instrumentation... In this paper, we will focus on DC operation of microdischarges working in helium or in argon. The microreactor geometry was investigated to achieve the best results in terms of life time and ignition. Although we were able to ignite up to 1024 microdischarges (100 μm diameter holes), we observed many spikes on the current waveform, which indicate that microplasmas are not so stable. The quite short life time of our microdevices which varies from few minutes to few hours could be linked to these spikes, which actually cause significant damages. Taking into account our observations by Scanning Electron Microscope, our optical characterization and our electrical measurements, we propose a mechanism explaining the appearance of the damages, which shorten the lifetime of our microdischarges. Finally, we will give some indications to delay the damage mechanisms and to increase the life time of the microplasma arrays.

References

[1] J G Eden, S-J Park, N P Ostrom, S T McCain, C J Wagner, B A Vojak, J Chen, C Liu, P von Allmen, F Zenhausern, D J Sadler, C Jensen, D L Wilcox and J J Ewing, *J. Phys. D: Appl. Phys.* **36** 2869–2877 (2003)

[2] K. H. Schoenbach, R. Verhappen, T. Tessnow, P. F. Peterkin, W. Byszewski, *Appl. Phys. Lett.* **68**, 13 (1996)

9:20am **PS+EM-MoM4 A Foldable Microplasma-Generation Device on a Paper Substrate Operating under Atmospheric Pressure**, *Y.J. Yang, J.H. Tsai, Y.C. Liao, Y.W. Lu, C.C. Hsu*, National Taiwan University, Taiwan, Republic of China

The fabrication of plasma generating devices on paper substrates is presented. The device was fabricated using a screen print process. Stable helium plasmas were ignited in two parallel electrodes with a gap of 237 to 710 μm by a DC power source. When the plasma was ignited with a 0.2 μL salt solution droplet with trace amount of metallic elements applied to the discharge gap, clear metallic emission lines emanated from the plasma. The result suggests that this paper-based device can be used in analytical applications. We demonstrate that a stable helium plasma can be sustained when the substrate is flat, rolled, and folded along various orientations. Microarrays were also fabricated on paper substrates. Stable array of discharges can be ignited by an AC power source with a frequency between 50 Hz to 10 kHz. Preliminary results show that a 10*10 discharge array can

be ignited under different atmospheres such as argon, helium, and air by properly adjusting the parameters. This work was supported by National Science Council of Taiwan, the Republic of China (100-2628-E-002-012 and 101-3113-E-002-002).

9:40am **PS+EM-MoM5 Cold Atmospheric Microplasma Arrays for Processing of Flexible Materials**, *J. Hopwood, A. Hoskinson, C. Wu, N. Miura*, Tufts University **INVITED**

Microplasmas offer a pathway to atmospheric pressure plasma processing using low-temperature, low-cost substrates. Unlike arc and torch technologies, the atmospheric microplasma typically operates near room temperature. Corona discharges share this distinction, but modern microplasma devices produce electron densities that are several orders of magnitude greater than the corona. The combination of low gas temperature and high electron density suggests that a unique process window exists for deposition, etching, and surface modification of flexible materials at atmospheric pressure. In this lecture, we describe the plasma physics of a steady-state microplasma excited by 1 GHz microwave power. Spatially resolved laser diode absorption, imaging spectroscopy, and electrical probe measurements show that the individual microdischarge has an intense inner core surrounded by a cooler region that is rich in metastable atoms. These physical insights are combined with data from deposition experiments using acetylene mixed with a helium gas flow. High densities of electrons and energetic species produced by steady-state microplasmas are believed to be crucial to quality film formation at one atmosphere. Finally, we explore scaling the microplasma toward roll coating geometries. Linear arrays of microplasmas are excited from a single microwave power source through the use of resonant energy sharing. This technique allows over 100 microplasmas to operate in parallel without the usual problem of instabilities induced by ionization overheating and negative differential discharge resistance. This work was supported in part by the U.S. Department of Energy under award No. DE-SC0001923 and by the National Science Foundation under Grant No. CBET-0755761.

10:40am **PS+EM-MoM8 Nucleation of Nanodiamond Clusters at Ambient Pressure via Microplasma Synthesis**, *A. Kumar, P.A. Lin, A. Xue, R.M. Sankaran*, Case Western Reserve University

Since their discovery, nanodiamonds have been an active area of research due to their unique size, chemical stability, high thermal conductivity, and biocompatibility.¹ Nanodiamonds have been detected in outer space (meteorites, interstellar dust) and synthetically produced by high pressure/high temperature (HPHT) and detonation processes. In addition to their potential technological use, the formation of nanodiamond is of great scientific interest. While bulk graphite is more stable than bulk diamond at lower pressures and temperatures (e.g. ambient conditions), recent modeling has suggested that nanometer-sized particles of diamond-phase carbon could be thermodynamically favored at these same conditions as a result of surface energy considerations.²

Previously, microplasmas have been shown to be capable of nucleating high-purity nanometer-sized metal nanoparticles from vapor precursors.³ Here, we present a study of nanodiamond synthesis at atmospheric pressure using a similar microplasma process. Ethanol vapor was used as a carbon precursor for the nucleation of carbon clusters. Aerosol measurements confirm that carbon clusters less than 6 nm in mean diameter are nucleated in the microplasma. *In situ* optical emission spectroscopy (OES) indicates the presence of C₂ dimers and atomic H species which have been linked to diamond nucleation. The collected product is characterized by several techniques including micro Raman spectroscopy, X-ray diffraction (XRD), X-ray photoelectron spectroscopy (XPS), and high-resolution transmission electron microscopy (HRTEM). Results confirm the presence of nanodiamond with uniform sizes of *ca.* 3 nm in diameter and crystal structures corresponding to known phases of diamond. The synthesis of nanodiamond at low pressure may allow new technologies to be realized, and help explain their formation in extraterrestrial material.

1. V. N. Mochalin *et al.*, "The properties and applications of nanodiamonds", *Nat. Nanotech.* **7**, 11 (2012).
2. P. Badziag *et al.*, "Nanometre-sized diamonds are more stable than graphite", *Nature* **343**, 244 (1990).
3. A. Kumar *et al.*, "New insights into plasma-assisted dissociation of organometallic vapors for gas-phase synthesis of metal nanoparticles", *Plasma Proc. Polym.*, in review.

11:00am **PS+EM-MoM9 Atmospheric Pressure Plasma Effects on the Adhesive Bonding Properties of Stainless Steel and Epoxy Composites**, *T.S. Williams, H. Yu, P. Yeh, J. Yang, R.F. Hicks*, University of California, Los Angeles

An atmospheric pressure helium and oxygen plasma has been used for the surface preparation of 410 stainless steel and carbon-fiber epoxy laminates

prior to bonding them together. Lap shear results for stainless steel coupons and carbon-fiber epoxy laminates demonstrated an 80% and a 150% increase in bond strength, respectively, after plasma activation. Following 7 days of aging, wedge crack extension tests revealed a crack extension length of 7.0 mm and 2.5 mm for the untreated and plasma activated steel. The untreated stainless steel had 30% cohesive failure compared to 97% for steel activated with the plasma. Surface analysis by X-ray photoelectron spectroscopy showed that carbonaceous contamination was removed by plasma treatment, and specific functional groups, e.g. carboxylic acids, were formed on the surface. These functional groups promoted strong chemical bonding to the epoxy film adhesive. Atmospheric pressure plasmas are an attractive alternative to abrasion techniques for surface preparation prior to bonding. The process is easily automated, does not damage the materials, and has no environmental, health and safety concerns.

11:20am **PS+EM-MoM10 Numerical Simulation of Gas Heating in a Capacitively Coupled Microcell Plasma at Atmospheric Pressure**, *T. Yagisawa, T. Makabe*, Keio University, Japan

A microcell plasma at atmospheric pressure has been widely investigated. One of the biggest advantages is in the capability to produce a small-size and high-density plasma, broadening a range of applications such as nano-material synthesis, light sources, biomaterial processing, green technology and so on. With decreasing the size of the reactor, the ratio of volume to surface area also decreases. Under these circumstances, the contribution of the wall surface to the loss of charged and neutral particles becomes much larger. The energy is accumulated in the plasma in the form of a thermal energy by the interaction between energetic ions and gas molecules and the ion impact on the wall. Therefore, the effects of local heating of gas molecule on the plasma structure is of great importance particularly in a microcell plasma at high pressure.

In this study, the two-dimensional (2D) structure of a capacitively coupled microcell plasma (CCP) driven at radio frequency (13.56 MHz) with the power of ~ 4.7 W cm⁻³ is numerically investigated in a sealed cylindrical chamber at atmospheric pressure. Pure argon is considered as a parent gas molecule, where electron, Ar⁺, Ar₂⁺ and long-lived metastable atom (Ar^m) are traced in the simulation. In order to discuss the effects of local gas heating, the governing system consisting of a coupled set of models is developed: a neutral transport model including the gas temperature T_g, a conventional plasma model in gas phase, as well as a heat conduction model in solid phase. Large amount of metastable atom $\sim 10^{14}$ cm⁻³ makes huge influence on the plasma structure via stepwise ionization process caused by low energy electrons (~ 4.3 eV), as well as metastable pooling. The temperature dependence of the thermal conductivity ($\sim T_g^{1/2}$) of argon is considered and the result is compared with that of constant thermal conductivity. The local peak of gas temperature T_g ~ 600 K appears due to the Joule heating by energetic ions in the sheath region in front of the powered electrode, resulting in the local reduction of gas density N_g(r) under the constant gas pressure. Taking the gas heating into account, electron density increases by the enhancement of reduced field E/N_g(r). In addition, electron density distribution slightly expands toward the radial direction.

11:40am **PS+EM-MoM11 Reactions at the Interface of Plasmas and Aqueous Electrodes: Identifying the Role of Electrons**, *M. Witzke*, Case Western Reserve University, *P. Rumbach, D.B. Go*, University of Notre Dame, *R.M. Sankaran*, Case Western Reserve University

Plasmas formed at the surface of or inside liquids have been of historical interest for the potential to mediate electrochemical reactions with gaseous species.¹ Recently, there has been technological interest in plasma/liquid systems for a wide range of applications including nanomaterials synthesis, water treatment, and medicine. However, the nature of reactions at the plasma/liquid interface remains poorly understood. Specifically, since plasmas are a source of electrons, ions, UV light, and radicals, it has been difficult to isolate and identify the role of the various species on reactions that occur in the liquid phase.

Here, we present evidence of electrolytic reactions at the plasma/liquid interface. Experiments were carried out with a non-thermal, atmospheric-pressure, direct-current microplasma jet formed at the surface of an aqueous electrolyte. The plasma was operated as the cathode with a Pt foil immersed in solution as the anode. To isolate the role of electrons, we selected model electrolytic reactions such as the conversion of ferricyanide [Fe(CN)₆³⁻] to ferrocyanide [Fe(CN)₆⁴⁻] which can be easily monitored by UV-vis absorbance spectroscopy.² Cyclic voltammetry was performed to verify that ferricyanide was not dissociated. Alternatively, using acidic solutions, hydrogen gas was detected by mass spectrometry, indicating that protons (H⁺) are electrochemically reduced by the plasma.³ Overall, these results reveal the significant role electrons can play in plasma/liquid systems.

1. J. Gubkin, *Ann. Phys. Chem. N. F.* **32**, 114 (1887).
2. M. Witzke *et al.*, *J. Am. Chem. Soc.* **133**, 17582 (2011).

Plasma Science and Technology Room: 25 - Session PS-MoM

Advanced FEOL/Gate Etching 1

Moderator: L. Diao, Mattson Technology

8:20am **PS-MoM1 Selective Etching of Spacer with Pulsing in Inductively Coupled Plasmas for FinFET Devices**, *B. Zhou, M. Titus, P. Friddle, M. Robson, G. Upadhyaya, G. Kamarthy*, Lam Research Corp, *S. Kanakasabapathy, E. Franke*, IBM Corp

The transition to 14 nm technology node has introduced an architectural shift from traditional planar devices to complex three-dimensional FinFET structures. A primary etch challenge for making FinFET devices is that of spacer etch wherein the topography of the FinFET devices requires the fin surface (Si) to withstand substantial over-etch in order to remove the spacer on the fin sidewalls. Typical targets for this etch comprises of < 1nm Si recess, good spacer profile fidelity, complete spacer removal on fin sidewalls and < 2nm spacer CD loss. With conventional etch methodologies, the process window for achieving these targets is narrow due to competing deposition and etch species that simultaneously co-exist in the plasma. Simply lowering the electron temperature or lowering the ion energy is not a solution since there is a tradeoff between spacer CD loss and Si recess. In this presentation, we will demonstrate that by using pulsing, the deposition and etch phases can be separated thereby yielding a wide process window and breaking the tradeoff to enable FinFET spacer etch. Various pulsing schemes will be contrasted with conventional continuous mode operation along with a discussion of the compatibility of the pulsed spacer process with downstream integration.

8:40am **PS-MoM2 Evaluation of Novel Spacer Etch Processes using a New Gas**, *S. Engelmann, E.A. Joseph, N.C.M. Fuller, W.S. Graham, E.M. Sikorski*, IBM T.J. Watson Research Center, *M. Nakamura, G. Matsuura*, Zeon Chemicals L.P., *H. Matsumoto, A. Itou, T. Suzuki*, Zeon Corporation

The spacer etch process is a very critical element in the CMOS device process flow as it ensures and enables the electrical isolation of Source/Drain and Gate regions. We observed that during conventional spacer processes, very little difference in plasma polymer deposition onto the respective substrates could be noted. [1] A successful Nitride Spacer process was rather facilitated by a silicon etch process that was selective to oxide, where excess oxidation lead to a conversion of Silicon to Silicon oxide. This also means that the etch rates of the Nitride are limited by the simultaneous oxidation of the nitride. A potential solution to overcome this limitation would be to control the etch rate by polymer thickness, similar to high selectivity oxide etching. An evaluation of this approach has yielded similar results as the general etch mechanism proposed by Standaert *et al.* [2] A novel etch chemistry was also evaluated that enables a different etch mechanism that cannot be described by the general model.

The impact of this novel mechanism on spacer etch processes was evaluated for both, capacitive and inductive discharges. We furthermore evaluated the impact of this novel process on planar and non-planar device structures. The novel gas chemistry has also been evaluated to enable an oxygen free spacer process. We found that the lateral spacer loss can be eliminated and that Si loss can be effectively reduced by employing the novel process. The SiN footing can be effectively reduced by fine-tuning the ion/neutral ratio of the plasma discharge. The best results to date from a PDSOI 22nm testsite have yielded an SOI loss of about 2nm which is able to maintain all SiN on the gate sidewall while keeping the HM loss to about 4nm and reducing the SiN foot to less than 3nm.

[1] S. Engelmann *et al.*, AVS 58th Int. Symp. & Exhibit. (2011)

[2] M. Schaepkens *et al.*, J. Vac. Sci. Technol. A 17, 26 (1999)

9:00am **PS-MoM3 Anisotropic and Selective Etching of Novel Multifunctional Materials**, *J.P. Chang*, University of California, Los Angeles

INVITED

The introduction of new and improved materials into silicon based integrated circuits is a major contributor in the recent decade to enable the scaling of circuit density and performance in analog, logic, and memory devices. Many new materials, such as complex metal oxides, magnetic materials and phase change materials, are much harder to pattern, thus pose significant challenges to the design and selection of plasma etching

chemistries. This talk focuses on understanding the plasma-surface interaction and reaction kinetics, offers an unique approach in that thermodynamics analysis guides the selection of gas-phase chemistry, and establishes a kinetics-based model containing salient attributes of the etch process. The significant gain deriving from this unique approach is the ability to assess a large array of materials, which possess different properties that dictates a careful balance between etch anisotropy and selectivity. Both theoretical and experimental results from recent research will be discussed using complex metal oxides and magnetic materials are model systems.

9:40am **PS-MoM5 High Selective Etching of SiN Based Material Over Si and SiO₂ using Evanescent Microwave Plasma for FINFET Spacer Applications**, *A. Raley, A. Ranjan, H. Kintaka, B. Messer, T. Mori, K. Kumar, P. Biolsi*, Tokyo Electron Technology Center, America, LLC, *A. Inada*, Renesas Electronics, *R. Jung, S. Kanakasabapathy*, International Business Machines – Research Group

For smaller than 22nm technology node devices, a FinFET (3-D) gate structure is needed to reduce gate leakage, decrease power consumption, increase drive current and control short channel effects. FinFET gate spacer etching presents challenges for conventional RIE process, since it requires highly anisotropic and selective etching of Silicon Nitride over Si/SiO₂. Microwave power was delivered through radial line slot antenna generating high density evanescent microwave plasma. High density evanescent microwave plasmas with low self-bias at the wafer enables a highly selective and anisotropic etching of spacer. The bulk electron energy distribution determines the gas phase reaction rates that generate various radicals and ionic species. The etchant, passivant and ion flux to the wafer can be controlled by the energy distribution of Bulk electrons (T_e). T_e can be tuned in by adjusting the microwave power. High SiN selectivity over Si and SiO₂ was achieved on blanket as well as patterned wafer using the evanescent microwave plasma etcher. In general, selectivity is achieved by controlling the polymer layer difference over SiN/Si/SiO₂. The difference of pattern wafer/blanket wafer etch rates/selectivities can be explained by differences in transport of by ions and radicals through high aspect ratio features. The effects of loading of SiN, Si and resist materials on etch rates and selectivity will be reviewed.

This work was performed by the Research and Development team at TEL Technology Center America in joint development with IBM Research Alliance Teams in Albany, NY 12222. This work was performed by the Research Alliance Teams at various IBM Research and Development Facilities

10:00am **PS-MoM6 Highly Selective and Controllable Si₃N₄ Etching on Si and SiO₂ for sub-22-nm Gate Spacer using CF₃ Neutral Beam with O₂ and H₂**, *D. Nakayama, A. Wada, T. Kubota*, Tohoku University, Japan, *M. Haass, R.L. Bruce, R.M. Martin, N.C.M. Fuller*, IBM TJ Watson Research Center, *S. Samukawa*, Tohoku University, Japan

Silicon nitride is used as a gate sidewall spacer for aggressively scaled complementary metal-oxide-semiconductor (CMOS) devices because of their high thermal stability and excellent insulating property. Therefore, silicon nitride (Si₃N₄) etching (patterning) is one of the critical processes in sub-22-nm-CMOS device fabrication. During the patterning of the silicon nitride spacer film, damage to the Si surface typically occurs, resulting in silicon (Si) and Si dioxide (SiO₂) recess in the source/drain and shallow trench isolation (STI) respective regions. Additionally, loss of spacer film close to the top of the gate structure can occur during the excessive “over etch” necessary to enable a manufacturable process. The advent of non-planar device geometries only exacerbates the aforementioned challenges. Hence, extremely high selectivity of silicon nitride to both Si and SiO₂ is extremely critical.

We developed an alternative etching process to solve these problems using a “damage-free” neutral beam (NB) etching process. A typical NB apparatus consists of plasma and process chambers that are separated by a carbon aperture. The carbon aperture can effectively neutralize the charged particles and eliminate irradiation of UV photons from plasma when the plasma passes through it. Therefore, etching can proceed without any UV-induced damage caused by charged particles or high-energy photons from the plasma.

In this study, we proposed neutral beam etching using a new gas chemistry of CF₃I in addition with oxygen (O₂) and hydrogen (H₂) gases for the sidewall spacer etching process. By using CF₃I, we can ensure that an energetic neutral beam comprised primarily of CF₃ is generated and, as such, becomes the main etching species for Si₃N₄ during the patterning process. Additionally, surface polymerization and surface oxidation on SiO₂ and poly-Si can be precisely controlled by addition of O₂ and H₂ gases, respectively. As a result, moderately high selectivity of Si₃N₄ to both of Si (6.2:1) and SiO₂ (18.6:1) could be achieved by optimizing the ratio of CF₃I/O₂/H₂. Additionally, on relaxed ground rule structures at ~ 240nm

pitch and gate CD (L_{gate}) \sim 40nm, an optimized NB etching condition achieves complete removal of the spacer from the gate sidewall with negligible spacer loss at the top of the gate structure and $<$ 2 nm SOI loss. These results demonstrate the potential of silicon nitride etching process using neutral beams for fabricating sub-22-nm gate sidewall spacers.

10:40am **PS-MoM8 Highly Selective Etching of Titanium Nitride Over Tantalum Nitride in Inductively Coupled Plasma**, *W. Zhu, H. Shin, S. Sridhar, L. Liu, V.M. Donnelly, D.J. Economou*, University of Houston, C. Lenox, T. Lii, Texas Instruments

The etching properties of metal nitrides (TiN, TaN) for high-k metal-gate integration were investigated in a Faraday-shielded inductively coupled plasma. The effect of operating conditions such as pressure, bias, and gas composition in HCl/He plasmas were explored for isotropic, highly selective etching of TiN over TaN. High selectivity is required for advanced device architectures incorporating metal gates integrated with high-k gate dielectrics and etch-stop layers. Etch rates were obtained separately for TiN and TaN blanket films on Si using end-point detection (by monitoring the Si 288nm emission signal) and reflectance measurements using a He-Ne laser, verified by post-etching TEM cross-sectional profiles. The etching rates were measured to be 130 ± 20 and 60 ± 10 nm/min for TiN and TaN, respectively, using 30% HCl/He chemistry at 70mTorr and 400W in continuous wave plasma with no bias on the substrate. The higher etching rate of TiN compared to that of TaN can be attributed to the lower binding energy of TiN and higher volatility of $TiCl_4$ etch byproducts. The etching selectivity was 2:1 (TiN:TaN) under the condition investigated. Higher selectivity between TiN and TaN was achieved by adding trace amounts of O_2 (O_2 partial pressure $< 1 \times 10^{-4}$ Torr): for very small oxygen additions, the etching rate of TiN remained unchanged, whereas that of TaN decreased significantly. At high enough additions of O_2 , etching of both TiN and TaN was completely suppressed. A narrow window of selectivity was found by varying O_2 partial pressure. The film surface was characterized after etching using X-ray photoelectron spectroscopy (XPS). Cl_2/He plasmas were also studied and their similarities and differences with HCl/He plasmas will be discussed.

Work supported by Texas Instruments.

11:20am **PS-MoM10 Detailed Analysis of Si Substrate Damage Induced by HBr/ O_2 - and H_2 -Plasma Etching and the Recovery Process Designs**, *Y. Nakakubo, A. Matsuda*, Kyoto University, Japan, *M. Fukasawa*, Sony Corporation, Japan, *Y. Takao*, Kyoto University, Japan, *T. Tatsumi*, Sony Corporation, Japan, *K. Eriguchi, K. Ono*, Kyoto University, Japan

Hydrogen-containing plasmas have been widely used for fabricating Si-based electronic devices such as metal-oxide-semiconductor field-effect transistor (MOSFET). Plasma-induced Si substrate damage during shallow trench isolation and gate electrode formation processes has become one of the critical issues because the damaged structure is believed to not only degrade the electric performance but also enhance the parameter variations resulting in yield loss in mass production [1]. Due to its light mass, a hydrogen atom from plasma can penetrate deeper in Si substrate, and, consequently, forms the thicker damaged layer leading to the larger amount of Si loss in the source/drain extension region of MOSFET called "Si recess" [2]. Although the recovery mechanism of Si damage has been extensively studied, there have been few comprehensive process-design guidelines by taking into account the electrical characteristic degradation. In this study, we report detailed analyses of Si-damage recovery dynamics using a capacitance-voltage (C-V) technique, and provide respective recovery process guidelines for HBr/ O_2 - and H_2 -plasma cases. Silicon wafers with thermal-oxide layer (2 nm) were damaged by HBr/ O_2 - and H_2 -plasma treatments. Various annealing processes in N_2 ambient with different "thermal budgets" were employed to address the impacts of the temperature and budget on the damage recovery. An SiO₂-Capping layer was formed on some samples to simulate structural constraints in present-day MOSFET processes. Using the quantitative C-V technique (1/C₂-based analysis), we found that, although HBr/ O_2 -plasma induced a larger amount of Si damage (defect site), wet-etch stripping process was more effective due to thinner damaged layer thickness, further, the annealing process with temperatures higher than 850 °C was found to be able to cure the structural defects. As for H_2 -plasma cases, on the other, the wet-etch was "insufficient" to remove the defects, resulting in a high conductive layer. Moreover, we observed that the annealing temperature ($>$ 1050 °C) rather than the budget was a primal parameter to cure the damage. The obtained results may be explained by "the defect-density or structural-constraint effect". The present findings imply an important and useful guideline of the recovery process design of H-containing-plasma damage in future advanced devices. [1] K. Eriguchi *et al.*: J. Vac. Sci. Technol. A **29**, 041303 (2011). [2] M. Fukasawa *et al.*: J. Vac. Sci. Technol. A **29**, 041301 (2011).

11:40am **PS-MoM11 Time-modulated Plasma Etching for Next Generation Devices**, *S. Sriraman, Y. Wu, G. Kamarthy, C. Rusu, J. Holland, A. Paterson, V. Vahedi*, Lam Research

Plasma etching has facilitated the continuation of Moore's Law from $> 1\mu m$ to now less than 20 nm and is used to enable next-generation semiconductor device technology. While etching is used to compensate for incoming lithographic limitations as well as non-uniformities from up-stream processes, it also offers ways to counter fundamental limitations of pattern dependent etching and atomic-scale mixing. In this context, time-modulated plasma etching is the key to address challenges arising in critical etch applications for < 20 nm technology nodes.

This paper will aim to discuss some fundamental factors in consideration for time-modulated plasma etching in a Transformer Coupled Plasma (TCPTM) chamber and its outcomes on representative process applications. Using a combination of experimental results, diagnostics, and modeling & simulation, the advantages of different types of time-modulated plasma and their ability to control basic plasma properties will be covered. The role and benefits of independently controlling ions and neutrals to overcome limitations in etching and their applicability to next generation device architectures will be discussed.

Advanced Surface Engineering
Room: 22 - Session SE+NS-MoM

Nanostructured Thin Films and Coatings I: Interface Aspects

Moderator: J. Patscheider, EMPA, Switzerland

8:40am **SE+NS-MoM2 Ion-guided Phase Separation of Carbon-Nickel Composite Films during Ion Beam Assisted Deposition: 3D Sculpting at the Nanoscale**, *G. Abrasonis*, Helmholtz-Zentrum Dresden-Rossendorf, Germany, *M. Krause*, Helmholtz-Zentrum Dresden-Rossendorf and Technische Universität Dresden, Germany, *T.W.H. Oates*, Leibniz-Institut für Analytische Wissenschaft, Germany, *A. Mücklich, S. Facsko*, Helmholtz-Zentrum Dresden-Rossendorf, Germany, *C. Baetz, A. Shalimov*, Helmholtz-Zentrum Dresden-Rossendorf, Germany and European Synchrotron Radiation Facility, France, *S. Gemming*, Helmholtz-Zentrum Dresden-Rossendorf, Germany

Ion assistance during film growth provides unique opportunities to influence the microstructure due to energy transfer and imposed directionality. During nanocomposite film growth at low temperatures, phase separation occurs at the growing film surface. Ion-assistance is a key parameter to control the surface processes during multiphase film growth, and hence the resulting nanocomposite morphology. A systematic study of ion irradiation as a pure energy and momentum transfer agent in the context of surface diffusion assisted phase separations is, however, lacking. Here the influence of low energy (50-130 eV) assisting Ar^+ ion irradiation on the morphology of C-Ni thin films will be reported. Ion-beam assisted deposition (IBAD) promotes the columnar growth of carbon encapsulated metallic nano-columns at low deposition temperatures for Ar^+ ion energy ranges of 50-100 eV. Moreover, the momentum transfer results in a tilting of the columns relative to the film surface. The potential to grow complex matrix encapsulated metallic structures such as chevrons is demonstrated. Furthermore, a window of deposition conditions will be reported where the ion assistance leads to the formation of regular 3D nanopatterns with well-defined periodicity. The influence of such anisotropic film morphology on the optical properties is highlighted.

Acknowledgements: Funding by the European Union, ECMP-Project D1, "Nanoskalige Funktionsschichten auf Kohlenstoffbasis", Projektnummer 13857 / 2379, is gratefully acknowledged.

9:00am **SE+NS-MoM3 Interface Phenomena in Nanostructured Thin Films and Coatings**, *D. Rafaja*, Freiberg University of Technology, Germany **INVITED**

The properties of nanostructured thin films and coatings are strongly influenced by the structure of internal interfaces. Thus, the understanding of the formation of the interfaces and the knowledge of the relationship between the microstructure and the materials properties are the first steps in designing nanostructured materials with tailored properties. This talk will focus on partially coherent interfaces between adjacent crystalline phases in nanostructured thin films and coatings, discussing the mechanisms of their formation, showing the capabilities of experimental methods for microstructure analysis to detect these interfaces and to describe their structure on the atomic scale, and recognizing the influence of the interfaces on the materials properties.

The interface phenomena and their impact on hardness and thermal stability of nanostructured thin films and coatings will be illustrated on physical vapor deposited transition metal nitrides containing aluminum and/or silicon, where the internal interfaces form as a consequence of the decomposition of metastable supersaturated solid solutions. It will be shown how the local fluctuations of the chemical composition arising during the deposition process and the local strain fields resulting from differences in the interatomic distances at partially coherent interfaces influence the decomposition process and the stability of the metastable phases.

The description and quantification of the interface phenomena on atomic scale would be impossible without a detailed microstructure analysis that is required to reveal the constitution of the nanostructured materials, to reproduce the structure of the internal interfaces and to assess the coherence of the interfaces. Hence, this talk will also recapitulate the recent developments in the microstructure analytics on the nanostructured thin films and coatings.

9:40am SE+NS-MoM5 Mechanical Properties, Fracture Toughness, and Thermal Stability of CrN/AlN Superlattice and Multilayer Thin Films, M. Schlögl, B. Mayer, J. Paulitsch, J. Keckes, C. Kirchlechner, P.H. Mayrhofer, Montanuniversität Leoben, Austria

Transition metal nitrides, such as CrN are highly attractive materials for a wide range of applications due to their outstanding properties like high hardness, excellent corrosion and oxidation resistance. Consequently, many research activities deal with their synthesis-structure-properties-relations. However, it has been reported that CrN/AlN superlattice coatings improve the mechanical properties compared to single CrN especially when keeping the AlN in its metastable cubic phase. Hence, we investigated the influence of the layer thickness of CrN on the stabilization of c-AlN and the critical layer thickness for AlN before transforming into the stable wurtzite phase. Furthermore, stress measurements and thermal stability were accomplished by the in-situ wafer curvature method during vacuum annealing to 700°C, differential scanning calorimetry to 1500°C and hardness measurements after annealing up to 1100°C.

The fracture toughness of the coatings is studied by means of in-situ scanning electron microscopy and transmission electron microscopy microbending and microcompression tests. The small test-specimens are prepared by focused ion beam milling of individual free-standing thin films. As generally monolithic coatings with their columnar structure provide low resistance against crack formation and propagation we perform our studies for CrN films, CrN/AlN multilayers and the CrN/AlN superlattice as mentioned above. Especially the multilayers and superlattices provide additional interfaces perpendicular to the major crack-propagation-direction. Adjusting the AlN layer-thicknesses to allow for cubic or wurtzite structure enables to study the influence of the extremely stress sensitive cubic-to-wurtzite AlN phase transformation on the crack propagation.

The microtests clearly demonstrate that the monolithic CrN as well as the CrN/AlN multilayer coating with the wurtzite AlN layers crack with the behavior and features for brittle fracture. Contrary, the CrN/AlN multilayer coatings composed of cubic stabilized AlN layers are able to provide resistance against fatal crack propagation. Hence, they allow for significantly higher loads during the microbending and microcompression tests. Detailed structural investigations, in-situ and after the tests, suggest that the cubic AlN layers, which are stabilized by coherency strains in the CrN/AlN multilayer coatings, phase transform with the connected nature expansion when experiencing additional strain fields and thereby hinder crack propagation.

10:00am SE+NS-MoM6 High-temperature Nanoindentation of Hard Coatings, M. Rebelo de Figueiredo, University of California Berkeley, M. Tkadletz, Materials Center Leoben, Austria, M. Schlögl, R. Hollerweger, P.H. Mayrhofer, C. Mitterer, Montanuniversität Leoben, Austria, P. Hosemann, University of California Berkeley

In the past decades, measurement techniques to probe the mechanical properties of hard coatings have been evolved dramatically and nowadays a wide variety of methods and devices are available. Within the field of evaluating the hardness of coating materials, nanoindentation has been established as a standard method utilizing the Oliver and Pharr approach. The measurements are commonly performed at room temperature. Industrial applications like metal cutting, however, demand resistance to wear also at temperature levels of up to 1000°C, which can easily be reached in the contact zone between a coated tool and the machined part. Therefore, knowledge about the mechanical properties of hard coatings at elevated temperatures is of vital importance. Nanoindentation devices allowing to go to temperatures as high as 750°C became available in recent years. While it appears simple to install heating devices in a nanoindenter, the minimization of the thermal drift, tip durability, and environmental control are a particular challenge to perform measurements at these temperatures. Therefore, significant efforts in monitoring all effects of a

measurement performed at these conditions need to be spent in order to gain valid indentation data.

Within the present work, a series of different hard coatings were analyzed, utilizing nanoindentation experiments up to 750°C. The coatings evaluated cover selected samples representing the state-of-the-art employed in cutting operations like Al₂O₃ and TiAlN as well as newly developed coating materials like TiAlTaN. Possibilities and experimental limitations of high-temperature nanoindentation are critically discussed. A sound knowledge of the dependence of hardness on microstructural changes occurring at elevated temperatures provides the basis for the further development of coating materials and design.

10:40am SE+NS-MoM8 Improving the Phase Stability of Metastable Aluminum Oxide Thin Films, F. Nahif, H. Bolvardi, D. Music, S. Mráz, J.M. Schneider, RWTH Aachen University, Germany

Charge state resolved ion energy distribution functions (IEDFs) of Al⁺, Al²⁺ and Al³⁺ were measured as a function of Ar

pressure in the range from 5.7×10^{-5} to 2.13 Pa (0.01 to 256 Pa cm). A close to monoenergetic beam of Al⁺ ions was obtained in an Ar/O₂ mixture at 128 Pa cm. Al₂O₃ films are deposited employing this monoenergetic Al⁺ beam using a substrate bias potential to increase the ion energy. A critical Al⁺ ion energy of 40 eV for the formation of the α -Al₂O₃ phase at a substrate temperature of 720 °C is determined. This energy is used as input for classical molecular dynamics and Monte-Carlo based simulations of the growth process, as well as *ab initio* calculations. The combination of theory and experiment indicates that in addition to the well known surface diffusion the previously non considered diffusion in sub-surface regions is an important atomistic mechanism in the phase formation of Al₂O₃. Using density functional theory and cathodic arc deposition experiments the effect of Si and Y addition on the stability of γ - and α -Al₂O₃ has been investigated. Si additives clearly shift the relative stability towards the γ -phase which can be understood based on the electronic structure. As the additive concentration increases, strong silicon-oxygen bonds are formed giving rise to the observed stabilization of the γ -phase.

11:00am SE+NS-MoM9 Thermal Stability of (Al_xCr_{1-x})₂O₃ Solid Solution Coatings Grown by Cathodic Arc Evaporation, V. Edlmayr, M. Pohler, University of Leoben, Austria, I. Letofsky-Papst, Graz University of Technology, Austria, C. Mitterer, University of Leoben, Austria

Corundum-type (Al_xCr_{1-x})₂O₃ coatings were grown by reactive cathodic arc evaporation in an oxygen atmosphere using AlCr targets with an Al/Cr atomic ratio of 1. Since the (Al_xCr_{1-x})₂O₃ solid solution shows a miscibility gap below 1300°C, where spinodal decomposition is predicted, the microstructural changes upon annealing were investigated by a combination of transmission electron microscopy, X-ray diffraction, Raman spectroscopy and differential scanning calorimetry. The as-deposited coating consists primarily of the corundum-type (Al_xCr_{1-x})₂O₃ solid solution, with smaller fractions of cubic (Al_xCr_{1-x})₂O₃. An additional Al-rich amorphous phase and a Cr-rich crystalline phase stem from the droplets incorporated. The corundum-type (Al_xCr_{1-x})₂O₃ was still present after vacuum annealing at 1050°C for 2 hours, whereas additional α -Al₂O₃ and Cr₂O₃ phases were formed due to decomposition of the cubic (Al_xCr_{1-x})₂O₃ phase. Likewise, Cr and Cr₂O₃ have been detected in the annealed coating, most probably originating from the partial oxidation of Cr-rich droplets. Upon crystallization of the amorphous phase fractions present, γ -Al₂O₃ is formed, which partially transforms in α -Al₂O₃. No evidence for decomposition of the corundum-type (Al_xCr_{1-x})₂O₃ solid solution could be found within the temperature range up to 1400°C.

11:20am SE+NS-MoM10 Protective Coatings Against Corrosion and Wear for 3D Components with Combined ALD and PVD Techniques, S. Ek, Picosun, Finland

Corrosion-related problems have always been a major challenge in various industries because of the components' shortened lifetime. Huge efforts are being made to improve the current corrosion protection procedures and to develop new corrosion preventing techniques. The objective is to find more efficient, environmentally sustainable, and cost-effective solutions for advanced corrosion protection of materials. However, in some applications it is not only corrosion protection that is needed but also wear resistance is required.

Relatively thick PVD coatings are generally used in applications where wear resistance is required. However, achieving simultaneous corrosion protection with that kind of coatings is challenging because the coating doesn't grow conformally and uniformly enough on the nano/microscale details of the surface of the protected material. This is where ALD coatings are needed: they enable reliable, long-term corrosion resistance through dense, uniform and conformal layers and they block the possible cracks, pinholes and nano/microscale voids and irregularities of the PVD layer, thus improving and securing the performance of the PVD coatings. At the same

time, ALD contributes to structural strengthening and better chemical stability.

The choice and composition of the ALD coatings for corrosion protection depend on the substrate material and the kind of environmental conditions to which the protected components are exposed. Especially, certain metal oxides or their laminates or mixtures deposited by ALD form efficient and functional corrosion protection layers. Optimization of the protective thin film thickness and composition has been performed during the last three years in the European Union 7th Framework Program collaborative project CORRAL ("Corrosion protection with perfect atomic layers" [CPFP213996-1]).

In the present work, high-quality coatings with less than 0.001 % porosity were achieved. The coatings were able to seal 100Cr6 steel substrates for over 800 h in neutral salt spray tests (NSS). The lifetime of 3D test components was increased by a factor of 3-10 depending on the substrate material.

Surface Science

Room: 21 - Session SS-MoM

Nonequilibrium and Nonlinear Processes

Moderator: D. Diesing, University of Duisburg-Essen, Germany, E. Karpov, University of Illinois at Chicago

8:20am **SS-MoM1 Hot Electron Flow Generated by Photon Absorption Probed with Metal-Semiconductor Nanodiodes**, *J.Y. Park, Y.K. Lee*, KAIST, Republic of Korea

A continuous flow of hot electrons that are not at thermal equilibrium with the surrounding metal atoms is generated by the deposit of energy from the external source to the surface through nonadiabatic electronic excitation. Here we show that hot electron flow generated on a gold thin film by photon absorption (or internal photoemission) is amplified by localized surface plasmon resonance. This was achieved by direct measurement of photocurrent on a chemically modified gold thin film of metal-semiconductor (TiO₂) Schottky diodes. Photons coupled into the modified gold thin film excite surface plasmon resonance, which enhances hot electron flows going over Schottky barrier between the gold film and TiO₂. The short-circuit photocurrent obtained with low-energy photons is consistent with Fowler's law, confirming the presence of hot electron flows. The morphology of the metal thin film was modified to a connected gold island structure after heating such that it exhibits surface plasmon. Photocurrent and optical measurements on the connected island structures revealed the presence of a localized surface plasmon at 550 ± 20 nm. The results indicate an intrinsic correlation between the hot electron flows generated by internal photoemission and localized surface plasmon resonance. We discuss the effect of dye molecules or metal nanowires on gold film in the efficiency of internal photoemission.

8:40am **SS-MoM2 The Nature of Charge Transfer at Metal-Liquid Interface: Equilibrium vs. Non Equilibrium Processes**, *D. Bürstel, M. Scheele, I. Nedrygailov, D. Diesing*, University of Duisburg-Essen, Germany

The hydrogen evolution reaction is one of the key reactions in catalysis whereby protons from a liquid phase discharge at a metal surface and form atomic hydrogen. A correlation between the reaction rate and the chemisorption energy of the metal-hydrogen species (so called Volcano plot) was motivated for decades by an exponentially increasing reaction rate originated from a stronger chemisorption energy by arguments from the equilibrium thermochemistry. Progress in the study of metal-gas phase interactions points to electronically excited states, when atoms adsorb on a metal or chemical reactions with molecules occur. Up to now metal-liquid interfaces are not in the focus of research activities considering non equilibrium processes in the course of interfacial chemical reactions. We show experimental concepts how reactions on metal-liquid interfaces can be reviewed with respect to the existence of chemically induced electronic excitations. In a theoretical model we show that even small deviations from the electronic equilibrium may change the rate of the discharge reaction of protons on metal surfaces.

9:00am **SS-MoM3 Probing Surface Chemical Reactions with Metal Nanofilm - Semiconductor Schottky Diodes**, *I. Nedrygailov, E. Hasselbrink, D. Diesing*, University of Duisburg-Essen, Germany

Most catalytic chemical reactions are complex processes, which include a variety of steps such as molecular and dissociative adsorption on a solid surface, interactions between intermediates, and desorption of products from the surface to the gas phase. Considerable effort has been made to

achieve a detailed microscopic understanding of the dynamics of these processes using different experimental and theoretical methods, nevertheless still little is known about the routes of energy transfer accompanying the gas-surface interactions. As shown by McFarland, Nienhaus and coworkers, dissipation of chemical energy, released in catalytic reactions on metals, may proceed non-adiabatically by transferring a part of the energy into electronic degrees of freedom. This process is caused by a nonequilibrium state of the adsorbate surface complex and leads to the excitation of highly energetic (hot) electrons and holes in the metal surface. Detection of the excited charge carriers in metals is rather challenging because they relax within some 10 fs due to scattering processes (including electron and phonon pathways). A loophole is the use of metal nanofilm - semiconductor Schottky diodes. A ballistic transport of the excited charge carriers from the metal surface, where the excitation takes place, into the underlying semiconductor is possible in such diodes allowing for the direct detection of the hot electrons and holes as a chemicurrent. Detailed studies of chemicurrents can further our knowledge about the role of electronic and nuclear degrees of freedom in the dissipation of the chemical energy and thereby can give us a key for understanding of surface dynamics. In this contribution, we report on our methodology of nanofilm Pt-SiO₂-Si Schottky diodes manufacturing and their application as detectors for chemically induced currents. We show experimental results with currents of up to several μ A detected in the Pt-SiO₂-Si diodes while the Pt top electrode is exposed to molecular hydrogen, oxygen or their mixtures with different molar ratios and a pressure in the range of 1 - 10 mbar. Thermal effects and electronic excitations in the Pt top electrode of Pt-SiO₂-Si diodes, caused by the water formation reaction, are considered as possible sources of the observed currents.

9:20am **SS-MoM4 Non-adiabatic Electronic Effects in Multiquanta Energy Transfer and Reactions at Metal Surfaces: Do We Need to Go Beyond the Electronic Friction Picture?**, *D.J. Auerbach*, University of California, Santa Barbara, *K. Golibrzuch*, University of Göttingen, Germany, *A. Kandratsenka*, Max Planck Institute for Biophysical Chemistry, Germany, *R. Cooper, C. Bartels*, University of Göttingen, Germany, *I. Rahinov*, The Open University of Israel, *A.M. Wodtke*, University of Göttingen, Germany

Interactions of molecules at metal surfaces can result in nonadiabatic electronic energy exchange with the metal. This complicates theoretical strategies designed to simulate surface reactivity, most of which today are based on the assumption that the electronic motion can be treated adiabatically, i.e. within the Born-Oppenheimer approximation. One widely applied electronically nonadiabatic theory that makes the leap beyond the Born-Oppenheimer approximation is "electronic friction". In this method coupling of adsorbate motion to metal electrons is treated as a weak perturbation involving frictional forces modifying the molecular dynamics in a systematic and simple way.

Recent experiments on multiquantum vibrational excitation at metal surfaces suggest that at least for certain systems, multi quantum transitions involve energy transfer between the molecule and a single electron hole pair of the solid. These processes might better be described as an electron transfer reaction than as friction. These results suggest that theoretical approaches that go beyond electron weak coupling and electronic friction will be needed to properly treat electronically nonadiabatic effects in surface chemistry.

9:40am **SS-MoM5 Experimental Evidence of Non-adiabatic Effects in Gas-Surface Interactions**, *H. Nienhaus*, University of Duisburg-Essen, Germany **INVITED**

The perturbation of the electronic system during gas-metal interactions can cause significant electronic excitations with lifetimes on the femtosecond timescale [1]. Such non-adiabatic processes occur when electronic states are injected below the Fermi level such rapidly that the occupation of the states by resonant charge transfer is delayed. According to Zener's criterion [2] this happens more likely in cases of fast nuclear motion and of low coupling between gas particle and metal states. Experimental evidence of chemically induced electronic excitations is gained by detecting exoelectron emission into the vacuum, surface chemiluminescence and internal hot hole or hot electron chemicurrents. The latter method uses thin-film electronic devices with internal potential barriers as high-pass energy filters. Metal-semiconductor (Schottky) diodes are the most prominent examples for sensitive detectors of both, hot charge carriers and chemiluminescence photons. Independent measurements of the phenomena uncover the various excitation mechanisms. An empty state below the Fermi level may inject a hot hole into the band of occupied electronic metal states or can be filled after Auger relaxation leading to an excited electron in the metal surface. For the oxidation of metals these two fundamental processes can be experimentally distinguished. In addition, it is shown that rapid state injection does not necessarily imply the dissociation of the oxygen molecule as peroxide formation also leads to a significant excitation of the electronic

system. The non-adiabatic energy transfer can be associated with a rapid intermolecular motion of the oxygen atoms during the reactive collision. The interaction of chlorine with potassium will be discussed as an example for a strong chemiluminescence reaction. By use of K/Ag/Si-multilayer Schottky diodes the coupling between emitted photons and Ag surface plasmons leads to an enhanced photocurrent in the device at a typical Ag film thickness of around 50 nm. Competing effects in the devices due to adiabatic energy dissipation, e.g., local heating of the system, are discussed. In the experiments such can be either certainly excluded or clearly separated from the non-adiabatic signatures.

[1] B.I. Lundqvist et al. in : Handbook of Surface Science, Vol. 3, Eds.: E. Hasselbrink and B.I. Lundqvist (North-Holland, Amsterdam, 2008), pp. 430-524.

[2] C. Zener, Proc. R. Soc. Lond. A 137 (1932) 696.

11:20am SS-MoM10 Analysis of Chemicurrent Components Induced by Hydrogen Oxidation on Pt/n-GaP and Pt/n-SiC Planar Schottky Nanostructures, S. Dasari, M. Hashemian, E. Karpov, University of Illinois at Chicago

Studies of chemically induced hot electron flow over Schottky barriers in planar metal-semiconductor nanostructures provides interesting possibilities for electrolyte-free conversion of chemical energy into electricity in solid-state devices and ultra-fast sensor applications. A method is described here to separate the hot electron current contribution to the total generated current based on in-situ resistive heating of cathode nanolayer of the Schottky structure. The total current is comprised of the hot electron and thermal components. The method preserves usability under application-relevant conditions requiring lower sample temperatures and higher pressures of a reactive gas mixture. Analysis of the current induced during oxidation to water of molecular hydrogen in 60-150 Torr mixtures on Pt/n-GaP nanostructure surface at 341-433 K is performed. Hot electron contribution to the total current has a nonmonotonic dependence on temperature, and its fraction reaches 25% at 341 K and 32% at 433 K. We also found that adsorption of molecular hydrogen and nitrogen gases on Pt/SiC planar nanostructure at normal atmospheric conditions leads to generation of a detectable chemicurrent only in the case of hydrogen. Nitrogen admission conditions were tuned to imitative an equal or greater thermal effect of adsorption as observed during admission of hydrogen gas; therefore the recorded chemicurrent cannot be thermally driven. Adsorptive chemicurrents can occur from admission of hydrogen to samples not only at pre-vacuum conditions, as in earlier studies, but also in reactive and inert gas mixtures at normal atmospheric pressure.

11:40am SS-MoM11 Enhanced Chemicurrent Effect of H₂ Oxidation on Porous MIM Nanostructures, E. Karpov, M. Hashemian, S. Dasari, University of Illinois at Chicago

Understanding of the basic charge transfer processes at solid interfaces with reactive gas mixtures is a pathway toward advanced sensing, novel catalytic and energy conversion applications. In particular, currents induced in surface reactions on catalytic nanofilms forming Schottky or MOS type contact with a semiconductor substrate have received considerable attention during the last decade. Physical nature of these currents is intriguing, since the Schottky nanofilm device contains no explicit ion conductive layer, and it resembles a photovoltaic cell much closer than an electrochemical device. In this presentation we report on observation stationary chemicurrents in the 0.1 mA/cm² range induced by molecular hydrogen oxidation on surface of porous Pt/TiO₂/Ti nanostructures with a potential barrier at room temperature conditions. Possible physical and chemical mechanisms of the current production are discussed.

Thin Film

Room: 11 - Session TF-MoM

ALD Enabled Applications

Moderator: W.M.M. Kessels, Eindhoven University of Technology, the Netherlands

9:00am TF-MoM3 Atomic Layer Deposition Films as Diffusion Barriers for Silver Artifacts, A.E. Marquardt, University of Maryland, E. Breitung, E-Squared Art Conservation Science, G. Gates, T. Drayman-Weisser, The Walters Art Museum, G.W. Rubloff, R.J. Phaneuf, University of Maryland

In this work we investigate atomic layer deposition (ALD) to create transparent oxide diffusion barrier coatings to reduce the rate of tarnishing for silver objects in museum collections. Elevated heating and H₂S pressure tests determined the effect of various thicknesses of Al₂O₃ ALD thin films,

ranging from 5 to 100nm thick, and the effect of annealing temperature on the thickness of the tarnish layer (Ag₂S) created at the interface of the ALD coating and the silver substrate. Reflectance spectroscopy and an integrated sphere spectrophotometer were used to measure the thickness of the tarnish layer and indicate the effectiveness of the Al₂O₃ ALD thin films in reducing the tarnishing rate of silver while minimally affecting the visual appearance of the silver. X-ray photoelectric spectroscopy (XPS), and time of flight secondary ion mass spectroscopy (TOF-SIMS) analysis determined the concentration profile of sulfur through the ALD oxide film. A model for predicting the tarnishing kinetics of sulfur diffusion through ALD oxide films is established, influenced by the composition of the alloy, phase of sulfide at the interface, and non-uniformity of diffusion due to pinhole and concentration dependence. Evidence was found for the slow diffusion of sulfur through the bulk of the films and faster diffusion through pinholes in the ALD oxide films.

9:20am TF-MoM4 Quasi-ALD for Deposition of a Water Resistive Barrier Layer and Prevent Electronic Devices from Water Shock, V. Gupta, M.R. Linford, Brigham Young University

Water resistant surfaces and devices have an ever increasing importance in various areas of technology, including electronics (e.g., cell phones), fabrics, shoes, chemical handling equipment, and hearing aids to name only a few. However, while important and effective against splashes, ultrathin hydrophobic films are not always sufficient for water proofing devices. Herein we describe the development of a water resistant barrier layer, deposited by a method similar to atomic layer deposition, which can also be made hydrophobic by deposition of fluorosilanes, for imparting improved protection against water to underlying surfaces and devices. The resulting barrier has been found effective in resisting the infiltration of water and preventing underlying surfaces such as electronic circuits from water shock. The precursors we use appear to have low toxicity in their molecular and (especially) deposited form, are inexpensive, have good vapor pressures so they can be deposited at low temperature, and can be deposited in a straightforward manner because of their high reactivity. Different plasma pre-treatments of substrates have been studied, although good uniformity in the deposition takes place on substrates, such as Si/SiO₂ and nylon, that have not been primed in any way. Film growth on Si/SiO₂ and nylon spin coated onto Si/SiO₂ has been monitored by spectroscopic ellipsometry, which shows consistent increases in film thickness with deposition cycles, contact angle goniometry, which shows similar wetting properties for all layers of the films and is consistent with deposition of a constant surface chemistry, XPS, which shows the expected elements in the film, AFM, which provides surface roughness, and ToF-SIMS, which is also a probe of the surface chemistry. This barrier layer has been tested on model circuit boards and results are consistent with both the number of layers deposited and their mode of deposition. That is, water damage shows a proportional decrease with an increase in the number of the above mentioned layers. This process appears to be applicable on multiple substrates ranging from inorganic to organic surfaces. Presently we are working on increasing the number of layers and more effective crosslinking of the films. Additional film characterization will also be done by RBS and NRA.

9:40am TF-MoM5 Atomic Layer Deposition for Astronomy and Space Applications, F. Greer, Jet Propulsion Laboratory/California Institute of Technology

INVITED
Future UV, X-ray, infrared, and sub-millimeter telescopes and spectrometers have the potential to revolutionize our understanding of the formation and habitability of the modern universe. Star formation, dark energy, and the composition of the intergalactic medium are only some of the key scientific topics that can be addressed by UV astronomy and astrophysics. Infrared astronomy enables the hunt for new planets and stars, even through clouds of interstellar dust, while sub-millimeter astronomy can probe the fine structure of the cosmic microwave background, giving glimpses into the early universe immediately following the Big Bang. While existing technology has allowed us to probe deep into the universe, materials or fabrication challenges still limit the sensitivity and capability of the detectors and instruments used in these applications. In this talk, we will first discuss, in general, how the precision and control afforded by atomic layer deposition can be used to substantially increase the capability of astronomers to make new discoveries. Then, we will focus on specific cases to show the impact of ALD films on the coating, passivation, and fabrication of UV, infrared, and submillimeter detectors, respectively. For example, atomic layer deposition coatings utilized in UV instruments, once fully optimized, can yield as much as a 100X increase in signal to noise ratio over conventional technology. Here, we will demonstrate how small changes in nucleation and growth conditions of ALD fluorides, oxides, and transition metal nitrides have a significant effect on the performance of these detectors and other instrument components, even for films with comparable indices of refraction and resistivity. We will also discuss the novel ALD chemistries that we have pursued, e.g. for MgF₂ deposition, in

order to achieve reliable processes. Finally, this presentation will detail the unique surface engineering approaches such as the combination of atomic layer deposition and MBE, demonstrating the advantages that are obtained by achieving atomic level precision at key steps in detector fabrication processes.

10:40am TF-MoM8 ALD-Enabled Pt/HfO₂/Ti and Pt/TiO₂/Ti Tunneling Diodes with Enhanced Tunneling Characteristic, O. Ajayi, G. Mumcu, J. Wang, University of South Florida

Due to its unique resistive switching capability, Metal-Insulator-Metal (MIM) diodes have attracted substantial interests ever since 1960's. The early generation of MIM device (point-contact diode) is composed of a sharp metal tip placed right on top of a planar metal electrode coated with an ultra-thin layer of insulator. It has been envisioned that MIM diodes hold great promise for detecting and mixing high frequency signals up to Terahertz (THz) range. Particularly, several prior works have suggested for operation at THz frequencies, the MIM diodes are anticipated to outperform heterojunction diodes, which have limited cutoff frequency (<3THz). Hence, the MIM devices are well-suited for a wide range of applications in security, imaging and energy scavenging. In lieu of this, microfabricated MIM diodes with low zero-bias impedance have been actively pursued in this work for a strategically-designed antenna-coupled detector with high responsivity.

With introduction of ultra-thin tunneling layer sandwiched between two planar metal electrodes, the microfabricated MIM diodes are amenable for direct integration with ICs. In particular, we have devoted most of our efforts on developing techniques to improve the overall diode characteristics through tuning its tunneling properties. The effective junction capacitance and resistance limit the operation frequency range of tunneling diode. The key factors that affect the frequency range of tunneling diodes are the junction area, defect density, permittivity and thickness of the tunneling layer. For the MIM diode, a small deviation in tunneling barrier thickness can cause a significant change in the junction resistance and its I-V responses. Hence, atomic layer deposition (ALD) process was employed which offer superb uniformity, low defect density, and precise thickness control of the tunneling layer. In this work, MIM diodes with a variety of junction areas ranging from 3 μm^2 to 100 μm^2 have been fabricated with different ALD thin films (e.g., TiO₂ and HfO₂) of varied thicknesses. By systematic investigation of the measured I-V characteristics for MIM devices with a variety of junction materials, junction thickness and junction area, it is evident that the performance of the MIM tunneling diodes can be greatly enhanced through optimizing junction properties (material, thickness, area, etc.). As compared to similar devices reported previously, we have successfully demonstrated high-yield MIM diodes with 1.5nm-thick tunneling junction with unprecedented low junction resistance in the range of 500 Ω or even less, thus resulting in greatly enhanced responsivity.

11:00am TF-MoM9 Uniform Adsorption of Ligand Free Ag Nanoparticles onto TiO₂ Thin Films Deposited by Atomic Layer Deposition, J.C. Halbur, J.S. Jur, North Carolina State University

Nanoparticle modification of inorganic thin films, such as TiO₂ or Al₂O₃, represents a method to enhance or alter the catalytic, antimicrobial, or responsive behaviors of a material. The use of nanoparticle inks for application is challenging, as the nanoparticles tend to be stabilized using surfactants or other molecules during the synthesis process, and these ligands can interfere with or prevent nanoparticle adsorption onto the oxide. This work shows the efficacy to attach ligand-free Ag nanoparticles onto TiO₂ surfaces formed by atomic layer deposition (ALD). Sonochemical synthesis is used to create Ag NPs of 14-20 nm diameter in an aqueous solution at room temperature without the need for additives such as stabilizing agents. After ALD of TiO₂ thin films onto polymer substrates, a facile dip coating process at ambient conditions results in the uniform decoration of the ligand free Ag nanoparticles on the TiO₂ surface. The efficiency of nanoparticle adsorption is examined by TEM and EDS. Finally, the photocatalytic degradation of methylene blue is used to assess the photocatalytic efficiency of the fiber based composite.

11:20am TF-MoM10 Alloy Films Grown Using Al₂O₃ ALD and Alucone MLD: Critical Tensile Strains, Water Vapor Transmission Rates and Compliant Interlayers, S.H. Jen, B.H. Lee, S.M. George, University of Colorado, Boulder, P.F. Carcia, R.S. McLean, DuPont Central Research and Development

Hybrid organic-inorganic alloy films can be grown using Al₂O₃ ALD and alucone MLD. These alloy films may display the excellent gas diffusion barriers properties of Al₂O₃ ALD films and also may be more flexible than Al₂O₃ ALD films. Critical tensile strains (CTSs) and water vapor transmission rates (WVTRs) were measured for the ALD:MLD alloy films using trimethylaluminum, ethylene glycol and H₂O as the reactants. The alloy composition was controlled by varying the ratio of ALD: MLD cycles

during film growth. The CTS reached its highest values of ~1.0 % for the 3:1 alloy. The WVTR decreased 4 orders of magnitude versus alloy composition. The 7:2, 5:1 and 6:1 alloys had the lowest WVTRs of ~1 $\times 10^{-4}$ g/m²/day at the sensitivity limit. These alloys are more flexible than Al₂O₃ ALD and may serve as gas diffusion barriers for flexible thin film devices. The alucone MLD film was also used as a compliant interlayer to minimize stress caused by thermal expansion mismatch between Al₂O₃ ALD films and Teflon FEP substrates. Without the alucone MLD interlayer, the Al₂O₃ ALD films are susceptible to cracking resulting from the high coefficient of thermal expansion mismatch between Al₂O₃ ALD and Teflon FEP. With an alucone compliant interlayer, the Al₂O₃ ALD film has a crack density that is reduced progressively versus alucone interlayer thickness.

Vacuum Technology

Room: 14 - Session VT-MoM

Vacuum Gauging and Metrology

Moderator: G.A. Brucker, Brooks Automation, Inc., Granville-Phillips Products

8:20am VT-MoM1 Sapphire-based Capacitance Diaphragm Vacuum Gauge Operating at 500 °C, T. Ishihara, H. Tochigi, J. Yoshinaga, M. Nagata, Azbil Corporation, Japan

Growing demand of low temperature processing for environmental concern in semiconductors and related technologies, such as organic electroluminescent display processing, now require process materials handling temperature to be higher (250-500°C) than it used to be, especially in vacuum deposition processing. In these applications, self-heating absolute manometers consist of nickel base alloy or ceramics operated up to 200°C are used to avoid deposition. Because of the plasticity of the diaphragm itself or bonding materials, if self-heating temperature becomes higher, characteristics of sensors become worse. So there is strong demand for manometers, which operate stable at 250-500°C. Authors have developed entirely sapphire-based capacitive pressure sensor chip utilizing Micro-Electro-Mechanical Systems technologies that is suitable for high temperature application. In this paper, we present packaging techniques of the sensor chip to construct the sapphire-based capacitance diaphragm vacuum gauge. Fig.1 and 4 show schematic cross-sectional views of a sapphire CDVG, bonding interface, and sensor chip respectively. In the pressure gauge with 0-133.32Pa absolute, packaging requires low mechanical stresses from the exterior metal body to the sensor chip. Generally, braze, solder, and glass are used for packaging, especially for bonding the sensor chip onto the metal body. But these intermediate bonding materials generate higher stress on sensor chip and its creep yields sensor zero point drift or span drift. To avoid these mechanical stresses, the sapphire chip is first bonded to a sapphire disc, which in turn is bonded to the metal body without any intermediate materials. We adopted solid-state bonding techniques, in which 1-10 MPa pressure is applied at bonded parts at a temperature of at least 900°C. Fig. 2 and 3 show the TEM images of bonded sapphire-metal and sapphire-sapphire interfaces used in this package respectively. These images show no observable interlayer, indicating perfect bonding at the atomic level. Fig. 5 shows the pressure sensitivities of this sensor at 500°C, in which error of the span is under 0.05Pa. In Fig. 6 the temperature dependence of zero and span of the sensor at from 200 to 500°C are presented. The span shift at this temperature range is only 0.52Pa. Fig. 7 shows the zero drift at 500°C. About 0.1%FS zero-shift can be seen for 600 hours. Sensor output resolution can be estimated at 0.0039Pa from Fig.8. These results show excellent performance of the sapphire CDVG over 200°C. With advanced packaging technologies, we have realized a sapphire-based manometer that can operate at 500°C, which enables measurement and controls of advanced processes.

8:40am VT-MoM2 On the Stability of Capacitance Diaphragm Gauges, M. Wüest, C. Strietzel, INFICON Ltd, Liechtenstein

Capacitance Diaphragm Gauges (CDG) are extensively used in critical coating industries due to their stated accuracies. However, the process to which the gauge is exposed to as well as the ambient environment can influence the accuracy of the gauge. Observed effects include e.g. zero pressure drift, span drift, noise, or depositions on the membrane. In this talk we will explore these influences on the accuracy.

9:00am VT-MoM3 A Truly Cold Vacuum Gauge for Ultra-high Vacuum and Extreme-high Vacuum Employing a Hydrogen Adsorber, G.A. Mulhollan, Saxet Surface Science

INVITED
Conventional gauging techniques for ultra-high vacuum (UHV) and extreme-high vacuum (XHV) employ a hot filament or a plasma discharge, thereby ionizing the background gas molecules so that they can be collected

and signal processed, to meter the vacuum pressure. Filaments emit heat and electrons, both of which can raise the system pressure. Stray electrons and ions from cold cathode discharges can have much the same effect. XHV metering limiting characteristics include x-ray induced errors and extinguished discharges. At UHV and XHV pressures, the predominant gas species is hydrogen. Little error is incurred in the total vacuum pressure value if only the hydrogen pressure is metered via absorption. While several techniques sensitive to hydrogen adsorption in the pressure ranges of interest could be employed to take advantage of this fact, careful consideration led to the selection of the titania nanotube array as the active element for a hydrogen absorbing vacuum gauge. Such arrays exhibit very large responses to hydrogen at atmospheric pressures.

In this relative gauging method, the titania nanotube array is mounted onto a UHV/XHV compatible header which in turn is affixed to a floating feedthrough. The feedthrough permits a bias to be applied across the array, resulting in current flow. The ensuing current flow, together with the bias value, allows an effective resistance to be calculated. The value of this resistance is proportional to the cumulative hydrogen impingement and restorative exposure history of the array, thereby enabling hydrogen as a vacuum constituent to be monitored. The metering activity is completely quiescent with respect to stray charged particle and heat generation. The ensuing gauging process has been shown to deliver excellent hydrogen gas response in vacuum. Enhanced sensitivity for XHV vacuum monitoring is achieved through illumination boosting. Alternate sensor materials, restorative methods and ultimate sensitivity limits will be discussed.

9:40am **VT-MoM5 Investigation of Pumping Combinations to Achieve XHV**, *M.L. Stutzman, P.A. Adderley*, Thomas Jefferson National Accelerator Facility, *M.A. Mamun*, Old Dominion University, *M. Poelker*, Thomas Jefferson National Accelerator Facility

The spin-polarized electron beam used at Jefferson Lab's nuclear physics accelerator is generated through photoemission from a strained-superlattice GaAs/GaAsP photocathode. The operational lifetime of the photogun depends strongly on the pressure in the system since residual gasses are ionized by the electron beam and accelerated into the photocathode causing damage. To date, photoguns at Jefferson Lab have relied on NEG and ion pumps. Incremental vacuum improvements have been made through a combination of better bake protocol, chamber heat treatment, NEG pump geometry and activation protocol, improved ion pump technology and the addition of a load-lock to enable photocathode replacement without venting the photogun. This work describes pressure measurements inside a gun-style vacuum chamber with a commercial bakeable cryopump in addition to the NEG and ion pumps. Much of the talk will focus on an assessment of our ability to measure the pressure in the system using three commercial UHV/XHV vacuum gauges.

10:00am **VT-MoM6 Beyond Mercury Manometers: Are Optically-Based Primary Standards for Realization of the Pascal Within Reach?**, *J.H. Hendricks, J.A. Stone, G.F. Strouse, D.A. Olson, J.E. Ricker*, National Institute of Standards and Technology

We propose to fundamentally change the method for realizing and disseminating the SI unit of pressure and vacuum, the pascal. The underlying metrology behind this advance is the ultra-accurate determination of the refractive index of gases by picometer optical interferometry. For the pascal an optical-based primary pressure standard will improve accuracy and allow the complete replacement of all mercury-based pressure standards. Pressure and vacuum standards based on refractive index could significantly reduce measurement uncertainties with the added advantage of eliminating the need for mercury manometers, which are expensive to operate and have environmental and health hazards. Mercury manometers currently serve as primary standards at 11 National Metrology Institutes (including NIST and PTB). Developing an optical-based pressure standard is central to the NIST measurement science mission, as it will improve NIST realization and dissemination of an important SI unit and will provide a needed improvement in accuracy (3X to 10X) across many industrial sectors (e.g. aerospace, energy, and advanced manufacturing) and benefit other government agencies (e.g. DoD, FAA, NASA, DARPA, and the EPA). The primary goal of the research is to develop a laser-based, SI-traceable pressure standard (1.5 ppm, k=1) along with a transportable version that can be deployed to industry covering a range of 1 Pa (vacuum) to 400 kPa (4 atmospheres pressure). The two instruments that will be developed are referred to as a variable-length optical cavity (VLOC) and a fixed-length optical cavity (FLOC). When either instrument is used as a pressure standard it is referred to as an optical interferometer manometer (OIM). The primary technical challenge involves building an apparatus to generate and precisely measure equal displacements of Fabry-Perot interferometer mirrors in vacuum and in a helium environment to picometer accuracy, thus determining refractive index in a manner that allows absolute measurement of pressure or temperature if one of these two quantities is known. More specifically, the

refractive index, n , as measured by the VLOC, is intrinsically related to density such that $n-1$ depends on P/T , where P is the pressure and T is the temperature. The current state of primary mercury manometers in use at NIST will be discussed along with technical challenges of developing an optical based primary standard.

10:40am **VT-MoM8 Reduction of Statistical Scatter of Spinning Rotor Gauge Readings by Operation at Higher Rotational Frequency**, *J. Setina*, Institute of Metals and Technology, Slovenia

First spinning rotor gauge (SRG) controllers had a fixed window of operational frequency from 405 to 415 Hz. Newer controllers have a much wider range of possible rotor frequencies from 405 Hz to 810 Hz. Most users still prefer lower rotor frequencies because the SRG residual drag and its frequency dependence increases significantly with increased rotor speed. However, by increasing rotor speed the number of revolutions in a fixed sampling interval is also increased, which means reduction in statistical scatter of readings. From operational theory of SRG the standard deviation of readings shall decrease proportional to $(\text{frequency})^{-1/2}$ but we have found that in reality it decreases much more. At fixed sampling interval we get 4 times or more reduction of standard deviation when rotor frequency is increased from 410 Hz to 800 Hz. The reason is that when operational frequency increases, the amplitude of induced signal in pickup coils for detection of rotor frequency also increases. In a separate experiment we have observed that with stronger pickup signal the standard deviation of readings decreases. For applications where shorter response time of SRG is critical and frequency dependence of residual drag can be corrected or tolerated, we recommend operation at highest rotational frequency. We have found that typical standard deviation at rotor frequency 800 Hz and sampling interval of 5 s is smaller than at rotor frequency 410 Hz and sampling interval of 10 s.

11:00am **VT-MoM9 Long-Term Stability of Hot-Filament Metal-Envelope Enclosed Ionization Gauges**, *J.A. Fedchak*, National Institute of Standards and Technology

Hot-filament ionization gauges are used as secondary standards by calibration laboratories and as transfer standards in intercomparisons among metrology laboratories. A quantitative measurement of gauge stability with respect to the gauge calibration factor is critical for these applications. In addition, gauge stability is important for those who use gauges for process monitoring and control, and for monitoring vacuum quality. We determined the long-term calibration stability of hot-filament metal-envelope enclosed ionization gauges based upon the analysis of repeat calibrations of nine gauges over a 15 year period. All of the gauges were Bayard-Alpert type ionization gauges with an integral metal-envelope surrounding the hot-filament, grid, and collector. The gauges were calibrated repeatedly at the National Institute of Standards and Technology (NIST), but are owned by organizations external to NIST. In all cases, the gauges were removed from the NIST high-vacuum standard after calibration, shipped back to the gauge-owner, and were returned to NIST at a later date (more than 1 year) for re-calibration. Here we present results of the stability study along with discussion of the NIST high vacuum standard and ionization gauge calibration methods.

11:20am **VT-MoM10 Non-Destructive Gas Pressure Measurements Inside Sealed Vacuum Devices**, *R.S. Goeke, T.P. Hughes*, Sandia National Laboratories

Measuring the pressure inside sealed vacuum devices is a difficult proposition that typically requires destructive analysis. While commercial vacuum pressure gauges can be applied to large vacuum envelopes, the gauge's large volume and mass make them impractical for the small volumes of many vacuum devices. Incorporation of smaller volume pressure gauges such as the spinning rotor gauge or capacitance manometers can interfere with the device functionality. Measurements on these small vacuum devices can be done by a destructive technique where the device is punctured inside a calibrated ultra-high vacuum (UHV) vessel. With this technique the tube pressure is calculated from the changes in pressure of the UHV chamber and ratio of the chamber volume to tube volume. We have developed a non-destructive method by which the pressure inside high vacuum devices can be characterized without modifying or damaging the vacuum envelope. The approach transforms the existing vacuum device into a Penning or Redhead style ion gauge. We take advantage of the device features such as existing electrodes and high voltage standoff capability. By creating optimized crossed electrical and external magnetic fields around the vacuum envelope, we can generate a self-sustained Townsend discharge current which can be directly related to pressure. This technique is similar to the cold cathode gauge first developed by Penning, which was later modified by Redhead into the inverted magnetron gauge. In a typical cold cathode gauge the electrodes are a cylindrical design, with coaxial symmetry, which enables application of a uniform cross magnetic field. In many vacuum devices this coaxial

electrode symmetry is not available. We overcome this obstacle by applying a ring-shaped magnetron magnet to the cathode electrode of a sealed vacuum device. In this arrangement the magnetic fields are not uniform, but the electron paths can still be significantly increased and even trapped resulting in enough ionization for a sustained discharge. The experimental technique to measure the time dependent pressure inside sealed vacuum devices non-destructively will be discussed. The novel concept of this technique is that we use the existing vacuum device as its own measurement gauge, with only the application of external fields and instrumentation. We have experimentally demonstrated a measurement range of 10^{-6} to 10^{-2} torr. A computer model of electron paths with some simple electrode geometries has been developed from which basic design guidelines can be derived. The model uses the Aleph finite-element particle-in-cell code developed at Sandia National Laboratories.

Sandia National Laboratories is a multi-program laboratory managed and operated by Sandia Corporation, a wholly owned subsidiary of Lockheed Martin Corporation, for the U.S. Department of Energy's National Nuclear Security Administration under contract DE-AC04-94AL85000

11:40am **VT-MoM11 Vacuum Gauge Operation in Noisy Accelerator Environments**, *L. Smart*, Brookhaven National Laboratory

In the BNL Collider-Accelerator vacuum systems, many gauges are installed near subsystems that present challenges to obtaining noise-free gauge readings. Superconducting magnets, beam diagnostics & control elements, and even sunlight are some of the major contributors to nuisance variations in indicated pressure. Sometimes tried-and-true abatement techniques cannot be implemented, so compromises must be made. Observations and mitigation solutions for hot cathode, cold cathode, and convection-pirani gauges will be presented.

Monday Afternoon, October 29, 2012

Actinides and Rare Earths Focus Topic
Room: 6 - Session AC+TF+SS+MI-MoA

Actinides and Rare Earths: Thin Films and Surface Science

Moderator: R.K. Schulze, Los Alamos National Laboratory

2:00pm **AC+TF+SS+MI-MoA1 Rare Earth 4f Hybridization in Gallium Nitride.** *J.W. McClory, S.R. McHale*, Air Force Institute of Technology, *L. Wang, W.N. Mei*, University of Nebraska-Lincoln, *J.C. Petrosky*, Air Force Institute of Technology, *J. Wu, R. Palai*, University of Puerto Rico – San Juan, *Ya.B. Losovyj*, Louisiana State University, *P.A. Dowben*, University of Nebraska-Lincoln

INVITED

The location of the Gd, Er and Yb 4f states within the GaN valence band has been explored both experimentally and theoretically. The 4d – 4f photoemission resonances for various rare earth doped GaN thin films (RE = Gd, Er, Yb) provide an accurate depiction of the occupied 4f state placement within the GaN valence band. The resonant photoemission show that the major Er and Gd rare earth 4f weight is at about 5-6 eV below the valence band maximum, similar to the 4f weights in the valence band of many other rare earth doped semiconductors. For Yb, there is very little resonant enhancement of the valence band of Yb doped GaN, consistent with a largely 4f^{14-d} occupancy. The placement of the rare earth 4f levels is in qualitative agreement with theoretical expectations.

2:40pm **AC+TF+SS+MI-MoA3 Revisiting the Yb Electronic Structure with Low-Energy Photoemission Spectroscopy.** *F. Offi*, CNISM and Univ. Roma Tre, Italy, *P. Vilmercati, L. Petaccia, S. Gorovikov*, ELETTRA Sincrotrone Trieste, Italy, *A. Ruocco*, CNISM and Univ. Roma Tre, Italy, *M.I. Trioni*, CNR-ISTM, Milano, Italy, *A. Rizzo*, CNISM and Univ. Roma Tre, Italy, *A. Goldoni*, ELETTRA Sincrotrone Trieste, Italy, *G. Stefani*, CNISM and Univ. Roma Tre, Italy, *G. Panaccione*, CNR-IOM, Basovizza-Trieste, Italy, *S. Iacobucci*, CNI-IFN, Rome, Italy

The peculiar electronic structure of rare-earth elements and compounds is mostly defined by the partially filled 4f band. Of particular interest is the investigation of the valence states, which is linked to the degree of hybridization of f electrons with delocalized s-d bands. In the simple case of Yb, the 4f states are fully occupied with a Fermi level of 6s character and a 2+ valency. However, the occupation of the Yb valence band has been the subject of several investigations over the years, intended in particular to separate the contribution of 5d states. Early experimental photoelectron emission (PES) spectra at very low excitation energy ($h\nu < 10$ eV) have reported a spectral modulation in the region close to the Fermi level that was attributed to the emission from a 5d band. The poor energy resolution did not allow however a detailed investigation of such spectral features. In recent years this low energy photoemission spectroscopy (LEPES) encountered a renewed interest, under the stimulus of the extremely high energy resolution obtainable with laser excited LEPES and given the expectation of a large increase of the bulk sensitivity at these low energies. We monitored the 4f spectral intensity in polycrystalline Yb films in the LEPES regime (between 5.5 and 21 eV photon energy, with experiments at the BaDELPH beamline of the ELETTRA synchrotron radiation facility), observing a moderate increase of the electron attenuation length and, thus, a moderate increase of the information depth when we reach the lowest energies. By lowering the photon energy below about 11 eV a prominent peak at the Fermi level is observed. The analysis of its intensity variation versus photon energy and the comparison of the experimental spectra with *ab initio* density of states (DOS) calculations allow to attribute this structure to a p band crossing the Fermi level, enhanced at selected photon energies due to the influence of the empty DOS, probably amplified by a photoionization cross section effect and by the general increase of the photoelectron yield at low photon energy. In this respect LEPES may thus be considered as a probe of the joint DOS.

3:00pm **AC+TF+SS+MI-MoA4 Erbium Rare Earth Thin Film Hydride Stress Studies as a Function of Processing Techniques.** *J.L. Provo*, J.L. Provo Consulting

An important part of understanding the behavior of rare earth, Group 3A and 4A thin film hydrides is the determination of indirect effects such as stress in the film lattice which can lead to film flaking. In this study, special vacuum sample containers were prepared to observe and record basal-plane film stress levels, and film flaking (optical observations).

The special vacuum sample containers contained erbium deuteride (ErD₂) and erbium tritide (ErT₂) films on AT and BT quartz resonator substrates with chromium underlays in pairs prepared by air-exposure, (in-situ)

evaporate-load and reactive evaporation hydriding techniques. The erbium deuteride samples were prepared as controls for aging studies. All samples were processed with PVD Electron Beam deposition techniques, hydriding techniques mentioned above and a 450°C temperature bakeout and exhaust in consideration of the $\alpha \rightarrow \beta$ crystal phase transformation in crystalline quartz at 573°C.

Samples for the measurement of initial film deposition stress as a function of hydride processing and for the determination of stress produced in ErT₂ films due to the generation of helium-3 with time (i.e., tritium decay) were designed to utilize the double-resonator technique developed by EerNisse(1). Measurements of mass change and induced film stress were determined by frequency measurement changes obtained with a precision frequency counter, data being taken from the output of a one transistor Colpitts type driving oscillator circuit in which the crystal is an integral part.

A summary of initial film deposition stress (tensile) and film aging accumulative stress (compressive) for the erbium films from the different deposition and hydriding techniques is given. Reactively evaporated erbium occluder films were seen to have an initial film deposition tensile stress approximately 5 times less than (in-situ) evaporate-load films and 11 times less than air-exposed loaded films. Accumulative aging compressive stress for erbium occluder films were shown to be more variable but data indicate that reactively evaporated film aging stress is less than that of (in-situ) evaporate-load and air-exposed tritided films.

(1)-J. Appl. Phys. 43, 1330 (1972)

3:40pm **AC+TF+SS+MI-MoA6 Splat Cooling Technique Contributing to Understanding of Uranium Systems.** *L. Havela*, Charles University, Czech Republic, *A. Gonçalves, J.-C. Waerenbogh, L. Pereira*, ITN Sacavém, Portugal, *I. Tkach*, Charles University, Czech Republic, *N.-T. Kim-Ngan*, Pedagogical University Cracow, Poland, *T.B. Scott*, University of Bristol, UK

The splat cooling technique is one of the methods of ultrafast cooling of a melt, particularly suitable for small amounts of material. In particular cases it can help to overcome constraints imposed by thermodynamics. One of them was the issue of magnetic properties of non-stoichiometric Laves phase UFe₂. This compound has a ferromagnetic ground state (with both U and Fe magnetic moments). An excess of U, achieved by quenching, led to the decrease of T_c from 162 K for pure compound to 112 K for UFe_{1.7} [1]. Quenching was, however, unable to provide Fe-rich material, with expected increase of T_c. Using splat cooling of a series of materials with various off-stoichiometry from UFe₂ to UFe₆ we found that the cubic Laves phase structure (with sub-micron grains) can absorb excessive Fe up to the stoichiometry UFe_{2.3}. Additional excess leads to the segregation of α -Fe [2]. The increase of T_c up to 230-240 K was the impact on magnetic properties. The spontaneous magnetization also increases from 1.0 μ_B /f.u. in UFe₂ to 1.9 μ_B /f.u. in UFe_{2.3}. ⁵⁷Fe Mössbauer spectroscopy reveals that the excessive Fe atoms enter the U sublattice and develop higher magnetic moments (approx. 1.0 μ_B /Fe).

Applying the splat cooling technique on pure and doped U metal had the aim to stabilize the high temperature bcc phase (γ -U) to low temperatures, to be able to establish its basic electronic properties. In particular, changes in magnetic characteristics and electronic specific heat can be expected due to the modest volume expansion comparing to orthorhombic α -U. We found that splat cooling reduces the necessary concentration of dopants and U with 12 at.% Mo has no traces of α -U. The Sommerfeld coefficient $\gamma = 19$ mJ/mol K² estimated for pure γ -U is enhanced comparing to 11 mJ/mol K² for pure U splat, which is close to values given in literature [3] for the U metal. The splats exhibit a superconducting ground state with T_c ranging from 1.24 K for pure U to 2.11 K for 15 % Mo. The γ -U superconductivity is characterized by a large critical field exceeding 6 T and a sharp λ -type anomaly in specific heat C_p(T) with the size corresponding to the BCS theory. The superconductivity of a pure U splat, which contains only traces of γ -U, has much lower critical field (0.33 T) and the weak anomaly in C_p(T) does not convince about the bulk character of superconductivity.

This work was supported by Grant Agency of the Czech Republic under the grant No. P204/10/0330.

[1] A.T. Aldred, J.Magn.Magn.Mater. 10, 42 (1979).

[2] L. Havela et al., Intermetallics 19, 113 (2011).

[3] J.C. Lashley et al., Phys. Rev. B 63, 224510 (2001).

4:00pm **AC+TF+SS+MI-MoA7 Investigation of Rare Earth Doped Lithium Tetraborate Glasses with XAFS and Emission and Excitation Spectroscopy**, *T.D. Kelly, J.W. McClory, D.A. Buchanan, A.T. Brant, J.C. Petrosky*, Air Force Institute of Technology, *Ya.B. Losovyj*, Louisiana State University, *V.T. Adamiv, Ya.V. Burak*, Institute of Physical Optics, *P.A. Dowben*, University of Nebraska-Lincoln

The local structure of rare earth doped lithium tetraborate ($\text{Li}_2\text{B}_4\text{O}_7$) glasses has been studied by extended x ray absorption fine structure (EXAFS) at the rare earth L shells and by optical emission and excitation spectroscopies. The samples investigated were 1% rare earth doped by weight with Gd and Nd. The EXAFS signal was recorded in fluorescence mode with the energies calibrated for Nd L1 and L3 edges and Gd L3 edge. X rays were applied to the samples to activate emission and excitation centers in the glasses. The spectra were analyzed to determine rare earth occupation sites in the lithium tetraborate crystal structure and the emission and excitation lines due to rare earth doping.

4:40pm **AC+TF+SS+MI-MoA9 Eu-implanted p-type GaN: Charge-Driven Luminescence Hysteresis and Identification of a Possible Charge-State-Alternation Resonance of the Mg Acceptor**, *K.P. O'Donnell, P.R. Edwards, R.W. Martin*, Strathclyde University, Scotland, UK, *K. Lorenz, E. Alves, V. Darakchieva*, ITN Sacavém, Portugal, *M. Bockowski*, Unipress, Poland

Europium-doped p-type GaN shows *spectral switching* and *luminescence hysteresis* when samples are temperature-cycled between room temperature and 20 K (*K.P. O'Donnell et al, Late News paper at ICPS2012, Zurich*). An explanation of this unusual behaviour may be found in the charge-state dependence of the local structure of the Mg acceptor in GaN, recently modelled by J.L. Lyons et al., (*Phys. Rev. Lett.* 108, 156403 (2012)). Eu ions, sensitive to their local environment, may act as 'spectators' of the charge-induced local distortions. The dominant impurity-induced luminescence spectrum at RT (hereafter, Eu0) *switches completely* to another spectrum (Eu1) when samples are cooled below 25 K. Upon subsequent warming of the sample, Eu1 fades with increasing temperature, as expected, but Eu0 *does not reappear* until the temperature exceeds 150 K; its recovery is complete only above 210 K. The noted temperature extremes correspond to hole localisation (carrier freeze-out) and delocalisation, respectively. Here, we extend Lyons' model to consider the possibility of observing the resonance in which the acceptor alternates rapidly between neutral and negative charge states, leading to a spatial oscillation of the associated defect between Eu0 and Eu1 forms, and describe the possible spectral identification of this resonance.

Applied Surface Science

Room: 20 - Session AS-MoA

Quantitative Surface Chemical Analysis, Technique Development, and Data Interpretation - Part 2

Moderator: J.A. Ohlhausen, Sandia National Laboratories, S. Suzer, Bilkent University, Turkey

2:00pm **AS-MoA1 Polyatomic and Gas Cluster Ion Beam Depth-Profiling: A Model Indicating the Most Appropriate Source for an Arbitrary, Known Polymer Matrix and Estimates of Polymer Sputter Rates**, *P.J. Cumpson, N. Sano*, NEXUS XPS Facility, Newcastle University, UK

There has been excellent progress in the SIMS community in recent years[1,2] to identify the optimum conditions and primary ions for SIMS depth-profiling of polymers. A key step forward was the identification of Type I and Type II behaviour[3], in which polymer damage is dominated by cross-linking and polymer backbone bond-scission respectively. In many cases it is difficult, especially for a non-expert, to judge which of these two types a given polymer matrix is likely to be. For example, PAA, PMAA, PMA and PMMA are of types I, II, I and II respectively, even though their structures are very similar.

We examine this system in detail, largely in the context of XPS where polyatomic and cluster ion sources are set to become much more popular. We develop equations based on a 3D Ising "resistor removal" model. Some of the difficult parameters in this model can be estimated from literature values for rates of cross-linking and bond scission of polymers seen in radiation treatment at much higher energies. This model leads to some reasonably simple equations allowing analysts to make objective estimates of (a) which primary ion source is most appropriate for a particular polymer matrix, and (b) an estimate of the sputter-rate, for any arbitrary polymer matrix whose repeat unit is known.

The reliability of the model is tested using measured sputter rates for samples of 20 polymers using polyatomic (coronene) and GCIB (argon cluster) sources. White-light interferometry combined with a novel kinematic mount for semi-automatic measurement of sputter crater volume have accelerated and improved the accuracy of these measurements.

Finally, based on the new model, we tabulate and plot estimated values for 103 polymers of technological significance.

[1] N. Winograd, *Anal Chem* 77 (2005) 143A

[2] J. S. Fletcher, X. A. Conlan, E. A. Jones, G. Biddulph, N. P. Lockyer, J. C. Vickerman, *Anal Chem* 78 (2006) 1827

[3] C. M. Mahoney, *Mass Spectrometry Reviews*, 29 (2010) 247

2:20pm **AS-MoA2 XPS Profiling of Biosensor Materials with Argon Cluster Ions**, *P. Mack, R.G. White, T.S. Nunney*, Thermo Fisher Scientific, UK, *J.J. Pireaux, P. Louette, N. Wehbe, L. Houssiau*, FUNDP, Namur, Belgium

Sensors for biological compounds are becoming increasingly important in a wide variety of applications. These devices are typically composed of complex stacks of thin/ultrathin layers of biochemical compounds. The overall behaviour of the sensor is strongly influenced by the elemental and chemical properties of the individual layers, but the interactions at layer interfaces may also have an effect.

There is an increasing requirement for compositional profiling of these devices, combining the chemical selectivity and surface specificity of XPS with some kind of ion beam sputtering. Traditional methods such as argon monomer ion profiling can result in a high degree of chemical modification during the acquisition of depth profiles for organic materials. Over the last few years, there have been numerous studies and investigations into the use of argon cluster beams for depth profiling with the goal of preserving chemical information during analysis of organic materials.

This talk will present data from cluster profiling studies of amino acid based biosensors. The chemical variation between amino acid layers is very subtle, but it will be demonstrated that the combination of rapid acquisition XPS and argon cluster profiling is able to characterise the changes in chemistry throughout the layer stack.

2:40pm **AS-MoA3 ToF-SIMS and NanoSIMS Imaging of Uranium Distributions in the Sediment of Hanford Site**, *Z. Zhu, Z. Wang*, Pacific Northwest National Laboratory

Nuclear materials processing over the past seventy years has left approximately 55 million gallons of nuclear wastes stored in underground tanks at Hanford site. Some of these wastes are leaking into the ground and the DOE has been working on developing remediation technologies. As a part of these activities, sediment samples have been extensively studied to understand chemical speciation and aqueous mineral chemistry. Although concentrations and distributions of radioactive elements, such as uranium (U), plutonium (Pu), and technetium (Tc) are of great interest, U is the most important one because its concentration in the wastes is significantly higher compared to other radioactive elements. Previous studies show that the sediment samples contain low concentration of U (<10 ppm). However, non-uniform distribution of U is found, and the U appears to be mainly in micron- or sub-micron-size particles. Although an understanding of the chemistry and speciation of these particles is important, it is extremely difficult to obtain the composition of these particles using conventional analytical capabilities such as AES, XPS, and SEM/EDX because of the low concentration of U in the samples. Secondary ion mass spectrometry (SIMS) can be effectively used to discover the chemical components of these U-containing particles with excellent sensitivity and decent spatial resolution. We used ToF-SIMS and Nano-SIMS to image some of these U-containing particles in the sediment samples. Preliminary results indicated that U was present across the sample at lower concentrations, while spots of sub-micron particles with much higher U concentrations were irregularly distributed. The major elements in these "hot" spots appeared to be uranium, sodium, phosphorus, and oxygen.

3:00pm **AS-MoA4 ToF-SIMS MCs_x^+ Dual Beam Depth Profiling with Improved Dynamic Range**, *S. Kayser*, ION-TOF GmbH, Germany, *N. Havercroft*, ION-TOF USA, Inc., *F. Kollmer, R. Moellers, E. Niehuis*, ION-TOF GmbH, Germany

In recent years MCs_x^+ depth profiling has become increasingly popular for the analysis of thin films using Time-of-Flight SIMS (ToF-SIMS). The MCs_x^+ mode offers quantitative or semi-quantitative SIMS data and allows for the measurement of electropositive and electronegative elements simultaneously by detecting MCs^+ and MCs_2^+ , respectively. In addition, the use of heavy cluster ions like Bi_3^+ or C_60^+ allows for a significant increase of the MCs_x^+ yields by a factor of up to 1000 with respect to Ga as primary ion projectile and leads to a remarkable improvement of the achievable detection limits [1].

However, one disadvantage of current TOF-SIMS instruments for the quantification in MCs_x^+ mode is the limited dynamic range, which restricts the possibility of achieving high sensitivity on the MCs_x^+ clusters and of using the Cs_x^+ intensity for normalization. The normalization is especially important for the analysis of layer systems where sputter rates or the cesium surface concentration might change from layer to layer. This requires a registration system which is able to detect more than 100 secondary ions of a specific element per primary ion gun pulse with high linearity.

We have developed a new registration system for TOF-SIMS, which increases the useable dynamic range by a factor of 100 i. e. 1E7 counts/sec with an excellent linearity. In addition, the maximum pulsed primary ion current of the bismuth liquid metal ion gun was increased in order to further improve the detection limits for low concentration elements. In this paper we will discuss the characteristics of this new experimental setup and the benefits for the quantitative depth profiling in the MCs^+ mode.

[1] E. Niehuis, T. Grehl, F. Kollmer, R. Moellers, D. Rading, SIMS Europe, Munster, 2006

3:40pm AS-MoA6 Surface Diffusion of Carbon on Metals and Complications for Auger Spectroscopy of Carburized Steels, *W.D. Jennings*, Case Western Reserve University **INVITED**

The development of low temperature colossal super saturation of stainless steels produces carburized case hardened materials with superior corrosion resistance and mechanical properties. Auger characterization of these materials requires line scan analysis of steel cases that contain substantial carbon concentration. Long acquisition times and surface migration of contaminating carbon complicate the measurement process, and lead to the need for continuous ion sputtering during acquisition of Auger spectra. This process in turn leads to the further complication of differential sputtering effects which alter the apparent composition of the material. This study details the corrections to the Auger relative sensitivity factors needed to achieve accurate characterization of these materials. Fundamental measurements of carbon surface diffusion are also presented.

4:20pm AS-MoA8 Charge Referencing Complex Organic Materials in XPS using Hexatriacontane, *L. Lohstreter*, Medtronic, Inc.

Excess charge build up on insulators can obscure interesting chemical shifts during XPS analysis. The common practice to correct for this is to charge reference the C1s peak of organic materials to 285 eV, the C-C, C-H bond that is ubiquitous due to atmospheric hydrocarbon contamination. However, for samples with complex organic chemistry, it is often the very information within the C1s envelope that is in question. Moreover, the peak can be convoluted with no distinct shoulders. This makes shifting the maximum of the peak to 285 eV a dubious process with little assurance that it will correlate to the true chemistry of an unknown sample. This work will show that even unknown, complex C1s envelopes can be accurately charge referenced with a combination of an application of hexatriacontane to the surface and spectral subtraction. Applications in model material characterization and plasma treated surfaces will be discussed.

4:40pm AS-MoA9 PADI: Ambient Surface Analysis of Polymers and Molecules – Metrology Development for Reliable Analysis, *T.L. Salter, I.S. Gilmore*, National Physical Laboratory, UK

Reliable and repeatable measurements are essential for the strong uptake of any analytical technique. Ambient surface mass spectrometry has demonstrated exciting and revolutionary measurement capability but for wider acceptance in industry they need a secure metrology foundation. Plasma sources are increasingly being used since the development of DART (direct analysis in real time) in 2005 and subsequent imaging methods such as PADI (plasma assisted desorption ionisation)² and LTP (low temperature plasma)³. Here, we commence establishing the essential metrology for PADI, which has already been shown to be successful at analysing pharmaceuticals² and personal care products⁴. A detailed study of the instrumental contributions to the spectral repeatability is conducted. Firstly, we identify and separate out the contributions to the repeatability (relative standard deviation) of the peak intensities. We show that the Thermo LTQ-Orbitrap mass spectrometer used in the study has a noise distribution approximately as expected for random noise. However, the standard deviation of the peak intensity is proportional to the peak intensity which is clearly not random but related to systematic effects in the source operation. Optimisation of the plasma source is essential for ensuring robustness and reliability. We show how the signal varies with geometry, helium flow rate and plasma power. Thermal imaging of the sample surface shows that the temperature rises approximately linearly with plasma power and at 19 W is 70°C. To reduce the effects of damage for surface sampling, we recommend keeping the surface temperature below 40 °C by operating at less than 15 W. General guidance is given for practical analysis. Importantly, PADI can analyse a wide variety of polymers. Analysis of polymers gives mass spectra with repeating series containing different

fragments and adducts. Preliminary studies of sample surfaces after PADI analysis show that the chemical damage, quantified by XPS, is less than 10%. With the recommended operating parameters, the plasma erodes the polymer sample at a rate of 0.87 nm s⁻¹ (for PMMA). This shows the potential for polymer depth profiling.

References

1. RB Cody, JA Laramee, HD Durst, *Analytical Chemistry* **2005**, *77*, 2297.
2. LV Ratcliffe, FJM Rutten, DA Barrett, T Whitmore, D Seymour, C Greenwood, Y Aranda-Gonzalvo, S Robinson, M McCoustra, M. *Analytical Chemistry* **2007**, *79*, 6094.
3. JD Harper, NA Charipar, CC Mulligan, XR Zhang, RG Cooks, Z Ouyang, *Analytical Chemistry* **2008**, *80*, 9097.
4. TL Salter, FM Green, N Faruqi, IS Gilmore, *Analyst*, 2011, *136*, 3274.

5:00pm AS-MoA10 Ion Beam Analysis of Surfaces and Thin Films, *L.S. Wielunski, R.A. Bartyński*, Rutgers University

Rutherford Backscattering (RBS) of ~2MeV He ions is well known technique used in surface and thin film analysis. This technique is very sensitive to heavy elements (Au, Pt, Hf, In, Ru) present on surface or in thin film on lower mass substrate (Si, Ti, Cr, Fe, Ge), but have very limited sensitivity for low mass elements on heavy mass substrates. Numbers of examples will be shown for both cases.

Nuclear reaction analysis (NRA) is very good alternative for detection of low mass elements in a heavy elements substrates. This technique uses similar experimental set-up as RBS but is using a different ion beam and it detects different particle. Examples will be shown for Li detection on steel and in LiFePO₄ crystal.

Detection of Hydrogen is not possible using RBS in a typical RBS geometry, and NRA can detect Hydrogen, but it require special high energy ¹⁵N beam (7MeV), but He Forward Scattering (FS) or Elastic Recoil Detection (ERD) can be used for Hydrogen detection and profiling. Examples of ERD will be shown and discussed.

Each of these techniques has its own limitations and advantages. Depth resolution and sensitivity will be discussed in details.

Biomaterial Interfaces

Room: 23 - Session BI-MoA

Cell-Surface Interactions: High Throughput Methodologies

Moderator: M.R. Alexander, University of Nottingham, UK

2:00pm BI-MoA1 3D Niche Microarrays for Systems-Level Analyses of Stem Cell Fate, *A. Ranga, M. Lutolf*, École Polytechnique Fédérale de Lausanne, Switzerland **INVITED**

Proper tissue maintenance and regeneration relies on intricate spatial and temporal control of biochemical and biophysical microenvironmental (or 'niche') cues, instructing stem cells to acquire particular fates, for example remaining quiescent or undergoing self-renewal divisions. Despite rapid progress in the identification of relevant niche proteins and signaling pathways using powerful *in vivo* models, many stem cell types cannot be efficiently cultured *in vitro*. To address this challenge, we have been developing biomaterial-based approaches to display stem cell regulatory signals in a precise and near-physiological fashion, serving as powerful artificial microenvironments to probe and manipulate stem cell fate. In this talk I will discuss recent efforts in my laboratory to develop three-dimensional microarrayed artificial niches based on a combination of biomolecular hydrogel engineering and liquid handling robotics. This platform allows key biochemical and biophysical characteristics of stem cell niches to be mimicked and the physiological complexity deconstructed into a smaller, experimentally amenable number of distinct signaling interactions. The systematic deconstruction of a stem cell niche may serve as a broadly applicable paradigm for defining and reconstructing artificial niches to accelerate the transition of stem cell biology to the clinic.

2:40pm BI-MoA3 Microfluidic Gradient Systems to Generate Defined Cell Microenvironments and Study Cellular Fate Processes, *P. Wallin, E. Bernson, J. Gold*, Chalmers University of Technology, Sweden

Cell microenvironments are the main driving force in cellular fate processes and phenotype expression *in vivo*. In order to mimic specific stem cell niches, and study cellular responses under those conditions in detail, we need the ability to create and control cell micro environments *in vitro*. This includes the capability to modify growth substrate surface properties, liquid

composition as well as cell-cell interactions in cell culture systems. Microfluidic systems offer the possibility to modify liquid mixtures on the cellular length scale in a highly defined manner. In particular, the ability to generate spatially- and temporally- controlled liquid gradients is of high relevance to study concentration dependent cell responses.

We are using a diffusion-based gradient generator that has been characterized both by computational fluid dynamic simulations, as well as experimentally. The micro fluidic network was used to investigate HUVEC endothelial cell migration along chemottractant VEGF gradients when simultaneously grown on a continuous gradient in spacing of cell attachment peptide (cRGD) via functionalized Au nanoparticles (65-85nm spacing over 6 mm). The aim of this study is to ascertain how cell migration is affected by the spacing of attachment peptides. This has been achieved by forcing cells to migrate in a chemotratrative gradient on a gradient substrate which will have portions that do not support mature focal adhesion formation or cell spreading. The same microfluidic network was also used in combination with a micro grooved growth substrate to study myoblast differentiation and alignment in response to simultaneous chemical (specifically, gradients in media composition) and topographical stimulation. This was performed in order to define the growth media and to optimize its composition.

The developed platform allows monitoring phenotype expression of cells in situ in highly controlled gradient environments of soluble factors in combination with different cell culture substrate properties. The detailed investigation of specific cellular responses to those stimuli is very difficult and timeconsuming with standard cell culture techniques.

The research leading to these results has received funding from the EU 7th Framework Programme (FP7/2007---2013) under grant agreement NMP3---SL---2009---229294 NanoCARD, and from Vinnova under contract no: 2009---00227.

3:00pm BI-MoA4 What Makes the Heart Grow Fonder? High Throughput Screening of Synthetic Surfaces for Cardiomyocyte Culture, A.K. Patel, M.R. Alexander, M.C. Davies, University of Nottingham, UK, D.G. Anderson, R. Langer, Massachusetts Institute of Technology, C. Denning, University of Nottingham, UK

Human pluripotent stem cell (hPSC) derived cardiomyocytes hold the potential to strengthen pharmaceutical toxicity testing and to provide disease models for development of treatment targets¹. The maturation and maintenance of the cardiomyocyte phenotype may be controlled by the manipulation of the substrate supporting the cells². However, the surfaces currently in use still fall short of producing cardiomyocytes of adult maturity. Standard culture-ware requires coating with biological substrates such as fibronectin which can be expensive and subject to poor reproducibility due to batch variation.

We are exploring an alternative, combinatorial materials high throughput screening approach³ to identify novel materials that can improve cardiomyocyte culture. Polymer microarrays comprising of 6 replicates of 116 acrylates and acrylamides are fabricated using contact printing. Cardiomyocytes derived from the HUES7 human stem cell line are seeded onto the arrays. Immunostaining of nuclei (DAPI) and the cardiomyocyte specific motor protein, sarcomeric alpha actinin is performed to visually estimate cell function and maturity and enable quantification of cell attachment in a high throughput manner using automated fluorescence microscopy and image analysis software. Surface characterisation of the arrays is performed using time of flight secondary ion mass spectrometry. Partial least squares (PLS) regression analysis allows for correlation of cell attachment with key molecular ions identified from mass spectrometry⁴.

Successful monomers that permit cardiomyocyte attachment, spreading and contraction are identified from the first generation homopolymer microarray and are mixed pair-wise to form second generation microarrays. This diverse library of copolymers enables unique combinations of chemical moieties to be investigated. Hit monomers and combinations identified to be synergistic can be analysed for their effect on cardiomyocyte function including electrophysiology measured by patch clamping, myofibril alignment and gene expression.

The lead materials generated by this approach are the first step in a discovery process for novel synthetic biomaterials capable of enhancing the culture of cardiomyocytes to move towards more reproducible, economical and defined conditions.

References:

1. Matsa E. *et al. European Heart Journal.* 2011;32(8):952-62
2. Engler A. *et al. The Journal of Cell Biology.* 2004;166(6):877-887
3. Hook A. *et al. Biomaterials.* 2010;31(2):187-198
4. Yang J. *et al. Biomaterials.* 2010;31(34): 8827-8838

4:20pm BI-MoA8 High-throughput Discovery of Polymers for Stem Cell Culture, A.D. Celiz, University of Nottingham, UK, M. Mahlstedt, A.L. Hook, D.J. Scurr, University of Nottingham, UK, D.G. Anderson, R. Langer, Massachusetts Institute of Technology, D.A. Barrett, C. Denning, L. Young, M.C. Davies, M.R. Alexander, University of Nottingham, UK

Numerous regenerative medicine procedures are already in clinical trials or in the pipeline and if these succeed and reach the clinic, stem cell factories will be needed to meet demand for the billions of cells required per intervention. Current protocols for stem cell culture employ poorly defined biological substrates such as Matrigel™, and/or non-human feeder cell layers which exhibit batch-to-batch variability, and are a potential source of pathogens. More recently, recombinant protein surfaces have been successfully employed, but these are not always cost effective for high-throughput culture methods. Consequently, there is significant research into xeno-free culture alternatives that use fully defined culture media and synthetic substrates. To discover materials for application as substrates, we have used high-throughput polymer arrays with which to fabricate chemically defined and scalable stem cell culture systems. A combinatorial chemical polymer library can be synthesized as a microarray on-slide allowing cell response of hundreds of different materials on a single glass slide, enabling hit materials to be identified in an automated manner^[1]. High-throughput surface characterization (HT-SC) can be performed on the polymer microarray to (i) rapidly evaluate the surface chemistry of each individual spot and (ii) identify surface structure-property relationships in the complex and large datasets generated.⁽²⁾

In this study, a polymer library substantially increased in number and diversity compared with previous studies is prepared by printing (meth)acrylate monomers in pair-wise combination on a polyHEMA coated slide. HT-SC is carried out using time-of-flight secondary-ion mass spectrometry, X-ray photoelectron spectroscopy, atomic force microscopy and water contact angle to characterize all polymer surfaces. Human pluripotent stem cell (hPSC) attachment is probed using automated fluorescence microscopy. This suite of HT-SC techniques has allowed the identification of 'hit' materials that support the expansion and proliferation of hPSCs. Human embryonic stem cell lines (HUES7 and H9) are screened for attachment in 3 different media; mouse embryonic fibroblast-conditioned media (MEF-CM), StemPro® and mTeSR®1 without any protein preconditioning to provide an insight into the impact of material surface properties on cellular interactions. The hits identified represent novel platforms for hPSCs culture without the need for any protein preconditioning and show great potential for development into future synthetic culture systems.

[1] Anderson, D. G. *et al. Nat. Biotechnol.* **22**, 863 - 866 (2004).

[2] Mei, Y. *et al. Nat. Mater.* **9**, 768 - 778 (2010).

4:40pm BI-MoA9 Plasma Polymer Films at the Interface: Biomaterial Applications, B.R. Coad, University of South Australia

Biomaterial research is primarily concerned with mediating the interaction of biological species at the surface of materials. Therefore, research into new ways of coating and derivatizing surfaces is advancing this field. Coating surfaces with thin plasma polymer layers is advantageous because fragmentation and recombination of organic compounds in the plasma phase allows for surface deposition leading to covalent anchoring of polymer networks that retain the functionality of the parent compounds. This is useful as a platform strategy, providing a substrate-independent path for modifying different classes of bulk materials so that they retain their bulk properties (hardness, softness, conductivity, inertness etc.).

In this presentation, we show how deposited plasma polymers form interlayers that allow further surface modification of 1) surface chemistry and 2) surface topology and relate these to their use as biomaterials.

In the first approach, we have constructed a bioconjugation platform that allows for covalent capture of proteins in a gradient fashion. Simultaneous gradient plasma polymerization of two compounds under a mask along a moving stage allows for an increasing surface density of reactive aldehyde groups to be placed alongside an inert hydrophilic spacer allowing for specific, yet variable attachment to be mediated across the surface. We have used this platform to capture streptavidin on the surface to which we have bound biotinylated signaling probes to investigate T-Cell binding and specificity. This platform is shown to be useful in further immunological studies investigating T-Cell binding to gradients of assembled human major histocompatibility complex analogs.

In the second approach, the surface topology has been modified with polymer brushes. With controlled radical polymerization from a novel macroinitiator, it is possible to generate polymer brushes of variable thickness and density which in turn modify the surface interaction with proteins and cells. Polymer chains which are present in highly ordered array provide an entropic barrier to surface fouling and cell attachment. The advantage of using plasma polymer interlayers is that the substrate-independent procedure allows for coatings with the same topology to be

grafted, for example, from the surface of a hard, inert metal or from a flexible, polymeric film.

We conclude by showing a few other examples of the use of plasma polymerization for biomaterials applications from our latest work.

5:00pm BI-MoA10 A High Throughput Strategy for Studying Protein Pre-adsorption to Materials Developed for Stem Cell Culture, M. Hammad, University of Nottingham, UK, *D.G. Anderson, R. Langer*, Massachusetts Institute of Technology, *M.R. Alexander, M.C. Davies*, University of Nottingham, UK

Improved biomaterials are required for application in areas such as regenerative medicine, biosensors, and medical devices. The performance of such materials is often dependent on their surface properties which can influence factors such as cell attachment and *in-vivo* biocompatibility and assimilation. High throughput (HT) materials discovery techniques have been developed to gain a greater fundamental understanding of the nature of the cell-surface interaction[1]. We have developed polymer microarray systems using several hundred unique polymers synthesised rapidly on-slide enabling parallel assessment of cell-surface response[2]. HT materials discovery is thus possible when this platform is combined with HT surface characterisation derived structure activity relationships[3].

The response of cells to these materials is controlled by the identity and conformation of the proteins adsorbed to the surface, which is in turn controlled by the chemistry of the underlying substrate. The complex nature of protein adsorption and their diversity in typical culture conditions makes this a difficult process to follow *in-situ*. Flaim et al. illustrated how printing of extracellular matrix (ECM) proteins can be used to investigate their role in stem cell differentiation and adhesion on a hydrogel surface[4]. We use an adaptation of this methodology to analyse proteins adsorbed to a range of polymer surfaces in the form of spots on the array using piezo dosed solutions of ECM proteins. We have achieved this on polymer microarray systems, illustrating the ability to control both the pre-adsorption and also surface protein composition. Surface chemical analysis techniques including X-ray photoelectron spectroscopy and secondary ion mass spectrometry are used to characterise the protein identity and distribution at the surface. Polymerisation was achieved using the deposition of monomer solutions by piezo dispensing nozzles in an array format onto pHEMA coated substrates before the slides were irradiated with a long wave UV source. ECM protein solutions were then printed on the polymer spots allowing cell response to be correlated with protein surface composition using the same apparatus.

1. Hook, A.L., et al. *Biomaterials*, 2010. (2): p. 187-198.
2. Anderson, D.G., S. Levenberg, and R. Langer *Nature Biotechnology*, 2004. (7): p. 863-866.
3. Mei, Y., et al *Nature Materials*, 2010. (9): p. 768-778.
4. Flaim, C.J., S. Chien, and S.N. Bhatia *Nature Methods*, 2005. (2): p. 119-125.

5:20pm BI-MoA11 Combinatorial Development of Biomaterials for Pluripotent Human Stem Cell Culture, Y. Mei, Clemson University
Pluripotent human stem cells include human embryonic stem cells (hESCs) and more recently developed human induced pluripotent stem cells (hiPSCs). These cells can replicate indefinitely in culture and can differentiate into all types of cells in human body. Thus, they hold remarkable promise as cell source for regenerative medicine and tissue engineering applications. However, hESCs and hiPSCs are currently cultured on a feeder cell layer of mitotically inactivated mouse embryonic fibroblasts (mEFs) or Matrigel™, extracellular matrix (ECM) protein mixtures secreted by mouse carcinoma cells. The utilization of mouse feeder cells and Matrigels as substrates leads to cell populations unsuitable for replacement therapy.

To address the challenge, we recently developed a high throughput polymer microarray technology to rapidly synthesize and test thousands of microscale substrates for hESC and hiPSC culture. In this study, 22 acrylate monomers were used to construct polymer arrays containing 496 different materials with diversified properties. Material properties including surface wettability, indentation elastic modulus, surface roughness and surface chemistry of each polymeric substrate in the array were quantified using high throughput methods. The results were then used to establish structure-function relationships between material properties and biological performance. Surface chemistry was shown to have controlling effects on hES cell undifferentiated growth while indentation elastic modulus or roughness had less pronounced effects on growth. The optimal ("hit") surface was defined as certain oxygen containing ions and hydrocarbon ions in time of flight secondary ion mass spectrometry [ToF-SIMS] analysis. The "hit" surfaces can effectively enhance adsorption of vitronectin and engagement with integrin $\alpha_3\beta_1$ and $\alpha_5\beta_1$ to promote self-renewal of hESCs and hiPSCs.

Based on the structure-function relationship, favorable substrates for hESC and hiPSC culture was developed by exposing polystyrene (PS), a typical cell culture plastic, to an optimized dose of short wavelength ultraviolet (UV) light. In this way, key chemical moieties supporting self-renewal of hESCs and hiPSCs (e.g. hydrocarbons and ester/carboxylic acid) can be introduced onto the surface of PS. PS surfaces treated with the optimal dose of UV (i.e. UVPS) can support more than three times more cells per area than traditional mouse embryonic fibroblast (mEF) feeder cells, the current gold standard. As "hit" polymers, UVPS can promote adsorption of vitronectin to support self-renewal of hESCs and hiPSCs.

Spectroscopic Ellipsometry Focus Topic **Room: 19 - Session EL+TF+BI+AS+EM+SS-MoA**

Spectroscopic Ellipsometry: From Organic and Biological Systems to Inorganic Thin Films **Moderator: M.S. Wagner, The Procter & Gamble Company**

2:00pm EL+TF+BI+AS+EM+SS-MoA1 Biochemical Optical Sensors Based on Highly-Ordered Slanted Columnar Thin Films, D. Schmidt, K.B. Rodenhausen, University of Nebraska-Lincoln, *J. VanDerslice, T.E. Tiwald, J.A. Woollam Co., Inc., E. Schubert, M. Schubert*, University of Nebraska-Lincoln

Highly-ordered three-dimensional nanostructure thin films offer substantially increased surface area for attachment of organic layers, and in addition, new detection principles due to the physical properties of the nanostructures. For example, upon material attachment the optical birefringence of the nanostructures changes due to screening of polarization charges. Because of these advantages, highly-ordered three-dimensional nanostructure thin films lend themselves as suitable candidates for studying of organic attachments as well as for low-cost humidity sensing, for example.

We utilize glancing angle electron-beam deposition for fabrication of highly spatially coherent metal slanted columnar thin films. Subsequently, the nanostructures may be further functionalized with thin conformal coatings by means of atomic layer deposition. The ellipsometry model analysis and resulting anisotropic optical properties of hybrid metal slanted columnar thin films determined by generalized spectroscopic ellipsometry in the visible and near-infrared spectral region will be discussed. We will be reviewing research in this area and report in particular on *in-situ* monitoring of organic attachments using ellipsometry combined with quartz crystal microbalance with dissipation. Exemplarily, we discuss studies of fibronectin protein adsorption, octanethiol chemisorption (self-assembled monolayer growth) on platinum coated titanium slanted columnar thin films as well as relative humidity sensing.

2:20pm EL+TF+BI+AS+EM+SS-MoA2 Studies of Optical Properties of Hybrid J-aggregates and Nanocrystal Quantum Dots Layers for Photonic Applications, K. Roodenko, H.M. Nguyen, L. Caillard, A. Radja, O. Seitz, Yu.N. Gartstein, A.V. Malko, Y.J. Chabal, The University of Texas at Dallas

The integration of organic materials and inorganic nanocrystal quantum dots (NQDs) on the nanoscale offers the possibility of developing new photonic devices that utilize the concept of resonant energy transfer between an organic material and NQDs. Electromagnetic coupling that takes place between excitons—bound electron-hole pairs—at the interfaces of the hybrid composite can be utilized for light-emitting, photovoltaic and sensor applications.

As the key ingredients for the nanocomposite material system reported in this work are the J-aggregates (JA, dye self-assembled molecules) that have exceptional optical absorption due to their strong oscillator strength. NQDs on the other hand combine a variety of important properties, such as high quantum yields, excellent photo- and chemical stability, and size dependent, tunable absorption and emission. Excitation energy transfer in NQDs / J-aggregate hybrids is characterized by their strong excitonic transitions at room temperature with spectrally well-defined absorption and emission.

In order to understand the energy transfer mechanisms in such complex systems, optical properties of JA and NQDs/JA hybrid systems were characterized by means of spectroscopic ellipsometry and polarized IR spectroscopy.

Spectroscopic ellipsometry in 0.6-5 eV spectral range was employed to study optical properties of J-aggregates drop-casted on silicon surfaces. Thin JA films were found to exhibit strong optical anisotropy due to the specific molecular orientation of thin layers on Si substrates. Variation of optical properties due to the deposition of nanocrystal quantum dots (NQDs) was systematically studied for applications in new photonic devices

that utilize excitonic energy transfer from NQDs to JA layer. Ellipsometric results were cross-referenced with atomic force microscopy (AFM) data to derive a quantitative understanding of the distribution of NQDs upon deposition on JA layer. Integration of hybrid colloidal NQD/JA structures could be potentially attractive for a range of optoelectronic applications.

2:40pm **EL+TF+BI+AS+EM+SS-MoA3 Love and Death, the Story of Most Proteins and Most Surfaces as Told by Spectroscopic Ellipsometry**, T. Benavidez, K. Chumbuni-Torres, J.L. Felhofer, C.D. Garcia, The University of Texas at San Antonio **INVITED**

Biosensors are analytical platforms that integrate a biological recognition element with a signal transducer. Because they have the potential to provide rapid, real-time, and accurate results, biosensors have become powerful tools in clinical and biochemical settings. Our group is particularly interested in the development of electrochemical biosensors based on enzymes adsorbed to nanomaterials. When integrated to microfluidic devices, these sensors offer sensitivity, portability, low cost, and the possibility of analyzing turbid samples. Adsorption was selected to immobilize the biorecognition element because it is one of the simplest and most benign methods, avoiding cross-linking reactions or additional components (such as entrapping polymers). Most importantly, as adsorption is a required (and sometimes limiting) step for any immobilization mechanism, the identification of key variables influencing this process can be applied to a variety of strategies. Although several techniques have been used to study the adsorption of proteins to nanomaterials,¹ only a few of them provide information about the kinetics of the process in real time. This is a critical aspect, as most of the post-adsorption conformational changes occur within a few minutes after the interaction.² Among those, reflectometry was used by our group to perform the first kinetic study related to the interaction of proteins with carbon nanotubes.³ These kinetic studies have been recently extended to the interaction of enzymes (D-amino acid oxidase,⁴ catalase,⁵ and glucose oxidase⁶) by variable angle spectroscopic ellipsometry, which enabled a more thorough analysis of the interaction process with a much more versatile experimental design.^{7,8} The use of VASE demonstrated that a number of variables, (being the amount of enzyme only one of them) can influence the biological activity of proteins adsorbed to the substrate. Furthermore, our results indicate that the activity of enzymes adsorbed to nanomaterials can be directly related to the kinetics of the adsorption process (dG/dt).⁵

Please see supplemental document for figures and footnotes.

3:40pm **EL+TF+BI+AS+EM+SS-MoA6 Detailed Photoresist and Photoresist Processing Studies using Spectroscopic Ellipsometry**, C. Henderson, Georgia Institute of Technology **INVITED**

Spectroscopic ellipsometry has become an invaluable tool for the study of a wide variety of thin film systems. In particular, it has become extremely valuable in the development and study of advanced photoresists and of lithographic processes used in the production of integrated circuits and other related semiconductor devices. In our work, we have used spectroscopic ellipsometry to study a variety of problems related to photoresists including swelling phenomena, exposure induced refractive index changes, and ultra-fast dissolution phenomena. We have combined spectroscopic ellipsometry with quartz crystal microbalance techniques to simultaneously study thin film optical properties, thickness, film mass, and film modulus. Such techniques have been particularly useful in understanding the dissolution properties of polymeric photoresists developed for 193 nm lithography. This talk will review some of the applications for spectroscopic ellipsometry in this field and in particular will highlight some of the results of our work made possible using spectroscopic ellipsometry.

4:20pm **EL+TF+BI+AS+EM+SS-MoA8 Ellipsometric Characterization of a Thin Titaniumoxide Nanosheets Layer**, H. Wormeester, G. Maidecchi, S. Kumar, A. Kumar, A. ten Elshof, H.J.W. Zandvliet, MESA+ Institute for Nanotechnology, University of Twente, The Netherlands

The photochemical properties of titaniumoxide make this a widely studied material. Of special interest is a thin nanostructured layer of such a material. A variety of a nanostructured material is the single sheet titaniumoxide that can be obtained by delaminating a layered titanate, with stoichiometry $Ti_{1-x}O_{2-4x}$ ($x=0.0875$). The slight titanium deficiency leads to a negatively charged nanosheet that can be used as a building block in a layer by layer assembled composite film [1]. In this work we used Langmuir Blodgett to deposit successive thin layers of nanosheets. The electronic properties of these layers were investigated with ellipsometry and Scanning Tunneling Microscopy (STM). The optical spectra show the well known absorption peak at 4.6 eV for titaniumoxide nanosheets. The optical spectra can be well modeled with a Cody-Lorentz dielectric function profile providing a bandgap of ... eV, a value also found from STM IV spectroscopy. The

Cody-Lorentz profile also indicates a slight below band gap light absorption by the nanosheet material.

[1] T. Sasaki, Y. Ebina, T. Tanaka, M. Harada, M. Watanabe and G. Decher, Chem. Mater. 2001, 13, 4661

4:40pm **EL+TF+BI+AS+EM+SS-MoA9 Preparation of Abrupt LaAlO₃ Surfaces Monitored by Spectroscopic Ellipsometry**, C.M. Nelson, M. Spies, L.S. Abdallah, S. Zollner, Y. Xu, H. Luo, New Mexico State University

LaAlO₃ is a polar perovskite oxide, used as a single-crystal substrate in oxide epitaxy. It has created much interest for novel electronic applications, because a two-dimensional electron gas is formed at LaAlO₃/SrTiO₃ heterostructures. The purpose of our work is twofold: First, we are interested in an accurate determination of the complex refractive index of LaAlO₃ at room temperature. Second, we studied the impact of various cleaning methods on the abruptness of the LaAlO₃ surface.

We obtained a commercial single-side polished LaAlO₃ substrate with 2-inch diameter and a (100) pseudo-cubic surface orientation. The surface was polished with an rms roughness below 0.8 nm. We determined the ellipsometric angles ψ and Δ for LaAlO₃ at 300 K from 0.7 to 6.5 eV. For a bulk insulator with a clean smooth surface, the phase change Δ should be zero or π below the band gap. In practice, this never happens, because surfaces are covered with overlayers (adsorbed organic or water vapors). Surface roughness has a similar effect on the ellipsometric spectra as a surface overlayer. Even for an abrupt bulk/air interface, there is a thin (~0.5nm) transition region where the electron wave functions leak from the crystal into the ambient. For the as-received sample, the data were described with a Tauc-Lorentz model for LaAlO₃, plus 2.1 nm of surface layer thickness (described as an effective medium with 50% density of the bulk). After ultrasonic cleaning in acetone, the overlayer thickness decreased to 1.8nm. Next, we mounted the wafer in a UHV cryostat, pumped down to below 10⁻⁸Torr, and acquired an ellipsometric spectrum at 70°. The surface layer thickness was reduced to 1.2 nm, presumably because a part of the adsorbed surface layer (especially water) desorbed under vacuum.

So far, everything worked as expected, but here it gets interesting: We heated the sample to 700 K for about an hour to desorb the remaining surface overlayer. After cooling down to 300 K, we measured the ellipsometric angles again at 70° angle of incidence from 0.7 to 6.5 eV. The ellipsometric angle Δ at 2 eV was reduced to below 0.2°, consistent with a surface layer thickness of less than 1 Å, much less than the surface roughness specified by the supplier (8 Å).

In conclusion, a macroscopically smooth and clean LaAlO₃ surface was prepared by ultrasonic cleaning of the wafer in acetone, followed by heating in UHV to 700 K. The resulting surface layer thickness was below 1 Å, as measured by spectroscopic ellipsometry. We will report Tauc Lorentz parameters. We will also describe the temperature dependence of the LaAlO₃ dielectric function from 77 to 700 K. This work was supported by NSF (DMR-11104934).

5:00pm **EL+TF+BI+AS+EM+SS-MoA10 Determination of the Refractive Index of a Gold-Oxide Thin Film Using X-Ray Photoelectron Spectroscopy and Spectroscopic Ellipsometry**, K. Cook, G.S. Ferguson, Lehigh University

A two-step procedure will be presented for measuring the complex refractive index of an electrochemically produced oxide film on a gold surface. In the first step, the composition and the thickness of the oxide film were determined using angle-resolved X-ray photoelectron spectroscopy. The experimental composition defined the system, thereby avoiding assumptions about the film stoichiometry that would otherwise be required. The value of thickness derived from these measurements was then used to calculate n and k from ellipsometric data collected across the visible spectrum (350 - 800 nm).

High-k Dielectrics for MOSFETS II

Moderator: C.L. Hinkle, University of Texas at Dallas, H.J. Kim, National Institute of Aerospace (NIA)

2:00pm **EM+TF+OX+GR-MoA1 "6.1" Family: The Next Generation of III-V Semiconductors for Advanced CMOS: Epitaxial Growth and Passivation Challenges.** C. Merckling, A. Alian, A. Firrincelli, S. Jiang, M. Cantoro, J. Dekoster, M. Caymax, M. Heyns, IMEC, Belgium **INVITED**
The integration of high carrier mobility materials into future CMOS generations is presently being studied in order to increase drive current capability and to decrease power consumption in future generation CMOS devices. If III-V materials are the candidates of choice for n-type channel devices, antimonide-based III-V semiconductors present the unique property of owning both high electrons (InSb) and holes (GaSb) mobilities, which triggered much of the interest in these III-Sb compounds for advanced CMOS. Moreover recent simulations have demonstrated that higher hole mobility could be found in strained III-antimonides compounds, suggesting the possibility of an all III-antimonide solution for full III-V based CMOS. In this work we studied the heteroepitaxy of 6.1 family semiconductors (GaSb, AlSb & InAs) on various III-V and Si substrates as well as the passivation of such semiconductors.

The relatively large lattice parameter of "6.1" semiconductors makes the growth and the integration on standard surfaces difficult. But is it possible to grow such semiconductors fully relaxed with low defect density due to the formation of a highly periodic array of 90° misfit dislocations at the III-Sb/substrate interface. In this contribution both MBE and MOVPE growth techniques have been studied in order to propose novel integration scheme on Si substrate.

In a second part, we will focus on the passivation of these III-V semiconductors. Because III-V surfaces are very sensitive to oxygen compounds, this will generate the formation of native oxide. This undesirable interlayer will contribute aggressively to the high density of surface states within the energy band gap, resulting in Fermi level pinning which disturbs the basic III-V MOSFET-operation. In this context both ex-situ and in-situ Al₂O₃ high-κ gate dielectric deposition by standard ALD or MBD processes is reported. The interface is abrupt without any substantial interfacial layer, and is characterized by high conduction and valence band offsets. Finally, MOS capacitors showed well-behaved C-V with relatively low D_{it} along the band gap. Such a D_{it} profile is promising for the future devices and suggests possibility to attain a low subthreshold swing.

2:40pm **EM+TF+OX+GR-MoA3 Improving Nucleation and Passivation of Ge(100) via H₂O and H₂O₂ Dosing.** T. Kaufman-Osborn, K. Kiantaj, J.S. Lee, A.C. Kummel, University of California San Diego
Germanium is a promising candidate for potential channel materials due to its higher hole and electron mobility. To minimize the oxide-semiconductor interfacial defect density, a proper passivation layer must be used before the oxide layer is deposited. In this study, a monolayer of H₂O chemisorbrates is shown to activate TMA chemisorption due to the Ge-OH bonds catalyzing the formation of an ultrathin passivation layer which can serve as an ideal ALD nucleation template on a Ge surface. However, since H₂O chemisorption results in equal density of Ge-H and Ge-OH sites on the Ge(100), H₂O can only provide a maximum of 0.5 monolayer of Ge-OH sites, limiting the TMA nucleation density. By using H₂O₂ dosing, the density of Ge-OH sites can be doubled thereby increasing the potential TMA nucleation density. This study compares the passivation of the Ge(100) surface via H₂O and H₂O₂, for the application of nucleating ALD growth on the surface, using scanning tunneling microscopy (STM) and scanning tunneling spectroscopy (STS).

A saturation H₂O dose onto Ge(100) resulted in 0.85 ML coverage of -OH and -H species chemisorbed on the surface. The remaining unreacted atoms on the surface have half filled dangling bond states causing a large local amount of conduction band edge states in the bandgap. The Ge-OH and Ge-H sites on the surface have limited thermal stability. Annealing the H₂O/Ge(100) sample to 100°C significantly reduces the H₂O coverage due to the recombinative desorption of H₂ or H₂O.

A saturation dose of H₂O₂ on Ge(100) at 250°C results in a coverage of 0.95 ML of Ge-OH species chemisorbed on the surface with very few unreacted sites. Compared to a H₂O dose, H₂O₂ provides more than double the number of reactive Ge-OH sites thereby increasing the number of potential ALD nucleation sites. In contrast to the H₂O passivated surface, annealing the H₂O₂/Ge surface to 100°C generates no additional dangling bond sites and even eliminates the dangling bonds present from the 250°C dose and forms a highly ordered surface of Ge-OH bonds. The improved coverage of

Ge-OH sites allows for increased nucleation density of O-Al bonds and also minimizes the dangling bonds which are considered as the major source of interfacial trap states (Dit). The improved thermal stability allows for an increased thermal budget during ALD cycles. STS measurements show that TMA nucleation on the H₂O₂ functionalized Ge(100) surface unpins the Fermi level and has a wide bandgap with no band edge states demonstrating very good interface quality.

3:00pm **EM+TF+OX+GR-MoA4 Electrical and Physical Characteristics of High-k/Metal Gate MOS Devices on MBE-Grown Germanium on Silicon Using Aspect Ratio Trapping.** S.R.M. Anwar, C. Buie, N. Lu, M.J. Kim, C.L. Hinkle, University of Texas at Dallas

Due to its high hole mobility and relative compatibility with Si CMOS processing, Ge has long been considered as a replacement channel material for PMOS devices. Selective area growth of Ge channels on bulk Si substrates would be ideal for minimizing fabrication costs and allowing the co-implementation of other materials (III-Vs for NMOS). However, due to the 4.2% lattice mismatch between Ge and Si, unacceptably high dislocation densities (~10⁹ cm⁻²) are created during this heteroepitaxy.

In this work, we investigate the fabrication of MOS gate stacks on MBE-grown Ge on Si using Aspect Ratio Trapping (ART)^{1,2} to reduce Ge defect density. ART is a growth technique that allows for the reduction of defects for lattice mismatched materials by trapping the threading dislocations into the sidewalls of patterned nanoscale trenches in which the epitaxial growth takes place. This technique has the added benefit of producing the necessary geometric structure required for highly scaled tri-gate devices while reducing defect density simultaneously. Surface roughness and defect density dependence on growth temperature and growth rate will be discussed as will be the effect of varying the trench geometry. RHEED, XRD, XPS, TEM, EPD, AFM, SEM, and IPE data are correlated with growth conditions to produce high quality heteroepitaxial growth. Data will be presented demonstrating the use of low-temperature buffer layers in conjunction with low-growth rate bulk Ge results in a reduction in threading dislocations of 2-3 orders of magnitude.

MOS devices were fabricated on the MBE-grown Ge on Si samples. A high-quality interface was obtained using a DI-H₂O surface functionalization by pre-pulsing the H₂O 50 times in the atomic layer deposition (ALD) chamber at 250 °C.³ A thin interfacial Al₂O₃ film was deposited by ALD at 250 °C followed by forming gas anneal (FGA) performed for 30 minutes at 350 °C. This FGA step converts the surface functionalized oxide to a thin layer of GeO₂ resulting in improved electrical performance. 2.5 nm of HfO₂ was then deposited by ALD. 10 nm of RF sputtered TiN was deposited as the gate metal followed by low-temperature anneals in various ambients to tune the effective work function of the HfO₂/TiN gate stack.⁴ A final FGA for 30 minutes at 350 °C completed device processing. These devices show excellent PMOS characteristics and will be discussed.

This work is supported by the SRC Global Research Corporation.

- 1 J.-S. Park, *et al.*, Appl. Phys. Lett. **90**, 052113 (2007).
- 2 J. Bai, *et al.*, Appl. Phys. Lett. **90**, 101902 (2007).
- 3 S. Swaminathan, *et al.*, J. Appl. Phys. **110**, 094105 (2011).
- 4 C. L. Hinkle, *et al.*, Appl. Phys. Lett. **100**, 153501, (2012).

3:40pm **EM+TF+OX+GR-MoA6 In Situ Infrared Spectroscopy Study on the Temperature Dependence on the Growth Mechanism of Atomic Layer Deposition of Al₂O₃ on InP(100).** W. Cabrera, The University of Texas at Dallas, I.M. Povey, Tyndall National Institute, Y.J. Chabal, The University of Texas at Dallas

One of the current challenges in fabricating III-V-based electronics is the growth of an interfacial layer during the atomic layer deposition (ALD) of high-κ dielectrics on III-V substrates, which has led to poor quality electrical properties. A process that can mitigate this problem is the "clean-up" effect that occurs when trimethylaluminum (TMA) is deposited by atomic layer deposition during the formation of Al₂O₃. A recent theoretical study suggests that the principal pathway in the "clean-up" effect of TMA on the native oxides of GaAs and InGaAs involves oxygen gettering¹. In this work, *in-situ* infrared absorption spectroscopy has been used to investigate the temperature dependence of the native oxide and the interface formation during Al₂O₃ deposition using TMA and deuterium oxide (D₂O) on chemically-treated InP(100) surfaces. Upon annealing a degreased sample to 300°C, compositional changes are observed, as evidenced by new absorption features in the region of 900-1250 cm⁻¹ of the infrared spectrum prior to TMA exposure. The initial native oxide, comprised in part of In(PO₃)₃ is transformed into an InPO₄-rich surface. Upon TMA exposure at 300°C, there is a clear loss of In(PO₃)₃ and gain of InPO₄ (at 1007 and 1145 cm⁻¹, respectively) along with the formation of Al-O bonds (absorption band at 800 cm⁻¹)². These observations are consistent with the "clean up" effect observed on GaAs₃ and InGaAs₄, and on InP(100)⁵

where TMA preferentially withdraws oxygen from the native oxide forming Al-O bonds. However, the TMA reduces In(PO₃)₃ and fosters the formation of InPO₄. Furthermore, TMA exposure of the native oxide at lower deposition temperatures (150°C) gives rise to methoxy (CH₃) formation as evidenced by the appearance of a band centered at 1475 cm⁻¹. This indicates that TMA not only withdraws oxygen from the native oxide but also transfers a methyl group to the surface oxygen, which may lead to carbon contamination at the interface. Al₂O₃ oxide films are formed after 10 TMA and D₂O cycles on both degreased native oxide and chemically treated (HF and (NH₄)₂S) InP(100) substrates, although the quality is higher on the (HF and (NH₄)₂S)-treated surface. A more clearly defined LO phonon mode is detected for that surface, suggesting that a denser oxide is formed.

- 1 S. Klejna et. al, *J. Phys. Chem. C*, **116**, (2012) 643-654
- 2 M. M. Frank et. al, *Appl. Phys. Lett.* **82** (2003) 4758
- 3 C. L. Hinkle et. al, *Appl. Phys. Lett.*, **92** (2008) 071901
- 4 M. Milojevic, et. al *Appl. Phys. Lett.*, **93**, (2008) 202902
- 5 B. Brennan et. al, *Appl. Phys. Exp.*, **4** (2011) 125701

4:00pm **EM+TF+OX+GR-MoA7 Ultimate Scaling of High-k Gate Dielectrics: Current Status and Challenges**, *T. Ando, M.M. Frank, E.A. Cartier, B.P. Linder, J. Rozen*, IBM T.J. Watson Research Center, *K. Choi*, GLOBALFOUNDRIES, *V. Narayanan*, IBM T.J. Watson Research Center
INVITED

Current status and challenges of aggressive equivalent-oxide-thickness (EOT) scaling of high-k gate dielectrics via higher-k (>20) materials and interfacial layer (IL) scavenging techniques are reviewed [1]. La-based higher-k materials [2, 3] and La-silicate IL with HfO₂ [4] showed aggressive EOT values (0.5–0.8 nm), but with large effective workfunction (EWF) shifts toward the Si conduction band edge, limiting their application to nFET. Further exploration for pFET-compatible higher-k materials is needed. Meanwhile, IL scavenging is a promising approach to extend Hf-based high-k dielectrics to future nodes [4, 5]. Remote-scavenging techniques enable EOT scaling below 0.5 nm. We will review IL scavenging techniques from the viewpoints of (1) IL growth condition; (2) Choice of scavenging element; (3) Location of scavenging element; (4) Choice of high-κ material and (5) Maximum process temperature. Careful choice of materials and processes based on these considerations is indispensable. Mobility-EOT trends in the literature suggest that short-channel performance improvement is attainable with aggressive EOT scaling via IL scavenging or La-silicate formation. However, extreme IL scaling is accompanied with loss of EWF control [6] and with severe penalty in reliability [7]. Therefore, highly precise IL thickness control in an ultra-thin IL regime (<0.5 nm) will be the key technology to satisfy both performance and reliability requirements for future CMOS devices.

This work was performed by the Research alliance Teams at various IBM Research and Development Facilities.

- [1] T. Ando, *Materials* **2012**, *5*, 478-500 [2] H. Arimura et al., *Electron Device Lett.* **2011**, *32*, 288–290 [3] L. F. Edge et al., *Appl. Phys. Lett.* **2011**, *98*, 122905 [4] T. Ando et al., *IEDM* 2009, 423-426 [5] L. Å. Ragnarsson et al., *IEDM* 2009, 663-666 [6] T. Ando et al., as discussed at *SISC* 2011 [7] E. A. Cartier et al., *IEDM* 2011, 18.4.1-18.4.4

4:40pm **EM+TF+OX+GR-MoA9 AR-XPS Study of Al₂O₃/In-based III-V Interfaces after Annealing under Vacuum at Low Temperature**, *E. Martinez, H. Grampeix, O. Desplats*, CEA, LETI, MINATEC Campus, France, *A. Herrera-Gomez, O. Ceballos-Sanchez*, CINVESTAV-Unidad Queretaro, Mexico, *J. Guerrero, K. Yckache, F. Martin*, CEA, LETI, MINATEC Campus, France

III-V semiconductor substrates are a potential solution for MOSTETs down scaling below the 16 nm technological node. Indium based semiconductors, such as InGaAs, InAs and InP are promising compounds to improve the speed of operation. The quality of the interface between these high mobility substrates and the gate oxide is of crucial importance to preserve the devices electrical properties. Aluminium oxide is used to remove the As oxide (“self-cleaning” effect). The gate-last scheme is preferred to control of the high-k/III-V since it involves low temperature post deposition annealing [1]. State-of-the-art control of this interface has been obtained with annealing at 400°C under vacuum [2]. In this work we focus on the impact of low temperature annealing under vacuum on the quality of the Al₂O₃/In-based III-V interfaces. We have studied the interfacial oxides formed between alumina and III-V substrates such as InGaAs, InAs and InP. Annealing at 600°C under ultra high vacuum (UHV) is first performed and compared to thermal treatments at 600°C and 400°C at 3 × 10⁻⁴ mbar. Substrate passivation is done with NH₄OH (4 %). The 3-nm thick alumina is deposited by Atomic Layer Deposition (ALD) using TMA and H₂O as precursor and oxidant. Angle-resolved photoelectron spectroscopy (AR-XPS) has been carried out to investigate the interfacial chemical bonding

states. Consistent and robust analysis of the As 3d, P 2p, Ga3d and In 3d core levels was carried out through the simultaneous fitting method [3]. At 600°C, we show that, on InGaAs, no interfacial oxides are created after annealing under UHV, whereas a thin interfacial InGaO_x is observed under secondary vacuum. A clear difference between the three substrates is observed after annealing at 400°C under 3 × 10⁻⁴ mbar. In particular, the indium oxidation and the relative stability of interfacial oxides are substrate dependant. On InAs, indium hydroxide is formed after annealing, by OH release from TMA/H₂O deposited alumina. This is not the case with additional elements such as Ga and P, which react with residual species to create their respective oxides. On InGaAs, a regrowth of InGaO_x is observed after anneal, as a result of preferential oxidation of Ga. On InP, the InPO_x interfacial oxide seems to decrease after anneal. **Acknowledgements** This work was performed with financial support from the MOS35 project funded by the French National Research Agency. Measurements were carried out at the NanoCharacterization Centre (NCC) of MINATEC. [1] H. Zhao et al., *Appl. Phys. Lett.* **95**, 253501 (2009) [2] Y. Urabe et al., *Appl. Phys. Lett.* **97**, 253502 (2010) [3] J. Muñoz-Flores et al., *J. Electron. Spec. Rel. Phen.* **182**, 81 (2011)

5:00pm **EM+TF+OX+GR-MoA10 Effect of a H₂ Plasma Pre-treatment on the Reduction of Native Oxides at the PEALD Al₂O₃/InAs Interface**, *E. Cleveland, L. Ruppalt, J.B. Boos, B. Bennett, J. Champlain, S.M. Prokes*, Naval Research Laboratory

The integration of high-κ dielectrics with high mobility III-V semiconductor materials has attracted extensive interest recently as an alternative to Si-based complementary metal-oxide semiconductor (CMOS) applications at the 16 nm node and beyond. Among the III-V semiconductors, InAs is a promising material as the channel material in metal-oxide-semiconductor field-effect transistors (MOSFETs) due to its extremely high electron mobility and high saturation velocity. However, problems arise in the fabrication of high performance channel MOSFETs due to the poor quality of the gate oxide/InAs interface. InAs has a highly reactive surface and on exposure to air will form a native oxide layer composed of In₂O₃ and As₂O₃. The complexity of these native oxides leads to the formation of a relatively high density of interface states which in turn act as charge traps thus pinning the Fermi level and degrading device performance. Wet-chemical treatments based on HCl and (NH₄)₂S have been found to be an effective means of removing these oxides, however, due to the rapid re-oxidation and lack of reproducibility a better means of interface cleaning is needed. Recently, there has been much interest in the field of surface cleaning combined with atomic layer deposition (ALD) in order to deposit high quality dielectrics on III-V semiconductor materials, such as InAs and GaSb. Therefore, we examined the use of a H₂ plasma as a means to obtain an oxide-free InAs interface prior to the deposition of high-κ Al₂O₃ via plasma enhanced atomic layer deposition (PEALD). Ex-situ XPS, AFM, and C-V measurements were performed to establish the effect of the plasma exposure time, temperature and rf power on the removal of the native oxide. It will be demonstrated that by removing or reducing the native oxides on the InAs surface that the density of interface defects at the Al₂O₃/InAs interface can be reduced and enhance the electrical performance. Similar work done on GaSb will be discussed, where XPS spectra revealed a significant reduction in Sb-O features for longer H₂ plasma exposures as the peaks associated with Ga-O increased. C-V measurements of fabricated MOSCAPS also found that samples treated with longer H₂ plasma exposures exhibited better C-V characteristics.

Energy Frontiers Focus Topic
Room: 15 - Session EN+TF-MoA

Chalcogenide Solar Cells I
Moderator: J. Luther, NREL

2:00pm **EN+TF-MoA1 Research Strategies and Results Toward Improving Thin Film CdTe Photovoltaic Devices Beyond 20% Conversion Efficiency**, *T.A. Gessert*, National Renewable Energy Laboratory
INVITED

Recent studies of thin-film CdS/CdTe photovoltaic (PV) devices have suggested that significantly higher device performance will not be achieved unless recombination in the CdTe is reduced. Specifically, unless high recombination in the CdTe quasi-neutral region is reduced, benefits of increasing CdTe net-acceptor doping cannot be realized—because resulting higher open-circuit voltage will be accompanied by lower fill factor. Although some control of CdTe recombination has been achieved historically through the careful incorporation of oxygen, chlorine, and

copper, many technologists believe a more promising avenue to higher device performance is by understanding and controlling the defects in the as-deposited CdTe. This is supported by theoretical studies that suggest much of the improvement associated with oxygen, chlorine, and copper is due to the interaction of these species with intrinsic defects related cadmium and tellurium (i.e., vacancies, interstitial, and anti-site defects). Although CdTe is a relatively simple semiconducting material that exists only near its 50%/50% composition, even at thermodynamic equilibrium, the material can sustain a small stoichiometric deficiency (~0.01%). Even this small extent of stoichiometry variation can produce intrinsic defects at a sufficient concentration to significantly alter device performance. Further, the typical techniques used in PV film deposition are not equilibrium processes, and so the extent of non-stoichiometry could be greater. Several research projects at NREL are currently focused on altering CdTe deposition and post-deposition processes to allow for an enhanced control of the as-deposited intrinsic defects. Related defect changes are being assessed using a combination of device analysis, time-resolved photoluminescence, low-temperature photoluminescence, and microscopic techniques. The presentation will discuss initial results where process changes expected to alter the as-deposited defects also affect junction evolution and device functionality. *This abstract is subject to government rights.*

2:40pm EN+TF-MoA3 Nanocrystal-Ink and Soluble-Precursor Routes to Earth Abundant Element Kesterite Solar Cells, H.W. Hillhouse, University of Washington **INVITED**

Given the terawatt scale of future energy needs, the most promising future photovoltaic materials should be Earth abundant with their primary mineral resources distributed across several geographic regions and their supply chains robust to reduce concerns of price volatility. In addition, the process of forming the solar cell should be scalable, low-cost, and not utilize dangerous or toxic materials. The strongest initial candidate appears to be kesterite structures of $\text{Cu}_2\text{ZnSnS}_4$ (CZTS) and similar materials. The presentation will review the progress in developing photovoltaics devices based on these materials and our group's recent experimental and modeling results.

CZTS thin film solar cells have historically been synthesized by evaporating or sputtering metals (Cu, Zn, & Sn) followed by sulfurization or selenization. More recently, two potentially low-cost high-throughput approaches have been demonstrated that form the quaternary or pentenary chalcogenide directly from solution-phase processes. One is based on first synthesizing multinary sulfide nanocrystals and then sintering them to form a dense layer. The other approach utilizes molecular precursors dissolved in hydrazine. Both new approaches reach their highest device efficiencies by incorporating Se to form $\text{Cu}_2\text{ZnSn}(\text{S}_x\text{Se}_{1-x})_4$ devices, and each has yielded substantially higher efficiency devices than the best vacuum deposited absorbers. The hydrazine route has yielded the most efficient CZTS-based devices thus far. The presentation will highlight our recent progress in CZTS-based nanocrystal-ink devices. In particular, we have shown that germanium may be alloyed with CTZS (at least up to Ge/(Sn+Ge) ratios of 0.7) to form $\text{Cu}_2\text{Zn}(\text{Sn,Ge})\text{S}_4$ nanocrystals that have an increased bandgap. The defect chemistry is serendipitous, and yields devices at with greater than 8% power conversion efficiency. This exciting prospect may be used to create a back surface field and direct carriers in a similar manner to how gallium is used in high efficiency CIGS devices. In addition, we will report recent results from high throughput experiments focused on identifying doping and passivation agents.

3:40pm EN+TF-MoA6 Developing Earth Abundant and Quantum Dot Materials for Thin-Film Photovoltaics, M. Law, University of California Irvine **INVITED**

This talk describes projects in our group to develop thin-film photovoltaics based on earth-abundant iron pyrite (FeS_2) active layers and PbSe quantum dot (QD) solids. I will first introduce the promise and challenge of pyrite, describe solution- and gas-phase syntheses of pyrite films, and present preliminary electrical characterization of pyrite layers and device stacks. Then I will switch gears to highlight several projects focused on the chemistry/physics of QD solids, including our use of atomic layer deposition to produce environmentally-robust PbSe QD films with long carrier diffusion lengths for next-generation solar cells.

4:20pm EN+TF-MoA8 Synthesis of Photovoltaic $\text{Cu}_2\text{ZnSnS}_4$ via Ex Situ Sulfidation of Co-Sputtered Cu-Zn-Sn Thin Films, M. Johnson, M. Manno, X. Zhang, C. Leighton, E.S. Aydil, University of Minnesota

$\text{Cu}_2\text{ZnSnS}_4$ (CZTS) is an emerging low-cost solar absorber for thin film photovoltaics based on non-toxic, high earth-abundance elements. While *ex situ* sulfidation of Cu-Zn-Sn precursor films in S vapor is a popular synthesis route for CZTS, much remains to be understood with regard to the sulfidation mechanisms, microstructural control, and structure-property relationships. In this work, DC magnetron co-sputtered Cu-Zn-Sn films, of

varying composition, were sealed with 1.0 mg of S in evacuated (10^{-6} Torr) quartz ampoules, and then isothermally heat treated at sulfidation temperatures in the range $100^\circ\text{C} \leq T_S \leq 700^\circ\text{C}$. The films were then characterized structurally by scanning electron microscopy, Raman spectroscopy, and X-ray diffraction, and electrically via resistivity measurements between 4.2 K and 300 K. We find that the phase purity of the resultant films depends strongly on T_S , with complete conversion of the precursor film to CZTS occurring only at $T_S \geq 550^\circ\text{C}$. The final phase purity of *ex situ* sulfidized CZTS films is however remarkably insensitive to modest amounts of excess Zn and Sn in the Cu-Zn-Sn precursor film. Excess Zn or Sn in the precursor is readily ejected during sulfidation, via elemental or binary sulfide evaporation, respectively, while Sn-deficiency can also be corrected by introducing elemental Sn to the sealed quartz ampoule. However, due to the low melting point of Sn, and the absence of appropriate Sn-Zn alloys, the precursor composition *does* play a significant role in defining the final CZTS film microstructure, and the lateral homogeneity. In addition to detailed discussion of the physics and chemistry underlying the above observations we will also provide data on the transport properties of such films, including observations of hopping conduction.

Work supported by NSF (CBET-0931145) and IREE (RL-0004-11)

4:40pm EN+TF-MoA9 Crossover from Intergranular Hopping to Conventional Charge Transport in Pyrite FeS_2 Thin Films, X. Zhang, M. Manno, A. Baruth, M. Johnson, E.S. Aydil, C. Leighton, University of Minnesota

Pyrite FeS_2 is undergoing a tremendous resurgence of interest as a candidate thin-film solar absorber based on abundant, low-cost, non-toxic elements. Historically, FeS_2 -based Schottky solar cells have suffered from low open circuit voltages (~100 mV), and thus low efficiency, although the origins of this behavior are not entirely clear. In fact, even the electronic properties of FeS_2 are not well understood, including the conduction mechanisms and doping behavior. Understanding these issues could contribute significantly to improvements in FeS_2 -based solar cells, particularly if doping can be understood and controlled. In this work, we present a comprehensive study of the conduction mechanism in FeS_2 thin films synthesized via the *ex situ* sulfidation of Fe films in a S vapor at sulfidation temperatures in the range $100^\circ\text{C} \leq T_S \leq 700^\circ\text{C}$. The resultant films were characterized structurally, using X-ray diffraction, scanning electron microscopy, energy dispersive spectroscopy, and confocal Raman microscopy; electrically, via transport and magnetoresistance measurements between 4.5 and 300 K; and magnetically with high-sensitivity dc magnetometry. At T_S around 500°C we observe a crossover in the conduction mechanism from some form of hopping conduction to a more conventional band transport-type mechanism. Through detailed analysis of the hopping parameters, measurement of the Fe spin-state, and simple calculations based on S diffusion in Fe, we demonstrate that intergranular hopping occurs via highly conductive, S-deficient, nanoscopic grain cores separated by nominally stoichiometric FeS_2 shells. We find that the approach towards more conventional band transport as T_S is increased above 500°C is due to an increase of S diffusion into the FeS_2 grains. Moreover, this conduction mechanism crossover is found to be accompanied by a sign reversal of the Hall coefficient, from hole-like (in the hopping regime) to electron-like. In addition to placing hard constraints on the conditions under which useful properties can be obtained from FeS_2 synthesized under diffusion-limited conditions, these results also highlight potential problems with prior conclusions on the dominance of *p*-type behavior.

The work was supported by the Initiative for Renewable Energy & the Environment, IREE (RL-0004-11). Part of this work was carried out in the University of Minnesota Characterization Facility, a member of the NSF-supported Material Research Facilities Network.

5:00pm EN+TF-MoA10 Plasma Assisted Synthesis of Pyrite Absorbers, R. Morrish, R. Silverstein, C.A. Wolden, Colorado School of Mines

Pyrite (FeS_2) is a non-toxic, earth abundant chalcogenide with desirable characteristics for application as a photovoltaic absorber including a modest band gap of 0.95 eV and a large optical absorption coefficient ($>10^5 \text{ cm}^{-1}$). Although theoretically capable of $>20\%$ efficiency, to date pyrite devices have displayed poor performance. One key challenge has been the production of stoichiometric material that is free of impurity phases. Conventional approaches employ thermal sulfurization of iron-based films or precursors. These routes inherently produce contaminate phases (troilite, pyrrhotite, marcasite), that once formed, are difficult to completely remove. Thermodynamics suggests that hematite ($\alpha\text{-Fe}_2\text{O}_3$) may be directly converted to pyrite in the presence of sufficiently high sulfur activity. In this work, we demonstrate pyrite synthesis using a H_2S plasma to sulfurize hematite nanorods produced using chemical bath deposition. Conversion to pyrite was achieved by exposure to a 90% Ar-10% H_2S plasma at moderate temperature (350 - 450 $^\circ\text{C}$). The application of plasma dramatically

enhances both the rate of conversion and the quality of the resulting material. Composition analysis using both Raman and X-ray photoelectron spectroscopy confirm that the resulting pyrite is free of common impurity phases. The degrees of sulfur incorporation could be precisely controlled by plasma exposure, and the apparent optical band gap could be systematically reduced from 2.2 to 1.0 eV. Electron microscopy images showed the surface maintained a nanostructured architecture following sulfurization, and a 150 nm thick film was sufficient to absorb 99% of incident visible light. In this presentation we discuss the kinetics of this solid state transformation, as well as report on the optoelectronic properties of these materials.

Graphene and Related Materials Focus Topic Room: 13 - Session GR+EM+ET+NS+TF-MoA

Electronic Properties and Charge Transport

Moderator: T.W. Michely, Universität zu Köln, Germany

2:00pm **GR+EM+ET+NS+TF-MoA1 Influence of Substrate Offcut on Electrical and Morphological Properties of Epitaxial Graphene, R.L. Myers-Ward, V.D. Wheeler, L.O. Nyakiti, T.J. Anderson, F.J. Bezares, J.D. Caldwell, A. Nath, N. Nepal, C.R. Eddy, Jr., D.K. Gaskill, U.S. Naval Research Laboratory**

The promise of graphene-based device technologies is critically dependent on uniform wafer-scale graphene films and is most directly met through epitaxial graphene (EG) growth on silicon carbide (SiC) substrates. An essential parameter which influences this uniformity is the substrate offcut, as any deviation will result in a local change in the terrace width, impacting the growth rate and step-bunched heights observed after EG formation. For nominally on-axis SiC substrates, typical offcuts can range from $\sim 0^\circ$ to $\sim 1^\circ$ off-axis toward the [11-20] direction. Offcuts approaching 0° produce wide terraces with short step-bunched heights which offers the possibility of reduced anisotropy of transport properties [M. Yakes, et al., Nano Lett. **10**(5), 1559 (2010)] and improved EG layer uniformity. Thus, it is of interest to understand the influence of substrate offcut on carrier mobility, surface morphology, step heights, and graphene growth rate. This study investigates EG grown on a unique single 3-inch substrate possessing a large variation in offcut, from $+0.1$ to -1° toward the [11-20] direction, enhancing the information obtained on offcut influence while eliminating other substrate influences. X-ray diffraction rocking curve and peak position maps of the (0012) reflection were performed prior to growth to evaluate the crystalline quality and local offcut, respectively. Electron mobilities of EG films were determined by van der Pauw Hall measurements. Surface morphology of the EG was investigated with scanning electron microscopy, while the step heights and terrace widths were measured using atomic force microscopy.

For a given set of conditions (1620°C for 30 min in 10 slm Ar), the EG morphology is dominated by straight steps that become wavy in character as the offcut decreases to zero degrees. Close to zero degrees, the step direction rotates from [11-20] to the [1-100] direction and the steps become further distorted. The step bunch heights generally decreased (from 8 to 3 nm) as the offcut decreased and the terrace widths increased (from 0.3 to ~ 3 μm); however, for the latter, the trend is interrupted near zero degrees offcut. In addition to such morphological assessments, the impact of growth parameters, where the growth temperatures investigated were 1540, 1580 and 1620 °C and growth times were 15, 30 and 45 min, on the electrical and structural properties of EG grown on this unique substrate will be reported. For example, samples grown at 1540 °C for 30 min on witness substrates with offcuts ranging from ~ 0.4 to 0.9° had large area mobilities ranging from 780 to 1100 cm^2/Vs , where larger offcuts led to lower mobilities.

2:20pm **GR+EM+ET+NS+TF-MoA2 Direct Determination of Dominant Scatterer in Graphene on SiO₂, J. Katoch, D. Le, T.S. Rahman, M. Ishigami, University of Central Florida**

Freely suspended graphene sheets display high-field effect mobility, reaching 2×10^5 $\text{cm}^2/\text{V s}$. Yet, suspended graphene sheets are fragile and impractical for most experiments and applications. Graphene sheets on SiO₂ are easier to handle but possess low-carrier mobilities, which can vary by an order of magnitude from sample to sample. Poor and unpredictable transport properties reduce the utility of SiO₂-bound graphene sheets for both fundamental and applied sciences. Therefore, understanding the impact of substrates is crucial for graphene science and technology.

We have measured the impact of atomic hydrogen with kinetic energy less than 250 meV on the transport property of graphene sheets as a function of hydrogen coverage and initial, pre-hydrogenation field-effect mobility. The

saturation coverages for different devices are found to be proportional to their initial mobility, indicating that the number of native scatterers is proportional to the saturation coverage of hydrogen. In order to understand this correlation between the field effect mobility and the apparent affinity of atomic hydrogen to graphene, we have performed a detailed temperature programmed desorption study on hydrogen-dosed graphene sheets. Atomic hydrogen is found to physisorb on graphene with activation energy for desorption of 60 ± 10 meV, consistent with our theoretical calculations. The associated charge transfer expected for such small desorption energy indicates that atomic-scale defects and ripples are not responsible for determining the mobility of graphene on SiO₂ and that charged impurities in substrates define the transport property of graphene on SiO₂.

1. J. Katoch, J.H. Chen, R. Tsuchikawa, C. W. Smith, E. R. Mucciolo, and M. Ishigami, Physical Review B Rapid Communications, **82**, 081417 (2010).

2:40pm **GR+EM+ET+NS+TF-MoA3 Tuning Electronic Properties of Graphene by Controlling its Environment, K.I. Bolotin, Vanderbilt University**

INVITED
Every atom of graphene, a monolayer of graphite, belongs to the surface. Therefore, the environment of graphene -- the substrate onto which graphene is deposited and any coating on top of graphene -- intimately affects the properties of graphene. In this talk, we demonstrate that both the mechanical and electrical properties of graphene can be tuned by varying its environment.

First, we discuss the dependence of electrical transport in graphene on the dielectric constant (k) of graphene's environment. For graphene in vacuum ($k=1$) we observe very strong electron-electron interactions leading to robust fractional quantum Hall effect at temperatures up to 15K. By suspending graphene in liquids, we explore the regime of dielectric constants between ~ 1.5 and ~ 30 . We observe the dependence of carrier scattering in graphene on k and demonstrate large values for room temperature mobility ($>60,000$ cm^2/Vs) in ion-free liquids with high k . We also explore the rich interplay between the motion of ions inside liquids and transport of electrons in graphene. We observe signatures due to streaming potentials and Coulomb drag between ions in the liquid and electrons in graphene.

We also briefly address the mechanical properties of graphene and their dependence on graphene's environment. We demonstrate that the built-in strain, the substrate adhesion force and even the thermal expansion coefficient of graphene depend on the substrate supporting graphene.

3:40pm **GR+EM+ET+NS+TF-MoA6 Study of Impurity-Induced Inelastic Scattering on Suspended Graphene by Scanning Confocal Micro-Raman Spectroscopy, L.W. Huang, C.S. Chang, Academia Sinica, Taiwan, Republic of China**

We utilized a polymer-based procedure to transfer the CVD-grown graphene onto a TEM copper grid. The heat treatment was performed on the graphene membrane in an argon/ hydrogen (Ar/H₂) atmosphere at 400 °C. After the transfer and heat treatment, TEM images, acquired by an ultra-high-vacuum transmission electron microscopy (UHV-TEM), demonstrated areas with distinguishable impurity distribution on the suspended graphene membrane. These areal impurity distributions can also be mapped by the scanning Raman spectroscopy correspondingly, indicating the influence of impurity-induced inelastic scattering. The results of this experiment show that the intensity ratio of Raman spectra 2D band over G band (I_{2D}/I_G) is proportional to minus fourth power of the inelastic scattering rate.

4:00pm **GR+EM+ET+NS+TF-MoA7 The Adsorption of Molecules with Large Intrinsic Electrostatic Dipoles on Graphene, L. Kong, Univ. of Nebraska-Lincoln, G.J. Perez Medina, Univ. of Nebraska-Lincoln, Univ. of Puerto Rico, J. Colón Santana, Univ. of Nebraska-Lincoln, L. Rosa, Univ. of Nebraska-Lincoln, Univ. of Puerto Rico, L. Routaboul, P. Braunstein, Maître de conférences de l'Université de Strasbourg, France, B. Doudin, Institut de Physique et Chimie des Matériaux de Strasbourg, France, C.-M. Lee, J. Choi, Kyung Hee Univ., Korea, P.A. Dowben, Univ. of Nebraska-Lincoln**

Both gold and graphene are excellent conductors, and one might expect that both conductors would fully screen the photoemission and inverse photoemission final states of a molecular adsorbate, but in fact this is not the case. The comparison of the electronic structure of p-quinonoid zwitterionic type molecules with a large intrinsic dipole of 10 Debyes adsorbed on both gold and graphene on copper substrates, shows that the

interaction between the adsorbate molecules and graphene is very weak, confirming that graphene is chemically inert. We find that the photoemission and inverse photoemission final states are well screened for p-quinonoid zwitterionic dipolar molecules on gold. This is not observed in the case of this quinonoid zwitterion adsorbed on graphene on copper. This weaker screening is evident in a larger highest occupied molecular orbital to lowest unoccupied molecular orbital gap for the molecules on graphene. The larger highest occupied molecular orbital to lowest unoccupied molecular orbital gap for the molecules on graphene indicates that a much weaker screening on the photoemission and inverse photoemission final states for these dipolar molecules on graphene than that on gold. This work is reviewed in the context of other studies of molecular adsorption on graphene.

4:20pm **GR+EM+ET+NS+TF-MoA8 Growth of and Interactions in Epitaxial Graphene Layers**, *A. Bostwick*, Lawrence Berkeley National Laboratory, *A. Walter*, *Th. Seyller*, Lawrence Livermore National Laboratory, *K. Horn*, *E. Rotenberg*, Lawrence Berkeley National Laboratory **INVITED**

The electronic properties of graphene has been investigated using angle-resolved photoemission spectroscopy at the MAESTRO* facility of the ALS** synchrotron in Berkeley, California. This laboratory is unique in its ability to grow sophisticated samples for *in situ* study using angle-resolved photoemission spectroscopy, and to subtly alter their properties by engineering their surfaces by chemical doping or thickness control. In this talk I will discuss the electronic properties of graphene, focusing on the role of dopants to control the charge density and as defects to disrupt the metallic conduction. By measuring the spectrum of "plasmaronic" quasiparticle excitations, we can demonstrate the scale-free nature of the Coulomb interaction in Dirac systems. Such effects are readily observed on quasi-free standing graphene samples doped with long-range scatterers. Doping with short-range scatterers, on the other hand, results in a loss of conduction which we interpret as a manifestation of strong (Anderson) localization.

*Microscopic and Electronic Structure Observatory

**Advanced Light Source

5:00pm **GR+EM+ET+NS+TF-MoA10 Squeezing of the Graphene Dirac Cone Observed by Scanning Tunneling Spectroscopy**, *J. Chae*, *S. Jung*, *Y. Zhao*, *N.B. Zhitenev*, *J.A. Stroscio*, Center for Nanoscale Science and Technology / NIST, *A. Young*, *C. Dean*, *L. Wang*, *Y. Gao*, *J.C. Hone*, *K.L. Shepard*, *P. Kim*, Columbia University

The single-particle spectrum of graphene is described by massless Dirac quasiparticles with a linear energy-momentum dispersion relation. In this talk I examine the effect of electron interactions on the graphene energy dispersion as a function of both excitation energy E away from the Fermi energy and density n . To analyze the dispersion, we measure the Landau levels (LLs) in graphene on a hexagonal boron nitride (hBN) insulator in low magnetic fields by scanning tunneling spectroscopy. The experiments were performed in a custom designed cryogenic scanning tunneling microscope system operating at 4 K with applied magnetic fields from 0 T to 8 T. The graphene devices were fabricated by the method detailed in Dean *et al.* [1]. The disorder in graphene on hBN is reduced in comparison with the previous measurements in graphene on SiO₂ [2] allowing us to observe the LLs in fields as low as 0.5 T. By fitting the LL energies obtained at constant density, we find that the energy dispersion remains linear, characterized by a momentum-independent renormalized velocity. However, the renormalized velocity is density dependent, showing a strong increase as the charge neutrality point is approached. The overall spectrum renormalization can be described as a *squeezing* of the Dirac cone angle due to electron-electron interactions at low densities. Interestingly, we also find that the renormalization of the dispersion velocity is affected by the local disorder potential and magnetic field, which is not described by current theory.

[1]. C. Dean, A. Young, I. Meric, C. Lee, L. Wang, S. Sorgenfrei, K. Watanabe, T. Taniguchi, P. Kim, K. L. Shepard, and J. Hone, *Nature Nanotech.* 5, 722–726 (2010).

[2]. S. Jung, G. M. Rutter, N. N. Klimov, D. B. Newell, I. Calizo, A. R. Hight-Walker, N. B. Zhitenev, and J. A. Stroscio, *Nature Phys.* 7, 245–251 (2011).

5:20pm **GR+EM+ET+NS+TF-MoA11 Interfacial Interaction of Graphene and Metal Surfaces Investigated by Resonant Inelastic X-ray Scattering**, *L. Zhang*, University of Science and Technology of China, Advanced Light Source, *J.H. Guo*, Advance Light Source, *J.F. Zhu*, University of Science and Technology of China

The synthesis of graphene on metal surfaces by chemical vapor deposition (CVD) is the most promising method to prepare single-layer and large-area

graphene, which is a prerequisite for the fabrication of graphene-based electronic devices. Therefore, the graphene/metal interfaces have attracted much attention due to their importance in graphene synthesis by CVD processes. In this presentation, we report our recent studies on the electronic structure and band dispersion of graphene on different metal surfaces (Cu, Ir and Ni) by the means of X-ray absorption spectroscopy (XAS), X-ray emission spectroscopy (XES) and resonant inelastic X-ray scattering (RIXS). The XAS spectra for graphene on metal surfaces show strong π^* and σ^* resonant features, indicating that the single-layer graphene films preserve the intrinsic symmetry of graphite. The resonant XES spectra of graphene on different metal surfaces change dramatically, especially for the features of π^* resonances, which can be directly related to the different strength of hybridization between graphene and metal substrates. These significant spectra changes have been proved to be an effective measure for the bonding strength of graphene on different substrates: strong band dispersion can be observed when the interaction between graphene and metal substrate is weak (such as Cu), while the band dispersion is seriously disturbed when a strong hybridization between graphene and metal substrate (such as Ni) exists. These results provide basic understanding of graphene/metal interfacial interaction, which helps to develop graphene-based electronic devices with high performances.

MEMS and NEMS

Room: 10 - Session MN-MoA

Multi-scale Interactions of Materials and Fabrication at the Micro- and Nano-scale

Moderator: M. Metzler, Cornell University

2:00pm **MN-MoA1 Acute Stress in Silicon Nitride**, *J.M. Parpia*, *V.P. Adiga*, *B. Ilic*, *R.A. Barton*, *R. De Alba*, Cornell University, *I. Wilson-Rae*, Technische Universität München, Germany, *H.G. Craighead*, Cornell University **INVITED**

Mechanical structures fabricated from highly stressed silicon nitride films exhibit some of the highest Q (Quality factor) values observed in MEMS/NEMS structures at room temperatures. By varying the diameter and thickness of high stress silicon nitride circular "drum" structures, we observe that the dissipation follows generally predictable behaviors. Qualitatively we see that the fundamental out-of-plane resonance mode has the lowest Q in large structures (though it can still exceed 10^5). As higher modes with radial nodal lines (described as cake like modes) are added, the Q increases. Modes that add a nodal line at a constant radius also have higher Qs, but the Q improvement over the fundamental is not large, and can also lead to lowering of the Q in small structures. Generally thinner more uniform cross section structures reveal the higher Qs. As higher order resonances are excited, the product of the frequency times Q (fQ) tends to a constant. Many of these behaviors are consistent with recent models. This presentation will describe the results obtained as the diameter and thickness of the devices of these structures was varied.

2:40pm **MN-MoA3 In Situ SEM Micro Tension Tests on Nanoscale Single Crystal Metals and Nanocrystalline Metals**, *M. Yilmaz*, *J.W. Kysar*, Columbia University

We developed a microscale uniaxial tension test MEMS device for in-situ SEM experimentation, with potential use for in-situ TEM experiments as well. We have characterized batch compatible integrated ultra-thin nanocrystalline gold nanoscale samples (~40nm thick), as well as externally integrated single crystal gold, and single crystal gold-silver thin-film nanoscale samples (~100nm thick) for their mechanical properties in-situ SEM.

The MEMS device is composed of an electrostatic comb-actuator, and two displacement sensors, with the purpose to mechanically characterize nanoscale samples that are located between the two displacement sensors. Sub-pixel resolution Digital Image Correlation (DIC) on SEM micrographs is used as displacement tracking technique in order to quantitatively characterize the displacement fields of the displacement sensors so as to obtain the force-elongation (hence, stress-strain) behavior of the tested samples. From the stress-strain behavior of the tested nanoscale specimens, we experimentally obtained fundamental material properties such as Young's modulus, and critical resolved shear stress for single crystal materials, and Young's modulus for nanocrystalline ultra-thin gold samples.

The method we apply in this study is the first in its field with the capability to integrate such small samples to MEMS with monolithic microfabrication. Although we worked with ultra-thin film gold, and thin-film gold and gold-silver alloy, the method can be adapted to other materials of interest, such as metals, carbon nanotubes, and graphene.

The results of the experiments are of interest to microelectronics industry, and materials research community.

3:40pm MN-MoA6 Fabrication and Testing of Suspended Piezoelectric Nanocomposite Membranes, J.R. Fox, S.B. Horowitz, J.P. Cortes, M.S. Allen, A.D. Mathias, L.A. Barkett, Ducommun Miltec, M. Sanghadasa, U.S. Army Aviation and Missile Research Development and Engineering Center
The fabrication and testing of a novel piezoelectric microphone consisting of a suspended nanocomposite membrane of oriented hydrothermally-grown ZnO nanorods in a matrix of SU-8 photopolymer is detailed. High aspect ratio ZnO nanorods (0.5 – 1 microns long) were grown using a low temperature hydrothermal process on a patterned gold electrode on a wet-oxidized wafer. Then SU-8 photoresist was spin-coated over the rods to a thickness of approximately 1 micron and subsequently exposed and developed to reveal access to the bottom bond pads of the structure. A top electrode was deposited via sputtering and patterned on the SU-8 polymer. Finally a deep reactive ion etch (Bosch process) through-wafer silicon etch was used to release the nano-piezo-membranes in diameters of 50-400 microns. The infiltration of SU-8 photopolymer into the nanorods was observed to improve during long post-exposure bakes of the polymer as well as produce an improvement in vacuum compatibility of the polymer. Laser Doppler vibrometry (LDV) was used to characterize the actuation of the nano-piezo-membrane both under application of a driving potential as well as during acoustic load from a plane-wave tube.

4:00pm MN-MoA7 Fabrication of Nanoelectromechanical Systems via the Integration of Glancing Angle Deposition Thin Films, J.N. Westwood, V.T.K. Sauer, J.K. Kwan, University of Alberta, Canada, W.K. Hiebert, National Institute for Nanotechnology, Canada, J.C. Sit, University of Alberta, Canada

Nanoelectromechanical systems (NEMS) have been shown to be far more sensitive than microelectromechanical systems (MEMS). However, their smaller size also reduces the surface area of the device. This is problematic when scaling gas- and mass-sensing MEMS to the nanoscale regime because it reduces the area for analyte adsorption. Nanostructured thin films grown by glancing angle deposition (GLAD) provide a potential solution to this issue. GLAD thin films, deposited by evaporation at highly oblique angles between the source and the substrate, have extremely high surface area which can be used to counteract the decreased surface area of NEMS. The low density of GLAD films permits the increase in surface area without adding significant mass. Successful surface functionalization of GLAD films has also been demonstrated. These factors indicate that GLAD films are promising candidates for NEMS sensor applications. A major drawback, however, is that GLAD films are very difficult to pattern using lithography because they are incompatible with the wet processes required for photoresist development and removal. We have devised an alternative process that requires no lithographic patterning of the GLAD by depositing the films on patterned and released NEMS doubly clamped beams. The NEMS are fabricated from silicon-on-insulator wafers by etching away the oxide layer to give released silicon NEMS. Silicon dioxide GLAD films are then deposited. The GLAD films show good uniformity and limited edge effects. These GLAD-coated NEMS, or GLEMS, show significant potential for sensing applications. There are many parameters available for future optimization, including beam dimensions and GLAD film deposition parameters.

4:20pm MN-MoA8 Electroactive Polymeric MEMS Actuators Fabricated by Thermal Imprinting of P(VDF-TrFE-CFE) and Poly(dimethylsiloxane) (PDMS), J. Shkovsky, L. Engel, A. Reuveny, Y. Sverdlov, Y. Shacham-Diamand, D. Schreiber, S. Krylov, Tel Aviv University, Israel

The rapidly developing field of polymeric electronic and microelectromechanical (MEMS) devices has attracted much attention in recent years. Applications of polymeric MEMS devices include thin film transistors, waveguides for optical sensors, stretchable electronics as well as electroactive polymers (EAP) and dielectric elastomers actuators (DEAs). Polymeric actuators are distinguished by their very low fabrication cost, are often biocompatible, demonstrate large strain under small forces, exhibit fast response times, relatively large actuation forces and high efficiency. Because the electric fields required for the actuation of these devices are relatively high, of the order of tens or even hundreds of V/mm, reduction of the thickness of the polymeric layers is crucial for reducing operational voltages. Thin layers of polymeric materials in MEMS devices are typically formed by spin-coating using diluted solutions of the uncured polymer. However, the spin-coating of polymers into micron scale films is challenging as there are strict requirements for film thickness, uniformity, process integration and defect density.

In this work we report on a novel fabrication process based on thermal imprinting for the formation of micron-scale, freestanding, layers of two

polymeric materials, the dielectric elastomer poly(dimethylsiloxane) (PDMS) and the electroactive relaxor P(VDF-TrFE-CFE). We have fabricated freestanding, smooth, defect-free membranes with thicknesses in the range of 0.4–4.8 μm and with diameters of several millimeters. Since the ability to detach the membrane from the chips after imprinting is critical for the production of freestanding layers, the adhesion between the polymers and the silicon (Si) stamp and the Si substrate is reduced by the deposition of a hydrophobic dodecyl-trichlorosilane monolayer on the chips prior to imprinting. We demonstrate the feasibility of patterning the devices at the time of imprinting to create freestanding patterned micron-scale structures. A simple device made up of a freestanding circular membrane with electrodes on the circumference demonstrating the application of the method is presented. The results of the device's electromechanical characterization revealed that a free-standing PDMS membrane 1 mm in diameter and 5.3 mm thick demonstrated displacements of 5 mm at an actuation voltage of 300 V.

Acknowledgements

This project was supported by Arkema/Piezotech. P(VDF-TrFE-CFE) materials were supplied by Piezotech S.A.S

4:40pm MN-MoA9 A CMOS MEMS Gas Sensor Using Monolayer Protected Gold Nano-Clusters Coating on Three-Dimensional Interdigitated Electrodes, Y.C. Chen, C.Y. Chang, National Taiwan University, H.L. Lu, C.-J. Lu, National Taiwan Normal University, W.-C. Tian, National Taiwan University

In this work, a novel gas sensing platform using the TSMC 0.35 μm CMOS-MEMS process was developed. Three-dimensional interdigitated sensing electrodes (3D IDEs) with a polysilicon microheater and a polysilicon thermometer were integrated in this CMOS-based platform. Compared to conventional 2D IDEs, our 3D IDEs not only extended the sensing surface area to the vertical sidewalls but also decreased the gap (the inter metal dielectric layer, IMD, thickness) between electrodes. The microheater of 2.6k Ω resistance and the thermometer of 2k Ω resistance were designed to provide on-chip heating, which could facilitate the deposition and/or activation of the sensing material. The sensing material, monolayer protected gold nanocluster (AuC₈), was coated onto the electrodes through the air brush spraying. The sensor performance was demonstrated with three compounds (Octane, Butanol, and Toluene) of concentrations in the range of 2000ppm to 5000ppm and manifested the good linearity and sensitivity.

The backend of CMOS processes for interconnects were utilized to provide microstructures which offer many potential advantages for sensors including low power consumption, low fabrication cost, high sensitivity and reliability. In the CMOS etching process, the design rules of a released (RLS) mask limit the minimum gap between electrodes to 3 μm . Hence, 3D IDEs were used to decrease the gap between electrodes to 1 μm (the IMD thickness) so as to increase the sensitivity of the designed sensor as well as to lower the resistance of the deposited sensing material. In addition, the consumption of the sensing material was reduced significantly.

When exposing to Toluene at different concentrations, the transient responses of the sensor were changed accordingly. The exceptional linearity of the sensor responses on targeted compounds at high concentrations was demonstrated. The great sensitivities, defined as the ratio of the impedance before and after exposing to the target gas, of the three compounds were obtained (Toluene: 3.66E-5/ppm, Octane: 3.30E-5/ppm, and Butanol: 5.71E-5/ppm). The differences in sensitivities are largely affected by the target gas and its affinity to AuC₈ surface. These variations in sensitivity for different compounds can enhance the specificity of our CMOS-based gas sensor platform.

5:00pm MN-MoA10 Integration of Functionalized Biological Nanostructures with Conventional Transducer Fabrication Schemes, X. Fan, N. Siwak, A. Brown, J. Culver, R. Ghodssi, University of Maryland
Nanoscale technologies have the potential to revolutionize a broad range of fields. Already, there have been a plethora of synthesis and fabrication techniques of nanostructures and devices utilizing both organic and inorganic materials. Biological molecules have transformed chem-bio detection, due to their innate ability to be tailored and engineered via genetics. These nanostructures can be versatile in their various binding properties making them attractive for a variety of applications. These biomolecules, often self-assembled or synthesized with a bottom-up approach, are used for scaffolding and functionalization purposes, while inorganic materials utilize conventional top-down lithographic techniques to

pattern transducers. The integration of these two different technologies is challenging due to fabrication incompatibility. While inorganic materials are robust, biomolecules are highly sensitive to pH levels, temperature, and chemical compositions, making them incompatible with top-down techniques. Thus, their integration is often withheld until the final step of device fabrication. This prevents further backend processing once the biomolecules have been deposited, limiting the degree of integration of nanoscale platforms and restricting the full potential of nanotechnology.

Our team has developed a method to pattern a type of nano-biomolecules onto the active region of a photonic device using a hybrid top-down and bottom-up approach. An optical ring resonator, highly sensitive to refractive index changes, was fabricated using E-beam lithography to investigate the assembly of biomolecules on its surface. *Tobacco mosaic virus* (TMV) was then self-assembled onto the transducer's active area. TMV is a rod like structure with coat proteins that are genetically modified to allow for the self-assembly of viruses onto surfaces and the expression of functionalization on the outer surface. The TMV structure is stable in a pH 2-11 and temperature up to 60°C that survives the conventional lift-off patterning process. This enables the patterning and alignment of biologically functionalized structures on lithographically fabricated transducers post self-assembly.

By integrating TMV structures onto the surface of the ring resonator, we will report on the optical properties of the TMV assembly, including its refractive index and optical loss, for sensing applications. This photonic platform with patterned TMV provides a compatible process to integrate biological nanostructures with conventionally fabricated transducers. This integration scheme we have developed will allow for an additional degree of control when developing nanoscale based hybrid platforms.

5:20pm **MN-MoA11 A Novel Computational and Experimental Methodology for Development of Therapeutic Microdevices for Rapid Reconstitution**, *S. D'hers*, Buenos Aires Institute of Technology, Argentina, *A. Alexander-katz*, *N.M. Elman*, Massachusetts Institute of Technology

Rapid Reconstitution Packages (RRPs) represents a breakthrough microfluidic platform to use pharmaceutical drugs in ambulatory settings without the need for refrigeration. RRP were designed as microfluidic cartridges, keeping drugs in lyophilized form (powder) for years and perform on demand reconstitution in the order of milliseconds. The unique integration of a dual multi-scale computational and experimental model with nano-materials and microfluidics provides the scientific basis towards the development of an ultra-portable platform for long term storage and extremely rapid reconstitution. The device architecture consisted of mixing microstructures, fabricated with Stereo Lithography Apparatus (SLA) with biocompatible materials. Rapid prototyping provided a quick turnaround experimental model for validating computational models, rendering a unique methodology for optimization. Experimental setup was intended to emulate temperature fluctuations in ambulatory environments. Experiments were performed using standard analytical methods on RRP containing drugs exposed to temperatures in the range of 25-65 C. High Performance Liquid Chromatography (HPLC) assays for quantifying reconstitution, and Enzyme-Linked Immunosorbent Assays (ELISA) for activity were performed. Several drugs were tested, including atropine for resuscitation, and tissue plasminogen activator (tPA) for treatment of thrombosis. The design was optimized in parametric software and tested for manufacturability and functionality using Computed Fluid Dynamics (CFD) analyses. Design optimization using the CFD models was performed with the goal of reducing drug retention in the device and tailoring drug concentration profiles during activation. A consistent fluidic representation was adopted to model drug dissolution and diffusion. The numerical scheme was validated through computational and laboratory tests for drug dose and concentration profile. Experimental results reveal the importance of the combined use of computational and experimental techniques. The convergence of these unique techniques allows exploitation of physical processes at the nanometer and micrometer scales to investigate the lyophilization and reconstitution processes, overall rendering a synergistic computational and experimental methodology for development of therapeutic microdevices. The use of RRP will result in significant improvement in logistics for a number of civilian and military applications.

Nanomanufacturing Science and Technology Focus Topic

Room: 16 - Session NM+NS+MS+EM-MoA

ALD and Scalable Processes for Nanomanufacturing

Moderator: T.S. Mayer, Penn State University

2:00pm **NM+NS+MS+EM-MoA1 From R&D Towards Industrial Atomic Layer Deposition: Challenges in Scaling up**, *M. Putkonen*, Beneq Oy, Finland

More and more ALD-enabled applications are emerging. Most of the ALD processes and applications are first demonstrated by small scale experiments. In optimal cases, the innovations lead to material-application combinations which have solid commercial interest. In the subsequent verification and pilot production phase, there is need for increased throughput and reduced costs also for the ALD processed materials.

There are two main features of ALD, that should be optimized when industrial scale production is being considered. Firstly, in large-area coating processes, more attention should be paid to the properties of the precursors. For large-area coatings, large doses of precursors are delivered to the substrates, preferably in very short pulses in order to keep the total cycle time as short as possible. This often requires either DLI-type sources or increased vapor pressure (i.e. increased thermal stability of metal precursors). In addition, although the ALD chemistry should be surface controlled and not dependent on the substrate surface area, deposition rates and film uniformities are habitually dependent on the tool configuration.

Secondly, ALD has so far been largely confined to laboratories due to non-availability of efficient, larger scale, high-throughput ALD systems. Whereas sputtering and CVD have been mainstream coating tools for decades, ALD has only recently started to gain acceptance as a mainstream industrial coating method. For example, ALD is widely seen as the desired manufacturing technology for producing high-quality functional layers for solar cells and packaging materials, but ALD is commonly considered too slow for high throughput manufacturing. However, large-area batch ALD tools, such as the Beneq P800, can operate up to 10 m² batch sizes and still maintain ALD cycle times in the range of 3-5 s. Currently, industrial ALD is diffusing into various industrial thin film areas where single wafer, batch or roll-to-roll ALD is the preferred coating method.

In this presentation, we discuss the different requirements for single wafer, conventional batch, cross-flow batch as well as spatial ALD deposition processes and tools for large throughput applications. In addition to conventional Al₂O₃ and TiO₂ processes, SiO₂ processes are used as examples when scaling up chemistry from single wafer to batch ALD. In addition, process transfer from an R&D scale Beneq TFS 200R rotating drum reactor to the true roll-to-roll Beneq WCS 500, developed for OLED encapsulation applications, is discussed in detail. Results of the studies using this system are presented including temperature dependence of growth rate, RI and WVTR measurements.

2:20pm **NM+NS+MS+EM-MoA2 Enabling ALD for Semiconductor Manufacturing**, *D. Chu*, Applied Materials Inc. **INVITED**

Atomic layer deposition (ALD) is being extensively studied for semiconductor applications because of its precise, atomic level thickness control for very thin films; ALD is extremely conformal and the overall thermal budget is lower than its CVD alternatives. However, ALD is inherently slow which makes it cost prohibitive.

Adoption of ALD processes into manufacturing requires consideration of multiple factors. At Applied Materials, we focus on three main areas to enable ALD for volume manufacturing.

1. Atomic level engineering to create differentiated solutions that boost device performance.
2. Tool architecture and methods to allow integration of multiple films without vacuum break. This is particularly of importance when films scale to Angstrom level, stability of the film becomes an issue. Extendable tool architectures allow integration of other films such as capping layers and pre-post treatments to address this issue
3. Accelerate adoption of standalone ALD films by improving manufacturability and productivity while maintaining single wafer performance

Example applications and challenges for each area will be discussed in this paper.

3:00pm NM+NS+MS+EM-MoA4 Migration to ALD Techniques in the Semiconductor Industry: Pattern Effects, Microloading and Film Thickness Variability in Dielectric Thin Films Deposition, M.P. Belyansky, IBM Semiconductor R&D Center

The continuation of scaling in the microelectronics industry is having a profound effect on thin film deposition techniques and processes. One of the consequences of the scaling is a decrease in average film thickness to accommodate the shrinking device dimensions which amplifies the problem of film thickness variability. Most of the CVD deposition techniques and tooling are reaching the limit of reliable thickness control of very thin films. At the same time, circuit designs are becoming more complex, which leads to significant pattern density variation on macro scale. Therefore CVD technology is facing a tremendous challenge in controlling film thickness and properties across variable pattern density which has been one of the major reasons that facilitated the transition to ALD-like deposition techniques and processes in the industry.

The paper discusses the microloading effect (dependence of thin film deposition rate on pattern density) as well as other manifestations of pattern effects in the semiconductor manufacturing. The data shows the effect of microloading on the variation of as deposited film thickness across features of different size as well as for identical features with different pattern density in the surrounding areas. The microloading performance of CVD and ALD silicon oxide and silicon nitride dielectric thin films is covered as well as methods aimed at quantifying and improving thin film variability. The effects of major process parameters, precursor chemistry and tool design on the thin films microloading performance are delineated. Thin films step coverage over a nano scale feature and pitch to pitch film thickness dependence for CVD and ALD dielectric processes are also discussed.

3:40pm NM+NS+MS+EM-MoA6 Interface Analysis of PEALD TaCN Deposited on HfO₂ using Parallel Angle Resolved X-ray Photoelectron Spectroscopy for sub-20nm Gate Last CMOS Transistors, F. Pierrat, ST Microelectronics, France, V. Beugin, R. Gassilloud, P. Michallon, CEA Grenoble, France, L. Dussault, B. Pelissier, LTM - MINATEC - CEA/LETI, France, C. Leroux, CEA Grenoble, France, P. Caubet, ST Microelectronics, France, C. Vallée, LTM - MINATEC - CEA/LETI, France

Sub-20 nm high-k/metal CMOS devices require about 2 nm thin metal gate electrode with adapted work function (WF) and chemical inertness regarding the high-k dielectric sub-layer. TaCN material deposited by Plasma Enhanced Atomic Layer Deposition (PE-ALD) has been investigated as a possible gate electrode candidate [1-2]. Depending on the carbon content TaCN can presents a *p-type* behavior with a WF from 4.5 to 4.7eV [3]. Besides plasma used for deposition may have an impact on the under-layer dielectric such as an increase of the EOT [4]. A deviation from bulk material characteristics of the metal gate WF is induced by the intimate bond linking environment at high-k/TaCN interface, but these chemical mechanisms are still unclear. Thus, in this work, interface of TaCN and HfO₂ dielectric is carefully analyzed by X-Ray Photoelectron Spectrometry (XPS), using Ta4f, Hf4f, O1s, C1s, N1s and Si2p core levels, and obtained bonding environments are correlated to work function extracted from MOS capacitors.

Thanks to chemical stability of SiO₂ [5], bonding environments of TaCN/SiO₂ and HfO₂/SiO₂ stacks were chosen as reference for XPS analysis. Then, by comparing TaCN deposited on HfO₂ spectra with these references, the evolution of the chemical environments can be determined, thus a mechanism of interaction between the two materials is proposed. Furthermore, it appeared that, when deposited on HfO₂, TaCN oxidation is higher than on SiO₂, which is attributed to the higher capacity of HfO₂ to have O deficiency [6].

In addition, TaCN/HfO₂/SiO₂ stack was measured using Parallel Angle Resolved XPS (PARXPS) in order to build a depth composition profile. This profile confirms the modifications of chemical environment such as oxidation of the electrode close to high-k/metal interface, it also shows N penetration in HfO₂, which could be induced by plasma densification.

Finally, electrical results from MOS capacitors with TaCN/HfO₂/SiO₂ stacks and TiN/W plug have shown an evolution of the *p-like* metal flat band voltage (V_{fb}) with plasma conditions. The modifications of chemical bonding environment observed at the high-k/metal interface can give insight on this deviation of V_{fb} with plasma.

[1] W. S. Hwang, D. Chan, B. Jin Cho, IEEE Transactions on Electron Devices, 55, (2008)

[2] H. Zhu and R. Ramprasad, Journal of Applied Physics 109, 083719 (2011)

[3] H. N. Alshareef, et al., Electrochemical and Solid-State Letters, 11, H182 (2008)

[4] H. C. Shin and C. Hu, Semiconductor Science Technologie, 11, 463, (1996)

[5] M. Zier, et al., Applied Surface Science 252, 234 (2005)

[6] G. D. Wilk, R. M. Wallace and J. M. Anthony, Journal of Applied Physics 89, 5243 (2001)

4:20pm NM+NS+MS+EM-MoA8 Atmospheric Pressure Atomic Layer Deposition of Al₂O₃ using Trimethylaluminum and Ozone, M.B. Mousa, D.H. Kim, C.J. Oldham, G.N. Parsons, North Carolina State University

Atomic layer deposition (ALD) is used for nanoscale coatings with high uniformity and precise thickness control. Currently, most commercial ALD processes operate in batch mode. Expanding to ambient pressure can increase throughput and facilitate its integration for applications such as smart textiles, flexible electronics and synthetic polymer coatings. We find that under certain flow conditions in the trimethylaluminum (TMA)/water ALD process for Al₂O₃, increasing the reactor pressure from ~2 Torr to 760 Torr can produce excess film growth per cycle.

For this work, we studied ALD of Al₂O₃ using TMA/O₃ and compared growth at ~2 Torr to that at 760 Torr in a flow tube reactor. We measured film thickness by ellipsometry and surface morphology by AFM. Also, we plan to monitor in-situ growth using a quartz crystal microbalance (QCM). At 2 Torr, by changing the ozone and TMA exposure times, we saw clear ALD saturation at ~0.45 Å/cycle at 170°C. A shorter purging time after the ozone exposure tends to increase the growth per cycle. Deposition at higher pressure results in growth rates between ~0.3 and 0.6 Å/cycle at 205°C, with lower growth rates obtained under higher gas flow rate conditions. For both the water and O₃ processes at 760 Torr, a low gas flow rate of 0.5 standard liters per minute (slm) in our flow-tube reactor leads to a high growth rates of ~3 Å/cycle (for water) and 0.6 Å/cycle (for O₃). For the water process at 760 Torr, increasing the flow rate to 10 slm somewhat decreases the growth per cycle to ~1.35 Å/cycle. However, for the O₃ processes at 760 Torr, we need only a relatively small increase to 1.5 slm to achieve growth of 0.3 Å/cycle. This could be due to enhanced ozone desorption kinetics compared to the rate of water desorption under the conditions used. Also interestingly, we find for the water process that films deposited at high pressure have higher surface roughness than films deposited at low pressure. These results will help to identify the key parameters for new continuous atmospheric pressure ALD reactors designs.

4:40pm NM+NS+MS+EM-MoA9 An Industrial Solution for Surface Passivation of c-Si using AlO_x Film Deposited by In-line Atmosphere Chemical Vapor Deposition, K. Jiang, Gebr. Schmid GmbH + Co, Germany, K.O. Davis, University of Central Florida, C. Demberger, H. Zunft, H. Haverkamp, Gebr. Schmid GmbH + Co, Germany, W.V. Schoenfeld, University of Central Florida, D. Habermann, Gebr. Schmid GmbH + Co, Germany

Among the different dielectric passivation layers for crystalline silicon (c-Si) solar cells, AlO_x has recently received a great attention due to its excellent chemical and field effect passivation performance for p-type c-Si surface. It offers great promise as a rearside passivation material for passivated emitter and rear cell (PERC) designs. However, up to this point in time, most of the development has been based on laboratory scale deposition systems and methods. Common approaches for synthesizing these passivation layers are thermal or plasma-assisted atomic layer deposition (ALD), whose deposition rates are typically too low (< 10 nm/min) to be compatible with high-volume manufacturing. Other deposition methods like PECVD or spatial separated ALD enable an increase in deposition rate by one order of magnitude (i.e. 100 nm/min). An industrially-compatible deposition technique with low processing cost, easy-handling, compact size, and high throughput that still retains comparable passivation performance to ALD films remains a challenging task.

Using an in-line atmosphere chemical vapor deposition (APCVD) tool, we have synthesized amorphous AlO_x films from precursors of trimethylaluminum and O₂, yielding a maximal deposition rate of up to 150 nm/min per wafer. Deposition rate is determined by the film thickness divided by wafer transportation time through the CVD injector. Both top view and the cross-sectional SEM images present an intact AlO_x/Si interface. A smooth surface is shown without any outgassing (blistering) after deposition and a subsequent firing step. The as-deposited layers exhibit an over stoichiometric O/Al ratio of 1.65~1.75 due to the incorporation of an OH group inside the layer. For both high and low doped p-type c-Si wafers deposited with APCVD AlO_x, excellent surface passivation is achieved with a maximum effective surface recombination velocities (S_{eff,max}) of 8 cm/s following by a firing step. These findings are attributed to the buildup of a large negative charge (Q_f ≈ -3 × 10¹² cm⁻²) and low interface defect density (D_{it} ≈ 4 × 10¹¹ eV⁻¹cm⁻²) following the firing process. It is believed that the incorporated OH group plays an essential role during the firing step. During the annealing/firing step, a certain degree of

dehydration takes place (i.e. Al sites bonded OH termination start to bond via an O bridge), which may involve an octahedral to tetrahedral coordination change. This could facilitate the negative charge formation and release of atomic H for passivating the Si dangling bonds at the AlO_x/Si interface.

This data implies a high application potential of APCVD AlO_x for low cost industrial solar cell applications.

5:00pm **NM+NS+MS+EM-MoA10 Solution Based Processing of Floating Gate Memory using Additive-Driven Self-Assembly and Nanoimprint Lithography**, *J. Watkins*, University of Massachusetts **INVITED**

Polymer and polymer-inorganic hybrid materials organized at the nanoscale are at the heart of many devices that can be created on flexible substrates for applications in energy generation and storage, microelectronics, optoelectronics, communications and sensors. The challenge is to produce these materials using process platforms and materials sets that are environmentally and economically sustainable and can be scaled for cost-effective, high value-added manufacturing. Here we describe a resource efficient, additive approach based on roll-to-roll coating of self-assembled hybrid materials. Specifically we report that nanostructured templates with periodic spherical, cylindrical, and lamellar morphologies exhibiting sub-10 nm domains can be easily obtained through the blending of commercially available disordered polymer surfactants with commodity homopolymers that selectively associate with one segment of the surfactant. We further demonstrate that order in the surfactant systems and in block copolymer templates can be induced by nanoparticle additives that undergo multi-point hydrogen bonding with one of the segments of the polymer template. These additives, which include metal and semiconducting nanoparticles, fullerenes, and other active components, impart functionality to the device. The strong interactions further enable particle loadings of more than 40% in the target phase, resolving a crucial constraint for many applications. These systems can be scaled in our newly constructed R2R processing facility, which includes a custom microgravure coater for hybrid materials that is equipped for in-line substrate planarization and a precision R2R UV-assisted nanoimprint lithography (NIL) tool.

We illustrate the capabilities of these approaches by the fabrication of floating gate field effect transistor memory devices. For this application, the charge trapping layer is comprised of well-ordered polymer/gold NP composites prepared via additive-driven self-assembly; the addition of gold nanoparticles that selectively hydrogen bond with pyridine in poly(styrene-*b*-2-vinyl pyridine) copolymers yields well-ordered hybrid materials at gold nanoparticle loadings of more than 40 wt.%. The charge trapping layer is sandwiched between a dielectric layer and a poly(3-hexylthiophene) semiconductor layer. We can achieve facile control of the memory windows by changing the density of gold nanoparticles. The devices show high carrier mobility (> 0.1 cm²/Vs), controllable memory windows (0~50V), high on/off ratio (>10⁵) between memory states and long retention times. Strategies for patterning of the device using NIL will be discussed.

Nanometer-scale Science and Technology

Room: 12 - Session NS+SP-MoA

Nanopatterning and Nanolithography

Moderator: P.E. Sheehan, U.S. Naval Research Laboratory

2:00pm **NS+SP-MoA1 Optical Properties of As-Prepared and Annealed Gold Nanostructures Fabricated by Interference Lithography**, *A.B. Tsargorodskaya*, University of Sheffield, UK, *A.V. Nabok*, Sheffield Hallam University, UK, *A.J. Lee*, University of Leeds, UK, *G.J. Legget*, University of Sheffield, UK

Gold nanostructures were fabricated by interferometric lithography (IL) with a view to their application for optical bio-sensing based on localized surface plasmon resonance. This approach relies upon very modest instrumentation, high processing speed and capacity for fabrication of dense arrays of nanostructures over macroscopic areas. The dimensions and morphology of nanostructures obtained were characterized by AFM/SEM. The arrays of 65-200nm wide and 125-400nm long gold nano-dots and nano-rods with spacing of 120-220nm were fabricated by IL.

UV-vis absorption spectra of gold nanostructures showed a characteristic peak at ca. 520nm associated with localized surface plasmons. A spectroscopic ellipsometry study of the gold nanostructures was carried out. Raman spectra of a thin film of phthalocyanine adsorbed on gold nanostructures showed an enhancement of Raman scattering of up to 200 times compared with the same film deposited on continuous gold layer.

Post-lithographic processing by annealing was found to improve the optical properties of the nanostructure arrays still further. Annealed samples appear higher and smaller compared to as-prepared samples. AFM images show that all the samples annealed at between 450-470°C for 50-120min retain a regular pattern. XRD analysis of annealed gold nanostructures evinces formation of crystal clusters on the surface.

In order to demonstrate the biosensing capabilities of annealed and as-prepared nanostructures, the LSPR response of nanostructures to changes in the bulk refractive index (RI) was investigated. The RI sensitivity of the annealed samples is found to be 145nm/RIU. Compared to the RI sensitivity value of the as-prepared sample (52.5nm/RIU) this value is ~2.7 times higher due to smaller size of nanostructures and larger spacing between them.

A model biosensing of streptavidin-biotin binding and BSA were successfully performed on as-prepared and annealed gold nanostructures. Measurements were based on the LSPR shift induced by local RI change when proteins are immobilized on the nanostructures. Streptavidin concentrations were washed over the nanostructured surface in cumulative succession ranging from 0.1µg/ml to 0.1mg/ml, followed by an identical protocol with biotin. Characteristic increases and saturation are noted through shifts in the absorption of the LSPR peak at ca. 635nm. Annealed nanostructures demonstrated a higher detection limit (DL) compare to as-prepared one: the DL for BSA is 1.5fM and 50pM for annealed and as-prepared nanostructures, respectively. Our results demonstrate the potential of interference lithography for the application of plasmon-based biosensing devices.

2:20pm **NS+SP-MoA2 Fast Turnaround 3D Nanolithography using Heated Probes – from Nanofabrication to Directed Assembly**, *A.W. Knoll*, P. Paul, IBM Research - Zurich, Switzerland, *F. Holzner*, IBM Research - Zurich, ETH Zurich, Switzerland, *J.L. Hedrick*, IBM Research - Almaden, *M. Despont*, IBM Research - Zurich, Switzerland, *C. Kuemin*, IBM Research - Zurich, ETH Zurich, Switzerland, *H. Wolf*, IBM Research - Zurich, Switzerland, *N.D. Spencer*, ETH Zurich, Switzerland, *U. Duerig*, IBM Research - Zurich, Switzerland **INVITED**

A novel thermal scanning probe lithography (tSPL) method based on the local removal of organic resist materials has been developed at the IBM Research Laboratory in Zurich [1-3]. A polymeric polyphthalaldehyde resist [2-4] responds to the presence of a hot tip by local material decomposition and desorption. Thereby arbitrarily shaped patterns can be written in the organic films in the form of a topographic relief, constrained only by the shape of the tip. The combination of the fast 'direct development' patterning of a polymer resist and the in-situ metrology capability of the AFM setup allows to reduce the typical turnaround time for nano-lithography to minutes.

Patterning rates of 500 kHz have been achieved. For this, the mechanics and drive waveform of the scan stage were optimized, achieving high speed linear scanning with an overall position accuracy of ± 10 nm over scan-ranges and scan-speeds of up to 50 µm and 20 mm/s, respectively. A pre-tension-and-release strategy was used to actuate the cantilever above its resonance frequency of 150 kHz.

Fabrication of three dimensional patterns is done in a single patterning step by controlling the amount of material removal at each pixel position. The individual depths of the pixels are controlled by the force acting on the cantilever.

The structuring capability in the third dimension adds an entirely new feature to the lithography landscape and finds applications e. g. in multi-level data storage, nano/micro-optic components and directed positioning of nanoparticles. For the latter, shape-matching guiding structures for the assembly of nanorods of size 80nm × 25nm have been written by thermal scanning probe lithography [4]. The nanorods were assembled into the guiding structures by means of capillary interactions. Following particle assembly, the polymer was removed cleanly by thermal decomposition and the nanorods are transferred to the underlying substrate without change of lateral position. As a result we demonstrate both the placement and orientation of nanorods with an overall positioning accuracy of ≈ 10 nm onto an unstructured target substrate.

[1] D. Pires, J. L. Hedrick, A. De Silva, J. Frommer, B. Gotsmann, H. Wolf, M. Despont, U. Duerig, and A. W. Knoll, *Science* **328**, 732 (2010).

[2] A. W. Knoll, D. Pires, O. Coulembier, P. Dubois, J. L. Hedrick, J. Frommer, U. Duerig, *Adv. Mat.* **22**, 3361 (2010).

[3] P. C. Paul, A.W. Knoll, F. Holzner, M. Despont and U. Duerig, *Nanotechnology* **22**, 275306 (2011).

[4] F. Holzner, C. Kuemin, P. Paul, J. L. Hedrick, H. Wolf, N. D. Spencer, U. Duerig, and A. W. Knoll, *NanoLetters*, **11**, 3957 (2011).

3:00pm **NS+SP-MoA4 Laser Assisted Electron Beam Induced Deposition of Platinum**, *N.A. Roberts*, University of Tennessee Knoxville, *J.D. Fowlkes*, Oak Ridge National Laboratory, *G.A. Magel*, *T.M. Moore*, Omniprobe, Inc. an Oxford Instruments Company, *P.D. Rack*, University of Tennessee Knoxville

We introduce a laser assisted electron beam induced deposition (LAEBID) process which is a nanoscale direct write method that implements a synchronized electron beam induced deposition (EBID) process with a pulsed laser step for thermal desorption of the reaction by-product. The pseudo-localized (~ 100 nm spot), pulsed laser enables thermal desorption of the reaction by-product without the issues associated with bulk substrate heating, which shortens the precursor residence time and distort pattern fidelity due to thermal drift. Current results show a significant purification of platinum deposits (~35% Pt) with the addition of synchronized laser pulses as well as a significant reduction in deposit resistivity. Measured resistivity from platinum LAEBID structures (1.2×10^4 mW-cm) are more than 3 orders of magnitude lower than standard EBID platinum structures (2.2×10^7 mW-cm) from the same precursor and are lower than the lowest reported EBID platinum resistivity with post-deposition annealing (1.4×10^4 mW-cm).

3:40pm **NS+SP-MoA6 Parallel Stacking of Extended π -conjugated Molecules on Si(100)-H Surface**, *M.Z. Hossain*, Gunma University, Japan, *H. Kato*, Osaka University, Japan, *M. Kawai*, The University of Tokyo and RIKEN, Japan

Understanding and controlling of intermolecular interaction in highly organized π -conjugated molecules is crucial for the development of the high performance organic devices. Molecule-molecule interaction through frontier orbital states is assumed to be substantially varies with the packing pattern and intermolecular distance. H-terminated Si(100) surface has appeared as an ideal template for controlled stacking of π -conjugated molecules, where the intermolecular distance is defined by the dimer-dimer distance on the surface. To date, a number of studies have been reported on the controlled growth of different types of molecular assemblies and their junctions on the surface. It is expected that intermolecular interaction between such assemblies should strongly varies with substituent and extent of π -conjugation of the molecules. Here we report various nanopattern formation with some simple acene molecules such as 9-vinyl anthracene, 2-vinyl naphthalene and styrene on H-terminated Si(100) using scanning tunneling microscope (STM) and ultraviolet photoelectron spectroscopy (UPS).

Controlled stacking of styrene molecules on H-terminated Si(100) surface through chain reaction mechanism is well known. Self-directed growth of molecular stacking is exclusively directed along the dimer row on the surface, where the phenyl rings are stacked in parallel along the dimer row. Unlike styrene molecule, 9-vinyl anthracene forms both orderly stacking pattern along the dimer row and disorderly nanopattern on the surface. The relative appearances of these orderly and disorderly nanopatterns in STM images depend on the applied sample bias while scanning. At lower bias, the orderly pattern appears much brighter than that of the disorderly pattern. This contrast difference between two structures relates to the enhanced π - π interaction in the case of orderly stacked nanopattern. We also observe that the orderly nanopattern of anthracene molecules undergoes reversed chain reaction very frequently compared to that of styrene molecule.

The 2-vinyl naphthalene molecules form relatively shorter assemblies along the dimer row. Some short disorderly structures are also seen in STM images. UPS measurements of different surfaces containing high-density nanopatterns of these acene molecules have been performed. The observed peaks in UPS spectra are reasonably in agreement with the theoretical calculations reported earlier. The details of the UPS spectra and the reaction mechanism of each molecule forming different nanopatterns will be discussed.

4:00pm **NS+SP-MoA7 Kinetics of disilane reaction on Si(100)-(2x1): Flux, Temperature, and H-coverage Dependence**, *D. Dick*, *J.-F. Veyan*, University of Texas at Dallas, *P. Mathieu*, Mc Gill University, Canada, *J.N. Randall*, Zyvex Laboratories, *Y.J. Chabal*, University of Texas at Dallas

Atomic Layer Epitaxy (ALE) is a fundamental process in the Atomically Precise Manufacturing (APM) of nanoscale devices. Si₂H₆ has been shown to be a good precursor molecule for patterned growth on Si(100) using Chemical Vapor Deposition (CVD). For ALE of silicon, three parameters have to be considered: the incident Si₂H₆ flux, the temperature, and partial H coverage of the surface. These parameters have been investigated experimentally using in-situ infrared absorption spectroscopy to characterize the nature and coverage of species on a Si (100)-(2x1) surface in a well-controlled environment (2x10⁻¹⁰ Torr base pressure).

The flux dependence was studied over two orders of magnitude and temperature dependence from 173 K to 473 K for varying fluxes. It was found that the nature of SiH_x species formed at the surface was strongly

dependent on the flux, with higher silanes (e.g. x>1) for higher fluxes. Furthermore, the time required for saturation also decreased with increasing flux and temperature.

The impact of partial H coverage was also investigated with H coverage from 0.01 To 1ML Monolayer, achieved by partial desorption of a H saturated surface. On the substrate's surface has been also investigated with FT-IR under UHV conditions. It has been found that even a very small amount of Hydrogen (~1% ML) substantially reduces the chemisorption of disilane on the clean parts of Si(100)-(2x1).

This complex dependence on flux and temperature arises from the complex and highly temperature dependent adsorption/dissociation behavior of disilane on Si(100). The dependence on partial H coverage highlights the spatial requirements of the dissociation products, as uncovered in our earlier work.¹

¹ J.-F. Veyan, et al., Journal of Physical Chemistry C 115, 24534.

4:20pm **NS+SP-MoA8 SPM Lithography on Silicon Reconstructed and Hydrogen-Passivated Surface**, *J. Fu*, *K. Li*, *N. Pradeep*, *L. Chen*, *R. Silver*, National Institute of Standards and Technology

We are using Scanning Probe Microscope (SPM) to write patterns directly on a single crystal silicon surface that was reconstructed and hydrogen-passivated in the ultra high vacuum (UHV) chambers, and are followed by the process of reactive ion etching to transfer the patterns into the silicon bulk. The patterns were written either by an atomic force microscope (AFM) in the ambient or by a scanning tunneling microscope (STM) in UHV chambers and was immediately proceeded by an oxidation process in a separate vacuum chamber. AFM or STM patterned samples were immediately transferred to a RIE chamber via an argon back-filled inflatable glove box.

In terms of patterning, the AFM in the ambient environment and the STM in the UHV both can perform lithography; however, the mechanism are quite different: the AFM is adding species, OH⁻, to the surface, and the STM is removing species, H, from the silicon surface.

The features patterning by the AFM prior to RIE process were 1~2nm in height, and were 15~20nm height after RIE and 6nm wide (FWHM) that were measured and confirmed by a critical dimension AFM (CD-AFM). For the features patterning by STM, it was conjectured the height were 0.2~0.3nm prior to RIE. After the RIE process, the height was measured to be 0.7nm.

4:40pm **NS+SP-MoA9 Ultra-High Frequency Surface Acoustic Wave Generation in Silicon Using Inverted Nanoimprint Lithography**, *S. Büyükköse*, University of Twente, Netherlands, *B. Vratzov*, NT&D – Nanotechnology and Devices, Germany, *D. Ataç*, *J. van der Veen*, University of Twente, Netherlands, *P.V. Santos*, Paul-Drude-Institut für Festkörperelektronik, Germany, *W.G. van der Wiel*, University of Twente, Netherlands

Surface acoustic waves (SAWs) are widely used and very important phenomena in both research and industry. SAWs are mechanical vibrations propagating along the surface by confining the acoustic energy over a depth of typically one wavelength. In piezoelectric materials, they can be excited through the inverse piezoelectric effect by using interdigital transducers (IDTs): two interlocking comb-shaped metallic electrode pairs. A piezoelectric potential wave accompanies the mechanical wave. The unique SAW properties make them suitable for wide range of applications. Among the most exciting applications of SAWs are acousto-optical modulators as well as the control of excitons, electrons, and spins in semiconductors. For almost all SAW applications, there is a strong demand for higher frequencies, for example to enhance processing speed or to reach the quantum regime. There are two main factors determining the IDT resonant frequencies: the acoustic properties of the substrate, and the IDT period constrained by lithography resolution. In latter case, the resolution of standard photolithography (minimum finger width of approx. 0.5 μ m) limits the operation frequency to around a few GHz, even for high acoustic-velocity substrates.

In this study, an alternative lithography technique, "step-and-flash nanoimprint lithography" (SFIL), with a novel material system for lift-off was used to reach very high resolution and higher reproducibility. Hydrogen silsequoxane (HSQ) was used as a planarization layer and an excellent etching mask to get inverted replication of the IDT features on the SFIL template. A sufficient undercut profile of the electrode features, which is essential for metal lift-off at nanoscale, was successfully achieved. Very high critical dimension (CD) control has been obtained for the electrode dimensions from 125nm down to 65 nm. While this method has the advantage of EBL resolution, it is nearly substrate independent with higher throughput compared to EBL. For the IDT fabrication, we have deliberately chosen a rather standard Si substrate to demonstrate that our method can result in extremely high-frequency SAW devices, which can be

monolithically integrated with common electronic circuitry. Integration of high-frequency SAW devices is normally restricted by the incompatibility of piezoelectric films with CMOS processing. We showed that SAW delay line devices with 125nm down to 65 nm metal lines can reach resonance frequencies up to 16 GHz in ZnO/SiO₂/Si multilayer system, which is the highest frequency for ZnO based transducers on Si reported so far. The finite element analysis confirmed the results and showed good agreement with the experiment.

5:00pm **NS+SP-MoA10 Variance of Proximity Effect Correction Parameter Measured on Silicon**, *D.A. Czuplewski, L.E. Ocola*, Argonne National Laboratory

We present data showing that the relative intensity of the backscattered electrons, h , to primary write electrons varies depending on the experimental setup. Our data is consistent with the wide range in values reported in the literature for h . The value of h was determined using a doughnut and cross method [1] where the range of the backscattered electrons was measured to an uncertainty of less than 1%. We find that using this method to determine h provides values that are dependent on the dose of the doughnut. Such a result raises questions on the effectiveness of standard proximity effect correction models (PEC) if they rely on a single h value. Standard PEC models attempt to load level the dose received by the desired pattern in the e-beam resist from all sources of electrons, including the forward and backward scattered electrons during an electron beam exposure.

The relative dose of the backscattered electrons was measured using a set of intersecting lines at the center of tori patterns in a doughnut and cross method [1], (Fig. 1). The backscattered electron dose contribution was varied by changing the dose of the tori with respect to the dose of the intersecting lines as can be seen in Fig. 2. The expected behavior would be a consistent ratio of the backscattered contribution and the line dose; however, as the backscattered electron dose is decreased, the relative contribution to the pattern increases faster than the line dose contribution (Fig. 3). The causes of this phenomenon are not certain yet, but the implications could change existing PEC models. Through further study of this phenomenon, it is possible that the models used in PEC could be updated to accommodate this data and therefore give more accurate dose assignments.

[1] D. A. Czuplewski, L. E. Ocola, *Appl. Phys. Lett.* **99** 192105 (2011).

5:20pm **NS+SP-MoA11 Nanopatterning of Poly(N-isopropylacrylamide) based Hydrogel – Gold Nanoparticle Composite**, *K.J. Suthar, D.C. Mancini, R.S. Divan*, Argonne National Laboratory, *O.N. Ahanotu*, University of Michigan

This paper presents the nanopatterning of the hydrogel-gold nanocomposite. We synthesized water based colloidal suspension of covalently bound gold nanoparticles (5-10nm) on the backbone of Poly(Allyl amine) by reduction of gold salt on the amine groups of polymeric chain. Poly(N-isopropylacrylamide) was dissolved in Poly(Allyl amine) based gold colloidal solution. This solution then spun-coated on Hexamethyldisilazane primed Si wafer for nanolithography. The hydrogel precursor was dried in air. Resulting thickness of the hydrogel precursor was approximately 1 μ m. The samples were then exposed to 110-180 μ C/cm² e-beam. The exposure dose was optimized for different thickness of precursor. Different characterization techniques such as UV-vis spectroscopy, differential scanning calorimetry, FTIR, scanning electron microscopy, and atomic force microscopy were employed for characterization. Thus, gold nanoparticles were incorporated into a three dimensional, cross-linked, polymeric hydrogel network by nanopatterning technique. With the ability of hydrogels to expand or contract with changes in pH and temperature, the spacing between nanoparticles can be controlled, allowing a single material being able to resonate at different frequencies. The ability to perform lithography to form a patterned hydrogel with homogeneous nanoparticles opens the door to development of nanoswitches, sensors, MEMS as well as drug delivery devices.

Oxide Heterostructures-Interface Form & Function Focus Topic

Room: 7 - Session OX+SS+TF+MI-MoA

Chemistry of Oxide Surfaces and Interfaces

Moderator: M. Engelhard, EMSL, Environmental Molecular Sciences Laboratory

2:00pm **OX+SS+TF+MI-MoA1 Investigation of Al₂O₃ Nanostructure Surfaces Using Charge Optimized Many Body Potentials**, *D.E. Yilmaz, T. Liang, S.B. Sinnott, S.R. Phillpot*, University of Florida

Aluminum oxide nanostructures have drawn attention due to their interesting physical and optical properties. In particular, photoluminescence peaks for these systems are attributed to oxygen vacancies and surface effects. Here, we apply third-generation Charge Optimized Many Body (COMB) potentials for the Al-A1₂O₃ system to investigate the properties of Al₂O₃ nanoparticle surfaces. In particular, the elastic properties and local atomistic strain distribution of nanoparticles with a range of sizes are determined, and the corresponding vibrational spectra are determined. The effect of oxygen vacancies and adsorbed surface atoms on the local strain and vibrational spectra are also determined. This work is supported by the National Science Foundation (DMR-1005779).

2:20pm **OX+SS+TF+MI-MoA2 Manipulating Ferroelectric Surfaces for Direct NO_x Decomposition**, *M.W. Herdich, A. Kakekhani, S. Ismail-Beigi, E.I. Altman*, Yale University

Current technology for removing nitrogen oxides from engine exhausts relies on nearly stoichiometric air to fuel ratios. Under these conditions, the concentrations of CO and unburned hydrocarbons in the exhaust stream are high enough to efficiently remove adsorbed oxygen from the platinum based catalysts in catalytic converters, ensuring that the catalysts do not become saturated with adsorbed oxygen. Direct catalytic decomposition of NO_x to N₂ and O₂ in the presence of excess O₂ would eliminate the need for reducing species in automobile engine exhaust streams, allowing these engines to be run more efficiently. We have been investigating the potential of ferroelectric supports to modify the behavior of supported layers to enable direct NO_x decomposition. Our approach involves first principles density functional theory and surface science techniques. Using both approaches we have investigated the interactions of N, O, and NO with bare ferroelectric lead titanate surfaces and surfaces modified to expose catalytic layers, in particular Ru oxides. Theory indicates that the behavior of the PbTiO₃ surface towards these species is sensitive to the polarization direction and termination of the ferroelectric and that stable RuO₂-terminated surfaces can be created by manipulating the termination of the substrate. Experiments take advantage of plasma sources that allow the behavior of O and N atoms to be studied individually and epitaxial growth to manipulate the termination of the ferroelectric support. Favored reaction pathways are assessed using theory and temperature programmed desorption and related mass spectrometry methods.

2:40pm **OX+SS+TF+MI-MoA3 Catalyst Synthesis by Atomic Layer Deposition**, *P.C. Stair*, Northwestern University & Argonne National Laboratory

INVITED

Atomic Layer Deposition (ALD) has enormous potential for the synthesis of advanced heterogeneous catalysts with control of composition and structure at the atomic scale. The ability of ALD to produce conformal oxide coatings on porous, high-surface area materials can provide completely new types of catalyst supports. At the same time ALD can achieve highly uniform catalytically active metal and oxide phases with (sub-) nanometer dimensions.

Vanadium oxide species supported on high surface area oxides are among the most important catalytic materials for the selective, oxidative conversion of hydrocarbons to useful chemicals. In our laboratory ALD has been used to synthesize both the catalytic vanadium oxide and the supporting oxide on both high surface powders and anodic aluminum oxide (AAO) nanoliths. These materials have been characterized by SEM, XRF, ICP, UV-Vis absorption spectroscopy, Raman spectroscopy and evaluated for the oxidative dehydrogenation (ODH) of cyclohexane.

More recently we have studied the synthesis of supported metal particles and developed what we call "ABC-type" ALD in which metal nanoparticles and support materials are grown sequentially in each ALD cycle. This method makes possible the synthesis of exceptionally small particles, ca. 0.5 nm. Using additional ALD support layers at the conclusion of the growth, the metal particles can be stabilized against sintering while still remaining active at high temperatures and reaction conditions. Moreover, the catalysts resist coke formation which is a leading cause of catalyst deactivation.

These properties are imparted as a result of anchoring step and edge atom sites while leaving facet sites open for catalysis.

3:40pm **OX+SS+TF+MI-MoA6 Energy Alignment at Organic/Oxide Interfaces: The Influence of Adsorption Geometry and Chemical Bond on Interface Dipole.** *S. Rangan, C. Ruggieri, S. Coh, R.A. Bartynski, K. Chitre, E. Galoppini*, Rutgers University

The lack of control of the energy alignment at the interface between an organic layer and an oxide substrate remains a limitation to the performance of promising technologies such as dye sensitized solar cells, organic light emitting diodes or organic thin film transistors. The energy alignment depends not only on the choice of the starting materials, but also on more subtle parameters such as oxide surface termination or defects, and molecular layer preparation mode.

In an effort to disentangle the different aspect of the interface of an organic/oxide system, we have studied simultaneously the adsorption geometry and the energy alignment of the Zn(II) tetraphenylporphyrin (ZnTPP) molecule on the TiO₂(110) and ZnO(11-20) surfaces. Two approaches have been pursued: 1) in-situ evaporation of the ZnTPP on a clean oxide surface prepared in ultra-high vacuum resulting in weakly bound multilayers or monolayers 2) ex-situ sensitization in a solution of ZnTPP derivative, modified with COOH anchoring group for chemisorption at the oxide surface.

Scanning tunnel microscopy has been used to characterize the clean oxides and the ZnTPP adsorption modes. X-ray photoemission, ultra-violet photoemission and inverse photoemission spectroscopies have allowed the exploration of both occupied and unoccupied states of the electronic structure, resulting in the full characterization of the energy alignment at the surface as a function of the molecular overlayer thickness. The electronic transport gap, obtained from the latter experimental techniques has also been compared to the optical gap obtained from reflection electron energy loss spectroscopy, thus allowing the characterization of bound excitonic states.

The effect of the ZnTPP/oxide interface preparation, as well as the effect of the oxide substrate on the energy alignment will be presented. The discussion will be extended to metallic substrates such as Ag(100) and Au(111) surfaces

4:00pm **OX+SS+TF+MI-MoA7 Energy-Level Alignment at Organic/Oxide Interfaces.** *M.T. Greiner, Z.-H. Lu*, University of Toronto, Canada **INVITED**

Oxide/organic interfaces play an important role in many organic electronic device designs. Oxides are frequently used as buffer layers to tune the energy-level alignment between electrodes and organic semiconducting layers, and thus allow for efficient hole/electron injection. As per the 'integer charge-transfer' (ICT) model, energy-level alignment at electrode/organic interfaces is governed by the electrode's Fermi level and the organic molecule's oxidation/reduction potential. While the ICT model was originally proposed for organic/organic interfaces, it also applies to a broad range of transition metal oxides. In this presentation we will discuss the energy-level alignment (ELA) of several organic semiconductors with transition-metal oxides. We will show that ELA is primarily governed by an oxide's work function, and that ELA is relatively insensitive to oxide electronic structure. As transition metal oxides can exhibit a wide range of work functions (~ 2 - 7 eV), and can possess a wide range of electronic properties (p-type to n-type) they are very versatile materials for use in organic electronics. We will their properties—such as work function and electronic structure—can best be utilized for use as buffer layers in organic light-emitting diodes and organic photovoltaics.

4:40pm **OX+SS+TF+MI-MoA9 Variable Kinetic Energy XPS of the Buried P3HT/ITO Interface.** *M.T. Brumbach*, Sandia National Laboratories, *J.C. Woicik*, National Institute of Standards and Technology

The characterization of buried interfaces is difficult and often has to be performed by post-processing methods where the interface is revealed, disturbed, and possibly altered by environmental exposure. Variable kinetic energy X-ray photoelectron spectroscopy (VKE-XPS) offers the ability to tune the depth of analysis while the use of hard X-rays allows for a deeper analysis. The combination of variable energy hard X-rays for XPS (HAXPES) allows for systematic evaluation through a buried interfacial region. An important inorganic/organic interface for use in organic photovoltaic devices is the poly(3-hexylthiophene) (P3HT) interface with indium tin oxide (ITO). In this work P3HT/ITO buried interfaces were examined using X-ray energies from 2.2-3.9 keV. The ITO surface was additionally prepared using different pretreatment conditions. The P3HT film protected the ITO surface from adventitious adsorbents and allowed for sensitivity to the buried ITO surface. Robust peak fitting parameters were obtained to model the O 1s and In 3d lineshapes. The deconvolution of these lineshapes allowed for the clear identification of a surface layer on the

ITO which is oxidized to a greater extent than the underlying bulk ITO. The surface oxide layer, composed of indium oxide and indium hydroxide, is deficient of oxygen vacancies and would therefore be expected to act as an insulating barrier on the ITO surface. Peak fitting conditions allowed for an estimation of the thickness of this insulating layer. Sandia National Laboratories is a multi-program laboratory managed and operated by Sandia Corporation, a wholly owned subsidiary of Lockheed Martin Corporation, for the U.S. Department of Energy's National Nuclear Security Administration under contract DE-AC04-94AL85000.

5:00pm **OX+SS+TF+MI-MoA10 Organic Molecules Adsorbed on the ZnO(10-10) Surface: An Infrared Reflection Absorption Spectroscopy Study.** *M. Buchholz*, Karlsruhe Institute of Technology, Germany, *H. Noei, Y. Wang*, Ruhr University Bochum, Germany, *A. Nefedov, Ch. Wöll*, Karlsruhe Institute of Technology, Germany

Except for gold, every metal forms an oxide on its surface when exposed to the ambient atmosphere. The understanding of chemical processes taking place on metal oxide surfaces are thus of crucial importance. One of the most important oxides is ZnO. As a result of its semiconducting and optical properties, this material is used in many applications such as gas sensors, thin film solar cells, as well as in photocatalysis and photooxidation[1]. The important surfaces of ZnO are the polar Zn- or O-terminated ZnO(0001) and ZnO(000-1) as well as the mixed-terminated ZnO(10-10) surface. The latter is the dominating surface for ZnO powder particles and energetically most favorable.

Here we report on the adsorption of formic acid and maleic anhydride (MA) molecules on the mixed-terminated ZnO(10-10) surface. Formic acid is a good model molecule for understanding the anchoring of carboxylic dye molecules in dye-sensitized solar cells. The choice of MA is motivated by the importance of the industrial process where MA is hydrogenated using Cu/ZnO catalysts. The identification of the reaction mechanism requires the identification of intermediates using IR-spectroscopy[2].

In last decades numerous IR investigations of oxide powders have been reported. An unambiguous assignment of the features present in the complex powder IR spectra, however, is only possible on the basis of reference data recorded for well-defined systems, e.g. surfaces of single crystals with defined orientation. Unfortunately, Infrared Reflection Absorption Spectroscopy (IRRAS) studies of molecular adsorbates on oxide single crystals, and, in particular on ZnO, are extremely scarce due to the fact that the sensitivity of IRRAS to adsorbate vibrations is two orders of magnitude lower for oxides than for metals. Whereas in case of TiO₂ recently with improved experimental setups adsorbate vibrations have been observed for a number of cases[3], to our knowledge molecular vibrations on clean ZnO single crystal surfaces have not yet been reported. With our novel UHV-IRRAS setup[4] high-quality IR spectra of different molecular adsorbates on ZnO(10-10) could be recorded in a routine fashion. In this presentation the obtained results will be presented and discussed.

M. Buchholz gratefully acknowledges the financial support from the Helmholtz Research School "Energy-Related Catalysis".

[1] C. Wöll, Prog. in Surf. Sci. **2007**, 82, 55-120.

[2] S. G. Girol, T. Strunskus, M. Muhler, C. Wöll, *J. Phys. Chem. B* **2004**, 108, 13736-13745.

[3] M. C. Xu, H. Noei, M. Buchholz, M. Muhler, C. Wöll, Y. M. Wang, *Catal. Today* **2012**, 182, 12-15.

[4] Y. Wang, A. Glenz, M. Muhler, C. Wöll, *Rev. Sci. Instrum.* **2009**, 80, 113108-113106.

5:20pm **OX+SS+TF+MI-MoA11 In Situ Interface Analysis of Self-Assembled Monolayers on Metal Surfaces at High Water Activities by Means of a PM-IRRAS/QCM-Setup.** *I. Giner, M. Maxisch, G. Grundmeier*, University of Paderborn, Germany

Aluminum and its alloys are widely used as engineering material and in a wide range of applications ranging from the aviation industry to the automotive and construction industries. As almost all engineering metals, aluminum under ambient conditions is covered by a native oxide film which alters significantly its surface physical and chemical properties. For corrosion protection and adhesion promotion, oxide covered aluminum surfaces are coated with organic films. Ultra-thin films or even monomolecular layers of organic acids like self-assembled monolayers (SAMs) of organophosphonic and organocarboxylic acids have been investigated as new advanced interfacial layers for aluminum alloys.¹ However, the stability of the self-assembled monolayers under environmental conditions is an aspect for technical applications. Different studies concerning to the stability and structure of the self-assembled monolayers under high humidity's conditions have been performed.² These studies revealed that the organic film decreased the amount of interfacial water layer but cannot prevent the water diffusion through the monolayer.³ The aim of the present work is to establish an in-situ setup combining

quartz crystal microbalance (QCM) and PM-IRRAS to study the chemistry of passive films and adsorbed organic monolayers at high humidity. The metal coated quartz was used as the reflecting substrate for the PM-IRRAS measurement. Thereby, the structure of the monolayer, the amount of adsorbed water and the chemical state of the surface layer in the presence of an adsorbed water layer could be analysed in-situ. The surface hydroxyl density prior to organic molecule adsorption was adjusted by means of low temperature Ar- and H₂O- plasma treatments. Adsorption studies of H₂O on nonadecanoic carboxylic acid (NDA) monolayer modified surfaces in comparison to bare oxide covered aluminum surfaces showed, that the NDA monolayer leads to a reduced amount of adsorbed water based on the inability of water to form hydrogen bonds to the low energy aliphatic surface chemistry. Moreover the kinetics of chemisorption of water indicated by the oxyhydroxide peak growth at SAM/metal interfaces could be significantly inhibited. Furthermore, it is noticeable that interfacial carboxylate group coordinatively bound the oxide as well as the orientation of the NDA monolayer is not affected by the adsorption of several monolayers water. *Bibliography* 1. Thissen, P et al. *Langmuir* **2010**, *26*, (1), 156-164 2. Thissen, P et al. *Surface & Coatings Technology* **2010**, *204* (21-22), 3578-3584. 3. Maxisch, M et al. *Langmuir* **2011**, *27* (10), 6042-6048

Plasma Science and Technology Room: 24 - Session PS+BI-MoA

Applications of (Multiphase) Atmospheric Plasmas (including Medicine and Biological Applications)

Moderator: G.Y. Yeom, Sungkyunkwan University, Korea

2:00pm **PS+BI-MoA1 Plasmas in Saline Solution Sustained Using Bipolar Pulsed Power Source – Tailoring the Discharge Behavior Using the Negative Pulses.** *H.W. Chang**, *C.C. Hsu*, National Taiwan University, Taiwan, Republic of China

Plasmas in saline solutions have been extensively studied due to their wide applications. In this work, plasmas ignited in saline solution were studied. The plasma system consisted of two electrodes immersed in 0.2 M NaCl saline solution. The electrode where the plasma was ignited was a 0.5 mm-diameter Pt wire covered by a glass tube to precisely define the area exposed to the solution. The grounding electrode was a bare platinum wire with the same diameter. Diagnostic tools used included voltage and current probes, an optical emission spectrometer, and a photomultiplier tube. We studied plasmas driven by a bipolar pulse power source using repetitive positive and negative voltage pulses with adjustable width and amplitude. We used the positive voltage pulses to ignite the plasma while using the negative voltage pulses to tailor the electrolytic gas formation amount. Conditions with the positive voltage pulse fixed at +600 V with an 80 μs duration, and the negative pulse varying from 0 to 80 V with the duration ranging from 0 to 20 ms were tested. By changing the duration of each voltage pulse, the bubble dynamics and the plasma behavior can be effectively controlled. By increasing the negative voltage pulse amplitude, we observed a decrease in the maximum currents before the ignition of the plasma from 1.75 to 1.0 A. The time required for plasma ignition upon the onset of the positive voltage pulse was reduced. The above observations can be well explained by the coverage of the electrode surface by electrolytic gas. Optical emission spectroscopy showed that $I_{\text{H}}(656 \text{ nm})/I_{\text{Na}}(588 \text{ nm})$ ratio increases from zero to 0.0035 when the negative voltage pulse amplitude increases from 0 to 80 V. This clearly showed hydrogen, the electrolytic gas, content in the bubble increased with the increase in negative voltage pulse amplitude. This work was supported by National Science Council of Taiwan, the Republic of China (100-2628-E-002-012 and 101-3113-E-002-002).

2:20pm **PS+BI-MoA2 Low Temperature Plasma Deactivation of Endotoxic Biomolecules: The Effects on Lipid A.** *T.-Y. Chung*, *J.-W. Chu*, *D.B. Graves*, University of California Berkeley, *E. Bartis*, *J. Seog*, *G.S. Oehrlein*, University of Maryland

Effective removal of infectious organisms and/or biomolecules from medical instruments is essential to prevent infections and disease transmission. Intricate modern instruments are difficult to clean via thermal sterilization since they are often heat sensitive. Furthermore, bacterial endotoxin and prion proteins are known to be particularly resistant to conventional sterilization procedures.[1, 2] Low-temperature plasma is a promising option for surface sterilization of bacteria and deactivation of harmful biomolecules, but mechanisms of endotoxic biomolecule deactivation are poorly understood.[3] Using a vacuum beam system, we

study the effects of vacuum ultraviolet (VUV) radiation, oxygen and deuterium radicals on lipid A, the immune-stimulating region of lipopolysaccharide (LPS). The endotoxic activity of lipid A samples is monitored by measuring the secreted interleukin-1β (IL-1β) in human whole blood. The results obtained from *ex situ* transmission Fourier transform infrared (FTIR) spectroscopy, *in situ* quartz crystal microbalance (QCM), *in situ* residual gas analysis and *ex situ* electrospray ionization mass spectrometry (ESI-MS) show that VUV photons cause bulk modification to the penetration depth of photons, ~200 nm. On the other hand, radicals mainly cause chemical etching and modification near the surface of lipid A films. Although the radical-induced etch yield of lipid A is much lower than VUV-induced photolysis, secondary ion mass spectrometry (SIMS) and human whole blood-based assay demonstrate that O and D radicals alter the film surface, leading to significant reduction of film endotoxicity. Important structures governing the endotoxic activity of lipid A, e.g. the fatty acid chains and the phosphate groups, are greatly reduced after radical exposure. Qualitatively similar results are observed when LPS films are exposed to either H atoms or VUV photons in low-pressure plasma. The deactivation effects of low energy ions and atmospheric pressure air plasma on lipid A films will also be presented.

[1] K. L. Williams, ed., *Endotoxins: Pyrogens, LAL Testing and Depyrogenation*, Informa Healthcare USA, Inc., New York, 2007.

[2] W. A. Rutala and D. J. Weber, *Infect. Control Hosp. Epidemiol.* **31**, 107 (2010)

[3] A. von Keudell et al., *Plasma Process. Polym.* **7**, 327 (2010)

2:40pm **PS+BI-MoA3 Nonthermal Bioplasma Sources and its Interactions to the Microbial, Fungal, Yeast and Living Cells.** *E.H. Choi*, *Y. Kim*, *G.S. Cho*, *G. Kwon*, *B.K. Min*, *H. Uhm*, Kwangwoon University, Republic of Korea, *P. Suanpoot*, Maejo University Phrae Campus, Thailand, *G. Lee*, *R. Jung*, *B. Park*, Kwangwoon University, Republic of Korea

INVITED
We have investigated the atmospheric pressure (AP) nonthermal bioplasma sources and their characteristics as well as their interactions with biological cells of microbial, fungal, yeast, and living cells. The electron temperature and plasma density are measured to be about 1.1 eV~ 1.5 eV and $(1\sim 3)\times 10^{12} \text{ cm}^{-3}$, respectively, for the direct plasma jet and dielectric barrier discharge (DBD) plasma under Ar gas flow. The densities for the reactive oxygen species (ROS) such as the hydroxyl radicals (OH), superoxide anions (O₂⁻), and nitric oxide (NO) have also been investigated in these AP direct plasma, respectively, inside the saline culture media by the ultraviolet optical absorption spectroscopy. Herein, we have investigated the basic interactions of these AP nonthermal bioplasma with the living organisms in morphological and biomolecular aspects. We found that the secondary electron emission coefficient of the biological surface has been drastically increased by atmospheric bioplasma, which indicates the biological surface to be oxidized especially by the hydroxyl (OH) radical species. In order to elucidate the basic mechanisms for the cell shrinking and apoptosis leading to a cell death by the nonthermal bioplasma, the cell membrane potential changes have been measured and investigated inside the culture media based on the ROS density as well as cell capacitances. It is also found that the molecular electron energy band structure in these biological cells have been modified and shifted toward the vacuum surface energy level by the AP nonthermal bioplasmas due to cell oxidation, mainly caused by OH radicals. We have also investigated the confocal Raman spectroscopy and circular dichroism as well as various biological assays to clarify these characteristics.

3:40pm **PS+BI-MoA6 Deactivation of Lipopolysaccharide and Lipid A by Radicals Produced in Inductively Coupled Plasmas.** *E. Bartis*, University of Maryland, *T.-Y. Chung*, *J.-W. Chu*, *D.B. Graves*, University of California Berkeley, *J. Seog*, *G.S. Oehrlein*, University of Maryland

Low temperature plasma (LTP) treatment of surfaces has been shown to degrade and sterilize bacteria as well as deactivate harmful biomolecules [1]. However, a major knowledge gap exists regarding which plasma species e.g. ions, VUV photons, and reactive radicals, are responsible for the modifications required for deactivation. Lipopolysaccharide (LPS) and lipid A, the toxic element of LPS, are the main components of the outer membrane of Gram-negative bacteria and are notoriously difficult to remove from surfaces by traditional sterilization methods [2]. In this study, LPS- and lipid A-coated silicon substrates were exposed to low pressure plasma-generated Ar and H radicals isolated from an inductively coupled LTP source by employing a gap structure [3] to examine the effects of plasma composition on etch rates and chemical properties. Bioactivity of LPS was measured using an enzyme-linked immunosorbent assay (ELISA). Ar neutrals caused a 5% reduction in bioactivity whereas exposure to H radicals using the same plasma operating conditions caused a 25% reduction in bioactivity. Ellipsometric data shows that H radical-only exposures cause less than 2 nm of material removal, indicating that surface

* Coburn & Winters Student Award Finalist

modification is the major cause of deactivation and that complete etching and removal is not necessary. These modifications can inhibit the binding of receptor molecules, whose binding depends on a variety of interactions such as hydrophobic and electrostatic interactions and lock-and-key mechanisms. After plasma processing, samples were characterized by vacuum transfer to x-ray photoelectron spectroscopy (XPS) to study the chemical changes occurring on the film surface. With XPS, we observed that plasma-generated H radicals produce a C-rich surface by effectively removing O, N, and P, the latter of which is from phosphate groups that contribute to the pyrogenicity. The C 1s spectra shows a clear loss of N-C=O and O-C=O groups. This loss leads to the removal of lipid A's aliphatic chains, which are responsible for its toxicity. Direct H₂ plasma treatments also remove O, but fast material removal causes an increase in N and P due to the exposed core and O-chain on LPS. Radical-only ELISA results will be compared to direct and VUV-only treatments where material removal is significantly greater. This result is especially true for direct Ar plasmas, where modification/etching is dominated by ion bombardment. Our results compare favorably with complementary VUV/radical beam studies of lipid A.

[1] A. von Keudell et al., *Plasma Process. Polym.* **7**, 327 (2010)

[2] E. T. Rietschel et al., *FASEB J.* **8**, 217 (1994)

[3] L. Zheng et al., *J. Vac. Sci. Technol. A* **23**, 634 (2010)

4:00pm PS+BI-MoA7 Localised, Non-Contact Surface Modification with Microplasma for Biotechnological Applications, S.A. Al-Bataineh, E.J. Szili, D.A. Steele, N.H. Voelcker, H.J. Griesser, R.D. Short, University of South Australia

Localised surface modification of "open" surfaces is important for many biotechnological applications. In this study, we describe the utilisation of microcavity plasma arrays for localised surface modification of materials in a non-contact approach. In contrast to the current methods for localised surface modification, our method achieves spatially controlled surface modification without the use of a physical mask, photolithography or contacting the surface. Therefore, it provides the opportunity to reduce the number of modification steps and thus the cost of surface engineering processes. To this end, a 7 x 7 microcavity plasma array device (each cavity is separated by 500 µm and has a diameter of 250 µm with a depth of 55 nm) was manufactured and operated in helium at atmospheric pressure to generate, under optimised operating parameters, spatially separated modified regions on passivated surface coatings. The microplasma-patterned coatings were then used to control the spatial distribution of biomolecules such as proteins by allowing protein adsorption onto the modified regions whereas the rest of the coating remains non-fouling. Therefore, this approach resulted in spatially separated areas of immobilised protein. These surfaces were also used to control the spatial distribution of other biomolecules as well as living cells.

4:20pm PS+BI-MoA8 Biocompatible Nanocomposites Synthesized by Gas-Liquid Phases Plasmas, T. Kaneko, Q. Chen, R. Hatakeyama, Tohoku University, Japan

INVITED

Recently, multiphase plasmas, particularly gas-liquid phases plasmas have attracted much attention as fundamental and application researches [1], because the non-equilibrium plasmas in gas phase can produce the various kinds of chemically active ions and radicals which react with nano- and biomaterials stably existing in liquid. As one of the promising applications of the gas-liquid interfacial discharge plasmas (GLIDPs), the synthesis of various kinds of nanoparticles [2] is advantageous in that toxic reducing agents are unnecessary and the synthesis is continuous during the plasma irradiation. In addition, the GLIDPs are also used in the biomedical field, for example, the synthesis of gold nanoparticles (AuNPs) conjugated with biomolecules such as DNA. The DNA conjugated AuNPs (DNA-AuNPs) work as vectors to deliver DNA into living cells because the AuNPs can be efficiently manipulated by a light field. Furthermore, the DNA-AuNPs are attempted to be encapsulated into carbon nanotubes (CNTs) to protect the DNA from the ambient environment.

The GLIDP is generated between the bottom liquid and top metal electrodes in Ar gas (20 kPa) by applying a pulse voltage (20 kHz) to the liquid electrode. The liquid electrode consists of aqueous chloroauric acid trihydrate (HAuCl₄·3H₂O) (0.1 mg/ml) with DNA. A single-stranded DNA is used as the conjugated material, which consists of 30 bases of cytosine or guanine. In the synthesis of the DNA-AuNP encapsulated CNTs, double-walled carbon nanotubes (DWNTs) are adopted to be used because of their large inner diameter.

Depending on the DNA concentration, the resultant water-soluble AuNPs take on pink and purple. The different colors originate from the particle size and interparticle distance which determine the absorption wavelength of the

surface plasmon resonance of the AuNPs. Interestingly, these phenomena depend on the types of DNA base, which are attributed to the difference in the binding energy of the DNA base. Therefore, we can control the size and assembly of the AuNPs by changing the DNA type and concentration [3].

In order to encapsulate the negatively charged DNA-AuNPs into the DWNTs, a positive DC voltage is applied to the DWNTs put on the substrate immersed in the GLIDP. The transmission electron microscope images of the resultant products show that the number of the DNA-AuNPs encapsulated into DWNTs increases with an increase in the positive DC voltage.

[1] T. Kaneko, K. Baba and R. Hatakeyama: *J. Appl. Phys.* **105**, 103306 (2009).

[2] T. Kaneko, Q. Chen, T. Harada and R. Hatakeyama: *Plasma Sources Sci. Technol.* **20**, 034014 (2011).

[3] Q. Chen, T. Kaneko, and R. Hatakeyama: *Chem. Phys. Lett.* **521**, 113 (2012).

5:00pm PS+BI-MoA10 Organization of Dielectric Barrier Discharges in the Presence of Structurally-Inhomogeneous Wood Substrates, O. Levasseur, Université de Montréal, Canada, A. Bouarouri, N. Naudé, R. Clergereaux, N. Gherardi, Université de Toulouse, UPS, INPT, LAPLACE, France, L. Stafford, Université de Montréal, Canada

There has been a growing interest in the use of dielectric barrier discharges (DBDs) for many applications, especially for the treatment of heat-sensitive materials such as polymers. Some studies have also reported a self-organization of these discharges which can manifest itself in two ways : i) the auto-organization of filaments or micro discharges in a filamentary DBD or ii) the formation of regular spatio-temporal patterns in a glow-like discharge. Several types of patterns such as hexagonal arrays or concentric rings have been observed for various gases and system configurations. We have recently extended the range of applications of DBDs to the functionalization of wood surfaces with the objective of improving its durability following natural weathering. However, the application of DBDs to the modification of wood presents additional complications compared to traditional substrates due not only to the highly porous nature of wood which can produce significant outgassing but also to the presence of "early" vs. "late wood" sections which can introduce local modification of the properties of the dielectric exposed to plasma. In this work, we examine the organization of DBD in the presence of complex wood substrates using optical imaging and current-voltage (I-V) characteristics. For Douglas pine samples, the structural inhomogeneities of the wood substrate was found to produce non-uniform light emission patterns while maintaining homogeneous-like I-V characteristics. Experiments performed on samples with various fractions of "early" vs. "late" wood sections showed that the plasma emission was always more intense on the "early" wood. The charge flow pattern was also analyzed using surface potential measurements. Both sections exhibited decaying behaviors, with time constants, t , of 40 s for late wood and 10 s for early wood. Based on these results and the predictions of a simple electrical model of the discharge, the organization was ascribed to a spatial modulation of the relative dielectric permittivity on "early" versus "late" wood affecting the local voltage applied to the gas, and thus the local discharge current which is directly related to the plasma emission.

5:20pm PS+BI-MoA11 Role of Substrate Outgassing on the Formation Dynamics of Either Hydrophilic or Hydrophobic Wood Surfaces in Atmospheric-Pressure, Organosilicon Plasmas, O. Levasseur, L. Stafford, Université de Montréal, Canada, N. Gherardi, N. Naudé, Université de Toulouse, UPS, INPT, LAPLACE, France, P. Blanchet, FPlnnovations, Canada, B. Riedl, Université Laval, Canada, A. Sarkissian, Plasmionique, Canada

Dielectric barrier discharges (DBDs) were thoroughly investigated over the last several years with one of the main goals being the achievement of a homogeneous discharge at high operating pressure in various gas mixtures. This keen interest is mainly driven by the fact that atmospheric-pressure DBDs present major advantages over low-pressure plasmas for polymer treatments, one of the most important being the ability to work with cold plasmas without the use of high-end vacuum pumping systems. Over the last decade many precursors, such as organosilicon compounds like hexamethyldisilazane (HMDSN) and hexamethyldisiloxane (HMDSO), were added to these cold, atmospheric-pressure plasmas for PECVD applications and a wide variety of coatings have been obtained by such methods. Application of DBDs to the treatment of polymers is however much more challenging than for conventional substrates such as Si or SiO₂. This can be not only be attributed to the highly complex chemical nature of most polymers but also to their generally porous microstructure which can release impurities in the discharge either from plasma-substrate chemical reactions or from sample outgassing (if not pumped-down beforehand). Such impurities can greatly alter the discharge stability and gas-phase kinetics which are both known to play an important role on the plasma

deposition dynamics. In this work, we capitalize on the very porous nature of wood to examine the influence of substrate outgassing during PECVD on the stability of a N_2 -HMDSO discharge and on the evolution of the properties of plasma-deposited thin films over sugar maple and black spruce wood samples. Current-voltage characteristics revealed a transition from a filamentary to a homogeneous discharge with increasing plasma treatment time, t . Based on optical emission spectroscopy, the filamentary behavior was ascribed to the release of air and humidity from the wood substrate following plasma exposure which produced significant quenching of N_2 metastables. This effect vanished at longer treatments times due to the nearly complete “pumping” of products from the substrate and the progressive deposition of a “barrier” layer. Analysis of the surface wettability through static, water contact angles (WCAs) and of the surface composition through FTIR and XPS indicated that for $t < 10$ min, the wood surface was more hydrophilic due to the formation of a SiO_x layer, a typical behavior for HMDSO deposition in presence of oxygen. On the other hand, for $t > 10$ min, the static WCA increased from $\sim 50^\circ$ up to $\sim 140^\circ$ due to the deposition of hydrophobic $Si(CH_3)_3$ -O- $Si(CH_3)_2$ and $Si(CH_3)_{3.2}$ functional groups.

Plasma Science and Technology

Room: 25 - Session PS2-MoA

Plasma Modeling

Moderator: E. Despiou-Pujo, LTM-CNRS

2:00pm **PS2-MoA1 Tailored Ion Energy Distributions on Plasma Electrodes**, *P. Diomede, D.J. Economou, V.M. Donnelly*, University of Houston **INVITED**

Control of the energy of ions bombarding a substrate is important for both plasma etching and deposition. As device dimensions keep shrinking, requirements on selectivity and substrate damage become ever more stringent. Such requirements impose strict limits not only on the mean ion energy but also of the ion energy distribution (IED). The IED may be controlled by applying judicious bias voltage waveforms on the substrate, or on a “boundary electrode” in contact with the plasma. A Particle in Cell simulation with Monte Carlo Collisions (PIC-MCC) was employed to predict the IEDs resulting by the application of a variety of voltage waveforms (steps, staircases, etc.) on a plasma electrode in the afterglow of power-modulated plasmas. IEDs with distinct energy peaks at controlled location, spacing, and fraction of ions under each peak, were obtained by properly selecting the applied waveform. The effect of gas pressure on the IEDs was also studied. A semi-analytical equivalent-circuit model was developed to solve the “inverse problem”, i.e., to find the voltage waveform that results in a desired IED. The model allowed rapid calculation of the IED, and model predictions were in agreement with experimental data and the results of the much more computationally intensive PIC simulation. Work supported by DoE Plasma Science Center and NSF.

2:40pm **PS2-MoA3 Self-Consistent Multi-Dimensional Modeling of Inductively Coupled Plasmas**, *A. Agarwal, J. Kenney, M.-F. Wu, S. Rauf, K. Collins*, Applied Materials Inc.

Plasma etching of microelectronic structures at advanced technological nodes ($< 2x$ nm), especially complicated structures such as multi-gate MOSFETs and 3D memory stacks, places great emphasis on uniformity of the process.[1] Asymmetries, either azimuthal or radial, can arise in inductively coupled plasma (ICP) sources due to the input and pumping locations of feedstock gases, voltage and current variations along the coils, and other particulars of the reactor configuration.[2] While two-dimensional plasma models are adequate to tackle radial non-uniformities during design of ICP systems, these models usually do not address the circuit issues and are incapable of investigating azimuthal asymmetries.

In this work, results from a two-dimensional plasma model, HPEM[3], modified to include match-side circuit calculations, will first be discussed to highlight the effect of coil voltages on capacitive coupling in ICPs. The model is validated using voltage and current measurements in the match and along the coils. The consequences of capacitive coupling on the plasma and ion energy distribution characteristics will be discussed.

With increasing coil dimensions, voltage and current can vary along the coils which can produce azimuthal asymmetries. Mitigation of these non-uniformities requires a careful antenna design. However, as these azimuthal non-uniformities cannot be predicted by a two-dimensional model, a three-dimensional model is required to help with antenna design for ICPs. We discuss results from three-dimensional modeling of ICPs using the plasma-electromagnetics modeling code, Mira.[4] Mira is a fully electromagnetic fluid plasma model which self-consistently computes the electromagnetic fields using the finite-difference time domain (FDTD) technique. By virtue

of the fully electromagnetic nature of the model, both capacitive and inductive fields are self-consistently included while computing the power deposition in the plasma. The effect of various azimuthally asymmetric reactor configurations and coil designs on plasma uniformity will be discussed.

[1] K. Ahmed and K. ScheuGRAF, IEEE Spectrum 48 (11), 50 (2011).

[2] J.A. Kenney, S. Rauf, and K. Collins, J. Appl. Phys. 106, 103302 (2009).

[3] M.J. Kushner, J. Phys. D 42, 194013 (2009).

[4] S. Rauf, Z. Chen, and K. Collins, J. Appl. Phys. 107, 093302 (2010).

3:00pm **PS2-MoA4 Feature Profile Modeling of STT-MRAM Etch**, *P. Stout*, Applied Materials Inc.

Results of feature profile evolution modeling of a STT-MRAM (Spin Transfer Torque - Magnetoresistive Random Access Memory) etch process will be discussed. STT-MRAM is a promising candidate for future memory. This non-volatile RAM has fast read/write, is scalable to DRAM (dynamic random access memory) cell sizes, has low power, and has possible multi-bit multi-level capability. This talk will address modeling the pattern definition of the MTJ (magnetic tunneling junction) stack through an etch process. The feature model used for the study is a 3D Monte Carlo model. The MTJ stack consists of many metals which are not easily etched (i.e., mostly non-volatile etch by-products) such as CoPt, Ru, CoFeB, and MgO. Thus, the feature model assumes mostly physical sputtering as the etch mechanism. The material emission model is also important in a physically dominated etch process. The impact of different material emission models on the final profile will be discussed. The main issue is removal of metal sidewall deposits which are the result of the re-deposition of the sputtered MTJ layers. The thickness of the re-deposited metal on the sidewall decreases from bottom to top. The closer the sidewall is to the sputter source at the feature bottom the thicker the deposit. The thickness is also heavily influenced by the geometry of the mask. Given the physical nature of the etch line-of-sight of incoming ions and outgoing metal is important. Negative sidewall slopes can also influence the morphology of the re-deposited metal. The square shaped pillar patterns modeled have non-uniform deposit around the circumference of the feature with larger metal at the corners. The etch front is also more non-uniform due to the length difference from corner to corner vs side to side for the features. Smaller aspect ratio features will allow removal of more MTJ metal but may have less of an impact on the final CD at the MgO layer. Material sputter emission models which are more focused lead to thicker deposits in sputtered layers, spottier deposits on patterned sidewalls, and ledge formation. The difficulty in removing the metal sidewall deposits leads to strategies such as the use of off-angle ion beams. Off-angle ion beams take advantage of the off-angle peaks in the ion yield curves. The number of steps per rotation and the off-angle value influence the final profile. Fewer steps / rotation lead to more non-uniform etch fronts. Larger off-angles lead to larger yield numbers for the sidewall deposited metal but will also be shadowed by nearby features limiting the depth where the metal removal takes place.

3:40pm **PS2-MoA6 Development of a New Industry Focused Plasma Simulation Tool**, *A.I. Williams*, University College London, UK, *S. Lopez-Lopez*, Quantemol Ltd., UK, *W. Brigg, J. Tennyson*, University College London, UK

Plasma processes are routinely used in a number of industrial settings, for applications varying from silicon chip etching to thin-film deposition for solar cells. In the majority of these cases the techniques and procedures used to create the required plasmas are obtained by initial experimental trial and error. Thus, this advancement has been led in a large part by the technical ability of the engineers in charge of the equipment. This model has worked so far, however, with more and more complex plasma chemistries being developed and the continual drive for efficiency, simulations are becoming another implement in the engineer's toolset. This poses interesting requirements on any simulation software which is aimed toward industry, such as: reliability, simulation speed and ease of set-up. It is the goal of the new coding project at UCL and Quantemol Ltd. to tackle these issues and more, to produce a simulation tool specifically targeted to industrial applications.

This new software will allow the simulation of full 3D geometries, implementing a finite element method (FEM) to solve the required partial differential equations and a hybrid simulation method to improve runtime. We intend to implement the following features:

An underlying robust FEM library, which includes automated mesh refinement.

Parallel computation of the FEM to decrease runtime.

Simplification of plasma chemistry creation with a look at automatic generation through linking with pre-built databases.

Automated selection of plasma models through algorithmic selection to help speed up the set-up and improve the quality of simulations.

A robust test suite of simulations to assure validity of results.

At the conference the latest research issues about, and the development towards the above features will be reported.

4:00pm **PS2-MoA7 Mechanism of Generating Ions and Radicals in Fluorocarbon Plasma Investigated by Reaction Model Analysis**, *Y. Kondo**, *Y. Miyawaki, K. Takeda, H. Kondo, K. Ishikawa, T. Hayashi, M. Sekine, M. Hori*, Nagoya University, Japan

Excellent etch properties such as high etch rate, high selectivity, fine profile, are required for interlayer dielectric film processing for ULSI circuits to achieve high device performances. The etch properties depend on the composition and amount of active species, i.e. ions and radicals which are strongly correlated with the molecular structure of feedstock gas. To choose the most appropriate feedstock gas for designing a specific etch process, it is favorable to understand the detailed relationship among gas molecule structure, active species and etch performance. It may also lead to suggest a new gas with extreme high performance.

In previous study, we have developed a SiO₂ etch process using CF₃OOCFCF₂ (C₃F₆O). C₃F₆O has characteristic molecular structures such as an ether bond, a CF₃ group and a double bond. Relatively high etch rate for SiO₂ is expected for the C₃F₆O plasma chemistry since the major fragment ion of C₃F₆O is CF₃⁺ that is known to show high etch yield for SiO₂[1]. Detailed relationship among the gas molecule structure, etch species and etch performance, however, has not clarified so far.

In this study, we have developed a chemical model of reactions in C₃F₆O/Ar plasma and simulated it using chemical kinetics simulation software, CHEMKIN. The experimental results were compared with the results obtained by the model. Then, we clarified the generation pathway of ions and radicals, and evaluated effects of the difference of these pathways on the composition of active species. Then we considered the relationship between molecule structure and the generation of active species.

Electron induced dissociation channels of C₃F₆O were evaluated by analysis of cracking patterns measured using a quadruple mass spectrometer. Cross-section for ionizing dissociation of C₃F₆O was estimated through a range between a few to 50 eV for electron energy [2]. Reaction constants for this dissociative ionization were calculated by integrating over whole electron energy range assuming the electron temperature as 3 eV. Using these constants and constants on previous model for CF₄, C₂F₆, and C₄F₈ chemistry [3, 4], the chemical model of gas phase reactions in the C₃F₆O/Ar plasma was constructed, and enabled us to estimate the concentrations for gas phase species. We also evaluated the dependence of the concentrations on electron density, partial pressure of feedstock C₃F₆O gas and residence time.

[1] K. Karahashi, et al. : J. Vac. Sci. Technol. A **22**, 1166 (2004).

[2] H. Toyoda, et al. : Jpn. J. Appl. Phys. **36**, 3730 (1997).

[3] G. I. Font et al., J. Appl. Phys. **91** (2001) 6.

[4] A. V. Vasenkov et al., J. Vac. Sci. Technol. A **22** (2004) 3.

4:40pm **PS2-MoA9 Excitation of Ion Acoustic Waves by Electron Beams**, *I.D. Kaganovich*, Princeton Plasma Physics Laboratory, *D. Sydorenko*, University of Alberta, Canada, *E. Tokluoglu, E.A. Startsev, A.V. Khrabrov*, Princeton Plasma Physics Laboratory, *L. Chen, P. Ventzek, R. Sundararajan*, Tokyo Electron America

The interaction of an electron beam with plasma is of particular importance for hybrid DC/RF coupled plasma sources used in plasma processing. A high frequency (HF) electron plasma wave resonant with the high-energy beam may decay into another HF wave and an ion acoustic wave. The new HF wave may have lower phase speed than the original HF wave. Electron acceleration by the slower HF wave may explain the low-energy peak in the electron energy distribution function measured in plasma processing devices [1]. In the present paper, the collisionless electron heating in a hybrid RF-DC plasma source is studied using the particle-in-cell code EDIPIC. [2,3] In simulation, electrons emitted from the cathode surface are accelerated through a dc bias electric field and form an 800 eV electron beam entering the bulk plasma. The beam excites electron plasma waves through the two-stream instability. High localized plasmon pressure creates ion acoustic waves in the process similar to the modulation instability.

Eventually, coupling between electron plasma waves and ion acoustic waves deteriorates HF oscillations, which leads to bursting behavior.

[1] L. Chen and M. Funk, Langmuir wave standing wave resonance in DC/RF plasma, Proceedings of ICRP 2010.

[2] D. Sydorenko, A. Smolyakov, I. Kaganovich, and Y. Raitses, Phys. Plasmas, **14**, 013508 (2007).

[3] D. Sydorenko, I. Kaganovich, Y. Raitses, A. Smolyakov, Phys Rev Lett., **103**, 145004 (2009).

5:00pm **PS2-MoA10 Multi-Peaked and Stepped Electron Velocity Distributions in RF-DC Discharges with Secondary Emission**, *A.V. Khrabrov, I.D. Kaganovich*, Princeton Plasma Physics Laboratory, *D. Sydorenko*, University of Alberta, Canada, *E. Tokluoglu, E.A. Startsev*, Princeton Plasma Physics Laboratory, *L. Chen, P. Ventzek, R. Sundararajan*, Tokyo Electron America

In RF-DC (hybrid) capacitive-coupled discharges, secondary electrons emitted from the electrodes undergo a complicated motion defined by acceleration in, and bouncing between a steady and an oscillating sheath. For the electrons that return to the RF electrode, the arrival phase is a multi-valued function of the phase in which they were emitted. This basic property leads to a velocity distribution with multiple peaks. The phase of arrival can also be discontinuous, which corresponds to a distribution containing steps. We have observed such distributions in numerical test-particle simulations, and analyzed the observed structure of the electron distributions.

5:20pm **PS2-MoA11 Simulations of the Radial Line Slot Antenna Plasma Source**, *P. Ventzek*, Tokyo Electron America, *S. Mahadevan*, Esgee Technologies, *J. Yoshikawa*, Tokyo Electron Technology Development Institute, INC., *L. Raja*, University of Texas at Austin, *T. Iwao*, Tokyo Electron Technology Development Institute, INC., *L. Chen, R. Sundararajan, J. Zhao*, Tokyo Electron America, *T. Nozawa, K. Ishibashi*, Tokyo Electron Technology Development Institute, INC., *R. Upadhyay*, Esgee Technologies

The Radial Line Slot Antenna plasma source couples microwave power through a slot antenna structure and window to a plasma characterized by a generation zone adjacent to the window and a diffusion zone that contacts a substrate. The diffusion zone is characterized by a very low electron temperature. This property renders the source useful for soft etch applications and thin film processing for which low ion energy is desirable. The coupling between the microwave applicator, slot antenna, coupling window and plasma is complex and the subject of many investigations more often than not electromagnetic wave analysis. Another way to look at the coupling is that of a microwave network ending in a plasma load. A systematic analysis of the interrelationship between slot geometry, position and basic coupling window characteristics is presented revealing the complex impedance relationship between critical elements. We will begin presenting results from 2 dimensional plasma simulations illustrating sensitivity of the coupling to slot location using a single slot then go on to more complex examples. The plasma load itself adds additional challenges. In particular the importance of the high frequency behavior of the electron energy distribution function on the plasma load will be presented. Ignoring the impact of the driving frequency on the electron energy distribution function leads to significant variation in plasma predicted densities.

Advanced Surface Engineering Room: 22 - Session SE+NS-MoA

Nanostructured Thin Films and Coatings II: Multifunctional Properties

Moderator: E. Broitman, Linköping University, Sweden

2:00pm **SE+NS-MoA1 Layered Binary Metal Oxide Solid Lubricants for High Temperature Moving Assemblies**, *S. Aouadi, D. Stone*, Southern Illinois University Carbondale, *A. Martini*, University of California Merced, *C. Muratore, A.A. Voevodin*, Air Force Research Laboratory

INVITED

Oxides exhibit an unparalleled variety of physical properties that give them great promise for many applications in optics, magnetism, and electronics. Oxides that possess layered crystal structure inherently display anisotropic properties as a result of their non-symmetrical crystal structure. This flexibility in their structural skeleton offers a great opportunity to create new materials with designed functionality. This paper provides an overview of the current research developments in understanding how a class of layered binary metal oxides is effective at reducing friction at moderate and high temperatures. Oxides, known to be abrasive at low temperatures, are

* Coburn & Winters Student Award Finalist

particularly desirable lubricious materials at high temperatures considering that most materials will oxidize in air under these conditions. Four different, non-exclusive, mechanisms are reported to cause their enhanced lubricity: (1) oxide softening due to the working temperatures between 0.4-0.7 of the absolute melting temperature (T_m), (2) melting of the oxide by exceeding T_m , (3) the creation of a material with a lamellar crystal structure with weak interplanar bonds, and, (4) shearing due to dislocations or grain boundary sliding. We will focus on understanding the fundamental mechanisms that impart their advantageous material properties at high temperatures using computational (density functional theory and molecular dynamics simulations) and experimental tools (in situ Raman spectroscopy, X-Ray diffraction, scanning electron microscopy, and transmission electron microscopy). The frictional and wear properties of these materials, tested in various controlled environmental conditions, will be discussed in detail.

2:40pm SE+NS-MoA3 Free-standing Nanoscale Gold Pyramidal Films with Milled Nanopores, J.A. Grant-Jacob, W.S. Brocklesby, T. Melvin, Optoelectronics Research Centre

Thin films of micro and nanostructured metals are important for the construction of plasmonic devices and microelectromechanical systems (MEMs). The fabrication of individual metallic, pyramidal shells as well as ultra-smooth metal films with grooves, bumps, pyramids and holes has previously been demonstrated^{1,2}, as has direct raster milling with 5 nm machining precision in 100 nm thick gold films³. Routine fabrication of micro and nanostructured thin films is desirable. In this work, the fabrication of arrays of nanoscale pyramidal structures in free-standing gold films is demonstrated, and single nanopores are milled into the nanostructures for DNA translocation.

Silicon Klarite® pyramidal micro-structured substrates are an effective tool for surface enhanced Raman scattering (SERS) experiments, owing to the strong field enhancement within the pyramids. Here, the substrates are used as moulds for creating pyramidal structured gold as free-standing thin films. The silicon substrates contain an array of pyramids etched into a 4 mm x 4 mm square region on the substrate's surface. These pyramids are 1.5 μm x 1.5 μm square and 1 μm deep on a pitch of 2 μm . An Edwards E306A Thermal Evaporator is used to coat silicon samples in a 50 nm layer of Teflon® and then a 100 nm layer of gold. Epoxy is then deposited on top of the gold layer using a pipette. Once the epoxy has cured, the epoxy together with the gold is mechanically lifted from the Teflon® coated substrate. The gold-coated epoxy is then placed over a micron-sized aperture and the epoxy dissolved away using acetone. Initial imaging is performed using a Carl Zeiss SMT, Inc., Evo® scanning electron microscope (SEM), while the subsequent imaging and milling of 50 nm holes through the free-standing gold is carried out using a Carl Zeiss SMT, Inc., Orion® Plus helium ion microscope (HIM). These films are suspended over micron-sized apertures for integration into platforms already proven for DNA translocation, and to optically interrogate the structures using Raman based techniques.

¹ Q. Xu, I. Tonks, M.J. Fuerstman, J.C. Love, and G.M. Whitesides, *Nano Letters* **4**, 2509-2511 (2004).

² P. Nagpal, N.C. Lindquist, S.-H. Oh, and D.J. Norris, *Science* (New York, N.Y.) **325**, 594-7 (2009).

³ L. Scipioni, D.C. Ferranti, V.S. Smentkowski, and R. a. Potyrailo, *Journal of Vacuum Science & Technology B: Microelectronics and Nanometer Structures* **28**, C6P18 (2010).

3:00pm SE+NS-MoA4 Synthesis of Superhydrophobic PTFE-like Thin Films by Self-Nanostructuring in a Hybrid Plasma Process, F. Henry, University of Mons, Belgium, F. Renaux, S. Coppée, Materia Nova Research Center, Belgium, R. Lazzaroni, University of Mons, Belgium, N. Vandecasteele, F. Renters, ULB, Belgium, R. Snyders, University of Mons, Belgium

Superhydrophobic Poly(tetrafluoro-ethylene) (PTFE) like thin films were grown using a plasma-based hybrid process consisting on sputtering a carbon target in a Ar/CF₄ atmosphere. The influence of the bias voltage applied to the substrate (VBias) as well as of the gas mixture composition (%CF₄) on the chemical composition, the wettability and the morphology of the deposited thin films were evaluated.

The chemical composition measured by X-Ray photoelectron spectroscopy (XPS) reveals that the fluorine content is lower than in conventional PTFE (50 at.% maximum > 66%) and that it decreases when VBias increases (from 50 at.% for VBias = -100 V to 30 at.% for VBias = -200 V). This behaviour is associated with the preferential etching of the fluorine atoms during the plasma-assisted growth of the films. Consecutively to this etching, a self-nanostructuring enhanced by increasing VBias, is observed. As a consequence, the water contact angle (WCA) measurements range from 70° up to 150° depending on (i) the fluorine content and (ii) on the magnitude of the nanostructuring. In addition, for the films presenting the highest WCA angles, a small hysteresis between the advancing and

receding WCA is observed (< 10°) allowing these films to fulfil completely the requirements of superhydrophobicity.

In order to get more understanding on the wettability mechanisms of these surfaces, the topology of the films has been evaluated by atomic force microscopy (AFM). The data reveal, for all films, a dense and regular structure composed by conic objects for which the dimensions increase with VBias. We were able to correlate the ratio of the average height (AvH) of the objects and the average distance (AvD) between them with the WCA. Theoretical evaluations of the WCA using the Wenzel and Cassie equations with, as inputs, the features of the deposited thin films surfaces measured by AFM suggest that the wetting regime is intermediate between these two ideal situations.

3:40pm SE+NS-MoA6 Creation of Highly Functionalized Polymer-Metal Oxide Nanomaterials Using A Novel Rotating Drum Plasma Reactor, J.C. Shearer, E.R. Fisher, Colorado State University

The use of nanoparticles in biological applications has grown rapidly in recent years. Understanding the surface chemistry and protein-nanoparticle interactions is critical in the fabrication of biomedical devices. Some nanoparticle surfaces are not compatible with specific applications, and thus must be modified to make them viable. Plasma processing of nanomaterials is an effective method for functionalization and encapsulation of nanoparticles. Our lab has designed a rotating drum inductively coupled plasma reactor that has afforded the ability to create specifically tailored nanoparticle surfaces. The rotating drum apparatus was utilized to encapsulate Fe₂O₃ and Au nanoparticles with various polymer films. Allyl alcohol, allylamine, and acrylic acid plasmas were used to incorporate alcohol, amine, and carboxylic acid functionality to nanoparticle surfaces, respectively. Tailoring of film composition was achieved by lowering the duty cycle (d.c.) of the plasma to facilitate less fragmentation of the monomer. This resulted in the deposited films being more stoichiometrically similar to the parent monomer gas and thus having a high concentration of functional groups present within the film. For example, the alcohol functionality of plasma polymerized allyl alcohol films on Fe₂O₃ nanoparticles can be substantially increased by lowering the d.c. of the plasma from 100 % to 10 %. Specifically, x-ray photoelectron spectroscopy elemental analysis shows that films deposited under low d.c. conditions increase O/C ratios from 0.17 to 0.35, which is comparable to that of the parent monomer (0.33). FTIR data reveal complementary results, where increases in OH functionalities are observed for low d.c. plasmas. Electron microscopy confirms there is no appreciable change in size and shape of the nanoparticles upon plasma treatment. The solubility and stability of the encapsulating films were analyzed to measure the longevity of the particles in biological systems. Highly functionalized films were also deposited onto supported nanoparticle substrates to investigate how plasma processing affects surface roughness, as this can affect cell adhesion. We have demonstrated that plasma processing can change the RMS roughness of supported nanoparticles by 0.2 μm , thereby affording the ability to tailor the roughness of a surface for specific cell interactions. A variety of gas-phase and surface analysis data will be presented to show how plasma processing can tailor the composition of deposited films of as a function of plasma parameters and gas-phase species. Understanding how these films are produced will undoubtedly advance the fabrication of novel biomedical devices.

4:00pm SE+NS-MoA7 Field Emission Dynamic Investigation of the Polymer-MWCNT Composite Films Depending from Vacuum Conditions, E.O. Popov, A.G. Kolosko, M.V. Ershov, S.V. Filippov, A.F. Ioffe Physico-Technical Institute, Russian Federation

It is obvious that research I-V characteristics remains the basic criterion of an estimation of field emission process. However the techniques, allowing to do exhaustive conclusions about the physical processes occurring on nano dimensional emission sites by macroscopical values of a current and voltage does not exist yet. Especially it is expressed at research of dynamics of field emission, the phenomena accompanying functioning flat multityps cold cathodes (emitters).

Attempts to observe other phenomena that can accompany emission processes, except for observation of I-V characteristics, are being made. There are the registration of radiation of the emitter and the anode, heating of electrodes, change of vacuum conditions, mass spectrometer researches. Application of computer processing during record I-V characteristics opens additional possibilities of knowledge of evolution and emitter work, allows to approve models of physical processes is directly during emission experiment.

In our work was developed the technique of multichannel record and *in situ* data processing about evolution of field emitters. On-line processing of signals is performed on the basis of own program written on Labview 10. The technique includes multichannel system of gathering of signals of a current and voltage, record of vacuum values and temperature. As a part of

mass spectrometer installation the given system collects the data about kinetics allocation of the volatile products accompanying emission process. Data for representation in a kind convenient for the analysis is in addition processed: beta values of field increasing, active resistance of inter-electrode gap, visualization of height of emitters and the estimation of a total emitting surface and number of the emission centers is made.

Some characteristic areas in dependence SK [1,2] which are treated as desorption gases from surface MWNT, area of growth of number of sites without change of the geometrical sizes (almost vertical growth SK), area of smooth change of geometry of the emitter (increase in intensity of a field and increase in the area of the emitter - intercept increasing) have been found out.

[1] M. Kawasaki, Z. He, Y. Gotoh, H. Tsuji, J. Ishikawa, *J. Vac. Sci. Technol. B* 28, (2010) C2A77.[2] E.O.Popov, M.V. Ershov, *IEEE, 24th INVC*, Wuppertal, (2011) 158.

4:20pm SE+NS-MoA8 Cost Efficiency Trade Off in Nanostructured Thermoelectric Energy Conversion Systems, A. Shakouri, K. Yazawa, Birck Nanotechnology Center, Purdue University **INVITED**

Energy consumption in our society is increasing rapidly. A significant fraction of the energy is lost in the form of heat. In this talk we introduce thermoelectric devices that allow direct conversion of heat into electricity. Some new physical concepts and nanostructures make it possible to modify the trade-offs between the bulk electrothermal material properties through the changes in the density of states, scattering rates and interface effects on the electron and phonon transport. We will review recent experimental and theoretical results on nanostructured materials as well as solid-state thermionic power generation devices. Theory and experiment are compared for several III-V and nitride nanocomposites and multilayers. Potential to increase the energy conversion efficiency and bring the cost down to \$0.1-0.2/W will be discussed.

5:00pm SE+NS-MoA10 The Effects of Interfacial Bond Stiffness on Heat Transport: An Experimental Study Using Self-Assembled Monolayers, M.D. Losego, M. Grady, N.R. Sottos, D.G. Cahill, P.V. Braun, University of Illinois at Urbana Champaign

Compared with our ability to precisely control the flow of electrons or light within a material, our capacity to design the flow of heat, particularly at the nano-scale, is rather rudimentary. For example, billions of microscopic transistors with coordinated electronic transport are routinely fabricated for computers, cell phones, and iPods. In contrast, thermal management is largely limited to macroscopic solutions (e.g. fans, insulation). Examples of confining and controlling heat with precision at micro- or nanometer length scales are relatively rare

Crucial to nanoscale thermal management is an understanding of interfacial heat transport. Interfaces between two materials act as a barrier to heat flow. For nano-scale systems, interfacial heat conduction and not just bulk thermal conductivity is important and possibly dominant in controlling heat transfer. However, thermal transport across interfaces is still not well understood. Historically, differences in bulk acoustic properties and/or phonon densities of states have been used to explain the interfacial thermal boundary resistance. However, more recently, atomic level structural features, such as interfacial roughness and interfacial bonding, have been proposed as contributors to the thermal boundary resistance.

This talk will describe experimental work that attempts to validate recent molecular dynamics (MD) simulations suggesting that interfacial thermal conductance can be strongly modulated by adjusting the strength of interfacial bonds. Our experimental system consists of self-assembled monolayers (SAMs) on SiO₂ substrates having either methyl or mercapto terminations. Gold films are transfer printed onto these surfaces forming either a van der Waals or covalent bond respectively. The interfacial thermal conductance across the Au/SAM interface is measured via time-domain thermoreflectance (TDTR) and found to increase by nearly 2x when the interface is switched between a van der Waals interaction and a covalent bond. The interfacial bond stiffness is independently measured using picosecond acoustics. Together these experiments represent the first clear demonstration of how changing the stiffness of a single atomic-scale interfacial bonding layer affects thermal conductance.

To further elucidate the mechanism for this change in interfacial thermal conductance, we will present temperature dependent thermal conductance measurements. This data reveals that high frequency phonon modes cannot traverse interfaces with lower stiffness. Finally, we will show proof-of-concept experimental results that outline a scheme for designing materials with specified values of interfacial thermal conductance.

5:20pm SE+NS-MoA11 Growth, Nanostructure Formation, and Physical Properties of Single-Phase, Epitaxial, SrTiO₃-TiO₂ Nanocomposites: A Topological Insulator Approach to High-T Thermoelectrics, B.M. Howe, Air Force Research Laboratory, E. Thomas, University of Dayton Research Institute, D. Dudis, Air Force Research Laboratory

Here, we present a novel approach towards creating efficient thermoelectric materials for energy conversion and thermal management under high-temperature and oxidizing environments. Several transition-metal oxide systems have recently been investigated, however most studies involve the doping of single-phase compounds to enhance electrical conductivity; while very few address decreasing thermal conductivity (in the same direction as electron transport). Thus, we present an investigation into the growth, nanostructure formation, and physical properties of epitaxial, immiscible SrTiO₃-TiO₂ nanocomposites. Sr_(1-x)Ti_(1+x)O_(3+2x) layers with 0 ≤ x ≤ 0.67 were grown on SrTiO₃ (001) substrates at 700°C in 1 × 10⁻⁶ Torr O₂ by high-vacuum pulsed laser deposition using a KrF excimer laser (λ = 248nm) operating at 10 Hz pulse rate and 1.7 J/cm² fluence. HRXRD and XTEM results show that perovskite-structure layers grow epitaxially with a cube-on-cube orientational relationship to the substrate. The lattice parameter increases linearly while crystalline quality decreases from x=0 to x=0.67. We find a remarkably broad metastable single-phase field given the immiscible nature and crystal structure mismatch of the two alloy components. Alloying SrTiO₃ with TiO₂ leads to the formation of nanostructured compositional modulations due to the onset of spinodal decomposition, resulting in increased in electrical conductivities (due to the formation of 2D electron gas layers at the SrTiO₃-TiO₂ interfaces), decreased thermal conductivities, and enhanced thermoelectric figure of merit, large enough to compete with current state-of-the-art high-temperature thermoelectric materials.

Surface Science

Room: 21 - Session SS-MoA

Surface Dynamics

Moderator: D.J. Auerbach, University of California, Santa Barbara

2:00pm SS-MoA1 Creation and Reaction of Solvated Electrons at the Vacuum-Liquid Interface, W.A. Alexander, Montana State University, J.P. Wiens, University of Wisconsin-Madison, T.K. Minton, Montana State University, G.M. Nathanson, University of Wisconsin-Madison **INVITED**

Over the last 70 years, thousands of reactions between solvated electrons and dissolved species have been investigated in water and other protic solvents. Electrons born at the surface of the solvent, however, may react differently than those created within it. In this talk, I will describe gas-liquid scattering experiments using an impinging beam of sodium atoms that ionize upon contact and create electrons at the surface of liquid glycerol. We find that these electrons produce hydrogen atoms and hydrogen molecules, hydroxide ions and water, and glycerol radicals. Remarkably, nearly half the hydrogen atoms created near the surface escape into vacuum before reacting with the solvent.

2:40pm SS-MoA3 Liquid-Crystal to Solid-Crystal Phase Transition in Flexible Aryl-Triazole Oligomer Adsorbates at the Liquid / HOPG Interface, B. Hirsch, K. McDonald, A. Flood, S.L. Tait, Indiana University - Bloomington

Supramolecular self-assembly at the liquid / solid interface is a powerful strategy for the bottom-up fabrication of complex and well-ordered structures. In order to achieve greater functionality, molecules with functional groups that possess symmetries other than those of the substrate must be included. Here, we explored this idea by integrating the pseudo-C5 triazole moiety into an oligomer through facile synthesis using well-known click chemistry. The molecules initially adsorbed without direct commensuration with HOPG (high oriented pyrolytic graphite) in a lamellar-like liquid-crystalline phase. Subsequent molecular conformational changes are believed to enable a spontaneous phase transition to a more condensed crystalline phase. The crystalline phase forms a dynamic bilayer, in which ripening of the second layer domains was observed. We will present scanning tunneling microscopy (STM) snapshots of this evolution and discuss the dynamics associated with these phase transitions and bilayer formation. Packing models and phase dependence on experimental conditions will be presented. This work lays the foundation for extending the library of self-assembling molecules to develop higher functionality at surfaces.

3:00pm **SS-MoA4 State-Resolved Studies of Methane Activation: Mechanistic Insights into Gas-Surface Reactivity**, *A.L. Utz*, Tufts University

Gas-surface reactivity measurements performed with vibrational and rotational state selected reagents provide precise energetic resolution that can be exploited to uncover important aspects of gas-surface reactivity. This talk will focus on two examples. In the first, we explore the surface temperature dependent reactivity of methane (CH_4) molecules prepared in the ν_3 C-H stretching state. We find that at low incident kinetic energy, thermal excitation of the Ni(111) surface can increase reaction probability by nearly three orders of magnitude. Calculations from the Jackson group provide insight into the origin of this effect. As a second example, we will describe recent experiments that compare the reactivity of the symmetric (ν_1) and antisymmetric (ν_6) C-H stretching states in di-deutero methane, CH_2D_2 , on Ni(111). That work explores how the vibrational symmetry of the reactant molecule may influence the rate and pathway of rapid intramolecular vibrational energy redistribution (IVR) that occurs just prior to reaction, and it tests whether vibrationally adiabatic models for methane activation in the gas phase are also applicable to methane reactivity on a metal surface.

Taken together, the work highlights how general patterns of energy flow within the gas-surface reaction complex can influence reactivity patterns, and how the kinetics of energy redistribution might be used to control or enhance the rate or selectivity of reactions on surfaces.

3:40pm **SS-MoA6 Autocatalytic Decomposition Mechanism of Aspartic Acid on Cu(110) Surfaces**, *B.S. Mhatre, A.J. Gellman*, Carnegie Mellon University

Surface explosions are surface reaction mechanisms wherein an autocatalytic increase in the reaction rate results in the reaction proceeding to completion over a very narrow temperature range during heating. While several substrate-adsorbate systems exhibiting decomposition via surface explosion mechanism have been identified, a detailed understanding of the mechanism remains unclear. We have successfully identified aspartic acid as a suitable probe for studying surface explosion mechanism on Cu(110) surface. Because a wide range of isotopically labeled varieties of aspartic acid are commercially available, we have been able to conduct a detailed investigation of its autocatalytic reaction mechanism. Using specifically labeled aspartic acid molecules, we have identified the reaction products and identified the origins of atoms in the decomposing aspartic acid molecules. The explosive nature of the reaction mechanism has enabled us to study its kinetics using isothermal methods by heating the Cu(110) surface to a constant temperature and then monitoring the product desorption as a function of time. We observe a significant lag time during which nucleation of the reaction is occurring without observable desorption of products. Once the reaction begins, it proceeds to completion over a relatively short time period. Our preliminary studies on chiral Cu(643)^{R&S} surfaces indicate that aspartic acid exhibits enantiospecific surface decomposition kinetics. The ultimate objective of this work is to be able to identify the mechanism and in particular, the steps in the mechanism which are responsible for the enantiospecificity.

4:00pm **SS-MoA7 Quantum Tunneling Driven Assembly and Diffusion of Hydrogen and Deuterium on Cu(111)**, *A.D. Jewell**, Tufts University, *G. Peng*, University of Wisconsin Madison, *G. Kyriakou*, Tufts University, *M. Mavrikakis*, University of Wisconsin Madison, *C.H. Sykes*, Tufts University

Hydrogenation reactions are central to the petrochemical, fine chemical, pharmaceutical, and food industries and are of increasing interest in energy production and storage technologies. The processes of molecular adsorption, dissociation, diffusion, association, and desorption are important surface phenomena in heterogeneous catalysis. Typical heterogeneous catalysts often employ alloys based on platinum, palladium, rhodium and ruthenium. While these metals are active at modest temperature and pressure, they are not always 100% selective and are expensive.

Given that molecular hydrogen (H_2) dissociation is often the rate limiting step, one strategy is to engineer the minimal catalytic ensemble that will activate H_2 but leave the other reactants untouched. We describe a system which offers low dissociation barriers at one location on the surface and weaker binding in other regions. The Pd/Cu surface alloy was prepared in the dilute limit in which 1% Pd resides as individual, isolated substitutional atoms in a 99% Cu(111) surface. In terms of adsorption, these Pd atoms significantly lower the barrier to H_2 dissociation and allow the spillover of H atoms onto the Cu surface.[1]

* Morton S. Traum Award Finalist

This system also offers the opportunity to study the diffusion, association, and assembly of large quantities of H and D on the Cu(111) surface. Through careful low-temperature scanning tunneling microscopy (STM) tracking experiments we show that quantum tunneling effects dominate the diffusion properties of H and D on the Cu surface.[2] With this direct visualization and quantification of quantum tunneling effects in adatom diffusion, we reveal two types of weak interactions between H adatoms, which lead to assembly into small clusters and larger assemblies of small clusters. We show that the self-assembly of H into large islands is, in fact, a tunneling effect resulting from inter-atom energy being much smaller than the diffusion barrier. We further demonstrate that these latter effects are not at play for D. Density Functional Theory (DFT) calculations provide estimates for both diffusion and interaction energies. Theory also provides quantum tunneling probabilities that agree well with experiment.[2]

References:

- [1] G. Kyriakou, M.B. Boucher, A.D. Jewell, E.A. Lewis, T.J. Lawton, A.E. Baber, H.L. Tierney, M. Flytzani-Stephanopoulos, and E.C.H. Sykes, *Science* **335**, 1209 (2012).
- [2] A.D. Jewell, G. Peng, G. Kyriakou, M. Mavrikakis, E.C.H. Sykes, in preparation.

4:20pm **SS-MoA8 H Absorption Depth Profiling Measurement at Ultra-thin Pd(111) Film by Thermal Desorption Spectroscopy**, *Y. Aoki, S. Nakajima, H. Hirayama*, Tokyo Institute of Technology, Japan

Palladium is a peculiar metal with non-activated dissociation and bulk incorporation of hydrogen. Previous studies of H thermal desorption spectroscopy (TDS) at Pd(111) indicated that large H_2 exposures at $\sim 100\text{K}$ induce a non-saturating desorption signal which is so called as α peak at 180 K [1]. The absorption origin of the α peak was inferred as the hydrogen located in subsurface sites just below the top surface Pd atoms layer, where it is stabilized at low temperatures by an energy barrier with respect to bulk sites. However, a hydrogen depth profiling measurement by nuclear reaction analysis (NRA) at the Pd(001) surface indicated that the α_1 peak (which regards as α peak at the Pd(111)) has to be assigned to the deeper located H in the 0-50 monolayer [ML] subsurface region [2]. The actual H depth distribution however was difficult to assess precisely with NRA, since the beam induced local heating was suspected to cause a partial escape of H from detection by diffusion into the bulk. To investigate the α -H origin without any heating ambiguity, TDS has been observed at well-defined ultra-thin Pd(111) films. Controlling the Pd film thickness enables us to seek the α -H depth profiling.

Pd film was deposited at the 50 ML of Ag(111) coated Si(111) surface by a Knudsen cell at room temperature. The Pd surface structure was characterized by a reflection high-energy electron diffraction (RHEED) and an atomic force microscopy (AFM). Pd(111) film grew layer-by-layer at the Ag(111) surface when grown at room temperature without any interdiffusion. The lattice constant mismatch between Pd and Ag of 4.9 % expanded the Pd lattice constant when the Pd thickness (θ_{Pd}) was below 80 ML. It recovered the bulk lattice constant at $\theta_{\text{Pd}} > 80$ ML. H_2 was exposed to the Pd(111) surface at 102 K with an exposure pressure of 1×10^{-4} Pa. By integrating α -TDS signal, α -H absorption amount of H_2 exposure dependence ($< 4 \times 10^4$ L) and of θ_{Pd} dependence (< 560 ML) were observed.

H absorption on the Pd film ($\theta_{\text{Pd}}=420$ ML) saturated as ~ 8 ML at the maximum exposure of 4×10^4 L. The averaged α -H concentration corresponded to 1.9 %. The θ_{Pd} dependence of α -H at the exposure of 4050 L showed that the α -H absorption increased with θ_{Pd} (maximum θ_{Pd} was 560 ML). H concentration at $\theta_{\text{Pd}}=80$ ML was 1.8 % which was close to the saturated concentration, it decreased to 1.2 % at $\theta_{\text{Pd}}=560$ ML. Our result indicated that the α -H absorption progress from near the surface region, but it possibly to absorb at the deeper bulk region than that of the previous NRA measurement at the high exposures.

References:

- [1]. G. E. Gdowski *et al.* Surf. Sci. 181, L147 (1987).
- [2]. M. Wilde *et al.* Surf. Sci. 482, 346 (2001).

4:40pm **SS-MoA9 Novel Insight Into the Formation Mechanism of Subsurface Hydrogen at Pd(110) Surfaces**, *S. Ohno, M. Wilde, K. Fukutani*, The University of Tokyo, Japan

The present study investigates the microscopic hydrogen (H) absorption mechanism at palladium (Pd) (110) single crystal surfaces. The unique properties of H-Pd interactions such as non-activated H_2 dissociation and facile bulk absorption are well known, yet an accurate atomic-level understanding of the H transportation across the surface, i.e., penetration into the Pd interior and hydride formation during absorption as well as the H release into the gas phase has not been achieved. We apply $^1\text{H}(^{15}\text{N}, \alpha \gamma)^{12}\text{C}$

resonant nuclear reaction analysis (NRA) for nondestructive H depth profiling in combination with thermal desorption spectroscopy (TDS) to quantitatively reveal the H-concentration-depth distribution and to unambiguously assign characteristic TDS features to surface-adsorbed and subsurface-absorbed H-species. To obtain additional insight into the release mechanism during thermal desorption of the H states absorbed in the Pd interior, the internal state distribution of desorbing H₂ molecules is characterized with a rovibrational state selective resonance-enhanced multiphoton ionization (REMPI) technique.

TDS experiments using isotope labeling for the surface-adsorbed and subsurface-absorbed H states reveal that two parallel absorption routes exist that lead to two distinctly different depth distributions of Pd hydride in the near-surface region which give rise to separate TDS signatures (α_1 at T=160 K and α_3 at T>190 K), respectively. The first absorption pathway involves only a few (~4%) minority sites (presumably defects) at which penetration is highly efficient and leads to in-plane localized nucleation of hydride that remains concentrated within a few nanometers below the surface (α_1 state). The second absorption route proceeds on regular terraces with a significantly slower penetration rate per site so that subsurface H diffusion leads to a more extended hydride depth distribution (α_3 state, several tens of nm below the surface). A clear difference between the two H absorption states (α_1 , α_3) is also seen in the REMPI internal-state populations of desorbing H₂. Both absorption pathways critically require gas phase H₂, replace surface-adsorbed H atoms with the gas phase isotope, and have activation energies (< 100 meV) much smaller than expected for the isolated subsurface migration of chemisorbed H. The results are accounted for by a concerted mechanism, in which pre-adsorbed H transits into the subsurface while its vacated adsorption site is simultaneously refilled by a nearby 'nascent' H atom in a state of high potential energy, which is supplied through gas phase H₂ dissociation at vacancies in the chemisorption layer.

5:00pm **SS-MoA10 Glide-Plane-Specific Selectivity of HREELS Demonstrated in H:Si(110)-(1x1) Phonon Dispersion**, *T. Yamada*, RIKEN, Japan, *S.Y. Matsushita*, Tohoku University, Japan, *H. Kato*, Science University of Tokyo, Japan, *A. Kasuya*, *S. Suto*, Tohoku University, Japan

We observed the consequence of surface glide-plane symmetry over the phonon vibration on a typical, well-defined silicon wafer. We recorded surface phonon dispersion curves on hydrogen-terminated Si(110)-(1x1) by means of high-resolution electron energy loss spectroscopy (HREELS). This surface, H:Si(110)-(1x1), was prepared by etching a Si(110) wafer in 40% aqueous solution of NH₄F. H:Si(110)-(1x1) structure involves a glide-plane symmetry, denoted as *p2mg*, along the short segment of the rectangular unit cell, containing two H-Si bonds. This glide-plane symmetry is also lucid in the extinction rule observed in the pattern of low energy electron diffraction (LEED). The normal vibrational modes are doubled into the in-phase and anti-phase modes. However, for the phonons propagating along the glide plane, ones of those pairs are excluded according to the wave vector. The H-Si symmetric stretching, anti-phase out-of-plane bending, and anti-phase in-plane bending exist only for the wave vectors in the 1st Brillouin zone, and the others exist only in the 2nd Brillouin zone. The impact scattering selection rule furthermore limits the normal modes visible to HREELS. We have verified this special case of phonon dispersion by recording angular-resolved vibrational spectra. The surface phonon dispersion curves were recorded over the 1st and 2nd Brillouin zones, by adjusting the angular configuration as well as the incident electron energy. The experimental dispersion curves are in a fair agreement with the theoretical prediction [2]. However, along Γ -X direction, the H-Si stretching mode (~2080 cm⁻¹) just composes a single branch as a concatenation of the symmetric mode in the 1st Brillouin zone, and the asymmetric mode in the 2nd Brillouin zone. Similarly, the out-of-plane bending (~680 cm⁻¹) curve is also single. This is due to the glide-plane symmetry. The in-plane bending modes are all cancelled by the EELS impact selection rule. As for the propagating direction vertical to the glide plane (Γ -X' direction), the pairs of stretching and out-of-plane bending appear simultaneously. The sub-surface phonon modes (< 600 cm⁻¹) also follow the same rule. This is a special case for the glide-plane symmetry, reflected over the reciprocal unit cell as the property of phonon waves propagating along the surface.[1] M. Eremtchenko et al., Surf. Sci. 582 (2005) 159.[2] V. Gräschus et al., Phys. Rev. B 56 (1997) 6482.

Thin Film

Room: 11 - Session TF+EN-MoA

ALD for Energy

Moderator: R.K. Grubbs, Sandia National Laboratories

2:00pm **TF+EN-MoA1 Atomic Layer Deposition for the Synthesis of Nanostructured Catalysts**, *J.W. Elam*, *C. Marshall*, Argonne National Lab, *E. Stach*, *F. Ribeiro*, Purdue Univ., *J. Greeley*, Argonne National Lab, *J. Notestein*, *K. Poepelmeier*, Northwestern Univ., *L. Curtiss*, Argonne National Lab, *M. Kung*, *P.C. Stair*, Northwestern Univ., *L. Winans*, Argonne National Lab, *S. Nguyen*, Northwestern Univ. **INVITED**

The successful transition to an energy economy based on biomass will require radical advances in catalyst science. This challenge demands a new paradigm in catalyst synthesis whereby inorganic components can be assembled at the atomic scale to yield complex, multifunctional catalysts rivaling Nature's enzymes in their specificity. To this end, we have developed a novel approach combining templated synthesis for shape-selectivity with the atomically-precise positioning of discrete functionalities. In this approach we begin with a supporting scaffold for catalyst growth upon which we chemically attach molecular templates. Next, atomic layer deposition is used to build a structure around each template in an atomically precise, layer-by-layer fashion where the thickness and composition can be tuned at each layer. Finally, the template is removed yielding a "nanobowl" defining a structured catalytic environment. The molecular template can be synthesized to contain bulky organic ligands surrounding a catalytic atom or cluster which remains anchored to the bottom of the bowl after ligand removal. Furthermore, one or more layers in the bowl wall can be selected to serve as a co-catalyst (e.g. Lewis acid group) positioned at a well-defined distance from the catalyst at the bottom of the bowl. This presentation will review our recent progress synthesizing, characterizing, modeling, and testing these unique catalytic materials.

2:40pm **TF+EN-MoA3 Using Metalcone Films Grown by Molecular Layer Deposition to Form Conducting Metal Oxide-Carbon Composite Films**, *A. Abdulagatov*, *K. Terauds*, *J. Travis*, *A. Cavanagh*, *R. Raj*, CU Boulder, *S.M. George*, University of Colorado, Boulder

Metalcone films grown using molecular layer deposition (MLD) techniques with metal and organic precursors are metal alkoxide polymers. These hybrid organic-inorganic films can serve as precursors to conducting metal oxide-carbon composite films. In this study, titaniconc MLD films were deposited by sequential, self-limiting exposures of TiCl₄ and glycerol at 150°C. These films were then annealed in argon at temperatures ranging from 500 to 1200 °C. Under argon, the hydrogen is removed from the hybrid organic-inorganic titaniconc films and the carbon remains. Raman spectroscopy measurements showed the progressive growth and sharpening of the D and G signature peaks for graphitic carbon after annealing from 600 to 900 °C. The sheet resistance of the annealed films was also found to progressively decrease with increasing annealing temperature. X-ray photoelectron spectroscopy depth profiling confirmed the presence of carbon throughout the annealed film. X-ray diffraction measurements also observed the formation of rutile TiO₂ diffraction peaks. The annealing of metalcone MLD films in argon is a general method to deposit metal oxide-carbon composite films. Conducting metal oxide-carbon composite films are desirable because many electrochemically important metal oxides have low electrical conductivities. The metal oxide-carbon composite films with graphitic carbon have much higher electrical conductivities that will enable their electrochemical application for Li ion batteries and pseudocapacitance supercapacitors.

3:00pm **TF+EN-MoA4 In Situ Growth Study and Material Characterization of Plasma-Assisted Atomic Layer Deposition of Palladium**, *M.J. Weber*, *A.J.M. Mackus*, *M.A. Verheijen*, *N. Leick-Marius*, *A. Bol*, *W.M.M. Kessels*, Eindhoven University of Technology, Netherlands
Palladium thin films are object of great interest in catalysis, as well as in hydrogen sensing, storage and generation. Noble metals such as Palladium are the most effective if deposited as ultrathin films on a large surface area. Atomic layer deposition (ALD) is considered to be the method of choice to grow ultrathin films on various substrates with demanding surface topologies. This contribution will present *in situ* and *ex situ* studies of Palladium films grown by plasma-assisted ALD. The Pd films were deposited on alumina at 100°C using Pd(hfac)₂ (hfac= hexafluoroacetylacetonate) as the precursor, and H₂ gas and H₂ plasma as reducing agents. *In situ* spectroscopic ellipsometry (SE) has been used to monitor the film growth and obtain detailed information about the optical properties of Palladium. The nucleation and subsequent island growth have been characterized by Transmission Electron Microscopy (TEM). X-Ray

diffraction, X-ray photoelectron spectroscopy and Rutherford backscattering spectrometry have been carried out in order to characterize the grown films. The thermal ALD process only allowed for growth of Pd on a Pd or Pt seed layer, while the plasma-assisted ALD process also led to growth on an alumina surface. In both cases the steady-state growth rate was $\sim 0.17 \text{ \AA/cycle}$ as determined by *in situ* SE. The observed selective growth on catalytic Pd or Pt seed layer of the thermal process holds promises for nanopatterning applications, whereas the plasma-assisted process can be used to deposit Pd nanoparticles and films at low-temperature on oxide substrates, which has considerable potential for catalysis and hydrogen sensor applications.

3:40pm TF+EN-MoA6 ALD-enabled Nanostructures for High Rate Li-ion Storage. *X. Chen, H. Zhu, L. Hu, G.W. Rubloff*, University of Maryland
A major challenge for Li-ion batteries is to achieve high rates (power) by overcoming the long charge/discharge time caused by low Li diffusivity in active storage materials. Nanostructured electrodes provide a potential solution by reducing the thickness of active storage layers, since the diffusion time is proportional to the square of diffusion length. Our strategy to improve the rate performance of Li-ion battery is to use atomic layer deposition (ALD) to grow thin active battery materials on highly conductive current collecting scaffolds with high surface area. The unprecedented conformality of ALD allows maximum utilization of high surface area, while the highly conductive scaffold facilitates easy electron transport and Li^+ migration in electrolyte as also needed for high power. We report two embodiments of this heterogeneous nanostructure configuration, both with ALD V_2O_5 storage layers.

First, we used highly porous multiwall carbon nanotube (MWCNT) sponge as the scaffold. The V_2O_5 -MWCNTcoaxial sponge achieves a stable high areal capacity as $816 \mu\text{Ah}/\text{cm}^2$ over voltage range 4.0-2.1 V at current density of $1.1 \text{ mA}/\text{cm}^2$ (i.e., 1C rate). This capacity is 450X that of a corresponding planar V_2O_5 thin film cathode. For the same voltage range but 50X higher current, the areal capacity of the V_2O_5 -MWCNT sponge is $155 \mu\text{Ah}/\text{cm}^2$, giving a high power density of $21.7 \text{ mW}/\text{cm}^2$. The areal capacity increases further to $1284 \mu\text{Ah}/\text{cm}^2$, when cycled over a larger voltage window (4.0-1.5 V), but this incurs deteriorated cycling performance as expected from the intrinsic properties of V_2O_5 .

Second, we employed well-ordered anodic aluminum oxide (AAO) templates to with ALD current collecting layers as a scaffold for the storage material. ALD TiN was first deposited into the AAO nanopores to form current collecting nanostructures, after which ALD V_2O_5 was deposited on TiN as the active Li storage medium, with both layer thicknesses precisely controlled and highly conformal. The resulting structures, with electrolyte filling the remaining pore volume, provide test structures to understand regimes where either Li^+ transport or electron transport can be rate-limiting.

4:00pm TF+EN-MoA7 Enhancement of the Heat Recovery Mechanism in Infrared Photovoltaic Devices Promoted by Thin Planar ALD Oxide Films. *A.J. Vincent-Johnson, H.S. Mann, Y. Schwab*, James Madison University, *A.E. Masters*, Custom Thermoelectrics Inc., *X. Hu, G. Scarel*, James Madison University

Infrared photovoltaic devices absorb infrared radiation and transform it into electricity through the heat recovery mechanism [1,2]. In thin planar oxide films, the mechanism is mediated by the excitation of radiative polaritons, as shown by investigations carried out immediately after beginning the exposition to infrared radiation [1,2]. Here we present the results of our investigation on the evolution of the heat recovery mechanism; and the electricity production over time through illumination by infrared radiation. We compare the results on systems including atomic layer deposited (ALD) Al_2O_3 , Al foil, and the bare thermoelectric power generator used for the detection of the heat recovery mechanism. We show that ALD oxide films promote the largest amount of electricity production under long term exposition to both polarized and non-polarized infrared radiation.

[1] A.J. Vincent-Johnson, K.A. Vasquez, J.E. Bridstrup, A.E. Masters, X. Hu, and G. Scarel, *Appl. Phys. Lett.* **99**, 131901 (2011).

[2] A.J. Vincent-Johnson, A.E. Masters, X. Hu, and G. Scarel. Submitted.

4:20pm TF+EN-MoA8 Ultra-thin TiO_2 Blocking Layer by Atomic Layer Deposition for Dye-Sensitized Solar Cells. *D.H. Kim, M. Woodroof, K.M. Lee, B. Kalanyan, G.N. Parsons*, North Carolina State University

In dye-sensitized solar cells (DSSCs), one of major recombination routes occurs at the interface of fluorine-doped tin oxide (FTO) glass and electrolyte solution. Typically, a thin and compact blocking layer (B/L) on the FTO-glass has been introduced to reduce electron loss before mesoporous TiO_2 layer integration. A variety of deposition methods have been tried and studied to make efficient B/L on the FTO-glass. Optimal thickness that suppresses the recombination on the interface of FTO glass

and electrolyte, is typically 25 to 450 nm, depending on deposition methods and conditions. Compared to other methods, atomic layer deposition (ALD) with TiO_2 is not well established and investigated for blocking layers even though it is a valuable process in making pin-hole, crack-free, and dense TiO_2 films.

In this study, ALD TiO_2 was performed on FTO-glass with titanium isopropoxide and H_2O as precursors, producing B/L thickness from 5 to 100 nm. Cells without mesoporous titania but with ALD TiO_2 B/L were also made. We find the optimal thickness of the ALD TiO_2 blocking layer is 10 nm. This blocking layer thickness significantly reduces recombination, resulting in an average overall efficiency of 8.5%, compared to 7.1% for similar cells without the blocking layer present. We also find that a blocking layer of 4.3 nm effectively prevents electrons of FTO surface from recombining with I_3^- in the electrolyte. On the other hand, a thick ALD TiO_2 blocking layer in excess of 10 nm tended to reduce the overall efficiency because the thick ALD TiO_2 film increases the charge transfer resistance and hinders the electron transport to FTO-glass. This work contributes to understand effective blocking layer from TiO_2 ALD process for DSSCs and other high-performance electrical devices

Vacuum Technology

Room: 14 - Session VT-MoA

Gas Flow, Leaks, Permeation and Mass Analysis

Moderator: J.A. Fedchak, National Institute of Standards and Technology

2:00pm VT-MoA1 First International Comparison of Standard Leak Calibrations of Metrological Institutes. *K. Jousten*, PTB, Germany, *K. Arai*, NMIJ, Japan, *U. Becker, O. Bodnar*, PTB, Germany, *F. Boineau*, LNE, France, *J.A. Fedchak*, NIST, *V. Gorobey*, VNIM, Russian Federation, *W. Jian*, SPRING, Singapore, *D. Mari*, INRIM, Italy, *P. Mohan*, NPL/I, India, *J. Šetina*, IMT, Slovenia, *B. Toman*, NIST, *M. Vicar*, CMI, Czech Republic, *YH. Yan*, NIM, China **INVITED**

The measurement of leak rates has become an important test in industry for function tests, quality and safety management, and for environmental protection. Leak tests are performed not only for vacuum chambers, but also for various containers like electrical high power switches, pace makers, refrigerating systems, isolation vacuum, rims, and tanks. The leak tests are performed by leak detectors which mainly use helium as test gas. Traceability to the SI units is given by calibrated standard leaks that emit a well known flow rate of typically helium gas. Many National Metrological Institutes (NMIs) provide such traceability in their vacuum sections. The NMIs that signed the mutual recognition arrangement committed themselves to prove equivalence of their calibration measurement capabilities. The test of equivalence is a comparison where a transfer standard is calibrated at the participants' facilities and the results compared. The difference between the laboratory result and a reference value or a bias of a laboratory must not exceed the uncertainty of this difference or the bias. To test equivalence of standard leak calibrations NMIs from 11 countries performed a comparison with two helium permeation leaks as transfer standards. The leak rates were $4\text{E-}11 \text{ mol/s}$ for standard leak L1 ($1\text{E-}4 \text{ Pa L/s}$ at 23°C) and $8\text{E-}14 \text{ mol/s}$ ($2\text{E-}7 \text{ Pa L/s}$ at 23°C) for L2 respectively. For the latter, only 6 NMIs had measurement capabilities. Since leak rates from permeation leaks decrease with time, special evaluation procedures had to be applied to calculate a reference value and to compare the results of the NMIs. Also a statistical method was applied to evaluate a possible bias of a laboratory. Most of the 11 laboratories proved equivalent in the case of transfer standard L1 and all for L2. These results will be published and serve as basis for mutual recognition of calibration results.

2:40pm VT-MoA3 Comparison of the Flow Ratio of the Permeation Type Helium Standard Leaks and the Gas Flow Generator Composed with a Small Conductance Element Made by Sintered Stainless Steel. *N. Takahashi*, ULVAC Inc., Japan, *H. Yoshida*, AIST Japan

The possibility of the gas generator with a small conductance element made by sintered stainless steel as a small gas flow standard is examined.

Helium leak test is one of an important way for the non-destructive testing. Helium standard leaks are usually used for the calibration and for the adjustment of the sensitivity of helium leak detectors. Characteristic and calibration of the helium standard leaks were well studied from late 1980's to middle 1990's (1-6). However, the flow ratio of the one unit of standard leak is fixed. Helium flow ratio by the permeation through glass element usually shows large temperature dependence.

On the other hand, the gas flow generator composed with a small conductance element made by sintered stainless steel was reported as a variable, stable and wide range gas flow generator for the vacuum gauge calibration [7]. We examined and made comparison of the helium gas flow ratio between the gas generator and the permeation type helium standard leaks. The flow ratios of the permeation type helium standard leaks are traceable to AIST/NMIJ. The relation of the helium gas flow generated by the generator and the permeation leaks was good agreement with less than 5% of difference. The generator generates wide range of helium gas flow less than 10⁻⁵ Pa·m³/s. This experiment was performed on the ultra high vacuum equipment, which residual pressure was lower than 10⁻⁷ Pa, with a quadrupole mass spectrometer. The generator is also useful for the wide range, stable and easy way of calibration of standard leaks. Stability, conformity of the generator is also reported.

- 1) L. E. Bergquist, et al., *JVST A* **7**, 1989, 2414.
- 2) M. V. Iverson, et al., *JVST* **20**, 1982, 982.
- 3) J. M. Ball, *JVST A* **6**, 1988, 2860.
- 4) W. G. Bley, *Vacuum* **41**, 1990, 1863.
- 5) P. J. Abbott, et al., *JVST A* **14**, 1996, 1242.
- 6) C. D. Ehrlich, et al., *JVST A* **10**, 1992, 1.
- 7) H. Yoshida, et al., *Vacuum* **86**, 2012, 838.

3:00pm VT-MoA4 Porous Plug Made of Sintered Stainless Steel used as Standard Conductance Element, H. Yoshida, K. Arai, T. Kobata, National Institute of AIST, Japan

A porous plug made of sintered stainless steel, which is named as standard conductance element (SCE), has been developed as an open-type standard leak element for in-situ calibration of ionization gauges (IGs) and partial pressure analyzers [1]. Since the pore size of sintered filter is less than 1 micro meter, the molecular flow condition is realized up to 10 kPa of the upstream pressure of SCE. Therefore, four useful characteristics shown in below are available. (1) Flow rate is proportional to the upstream pressure of SCE. (2) Introducing various gas species with known flow rate is available by applying this single leak element. (3) Calibration using mixture gases is available. (4) Dependence of flow rate on the temperature is small and easy to compensate. In addition, the molecular conductance C_s of SCE has good long-term stability of less than 3 %/year typically. No significant influence is observed by introducing water vapor and bake-out. Since SCE with C_s from 1x10⁻¹⁰ m³/s to 2x10⁻⁹ m³/s is available, the flow rate of less than around 10⁻⁵ Pa·m³/s is generated with various gas species.

Three typical applications of SCE are introduced. First is the quantization of the gas desorption rate for thermal desorption spectroscopy (TDS) [2]. The gas desorption rate was measured by a quadrupole mass spectrometer (QMS) which was calibrated by SCE with H₂, H₂O, N₂, CO, and CO₂ gases. Second is the measurement of the effective pumping speed S_{eff} of cryopump in the range from 10⁻⁹ Pa to 10⁻⁶ Pa [3]. H₂, CH₄, N₂, and Ar gases with known flow rate Q were introduced into the test chamber with the cryopump through SCE, and measured the pressure increment p by extreme high vacuum gauges. Pressure indications of the gauges were compensated by relative sensitivity factors for N₂. The last one is the in-situ calibration of IG and QMS. The standard pressure p was obtained from Q divided by S_{eff} , where Q and S_{eff} were determined by using SCE and conductance modulation method, respectively. The sensitivity of IG and QMS were measured for H₂, He, CH₄, H₂O, Ne, CO, N₂, C₂H₄, C₂H₆, O₂, Ar, C₃H₆, CO₂, N₂O, and C₃H₈.

These results show that SCE seems to satisfy almost all of requirements for the quantitative measurements in high and ultrahigh vacuum. SCE will be used as a new vacuum standard device.

- [1] H. Yoshida, et al., *Vacuum* **86** (2012) 838-842.
- [2] S. Inayoshi, et al., 52th Annual Symposium of the Vacuum Society of Japan (AVSSJ-52), Tokyo, Japan, 2011.
- [3] M. Yamamoto, et al., Proceedings of international particle accelerator conference (IPAC2011), San Sebastian, Spain, 2011, 979-981.

3:40pm VT-MoA6 Measurement of Gas Transport in Solids by a Saturation/Outgassing Method, L. Wang, J.A. Tanski, R.Y. Weinberg, Los Alamos National Laboratory

Common flow techniques for measuring gas transport properties in solids requires the formation of a membrane which serves as a barrier to the movement of gas and the formation of leak-tight seal so the gas is diffusing through the membrane. However, for many materials, especially brittle non-metallic ionic solids, meeting these two requirements are difficult. In this study, an alternative method based on first saturating the material with the gas at a known pressure and subsequently allowing the absorbed gas to

diffuse out to a static vacuum environment was developed for measuring gas transport properties of this type of materials. The method uses a sample of a well-defined geometry, in this case a right cylinder, and a computer program (DiSol) was developed to model the desorption process and extract diffusivity and solubility from the measured outgassing curve. To demonstrate the viability of the method, helium transport in a high-density polyethylene (HDPE) cylinder was measured, and the results obtained compared well with the published diffusivity and solubility values. The details of the method and the HDPE data obtained in this study will be presented.

4:00pm VT-MoA7 Report on Workshop on Measurement Characteristics and Use of Quadrupole Mass Spectrometers for Vacuum Applications, K. Jousten, Physikalisch Technische Bundesanstalt, Germany, J. Šetina, Institute of Metals and Technology, Slovenia, R. Ellefson, REVac Consulting

The ISO Technical Committee (TC) 112 is responsible for international standards in the field of vacuum technology. Supporting TC112 are three working groups (WG): WG1 is responsible for vacuum pumps, WG 2 for vacuum instrumentation and WG 3 for vacuum hardware. Hence, the WG 2 is responsible for total and partial pressure measurement in vacuum. In 2006, WG 2 began a project towards standardization for the specification and calibration of quadrupole mass spectrometers (QMS). A new ISO (Draft) standard 14291 "Definitions and specifications for quadrupole mass spectrometers" will be published in 2012. Additionally WG 2 is working on documenting the proper use of a QMS and establish a standard for meaningful calibration procedures. In support of this ISO goal, the European Metrology Research Programme has established a project IND12 "Vacuum metrology for production environments" to open new measurement capabilities for vacuum and to help industry to characterize vacuum in industrial environments.

One of the focuses of this IND12 effort is to address traceability to national measurement standards for partial pressure measurements and outgassing rate measurements for materials characterization in industry. To gather current status on such methods, a workshop on calibration of the QMS for industrial use was held in Bled, Slovenia. Quadrupole mass spectrometers are widely used to measure partial pressures in vacuum although the performance and accuracy of these measurements is the subject of ongoing discussion among users. The wide range of partial pressure measurement needed from UHV/XHV (10⁻¹⁰ Pa) to 1 Pa emphasizes that one type of QMS does not address all applications. From presentations at this workshop, application-specific data on performance of QMS types gives guidance for selection of a QMS type for an application. Talks were given on setup and ion source operation recommendations; initial calibration methods for an application and *in situ* calibration methods for verification or recalibration of a QMS during use. The fact that QMS electron energies differ by application and manufacturer leads to the requirement that gas species calibration is needed for each QMS for accurate partial pressure or compositional analysis. Papers on the electron-ion space charge at pressures > 10⁻⁴ Pa in ion sources were given together with gas interference where addition of a partial pressure of a new chemical species B gives a different ion current output for species A (when A is known to be at its original partial pressure). Results of these talks at the workshop will be summarized in this presentation.

4:20pm VT-MoA8 Mass Spectrometry a Mile Deep: Issues and Solutions for Underwater Vacuum Systems, R.T. Short, SRI International INVITED

There are numerous advantages to performing in situ chemical analyses in the field rather than collecting samples for laboratory analysis. These include reducing the possibility for sample contamination or degradation, significantly improving the spatial and temporal resolution of analyses, and providing the ability to implement adaptive sampling strategies by receiving the analytical information in real-time or near real-time. Many analytical instruments, such as mass spectrometers (MSs), require high vacuum for operation. Vacuum systems for these portable instruments must be reasonably small, low-power, and often more rugged than needed for laboratory operation. Underwater instruments of this type have the additional requirements that the vacuum systems must be self-contained (or exhaust to a high-pressure environment) and the sampling interfaces must withstand pressure differentials greater than 1 atmosphere – hydrostatic pressure increases by approximately 1 bar for every 10 m depth in the ocean. Consequently, all of these constraints must be taken into account when selecting or building vacuum systems for these applications.

Several groups around the world have been working on developing and using underwater MSs for in situ chemical measurements in oceans, lakes, and rivers – at times over a mile deep. To date, all of these operational underwater MSs have employed membrane-inlet interfaces to introduce analytes into the vacuum of the MS. Analytes that are soluble in the membrane material (typically polydimethylsiloxane or Teflon) permeate

through the membrane and evaporate into the ion source of the MS, where they are ionized by an electron impact source. For operation at depth, the membrane must be supported by a porous frit to withstand the increased hydrostatic pressure. Membrane inlet MSs are very effective at detecting and quantifying dissolved gases, light hydrocarbons, and volatile organic compounds, often at trace levels.

Design considerations for underwater MSs will be discussed in this presentation, along with examples of specific components chosen for the vacuum systems. In particular, the focus will be on problems with operating vacuum systems under these often extreme and harsh conditions, along with solutions to mitigate these problems. In addition, we will present examples of deployments of underwater MSs for a variety of applications on a number of unmanned deployment platforms.

5:00pm VT-MoA10 Performance Optimization for Autoresonant Ion Trap Mass Spectrometers, G.A. Brucker, J. Rathbone, B. Horvath, Brooks Automation, Inc., Granville-Phillips Products

A new generation of residual gas analyzers based on autoresonant ion trap mass spectrometry (ARTMS) technology has recently become commercially available and is rapidly gaining market acceptance for vacuum processing applications. Recent investigations into this novel ion trap technology have focused on a detailed understanding of the role of ion generation and storage on the mass spectrometer's performance. The rate of ion formation, the initial energetics of the ions stored inside the trap, the shape of the electrostatic trapping potential and the characteristics of the radiofrequency signal sweep used to eject the ions all have a significant impact on the performance of an ART MS instrument. Unit-to-unit variations in ion formation rates and energetics due to mechanical assembly tolerances, can lead to slight variations in ion trap performance which can be easily corrected through adjustment of the electron beam focusing optics and the shape of the electrostatic trapping potential. This presentation describes a straight forward methodology that has been developed in our research laboratory to manually optimize ion trap performance during routine measurements and also an automated tuning procedure (Auto-Tune) that is built into the control software and can be used to restore trap performance each time an ART MS sensor is fitted with a new filament assembly.

5:20pm VT-MoA11 Differential Pumping Method for a Fast Partial Pressure Analyzer of Recent Design to Extend its Upper Pressure Limit Up to the Torr Range, P.C. Arnold, T.C. Swinney, Brooks Automation, Inc., Granville-Phillips Products

The upper pressure limit of a partial pressure analyzer (PPA) was extended by differential pumping so that gas composition of process pressures are evaluated. The selection of orifice size for differential pumping, first by calculation, then by empirical data, is presented. The range of a linear relation for reduced total pressure vs. process pressures in the millitorr range for several gases is presented. The validity for scans of multiple gas species for 0 – 130 amu was also evaluated by testing, comparing scans in the high pressure region to those in the reduced pressure region. The application of this method for an autoresonant ion trap will be presented for the first time in this pressure reduction protocol as it provides measurement of fast transients at these higher pressures. Trade-offs for orifice sizes and pressure reduction ratios will be discussed. The test set-up as it relates to the AVS Recommended Practices and the conclusions for pressure ranges that it provides will be given.

Tuesday Morning, October 30, 2012

Actinides and Rare Earths Focus Topic

Room: 6 - Session AC+EN-TuM

Energetic Materials Issues for Nuclear Power: Fuels, Corrosion and Waste Disposal

Moderator: J.G. Tobin, Lawrence Livermore National Laboratory

8:00am AC+EN-TuM1 Novel Concepts for Enhanced Metallic Nuclear Fuel Performance, *J.R. Kennedy, R.D. Mariani, D.L. Porter, S.L. Hayes, H.J.M. Chichester*, Idaho National Laboratory, *A.E. Wright, Y.S. Kim, A.M. Yacout, G.L. Hofman*, Argonne National Laboratory, *R.P. Omborg, D.J. Senior*, Pacific Northwest National Laboratory

INVITED

The Advanced Fuels Campaign of the Fuel Cycle Research and Development (FCRD) program of the Office of Nuclear Energy (DOE/NE) is charged with the mission to develop and qualify fuel forms that can be used 1) to close the nuclear fuel cycle, 2) to increase fuel performance in reactor, and 3) to be accident tolerant. In the first case, metallic fuels composed of (U,Pu,Np,Am)Zr alloys are being developed with the intention to transmute the transuranic isotopes in fast spectrum reactors. In the second case, increasing fuel performance, fuel forms are being developed that may, for example, allow higher levels of burnup in either fast spectrum or thermal spectrum reactors (lightwater reactors - LWR). In the final case, fuel forms that have an inherently higher level of tolerance to off-normal conditions are being developed in response to the Fukushima Daiichi accident. A number of innovative concepts will be presented with respect to the above including decreased fuel smear densities, annular fuel forms, cladding coatings or liners to prevent fuel-cladding chemical interactions, gas vented fuel pin designs, advanced fabrication methods such as fuel-clad co-extrusion, U-Mo based fuel alloys, and, of particular interest to this session's topical area, targeted fuel alloy additions into the actinide fuel composition that will sequester rare earth fission product migration to the fuel-cladding interface. Rare earth fission products have been implicated in enhancing detrimental fuel-cladding chemical interactions. These fuel development activities are a collaboration of Idaho National Laboratory with Argonne National Laboratory and with Pacific Northwest National Laboratory.

8:40am AC+EN-TuM3 Low Temperature Oxidation of Plutonium: A Mott-Cabrera Mechanism, *P. Rousset*, AWE, UK, *A.J. Nelson*, Lawrence Livermore National Laboratory

INVITED

X-ray photoelectron spectroscopy was used to study the oxidation of d-stabilized plutonium between 190K and 300K. The gas-solid reaction on this highly reactive surface depends on the surface energy, electronic structure and temperature along with radiological dissociation of the O₂ molecule. The initial oxidation of sputter cleaned Pu metal by O₂ forms Pu₂O₃ followed by formation of PuO₂ on the Pu₂O₃ surface. Angle-resolved measurements indicate that the PuO₂ layer thickness is limited to 1.2 nm after continued O₂ dosing at the lower temperatures. These results suggest the Mott-Cabrera mechanism of oxidation at low temperature where the rate limiting step is the diffusion of O⁻ anions through the oxide film to the oxide/Pu interface increasing only the thickness of the Pu₂O₃ layer.

This work was performed under the auspices of the U.S. Dept. of Energy by Lawrence Livermore National Laboratory under Contract DE-AC52-07NA27344.

9:40am AC+EN-TuM6 The Sputtering Yields of Depleted Uranium and Uranium Carbide Bombarded and Alloyed by Either 30 keV Gallium or 16 keV Cesium Ions, *W.J. Siekhaus, N.E. Teslich, P.K. Weber*, Lawrence Livermore National Laboratory

A sample of depleted uranium was abraded with 1200 grid SiC paper and subsequently polished with 3µm and 1µm diamond to a mirror finish. Areas 20µm x 20µm wide that included uranium carbide inclusions were ion-etched with 30 keV Gallium ions with a current of 2.8 nA, for up to 5 minutes. The depths of the "craters" thus generated were measured by electron microscopy and by profilometry and the ratio of the number of uranium atoms removed and the ion fluence was used to determine the sputtering yield for both uranium and uranium carbide.

We show the results in SEM images of sputtered areas and depth measurements on "craters" that include uranium carbide inclusions.

The same procedure was used to determine the sputtering yield of 16keV Cesium ions bombarding uranium. At their respective energies the depth of penetration of Gallium and Cesium (109Å and 50Å, respectively, as calculated by the TRIM[1] code) is much smaller than the crater depths.

The measured depth increases represent therefore the sputtering yields of the Uranium-Gallium and Uranium-Cesium alloys created by ion implantation, since sputtered atoms originate almost exclusively from the first atomic layers of the substrate[2]. Comparison of the measured sputtering yields with those of pure U using Matsunami's equation[3] demonstrates the effect of alloying on sputtering yield.

This work performed under the auspices of the U.S. Department of Energy by Lawrence Livermore National Laboratory under Contract DE-AC52-07NA27344.

[1] Sputtering by Particle Bombardment. Behrisch, R. Ed. Springer Verlag GmbH., 2007.

[2] Burnett, J.W. et al., Journal of Vac. Science & Technology A., **6**, 3, 2064-2068, 1988.

[3] Matsunami, N. et al., Atomic Data and Nuclear Data Tables, **31**, 1-80, 1984.

10:40am AC+EN-TuM9 Actinide Subsurface Chemistry in Waste Isolated Pilot Plant, Recent Development, *M. Borkowski, J.-F. Lucchini, M.K. Richmann, D.T. Reed*, Los Alamos National Laboratory

Waste Isolation Pilot Plant (WIPP) is designed to permanently dispose radioactive waste generated by the US defense program. Waste is placed in a salt bed 2150 feet below the ground level. During the regulatory time repository may be filled with brine and interaction of brine components with actinide is objective of the Actinide Chemistry Repository Science Program. One of the brine components is borate (up to ~160 mM), present in the brine by the dissolution of Borax mineral. Borate chemistry especially in basic media is still unknown and in this study the interesting borate speciation in the basic media is presented. Recently it was reported that neodymium, analog for trivalent actinides, is complexed by tetraborate ion with log K ~4 and that plutonium forms a stronger complex than that of neodymium. Also neptunium (V) forms complexes with borate and spectrophotometric evidence will be presented. Further investigations of borate chemistry and borate complexing properties are also discussed. Complexation power of different polyborate forms may be different. Some are able to form a covalent bond but other forms can only attract cation by a weak electrostatic interaction. Borate provides a wide range of pH buffering capacity from 6 to 12.

11:00am AC+EN-TuM10 XPS Study of Uranium Oxides with Various Precipitating Agents, *K.S. Holliday*, Lawrence Livermore National Laboratory, *J. Plaue*, University of Nevada, Las Vegas, *W.J. Siekhaus, A.J. Nelson*, Lawrence Livermore National Laboratory

X-ray photoemission spectroscopy (XPS) and Auger electron spectroscopy (AES) are powerful tools for materials characterization by determining chemical shifts in core level spectra. By combining XPS data with the X-ray excited Auger transitions one is able to have a two dimensional analysis based on both initial state effects and final state relaxation energies. Specifically, combining the chemical shift of the U NOV Auger lines with the chemical shift of the U 4f photoelectron lines defines the Auger parameter (difference in the binding energy of the photoelectron and Auger lines) and results in a reliable method for determining oxidation states independent of calibration. Here, XPS analysis of core-level excitation and X-ray excited Auger transitions were combined to determine the Auger parameter and produce chemical state (or Wagner) plots for various uranium and thorium compounds. In addition this method is combined with valence band spectra to characterize uranium oxides precipitated with different reagents. The calcination of these precipitates is followed at various temperatures in an effort to identify unique characteristics associated with the precipitating reagent.

Applied Surface Science

Room: 20 - Session AS+BI-TuM

Practical Surface Analysis

Moderator: A. Belu, Medtronic, Inc., D.L. Pugmire, Los Alamos National Laboratory

8:00am AS+BI-TuM1 Clinical Application of Surface Analysis Technologies - Needs, Requirements and Challenges, *J. Schnekenburger*, Muenster University, Germany

INVITED

Surface analysis technologies offer tremendous applications in clinical fields. The interface of cells and materials is a crucial determinant for

implant integration, artificial organ regeneration and stem cell differentiation. Cells are highly sensitive not only to chemical but also to structural determinants of their environment. Material softness, roughness and distance of adhesion points are known factors for adhesion, differentiation and the maintenance of cell function. The characterization of cell environments and surfaces for advanced cell culture by surface analysis technologies is a key element of the successful generation of bioimplantable materials and tissue regeneration.

Dental implants and liver regeneration are high impact examples for surface analysis needs. Dental implants should have a structure and chemical composition which facilitates osteoblast adhesion and bone development but impairs microbial growth and adhesion. Different implants were characterized and cell adhesion presented. The regeneration of functional liver cells from mesenchymal stem cells would allow the replacement of donor organs by cell implants. Stem cell differentiation not only requires genetic reprogramming and soluble factors but also a three dimensional environment with key elements of mature hepatocyte surrounding. These surface structures need to be identified and transferred in tissue culture dishes.

The analysis of cells and tissues as materials is challenging. The clinical environment requires technology application processes different from material science. Clinical routine analysis is cost driven and performed by technicians or MDs without deeper technical training. Expert personnel are available only in high throughput clinical centers. Also research is based on understanding the molecular determinants like DNA and proteins rather than material aspects. Furthermore cells and tissues need preparation since biological material can not be measured in high vacuum. The preparation like chemical fixation limits the analysis to specific time points of biological processes and may alter the samples compared to the original state. The combination of technologies like mass spectrometry or scanning electron microscopy with atomic force microscopy or digital holography allows the analysis of preparation artifacts and the generation of reliable data.

Overcoming the current restrictions surface analysis technologies have the potential to replace the biomedical gold standard light microscopy and fluorescence microscopy in the high resolution and three dimensional structural and chemical analysis of biological samples.

8:40am AS+BI-TuM3 The Application of XPS to the Study of Protein Lyophilizates, S.J. Coultas, J.D.P. Counsell, A.J. Roberts, S.J. Hutton, C.J. Blomfield, Kratos Analytical Ltd, UK, R. Geidobler, G. Winter, Ludwig-Maximilians-University, Germany

Long term storage of proteins is most often achieved by freeze drying (lyophilization). For this to be successful it is essential that the process retains the stability and biological activity of the protein. Despite its widespread use there are still problems associated with the process, not least the aggregation of the protein at the ice/liquid interface which develops during the freezing stage. To overcome this problem excipients are commonly used to ease the stresses at this interface and stabilise the protein. Polysorbates are commonly used for this purpose but there has been recent interest in using other excipients.

X-ray photoelectron spectroscopy (XPS) is ideally suited to the study of these materials due to its surface sensitivity (1-10 nm) and the quantitative nature of the data.

In this study we use XPS to investigate the protein stabilisation mechanism in lyophilizates produced using different excipients. We show there to be clear differences in the surface chemistry of the resultant lyophilizates. We also investigate the effect of temperature on the protein surface chemistry and stability.

9:00am AS+BI-TuM4 Characterization of Real-World Surfaces and Interfaces of Devices in the Biomedical Industry, W. Theilacker, A. Belu, L. Lohstreter, L. LaGoo, Corporate Technology and Innovation, Medtronic, Inc.

This presentation will highlight the use of surface analysis methods for the characterization of medical devices. Examples will be presented to demonstrate a range of practical applications in solving industrial problems. A multi-technique approach is used to better understand issues of cleanliness, adhesion, and intentional surface modification with regards to pacemakers, leads, and other cardiovascular devices. Oftentimes the samples provided are non-ideal for surface sensitive techniques, e.g. they are large, non-flat, and have been handled, or have been in contact with other materials. This presentation will also address approaches for characterization of real-world, non-ideal samples. The surface is an important zone as it is the interface between a material of interest and its environment. Knowledge of interface chemistry is critical for understanding how a biomaterial or drug delivery system will interact with the biological environment of the body. For other materials, particularly those that are employed in the manufacture of medical devices, evaluation of the surface

is important to further understand issues with welding, adhesion, contamination, discoloration, etc. Many techniques may be utilized in order to gain a comprehensive understanding of surface morphology and chemistry, including traditional techniques such as SEM-EDS (scanning electron microscopy energy dispersive spectroscopy), IR (infrared) spectroscopy, along with other techniques such as confocal Raman microscopy, interferometry, ellipsometry, XPS (x-ray photoelectron spectroscopy), and TOF-SIMS (time-of-flight secondary ion mass spectrometry). A comparison of the techniques will be made to help elucidate which method or methods are best for specific problems. Further, the power of and the problems with data acquisition and interpretation will be highlighted with regards to each technique.

9:20am AS+BI-TuM5 Ageing Processes Occurring on Nanoscaled Aminated Surfaces as Observed by ToF-SIMS/PCA, NEXAFS Spectroscopy and XPS, W.E.S. Unger, BAM Federal Inst. for Materials Res. and Testing, Germany, H. Min, BAM Federal Inst. for Materials Res. and Testing and KAIST Korea, S. Swaraj, BAM Federal Inst. for Materials Res. and Testing and Soleil Synchrotron France, P.-L. Girard-Lauriault, BAM Federal Inst. for Materials Res. and Testing and McGill Univ. Toronto, A. Lippitz, BAM Federal Inst. for Materials Res. and Testing, Germany

Ulthran organic surfaces covered by amines as coupling sites are often used in recent technologies as biosensing, adhesion in composite materials and layer-by-layer deposition of nano structures on self-assembled monolayer platforms. Ageing processes occurring with those aminated surfaces have to be regularly controlled in order to guarantee their functionality in applications.

We used a combined XPS, NEXAFS spectroscopy and ToF-SIMS/PCA approach to follow ageing of different kinds of amino-terminated surfaces stored on ambient air up to ~1 year. Test samples have been prepared as (1) aliphatic and aromatic aminosilanes on glass slides, (2) aminothiols prepared as self assembled monolayers and (3) by different plasma polymerization technologies (low pressure and atmospheric pressure DBD plasma polymerization).

The observation common to all investigated films is that the ageing process ends with a formation of amides which has been clearly proven by NEXAFS N K-edge spectra and PCA of ToF-SIMS data. However the kinetics of the ageing processes, the decay of amines, has been found to be rather different for the different kinds of samples investigated. The susceptibility of plasma deposited films is much higher due to the radicals inherently produced by the deposition technique. Furthermore storage conditions have been found at which the decay of amines in course of ageing can be suppressed to some extent.

9:40am AS+BI-TuM6 Signature Discovery in Explosives and Bioagents using Imaging Mass Spectrometry, C.M. Mahoney, Pacific Northwest National Laboratory

Recent terrorist attacks, both in the US and abroad, have indicated that significant improvements in intelligence operations are required for adequate prevention and prosecution of terrorist acts. This includes the ability to accurately and rapidly attribute pre-detonated and post-detonated explosive devices and/or other weapons-based material to a particular source, and/or region of the world. Surface mass spectrometry methods have the potential to greatly advance the field of forensics science, allowing for simultaneous elemental, isotopic and molecular imaging on a sub-micron to nano-scale range, with superior chemical specificity and sensitivity. With recent advancements in the field of surface mass spectrometry, the versatility of these methods has increased dramatically, allowing for the direct analysis of samples at atmospheric pressure (e.g. Desorption ElectroSpray Ionization or DESI). The potential for 3-D molecular analysis in soft samples with depth resolutions on the order of 5 nm has also been realized with advent of the gas cluster ion beam (GCIB) source. Finally substantial improvements in the mass resolving power (by at least a factor of 10) has been observed when employing FT-MS mass spectrometers, allowing for even greater improvements in the chemical specificity. Here we describe our efforts to develop a suite of advanced mass spectral analysis and imaging techniques for the characterization and attribution of plastic explosives and other complex explosive mixtures from around the world. We will also provide initial feasibility studies for the characterization and differentiation of biological agents based on their unique molecular fingerprints. With the development of these very powerful "chemical signature microscopes" it is expected that significant advancements will be made in the field of forensics, both on the home front, and abroad.

10:40am **AS+BI-TuM9 Topography and Field Effects in the Inner Side of Micro via Hole using ToF-SIMS**, *J.C. Lee, Y.K. Kyoung, I.Y. Song*, Samsung Advanced Institute of Technology, Republic of Korea, *S. Iida*, Ulvac Phi, Japan

Surface topography is often important role in the functionality and activity of electronic devices including MEMS, composite materials, catalysts, sensors, biomedical, and packaging of semiconductor devices. Especially, trench structure such as via hole or etched pattern is one of the important processes in the through silicon via or ball grid array. If there is contaminated on the wall or bottom of via hole, it may cause contact failure between integrated circuits and printed circuit board (PCB) because of increasing contact resistance. For the recent decade, many research activities are focused on the quantitative analyses of topographic samples using TOF-SIMS. However, the most of results were focused on the nanowire, nano particle, and etched surface, it is relatively rarely dealt with the trench shape sample. It is not easy to characterize the contaminant level of ~ppm or less on the bottom of trench shape sample such as via hole. It is well known that a ToF-SIMS is one of powerful tools to analyze organic contaminants. However there are some limitations to apply it to the trench shape sample because of high sample bias voltage and short focal length of emersion lens of ToF-SIMS analyzer. If we want to characterize contaminants on the bottom of via hole using a ToF-SIMS, the side wall of via hole should be removed by mechanical treatments. In this study, we aim to establish an optimized method that is able to characterize the bottom and wall of via hole of BGA using ToF-SIMS without any mechanical or chemical treatments. This is performed by combining ToF-SIMS experiments using via hole systems with computer modeling using SIMION.

For this study, trench structure samples with the diameter of 90 μ m and width of 90 μ m were used for TOF-SIMS imaging. Via holes were fabricated by laser drilling method. Samples were mounted on the sample holders which were specially designed with tilted angles of 15, 28, and 40 degrees surfaces for this experiment. Secondary ion trajectory and potential contour were calculated using SIMION for 0, 15, 28, 40 degree tilted samples for understanding the angle dependence of field effects.

According to the simulation results, secondary ions ejected from near corner between wall and bottom of via hole are aimed to diagonal direction due to Coulomb repulsive force between secondary ions and wall of via hole. When specially designed 40 degree tilted angle sample holder which is based on simulation result is used, the bottom and wall of via hole of BGA can be fully characterized using ToF-SIMS without any mechanical treatment.

11:00am **AS+BI-TuM10 Using XPS to Probe the Surface Chemistry of Ionic Liquids**, *J.D.P. Counsell, S.J. Coultas, A.J. Roberts, S.J. Hutton, C.J. Blomfield*, Kratos Analytical Ltd., UK

Ionic liquids have attracted much attention due to their possible "green chemistry" applications. Due to the recent use of ionic liquids as corrosion resistant thin-films, it has become important to fully understand the complex nature of their surface environments.

A series of commercially available ionic liquids (e.g. [BMIM][PF₆]) were studied and characterised using x-ray photoelectron spectroscopy. Angle-resolved experiments indicate an increased concentration of the organic cation in the liquid's surface. The surface composition becomes enriched with contributions from the linear alkyl substituent of the cation which is significantly greater than that expected from the nominal stoichiometry. A maximum entropy method algorithm was used to build an accurate structure of the surface and near-surface region

We also explore the possibilities of using ionic liquids as potential new reference standards. They present the opportunity to offer a clean reference surface without the need for ion sputtering and present a number of core level peaks for spectrometer energy scale and transmission function calibration and validation.

11:20am **AS+BI-TuM11 XPS Profiling and Work Function Mapping of a Damaged Solar Cell**, *B. Strohmaier*, Thermo Fisher Scientific, *P. Mack, T.S. Nunney, J. Wolstenholme*, Thermo Fisher Scientific, UK

In many areas of materials technology, it is important to control both the chemical composition and the electrical properties of the material. One example of this need is in the manufacturing of solar cells. In this case, the solar cell is based on a thin film of CIGS (Cu (In, Ga) Se₂). The full structure of the device includes an upper electrode containing indium tin oxide (ITO), zinc oxide, and cadmium sulfide. The whole structure is separated from a steel substrate using layers of molybdenum and chromium.

It has been demonstrated previously that X-ray Photoelectron Spectroscopy (XPS) is the ideal technique for characterizing the compositional depth profiles of CIGS solar cells, similar to the one described above. Using XPS it is possible to measure elemental composition gradients in the CIGS layers

(allowing engineers to tune the band gap of the device) and also to investigate chemistry at interfacial layers. XPS can also be used to measure another very important parameter of solar cells, i.e. the work function. This measurement relies upon the spectrometer being accurately calibrated and the photon energy being accurately known. On a modern XPS instrument, internal standard samples (copper, silver, and gold) may be used to automatically calibrate the XPS binding energy scale. The photon energy can be checked by measuring the position of an X-ray induced Auger peak on the binding energy scale and adding it to the known kinetic energy for that peak in the Auger spectrum.

This work demonstrates the use of XPS to characterize a damaged solar cell, using depth profiling to identify the delamination zone in the solar cell stack. The surface of the delaminated cell has also been mapped for elemental and work function information.

11:40am **AS+BI-TuM12 Application of XPS Imaging Analysis in Understanding of Interfacial Delamination and Related Problems**, *H. Piao*, General Electric Global Research Center, *N. Fairley*, Casa Software Ltd, UK, *J. Walton*, The University of Manchester, UK

The recent development of X-ray Photoelectron Spectroscopy (XPS) instrumentation with near-micron spatial resolution has advanced the capability of elemental and chemical state imaging. This work extends the application of imaging XPS to the analysis of real world samples. The presentation also focuses on description of radiation damage of polymers encountered in XPS imaging analysis. The imaging analysis can cause extensive damage to polymers since the acquisition time for creating datasets can be excessive. Understanding of radiation damage in polymers is necessary for successful and validated application of XPS spectromicroscopy.

Keywords: XPS, chemical states, imaging, delamination.

Biomaterial Interfaces

Room: 23 - Session BI+SS+AS-TuM

Biomolecules at Interfaces

Moderator: P. Kingshott, Swinburne University of Technology, Australia

8:20am **BI+SS+AS-TuM2 Computer Simulation of Water-Mediated Adhesion between Organic Surfaces**, *A.J. Pertsin, M.H. Grunze*, University of Heidelberg, Germany

The adhesive forces operating between various surfaces in aqueous media are of interest in many areas ranging from biology to electronics. This refers, in particular, to surfaces formed by self-assembled monolayers (SAMs) on solid substrates to modify the surface-sensitive properties of the latter. Another important example is provided by supported lipid bilayers, where the water-mediated bilayer-substrate adhesion determines the stability of the system. The present study is concerned with surfaces formed by a hydrophobic methyl-terminated SAM (C-SAM), a hydrophilic carboxyl-terminated SAM (hereafter, O-SAM), and a phosphatidylethanolamine (PE) bilayer. The surface-water-surface system was treated as an open one using the grand canonical Monte Carlo technique. The free energies of adhesion were evaluated by integration of simulated pressure-distance relations. For SAMs, both symmetric and asymmetric confinements were considered, as formed by like and unlike SAMs, respectively. As the confinement was increased, water confined by the C-SAMs experienced capillary evaporation. As a consequence, the adhesion energy was mainly determined by the direct interaction between bare C-SAMs. In the asymmetric SAM system, an incomplete capillary evaporation was observed, with the number of water molecules dropped by more than an order of magnitude. The remaining water molecules were all adsorbed on the O-SAM, while the C-SAM was separated from the rest of the system by a thin vapor layer. The calculated free energies of adhesion were in acceptable agreement with available experimental data. Unlike the SAM systems involving the hydrophobic C-SAM, the PE/water/C-SAM system did not experience capillary evaporation up to the highest confinements tried. A likely reason is a high molecular-level "roughness" of the PE/water interface due to a deep penetration of water in the PE bilayer. The pressure-distance dependence showed a slightly repulsive region with a depth comparable with the statistical uncertainty in pressure. By contrast, the pressure-distance curve of the PE/water/O-SAM system showed a well-defined minimum with a depth of about 0.7 kbar. The integration of this curve resulted in an adhesion free energy of 19 \pm 3 mJ/m², close to the value obtained for the O-SAM/water/O-SAM and O-SAM/water/C-SAM systems (~25 mJ/m²).

8:40am **BI+SS+AS-TuM3 Adsorption from Saliva - Properties of Adsorbed Layers and Comparison with Other Systems**, *T. Arnebrant, L. Lindh, J. Sotres*, Malmö University, Sweden **INVITED**

Adsorbed salivary protein layers will cover soft and hard surfaces in the oral cavity, where they fulfill a protective function influencing adhesion and wear, and also surfaces of devices exposed to saliva. Properties of salivary films will depend on the characteristics of the surface on which they are formed as well as solution conditions (salt, pH) and will affect surface properties such as wettability and charge. Moreover, normal and lateral forces between surfaces bearing salivary films will be distinctly different than for bare surfaces. Such changes in surface properties and interactions may be relevant not only for events at oral interfaces but also for the operation of monitoring or sampling devices immersed in or exposed to saliva. Here, we show how a combined characterisation of these systems through different surface techniques provides important information on the role of this body fluid which is not available through more common chemical or biochemical approaches. The presentation will describe adsorption characteristics of salivary proteins from the total secretion as well as for purified fractions including single protein preparations. Influence by surface properties and ambient (solution) conditions will be outlined. Data on structure of salivary films as obtained by *in situ* ellipsometry, QCM-D and neutron reflectivity will be reported. Furthermore, SFA and AFM measurements of DLVO, steric, adhesive and frictional forces between surfaces bearing salivary films will be discussed. A new method for estimating the strength of salivary films based on simultaneous recording of roughness and friction data from AFM will also be described.

References: Protein Adsorption in the Oral Environment, Arnebrant T, In Biopolymers at Interfaces 2nd ed. (M. Malmsten Ed.) Marcel Dekker, 2003, pp 811-856

Friction force spectroscopy as a Tool to Study the Strength and Structure of Salivary Films. Sotres J., Liselott L., Arnebrant T. 2011. *Langmuir*, 27 (2011), 13692-13700.

9:20am **BI+SS+AS-TuM5 An Atomic Force Microscopy Based Method for the Determination of Protein Stability**, *O. Croad*, University of Nottingham, UK, *S. Rigby-Singleton*, Molecular Profiles Ltd., UK, *C.J. Roberts, D.J. Scott, P.M. Williams, S. Allen*, University of Nottingham, UK

A method for the early detection of instability and aggregation propensity of proteins and other biological macromolecules would be valuable for the rapid development of novel biopharmaceutical formulations. The aim of this study was to investigate the potential of atomic force microscopy (AFM) based adhesion force measurements to meet this need. We report the first key step in demonstrating this approach; a clear relationship between how frequently an AFM probe adheres to a protein coated surface and the fraction of unfolded proteins on that surface. Instability and subsequently protein denaturation are commonly linked with protein aggregation, and hence formulation failure. It was found that for the protein bovine serum albumin (BSA), the adhesion between AFM tips and protein-coated samples occurred much more frequently as either the concentration of a denaturant or temperature was gradually increased. We compared this behaviour with fluorescence based studies of the BSA unfolding in solution. Both methods provided us with almost identical ΔG values of stability and 50% unfolding ($[D]^{50\%}$) values. The data demonstrates for the first time, an AFM based method for protein stability determination. Interestingly, the method also appears to be a good reporter of the protein solution behaviour. With further development this approach could be utilized to screen for instability and aggregation propensity of a given protein therapeutic, in a range of conditions. The ultimate aim is to create a robust technique that can be performed rapidly and routinely.

9:40am **BI+SS+AS-TuM6 Von Willebrand Factor A1 Domain Structure and Function Changes on Surfaces**, *E. Tronic, W. Thomas, D.G. Castner*, University of Washington

The clotting protein von Willebrand Factor (VWF) binds to platelet receptor glycoprotein 1ba (GP1ba) when VWF is activated, such as when VWF is exposed to a surface or is under high shear. However, the mechanism of surface activation is not known. This study characterizes function and adsorption behavior of the VWF A1 domain, which contains the GP1ba binding site. Surfaces tested are glass, polystyrene, and tissue culture polystyrene. Highest VWF A1- GP1ba binding is observed when A1 is adsorbed onto polystyrene, as measured by platelet rolling velocity in a parallel plate flow chamber assay. X-ray photoelectron spectroscopy (XPS) showed comparable A1 amounts are present on each surface, suggesting functional differences were not explained by differences in surface coverage. A1 surface structure was investigated using ELISA, time-of-flight secondary ion mass spectrometry (ToF-SIMS) and near-edge x-ray absorption fine structure (NEXAFS). Using monoclonal antibodies binding to a nonlinear epitope within A1, ELISA showed lower antibody binding

for A1 adsorbed to polystyrene than to glass or tissue culture polystyrene. ToF-SIMS was used to identify differences in amino acid exposure, and NEXAFS showed different amide backbone ordering on the three surfaces. These studies demonstrate that the surface dependence of A1 function is likely due to differences in adsorbed surface orientation and/or conformation. This is an important consideration in *in vitro* models, where A1 is typically immobilized onto synthetic surfaces, and is also of interest for blood-contacting biomaterials. Additional studies have been done on A1 and two A1 mutants adsorbed on collagen coated tissue culture polystyrene. One mutant exhibits similar ELISA and ToF-SIMS results to the wild type A1, while the other mutant exhibits differences. This indicates that mutations in A1 can affect the conformation/orientation changes that result from A1 adsorption onto collagen.

10:40am **BI+SS+AS-TuM9 Combining Catalysis and Self-Assembly: Towards Evolvable Soft Matter**, *R. Uljin*, University of Strathclyde, UK **INVITED**

Molecular networks are key to the adaptiveness of biological systems and it would be very useful if this concept could be introduced into simple man-made functional materials, which could adapt to changing environments. In biology, adaptiveness (as a consequence of evolution) is achieved through a combination of catalysis, self-assembly, molecular recognition and compartmentalisation. These individual molecular processes are closely linked, a situation which may be achieved in laboratory based systems by sharing of building blocks between these individual processes, thereby giving rise to networked systems that are highly responsive and adaptive to changing external conditions. We have made the first steps towards developing evolvable materials, and will present progress in (i) structure/function relationships in peptide self-assembly, (ii) development of catalytic peptides, (iii) self-selecting peptide libraries achieved by combining fully reversible amino acid exchange in self-assembling peptide systems. The overall aim of this area is to produce laboratory made molecular materials that incorporate the above features and are able to adapt and change their properties in response to external environmental changes. Potential applications in biomaterials science will be discussed.

11:20am **BI+SS+AS-TuM11 Bio/Nano Interfaces of De Novo Design: Small Proteins with Large Potential**, *M.G. Ryadnov*, National Physical Laboratory, UK

Our ability to manipulate function at interfaces in native and near-native environments is critical for the fabrication of nanostructured materials and devices. Biomolecular self-assembly lends itself to robust bio-nano systems. However, exact construction strategies to enable desired applications stumble upon the lack of control over self-assembly processes. De novo peptide design provides a saving solution to this.[1] Small proteins can be designed to deliver functions that are otherwise accessible only to macromolecular subcellular complexes. Examples include gene delivery systems,[2] fibrillar microscopic structures for tissue repair[3] and responsive antimicrobial agents[4]. A key factor in all such designs is their structural and functional relevance to native self-assembling structures, be these viruses, extracellular matrices or host defence systems. Thus, this is our ability to construct such materials at will that advances the development of efficient bio/nano-interface technologies.[5] **References** 1. Ryadnov, M. G. (2012) Prescriptive peptide design. In *Amino acids, peptide and proteins*. (Farkas, E. & Ryadnov, M. G., eds.) SPR, RSC Publishing (2012), v.37. 2. Lamarre, B., Ravi, J. & Ryadnov, M. G. (2011) GeT peptides: a single-domain approach to gene delivery. *Chem. Commun.*, 47, 9045-9047. 3. Bella, A., Ray, S., Shaw, M. & Ryadnov, M. G. (2012) Arbitrary self-assembly of peptide extracellular microscopic matrices. *Angew. Chem. Int. Ed.*, 51, 428-431. 4. Ryadnov, M. G., Mukamolova, G. V., Hawrani, A. S., Spencer, J. & Platt, R. (2009) RE-coil: an antimicrobial peptide regulator. *Angew. Chem. Int. Ed.* 48, 9676-9679. 5. Ryadnov, M. G. (2009) *Bionanodesign: Following the Nature's touch*. RSC Publishing, 250 pp.

11:40am **BI+SS+AS-TuM12 Application of CD and SRCD Techniques to the Study of Protein/Nanoparticle Complexes**, *G. Ceccone, S. Laera, L. Calzolari, D. Gilliland*, EC-JRC-IHCP, Italy, *R. Hussein, G. Siligardi*, Diamond Light Source, UK, *F. Rossi*, EC-JRC-IHCP, Italy

Nanotechnology is having a large impact in very different scientific fields and the use of nanotechnology-based materials is not just limited to research laboratories, but has already been applied in several industrial sectors and into real products as disparate as medical diagnostic tools, drug delivery systems, cosmetics, and consumer products.

In particular, engineered nanoparticles (ENPs) are used in different applications such as cosmetics, food and medicine and currently more than 600 products containing nanomaterials are already on the market[1,2,3]. At the same time there is a growing public concern about the safety of ENPs since it has been demonstrated that those intended for industrial and medical applications could cause adverse effects in mammals or aquatic

organisms by specific mechanisms depending on their physical chemical properties[4]. However, the interaction of nanomaterials with complex matrices is far to be understood. In fact, although it is now increasingly accepted that the surface of nanoparticles in a biological environment is modified by the so called "protein corona"[5,6], the importance of the detailed structure of the adsorbed protein-solution interfaces is still not much addressed in the nanotoxicology literature[7].

In this work, we report the use of Circular Dichroism (CD) and Synchrotron Radiation Circular Dichroism (SRCD) to detect changes in the secondary structure and stability of different classes of proteins interacting with nanoparticles. In particular, we show that by using the SRCD we can detect structural changes of proteins in the nanomolar concentration range when they form protein-nanoparticle complexes[8]. Furthermore, the adsorption of protein on NP modifies their melting point in a composition and size dependent manner, indicating once more that the protein corona formation is strongly depending on the nanoparticles physico-chemical properties. For instance, while the presence of Au NPs do not influence the thermal unfolding process of human serum albumin (HSA), a significant decrease of the HSA melting temperature (about 6°C) is observed in presence of Ag NPs.

-
- [1] R.A. Petros, J. M. DeSimone, *Nature Rev.*, **9**, (2010), 616.
 - [2] G.J. Noynek et al., *Crit. Rev. Toxicol.*, **37**, (2007), 251.
 - [3] N. Sozer, J.L. Kokini, *Trends in Biotechnol.*, **27(2)**, (2009), 82.
 - [4] G. Obersdorter et al., *Env. Health Persp.* **113**, (2005), 823
 - [5] I. Lynch, K. A. Dawson, *Nanotoday*, **3(1-2)**, (2008), 40
 - [6] M.P. Monopoli et al., *J. Am. Chem Soc.*, **133**, (2011), 2525
 - [7] P. Sabatino et al., *J. Coll Interface Sci.*, **314**, (2007), 389
 - [8] S. Laera et al., *Nano Lett.***11**, (2011), 4480.

Electronic Materials and Processing

Room: 9 - Session EM-TuM

Electrical Testing and Defects in III-V's

Moderator: E.M. Vogel, Georgia Institute of Technology,
E.X. Zhang, Vanderbilt University

8:00am EM-TuM1 Characterization, Modeling and Control of Fermi Level Pinning Phenomena at III-V High-k MOS Gate Stack Interfaces, H. Hasegawa, Hokkaido University and RIKEN, Japan **INVITED**

III-V high mobility channel materials are currently drawing attention as possible material candidates for devices to continue scaling of CMOS transistors on the Si platform. Here, construction of high performance high-k MOS gate stacks is the key issue. Such gate stacks are also needed for various gate controlled III-V nanowire and nanodot devices for "Beyond CMOS" applications.

The purpose of this paper is to review the present status of understanding and control of "Fermi level pinning (FLP)" phenomena at III-V metal-gate high-k gate stack interfaces whose atomic level control is vitally important for success of above approaches. FLP at the insulator-semiconductor (I-S) interface deteriorates efficiency and stability of gate control of carriers while FLP at the metal-insulator (M-S) interface deteriorates the control capability of the threshold voltage of the MOSFET.

First, various models on FLP at I-S and M-S interfaces are reviewed, paying attention to chemical trends of pinning at Schottky barriers and MOS capacitors formed on GaAs and other III-V materials. Extremely complicated C-V behavior of ALD high-k dielectric/GaAs MOS capacitors is explained by the authors' disorder induced gap state (DIGS) model [1] where a U-shaped donor-acceptor gap state continuum causes pinning. Importance of the location of the charge neutrality level (CNL) [2] is pointed out for channel material selection, showing superiority of InGaAs over GaAs and others.

Then, various efforts to remove FLP at III-V I-S interfaces by inserting interface passivation layers are reviewed. In particular, authors' efforts to realize pinning-free high-k MOS interfaces on GaAs and InGaAs, using the silicon interface control layer (Si ICL) are described. Here, the Si ICL is an MBE-grown ultrathin Si interlayer which is proposed first by the authors [2,3] and now extended to construction of high-k MOS gate stacks. The structure has been investigated by XPS, contactless C-V and STM/STS methods and by ex-situ PL and MOS C-V measurements [4-7].

Finally, the FLP issue at metal-high-k Schottky interfaces is briefly discussed.

- [1]H. Hasegawa and H. Ohno, *J. Vac. Sci. Technol.*, **B4**, 1130 (1986) [2]H. Hasegawa, M. Akazawa et al *J. Vac. Sci. Technol.* **B 7**, 870 (1989). [3]H. Hasegawa, M. Akazawa, et al *Jpn. J. Appl. Phys.*, **27**, L2265 (1988) [4]M. Akazawa and H. Hasegawa, *J. Vac. Sci. Technol.* **B25**, 1481(2007) [5]M. Akazawa and H. Hasegawa, *J. Vac. Sci. Technol.* **B26**, (2008)1569 [6]M. Akazawa, A.Domanowska, B. Adamowicz and H. Hasegawa, *J. Vac. Sci. Technol.* **B27**, 2028(2009) [7]M. Akazawa and H. Hasegawa, *Appl. Surf. Sci.*, **256**, 5708(2010)

8:40am EM-TuM3 An Investigation into the Origin of Anomalous Frequency Dispersion in Accumulation Capacitance of MOS Devices on III-V Substrates, R.V. Galatage, D.M. Zhernokletov, H. Dong, B. Brennan, C.L. Hinkle, R.M. Wallace, University of Texas at Dallas, E.M. Vogel, Georgia Institute of Technology

Anomalous frequency dispersion in accumulation is a commonly observed feature in experimental capacitance-voltage (C-V) characteristics of III-V metal-oxide-semiconductor (MOS) devices. Different models have been proposed to explain the origin of this frequency dispersion. One model attributes this dispersion to tunneling of the carriers into a disordered region caused by oxidation of the III-V substrate which is close to the interface between the III-V substrate and an insulator.^{1,2} Another model attributes this dispersion to border traps located inside the high-k dielectric.^{3,4} In this work, we use both HfO₂ and Al₂O₃ with several interface treatments to differentiate between these two models.

MOS capacitors are fabricated on As-decapped n-In_{0.53}G_{0.47}As and n-GaAs substrates with either atomic layer deposited (ALD) HfO₂ or Al₂O₃ dielectrics. An As-cap initially grown on the n-In_{0.53}G_{0.47}As surface to avoid spurious oxidation is thermally desorbed to leave a pristine surface. ALD HfO₂ and Al₂O₃ is then deposited onto substrates prepared with several conditions: (1) *in situ* on the oxide free surface, (2) *ex situ* with a 10% ammonium sulfide and immediate transfer to ALD (<3 min exposure to air), (3) *ex situ* with a 10% ammonium sulfide treatment and ~30 min exposure to air prior to ALD. Companion GaAs samples receive similar *ex situ* ammonium sulfide treatments, air exposure times and ALD dielectrics for comparison. A detailed analysis of the effect of the different disordered region thicknesses and different dielectrics on the accumulation frequency dispersion and interface trap density (D_{it}) distribution will be presented. Correlation of electrical results to X-ray photoelectron spectroscopy (XPS) analysis will also be presented.

This work is sponsored by SRC FCRP Materials Structures and Devices Center and the National Science Foundation under ECCS Award No. 0925844.

- [1] H. Hasegawa and T. Sawada, *IEEE Trans. Electron Devices* 27(6), 1055 (1980).
- [2] A. M. Sonnet, C. L. Hinkle, H. Dawei, G. Bersuker, and E. M. Vogel, *IEEE Trans. Electron Devices*, 57, 2599 (2010).
- [3] Y. Yuan, L. Q. Wang, B. Yu, B. H. Shin, J. Ahn, P. C. McIntyre, P. M. Asbeck, M. J. W. Rodwell, and Y. Taur, *IEEE Electron Device Lett.* 32 (4), 485 (2011).
- [4] E. J. Kim, L. Wang, P. M. Asbeck, K. C. Saraswat, and P. C. McIntyre, *Appl. Phys. Lett.* 96 (1), 012906 (2010).

9:00am EM-TuM4 Evaluation of Atomic Layer Deposited High-k Dielectrics on GaAs, H.J. Lim, Y.J. Choi, S.H. Lee, Seoul National University, Republic of Korea, J.H. Ku, N.I. Lee, Samsung Electronics Co. Ltd., Republic of Korea, H.J. Kim, Seoul National University, Republic of Korea

GaAs is a promising channel material for sub-20nm logic MOSFET due to high electron mobility. However the instability of its native oxide is considered to generate high density of interface states that can induce Fermi level pinning and frequency dispersion in capacitance-voltage (C-V) curve. Although a variety of dielectric materials have been investigated over the past 4 decades to improve interface properties, a few positive results have been reported: Ga₂O₃ (Gd₂O₃) grown by molecular beam epitaxy (MBE) and Al₂O₃ and HfO₂ grown by atomic layer deposition (ALD). In this study, n-type GaAs MOSCAP's were fabricated with ALD SiO₂, Al₂O₃, La₂O₃, and HfO₂, and measurements of C-V hysteresis, flatband voltage shift (ΔV_{fb}), and frequency dispersion were performed to investigate the dependence of electrical properties on dielectric materials and to find dielectrics suitable for a stable MOSCAP operation.

Only HfO₂ revealed good electrical characteristics with a C-V hysteresis of < 80 mV and ΔV_{fb} of 40 mV under constant stress time and voltage, while SiO₂, Al₂O₃, and La₂O₃ showed significantly degraded characteristics with a C-V hysteresis of > 700mV hysteresis and ΔV_{fb} of 200mV. But even though a single HfO₂ dielectric layer had good electrical characteristics, the stacked HfO₂/SiO₂ dielectric layer on GaAs showed the degraded characteristics like a single SiO₂ layer, indicating that the electrical characteristics were mainly dependent not on bulk properties but on the interface properties with

GaAs. X-ray photoelectron spectroscopy (XPS) analysis revealed that SiO₂, Al₂O₃, and La₂O₃ dielectrics produced more elemental As (As⁰) than HfO₂ did at the interface. In addition, for SiO₂, Al₂O₃ and La₂O₃ dielectrics, As were detected on the top surface of dielectrics by Auger electron spectroscopy (AES) measurement, implicating that the origin of degradation was related with the amount of elemental As, which might diffuse out and induce vacancy defects during subsequent annealing process, at the interface.

Frequency dispersion characteristics in a C-V measurement were also compared. HfO₂ showed huge frequency dispersion of about 280 % ($\Delta C_{1kHz-1MHz}/C_{1MHz}$) while SiO₂, Al₂O₃, and La₂O₃ resulted in the relatively small dispersion of about 50% unlike the C-V hysteresis tendency. However, HfO₂ on thin SiO₂ led to small dispersion similar to SiO₂. Frequency dispersion was strongly correlated with the interface state density (D_{it}). Therefore, we can conclude that both hysteresis and frequency dispersion in a C-V measurement are dependent on the interface properties of dielectrics, especially the amount of elemental As and Dit level, respectively.

9:20am EM-TuM5 High Energy XPS and Electrical Characterisation Studies of Metal Oxide Semiconductor Structures on Si, GaAs and InGaAs, G.J. Hughes, L.A. Walsh, Dublin City University, Ireland, P.K. Hurley, J.H. Lin, Tyndall National Laboratory, Ireland, J.C. Woicik, National Institute of Standards and Technology **INVITED**

In this work synchrotron radiation based hard x-ray photoelectron spectroscopy (HAXPES) measurements have been used to study the intrinsic electronic properties of high-k dielectric metal oxide semiconductor (MOS) structures on Si, GaAs and InGaAs substrates. The MOS structures were prepared with both high (Ni) and low (Al) workfunction metal layers 5nm thick on both n and p doped semiconductor substrates. CV and IV measurements were also performed on an identical sample set where the top metal contact was 160 nm thick to facilitate electrical measurements, and Ni was replaced with Ni/Au, 70/90 nm thick, respectively. The 4150 eV photon energy used in the HAXPES measurements gave a photoemission sampling depth of ~15 nm ensuring that signals were simultaneously detected from the substrate, the 8 nm thick dielectric layers as well as the top metal contact. The binding energy of core levels in photoemission are referenced with respect to the Fermi level, therefore changes in the binding energy of a particular core level reflect differences in the position of the Fermi level in the semiconductor band gap. For the MOS structures fabricated using SiO₂/Si, changes in the Fermi level positions and differences in the potential drops across the dielectric layers have been directly correlated with the metal workfunction differences observed in the CV and GV measurements. The MOS structures on ammonium sulphide passivated n (Si - 5x10¹⁷ cm⁻³) and p (Zn - 5x10¹⁷ cm⁻³) doped GaAs substrates were fabricated by the atomic layer deposition (ALD) of 8 nm thick Al₂O₃ dielectric layers. A binding energy difference of 0.6 eV was measured between the GaAs core levels of the n and p doped substrates, independent of metal work function indicating that the Al₂O₃/GaAs interface is strongly pinned. Lattice matched 0.2 μm thick In_{0.53}Ga_{0.47}As layers, with both n and p doping (~4x10¹⁷ cm⁻³), were grown by MOCVD on InP⁺ and p⁺ substrates, respectively. Al₂O₃ dielectric layers 8 nm thick were then deposited ex-situ by ALD on the native oxide and ammonium sulphide treated InGaAs surfaces. Binding energy measurements for the core levels of native oxide covered n-type doped InGaAs substrates with no metal cap were found to be consistently (~0.3 eV) higher than p-type samples reflecting the fact that the Fermi level is in a different position in the band gap. Deposition of the metals with different workfunctions resulted in limited movement of the Fermi level, indicating the partially pinned nature of the InGaAs/Al₂O₃ interface. Corresponding changes in the potential across the dielectric layer were also measured.

10:40am EM-TuM9 Metastable Centers and Localized States in AlGaN/AlN/GaN Heterostructures Studied by C-V, Admittance Spectroscopy, and DLTS, A.Y. Polyakov, N.B. Smirnov, A.V. Govorkov, E.A. Kozhukhova, Institute of Rare Metals, Russian Federation, S.J. Pearton, F. Ren, L. Lu, University of Florida, S.Y. Karpov, Soft-Impact, Ltd, Russian Federation, W. Lim, Samsung LED, Republic of Korea

A set of AlGaN/AlN/GaN high electron mobility transistor (HEMT) structures with Al composition in the AlGaN barrier changing from 20% Al to 50% Al was grown by metalorganic chemical vapor deposition (MOCVD) on sapphire and studied by means of capacitance-voltage C-V measurements, admittance spectroscopy, reverse deep levels transient spectroscopy. C-V and admittance measurements were performed in the dark and after illumination. The results suggest the presence in the AlGaN barriers of deep negatively charged traps of high concentration measurably shifting C-V characteristics to more positive voltages. The density of negatively charged centers can be increased by cooling at high reverse bias. These centers are believed to have a relatively high barrier for capture of electrons. Their thermal activation energy is estimated as 0.6-0.85 eV, the

optical ionization energy is close to 1.7 eV. The presence of such centers explains lower than expected from modeling threshold voltages of the studied structures. Admittance spectroscopy also reveals consistent presence of features corresponding to apparent activation energy 0.11-0.13 eV for measurements at reverse voltages corresponding to a peak in AC conductance dependence on bias. These peaks in conductance and steps in admittance were attributed to transitions from the ground state in the triangular well near the AlN/GaN interface to the quasi continuum of excited states in the well with subsequent thermal emission into the conduction band. For samples illuminated at low temperature admittance spectra show unusual peaks in conductance with the activation energy close to the activation energy of thermal emission from the traps responsible for persistent photoconductivity.

11:00am EM-TuM10 Characterizations of Proton-irradiated GaN and 4H-SiC by KOH Etching, H.-Y. Kim, Korea University, Y.J. Shin, W. Bahng, Korea Electrotechnology Research Institute, J. Kim, Korea University

We investigated the variations of the free electron concentrations and the etch pits such as threading screw dislocation (TSD), threading edge dislocation (TED) and mixed dislocation on proton-irradiated GaN and 4H-SiC. High energy protons create the radiation-induced defects (RD) such as single V_{Si}, V_C and interstitials, which can act as the carrier traps. Before proton irradiation, the energy loss and the penetration depth of the high-energy protons were assessed by Monte Carlo simulation (SRIM). Proton irradiations were performed on the sidewall and backside (carbon face of 4H-SiC) of the samples to examine the experimental proton-penetration depth. The irradiated fluence of the 6 and 8 MeV protons were 5x10¹⁵ cm⁻². High-energy protons gradually lose their energy by Coulomb interactions until they approach to specific depth where protons collide with the lattice atoms and create the point defects. The free electron concentrations of pre-irradiated GaN and 4H-SiC were 4x10¹⁶ cm⁻³ and 5x10¹⁸ cm⁻³, respectively. The free carrier concentrations of proton irradiated GaN and SiC showed less than 1x10¹⁶ cm⁻³, which can be calculated from the Raman scattering. After proton irradiation, 4H-SiC was etched in molten KOH at 530 °C for 3 min to compare the shape of the etch pits before and after proton irradiation. It was reported that the different kinds of etch pit were apparently distinguished at low-doped SiC, while the classification of the etch pit on highly doped SiC were very difficult. We observed the effect of the free carrier concentrations to the shape and the size of the etch pits. The results of molten KOH etched proton irradiated 4H-SiC showed different etch pits which were clearly distinguished. The TSDs were approximately 2-3 times larger than TEDs in proton-irradiated sample. After 1700 °C thermal annealing, the free electron concentrations were partially recovered. The differences of TEDs and TSDs were less evident after thermal annealing due to the recovery of the free electron concentrations. More details will be discussed.

11:20am EM-TuM11 Trapping Centers in High -k Dielectrics for MOS Devices, P. Lenahan, Pennsylvania State University **INVITED**

This presentation will review experimental evidence with regard to trapping centers in high dielectric constant gate stacks in metal oxide semiconductor (MOS) devices. The presentation will deal primarily with hafnium oxide based systems on silicon. The presentation will include discussion of silicon/dielectric interface traps, trapping centers within the interlayer dielectric between the silicon and the high -k material, and defects in hafnium oxide. Most of the experimental evidence with regard to the physical and chemical nature of these trapping centers comes from electron paramagnetic resonance (EPR) and electrically detected magnetic resonance (EDMR). The presentation will thus emphasize EPR and EDMR measurements along with "electronic" measurements on these systems. An attempt will be made to link device processing, defect structures, and defect densities to the electronic properties of these high -k MOS systems.

Energy Frontiers Focus Topic

Room: 15 - Session EN+TF-TuM

Chalcogenide Solar Cells II

Moderator: H.W. Hillhouse, University of Washington

8:00am EN+TF-TuM1 Thin Film Solar Cells: Present Status and Future Prospects, C.S. Ferekides, University of South Florida **INVITED**

Thin film photovoltaics (TF PV) have long been viewed as a low cost option for solar electricity. Two very promising TF technologies are based on Cu(In,Ga)(S,Se)₂ (CIGS) and CdTe. The former has achieved the highest thin film laboratory efficiency (over 20%) and the latter is the lowest cost PV product on the market today (@ \$0.74/Watt). Recently, another thin

film technology based on the kesterites $\text{Cu}_2\text{ZnSn}(\text{S,Se})_4$ (CZTS) has received significant attention due to the abundance of the constituent elements, and small area cells have reached the 10% efficiency level. Despite all the successes achieved at the laboratory and manufacturing environments, TF technologies continue to face challenges some of which are unique to the specific material system. The presentation will provide an overview of thin film photovoltaics by comparing and contrasting the devices and technologies described above. Material, device and fabrication issues will be discussed with emphasis placed on some of the unique aspects of each technology: the need for sodium for CIGS and the importance of the co-evaporation process, the use of a chloride based treatment for CdTe and the challenge in forming back contacts to this device, and the loss of tin for CZTS.

8:40am EN+TF-TuM3 Materials and Process Options for $\text{Cu}(\text{InGa})\text{Se}_2$ Thin Film Solar Cells, W.N. Shafarman, University of Delaware INVITED

Two approaches to depositing thin films of $\text{Cu}(\text{InGa})\text{Se}_2$ and related alloys have been developed in the laboratory and are being implemented in large scale photovoltaics manufacturing. Precursor reaction processes use precursor films containing Cu, Ga, and In deposited by methods such as sputtering, printing, or electrodeposition chosen to provide potential manufacturing benefits. These are reacted in hydrogen selenide gas or elemental Se vapor to form the semiconductor absorber layer. Elemental co-evaporation is a single step process in which fluxes of all species are delivered to a hot substrate. Advantages and critical issues for these processing approaches will be compared. One of the materials options for $\text{Cu}(\text{InGa})\text{Se}_2$ -based absorber layers is the opportunity to alloy the film to increase its bandgap. This is desirable because the increased solar cell voltage can be advantageous for large scale module performance. Wider bandgap can be achieved by increasing the relative Ga content or by alloying with S, Al or Ag, but in all cases the cell efficiency decreases as the absorber layer bandgap increases beyond 1.2-1.3 eV. Alloying and composition control is generally straightforward using co-evaporation since these alloys form continuous solutions. With precursor reaction, however, chemical pathways to film formation are partly controlled by preferential reaction of Se with In instead of Ga, leading to aggregation of the Ga at the back of the film and, effectively, low bandgap. Multi-step reaction profiles can be used to control through-film composition in this case. For wide bandgap cells, recent results with the combination of Ag alloying and higher Ga content show promise. This includes improved optical properties, evidence of reduced structural disorder and improved performance with high open circuit voltage solar cells. The incorporation of Ag in both the precursor reaction and co-evaporation processes will be described.

9:20am EN+TF-TuM5 Why Are We Making CIGS Solar Cells from Cu-poor Material?, S. Siebentritt, University of Luxembourg INVITED
CIGS can be prepared single phase in a large range of Cu-poor compositions. When prepared under Cu-excess a secondary phase of Cu selenide is formed which can be etched. Record solar cells as well as commercial modules are prepared from Cu-poor absorbers. However, the transport and recombination properties of material prepared under Cu-excess are superior. It has been known that the interface in cells with absorbers prepared under Cu-excess leads to increased recombination and thus limits the efficiency. The properties of the surface of CIGS absorbers prepared under Cu-excess is not well understood so far. We are preparing solar cells with absorbers grown under Cu-excess, where we make the surface Cu-poor to get the best from both worlds.

10:40am EN+TF-TuM9 $\text{Zn}_x\text{Cd}_{1-x}\text{S}$ Thin Films for Chalcopyrite Solar Cells Deposited through Batch and Continuous-Flow Chemical Bath Deposition, B.S. Tosun, C. Pettit, S.A. Campbell, E.S. Aydil, University of Minnesota

Copper indium gallium diselenide (CIGS) thin film solar cells already exceed 20% overall power conversion efficiencies. These high efficiencies are achieved using an n-type cadmium sulfide (CdS) buffer layer deposited on the p-type CIGS absorber using chemical bath deposition. CdS buffer layers are also used in the emerging copper zinc tin sulfide/selenide (CZTSSe) based solar cells. In some cases, it is desired to grade and widen the band gap of the buffer layer away from the CdS-absorber interface by alloying CdS with Zn to form $\text{Zn}_x\text{Cd}_{1-x}\text{S}$ films. In this work, we demonstrate the ability to manipulate Zn fraction, x , as a function of distance from the absorber-buffer layer interface and investigate the fundamental factors that govern the evolution of the film composition as a function of depth. Specifically, $\text{Zn}_x\text{Cd}_{1-x}\text{S}$ films were grown from solutions containing cadmium sulfate ammonium hydroxide, ethylenediaminetetraacetic acid disodium, zinc sulfate and thiourea in two different types of chemical baths, a traditional batch-type chemical bath and a continuous-flow chemical bath. By changing the initial concentrations of Zn and Cd sulfate in the batch-type chemical bath deposition, the entire range of overall compositions

ranging from primarily cubic ZnS to primarily hexagonal CdS could be deposited. Using Auger depth profiling, we show that a CdS rich layer forms at the film/substrate interface due to the faster reaction of Cd than Zn. The formation of Cd-rich $\text{Zn}_x\text{Cd}_{1-x}\text{S}$ layer at film/substrate interface followed by Zn-rich $\text{Zn}_x\text{Cd}_{1-x}\text{S}$ is favorable for solar cells. Thicker films with increasing band gap towards the surface can be deposited to increase the shunt resistance without sacrificing light transmission. In addition, we have developed a continuous chemical bath deposition system that allows deposition of $\text{Zn}_x\text{Cd}_{1-x}\text{S}$ films on 4-inch diameter substrates at temperatures as high as 80 °C without significant liquid temperature rise and without homogeneous nucleation and growth. Structure and composition of the films from the batch and continuous flow systems will be discussed and compared.

11:00am EN+TF-TuM10 Selenization of Cu-Ga-In Precursors for Synthesis of CIGS Absorbers: Equilibrium and Kinetic Studies, C. Muzzillo, R. Krishnan, University of Florida, W.K. Kim, Yeungnam University, Republic of Korea, E.A. Payzant, Oak Ridge National Laboratory, Y.H. Sohn, B. Yao, University of Central Florida, J. Shen, General Research Institute for Non-ferrous Metals of Beijing, China, C. Campbell, National Institute of Standards and Technology, T.J. Anderson, University of Florida

The emerging $\text{CuIn}_x\text{Ga}_{1-x}\text{Se}_2$ (CIGS) PV industry is primarily differentiated on the basis of the process used to synthesize the CIGS absorber. The most common approach is a 2-step metal deposition/selenization with differentiation occurring on the method of metal deposition and Se source for selenization. Typical champion cell efficiencies, however, are slightly lower for 2-step processes as compared to co-evaporation. This has been attributed to difficulty in creating a 'U-shaped' Ga profile, void formation near the back contact, and differences in diffusion/reaction rates of Ga and In during synthesis. Furthermore, cost pressures are driving reduction of the selenization time (up to 8 hr) and thinning of the absorber layer. A better understanding of the thermodynamic and kinetic elements of the precursor Cu-Ga-In metal system offers the potential to exploit faster pathways, assist in scale-up, and ensure robust processing of CIGS. This study includes a critical assessment of thermochemical and phase equilibria data of the Cu-Ga-In ternary metal system. The calculated phase diagram includes 11 binary intermetallic phases and no ternary compounds. Of particular interest are the 4 phases which exhibit ternary solubility: $\alpha\text{-Cu}$ (fcc), $\gamma\text{-Cu}_9(\text{Ga}_x\text{In}_{1-x})_4$ (sc), and $\eta\text{-Cu}_{16}(\text{In}_x\text{Ga}_{1-x})_9$ (hcp) are all modeled with a sublattice formalism, and an ionic two-sublattice liquid model is employed. Time-resolved *in situ* high temperature X-ray diffraction data for selenization of metallic precursors have also been collected. Reaction pathways and kinetics of temperature ramp and isothermal anneal experiments have both been examined, and kinetic rate parameters for the Avrami and parabolic growth models have been estimated from the data. As examples, MBE deposited bilayer metal precursor structures (e.g. CuIn/CuGa) and elemental stacked layers (e.g. $(\text{Cu}/\text{Ga}/\text{In})_n$) were selenized and the Ga distribution measured. The formation of $\text{Cu}_{11}\text{In}_9$, textured indium, and the solid solution $\gamma\text{-Cu}_9(\text{Ga}_x\text{In}_{1-x})_4$ were also evident as well as formation of CuGaSe_2 and CIGS simultaneously for selected structures. Rietveld refinement of temperature ramped selenized samples was performed to estimate the Ga distribution. TEM-EDS results confirm that the Ga distribution after selenization depended on the order of deposition of the precursor structure. The samples were further characterized by SEM (microstructure) and ICP (final composition). The activation energy for formation of CIGS was estimated from isothermal studies, and gave values of $76(\pm 14)$ for the glass/Mo/CuIn/CuGa and $93(\pm 4)$ and $101(\pm 9)$ kJ/mole for the glass/Mo/CuGa/CuIn precursor.

11:20am EN+TF-TuM11 Fabrication of $\text{CuIn}_{1-x}\text{Ga}_x\text{S}_2$ Thin-Film Solar Cells on Single Layer Molybdenum, A. Kaul, E. Schneller, N. Shiradkar, S. Pethe, N. Dhere, Florida Solar Energy Center, University of Central Florida

Considering the various advantages of a single pass operation, efforts have been made to develop a recipe for device quality single layer molybdenum back contact film that has good adhesion to the soda-lime glass substrate and at the same time lower resistivity values. $\text{CuIn}_{1-x}\text{Ga}_x\text{S}_2$ (CIGS2) thin film solar cells with reasonable efficiencies were successfully fabricated on the single layer molybdenum film without any signs of peeling or back contact degradation during processing. The molybdenum films were also subjected to various processing conditions of temperature and gas ambient and the subsequent results from these tests are also being presented.

11:40am EN+TF-TuM12 Investigation of Elemental Composition for $\text{Cu}(\text{InGa})\text{Se}_2$ Thin Films by Various Analytical Techniques, J.H. Lee, S.H. Kim, J.-H. Yoon, S.-O. Won, Y.H. Lee, Korea Institute of Science and Technology, Republic of Korea

$\text{Cu}(\text{InGa})\text{Se}_2$ (CIGS) solar cells are very promising films for use in photovoltaic devices, as they feature a high absorption coefficient and a

high conversion efficiency at a relatively low manufacturing cost. In order to develop an efficient CIGS solar cell, the relative ratio of the major elements should be determined quantitatively. In this study, a quantitative analysis of Cu(InGa)Se₂ (CIGS) was performed using an electron probe micro analysis (EPMA), x-ray fluorescence (XRF), inductively coupled plasma-optical emission spectrometry (ICP-OES), Auger electron spectroscopy (AES), time-of-flight secondary ion mass spectrometry (TOF-SIMS), and dynamic secondary ion mass spectrometry (dynamic SIMS). Surface roughness was observed by using atomic force microscopy (AFM) to identify the effect of the surface roughness on the reproducibility of the measurements. The relative sensitivity factors (RSF) of AES and SIMS were obtained by using ungraded CIGS thin film of known composition as the standard sample. Quantitative analysis of several CIGS samples were performed using the relative sensitivity factor (RSF) value calculated from the depth profile results of the standard film. The Cu/(In+Ga) ratio and the Ga/(In+Ga) ratio of SIMS results are relatively reproducible and close to those of the AES results. Overall, results from Composition of CIGS thin films by a variety of analytical methods were compared and their discrepancies were interpreted.

Exhibitor Technology Spotlight

Room: West Hall - Session EW-TuM

Exhibitor Technology Spotlight

Moderator: D. Surman, Kratos Analytical Inc.

10:00am **EW-TuM7 ORION Nanofab: Fabricating sub 10 nm Nanostructures using the Helium Ion Microscope**, *D. Elswick*, Carl Zeiss
The helium ion microscope (HIM) takes advantage of an atomically sharp source to emit a beam of focused He ions so the microscopist today can go beyond imaging resolutions achieved in the Scanning Electron Microscope (SEM). Imaging with ions rather than electrons offers many advantages including the ability to image uncoated non conducting samples at high resolution without damage. Additionally, helium ions can be used to sputter material for nanolithography and nanopatterning applications where sub 10 nm structures are desired. A gallery of helium ion microscopy results will be presented to showcase the capability and performance of this novel microscope. The HIM has proven invaluable at characterizing uncoated biological samples as well as other soft materials. Features sizes and material removal via conventional Ga FIB systems is now surpassed using HIM. The HIM-FIB has touched a wide array of applications that range from nanomachining 5 nm pores for single molecule detection to patterning devices in graphene and creating nanophotonic devices in thin films.

10:20am **EW-TuM8 AM-FM and Loss Tangent Imaging—Two New Tools for Quantitative Nanomechanical Properties**, *R. Proksch, I. Revenko, S. Hohlbauch, J. Cleveland, N. Geisse, A. Moshar, J. Bemis, C. Callahan, K. Jones*, Asylum Research

Amplitude-modulated Atomic Force Microscopy (AM-AFM), also known as tapping mode, is a reliable and gentle imaging method with widespread applications. Previously, the contrast in AM-AFM has been difficult to quantify. In this work, we introduce two new techniques that allow unambiguous interpretation of material properties. AM-FM imaging combines the features and benefits of normal tapping mode with quantitative and high sensitivity of frequency modulated (FM) mode. Briefly, the topographic feedback operates in AM mode while the second resonant mode drive frequency is adjusted to keep the phase at 90 degrees, on resonance. With this approach, frequency feedback on the second resonant mode and topographic feedback on the first are decoupled, allowing stable, robust operation. The FM image returns a quantitative value of the frequency shift that in turn depends on the sample stiffness and can be applied to a variety of physical models. Loss tangent imaging is a recently introduced quantitative technique that recasts phase imaging into a term that includes both the dissipated and stored energy of the tip sample interactions. Quantifying the loss tangent depends solely on the measurement of cantilever parameters as a reference position. These two quantitative techniques can be performed simultaneously. To illustrate this, we will present an example of a micro-cryotomed, cross-sectioned area of a coffee bag packaging material that has been imaged. The loss tangent image shows the highly lossy "tie" layers connecting the low loss metal layer with two vapor-barrier polymer layers. The AM-FM image shows the relative stiffness of the five layers, with the metal layer being the stiffest and the tie layers the softest. As a second example, we imaged graphene deposited onto SiO₂, where the softer graphene layer showed a lowered resonance and the loss tangent imaging revealed a dissipative region between SiO₂ and graphene.

Graphene and Related Materials Focus Topic Room: 13 - Session GR+AS+EM+MI+MN-TuM

Optical, Magnetic, Mechanical and Thermal Properties

Moderator: K.I. Bolotin, Vanderbilt University

8:00am **GR+AS+EM+MI+MN-TuM1 Characterization of Magnetically Tunable Iron Nanorod Coated Graphene Nanoplatelets**, *S.D. Johnson, M.H. Gowda, S.-F. Cheng, N.Y. Garces, B. Feigelson, F.J. Kub, C.R. Eddy, Jr.*, U.S. Naval Research Laboratory

Composites made from iron coated graphene nanoplatelets (GNPs) show promise for applications such as, magnetic switches, electromagnetic interference shielding, and electromagnetic waveguides due to the large conductivity of GNPs combined with the magnetism of iron. Additionally, this composite can be easily formed into millimeter thick sheets making it a promising composite for other applications.

We report a novel method to synthesize iron oxide compound onto GNP using microwave hydrothermal synthesis at 60° C and reaction times between 10 and 120 minutes. Scanning electron microscopy imaging reveals iron oxide nanorods approximately 100 nm long adhered to the GNPs for reaction times as short as 10 minutes. X-ray photoemission spectroscopy reveals that the iron/carbon ratio remains constant across these reaction times. The resistivity of the composite increases with reaction time from 0.2 to 0.6 ohm-cm. Saturation magnetization and coercive field values follow a decreasing trend with increasing reaction time. From 10 to 120 minutes saturation magnetization decreases by 70% from 170 emu/g and coercive field decreases by 40% from 52 Oe. Remnant magnetization of around 0.7 memu/g remains constant throughout. We also report the temperature-dependent magnetic response of the compound across the Morin transition, which for submicron particles of α -Fe₂O₃ is near 250 K.

Preliminary results suggest that while the nanorod size and quantity remains constant with reaction time, the resistive and magnetic properties change. This may suggest that we are tuning the magnetism of the system by changing the iron structure between the ferromagnetic γ -Fe₂O₃ and the antiferromagnetic α -Fe₂O₃.

8:20am **GR+AS+EM+MI+MN-TuM2 Dynamical Origin of Blue Photoluminescence from Graphene Oxide**, *A.L. Exarhos, M.E. Turk, P.M. Vora, J.M. Kikkawa*, University of Pennsylvania

The tunable broadband emission from graphene oxide (GO) has sparked significant interest in research regarding its potential for band gap engineering. Here, we use polarization sensitive time-resolved optical spectroscopy to study the spectral diffusion and sub-picosecond dynamics of the excited carriers in GO and photo-exposed GO, where photo-exposure has been demonstrated to constitute a reducing condition. In steady state measurements, a significant blueshifting of the photoluminescence (PL) is observed with photo-exposure. This blueshift correlates with a marked difference in the temporal behavior of the PL from GO and photo-exposed GO. The PL spectra are very similar at short delay times, but an increased non-radiative recombination rate in the exposed GO leads to a decreased lifetime in the material. Utilizing in-plane polarization memory measurements, we examine the electron-hole polarization in these systems which can probe excitonic effects and help to provide a better understanding of the role of the sp² graphene lattice in GO and exposed GO. We further discuss the relevance of our data to the origins of PL in these systems.

A.L.E. gratefully acknowledges the support of NSF DMR-0907226. M.E.T., P.M.V., and the construction of a Kerr gate system are supported by the Department of Energy Office of Basic Energy Sciences Award DE-SC0002158.

8:40am **GR+AS+EM+MI+MN-TuM3 Spin-Transport and Magnetism in Graphene**, *R. Kawakami*, University of California, Riverside **INVITED**

Graphene is an attractive material for spintronics due to its high mobility and the low intrinsic spin-orbit and hyperfine coupling, which should lead to excellent spin transport properties. In 2007, graphene became the first material to exhibit gate tunable spin transport and spin precession at room temperature. However, the spin injection efficiency was low and the spin lifetime was much shorter than predicted theoretically. In this talk, I will report on our progress in this area. The low spin injection efficiency into graphene is due to the conductivity mismatch between the ferromagnetic metal (Co) spin injector and the single layer graphene (SLG). To alleviate this problem and enhance the spin injection efficiency, we developed atomically smooth MgO tunnel barriers by utilizing a TiO₂ seed layer. With tunneling contacts, the non-local spin signal is found to be as high as 130 ohms at room temperature, with a spin injection efficiency of 30%. In addition to improving the spin injection efficiency, the tunneling contacts were found to improve the spin lifetime as well. This indicates that the short

spin lifetimes reported before are due to the contact-induced spin relaxation from the ferromagnetic electrodes. Using tunneling contacts, we investigate spin relaxation in single layer graphene (SLG) and bilayer graphene (BLG). At low temperatures, contrasting behaviors of gate voltage dependence of the spin lifetime are observed between SLG and BLG, which suggest different mechanisms for spin relaxation in SLG and BLG. A final topic of interest is magnetism and the formation of magnetic moments in graphene. While there is substantial theoretical work on magnetic moments generated by hydrogen adatoms and lattice vacancies, the experimental situation is less clear. We have developed a new method for detecting magnetic moment formation based on scattering of pure spin currents in graphene spin valves. We will report the progress on our efforts to identify magnetism with this approach.

10:40am **GR+AS+EM+MI+MN-TuM9 A "How To" for Magnetic Carbon.** *H. Ohldag*, SLAC National Accelerator Laboratory, *E. Arenholz*, *T. Tylliszczak*, Lawrence Berkeley National Laboratory, *D. Spemann*, *R. Hoehne*, *P. Esquinazi*, *M. Ungureanu*, *T. Butz*, University of Leipzig, Germany

While conventional wisdom says that magnetic materials have to contain some metallic atoms, the confirmation of intrinsic magnetic order in pure metal free carbon represents an ultimate and general scientific breakthrough because of the fundamental importance of carbon as an elemental building block of organic as well as inorganic matter. The common controversy raised across all disciplines is whether the magnetism of carbon is intrinsic or induced by other elements. We address this controversy by providing clear experimental evidence that metal free carbon can be ferromagnetic at room temperature using dichroism x-ray absorption spectro-microscopy. For this purpose we acquired soft x-ray microscopy images of magnetic structures on a thin carbon film that have been produced by irradiation with a focused 2.25MeV proton beam. Our element specific magnetic probe shows no indication of magnetically ordered Fe, Co or Ni impurities in these samples. In a second step we investigate the particular electronic states that are involved in carbon magnetism and find that the carbon p-states as well as C-H bonds show a magnetic moment, indicating that hydrogenation plays a crucial role in developing the ferromagnetic order. Our surface sensitive approach reveals that the magnetism at the surface of the irradiated graphite samples is much larger than in the bulk of the sample. We observe a surface magnetic moment similar to what is typically present in classical ferromagnetic 3d transition metals.

REFERENCES

P.Esquinazi et al., *Magnetic order in graphite: Experimental evidence, intrinsic and extrinsic difficulties*, Journal of Magnetism and Magnetic Materials, Vol 322, 1156 (2010).

H. Ohldag et al. *p-Electron ferromagnetism in metal free carbon probed by soft x-ray dichroism*, Phys. Rev. Lett. 98, 187204 (2007) H. Ohldag et al., *The role of hydrogen in room temperature ferromagnetism at graphite surfaces*, New J. Phys. 12 123012 (2010)

11:00am **GR+AS+EM+MI+MN-TuM10 From Graphene to Amorphous Carbon by Sublimation and Condensation.** *B. Steele*, *R. Perriot*, *V. Zhakhovsky*, *I.I. Oleynik*, University of South Florida

The mechanisms of the non-equilibrium melting process of graphene and the structure of the liquid phase of carbon was studied by molecular dynamics (MD). Graphene undergoes a non-equilibrium melting process at high temperature and low pressure as the carbon chains are formed out of the graphene sheet, thus making up a transient liquid phase of carbon. As the chains expand the material sublimates to a low dense gas of carbon chains. Under higher pressure the gas phase will condense to an intermediate porous phase of carbon with a significant sp² fraction of atoms, followed by the liquid phase, and finally an amorphous phase. Mechanisms of melting of graphene, including formation of topological and Stone Wales (SW) defects in two and three dimensions will be discussed.

In Situ Microscopy and Spectroscopy Focus Topic Room: 7 - Session IS+AS+SS+EN-TuM

In Situ Spectroscopic Studies of Catalysis and Gas-Solid Reactions

Moderator: B. Roldan Cuenya, University of Central Florida

8:00am **IS+AS+SS+EN-TuM1 Ambient Pressure XPS for Alternative Energy Research and Environmental Science.** *H. Bluhm*, Lawrence Berkeley National Laboratory **INVITED**

Solid/vapor and liquid/vapor interfaces play a major role in many processes in the environment and technology. Examples include heterogeneous catalysis, fuel cell technology, aerosol chemistry, and weathering of minerals and rocks. The measurement of these interfaces under realistic conditions of gas pressure and temperature has gained increasing importance over the last decades. Ambient pressure photoelectron spectroscopy (APXPS) is a promising technique for the investigation of liquid and solid surfaces in the presence of gases at pressures in the Torr range. The heart of an APXPS instrument is a differentially pumped electrostatic lens system that separates the sample, which is in a gas atmosphere at pressures of up to 5 Torr, from the electron spectrometer, which is kept in vacuum. This talk will discuss the history and basics of APXPS and show examples of the application of APXPS to the study of aqueous solution, metal oxides, soot, and fuel cell electrodes under reaction conditions.

8:40am **IS+AS+SS+EN-TuM3 In Situ Soft X-ray Photon-in/Photon-out Spectroscopy of Photo-electrochemical Reactions of Hematite in Water Splitting.** *J.H. Guo*, Lawrence Berkeley National Laboratory, *A. Braun*, Empa, Swiss Federal Laboratories for Materials Science and Technology, *K. Sivula*, Ecole Polytechnique Fédérale de Lausanne (EPFL), Switzerland, *D. Bora*, Lawrence Berkeley National Laboratory, *J.F. Zhu*, *L. Zhang*, University of Science and Technology of China, *M. Grätzel*, Ecole Polytechnique Fédérale de Lausanne (EPFL), Switzerland, *E.C. Constable*, University of Basel, Switzerland

Hydrogen fuel generation by solar water splitting in photoelectrochemical cells (PEC) is one of the first steps in artificial photosynthesis and an essential part of the holy grail of solar energy conversion. Iron oxide, literally "rust", is an interesting PEC photoanode material because of its affordability, good stability, good spectral match of the solar spectrum, and yet controversial because of its poor electronic structure. At present, iron oxide is taking center stage as prospective PEC anode material.

PEC electrodes are typically semiconducting metal oxides to form electron-hole pairs when struck by light. In the photoanodes such as hematite, the generated holes must diffuse to the iron oxide surface where they can oxidize water to oxygen. However, the electronic structure of iron oxide is such that the photogenerated holes tend to recombine and annihilate with the electrons before reaching the surface and performing the required chemical work on water splitting. Currently, researchers worldwide try to understand the peculiarities of iron oxide so as to invent strategies to improve this material.

The Advanced Light Source produces soft X-rays which are optimally suited to study the electronic structure of electrode materials and which can detect electron holes. But the holes needed for solar water splitting by iron oxide require an anodic electric bias plus the illumination. Moreover, the holes are transitional and quite elusive. Also, soft X-rays cannot easily peek into a PEC cell. The unique design of the in-situ cell at the ALS has overcome the burden [1-3]. Recently the experiment has been performed for studying, under in-situ and operando conditions, the hole generation in a specifically designed photoelectrochemical cell. The oxygen valence band signature was recorded while tuning the PEC relevant parameters, two different types of holes in the valence band near the Fermi energy are discovered [4].

References:

[1] "X-ray Emission Spectroscopy of Hydrogen Bonding and Electronic Structure of Liquid Water", J.-H. Guo et al., Phys. Rev. Lett. **89**, 137402 (2002).

[2] "Electronic Structure of Cobalt Nanocrystals Suspended in Liquid", H. Liu et al., Nano Lett. **7**, 1919 (2007).

[3] "In situ soft X-ray absorption spectroscopy investigation of electrochemical corrosion of copper in aqueous NaHCO₃ solution", P. Jiang et al., Electrochem. Comm. **12**, 820 (2010).

[4] "Direct Observation of Two Electron Holes in a Hematite Photoanode during Photoelectrochemical Water Splitting", A. Braun et al., J. Phys. Chem. C **116**, 16870 (2012).

9:00am **IS+AS+SS+EN-TuM4 XANES and Ambient Pressure XPS (APXPS) Study: Investigations of the Local Structure and Final-State Effect in Partially Reduced SnO_x Nanoislands on Pt(111).** *S. Axnanda, Z. Liu, B. Mao*, Lawrence Berkeley National Laboratory

Heterogeneous catalysts consisting of small particles having a high concentration of structural defects and under-coordinated sites make up the majority of the catalytic processes in industrial chemistry. One important recent example of interest shows that the interface-confined coordinatively unsaturated ferrous (CUF) sites together with the metal supports (FeO_x/Pt(111)) are active for dioxygen activation which causes the ensemble to be highly efficient for CO oxidation at low temperature under typical operating conditions of a proton-exchange membrane fuel cell.[1-2] In this work, we report another spectroscopic evidence to further confirm an enhanced reactivity at the edges of small catalyst particles. The system in interest is partially oxidized SnO_x (Sn²⁺) nanoislands supported on Pt(111) for ethanol oxidation reaction (EOR), an electrode material in a direct alcohol fuel cell (DAFC). Our findings suggested that SnO_x/Pt(111) inverse catalysts have improved activity for EOR in acidic media as compared to a bare Pt(111) surface.[3] We also found that the most active surface had a small coverage of SnO_x (0.3- 0.4 ML). Water activation at low potentials is currently attributed to be the promoting effect of SnO_x nanoparticles, since this enhances the oxidation of chemisorbed CO formed on Pt sites during the EOR.[4] To better understand this increased activity, we performed study with the goal to indicate the actual state of Sn in SnO_x nanoislands before and after the SnO_x /Pt(111) is used in EOR showing the increased activity: purely oxide Sn or mixed Sn alloy and Sn oxide, using a combination of APXPS and XANES techniques. BE shift in the XPS core-line spectra of Sn and O, soft X-ray XANES spectra (Sn M_{4,5}-edge, O K-edge) will be collected and compared to the corresponding XPS spectra (Sn 3d, O 1s) to explain the actual state of Sn before and after the SnO_x/Pt(111) is used in the EOR.

1. Fu, Q., et al., Interface-Confined Ferrous Centers for Catalytic Oxidation. *Science*, 2010. 328: p. 1141.
2. Deng, X., et al., Reactivity Differences of Nanocrystals and Continuous Films of α -Fe₂O₃ on Au(111) Studied with In Situ X-ray Photoelectron Spectroscopy. *J. Phys. Chem. C*, 2010. 114: p. 22619.
3. Zhou, W.P., et al., Enhancement in Ethanol Electro-Oxidation by SnO_x Nanoislands Grown on Pt(111): Effect of Metal Oxide-Metal Interface Sites. *Journal of Physical Chemistry C*, 2011. 115: p. 16247.
4. Axnanda, S., W.P. Zhou, and M.G. White, CO Oxidation on Nanostructured SnO_x/Pt(111) surfaces: Unique Properties of Reduced SnO_x. *Phys. Chem. Chem. Phys.*, 2012. Submitted.

9:20am **IS+AS+SS+EN-TuM5 Epitaxial Strontium Substituted Lanthanum Cobalt Oxides Investigated using In Situ Ambient Pressure X-ray Photoelectron Spectroscopy Near Operating Conditions Under Applied Potentials.** *E. Crumlin, E. Mutoro*, Massachusetts Institute of Tech., *Z. Liu*, Lawrence Berkeley National Lab, *M.D. Biegalski*, Oak Ridge National Lab, *W.T. Hong*, Massachusetts Institute of Tech., *H.M. Christen*, Oak Ridge National Lab, *H. Bluhm*, Lawrence Berkeley National Lab, *Y. Shao-Horn*, Massachusetts Institute of Tech.

Operating conditions for solid oxide fuel cell (SOFC) are typically at high temperatures (~500 – 1000 °C) and ambient pressures (~1 atm). We have to understand how the physical and chemical properties of SOFC materials, particularly the cathode which is responsible for a majority of the fuel cells area specific resistance, change under operating conditions. Such data can provide insights into the mechanism of the oxygen reduction reaction (ORR) which may lead to material development strategies to improve the cathode performance. However, these operating conditions are far away from conventional characterization techniques that are often applied at room temperature or even in ultrahigh vacuum (UHV). Our recent work using *in situ* ambient pressure X-ray photoelectron spectroscopy (APXPS) has shown that (001) oriented epitaxial films of La_{0.8}Sr_{0.2}CoO_{3- δ} (LSC₁₁₃) can exhibit Sr enrichment in the near-surface perovskite lattice structure ("lattice") as temperatures were raised from 220 °C to 520 °C in a $p(\text{O}_2)$ of 1×10^{-3} atm. In contrast under the same conditions, a bulk pellet of LSC demonstrated no changes in Sr content within the "lattice" region. The Sr enrichment is believed to play a key role in the observed one order of magnitude enhancement in ORR activity (as measured by the surface exchange coefficient, k^0) of the (001) epitaxial films relative to bulk LSC₁₁₃. In this work, we continue the previous investigations of the chemical properties of (001) epitaxial LSC₁₁₃ as a function of temperature cycling between 220 °C and 520 °C at a $p(\text{O}_2)$ of 1×10^{-3} atm. Additionally, the comparison of LSC₁₁₃, (La_{0.5}Sr_{0.5})₂CoO_{4- δ} (LSC₂₁₄), and LSC₂₁₄-decorated LSC₁₁₃ (LSC_{113/214}) at $p(\text{O}_2)$ of 1×10^{-3} atm as a function of temperature and under applied cathodic potentials will be presented in order to provide insights into the physical origin responsible for the observed ~3 orders of magnitude ORR activity enhancement of LSC_{113/214} relative to (001) epitaxial LSC₁₁₃.

9:40am **IS+AS+SS+EN-TuM6 Probing Nitrogen and Metal Speciation in Non-Platinum Electrocatalysts by Ambient Pressure X-ray Photoelectron Spectroscopies and DFT Calculations.** *K. Artyushkova, B. Halevi, A. Serov*, The University of New Mexico, *B. Kiefer*, New Mexico State University, *P. Atanassov*, The University of New Mexico

X-ray Photoelectron Spectroscopy (XPS) has been the main surface analysis method for determining the chemical environment and coordination of nitrogen and transition metal (TM) in the non-precious group metal oxygen reduction reaction (ORR) electrocatalysts. Even though there is an agreement that Me-N_x serve as one of the possible active sites in ORR, the distribution of Me-N₂ vs Me-N₄ centers and their specific role still remains unresolved. XPS which heavily relies on use of reference spectra in accurate identification of species cannot address this issue directly as no reference compounds with Me-N₂ moieties are available. The assignment of peaks and nitrogen coordination is not straightforward due to overlapping peaks that appear within a narrow energy window of 2.5-eV and the full width half maximum (fwhm) for individual species is on the order of 1.2-1.5-eV. Being able to calculate binding energy shifts based on molecular structure can be very important tool for assisting in this task. We will report on BE shifts that have been calculated at the DFT level and their comparison to experimentally obtained values for metal-less and metal-containing porphyrins. Information obtained from the DFT calculations will be used as input into curve-fitting XPS spectra for various model N-Me containing compounds as well as from electrocatalysts. We will compare chemical information derived from conventional XPS as well as *in-situ* ambient-pressure XPS using variable energy synchrotron source.

10:40am **IS+AS+SS+EN-TuM9 Resolving Growth of Palladium Nanocatalysts Using In Situ FT-IR, XAS and PDF under Practical Atomic Layer Deposition Conditions.** *Y. Lei, J. Lu, B. Liu, H. Zhao, J. Greeley, P. Chupas, J. Miller, J.W. Elam*, Argonne National Laboratory

Nanostructured Pd catalysts prepared by ALD have been demonstrated highly active for alkene hydrogenation, methanol decomposition reaction, and alcohol oxidation for fuel cells. Development of supported Pd nanoparticles with Controlled size/structure relies on the fundamental understanding of the two half reactions with high precision during Pd ALD. However, evolution of Pd surface species, as well as the subsequent nucleation and growth of palladium nanoparticles during Pd ALD is still not clear.

Mechanism of assembly of highly dispersed Pd nanoparticles on TiO₂ surfaces from palladium hexafluoroacetylacetonate (Pd(hfac)₂) were investigated by means of *in situ* Infrared (IR) spectroscopy, X-ray absorption spectroscopy (XAS) and pair distribution function (PDF) under practical atomic layer deposition condition simultaneously. Density function theory simulation was applied to understanding the reaction mechanism. On chlorine-containing TiO₂ surface, Pd(hfac)₂ primarily adsorbed on TiO₂ surface as Pd(hfac)Cl₂* species, confirmed by both XAS and DFT calculations. *In-situ* FT-IR results reveal that deligation of Pd(hfac)Cl₂* species began at as low as 100 °C with the present of formalin. Further on, *in-situ* XAS results indicated that cleavage of Pd-O bond occurred first, followed by cleavage of Pd-Cl bond. Sequentially, Pd atoms started to gain mobility and agglomerate to small nanoparticles. The hfac ligands spilled to TiO₂ surface as site blockers for ALD. The surface poisons were eventually removed at 225 °C. Nano-size palladium-carbon phase was also found after long exposure of formalin. Atomic resolution aberration-corrected STEM image showed one nanometer size crystalline Pd particles were synthesized using ALD. The catalytic performance of these Pd nanocatalysts was further demonstrated in several applications.

In summary, dynamic growth of Pd nanocatalysts was obtained utilizing a combination of *in-situ* techniques.

11:00am **IS+AS+SS+EN-TuM10 Catalyst Characterization using In Situ XAS and XPS: From Nanoparticles Synthesis to Evolution of Structural/Electronic Properties under Reaction Conditions.** *A.M. Karim*, Pacific Northwest National Laboratory

Catalysts are used to facilitate the important industrial chemical processes, leading to products valued in the trillions of dollars annually just in the U.S and most catalysts used in large-scale processes are solids. To maximize the number of sites available for reaction, catalysts are typically comprised of metallic/metal oxide nanoparticles dispersed on high surface area supports. The activity and selectivity of metallic nanoparticles strongly depend on their size, shape and composition [1-8]. In order to design more active and selective catalysts, it is essential to identify the catalytically active sites and understanding their geometric and electronic properties which requires: (1) synthesis of well-defined catalyst structures and (2) the ability to correlate individual reaction pathway(s) with the type of active site(s) available on the catalyst surface under reaction conditions.

This talk is going to cover our work on *in situ* characterization of nanoparticles from the synthesis stage to the evolution of their structural/electronic properties under reaction conditions using X-ray photoelectron and X-ray absorption spectroscopies. The catalyst systems that will be covered include:

Pd nanoparticles synthesis in solution: Understanding the nucleation and growth mechanisms.

Supported Pt, PtRe and PtNi nanoparticles under aqueous phase reaction condition: Correlating the structural and electronic properties with the catalytic activity and selectivity.

References:

- [1] Boudart, M. *Adv. Catal.* 1969, 20, 153.
- [2] Boudart, M. *Journal of Molecular Catalysis* 1985, 30, 27.
- [3] Ichikawa, S.; Poppa, H.; Boudart, M. *Journal of Catalysis* 1985, 91, 1.
- [4] Somorjai, G. A.; Carrazza, J. *Industrial & Engineering Chemistry Fundamentals* 1986, 25, 63 [5] Liu, Z.; Hu, J. E.; Wang, Q.; Gaskell, K.; Frenkel, A. I.; Jackson, G. S.; Eichhorn, B. *Journal of the American Chemical Society* 2009, 131, 6924.
- [6] Alayoglu, S.; Nilekar, A. U.; Mavrikakis, M.; Eichhorn, B. *Nature Materials* 2008, 7, 333.
- [7] Sinfelt, J. H. *Journal of Catalysis* 1973, 29, 308.
- [8] Sinfelt, J. H. *Accounts of Chemical Research* 1977, 10, 15.

11:40am **IS+AS+SS+EN-TuM12 *In Situ* Study of the Oxidation of CO over Ir(111)**, J. Knudsen, Lund University, Sweden, Y. Moriya, Keio University, Japan, J. Schnadt, M.A. Arman, E. Grånäs, Lund University, Sweden, H. Kondoh, Keio University, Japan, J.N. Andersen, Lund University, Sweden

The platinum group metals are known to be excellent catalysts for the oxidation of carbon monoxide, and the reaction mechanisms over the surfaces of these metals have been studied for a long time. Nevertheless, only during recent years a new picture has emerged which suggests that the catalytically active phase often is formed first under reaction conditions – which implies realistic pressures rather than ultrahigh vacuum (UHV) – and that it is different from the adsorption structures known from UHV experiments. In the case of the Pt(111) surface a very oxygen-rich chemisorbed phase has been suggested as the catalytically active phase [1], whereas a surface oxide has been suggested for the Ru(0001) surface [2]. Thus, for each different surface different phases and mechanisms might be at play, and, moreover, the phase might depend quite strongly on the conditions (pressure and temperature) used.

With this in mind we have studied the CO oxidation reaction over the Ir(111) surface and the related adsorption systems of CO and oxygen on Ir(111) using a combination of *in situ* Ambient pressure x-ray photoelectron spectroscopy (APXPS) – carried out at the new APXPS instrument at the Swedish synchrotron radiation facility MAX IV Laboratory – and *ex situ* Scanning tunnelling microscopy (STM) and x-ray photoelectron spectroscopy (XPS) measurements performed in UHV.

A recent surface x-ray diffraction study reports different oxygen phases for the Ir(111) surface at oxygen pressures from 10^{-6} to 100 mbar – chemisorbed oxygen, a trilayer, a multilayer oxide, and a bulklike oxide [3]. Concentrating on pressures at around 1 mbar, we find a variety of oxygen-rich structures. The corresponding CO adsorption phase formed at 1 mbar CO pressure is an assembly of separated CO_{16} clusters with the CO molecules sitting in on-top sites [4].

The reactivity at 1 mbar total pressure ($\text{O}_2:\text{CO}$ ratio 9:1) and at different temperatures was studied by APXPS and simultaneous monitoring of the gas composition. We find that the phase with the highest activity for the oxidation of CO is a surface phase which contains both CO and oxygen. By comparing with the measured adsorption structures of oxygen we find that the oxygen structure is quite similar to the $\text{p}(2\times 1)\text{-O}$ structure formed on Ir(111) under UHV conditions. This contrasts with what is found for other platinum group metals such as the Pt(111) surface [2], for which CO oxidation is favoured over oxygen rich phases.

- [1] A. L. Gerrard, J. F. Weaver, *J. Chem. Phys.* **123** (2005) 224703.
- [2] H. Over et al., *Science* **287** (2000) 1474.
- [3] Y. B. He et al., *J. Phys. Chem.* **112** (2008) 11946.
- [4] L.-M. Yang, S.-L. Yau, *J. Phys. Chem. B.* **104** (2000) 1769.

MEMS and NEMS

Room: 10 - Session MN-TuM

Optomechanics and Photonic MEMS and NEMS

Moderator: W.K. Hiebert, University of Alberta and The National Institute for Nanotechnology

8:40am **MN-TuM3 Focused Ion Beam Fabrication for Nanophotonics and Microsystems Integration**, I.W. Jung, Argonne National Laboratory
INVITED

Focused ion beam (FIB) fabrication has become an invaluable tool to pattern nanoscale features on a vast range of materials otherwise not available due to the limitations on selectivity of chemical based reactions for etching. In addition, direct milling to create features allows precision patterning on a variety of surface topology. In this talk, we present work on using the FIB to pattern and integrate nanophotonic elements, e.g. photonic crystals, and microelectromechanical systems for novel device applications. In addition, we explore how the FIB can also be used for applications in integration of microsystems with plasmonic structures to achieve precision control of light-matter interactions at the nanoscale.

9:20am **MN-TuM5 Nanomechanical Resonator Detection using Racetrack Resonator Structures for Use in Mass Sensing**, V.T.K. Sauer, Z. Diao, M.R. Freeman, W.K. Hiebert, University of Alberta and The National Institute for Nanotechnology, Canada

Nano-optomechanical systems have been demonstrated as an excellent mechanism for detecting the motion of nanomechanical resonators. They have very high displacement sensitivities and also very large frequency detection bandwidths. These properties make nano-optomechanical systems a promising platform for on-chip inertial mass sensing. By mass loading a resonating mechanical device, the mass of the analyte can be determined by measuring the frequency change this addition of mass causes. The high displacement sensitivities and large operational bandwidth allow for smaller mechanical resonators to be measured which allows for smaller masses to be detectable. Both cantilevers and doubly clamped beams have been detected using the interaction of the evanescent fields from photonic structures such as waveguides, ring/racetrack resonators and toroid structures. Many of these devices incorporate the mechanical resonator directly into the photonic element, but for optimal use in a mass sensing system it is preferable that any added mass not interact directly with the photonic modes. This can cause losses or other uncontrollable effects that negatively impact the operation of the mass sensor. To avoid this, the mechanical element should interact with, but still be external to, the optical cavity structure. Here, cantilever beams 0.5 to 5 μm long and doubly clamped beams 3 to 10 μm long are fabricated 70 to 170 nm from a ring resonator optical cavity. As a beam oscillates in the plane of the wafer, toward and away from a ring resonator, it modulates the ring's effective index. This causes a phase shift in the ring which is detected by a probe laser. The beams are actuated using a power modulated pump laser which uses an optical gradient force to pull the beams toward the optical structure. To increase their mass sensitivity, the devices are implemented into a phase-locked loop and their frequency stabilities are measured.

9:40am **MN-TuM6 Fabrication and Characterization of Ultra-Fast Electrostatically-Actuated Surface Micro-Machined Aluminum Mirrors**, J.R. Fox, A.D. Mathias, J.P. Cortes, M.S. Allen, S.B. Horowitz, Ducommun Miltec, M.G. Temmen, M. Sanghadasa, U.S. Army Aviation and Missile Research Development and Engineering Center

The design, optimization, fabrication, and characterization of an electrostatically-actuated, surface micro-machined aluminum, torsional-beam micro-mirror is presented. The design was optimized to produce a 5 degree tilt of the 20 x 20 micron mirrors with a settle time of less than 6 microseconds with a 190 V electric potential across a 3 micron gap. The design is repeated in 25 x 25 arrays for high-speed deflection of incident light as an optical shutter. Utilization of the COMSOL Multiphysics finite element analysis environment for parameterization of geometries is described and the resulting optimized micro-mirror design is detailed. Fabrication of micro-mirrors via argon ion-mill patterning of aluminum over sacrificial resists and their subsequent dry release with oxygen plasma will be described. The micro-mirrors were then subjected to scanning electron microscopic examination, and laser-Doppler vibrometry was used to examine micro-mirror actuation performance.

10:40am **MN-TuM9 A Comparison of Different Releasing Methods in Fabricating Nano-Optomechanical Devices**, *Z. Diao*, National Institute for Nanotechnology, NRC Canada and University of Alberta, Canada, *V.T.K. Sauer, J.E. Losby, M.R. Kan, M.R. Freeman*, University of Alberta and The National Institute for Nanotechnology, Canada, *W.K. Hiebert*, National Institute for Nanotechnology, NRC Canada and University of Alberta, Canada

Nano-optomechanical systems (NOMS), in which guided light is utilized to actuate and transduce the motion of nanomechanical resonators, have received intense attention in recent years [1, 2]. This actuation and transduction scheme offers unprecedented displacement sensitivity and ultrahigh bandwidth, which is also able to be fully integrated with state-of-the-art opto-electronic and semiconductor technology. It can be envisioned that NOMS will see a large variety of applications in mass sensing, gradiometry, and high precision frequency counting.

Strong optical forces and large evanescent field gradient, both critical factors in defining the actuation efficiency and the motion transduction sensitivity in a nano-optomechanical system, only exist in a distance smaller than the wavelength of light from the nanophotonic waveguide. This requires the nanomechanical resonator in NOMS to be brought in close proximity to adjacent nanophotonic structures (normally in the range of 100 – 300 nm). A well known device failure mechanism in this case is stiction of released structures due to attractive forces with adjacent surfaces. A critical point drying process is so far conventionally utilized in NOMS fabrication to remedy this issue [1, 2].

In this work we report on our attempt in utilizing alternative device releasing protocols in fabricating NOMS structures. The test structure selected is a several tens of micrometers long doubly clamped beam embedded in a race-track nanophotonic resonator. The entire device was fabricated on a silicon-on-insulator substrate with deep-UV lithography. The race-track resonator possesses an optical quality factor of a few tens of thousands and a finesse of ~ 20 . The large finesse of the optical resonator allows sensitive motion transduction in which thermomechanical noise of a $\sim 10 \mu\text{m}$ long device was able to be detected. Device releasing methods tested include sublimation drying with dichlorobenzene and cyclohexane, and hard masked hydrofluoric acid vapour etching. Finally, we also discuss the influence of different device releasing methods on the photonic properties of the system and the undercut profile.

[1] M. Li et al., *Nature Photon.* **3**, 464 (2009).

[2] J. Roels et al., *Nature Nanotech.* **4**, 510 (2009).

11:00am **MN-TuM10 Optomechanical Experiments with Large Area Graphene Membranes**, *V.P. Adiga, R.A. Barton, I.R. Storch, B.R. Ilic, C.B. Wallin, P.L. McEuen, J.M. Parpia, H.G. Craighead*, Cornell University

Large area, ultra-thin membranes are useful as mechanical resonators whose mechanical degree of freedom can be easily controlled using light due to low spring constants and resonator mass. In this regard, there are advantages associated with using two dimensional materials like graphene and ultrathin silicon nitride. However, achieving large area suspended devices with high mechanical quality (Q) factors in these high surface-to-volume-ratio resonators has been a challenge. Recently it has been observed that the Q of these membranes can be significantly improved by a combination of tensile stress, resonator geometry and optimized fabrication techniques. Here we fabricate CVD grown, electrostatically tunable graphene drums of diameter up to 100 μm and measure high quality factors (up to 4000) at room temperature. We then use lasers to control the amplitude of mechanical vibrations using the back action provided by the photothermal effect. We can effectively cool (increase the effective damping) or heat (decrease the effective damping leading to self oscillation) the graphene membrane in a Fabry-Perot cavity formed by the membrane suspended over prefabricated trench, with cavity detuning provided by a highly reflective movable mirror. The strong optomechanical coupling observed in these membranes is due to the low mass and relatively strong absorption in the atomic monolayer.

1) *Cavity Optomechanics with Graphene Resonators*, R. A. Barton et al, Submitted.

11:20am **MN-TuM11 Optomechanics of Graphene Resonators**, *R.A. Barton, I.R. Storch, V.P. Adiga, R. Sakakibara, B.R. Cipriany, B.R. Ilic, S. Wang, P. Ong, P.L. McEuen, J.M. Parpia, H.G. Craighead*, Cornell University

By virtue of their low mass and stiffness, atomically thin mechanical resonators are attractive candidates for use in optomechanics. Graphene, in particular, is an ideal material to investigate as it possesses excellent electrical and mechanical properties as well as a strong interaction with

light over the entire visible range. Here, we demonstrate photothermal back-action in a graphene mechanical resonator comprising one end of a Fabry-Perot cavity. As a demonstration of the utility of this effect, we show that a continuous wave laser can be used to cool a graphene vibrational mode or to power a graphene-based tunable-frequency oscillator. In addition to enabling studies of fundamental physics, the remarkable sensitivity of graphene optomechanical resonators and their ability to operate over a broad range of wavelengths and mechanical frequencies makes them attractive for applications.

Nanomanufacturing Science and Technology Focus Topic

Room: 16 - Session NM+MS-TuM

All Invited Session: Challenges of Nanomanufacturing from an Industrial Perspective

Moderator: S. Butler, Texas Instruments, B.R. Rogers, Vanderbilt University

8:00am **NM+MS-TuM1 Challenges of Nanomanufacturing from an Industrial Perspective**, *A. Sekiguchi*, Tokyo Electron Limited **INVITED**

In the semiconductor industry, we have been able to benefit from cost reductions associated with physical scaling of memory and logic devices for decades. By reducing the physical dimensions of our devices from generation to generation, we have been able to drive bit cost of memory and processing power cost of our logic devices with ease. Today however, challenges associated with atomic scale manufacturing and control are daunting, to say the least. Dimensional controls are in the single nm range, six sigma, for lateral scales, and in the sub-Angstrom range for critical film thicknesses. The talk will describe the device level challenges that we face in this era of nano-scale manufacturing, explore options that we have in terms of patterning at 1x nm node and below, and discuss process options that will be needed in the next generation of devices.

9:00am **NM+MS-TuM4 PRINT® Nanomanufacturing Technology-Precisely Engineered Particles for Life Science Applications**, *M. Hunter*, Liquidia Technologies, INC. **INVITED**

Nanomedicine, an offshoot of nanotechnology, refers to highly specific medical intervention at the molecular scale for treating and curing disease or repairing damaged tissues, such as bone, muscle, or nerves. At this size scale – about 500 nanometers or less – biological molecules and structures operate inside living cells. The pharmaceutical industry continues to evaluate the potential of these new technologies to alleviate the burden of rising research costs, improve the speed and efficiency of the discovery process, and create high-value new generation therapeutics. While nanotechnology is widely seen as having huge potential, the pharmaceutical industry remains skeptical that success at the bench scale can successfully be translated into high volume products.

Liquidia's PRINT® technology (Particle Replication in Non-Wetting Templates) is one example of a breakthrough in micro- and nanoparticle manufacturing that allows complete control over particle size, shape and chemical composition. Since its inception, Liquidia has been addressing nanoparticle manufacturing scale-up by adapting the PRINT particle fabrication process to merge the high-volume production methodologies of roll-to-roll processing and the high precision fabrication methods of the microelectronics industry. Using PRINT technology, Liquidia has the ability to rapidly scale up cGMP manufacturing of particles with unprecedented control over the composition and geometry. This creates the unique ability to manufacture high volumes of complex micro- and nanostructured objects in a number of particle geometries and a variety of materials in a cost paradigm that is very attractive. Using manufacturing methodologies developed and proven in other industries including the printing, film and medical device industries, Liquidia plans to scale its particle manufacturing capabilities to supply commercial quantities for a variety of industries, including diagnostics, vaccines and therapeutics.

10:40am **NM+MS-TuM9 High Productivity Combinatorial R&D Technologies for Cost-Effective Nanomanufacturing**, *D. Lazovsky, C. Hunter*, Intermolecular, Inc. **INVITED**

Nanomanufacturing is inherently more challenging than the production of micron-scale and larger device structures, as interface effects increasingly dominate device performance for nano-scale devices. Theoretical understanding of such effects lags the results of practice, so empirical experimentation is necessary to simultaneously co-optimize multiple critical elements. Such co-optimization using traditional research and development (R&D) methods is typically inefficient, slow and expensive.

Cost-effective nanomanufacturing starts with the development of an optimized device structure, which depends upon our ability to learn about material interactions. For example, while a basic photovoltaic (PV) cell can be made with just 4 layers (n- and p-regions, two contacts), thin-film PV cells designed for optimum efficiency today use additional 10-50nm thick layers to modify band-gaps, optimize light reflection, and extract maximum current.

Even if an optimized nanodevice structure has been identified, it cannot be trivially transferred to high-volume manufacturing (HVM). Different tooling alters process conditions, which generally results in non-optimal final device performance as well as manufacturing yield losses. As an example, while the champion Cu(In,Ga)Se₂ (CIGS) cell from a lab has reached >20% conversion efficiency, the best reported from HVM lines today is only ~14%.

Once a nanomanufacturing line is running, experiments are needed to enhance device performance and improve line yield. However, it is inefficient to do R&D using the production line since the experiments must compete with manufacturing runs, and the HVM tools are generally not ideal for experiments. With inefficiency in R&D learning cycles, improving yield is slow and expensive.

A more efficient approach uses a high productivity combinatorial (HPCTM) platform—such as that developed by Intermolecular—to dramatically accelerate R&D by 10-100x relative to traditional methods. With unique combinatorial process tools, throughput-matched characterization, and an informatics analysis and data management system, in less than a year we developed a world-class 17.7% active-area efficiency CIGS PV cell using a two-step sulfur-free process flow.

Intermolecular's HPC platform is purpose-built for the R&D of semiconductor and clean-energy products, and is used in Collaborative Development Programs (CDPs) with a growing number of customers. For example, leading-edge semiconductor memory chips today use dielectrics and metal electrode layers that are only 1-10 nm thick, and HPC technology has accelerated R&D learning-cycles and time-to-market for our customers producing such memory chips.

Nanometer-scale Science and Technology

Room: 12 - Session NS+EN-TuM

One-Dimensional Nanowires and Nanotubes

Moderator: M.C. Hersam, Northwestern University

8:00am NS+EN-TuM1 **Direct Observation of Selective Band Engineering of an Isolated Subnanometer Wire.** *I. Song, D.-H. Oh, C.-Y. Park, J.R. Ahn*, Sungkyunkwan University, Republic of Korea

Band engineering has been achieved mainly by substituting an atom of a pristine nanomaterial with an extra atom. At the ultimate nanometer scale, subnanometer scale, a nanowire becomes closer to an ideal 1D system and the band engineering by the atomic substitution enters a different regime. The strong disorder by the atomic substitution tends to break a pristine 1D system. In the band engineering of the subnanometer wire (hereafter subnanowire), we need to find a way of circumventing the dilemma of doping and disorder. There is another challenging problem to find out a conclusive experimental proof that its electronic band structure is changed within a single isolated subnanowire. A unique experimental way is to measure its electronic band structure by angle-resolved photoemission spectroscopy (ARPES). Because a photon beam in ARPES measurement cannot be focused down to subnanometer scale, a single subnanowire cannot be used and rather subnanowires have to be aligned along a specific direction on a surface. A fundamental requirement to resolve the puzzling problem is that subnanowires have to be aligned by a self-assembly method. In comparison to the atomic structure, its electronic structure is required to be decoupled to observe a 1D electronic structure change of a single isolated subnanowire by a dopant. In this study, self-assembled subnanowires on a stepped surface, Au-induced subnanowires on a Si(553) surface, were chosen. A Si(553) surface, which is one of stepped Si(111) surfaces, has an appropriate terrace width to assemble subnanowires along its step edge direction and its step edge structure can decouple subnanowires electronically. Three different metallic subnanowires exist on its single terrace and each metallic wire has only a single metallic band. After extra Au atoms were adsorbed on the self-assembled subnanowires at room temperature, only one of metallic bands moved rigidly to a higher binding energy without a change in other metallic bands, which was directly observed by ARPES measurement. Here we note that if the three metallic subnanowires are coupled electronically to each other, all of the three metallic bands have to shift rigidly. This experimentally proves that only one of self-assembled multiple metallic wires can be controlled

electronically by a dopant and the electronic structure of an isolated wire can be controlled down to a subnanometer scale.

8:20am NS+EN-TuM2 **Growth of ZnO Nanowires on Retroreflector Microspheres and the Resulting Plasmonic Light Channeling Properties.** *S.M. Prokes, O.J. Gembocki, E. Cleveland*, Naval Research Laboratory

We investigated the growth of ZnO nanowires on retroreflectors in order to potentially enhance the optical response of these composite structures. Results show that the growth of ZnO aligned NW arrays can be achieved on the retroreflectors, but it occurs far away from the Zn vapor source compared to the standard ZnO nanowire growth on a flat Si substrate. In the case of the ZnO nanowires on flat Si, the nanowires that formed in nearly aligned arrays were short and significantly thicker, suggesting that the growth occurred both longitudinally and laterally in this process. For the NW growth on the curved retroreflectors, as the distance from the vapor source increased, the NW density increased and for the substrates farthest from the source, growth of nearly aligned NW arrays was noted. Initially, the ZnO growth on the retroreflectors resulted in a high rate of deposition of a polycrystalline ZnO film and as the amount of Zn vapor decreased, the vapor-solid (VS) nucleation of random NWs began, and aligned nanowire arrays only formed where the vapor supply was the lowest. The fact that it is more difficult to nucleate and grow ZnO NW arrays on the retroreflectors is likely due to the surface roughness, as well as the crystal structure of the retroreflector bead.

Once nearly aligned arrays of ZnO nanowires on the retroreflectors were formed, we investigated their optical properties by forming ZnO/Ag composite NW structures and using a self assembled monolayer of benzenethiol to measure a surface enhanced Raman (SERS) response. The ZnO/Ag NW composites were formed by atomic layer deposition (ALD) of Ag, and the surface enhanced Raman (SERS) response was measured and compared to nanowire composites deposited on a flat Si substrate. Results indicated that the SERS response was 29 times greater in the case of the ZnO/Ag NW aligned arrays grown on the retroreflectors. Since one would only expect a factor of 4 enhancement due to the light reflecting properties of the retroreflector, it is suggested that the enhancement in the SERS signal is due to light channeling by the nearly aligned nanowire arrays as a result of plasmonic effects. These results have been modeled using COMSOL electric field simulations, which support the light channeling concept.

8:40am NS+EN-TuM3 **Optical and Electrical Characteristics of Al-doped ZnO Nanowires Grown by Chemical Vapor Deposition.** *G. Shen, N. Dawahre, J. Waters, J. Krafcik, S.M. Kim, P. Kung*, University of Alabama, Tuscaloosa

Zinc oxide (ZnO) is a well-known major semiconductor material for optoelectronic devices due to its wide bandgap (~3.3 eV) and large exciton binding energy (~60 meV). One dimensional ZnO nanowires have been successfully synthesized by various techniques ranging from as simple as thermal chemical vapor deposition and solution growth, to more complex such as metal organic chemical vapor deposition, with good structural, optical and electrical properties. These are promising as an alternative to indium tin oxide as a more abundant, lower cost transparent window for a number of optoelectronic devices, including photovoltaics, while at the same time offering potentially more efficient electron charge transport. ZnO is also capable of harvesting the short wavelength spectral bands more efficiently.

In this work, we present the growth, doping and characterization of vertical well-aligned ZnO nanowire arrays. The wires are synthesized without metal catalyst by thermal chemical vapor deposition on basal plane sapphire substrates following the carbo-thermal reduction of zinc oxide powder. Control of the aluminum doping is accomplished by adjusting the ratio of Al and ZnO in the source material. The effects of doping and synthesis conditions on the nanowire optical and electrical properties are investigated through a number of techniques. The concentration of Al in the crystal is determined by energy dispersive spectroscopy, while atom probe tomography enables us to investigate the distribution of aluminum within the ZnO matrix. Micro-Raman spectroscopy and micro-photoluminescence, including their temperature dependence, are used to probe the vibrational and optical properties of the nanowires as a function of doping. It is observed that a defect related radiative green emission in ZnO is significantly reduced after Al doping. The electrical characteristics of undoped and doped nanowires are compared by leading electrical nano-connections to individual nanowires, which show a more than 1 order of magnitude decrease in the resistivity after doping down to 1 ohm.cm.

9:00am NS+EN-TuM4 **Rational Defect Engineering in Silicon Nanowires.** *N. Shin, M. Filler*, Georgia Institute of Technology
Group IV nanowires synthesized via the vapor-liquid-solid (VLS) technique do not frequently exhibit planar defects and/or polytypic domains. Even in

group III-V nanowires, where these structural motifs are common, rational control of their position remains challenging. Since defect energetics are similar in both systems, the observed structural differences are especially striking and indicate that the underlying physical phenomena are not sufficiently well understood. Here, we demonstrate how user-defined changes in surface chemistry near the triple-phase line can introduce twin planes and stacking faults during the growth of <111> oriented Si nanowires. More specifically, the addition of atomic hydrogen during Si nanowire growth enables {111} defects that begin at the <112> sidewall and continue to propagate across the nanowire even after the flux of atomic hydrogen ceases. Real-time *in-situ* infrared spectroscopy measurements reveal that covalent Si-H bonds are responsible for the defect initiation process and a simple mechanistic model will be presented to explain these results. Our findings are an important step toward a fundamental understanding of the chemistry that governs semiconductor nanowire synthesis and suggest a new route to engineer the properties of Si.

9:20am **NS+EN-TuM5 Ultrafast Carrier Dynamics of Si Nanowires Grown by LPCVD**, *A. Seyhan*, Tokyo Institute of Technology and Nigde University, Turkey Japan, *T. Ishikawa*, *S. Koshihara*, *M. Simanullang*, *K. Usami*, *S. Oda*, Tokyo Institute of Technology, Japan

This paper report the ultrafast carrier dynamics in silicon nanowires (NWs) grown by vapour-liquid-solid (VLS) mechanism in the low pressure chemical vapour deposition (CVD) reactor at 425°C. The femtosecond transient absorption measurements were studied by tuning probe wavelength in visible range to investigate the effect of pump and probe beam polarization, NW diameter, and pump fluence on the carrier dynamics. The fast carrier relaxation with lifetime of several picosecond in Si NWs can be attributed to surface trap states. This study has important implications in the understanding of ultrafast carrier dynamics of Si NWs.

9:40am **NS+EN-TuM6 Selective Deposition of Germanium Nanowire Segments via a Hybrid Oxide-Stabilized/Vapor-Liquid-Solid Growth Method**, *C.J. Hawley*, *T. McGuckin*, *J.E. Spanier*, Drexel University

The introduction low levels of oxygen during the vapor-liquid-solid growth (VLS) of germanium nanowires causes an oxide sheath to form at the catalyst/nanowire/vapor interface for the extent that the growth persists. This results in extremely high aspect ratio nanowires due to the removal of homoepitaxial deposition and the finite energy required for heterogeneous nucleation of germanium on its oxide. Furthermore, with the removal of oxygen, the catalyzed oxide sheath terminates and conventional growth with finite sidewall deposition dominates subsequent growth. The successful transition between the aforementioned oxide-stabilized and conventional VLS regimes can be deliberately manipulated to grow finite conical nanowire segments with discontinuous changes in diameter.

Work was supported by the U.S. Army Research Office (W911NF-08-1-0067).

10:40am **NS+EN-TuM9 Electronics and Opto-Electronics with Semiconducting Carbon Nanotube Arrays**, *M.B. Steiner*, IBM TJ Watson Research Center **INVITED**

While field-effect transistors made of single semiconducting carbon nanotubes have excellent electrical DC characteristics, the measurement of their AC characteristics is complicated and their output current is not sufficient for technological applications. Utilizing an array of semiconducting carbon nanotubes could resolve these problems. However, there are issues associated with the separation of carbon nanotubes with respect to the electronic type, their aligned assembly in high densities, as well as the scaling of device dimensions.

In this talk, I will present recent advancements with respect to the solution-assisted, electric-field driven assembly of highly separated (>99%) semiconducting carbon nanotubes into regular arrays on a device platform with embedded electrodes. The planar device platform is based on manufacturing processes known to the semiconductor industry and provides a basis for future enhancements of the carbon nanotube assembly and the scaling of critical device dimensions. Electrical transport measurements (AC and DC) of assembled carbon nanotube array transistors reveal intrinsic current gain cut-off frequencies of 150GHz and electrical current saturation behavior at a gate length of 100nm. The requirements for future applications of carbon nanotube array transistors in high-frequency electronics will be discussed.

In the second part of my talk, I will discuss high-resolution optical mapping of the internal electrostatic potential landscape of carbon nanotube array devices. Laser-excited photocurrent measurements provide insights into the physical principles of device operation and reveal performance-limiting local heterogeneities that cannot be detected with the electron microscope. The experiments deliver photocurrent images from the underside of nanotube-metal contacts and enable the direct measurement of the charge carrier transfer length at a nanotube-metal interface. Moreover, the external

control of the electrostatic potential profile in carbon nanotube array devices by means of local metal electrodes is demonstrated. The results are important for the design and optimization of optoelectronic devices based on carbon nanotube arrays, such as polarized light detectors and emitters.

11:20am **NS+EN-TuM11 Observation of the Impact of Pseudospin Conservation in Carbon Nanotubes**, *R. Tsuchikawa*, University of Central Florida, *Z. Zhang*, *X. Guo*, *J.C. Hone*, Columbia University, *M. Ishigami*, University of Central Florida

It has long been accepted that pseudospin conservation in metallic carbon nanotubes prevents backscattering by long-range potentials such as Coulomb potential. This unique property is expected to be valid only for metallic nanotubes [1]. Here, we have directly tested this yet untested theoretical result by measuring the impact of charged impurities on transport property of chiral-angle known carbon nanotubes. Single-walled carbon nanotubes (SWNTs) were grown to as long as a few hundred microns with minimal number of defects, followed by Rayleigh scattering spectroscopy to identify the chirality. In order to minimize the extrinsic impurities, electron transport measurements were performed in an ultra high vacuum environment after cleaning nanotubes down to atomic scale. Furthermore, we employed length-dependent resistance measurements to eliminate the impact of the metal-nanotube contact. Finally, transport property was measured at increasing coverage of cesium to determine the impact of charged impurities. Our results show chiral angle dependence of the impact of cesium and enable us to directly test the properties of pseudospin in carbon nanotubes.

1. P.L. McEuen, M. Bockrath, D.H. Cobden, Y.-G. Yoon, and S.G. Louie, Disorder, Pseudospin, and Backscattering in Carbon Nanotubes, Physical Review Letters, 83, 5098 (1999)

11:40am **NS+EN-TuM12 Properties and Application of Electronically Monodisperse Carbon Nanomaterials Functionalized with Nonionic Block Copolymers**, *J.-W.T. Seo*, Northwestern University

Carbon nanomaterials, including carbon nanotubes and graphene, have garnered significant attention from the research community in recent years. In an effort to refine their properties and better integrate them into device structures, chemical functionalization methods have been employed including aqueous dispersion with ionic surfactants, proteins, and DNA. While these strategies have proven effective for tuning the optical properties of carbon nanomaterials, the residual charge from the ionic dispersants complicate efforts to utilize them in electronic and/or electrochemical technologies. In contrast, we demonstrate here that nonionic, amphiphilic block copolymers (e.g., Pluronics and Tetronics) are effective surfactants for grapheneⁱ and carbon nanotubes,ⁱⁱ thus yielding chemically and electronically monodisperse samples without spurious charged impurities.

Pluronics and Tetronics are biocompatible block copolymers that are composed of hydrophilic polyethylene and hydrophobic polypropylene oxide domains. By tuning the relative length of these domains, their dispersion efficiency for carbon nanomaterials can be tailored. For example, Pluronics possess the ability to sort semiconducting single-walled carbon nanotubes (SWCNTs) via density gradient ultracentrifugation with shorter hydrophobic domains resulting in higher purity levels. Furthermore, Pluronic F68 has shown pH-sensitive, switchable sorting affinity towards both metallic and semiconducting SWCNTs, thus providing a novel route for the production of electronically monodisperse SWCNTs that are encapsulated with biocompatible, nonionic speciesⁱⁱⁱ. In addition to biomedical applications, the nonionic character of these block copolymers yields more reliable and enhanced performance of SWCNT-based electronic and electrochemical devices such as thin film transistors and lithium ion batteries.

Plasma Science and Technology

Room: 24 - Session PS1-TuM

Plasma Diagnostics, Sensors and Control 1

Moderator: V. Nagorny, Mattson Technology

8:00am **PS1-TuM1 Monitoring Plasma Etch Processes with Wave Cut-Off, Langmuir, and Radio-Frequency Probes**, *M.A. Sobolewski*, National Institute of Standards and Technology (NIST) **INVITED**

In industrial plasma etching processes, etch rates, profiles, and the critical dimensions of etched features may depend very sensitively on ion current density and other plasma parameters. The reproducibility of plasma conditions is thus an important concern, but the many mechanisms that can cause plasma properties to vary during processing have not been much studied. Here, such mechanisms were investigated using a wave cut-off

probe and a Langmuir probe, in tetrafluoromethane/argon plasmas in an rf-biased, inductively coupled plasma reactor. The wave cut-off probe provided measurements of plasma electron density every few seconds. Because it is based on a frequency measurement, it can precisely measure small changes in electron density, often as small as 1%. Internal resonances in the cut-off probe, however, can degrade this precision. The Langmuir probe provided measurements of the ion current density, electron and ion densities, and electron energy distribution function, with a time resolution of tens of seconds.

Several different phenomena were investigated. First, we investigated the changes in plasma electron density that occur when the rf bias is turned on or off. Analysis shows that such changes can be explained by the stochastic heating of electrons by rf bias power, the interaction of the rf bias and the inductive source, and perturbations in gas composition caused by etch products. Second, we investigated the changes in all plasma parameters that occur when etches of silicon dioxide films on silicon substrates reach endpoint. Analysis shows that the changes observed at etch endpoint were primarily due to changes in gas composition, rather than changes in electron emission from the wafer surface. Third, we also observed nonidealities in the inductive source that affect its ability to maintain constant plasma parameters.

Simultaneous with these measurements, the rf current and voltage were measured outside the reactor, in the rf bias and inductive source circuitry. These external measurements were strongly correlated to — and explained by — the wave cut-off and Langmuir probe data. These results strongly suggest that nearly all of the phenomena observed here can be monitored equally well by external rf measurements, instead of invasive probes.

8:40am PS1-TuM3 Impact of Self-Absorption on Emission Spectral Lines for Non-Equilibrium Plasma Source, *E. Gudimenko, V. Milosavljevic, S. Daniels*, Dublin City University, Ireland

Precise optical measuring techniques of spectral lines are necessary for low pressure plasma semiconductor manufacturing analysis. Problems which add to the inaccuracy of the optical measuring techniques include spectral line broadening mechanisms such as self-absorption.

Self-absorption has been widely neglected or its importance overlooked for plasma diagnostics.

In this study several different techniques are used to examine the impact of self-absorption on emission spectral lines from a reactive ion etch (RIE) plasma chamber, measured using a high resolution optical spectrometer. The experiments are performed in an Oxford Instruments plasma lab 100 RIE chamber which operates at a standard single frequency (GEC) 13.56 MHz with maximum RF power of 600 W. The OES spectrums were taken with a Horiba Jobin Yvon Czerny-Turner design Auto MicroHR spectrometer with focal length of 140 mm and spectral resolution of 0.25 nm at 400 nm wavelength.

One technique which is used is to check line intensity ratios within multiplets which abide by so-called LS-coupling rules. The time or spatial fluctuation in the observed intensity of the strongest or metastable line within the multiplet, in respect to the weakest spectral line in the same multiplet shows that self-absorption is present. Another technique which is examined is to change the optical path length by measuring the plasma from different points or different viewports on the plasma chamber. If the increase in signal intensity changes corresponding to optical path length, there is no self-absorption.

A Design of Experiments (DOE) has been used to cover the multidimensional external parameter space e.g. power, pressure, flow rate and chemistry. The results from the techniques are compared to each other for accuracy and the impact of self-absorption is then quantified. In this work the influence of self-absorption of neutral Argon and Oxygen spectral lines for a range of parameters in an RIE plasma chamber has been studied. Almost all the measured spectral lines have been affected, up to some level, by self-absorption. Some spectral lines shapes are changed by self-absorption up to 60%. One of the most widely used actinometry spectral lines for plasma diagnostics, Argon 750 nm, has its intensity affected by self-absorption by up to 40%.

Correction of self-absorption is a necessary step for OES based plasma diagnostics. In the case of Actinometry calculation correction of self-absorption could change the final result up to 20%.

This material is based upon works supported by Science Foundation Ireland under grant No.08/SRC/11411

9:00am PS1-TuM4 Real-Time Plasma Deposition Thickness Control using In Situ Optical Emission Interferometry, *D.J. Johnson, K.D. Mackenzie, C.W. Johnson, L. Martinez*, Plasma-Therm LLC

Measurement of the thickness of a growing film as it is deposited can provide real advantages in a production environment. Consistent film thickness is achieved despite long term process drifts and machine to

machine variations in deposition rate. Also the time lost due to system re-qualification after routine cleans and maintenance procedures can be reduced significantly.

In this work film thickness is measured in situ in a PECVD system by reflectance techniques, using the plasma emission as a light source (Optical Emission Interferometry, OEI). A parallel plate deposition system is described in which the plasma emission reflected from the substrate is monitored through one of the gas introduction holes in the upper electrode. During the deposition of silicon dioxide and silicon nitride films, the emission bands from molecular nitrogen in the 300 – 400nm region are used for measurement purposes. As the film thickness increases the reflected intensity undergoes a cyclical variation due to interference effects. The film thickness change for one complete cycle is known from the values of the wavelength and the refractive index of the film at that wavelength. The number of interference cycles, including fractional cycles is counted and the film thickness calculated in real time as the film is deposited. The process is terminated when the desired film thickness is reached. An example is shown where the long term variation in film thickness is significantly reduced as compared to running a process terminated by time alone.

For thin films (eg < 100nm) a series of interference cycles is not generated, so the “peak counting” approach cannot be used. Instead, multiple wavelengths (multiple nitrogen bands) are monitored, generating more data points which permits a more accurate determination of the film thickness. This approach is applied to the deposition of a 50nm silicon nitride film.

The above approaches strictly measure change in film thickness, not absolute film thickness. It is shown that by monitoring the complete spectrum and calculating the spectrum change with time, the result is equivalent to the differential of the film's reflectance spectrum. From this the absolute film thickness is calculated. This is particularly useful for the deposition of thicker films where a final film thickness is required, despite a variable or unknown starting film thickness. Although not discussed here, the same approach can be used when etching thick films down to a final required thickness.

9:20am PS1-TuM5 Subsequent Temporal Change of Gaseous H and N Radical Density in Plasma after Different Processes, *T. Suzuki, A. Malinowski, K. Takeda, H. Kondo, K. Ishikawa*, Nagoya University, Japan, *Y. Setsuhara*, Osaka University, Japan, *M. Shiratani*, Kyushu University, Japan, *M. Sekine, M. Hori*, Nagoya University, Japan

A precise shape control at less than 1 nm scale is demanded in large-scaled-integrated-circuits (LSI) fabrication of the 10-nm half pitch and beyond. In realization of super-fine plasma etching process, surface reactions of ions and radicals play important role because they determine etched feature^[1]. Thus control of actual plasma parameters such as substrate temperature, radical density, and electron density is required. It has been proved that the radical density is changed as a result of emission into bulk plasma both of etching products and adsorbed species on chamber wall. However, investigation of influence of inner wall condition on bulk radical density has not been studied yet. Thus, in this study we focused on gaseous radical density in H₂/N₂ plasmas, and investigated temporal changes subsequently after different kind of plasmas where inner wall condition could be changed.

Measurements of gaseous radical densities have been carried out by the Vacuum Ultra Violet Absorption Spectroscopy (VUVAS) equipped with a micro-discharge hollow cathode lamp (MHCL)^[2]. In this case we measured transition lines for Lyman α at 121.6 nm for H atoms and $^4P_{5/2}$ - $^4S_{3/2}$, $^4P_{3/2}$ - $^4S_{3/2}$ and $^4P_{1/2}$ - $^4S_{3/2}$ at 120.0 nm for N atoms. H₂/N₂ plasma was generated in a 100-MHz capacitively coupled plasma (CCP) reactor with H₂/N₂ gas mixture ratio of 75/25. Applied power was 400W (100 MHz) for upper electrode, and 200W (2 MHz) for bottom electrode respectively. The gaseous radical densities for the H₂/N₂ plasmas were monitored subsequently after different plasmas, (a) seasoning condition of H₂/N₂ plasma, (b) O₂ plasma, and (c) air exposure.

First, temporal changes for N radical density in the H₂/N₂ plasma subsequently, after the various plasma exposures were compared. In case of (a) seasoning, the N density was stable. On the other hand, the N radical densities were much varied after (b) O₂ plasma, and (c) air exposure. Notably, the density just after H₂/N₂ plasma ignition reached value which is more than twice higher when compared to stabilized value for (a) seasoning. Interpretation can be given as etched products or process gases were adsorbed on inner wall surface at the previous process, and then those species were desorbed from the wall into bulk plasmas in the subsequent processes. In accordance with organic low-*k* etching using H₂/N₂ plasmas, when a ratio of H radical and N radical (H/(H+N)) was changed more than 15% against an optimal original value, a shape of etched feature is resulted in modifications with scales of 10 nm^[1].

[1] M. C. Sung *et al.*, J. Appl. Phys. **107**, 113310 (2010).

[2] S. Takashima *et al.*, J. Vac. Sci. Technol. A **19**, 599 (2001).

10:40am **PS1-TuM9 Experimental Implementation of Real-time Multivariable Control of a Capacitively Coupled Plasma**, *Y. Zhang, B.J. Keville, C. Gaman, A. Holohan, M. Turner, S. Daniels*, Dublin City University, Ireland

The ever-increasing demand for higher device density in integrated-circuit fabrication has resulted in stringent requirements in respect of quality, reliability and precision of all fabrication processes in semiconductor manufacturing. *Reactive Ion Etching* (RIE) is a critical technology used at many stages of the manufacturing process. At present, most semiconductor manufacturing equipment is operated in open loop mode. Consequently, key plasma parameters such as ion flux and radical densities at the substrate surface are sensitive to drift in tool subsystems, changes in wall condition and wafer loading, for example. Such disturbances may affect process metrics such as etch depth and anisotropy and result in a significant degradation in device yield and performance.

In this presentation, we describe the implementation of a multi-variable *Linear Quadratic Gaussian/Loop Transfer Recovery* (LQG/LTR) controller to regulate key plasma parameters in an updated Mini-lab RIE 80 capacitively coupled chamber. The custom designed, real-time data-acquisition and control system has been implemented in Labview on a National Instrument CompactRIO real-time controller, which has been interfaced to a hairpin resonance probe and an optical emission spectrometer, the Ocean Optics USB4000. Experimental results are presented which compare the performance of the multivariable LQG/LTR controller to that of a suite of decentralised *single-input-single-output* (SISO) controllers.

This research forms part of program to implement multivariable closed-loop control on an industrial *Electron Cyclotron Resonance* (ECR) plasma etch chamber. The presentation concludes by describing progress in this part of the program.

11:00am **PS1-TuM10 Multivariable Control of a Capacitively Coupled Plasma**, *B.J. Keville, Y. Zhang, M. Turner*, Dublin City University, Ireland

Present practice in reactive ion etching specifies etch recipes in terms of inputs such as gas flow rates, RF power and pressure. However, ostensibly identical chambers running identical recipes may produce very different results. Extensive ‘chamber matching’, i.e. initial iterative, empirical tuning of the process recipe, which entails time-consuming, ex situ statistical analysis of etch metrics, is required to ensure that an etch chamber produces acceptable results. Once matched, etchers are run ‘open loop’ and are thus sensitive to disturbances such as actuator drift, wall seasoning and substrate loading, which may have deleterious effects on process metrics such as etch depth, uniformity, anisotropy and selectivity. An alternative approach, which would reduce sensitivity to disturbances of the plasma generating process, would be to specify a recipe in terms of plasma quantities such as radical densities, and to regulate these in real time by adjusting the inputs with a suitable multivariable control algorithm.

Multivariable closed loop control of an $SF_6/O_2/Ar$ plasma in an Electron Cyclotron Resonance (ECR) etcher is the focus of a major research program in the National Centre for Plasma Science and Technology (NCPST) in Dublin City University (DCU). As an intermediate step, a multivariable LQG/LTR control algorithm has been implemented on a capacitively coupled plasma using the same gas mixture. This presentation describes the design of the algorithm, and its efficacy is demonstrated via simulation with a variety of disturbances. The performance of the multivariable algorithm is compared to that of a suite of decentralised single-input-single-output (SISO) controllers.

11:20am **PS1-TuM11 Single and Multi-Point Ion Energy Distributions in a VHF+RF Commercial Reactor Measured by Novel In-Wafer Ion Energy Analyzer**, *B.G. Lane, M. Funk, L. Chen, R. Sundararajan, J. Zhao*, Tokyo Electron America

The energy distribution of the ions impacting the wafer is a key determinant of process results. A novel, all silicon, minimally perturbing, non-contaminating, in-wafer, 2 and 3 layer ion energy analyzer described elsewhere in this conference is used to measure ion energy distributions for a variety of realistic processing conditions in a commercial VHF + 13.56 MHz RF reactor with no modifications to its basic geometry or RF delivery system. Spectra with energies as high as 1 keV are measured with resolution on the order of 1%. Total ion transmitted flux as well as the floating potential of the plasma exposed 1st grid relative to ground are measured in addition allowing estimates of the plasma potential at the sheath edge. Measured energy spectra are compared to particle simulations aiding in the interpretation of the spectral features. We show data and discuss the splitting of the high energy peaks due to finite ion sheath crossing time effects and how this splitting scales with frequency, power and pressure. We discuss how such splitting can be used to estimate the ion density at the sheath edge. We discuss the origin and scaling of charge exchange peaks. We use the identification of atomic and molecular oxygen ion peaks to

estimate the resolution of the diagnostic. The use of VHF to obtain narrow ion energy distributions at moderate ion energies will be highlighted. Spectra using a multi-point, 2 layer variant of the ion energy analyzer design were obtained at 4 radial locations for a variety of conditions in argon and oxygen plasmas. These spectra quantify center to edge variations and reveal unique spectral features due to pre-existing modifications to the test reactor's upper counter electrode surface. We believe that these may be the first reported measurements of ion energy distribution functions for some of the more extreme conditions investigated and some of the first reported multi-point ion energy spectra for a commercial plasma reactor.

11:40am **PS1-TuM12 Characterizing Electron Beam Generated Plasmas for Plasma Processing Applications**, *D.R. Boris, R. Fernster, S.G. Walton*, Naval Research Laboratory

Electron beam generated plasmas have a variety of unique features that make them distinctive plasma sources for materials processing. They are characterized by high plasma density, very low electron temperature, and unique gas phase chemistries that distinguish them from discharge based plasmas. This work presents frequency probe and Langmuir probe measurements (where applicable) of plasma density over a range of 10^9 to 10^{12} cm⁻³ in a variety of processing plasma chemistries. This work also features the effect of varying gas chemistry on energy distribution function measurements as well as OES (optical emission spectroscopy) and mass spectrometry measurements.

Plasma Science and Technology Room: 25 - Session PS2-TuM

Advanced FEOL/Gate Etching 2

Moderator: J.P. Chang, University of California at Los Angeles

8:00am **PS2-TuM1 Gate-Silicon Etching using Evanescent Microwave Plasma for 22nm Technology Node and Beyond**, *A. Ranjan, S. Voronin, H. Kintaka, K. Kumar, P. Biolsi*, Tokyo Electron Technology Center, America, LLC, *R. Jung, S. Kanakasabapathy*, International Business Machines – Research Group, *A. Banik*, IBM T.J. Watson Research Center

Moore's law dictates continuation of shrinkage of transistors to make smaller, faster and less power-consuming devices at lower cost. FinFET (3-D) devices are needed to continue Moore's law. Anisotropy and selectivity requirements in FEOL etches (e.g., FinFET gate) are becoming very demanding and conventional RF plasma sources are hitting their limits to achieve such requirements. Microwave power delivered through radial line slot antenna generates over-dense evanescent microwave plasma just below top dielectric plate, and the electrons cool down (1eV or less in wafer region) due to inelastic collisions with the background gas. Low electron temperature (T_e), low self-bias (Vdc) and low plasma potential in evanescent microwave plasmas enable ‘soft’ etching for the 22nm generation and beyond technology nodes. In this study, Si-gate etching was performed in an evanescent microwave plasma system to achieve high selectivity over silicon oxide and silicon nitride with vertical profile. In addition to low self-bias, low T_e is required to obtain high Si selectivity over SiO₂ due to low-dissociation of by-products in evanescent microwave plasmas. Re-dissociated by-products (e.g., SiBr_x*) pull out O- from SiO₂ resulting in loss of Si selectivity over SiO₂. Low T_e (low re-dissociation) also helps with control of iso-nested CD-loading. High ion-flux with low T_e plasma yields vertical profile of Si independent of aspect ratio and with minimal iso-nested CD-loading. Various other interesting aspects will also be presented.

This work was performed by the Research and Development team at TEL Technology Center America in joint development with IBM Research Alliance Teams in Albany, NY 12222. This work was performed by the Research Alliance Teams at various IBM Research and Development Facilities.

8:20am **PS2-TuM2 Tracking Line Width Roughness Improvement during Gate Plasma Patterning**, *L. Vallier, E. Pargon*, CNRS, France, *N. Posseme*, CEA, LETI, MINATEC Campus, France, *L. Azarnouche*, CNRS, France, *S.D. Nemani, C. Rosslee, T. Pham*, Applied Materials Inc. The effect of line width roughness (LWR) on the performance characteristics of transistor gates becomes problematic as the critical dimension (CD) of the gate decreases. Minimizing the magnitude of LWR

in patterned features is becoming mandatory for the next technological nodes and is actually requested by the International Technology Roadmap for Semiconductor. Showing up particularly at 193nm wavelength exposure, the photoresist (PR) LWR is the main contributor to the final LWR measured in silicon gates following plasma patterning; therefore most of the effort is focused on the PR LWR reduction prior to the plasma transfer. At the same time, it was observed that the magnitude of LWR decreased when transferred from resist into the gate material. Plasma action might further help in the LWR reduction. In this work we have implemented the Power Spectrum Density (PSD) method as a measure of the LWR spatial frequencies distribution of a line, to monitor its evolution during the patterning of silicon gates with plasma etching process, starting from the PR after lithography up to the Silicon gate line. Thanks to the PSD method, noise coming up from CD SEM pictures of PR lines acquired at very low electron fluency can be subtracted, enabling a real LWR measure of the line with associated frequencies. A robust protocol for the CD SEM data treatment was developed and applied to various process conditions, aiming to obtain the best LWR reduction. Several cure treatment of the PR, achieved prior to the plasma etching of the gate, were investigated with the combination of UV light, plasma exposure using different gas chemistries, thermal treatment, pulsed plasma and E-beam exposure. This work confirms that the etch process can reduce the magnitude of roughness in silicon over a range of mid and high spatial frequencies, that is smoothing the line, however the extent of this roughness reduction vanishes as the resist LWR reaches its minimum. These results demonstrate that plasma action during the gate etch cannot improve the LWR much and post-etch LWR in silicon may be limited by the minimum LWR achievable in resist, therefore pushing for efficient PR cure treatment where plasma exposure play a key role. Based on the PR material used in this study which presents a 6.5 nm initial LWR value after lithography, a LWR of 2.9 nm was measured after the best LWR reduction process highlighting the need for further improvement to match the LWR requirement of the next technological nodes.

8:40am **PS2-TuM3 Plasma Prize Talk: Grand Challenges in Etch, R. Gotscho*, S. Sriraman**, Lam Research **INVITED**

Plasma etching has enabled the perpetuation of Moore's Law from >1 um to now less than 20 nm. More than ever, plasma etching is used to enable the extension of semiconductor device fabrication into the nanoelectronics age. The industry has always faced etch challenges due to scaling laws, especially as we begin to manufacture features that require atomic etch precision. Etch precision is especially challenging as the industry moves to 3D architectures, as we are etching electrically active layers in structurally complex features. Also, though we've always had to etch high aspect ratios, the fundamental challenge of aspect ratio dependent etching is now through alternating thin materials. The additional challenge to control wafer edge effects and reduce cost of consumables is ever more critical with compounding effects of multiple passes needed to compensate for lithographic limitations. In this presentation, I will give an overview of where we currently stand on our understanding of the origins and some solution approaches to the grand challenges in etch.

9:20am **PS2-TuM5 Spacer Patterning for Trigate SOI Devices, S. Barnola, P. Pimenta-Barros, L. Desvoivres, J. Pradelles, S. Barraud**, CEA, LETI, MINATEC Campus, France

Demonstrations of Trigate SOI devices recently reported highlight a better scalability with improved subthreshold slope and immunity to short channel effect for aggressively scaled CMOS Si devices. However, there are several key challenges in these devices to achieve high performance. Extremely narrow and uniform silicon fins are required combined with increased fin pitch in order to improve the effective channel width and then, the drive current. This work aims to demonstrate Si fin pattern with a width of 10nm and a fin pitch of 35nm. It is not possible to create 10nm dense active features by using only 193nm immersion lithography because of its optical limitations. Consequently, several approaches have been developed in order to reach ITRS predictions, such as e-beam lithography, Extreme UV, negative tone development, block copolymer, and Self-Aligned Double Patterning (SADP). Regarding the technical issues that remain to be solved for each approach, SADP is one of the most promising solutions for the 14nm technology node and below. SADP approach includes at least 3 steps (lithography, spacer deposition, spacer and Si etching) to divide by 2 the pitch of the 1st lithography. For practical reasons and for reducing the number of SADP steps, e-beam lithography has been used to create the "mandrel" patterns that support the spacers. The e-beam initial pitch is 70nm, whose CD has to be reduced to 25nm by a trimming step to reach the final 35nm pitch after SADP. The integration scheme investigated in this work includes the following steps: e-beam lithography with trilayer stack,

resist trimming, trilayer etching, SiARC removal, spacer deposition, spacer etching and SOC stripping. All plasma etching steps were carried out on 300mm ICP LAM VERSYS. One of the major challenges of this SADP integration was to limit the Si and SiO₂ consumption from the SOI substrate during the SADP process steps. We also had to consider the impact of the non-symmetrical spacers on the micro-loading effect during Si etching. Integration scheme with a buffer layer has been investigated to limit the Si and BOX consumption, but this approach makes CD control more complicated. Thus, we have compared the two integration schemes, with and without buffer layer, in term of CD control and profile to achieve the requirements for this FEOL application for SOI technology.

9:40am **PS2-TuM6 Key Challenges in FinFET FEOL RIE Processing at the 14nm CMOS Node and Beyond, R.M. Martin, A. Banik, J. Chang, R. Jung, S. Kanakasabapathy, M. Kobayashi, Q. Lin, B.G. Morris, S.C. Seo, T. Standaert, K. Stein, R. Sreenivasan, H. Wang, M. Yang, Q. Yang, Y. Yin, IBM Corporation, D.H. Choi, R. Kambhampati, T. Kwon, GLOBALFOUNDRIES**

For CMOS nodes at 22nm and below, the gate critical dimensions become small enough so that conventional methods for addressing issues such as short channel effects on planar devices become ineffective. Fortunately, alternative non-planar devices are becoming mature enough so that they can be used at these next generation technology nodes. Development of new processes to build such three dimensional structures present new challenges for both lithography and plasma etching. In this presentation, we will review processes for building finFET devices in the front end of line (FEOL) from a patterning perspective. Below 80nm print pitch, double patterning methods such as sidewall image transfer (SIT) and pitch split can be employed, however, these more complex methods require additional precision in the plasma etching profile and selectivity to avoid issues such as pitch walking and line edge roughness. Furthermore, at these smaller dimensions and with the complication of 3 dimensions, issues such as RIE lag become much more apparent. Challenges such as these, and some of their potential solutions will be discussed.

This work was performed by the Research Alliance Teams at various IBM Research and Development Facilities.

10:40am **PS2-TuM9 Patterning Options for 14nm Node and Beyond, Y. Yin, R. Jung, F. Lie, M. Beard, B.G. Morris, M. Hartig, S. Kanakasabapathy, IBM Res. at Albany Nanotech, Y. Mignot, STMicroelectronics, Y. Xu, C. Koay, IBM Res. at Albany Nanotech, L. Jang, GLOBALFOUNDRIES, N. Saulnier, J. Abdallah, H. Chen, IBM Res. at Albany Nanotech, M. Tagami, Renesas Electronics, K. Akarvardar, S. Akarvardar, GLOBALFOUNDRIES, J. Arnold, T. Spooner, M. Colburn, IBM Res. at Albany Nanotech**

Beyond the 22nm node, limitations of traditional patterning processes become critical. Conventional 193nm immersion lithography is not able to resolve features below 40nm half pitch with a single exposure for Front, Middle and Back Ends of Line. Patterning vias at appropriate CD and spacing is equally challenging. Until further wavelength scaling through Extreme Ultraviolet (EUV) the industry's attention is focused on Double Patterning. Pitch Splitting (PS) Lithography and Sidewall Image Transfer (SIT) are the two broad categories of techniques that have been under evaluation for sub-22nm nodes. Moreover, as we keep shrink the key features to dimensions of interest to sub-14nm nodes, innovations on existing double patterning techniques and the introduction of emerging patterning techniques such as directed self-assembly are needed in order to enable sub-40nm pitch features patterning. In this talk we will address the innovations further needed on existing double patterning methods and discuss the opportunities and challenges of emerging advanced patterning techniques in order to meet the patterning requirements for 14nm node and beyond. This work was performed by the Research Alliance Teams at various IBM Research and Development Facilities.

11:00am **PS2-TuM10 High-Efficiency Downstream Plasma Processes, L. Diau, R. Elliston, A. Kadavanich, C. Lee, V. Nagorny, H. PhanVu, O. Todor, V. Vaniapura, Mattson Technology**

Photoresist (PR) strip processes continue to improve with major IC technology node advances and architecture changes. One of the new technologies currently being implemented for the 2x nanometer node, high-κ metal gate (HKMG) has emphasized the need for enhanced reducing chemistry processes, which are also widely used in other strip-over-metal applications. Three-dimensional vertical architectures present great challenges for high aspect ratio (HAR) processing, and stacked structures often require low-temperature process capability. Control specifications for critical processes are further tightened as more new materials are introduced at advanced geometries. Industry-wide strip process enhancements have diverged into two directions: increasing RF power or adding bias. In either case, wafer surface temperature increases significantly, which introduces

* 2011 Plasma Prize Winner

pattern damage. Furthermore, there is increased risk of plasma-induced damage (PID). A new Mattson Technology dry strip source provides a solution to these challenges.

Based on the company's proprietary Faraday-shielded inductively coupled plasma (ICP) source technology, the new source offers these distinctive features: (1) a specially designed plasma generation volume with improved electron confinement that provides high efficiency of electron heating and enhanced plasma stability, and (2) a gas injection system that directs all the gas flow through this volume to increase efficiency of gas utilization. This results in efficient use of process inputs (power, gases) while simultaneously widening the operational window in terms of pressure, power, temperature.

The new source demonstrated significant increase of the PR removal rate and reduction of non-uniformity across different chemistries. One major benefit was observed with pure reducing chemistry. The new source with high power nearly doubled the ash rate, at 20% H₂ in N₂ with non-uniformity of <5%. Its impact on critical dimension (CD) and sheet resistance (Rs) were minimum and enabled better strip over metal process. O₂-rich reducing chemistry with high power was used in HAR PR removal in the middle-end-of-line (MEoL) contact container. It showed improved residue removal capability with challenging AR. One more time, Rs was well controlled over exposed metal liner with high power. CF₄-containing chemistry for amorphous carbon hard mask removal demonstrated improved productivity and selectivity over oxide and nitride at extremely low temperatures. Avoiding high power usage, the enriched reactant species allow HDIS process with dry only residue free, less pattern damage, lower silicon (Si) loss and controlled oxidation with different chemistries.

11:20am **PS2-TuM11 Challenges for Sub 20nm STI Etch**, *H. Zhou, X. Ji, S. Srinivasan, J. He, X. Hua, D. Heo, J. Choi, A. Khan, A. Agarwal, S. Rauf*, Applied Materials Inc.

With the feature size scaled down below 20nm, the plasma etching technology for shallow trench isolation (STI) becomes very challenging. The aspect ratio of the isolation trench can be as high as 20:1, and the space CD variation from double patterning is no longer negligible. Advanced processes and hardware are then required for the sub 20nm STI etch to minimize the depth loadings, i.e. intra-cell loadings. First approach is to trim the mask at the beginning to reduce the aspect ratio of the mask. With trimmed mask, the intra-cell loading is reduced. Second approach is realized with pulsed plasma. The period of pulsed plasma is ~ms, which is comparable to the residence times of typical plasma etch conditions. During the off cycle, the radicals/ions/byproducts have extra time to move out of the trench or act on the sidewall independently, and the sidewall polymer deposition is better managed. The advantage of pulsed plasma has been demonstrated with both 13MHz and 2MHz bias frequencies. Synchronized pulsed plasma etching has shown at least 40% improvement on CD-dependent depth loading than continuous wave plasma process. Moreover, 2MHz bias frequency also helps to round the trench bottom with higher energized ions. Another challenge for sub 20nm STI etch is profile control at extreme edge. Because of the plasma sheath bending effect, extreme edge trenches tend to tilt toward the wafer center. This issue can be fixed with a novel improvement of bottom electrode, which also improves the depth uniformity across the wafer. The ion flux with the novel bottom electrode is more uniform, in particular at the extreme edge locations. Compared to the standard electrode, the center to extreme edge trench depth variation has been reduced from 14.55% to 4.42% with the novel bottom electrode. Challenges for sub 20nm STI etch also include in-situ etching and line bending prevention, which will be also discussed.

Advanced Surface Engineering

Room: 22 - Session SE+PS-TuM

Pulsed Plasmas in Surface Engineering

Moderator: C. Mitterer, University of Leoben, Austria

8:00am **SE+PS-TuM1 Strong Localization of Ionization in High Power Impulse Magnetron Sputtering in Reactive and Non-Reactive Gas Environments**, *A. Anders*, Lawrence Berkeley National Laboratory
INVITED

Self-organized structures of plasmas in high power impulse magnetron sputtering (HiPIMS) have recently been observed by several groups. The structures move along the racetrack in the ExB drift direction but only with about 10% of the electron drift velocity (E and B are the electric and magnetic field vectors). The bright structures are zones of concentrated ionization: they can be related to the amplification mechanism of self-sputtering and gas recycling. The ionization zones can readily be observed with fast cameras providing time resolution of 1 microsecond or better. The

situation will be illustrated with images taken with a gated intensified frame image camera (Princeton Instruments) and with an intensified streak camera (Hamamatsu). Both end-on and side-on views to the magnetron are utilized. The side-on view reveals that each dense ionization zone is associated with an electron beam leaving the target region. Such beam maintains the quasi-neutrality of the plasma as ions are "evacuated" towards the target. The motion of the ionization zones is not a motion of plasma but a displacement of the region of greatest ionization. Its speed is mainly limited by the inertia of ions. The mechanism will be discussed and supported with images taken for various targets in noble and reactive gas atmospheres. Finally, the consequences of the localization of ionization for film formation will be considered in the greater context of energetic condensation.

8:40am **SE+PS-TuM3 The Magnetic Field Configuration's Effect on Plasma Parameters in High-Power Pulsed Magnetron Sputtering**, *H. Yu, L. Meng, P. Raman, T.S. Cho, D.N. Ruzic*, University of Illinois at Urbana Champaign

Magnetic field design is crucial in DC magnetron sputtering operation, but has been largely overlooked in high power pulsed magnetron sputtering (HPPMS). In a HPPMS discharge, plasma disperses after each short pulse, unlike in the DC operation which requires a good magnetic confinement to maintain the plasma. It is thus interesting to study the effect of magnetic field configuration on HPPMS discharge for further optimization. A special magnet pack was fabricated with the magnet positions fully adjustable. Different designs were made, with the corresponding magnetic field calculated by Comsol. For example, the magnetic field (B) strength in the racetrack was varied, as 200, 500, and 800 Gauss. Different racetrack shapes were used, such as ring-like and bean-like. Designs were also made to have incomplete racetrack, and weak racetrack in which piles of magnets were placed evenly across the whole pack and polarities of adjacent piles were opposite. These magnetic configurations were then tested in a large magnetron system with a 36 cm target using a conventional HPPMS plasma generator. The I-V discharge characteristics were measured. A time-resolved triple Langmuir probe was employed to study the temporal evolution of electron temperature (T_e) and density (n_e) across the substrate. Ionization fractions of sputtered metal were also measured using quartz crystal microbalance combined with electrostatic filters. The results showed that higher B field strength and longer racetrack produced higher pulse current. The 500 Gauss configuration however had higher n_e in the pulse than 800 Gauss did, likely because it allowed easier plasma diffusion. In all the designs with a racetrack, the distribution of n_e on the substrate was non-uniform that n_e was typically about 10 times higher right below the racetrack than at the center. The weak racetrack configuration was found to work and showed certain superiority over the normal DC magnet design. The plasma was generated from almost the entire target surface indicating an improvement in target utilization without the need for rotation. The discharge current was comparable with the racetrack designs. Furthermore, the plasma density distribution over the substrate was very uniform.

9:00am **SE+PS-TuM4 Plasma Generation and Transport in High-Power Pulsed Magnetron Sputtering**, *L. Meng, H. Yu, T.S. Cho, D.N. Ruzic*, University of Illinois at Urbana Champaign

High power pulsed magnetron sputtering (HPPMS) processes, including its potential application in interconnect metallization during microfabrication, require a precise control of fluxes and energies of various plasma species. A more fundamental understanding of the pulsed discharge mechanisms and the underlying physics thus becomes necessary. In a 36 cm planar magnetron system, a triple Langmuir probe was used to study the time-resolved behaviors of the HPPMS plasma under various discharge and pulsing parameters, as well as at different positions extending from the target surface. The pulsed plasma was shown to be established through multiple stages. And the 3-dimensional probe characterization depicted a scenario of plasma expansion from the plasma-confined racetrack, producing high density peaks up to 10^{19} m^{-3} into the pulse-off period. The delay time of these peaks from the pulse-off edge varied from several to several hundred μs with different probe positions, and was found to depend on the plasma density in the racetrack which affects the diffusion constant, and the temporal location of the peak plasma density in the racetrack as well. In addition to the probe measurements in the vicinity of the racetrack, a special setup with quartz crystal microbalance and current collecting plate behind orifices drilled in the target was designed. Ion fluxes to the cathode were directly measured, while the metal ion and argon ion fluxes were distinguished time-averagely. The self-sputtering theory of HPPMS is supported by a higher metal ion fraction measured at a higher pulse peak current. Based on the above experiments, a 1-dimensional time-dependent HPPMS discharge model was developed incorporating the surface reactions, ionization process in the plasma, and plasma diffusion. It was able to describe the essential processes of plasma buildup and dispersion, and to predict some important plasma properties such as density and

ionization fraction from the basic inputs of magnetic field, discharge and pulsing parameters, etc.

9:20am **SE+PS-TuM5 Metallic Film Modification through the Use of Non-standard HiPIMS Waveforms**, *P.M. Barker, E. Lewin, J. Patscheider*, EMPA, Switzerland

High power impulse magnetron sputtering, HiPIMS, has been the source of significant scientific interest in recent years. HiPIMS consists of a high voltage / high current pulse, followed by a long off-period resulting in low duty cycles. In the present study additional control parameters are explored by using non-standard HiPIMS waveforms, consisting of pulse sequences. These pulse sequences consist of a number of micro-pulses, which can be varied in length. In a further novel approach to HiPIMS, the pulses were also applied in a bi-polar manner, with a positive voltage supplied to the same target between negative voltage pulses. Films have been grown using varied pulse sequences, in both uni- and bi-polar mode, and compared to materials grown both by traditional, single pulse, HiPIMS and dcMS. The deposition of Ti metal was chosen as a model system, and the attained coatings were analysed using X-ray diffraction, XRD, scanning electron microscopy, SEM, and X-ray photoelectron spectroscopy, XPS. An increased deposition rate, relative to a comparable standard HiPIMS pulse, was observed. The coating microstructures show increased smoothening of the coating surface and shallower surface oxidation for samples deposited using micro-pulsed HiPIMS.

10:40am **SE+PS-TuM9 Reactive Modulated Pulse Power Magnetron Sputtering of Molybdenum Oxides: Optical Behavior as a Function of Process Parameters**, *N.R. Murphy*, Air Force Research Laboratory, *L. Sun*, General Dynamics Information Technology, *J.T. Grant*, University of Dayton Research Institute, *J.G. Jones, R. Jakubiak*, Air Force Research Laboratory

Molybdenum oxide, a material prized for its ability to facilitate thermochromism and electrochromism, has displayed considerable sensitivity to oxygen concentrations present during reactive DC magnetron sputtering. Typical depositions performed using continuous reactive DC magnetron sputtering have demonstrated low deposition rates and limited control over stoichiometry as a result of oxygen induced target poisoning. In the following study, molybdenum oxide films were deposited using reactive modulated pulse power magnetron sputtering (MPPMS) using a 99.999% pure molybdenum sputtering target within an argon-oxygen atmosphere. At a pressure of 10 mTorr, the oxygen concentration was varied between 1 and 20%. The resulting films were characterized by way of in-situ spectroscopic ellipsometry, x-ray photoelectron spectroscopy, x-ray diffraction and UV-visible spectroscopy. The as-deposited films were determined to be amorphous by way of x-ray diffraction analysis and were analyzed without any prior heat treatment. *In-situ* spectroscopic ellipsometry was conducted throughout the deposition process, monitoring real time changes in the refractive index, extinction coefficient and thickness of the film.

11:00am **SE+PS-TuM10 Cathodic Arc Plasma of AlCr Composite Cathodes in Inert and Reactive Atmospheres**, *R. Franz, J. Wallig*, Lawrence Berkeley National Laboratory, *P. Polcik*, PLANSEE Composite Materials GmbH, Germany, *A. Anders*, Lawrence Berkeley National Laboratory

In the past, the distributions of ion charge states of vacuum arcs have been studied in great detail under various conditions, including their dependence on arc current level, strength of a magnetic field (if present), pressure and kind of background gases, and the distance from the plasma-producing cathode spots. Most of the work was done using pure elementary cathodes since the presence of two or more elements in the cathodes would most likely further complicate the situation when studying the physics of cathodic vacuum arcs. However, in many practical applications ternary or quaternary thin films are used. For their synthesis it is common to employ composite cathodes consisting of the elements of interest.

In the field of hard and wear-resistant coatings, thin films based on the system aluminium and chromium represent the state of the art. With the addition of nitrogen and/or oxygen ceramic coatings covering a wide compositional range can be synthesised. In the present study, a time-of-flight spectrometer was used to investigate the arc plasma composition in terms of elemental and ion charge state composition when using Al_xCr_{1-x} ($0 \leq x \leq 1$) composite cathodes in different gaseous environments, i.e. in vacuum as well as argon, nitrogen and oxygen atmosphere. The observed ion distributions were interpreted in the established framework of plasma generation at cathode spots and ion-gas interactions.

Surface Science

Room: 21 - Session SS-TuM

Surface Reactivity of Oxides

Moderator: A.L. Utz, Tufts University

8:00am **SS-TuM1 Preparation, Characterization and Catalytic Activity of Model WO_3 Catalysts**, *Z. Dohnalek*, Pacific Northwest National Laboratory **INVITED**

Supported early transition metal oxides have important applications in numerous catalytic reactions. In our studies, conversion of small aliphatic alcohols to alkenes, aldehydes/ketones, and ethers is employed to probe the structure-activity relationships on model WO_3 catalysts. To understand how the structure and binding of WO_3 species affect catalytic properties we prepared a number of well-characterized systems. Direct sublimation of WO_3 solid was used to generate cyclic gas-phase (WO_3)₃ clusters. As shown in our matrix isolation experiments, sublimation leads to pure (WO_3)₃ clusters. The (WO_3)₃ clusters were embedded in alcohol matrices and their support-free chemistry was explored in subsequent temperature programmed reaction experiments. Model supported catalysts were created by depositing (WO_3)₃ clusters on $TiO_2(110)$ and $FeO(111)$ and subsequently characterized using scanning tunneling microscopy and surface sensitive spectroscopies. In other studies, epitaxial and nanoporous thin WO_3 films were prepared on Pt(111). The catalytic chemistry of all the systems is compared and contrasted with that observed on unsupported (WO_3)₃ clusters. Calculations employing Density Functional Theory provide molecular-level mechanistic insight into the role structure and binding of (WO_3)₃ clusters to the support plays in determining their catalytic properties.

This work was supported by the US Department of Energy, Office of Basic Energy Sciences, Division of Chemical Sciences, Geosciences & Biosciences and performed in Environmental Molecular Sciences Laboratory (EMSL), a national scientific user facility sponsored by the Department of Energy's Office of Biological and Environmental Research and located at Pacific Northwest National Laboratory (PNNL). PNNL is a multiprogram national laboratory operated for DOE by Battelle.

8:40am **SS-TuM3 EUV Photon Enhanced Oxidation of Carbonaceous Layer at a TiO_2 Film Surface**, *N.S. Faradzhev, J.T. Yates, Jr.*, University of Virginia, *S.B. Hill, T.B. Lucatorto*, National Institute of Standards and Technology

We report the photo oxidation of a carbonaceous layer originally grown by 92 eV radiation-induced chemistry. The C film is supported on a surface of a nm thick amorphous TiO_2 film. Photo oxidation is achieved using various oxygen-containing molecules. The TiO_2 film mimics one of the possible protective layers of EUV Lithography optics, and the C film mimics optics contamination produced by 92 eV photons in a EUVL stepper apparatus. The C layer (~4 nm) is deposited by photodecomposition of the linear hydrocarbon molecule, *n*-tetradecane, using the NIST synchrotron ultraviolet facility (SURF III) in an UHV cell. The kinetics of C growth and C removal are monitored in real time using *in situ* single wavelength ellipsometric measurements. After each set of experiments, *ex-situ* XPS is used to detect the residual thickness of the carbonaceous film and the changes in its chemical state. We found that exposure to a vapor beam of several O-containing molecules has little or no effect on the C film in the dark. In the presence of EUV photons, the ability of these molecules to volatilize carbon as either CO or CO₂ increases significantly. The carbon removal rate increases with the partial pressure of the oxidizer. The substrate temperature has little effect on the carbon removal rate and this is in contrast to the rate of radiation-induced C growth that exhibits a very strong temperature dependence. The rate of removal of C depends upon the EUV irradiation and does not occur appreciably in the dark.

Although the studies are not finished yet, our results indicate that processes of C growth and C removal may proceed via different routes. In an earlier study, we found that during C growth, the hydrocarbon molecule arrives at the surface in its ground state and forms a weak bond to the bare or C-covered TiO_2 surface. The molecule is not trapped permanently and will thermally desorb within a characteristic time. It can also be either photo-desorbed or photo-decomposed to produce the carbonaceous film via direct (photo excitation) or indirect (secondary electron excitation, e.g. DEA) processes. For photo oxidation, the first step requires the formation of a strong bond of the oxidizer molecule to the surface. An oxidizer molecule will either arrive at the surface in an electronically excited molecular state or arrive in its ground state and find an EUV-activated long-lived electronically excited state at the surface. In both cases, the oxidizer molecule will stay on the surface for a sufficiently long time to decompose and react to produce a volatile product (e.g. CO).

This study is being performed as a part of EUVL Contamination cooperative research at NIST and UVA.

9:00am **SS-TuM4 Reactions of Water with Vacuum Fracture Surfaces of Sodium-Aluminosilicate Glass: Effects of Composition on Reactivity**, *K. Adib, J.E. Dickinson*, Corning Incorporated

We have synthesized different ternary $\text{SiO}_2:\text{Al}_2\text{O}_3:\text{Na}_2\text{O}$ glasses containing bridging oxygens and non-bridging oxygens (NBO) and fractured them in ultrahigh vacuum to produce pristine surfaces. X-ray photoelectron spectroscopy of oxygen core levels and valence band were used to determine the fraction of non-bridging oxygens (SiONa) to bridging oxygens (SiOSi and SiOAl) on the vacuum fractured surfaces. For those glasses where the NBO fractions of the total oxygen were held constant, a 0.2 eV variance was observed in the binding energies of the NBO O1s core levels consistent with substantial changes, as a function of composition, in the ionicity of the bond between the NBO and sodium. The fracture surfaces were then exposed to partial pressures of H_2O at ambient temperature. It was observed that water reacts primarily with the NBO's to produce SiOH in place of SiONa. Non-bridging oxygens from glass compositions that contained less alumina had lower electron binding energy and were more likely to react with water. Molecular dynamics simulations were used to elucidate the role of H_3O^+ in the reaction of water with the non-bridging oxygens.

9:20am **SS-TuM5 Reactivity of Highly-hydroxylated $\text{TiO}_2(110)$ Surface Prepared via Carboxylic Acid Adsorption and Photolysis**, *I. Lyubnitsky, Y.G. Du, N.G. Petrik*, Pacific Northwest National Laboratory, *N.A. Deskins*, Worcester Polytechnic Institute, *Z.-T. Wang, M.A. Henderson, G.A. Kimmel*, Pacific Northwest National Laboratory

We present a novel, photochemical approach to prepare a highly-hydroxylated $\text{TiO}_2(110)$ and discuss the reactivity of the resulting surface. $\text{TiO}_2(110)$ surfaces with an OH_b coverages up to 0.5 ML have been obtained upon trimethyl acetic acid (TMAA) dissociative adsorption and subsequent photolysis at 300 K. The formation and chemistry of such surface have been examined at the atomic level by a combination of scanning tunneling microscopy, temperature-programmed desorption, photo stimulated desorption, and density functional theory methods. Deprotonation of TMAA molecules upon adsorption produces both surface bridging hydroxyls (OH_b) and bidentate trimethyl acetate (TMA) species with saturation coverage of near 0.5 ML. The TMA species can be selectively removed by ultra-violet light irradiation while OH_b 's survive photolysis. At high coverages, the OH_b species typically occupy second-nearest neighbor sites along the bridging oxygen row locally forming linear (2×1) structures of different lengths, although the surface is less ordered on a long scale. The annealing of the highly-hydroxylated surface leads to hydroxyl recombination and H_2O desorption with $\sim 100\%$ yield, thus ruling out the diffusion of H into the bulk. In agreement with experimental data, theoretical results show that the recombinative H_2O desorption is preferred over both H bulk diffusion and H_2 desorption processes.

9:40am **SS-TuM6 Infrared Spectroscopy of CO_2 Adsorbed on $\text{TiO}_2(110)$** , *N.G. Petrik, G.A. Kimmel*, Pacific Northwest National Laboratory

We have studied the adsorption of CO_2 on $\text{TiO}_2(110)$ using reflection-absorption infrared spectroscopy (RAIRS) and temperature programmed desorption (TPD). Infrared spectra were obtained for s- and p-polarized light with the plane of incidence parallel and perpendicular to the [001] azimuth of $\text{TiO}_2(110)$. As a result, the RAIRS provide detailed information on the adsorption geometry for the CO_2 versus coverage. Initially, CO_2 adsorbs in vacancies in the bridge-bonded oxygen (BBO) rows with the peak for the asymmetric stretch seen at 2346.5 cm^{-1} for both s- and p-polarized light. Hydroxylation or oxidation of the vacancies suppresses this feature. After filling the vacancies, CO_2 adsorbs on Ti_{5c} sites ($\text{CO}_2(\text{Ti})$). The asymmetric stretch for $\text{CO}_2(\text{Ti})$ starts at $\sim 2342 \text{ cm}^{-1}$ and then red-shifts to 2332 cm^{-1} at 1 ML. CO_2 TPD spectra show that the shift in the RAIRS spectra correlates with a decrease in the CO_2 binding energy from ~ 47 to $\sim 34 \text{ kJ/mol}$ as the coverage increases from 0 to 1 ML. For $\text{CO}_2(\text{Ti})$, the absorbances for the s-polarized spectra are similar for both azimuths indicating that the ensemble-average of the adsorbed CO_2 has approximately equal components along both azimuths. The p-polarized RAIRS spectra show that $\text{CO}_2(\text{Ti})$ also adsorbs with a component normal to the surface. Between 1 and 1.5 ML, CO_2 adsorbs on BBO sites. These CO_2 absorb only s-polarized light with its plane of incidence parallel to the BBO rows indicating that the molecules are oriented parallel to the surface and perpendicular to the BBO rows. The CO_2 RAIRS spectra are compared with STM results and DFT theory to provide detailed insight into its molecular orientation and coverage-dependent mobility.

10:40am **SS-TuM9 Low-temperature Dissociation of CO_2 on Ni/CeO₂/Ru(0001) Model Catalyst**, *D.D. Kong*, University of Science and Technology of China, *K.-H. Ernst*, EMPA, Switzerland, *J.F. Zhu*, University of Science and Technology of China

Model Ni/CeO₂(111) catalysts were prepared by depositing nickel atoms onto well-ordered cerium oxide films grown on Ru(0001) and were investigated using photoelectron spectroscopy (XPS) and reflection absorption infrared spectroscopy (RAIRS). It is found that the fully oxidized CeO₂ thin films are slightly reduced to CeO_{1.97} after 0.2 ML Ni deposition. When CO_2 is exposed to the surface of clean CeO₂(111) film at 97 K, the physisorbed linear molecular CO_2 and carboxylate species are observed. However, on the CeO₂(111) surface covered with 0.6 ML Ni, CO_2 immediately dissociates upon adsorption at 97 K, leading to the formation of Ni-CO adsorbates and partial oxidation of Ni nanoparticles. This dissociation activation of CO_2 is inhibited when Ni nanoparticles on CeO₂ are pre-oxidized. In contrast to the results reported for CO_2 adsorption on Ni single-crystals where the dissociation temperature was found to be higher than 240 K, the much lower dissociation temperature ($\sim 97 \text{ K}$) for CO_2 on Ni nanoparticles supported on CeO₂(111) suggests that the Ni/CeO₂ catalyst exhibits high activity toward CO_2 activation.

11:00am **SS-TuM10 Adsorption and Diffusion of Acetone on Rutile $\text{TiO}_2(110)$** , *B. Zhang, Y. Xia*, Baylor University, *J. Ye, Q. Ge*, Southern Illinois University Carbondale, *Z. Zhang*, Baylor University

Understanding the surface reaction processes of acetone on metal oxide surfaces is important for photo-oxidation of toxic organic molecules. We have studied the adsorption and the diffusion of acetone on reduced rutile $\text{TiO}_2(110)$ surfaces using variable temperature scanning tunneling microscopy (STM). At room temperature (RT) acetone molecules prefer to adsorb on bridging-bonded oxygen vacancy sites. The sequential isothermal STM images show that acetone molecules are mobile at RT. They hop between unoccupied vacancy sites via both apparent along-row diffusion and apparent cross-row diffusion processes. Images obtained at temperatures below RT show that there are two barriers involved in these diffusion processes: (1) the diffusion barrier along the Ti row, and (2) the barrier from the vacancy site to the neighboring Ti row. The latter is the rate limiting step. DFT calculations agree with experimental results.

11:20am **SS-TuM11 Variations in Reactivity for Acetaldehyde and Acetic Acid with the Crystallographic Orientation of Cerium Oxide Thin Films**, *P.M. Albrecht, D.R. Mullins*, Oak Ridge National Laboratory

Cerium oxide is a vital component in many heterogeneous catalytic processes. The various crystallographic faces of ceria present significantly different surface structures and compositions, which may result in an orientation-dependent catalytic reactivity. The structure and composition determine the availability of adsorption sites, the spacing between those adsorption sites, and the ability of surface O to participate in a reaction. The adsorption and reaction of various oxygenated hydrocarbons on cerium oxide surfaces are of interest from the standpoint of understanding the catalytic properties of the material. Studies on the interactions of alcohols, aldehydes, ketones, and carboxylic acids on well-defined CeO₂ surfaces have been motivated predominantly by the rich chemistry produced by the variation in the Ce oxidation state and the associated O vacancies. Alcohols, carbonyls, and carboxylic acids vary significantly in their strength of interaction with the surface and consequently in their reaction products. Here, we report a study of the adsorption and dissociation of acetaldehyde (CH_3CHO) on CeO₂(100). CeO₂(100) films were grown by pulsed laser deposition on Nb-doped SrTiO₃(100). In addition to the fully oxidized CeO₂(100) surface, experiments were conducted on reduced surfaces containing $\sim 60\%$ Ce^{3+} ($\text{CeO}_{1.7}$) prepared by methanol exposure at 660 K. Reaction products were monitored by temperature programmed desorption (TPD), and surface intermediates were determined by soft x-ray photoelectron spectroscopy (sXPS) and near-edge x-ray absorption fine structure (NEXAFS). The key result is that acetaldehyde reacts with oxidized CeO₂(100), whereas it does not react with oxidized CeO₂(111). The most intense products are CO, CO_2 , and water, with trace amounts of crotonaldehyde and acetylene. On reduced CeO_{1.7}(100), the oxygenated products are largely eliminated and ethylene and H_2 are produced. Residual C is also left on the surface. Recent results indicate that the chemistry of acetic acid (CH_3COOH) is also significantly different on CeO₂(100) compared to CeO₂(111). Acetone is a major product on CeO₂(100) whereas only a trace amount of ketonization occurs on CeO₂(111). Research sponsored by the Division of Chemical Sciences, Geosciences, and Biosciences, Office of Basic Energy Sciences, US Department of Energy, under contract DE-AC05-00OR22725 with Oak Ridge National Laboratory, managed and operated by UT-Battelle, LLC. Use of the National Synchrotron Light Source, Brookhaven National Laboratory, was supported by the US Department of Energy, Office of Science, Office of Basic Energy Sciences, under Contract No. DE-AC02-98CH10886.

11:40am **SS-TuM12 The Entropies of Adsorbed Molecules**, C.T. Campbell, J.R.V. Sellers, University of Washington

Adsorbed molecules are involved in many reactions on solid surface that are of great technological importance. As such, there has been tremendous effort worldwide to learn how to predict reaction rates and equilibrium constants for reactions involving adsorbed molecules. Theoretical calculation of both the rate constant and equilibrium constant for such reactions require knowing the standard entropy and enthalpy of the adsorbed molecule. While much effort has been devoted to measuring and calculating the enthalpies of well-defined adsorbates, few measurements of the entropies of adsorbates have been reported. We present here a new way to determine the standard entropies of adsorbed molecules (S_{ad}^0) on single crystal surfaces from temperature programmed desorption data, prove its accuracy by comparison to entropies directly measured using equilibrium adsorption isotherms on MgO(100), and apply it to published data to extract new entropies. Most importantly, when combined with reported entropies, we find that at high coverage they linearly track the entropy of the gas-phase molecule at the same temperature (T) as:

$$S_{ad}^0(T) = 0.70 S_{gas}^0(T) - 3.29R,$$

with a standard deviation of only 2R from 0 to 60R, where R is the gas constant. These entropies, which are $\sim 2/3$ of that for the gas, are huge compared to most theoretical predictions (e.g. the harmonic approximation commonly employed in combination with DFT estimates of reaction barriers). This relationship applies at temperatures where desorption rates are fast enough to perform EAI and TPD measurements ($\sim 10^{-3}$ to 100 monolayers/s). It provides an important tool to aid in estimating equilibrium constants and rate constants for reactions where these adsorbates are involved, as proven here for prefactors in the Arrhenius rate constant for desorption. The prefactor can be estimated as:

$$v = (k_B T/h) \exp\{0.30 S_{gas}^0(T)/R + 3.29 - 9.31 \ln[(m/m_{Ar})(T/298K)]\},$$

where m/m_{Ar} is the mass of the adsorbate relative to Ar. For longer adsorbed molecules where $S_{gas}^0(T)$ exceeds 60 K (e.g. linear alkanes with >11 carbons), their entropies remain a constant 20.7R below gas entropies, and $\sim 10.4R$ below Trouton's Rule for liquid entropies.

Work supported by NSF under CHE-1010287.

Thin Film

Room: 11 - Session TF-TuM

ALD Reactions and Film Properties

Moderator: H. Kim, Yonsei University, Korea

8:40am **TF-TuM3 Growth Simulations for Atomic Layer Deposition: Adsorption, Elimination and Densification Reactions**, S. Elliott, M. Shirazi, Tyndall National Institute, Ireland **INVITED**

The central idea in chemical vapour deposition (including atomic layer deposition, ALD) is that the thermodynamic tendency of atoms to aggregate and bond into a solid film can be delayed by surrounding the atoms with ligands and transporting the molecular complex as a vapour. Deposition thus involves adsorption of the molecule, removal of ligands and a concomitant increase in atomic coordination number as the solid is formed. The focus is often on adsorption and ligand removal, while the change in coordination during growth, which has been termed 'densification' [1], has often been neglected.

We apply first principles density functional theory (DFT) to the $Hf(NR_2)_4 + H_2O$ system for the ALD of HfO_2 , which reveals how important densification can be in explaining the characteristics of oxide ALD. We consider $R=Me$ but expect that similar reactions occur for larger R. Transfer of H from the surface to the ligand is strongly affected by rotation of the ligand around the Hf-N bond, which in turn depends on the crowding associated with proximity of Hf to the surface. Dissociation of $HfNR_2$ is facilitated if multiple ligands on an adsorbed Hf centre are protonated, contrary to the usual assumption of dissociation one by one. Once sufficient protonated ligands have desorbed, Hf is freed up to bond to more surface O (densification), with substantial release of energy. Thus this example illustrates the importance of densification reactions in transforming molecular precursors into solid films.

Next, we use the DFT activation energies for this reaction mechanism as inputs to a Kinetic Monte Carlo (KMC) model to explicitly model film growth over multiple ALD cycles. KMC allows a large set of inter-dependent events (such as growth reactions) to be combined into a sequence over a variety of timescales. It is therefore suitable for the coarse-graining in time that is necessary in order to simulate ALD cycles [2]. We have modified the KMC modules of the SPPARKS code [3] for oxide growth by ALD. We include 162 possible reactions (each with DFT-derived activation

energies) at 8000 reaction sites under typical values of temperature and pressure. The results show which reactions predominate, how layer-by-layer growth takes place and how roughness evolves in time.

We gratefully acknowledge funding from Science Foundation Ireland under the Strategic Research Cluster 'FORME' (www.tyndall.ie/forme) and coding support and computing time at the SFI/HEA funded 'Irish Centre for High End Computing'.

[1] S. Olivier et al., Chem. Mater., 2008, 20, 1555-1560.

[2] A. Esteve et al., J.Chem. Theory Comput., 2008, 4, 1915-1927.

[3] A. Slepoy et al., J. Chem. Phys., 2008, 128, 205101.

9:20am **TF-TuM5 Optimization of Properties of Al-doped ZnO Films Deposited by Atomic Layer Deposition**, Y. Wu, P.M. Hermkens, B.W.H. van de Loo, H.C.M. Knoops, F. Roozeboom, W.M.M. Kessels, Eindhoven University of Technology, the Netherlands

ZnO is widely used in solar cell windows, and as active layers in gas sensors. Often Al-doping is applied to decrease its resistivity. However, the chemical environment and electrical properties of Al-doped ZnO are not fully understood and the doping efficiency of Al is not optimized yet. In this work, 40 nm Al-doped ZnO layers were deposited on 450 nm SiO_2/Si -substrate at 250 °C by ALD using $ZnEt_2$, $AlMe_3$ and water vapor as precursors. The Zn-O/Al-O cycle ratios were varied corresponding to an Al-content ranging from 0 at.% to 17.4 at.%. The resistivity improved from 8.2 $m\Omega\cdot cm$ for intrinsic ZnO to an optimum of 2.2 $m\Omega\cdot cm$ at 6.8 at.% Al-content. The stoichiometry, distribution and chemical environment of Zn, Al and O elements were studied by angular-resolving and depth-profiling X-ray photoelectron spectroscopy (XPS). With XPS sputter depth profiling we could distinguish the individual ZnO and Al-O lamellae in the films grown with high cycle ratios, whereas films grown with low cycle ratios showed a more homogeneous composition. The binding energies of Al 2p3 and Zn 2p3 increase by 0.23eV and 0.44eV for intrinsic ZnO to highest doped AZO, respectively. This shift is ascribed to an increase of the Fermi level, and secondly, to the delocalization of bonded electrons from Zn_{Zn}^0 to Al_{Zn}^+ .

Ex-situ SE and Fourier transform infrared spectroscopy were applied to measure the optical properties, from which the carrier concentration and intra-grain mobility were extracted by modeling. The relative permittivities ϵ_1 and ϵ_2 were obtained from the modeling as well and the optical band gap was determined by Tauc-plot fitting. The optical band gap increases from 3.29 eV for intrinsic ZnO to 3.77eV for the highest doped AZO (17.4 at.% Al), corresponding to the Burstein-Moss effect and an increase of the Fermi level. Meanwhile, the total mobility was determined by Hall measurement. Combined with the intra-grain mobility, the mobility at grain boundaries (GB) can be calculated. The result shows that with increasing Al%, the barrier at GB decreases at first due to an increased Fermi level and increases next due to alumina clustering at the GB. The Al-doping efficiency, as calculated from the carrier concentration, shows that the doping of Al in ZnO phase is saturated at 6.8 at.% Al. Above this value, the Al incorporated mainly forms alumina at GB, which decreases the mobility while hardly leading to higher carrier concentrations.

In summary, the chemical and electrical properties of Al-doped ZnO were measured and explained properly, and the doping efficiency was optimized at 6.8 at.% Al, which is useful for further study and applications.

9:40am **TF-TuM6 Growth Inhibition of Al_2O_3 on InGaAs by Atomic Layer Deposition**, B. Granados, A.J. Muscat, University of Arizona

The chemical composition of the $In_{0.53}Ga_{0.47}As(100)$ interface during the growth of an aluminium oxide (AlO_x) layer deposited by ALD was studied after each half-cycle using *in-situ* X-ray photoelectron spectroscopy (XPS) to understand film nucleation and interface formation. Native oxide was removed from InGaAs using liquid HF (49%, followed by water rinse) and gas phase HF and compared to deposition directly on native oxide. *In situ* gas phase HF/ H_2O etching was run at 29°C and 100 Torr with an HF to water partial pressure ratio of 1.23. The ALD process consisted of pulses of trimethylaluminum (TMA) and H_2O at 170°C. The AlO_x film thickness was estimated from the Al 2p peak area and the attenuation of the As 3d bulk signal due to an assumed homogenous Al_2O_3 overlayer. An AlO_x film with a thickness of 11.2 ± 2.5 Å was deposited during the first pulse of TMA on both liquid and gas phase HF treated samples and a film with a thickness of 12.8 ± 2.5 Å was deposited on InGaAs covered by native oxide. These thicknesses correspond to approximately 3 ML of Al_2O_3 , which could indicate the formation of islands. Remarkably the thickness was equivalent starting from an As-rich interface in the case of liquid HF, a Ga-rich interface in the case of gaseous HF that contained both oxides and fluorides, and an nearly stoichiometric surface in the case of native oxide. After three complete ALD cycles the thickness of the AlO_x film was 12.9 ± 2.5 Å on liquid HF treated, 9.2 ± 2.5 Å on gas phase HF treated, and 14.1 ± 2.5 Å on the native oxide of InGaAs, indicating that the first pulse reacts with most

of the sites on the surface. The density of methyl groups after the first pulse was estimated to be 12 methyl groups/nm² on the liquid HF treated surface based on XPS. Approximately half of the methyl groups were hydrolyzed by the first water pulse, depositing an estimated 6 hydroxyl groups/nm². The second TMA pulse returned the methyl density to approximately the same value after the first TMA pulse. After the first ALD cycle the samples entered into a growth inhibition period. The growth rate per cycle (GPC) during cycles two and three dropped from 2.5 ML/cycle to 0.4 ML/cycle on the liquid HF treated surface and to 0.0 ML/cycle on the gas phase HF treated surface, and from 3.4 ML/cycle to 0.2 ML/cycle on the native oxide of InGaAs. This growth inhibition after the first pulse of TMA must be caused by the formation of Al-CH₃ moieties on the surface that are less reactive than both the initial surface and Al₂O₃. Understanding the surface reactions involved in the nucleation phase and early cycles of ALD is important in achieving control of the III-V-dielectric interface.

10:40am **TF-TuM9 Nanoindentation and Flexure Related Effects Due to Reactive Subsurface Growth of Atomic Layer Deposition Aluminum Oxide on Polyamide-6**, *Y. Sun*, North Carolina State University, *M.P. Goertz, J.A. Palmer*, Sandia National Laboratories, *R.P. Padbury, J.S. Jur*, North Carolina State University

In this study, we investigate the nanoindentation characteristics and crack formation with flexure of nanoscale atomic layer deposition (ALD) alumina on polyamide-6 (PA-6) films. Initial ALD processing PA-6 is shown to form a subsurface hybrid layer by reaction between ALD precursors and the polymer backbone, followed by standard Al₂O₃ surface formation in subsequent cycling. Over an exposure temperature from 60 to 120 °C, the degree of hybrid layer formation varies significantly. Transmission electron microscopy shows that the thickness of the underlying hybrid layer is increased at lower temperatures, up to 120 nm for 100 ALD cycles of trimethylaluminum and water on PA-6. At 120 °C processing, no hybrid layer is observed. The elastic modulus and hardness evaluated by nanoindentation show a corresponding decrease in value with the thickness of the hybrid layer. Flexure testing shows that both crack density and critical tensile strain is decreased for films processed at lower temperatures that have an increased thickness of the underlying hybrid layer. This analysis shows that the nucleation behavior of the ALD thin films on polymers plays an important role in understanding the mechanical performance of the thin films. This work has important consequences in the how ALD materials need to be applied and evaluated on polymers for application as diffusion barrier layers.

11:00am **TF-TuM10 The Importance of Oxygen-Induced Ripening in the Nucleation of Platinum Atomic Layer Deposition**, *A.J.M. Mackus, M.A. Verheijen, N. Leick, W.M.M. Kessels*, Eindhoven University of Technology, Netherlands

Platinum thin films and particles on oxide surfaces are interesting for various applications in microelectronics and catalysis. Atomic layer deposition (ALD) of Pt from MeCpPtMe₃ precursor and O₂ gas has recently emerged as a promising technique to fabricate these structures on demanding topologies such as high-aspect ratio surfaces or porous catalyst supports. The surface reactions of Pt ALD are governed by dissociative chemisorption of O₂ at the Pt surface, and catalytic combustion and dehydrogenation of the MeCpPtMe₃ precursor ligands,¹ which is limited during nucleation on oxides due to the absence of a catalytic surface. In this work, it is established that a parameter that has not been investigated so far, the O₂ exposure (i.e. pressure × time) during the reactant half-reaction of the ALD cycle, plays a crucial role during the nucleation of Pt ALD. Under influence of the oxygen, deposited Pt atoms diffuse over the surface and form small islands, and these islands subsequently catalyze the surface reactions of Pt ALD. As a result, the nucleation delay for Pt growth decreases with increasing O₂ exposure. It is shown that the particle ripening is absolutely essential for the Pt ALD growth to occur. For low O₂ exposures, there is no growth at all on Al₂O₃ substrates. The O₂ exposure can be used as a parameter to tune the nucleation behavior, and this has some important consequences for the applications. For example, the O₂ exposure dependence can be exploited to minimize the nucleation delay for the deposition of ultrathin closed Pt films, to fabricate particles with a narrow size distribution for catalysis applications, or to obtain selective growth on seed layer patterns for nanopatterning applications.²

[1] A.J.M. Mackus, N. Leick, L. Baker, W.M.M. Kessels, *Chem. Mater.*, (accepted for publication).

[2] A.J.M. Mackus, J.J.L. Mulders, M.C.M. van de Sanden, W.M.M. Kessels, , 116102 (2010)

11:20am **TF-TuM11 Plasma Assisted Atomic Layer Deposition of Pt and PtO_x in High Aspect Ratio 3D Structures**, *I.J.M. Erkens, M.A. Verheijen, F. Roozeboom, W.M.M. Kessels*, Eindhoven University of Technology, Netherlands

High aspect ratio (AR) nanostructured films of noble metals and noble metal oxides with large specific surface areas can have a wide variety of applications in many fields such as catalysis, sensing and energy storage. Atomic layer deposition (ALD) has become the method of choice for depositing thin films conformally in high AR structures.(1) To achieve high conformality, saturation of the surface reactions has to be achieved throughout the three-dimensional (3D) structure. For plasma assisted ALD, reaching conformal deposition in high AR structures is less straightforward than for thermal ALD due to surface recombination loss of plasma radicals.(2) In our contribution we demonstrate that plasma assisted ALD can be used to deposit Pt in high AR 3D structures with high conformality. We also describe the sample preparation technique that allowed the conformality to be analyzed using transmission electron microscopy (TEM). Depositions were performed on high AR trenches, pre-etched in silicon (AR = 1.3 - 34), and in anodized aluminum oxide (AAO) (pore diameter = 70 nm, depth = 20 μm). The results for coating the Si trenches demonstrate that for the plasma assisted ALD process, pulses of 3 s (MeCp)PtMe₃ and 3 s O₂ plasma are sufficient to deposit Pt coatings with 95-100% conformality up to AR = 20. For AR = 20 the conformality was quantified using TEM. For this purpose, a cross-sectional TEM sample of a trench was prepared by first cleaving the Si substrate exactly through the trench heartline. A lift-out TEM sample was subsequently prepared using Focused Ion Beam (FIB) milling orthogonal to the cleavage plane (i.e. to the side wall of the trench). This provided a TEM sample in which the entire sidewall of the 20 μm deep trench was electron transparent, which allowed the layer thickness as a function of depth to be determined with high precision. The TEM images of individual Pt nanotubes deposited in the AAO pores were used to determine wall thickness as a function of depth, and showed the grain structure of the deposited Pt in great detail. In our contribution we will also report on the high AR conformality of other noble metal and noble metal oxide plasma assisted ALD processes (e.g., PtO_x and Ir).

(1) P. Banerjee, I. Perez, L. Henn-Lecordier, S. B. Lee, and G. W. Rubloff, *Nature Nanotechnology* **4**, 292 (2009).

(2) H. C. M. Knoops, E. Langereis, M. C. M. van de Sanden, and W. M. M. Kessels, *J. Electrochem. Soc.* **157**, G241-G249 (2010).

Tribology Focus Topic

Room: 19 - Session TR+BI-TuM

Self Healing Coatings, Bio-Inspired Design, and Frictional Properties of Biological Materials

Moderator: D. Irving, North Carolina State University, M.O. Robbins, Johns Hopkins University

8:20am **TR+BI-TuM2 Friction at Hydrogel Contact Lens Surfaces**, *S.S. Perry, S. Huo, A. Rudy*, University of Florida **INVITED**

The surfaces of six types of silicone hydrogel (SH) contact lenses (PureVision®, O₂ OPTIX®, ACUVUE® Oasys®, ACUVUE® TruEye®, Biofinity®, DAILIES TOTAL1®) and the pHEMA-based ACUVUE® 2 have been analyzed using atomic force microscopy (AFM) in aqueous environment. The elastic modulus, frictional, and adhesive properties of each lens were evaluated using calibrated instrumentations, providing a basis for comparing the distinctive surface properties of these lenses. Cantilevers modified with 5-μm (diameter) silica colloidal probes were employed throughout the experiments. Elastic modulus was measured by indenting the probe into the surface of the hydrogel in a controlled manner (i.e. approach speed and maximum applied force), such that the maximum indentation depth was restricted to sub-micron levels. A modulus value was obtained by fitting the characteristic force versus indentation behavior to a mathematical model. The frictional force was measured for the sliding contact of the probe and the surface at the length scale of 500 nm and with applied loads up to 20 nN. The friction coefficient was realized by evaluating the linear dependence of friction force on applied normal load. The lenses examined exhibited an order of magnitude difference—from the softest to the stiffest sample—in modulus value, generally reflective of the distinct surface treatments they received during manufacturing. For example, the pHEMA-based ACUVUE® 2 was shown to have a modulus between 100 and 130 kPa, whereas PureVision®'s was an order of magnitude higher in value. The frictional properties of the lenses followed a similar trend in that the lenses with surface treatment, such as PureVision® and O₂OPTIX®, generally exhibited coefficients of friction five times greater than that of a non-treated lens such as ACUVUE® OASYS®. The elastic modulus and

frictional properties of different lenses evaluated on a nanoscopic level by AFM depict a strong correlation between the surface treatments and the apparent mechanical behaviors of the lenses.

9:00am TR+BI-TuM4 Linking Cartilage Structure, Lubrication, and Osteoarthritis, D.L. Burris, University of Delaware

Cartilage is known for exceptionally low friction coefficients during sliding, but its wear resistance is arguably more remarkable. Conventional wisdom suggests that cartilage wears gradually with use and that osteoarthritis is the inevitable consequence. This notion is refuted by the scientific literature. Dissections of mature, healthy, and active joints consistently reveal smooth, glossy, damage-free articulating surfaces that can only occur if tissue recovery matches wear. Cartilage recovery is extremely slow due to a lack of vasculature and numerous lubrication mechanisms have been proposed to explain extremely low in-vivo wear rates. Osteoarthritis (OA) is characterized by progressive wear and caused by a system destabilizing input (e.g. biochemistry, acute injury, altered loading, and joint instability). In certain joint-destabilized animal models, for example, a localized defect (~50 μm wide) is visible in as little as a week, and bone-on-bone contact occurs on the order of 6 months. Recent studies suggest that interstitial lubrication, a mechanism that reduces frictional and normal stresses by nearly 100X, is the dominant protective mechanism of cartilage. Localized surface damage can disrupt the very specific structural features responsible for the unique interstitial fluid pressurization mechanism. We hypothesize that localized surface damage can initiate OA-like degradation if it is sufficiently disruptive to the interstitial lubrication mechanism. In this paper, we present friction and wear measurements designed to explore this novel mechanical hypothesis of OA initiation and progression.

9:20am TR+BI-TuM5 Self Healing Materials: A New Approach to Make Materials Perform More Reliably under Harsh Conditions, S. van der Zwaag, M. Valefi, S. Garcia, M.R. de Rooij, Delft University of Technology and University of Twente, the Netherlands INVITED

Currently all engineering materials are designed on the basis of the 'damage prevention' paradigm i.e. the microstructure is designed such that damage forms as late as possible and grows slowly, but no mechanisms are built in which can reduced damage once formed. Materials in nature on the other hand seem optimised on the basis of 'damage management' paradigm, i.e. the occurrence of damage is taken as unavoidable and the material has the in-built ability to repair the damage during less demanding stages of the loading cycle. In this presentation we will show various approaches to self healing behaviour in a wide range of material classes and also show how self healing concepts can be used to mitigate tribological damage in both ceramics and polymeric materials. The experimental results are supported by a simple mechanical model.

10:40am TR+BI-TuM9 Surface Analytical and Tribological Characterization of Diamonlike Boundary Films Extracted from Base Mineral and Synthetic Oils, A. Erdemir, O.L. Eryilmaz, Argonne National Laboratory

In this study, we explored the possibility of deriving carbon-based boundary films directly from base lubricating oils during tribological tests. For this purpose, we first designed and deposited a series of catalytically active nanocomposite coatings on some steel substrates and by adjusting the ratios of softer phases made out of known catalysts and harder nitride phases (that are also catalytically active), we were able to extract carbon-based boundary films from the base oil molecules and deposit them as protective boundary films on rubbing surfaces. Using UV Raman and variety of other surface and structure analytical techniques, we were able to confirm that these boundary films were indeed similar to those diamonlike carbon films that are typically synthesized using CVD and PVD methods. Some of the main characteristics of resultant DLC boundary films were: very low friction coefficients (less than 0.05) even under extreme sliding conditions and very high resistance to wear and scuffing. In this paper, we will provide insight into the structural and chemical nature of these tribofilms and explain fundamental mechanisms for their impressive tribological properties under severe test conditions.

11:00am TR+BI-TuM10 Data-driven Model for Estimation of Friction Coefficient via Informatics Methods, E.W. Bucholz, University of Florida, C.S. Kong, Iowa State University, K.R. Marchman, F.-Y. Lin, W.G. Sawyer, S.R. Phillpot, University of Florida, K. Rajan, Iowa State University, S.B. Sinnott, University of Florida

The rapid development of new mechanical assemblies capable of operating in extreme conditions requires the rapid determination/estimation of friction. Often, during the design phase, materials friction coefficients are unknown. Here, data mining and materials informatics methods are used to generate a predictive model that enables efficient high-throughput screening of ceramic materials, some of which are candidate high-temperature solid-

state lubricants. Through the combination of principal component analysis and recursive partitioning using a small dataset comprised of intrinsic material properties, we develop a decision tree based model comprised of if-then rules, which estimates the friction coefficients of a wide range of materials derived from the interrelationships between the intrinsic material properties. This predictive model lays the foundation for new studies in predictive modeling and tailoring materials with specific tribological characteristics. It is applied to predict the tribological performance of a range of different materials.

This work is supported by the Office of Naval Research.

11:20am TR+BI-TuM11 Structure, Lateral Flow, and Self-Healing of a Bound-and-Mobile Lubricant Film, S.H. Kim, Pennsylvania State University INVITED

There have been a significant amount of efforts to develop boundary lubrication films that have the bound and mobile natures at the same time. As an effort to develop a more efficient boundary film lubrication method, a new bound-and-mobile lubricant molecule was synthesized and its lubrication and self-healing capability was studied. Low-molecular-weight silicone molecules with cationic side groups can form bound-and-mobile boundary lubrication film on silicon oxide surface. Both nano- and macro-scale tribological tests revealed superior lubrication performance of the silicone polymer with cationic side chains (called cationic lubricant polymer, CPL) over the neutral silicone oil. The multilayer CPL films exhibited characteristic topographic features due to ionic interactions within the polymeric film. In the macro-scale, the effects of ionic content and environmental condition on self-healing will be discussed to demonstrate the wear resistance and self-healing capability. In the nanoscale, the results of disjoining pressure and viscosity measurements help understand the lateral spreading of the mobile layer and identify the mobile species. The CPL-coated surfaces are hydrophobic which prevents the detrimental effects of humidity on wear of silicon. In addition, the hygroscopic nature of CPL allows humidity to be absorbed into the film, which enhances the self-healing capabilities. By texturing the silicon surface with nanowells, self-healing can be enhanced when the nanowells are filled with CPL. The nanowells serve as CPL reservoirs that are readily available for self-healing within the wear track for faster cycle intervals. However, the nanowells deteriorate the self-healing from surrounding the contact region due to the refilling of the empty nanowells.

Vacuum Technology

Room: 14 - Session VT-TuM

Pumping, Gas Dynamics and Modeling

Moderator: L. Wang, Los Alamos National Laboratory

8:00am VT-TuM1 Gas Dynamics Modelling for Particle Accelerators, O.B. Malyshev, STFC Daresbury Laboratory, UK INVITED

Design of accelerator vacuum chamber requires an input from different scientific disciplines such as surface science, material science, gas dynamics, particle beam dynamics, and many others. Although vacuum scientists work on the boundary field between these disciplines the gas dynamics is one that allows jointing all these to the vacuum science for particle accelerators.

The particle accelerator requirement to vacuum defined by beam gas interactions that should be negligible comparing to the other phenomena and effects limiting the quality of the beam, so these requirements are in free molecular regimes: HV, UHV or even XHV. At such low pressures the main source of gas in the vacuum chamber is molecular desorption from materials used for vacuum chamber and in-vacuum components.

The outgassing rates depends on material, its cleaning procedure, treatments (polishing, etching, coatings, bakeout, etc.), time in vacuum, irradiation bombardment by particles (photons, electrons, ions, etc.) and accumulated irradiation dose. Therefore, the outgassing rates vary in very wide range.

The gas dynamic is used to design the research facilities to accurately measure and to study outgassing rates at different conditions, then it used for data analysis. By applying these data to the accelerator vacuum design one have to consider that outgassing is often non-uniform and changes with time with different functions. Full 3D modelling is possible with TPMC codes, however, it is time consuming work and not ideal for pumping and design optimization, so it is used for components or for finalized design. Meanwhile, during the optimization study the most time-efficient way is using 1D diffusion model where all parameters are defined as a function of longitudinal coordinate (along the beam path).

The examples accelerator vacuum chamber designer should also consider such effects as thermal outgassing, photon, electron and ion stimulated

desorption, beam induced electron multipacting and ion induced pressure instability.

8:40am VT-TuM3 Transient Flow of Rarefied Gas through a Short Tube, F. Sharipov, Federal University of Parana, Brazil

Steady flows of rarefied gases through orifices, slits, short tubes, and channels are well studied. In spite of the high practical interests to the transient flows of rarefied gases, the problem of short tube flow has not been studied from this viewpoint. The aim of the present work is to study transient rarefied gas flow through a short tube on the basis of the direct simulation Monte Carlo method. The mass flow rate and flow field are calculated as a function of the time in the transitional and hydrodynamic regimes with respect to the gas rarefaction. Two values of the pressure ratio, i.e., 0.1 and 0.5, and two values of the aspect ratio, i.e. 1 and 5, are considered. A characteristic time equal to that needed to cross the tube radius with the most probable molecular speed is introduced. The typical time to establish the stationary flow is calculated. The flow field past the tube reaches the steady state during the same time in the transitional regime and it takes a longer time in the hydrodynamic regime.

9:00am VT-TuM4 Experimental Results and Direct Simulation Monte Carlo Modelling of a High-Performance Large-Scale Cryopump, S. Varoutis, Chr. Day, X. Luo, H. Haas, Karlsruhe Institute of Technology, Germany, **F. Sharipov**, Federal University of Parana, Brazil

The main duty of the vacuum pumping system of fusion devices is to pump out the fusion exhaust gas. Due to the fact that very high throughputs have to be coped with, large pumping speeds are required. This is typically provided by cryogenic pumping, supplied with cryogen medium at 4 K and 80 K. The concept for the cryosorption vacuum system of ITER, the next generation fusion experiment currently being built in Europe, has been developed at the Karlsruhe Institute of Technology (KIT). As a result to the large gas flows, which are unusually high for a cryopump, the pumps are operated in the transitional regime. A further development and improvement of the system requires a corresponding numerical modelling of the gas flow inside the pump housing and near the cryopanel section.

The aim of the present work consists of the computational investigation of a 2D axisymmetric complex geometry of a model cryopump by the Direct Simulation Monte Carlo (DSMC) method. Since the flow close to the cryopanel can be assumed free molecular due to low pressure levels, the capture coefficient of the cryopanel can be estimated by applying the Test Particle Monte Carlo method. Then, this information can be used as input data to the corresponding DSMC simulations. The macroscopic parameters of practical interest as the bulk velocity, the pressure and the temperature in the whole flow field, have been calculated as a function of the incoming gas throughput and of the pump inlet valve position. Furthermore, the present numerical results have been thoroughly compared with corresponding experimental results obtained at KIT for the case of an ITER model cryopump.

The importance of these calculations is based on the fact that they can provide information for quantities which are not accessible for measurement during pump operation and that they can be used for prediction of the pump behavior. This paper describes a post-operational investigation of a built pump and is thought as a proof-of-principle test to include this approach in the design process of a future pump development.

9:20am VT-TuM5 Development of a PhD-level course in Vacuum Science and Technology, P. Eklund, Linköping University, Sweden

There are many available courses in Vacuum Technology, including those offered by the AVS. They typically have an engineering-oriented approach aimed at the practical user of vacuum system. When I started teaching a PhD-level course in Vacuum Science and Technology, I was faced with a different – pedagogical and scientific – challenge. The attendees are PhD students who work, or will work, with vacuum in their PhD research and future careers, but most are not vacuum practitioners per se. Neither is the teacher. In such a course, the students need to achieve an in-depth understanding of the science of vacuum and how it can ultimately affect their research. Here, available textbooks on the topic of “Vacuum Technology” are not at PhD level – they tend to be “engineering user’s guides” or similar.

In achieving this, a clear definition of the objectives is essential. In a PhD course, the aim is to give students a thorough understanding of how vacuum components and vacuum systems work, and the fundamental physics and chemistry behind them – emphasizing the latter part, in contrast to a more engineering-oriented course. Among others, this means that students should understand and be able to define the vacuum concepts (ideal, rough, low, high, ultrahigh, etc...), understand and be able to explain in own words the kinetic theory of gases, the principles for gas flow at low pressures, and physico-chemical phenomena in vacuum (evaporation, condensation, solubility, permeation, adsorption, absorption, desorption). They should

also be able to apply the knowledge and understanding listed above to practically and theoretically relevant situations in vacuum science and technology, communicate this understanding orally and in writing, and be able to critically reflect on scientific articles relevant to vacuum science and technology.

Here, I will discuss my pedagogical and scientific approach to such a course and how to align the course activities for the PhD students to reach the above goals. I will also discuss the examination format, and why I have found it to be particularly suitable for this type of course. It is a combination of continuous examination in connection with the lectures and home examination, which also contains an assignment connecting the course content to the laboratory work of the students. The continuous examination is not mandatory, but gives credits for the home examination. The mandatory parts of the course are examined through peer review and an ending seminar.

10:40am VT-TuM9 A Comparison between Numerical and Analytical Models of Turbomolecular Drag Pump’s Stages, I.F. Cozza, Agilent Technologies, Italy, **M. Rose**, PI-DSMC, Germany, **R. Arpa, H. Telib**, Optimad Engineering S.R.L., Italy

The design and optimization of vacuum pumps requires a deep knowledge of the internal gas-dynamics, and a large trial-and-error process to fix the design parameters. A common practice in the TMDP’s industry is to perform an experimental design of new pumps, by testing the global performances of prototypes. This approach has two drawbacks: it doesn’t give indications on the details of the internal fluid dynamics of the problem, and the design and realization of prototypes has significant costs and requires long times, that could affect the time-to-market of new products.

In this framework, an accurate and efficient numerical analysis tool could meet these needs. This tool should model the tridimensional, local flow features, such as pump leakage and development of the rarefied gas flow along the curved channels, and take into account the inertial forces.

In this work, two approaches will be presented: a full 3D Direct Simulation Monte Carlo numerical analysis of the Siegbahn drag stages, and a semi-analytical approach based on the numerical solution of the Linearized Boltzmann Equations.

The DSMC simulations have been performed using a DSMC software package called PI-DSMC. The sampling and collision cells were generated automatically from a triangular mesh describing the shape of the solid body. The reflection of molecules by the walls was investigated to choose the proper particle/surface interaction model. The temperature of the rotor, the stator and the gas at the inlet have a fixed value. The effect of rotor temperature on the performances of the stage has been investigated. The collisions between nitrogen and hydrogen molecules were modeled using the variable hard sphere model with the common parameters.

The semi-analytic model is developed for steady flows in spiral molecular drag stages, and it is based on the solution of the Boltzmann Equation (BE) with a BGK closure. The order of the original problem is reduced in the physical space to 2D, by introducing assumption of locally known flow development of the distribution function along the spiral channel. Thus, 2D-BE calculations of the flow rates and stresses will be performed in a finite number of sections, suitably positioned along the spiral channel, from the outlet to the inlet, in order to recover the integral performances of the pump. The original BGK equation is linearized in the most significant parameters (rotational speed and pressure gradients), and solved in the reference cross-section, by means of a DVM scheme. Maxwell diffuse boundary conditions and impermeability are provided at walls. The local values of pressure and torque are obtained consistently by enforcing the mass flow.

11:00am VT-TuM10 Improved Modelling and Measurement of the Rotor Temperature of Turbo-Molecular Pumps in Magnetic Fields, A. Jansen, KIT, IEKP, Germany, **N. Kernert**, KIT, IKP, Germany, **J. Wolf**, KIT, IEKP, Germany

When designing a vacuum system with turbo-molecular pumps (TMP) in an external magnetic field, one needs to know the influence of eddy currents on the rotor temperature to ensure safe operating conditions. The KATRIN neutrino experiment will operate about 20 TMPs in the vicinity of superconducting magnets, pumping out tritium gas from the electron beam-line of the experiment. In a dedicated test setup with Helmholtz coils systematic studies have been conducted, investigating the rotor temperature and stability for TMPs with magnetic and ceramic bearings at full speed. The rotor temperature was monitored with an infra-red pyrometer as a function of gas load, magnetic field strength and direction of the field. For interpretation of the data and predictions for different operating conditions an empirical model has been developed, describing the rotor temperature versus time as a function of gas flow and magnetic field, using 5 pump-specific parameters, which characterize heating effects of eddy currents and gas friction as well as cooling by radiation loss and convection. Since this approach assumes a homogeneous field, we extended the model, replacing

the field and friction terms by the motor current of the pump, which compensates the retarding effects of eddy currents and gas flow. This new model can now be used for inhomogeneous magnetic fields.

KATRIN is supported by the German BMBF project 05A11VK3, the Helmholtz Alliance Astroparticle Physics and HGF.

11:20am VT-TuM11 Test of Temperature-Dependent NEG Activation and Stability of Gold-Plating in the KATRIN Experiment, W. Gil, L. Bornschein, J. Wolf, Karlsruhe Institute of Technology, Germany

The Karlsruhe Tritium Neutrino (KATRIN) experiment will measure the neutrino mass with an unprecedented sensitivity of $0.2 \text{ eV}/c^2$ by investigating β -electrons from tritium decay. While the electrons are magnetically guided through a beam tube to the spectrometer by superconducting solenoids, the tritium flow rate from the source has to be reduced by at least 14 orders of magnitude by differential pumping and cryo-sorption. The last stage of the pumping section is the 7 m long cryogenic pumping section (CPS), using a pre-condensed argon-frost layer to capture tritium molecules. For reducing the adsorption of tritium on the wall of the beam line and for more efficient regeneration of the cryo-pump its inner surface has been gold-plated, using a standard industrial galvanic process. Non-evaporable getter (NEG) strips (SAES St707) will be installed inside the last meter of the beam tube of the CPS as a fallback system, protecting the spectrometer in case of a failure of the cryogenic system. The standard NEG activation temperature is 450°C for about 60 min, but can be reduced with prolonged activation time. However, the activation temperature in the CPS should be as low as possible with respect to the superconducting solenoids around the beam tube and the stability of the gold-plating. Therefore, a test has been set up, optimizing the activation temperature and time with regard to the NEG's pumping efficiency, the stability of the gold-plating, and the safety of the magnets. This paper presents results of the temperature-dependent NEG activation efficiency and the influence on the gold-plating.

11:40am VT-TuM12 Improving the Pump Down of UHV Systems by the Additional Pumping Speed Provided by NEG Pumps, F. Siviero, A. Bonucci, A. Conte, L. Caruso, L. Viale, P. Manini, SAES Getters, Italy

The study of pump down processes is one of the basic topics of vacuum technology since its early days. Its relevance from the practical point of view is very high in a variety of systems including large machines like accelerators, surface science equipment, scanning/transmission electron microscopes and many other analytical systems and sealed off devices. At present the bake-out of these systems may require days to weeks, resulting in a considerable use of time and energy. Here we report on a series of experiments aimed at investigating how an increase of the total pumping speed during the pump down influences the behaviour of the main gases of interest, i.e. water and hydrogen. Several pumping configurations are compared, including turbo molecular pumps, large sputter ion pumps (SIP), Non Evaporable Getter (NEG) and a new SIP/NEG combination pump called NEXTor[®] [1]. The most relevant desorption models and their predictions for the pump down processes are expressed in an explicit form and compared with the experiments. The results of the study confirm that water desorption can largely benefit from an increase of the available pumping speed, due to the reversible nature of its adsorption kinetics. As far as hydrogen is concerned, a higher pumping speed at the end of the bake provides a lower partial pressure. This translates into the possibility of either reducing the duration of the bake-out process or improving the ultimate achievable vacuum, both issues having practical interest in vacuum systems for research and industrial applications.

[1] NEXTor is an International Trademark registered by the "Madrid System" property of SAES Getters S.p.A.

Tuesday Lunch, October 30, 2012

Exhibitor Technology Spotlight

Room: West Hall - Session EW-TuL

Exhibitor Technology Spotlight

Moderator: D. Surman, Kratos Analytical Inc.

12:20pm EW-TuL2 Complementary Nature of XPS and Raman Techniques, R. Kershner, T. Nunnery, Thermo Fisher Scientific

The increasingly complex nature of structure-property investigations in bulk, nanostructured, and thin-film applications has demanded a renewed focus on complementary techniques for chemical and structural analysis. At the same time, the most successful experimental protocols will take advantage of minimal sample preparation, straightforward data collection, and unambiguous interpretation of results. In this talk, we present a broad overview of the rich chemical and structural information provided by both Raman and X-ray Photoelectron Spectroscopies, with an emphasis on applications that derive significant benefit from leveraging both techniques in a complementary fashion. While both XPS and Raman can be used to generate complex datasets using a variety of advanced sampling approaches, the real power lies in the user's ability to generate answers to challenging problems without the need for an in-depth understanding of the technique itself. Specific examples will be given that demonstrate how both approaches are essential to uncovering the fundamental science behind functionalization of thin graphene films, characterization of one-dimensional carbon materials, and other applications -- allowing anyone to quickly develop expertise in new and emerging fields.

12:40pm EW-TuL3 Multi-Dimensional XPS Profiling from Thermo Fisher Scientific, A. Bushell, R.G. White, T.S. Nunnery, P. Mack, A.E. Wright, Thermo Fisher Scientific, UK

X-ray Photoelectron Spectroscopy (XPS) provides crucial surface specific chemistry information when evaluating any surface modification, thin film coating or the composition of electronic devices. Depth information from inorganic materials can be obtained by removing material by use of Ar ion sputtering, but organic material can be adversely affected by this process. More recently, noble gas cluster ion beam sources have been developed for profiling of organic materials. The development of a combined monatomic and gas cluster ion source (MAGCIS) allows for a single depth profile experiment to have both cluster and monatomic etching stages. This is ideal for the depth profiling of devices and structures with mixed inorganic and organic layers.

When dealing with the analysis of small features, such as bond pads and tracks for electronic devices, Parallel Imaging XPS provides unmatched spatial resolution for XPS analysis. Reconstructing a spectrum from a chosen area on a spectroscopic parallel XPS image gives the analyst absolute confidence in the area from which that spectrum was obtained. The combination of retrospective spectroscopy from image stacks with a depth profiling capability within a single experiment gives the surface scientist a valuable tool for parallel multi-point depth profile analysis. Processing the large multi-dimensional data sets produced from such experiments requires a sophisticated range of statistical analysis tools, provided within the *Avantage* software.

This presentation will provide examples of data acquired from the Thermo Scientific XPS product range, demonstrating the above capabilities.

1:00pm EW-TuL4 Organic Depth Profiling using XPS – Pro's and Con's of Different Polyatomic Species, C. Blomfield, S. Hutton, Kratos Analytical Ltd, UK, D. Surman, Kratos Analytical Inc.

XPS depth profiling of organic materials while retaining chemical information has traditionally been problematic. The advent of polyatomic ion species for sputtering has substantially changed the way depth profiling can be carried out. A variety of ion species have been developed such as C60, Coronene and Ar clusters all of which seem to have particular areas (types of materials) that they are suited to. This presentation discusses several of these ion species and what their advantages and disadvantages are and how they can be applied. Examples will be shown ranging from polymers to organic PV materials as well as some inorganic materials.

1:20pm EW-TuL5 What's New from Physical Electronics, J.F. Moulder, Physical Electronics

The latest innovations in XPS, AES, and TOF-SIMS instrumentation from Physical Electronics will be presented.

1:40pm EW-TuL6 KolibriSensor and Tyto: New Milestones in Scanning Probe Microscopy, T. Hänke, Y. Dedkov, A. Pioda, T. Kampen, A. Thissen, SPECS Surface Nano Analysis GmbH, Germany

The KolibriSensor™ from SPECS represents a new quartz sensor on the market that excels in its performance and its reliability. It is based on a symmetrical length extension resonator. The high resonance frequency of 1 MHz and the good signal-to-noise ratio allows for faster data acquisition in scanning microscopy and force spectroscopy. Oscillation amplitudes may be set below 20 pm. High stiffness prevents snap-in and the low noise floor continues to give a good frequency shift signal. The tip of the KolibriSensor™ has a separate contact, guaranteeing clean separation of the signals from the tunneling tip and from the quartz force sensor. The new Tyto scan head from SPECS is a milestone in the technology of Scanning Probe Microscopy. The modular design allows for various experimental configurations and for the usage of different sensors. A kinematic mount is used for both the sample and sensor and this feature is combined with accurate position sensors. For the first time, this enables different sensors to access identical locations on a sample and to repeat the procedure after successive sample preparation steps. This opens up opportunities for new experiments and will advance the research of surfaces at the nanometer scale. Additional features of the Tyto scan head are: Four openings for in-situ evaporation, two specular ports for simultaneous optical experiments, and large front openings and windows situated on each side of the body and at the back for broad visual inspection of the sample and sensor. Various sample receptors can be installed in the Tyto scan head, with four or twelve electronic contacts to the sample. Optional extra features include a calibrated Cernox temperature sensor located directly under the sample plate, and a small heater to control the sample temperature to within 1 mK.

Tuesday Afternoon, October 30, 2012

Applied Surface Science

Room: 20 - Session AS+BI-TuA

Surface Analysis of Materials Using Vibrational Techniques (2:00-3:20 pm)/ Multi-Technique Analysis (4:00-6:00 pm)

Moderator: D. Roy, National Physical Laboratory, UK, C. Szakal, National Institute of Standards and Technology

2:00pm AS+BI-TuA1 Vibrational Spectrum and Stability of the Long-Debated Models for the $(\sqrt{7}\times\sqrt{7})R19^\circ$ Phase of S/Cu(111). *M. Alcántara Ortigoza, M. Aminpour, T.S. Rahman*, University of Central Florida

Recently, the structure of the copper sulfide overlayer formed on Cu(111) upon sulfur exposure has attracted attention because it serves as a substrate to form MoS₂ monolayers and MoS_x nanostructures in a controlled manner, which may have numerous technological applications. In the past, at least eight experimental techniques have been used to characterize the $(\sqrt{7}\times\sqrt{7})R19^\circ$ Cu-S overlayer on Cu(111) and to support or refute a large number of possible models but, as yet, at least three models are still in dispute. In this study, we provide firmer arguments to resolve the structure of CuS/Cu(111) at the atomic scale. Specifically, we perform density-functional-theory calculations of the total energy and the vibrational spectrum of the proposed structures to (1) attest their dynamical stability; (2) compare their thermodynamic stability as obtained from the total free energy; and (3) provide the vibrational frequencies that uniquely fingerprint these structures and which may serve for further experimental confirmation or refutation.

This work was supported in part by DOE grant DE-FG02-07ER15842

[1] Kim et al., Langmuir 27, 11650 (2011)

[2] Alfonso J. Phys. Chem. C 115, 17077 (2011)

2:40pm AS+BI-TuA3 First-principle Investigation of the Stability and Vibrational Spectrum of MoS_x Nanostructures Grown on Cu(111). *M. Aminpour, M. Alcántara Ortigoza, T.S. Rahman*, University of Central Florida

Recent experiments have successfully synthesized MoS_x nanostructures in a controlled manner by evaporating Mo adatoms on the copper sulfide monolayer that forms on Cu(111) upon sulfur preloading[1,2]. Based on STM observations and total-energy calculations based on density functional theory, including *ab initio* van-der-Waals interactions, several structures for MoS_x/Cu(111) have been proposed. In this study, we investigate the plausibility of those structures and provide elements for further experimental substantiation or refutation. Namely, we perform density-functional-theory calculations (also including *ab initio* van-der-Waals interactions) of the total energy and the vibrational spectrum of the proposed structure to (1) attest their dynamical stability; (2) compare their thermodynamic stability as obtained from the total free energy; and (3) provide the vibrational frequencies that uniquely fingerprint the proposed structures.

[1] Kim et al., Langmuir 27, 11650 (2011)

[2] Le et al., PRB 85, 075429 (2012)

This work was supported in part by DOE grant DE-FG02-07ER15842

4:40pm AS+BI-TuA9 New Desorption Mass Spectrometry Approaches for Inorganic Particle Analysis. *C. Szakal, A.R. Konicek, M. Ugelow, D.S. Simons, A. Herzing, R.D. Holbrook*, National Institute of Standards and Technology

Chemical characterization of inorganic particles becomes more difficult as the particle sizes decrease. For application areas ranging from semiconductor failure analysis to nanotoxicology, the distinct chemical signatures of both the surface and bulk of particles can provide insight into system mechanisms and behavior. New methods that aim to explore the surface chemistry of inorganic nanoparticles for both their elemental and organic overlayer signatures will be presented. Specifically, the “static” nature of time-of-flight-secondary ion mass spectrometry is used to provide mass spectral characterization at the very surfaces and sub-surfaces of well-prepared (via drop-on-demand inkjet printing) and well-characterized (via scanning transmission electron microscopy and ultraviolet-visible spectroscopy) nanoparticle aggregates. This information can potentially be combined with full aggregate analysis using more elementally sensitive dynamic SIMS instrumentation once target species are identified with ToF-SIMS. Both sets of SIMS data can be used to obtain a chemical distribution

of signals throughout the particle depths. Additionally, the question of whether the centers of inorganic nanoparticle aggregates are chemically similar to the overall aggregate surfaces will be explored.

5:00pm AS+BI-TuA10 TOF SIMS Analyses of Ga Concentration as a Function of Distance from FIB Milled Features. *C. Santeufemio*, University of Massachusetts, *B.P. Gorman*, Colorado School of Mines, *C. Zhou, F.A. Stevie*, North Carolina State University, *L.A. Giannuzzi*, L.A. Giannuzzi & Associates LLC

Focused ion beams are routinely used for site-specific specimen preparation, nanopatterning, and analysis. It is important to know whether the primary ion beam is present outside the region targeted for ion beam modification. A previous report showed that $> 1E12$ atoms/cm² of Ga was detected up to several millimeters away from a focused ion beam (FIB) milled feature [1]. In this work, we reproduce this earlier report using a blind study of 2 different state-of-the-art Ga-FIB columns. Each column was used to FIB mill a 100 μm x 100 μm square into a (100) Si wafer at 30 keV with a nominal beam current of 20 nA at constant dose. Time of flight secondary ion mass spectrometry (TOF SIMS) was used to measure Ga depth profiles and Ga surface concentration at a distance up to 6.5 mm from the FIB milled square. In column “A,” $> 1E12$ atoms/cm² of Ga was detected up to ~ 5 mm from the FIB milled square. Column “B” showed considerably less Ga with $> 1E12$ atoms/cm² detected within ~ 250 μm from the FIB milled square. The depth profiles show that the Ga concentration was fairly uniform to a depth of ~ 2 nm from the surface for column “A” and ~ 1 nm into the surface for column “B”. Using SRIM [2] simulations we determine that these implantation depths correspond to an ion energy < 500 eV. The consequences of the presence of Ga at long distances from desired FIB milled features will be discussed.

[1] U. Muehle, R. Gaertner, J. Steinhoff, W. Zahn, “Characterisation of Ga-distribution on a silicon wafer

after inline FIB-preparation using inline ToFSIMS,” M. Luysberg, K. Tillmann, T. Weirich (Eds.): EMC 2008, Vol. 1: Instrumentation and Methods, pp. 749–750, DOI: 10.1007/978-3-540-85156-1_375, © Springer-Verlag Berlin Heidelberg 2008

[2] www.srim.org

5:20pm AS+BI-TuA11 The Surface Characterization of Oligo(Ethylene Glycol) Functionalized Gold Nanoparticles. *A. Rafati, D.G. Castner*, University of Washington

Extensive surface analysis of available gold nanoparticles (AuNPs) is crucial to understand how their production and functionalization affects their final properties. This information is needed to improve the performance of engineered nanoparticles in research and commercial applications. Ethylene glycol functionality is desirable owing to the benefits such as the reduction of protein adhesion which if not properly controlled can lead to activation of an immune response and/or clearance.

In this work AuNPs ~14nm and ~40nm in diameter are synthesized and functionalized with 1-undecanethiol (HS-CH₂)₁₁ terminated with either (OEG)₄OH or (OEG)₄CH₃. The AuNPs were characterized with transmission electron microscopy (TEM), time of flight secondary ion mass spectrometry (ToF-SIMS), X-ray photoelectron spectroscopy (XPS), attenuated total reflectance Fourier transform infrared spectroscopy (ATR-FTIR) and low energy ion scattering (LEIS). These studies provided both qualitative and quantitative information about the functionalization of the AuNPs with an OEG containing monolayer.

TEM showed the 14nm AuNPs had a narrower size distribution and more spherical shape than the 40nm AuNPs. ToF-SIMS clearly differentiates the two SAMs based on the C₃H₇O⁺ peak attributed to the CH₃ terminated SAM. Angle-resolved XPS high-resolution C1s spectra from flat gold samples at photoelectron take-off angles of 0°, 55° and 75° from the surface normal shows an increase in the ether component and reduction in CH with an increase in take-off angle. The changes in these values are comparable for both SAMs. This illustrates the increased presence of ethylene glycol monomers in the outer surface region and shows little difference between the two types of terminal functional groups. The 40 nm AuNPs show a slightly greater surface OEG concentration than 14 nm AuNPs, possibly indicating a more vertically oriented SAM on the 40 nm AuNPs. FTIR indicates similar crystalline CH₂ backbones for all samples, however it appears the structure of OEG head groups are less crystalline on the 14nm AuNPs. This likely results in thicker and/or higher density SAMs on the 40 nm AuNPs compared to the 14nm AuNPs. This is consistent with the nearly identical XPS determined surface elemental compositions determined for OEG SAMs on the two different sized AuNPs. This is contrary to previously XPS results observed for AuNPs functionalized with COOH SAMs [1].

1. Techane, S.D., L.J. Gamble, and D.G. Castner, *Multi-technique Characterization of Self-assembled Carboxylic Acid Terminated Alkanethiol Monolayers on Nanoparticle and Flat Gold Surfaces*. J Phys Chem C Nanomater Interfaces, 2011. **115**(19): p. 9432-9441.

5:40pm **AS+BI-TuA12 Characterization Challenges of Ceria Nanoparticles: When is a Nanoparticle Not a Nanoparticle?**, *D.R. Baer, P. Munusamy, A.S. Karakoti*, EMSL, Pacific Northwest National Laboratory, *S.V.N.T. Kuchibhatla*, Battelle Science and Technology India, *S.S. Seal*, University of Central Florida, *S. Thevuthasan, C.F. Windisch, Jr.*, EMSL, Pacific Northwest National Laboratory

Cerium oxide (ceria) nanoparticles are widely studied for their current and potential use in catalytic, energy, environmental protection and bio-medical applications. The performance of ceria in many of these applications depends on the ability of cerium to switch between +3 and +4 oxidation states. Unfortunately the physical and chemical properties of ceria nanoparticles reported in the literature are often in consistent and at times contradictory. Our research involves examination of the properties of ceria nanoparticles as they apply to materials science research and impact biological systems. We have found that it is possible to obtain what appears to be a self-consistent understanding of these particles by integrating dynamic light scattering, surface potential and UV-Vis adsorption measurements made in solution with *ex situ* x-ray photoelectron spectroscopy (XPS), x-ray diffraction (XRD) and transmission electron microscopy (TEM) observations. These measurements have demonstrated that a simple understanding of the chemical state of ceria nanoparticles as dependent on size is not adequate and has led to some of the inconsistent results in the literature. However, Raman and microXRD of wet ceria nanoparticles (pseudo *in situ*) show that the nature of the particles in solution is even more complex than indicated the above measurements. Raman and microXRD measurements indicate that both the chemical state and structure of the smallest nanoparticles can change depending on the nature of the solution. In solutions with low oxygen activity these particles have a ceria structure with cerium in +3 oxidation state while in highly oxidizing conditions the chemical state switches to +4 but the structure can be highly defected (XRD) and appears to be some type of cerium oxyhydroxide (Raman). The extent of the transformation depends on the size of the particles and appears complete for the smallest particles and partial or possibly not present for larger particles. These measurements demonstrate that the environment, size and time can impact the nature of these particles and that a variety of analysis methods – *in situ* as well as *ex situ* – are required for comprehensive understanding of ceria nanoparticle behaviors. Acknowledgement - Aspects of the work have been supported by the National Institute of Environmental Health Sciences under grant NIH U19 ES019544. Portions of this work were conducted in the Environmental Molecular Sciences Laboratory, a DOE user facility operated by Pacific Northwest National Laboratory for the Office of Biological and Environmental Research of the DOE.

Biomaterial Interfaces

Room: 23 - Session BI+AS-TuA

Characterization of Biointerfaces

Moderator: L. Meagher, CSIRO Materials Science and Engineering, Australia

2:00pm **BI+AS-TuA1 Surface Characterization Meets Cells and Proteins**, *B.D. Ratner*, University of Washington **INVITED**

Surfaces such as Ni(100) and Si(100) have been extensively studied and each has been found to be more complicated than simple geometric models would suggest. In this context, consider more mobile surfaces than these precisely defined crystal surfaces that are comprised of 20 amino acids integrated into hundreds of different proteins. Also, these surfaces may contain lipids and complex saccharide structures. It should be apparent that these surfaces can be staggeringly complex, and yet, as with surfaces in general, they efficiently catalyze complex reactions. But they do this at room temperature and atmospheric pressure in a way that makes life possible. For these reasons, the ability to characterize such surfaces will certainly lead to advances in surface design and surface functionality. Tools taken from the “surface science tool chest” can be applied in special ways to complement the tools developed by biologists for molecularly characterizing such surfaces. This talk, primarily focused on electron spectroscopy for chemical analysis (ESCA) and secondary ion mass spectrometry (SIMS), will start with analysis of amino acids and peptides, move to adsorbed protein films and finally consider complex surfaces such as decellularized extracellular matrices and cell monolayers.

2:40pm **BI+AS-TuA3 Using Binary Solvent Mixtures Produces High Graft Density Poly (Ethylene Glycol) Layers**, *A.R. Arcot*, Aalto University, Finland, *S. Zhang, R.L. Meyer, R. Ogaki*, Aarhus University, Denmark, *P. Kingshott*, Swinburne University of Technology, Australia

The success of PEG based non fouling surfaces depends on several factors such as graft density [1] and nature of head group-substrate interaction. [2] The ‘grafting-to’ technique though simple, often results in low pinning density when compared to ‘grafting-from’ technique. [3] This limitation of ‘grafting-to’ technique can be overcome by grafting under reduced solubility conditions. [4] We demonstrate a simple and versatile way to coat surfaces with PEG at high graft density using binary solvent mixtures, where a poor and a good PEG solvent are mixed with the PEG. The addition of poor solvent decreases the hydrodynamic radius of PEG molecules and hence results in thicker films due to diminished steric repulsion (Supplementary Fig 1a and 1b). The ‘good’ and ‘poor’ solvent pair was chosen based on solubility parameter distance calculated from Hansen solubility parameters. [5]

The PEG thiol films on gold formed from acetone-ethanol mixtures were analyzed using x-ray photoelectron spectroscopy (XPS), ellipsometry and atomic force microscopy. The PEG film gets thicker with more ethanol, which is a poorer solvent for PEG (Supplementary table 1). The high resolution sulfur 2p spectra confirmed the absence of precipitate particles. Grafting under high ionic strength conditions used by Kingshott et al. was used as reference for comparison. [4] The PEG thiol films were exposed to fetal bovine serum (FBS) and it was observed that thicker films could resist protein adsorption better than thin films that were formed from high solubility conditions. This method of using binary solvent mixtures can be extended to any polymer-substrate system by choosing appropriate ‘good-poor’ solvent pair. To demonstrate this point we also studied 5 kDa PEG silane films grafted using acetone-diethyl ether solvent mixture.

References:

1. L. D. Unsworth, H. Sheardown and J. L. Brash, *Biomaterials* (30), 5927-5933 (2005).
2. P. Kingshott, J. Wei, D. Bagge-Ravn, N. Gadegaard and L. Gram, *Langmuir* (17), 6912-6921 (2003).
3. N. Luo, J. B. Hutchison, K. S. Anseth and C. N. Bowman, *Macromolecules* (7), 2487-2493 (2002).
4. P. Kingshott, H. Thissen and H. J. Griesser, *Biomaterials* (9), 2043-2056 (2002).
5. B. A. Miller-Chou and J. L. Koenig, *Progress in Polymer Science* (8), 1223-1270 (2003).

3:00pm **BI+AS-TuA4 Adsorption Behavior of Serum Albumin on Nanocrystalline Apatites**, *K. Fears, D. Burden, C. Love*, U.S. Naval Research Laboratory, *D. Day*, Missouri University of Science and Technology, *T. Clark*, U.S. Naval Research Laboratory

The adsorption behavior of bovine serum albumin (BSA) on nanocrystalline hydroxyapatite (HA) and strontium apatite (SrHA) microspheres, derived from borate glasses, was assessed using circular-dichroism spectroscopy (ECD). Numerous reports have shown that surfaces which present nano-sized features can exhibit better cellular response than surfaces with features in the micron regime. The microspheres were incubated in BSA solutions (40 mg/mL; ~64% helix; ~1% sheet) to determine if BSA adsorbed in a fundamentally different manner than on bioinert yttria-alumina-silicate (YAS) spheres that induced minimal conformational changes (~56% helix; ~4% sheet). On the apatite spheres, BSA loss a substantial amount of its helical structure and strained disulfide bonds were detected. However, the protein density on the SrHA spheres was 50% lower than on the HA spheres, indicating that BSA has a higher affinity for irreversible adsorption on HA. 5,5'-Dithio-bis-(2-nitrobenzoic acid), was used to selectively modify free thiols post-adsorption, indicating that solvent-accessible free cysteines were present on the apatite spheres, despite the absence of a reducing agent. Subsequent BSA molecules, or other proteins *in vivo*, could potentially form intermolecular disulfide bonds leading to increased adhesion of proteins or support the formation of macroscopic protein structures.

4:00pm **BI+AS-TuA7 Quantitative Characterization of Cells in Biofilms and on Surfaces**, *A.C. Areias, C. Sousa, G.P. Mendes*, University of Minho, Portugal, *P. Mack*, Thermo Fisher Scientific, UK, *S. Lanceros-Méndez*, University of Minho, Portugal, *D.Y. Petrovykh*, International Iberian Nanotechnology Laboratory, Portugal

Films of cells on solid substrates are encountered in a variety of biological and biomedical environments, including cells in biofilms that spontaneously colonize medical devices and multilayers of cells filtered from suspensions for analysis. Understanding the chemical properties of cells in such films is important for providing clues about the behavior of the cells or about the effects of treatments that had been applied to the cells. Similarly to other

types of surface-based systems, the characterization of cells on solid substrates poses several analytical challenges. In particular, the small number of cells on each sample, the interference from surface interactions, and the absorbance of the substrate material prevent the characterization of cells on surfaces by the standard optical methods that are used in solution. We show that protocols similar to those used for preparing samples for electron microscopy can be adapted to prepare biofilm samples for characterization by X-ray photoelectron spectroscopy (XPS). Modern XPS instruments also provide the functionality required for characterization of these complex samples, for example, sample charging on insulating substrates can be efficiently and consistently compensated. Finally, the Ar cluster ion beam technology that recently became available on XPS instruments provides additional capabilities for a more detailed characterization of cells in biofilms, which typically have thicknesses larger than the sampling depth of XPS. We characterized several types of fixed and dried cell samples, including biofilms and cells filtered from suspensions, to compare different preparation protocols and to identify qualitative and quantitative parameters that can be reliably obtained from XPS analysis of such films of cells. We will present the results of our comparative analysis and possible applications of our methodology for characterization of cells in biological and biomedical experiments.

4:20pm BI+AS-TuA8 Antimicrobial Multilayers and Their Analysis by Laser Desorption Postionization Mass Spectrometry, M. Blaze, C. Bhardwaj, A. Akhmetov, L. Hanley, University of Illinois at Chicago

Bacterial biofilms are structured communities of microbes encapsulated within a self-developed polymeric matrix which adhere to surfaces and display genetic expression distinct from freely floating bacteria. Biofilms are frequently found to populate medical devices, leading to significant problems of infection in the first few days after implantation. Polyelectrolyte multilayers are developed for the delayed delivery of antibiotics to inhibit biofilm growth on biomedical devices [1]. Ten layers each of chitosan and alginate are prepared on a gold substrate, then infused with a novel antibiotic compound. This antibiotic-infused multilayer is found to inhibit the growth of *Enterococcus faecalis* bacterial biofilms on membranes over an 18 hour exposure. Laser desorption postionization mass spectrometry (LDPI-MS) is used to characterize the antibiotic after synthesis [2]. LDPI-MS analysis shows that the antibiotic survives sterilization of the multilayer surface, but <1% of the antibiotic remains after exposure to the biofilm.

[1] M. Blaze M.T., L.K. Takahashi, J. Zhou, M. Ahmed, G.L. Gasper, F.D. Pleticha, and L. Hanley, *Anal. Chem.* 83(2011) 4962.

[2] A. Akhmetov, J.F. Moore, G.L. Gasper, P.J. Koin, L. Hanley, *J. Mass Spectrom.* 45 (2010) 137.

4:40pm BI+AS-TuA9 Combining Colloidal Probe Atomic Force and Reflection Interference Contrast Microscopy to Study the Mechanics of Biopolymer Films, R.P. Richter, CIC biomaGUNE, Spain; Joseph Fourier University, France; Max Planck Institute for Intelligent Systems, Germany, S. Attili, CIC biomaGUNE, Spain; Max Planck Institute for Intelligent Systems, Germany, V. Borisov, Institut Pluridisciplinaire de Recherche sur l'Environnement et les Matériaux, France

Highly solvated polymer films have naturally evolved as multifunctional interfaces in biological systems, e.g. as mucosal films, cellular coats or bacterial biofilms. Surface-confined polymer films are also becoming increasingly popular as biomaterials and in various (bio)technological applications. The mechanical response of such polymer films is not only important for functional performance, but it can also provide valuable information about the film's internal organization, interactions and dynamics.

Here, we present a method that combines colloidal probe atomic force microscopy (AFM) and reflection interference contrast microscopy (RICM) to measure the mechanical properties of thin and solvated polymer films. When analyzing such films, a fundamental problem in colloidal probe AFM experiments is to determine the distance at closest approach between the probe and the substrate on which the film is deposited. By combining AFM and RICM *in situ*, forces and absolute distances can be measured simultaneously, and experimental drifts that otherwise would pass unnoticed can be corrected (1).

We used the combined setup to quantify the compressive mechanics of films of end-grafted hyaluronan (HA brushes) (2). Hyaluronan is a polysaccharide that plays a vital role in the organization and function of pericellular coats and extracellular matrices in vertebrates, and that is also attractive for biomedical applications. We show that HA brushes can swell dramatically as a function of ionic strength or upon binding of the cartilage proteoglycan aggrecan. Detailed comparison of the experimental data with polymer theory reveals that hyaluronan is a prototype of a strongly charged, semiflexible polyelectrolyte with intrinsic excluded volume (3).

The novel combined AFM/RICM setup should be broadly applicable to quantify the mechanical properties of soft hydrated polymer films with precise control of probe-sample separation. The generated data on HA brushes represent a valuable reference for future quantitative studies of more complex HA-rich films and to refine theories of polyelectrolyte brushes of strongly charged and intrinsically stiff polyelectrolytes.

References:

- (1) Attili and Richter *Langmuir* **2012**, 28:3206;
- (2) Richter et al. *J. Am. Chem. Soc.* **2007**, 129:5306;
- (3) Attili et al. *Biomacromolecules* **2012**, in press.

5:00pm BI+AS-TuA10 Surface Modification of Silicone Hydrogels through Adsorption of Diblock Copolymers, Y.J. Huo, S.S. Perry, University of Florida

The interaction between an ethylene oxide-*block*-butylene oxide (EOBO) copolymer surfactant and the surfaces of four silicone hydrogel (SH) contact lenses—PureVision® (PV), O₂OPTIX® (O₂), ACUVUE® Oasys® (AO), and Biofinity® (BF)—was investigated using angle-resolved X-ray photoelectron spectroscopy (AR-XPS) following treatment in test solutions containing various concentrations of EOBO. The nature of this interaction was further understood by quantifying the amount of eluted EOBO from each lens following the same treatment using ultra performance liquid chromatography (UPLC). The elution study revealed a large disparity in the amount of EOBO uptake by the different samples following each solution treatment. The XPS results, however, suggested that the amount of EOBO retained on the surface of the lenses demonstrated a largely different trend. For example, AO and BF displayed little evidence of signal at binding energies characteristic of the EO blocks, whereas O₂ and PV exhibited a clear EO signature. The correlation between the elution and XPS results highlights the difference in the interaction mechanism of the EOBO copolymer with different lenses. For lenses such as O₂OPTIX®, this interaction is predominantly bound to the surface; for ACUVUE® OASYS®, however, EOBO was uniformly distributed through the lens structure.

5:20pm BI+AS-TuA11 Microfluidic Devices for High-Throughput Quantitation in Biology: From Biophysics to Diagnostics, S. Maerkl, Ecole Polytechnique Fédérale de Lausanne (EPFL), Switzerland INVITED Microfluidic devices promise to have a significant impact on human health, particularly in diagnostics and drug development. We have developed a suite of microfluidic devices for high-throughput protein biochemistry and applied them to a wide range of applications spanning from protein biophysics to diagnostics, drug development, and vaccine development. Here I will discuss a novel approach to obtaining hundreds of kinetic rate measurements of bimolecular interactions on a single microfluidic device. In a second example I will present a generic microfluidic platform capable of quantitating biomarkers from a wide variety of samples in high-throughput and ultra-low cost, which could ultimately supersede the classical ELISA assay. We applied this platform to vaccine development by quantitating the activation of dendritic cells in response to a large panel of binary adjuvant combinations.

**Electronic Materials and Processing
Room: 9 - Session EM-TuA**

**Materials and Processes for Advanced Interconnects
Moderator: J. Bielefeld, Intel Corporation, S. King, Intel Corporation**

2:00pm EM-TuA1 Interface Engineering of Porous and Non-Porous ILD Layers Using Molecular Layer Deposition for Interconnect Applications, J. Bielefeld, Intel Corporation, H. Zhou, P. Loscutoff, Stanford University, S. Clendenning, Intel Corporation, S.F. Bent, Stanford University

As the dimensions continue to scale in interconnect processing, having a stable and controlled interface between the metal line and the dielectric material becomes more and more important. Molecular Layer Deposition (MLD) has been investigated as a method of growing thin films on dielectric surfaces which act as metal barriers, as blocking layers and as adhesion promoters. The advantage of MLD growth over conventional self-assembled monolayer (SAM) processing is the ability of MLD to easily grow films of varying thickness with tunable chemical functionality.

In this paper, we will discuss the growth and thermal stability of poly-urea-based MLD thin films on both porous and non-porous Carbon Doped Oxide (CDO) dielectric surfaces and compare this work to similar MLD films

grown on conventional SiO₂. A variety of characterization techniques, including thermal stress test, secondary ion mass spectrometry, x-ray photoelectron spectroscopy, and electron microscopy, were used to determine film composition, film stability, film adhesion, and degree of penetration into porous substrates. We investigate the importance of surface preparation on the anchoring of MLD films to CDO surfaces. Surface preparation is especially important when growing controlled layers on the surface of a porous dielectric, and we show that surface treatments influence the depth of penetration of the MLD film within porous CDO. Finally, we examine the deposition of thin metal films on top of MLD coated CDO layers (both blanket and patterned) and we show that the metal deposition process impacts both the MLD stability and the metal penetration into the ILD.

2:20pm EM-TuA2 Synchrotron X-ray Scattering Investigation of Morphological Stability of Cu Thin Film Interfaces, A.P. Warren, University of Central Florida, M.F. Toney, Stanford Synchrotron Radiation Lightsource, K. Barmak, Carnegie Mellon University, I.I. Kravchenko, Oak Ridge National Laboratory, K.R. Coffey, University of Central Florida

Nanometric films of pure Cu continue to attract attention due to their widespread use as interconnect material in the semiconductor community. Among the various engineering and scientific challenges posed by the continued use of Cu is its high surface mobility, which is well known to result in both electromigration and stress induced void formation in interconnects. The use of barrier/adhesion layers greatly improves the reliability of Cu interconnects. Nonetheless, the diffusion of Cu along the Cu/barrier interface is not well understood. Addressing the thermal stability and morphological evolution of Cu/barrier interfaces with the intent of quantifying interfacial diffusivities is the ultimate goal of this research.

Synchrotron x-ray scattering was used to study the evolution of interface roughness with annealing for a series of Cu thin films. The films were encapsulated in SiO₂ or Ta / SiO₂ and prepared by sputter deposition. Specular x-ray reflectivity was used to determine the root mean square roughness for both the upper and the lower Cu / SiO₂ (or Cu / Ta) interfaces. The lateral roughness was studied by diffuse x-ray reflectivity. Annealing the films at 600°C resulted in a smoothing of only the upper interface for the Cu / SiO₂ samples, while the lower Cu / SiO₂ interfaces and both interfaces for the Ta encapsulated films did not evolve significantly. As a function of roughness wavelength, the upper Cu / SiO₂ interfaces exhibited a roughness decay with annealing that was only 12.5% of that expected for classical capillarity driven smoothing of a free surface.

Continued work is focusing on further quantifying the interface kinetics for Cu/barrier systems. Using e-beam lithography methods, we have patterned a grating onto the surface of Cu thin films. Subsequent encapsulation and annealing will be carried out to study the effects of time and temperature on the patterned interface.

2:40pm EM-TuA3 Interconnect Scaling for 10nm and Beyond, Z. Tokei, IMEC, Belgium **INVITED**

The rapid introduction of different interconnect schemes enabled sustained scaling towards advanced technology nodes. Enablers are dimensional and material scaling together with system level aspects. Both logic and memory chips require tight pitch interconnecting lines with some common aspects and at the same time some different requirements. From material and dimensional scaling point of view logic interconnects demand tight pitch metal lines with low-k dielectrics, while emerging memories demand high current (or voltage) through tight pitch metal lines embedded into silicon oxide or air gaps. Conventional interconnects are built using multilevel damascene recently added with multiple patterning techniques leading to increased complexity. In order to break down the barrier and pave the way for 10nm technologies and beyond further material innovation along with non-conventional integration schemes and potentially system architecture modification will be necessary. Copper interconnects will require less than 2nm cladding layer or eventually the complete omission of conventional Ta-based diffusion barriers. Copper based metallization is expected to extend to 15nm critical dimensions although the number of elements through alloying and various liners increases already today. At 10nm and below alternatives to Cu wiring without a reliability issue is a candidate. For thin film deposition self assembled mono-layers, electroless and CVD/ALD techniques are becoming important, while novel dielectrics increasingly rely on self-assembling chemistries. This talk will focus on options that are being considered for 10nm and beyond. While several aspects will be mentioned, the main emphasis will be put on material innovation. Examples and case studies will be detailed for dielectric and metal options along with the relevant material characterization. Examples include defect characterization in low-k materials, phase identification and stress measurements in metal lines.

4:00pm EM-TuA7 High Throughput Crystal Orientation Mapping of Nanometric Cu: Impact of Surface and Grain Boundary Scattering on Electrical Resistivity, X. Liu, Carnegie Mellon Univ., A. Darbal, Nanomegas, K. Ganesh, Univ. of Texas at Austin, G. Rohrer, D. Choi, Carnegie Mellon Univ., P. Ferreira, Univ. of Texas at Austin, B. Yao, T. Sun, A.P. Warren, Univ. of Central Florida, M.F. Toney, Stanford Synchrotron Radiation Lab, K.R. Coffey, Univ. of Central Florida, K. Barmak, Carnegie Mellon Univ.

Due to limitations in characterizing twin boundaries in nanocrystalline Cu, it has been difficult to account for twin boundary scattering in the quantitative analysis of the resistivity size effect. In this study, a recently developed high throughput electron diffraction based metrology method in the transmission electron microscope, known as ASTARTM, is employed to obtain crystal orientation maps in two SiO₂ and 6 SiO₂/Ta₃₈Si₁₄N₄₈ encapsulated nanocrystalline Cu thin films. In ASTARTM, a dedicated hardware unit is used for precession and automated scanning of a nanosized quasi-parallel electron beam probe. A high speed external optical camera is then used for rapid acquisition of spot diffraction patterns. The acquired spot patterns are indexed automatically using a template matching algorithm. Significant improvement in the reliability of the orientation maps is achieved with electron beam precession. The use of precession reduces the dynamical effects and increases the number of spots in the diffraction pattern. The use of rapidly acquired spot patterns and the robust template matching algorithm make ASTARTM highly suitable for obtaining large datasets of crystal orientations. Analysis of the orientation maps of the Cu films shows a significant fraction of incoherent twin boundaries, indicating a potentially higher resistivity contribution from twin boundary scattering than previously assumed. Including the mixture of coherent and incoherent twin boundaries in the study of the resistivity size effect shows that the contribution from grain boundary scattering is still the dominant resistivity size effect in Cu, compared to surface scattering. Inclusion of the twin boundary mixture in a quantitative model shows the resistivity data to be best described by the Fuchs Sondheimer surface scattering model and the Mayadas Shatzkes grain boundary scattering model, combined using Matthiessen's rule (simple summation), with a surface specularly coefficient, $p = 0.50$, and a grain boundary reflection coefficient, $R = 0.26$. These values can be compared with values of $p = 0.52$ and $R = 0.43$ obtained in previous studies where the presence of twin boundaries was not considered. The potential to separately quantify electron scattering at twin boundaries and non-twin grain boundaries, the role of surface roughness, measured by x-ray reflectivity using synchrotron radiation, and the role of voids, measured using high angle annular dark field imaging in the transmission electron microscope, will also be discussed.

4:20pm EM-TuA8 Developing Robust Ultra-Low-k Dielectric ($\kappa \leq 2.55$) Materials using Novel Characterization Techniques for the 20nm Node and Beyond, D.R. Kioussis, Z. Sun, Y. Lin, GLOBALFOUNDRIES, A. Madan, N. Klymko, C. Parks, S. Molis, IBM Semiconductor R&D Ctr, E.T. Ryan, GLOBALFOUNDRIES, E. Huang, S.M. Gates, A. Grill, IBM T.J. Watson Res. Center, B. Kim, J.K. Kim, Samsung Electronics Co. Ltd., Korea, D. Restaino, T.H. Lee, IBM Semiconductor R&D Ctr, S. Hosadurga, IBM Research Group, S.A. Cohen, IBM T.J. Watson Res. Center, K. Virwani, IBM Research - Almaden

As the semiconductor industry pushes feature miniaturization limits beyond the 20nm node, novel interline dielectric materials with low dielectric constants (k-value), so called ultra low-k (ULK) materials ($k < 2.55$), are targeted to prevent capacitive crosstalk, interline leakage and reduced power consumption of advanced integrated circuits (IC). These materials are commonly porous (>15%) and organic in nature, which necessarily incur compromises in either the thermal or mechanical integrity with respect to more traditional dense low-k and SiO₂ dielectrics. Porous organosilicate glass ULK films with k-values 2.4 - 2.55 deposited by PECVD and cured via UV irradiation were first put into production at the 45nm node to further minimize RC delay. These ULK materials incorporate a large number of methyl (Si-CH₃) groups and pores into Si-O based network structures. The methyl groups disrupt the Si-O bond network, which tend to lower density and also lower polarizability making the film hydrophobic. Lower density, reduced polarizability, and greater hydrophobicity decrease the k-value. Introduction of porosity is used to further lower the k-value but other critical film properties, such as fracture toughness are affected. A viable ULK material must survive "damage" sustained from a series of processing steps that include dual-damascene (DD) litho, RIE, stripping and cleaning, CMP, and packaging. The reliability of devices containing these multi-layer DD stacks depends heavily on the chemical and mechanical stability of the dielectric, as this is the material and structural template in which the IC functionality is laid. Damage mechanisms occur when ULK is exposed to RF-plasma during etching or ashing. Subsequent moisture adsorption leads to the increase of effective k-value degrading performance. The integration challenges of ULK are significant, such as plasma damage, chip packaging, and ILD/metal barrier compatibility issues. Substantial optimization of the ULK properties via quick turn methods is crucial for successful integration

in advanced 20 nm generations. This study will discuss optimization of the material properties of single or dual precursor based ULK films through the use of different process chemistry and tuning of material deposition and UV curing parameters to meet the integration and packaging requirements. Quick turn characterization techniques were used to determine critical film properties. Correlation between film properties to the degree of plasma damage and mechanical integrity of ULK will be shown. We will show that careful modification of the ULK properties to minimize damage resulted in the successful integration at the 20nm node.

4:40pm EM-TuA9 Reflection Electron Energy Loss Spectroscopy Investigation of Band Gap and Defect States in Low-k and High-k Dielectrics, B. French, S. King, Intel Corporation

Electrical leakage in high-k metal gate transistors and low-k/Cu interconnect structures is a growing, vital concern as the nano-electronics industry moves to sub-16 nm technology nodes and continues to implement new materials. In order to understand the various possible leakage mechanisms in low-k/Cu interconnects, knowledge of the band gap and defect states in low-k and high-k dielectrics is needed but has gone largely unreported in many cases. In this regard, we have utilized Reflection Electron Energy Loss Spectroscopy (REELS) to determine the band gap of numerous single crystalline and amorphous low-k and high-k dielectric materials. We demonstrate that for standard single crystalline materials such as Quartz, 6H-SiC, and GaN, REELS band gap measurements agree with known values. For amorphous low-k and high-k thin film materials, we further demonstrate that REELS band gap measurements in most cases agree with optical measurements of the same materials. However in some cases, we have observed that the REELS analysis can be complicated by the existence of defect states within the band gap of these materials. While troublesome for band gap measurements, we demonstrate that this sensitivity can be utilized to determine the energy level of various defects in pristine and sputter damaged low-k SiOC:H dielectrics and in some cases identify the chemical identity of the defect.

5:00pm EM-TuA10 The Effects of Plasma Exposure and Vacuum-Ultraviolet Radiation on Photopatternable Low-k Dielectric Materials, M.T. Nichols, K. Mavrakakis, University of Wisconsin-Madison, Q. Lin, IBM T.J. Watson Research Center, J.L. Shohet, University of Wisconsin-Madison

Silsesquioxane-based photopatternable low-k (PPLK) dielectric materials[1] are promising alternatives to existing low-k dielectrics due to the reduction of BEOL integration complexity. However, processing-induced damage due to reactive species and energetic particles has been previously found to be problematic for low-k organosilicate dielectrics. Thus, for successful integration, the effects of charged-particle bombardment and photon irradiation (particularly in the vacuum ultraviolet range) must be characterized. In order to examine these effects, I-V and C-V characteristics were made on PPLK samples before and after exposure to a variety of argon plasma exposure conditions. Plasma parameters were varied between each exposure so that each sample was subjected to a range of charged particle and photon fluxes. In order to examine the effects of photon irradiation alone, PPLK samples were also exposed to monochromatic synchrotron radiation over energies varying from 5 to 15 eV. It was found that both charged-particle bombardment and photon irradiation have deleterious effects, resulting in increased magnitude of leakage currents and increased flat-band voltage shifts. VUV-exposed samples also exhibited increased leakage currents, but this effect was found to be strongly dependent on photon energy.

This work has been supported by the Semiconductor Research Corporation under Contract 2008-KJ-1871 and by the National Science Foundation under Grant CBET-1066231.

[1] Q. Lin, S.T. Chen, A. Nelson, et al., **Proc. Of SPIE** 7639, 76390J (2010)

5:20pm EM-TuA11 A Survey of Alternative Methods for Curing Porous SiCOH Films, N. LiCausi, V. Kamineni, GLOBALFOUNDRIES, S. Ohsiek, H. Geisler, M. Weisheit, M. Majer, GLOBALFOUNDRIES, Germany, E.T. Ryan, GLOBALFOUNDRIES

SiCOH films have been used in advanced semiconductor devices to enable continued scaling of interconnect integration. The further scaling of ultra low *k*-value (ULK) films has necessitated a move to porous SiCOH films. Porosity is intentionally introduced to decrease the dielectric *k*-value and therefore reduce interconnect RC delay. However, this porosity also leads to reduced mechanical strength and presents substantial challenges to integration and packaging.

Nanoporous thin films can be formed with PECVD of a SiCOH film with embedded porogen clusters. The porogen can either be supplied by a second porogen precursor or using a single precursor containing an embedded porogen fragment. The porogen is then removed with curing. Currently the

industry favors UV assisted thermal curing to simultaneously drive out porogen (forming the porous structure) and enable cross-linking of the film matrix (Si-O-Si bond formation). However, prior investigation claims that this porogen is not completely removed, leaving porogen residue in the pores [1]. It is believed that cross-linking of the film matrix inhibits porogen removal and inversely, porogen residue prevents efficient cross-linking. Subsequently, this can lead to degraded electrical and mechanical performance.

A new approach under review uses a two-step curing procedure. First porogen is removed from the film with a novel film treatment. This step targets porogen removal, but does not cross-link the film's matrix. An example of this is remote H₂/He plasma (H radical exposure) [2]. After removing the porogen, a traditional UV assisted thermal cure strengthens the film and drives out any remaining porogen. We evaluated this and two similar approaches and observed the same qualitative trends. Generally speaking, when using conventional curing techniques there is an unavoidable tradeoff between *k*-value and mechanical performance. However, the two-step process results in films which have both increased mechanical strength and improved electrical performance.

Films have been evaluated electrically (*k*-value, breakdown voltage, leakage current). Film structure (porosity and pore size distribution), mechanical properties (Young's modulus) and film composition were measured with ellipsometry porosimetry, nanoindentation and XPS/FTIR, respectively. The UV absorption peaks related to porogen residue have also been measured using vacuum ultraviolet spectroscopic ellipsometry.

[1] A.M. Urbanowicz, K. Vanstreels, D. Shamiryan, S.D. Gendt and M.R. Baklanova, *Electrochem. Solid St.* **12** (2009).

[2] A.M. Urbanowicz, K. Vanstreels, P. Verdonck, D. Shamiryan, S. De Gendt and M.R. Baklanov, *J. Appl. Phys.* **107** (2010).

5:40pm EM-TuA12 Metallization Challenges in Integration of Soft Dielectric Materials, R. Chebiam, C. Jezewski, B. Krist, H. Yoo, J. Clarke, Intel Corporation

In order to take advantage of reduction in transistor gate delay at smaller dimensions, back-end interconnect (RC) delay has to be minimized. One of the methods of reducing the system capacitance is by reducing the dielectric constant of ILD's at each technology node. There is an observed trend that modulus and hardness of dielectric films degrades with decreasing *k* value. This is either due to increased carbon content or increased porosity. Ultra low-*k* materials (*k*<2.2) are well known to be susceptible to damage during the patterning process. However, there has been little focus on the damage resulting from the metallization process (barrier/seed, plate, and CMP). In this study we use a spin-on dielectric (*K*~2.2) with *E* =4.5GPa and *H*=0.3GPa to investigate metallization damage. The soft ILD shows little feature size blowout post metallization for large feature sizes (>100nm). However, feature size blowout of ~10-18 % is seen for sub 100nm features post metallization compared to pre-metallization. Feature blow out appears to be driven by dielectric densification and to a less extent from material etch out. Densification damages the dielectric by increasing the *k* value and hence must be minimized. The origin of the feature size blowout can be traced to an energetic barrier or seed deposition process. For example, a high resputter PVD barrier process has similar blowout compared to an ALD Liner process. When the energy of barrier /seed process was decreased blowout was reduced, but this was accompanied by poorer sidewall coverage which will result in degraded gapfill and reliability. The key challenge can then be highlighted as developing a low energy barrier/seed process that has good sidewall coverage (conformality) and no feature blowout to enable ultra low-*k* dielectrics integration.

**Energy Frontiers Focus Topic
Room: 15 - Session EN+TF-TuA**

**Thin Film, Heterostructured, and Organic Solar Cells
Moderator: M. Filler, Georgia Institute of Technology**

2:00pm EN+TF-TuA1 Photonic Materials for Solar Energy Conversion at the Thermodynamic Limit, H.A. Atwater, California Institute of Technology INVITED

Ever since serious scientific thinking went into improving the efficiency of photovoltaic energy conversion more than 50 years ago, thermodynamics has been used to assess the limits to performance, guiding advances in materials science and photovoltaic technology. Photovoltaics have advanced considerably, resulting in single-junction solar cells with a record efficiency of 28.8% and multi-junction cells with an efficiency of 43.5%. As impressive as these advances are, these record efficiencies and also today's manufactured cell efficiencies in the 10–18% range fall far short of

the thermodynamic limits. Why such a large gap? There is no fundamental reason, and in this talk, I will discuss methods for systematically addressing the thermodynamic efficiency losses in current photovoltaics that can enable a next phase of photovoltaic science and engineering – ultrahigh efficiency photovoltaics. This development takes advantage of recent advances in the control of light at the nanometer and micron length scales, coupled with emerging materials fabrication approaches, and will allow the development of solar cells with efficiencies in the 50–70% range.

Web resources:

<http://www.lmi.caltech.edu/>

<http://daedalus.caltech.edu/>

2:40pm **EN+TF-TuA3 Semiconducting Carbon Nanotubes as Polymer-Like Near-Infrared Bandgap Photoabsorbers**, M.S. Arnold, D.J. Bindl, M.-Y. Wu, M.J. Shea, University of Wisconsin Madison **INVITED**

We are pioneering the exploration of semiconducting carbon nanotubes as the light-absorbing components of polymer-inspired solar cells and photodetectors.[1-2] Carbon nanotubes are conjugated polymer-like materials with built-in long-range crystallinity that gives rise to exceptional charge and energy transport characteristics, strong light absorption tunable throughout the visible and near-infrared spectra, and outstanding stability in air. We have discovered how to efficiently harvest photogenerated charges and excitons from optically excited nanotubes by pairing them in donor / acceptor heterojunctions with more electronegative electron accepting semiconductors. In particular, semiconducting nanotubes form a type-II heterojunction with C60 fullerenes and C60 derivatives with energy offsets sufficient to drive electron transfer from the optically excited nanotubes to C60, with an internal quantum efficiency (QE) for exciton dissociation and charge transfer > 75%, for nanotubes of diameter < 1 nm and gaps > 1 eV. Thus, we have identified the nanotube / C60 materials pair as a promising basis for future nanotube-based light harvesting devices.

In order to further guide the implementation of nanotubes in devices, we have also characterized exciton transport in nanotube films and shown that excitons can migrate in films by two mechanisms: (i) over short distances of ~ 5 nm via slow inter-nanotube diffusion and (ii) potentially over much longer distances via rapid intra-nanotube diffusion. As a proof-of-principal, we have fabricated both bilayer and blended nanotube / C60 heterojunction devices, which are analogous to polymer solar cells with nanotubes taking on the role of the semiconducting “polymer”. Thus far, we have realized a peak external QE > 20% across 1000 – 1365 nm and a monochromatic power conversion efficiency of 7% at 1050 nm. Our results show that AM1.5G photovoltaic power conversion efficiency > 10% should be possible with future optimization of: (a) the nanotube bandgap (and diameter) distribution and (b) improved control over morphology.

[1] D. J. Bindl, M.-Y. Wu, M. S. Arnold, *Nano Letters* (2011).

[2] D. J. Bindl, A. S. Brewer, M. S. Arnold, *Nano Research* (2011).

4:00pm **EN+TF-TuA7 Understanding Vertical Stratification in Polymer:Fullerene Bulk Heterojunction Solar Cells**, M.D. Clark, Air Force Research Laboratory, M.L. Jepsersen, University of Dayton Research Institute, B.J. Leever, Air Force Research Laboratory

In the bulk heterojunction architecture of polymer-based solar cells (PSCs), the separate acceptor-donor phases form a bi-continuous inter-penetrating network by simultaneous casting from solution with morphological control stemming from external parameters such as thermal annealing, co-solvent inclusion, and drying conditions. While such treatments enhance device performance, a fundamental understanding of vertical concentration gradients within the fabricated active layer has been limited. In an effort to understand such morphological changes, several reports have explored 3D bulk heterojunction nanostructure using electron tomography,¹ ellipsometry,² neutron scattering,³ and spectroscopic techniques.⁴ This work, however, has yielded somewhat contradictory conclusions about fundamental network development and the origin of emerging concentration gradients. For example, some studies reported nearly equal blends at the PEDOT:PSS surface of annealed samples,^{2,4c} while others found P3HT^{1,4a,4c} or PCBM^{3,4b,4d,4f} preferentially decorating the buried interface. Several groups^{2b,3,4c,4f} further reported annealing causes PCBM diffusion towards the exposed surface, suppressing as cast vertical composition gradients. However, Xu et al.^{4b} detected PCBM migration towards the PEDOT:PSS interface upon annealing, while Xue et al.^{4a} suggested PCBM diffusion away from both interfaces. Here we report a combined experimental and theoretical analysis of phase segregation. The vertical stratification within a P3HT:PCBM bulk heterojunction solar cell is examined by depth profiling using both x-ray photoelectron spectroscopy (XPS) and time of flight

secondary ion mass spectrometry (ToF-SIMS), with the effects of thermal annealing and P3HT:PCBM ratio being explored. In addition, the vertical phase stratification is predicted on thermodynamic grounds based on measured interfacial energies of the PSC constituents. Using these results, a fundamental understanding of the thermodynamic driving force for bulk heterojunction phase segregation and vertical stratification is then presented.

References

1 van Bavel, S.S. et al. *Nano Lett.* **9**, 507 (2009).

2 (a) Germack, D.S. et al. *Macromolecules* **43**, 3828 (2010); (b) Campoy-Quiles, M. et al. *Nat. Mater.* **7**, 158 (2008).

3 Parnell, A.J. et al. *Adv. Mater.* **22**, 2444 (2010).

4 (a) Xue, B. et al. *J. Phys. Chem. C* **114**, 15797 (2010); (b) Xu, Z. et al. *Adv. Funct. Mater.* **19**, 1227 (2009); (c) Yu, B.-Y. et al. *ACS Nano* **4**, 833 (2010); (d) Vaynzof, Y. et al. *ACS Nano* **5**, 329 (2011); (e) Wang, H. et al. *Chem. Mater.* **23**, 2020 (2011); (f) Germack, D.S. et al. *Appl. Phys. Lett.* **94**, 233303 (2009).

4:20pm **EN+TF-TuA8 Novel, Single-Crystalline-like Silicon on Low-Cost, Flexible Substrates for High Efficiency Thin Film Photovoltaics**, V. Selvamanickam, P. Dutta, R. Wang, Y. Gao, M. Yang, G. Majkic, E. Galtsyan, University of Houston

Thin film photovoltaics (PV) is being pursued by several institutions as a lower cost alternative to crystalline wafer technologies. The use of much less materials and roll-to-roll continuous processing in thin film technologies have been touted as the pathway to low-cost PV. However, the efficiencies of production thin film Si solar cells are about one half that achieved with crystalline silicon. Hence, achievement of single-crystalline-like silicon photovoltaics on flexible, low-cost substrates can be game changing by combining high efficiency with low cost. We are developing such a technology by creation of an architecture that yields single-crystalline-like thin films even on polycrystalline or amorphous substrates. This technology has been very successfully demonstrated and being commercialized in the superconductor field and inserted in the U.S. electric power grid [1].

The enabler that we have employed in this work is a single-crystalline-like thin film template of MgO made by Ion Beam-Assisted Deposition (IBAD). Such IBAD films have been successfully employed as templates for epitaxial growth of cube-textured superconducting films on polycrystalline substrates with critical current densities as high as those achieved on single crystal substrates [1].

MgO templates made by IBAD on flexible metal substrate have been used for epitaxial growth of germanium films using intermediate oxide layers. All layers were deposited by reel-to-reel magnetron sputtering and strongly (400) textured Ge films with an in-plane texture spread of just 1° FWHM were achieved [2]. Optical properties of the germanium films are found to be comparable to that single crystal Ge and Hall mobility values over 700 cm²/Vs have been achieved. Epitaxial (400) textured silicon films have been grown by reel-to-reel magnetron sputtering on the Ge films. A continuous grading of germanium to silicon has been done to accommodate for the lattice mismatch. While excellent epitaxial growth has been achieved in Si and Ge on flexible metal substrates, the defect density of the films showed a high value of 10⁸ per cm². Cross sectional TEM of the multilayer architecture showed concentration of threading dislocations near the semiconductor-oxide interface. Defect reduction strategies are being employed and recent progress in use of single-crystalline-like templates on low-cost, flexible substrates for high-efficiency silicon photovoltaics will be discussed in this presentation.

1. V. Selvamanickam et al. *IEEE Trans. Appl. Supercond.* **19** (2009) 3225.

2. V. Selvamanickam et al. *J. Crystal Growth* **311**, (2009) 4553.

4:40pm **EN+TF-TuA9 High-Efficiency Multijunction Solar Cells Employing Dilute Nitrides**, V.A. Sabnis, H.B. Yuen, M. Wiemer, Solar Junction **INVITED**

Concentrating photovoltaic (CPV) systems have the opportunity to provide the lowest cost of electricity in hot, sunny climates. The advantages of CPV are based, in part, from the high performance offered by multijunction solar cells made from group III-V compound semiconductors. Unlike traditional PV, high concentration systems utilize mm-scale solar cells that comprise only 10-15% of the overall system cost. This low cost share means that increasing cell efficiency has significant leverage in driving down upfront capital costs and the leveled cost of electricity of a CPV project.

Production cell efficiencies for triple junction solar cells have reached 40% under concentration (25°C, AM 1.5D spectrum). We will review a number of exciting approaches for increasing cell efficiency that are being investigated world wide. Solar Junction has developed a set of dilute-nitride compound semiconductors that offer broad bandgap tunability over the infrared while retaining lattice matching to GaAs and Ge substrates. While significant efforts have been undertaken to develop dilute nitrides for multijunction solar cells over the last 15 years, these approaches have resulted in films that exhibited poor minority carrier properties resulting in low current drives and output voltages. Solar Junction has developed a molecular beam epitaxy process utilizing antimony as a surfactant that significantly enhances the minority carrier properties. Triple junction cells utilizing GaInNAsSb bottom junctions have achieved a world record efficiency of 43.5% under concentration. When used in conjunction with well known InAlGaP and AlGaAs compounds, GaInNAsSb films complete a lattice-matched epitaxial platform for enabling 4-, 5-, and 6-junction cells for achieving > 50% efficiencies in the coming years.

5:20pm **EN+TF-TuA11 Non-Radiative Carrier Recombination in InGaAs/GaAsP Strain-Balanced Superlattice Solar Cell**, *T. Aihara*, University of Miyazaki, Japan

An inserting of the quantum wells (QWs) to GaAs p-i-n solar cells could be a promising candidate to solve the current matching issue in the multi-junction solar cells[1]. We have successfully obtained the non-radiative recombination process for excitonic and subband absorptions in the GaAs/AlAs multiple QWs (MQWs) by using PPT methods [2]. In this study, we investigate escape, radiative and non-radiative recombination mechanisms of photo-generated carriers in the strain-balanced InGaAs/GaAsP MQWs or superlattice (SL) inserted into GaAs p-i-n solar cell structure to improve the photovoltaic performance. We then evaluated above three processes by using the surface photovoltage (SPV), photoluminescence (PL), and piezoelectric photothermal (PPT) spectroscopies, respectively. A InGaAs/GaAsP MQWs absorbing layer that inserted into GaAs p-i-n junction was composed of 10 stacks of 7.4-nm-thick InGaAs well and 10.8-nm-thick GaAsP barrier. For SL absorbing layer, ultra-thin GaAsP barriers of 3.7 nm thickness with 0.56-nm-thick GaAs buffer were prepared. All the layers were grown by metal-organic vapor phase epitaxy on the GaAs substrate. The PPT detects a heat generated by the non-radiative recombination by the PZT directly attached to rear surface of the sample. Figures 1 and 2 show the temperature change of PPT spectra of MQWs and SL with GaAs thin buffer samples, respectively. For MQWs sample, three peaks were observed and A-peak was concluded to be due to the excitonic transition associated with the electron transition between first electron (e1) and heavy-hole subbands (hh1) in QW. On the other hand, B-peak was concluded to be the electron transition between 1st minibands in conduction and valence bands in SL. As the temperature decreased, peak intensities of A and B increased, whereas corresponding SPV peaks decreased. The temperature dependence of PL, PPT, and SPV signal intensities can be fitted with the Arrhenius equation. Figure 3 shows the fitting results of PPT A (MQWs) and B (SL) and SPV A peaks. As shown in Fig. 3, activation energy of SL was smaller than that of MQWs. This result implied that carrier escape from the QWs was enhanced for the case of SL. References [1] K. W. J. Barnham and G. Duggan, *J. Appl. Phys.* 67 (1990) 3409. [2] P. Wang et al.: *Jpn. J. Appl. Phys.* 46 (2007) 6857.

5:40pm **EN+TF-TuA12 Piezoelectric Photothermal Spectra and Carrier Nonradiative Recombination in InGaAs/GaAsP Super Lattice Structured Solar Cells**, *T. Ikari, T. Aihara, Y. Nakano*, University of Miyazaki, Japan, *Y. Wang, M. Sugiyama, Y. Nakano*, University of Tokyo, Japan, *A. Fukuyama*, University of Miyazaki, Japan

Fabrication of multi quantum well (MQW) or superlattice (SL) structures embedded in an absorption layer of solar cell is a promising idea for developing higher efficient devices. This is because the quantum well can extend the absorption to longer wavelength region and enhance the short-circuit current. However, recombination centers for carriers are simultaneously generated at the boundaries, leading to the degradation of conversion efficiency. Although optical absorption and spectral response spectroscopy are usually used for investigating absorption and recombination mechanism in the solar cell, no direct technique for characterizing nonradiative recombination is presented. We have developed the piezoelectric photothermal (PPT) spectroscopy for detecting such nonradiative recombination in the QW [1]. Heat generated by a nonradiative recombination of photoexcited carriers were detected as PPT signal by using a piezoelectric transducer. In this paper, we report on the PPT spectra of InGaAs/GaAsP SL layer and show that this technique is sensitive and powerful to investigate the absorption spectra of SL. It is, then, becomes possible to discuss a recombination mechanism of the photo-excited carriers in the solar cell structure from the non-radiative transition point of view.

A strain-balanced InGaAs/GaAsP SL layer embedded into the intrinsic region of the GaAs p-i-n solar cell were prepared. The SL absorbing layer was prepared in the structure of InGaAs(3.7nm)/GaAsP(5.4nm) with 0.56-nm-thick GaAs buffer layer by MOVPE technique on the GaAs substrate [2]. PPT spectrum at 100K shows two dominant peaks. The conventional absorbance of SL and the PPT spectrum of the MQW (InGaAs(7.4nm)/GaAsP (10.8nm)) samples were also discussed for comparison. A signal from SL is more clearly observed in the PPT than the absorbance spectra. Although the step like signals accompanied with the exciton transition are well resolved for MQW samples, no step but broad peaks around 1.395 and 1.45 eV were observed for SL sample. The energies of these peaks were as expected from the calculation of the single QW without any interaction of the neighboring QW, i.e. tunneling. Since the wave function of quantized level spread into the next well for the SL structure, broad peaks were, then, observed. Although the step like density of states should appear even in the SL, drastic decrease of the PPT signal beyond the peak was observed. One possible reason is that the number of carriers that recombine nonradiatively inside the quantum well decreases by tunneling.

[1] T. Ikari, *et al.*, *Phys. Rev. B* 77 (2008) 125311.

[2] M. Sugiyama *et al.*: *J. Cryst. Growth* 315 (2011) 1.

Exhibitor Technology Spotlight

Room: West Hall - Session EW-TuA

Exhibitor Technology Spotlight

Moderator: D. Surman, Kratos Analytical Inc.

3:20pm **EW-TuA5 NEG Pumps Improving the Performance of Vacuum Systems**, *B. Garcia, E. Maccallini, P. Manini*, SAES Getters

The presentation will include a discussion of new and existing products and how NEG pump technology improves over all vacuum performance. The positive effect NEG Pump technology has on the bakeout process will be discussed as well.. Examples and data will be provided to support the discussion.

3:40pm **EW-TuA6 New Developments in Thin Film Deposition from Kurt J. Lesker Company®**, *S. Armstrong, D. Bingaman*, Kurt J. Lesker Company

In this spotlight the Kurt J. Lesker Company will update the industry on some of its new thin film deposition solutions.

Graphene and Related Materials Focus Topic

Room: 13 - Session GR+AS+NS+SP+SS-TuA

Graphene Characterization Including Microscopy and Spectroscopy

Moderator: J.C. Hone, Columbia University

2:00pm **GR+AS+NS+SP+SS-TuA1 High Resolution Real and Reciprocal Space Photoelectron Emission Microscopy on Heterogeneous Graphene/SiC(000-1)**, *K. Winkler, B. Kroemker*, 1Omicron NanoTechnology, Germany, *N. Barrett*, IRAMIS, Saclay, France, *E. Conrad*, GeorgiaTech

We present energy filtered electron emission spectromicroscopy with high spatial and wave-vector resolution on few-layer epitaxial graphene on SiC(000-1) grown by furnace annealing.

Conventional electron spectroscopy methods are limited in providing simultaneous real and reciprocal or k-space information from small areas under laboratory conditions. Therefore, the characterization of materials with only micron scale sample homogeneity such as epitaxially grown graphene requires new instrumentation. Recent improvements in aberration compensated energy-filtered photoelectron emission microscopy (PEEM) can overcome the known limitations in both synchrotron and laboratory environments. Here we report 2D maps of the k-parallel π - π * band dispersion in micron-scale regions and correlate them with spatially resolved chemical information on the same regions. Only the combination of high lateral, high energy, high k-resolution and controlled switching between real space and k-space allows detailed understanding of micron size sample sites with 1-3 layers graphene. The experiments underline the importance of simultaneous lateral, wave vector and spectroscopic resolution on the scale of future electronic devices in order to precisely characterize the transport properties and band alignments.

2:20pm **GR+AS+NS+SP+SS-TuA2 Evidence of Nanocrystalline Semiconducting Graphene Monoxide during Thermal Reduction of Graphene Oxide in Vacuum.** *C. Hirschmugl, E. Mattson, H. Pu, S. Cui, M. Schofield, S. Rhim, G. Lu, M. Nasse*, University of Wisconsin Milwaukee, *R.S. Ruoff*, University of Texas at Austin, *M. Weinert, M. Gajdardziska-Josifovska, J. Chen*, University of Wisconsin Milwaukee

As silicon-based electronics are reaching the nanosize limits of the semiconductor roadmap, carbon-based nanoelectronics has become a rapidly growing field, with great interest in tuning the properties of carbon-based materials. Chemical functionalization is a proposed route, but syntheses of graphene oxide (G-O) produce disordered, nonstoichiometric materials with poor electronic properties. We report synthesis of an ordered, stoichiometric, solid-state carbon oxide that has never been observed in nature and coexists with graphene. Formation of this material, graphene monoxide (GMO)[1], is achieved by annealing multilayered G-O. A combination of transmission electron microscopy and infrared microspectroscopy have provided critical experimental evidence to identify the novel structure. These results indicate that the resulting thermally reduced G-O (TRG-O) consists of a two-dimensional nanocrystalline phase segregation: unoxidized graphitic regions are separated from highly oxidized regions of GMO. GMO has a quasi-hexagonal unit cell, an unusually high 1:1 O:C ratio, and a calculated direct band gap of approximately 0.9 eV.

This work was supported by the NSF (CMMI-0856753 and CMMI-0900509). This work is based upon experiments performed at the Synchrotron Radiation Center. The SRC is funded by the University of Wisconsin-Madison and the University of Wisconsin-Milwaukee. Work performed at the SRC IRENI beamline been done with support from an NSF Major Research Instrumentation grant (DMR-0619759). The authors thank Bruker Technologies for the Grazing Angle Objective used for this work.

[1] Mattson, E.C. et al., ACSNano (2011) 5 (2011) 9710-9717.

2:40pm **GR+AS+NS+SP+SS-TuA3 Scanning Tunneling Spectroscopy of Epitaxial Graphene: Local Band Mapping and Wavefunction Engineering.** *P.N. First*, Georgia Tech **INVITED**

Because the crystalline orientation is determined prior to growth, epitaxial graphene (EG) on silicon carbide is an excellent material to consider for 2D wavefunction engineering, where device properties are designed through wavefunction confinement and material strain. In pursuit of this goal, we use scanning tunneling microscopy (STM) and spectroscopy (STS) to characterize the local structural and electronic properties of EG and a simple EG nanostructure. With some care, STS can be used to measure the full energy-momentum dispersion of both filled and empty states, on length scales determined by the coherence of the graphene wavefunctions. Applying a magnetic field introduces a field-tunable comb of discrete Landau level energies that we use to obtain high momentum resolution, to characterize the tip-induced surface potential, and to detect subtle interlayer interactions in a multilayer graphene stack. * Work performed in collaboration with NIST Center for Nanoscale Science and Technology ** Funded in part by NSF and by NRI-INDEX.

4:00pm **GR+AS+NS+SP+SS-TuA7 Intercalation of O₂ and CO Controlled by the Mesoscopic Structure of Graphene.** *E. Gränäs, J. Knudsen*, Lund University, Sweden, *U. Schröder, T. Gerber, C. Busse*, Universität zu Köln, Germany, *M.A. Arman, K. Schulte, J.N. Andersen*, Lund University, Sweden, *T.W. Michely*, Universität zu Köln, Germany

Intercalation of gases between epitaxial graphene and its substrate has become a topic of interest for studies due to, for example, the unique opportunities to modify the graphene-substrate interaction and the possibilities to perform chemistry under the graphene layer. Further, a profound knowledge about graphenes stability in gases at elevated temperatures and pressures is essential for, among other things, the correct interpretation of gas adsorption studies on graphene supported metal cluster arrays.

We have studied intercalation and etching of Ir(111) supported graphene upon gas exposure to common gasses such as O₂ and CO in the entire pressure interval from 10⁻⁸ to 0.1 mbar. Comparing perfect graphene layers without holes with graphene films, that only covers a fraction of the Ir(111) surface, we reveal that the holes - or more specific the graphene edges - are essential for intercalation.

For oxygen exposed graphene we develop a coherent picture of temperature dependent oxygen etching and intercalation. Using X-ray photoemission spectroscopy (XPS) and scanning tunnelling microscopy (STM) we show that a perfect graphene layer is stable against etching and intercalation up to 700 K, whereas at higher temperatures etching, but no intercalation, takes place. In contrast, a partial graphene coverage on Ir(111) enables dissociative oxygen adsorption on the bare Ir and subsequent intercalation underneath graphene flakes at 355 K and above. Intercalated oxygen

remains stable up to a temperature of 600 K, above this temperature it desorbs in the form of CO or CO₂. We have determined XPS and STM fingerprints for the intercalated oxygen structure and we unambiguously assign it to a p(2x1)-O structure similar to the one observed on clean Ir(111). The decoupling of the intercalated graphene film from the metal substrate is directly visualized through the inability to form well-ordered Pt cluster arrays on the O-intercalated areas of graphene on Ir(111). Further, we have identified the rate limiting step for oxygen intercalation to be unlocking of the graphene edge and propose that this takes place through bond breaking between graphene edge bonds and the Ir substrate.

Using a combination of high pressure X-ray photoemission spectroscopy (HP-XPS) and STM we also show that CO intercalation takes place at room temperature and pressures in the 1 mbar range. The adsorption structure of intercalated CO is determined to be (3√3 × 3√3)R30°, identical to the structure observed on clean Ir(111) upon high pressure CO exposure.

4:20pm **GR+AS+NS+SP+SS-TuA8 Long-range Atomic Ordering and Variable Interlayer Interactions in Two Overlapping Graphene Lattices with Stacking Misorientations.** *T. Ohta, T.E. Beechem*, Sandia National Laboratories, *J.T. Robinson*, Naval Research Laboratory, *G.L. Kellogg*, Sandia National Laboratories

We report a method to examine the effect of stacking misorientation in bilayer graphene by transferring chemical vapor deposited (CVD) graphene onto monolithic graphene epitaxially grown on silicon carbide (SiC) (0001). The resulting hybrid bilayer graphene displays long-range Moiré diffraction patterns having various misorientations even as it exhibits electron reflectivity spectra nearly identical to epitaxial bilayer graphene grown directly on SiC. These varying twist angles affect the 2D (G^{*})-band shape of the Raman spectrum indicating regions of both a monolayer-like single π state and Bernal-like split π states brought about by the differing interlayer interactions. This hybrid bilayer graphene fabricated via a transfer process therefore offers a means to systematically study the electronic properties of bilayer graphene films as a function of stacking misorientation angle.

The work at Sandia National Laboratories was supported by LDRD and by the US DOE Office of Basic Energy Sciences, Division of Materials Science and Engineering. Sandia National Laboratories is a multi-program laboratory managed and operated by Sandia Corporation, a wholly owned subsidiary of Lockheed Martin Corporation, for the U.S. Department of Energy's National Nuclear Security Administration under contract DE-AC04-94AL85000. The work at NRL was funded by the Office of Naval Research.

4:40pm **GR+AS+NS+SP+SS-TuA9 Chemically-resolved Interface Structure of Epitaxial Graphene on SiC(0001).** *J.D. Emery*, Northwestern Univ., *B. Detslefs*, European Synchrotron Radiation Fac., France, *H.J. Karmel*, Northwestern Univ., *V.D. Wheeler*, U.S. Naval Research Lab, *J.M.P. Alaboson*, Northwestern Univ., *L.O. Nyakiti, R.L. Myers-Ward, C.R. Eddy, Jr., D.K. Gaskill*, U.S. Naval Research Lab, *M.C. Hersam*, Northwestern Univ., *J. Zegenhagen*, European Synchrotron Radiation Fac., France, *M.J. Bedzyk*, Northwestern Univ.

The implementation of graphene into next-generation electronics will require production high-quality graphene at the wafer scale. One promising route for the production of wafer-scale graphene is to grow epitaxial graphene (EG) via thermal decomposition of Si-terminated SiC (SiC(0001)). This method produces high-quality EG, but is accompanied by the formation of the so-called "buffer layer" at the interface, which is known to affect the electronic properties of the graphene. Despite numerous efforts to determine the nature of the buffer layer, debate persists concerning its atomic and chemical structure. Here, we use the X-ray Standing Wave (XSW) technique to create a precise chemically-sensitive description of the distributions of Si and C at the interface. This technique, which combines X-ray scattering and X-ray Photoelectron Spectroscopy (XPS), is capable of locating coherent distributions of chemically distinct species above a single crystal surface. This allows for a more detailed description of the interface than those afforded by scattering or XPS alone. Our analysis shows that the buffer layer, which is present in both UHV and furnace-grown EG/SiC(0001), contains no substantial non-bulk or oxide silicon component, and is thus purely carbon. We identify two chemically distinct carbon species within the interface layer, each with a distinct location above the Si-terminated surface, and report their positions and distributions with sub-angstrom precision. These results help to clarify long-standing uncertainties about the interfacial structure of graphene/SiC(0001). Further, we also highlight the potential for XSW with XPS as a valuable tool in the structural determination of complex interfaces, such as functionalized, doped, or intercalated epitaxial graphene.

5:00pm **GR+AS+NS+SP+SS-TuA10 Formation of Graphene on SiC(000-1) in Disilane and Neon Environments**, *G. He, N. Srivastava, R. Feenstra*, Carnegie Mellon University

We have prepared graphene on the SiC(000-1) surface (the so-called C-face of the {0001} surfaces), by heating the SiC in a Si-rich environment produced either by using disilane ($\approx 10^{-4}$ Torr) or cryogenically-purified neon (1 atm). With the Si-rich environments, we obtain considerably better uniformity in the thickness for thin, \approx ML-thick graphene on the C-face compared to that observed in samples prepared in vacuum or in an argon environment. We also find that different interface structures occur in these environments. In particular, we find a graphene-like buffer layer forming at the interface, analogous to the well known behavior of the SiC(0001) surface (the Si-face).

Studies are performed using atomic force microscopy (AFM), low-energy electron diffraction (LEED), and low-energy electron microscopy (LEEM). For graphene prepared in vacuum, LEED patterns show a characteristic 3X3 pattern together with graphene streaks. In contrast, for the graphene produced in either the disilane environment ($\approx 10^{-4}$ Torr) or 1 atm of neon, LEED patterns reveals a complex $\sqrt{43} \times \sqrt{43} - R \pm 7.6^\circ$ arrangement along with graphene spots. This structure is somewhat similar to the well known $\sqrt{3} \times \sqrt{3} - R30^\circ$ "buffer layer" of the Si-face, with satellite spots surrounding the primary Si spots, and is interpreted as arising from a C-rich buffer layer on the SiC. Selected area diffraction on those surface areas reveals a wavevector magnitude precisely equal to that of graphene, thus proving that the buffer layer does indeed have structure very close to that of graphene (the pattern is interpreted as a distortion of the buffer-layer graphene due to bonding to the underlying SiC). Using LEEM, measurements from the buffer layer of the reflected intensity of the electrons as a function of their energy reveal a new characteristic reflectivity curve, not seen for vacuum-prepared graphene.

After oxidation of the samples, the $\sqrt{43} \times \sqrt{43} - R \pm 7.6^\circ$ spots disappear and $\sqrt{3} \times \sqrt{3} - R30^\circ$ spots appear on the surface. This latter behavior is interpreted as oxidation of the SiC surface beneath the buffer layer. Selected area diffraction on portions of the surface that were previously identified as buffer layer still reveal a wavevector magnitude precisely equal to that of graphene. However, LEEM reflectivity curves on those areas reveal a completely new spectrum, indicative of a "decoupling" of the buffer from the SiC. This decoupling is consistent with our interpretation of this new interface structure as being a graphene buffer layer on C-face SiC.

This work is supported by NSF.

5:20pm **GR+AS+NS+SP+SS-TuA11 Characterization of Few Layer Graphene Films Grown on Cu-Ni and SiC Substrates**, *P. Tyagi, J.D. McNeilan, J. Abel, F.J. Nelson, Z.R. Robinson, R. Moore, A.C. Diebold, V.P. LaBella, C.A. Ventrice, Jr., University at Albany - SUNY, A.A. Sandin, D.B. Dougherty, J.E. Rowe, North Carolina State Univ., C. Dimitrakopoulos, A. Grill, C.Y. Sung, IBM T.J. Watson Res. Center, S. Chen, A. Munson, Y. Hao, C.W. Magnuson, R.S. Ruoff, Univ. of Texas at Austin*

The electronic structure of graphene depends on the number of graphene layers and the stacking sequence between the layers. Therefore, it is important to have a non-destructive technique for analyzing the overlayer coverage of graphene directly on the growth substrate. We have developed a technique using angle-resolved XPS to determine the average graphene thickness directly on metal foil substrates and SiC substrates. Since monolayer graphene films can be grown on Cu substrates, these samples are used as a standard reference for a monolayer of graphene. HOPG is used as a standard reference for bulk graphite. The electron mean free path of the C-1s photoelectron is determined by analyzing the areas under the C-1s peaks of monolayer graphene/Cu and bulk graphite and results in a value of 12.3 ± 0.8 Å. With this electron mean free path, the graphene coverage of a film of arbitrary thickness can be determined from the areas under the C-1s peaks of the sample of interest, the monolayer graphene/Cu, and HOPG samples. Analysis of graphene coverages for graphene films grown on Cu-Ni substrates shows that a uniform monolayer is first formed before the growth of a second layer. The thickness of both the graphene overlayer and intermediate buffer layer has been determined on 6H-SiC substrates. Raman spectroscopy data have also been taken on these samples and compared to the overlayer coverages determined with XPS. This research was supported in part by the National Science Foundation (grant no. 1006350/1006411).

5:40pm **GR+AS+NS+SP+SS-TuA12 Thickness-related Electronic Properties of Single-layer and Few-layer Graphene Revealed by Single-pass Kelvin Force Microscopy and dC/dZ Measurements**, *J. Yu, S. Wu, Agilent Technologies, Inc.*

Graphene has attracted much attention recently due to their exotic electronic properties. Potential applications of graphene sheets as ultrathin transistors, sensors and other nanoelectronic devices require them supported on an insulating substrate. Therefore, a quantitative understanding of charge

exchange at the interface and spatial distribution of the charge carriers is critical for the device design. Here, we demonstrate that atomic force microscopy (AFM)-based technique Kelvin force microscopy (KFM) can be applied as an experimental means to quantitatively investigate the local electrical properties of both single-layer and few-layer graphene films on silicon dioxide. Our measurements indicate that the surface potential of single-layer graphene is 60 mV higher than that of the silica interfacial layer. The effect of film thickness on the surface potential of few-layer graphene is observed. For example, a 66 mV increase in the surface potential is detected for an eleven-layered film with respect to a nine-layer film. Furthermore, with the introduction of multiple lock-in amplifiers (LIAs) in the electronics for scanning probe microscopes, single-pass kelvin force microscopy and probing of the other electric property such as local dielectric permittivity via the capacitance gradient dC/dZ measurements are allowed by the simultaneous use of the probe flexural resonance frequency ω_{mech} in the first LIA targeting the mechanical tip-sample interactions for surface profiling, and a much lower frequency ω_{elec} (both in the second LIA and its second harmonic in the third LIA) for sample surface potential and dC/dZ measurements, respectively. In contrast to surface potentials, the dC/dZ measurements show that local dielectric permittivity of few-layer graphene films maintain at the same level regardless of the film thickness. Such simultaneous monitoring of multiple electronic properties that exhibit different behaviors in response to the graphene layers provides us a way to achieve both a comprehensive characterization and a better understanding of graphene materials.

In Situ Microscopy and Spectroscopy Focus Topic
Room: 7 - Session IS+AS+BI+ET+GR+NS-TuA

In Situ Studies of Organic and Soft Materials and In Situ Microscopy

Moderator: K. Artyushkova, The University of New Mexico, J.A. Eastman, Argonne National Laboratory

2:00pm **IS+AS+BI+ET+GR+NS-TuA1 Micronutrient Detection and Quantification from Data Obtained from Plasma Pencil Atmospheric Mass Spectrometry**, *M.J. Stein, E. Lo, C. Waterton, D.G. Castner, B.D. Ratner, University of Washington*

The analysis of micronutrient quantities is one component in the strategy to reduce the global burden of malnutrition-related disease. Accessibility of the proper equipment and equipment complexity impede nutrient testing in the areas that might benefit most from these studies. In this work, we present an analysis of micronutrients in a physiological range from blood plasma using plasma pencil atmospheric mass spectrometry (PPAMS), a method for sampling a sample's surface at ambient temperature and pressure conditions. The effectiveness of our PPAMS system is demonstrated using characteristic and tandem mass spectra on raw nutrient controls. Key micronutrient peaks and fragmentation patterns are observed. Next, we analyze a sample matrix of micronutrients in porcine plasma in which the nutrient concentrations are varied. Principal component analysis (PCA) is then employed on the spectra. The resulting PCA scores showed that these nutrients are separable at different nutrient concentrations to 95% confidence. The loadings peaks are shown to contain several of the key peaks observed in the raw nutrient powders as principal separators. The PPAMS technique is compared to several traditional techniques such as time-of-flight secondary ion mass spectrometry (ToF-SIMS) and electrospray ionization mass spectrometry (ESI-MS). Separation of the nutrients at concentrations relevant for human blood-based nutrient detection is possible in both ESI-MS and PPAMS. However, ToF-SIMS is found to require 5x to 1000x higher concentrations than PPAMS for folate, vitamin A, and iodine in order to achieve similar separation of the micronutrients. In addition to the qualitative information obtained from the PCA results, quantitative predictive values are obtained by the application of a Bayesian wavelet-based functional mixed model. Since the mass spectra are modeled as functions in this model, peak detection methods are not required and the final results utilized the full spectral response. The final predicted values are compared to the known concentration values and the mean standard error of prediction (MSEP) is calculated. The accuracy of the predictive model was found to be dependent on the ionization potential of the individual nutrients. Metallic-nutrients were hypothesized to be more sensitive to outside cationization effects than their larger organic counterparts. In addition to quantitation, the physical properties of the ionization process were explored. Using XPS and ellipsometry in conjunction with carefully timed exposures and concurrent fragment PCA, it is determined that the PPAMS ionization is a softer form of ionization than most vacuum-based techniques.

2:20pm **IS+AS+BI+ET+GR+NS-TuA2 *In Situ* Real Time Examination of the Thin Film Growth of Pentacene on Polymeric Dielectrics Using X-Ray Synchrotron Radiation: Unexpected Changes in the Evolution of Surface Morphology with Substrate**, T.V. Desai, A.R. Woll, J.R. Engstrom, Cornell University

We have examined the thin film growth of pentacene on SiO₂ and on three different polymeric dielectrics using *in situ* synchrotron x-ray scattering and *ex situ* atomic force microscopy (AFM). The polymeric dielectrics investigated spanned the range from a low surface energy hydrophobic surface (polystyrene, PS), to a medium surface energy hydrophobic surface (polymethylmethacrylate, PMMA), to a high surface energy hydrophilic surface [poly(ethylene imine), PEI]. We have also compared these results to pentacene growth on clean SiO₂. On all surfaces, pentacene forms a polycrystalline thin film, whose structure is that of the previously identified "thin film" phase. From *in situ* real-time x-ray scattering, we find that pentacene exhibits layer-by-layer (LbL) growth on all surfaces investigated, but the extent of LbL growth is a strong function of the underlying substrate. This result is unexpected as the transition to more 3D-like growth occurs for thicknesses where the underlying substrate is effectively almost entirely covered by the growing pentacene thin film. Layer-by-layer growth is significantly more prolonged on PEI (up to ~6 MLs), followed by SiO₂ and PMMA (up to ~4 MLs) and finally PS (up to ~3 MLs). This trend is also seen in the variation of both the roughness and the in-plane feature sizes of ~10 ML thick films, where the films are the smoothest, and the feature sizes are the largest for growth on PEI, whereas on PS, the films are roughest, and the feature sizes are the smallest. Concerning possible reasons for this behavior, we can exclude the effects of the structure of the crystalline thin film (they were the same in all cases), and the roughness of the polymeric dielectric (rms roughness differed by < 0.1 nm) as major contributing factors. Surface energy of the polymeric thin films, however, provided the best explanation for the observed behavior, suggesting that thermodynamic driving forces play an important role in the evolution of thin film structure. In terms of molecular scale phenomena, interlayer transport and step-edge crossing events may be influenced by the mobility of the near-surface polymeric layers in the underlying substrate, which can be quite different for the ultrathin PEI layers vs. the much thicker PMMA and PS thin films.

2:40pm **IS+AS+BI+ET+GR+NS-TuA3 *In Situ*, Real-Time Diagnostics of Colon Cancer and Inflammatory Bowel Diseases by Direct Combination of Endoscopy and Rapid Evaporative Ionization Mass Spectrometry**, Z. Takats, Imperial College, UK, L.A. Sasi-Szabo, University of Debrecen, Hungary, J. Kinross, Imperial College, UK, J. Balog, Medimass Ltd., L. Muirhead, K.C. Schafer, C. Guallar-Hoyas, Imperial College, UK

INVITED

Rapid identification of biological tissues is a long-standing problem on various fields of interventional medicine, with special regard to cancer diagnostics and cancer surgery. While histological techniques provide the ultimate solution for the cellular-level identification of cancer cells, the approach is extremely complex and time consuming. Nevertheless, accelerated version of histopathology (so-called "frozen section" method) is widely used for the intraoperative characterization of tissue samples removed from the surgical area. Since frozen section histology is less reliable than the traditional approaches, and the accelerated procedure still takes approx. 30 minutes for a single sample, there has been ongoing research for the development of more accurate and faster methods.

Molecular spectroscopy techniques including IR, Raman, solid state NMR and mass spectrometry have been used for the characterization of intact biological tissues and showed enormous potential for the differentiation of tissues with various histologies, including multiple different types of cancer.

Rapid Evaporative Ionization Mass Spectrometry is based on the observation that electrosurgical dissection of vital tissues involves the ionization of various tissue constituents, with special emphasis on membrane lipids. Electrosurgical methods employ electric current for the rapid heating and evaporation of tissue material and they are widely used both for dissection and coagulation on practically all fields of surgery. Hence, the direct combination of electrosurgery with mass spectrometry provides a tissue identification methodology, where the tissue manipulation part is already widely used by surgeons and fully approved from regulatory point of view. Electrosurgical methods are also employed on the field of endoscopy, both for coagulation and dissection. Combination of endoscopy with *in-situ* mass spectrometric tissue identification resulted in a diagnostic device which can potentially identify lesions in body cavities *in-situ*, in real-time.

Electrosurgical electrode assembly and ion transfer device were embedded into working channel of commercially available colonoscope. The device was coupled with a linear ion trap mass spectrometer, and the system was utilized during diagnostic colonoscopic interventions. Adenomae, adenocarcinomae and mucosal areas affected by inflammatory bowel

diseases were successfully identified, in complete agreement with histopathological examination.

4:00pm **IS+AS+BI+ET+GR+NS-TuA7 Nanocrystal Phase Transformations in ZBLAN Glass Ceramics**, J.A. Johnson, University of Tennessee Space Institute, C. Alvarez, Northwestern University, Y. Lui, Argonne National Laboratory, C.E. Johnson, University of Tennessee Space Institute, A. Petford-Long, Argonne National Laboratory

In-situ and *ex-situ* TEM investigations of fluorochlorozirconate (FCZ) glass have led to the discovery of previously unreported BaF₂ in the face-centered-cubic (FCC) and orthorhombic phases. These FCZ glasses are a class of material based on ZBLAN glasses, which are being developed for uses in advance mammography systems. The FCZs of interest have been doped with Eu (II) for use as either a scintillator or a storage phosphor material but need to be partially crystalline to show good optical properties. The photo-stimulated luminescence of this material, for use as storage phosphor, is attributed to the characteristic 5d-4f emission of Eu²⁺ present in the BaCl₂ nanocrystals. The crystals formed are known from XRD experiments to be hexagonal and orthorhombic BaCl₂ depending on the annealing temperature, 265 and 295°C respectively. *In-situ* and *ex-situ* TEM heating experiments were used to study the nucleation and growth process of the nanocrystals at the EMC. The nanocrystals nucleate and grow through-out the glass matrix when annealing FCZ glasses, therein producing a nanocomposite glass-ceramic system. The traditional BaCl₂ orthogonal phase in addition to the unreported FCC and orthogonal BaF₂ phase have been found in multiple ZBLAN compositions in which the content of Cl and F has been varied. This indicates that annealing FCZ glasses produces polymorphic crystals of both BaCl₂ and BaF₂, which vary in size from 10 nm to 100 nm.

Mössbauer Spectroscopy has also given indisputable evidence that the divalent Europium enters the nanocrystals.

4:20pm **IS+AS+BI+ET+GR+NS-TuA8 *In Situ* Microscopy of Organic Film Growth: Zn-Phthalocyanine on Ag(100)**, A. Al-Mahboob, J.T. Sadowski, Brookhaven National Laboratory

Metal phthalocyanines are attracting significant attention, owing to their potential for applications in chemical sensors, solar cells and organic magnets. As the electronic properties of molecular films are related to their crystallinity and molecular packing, the optimization of film quality is important for improving the performance of organic devices.

In this work, we studied the dynamics of nucleation and structural evolution of zinc-phthalocyanine (ZnPc) films on Ag(100) surface, employing real-time low-energy electron microscope (LEEM) complemented by DFT calculations. We have observed two different modes of ZnPc nucleation, depending on the growth temperature. At lower temperatures ZnPc nucleates in a double domain structure, with bulk-like square lattice similar to one reported by Dou et al. [2]. LEED patterns recorded in LEEM experiment show that ZnPc monolayer (ML) grows epitaxially, having a square lattice with $(4/3)\sqrt{13} \times (4/3)\sqrt{13} R33.69^\circ$ unit cell (denoted R33.69) with respect to the substrate lattice. At temperatures of 170°C or above, nucleation of less dense epitaxial ZnPc, having single domain orientation, was observed, with square lattice parameters exactly 5 times larger (5x5) than the Ag(100) substrate.

Utilizing LEEM to observe the ZnPc nucleation at varying substrate temperatures – from room temperature (RT) to 225°C – we have observed that the nominal ZnPc coverage required for the onset of nucleation has strong temperature dependence. The nucleation commences at about 0.2 ML at RT, while 0.7 ML is required at 190°C. At the same time the completion of 1st layer occurs at constant nominal coverage of ZnPc, independent of substrate temperature. Based on that observation, the delay in onset of nucleation could be understood as a result of increased equilibrium concentration of diffusing ZnPc molecules at higher temperatures. This is in contrast to a delay in nucleation and giant island growth observed during vacuum deposition of anisotropic molecules like pentacene (Pn), in which case the energy barrier for the reorientation of the molecule from diffusing state into its crystalline orientation plays a critical role [3]. Real-time tracking of the evolution of ZnPc island area at varying deposition conditions combined with DFT analysis revealed that the 5x5 structure has both, a detachment barrier with respect to attachment, and a pre-factor (or attempt frequency), lower than those for bulk-like structures, allowing for controlling of the resulting ZnPc structure.

[1] E. Bauer, Rep. Prog. Phys. **57**, 895 (1994).

[2] W. Dou et al, J. Chem. Phys. **133**, 144704 (2010).

[3] Al-Mahboob et al, Phys. Rev. **B 82**, 235421 (2010).

4:40pm **IS+AS+BI+ET+GR+NS-TuA9 In Situ Sub-Micrometer Scale Chemical Imaging with Scanning Transmission X-ray Microscopy**, *S.T. Kelly, P. Nigge*, Lawrence Berkeley National Laboratory, *A. Laskin, B. Wang*, Pacific Northwest National Laboratory, *A. Tivanski, S. Ghorai*, University of Iowa, *T. Tylliszczak, M.K. Gilles*, Lawrence Berkeley National Laboratory

Spatially resolved chemical information on length scales shorter than 50 nm has become crucial in many areas of science and engineering -- from analyzing the chemistry of geological and environmental samples to quantifying the detailed chemical structure of novel materials engineered on the nanoscale. Scanning transmission x-ray microscopy (STXM) allows collection of specific chemical speciation data on these length scales through the acquisition and analysis of near-edge x-ray absorption fine structure (NEXAFS) spectra at each image pixel. However, the full usefulness of the STXM instrument may ultimately be realized in the in situ analysis of chemical transformations by controlling the local sample environment.

In situ STXM/NEXAFS measurements have been made in several ways thus far, ranging from simple to very complex. Introducing gases directly into the microscope chamber is effective, yet the presence of the gas along the entire optical path of the x-rays reduces signal at the detector. Furthermore, gas choice with this configuration is limited to those compatible with the microscope components. Separate in situ reactor cells circumvent these limitations by confining the gaseous environment to a small region immediately around the sample. Several groups have used reactor cells to this end, with reactors ranging widely in complexity -- from simple cells with limited capability to complex systems which require substantial instrument reconfiguration.

Ideally, an in situ reactor for STXM should be capable, flexible, easy to install and configure, and easily fabricated. We have developed a gas phase STXM reactor cell to meet many of these requirements. The reactor mounts directly to the standard STXM sample mount (making installation relatively simple) and contains an integrated sensor to actively measure relative humidity inside the cell for experiments using water vapor. We present here recent results using the reactor cell to examine two different systems. In the first system, we observed the hygroscopic properties of mixed organic/inorganic aerosol particles at increasing levels of relative humidity. In the second system, we monitored carbon dioxide sorption in metal organic framework materials. The advantages afforded by this reactor (and future improvements to it) will enable new scientific discoveries across a wide range of fields.

5:40pm **IS+AS+BI+ET+GR+NS-TuA12 In Situ SEM and ToF-SIMS Imaging of Liquids for Biological Applications**, *L. Yang, X.-Y. Yu, Z. Zhu, S. Thevuthasan*, Pacific Northwest National Laboratory, *J. Cowin*, Cowin In-Situ Science, L. L. C.

A vacuum compatible microfluidic interface was developed to enable surface analysis of liquids. The unique feature of the liquid flow cell is that the detection window is open to the vacuum allowing direct probing of the liquid surface. The flow cell is composed of a silicon nitride membrane and polydimethylsiloxane; and it is fully compatible with vacuum operations for surface analysis. The aperture can be drilled through the 100 nm silicon nitride membrane by using the focused ion beam/scanning electron microscope (FIB/SEM). Alternatively the primary Bi⁺ ions in ToF-SIMS can be used to fabricate the aperture window in real-time. New results using this vacuum interface and recent development will be presented in this paper. Several aqueous solutions containing conjugated IgG gold nanoparticles and representative biological solutions were studied *in situ* using scanning electron microscope (SEM) and time-of-flight secondary ion mass spectrometry (ToF-SIMS). Characteristic signals of the conjugated gold nanoparticles were successfully observed through the aperture by both energy-dispersive X-ray spectroscopy (EDX) in SEM and ToF-SIMS. Comparisons were also made among wet and dry samples and liquid sample in the flow cell using SEM/EDX. Stronger gold signal can be observed in our novel portable device by SEM/EDX compared with the wet or dry samples, respectively. Our results indicate that analyses of the nanoparticle conjugated antibodies are better made in their native liquid environment. Our unique microfluidic flow cell permits *in situ* liquid observations. In addition, a variety of aqueous solutions relevant to biological systems were analyzed. Our results indicate that chemical imaging by SEM and ToF-SIMS is applicable in analyzing more complicated aqueous solutions when coupled with our novel portable microfluidic platform.

Magnetic Interfaces and Nanostructures
Room: 6 - Session MI+EN+BI-TuA

Fundamental Problems in Magnetism

Moderator: G.J. Szulczewski, The University of Alabama

2:00pm **MI+EN+BI-TuA1 Spintronics – Implications for Energy, Information and Medical Technologies**, *S.D. Bader*, Argonne National Laboratory and Northwestern University **INVITED**

Spintronics encompasses the ever-evolving field of magnetic electronics.[1,2] Fields such as spintronics are held the potential to extend the information technology revolution as the semiconductor road map reaches its end. A major issue with present day electronics is in its demand for increased power. Spintronics offers the possibility to communicate via pure spin currents as opposed to electric charge currents. The talk provides a brief perspective of recent developments to switch magnetic moments by spin-polarized currents, electric fields and photonic fields. Developments in the field of spintronics continue to be strongly dependent on the exploration and discovery of novel nanostructured materials and configurations. An array of exotic transport effects dependent on the interplay between spin and charge currents have been explored theoretically and experimentally in recent years. The talk highlights select promising areas for future investigation, and, features recent work at Argonne, [3,4] including, most strikingly, in the realm of medical applications. [5]

* Work supported by the U.S. Department of Energy, Office of Science, Basic Energy Sciences, under contract No. DE-AC02-06CH11357.

1. S. D. Bader and S. S. P. Parkin, "Spintronics," in *Ann. Rev. of Cond. Matt. Phys.*, 1, 71-88 (2010).
2. S. D. Bader, *Rev. Mod. Phys.* 78, 1-15 (2006).
3. O. Mosendz, J. E. Pearson, F. Y. Fradin, G. E. W. Bauer, S. D. Bader, A. Hoffmann, *Phys. Rev. Lett.* 104, 046601 (2010).
4. J. S. Jiang, J. E. Pearson, S. D. Bader, *Phys. Rev. Lett.* 106, 156807 (2011).
5. D.-H. Kim, E. A. Rozhkova, I. V. Ulasov, S. D. Bader, T. Rajh, M. S. Lesniak, V. Novosad, *Nature Mat.* 9, 165-171 (2010).

Samuel D. Bader, Materials Science Division and Center for Nanoscale Materials, Argonne National Laboratory, Argonne, Illinois 60439, and Department of Physics and Astronomy, Northwestern University, Evanston, Illinois 60208 USA

2:40pm **MI+EN+BI-TuA3 Multiscale Modeling for Spintronics**, *K.A. Mewes, T. Mewes, W.H. Butler*, University of Alabama **INVITED**

The next generation of spintronic devices relies strongly on the development of new materials with high spin polarization, optimized intrinsic damping and tunable magnetic anisotropy. Therefore technological progress in this area depends heavily on the successful search for new materials as well as on a deeper understanding of the fundamental mechanisms of the spin polarization, the damping and the magnetic anisotropy. My talk will focus on different aspects of materials with high spin polarization, low intrinsic relaxation rate and perpendicular anisotropy. Our results are based on first principles calculations in combination with a non-orthogonal tight-binding model to predict those material properties for complex materials which can be used for example in new spin based memory devices or logic devices. Future progress in spintronics not only requires a better understanding of the underlying physical principles but also hinges strongly on the development of theoretical models capable of describing the expected performance of realistic device structures. As an example I will discuss the challenges in the Spin Transfer Torque Random Access Memory. This memory is dense, fast and nonvolatile and has the capability of a universal memory possibly even replacing today's Dynamic Random Access Memory (DRAM).

4:00pm **MI+EN+BI-TuA7 Anomalous Magneto Transport in Amorphous TbFeCo Film with Perpendicular Magnetic Anisotropy**, *N. Anun'vat, M. Ding, J. Poon, S.A. Wolf, J.W. Lu*, University of Virginia

TbFeCo has attracted some interests because of its high perpendicular anisotropy and tunable magnetic properties for nanomagnetic and spintronics application. Due to the fact that electronic device is getting smaller, fundamental understanding of size and geometry dependent is crucial. In this study, we report a strong size dependence of the coercive field in 15 - 100nm thick Tb₃₀Fe_{63.5}Co_{6.5} films with MgO capping. Magneto Optical Kerr effect (MOKE) and Vibrating Sample Magnetometer are performed on unpatterned films. The films exhibited strong PMA characteristics. The films were then fabricated into Hall bars with 10 μm, 50 μm, 100 μm and 500 μm in width. From anomalous Hall effect (AHE), HC was determined for these patterned films. We observed coercivity

enhancement as the width of the hall bar decreases (up to 200% at room temperature). The temperature dependent of the coercivity is also studied. There exhibits the local minimum as the temperature change from 50 - 300K. The correlation between HCmin and dimensions of the hall bar are discussed. The magnetic domain structures and surface morphology analysis were performed using magnetic force microscopy and atomic force microscopy respectively. The variation in domain sizes, structures for different hall bars as well as possible origins of the coercivity enhancement are also discussed.

4:20pm **MI+EN+BI-TuA8 Magnetic Properties of Fe Clusters: A DFT+U vs Nano DFT+DMFT Analysis**, *A.K. Kabir, V. Turkowski, T.S. Rahman*, University of Central Florida

We use our recently proposed combined density-functional-theory/dynamical-mean-field-theory (DFT + DMFT) approach for molecules and nanosystems [1] to study the magnetic properties of Fe clusters consisting of 15, 17 and 19 atoms. This method has several advantages compared with the widely-used DFT + U approach for systems with localized electron states, the most important of which is that it takes into account dynamical correlation effects. These effects are especially important in the case when the kinetic (hopping) and the local Coulomb repulsion energies have the same order of magnitude. In particular, we study the size-dependence of the magnetic properties of the clusters by using the nanoDMFT code developed in our group using the iterated-perturbation theory approximation in the impurity solver. We find that the DFT+DMFT approach yields much better agreement for the magnetization with experimental data as compared to DFT and DFT+U methods, both of which generally overestimate the magnetization.

Work supported in part by DOE Grant No. DOE-DE-FG02-07ER46354

1. V. Turkowski, A. Kabir, N. Nayyar and T.S. Rahman *J. Phys.: Condens. Matter* 22, 462202 (2010) and *J. Chem. Phys.* 136, 114108 (2012)

4:40pm **MI+EN+BI-TuA9 Rationally-designed Iron Oxide Nanostructures for Bioimaging**, *Y. Bao*, The University of Alabama
INVITED

Iron oxide nanoparticles have been extensively studied in targeted delivery, localized therapy, and as contrast agents for magnetic resonance imaging (MRI). In fact, sugar coated iron oxide NPs have been clinically used as the liver/spleen-specific contrast agents in MRI, indicating the biocompatibility and potential of iron oxide nanoparticles in nanomedicine. This presentation will discuss how rationally designed iron oxide nanoparticles can achieve highly effective MRI contrast agents. The talk will primarily focus on the shape control of iron oxide nanoparticles and the surface functionalization. The formation and magnetic properties of various shaped-iron oxides (e.g., cubes, nanoworms, nanoplates, and nanowires) will be elaborated. In particular, ultrathin iron oxide nanowires will be discussed in details, such as synthesis, property, and their potential as MRI contrast agents.

5:40pm **MI+EN+BI-TuA12 3D Vector Magnetometry of Thin-Films using Generalized Magneto-Optical Ellipsometry (GME)**, *J.A. Arregi, J.B. González-Díaz, O. Idigoras, A. Berger*, CIC nanoGUNE Consolider, Spain

Generalized Magneto-Optical Ellipsometry (GME) has emerged in the last decade as a methodology to characterize magnetic materials with a high degree of precision, by means of utilizing the magneto-optical Kerr effect [1]. Compared to other magneto-optical characterization methods based on the same effect, GME has two key advantages: it can measure both the optical and magneto-optical constants, and it allows full vector magnetometry, all with one simple experimental set-up. The technique has been successfully employed in the study of diverse magnetization reversal processes, for the purpose of identifying spin-polarized electronic states in multiferroic materials [2], as well as for the measurement of the magnetization orientation using 2D vector magnetometry [3].

Even if some works have suggested the possibility to perform quantitative 3D vector magnetometry using the GME technique [4], actual measurements have not been demonstrated so far. Here, we extract the field dependent evolution of the three magnetization components during the reversal process. In order to do so, we exploit the different symmetries of the longitudinal, transverse and polar Kerr effect around different polarizer/analyzer crossing points, which allows us to separate the information of each of the magnetically induced contributions to the non-diagonal reflection matrix elements. By combining the presence of in-plane uniaxial anisotropy as well as out-of-plane applied magnetic fields in our Co and Co-alloy based thin films, we manage to monitor the evolution of the full magnetization vector as a function of the field.

In addition to this full vector magnetometry capability, we have recently improved this technique to enhance measurement reliability [5] and we also

extended its capabilities to characterize materials that are magneto-optically active and optically anisotropic at the same time [6].

References:

- [1] A. Berger and M. R. Pufall, *Appl. Phys. Lett.* **71**, 965 (1997)
- [2] M. Bastjan, S. G. Singer, G. Neuber *et al.*, *Phys. Rev. B* **77**, 193105 (2008)
- [3] A. Berger and M. R. Pufall, *J. Appl. Phys.* **85**, 4583 (1999)
- [4] K. Mok, N. Du, and H. Schmidt, *Rev. Sci. Instrum.* **82**, 033112 (2011)
- [5] J. A. Arregi, J. B. Gonzalez-Diaz, E. Bergaretxe, O. Idigoras, T. Unsal, and A. Berger, accepted for publication in *J. Appl. Phys.*
- [6] J. B. González-Díaz, J. A. Arregi, E. Bergaretxe, M. J. Fertin, O. Idigoras, and A. Berger, submitted to *Appl. Phys. Lett.*

Nanometer-scale Science and Technology

Room: 12 - Session NS+EN+GR-TuA

Nanomaterials in Two and Three Dimensions

Moderator: V.P. LaBella, University at Albany-SUNY

2:20pm **NS+EN+GR-TuA2 Nanopatterning of SPRi Sensor Surfaces for Sub-Nanomolar Biomarker Detection**, *M.A. Parracino, M.J. Perez Roldan, J. Hanus, V. Spampinato, G. Ceccone, P. Colpo, F. Rossi*, Nanobiosciences Unit, JRC, Italy

In this work we report the detection of low-molecular weight biomarkers on two kinds of nanostructured surfaces by using a SPRi sensor. Nanopatterned surfaces are fabricated by combining functionalization and patterning techniques. Two different methods were used for the surface nanopatterning: electro-beam lithography (EBL) and colloidal lithography (CL). Maltose binding protein (MBP) and transthyretin (TTR) are respectively immobilized on the two types of nanopatterns and used as biological recognition elements. Chemical contrast adhesive/non adhesive at nanoscale has been created in order to control protein binding at nanoscale. Plasma deposited (PEO)-like film was used as passivation layer to prevent non-specific binding of protein in between the protein adhesives nano-areas. All the fabrication steps of both surfaces have been carefully controlled and analyzed using several techniques such as AFM, XPS, and SEM. The gold nanostructures were 185 nm width lines, for the patterned created with EBL, and holes of 250 nm in diameters for the pattern fabricated using CL. The gold grating surface made using EBL was functionalized with sugar via a thiol-linker. Maltose Binding Protein (MBP) was bound on sugar modified surface in order to develop a competitive assay for maltose detection. In this competitive assay, the protein binding on the sugar functionalized surface depends on the concentration of his free competitor in solution: by measuring the protein binding, it is possible to evaluate the concentration of the small molecule in solution. In the second methods, NTA functionalized nanoholes in PEO like background were fabricated and subsequently activated with nickel (Ni II) for a selective immobilization of histidines tagged TTR, which underlies to a direct detection of Thyroxine 4 (T4). In both case, the biological intermediates, MBP and TTR, are selectively immobilized onto nanopatterned surfaces. The ligand protein binding on the nanostructure is higher than on the flat surface. The better ligand orientation and immobilization on the nanostructures results in analyte detection at sub-nanomolar concentration. The combination of nanopatterning features with the two different methods of detection presented in this work provides a description for a more generalized approach for the development of stable and reliable biosensor platforms for the detection of different small molecules having an high impact in environmental, and biomedical field.

4:00pm **NS+EN+GR-TuA7 Single Layer of MoS₂ on Close-Packed Metal Surfaces**, *D. Le, T.S. Rahman*, University of Central Florida

We present results of first principles electronic structure calculations, using van der Waals density functional theory, of the adsorption of a single layer of Molybdenum disulfide (MoS₂) on several close-packed metal surfaces. On Cu(111) we find three energetically equivalent stacking types and a Moiré pattern whose periodicity is in agreement with experimental findings [1]. The layer is found not to be purely physisorbed on the surface, rather there exists a chemical interaction between it and the Cu surface atoms. We also find that the MoS₂ film is not appreciably buckled, while the top Cu layer gets reorganized and vertically disordered. The sizes of Moiré patterns for a single layer of MoS₂ adsorbed on other close-packed metal surfaces are also estimated by minimizing the lattice mismatch between the film and the substrate. The Moiré patterns on Ir(111), Pt(111), and Ru(0001) are particularly interesting as the MoS₂ layer is found to bind more strongly on

them than on Cu(111). We compare the nature of the bond in these three substrates with that on Cu(111).

[1] D. Kim, D. Sun, W. Lu, Z. Cheng, Y. Zhu, D. Le, T. S. Rahman, and L. Bartels, *Langmuir* **27**, 11650 (2011).

* This work was supported in part by the U.S. Department of Energy under Grant No. DE-FG02-07ER15842.

4:20pm NS+EN+GR-TuA8 Chemically Exfoliated Two Dimensional Materials for Energy Applications, *M. Chowalla*, Rutgers University INVITED

Chemical exfoliation of layered two-dimensional materials such as graphite and transition metal chalcogenides allow access to large quantities of atomically thin nanosheets that have properties that are distinctly different from their bulk counterparts. Although 2D materials have recently become popular, their fabrication via exfoliation of bulk crystals has been known for decades. For example, Brodie first exfoliated graphite into atomically thin oxidized form of graphene in 1859. In the case of layered transition metal dichalcogenides (LTMDs) such as MoS₂, WS₂, MoSe₂, WSe₂, etc., Frindt et al. performed seminal work in the '70s and '80s. We have revived these techniques to obtain a wide variety of chemically exfoliated two-dimensional nanosheets and utilized these materials in wide variety of electronic and energy applications. In this presentation, I will highlight some of our key contributions with graphene oxide (GO) and LTMD nanosheets. Specifically, I will present their implementation into large area electronics, strategic implementation into solar cells, and as catalyst for hydrogen evolution.

5:00pm NS+EN+GR-TuA10 Isolation and Surface Structure of Ultrathin Nanosheets formed by Atomic Layer Deposition, *K.M. Lee, D.H. Kim, G.N. Parsons*, North Carolina State University

Ultrathin nanosheets are two-dimensional structures that are often exfoliated from layered compounds. The nanosheets are flat with large surface area (100's of nm²) but with very small thickness in several nm scale. A common example of a nanosheet is graphene which is exfoliated from graphite. Other nanosheet materials that are chemically exfoliated from layered crystals include MoS₂, VS₂, and many oxide materials such as MnO₂, TiNbO₅, or LaNbO₇. These materials show unique capabilities for nanoelectronic devices, photocatalysts, and electrochemical sensor applications. For our work, we explore atomic layer deposition (ALD) as an effective technique to fabricate metal oxide nanosheets with precisely controlling thickness and chemical composition. To form nanosheets, we spin-coated a substrate with polymer such as polymethylmethacrylate (PMMA), polyvinyl alcohol (PVA), or polyacrylic acid (PAA) as a sacrificial layer, then deposited TiO₂, Al₂O₃ or ZnO on polymer layer by ALD. Dissolving the polymer in solvent releases nanosheets from the substrate. We successfully attained two dimensional TiO₂ nanosheets with several hundred μm in lateral size and less than 10 nm in thickness. Attaining nanosheets with thickness near 1nm proved to be rather challenging. For Al₂O₃ and TiO₂, nanosheets with thickness of ~ 1 nm can be isolated by two-immiscible liquid separation process. For ZnO, the thinnest nanosheet obtained to date is closer to 15 nm. We characterized nanosheets using AFM to confirm their thickness and found that the surface structure and roughness depends on the materials and thickness. We also examined the functionality of TiO₂ nanosheets as an agent for photocatalytic degradation of organic dyes. This work demonstrates and defines the capabilities and limits for functional nanosheets fabrication by atomic layer deposition.

5:20pm NS+EN+GR-TuA11 All Solution Processed InGaO₃(ZnO)_m Thin Films with Layered Structure and their Thermoelectric Properties, *J.H. Kim, H.K. Cho*, Sungkyunkwan University, Republic of Korea

As the materials currently in use have been reached terminal and showed low productivity in a few field, the development of advanced materials are demanded. In the middle of atmosphere, low-dimensional nanostructures have been introduced in recent studies such as 1-D nanowire and 2-D superlattice. Among them, a multi-layered structure shows unique properties originating from the confinement of carriers in the two-dimensional layer. For example, LaFeO₃-LaCrO₃ superlattice structures fabricated by pulsed layer deposition (PLD) have shown enhanced ferromagnetism [1] and InGaO₃(ZnO)_m superlattice structure grown by sputtering method has improved thermoelectric properties [2].

These homologous series of RAO₃(MO)_m (R=In or rare earth elements; A=Ga, In, Al, or Fe ; M=Mg, Co, Cu, or Zn ; m=integer) comprise alternating stacks of RO₂⁻ and AO⁺(MO)_m layers and are candidate to exhibit the quantum effect due to its natural superlattice [3]. Despite these materials being widely investigated, the fabrication of RAO₃(MO)_m thin film with layered structure is limit due to their fabrication which requires expensive high-vacuum equipment and shows low productivity.

In this study, all solution process (an epitaxial ZnO buffer layer growth on sapphire substrate, amorphous IGZO layer on ZnO buffer layer by composition controlled solution process, and post-annealing at 900°C for 9hours) enables us to fabricate InGaO₃(ZnO)_m thin film with periodic superlattice structure. Crystallinity of thin film was analyzed by X-ray diffraction and TEM results. And also, TE properties such as Seebeck coefficient, electrical conductivity, thermal conductivity were evaluated to identify the degree of crystallization of superlattice with layered structure.

Reference

[1] K. Ueda, H. Tabata and T. Kawai, *Science*, 1998, **280**, 1064

[2] D. K. Seo, B. H. Kong and H. K. Cho, *Cryst. Growth Des.*, 2010, **10**, 4638

[3] J. L. F. Da Silva, Y. F. Yan and S. H. Wei, *Physical Review Letters*, 2008, **100**, 255501.

Plasma Science and Technology Room: 24 - Session PS1-TuA

Plasma Deposition and Plasma Enhanced ALD

Moderator: S. Agarwal, Colorado School of Mines

2:00pm PS1-TuA1 Looking Down the Rabbit Hole: Impact of Porosity in Plasma-deposited Inorganic Layers on Their Moisture Permeation Barrier Performance, *M. Creatore*, Eindhoven University of Technology, The Netherlands INVITED

Although very promising results in terms of moisture and oxygen permeation barrier properties have been achieved by organic/ inorganic multi-layers, the impact of the organic interlayer on the global barrier performance is still under discussion. It is generally considered that the organic interlayer acts as smoothing layer for the macro-defects present at the surface or in the barrier layer. It is also hypothesized that the organic interlayer infiltrates into the nano-pores present in the barrier layer, therefore affecting the barrier itself at microstructure level.

In the present work the moisture permeation barrier performance of multi-layers deposited by means of initiated- and plasma enhanced- CVD methods [1] is addressed, with the aim of unraveling the role of the organic interlayer. Calcium test measurements allowed discriminating between the water permeation through the macro-defects/pinholes and the permeation through the matrix porosity. It has been found that the improvement in terms of barrier properties, due to the filling/infiltration of the SiO₂ layer nano-pores by an organosilicon interlayer [2], universally correlates with the residual open micro- (i.e. < 2 nm) porosity in the inorganic (SiO₂ or Al₂O₃) layer, independently of the deposition method (PECVD or plasma-assisted ALD). The residual nano-porosity has been evaluated by means of ellipsometric porosimetry which allows carrying out adsorption/desorption isothermal of a probe molecule in the open porosity. In detail, only for WVTR values of the SiO₂-like layer larger than 10⁻³ g m⁻² day⁻¹, a barrier improvement factor is observed upon deposition of the organic interlayer, although limited to values between 5 and 10. This outcome, in combination with the evaluation of the macro-defect density upon organosilicon layer deposition on the SiO₂ layer, provides the evidence that smoothing plays a major role in the improvement of the barrier performance.

Next to the growth and characterization studies of the organosilicon/SiO₂ multi-layer, the control on the residual open nano-porosity of high growth rate roll-to-roll atmospheric pressure plasma deposited SiO₂ layers is addressed. Upon 2 nm thick Al₂O₃ layer deposition, the water vapor transmission rate of the SiO₂ layer decreases of a factor 10³, due to the filling of the residual SiO₂ nano-porosity.

[1] G. Aresta, J. Palmans, M.C.M. van de Sanden, M. Creatore, (2012), accepted for publication in *J.Vac. Sci. Technol.*

[2] G. Aresta, J. Palmans, M.C.M. van de Sanden, M. Creatore, (2012), *Microporous and Mesoporous Materials* **151**, 439.

2:40pm PS1-TuA3 Dual Etching and Deposition Mechanism of a Microwave Alcohol Plasma on Commercial Polymers for the Enhancement of Adhesion, *C.J. Hall, P.J. Murphy, H.J. Griesser*, University of South Australia

The use of polymers to replace traditional materials in the automotive, aerospace and other industries is continuing at a high pace. Polymers offer distinct advantages over glass and metals, such as weight, impact strength, and the ability to be formed into complex shapes. To ensure long service life, however, in some applications the polymers must be coated to provide protection from damage due to mechanical abrasion or chemical attack.

One such protective coating currently being developed is a microwave based PECVD coating using tetramethyldisiloxane (TMDSO) and oxygen. This system can be used to deposit an amorphous siloxane coating several microns thick, at industrially relevant speeds. PECVD has high deposition rates with no cure required; it can coat complex parts and has the ability to vertically grade the composition of the coating. These siloxane coatings can provide the polymers with protection from in-service wear and chemical attack. However, traditionally, adhesion of these coatings to many polymers has been marginal.[1]

In this study it has been found that plasma pre-treatments using vapours from the alcohol family are effective at modifying the adhesion of these coatings to five commercial polymers, polycarbonate (PC), polypropylene (PP), polystyrene (PS), poly(methyl methacrylate) (PMMA) and acrylonitrile butadiene styrene (ABS). We have observed that the plasma pre-treatment both etches the polymer and deposits a carbonaceous film some 10 to 20 nm thick. It has also been established that both of these mechanisms are required to improve adhesion. Of further interest is the observation that the pre-treatment time must be tailored depending on the polymer substrate. Optimum adhesion is only achieved after some critical time. For ABS and PS, less than 15 secs is adequate, however for polymers, such as PMMA and PC, treatment times up to 120 and 180 secs are necessary. The duration of pre-treatment appears to be related to the etch rate of the particular polymer. Investigation has revealed that the alcohol plasma creates hydroxyl radicals.[2,3] These radicals are capable of initial hydrogen abstraction from the polymer; however, the subsequent etching proceeds depending on the structure of the polymer. As such there is a need to tailor the pre-treatment time depending on the polymer being treated.

1. B. W. Muir, H. Thissen, G. P. Simon, P. J. Murphy, H. J. Griesser, *Thin Solid Films* **2006**, 500, 34.

2. C. Hall, P. Murphy, H. Griesser, *Plasma Process. Polym.* **2012**, *Accepted, In Press*, DOI: 10.1002/ppap.201100159.

3. C. Hall, P. Murphy, H. Griesser, *Plasma Process. Polym.* **2012**, *Accepted, In Pres.*

3:00pm **PS1-TuA4 The Roles of Ions and Neutrals in Growth Mechanisms of Plasma Polymer Films**, *A. Micheltore*, University of South Australia

Plasma polymers have been used since the 1960s and have found a wide range of applications. However the basic processes and mechanisms leading to plasma polymer film growth are poorly understood. Due to this lack of understanding, external parameters such as RF power and monomer flowrate are typically quoted in the literature, which provide no information on processes at the molecular level. Therefore reproducing films with different reactors is usually done by trial-and-error as the critical parameters determining growth processes are largely unknown.

Here we will discuss the roles of ions and neutrals in contributing mass to the film with a view to understanding the molecular processes by which plasma polymer films grow. The pivotal role of monomer chemical structure, specifically sites of unsaturation, in determining which growth mechanisms dominate will also be demonstrated.

4:00pm **PS1-TuA7 Defect Analysis and Mechanical Performance of Optoelectronic Thin Films Deposited on Flexible Substrates**, *R. Patel, C.A. Wolden*, Colorado School of Mines

Plasma deposition enables synthesis of optoelectronic thin films on flexible substrates at low temperature. The ultimate performance of these materials is controlled by defects such as pinholes or cracks. This work focuses on understanding the formation of such defects during both film synthesis as well as during the application of stress. A simple solvent-etch based technique is presented which can be used to visualize and quantify defects in both single and multi-layered films deposited on flexible substrates. This approach allows for quantitative evaluation of crack/defect density evolution. This technique is applied to both sputtered indium tin oxide (ITO) as well as alumina-silicone nanolaminates deposited on flexible polycarbonate films by plasma-enhanced chemical vapor deposition. The use of the nanolaminate architecture is shown to significantly attenuate pinhole density relative to single layers. In the case of sputtered ITO, an optimum thickness is identified that balances electronic performance with mechanical integrity. For both materials their performance under applied stress was examined using an automated bending test setup that explored mechanical failure as a function of applied strain and number bending cycles. The threshold strain for failure under the application of tensile/compressive stress was quantified by bending samples to a given radius of curvature. Below a critical strain these materials demonstrate robust performance during cycling, displaying their strong potential for device applications.

4:20pm **PS1-TuA8 Plasma Polymerization of Ethyl Lactate**, *S. Ligot*, University of Mons, Belgium, *F. Renaux*, Materia Nova Research Center, Belgium, *L. Denis*, University of Mons, Belgium, *D. Cossement*, Materia Nova Research Center, Belgium, *P. Dubois*, *R. Snyders*, University of Mons, Belgium

Biodegradable and derived from renewable resources, polylactide (PLA) has gained enormous attention as an alternative to conventional synthetic packaging materials. Nevertheless, PLA presents high water and gas permeability, which leads to a high degradation rate by hydrolysis of the ester bonds and therefore substantially limits its application for food packaging.

In order to improve the barrier properties of PLA substrate, we propose to cover it with a highly cross-linked PLA-based plasma polymer film (PPF) synthesized by Plasma Enhanced Chemical Vapor Deposition (PECVD). The control of both chemical composition and cross-linking degree would allow to tune the gas permittivity and, as a consequence, the degradation rate of the PLA substrate.

The present work reports on the study of the influences of the experimental parameters (RF power, working pressure and precursor flow rate) on the PPF films properties using a design of experiments tool. The PPF are studied in terms of chemistry and cross-linkage by XPS, FTIR spectroscopy and ToF-SIMS measurements. In addition, *in-situ* IR spectroscopy is used to probe the plasma in order to get a better understanding on the plasma-surface interactions during the growth process. It comes out that, in our conditions, the applied power is the key parameter controlling the PPF properties. By increasing it, the C/O ratio in the coatings increases from 2.5 to 9.3. The decrease of the oxygen content when applied power is increased is correlated with the loss of O=C=O and C-O functions from 15% to 0 % and from 21% to 5 %, respectively. The *in situ* FTIR data support this observation and suggest the formation of alkynes in the plasma.

4:40pm **PS1-TuA9 Functional Carbon Contained Film Formation using Neutral-Beam-Enhanced Chemical-Vapor-Deposition by Microwave Plasma**, *Y. Kikuchi*, Tohoku University and Tokyo Electron, Japan, *A. Wada*, *S. Samukawa*, Tohoku University, Japan

Carbon materials possess various functional properties by forming various structures of carbon atoms. Especially diamond-like carbon (DLC) film is one of the primary materials as alternative of metal electrodes in various devices, in contrast a carbon doped silicon oxide (SiCOH) is known as a low-*k* dielectric in ultralarge-scale integration (ULSI) devices. However, it is difficult to precisely control their properties using conventional plasma-enhanced chemical vapor deposition (PECVD). To solve this problem, we have developed a neutral-beam-enhanced chemical vapor deposition (NBECVD) process as an alternative to the conventional PECVD process. NBECVD can almost completely eliminate the irradiation of UV photons and electrons to the substrate surface by a carbon aperture, resulting in a damage-free deposition process. Moreover, the NBECVD can form a film through surface polymerization caused by bombardment of an energy-controlled Ar neutral beam on the surface with adsorbed precursors. We previously proposed controlling the molecular-level structures in SiOCH film on 2 inch wafer by using NBECVD process, which can control the film properties (*k*-value and modulus). Since the bombardment energy of the neutral beam can be precisely controlled by Ar plasma above a carbon aperture, selective dissociation of weak chemical bonds in the precursors is possible with applicable plasma source, which enables us to design the film structure by controlling the precursor structure.

In this study, we developed NBECVD equipment for 8 inch wafer selecting microwave plasma source and deposited DLC and SiCOH films. For DLC film, we used toluene as precursors to control sp²/sp³ bonds ratio and hydrogen content in the film. DMOTMDS was selected for SiCOH film as reported previously. As the results, we can form high-quality DLC films and high density and low-*k* SiCOH films on 8 inch wafer by controlling the film structure precisely.

5:00pm **PS1-TuA10 Nano-crystalline Silicon Deposition using a Layer-by-layer Technique**, *Z. Chen*, *M.N. Iliev*, *J.A. Mucha*, University of Houston, *Y.K. Pu*, Tsinghua University, China, *D.J. Economou*, *V.M. Donnelly*, University of Houston

Nano-crystalline silicon was deposited using a layer-by-layer technique in a novel reactor with two separate reaction regions for amorphous silicon deposition and nano-crystallization. Substrates were rotated between two internal plasma sources, with selectable processing times in each source. A capacitively-coupled plasma (CCP) with SiH₄/He feed gas was used to deposit thin hydrogenated amorphous Si layers that were then immediately exposed to a H₂ or D₂ inductively-coupled plasma (ICP). The reaction of H or D atoms induced crystallization in the films. With 2 or 4 substrates on opposite sides of a circular susceptor, one substrate was in the SiH₄ CCP, while another was in the H₂ or D₂ ICP. These two processes were performed sequentially and periodically to grow thin films. Raman spectroscopy was

used to characterize the films and determine the fraction of crystalline (510 and 520 cm^{-1} peaks) material in the a-Si:H layer (480 cm^{-1} peak). For the same total exposure times in each plasma, nearly the same total thickness films were deposited. Many short exposures to both plasmas were more effective in producing nano-crystalline Si than with one long exposure to each plasma. In addition, the fraction of nano-crystalline Si increased with increasing ratio of H_2 ICP-to-SiH₄/He CCP exposure time. Mass spectrometry was also used to monitor products produced in the D₂ plasma. During crystallization, etching was observed and SiD₂H₂ peaks were detected, with the strongest coming at $m/e=32$ (SiD₂⁺, SiH₂D⁺). These signals decayed to a small background over times that depended on the exposure time in the SiH₄/He CCP. The films were also characterized by spectroscopic ellipsometry and Fourier transform infrared absorption. By utilizing these characterization methods, the kinetics for crystallization was investigated and will be discussed.

5:20pm PS1-TuA11 Role of PEALD Reactor Wall Conditions on Radical and Ion Substrate Fluxes, M.J. Sowa, M.J. Sershen, G. Sundaram, J.S. Becker, Cambridge NanoTech, Inc.

Plasma Enhanced Atomic Layer Deposition (PEALD) relies on plasma generated species as co-reactants for one half of the cyclic, two-step deposition process. Plasma generated species include radicals, ions, electrons, and photons. PEALD research is still in its early stages and the community is just beginning to elucidate the roles of these species in the deposition process and ultimately in the resulting deposited film characteristics.

Plasmas can exhibit quite complex behavior. Without excellent Faraday screening, Inductively Coupled Plasmas (ICPs) will have some component of capacitive coupling between the induction coil and the plasma. This leads to various amounts of extension of the "remote" plasma into the ALD reactor as currents originating at the high capacitive potentials of the plasma source seek out a grounded counter electrode. The sink location for the capacitive currents would be expected to vary substantially depending on if the ALD reactor is coated with a conducting or insulating film.

Ideally the plasma source will deliver a high flux of radicals to the substrate surface. Recombination of radicals on reactor wall surfaces is one of mechanisms by which the radical flux is reduced between the remote source and the substrate. The wall/radical recombination rate is a function of the radical species, the wall material, and the wall temperature.

In a PEALD system which sees multiple film chemistries, at any given time the exposed coating on the reactor walls may be of various conducting or insulating materials. The plasma properties and the radical recombination properties, and thus the flux and characteristics of plasma generated species seen by the substrate, could be substantially different depending on the details of the wall films. Additionally, the wall characteristics could change during the deposition leading to drift in the process over the course of the deposition. This, in turn, could lead to within wafer and wafer-to-wafer non-uniformities.

We have investigated the role of various insulating and conducting wall films on the spatial radical flux and spatial ion flux and energy distribution. Measurements were made on multiple ICP sources designed to deliver radicals to a PEALD reactor in a remote plasma configuration. Measurements were made over a range of rf powers (50-300W), gas compositions (Ar, O₂, N₂, and mixtures), gas flow rates (10-400sccm), wall films (304L SS, Al₂O₃, Pt, ...), wall temperatures (RT - 200C), and probe/plasma source distances (150 - 450mm). Relative radical flux measurements are derived from the mass loss of photoresist coated QCM crystals. Ion data are derived from Langmuir probe measurements.

5:40pm PS1-TuA12 Tuning Material Properties in ALD ZnO Films: In Situ Plasma Treatments and Doping, M.A. Thomas, Stetson University, J.B. Cui, University of Arkansas at Little Rock

A variety of techniques has been used to modulate the material properties of atomic layer deposited (ALD) ZnO thin films. The structural, optical, and electrical properties of the various ZnO films were characterized by techniques such as scanning electron microscopy, atomic force microscopy, x-ray diffraction, photoluminescence, transmission/absorption, and resistivity and Hall effect measurements. The electrical properties of ALD ZnO are shown to be readily tunable by combining in-situ plasma treatments with standard thermal-ALD processes. This new ALD technique is labeled plasma enhanced thermal-ALD (PET-ALD) and is capable of significantly reducing or increasing the *n*-type conductivity in ZnO by employing either an O₂ or H₂ plasma, respectively. The resistivity of such PET-ALD films is controllable within more than seven orders of magnitude. Doped ZnO films are also readily obtained by inserting an appropriate number of dopant cycles in between the standard ZnO growth sequence. By adjusting the number of dopant cycles the optical and electrical properties of ZnO can also be well controlled. These ALD films possessing a wide range of structural, optical, and electrical properties, all of which can be

easily tuned with appropriate deposition parameters, serve as excellent candidates for use in a variety of electronic and optoelectronic devices.

Plasma Science and Technology

Room: 25 - Session PS2-TuA

Plasma Surface Interaction during Plasma Etching

Moderator: S. Shannon, North Carolina State University

2:00pm PS2-TuA1 Surface Interaction Mechanisms Enabling Plasma-Enhanced Strongly Time-Dependent Etching Rates, D. Metzler, E. Vogli, F. Hilpert, G.S. Oehrlein, University of Maryland

There is great interest in establishing directional etching methods capable of atomic scale resolution during fabrication of highly scaled electronic devices. We report a new concept to achieve controlled, self-limited etching of extremely thin layers of material using a polymer as a special case. The work was performed in a capacitively coupled plasma reactor. The polymer material is a 248nm photoresist. A complete process cycle consists of: O₂ exposure of the polymer material, exhaust of O₂ from the chamber, low energy Ar⁺ ion bombardment of the surface using Ar plasma to remove the oxygen-bonded carbon species, and Ar exhaust. This sequence is repeated up to 20 times to investigate reproducibility of each cycle and time dependent behavior. Controlled etching is based on deposition of a thin reactive layer during Ar⁺ sputtering from a polymer-coated electrode (polyimide-related material) within the chamber. The polyimide-related film deposition balances etching during the Ar⁺ ion bombardment step once the reactive layer has been removed, and enables control of the etching depth. Ar⁺ ion bombardment energies were selected so that once the oxygen-bonded carbon material and physisorbed layer had been removed, net etching ceased. If the ion energy is too small, deposition of sputtered polyimide-related material dominates over etching. When applying a too high selfbias voltage, significant pristine polymer etching takes place and a self-limited process cannot be achieved. Using real-time ellipsometric monitoring, we demonstrate strongly time-dependent etching rates. Starting with a high etch rate of ≈ 19 nm/min for 2 sec, it decreases within the next 5 sec to 0 nm/min, and therefore shows self-limitation. During the Ar etching step, the O₂ modified deposited reactive layer along with 0.13 nm unmodified polymer can be removed, while concurrent deposition prevents net etching of the unmodified polymer and enables achievement of self-limited etching cycles. This etch is believed to be directional enabled by the energetic ion bombardment of the surface. Subsequently, the reactive surface is modified by O₂ adsorption during the O₂ exposure step. Molecular oxygen does not spontaneously react with carbon-based polymers at room temperature, but can be adsorbed on an activated polymer surface to form a very thin layer of oxidized carbon material over unmodified polymer. A thickness increase of 0.6 nm per cycle is observed via real-time ellipsometry. Additional XPS studies allow the investigation of the surface material composition for further insight on the reactive layer deposited during the Ar⁺ etching step and the adsorbed layer during O₂ exposure.

2:20pm PS2-TuA2 Reactive Etching or Deposition Properties of Silicon Halide Ions in Gate Etching Processes, T. Ito, K. Karahashi, S. Hamaguchi, Osaka University, Japan

As semiconductor devices continue to miniaturize, a better understanding of basic reactions of etching and/or deposition processes on substrate surfaces has become more important than before for finer controls of device structures in the manufacturing processes. In typical gate etching processes by halogen plasmas (such as HBr plasmas), Si atoms that are desorbed from the substrate surface and enter the plasma may form silicon halide ions (such as SiBr⁺) or charge neutral radicals (such as SiBr) and serve as additional etchants. For example, silicon halide ions in the plasma may also be accelerated by the sheath voltage and re-enter the substrate surface. They also may interact with the sidewalls and deposit Si there. Therefore Si containing ions and charge-neutral species may affect etching yields and etched profiles. To clarify the roles of such species in gate etching processes, we have examined sputtering or deposition reactions of Si, Si₃N₄, and SiO₂ substrates with silicon halide ions, using a mass-analyzed ion beam system. The ion beam system allows one to irradiate a sample surface with a specific ionic species at a given incident energy under ultra-high vacuum conditions and evaluate the etching yields and surface chemical reactions. The surface chemistry can be examined by in situ X-ray photoelectron spectroscopy (XPS) and desorbed species by the etching reactions can be detected by a quadrupole mass spectrometer (QMS) installed in the vacuum chamber. In this study, etching yields of silicon by SiCl_x⁺ or SiF_x⁺ ion beams were evaluated with incident energies of 500 - 1000 eV. It has been found that, depending on the incident energy, these species tend to deposit Si on the

surface although they also simultaneously etch the substrate. Some properties of such etching/deposition processes may be understood from elementary reaction processes of Si deposition and halogen etching.

2:40pm PS2-TuA3 Cl Atom Reactions on Silicon Oxy-Chloride Layers Deposited on Chamber Walls in Chlorine-Oxygen Plasmas, A.K. Srivastava, University of Houston, R. Khare, Lam Research Corp, V.M. Donnelly, University of Houston

The effects of O₂ addition to a Cl₂ inductively-coupled plasma (ICP) on the heterogeneous reactions of Cl atoms during silicon etching has been studied, using the "spinning wall" method with line-of-sight mass spectrometry, optical emission spectroscopy and Auger electron spectroscopy. A cylindrical substrate embedded in the wall is rotated so that its surface periodically passes through the plasma chamber and then through the differentially pumped diagnostic chambers. Langmuir-Hinshelwood desorption products are detected as a function of time after leaving the plasma, established by the variable rotation frequency. A silicon wafer electrode placed inside the plasma chamber was etched for 10 min with -119 Vdc self-bias in a 2.5 mTorr, 400 W Cl₂ ICP, depositing etching products on the chamber walls and spinning substrate. The Si-electrode bias was turned off and the chamber walls were conditioned with a Cl₂ ICP for an hour. A silicon oxy-chloride (SiO_xCl_y) layer of stoichiometry Si:O:Cl = 1:0.38:0.38 was formed, with the O being a result of slow etching of the quartz discharge tube. No significant Cl recombination on this layer was observed (recombination probability, $\gamma_{Cl} < 0.001$). With the addition of 5% O₂ to the feed gas, the Si-wafer was again biased for 10 min to deposit SiO_xCl_y products on the chamber walls, which were then conditioned with a no-bias ICP for another hour, leaving a film with Si:O:Cl = 1:1.09:0.08. Cl recombination was observed on this surface, with $\gamma_{Cl} = 0.03$. No etch products were detected in the mass spectrometer and hence there is no significant etching of the silicon oxy-chloride layer deposited on the chamber walls at this oxygen fraction. On further treating the surfaces with a pure O₂ plasma for 60 min, the surface composition became Si:O:Cl = 1:1.09:0.04. On this surface the Cl-atom recombination was further enhanced, with $\gamma_{Cl} = 0.04$. We attribute this behavior to Cl recombination occurring at chlorinated O sites rather than chlorinated Si sites on silicon oxy-chloride surface, because of the weak Cl-O bond compared to the Cl-Si bond.

3:00pm PS2-TuA4 Molecular Dynamic Simulation of Possible Damage Formation at Vertical Walls of finFET Devices during Plasma Etching Processes, K. Mizotani, M. Isobe, S. Hamaguchi, Osaka University, Japan

Development of multi-gate field effect transistors (FETs) such as fin-type FETs (finFETs), which can suppress short channel effects, have been considered as a leading approach to continue to follow Moore's law after the current planer MOSFET technologies reach the size limitations. In finFETs, the Si vertical walls are typically designed to function as gate channels and therefore damages at the vertical walls possibly caused by ion bombardment during the gate etching processes must be minimized. During such etching processes, ions may impinge upon the vertical surfaces but their angles of incidence should be nearly grazing angles. Energetic ions at large oblique angles of incidence against the surface are often considered to be less harmful than those with normal angle of incidence if their incident energies are the same. However, a recent study [1] performed by mass-selected ion beam system has shown that H⁺ ion injection at 60 degree from the surface normal can form a deep damage later near the substrate surface. In addition, it is known that simultaneously injection of H⁺ ions and O atoms cause enhanced surface oxidation on the Si substrate [2]. In this study, we have used molecular dynamics (MD) simulations to study damages caused by ion bombardment with oblique angles of incidence. It has been found in MD simulations that light ions such as H⁺ can indeed cause a deep damaged layer near the substrate surface even at large angle of incidence whereas heavier ions such as Br⁺ ions cause less damages under the same conditions.

[1] T. Ito, K. Karahashi, K. Mizotani, M. Isobe, S.-Y. Kang, M. Honda, and S. Hamaguchi, Jpn. J. Appl. Phys. (2012) *in press*.

[2] T. Ito, K. Karahashi, M. Fukasawa, T. Tatsumi and S. Hamaguchi, Jpn. J. Appl. Phys. 50 (2011) 08KD02.

4:00pm PS2-TuA7 Real time In Situ Electron Spin Resonance (ESR) Study of Free Radicals on Materials Created by Plasmas, K. Ishikawa, Nagoya University, Japan, H. Horibe, Kanazawa Institute of Technology, Japan, M. Ito, Meijo University, Japan, M. Sekine, M. Hori, Nagoya University, Japan

INVITED

Introduction - To understand a mechanism of plasma-surface interaction, there needs analysis of reactions between plasmas and materials. It has long been appreciated that free radicals play important roles for controlling the reactions. The electron-spin-resonance (ESR) technique can detect the radicals - in particular dangling bonds - and thus we have developed

methods to utilize the ESR for this purpose [1]. In this study, we focused on ESR detection of free radical on materials interacted with plasmas.

Polymeric materials - An ESR system was connected to a plasma discharge system (2.45 GHz, 50 W) using a quartz tube with an inner diameter of approximately 9 mm. Gas (H₂, O₂, etc.) was flowed into the quartz tube and the pressure was maintained at approximately 100 Pa in the downflow region. ESR measurements were conducted using a standard X-band (9 GHz) spectrometer with a microwave resonator. The quartz tube and poly(methyl-methacrylate)(PMMA)-ralted polymer (methacrylic acid, ethylacrylate, ethyl-methacrylate, acrylic acid, etc.) film sample were inserted inside the ESR cavity in the down-flow region, typically 20 cm from the plasma discharge.

During exposure of gaseous radicals on the polymer surface, the *in situ* real-time ESR technique was detected creation of dangling bonds on surface at real time and provided to the microscopic understanding of chemical reactions on surfaces with gaseous radicals during plasma processes. We have successfully obtained information regarding the reaction mechanism with radicals generated by plasma induced surface interactions.

Biological organism - In another, fungal spores of *Penicillium digitatum* were diluted by sterilized water mixed surfactant (Tween 20) for avoiding clump of spores, and then dried it on a quartz plate. ESR observation of the spores was conducted during oxygen plasma exposure.

Decrease of ESR intensity was corresponded with inactivation behavior where no germination of the spores was observed, eg. no sprout on the mycelia after plasma exposure. Through clarification of individual effects of plasma emission lights, neutral and charged species, this behavior is interpreted that intercellular stable free radical such as quinones was destroyed by exposing oxidizing species generated in the plasmas.

Conclusion - The real time *in situ* ESR method has a great potential for analyzing the interactions with materials and plasmas.

Acknowledgments - This study was partly supported by the Knowledge Cluster Initiative (the second stage), Tokai region, MEXT.

1. K. Ishikawa *et al.*, J. Phys. Chem. Lett. 2, 1278 (2011).

4:40pm PS2-TuA9 Roles of Hydrogen for Hydrofluorocarbon (HFC) Plasma Etching of Silicon Nitride (SiN), S. Hamaguchi, K. Miyake, K. Mizotani, M. Isobe, T. Ito, K. Karahashi, Osaka University, Japan, M. Fukasawa, T. Tatsumi, Sony Corporation, Japan

Silicon nitride (SiN) is a chemical compound widely used in semiconductor devices or their manufacturing processes as, e.g., gate spacers, stress liners, or hard masks for reactive ion etching (RIE) processes. As to RIE processes of SiN, it has been known that the content of hydrogen (H) in a hydrofluorocarbon (HFC) plasma strongly affects the SiN etching rates. The goal of the present study is to clarify the reaction mechanism of SiN etching. Our earlier studies based on molecular dynamics (MD) simulations and ion beam etching experiments suggested that hydrogen in HFC plasma tends to reduce the thicknesses of a carbon-rich surface layer deposited on SiN during an HFC plasma etching process by forming volatile hydrocarbon species. In the present study, we examine to what extent hydrogen promotes the formation of volatile species containing Si and/or N, which would directly increase sputtering yields of SiN. Our beam experiments have indicated that, under carbon deposition conditions (with 1keV CF₂⁺ ion incidence), the hydrogen content in a SiN film has little effect on the deposition rate of a carbon rich film on SiN. In other words, hydrogen typically contained in the bulk of SiN is not sufficient (probably in quantity) to promote the formation of volatile species on the surface under such conditions to the extent that the deposition rate could be reduced. However, our MD simulation results have also indicated that, under direct interaction of a SiN substrate with HFC ion beams, Si containing volatile species can be indeed desorbed from the surface. The results suggest that, in the presence of a large amount of hydrogen, hydrogen termination of Si and/or nitrogen bonds in the SiN substrate surface region increases the etching rate of SiN.

5:00pm PS2-TuA10 Molecular Dynamics Analysis of Si Etching with Cl and Br Beams: Ion Incident Angle and Neutral Radical Flux Dependence, N. Nakazaki, H. Tsuda, Y. Takao, K. Eriguchi, K. Ono, Kyoto University, Japan

Profile anomalies and surface roughness are critical issues to be resolved in plasma etching of nanometer-scale microelectronic devices, which in turn requires a better understanding of the effects of ion incident energy and angle on surface reaction kinetics. In addition, incident neutral radicals also affect the surface reaction kinetics during plasma etching, and thus the etching characteristics are varied by the neutral-to-ion flux ratio. This paper presents a classical molecular dynamics (MD) simulation of Si etching by energetic Cl⁺ and Br⁺ ion beams and low-energy neutral Cl and Br radicals, using an improved Stillinger-Weber interatomic potential model for Si/Cl and Si/Br systems. Emphasis is placed on a systematic understanding of

plasma-surface interactions of Si/Cl and Si/Br systems, which are widely used in manufacturing microelectronic devices.

In the MD simulation, the substrate has a Si(100) surface, which is a square 32.58 Å on a side and contains 72 Si atoms in a monolayer (ML). The simulation cell initially contains 1440 Si atoms (20 ML) in a depth of 26.0 Å, where Si atoms in the bottom layer are fixed during simulation, while periodical boundaries are imposed in the horizontal direction. Energetic Cl⁺ and Br⁺ ions are injected toward the substrate surface from randomly selected horizontal locations above the target, and neutral Cl and Br atoms are introduced onto the surface prior to every ion incidence. The neutral-to-ion flux ratio was varied in the range $\Gamma_n/\Gamma_i = 0-100$. The ion incident energy was in the range $E_i = 20-300$ eV, and the ion incident angle was in the range $\theta_i = 0-90^\circ$. The kinetic energy of neutral atoms was taken to be 1 eV.

Numerical results indicated that in etching by beam only ($\Gamma_n/\Gamma_i = 0$), the surface reaction kinetics exhibit a characteristic of the ion-enhanced etching at lower ion energies, where the etching yield is maximum at normal incidence ($\theta_i = 0^\circ$), while a characteristic of the physical sputtering at higher energies, where the yield is maximum at off-normal incidence ($\theta_i = 60-70^\circ$). Similar inclinations for the ion incident angle were obtained with increasing Γ_n/Γ_i , although the thickness of the surface reaction layer increases a little and the etch yield increases significantly with increasing Γ_n/Γ_i . These imply that impinging ions disarrange the surface Si lattice and weaken the binding force of Si atoms on the top surface, and incident neutral radicals etch surface Si atoms whose binding force with the neighbor Si atoms becomes lower than that of Si atoms in the original diamond lattice. These effects are clearly observed for Si/Br system, as compared to for Si/Cl system.

5:20pm **PS2-TuA11 Controlling Correlations Between Ion and UV/VUV Photon Fluxes in Low Pressure Plasma Materials Processing.** P. Tian, M.J. Kushner, University of Michigan

The importance UV and VUV photon fluxes during plasma materials processing has been recognized through the damage these fluxes may cause in devices being fabricated and in adversely affecting the permittivity of low-k dielectrics such as SiOCH through demethylation. Recently, synergistic effects between ions and photons have been observed in the roughening of photoresist [1] and in sub-threshold etching of silicon in Cl containing gas mixtures.[2] The growing awareness of the importance of UV and VUV photon fluxes in low pressure plasma materials processing, and the possibility of there being synergies with ion fluxes, motivates development of methods to separately optimize UV/VUV and ion fluxes. For example, one may wish to maximize or minimize the overlap in time between the UV/VUV and ion fluxes depending on the particular process. In this talk, we report on results from a computational investigation of low pressure inductively and capacitively coupled plasmas with the goal of determining the degree to which UV/VUV and ion fluxes can be separately controlled. The model used in this investigation is a 2-dimensional plasma hydrodynamics model with radiation transport. Two strategies are being investigated. The first is pulsed plasmas which rely on the different time scales for production and transport of photons and ions to the substrate during the pulsed period to provide for some degree of separate control of the fluxes. The second is semi-remote plasma sources which rely on isolation of the photon sources and transport of ions to control the ratio of photon and ion fluxes to the substrate.

[1] T-Y. Chug, et al., Plasma Proc. Polymer **8**, 1068 (2011)

[2] H. Shin et al., J. Vac. Sci. Technol A **30**, 021306 (2012)

* Work supported by the Semiconductor Research Corp. and DOE Office of Fusion Energy Sciences

5:40pm **PS2-TuA12 Formation Mechanisms of Nanoscale Surface Roughness and Rippling during Plasma Etching and Sputtering of Si under Oblique Ion Incidence.** H. Tsuda, Y. Takao, K. Eriguchi, K. Ono, Kyoto University, Japan

Three-dimensional measurement and prediction of atomic-scale surface roughness on etched features become increasingly important for the analysis of line edge roughness (LER) and line width roughness (LWR) on feature sidewalls; however, the feature profiles are too small and/or too complex to measure the surface roughness on bottom surfaces and sidewalls of the etched features. To predict the surface roughness on atomic/nanometer scale, we have developed our own three-dimensional atomic-scale cellular model (ASCeM-3D) [1] and feature profile simulation. In this study, emphasis is placed on a better understanding of the formation mechanisms of nanoscale surface roughening and rippling during Si etching and sputtering under oblique ion incidence.

In the ASCeM-3D model, the simulation domain is divided into a number of small cubic cells of $L = \rho_{Si}^{-1/3} = 2.7$ Å, where $\rho_{Si} = 5.0 \times 10^{22}$ cm⁻³ is the atomic density of Si substrates. Ions and neutrals are injected from the top of the simulation domain, and etch and/or sputter products are taken to

be desorbed from etching surfaces into microstructural features, where two-body elastic collision processes between incident ions and substrate atoms are also taken into account to analyze ion reflection on etched feature surfaces and penetration into substrates. The ASCeM-3D takes into account surface chemistries based on the Monte Carlo (MC) algorithm [2-4], including adsorption and reemission of neutrals, chemical etching, ion-enhanced etching, physical sputtering, and redeposition of etch and/or sputter products on feature surfaces. The etch yield of ion-enhanced etching and sputtering depending on ion incident energy and angle is taken from the empirical models.

Numerical results indicated that the ripple structures occur on etched surfaces, depending on incident angle of ions. The surfaces are randomly roughened in the case of Cl₂ plasma etching for an ion incident angle $\theta_i = 0^\circ$ or normal incidence of ions. For increased $\theta_i = 45^\circ$, the ripples are formed perpendicular to the direction of ion incidence, while parallel to that of ion incidence for further increased $\theta_i = 75^\circ$. These imply that the angular dependence of energy transfer processes from an incident ion to substrate atoms largely affects the evolution of feature profiles and surface roughness on atomic/nanometer scale.

[1] H. Tsuda *et al.*, Jpn. J. Appl. Phys. **50** (2011) 08JE06.

[2] Y. Osano and K. Ono, J. Vac. Sci. Technol. B **26** (2008) 1425.

[3] H. Tsuda *et al.*, Thin Solid Films **518** (2010) 3475.

[4] H. Tsuda *et al.*, Jpn. J. Appl. Phys. **49** (2010) 08JE01.

Advanced Surface Engineering
Room: 22 - Session SE+PS-TuA

Atmospheric Pressure Plasmas

Moderator: H. Barankova, Uppsala University, Sweden,
P.H. Mayrhofer, Montanuniversität Leoben, Austria

2:00pm **SE+PS-TuA1 Plasma Medicine: The Journey of a New Field of Research, from Killing of Bacteria to Killing of Cancer Cells.** M. Laroussi, Old Dominion University **INVITED**

Research on the biomedical applications of low temperature plasmas started with few limited experiments mainly concerned with the ability of plasma to kill harmful microorganisms, especially bacteria as it relates to sterilization of abiotic and/or biotic surfaces (such as tissues). Low temperature plasmas produce a potent cocktail of highly reactive chemical species including reactive oxygen species (ROS) such as O, O₂⁻, and OH and reactive nitrogen species (RNS) such as NO and NO₂. These species are known to exhibit strong oxidative properties and can trigger signaling pathways in biological cells. For example oxidation of the lipids and proteins that constitute the membrane of biological cells leads to the loss of their functions. In such environment bacterial cells were found to die in minutes or even seconds, depending on the strain. Plasmas were also found to be an effective method to control the proliferation of biofilms. Biofilms are very resistant to chemicals found in detergents and even to antibiotics. Therefore, if not controlled, biofilms (including dental plaque, for example) could represent serious health hazards.

Experiments on eukaryotic cells demonstrated that under some conditions, low temperature plasmas appear to cause little damage to living animal and plant tissues. For example, skin fibroblast cells are found to remain viable under plasma conditions that can be lethal to bacterial cells. The proliferation of fibroblasts is an important step in the wound healing process. The ability of plasma to kill bacteria and to accelerate the proliferation of specific tissue cells opened up the possibility to use plasma for the healing of chronic wounds such as diabetic ulcers. Tens of thousands of amputations occur every year in the US alone because of the inability of present medical methods to heal chronic wounds.

Low temperature plasmas have been found to be able to trigger apoptosis in cancer cells. Apoptosis is a natural process of "programmed" cell death. Cancerous cells lose the ability to initiate such a killing process. However, mediated through its specific chemical species, plasmas can trigger the signaling pathway that can start the cascade of events that result in apoptosis. This unique plasma capability opened up the possibility to use plasma for cancer treatment.

Low temperature plasmas therefore constitute a new transformational approach to healthcare referred to as Plasma Medicine [1]. In this paper background work as well as new results both in fundamental understanding and applications will be discussed.

References

[1] M. Laroussi, "Low Temperature Plasmas for Medicine?", *IEEE Trans. Plasma Sci.* **37**, 714 (2009).

2:40pm **SE+PS-TuA3 VHF Atmospheric Glow Discharge: Electrical and Optical Characterization for Multiple Gases**, *B. Byrns, A. Lindsay, S. Shannon, A. McWilliams, S. Hudak, J. Cuomo*, North Carolina State University

Atmospheric plasmas have the potential to increase the efficiency of many processes involving interactions between materials and plasma due to the increased reactive species densities in the plasma. One challenge in the integration of these sources into high volume applications is the difficulty of producing large area, high density atmospheric plasmas without reaching thermal equilibrium or relying on the formation of arcs; a secondary challenge is the formation of these discharges without helium or other rare gas species that are typically used to sustain atmospheric glows. In this work a large area atmospheric pressure glow discharge operating at 162MHz has been created utilizing a VHF ballasting effect [1]. An electrical model paired with a simple global plasma model is used to characterize the electrical properties of the plasma. Several different feed gases including air, CO₂, nitrogen, and argon are used to validate the model and study the production of reactive species in the plasma volume; both of these endeavors also enable intelligent process setpoint design to achieve the necessary operating conditions for various gases. These measurements are made using various electrical and optical diagnostics including OES, B-loop probe measurements, and in-line RF metrology. The effects of increasing the pressure, through the use of nozzles, are examined and used to further refine and validate the system model. This greater understanding of the plasma allows for the potential to increase the size of the plasma, allowing for an increase in the number of reactive species and thus an increase in the efficiency for the treatment of surfaces. Currently the plasma is being studied for use in the removal of HDPE from surfaces as well as for the treatment of water. Preliminary results for both of these applications will be presented.

[1] Brandon Byrns et al 2012 J. Phys. D: Appl. Phys. 45 195204

* Work supported by the State of North Carolina, SERDP contract 1762, and by a generous gift donation from Advanced Energy Incorporated, Verity Instruments, and Bird Technologies.

3:00pm **SE+PS-TuA4 Atmospheric Pressure Glow Discharge for Point-of-Use Water Treatment**, *A. Lindsay, B. Byrns, S. Shannon, D. Knappe*, North Carolina State University

Treatment of biological and chemical contaminants is an area of growing global interest where atmospheric pressure plasmas can make a significant contribution. Atmospheric plasmas have demonstrated the potential to reform aqueous chemistry¹ and mitigate water contamination². One of the key challenges is scaling of these systems for volume processing. A large volume VHF coaxial plasma source has been developed that enables scale up of these systems under ambient air conditions, addressing volume processing and operating cost due to the absence of a noble gas carrier to sustain a volume glow.³ The 162 MHz atmospheric glow discharge presented here offers several features uniquely applicable for disinfection. Because of ballasting effects, attributable to the very high drive frequency, the electric discharge is maintained at a steady glow, allowing formation of critical non-equilibrium chemistry. High densities, $n_e = 10^{11}$ - 10^{12} , have been recorded. The atmospheric nature of the device permits straightforward and efficient treatment of material samples. Using air as a process gas, [H⁺] concentrations in 150 milliliter tap water samples have been shown to drop five orders of magnitude after five minutes of discharge exposure. Recent literature has demonstrated that increasing acidity is strongly correlated with a solution's ability to deactivate microbial contaminants.¹ The work presented here will explore the impact of treatment gas, system configuration, and power density on water treatment including disinfection and PFC abatement. An array of plasma diagnostics including optical emission spectroscopy and electrical measurement of plasma discharge condition are combined with post-process water chemistry analysis including Quanti-Tray analysis of coliform and E.coli bacteria, gas chromatography, and mass spectrometry. Continued development of volume processing atmospheric plasma disinfection technology offers promise for point-of-use treatments in developing areas of the world, potentially supplementing or replacing supply-dependent chemical and weather-dependent solar disinfection methods.

1. Traylor (2011) J. Phys. D: Appl. Phys. 44 (2011) 472001

2. Takeuchi (2011) IEEE Trans. On Plasma Sci. 39(12) 3358-3363

3. Byrns (2012) J. Phys. D: Appl. Phys. 45 (2012) 195204

* Work supported by generous gift donations from Bird Technologies, Advanced Energy, and Verity Instruments

4:00pm **SE+PS-TuA7 Cold Atmospheric Plasma in Liquids**, *H. Barankova, L. Bardos*, Uppsala University, Sweden

Atmospheric pressure plasmas and their applications, especially those based on non-thermal processes, have been extensively studied in the last decade,

with focus on surface treatment, coatings and gas conversion. Individual applications depend on the current status of development in atmospheric pressure plasma sources. The plasma source based on the Fused Hollow Cathode (FHC) geometry was developed for generation of plasma in liquids. Effect of various generation regimes on the performance of plasma and on plasma distribution in water is studied without and with different auxiliary gases. The paper also discusses importance of the plasma source/reactor design for control of plasma chemical kinetics and comments on advantages and limitations of atmospheric plasma.

4:20pm **SE+PS-TuA8 Characterization of Amorphous and Microcrystalline Si Films Grown in Atmospheric-Pressure Very High-Frequency Plasma**, *H. Kakiuchi, H. Ohmi, T. Yamada, A. Hirano, T. Tsushima, K. Yasutake*, Osaka University, Japan

Hydrogenated amorphous silicon (*a*-Si) and microcrystalline silicon (μ c-Si) prepared at low temperatures are promising thin film materials for use in large-area electronic devices. The goal of our study is to develop a highly efficient deposition process of good-quality *a*-Si and μ c-Si films on polymer substrates using an atmospheric-pressure (AP) plasma technology in which stable reactive plasma excited by a 150-MHz very high-frequency (VHF) power under AP is effectively used.

The experiments were conducted in an AP plasma CVD system that had a parallel-plate-type electrode (2x8 cm²), whose surface was coated by alumina of ~0.1 mm thickness. By supplying a VHF power through an impedance matching unit, AP He/H₂/SiH₄ plasma was stably confined in the narrow gap region (0.3–0.7 mm) between the electrode and a substrate. Under a constant process pressure of 1x10⁵ Pa, VHF power density (P_{VHF}), H₂ and SiH₄ flow rates, plasma gap and substrate heating temperature (T_{sub}) were varied as principal parameters. Si dusty particles formed by gas-phase condensation in the outside of the plasma region were completely removed by sucking the gas flow before their adhering to the substrate surface.

By examining the influence of gas residence time in the plasma on the film growth behavior, it was shown that the source SiH₄ gas was immediately decomposed after being introduced into the plasma region and contributed to the film growth. Under the condition of $P_{VHF} = 14$ W/cm², H₂ and SiH₄ flow rates of 500 and 50 SCCM, respectively (H₂/SiH₄ = 10), and $T_{sub} = 220$ °C, the film started to crystallize in only 0.3 msec. Both increasing P_{VHF} and H₂/SiH₄ ratio caused the decrease in gas residence time necessary for the phase transition of the resultant Si films. On the other hand, an excessively long gas residence time (> 1 msec) led to the formation of highly crystallized μ c-Si films even if H₂ was not added to the process gas mixture. However, such μ c-Si films showed poor electrical properties, which resulted from the sparse film structure without enough passivation of the grain boundaries with amorphous Si tissues. These suggest that the precise control of gas residence time is primarily important for the formation of good-quality *a*-Si and μ c-Si films using AP-VHF plasma, together with the optimization of P_{VHF} and H₂/SiH₄ ratio.

The *a*-Si and μ c-Si films deposited with high rates (>10 nm/s) in AP He/H₂/SiH₄ plasma were used as the channel layers of bottom-gate thin film transistors (TFTs). The performance of the TFTs will be presented in the conference.

4:40pm **SE+PS-TuA9 Atmospheric Plasma Polymerization of Esters: Tuning the Coating Chemistry by Tuning the Precursor Chemistry**, *B. Nisol, A. Batan*, Université Libre de Bruxelles, Belgium, *A. Kakaroglou, M. Wadikar, G. Scheltjens, G. Van Assche, B. Van Mele, I. De Graeve, H. Terryn*, Vrije Universiteit Brussel, Belgium, *F. Reniers*, Université Libre de Bruxelles, Belgium

The influence of the chemical environment of an ester function on the plasma polymerization process and on the chemical structure of the deposited coating is investigated, and the consequences on the coatings properties (barrier and adhesion) are discussed. Allyl methacrylate (AMA), n-propyl methacrylate (nPMA) and propyl isobutyrate (PIB) containing respectively two, one and no double bonds were injected in a home made dielectric barrier discharge reactor. Argon was used as the main plasma gas, and the power of the discharge was varied from 30 to 80 W. The thickness of the deposited coating was determined by visible spectroscopic ellipsometry and allowed to calculate the deposition rate. The surface chemistry was investigated by X-ray photoelectron spectroscopy (XPS) and the bulk structure was analyzed by reflection – absorption infrared spectrometry (IRRAS). Differential scanning calorimetry was used to probe the remaining unreacted groups in the coating. The results evidence a great change in the polymerization rate that depends on the presence of the double bonds. Moreover, the concentration of ester groups at the surface of the coatings also depends on the surrounding double bonds present in the precursor. Indeed, whereas the relative amount of ester groups in poly-AMA remains stable when increasing the plasma power, it drops drastically for poly-PIB. A stabilization of the ester groups by the double bonds is suggested.

Acknowledgements: this work is part of the GREENCOAT project, financed by the Brussels Region, and by the IAP project "physical chemistry of plasma surface interactions", funded by the Federal Government, Belgium.

Scanning Probe Microscopy Focus Topic

Room: 16 - Session SP+AS+BI+ET+MI+NS-TuA

Advances in Scanning Probe Imaging

Moderator: S. Allen, The University of Nottingham, UK, Z. Gai, Oak Ridge National Laboratory

2:00pm **SP+AS+BI+ET+MI+NS-TuA1 Molecules Investigated with Atomic Resolution using Scanning Probe Microscopy with Functionalized Tips**, L. Gross, F. Mohn, N. Moll, G. Meyer, IBM Research - Zurich, Switzerland **INVITED**

Single organic molecules were investigated using scanning tunnelling microscopy (STM), noncontact atomic force microscopy (NC-AFM), and Kelvin probe force microscopy (KPFM). With all of these techniques submolecular resolution was obtained due to tip functionalization by atomic manipulation. The techniques yield complementary information regarding the molecular structural and electronic properties.

Using NC-AFM with CO terminated tips, atomic resolution on molecules has been demonstrated and the contrast mechanism was assigned to the Pauli repulsion [1]. On the other hand, by using STM the molecular frontier orbitals, i.e., the highest occupied and the lowest unoccupied molecular orbitals (HOMO and LUMO), were mapped [2]. Using a CO terminated tip for orbital imaging with the STM, the resolution can be increased and the images correspond to the gradient of the molecular orbitals due to the *p*-wave character of the tip states [3]. Finally, KPFM reveals information about the distribution of charges within molecules by measuring the *z*-component of the electrostatic field above the molecule, as demonstrated on the hydrogen tautomerization switch naphthalocyanine [4].

References :

- [1] L. Gross *et al.* *Science* **325**, 1110 (2009).
- [2] J. Repp *et al.* *Phys. Rev. Lett.* **94**, 026803 (2005).
- [3] L. Gross *et al.* *Phys. Rev. Lett.* **107**, 086101 (2011).
- [4] F. Mohn *et al.* *Nature Nanotechnol.* **7**, 227 (2012).

2:40pm **SP+AS+BI+ET+MI+NS-TuA3 Functional Imaging of Jahn-Teller Dynamics at the Single-molecule Scale**, J. Lee, S.M. Perdue, A. Rodriguez Perez, P.Z. El-Khoury, V.A. Apkarian, University of California, Irvine

Taking advantage of both elastic and inelastic tunneling processes of a molecule isolated at the double-barrier tunneling junction of a scanning tunneling microscope, both static and dynamic parts of the Hamiltonian can be visualized with submolecular resolution. This is illustrated by imaging Jahn-Teller (JT) driven vibronic dynamics within Zn-etio porphyrin (ZnEtio), in its various reduced forms, in what may be regarded as nature's choice of a molecule as a controllable current switch. Unique interpretations are afforded through simultaneously recorded functional images, such as maps of: a) energy resolved differential current, b) spectrally resolved electroluminescence, c) conduction bistability, d) reduction/oxidation potentials (maps of charging and discharging). We focus on the radical anion, ZnEtio⁻, which is reduced by injecting an electron to a single ZnEtio molecule adsorbed on a thin aluminum oxide film grown on NiAl(110). In contrast with the neutral, the saddle-shaped radical anion lies flat on the surface of the oxide. The discharge map directly shows that the excess electron is localized in the ²p_x orbital of the entire porphyrin macrocycle, as a result of the JT active rectangular (B_{1g}) distortion of the molecule. The static JT potential leads to conduction bistability, with reversed switching polarity depending on whether tunneling electrons are injected in the occupied ²p_x orbital or the diamond (B_{2g}) coordinate which serves as a transition state that connects the p_x and p_y orbitals at the two B_{1g} minima. In addition to the JT switching, the dynamic JT states are directly imaged through electroluminescence spectra, induced by injection of a second electron in the anion. The spectra consist of a continuum due to radiative ionization of the dianion, and sharp Fano resonances of the vibronic progression of the JT active modes. A detailed analysis of the spectra yields the vibronic couplings and the wavefunctions. Vibronic structure is inherent in STM topographic images, and has hitherto not been fully recognized.

3:00pm **SP+AS+BI+ET+MI+NS-TuA4 Atomic and Chemical Resolution of Heterogeneous 1-D Metallic Chains on Si(100) by Means of nc-AFM and DFT**, M. Setvin, M. Ondracek, P. Mutombo, Z. Majzik, P. Jelinek, Institute of Physics of ASCR, Czech Republic

Scanning Probe techniques are widely used to image atomic and electronic structure of surfaces and nanostructures. However atomic and chemical resolution of complex nanostructures (e.g. molecules, nanoparticles or nanowires) is still the large challenge. Several methods (see e.g. [1-3]) have been already proposed to achieve the single-atom chemical resolution. In the work [3] it was showed that the single-atom chemical identification can be achieved via force-site spectroscopy measurements using Frequency Modulation Atomic Force Microscopy (FM-AFM). The validity of the method was demonstrated on semiconductor surface alloy composed of isovalent species (Si, Sn and Pb). In this particular case, the valence electrons of surface atoms possess very similar electronic structure close to sp³ hybridization with characteristic dangling bond state. Hence the maximum short-range force is mainly driven by the position of the dangling bond state with respect to the Fermi level.

In this work, we investigated atomic and chemical structure of heterogeneous 1-D chains made of III and IV group metals grown on Si(100) surface [4] by means of room-temperature (RT) FM-AFM measurements combined with DFT simulations. Here 1D chains consist of heterogeneous buckled-dimer structures with unknown chemical ordering. What more, the presence of buckled dimers composed by chemical species of different valence makes this system very challenging for true atomic and chemical resolution by means of SPM.

In this contribution, we will show first that FM-AFM technique even at RT is able to achieve atomic resolution of individual atoms forming dimers, much superior to the contrast obtained by the traditional STM technique. Secondly, we will demonstrate that the single-atom chemical identification is still possible combining the force-site spectroscopy at RT with DFT simulations even in such complex systems as the heterogeneous 1D metallic chains.

- [1] M. Schmid, H. Stadler, P. Varga *Phys. Rev. Lett.*, **70**, p. 1441 (1993)
- [2] L. Gross *et al.* *Science* **325**, 5944 (2009).
- [3] A. Foster *et al.* *Phys. Rev. Lett.* **102**, 256103 (2009).
- [4] Y. Sugimoto, P. Pou, M. Abe, P. Jelinek, R. Perez, S. Morita, O. Custance, *Nature* **446**, 64 (2007)
- [5] L. Magaud, A. Pasturel, and J.-Y. Veuillen, *Phys. Rev. B* **65**, 245306 (2002).

4:00pm **SP+AS+BI+ET+MI+NS-TuA7 Simple Routes to High Speed and Super Resolution AFM**, J.K. Hobbs, University of Sheffield, UK **INVITED**

Over the past two decades atomic force microscopy has developed to become the workhorse of molecular nanotechnology. However, despite this success, it has failed to deliver consistently in two areas where it arguably has most potential, namely sub-molecular resolution imaging and the following of processes in real time. Here our work to tackle these challenges will be discussed.

We have developed a new approach to reaching high resolution within a conventional AFM, based on torsionally driven T-shaped cantilevers, dubbed "torsional tapping AFM". The use of torsional oscillations gives improved dynamics (high Q-factor, high frequency), without excessively increasing the spring constant. The small offset of the tip from the axis of rotation gives improved lever sensitivity. Combined, these result in an approximately 12 fold improvement in sensitivity when compared to the same AFM with a conventional tapping cantilever. This improved sensitivity allows ultra-sharp whisker tips to be used in a routine manner, giving true molecular resolution even on soft materials presenting surfaces with tens of nanometres of topography. For example, individual polyethylene chains both in the crystalline phase, and at the interface with the amorphous phase, can be clearly imaged in a conventionally processed sample of plastic, with polymer chain-to-chain resolution down to 0.37 nm [1]. Data from semi-crystalline polymers to naturally occurring protein crystals will be presented.

High speed AFM requires methods for scanning rapidly, for maintaining tip-sample contact ("feedback"), and for constructing the topography image. We have shown that resonant scanners [2] give a robust method for rapid scanning. In a conventional AFM the feedback and the topographic image are inextricably linked. However, this places a limit on scan speed as it demands that the tip has reached equilibrium at each point on the image if the height is going to be accurately obtained. We have adopted a different approach, in which the height of the tip is directly measured using an interferometric approach, freeing the feedback loop to minimising tip-sample forces. This allows topographic images with height traceable to the wavelength of the interferometric laser to be obtained at imaging rates greater than one frame a second. Coupled with resonant scanners, giving

scan areas up to $40 \times 40 \text{ \mu m}^2$ an AFM platform capable of in-line industrial applications is obtained.

1. Mullin, N.; Hobbs, J. K., *Phys Rev Lett* **2011**,107

2. Humphris, A. D. L.; Miles, M. J.; Hobbs, J. K. *Appl Phys Lett* **2005**,86 (3)

4:40pm SP+AS+BI+ET+MI+NS-TuA9 A Scanning Probe Microscopy Study of Trimesic Acid Self-Assembly on Highly Oriented Pyrolytic Graphite. V. Korolkov, S. Allen, C.J. Roberts, S.J.B. Tendler, The University of Nottingham, UK

We have investigated trimesic acid (1,3,5-benzenetricarboxylic acid, TMA) adsorption on highly oriented pyrolytic graphite (HOPG) surfaces from aqueous medium at room temperature. Both atomic force (Peak Force Tapping mode) and scanning tunnelling microscopy were utilized to follow the adsorption dynamics and molecular arrangements. A chicken-wire arrangement for adsorbed molecules with an average pore size of $11 \pm 1 \text{ \AA}$ was established and observed using both scanning techniques. We found that this structure forms a monolayer within ~ 100 seconds of exposure of the HOPG surface to $50 \mu\text{M}$ TMA solution in H_2O . The monolayer structure was found to be stable for at least 48h under ambient conditions. STM was observed to lead to some desorption of TMA from a dynamically formed TMA film, and was only able to image the monolayer of TMA molecules in intimate contact with the HOPG. AFM revealed that TMA films formed using higher concentrations or longer adsorption times formed multilayers with similar molecular spacings and displayed an island growth morphology.

We have achieved an excellent resolution on an ambient running AFM. We have demonstrated that the combination of STM and AFM is essential, if not a must, to look at ultimate monolayers in the ambient conditions. Overall a facile green chemistry method for TMA monolayer fabrication from aqueous media on a HOPG surface has been established.

5:00pm SP+AS+BI+ET+MI+NS-TuA10 Understanding the Role of the Probe in SPM Imaging of Metal Oxides: New Opportunities for In-Depth Surface Analysis. H. Mönig, Univ. of Münster, Germany, M. Todorovic, Univ. Autónoma de Madrid, Spain, M.Z. Baykara, Yale Univ., T.C. Schwendemann, Southern Connecticut State Univ., J. Götzen, Ö. Ünverdi, E.I. Altman, Yale Univ., R. Perez, Univ. Autonoma de Madrid, Spain, U.D. Schwarz, Yale Univ.

Metal oxide surfaces play an indispensable role in a number of catalytic processes of technological and scientific importance. A fundamental understanding of the role that metal oxide surfaces play in such applications requires an experimental technique that allows analyzing chemical and electronic surface properties down to the atomic scale. The powerful method of three-dimensional atomic force microscopy (3D-AFM) in combination with scanning tunneling microscopy (STM) can be used towards this goal with great success. However the interpretation of results is not straightforward, particularly because the structure and chemistry of the probe tip employed in the experiments influences the measured data.

In this talk, using a combination of experimental STM data and density functional theory (DFT) calculations, we will study the effect of changing the tip structure and chemistry, as well as imaging parameters such as tip-sample distance and bias voltage on STM images obtained on the model surface of $\text{Cu}(100)\text{-O}$, a surface oxide layer consisting of nearly co-planar copper (Cu) and oxygen (O) atoms. We observe that STM image contrasts and atomic species with highest tunneling probability vary greatly with changing tip properties and imaging parameters. Reasonable matches between calculated and experimentally recorded STM images are observed, allowing the determination of particular tip models used in the experiments. Additionally, the effect of rotating the model tip structures with respect to the sample surface results in asymmetric features in simulated STM images, reproducing certain peculiar patterns observed experimentally. To sum up, the results presented here underline the significant role that the tip plays in SPM measurements and describe potential routes to optimize the gathered information through deliberate manipulation of tip properties as well as imaging parameters.

5:20pm SP+AS+BI+ET+MI+NS-TuA11 Characterizing the Best Tips for NC-AFM Imaging on Metal Oxides with Force Spectroscopy and Theoretical Simulations. D. Fernandez-Torre, Universidad Autónoma de Madrid, Spain, A. Yurtsever, Osaka University, Japan, P. Pou, Universidad Autónoma de Madrid, Spain, Y. Sugimoto, M. Abe, S. Morita, Osaka University, Japan, R. Perez, Universidad Autónoma de Madrid, Spain

Metal oxides play a key role in a wide range of technological applications. To optimize their performance, it is essential to understand their surface properties and chemistry in detail. Noncontact atomic force microscopy (nc-AFM) provides a natural tool for atomic-scale imaging of these insulating materials. Some of these materials, including ceria (CeO_2), and particularly titania (TiO_2), have been extensively studied with nc-AFM in the last few

years. Experiments on the rutile $\text{TiO}_2(110)$ surface show, at variance with STM, that a variety of different contrasts can be obtained, and frequent changes among different imaging modes are observed during scanning. The two most common contrasts are the “protrusion” and the “hole” mode imaging modes, that correspond, to imaging bright the positive or the negative surface ions respectively, but other contrasts like the “neutral” mode and the “all-inclusive” mode—where all the different chemical species and defects are imaged simultaneously—have been also identified.

Understanding the image contrast mechanisms and characterizing the associated tip structures is crucial to extract quantitative information from nc-AFM measurements and to identify the nature of the observed defects. While in many cases the same nc-AFM image can be explained by different models, and even different underlying tip-sample interactions, we show here that the combination of force spectroscopy (FS) measurements and first-principles simulations can provide an unambiguous identification of the tip structure and the image contrast mechanism. In particular, we show that the best tips to explain the protrusion and hole mode forces are TiO_x -based clusters differing in just one H atom at the tip apex, discarding previously proposed Ti-terminated tips that would lead to forces much larger than the ones observed in the experiments. The less frequent neutral and all-inclusive images are associated to Si tips where contamination is limited to just an O atom or OH group at the apex. These models provide a natural explanation for the observed contrast reversals by means of H transfer to/from the tip, an event that we indeed observe in our simulations. As tip contamination by surface material is common while imaging oxides, we expect these tips and imaging mechanisms to be valid for other oxides. Our results for the imaging of CeO_2 surfaces and of metal atoms (K, Pt) adsorbed on TiO_2 support this conclusion.

5:40pm SP+AS+BI+ET+MI+NS-TuA12 Direct Probe of Interplay between Local Structure and Superconductivity in $\text{FeTe}_{0.55}\text{Se}_{0.45}$. M.H. Pan, W.Z. Lin, Q. Li, B.C. Sales, S. Jesse, A.S. Sefat, S.V. Kalinin, Oak Ridge National Laboratory

A key challenge in high-temperature superconductivity is to determine the role of local crystallographic structure and chemical effects on the superconducting critical temperature, T_c . Iron chalcogenide superconductors ($111'$) are ideal model systems for deciphering the role of local effects on the superconductivity, primarily because they cleave leaving non-polar surfaces unlike other families of iron arsenide superconductors ($1111'$ or $122'$) and cuprates. Here, we explore the interplay between local crystallographic structure, composition and local electronic and superconductive properties. Direct structural analysis of scanning tunneling microscopy (STM) data allows local lattice distortions and structural defects across a $\text{FeTe}_{0.55}\text{Se}_{0.45}$ surface to be explored on a single unit-cell level. Concurrent superconducting gap (SG) mapping reveals suppression of the SG at well-defined structural defects, identified as a local structural distortion (Guinier-Preston zone). The strong structural distortion is related to the vanishing of the superconducting state. This study provides insight into the origins of superconductivity in iron chalcogenides by providing an example of atomic-level studies of the structure-property relationship.

Surface Science

Room: 21 - Session SS+NS-TuA

Reactivity of Size and Shape Selected Nanoparticles

Moderator: C.T. Campbell, University of Washington

2:00pm SS+NS-TuA1 2012 AVS Gaede-Langmuir Award Lecture: Surface Photochemistry on Compact Crystals and on Metal Nanoparticles. D. Menzel*, Fritz-Haber Institut, and Techn. Univ. Muenchen, Germany

INVITED

Adsorbing a molecule on a substrate changes its photochemistry. I shall briefly review characteristics of surface photochemistry, established mechanisms, and effects such as whether the substrate acts mainly as source or sink of electronic excitations of adsorbates, how long the latter survive, and how effects which influence their localization and delocalization influence the success rate of excitations. For laser excitation, linear and nonlinear response to excitations can occur.

Use of nanoparticles (MNPs) instead of bulk metals further changes surface photochemistry, mainly by changing the substrate optical excitations (e.g. the Mie plasmon of MNPs), and excitation lifetimes and efficiency (by confinement). This will be illustrated by data obtained in the past years in Berlin on NO dimers adsorbed on Ag NPs with varied size (2 to 10 nm)

* Gaede Langmuir Award Winner

supported on thin alumina films on NiAl single crystals, laser-excited with 2 to 5 eV, with in situ comparison with Ag(111). The main channel is photodesorption of NO; conversion to $N_2O + O$, and to NO(ad) stabilized by O also occur. Adsorption energies were characterized by TPD, cross sections (PCS) by photo-depletion, and desorbate energy distributions (translation, rotation, vibration) by TOF and REMPI analysis. Linear and nonlinear fluence dependencies of desorption signals have been found with ns and fs laser pulses, respectively. The main changes in NO photodesorption are found in the PCS which are strongly enhanced by plasmon excitation and more weakly by excitation confinement, and show clear size dependences interpreted by counteracting influences. The branching into the minor photoreaction channels is also changed at Ag NPs compared to Ag(111) which is due to varying PCS enhancement factors. The photochemical mechanism, however, as evidenced by state-resolved analysis of the desorbing NO molecules, remains the same – formation of transient negative ions by hot electrons in the substrate - for most of the investigated range (with an exception for high energy and small particles). With fs laser pulses further drastic PCS increases are found even at low fluences at the NPs but not at Ag(111). This nonlinear effect is explained by re-excitation of hot electrons confined in the NPs within a single laser pulse. But even here the individual dynamics stay the same. This action of NPs on the success probability of excitations with essentially unchanged dynamics appears to be the typical behavior for photochemistry on MNPs. Only in an unusual case (Xe/Ag NPs) we have seen a direct influence of plasmon excitation on desorption.

These findings may help in the understanding of photocatalysis on MNPs.

2:40pm SS+NS-TuA3 Photocatalytic Deposition of Au onto Ordered Linear Arrays of TiO₂ Nanoparticles, J. Taing, A. Margarella, Y. Liu, J.C. Hemminger, University of California Irvine

TiO₂ nanoparticles were decorated onto the step edges of highly oriented pyrolytic graphite (HOPG) via physical vapor deposition. Gold shells and nanoparticles were then grown on the TiO₂ nanoparticles using a photoelectrochemical cell whereupon a photocatalytic reduction mechanism is verified by photocurrent measurements. Samples of TiO₂ nanoparticles on HOPG, acting as a photoelectrode, were placed in a half-cell and immersed in either an electrolyte solution of 1.0 M NaCl or 1.0 M NaNO₃. Bare HOPG, acting as a counter electrode, was placed in a second half-cell and immersed in the same electrolyte solution. The two half-cells were connected by a salt bridge and the electrodes by a picoammeter. Upon irradiation of the TiO₂ nanoparticles by 365 nm UV light from a 200 W Hg lamp, photogenerated electrons produced a photocurrent. Subsequent to introducing 1 mL of 15 μ M HAuCl₄ into the cell containing the TiO₂ nanoparticles, the photocurrent decreased as a result of the reduction of Au³⁺ to Au on TiO₂. Scanning electron microscopy (SEM), transmission electron microscopy (TEM), x-ray dispersive spectroscopy (EDS), and x-ray photoelectron spectroscopy (XPS) were used to characterize the morphology, crystal structure, and chemical identity of the nanoparticles. Images of TiO₂ nanoparticles encapsulated in Au are included in the supplement.

3:00pm SS+NS-TuA4 Catalytic Activity of Gold-supported TiO₂ Nanocrystals Towards Simple Alcohols, D.V. Potapenko, Z. Li, Y. Lou, R.M. Osgood, Columbia University

Titanium oxide is a versatile photocatalytic material and it has been the subject of much research throughout the last two decades. Nanostructuring is one approach for tailoring the properties of a catalyst. Previously we have developed a method of preparation of structurally homogenous TiO₂ nanocrystals on Au(111) substrate through oxidation of Ti-Au surface alloy. In this work we explore catalytic properties of the nanocrystals through a series of temperature programmed desorption (TPD) studies with simple alcohols: ethanol and 2-propanol. Similarly to the single crystal TiO₂ rutile(110) surface, TiO₂ nanocrystals on Au(111) catalyze dehydrogenation of ethanol and 2-propanol into ethylene and propene. Dehydrogenation was observed in a wide range of temperatures from 400 to 550 K, which is lower than the temperature of the corresponding reaction on rutile(110). More interestingly, we have observed formation of acetone from 2-propanol on our TiO₂/Au(111) surface at around 450 K; this reaction was not observed on rutile(110). The reactivity patterns of TiO₂/Au(111) show strong dependence on geometry and structure of the nanocrystals.

4:00pm SS+NS-TuA7 Structure, Chemical State, and Reactivity Investigations of Size- and Shape-Selected Nanocatalysts under Operando Conditions, B. Roldan Cuenya, University of Central Florida
INVITED

The rational design of the next-generation of catalysts requires detailed knowledge of the correlation between structure, chemical composition, and reactivity. Even though Pt and Pd are among the most industrially relevant and widely investigated nanocatalysts, their complex interaction with

common reactants such as oxygen still provides many challenges to the scientific community. In this work, the relation between the structure and reactivity of nanocatalysts "at work" was obtained via X-ray absorption fine-structure spectroscopy, X-ray photoelectron spectroscopy, and mass spectrometry. Homogeneous size- and shape-selected metal nanoparticles (NPs) have been synthesized by means of diblock copolymer encapsulation.

The influence of the nanoparticle *shape* on the reactivity of Pt nanocatalysts on γ -Al₂O₃ will be described. Nanoparticles with similar size distributions (~0.8-1 nm) but with different shapes were found to display distinct reactivities for the oxidation of 2-propanol. A correlation between the number of undercoordinated atoms at the NP surface and the onset reaction temperature was observed. Furthermore, platinum oxides were found to be the active species for the partial oxidation of 2-propanol, while the complete oxidation was catalyzed by oxygen-covered metallic Pt NPs.

The evolution of the structure and oxidation state of ZrO₂-supported Pd nanocatalysts during the *in situ* reduction of NO with H₂ will also be discussed. Prior to the onset of the reaction, NO-induced redispersion of the Pd NPs over the ZrO₂ support was observed, and Pd^{δ+} species detected. This process parallels the high production of N₂O observed at the onset of the reaction (>120°C), while at higher temperatures (\geq 150°C) the selectivity shifts toward N₂. Interestingly, concomitant with the onset of N₂ production, the Pd atoms re-aggregate into large metallic Pd NPs, which were found to constitute the active phase for the H₂-reduction of NO. The evolution of the oxidation state of Pd and Pt NPs during the oxidation of NO and the role of the NP size will also be presented.

Our findings highlight the decisive role of the nanoparticle structure and chemical state in catalytic reactions and the importance of *in situ* reactivity studies to unravel the microscopic processes governing catalytic reactivity.

4:40pm SS+NS-TuA9 Particle Size, Support and Alloying Effects in Electrocatalysis: Relationships with Heterogeneous Catalysis, B.E. Hayden, University of Southampton, UK
INVITED

High-Throughput Physical Vapour Deposition (HT-PVD) based on Molecular Beam Epitaxy methods¹ has been used to synthesize libraries of catalysts which have subsequently been screened for their electrochemical activity and stability. A screening method is briefly described² which has been applied to measurements on model supported metal nano-particle HT-PVD catalyst libraries.

Considerable effort has been made to find alternative supports for platinum based catalysts in order to improve the particle stability and improve the three-phase boundary in fuel cell applications. HT-PVD model catalyst methodology has been applied to the study of support and particle size effects in electrocatalysis.³ Experiments have demonstrated the potential for using a support such as titania to induce CO oxidation electro-catalytic activity in gold particles,⁴ with an optimum particle size observed at ca. 3nm (Figure). No induced activity is observed for carbon supports. The similarities with the low temperature oxidations exhibited by supported Au in heterogeneous catalytic are highlighted. Extending this methodology to supported platinum based catalysts, the effect of particle size is demonstrated in the reduction of oxygen for the model carbon supported platinum catalysts, highlighting the limitations of catalyst dispersion. Supporting platinum on titania can result in a strong poisoning of the oxygen reduction catalysis.⁵

The combination of ab-initio theory and electrocatalyst screening also provides a powerful combination in the search for precious metal alloy and non noble metal alloy catalysts. Examples are given for anode hydrogen oxidation (HOR) catalysts such as Pd based,⁶ and tungsten copper⁷ alloys.

References

1. S. Guerin and B. E. Hayden; J. Comb. Chem. 8 (2006) 66-73.
2. S. Guerin, B.E. Hayden, et al.; J. Comb. Chem. 6 (2004) 149 - 158.
3. S. Guerin, B.E. Hayden, D. Pletcher, et al.; J. Comb. Chem. 8 (2006) 791-798.
4. B.E. Hayden, D. Pletcher and J.-P. Suchsland; Angewandte Chemie Int. Ed. 46 (2007) 3530-3532.
5. B.E. Hayden, D. Pletcher, J.-P. Suchsland et al.; Phys. Chem. Chem. Phys. 11 (2009) 1564-1570. *ibid*: Phys. Chem. Chem. Phys., 2009, 11, 9141-9148.
6. F. A. Al-Odail, A. Anastasopoulos, and B. E. Hayden; Phys. Chem. Chem. Phys. 12 (2010) 11398-11406. *ibid*; Topics in Catalysis 54 (2011) 77-82.
7. A. Anastasopoulos, J. Blake, John and B.E. Hayden; J. Phys. Chem. C, 115 (2011) 19226-19230.

5:20pm **SS+NS-TuA11 The Growth and Structures of Metal Nanoparticles on Ordered ZrO₂(111) Surfaces**, *Y. Han, S.W. Hu, Y.H. Pan, J.B. Hou, H.B. Pan, J.F. Zhu*, University of Science and Technology of China

Metal nanoparticles supported on zirconia have attracted much attention in recent years owing to their variety of technological applications such as heterogeneous catalysis and gas sensor operation. In particular, as catalysts, the interface properties of metal/ZrO₂ referring to the morphology, charge transfer, thermal stability and reactivity play crucial roles in determining their real applications. In this presentation, we report our recent studies on the growth, electronic structures and thermal stabilities of metal nanoparticles (Cu, Ag and Au) on well-defined ZrO₂ thin films by synchrotron radiation photoemission spectroscopy (SRPES) together with scanning tunneling microscopy (STM) and low electron energy diffraction (LEED). The well-defined ZrO₂(111) oxide thin films were epitaxially grown on Pt(111). It was found that the growth behavior of metals on ZrO₂(111) strongly depends on the morphologies of oxide surfaces and the interfacial interactions between the metal deposits and the ZrO₂(111) films. The binding energies of all three metal core-level peaks shift monotonically toward higher binding energy with decreasing the metal particle sizes. The contributions of initial and final state effects to the core level binding energy shifts are differentiated using the Auger parameters. At very low coverages, most likely Au forms Au⁺, while Ag remains the metallic state and Cu forms Cu⁺ on ZrO₂(111).

5:40pm **SS+NS-TuA12 Structure and Electronic Properties of Ni Nanoparticles Supported on Reducible CeO₂(111) Thin Films**, *Y.H. Zhou*, Xiamen University, Republic of China, *J. Zhou*, University of Wyoming

Ceria-supported Ni nanoparticles have been of great interest as ethanol and methane reforming catalysts for hydrogen production in fuel cell applications. Recent studies have indicated that the catalytic reactivity of these ceria-supported Ni nanoparticles can be influenced by the redox properties of ceria as well as the synergistic effect between the two. To elucidate the nature of their activity, we studied Ni particles deposited on fully oxidized CeO₂(111) and reduced CeO_{1.88}(111) thin films using scanning tunneling microscopy and x-ray photoelectron spectroscopy at the fundamental level. Ceria thin films were grown in situ on Ru(0001) under ultrahigh vacuum conditions. Ni was vapor-deposited onto ceria thin films. At 300 K, metallic Ni is the only species present on the reduced ceria. However, a small amount of Ni is oxidized to Ni²⁺ on CeO₂. Oxidation of Ni on CeO₂ can be facilitated by annealing as well as by depositing Ni at 500 K. Scanning tunneling microscopy studies show that Ni forms two-dimensional particles on ceria at room temperature, which suggests a strong Ni-ceria interaction. The particles can agglomerate into large three-dimensional structures with further heating. The structure and electronic properties of Ni metal particles on ceria were further compared to those of bimetallic Ni-Au and Ni-Rh particles.

Thin Film

Room: 10 - Session TF+AS-TuA

Modeling and Analysis of Thin Films

Moderator: D. Irving, North Carolina State University

2:00pm **TF+AS-TuA1 Nanoconfined Fluids: Fundamentals and Application to Ionic-Liquid-Based Supercapacitors**, *G. Feng, S. Li, P.T. Cummings*, Vanderbilt University **INVITED**

Phase transitions in nanoconfined fluids have been contentious for two decades. In the 1980s and early 1990s a large number of surface force apparatus (SFA) experiments on a variety of ultrathin nonpolar liquid films (e.g., such as dodecane, cyclohexane and octamethylcyclotetrasiloxane (OMCTS)), reached a common conclusion: When their confinement between molecularly smooth mica sheets reached the order of several molecular diameters (approximately 3 or less, depending on the fluid being studied) they exhibited behavior typical of the stick-slip response of a crystalline solid structure.

In contrast to the solid-like behavior under extreme nanoconfinement, when the mica surface separation is sufficiently large, the confined fluid exhibits bulk-like liquid behavior. Thus, a phase transition as a function of separation must exist. In this talk, we review the two-decade-old debate on the nature of this phase transition (first order vs continuous), and its effective resolution using very high fidelity molecular dynamics simulations. In particular, the origin of the phase transition from fluid to solid-like behavior is, unexpectedly, driven by electrostatic interactions

between ions in mica and partial charges on the atoms in the nonpolar organic molecules.

More recently, our interest in nanoconfined fluids has focused on novel energy storage devices: electrical double layer (EDL) capacitors, also called supercapacitors. Supercapacitors have attracted considerable attention, owing to their desirable properties, such as high power density, high capacitance, and excellent durability. As emerging electrolytes for these supercapacitors, room-temperature ionic liquids (RTILs) have attracted considerable attention due to their wide electrochemical windows, excellent thermal stability, non-volatility, relatively inert nature, and high ionic conductivity. With high specific surface area and electrical conductivity, nanoporous carbon-based materials are the most widely used electrodes for supercapacitors, including activated carbons, templated and carbide-derived carbons (CDC). Using molecular simulations, model porous carbon electrodes (e.g., CDC), supercapacitors composed of slit-shaped micropores ranging in size from 0.67 nm to 1.8 nm in an IL were studied to investigate the dependence of capacitance on pore size. The capacitance was found to show an oscillatory behavior with pore size. In good agreement with experiment, we find that, as the pore shrinks from 1.0 nm to 0.7 nm, the capacitance of the micropore increases anomalously. The persistence of oscillations in capacitance beyond 1.0 nm is a new theoretical prediction currently being probed experimentally.

2:40pm **TF+AS-TuA3 XPS Analysis of Monomolecular Films Prepared by Self-Assembly and Langmuir-Blodgett Techniques**, *G.G. Jernigan, F.K. Perkins, M.G. Ancona, A.W. Snow*, Naval Research Laboratory

Characterization of self-assembled monolayers (SAMs) using x-ray photoelectron spectroscopy (XPS) measurements of the gold (4f) attenuation from increasing molecular length alkane thiols were pioneered by Bain and Whitesides[1]. Since then, the gold attenuation has been used by many others as a method for determining the length/thickness of molecular films formed as SAMs on gold. We have done similarly with carboxylic acid (COOH) terminated alkane thiols SAMs deposited on gold with the aid of additives[2], and we obtained similar results. We discovered, however, that the attenuation of the sulfur (2p) signal did not correspond with the gold attenuation. Additionally, neither the gold or sulfur attenuation could correctly account for the observed carbon (1s) signal in the XPS measurements. This fact was originally noted, but not addressed, by Bain and Whitesides.

In conjunction with experiments, we will present our successful solution to the modeling of XPS measurements of molecular films prepared by self-assembly and by the Langmuir-Blodgett (LB) technique. In a classic alkanethiol SAM, one third of the surface gold atoms, typically, are bound to a thiol-terminated molecule, due to the steric effect of a radial shell created by the molecule. Thus, the gold signal is only partially attenuated by the molecule. Use of the attenuation of the sulfur signal associated with the S-Au bond (obtained by fitting the XPS signal), we find that we are able to correctly determine the electron escape depth (λ) for sulfur and carbon through the molecular film. Using a poly(thiomethyl methacrylate) thin film as a carbon and sulfur XPS standard combined with the correct λ , we developed a model for the packing density and molecular orientation of COOH terminated alkane thiols that is consistent with gold, sulfur, and carbon XPS measurements as a function of molecule length. We have expanded our model to include SAMs formed of sterically crowded tertiary thiols, where fewer molecules per gold atom can attach to the surface, and to LB films formed from carboxylic acid terminated alkanes on gold surfaces, where no sulfur linkage is made. The consistent interpretation provided by our model will be presented at the talk.

[1] C.D. Bain and G.M. Whitesides, *J. Phys. Chem.* **93**, 1670 (1989).

[2] A.W. Snow, G.G. Jernigan, and M.G. Ancona, *Analyt* **136**, 4935 (2011).

3:00pm **TF+AS-TuA4 The Dynamics of Atomic-Scale Transport on the Anisotropic Compound Surface TiN(001)**, *D.G. Sangiovanni, V. Chirita, L. Hultman*, Linköping University, Sweden, *I. Petrov, J.E. Greene*, University of Illinois at Urbana Champaign

We use classical molecular dynamics (MD) and the modified embedded atom method (MEAM) formalism to investigate the dynamics of atomic-scale transport on a low index anisotropic model compound, TiN(001). Our simulations, totaling 0.25 ms for each case study, follow the pathways and migration kinetics of Ti and N adatoms, as well as Ti_x complexes with x = 1, 2 and 3, all of which are known to contribute to the growth of TiN thin films by reactive deposition from Ti, N₂, and N precursors. The simulations

are carried out at 1000 K, a reasonable temperature for TiN(001) epitaxial growth. We find Ti adatoms to be the highest mobility species on TiN(001), with the primary migration path involving jumps of one nearest-neighbor distance d_{NN} between four-fold hollow sites along in-plane $\langle 100 \rangle$ channels. Long jumps, $2d_{NN}$, are also observed, but at much lower frequency. N adatoms exhibit much lower migration rates than Ti, diffuse only along in-plane $\langle 110 \rangle$ directions, and are unstable to associative formation of N_2 molecules which desorb at kinetic rates. As expected, TiN and TiN_3 complexes migrate at even lower rates with complex diffusion pathways involving rotations, translations, and roto-translations. TiN_2 trimers, however, are shown to have surprisingly high diffusion rates, comparable to that of Ti adatoms, due to, as revealed in our density functional theory (DFT) investigations, the significantly more symmetric charge transfer between trimer and terrace atoms, as compared with the charge distributions observed for dimers and tetramers.

4:00pm **TF+AS-TuA7 Multi-Method Calculations of the Thermodynamics of Film Deposition on Fuel Rods in Light Water Reactors**, *D.W. Brenner, A.D. Dongare, C.J. O'Brien*, North Carolina State University **INVITED**

Corrosion products in light water reactors are driven to deposit on the fuel rods, which reduces their efficiency and lifetime. The thermodynamics and kinetics that lead to this deposition are notoriously difficult to characterize *in situ* experimentally due to the extreme conditions of temperature and radiation within the reactor, and the relationship of deposits studied *ex situ* to processes under reactor conditions is unclear. It is thought that deposition is related to bubbles that form at the surface of the fuel rods due to sub-cooled boiling, but further details are lacking. We have been using first principles methods combined with molecular modeling to understand the thermodynamic driving force for this deposition, including how pH, pressure, temperature, and aqueous versus semi-aqueous “bubble” environments affects this driving force. The results of these calculations, which include studies of solvated ions, clusters and solid surfaces containing Ni, Fe, O, B, C and H will be presented along with ideas for suppressing deposition based on these results. The broader implications of our calculations for understanding and controlling film deposition in various types of aqueous environments will also be discussed.

This research is supported by the Department of Energy

4:40pm **TF+AS-TuA9 Toughness Enhancement in Transition Metal Nitride Thin Films by Alloying and Valence Electron Concentration Tuning**, *D.G. Sangiovanni, V. Chirita, L. Hultman*, Linköping University, Sweden

Enhanced toughness in hard and superhard thin films is a primary requirement for present day ceramic hard coatings, known to be prone to brittle failure during *in-use* conditions, in modern applications. Based on the successful approach and results obtained for TiN- and VN-based ternary thin films [1,2], we expand our Density Functional Theory (DFT) investigations to TiAlN-based quaternary thin films. $(TiAl)_{1-x}MxN$ thin films in the B1 structure, with $0.06 \leq x \leq 0.75$, are obtained by alloying with $M = V, Nb, Ta, Mo$ and W , and results show significant ductility enhancements, hence increased toughness, in these compounds [3]. Importantly, these thin films are also predicted to be hard/superhard, with hardness values comparable to TiAlN. For $(TiAl)_{1-x}WxN$ these results have been experimentally confirmed [4]. The general, electronic mechanism responsible for the ductility increase is rooted in the enhanced occupancy of d-t_{2g} metallic states, induced by the valence electrons of substitutional elements (V, Nb, Ta, Mo, W). This effect is more pronounced with increasing valence electron concentration (VEC), and, upon shearing, leads to the formation of a layered electronic structure, consisting of alternating layers of high and low charge density in the metallic sublattice. This unique electronic structure allows a selective response to tetragonal and trigonal deformation: if compressive/tensile stresses are applied, the structure responds in a “hard” manner by resisting deformation, while upon the application of shear stresses, the layered electronic arrangement is formed, bonding is changed accordingly, and the structure responds in a “ductile/tough” manner, as dislocation glide along the $\{110\}\langle -10 \rangle$ slip system becomes energetically favored [2]. The findings presented herein open new avenues for the synthesis of hard, yet tough, ceramic coatings, by tuning the VEC of alloying elements to optimize the hardness/toughness ratio in relevant applications.

[1] D. G. Sangiovanni et. al. Phys. Rev. B **81** (2010) 104107.

[2] D. G. Sangiovanni et. al. Acta Mater. **59** (2011) 2121.

[3] D.G Sangiovanni et. al. Thin Solid Films **520** (2012) 4080.

[4] T. Reeswinkel et. al. Surf. Coat. Technol. **205** (2011) 4821.

5:00pm **TF+AS-TuA10 Non-Destructive Element Specific Density Depth Profiling by Resonant Soft X-ray Reflectometry**, *S. Macke*, Max Planck - UBC Centre for Quantum Materials, Canada, *A. Radi*, University of British Columbia, Canada, *R. Sutarto*, Canadian Light Source, Canada, *G. Christiani*, *G. Logvenov*, Max-Planck-Institute for Solid State Research, Germany, *G. Sawatzky*, University of British Columbia, Canada, *B. Keimer*, Max-Planck-Institute for Solid State Research, Germany, *V. Hinkov*, Max Planck - UBC Centre for Quantum Materials, Canada

X-ray resonant reflectometry (XRR) is the ideal tool to study the depth resolved and element-specific electronic structure of multilayer films. Besides the structural parameters of thin films like thicknesses and roughnesses one is sensitive to the dielectric tensor of the film which allows to retrieve depth profiles of the magnetic, orbital[1] and valence configuration.

Due to the complex physics of reflectometry this measurement method needs sophisticated tools to analyze the results quantitatively [2]. The issues arising with this method are addressed and discussed.

By changing angle, energy and polarization of the incoming beam complete reflectivity maps can be measured leading in principle to an accurate picture of the depth resolved electronic states of thin films. The standard model used in reflectometry is based on compound layers with a defined thickness, roughness and dielectric tensor. But such a simple model is usually not capable to reproduce a full measured reflectivity map. The main reasons are especially contaminations, additional oxide layers and interdiffusion between layers.

However, introducing a layer system based on the element specific atomic density and scattering factors instead of dielectrics tensors allows more degrees of freedom for the system and allows to reproduce the reflectivity maps. Thereby the advanced model is capable to retrieve the element specific density profiles of thin films.

The method is introduced by analyzing a simple film of PrNiO₃ grown on an LSAT substrate. The reflectivity map is measured from 500eV to 1100eV.

[1] E. Benckiser et. al., Nature Materials **10**, 189 (2011)

[2] ReMagX, www.simulationcorner.net/ReMagX/

5:20pm **TF+AS-TuA11 Monte Carlo Radiation Model for Heat Transfer of Lamp for Advanced Thermal Annealing Process**, *K. Bera*, *J. Ranish*, *U. Kelkar*, Applied Materials, Inc.

Advanced thermal annealing process of semiconductor wafer uses lamp heating, specially for rapid thermal oxidation, silicidation, ion-implant anneal and spike anneal. As the technology node shrinks and the wafer size increases, wafer temperature uniformity becomes significant. The thermal modeling challenge includes complexity of the lamp filament and chamber configuration, and complex optical properties of semitransparent media. In order to analyze lamp heating, two-dimensional Monte-Carlo based radiation, and thermal conduction model for a single lamp is built using CFD-ACE+. The Tungsten lamp filament is immersed in Nitrogen. The single lamp is enclosed by a reflector, and protected at the top by a quartz plate. For the single lamp thermal model, effective surface area and volume of the coil are considered. The irradiance profile of the lamp at a distance of a few cm from the quartz plate compared well with the experimental data. The single lamp model is simplified using a cylindrical filament structure that matches the irradiance profile. The cylindrical filament structure is used in 3D chamber model that considers thermal convection in addition to radiation and conduction. In both single lamp and chamber models, for semi-transparent non-gray media, wavelength dependent real and imaginary parts of refractive indices are used in optical database to calculate thermal absorption. For gray material, surface emissivity of the material is defined. For reflective material, the degree of specularly on the surface is defined as well. For gas conduction, temperature dependent thermal properties are used. The single lamp power is varied by several hundreds of Watts. The irradiance profile shows a peak at the center that decays substantially as we move radially outwards. The effect of quartz plate thickness on irradiance profile is evaluated. The chamber model is used to determine wafer temperature distribution and transient thermal response for a range of lamp assembly power.

5:40pm **TF+AS-TuA12 First Principles Studies of Oxygen Transfer at Buried Metal/Metal Oxide Interfaces**, *C. Goldstein*, *E. Mily*, *J.-P. Maria*, *D.W. Brenner*, *D. Irving*, North Carolina State University

Heterogeneous material interfaces between metals and metal-oxides provide a unique opportunity to create active functional materials. The functionality of these heterostructures can hinge either on limiting or enabling oxygen transfer across the interface. For example, there has been recent research on how to use thin film metal/metal-oxide super-structures to control the power output generated by the exothermic exchange of oxygen across the as-deposited interface. In all of these heterogeneous systems, it is imperative to

fundamentally understand the mechanisms that facilitate oxygen exchange, as the dynamics are not currently well understood. In the work presented here, chemically accurate Density Functional Theory calculations have been used to predictively determine likely reaction pathways for oxygen transport in energetic nanocomposite materials and to characterize the stability of novel heterogeneous material interfaces. Our ultimate goal is to tune power output through an understanding of the mechanisms of oxygen transport across heterogeneous interfaces and within the super-structure. Several systems have been investigated, including more traditional thermite materials such as Al and Ti paired with Cu_2O . In these systems, the energy release is large, but there is also a high degree of strain when ideal systems are modeled. Other model systems were chosen based on structural similarity, minimal lattice mismatch, and the degree of exothermicity associated with oxygen transfer. Results on these systems will also be presented. Preliminary calculations simulate systems at various early stages to isolate factors that could influence the reaction, such as strain or initial barrier height. The results presented here show qualitative agreement between calculations and experimental observations. This project has been supported by the Army Research Office through grant # W911NF-10-1-0069 and the NSF Graduate Research Fellowship Grant # DGE0750733.

Thin Film

Room: 11 - Session TF2-TuA

ALD for Hybrid Films and Bioapplications

Moderator: S.M. Rosnagel, IBM T.J. Watson Research Center

2:00pm **TF2-TuA1 Characteristics of Nanomaterials Embedded in Atomic Layer Deposition Thin Films**, *J.S. Jur, P.J. Krommenhoek, J.C. Halbur*, North Carolina State University, *H.O. Everitt*, Duke University, *J.B. Tracy, G.N. Parsons*, North Carolina State University

Atomic layer deposition (ALD) is demonstrated as a method to fabricate NP embedded thin films, and provides new opportunities to alter the characteristic properties of nanomaterials. This work examines conducting and semiconducting ALD materials growth on nanoparticles and nanowires for opportunities to alter the optical behavior and conductive behaviors of nano-enabled materials. For example, gold nanoparticles (15 nm diameter) are embedded into dense inorganic zinc oxide nanofilms deposited by atomic layer deposition onto a fibrous textile template. By changing the dielectric field surrounding the nanoparticle with the ALD ZnO, the surface plasmon resonance is dampened, resulting in significant changes to the optical absorption behavior of the textile. The alteration of the surface plasmon resonance is examined with increasing nanoparticles concentration on the fiber surface and with increasing ALD coating thickness. For example, the absorption at 900 nm is enhanced by up to 4.8x for a 45 nm ZnO ALD coating. Minimal increase in absorption is observed with additional ZnO growth. Cathodoluminescence evaluation of ZnO ALD on Au nanoparticles -loaded nylon-6 produces a ~65% decrease in the defect luminescence and a corresponding ~80% increase in the band edge luminescence. In addition, an analysis of the electrical properties of nanoparticle and nanowire embedded ALD thin films are provided. Using externally fabricated nanomaterials and embedding them in ALD thin films offers the ability to study and understand near surface interactions that can alter the characteristics of the nanomaterials.

2:20pm **TF2-TuA2 ALD-Based Fabrication and Chromatographic Separations on Binder-Free, Carbon Nanotube-Templated Thin Layer Chromatography Plates**, *M.R. Linford, R.C. Davis, D.S. Jensen, S. Kanyal*, Brigham Young University, *M.A. Vail, A.E. Dadson*, Diamond Analytics

We recently reported the use of patterned carbon nanotube (CNT) forests as scaffolds for the microfabrication of silica-based thin-layer chromatography plates (TLC) (*Advanced Functional Materials* 2011, 21(6), 1132 – 1139). In this fabrication, CNTs were infiltrated by low pressure chemical vapor deposition of silicon using SiH_4 , which was then oxidized and hydrated. Thorough characterization by RBS, XPS, TEM, SEM, and ToF-SIMS has been performed on these materials, which has given us a considerable understanding of them, e.g., the structure of the $\text{Si/SiO}_2/\text{Al}_2\text{O}_3$ (30 nm)/Fe(6 nm) stack deposited prior to CNT growth has been confirmed, multiwall CNTs are grown in our process, CNT growth is base (bottom up) and not tip (top down), the thickness of the Fe catalyst layer plays a key role in the fabrication of our plates – when the catalyst layer is too thick CNT structures are unstable, etc. Fast and efficient separations were demonstrated on these plates.

Nevertheless, the oxidation of silicon in these materials leads to a volume expansion of the support, which appears to affect the A-term of the van

Deemter equation in our separations. That is, distortions in the material appear to adversely affect separations performed on them. Accordingly, we have now shown that TLC plates can be fabricated by (i) priming patterned nanotube forests with a few nanometers of amorphous carbon, followed by a layer of Al_2O_3 deposited by atomic layer deposition (ALD), (ii) deposition of SiO_2 in a fast (pseudo) ALD of this material, and (iii) oxidizing at a lower temperature (ca. 600 K) than was used previously to remove the CNTs. An amino bonded phase was created. The resulting TLC plates show 125,000 – 225,000 N/m in a baseline separation of four fluorescent dyes. An even more recent and newly developed microfabrication method in our laboratory of CNT-templated TLC plates also shows fast separations with 400,000 – 500,000 N/m in preliminary results. These separations rival (or exceed) those of HPLC/UPLC in both speed and efficiency. Separations of biological interest will be shown.

4:00pm **TF2-TuA7 Conductivity and Mechanical Stretching of Conductive ALD Coatings on Nonwoven Fiber Mats**, *W.J. Sweet, C.J. Oldham, G.N. Parsons*, North Carolina State University

Advanced sensing, responsive and protective electronic systems integrated with fibers and flexible textile media may lead to new solutions for functional device deployment and integration. A challenging aspect of conductive coatings on fibers is the observation that most good conductors, including doped metal oxides or metallic films, are not readily flexible when coated in thin film form onto polymer fibers. For this work, we use atomic layer deposition (ALD) to produce conformal coatings of conductive ZnO, Al:ZnO and others on complex nonwoven polypropylene and nylon fibers. We measured conductivity of the as-formed coated fibers as a function of deposition temperature and other process parameters. We also measured the mechanical response of the coated and uncoated fiber mats, including measuring the change in conductivity upon fiber mat stretching. We find that in all materials measured to date, the conductivity of the fiber mat decreases with increasing applied tensile stress. For example, for Al-doped ZnO on nylon deposited at 115°C, we obtained fiber mats with conductivity of 33 S/cm, and after a 10% strain, the conductivity drops to ~3.3 S/cm. Generally, the largest conductivity decrease occurs for the materials that are most conductive to start. However, results indicate a correlation between some process parameters, such as deposition temperature, and conductivity resiliency, showing possible directions to attain highly flexible and reliable conductive material integration. In this presentation we will summarize our results regarding mechanical resiliency and conductivity and identify key parameters needed to achieve stretchable fibers that are also highly conductive.

4:20pm **TF2-TuA8 Molecular Layer Deposition of Alucones and Zincones Using Hydroquinone**, *Y. Lee, S.M. George*, University of Colorado, Boulder

Alucones and zircones are metal alkoxide polymer films that can be grown using molecular layer deposition (MLD) techniques. In this study, alucones and zircones were grown using trimethylaluminum (TMA) and diethylzinc (DEZ) as the metal precursors and hydroquinone (HQ) as the organic reactant. HQ is an aromatic diol that has a rigid structure with a central benzene ring. The benzene ring may lead to interesting electrical conductivity and the rigid structure may help to avoid “double reactions”. Quartz crystal microbalance measurements and X-ray reflectivity (XRR) studies were employed to examine film growth. Individual mass gains after the TMA and HQ exposures were consistent with a TMA:HQ stoichiometry of 4:3 in the MLD film. This TMA:HQ stoichiometry suggests the presence of Al_2O_2 dimeric core species. In comparison, individual mass gains after the DEZ and HQ exposures were consistent with a DEZ:HQ stoichiometry of 1:1 in the MLD film. XRR studies measured growth rates at 150°C of 2.6 Å/cycle for TMA/HQ and 2.7 Å/cycle for DEZ/HQ. The alucone and zircon MLD films were also annealed in air at temperatures up to 350°C. There is evidence that the benzene rings polymerize after heating to 200°C. The films turn brown and a strong absorbance observed at ~320 nm is consistent with an expanded π -conjugated system. The polymerization of the benzene rings should change the mechanical properties of these annealed MLD films. Alucone and zircon films were also grown using tetrafluorohydroquinone to observe the effect of fluorination of the benzene ring.

4:40pm **TF2-TuA9 Organic-Inorganic Hybrid Thin Films Prepared by Ozone Assisted Molecular Layer Deposition (MLD)**, *J. Huang, M. Lee, A.T. Lucero, J. Kim*, The University of Texas at Dallas

Recently, organic thin films have been attracting attentions due to their flexibility and transparency which are suitable for large-scale display and flexible electronics applications. Alternatively, inorganic thin films have several benefits over organic thin films such as high functionality (e.g. high conductance, high dielectric constant or high polarization, etc). Potentially, organic-inorganic hybridization can widen the range of their applications, for both worlds, with new functionalities. A novel technique has been

reported using a modified atomic layer deposition (ALD) method, named molecular layer deposition (MLD), which can be applied to build an organic and inorganic hybrid stack. Hybrid thin films by MLD minimized the formation of defects during the growth of the organic and inorganic layers because they are deposited by sequential, self-limiting surface reactions similar to ALD process.

In this study, we investigated the growth characteristics of organic-inorganic laminates. We focused on 7-octenytrichlorosilane (7-OTS) and metal-oxide hybrid thin film, using ozone based MLD. 7-OTS is deposited by an exchanging reaction between functional group and water. The terminal vinyl group (C=C) of 7-OTS is converted into a carboxylic group (-COOH) through in-situ ozone (O₃) modification. Metal oxide is then deposited as a linker layer in-between of each OTS layers using conventional ALD precursors, such as diethyl zinc (DEZ) and water. We found out that MLD process is kinetically control, which mean for a very limited of time, if we need organic molecules to form chemical bonding on top of certain surface, some special process would be required. In our experiment, we used repeating pulse to get a good coverage of organic molecules. Besides, effect of depositing temperature, dosing time, even in-situ UV activation with variety of time, location and power will also be discussed.

Characterization of organic-inorganic hybrid thin films have been extensively investigated using transmission electron microscopy (TEM), scanning electron microscopy (SEM), atomic force microscopy (AFM), X-ray diffraction (XRD), X-ray photoelectron spectroscopy (XPS) and Fourier transform infrared spectroscopy (FTIR). Electrical characteristics of the hybrid films will also be reported.

This research is partially funded through Korea-US collaboration R/D program by MKE-COSAR-KETI.

5:00pm TF2-TuA10 Organic-Inorganic Hybrid Structure Formation via Sequential Vapor Infiltration, *H. Akyildiz, M. Yokus, R.P. Padbury, J.S. Jur*, North Carolina State University

Hybrid film formation onto polymer surfaces during atomic layer deposition (ALD) has inspired a number of processing schemes that promote precursor infiltration to increase the extent of hybrid reaction. These hybrid materials have shown opportunity in mechanical, electronic, biomedical and catalytic applications. In this work we utilize a sequential vapor infiltration (SVI) process, defined by subsets of consecutive precursor exposures, to understand the minimum precursor exposure required to saturate the formation of the hybrid material. As a test system, we examine consecutive exposures of trimethylaluminum followed by a H₂O exposure onto polyamide 6 (PA6). We investigate the effect of temperature, pressure, and exposure time on the mass change of high surface area PA6 fabrics (3 m²/g). A saturation in the mass increases is reached after ~10 TMA (0.2 sec dose, 30 sec hold) exposure cycles, resulting in a ~14 wt% increase at 30 °C and 1.5 wt% increase at 150 °C. Cross-sectional transmission electron microscopy shows a conformal surface modification of ~75 nm at 60 °C. The influence of water resident in the PA6 is examined by conducting a 120 °C *in situ* anneal prior to SVI processing, which results in a decreased of ~4 wt % at lower exposure temperatures. Still, the total mass increase is inversely proportional to temperature. A reaction-diffusion mechanism for the precursor penetration is proposed that considers a decrease in diffusion with an increased extent of reaction near the outer surface of the fiber. Application of these hybrid modifications to the mechanical and dielectric properties of the fabric is explored.

Tribology Focus Topic

Room: 19 - Session TR-TuA

Molecular Origins of Friction and Wear

Moderator: S.S. Perry, University of Florida

2:00pm TR-TuA1 Area, Stiffness, Friction and Adhesion of Contacts Between Rough Surfaces, *M.O. Robbins, L. Pastewka, T. Sharp*, Johns Hopkins University

INVITED

Many surfaces have roughness on a wide range of length scales that can be described by self-affine fractal scaling. This roughness has profound effects on contact and friction between experimental surfaces. The talk will present results for the load dependence of contact area, contact stiffness and friction for nonadhesive and adhesive surfaces with a self-affine fractal geometry. Simulations retain atomic structure for a few layers of atoms near the surface and use a Greens function method for an elastic continuum to determine the long-range elastic response. Under a broad range of conditions the area of intimate contact A_c between nonadhesive surfaces and the normal stiffness k_N are both proportional to the applied load. These

quantities are relatively insensitive to the atomic scale structure of surfaces, and even local plasticity. In contrast, atomic structure changes friction and tangential stiffness by orders of magnitude. For weak adhesion and strong roughness the linear relation between area, stiffness and load is retained, but the ratio of area to load increases. A simple scaling law predicts the change in ratio and why putty or tape sticks to walls but stiffer solids do not.

2:40pm TR-TuA3 Crystallographic Wear Patterns in Ionic Solids, *B.A. Krick, K.R. Marchman, S.B. Sinnott, W.G. Sawyer*, University of Florida

Ionic solids have simple and well known crystalline structures while spanning several orders of magnitude in wear rates; this makes them excellent candidates for fundamental studies in wear. Wear experiments on the (001) surface of rock-salts, including NaCl and MgO, revealed that the material wear rates have significant dependency on crystallographic wear direction. The materials experienced maximum wear when sliding in the <100> family of directions and minimum wear when sliding in the <110>. For MgO the wear rate in the <100> direction was approximately three times that in the <110> direction. Wear experiments were performed at angles relative to the [100] direction in six degree increments revealing wear as a sinusoidal function of direction with 90 degree periodicity. These results offer a direct link between material structure and the wear properties of a material.

3:00pm TR-TuA4 Measurements of Off-axis Friction Forces, *K. Kristiansen, X. Banquy*, University of California, Santa Barbara, *H. Zeng*, University of Alberta, Canada, *E. Charrault, S. Giasson*, Universite de Montreal, Canada, *J.N. Israelachvili*, University of California, Santa Barbara

Current measurements of frictional forces are usually done parallel to the sliding direction. However, when the distances between the moving surfaces and the dimensions of the lubricant approach the nanometer scale, the molecular structure and surface asperities can induce significant frictional forces that are not parallel to the sliding direction. We have developed a new sensor-actuator for the Surface Forces Apparatus which can measure forces and move two surfaces relative to each other in all 3 orthogonal directions with force resolution in the μ N range, and distance control in nm range in the normal direction and μ m range in the plane of the surfaces. I will present how "off-axis" (anisotropic) friction forces behave when shearing two atomically smooth crystalline (lattice) surfaces separated by nanometer thick layers of hexadecane. These anisotropic friction forces can induce complex transient and steady-state motions involving displacements perpendicular to the applied force and non-zero velocity at all stages of back-and-forth sliding.

4:00pm TR-TuA7 Temperature-dependent Atomic-scale Friction and Wear on NaCl(001), *X. Zhao, S.S. Perry*, University of Florida

Atomic-scale friction and wear were investigated by scanning a Si₃N₄ tip on NaCl(001) with variable temperature atomic force microscopy. In the absence of wear, an exponential increase in friction with decreasing temperature was observed. Atomic scale wear was detected through the formation of surface pits with a single atomic layer deep. From quantitative measurements of atomic displacement, microscopic wear coefficients were found to agree with known macroscopic wear properties of this ionic material. Both friction and wear exhibit a thermally activated behavior with different activation energies corresponding to the different energy dissipation processes. The thermal activation energy for friction and wear is ~ 0.12 eV and 0.82 eV, respectively, with wear obviously requiring more energy than friction.

4:40pm TR-TuA9 Ultra-Low Wear Nanocomposites: How Low Can We Go?, *A.A. Pitenis, B.A. Krick, J.J. Ewin, W.G. Sawyer*, University of Florida

Polytetrafluoroethylene (PTFE) is an excellent candidate material for solid lubrication applications due to its low friction coefficient and chemical inertness; however, its use is limited due to its high wear rate. Unfilled PTFE is known to suffer from subsurface crack propagation and subsequent delamination during sliding. To combat this high wear mode, fillers of various sizes have been added to a PTFE matrix to increase the wear resistance by typically one or two orders of magnitude by fracture toughening and load support mechanisms. Nanocomposites are the state of the art in ultra-low wear performance in fluoropolymer systems; polymer blends have been shown to achieve nearly zero wear with wear rates below 1×10^{-8} mm³/Nm. These low wear rates are consistently accompanied by visually distinct tribofilms at the interface of the bulk material and counterface. Experiments suggest that a combination of mechanical and tribochemical mechanisms are responsible for the development of these tribofilms and consequent ultra-low wear behavior.

5:00pm **TR-TuA10 Direct Measurement of Friction Forces and Shear Strengths at High-Speed Microscopic Contacts using a Probe and Quartz Resonator.** *B.P. Borovsky*, St. Olaf College

We present a study of the frictional properties of microscopic contacts (radius $\sim 1 \mu\text{m}$) in the high-speed regime ($> 1 \text{ m/s}$). Energy dissipation and lateral stiffness of the contact are measured with a transverse-shear quartz resonator in contact with a spherical probe. A transition from partial to full slip is observed at a critical amplitude of motion. Elastic and dissipated forces (identified with static and kinetic friction) are quantified and interpreted without the need for complex calibration procedures or detailed models of the interaction. Kinetic friction is observed to be independent of sliding speed. Measurements of the lateral stiffness at very low oscillation amplitudes allow evaluation of the contact area. For an interface subject to boundary lubrication, we find that friction increases sub-linearly with applied load, in direct proportion to contact area. We determine the corresponding interfacial shear strengths. Results from the technique demonstrated here may find application in contexts where high sliding speeds are routinely accessed, such as microelectromechanical systems (MEMS) and simulations of friction using molecular dynamics.

5:20pm **TR-TuA11 Isolating the Adhesive Component of Micro-Scale Rolling Friction via Vapor-Phase Lubrication.** *S. Misra, B. Hanrahan, R. Ghodssi*, University of Maryland, College Park

Microball bearings have been successfully utilized in several micro-machinery applications, providing low friction, low wear contact, long lifetimes, and device robustness. On all size scales, rolling friction arises from a combination of volumetric mechanical properties, surface chemical properties, and bearing geometries. On the micro-scale, surface effects are enhanced relative to volume, and geometries are dictated by microfabrication techniques. Due to these unique factors, there is not a comprehensive understanding of the fundamental source of rolling friction in microscale systems, but adhesion is theorized to dominate. Vapor-phase lubrication has been implemented to change the chemistry of the surface, specifically addressing the adhesive component of micro-scale rolling friction, leading to reduced friction and enhancing the overall understanding of the system. Future microball bearing supported microsystems will benefit from the work presented here due to a greater knowledge of the influence of adhesion on micro-rolling friction.

A custom silicon micro-turbine supported on ball bearings serves as the platform for the study of rolling friction. 440C stainless steel microballs (285 micrometers diameter) are housed in deep reactive ion-etched silicon raceways. The tribological properties of this device have been the focus of numerous previous studies. The micro-turbine is operated such that normal load and turbine speed can be independently controlled for normal load-resolved spin-down friction testing. The spin-down testing methodology reveals the relationship between friction torque and normal load, which is used to understand the fundamental sources of rolling friction. Vapor saturation techniques have been integrated within the turbine actuation scheme by bubbling nitrogen gas through heated liquid and then using it to actuate and provide normal load for the micro-turbine. A condenser is employed before the output to assure no liquid condenses within the raceway.

A water vapor-lubricated micro-turbine has demonstrated a 43% reduction of friction versus dry nitrogen at a normal load of 50mN in spin-down testing as well as a 37% increase in overall turbine performance. Additionally, with the introduction of vapor, the relationship between friction torque and normal load was fundamentally changed, revealing the significant influence of adhesion to the system. Vapor lubrication adsorbed on the surface of the ball and raceway lowers their surface energies, reducing the effect of adhesion. These results show the first conclusive demonstration of the adhesive component to micro-scale rolling friction by using vapor phase lubrication.

5:40pm **TR-TuA12 Electronic Friction at the Atomic Scale: Conduction, Electrostatic and Magnetic Effects.** *J. Krim*, North Carolina State University, *I. Altfeder*, Wright Patterson Air Force Laboratory

We have performed a magnetic probe microscopy study of levitation and atomic-scale friction for Fe on YBCO ($T_c = 92.5\text{K}$) in the temperature range 65 - 293 K, to explore electronic contributions to friction at the atomic scale. The samples were prepared with oxygen-depleted surfaces, with thin semiconducting surface layers present atop the bulk. Below T_c , the friction coefficient was observed to be constant at 0.19 and exhibited no correlation with the strength of superconducting levitation forces observed below T_c . The friction coefficient exhibited a change in slope within experimental error of T_c that increased progressively above T_c and reached 0.33 by room temperature. The results were analyzed within the context of underlying atomic-scale electronic and phononic mechanisms that give rise to friction, and it is concluded that contact electrification and static electricity play a significant role above T_c . Quartz crystal microbalance

studies of sliding friction studies of molecularly thin films in the presence and absence of magnetic fields, were also performed for both paramagnetic oxygen and diamagnetic nitrogen films on substrates in various magnetic states.

[1] I. Altfeder and J. Krim, J. Appl. Phys. (2012), in press

Supported by NSF and AFOSR

Vacuum Technology

Room: 14 - Session VT-TuA

Accelerator and Ultra-Clean Vacuum Systems

Moderator: L. Smart, Brookhaven National Laboratory

2:00pm **VT-TuA1 Design of the Vacuum System for the SuperKEKB Positron Ring.** *Y. Suetsugu, K. Kanazawa, K. Shibata, T. Ishibashi, H. Hisamatsu, M. Shirai, S. Terui*, High Energy Accelerator Research Organization, Japan

INVITED

A two-ring electron-positron collider with asymmetric energies, the SuperKEKB, has been designed as an upgrade of the KEKB B-factory (KEKB). The SuperKEKB aims for a maximum luminosity of $8 \times 10^{35} \text{ cm}^{-2} \text{ s}^{-1}$, which is approximately 40 times larger than that of the KEKB. The upgrade of the vacuum system is a key factor that will allow the SuperKEKB to achieve unprecedented high performance. As for the positron ring, most of the beam pipes are newly designed to reduce beam impedance and, especially, to manage the electron cloud effect (ECE), which is essential to keep the low-emittance beam stable. The beam pipes basically have antechambers at the both sides of a beam channel. Various vacuum components adaptable to the antechamber scheme with low beam impedance and high thermal strength had been developed. The bellows chambers, for example, have a comb-type RF-shield with the same cross section to the beam pipe, and the main vacuum pump consisting of NEG strips is inserted into one of the antechambers. The antechamber scheme is also effective to mitigate the ECE, that is, it structurally suppresses the photoelectron effect. A side wall of the antechamber, where the synchrotron radiation hit directly, is roughened so as to reduce photon reflections. In order to reduce secondary electron effect, on the other hand, the inner surface of beam channel is coated with titanium nitride (TiN). Furthermore, the longitudinal grooved surface and the clearing electrode are prepared for the beam pipes in dipole magnets and the wiggler magnets in the ring, respectively. In addition, the beam pipes in drift spaces are wound by solenoid coils. These mitigation techniques are the fruits of various theoretical and experimental studies so far. The SuperKEKB positron ring is the first one that will adopt these techniques in a large scale. The design of vacuum system has been mostly completed, and the mass production of beam pipes has started. The vacuum system design and some key issues for SuperKEKB positron ring will be reported here together with the present status.

2:40pm **VT-TuA3 Status of the FRIB Driver Linac Vacuum Calculations.** *B. Durickovic, P. Gibson, P. Guetschow*, Michigan State University, *R. Kersevan*, CERN, Switzerland, *D. Leitner, M. Leitner, L. Lingy, F. Marti, G. Morgan, M. Schein, M. Shuphtar*, Michigan State University

The Facility for Rare Isotope Beams (FRIB) is a heavy ion fragmentation facility to produce rare isotopes far from stability for low energy nuclear science. The facility will utilize a high-intensity, superconducting heavy-ion driver linac to provide stable ion beams from protons to uranium at energies greater than 200 MeV/u and at a beam power of up to 400 kW. The beam will be fragmented on a multilayer high power fragmentation target and separated in a high resolution fragment separator.

Two ECR ion source injectors will provide highly charged ions for the superconducting linac for efficient acceleration. In order to transport the heavy ions at the low velocities of the injection beam the vacuum systems need to be carefully designed to avoid beam losses due to charge exchange. For uranium $33+$, for example (one of the commissioning beams), the cross-section for electron capture from the residual gas is so large at low energies ($\sim 12 \text{ keV/u}$ in LEBT) that a residual gas pressure of 10^{-6} Torr would lead to unacceptable beam losses in the analyzing magnet.

Similarly, in the warm section of the superconducting linac, beam losses due to interaction of the beam with residual gas need to be minimized in order to keep the average uncontrolled beam loss well below 1 W/m as required for maintainability of the accelerator and safety considerations.

These beam loss requirements, as well as the need for managing vacuum levels in high loss regions such as beam stripping and collimation areas, led to the establishment of minimum baseline vacuum requirements for all areas of the accelerator system. In addition, the SRF cavities must be

protected from contamination that could possibly migrate from the stripper region, collimator systems, or target systems.

CAD vacuum models of each area are made based upon the accelerator lattice file, and Monte Carlo simulations of vacuum levels are performed using MolFlow+ to help determine or validate the vacuum hardware configuration needed to meet the baseline requirements. This talk will describe the FRIB facility vacuum requirements, and report on the methods and status of the FRIB vacuum calculations.

This material is based upon work supported by the U.S. Department of Energy Office of Science under Cooperative Agreement DE-SC0000661

4:00pm VT-TuA7 Contamination Control and Cleaning Techniques for Ultra Clean Vacuum Systems, H.G.C. Werij, N.B. Koster, J.C.J. van der Donck, A.J. Storm, R. Verberk, R. Versluis, TNO Technical Sciences, The Netherlands

INVITED

Cleanliness requirements in high-tech science and industry are getting more and more challenging. At the same time, the consequence of not properly adhering to these requirements could be devastating. Whereas the general way of working involves prevention, inspection/monitoring and cleaning, each particular application requires its own dedicated systems approach. For instance, is it particulate or molecular contamination we have to deal with? Do we really need an ultrahigh vacuum or should it be ultraclean with respect to certain contaminants? And what is the trade-off between ultraclean production and in-situ cleaning? Such questions have to be answered in order to find the solutions that are both adequate and cost-effective at the same time.

In the presentation several examples will be addressed, including delicate space instrumentation, (extreme ultraviolet) lithography tools and equipment for fusion energy (ITER). We will present how contamination should be dealt with in the design phase, which not only involves choice of materials, but also geometrical layout and handling. We will show that for certain applications the traditional approach of using ultra-high vacuum might not yield the optimum result. By introducing low-pressure ultraclean gases combined with differential pumping both molecular and particulate contaminants can be mitigated very efficiently, as is demonstrated in numerous experiments.

As far as inspection and monitoring is concerned, we will give a brief overview of several sensing technologies, currently being developed at TNO. These consist of ionization sensors and optical sensors, the latter being integrated nanophotonics sensors, which may be used to detect molecular contaminants. For particle detection down to 50 nm diameter an automated particle scanner has been developed, which will be touched upon as well.

In the field of cleaning, apart from more traditional methods like wet, CO₂, and ultrasonic cleaning, we will address plasma cleaning technology developed in-house. We will show experimental results obtained using our shielded microwave induced remote plasma setup and hydrogen radicals.

4:40pm VT-TuA9 Large Thermal Vacuum Chamber for TB/TV Tests and Optical Calibration of Space Instrumentation, R. Versluis, R. Verberk, E.C. Fritz, W.L.M. Gielesen, TNO Science and Industry, The Netherlands

Part of the TNO Space activities is the development and qualification of Optical Instruments for Space Applications. Especially the Earth Viewing Spectrographs constitute a significant part of the calibrations. Before these instruments will be launched into orbit they undergo a series of qualification tests, which typically consist of:

Performance test (PF)

Vibration test (VB)

Thermal balance/thermal vacuum test (TB/TV)

Performance test (PF)

Optical Calibration (OC)

TNO is building a Thermal Vacuum Chamber (TVC) in one of the TNO cleanrooms that can perform all of these tests (except the vibration tests) on these instruments. In this talk we will present an overview of the design, engineering, manufacturing and qualification activities that are related to this thermal vacuum chamber. The TVC will have an internal free volume of about 72 m³. The complete internal surface area of 100 m² will be entirely covered with a cooling shroud with temperature control between 95 K and 373 K. The required shroud temperature stability is less than 1 K_{pp}, the required steady state spatial homogeneity better than 5 K_{pp}. In order to reach low pump down times and allow testing of space instruments with relatively high outgassing rates, the required pumping capacity is between 5000 and 10000 L/s. Furthermore, a very high level of cleanliness is required to protect the space instrument optical system and TVC viewports from contamination, which could decrease the optical transmission, especially in the UV wavelength range. Contamination prevention is

especially important because the complete calibration test can last as long as a few months, during which the system will be at vacuum and deposition of contamination can affect the optical throughput. The TVC will be equipped with a residual gas analyzer, cold finger and thermal quartz crystal microbalance to perform online and offline contamination monitoring and analysis.

For the Optical Calibration the Space instrument will be integrated in a cradle with two rotational degrees of freedom. With this the complete Field Of View of all optical ports of the instrument can be illuminated by optical stimuli placed outside the vacuum vessel.

The presentation will highlight specific issues related with this type of test facility, such as standard and emergency procedures for evacuating and venting the chamber during cryogenic operation. Product assurance issues such as contamination prevention of the test object and test object integrity. Minimising leak rates and outgassing of feedthroughs and stages, particle contamination prevention and other issues of the tests performed at high vacuum and low or high temperatures.

5:00pm VT-TuA10 A Large Seismic Attenuation System in UHV, R. Takahashi, National Astronomical Observatory of Japan, Y. Saito, High Energy Accelerator Research Organization, Japan

Interferometer gravitational wave detectors require an ultra-high vacuum chambers which the laser beams pass through. KAGRA, the large-scale cryogenic gravitational wave telescope in Kamioka, has two 3-km vacuum tubes kept in ~10-7Pa of vacuum pressure so as to reduce scattering-effects due to residual gas molecules.

The interferometers consist of high quality mirrors, which should be isolated from ground vibration strongly. The vibration isolation system needs not only attenuation more than 109 at 100Hz but also reduction of root mean square motion of the mirrors. Many kinds of mechanisms for isolation at low frequencies have been suggested for gravitational wave detectors. We employed an inverted pendulum and geometric anti-spring filters as the isolator in KAGRA. We found diamond-like carbon (DLC) coatings are suitable for reduction of scattered light around the mirrors. The coatings have low outgassing, low reflectivity, and low scattering loss.

5:20pm VT-TuA11 Vacuum System of Cornell Energy-Recovery LINAC Prototype Injector, Y. Li, X. Liu, K.W. Smolenski, I. Bazarov, B.M. Dunham, Cornell University

A prototype electron injector was designed, constructed and operated at CLASSE, as an important first step toward the Cornell ERL (Energy-Recovery LINAC) based synchrotron radiation facility. The injector is designed to generate average beam current up to 100-mA, and electron beam energy ranging 5-MeV to 15 MeV. Main features of the injector include a laser-driven photo-emission electron source, a cryo-module containing superconducting RF cavities, electron beam transport beamlines equipped with a suite of beam diagnostic instrument, and a 600-kW electron beam stop. Recently, significant milestones were reached for the prototype injector. Most noticeably, we have achieved an average beam current of 52-mA at a beam energy of 5-MeV from activated GaAs photo-cathodes, breaking a long-standing world record of 32-mA from a laser-driven photo-emission electron source. There are many challenges in vacuum system design for the prototype injector. It needs to provide an extremely-high vacuum (XHV) environment for the photo-cathodes, flexibilities in beam transport beamlines for development of beam instrumentation, as well as sufficient vacuum pumping capacity to handle very large dynamic gas-load at the beam stop. In the past 3+ years of operations, the injector vacuum system has performed satisfactorily. To confirm the pumping performance, we calculated pressure profile along the main transport beamlines during the high beam current runs, and calculated pressure profile agreed well with the measured pressure profile. In this paper, we describe the design and the operational experiences of the prototype injector vacuum system, and address remaining operational issues arising from high beam current operations.

5:40pm VT-TuA12 Injection Vacuum System at the TPS, C.K. Chan, C.C. Chang, C.L. Chen, C.S. Yang, C. Chen, Y.H. Liu, K.H. Hsu, Y.T. Huang, H.P. Hsueh, S.N. Hsu, G.Y. Hsiung, J.R. Chen, NSRRC, Taiwan, Republic of China

The Taiwan Photon Source (TPS) is a 3 GeV synchrotron facility and aimed to have a low emittance electron beam maintaining the top-up operation. A 12-m long TPS injection section contains four kicker ceramic chambers (K1-K4) and one out-of-vacuum injection septum to provide the stored beam a horizontal bump for beam injection off axis. The kickers (K2, K3) and injection septum are placed in an adjustable plate, which can provide a

5 mm displacement for the injected beam close to the stored beam so as to decrease the kicker strength. The construction of the injection section is completed and we will describe the design, manufacturing process and some test results for the injection section.

Applied Surface Science

Room: Central Hall - Session AS-TuP

Applied Surface Science Poster Session

AS-TuP1 Sub-Micrometer Imaging of Lipids and Trace Elements in Various Cells with ToF-SIMS and Laser-SNMS. *H.F. Arlinghaus, F. Draude, S. Galla, A. Pelster, M. Körsgen*, University of Muenster, Germany, *J. Tentschert, H. Jungnickel, A. Haase, A. Luch*, German Federal Institute of Risk Assessment, Germany, *T. Schwerdtle, J. Muthing*, University of Muenster, Germany

In recent years, molecular imaging with submicron lateral resolution has become of more and more interest for characterizing specialized compounds in biological samples. As an example, nanoparticles (NPs) gain great commercial interest in the medical field due to their high mobility in human tissue. Despite broad applications close to the human body, so far, there is only little knowledge of possible toxicity. In this context, the distribution of NPs within cells is of particular interest. Moreover, not only the distribution of NPs but also elemental and molecular cellular distributions such as metabolites and lipids are interesting for medical research.

In this study, we used time-of-flight secondary ion mass spectrometry (ToF-SIMS) and laser-secondary neutral mass spectrometry (Laser-SNMS) to investigate different cells both unexposed and exposed in vitro to silver NPs (AgNPs) and arsenic species. To optimize the analysis, a special silicon wafer sandwich preparation technique was employed; this entails freeze-fracturing and washing of cell cultures that were grown on silicon wafers. The data showed that during freeze-fracturing, the cell membrane is often stripped from the cell, enabling direct analysis of the interior of the cells on one sandwich wafer and the remaining lipid membrane as a mirror image on the opposite wafer. During analysis, the signal from the nutrient materials was observed to diminish the contrast of the molecular signals in the images. By optimizing the preparation and washing procedures, both the contrast and the imaging resolution could be significantly increased due to higher molecular yields and lower background. With these optimization procedures it was possible to detect lipid ions in a higher mass range, especially from those membranes that were stripped from the cells.

Under these optimized conditions, several studies were performed to detect the distributions of trace elements in cells. One study dealt with AgNPs. In this context the uptake of AgNPs of human macrophages was measured with nanometer-scale resolution. 2D and 3D Laser-SNMS images clearly showed that AgNPs are incorporated by macrophages and in part agglomerate to silver aggregates with a diameter of ~3-7 μm . In a similar approach, the distribution of arsenic in cells was measured to obtain more information on the reasons why inorganic arsenic proves carcinogenic in humans. A comparison with ToF-SIMS data showed that especially the high elemental sensitivity of Laser-SNMS makes it possible to detect these trace elements in cells.

AS-TuP2 Comparative Study on the Methods to Determine the Interface Locations in SIMS Depth Profiling Analysis of Multilayer Films. *H.H. Hwang*, University of Science and Technology (UST), Republic of Korea, *J.S. Jang, H.J. Kang*, Chungbuk National University (CBNU), Republic of Korea, *K.J. Kim*, University of Science and Technology (UST), Republic of Korea

In-depth analysis by secondary ion mass spectrometry (SIMS) is very important for the development of electronic devices using multilayered structures, because the quantity and depth distribution of some elements are critical for the electronic properties. Correct determination of the interface locations is critical for the calibration of the depth scale in SIMS depth profiling analysis of multilayer films. However, the interface locations are distorted from real ones by the several effects due to sputtering with energetic ions.

In this study, we compared the three definitions for the determination of interface locations in SIMS depth profiling of multilayer films. Especially, we investigated the feasibility of 50 atomic % definition for Si/Ge and Si/Ti multilayer films by various SIMS analysis parameters. In 50 atomic % definition, the original SIMS depth profiles are converted into compositional depth profiles by the relative sensitivity factors (RSF) derived from the alloy reference films with well-known compositions determined by Rutherford backscattering spectroscopy (RBS).

The application of the 50% definition determined from the ion intensities was found to be very limited to specific systems showing clear interfaces. The definition of the interface by the dimer ions between the atoms in the two different layers was also difficult to apply due to the small intensity and the unclear variation at the interfaces.

AS-TuP3 Estimation of Useful Yield of Electrospray Droplet Impact/Secondary Ion Mass Spectrometry. *R. Takaishi, K. Hiraoka*, University of Yamanashi, Japan

The electrospray droplet impact secondary ion mass spectrometry (EDI/SIMS) has been developed as cluster SIMS[1]. EDI utilizes charged water droplets generated by ambient electrospray. The typical droplet is represented as $[(\text{H}_2\text{O})_{90,000} + 100\text{H}]^+$ with mass of $\sim 10^6$ u. The kinetic energy of droplets is about 10^6 eV with the velocity of 12 km/s. EDI/SIMS has the atomic/molecular level etching abilities[1][2]. EDI/SIMS was found to be applicable to many kinds of inorganic and organic material [1][3]. In spite of the shallow surface etching, relatively high secondary ion yields can be obtained by EDI.

The high ionization efficiency may be due to the occurrence of supersonic collision taking place between the droplet and the sample surface. In order to estimate the useful yield (i.e., total ions generated divided by the total molecules desorbed), mass spectra were measured for binary mixtures of C_{60} /Rhodamine B (1:1) and C_{60} /Aerosol OT (1:1). The equimolar samples were crushed and mixed in mortar and deposited on a stainless steel target as thin films using a spatula. This method was adopted from solvent-free MALDI. By assuming that (1) the desorption efficiency is the same for C_{60} , Rhodamine B and Aerosol OT, and (2) the desorbed ionic compounds directly give secondary ion signals, the useful yield was crudely estimated to be ~ 0.1 . This high value explains the high ionization efficiency of EDI/SIMS.

Reference

- [1] K. Hiraoka, D. Asakawa, S. Fujimaki, A. Takamizawa, K. Mori, *Eur. Phys. J. D38*, 225 (2006)
- [2] D. Asakawa, K. Mori, K. Hiraoka, *Appl. Surf. Sci.* 255 (2008) 1217
- [3] K. Hiraoka, K. Mori, D. Asakawa, *J. Mass. Spectrom.* 41 (2006) 894

AS-TuP4 Multivariate Analysis Models to Predict Surface Chemistry or Performance using ToF-SIMS Mass Spectra Datasets. *N. Sano, M.-L. Abel, J.F. Watts*, University of Surrey, UK

Latent (that is unintentional) adhesion between organics and inorganic surfaces is a well known phenomenon in many areas of materials science, e.g. the moulding of polymeric components and the storage of coated metal products where a polymeric surface is in intimate contact with the back of another sheet. A complete understanding of the adhesion and adhesion processes that occur at this interface may provide a key to obtaining optimum performance for a particular application.

In this work, we are considered with the effects of migration of organics to the surface of the polymeric host and their role at the polymer/inorganic interface. We have focused on three characteristic organics widely used as additives in a wide range of polymer formulations. In the samples we have studied, characteristic peaks from these additives dominate the ToF-SIMS analysis of the inorganic surface. In addition, surface chemistry of the inorganic surface induces different mechanical performances of the products. The storage period has the potential to play a significant role in the migration of minor components towards the interface under investigation, and data will be presented at two different periods (early and late stages).

In this study we show models using multivariate analysis describing how ToF-SIMS analysis can be applied to understand the surface chemistry of industrial materials. The behaviour of migration from the polymer to the inorganic side of the polymeric assembly induces three characteristic surface chemistries which influence mechanical performance. Our models show good predictions for a validation sample of materials.

AS-TuP5 Method for Cross-sectional Analysis Using FIB, ToF-SIMS and Multivariate Analysis. *J.A. Ohlhausen, M.J. Rye, P.G. Kotula, J.R. Michael, T.J. Garino*, Sandia National Laboratories

We have developed a method to create a cross-section of small samples for Time-of-Flight Secondary Ion Mass Spectrometry (ToF-SIMS) utilizing a Focused Ion Beam (FIB) approach. Using this method, a nearly ideal surface for elemental and molecular analysis of the cross-sectional surface is produced, thus providing complimentary information to other microanalytical techniques like scanning electron microscopy (SEM) and scanning transmission electron microscopy (STEM).

FIB is commonly used to create cross sections for SEM and STEM imaging and analysis. Benefits of this technique include controlled extraction area and high spatial resolution. Unfortunately, elemental analyses in the SEM and STEM are not sensitive to low-Z elements and have detection limits that may prevent the detection of some species of interest. Although ToF-SIMS produces lower spatial resolution ($\sim 200\text{nm}$), it has excellent low-Z

sensitivity and has detection limits in the ppm to ppb range. Traditional FIB lift-out sections have been used as cross sections for ToF-SIMS analysis, but they are typically fragile and difficult to handle, thus complicating ToF-SIMS analysis. We have developed a method to create cross sections of particles and small fragments of material that can be analyzed in the "as cut / as mounted" condition. Samples are placed on a traditional SEM mount, and then coated with a conductive layer of AuPd. With the use of special mounts, a cross section that is parallel to the sample surface is milled in the FIB. The resulting samples are sturdy, allowing the removal of the Ga implants by O₂ sputtering. The cross sectioned sample can now be analyzed with ToF-SIMS. Using data from ZnO multi-grain particles, we will show that ToF-SIMS analysis of the cross section yields elemental and molecular information with low detection limits. Additionally, we will demonstrate that multivariate analysis of ToF-SIMS data acquired by this technique is complementary to a FIB-STEM analysis.

§Sandia National Laboratories is a multi-program laboratory managed and operated by Sandia Corporation, a wholly owned subsidiary of Lockheed Martin Corporation, for the U.S. Department of Energy's National Nuclear Security Administration under contract DE-AC04-94AL85000.

AS-TuP6 XPS Depth Analysis of Metal/Polymer Multilayer by Electro Spray Droplet Impact, Y. Sakai, R. Takaishi, S. Ninomiya, K. Hiraoka, University of Yamaguchi, Japan

The electro spray droplet impact (EDI) has been developed for cluster SIMS [1]. EDI utilizes the charged water droplets as projectiles for reducing the sample surface degradations often encountered in atomic-ion SIMS. EDI projectiles are extremely large water cluster ions generated by an ambient electro spray (masses of several 10⁶ u). EDI is capable of atomic- and molecular-level etching with little damage after the irradiation. The EDI gun has been installed in X-ray Photoelectron Spectroscopy (XPS) instrument to analyze the dynamic etching processes during the EDI irradiation. This system has been applied to various organic and inorganic materials. A comparative study of Ar⁺ and EDI etching was performed. While selective etching was observed for almost all of the samples examined by Ar⁺, no chemical modification was recognized by EDI [2,3]. The multilayer metal/polymer samples are used for many practical applications such as transducer, optical device and packaging, etc. For example, the metal layers in integrated circuits are used as the electrical connection and barrier. The interface analysis of metal/ polymer multilayer is of significant importance to clarify the diffusion phenomena taking place between metal and polymer interface. Thus, the ion gun for the interface analysis that is capable of molecular-level etching with no chemical modification is highly demanded. Our preliminary experimental data showed that the EDI gun is very useful for metal/polymer interface analysis. In this report, the depth analysis of Cu/Polymer/Si by EDI etching will be presented. Reference [1] K. Hiraoka, D. Asakawa, S. Fujimaki, A. Takamizawa, K. Mori, Eur. Phys. J. D 38, 225 (2006) [2] Y. Sakai, Y. Iijima, D. Asakawa and K. Hiraoka, Surf. Interface Anal. 42, 658 (2010) [3] Y. Sakai, S. Ninomiya and K. Hiraoka, Surf. Interface Anal. 43, 1605 (2011)

AS-TuP7 A Combined HAXPES and Electrical Characterisation Study of Si and III-V based MOS Structures, L.A. Walsh, G.J. Hughes, Dublin City University, Ireland, P.K. Hurley, J.H. Lin, Tyndall National Laboratory, Ireland, J.C. Woicik, National Institute of Standards and Technology

The aim of this study was to use synchrotron radiation based HAXPES measurements to study the intrinsic electronic properties of both Si and III-V based MOS structures. High quality thermally grown SiO₂ layers, with a thickness of 8 nm, were grown on both n (5x10¹⁵ cm⁻³) and p (5x10¹⁵ cm⁻³) doped silicon. While Al₂O₃ layers 8nm thick were deposited on both n (Si - 5x10¹⁷ cm⁻³) and p (Zn - 5x10¹⁷ cm⁻³) doped GaAs, and n and p (~4x10¹⁷ cm⁻³ for both) doped InGaAs substrates. All substrates were treated by a wet chemical ammonium sulphide based passivation treatment. The samples for HAXPES analysis were capped with 5 nm Ni or Al blanket films by electron beam evaporation. For electrical characterisation, Ni/Au (70 nm/90 nm) and Al (160 nm) gate electrodes were patterned by electron beam evaporation and a lift off lithography process. HAXPES measurements using a photon energy of 4150 eV were used to probe the MOS structures in order to investigate the differences in substrate core level binding energies caused by changes in doping type, and metal work function. The sampling depth for these high energy photons was sufficient to detect core level peaks originating from the substrate, the 8 nm thick dielectric layer, and the top metal contact. The binding energy of core levels in photo emission are referenced with respect to the Fermi level, therefore changes in the binding energy of a particular core level reflect differences in the position of the Fermi level in the semiconductor band gap. For the MOS structures fabricated using SiO₂/Si, changes in the Fermi level positions and differences in the potential drops across the dielectric layers have been directly correlated with the metal workfunction differences observed in the

CV and GV measurements. A binding energy difference of 0.6 eV was measured between the GaAs core levels of the n and p doped substrates, independent of metal work function indicating the strong Fermi level pinning present at the Al₂O₃/GaAs interface. Binding energy measurements for the core levels of native oxide covered n-type doped InGaAs substrates with no metal cap were found to be consistently (~0.3 eV) higher than p-type samples reflecting the fact that the Fermi level is in a different position in the band gap. A binding energy difference of 0.25eV for the core levels of the n and p samples just with the Al₂O₃ dielectric layer present, indicating different Fermi level positions in the band gap. Deposition of the different workfunction metals resulted in limited change in the InGaAs core level binding energies, indicating the partially pinned nature of the Al₂O₃/InGaAs interface.

AS-TuP9 The Development of Charged Particle Lenses for High Spatial Resolution XPS Studies, R. Walker, Shimadzu Research Laboratory (Europe) LTD, UK

The development of selected area and imaging XPS made significant advances with the adoption of Magnetic Snorkel lenses. This lens type of an unconventional design, projects from its main bulk an axial magnetic field that enables focusing of charged particles with low optical aberrations. Simulation techniques, calculate typical lens aberration coefficients of spherical, Cs=3mm and chromatic, Cc=8mm. In the XPS application original theoretical expressions used to characterize this lens type, have been re-modeled, to use present day data and predict some future improvements with this and other lens types. The spatial resolution of present commercial instruments (3µm) is limited by signal to noise. With the large collection angles involved, it is shown that astigmatism is a major contribution that limits the spatial resolution. Furthermore the spatial resolution of the detected signals is insufficient to resolve the stigmatic foci of the astigmatism present in the XPS image. Snorkel lenses are positioned under the specimen and to enable sufficient working distance between the lens and the specimen surface, the lens is highly excited. Typical working distances measure 15mm. By refining the lens coil and iron circuit design, the lens excitation is increased to a maximum and a lens working distance of 19mm is achieved. Consequently with the Snorkel lens positioned in this manner, the thickness of sample will remain limited. A Snorkel lens may also be positioned above the specimen surface so that previous spatial constraints imposed on the specimen form no longer apply. The lens is conical in shape with a bore to focus the photoelectrons through. It will be shown that a Snorkel lens with a 45° access to the specimen surface and at a 2mm working distance has been experimentally proved with very low lens aberration coefficients (Cs, Cc) of 1mm. Calculations show that with only small increases to existing laboratory x-ray powers, it is possible to use this lens to image XPS spatial resolutions of 1µm with present day count rates. Snorkel lenses can have limitations with specimens that magnetize, particularly specimens with topography. Substitution of an Electrostatic accelerating lens for a Magnetic Snorkel lens may result in only a small deterioration of the detected photo electron photoelectron spatial resolution. The ultimate spatial resolution of an image exhibiting the same signal to noise is calculated to be 7µm (Electrostatic) as opposed to 3µm (present day Magnetic). Details of an accelerating electrostatic lens are shown, that is proved to operate reliably with no electrical breakdown.

AS-TuP10 Image Depth Profiling for Three-Dimensional Characterisation of Microelectronic Structures, B. Sgammato, A.E. Wright, A. Bushell, Thermo Fisher Scientific, UK

Microelectronic devices typically consist of elaborate three-dimensional structures, and careful control of chemical and structural properties is required for effective operation. Structures such as pads and bond pads must be carefully assessed for correct size, composition, layering and contamination levels. Supporting structures and substrates must also have the correct composition, integrity and electronic properties.

X-ray photoelectron spectroscopy (XPS) is a surface-sensitive material characterisation technique that offers sensitive chemical state information, and is already established as a method of choice for the analysis of microelectronic devices. Parallel XPS imaging offers high spatial resolution for observing the lateral distribution of chemical states at the surface of a material, and recent advances in spectroscopic imaging allow the generation of quantitative chemical state images for maximal information content.

Depth profiling, typically with ion beams, allows the gradual removal of material from a sample surface, so that XPS can be used to probe further than its characteristic nanometre-scale analysis depth.

The combination of spectroscopic parallel imaging and depth profiling, using the Thermo Scientific Escalab250Xi, permits unmatched spatial resolution combined with layering information, and permits the clear identification of subsurface structures and chemical states. The powerful, intuitive Avantage software datasystem makes data processing

straightforward, so that profile information from small parts of the sample are simple to generate.

AS-TuP11 Developing a Methodology for XPS Profiling of Biofilms and Biological Materials, *R.G. White*, Thermo Fisher Scientific, UK, *D.Y. Petrovykh*, International Iberian Nanotechnology Laboratory, Portugal, *A.C. Areias*, *C. Sousa*, *G.P. Mendes*, University of Minho, Portugal

Films of cells on solid substrates are encountered in a variety of biological and biomedical environments, including cells in biofilms that spontaneously colonize medical devices and multilayers of cells filtered from suspensions for analysis. Understanding the chemical properties of cells in such films is important for providing clues about the behavior of the cells or about the effects of treatments that had been applied to the cells.

X-ray Photoelectron Spectroscopy (XPS), with its combination of chemical selectivity and surface specificity, is an ideal technique for analysing these biofilms and multilayers, but it needs to be combined with profiling to more fully characterise the samples. It is well known that profiling with traditionally used argon monomers results in a high degree of chemical modification for most organic materials. Recent studies have shown, however, that argon cluster beams may be used for depth profiling of organic materials while preserving the chemical information.

This poster will present data from cluster profiling studies of biofilms and biomaterials. The methodology required for optimum profiling of these samples will be discussed, including an evaluation of XPS data acquisition protocols, as well as sputtering conditions.

AS-TuP12 XPS and Auger Analysis of Single and Multi-Layer Graphene Films: What is Graphene and What is Not?, *H.M. Meyer III*, *I. Vlassiuk*, Oak Ridge National Laboratory, *A.V. Sumant*, Argonne National Laboratory

Graphene has received unprecedented attention since 2010 when the Nobel Prize was awarded to Geim and Novoselov for “groundbreaking experiments regarding the two-dimensional material graphene.” Many graphene-related publications use the C 1s spectrum to demonstrate the existence or formation of graphene, but unique photoemission spectral signatures are difficult due to the inherent thinness of single or even multi-layer graphene. The difficulty is due to the surface sensitivity of XPS and Auger spectra and the analysis of spectra that include graphene, substrate-related carbon and possible adsorbed carbonaceous material on the graphene. This poster explores various XPS and Auger spectral features from studies of graphene grown by the CVD method on Cu (near-single layer) and Ni (multi-layer). In one study, graphene grown on Cu was heated in air to determine if the graphene provided any protection to the underlying Cu substrate. The results indicated not only oxidation (i.e. corrosion) protection, but that there was a time and heat dependence of the protection. To aid in the understanding of graphene vs. substrate contributions to the C 1s XPS spectrum, additional studies were performed on CVD-grown diamond substrates. Diamond substrates (very low oxygen and pure sp³-type carbon) offer an interesting contrast to most substrates that have inherent O and C contributions to the O 1s and C 1s spectra. Unique XPS and Auger related features of graphene will be highlighted in this poster.

AS-TuP13 XPS Sputter Depth Profiling of Organic Thin Films Using an Ar Cluster Ion Source, *A.J. Roberts*, *S.J. Hutton*, *C.J. Blomfield*, *W. Boxford*, Kratos Analytical Ltd., UK

A new 20 keV Ar cluster ion source has been used to successfully sputter profile through a range of organic thin films and multilayers. Samples were analysed using XPS between sputter cycles to allow the chemical composition of the sample to be probed as a function of depth into the material. Use of massive Ar cluster ions (1000 to 2000 Ar atoms per ion) promote the retention of sample chemistry throughout the depth profile. In this study we report the performance of the Ar cluster ion source on a range of organic thin films, from fields as diverse as organic PV materials, OLED's, cross-linked plasma polymers and multilayers. Analysis conditions were optimised to maximise retention of chemical functionalities and minimise ion induced interlayer broadening.

AS-TuP14 Quantitative XPS Depth Profiling of Mobile Ions in Soda-Lime-Silica Glasses using a Polyatomic Ion Source, *C.J. Blomfield*, *S.J. Hutton*, *W. Boxford*, Kratos Analytical Ltd., UK

Soda-lime-silica glass is widely used not only for architectural and automotive applications but increasingly in electrical devices as display panels and in photovoltaic applications. The role of mobile ions such as alkali or alkaline-earth ions in these glasses can affect the quality in architectural glass but can have a large impact on electrical device performance. It is important to know the concentration of these mobile ions in the glass surface region and deeper into the glass substrate to understand the leaching process.

Alkali migration has been a noted artefact of sputtering with monatomic Ar ion beams and the use of polyatomic ion beams more commonly applied to organic materials has been shown to yield some benefits in reduced migration without incorporation of C into the glass matrix.

In this investigation we compare the results with monatomic Ar ion sputtering and polyatomic (Coronene) for a number of soda-lime-silica glass samples.

AS-TuP15 XPS Assessment of the Thickness of Fe Oxide Layers using Standard and Active Shirley Background, *M. Bravo-Sanchez*, CINVESTAV-Unidad Queretaro, Mexico, *F. Espinosa-Magaña*, CIMAV Unidad-Chihuahua, Mexico, *A. Herrera-Gomez*, UAM-Azcapotzalco and CINVESTAV-Queretaro, Mexico

The thickness of metal oxide nanolayers can be assessed through X-Ray Photoelectron Spectroscopy (XPS) measurements. This is done by comparing the signal from oxide and metallic XPS peaks. The correct assessment of the oxide layer thickness depends on how accurate the peak areas are quantified through peak fitting. Since the oxide and metallic peaks overlaps in XPS spectra, the calculation of their areas could be tricky. This is specially the case for iron since the Fe 2p peak, which is the iron peak most employed in XPS experiments, is largely asymmetric. In this work, we show that the assessment of the peak areas can carry errors as large as 120% if the traditional Shirley background is employed. The problem is solved by the use of the “active” background removal method, in which the background intensity is optimized during the peak-fitting process. This method is described in detail, as well as its software implementation. The results are supported with High Resolution Transmission Electron Microscopy micrographs.

AS-TuP16 Active Fitting for Optimized Shirley Background Determination, *J. Muñoz-Flores*, UAM-Xochimilco, Mexico, *A. Herrera-Gomez*, UAM-Azcapotzalco and CINVESTAV-Queretaro, Mexico

To subtract the Shirley background to X-Ray Photoelectron Spectroscopy data it is necessary to choose two points, one at each side of the main features of the spectrum. It is common that these points are set close to the peaks to avoid other features present in the spectrum or simply because the data was not acquired with a wide enough energy range. The latter is a common error since it is difficult to discriminate by eye where the contribution of the peaks becomes negligible and the signal is completely due to the background. This is particularly true for peaks with large kurtosis (i.e., large Lorentzian widths) and even more for asymmetric peaks. In the traditional Shirley method, the background is forced to pass through the set points, not allowing any contribution of the peaks to the total signal at those points. As a consequence, the area of the peaks is usually underestimated. In this work we describe the error in the quantification of the peak areas as a function of the energy range and peak width when the traditional Shirley method is applied. This type of error can be avoided if the intensity of the Shirley background is optimized during the peak-fitting procedure, without the restriction of the background passing through the set points. This “active” method is described in detail, as well as its software implementation. By the use of simulated data, it is shown that the active method assesses the peak areas very precisely even when the data is obtained with a too-short energy range.

AS-TuP18 Atom Probe Tomography Analysis of Grain Boundaries in CdTe, *V.S. Smentkowski*, General Electric Global Research Center, *D.J. Larson*, *D.A. Reinhard*, *T.J. Prosa*, CAMECA Instruments Inc., *D. Olson*, Cambridge University, UK, *D. Lawrence*, *P.H. Clifton*, *R.M. Ulfig*, *T.F. Kelly*, CAMECA Instruments Inc.

Photovoltaic materials convert photons to electrical energy (e.g., solar cells) or convert electrical energy into light (e.g. light emitting diodes). Films based on the II-VI compound CdTe are currently regarded as one of the leading type II materials for development of cost-effective solar cells as the CdTe band gap is near ideal for photovoltaic conversion efficiency [1]. While theoretical efficiency values approach 30% [2], commercial and laboratory tests of CdS/CdTe heterojunctions range from ~10% to ~17%, respectively [3,4]. The presence of grain boundaries in these structures likely plays an important role in the observed efficiency. In the current work we investigate, for the first time, the applicability of atom probe tomography (APT) to characterize grain boundaries within the CdTe layer of a solar device. APT data were collected on a CAMECA LEAPTM 4000X HR operated at a base temperature of 40K with a laser energy of 3pJ, a repetition rate of 100kHz and an ion detection rate of 1%. Specimens for APT were prepared by standard focused-ion-beam milling methods [5] from a CdTe layer within a solar cell. Laser-pulsed APT spectra from CdTe-based alloys are quite complex [6,7]. There are two reasons for this: 1) Cd and Te each have eight isotopes and 2) Cd and Te field evaporate in a multitude of complex molecular ions species. The following ions were detected in mass spectra: Cd⁺, Te⁺, CdTe⁺, Cd₂⁺⁺, and Te₂⁺⁺, Cd₂Te⁺⁺ and

CdTe₂⁺⁺, Cd₂⁺, CdTe⁺ and Te₂⁺. In spite of the complex nature of these spectra, all of the peaks are identifiable as some combination of Cd and/or Te. This poster will show both the measured spectra and CdTe composition estimate, as well as 3D images revealing enhancement of S and Cl at a grain boundary.

References

- [1]. Z. Fang et al., *International Journal of Photoenergy* 2011 (2011) 297350.
- [2]. A. Bosio et al., *Progress in Crystal Growth and Characterization of Materials* 52 (2006) 247.
- [3]. M. Powalla & D. Bonnet, *Advances in OptoElectronics* 2007 (2007) 97545.
- [4]. <http://investor.firstsolar.com/releasedetail.cfm?ReleaseID=639463>
- [5]. D.J. Larson et al., *Ultramicroscopy*, 79 (1999) 287, M.K. Miller et al., *Micro. Microanal.*, 13 (2007) 428.
- [6]. P. P. Choi et al., *Microscopy Today*, 20 (2012) 18.
- [7]. D. J. Larson et al., *Microscopy and Microanalysis* (2012), in press.

AS-TuP19 Mapping of a Natural Lubricant Network on the Surface of Silicone Hydrogel Materials Using Surface and Bulk Chemistry Techniques, K.A. Wygladacz, D.J. Hook, M. Merchea, E.P. Maziarz, Bausch + Lomb

Commercial silicone hydrogel contact lenses (SiHy) are ophthalmic devices designed to correct vision as well as function as an ocular bandage for therapeutic purposes. Surface wettability, modulus, surface topography as well as bulk water content are some of the factors that influence lens comfort and performance. Contact lens surface wettability is believed to be an important factor in comfort as well as overall patient satisfaction. Tear confluence across a lens surface may be improved by the presence of well-chosen biomolecules, capable of retaining moisture. Very recently the application of a natural lubricant hyaluronate (HA), to a daily use multi purpose solution (MPS), Biotrue™ has been reported.

In these studies HA was used in conjunction with a surfactant system present in Biotrue™ MPS. The exclusive formulation of Biotrue™ was designed to improve hydration and wettability of various SiHy contact lens materials. Improvements in moisture retention are attributed to the use of high molecular weight HA present in Biotrue™ capable of high water retention. Presence of HA on a lens surface acts as a wetting agent and improves the properties of SiHy contact lens materials. To our knowledge there is no published literature reporting on a visualization method of HA on SiHy contact lenses surfaces.

The purpose of this research was to develop a direct method to demonstrate the presence of a HA network on the surface of SiHy contact lenses using surface chemistry techniques. Senofilcon A® and balafilcon A® were chosen to investigate the interaction of HA with SiHy materials. Atomic Force Microscopy (AFM) was applied to examine the topography of both materials in the hydrated and dehydrated state. The visualization of HA chains was done using Confocal Laser Scanning Microscopy (CLSM) and Differential Interference Contrast (DIC) microscopy using a dye selective for HA (Safranin).

Senofilcon A® and balafilcon A® were soaked in Biotrue™ for 4 hours. Lenses were then soaked in 3 mL of Safranin solution. After 3 min the samples were rinsed with DI water for 3 min to remove any unbound dye. Samples were imaged using an Olympus CLSM equipped with a DIC attachment. Individual confocal images were captured using an air objective sequentially across the sample. A large mosaic was generated using fiducial marks stitched together from the individual images. SiHy lenses incubated with Safranin solution but not exposed to Biotrue™ were characterized as control. Additionally applicability of X-ray Photoelectron Spectroscopy (XPS) for HA mapping on the lenses surface was examined. AFM was used in parallel to study modification of the lens surfaces with HA biopolymer.

AS-TuP20 Kinetics and Mechanism Studies of Copper Nano-Structures Formation on Functionalized Si Surfaces, J.M. Lin, University of Delaware, K.A. Perrine, University of California, Irvine, A.V. Teplyakov, University of Delaware

The manufacture of modern electronic devices has been longing for the higher control over chemical deposition processes and interface properties, as the electronic devices kept scaling down. As a result, a comprehensive understanding of surface reaction mechanisms between the precursor molecule and surface reactive sites is desired.

Numerous studies have addressed that chemically functionalized Si surfaces are promising solutions.

In this work, Copper (hexafluoroacetylacetonato) vinyltrimethylsilane, or Cu(hfac)VTMS, was used to deposit copper nanoparticles on several functionalized Si surfaces including H-Si(100), H-Si(111), NH₂-Si(100),

NH-Si(100), NH_x-Si(100), and OH-Si(100). With atomic force microscopy (AFM), infrared spectroscopy (MIR-FTIR), X-ray photoelectron spectroscopy (XPS) and temperature programmed desorption (TPD) supported with density functional theory calculations (DFT), we have investigated the reaction kinetics and mechanism of the surface reaction and the effects of Si surface functionalization on particle size control and elemental composition of the as-deposited film.

AS-TuP21 Dry Cleaning Methods for Single Reconstructions of (100) InGaAs Following Air Exposure and Post Annealing Conditions, W. Melitz, M. Edmonds, T.J. Kent, A.C. Kummel, University of California San Diego

In effort to further reduce the EOT scaling process while simultaneously maintaining low Dit and high mobility on III-V semiconductor surfaces, dry cleaning methods have been implemented to help create uniform and ordered semiconductor surfaces. The scaling of gate oxides on MOSFETs requires ALD oxide nucleation in every unit cell of the semiconductor channel surface, a process which depends having a highly ordered semiconductor with the minimization of surface defect sites which prevent ALD oxide deposition thereby inducing pihole formation. Through the use of in situ scanning tunneling microscopy (STM) and an atomic hydrogen cleaning technique, air exposed (001) InGaAs samples with an In/Ga rich 4x2 surface reconstruction and an As rich 2x4 surface have been restored to the order and cleanliness of MBE grown samples.

The InGaAs samples were exposed to air, containing NO_x, ozone, and hydrocarbons, and returned to UHV for STM atomic imaging. Imaging confirmed the surfaces became amorphous upon air exposure. The samples were exposed to 150L dose of atomic hydrogen at 380°C. After atomic hydrogen dosing, STM revealed the restoration of the ordered pure In/Ga rich 4x2 surface reconstruction with highly flat atomic terraces. Atomic H cleaning results in formation of deep etch features but a subsequent anneal at 460 °C for 30 min can reduce this effect. Etch pit density has been quantified for samples both after hydrogen dosing and after the post annealing process. Results showed a 98% reduction in etch pit density following the post annealing process [1]. For formation of the pure As-rich 2x4 reconstruction with no group III rich regions, a relatively small processing window was found introducing the air exposed sample to a 1800L dose of atomic hydrogen at 285°C to form the pure 2x4 reconstruction. Etch pit formation occurred following hydrogen dosing and the samples were subsequently annealed to 290°C for 30 minutes. Etch pit density was quantified for samples before and after post deposition annealing and results showed a decrease in etch pit density by 55% following the post annealing process.

[1] W. Melitz, J. Shen, T. Kent, A. C. Kummel, and R. Droopad, " InGaAs surface preparation for ALD by hydrogen cleaning and improvement with high temperature anneal," *J. Appl. Phys.*, vol. 110, p. 013713, 2011.

AS-TuP22 The Effect of Gas Environment on the Electronic and Optical Properties of Amorphous Indium Zinc Tin Oxide Thin Films, Y.R. Denny, S.Y. Lee, K.I. Lee, S.J. Seo, Chungbuk National University (CBNU), Republic of Korea, S. Heo, J.G. Chung, J.C. Lee, Samsung Advanced Institute of Technology, Republic of Korea, H.J. Kang, Chungbuk National University (CBNU), Republic of Korea

The electronic and optical properties of Indium Zinc Tin Oxide (IZTO) thin films were investigated by X-ray photoelectron spectroscopy (XPS) and reflection electron energy loss spectroscopy (REELS). IZTO thin films on a glass substrate have been prepared by RF magnetron sputtering. The composition ratios of In:Zn:Sn in IZTO thin films are 20:56.7:23.3. The films were deposited at the annealing temperature of 350 °C for 1 hour in air, oxygen mixed with water (annealed at 350°C), and 80% oxygen mixed with argon (without annealing). The XPS spectra shows that all IZTO thin films have the Sn-O, In-O, and Zn-O bonds. The REELS spectra revealed that the band gaps of IZTO thin films are 3.23 and 3.07 eV for water mixed oxygen and argon mixed oxygen, respectively. The value of band gap increased to 3.46 eV when the sample was annealed in air. All the measured band gaps by REEL are consistent with the optical band gaps determined by UV-Spectrometer. The average optical transmittance of all IZTO thin films in the visible light region was 86%. The sheet resistivity of IZTO thin films deposited in water and argon mixed oxygen was 5 times lower than that of air, which indicates that gas environment plays an important role in increasing the figure of merit (ϕ_{TC}) and thus improving the electrical and optical properties of IZTO thin films.

AS-TuP23 Modification of Metal – InGaAs Schottky Barrier Height by Atomic Layer Deposition of Ultrathin Al₂O₃ Interlayers. *L. Chauhan*, Dublin City University, Ireland, *S. Gupta, P. Jaiswal, N. Bhat, S.A. Shivashankar*, Indian Institute of Science Bangalore, India, *G.J. Hughes*, Dublin City University, Ireland

High indium content InGaAs is a leading candidate for n-channel devices in future generations of complementary metal-oxide-semiconductor (CMOS) technology due to its high electron mobility and high saturation velocity. In recent years significant progress has been made in improving the electrical quality of the high-k dielectric InGaAs interface by the atomic layer deposition (ALD) of high-k materials on passivated surfaces. An additional technological issue which needs to be addressed for metal oxide semiconductor field effect transistors (MOSFETs) fabrication is the relatively high source/drain (S/D) contact resistance which results from poor dopant activation in III-V semiconductors. One proposed solution to this issue is to fabricate metal S/D Schottky-barrier MOSFET devices which requires control over the barrier height at the metal-InGaAs interface. It has recently been reported that the insertion of an ultrathin layer dielectric layer at the contact interface between the metal and the semiconductor can help in releasing the Fermi level to obtain a rectifying contact.

In this study we investigate the effectiveness of the insertion of an ultrathin ALD deposited Al₂O₃ dielectric layer on the Schottky barrier formed at the interface between the metal and the InGaAs. Schottky contacts were fabricated on 1nm and 2nm Al₂O₃ layers deposited on native oxide and sulphur passivated In_{0.53}Ga_{0.47}As for both n and p doped substrates. To investigate the dependence of Schottky barrier height (SBH) on metal work function (WF), both low (Al~4.30 eV) and high (Pt~5.65 eV) WF metals were deposited on these surface.

Rectifying behaviour was observed for the p-type substrates for the Al-InGaAs and Al/Al₂O₃/InGaAs junctions and the SBH was measured to be ~0.60eV. Ohmic behaviour was observed on the Pt-InGaAs and Pt-Al₂O₃-InGaAs junctions regardless of the dielectric thickness. The Al₂O₃/InGaAs interfacial chemistry of these surfaces was investigated with x-ray photoelectron spectroscopy and no arsenic oxide was found on the Al₂O₃-native and sulphur treated InGaAs surfaces which suggests that on the native oxide InGaAs surface, Al₂O₃ deposition resulted in the consumption of the interfacial oxide.

Ohmic behaviour was observed on the all n-type metal/InGaAs and metal/Al₂O₃/InGaAs junctions regardless of the metal WF or thickness of the dielectric layer which suggests that the Fermi level is pinned near to the top of the conduction band for these InGaAs samples.

AS-TuP26 STM Imaging and Manipulation of a Three-Metal-Center Organometallic Molecule. *N.A. Wasio, R.C. Quardokus, Y. Lu, S.A. Kandel*, University of Notre Dame

The electronic properties of a trimetallic molecule, [$\{Cp^*(dppe)Fe(C\equiv C)\}_3(1,3,5-C_6H_3)\}$ (**Fe3**), are characterized to explore potential uses of these molecules in molecular-electronic devices. Scanning tunneling microscopy (STM) at 77 K under ultra-high vacuum is used to study the adsorption of **Fe3** on the Au(111) surface. Neutral **Fe3** and mixed-valence species (**Fe3⁺** and **Fe3²⁺**) are investigated, and STM images are shown to be sensitive to the intramolecular distribution of charge. Experimental data are compared to simulated theoretical results and tip-molecule manipulation is also explored.

AS-TuP27 Development of Advanced SIMS Single Stage Accelerator Mass Spectrometer Instrument at the Naval Research Laboratory. *K. Fazel, K. Grabowski, D. Knies, G. Hubler*, Naval Research Laboratory

The Naval Research Laboratory (NRL) will be constructing a SIMS Single Stage Accelerator Mass Spectrometer (SSAMS) instrument starting at the end of 2013 for use with nuclear forensics, cosmology, and other applications. The instrument will enable analysis of both positive and negative ions, and will have a molecular destruction capability. These features will address our goal to improve sensitivity and precision of select species, broaden the range of elements and isotopes to measure, and ease sample chemical pre-processing requirements.

To provide these features, the front portion of a Cameca IMS 6f will be combined with an NEC SSAMS system. The NEC SSAMS system will include a bipolar 300-kV air insulated single stage accelerator, custom multi-port 90° high mass resolution injection magnet ($ME/Z^2 = 2.6$ amu-MeV), 90° double focusing analysis magnet ($ME/Z^2 = 75$ amu-MeV), electrostatic spherical analyzer, and a molecular ion dissociator. High-speed electrostatic switching is also included in both magnets to allow high efficiency and precision of measurements of small sample particles. The multi-port injector magnet enables nearly continuous matrix normalization over a large mass range without having to change the magnetic field of the injector. The bipolar power supply for the accelerator allows measurement of both electropositive and electronegative elements, while the molecule destruction feature minimizes molecular interferences. Access to

electropositive elements should provide improved sensitivity for rare earth elements, Uranium, and Plutonium. Before NRL can apply the instrument, the fundamentals of the instrument must be established.

The fundamentals include establishing molecular destruction cross sections of anticipated molecular ions, charge state distributions, overall transmission, and molecule fragment patterns. Upon establishing the performance characteristics of the instrument, the NRL SIMS-SSAMS will be unique tool able to better understand the constituents of an unknown material in nuclear forensics, cosmology, and other applications.

AS-TuP28 Catalytic Effect of Ni in the Gasification of Flexicoke with Water Steam. *J.C. De Jesus, I.J. Gonzalez*, PDVSA Intevep, Venezuela (Bolivarian Republic of), *E.A. Rendon*, Universidad Central de Venezuela, (Bolivarian Republic of)

In Venezuela, the hydrocarbon refining industry produces approximately 400 TPD of flexicoke, a by-product of the Flexicoking™ process, a technology that thermally transforms heavy oils to lighter more valuable products. This solid material concentrates large amounts of vanadium and nickel, and it is usually traded for power generation or metal recovery. However, the indigenous metals in this carbonaceous solid present inherently an excellent dispersion and therefore some potential for complementary catalytic applications. For solid carbonaceous feedstocks, V has been reported to enhance combustion while Ni has shown a good activity to promote gasification with steam for the generation of valuable synthesis gas. However, most conclusions have been extracted from experiences at laboratory scale with synthetic samples, and not with real world ones collected from commercial plants. In this contribution, a real flexicoke sample obtained from a refinery is lixiviated with base and acid to allow the selective removal of each metal, and the assessment of the activity of the individual elements towards the promising gasification with steam is monitored in a thermogravimetric analyzer coupled to a quadrupole mass spectrometer for evolved gas analysis. Analysis by XPS permits the correlation of surface metal composition with catalytic activity monitored during the course of the test reaction. It is shown that Ni catalytically enhances the conversion of the flexicoke to CO and H₂ at a temperature much lower than the one observed thermally both in the original sample and in the fully demetalized carbon matrix. In addition, Ni activity is inhibited in the presence of V, presumably due to the formation of a deactivating layer on top of the Ni surface and, therefore, V must be selectively removed from the original material for the catalysis to take place.

Biomaterial Interfaces

Room: Central Hall - Session BI-TuP

Biomaterial Interfaces Poster Session

BI-TuP1 Response of Mesenchymal Stem Cells to Nano-Scale Rippled Silicon Surfaces. *O.Z. Andersen, A. Keller, D.C.E. Kraft, F. Besenbacher, M. Foss*, Aarhus University, Denmark

Proliferation of stem cells has been observed to be affected by surface roughness in the micro and nanometer range. Furthermore, when cultured on line patterns with dimensions in the sub-micrometer regime these have been found to adopt elongated morphologies and align with respect to patterns, often called contact guidance. Contact guidance has been observed to induce stem cell differentiation towards neurogenic and myogenic lineages. We have investigated the effect of rippled silicon substrates with different height and periodicity in the nanometer range on the behavior of human derived adult stem cells.

The substrates were prepared by irradiating silicon substrates with xenon ions with different energies and fluxes at angles of either 65° or 67° with respect to the surface normal. From this, substrates with nanoripples of different heights (h) and periodicities (λ) were obtained. As determined by AFM measurements the prepared substrates had ripple features ranging from h=3 nm with $\lambda=50$ nm up to h=70 nm with $\lambda=650$ nm. The cellular response towards these surfaces was investigated using human dental pulp stem cells (hDPSC). The cells (2,500 cell/cm²) were cultured for periods of 1, 3 and 4 days, fixed and used for assessing cellular proliferation, morphology, alignment with respect to the ripple structures and expression of the osteogenic markers Runx2 and ALPL and the myogenic markers GATA4 and MyoD1.

It is found that the ripple structures influenced cellular proliferation. An increase in proliferation was observed up until ripple structures with h=8 nm and $\lambda=170$ nm followed by a decrease as the ripples structures further increased in size. The decrease in proliferation for larger ripple structures was found to correlate with an increasing number of cells undergoing contact guidance. Furthermore, it was found that the cells cultured on the

ripple surfaces with features larger than $h=8$ nm and $\lambda=170$ nm had up-regulated expression of the myogenic markers.

The increasing ripple size is associated with larger RMS roughness values. Hence, the increase in cellular proliferation as the ripples grows in size, correlate well with literature on cellular behavior on rough samples. The decrease in proliferation observed with the larger ripple structure correlates with the increasing degree of contact guidance observed for these samples. We speculate that it could be related to changes in the cellular expression profiles. This is supported by the data from the immunohistochemistry. Especially the finding that the expression of MyoD1 is up-regulated with the larger ripple structures as this regulatory protein is known to be associated with cell cycle arrest.

BI-TuP2 *In Vitro* Cytotoxicity of Poly(*N*-isopropyl acrylamide), M.A. Cooperstein, H.E. Canavan, University of New Mexico

Poly(*N*-isopropyl acrylamide) (pNIPAM) is a thermoresponsive polymer that undergoes a conformation change in a physiologically relevant temperature range. Above its lower critical solution temperature (LCST, $\sim 32^\circ\text{C}$), pNIPAM is relatively hydrophobic, and cells can be easily cultured on pNIPAM-grafted surfaces. When the temperature is lowered, the polymer's chains extend and cells detach in intact sheets. It has previously been demonstrated that the NIPAM monomer is toxic; however, there are conflicting opinions as to whether the polymerized form of NIPAM is toxic. Since the cell sheets detached from pNIPAM could ultimately be used on humans, it is crucial to assess the cytotoxicity of surfaces coated with pNIPAM. Very few (<10) studies exist that investigate the cytotoxicity of pNIPAM, and their results are conflicting. Furthermore, the published studies are not comprehensive. Instead, they focus on isolated cell lines cultured on pNIPAM films generated using different methods, and use different assays to determine the degree of cytotoxicity. In this work, we present a comprehensive investigation of the cytotoxicity of pNIPAM-grafted surfaces. The cytotoxicity of pNIPAM is evaluated using different cell lines (endothelial, epithelial, smooth muscle, and fibroblasts), polymerization (free radical and commercially available pNIPAM) and deposition (spin coating and plasma polymerization) techniques, and cytotoxicity tests (MTS, Live/Dead, plating efficiency). The pNIPAM-coated surfaces are evaluated using X-ray photoelectron spectroscopy and goniometry. We find that there is lower cell viability on pNIPAM surfaces when compared to controls. The viability also seems to be deposition type dependent. This work will have valuable insights into the cytotoxicity of pNIPAM-coated surfaces, and therefore into the applicability of cells grown on these surfaces for use in human subjects.

BI-TuP3 Functionalization of Cerium Oxide Nanoparticles with Biocompatible Molecules to Prevent Surface Modification by Phosphate Ions, P. Mendez, S. Das, A. Kumar, S. Sudipta, University of Central Florida

Cerium oxide nanoparticles (CNP's) are a promising catalytic antioxidant in biological systems, exhibiting superoxide dismutase and catalase mimetic, and nitric oxide radical scavenging activity. Nanoceria exhibits redox activity by switching between Ce $3+$ and $4+$ depending on environment. CNPs have also been shown to protect cells against oxidative stress. Specific formulation of cerium oxide nanoparticle is non-toxic, non-immunogenic and well tolerated both *in vitro* and *in vivo* model, which provide the rational/platform for its biological applications. Recently CNPs have become increasingly popular in biological work, both *in vivo* and *in vitro*. We have previously shown these CNPs have some potential to treat wound care, cancer therapy, retinal protection and neurodegenerative diseases. However there are several factors to consider, one being its interaction with biological molecules in different buffers, media, and serum. The common anions are phosphate, sulfate and carbonate. In our previous work, CNPs interaction with sulfate and carbonate are proven not to alter the surface chemistry of CNPs, whereas phosphate anions do. The CNPs properties are surface dependent and phosphate anions are shown to modify the surface. Current study focuses on preventing the CNPs surface modification by phosphate buffer through functionalization. Dextran and polyethylene glycol (PEG) were used to functionalize CNPs. The functionalized CNPs were incubated with phosphate ions and changing their absorbance and emission characteristic was analyzed by Ultraviolet-visible spectroscopy (UV) and photoluminescence spectroscopy (PL). The results show that CNPs functionalized with Dextran prevented interaction with PBS (phosphate ions) and preserved the redox property of the nanoparticle. However, PEG coating fails to do so. Varying pH levels in the range of 6-8 had no significant effect on the phosphate ion interaction with CNPs surface. We further investigated the surface interaction of PEG-CNPs with phosphate, while varying the concentration (5% to 40%) and the chain length (300 molecular weight to 6000 molecular weight) of PEG. The results showed that increasing the concentration or chain length of PEG did not have any effect on phosphate and cerium surface interaction. Looking into the surface charge and morphology of PEG and Dextran will allow us

to gain further insight into what is occurring on the surface of these nanoparticles with phosphate ions. This basic study will help to engineer CNPs, which will be effective in biological applications and overall to prevent modification of CNPs surface.

BI-TuP4 Surface Topographic Patterns Functionalized with Different Biomaterials for Studying Neural Cell Behaviors, Y.P. Lu, M.Y. Lin, National Applied Research Laboratories, Taiwan, Republic of China

Micro- and Nano-patterned substrates functionalized with extracellular matrix (ECM) have been recognized as powerful tools for regulating cell behaviors and functions, because biomimetic features enable the study of cellular responses to specific external stimulations. Surface topography in micro- or nano-scale contributes to provide a physical niche to resemble the physiological environment, whereas biomolecules in ECM can provide a cell-favorable environment in the artificial materials. Independent combination of topographical fabricated scaffolds and biomaterials with bioactive features have provided a suitable *in vitro* cellular function study system. We developed two different characteristics of polymer chips with microstructure and functionalized peptide, including polydimethylsiloxane (PDMS) chip modified with poly-D-lysine (PDL) peptide on the surface and silicon wafer modified with laminin-1 peptide on the surface. The PDMS chip was composed of ridges and grooves around $10\ \mu\text{m}$ in width to form a stripe pattern with micro-meter scale. Another silicon substrate was prepared from micro-meter stripe pattern with nanorods in the grooves region. Neuron-like PC12 cells were then cultured on these 3D substrates and stimulated to manifest different behaviors, and induced cell differentiation with nerve growth factor (NGF) treatment. PC12 cells were cultured in biomimetic substrates impacted in several properties: Cells displayed contact guidance on both substrates and became elongated along the grating axis of scaffolds. When neuron cells cultured on the PDMS substrate, soma and neurite grew on the ridge, groove, or even lateral wall and formed the overlapping distribution. On the other hand, PC12 cells grew on the nanorod substrate functionalized with laminin and displayed contact guidance and became parallel elongated along the flat ridge plane. Some neurites were able to cross groove through the nanorod-supported laminin bridge. Results gained from this study provide the manipulation of neuron cell fate by using enhanced patterning techniques and would be valuable in various biomedical applications, including tissue engineering, neuron regeneration, and basic cell biology.

BI-TuP5 Nanoscale Characterization of Acid and Thermally Treated Collagen Fibrils and its Effects on the Cellular Responses of Osteoblast, Y.J. Park, KAIST, Republic of Korea, G.J. Choi, S.H. Kim, J.H. Hahn, T.G. Lee, KRISS, Republic of Korea, W.J. Lee, KAIST, Republic of Korea, D.W. Moon, KRISS, Republic of Korea

Type I collagen is a major extracellular matrix component and its hierarchical structure plays an important role in the regulation of cellular behavior. In order to study the effect of structure, surface chemistry, and mechanical properties change of collagen fibril on the cellular response, various collagen structures were prepared by different degrees of acidic and thermal treatment of native collagen fibrils. First, to study the microstructure and morphology of collagen, atomic force microscopy (AFM) was used due to its high spatial resolution and surface morphology specificity. Second, we applied time-of-flight secondary ion mass spectrometry (ToF-SIMS) to study the surface chemistry changes of collagen fibrils by utilizing the capability of providing molecular surface chemical information. Third, to observe the changes in the mechanical properties during acidic and thermal treatment of collagen fibrils, contact-resonance force microscopy (CR-FM) was applied because of its ability to provide not only nanoscale spatial resolution but also quantitative information about the mechanical properties. It was demonstrated that the change of microstructure, surface chemistry, and mechanical property of collagen induced by acidic and thermal treatment could be observed in molecular level using AFM, ToF-SIMS, and CR-FM. The structural, chemical, and mechanical properties of acid and thermally treated collagen fibrils could be correlated with the cellular responses such as cell morphology, cytoskeleton organization, and viability.

BI-TuP6 Comparison between Fabrication Techniques for Glass Microfluidic Microchannels, C. Vélez, S. Silva, Universidad de los Andes, Colombia, X. Wang, University of Florida, A. Gonzalez-Mancera, C. Leidy, J.F. Osma, Universidad de los Andes, Colombia, F. Ren, University of Florida

This work presents a comparison between three microfluidic fabrication techniques for shallow channels (less than $20\ \mu\text{m}$ depth) on glass including laser scribing, wet chemical etching using photoresist as a mask, and wet chemical etching using copper deposition as a mask. The purpose of this device is to perform optical particle tracking using a Four Roll Mill configuration. A JPSA excimer UV laser system was used to perform the laser scribing process. This process proves to be the fastest, allows for

better control over the etching rate, and produces smallest angles at the edges. On the other hand, wet etching with copper as a mask uses hydrofluoric acid to produce the channels, and the process proves to be better than etching with photoresist mask. Wet etching with copper as mask also shows better transparency at the bottom of the microchannels, which is perfect for optical tracking and a more homogeneous etching than laser scribing; however, it uses more time and there is less control over the etching rate. Complex geometrical patterns as semicircles and intersections were better obtained using wet etching with copper than the other two fabrication techniques. Liquid flowing inside complex geometry patterns was simulated with Comsol Multiphysics V 4.2. Final fabricated devices were tested with two micro-particle solutions: alginate particles and lipid vesicles in aqueous solutions.

BI-TuP7 Ceria-Gold-Chitosan Nanosystem with Improved Redox Activity and Enhanced Imaging, S. Barkam, S. Das, University of Central Florida, **P. Kulkarni, S. Mallik,** North Dakota State University, **S.S. Seal,** University of Central Florida

Research advances in nanoparticles constructs intended for biomedical applications have proved to be of major importance. This often presents serious challenges in terms of imaging or tracking of the nanoparticles. Our research aims at developing a system that has the effective characteristics of therapeutics and imaging modality. It is well known that Reactive oxygen species (ROS) and nitrogen species play a critical role in many oxidative stress associated disorders like cancer, neurodegeneration, radiation induced tissue damage. Ceria nanoparticles (CNPs) have proved to be potential redox active radical scavenging agents which also exhibit superoxide dismutase and catalase mimetic activity. These nanoparticles can potentially act as antioxidant which is attributed to its redox nature of switching the oxidation states from +3 to +4 mediated at the oxygen vacancies on the surface. Recent research has shown progress in the study of enhancing the contrast in imaging using gold nanoparticles by various microscopy techniques such as TEM, Computed tomography (CT) etc. Its marker ability is attributed to the strong plasmon enhanced absorption and increased light scattering ability which gives detailed information of the location of gold particles by combining optical and electronic microscopy. It is also proven to be non toxic and biocompatible *in vivo*. Our research attempts on providing a formulated coupling of the above notions to form a CNP-Chitosan-Gold integrated system. Addition of Chitosan helps in the reduction of HAuCl_4 to form gold nanoparticles and this polymer also enables the biocompatibility of the imaging agent. The activity of CNPs can be improved by surface modification through selective functionalization thereby enhancing the redox behavior and stability of the system.

BI-TuP8 The Effect of Light-Induced Surface Modification of Functionalized Ceria Nanoparticles towards Killing of Skin-Derived Cancer Cells, S. Barkam, S. Das, V.P. Perez, S.S. Seal, University of Central Florida

Malignant melanoma is the sixth most common cancer diagnosed in the United States. Surgery, chemotherapy and radiation are some of the successful techniques in killing tumor cells. However, in these techniques, it is not easy to distinguish tumor cells from the healthy one which inadvertently get exposed to chemical agent/radiation. Therefore it is required to develop an anti-cancer agent which selectively kills the cancer cells, while still protecting the normal tissues. In our preliminary work, we have shown that Dextran (1000Da) coated Cerium oxide nanoparticles (Dex-CNPs) selectively kills the cancer cells (50% killing at a concentration of $150\mu\text{M}$) without inducing toxicity to normal cells. However, the mechanism involved on how CNPs/Dex-CNPs attain the selectivity and efficiently kill the tumor cells is still unknown. In this study we have synthesized Dextran coated ceria nano particles (Dex- CNPs) with different surface oxidation state ratio ($\text{Ce}^{4+}/\text{Ce}^{3+}$) but similar shape and size. This will provide an in depth understanding of the key chemical and physical properties of the system that can improve its efficacy. The varied surface oxidation of the particles is achieved by exposing Dex-CNPs to light which initiates a color change from dark to pale yellow indicating the reduction of Ce^{4+} to Ce^{3+} . Interestingly we have found that the Dex-CNPs exposed to light have reduced cytotoxicity towards squamous cell carcinoma cell line (CCL30) compared to the protected one. Characterization of the same revealed that Dex- CNPs exposed to light have decreased $\text{Ce}^{4+}/\text{Ce}^{3+}$ surface oxidation ratio compared to the other. This provides more insight in useful synthesis of Dex-CNPs in terms of storage and handling. In summary, higher $\text{Ce}^{4+}/\text{Ce}^{3+}$ surface oxidation ratio is more efficient in hindering tumor growth by effectively hindering the tumor-stoma interaction.

BI-TuP9 Stability and Dispersion Characteristics of Ceria Nanoparticles in Biological Media, P. Munusamy, T. Suntharampillai, D.R. Baer, Pacific Northwest National Laboratory

Although nanoparticles have wide variety of biomedical applications, the characteristics that produce beneficial or toxic effects are not well

understood. Some ceria nanoparticles have gained high visibility for their redox active properties which appear to serve as free radical scavengers. Toxicity measurements of various types and sizes of ceria nanoparticles tested with a variety of *in-vitro* and *in-vivo* studies have many apparent inconsistencies. To accurately evaluate *in-vitro* and *in-vivo* testing results it is important to understanding the properties and behaviors of the ceria particles in the media in which the tests are conducted. In this work, ceria nanoparticles prepared by thermal hydrolysis process are used as a model nanoparticle to study there stability and dispersion characteristics. The particles behaviors in biological media such as aggregation and sedimentation rates were systematically evaluated by aggregation kinetic analysis and sedimentation studies. As one example, fetal bovine serum (FBS) which consists of multiple proteins components was found to be an effective dispersion agent forming a relatively robust surface layer with 24 hours. Data on mixtures of common biological media solutions show a variety of differing impacts. The type of kinetic data we have collected provides important information regarding behavior of nanoparticles in different dispersion media which valuable in understanding toxicity and other biological impact studies.

BI-TuP10 An Anti-biofilm Formation Design Strategy Based on Fibrous Topographical Cues, M. Kargar, A.S. Nain, B. Behkam, Virginia Tech

Biofilms tend to be significantly less responsive to antimicrobial stressors, compared with planktonic bacteria. Studies on the natural antifouling surfaces have shown that most of them have well organized micro/nanoscale surfaces features. This work aims at improving the current understanding of the effects of well-defined sub-micron surface topographies on microorganism-surface interactions with the ultimate goal of developing a bioinspired antifouling design framework based on topographical cues. To this end, model surfaces with well-defined surface topographies in form of highly aligned polystyrene nano fibers at controlled separation distances (diameter (D_f), 90 nm-900 nm and Separation distance (S_f): 0 nm-5000 nm) were fabricated using our previously developed pseudo-dry spinning method. *Pseudomonas aeruginosa* strain PAO1 (diameter (D_b) \approx 500nm, length (L_b) \approx 1800nm) was then presented on the nanofibrous surfaces in a 2.5-hour static retention assay. Scanning electron microscopy was utilized to quantify linear attachment density (number of bacteria/fiber length) and the degree of alignment between bacteria and fibers for all combination of fiber diameters ($D_f < D_b, D_f \approx D_b, D_f > D_b$) and spacing ($S_f < D_b, S_f \approx D_b, D_b < S_f < L_b, S_f > L_b$) at single cell level. Our experimental results demonstrate the presence of an optimum antifouling geometrical condition related to the minimum experimental adhesion density. This optimum condition occurs when the fiber diameter is close to the bacteria diameter ($D_f \approx D_b$) and the spacing is less than the bacteria diameter ($S_f < D_b$). Comparing to the bare surface this geometrical combination reduces bacterial adhesion by more than 40%. Additionally, the SEM images show that bacteria developed microcolonies (onset of biofilm formation) on the bare samples while the engineered surface inhibited colony formation. Our data reveal strong similarity between thermodynamic underpinnings of bacteria – surface interactions and vesicle– surface interactions. The thermodynamic principles governing the vesicle-rigid surface interactions were used to interpret the experimental data and explain the experimentally observed optimum antifouling topographical condition using an energy-based approach. Furthermore, a systematic design methodology for empirical determination of the optimum antifouling topographical condition for nanofiber textured surfaces is outlined.

BI-TuP11 Synthesis of Redox Active Cerium Oxide Nanoparticle with Varying Size and Shape by Manipulating the Chain Length of PEG, S. Das, C. Neal, A. Kumar, University of Central Florida, **A.S. Karakoti,** Pacific Northwest National Laboratory, **S.S. Seal,** University of Central Florida

The objective of this study is to ascertain the role of different molecular weights polyethylene glycol (PEG) solvents on the redox property of cerium nanoparticles. PEG with molecular weight of 300, 600, 1500, 3400 and 6000 were selected in this study for preparing 5mM cerium oxide nanoparticles (CNPs) in 20% PEG medium. The size and morphology of the particles were analyzed using TEM. Interestingly, the size and shapes of the nanoparticles were observed different in different chain length of the PEG nanoparticles from round to star shaped. The red-ox state of the samples was accessed at regular intervals, until stability was observed, using UV-Vis spectroscopy. Absorbance of each sample was recorded in the range of 250nm to 600nm. All the PEG-CNPs sample revealed stable peak at 298nm (characteristic of Ce^{3+}) with additional minor peak observed at 380nm for 1500, 3400 and 6000 PEG-CNPs sample. The biological activity measured by superoxide dismutase mimetic assay was found to be similar for all the PEG-CNPs. The current research suggests that by changing the chain length of the PEG it is possible to synthesize different

size and shape of the PEG-CNPs with similar redox activity for specific applications.

BI-TuP12 In Vitro Protein-Biofilm on Nanoparticles Characterized by ToF-SIMS, STEM and TEM, H.P. Wiesmann, J. Neunzehn, Technische Universität Dresden, Germany, F. Draude, H.F. Arlinghaus, University of Muenster, Germany

Time-of-flight secondary ion mass spectrometry (ToF-SIMS) was applied to detect and characterize different nano scaled protein coatings on gold nanoparticles. After washing the nanoparticles by various steps, the gold particles (diameter of about 10 to 20 nm) were coated with the proteins collagen type I and fibronectin and also different protein combinations in thin mono layers. The different nano-scaled protein layers on the cleaned gold nanoparticle surfaces were identified by detection of the protein typical amino acid mass peaks by time-of-flight secondary ion mass spectrometry.

In addition, the protein-coated particles were investigated by transmission electron microscopy to get information about the proteins structure and their layer thickness on the particle surfaces. It was possible to distinguish the protein coatings by their molecule thicknesses and to evaluate the different particle agglomeration influenced by the used proteins by the use of scanning transmission electron microscopy.

BI-TuP13 A Novel Method for the Bio-conjugation of Catalytic Nanoparticles, R. Draper, S. Das, S.S. Seal, University of Central Florida

This paper explores the possibility of using bio-conjugation to disperse nanoparticles into composite matrices for catalytic purposes. Solid state catalysis is a complex mechanism which can be drastically affected by catalyst size, morphology, surface condition, concentration, dispersal, and location to critical reaction sites. To better understand these mechanisms, as well as to tune solid catalysts to have the greatest specific effect, it is sometimes desired to arrange them into difficult to achieve, high free energy formulations. To overcome their natural characteristics, templating bio molecules can be used to arrange the particles into these difficult formulations to more completely understand the kinetics of the catalysis. One of the more prevalent methods of nanoparticle conjugation involves Watson-Crick base pairing, a method not suitable for aggressive solvents, or for conjugating many types of particles. Here we explore a novel method for biomolecule based nanoparticle conjugation with application to dispersion of catalytic particles in a solid matrix. The effects of these various dispersions are then studied using microscopic, spectroscopic, and calorimetric methods.

BI-TuP14 A Microfluidic Study of the Interaction of Haematopoietic Stem Cells with their Microenvironment, M. Hanke, C. Christophis, C. Leinweber, Institute for Functional Interphases, KIT, Karlsruhe, Germany, N. Baran, I. Taubert, P. Wuchter, A. Ho, University Hospital Heidelberg, Inner Medicine V, Germany, A. Rosenhahn, Institute for Functional Interphases, KIT, Karlsruhe, Germany

A microfluidic adhesion assay has been developed to quantitatively investigate the interaction of cells with interfaces under well defined flow conditions.[1] The device was applied to the study of the interaction of leukaemic cells and haematopoietic stem cells with hyaluronic acid surfaces. We found that beyond a critical shear stress the cell surface receptor CD44 mediates a catch bond, flow induced rolling of the cells on the surfaces[2], similar as observed for leukocytes during the extravasation process.[3] A similar rolling phenomenon occurred on mesenchymal stroma cells, which are present in the bone marrow niche creating the microenvironment required for haematopoietic stem cells to endlessly proliferate. The mesenchymal stroma cells inter alia secrete the stroma-cell-derived factor-1 alpha which has been reported to activate stem cell migration, mobilization and homing.[4] The effect of this chemokine on the movement of haematopoietic stem cells was also studied utilising a novel microstructured niche model.

[1] C. Christophis, M. Grunze, A. Rosenhahn, PCCP 2010, 12, 4498.

[2] C. Christophis, I. Taubert, G. Meseck, M. Schubert, M. Grunze, A. D. Ho, A. Rosenhahn, Biophys. J. 2011, 101, 585.

[3] L. Q. Jin, K. J. Hope, Q. L. Zhai, F. Smadja-Joffe, J. E. Dick, Nature Med. 2006, 12, 1167

[4] Jing DH, Fonseca AV, Alakel N, et al. Haematol-Hematol J. 2010, 95, 542-550.

BI-TuP16 Nonfouling Amphiphilic Polysaccharides, S. Bauer, M.P. Arpa-Sancet, Ruprecht-Karls University Heidelberg, Germany, J. Finlay, University of Birmingham UK, N. Aldred, Newcastle University, UK, M.E. Callow, J.A. Callow, University of Birmingham UK, A.S. Clare, Newcastle University, UK, A. Rosenhahn, Karlsruhe Institute of Technology, Germany
The potential of polysaccharides for fouling-resistant coatings lies in their chemical structure: due to the presence of ether- and hydroxyl-groups, they

are highly hydrophilic and able to form water-storing hydrogels. In this study, the free carboxyl-groups of two surface-tethered polysaccharides, hyaluronic acid (HA) and chondroitin sulfate (CS) were postmodified with the hydrophobic trifluoroethylamine. This strategy was chosen to study different effects: a blocking of free carboxyl groups to prevent complexation of bivalent ions and to preserve the resistance of these coatings in the marine environment, a shifting of the contact angle towards the minimum in the Baier curve and the introduction of amphiphilic properties due to the hydrophobic fluoro-groups. The coatings were tested towards their protein resistance and with different fouling relevant species to evaluate their resistance properties. Settlement and adhesion strength of the marine bacteria *Cobetia marina* and the two algae species *Ulva linza* and *Navicula perminuta* were reduced by the modification in case of HA based coatings. However, in case of CS coatings, the adverse effect was observed.

BI-TuP18 STM Characterization of Chemically Prepared Peptide-Functionalized Monolayers, A. Raigoza, L. Webb, The University of Texas at Austin

Proteins are able to express catalytic and sensing functions that current technologies are unable to reproduce. Instead, efforts have been focused on properly integrating this functionality with non-biological materials. Unfortunately, proteins are generally observed to lose function because of unfolding, aggregation, and overall loss of structure that occurs when a soft, solution-phase material is placed in the harsh structural and electrostatic environment that occurs on and near surfaces. To improve protein-surface interactions, we create a surface that is composed of peptides, which can be tailored for specific protein attachment. Here, we present scanning tunneling microscopy (STM) images of peptide-terminated monolayers on a gold surface created by functionalizing alkanethiol self-assembled monolayers. A Huisgen cycloaddition "click" reaction is used to tether the peptides to the surface at reactive locations that line up with modified residues on the peptide. STM is used to image the surface at each reaction step with molecular resolution. A complete surface reaction would generate a peptide density of approximately 0.6 peptides/nm², based on the distance between reactive azide functional groups and the theoretical size of our peptide. We estimate 0.4 peptides/nm² based on the area covered by peptides in our images.

**Spectroscopic Ellipsometry Focus Topic
Room: Central Hall - Session EL+TF+AS+EM+SS-TuP**

Spectroscopic Ellipsometry Poster Session

EL+TF+AS+EM+SS-TuP1 Ellipsometric Characterization of Iron Pyrite (FeS₂) and Samarium Sesquisulfide (Sm₂S₃) Thin Films, A. Sarkar, N.J. Ianno, University of Nebraska-Lincoln, J.R. Brewer, Rare Earth Solar

Iron pyrite (FeS₂) and samarium sesquisulfide (Sm₂S₃) are transition metal chalcogenides characterized as absorbing semiconductors with bandgaps of 0.95 eV and 1.8 eV respectively. Synthesis of both *n*-type and *p*-type samples have been reported in the form of single crystals and thin films for both materials. As a result of these properties they have received considerable interest as photovoltaic absorber materials. We present the characterization of FeS₂ and Sm₂S₃ thin films using spectroscopic ellipsometry. FeS₂ thin films were synthesized by sulfurizing DC magnetron sputtered iron films and reactive ion sputtered iron (III) oxide films in H₂S / Ar atmosphere. Sm₂S₃ thin films were synthesized by reactive ion sputtering of Sm in an H₂S / Ar atmosphere. This analysis gives the optical properties of chalcogenide films from near-UV (300 nm) to the mid-IR (20 μm). This can then be correlated to the structural and electronic properties as well. The analysis is corroborated with results obtained from Raman spectroscopy, scanning electron microscopy, profilometry, X-ray diffraction (XRD), and Van der Pauw measurements. The ellipsometric results can be used to access different processing methods for synthesizing FeS₂ and Sm₂S₃, to determine the presence of different phases and intermediate products. This work will lay the foundation for employing *in situ* ellipsometry as a process monitor and quality control tool during manufacture of earth abundant chalcogenide thin films.

EL+TF+AS+EM+SS-TuP2 Temperature Dependence of the Dielectric Function of Germanium by Spectroscopic Ellipsometry, A.A. Medina, L.S. Abdallah, S. Zollner, New Mexico State University

Germanium has important applications in photovoltaics as a substrate for III/V triple-junction solar cells, especially in space vehicles and for terrestrial concentrator-based applications. Unfortunately, the optical properties of germanium (complex refractive index and absorption

coefficient) and their temperature dependence (important to consider the effects of the space environment or the radiation-induced heating in concentrators) are not as well known as for silicon, which limits the accuracy of modeling for solar cells and Ge-based optical interconnects. In this work, we report precision measurements of the complex refractive index of germanium from 0.5 to 6.6 eV at room temperature using variable-angle spectroscopic ellipsometry. To improve accuracy, especially at photon energies below 2 eV, we used a Berek waveplate compensator. By cleaning a commercial Ge wafer in isopropanol followed by deionized water, we were able to reduce the native oxide thickness to 1.3 nm. Heating the wafer in UHV at 700 K did not reduce the oxide thickness further. (The oxide thickness can be determined with precision measurements of Δ below the band gap on a single-side polished wafer.) From the ellipsometric angles of the Ge wafer measured at three angles of incidence (65, 70, and 75°), we calculated the dielectric function from 0.5 to 6.6 eV, by correcting for the effects of a native oxide.

Mounting our wafer in a compact UHV cryostat allowed temperature-dependent measurements from 80 to 700 K at 70° angle of incidence. Using similar methods as described above, we determined the dielectric function at different temperatures. We also determined the critical-point parameters (amplitude, energy, phase angle, and broadening) of the E_0 , E_1 , $E_1+\Delta_1$, E_0' , and E_2 critical points as a function of temperature. To separate the non-resonant contributions from the critical-point line shapes, we calculated the second derivative of the dielectric function with respect to photon energy and fitted the result to analytical line shapes with two-dimensional critical points. In general, our results are in good agreement with those of Viña *et al.* However, our results cover a wider spectral range and are more accurate because of the use of a compensator. Work is in progress to form thermal oxides on Ge wafers by annealing in oxygen, which will allow a multi-wafer analysis for Ge similar to work on Si by Herzinger *et al.*

This work was supported by NSF (HRD-0803171 and DMR-11104934) and the New Mexico Louis Stokes Alliance for Minority Participation.

Reference: L. Viña, S. Logothetidis, M. Cardona Phys. Rev. B **30**, 1979 (1984).

In Situ Microscopy and Spectroscopy Focus Topic Room: Central Hall - Session IS-TuP

In Situ Microscopy and Spectroscopy Poster Session

IS-TuP2 In Situ Infrared Spectroscopic Studies of the Stability of Nanoporous Materials in Water Vapor for Gas Adsorption and Separation. K. Tan, N. Nijem, The University of Texas at Dallas, P. Canepa, Wake Forest University, Q. Gong, J. Li, Rutgers University, T. Thonhauser, Wake Forest University, Y.J. Chabal, The University of Texas at Dallas

The stability of nanoporous metal organic frameworks (MOFs) materials in water vapor is a critical issue that must be taken into account for its potential industrial applications such as energy carrier gases (H_2 , CH_4) storage, greenhouse gas CO_2 capture. Many previously reported MOFs structures decompose upon exposure to air, which results in a reduced gas uptake and limits their large scale application. In this context, the study of the interaction and possible reaction of water with MOFs is extremely important to obtain insight into the mechanism of MOFs dissociation in humid environments. In our study, the hydration process of prototypical MOFs $M(bdc)(ted)_{0.5}$ [$M=Cu, Zn, Ni, Co$; $bdc=1,4$ -benzenedicarboxylic acid; $ted=$ triethylenediamine] by water vapor was monitored by *in situ* infrared spectroscopy as a function of pressure and temperature. Infrared spectroscopic results from $M(bdc)(ted)_{0.5}$ compounds indicate that the condensation of water vapors into the framework is necessary to initiate the dissociation reaction of the metal-ligand bond; the stability or modification of $M(bdc)(ted)_{0.5}$ -compound structure upon exposure to water vapor critically depends on the central metal ions. Combining with results taken by *ex situ* Raman spectroscopy and X ray diffraction, we conclude that the hydrolysis reaction of water molecules with Cu-O-C group induces the $Cu(bdc)(ted)_{0.5}$ structure decomposition; for $Zn(bdc)(ted)_{0.5}$, $Co(bdc)(ted)_{0.5}$, the water molecules replace ted pillars and bond to the apical sites of the paddle wheel building units of $Zn_2(COO)_4$ and $Co_2(COO)_4$ by oxygen atoms; $Ni(bdc)(ted)_{0.5}$ is less susceptible to reaction with water vapors than the other three compounds under the same conditions. These experimental conclusions are well supported by first principles theoretical van der Waals density functional (vdW-DF) calculations of overall reaction enthalpies. This work constitutes the first systematic investigation of the decomposition mechanism of isostructural MOFs with different central metal ions in the presence of moisture. The findings within this work make it possible to determine the operating conditions of this class of MOFs with paddle wheel

secondary building units and provide guidance for developing more robust units.

IS-TuP3 Determination of the Mechanisms of Photooxidation of CdSe/ZnS Quantum Dots/Shells. L.J. Powell, S. Saurabh, M. Bruchez, Carnegie Mellon University, L.F. Allard, Oak Ridge National Laboratory, L. Qu, M. Bootman, Crystalplex Inc., R.F. Davis, Carnegie Mellon University

Realization of the potential of Quantum Dots (QDs) for biological, energy-efficient lighting and energy harvesting applications requires that their long-term photostability be improved, especially with regards to protection from photooxidation. The overarching objective of this project is the determination of the chemical and physical mechanisms of photooxidation of CdSe QDs. Pittsburgh-based Crystalplex, Inc. is providing 5 nm CdSe QDs for this research. Three integrated *in situ* characterization techniques are being used to observe changes in QD morphology, optical behavior, and surface chemistry during photooxidation conditions. We are conducting novel microstructural *in situ* experiments in an aberration-corrected STEM/TEM using a Protochips environmental chamber. Changes in the morphology of single QDs are observed in real-time under O_2 and N_2 atmospheres up to 1 atm while maintaining atomic resolution. Multiple series of digital micrographs and EDX data are shown. Single-molecule fluorescence microscopy experiments are allowing us to observe real-time changes in the photoluminescence (PL) behavior of single QDs. The QDs are exposed to 1 atm of either pure O_2 or an inert gas in an environmental chamber and excited with a 490 nm light source during measurements. Changes in blinking rates and PL intensities are analyzed with respect to the periods of exposure to O_2 and light. A series of images and associated statistical analysis are discussed in this poster. *In situ* XPS at CMU is being used to identify the chemical and bonding states of the reacting species. Analysis of the acquired spectra is also presented. These complementary *in situ* experiments allow us to assemble a description of the step-by-step photooxidation mechanism.

IS-TuP4 Coherent X-ray Imaging. T. Senkbeil, T. Gorniak, A. Buck, Karlsruhe Institute of Technology, Germany, K. Giewekemeyer, T. Salditt, University of Goettingen, Germany, A. Rosenhahn, Karlsruhe Institute of Technology, Germany

X-ray microscopy of hydrated biological samples – especially in the so-called water window of 284-540 eV – is of tremendous interest for life sciences due to the high intrinsic contrast of organic matter with respect to the aqueous background and the higher penetration depth compared to transmission electron microscopy. We present X-ray microscopy of cryogenic samples using the coherence-based imaging technique called ptychography.

Ptychography combines previous coherent X-ray diffraction imaging (CXDI) approaches with a scanning scheme, thus providing the ability to image bigger samples, like whole cells or bacteria. We have performed soft X-ray ptychography experiments using our dedicated vacuum chamber HORST at different soft X-ray beamlines at the synchrotron source BESSY II in Berlin, demonstrating chemical contrast and resolutions down to 50 nm in test samples. After upgrading our vacuum chamber with a cryo-sample stage, we now present first results of soft x-ray ptychography of cryogenic samples. Cryo-fixation preserves the natural hydrated state of biological specimens and eliminates the need for any further preparation step, which might possibly alter the ultra-structure. By keeping the sample at temperatures around 120 K at all times, recrystallization of the amorphous water is avoided and the effects of radiation damage during the scans are minimized.

MEMS and NEMS

Room: Central Hall - Session MN-TuP

MEMS and NEMS Poster Session

MN-TuP1 Tangential Momentum Accommodation Coefficients in Coated Microtubes. M. Hadj Nacer, I. Graur, P. Perrier, J.G. Mólans, Aix-Marseille Université, Ecole Polytechnique Universitaire de Marseille, France, M. Wüest, INFICON Ltd, Liechtenstein

The experimental setup based on the constant volume technique is developed to measure the mass flow rate through microtubes under isothermal stationary flow conditions. Four different working gases (helium, nitrogen, argon and carbon dioxide), and two surface materials (Stainless Steel and Sulfinert) are considered.

The Knudsen number calculated for the experimental conditions varies from 0.0001 (hydrodynamic regime) to 0.1 (slip regime). In this range the approach based on the analytical solution of the Stokes equation subjected

to the first order velocity slip boundary condition is used. The velocity slip coefficient and the Tangential Momentum Accommodation Coefficient (TMAC) are extracted from the experimental data of the mass flow rate using their analytical expressions.

The results are summarized in the tables representing the accommodation coefficients for the corresponding gas-surface material combinations. The influence of the molecular mass on the tangential momentum accommodation coefficient is discussed.

MN-TuP3 Development of Deposition and Etching Processes of Thick ZnS Films for Pixel Level Packaging of Infrared Focal Plane Arrays, B. Glück, ST Microelectronics, France, G. Rodriguez, G. Dumont, S. Barnola, CEA, LETI, MINATEC Campus, France

Because of its transparency in the medium and long wave infrared light (MWIR and LWIR) zinc sulphide (ZnS) is an attractive material to make optical windows for infrared devices. Moreover, its relatively low optical index can be used advantageously in association with high index material such as Germanium (Ge) to create an anti-reflecting coating. In our application a thick ZnS film of about 1.2 μm is deposited on top of the Ge to create the infrared window of a micro packaging structure for microbolometer devices in 200mm. This window has to be opened at the end of the process flow to realise the contacts. This study focuses on the deposition of ZnS by electron beam evaporation and its reactive ion etching to form the first layer of the IR-window. The integration of these processes in the fabrication of infrared focal plane arrays is presented in this work. In particular structure and morphology of the deposited ZnS films were investigated by X-ray diffraction, X-ray reflection, atomic force microscopy and scanning electron microscopy. Spectroscopic ellipsometry measurements were done to determine the optical properties. Concerning ZnS etching we developed a HBr based etch process that is also applicable to etch the Ge layer underneath using the same mask. The main process trends were investigated to maximise the etch rate and the selectivity to photoresist.

MN-TuP4 Low Damage Etching Process for Fabricating Micro Electro Mechanical Systems (MEMS) Devices using Neutral Beam, K. Miwa, Y. Nishimori, S. Ueki, BEANS Laboratory, Japan, M. Sugiyama, The University of Tokyo, Japan, T. Kubota, S. Samukawa, Tohoku University, Japan

We have developed low damage etching process suitable for fabricating micro electromechanical systems (MEMS) devices based on silicon by using neutral beam. For cutting edge three-dimensional (3D) MEMS devices, high aspect ratio structures are indispensable. In addition, the surface of the silicon device is required to be smooth enough to achieve excellent properties as electromechanical or optical devices. However, conventional processes using reactive ion enhanced etching (RIE) of silicon are likely to have rough surfaces called scallops or ripples on sidewalls. Furthermore, conventional plasmas used for etching process cause damages on the etched surfaces by ion and electron fluxes (charges) or vacuum ultraviolet/ultraviolet (VUV/UV) light emission from etching plasmas. In turn, neutral beam etching technology is able to achieve ultra-low damage etching and to obtain atomically flat silicon surfaces. Therefore, by using neutral beam we have developed novel dry process to fabricate silicon MEMS devices of which surface is smooth enough and have damage-less surfaces. The neutral beam was produced from an inductively coupled plasma (ICP) of pure Cl_2 gas in an etching tool. The ICP was generated by radio frequency (RF) wave (13.56 MHz) and the RF was time modulated at 10 kHz and the duty ratio was 50% (50 μs ON/ 50 μs OFF). Ions in the ICP were accelerated toward a carbon aperture and neutralized by colliding onto the aperture which was biased by applying 450 kHz alternating voltage. Two types of apertures are used for the experiment. The apertures have many small holes of its aspect ratio is approximately 10 and 20, respectively. We have found that the etched silicon trench profile by the neutral beam depend on bias voltage and aspect ratio (AR) of the aperture. In addition, mask material can change the trench shape. By optimizing these conditions to produce neutral beam, we have obtained silicon trenches which have perpendicular trench profile of its width is around 200 nm. No defects or damaged layer are seen in transmission electron microscope (TEM) observation of the trench sidewalls. The study was supported by new energy development organization (NEDO). Authors would like to thank to NEDO and project members in BEANS Laboratory.

MN-TuP5 Development of Test Instrument for the Mechanical Strength of Micro-nano Wires, A. Kasahara, M. Sasaki, H. Suzuki, M. Goto, M. Tosa, National Institute for Materials Science (NIMS), Japan

Recent nano-technology researches have created various advanced micro-nano materials.

In particular, there have been many reports on nano-meter-scale tubes and wires such as carbon nanotubes

and silicon wires.

We have prepared long crystal silicon wires with a diameter of several tens of nano meters at a temperature lower than 523k by using the low-pressure low-temperature CVD method too. To use these as materials for application to micro-nano electromechanical system, we need to fully understand their electric, chemical and mechanical properties.

However, we have not yet to see a genuine, flexible methodology for evaluating the key characteristic of mechanical strength essential to micro-nano structural materials development the nano scale equivalent of mechanical strength testers for ordinary materials. This time, we are developing the device which could support a bending or shearing test. We will discuss our recent results on mechanical strength measurement of micro-nano wires in diameter several nm through several thousand nm and in length several mm by means of prepared micro-nano mechanical strength measurement device.

MN-TuP6 Tin-Oxide Nanostructured Arrays Based Integrated MEMS Device for Low Temperature Hydrogen Detection, R.N. McCormack, University of Central Florida, N. Shtrato, University of Tennessee, U. Singh, S. Das, A. Kumar, H.J. Cho, University of Central Florida, R. Kalyanaraman, University of Tennessee, S.S. Seal, University of Central Florida

In the pursuit of an alternative fuel source, hydrogen gas appears to have the best potential. All hydrogen gas related processes require accurate monitoring for leaks during the storage, transportation and usage. The problem that arises with the use of hydrogen is its tendency to leak along with being highly explosive at 4-vol%. Most of the current metal oxide based chemi-resistors in use as detectors operate at elevated temperature (above 100 degree Celsius) in order to aid their sensor's response kinetics. This becomes a safety concern due to its proximity to the highly explosive hydrogen gas. The search for low temperature sensitive hydrogen sensing device is at the forefront of our research endeavor.

SnO_2 was deposited on SiO_2/Si substrates through the method of pulse laser deposition (PLD) to form thin film. Through the process of nanosecond pulse laser interference irradiation of the thin film, successfully architected SnO_2 nanoarrays were developed. These nanowire-like SnO_2 structures fabricated were uniformly distributed along the surface of the substrate. Dimensions of the nanostructure were obtained through Atomic Force Microscopy (AFM) and Scanning Electron Microscopy. Results obtained illustrate that the nanoarray's nanowires were ~ 8 nm in cross-sectional height and tens of microns in length. Both thin film and nanoarray were then incorporated into MEMS device. Tests of chemi-resistors were conducted at room temperature within the concentration limits of 300 to 9000 ppm under dynamic condition, simulating the actual environments of exposure. In comparison to SnO_2 thin film, the nanoarray illustrates a significantly larger electrical response upon exposure to concentrations as minimal as 600 ppm. Nanoarray exhibited a (drop in resistances by 2 orders of magnitude) 150 fold increase in electrical response in comparison to that of the thin film.

SnO_2 nanoarray incorporation into the MEMS platform has successfully produced a low temperature hydrogen sensor. The performance of the nanoarray showed promising applicability due to its fast response time, high electrical response and its robustness. Theoretical models of the depletion layer and the diffusive characteristic within SnO_2 were developed in order to exemplify the combined sensing mechanism due to the nanoarray's geometry. This research endeavor therefore combines aspect of interdisciplinary materials design and integration alongside MEMS design, experimental conduction and modeling of device mechanism in the development a gas detector.

MN-TuP7 Nanoimprint Block Co-polymer Enhanced Nanostructure Lithography, J. Zendejas, B. Wong, S. Franz, R. Candler, UCLA

As the demand for higher densities in microelectronic devices increase, the strain on current lithographic technologies becomes great. To achieve greater performance, smaller feature sizes are necessary and will require innovative lithographic technologies. One technique, called Nanoimprint Lithography (NIL) differs from traditional lithography in the exposure and development process, which is replaced by a process in which a resist on a substrate is imprinted by a patterned mold. The nano-scale reproducible patterns allow for a high-throughput technique that saves much processing time and cost. At the UCLA NRF, we are developing baseline recipes for producing nanoscale pattern transfers using PMMA and mr-I (Micro Resist Technologies) polymers. The ability to mass produce nanoscale patterns (C.D. <100 nm) will have a great impact on projects ranging from microelectronics to bioengineering. Using the NIL techniques learned at the UCLA NRF, two target applications have emerged. The cost effective means to produce nanoscale

patterns has made it possible to readily investigate; block copolymer (BCP) lithography and nanoimprint assisted DNA sequencing.

MN-TuP9 Electrostatic Deposition of a Micro Solder Particle Using a Single Probe by Applying a Single Rectangular Pulse, D. Nakabayashi, K. Sawai, P. Hemthavy, K. Takahashi, S. Saito, Tokyo Institute of Technology, Japan

Recently, demands for micromanipulation techniques have increased in order to realize highly functional microdevices such as MEMS. A technique to deposit a conductive microparticle onto a conductive substrate by using a single conductive probe as a manipulator has been proposed as one of the techniques. The technique can be used to increase the yield of a ball-grid-array (BGA), which is used for IC packaging, by fixing the individual soldering defect. Adhesion force between the probe and the microparticle is dominantly greater than gravitational force on the microparticle due to scaling law. Thus, repulsive force must be generated to detach the microparticle from the probe. In the technique, a solder particle with a diameter of 20–30 μm , initially adhering to the probe tip, is detached and deposited onto a substrate by applying a voltage between the probe and the substrate to exert an electrostatic force on the particle. However, when a constant voltage was applied, the detached particle mostly went out of the microscopic view due to the excessive impact of the collision between the particle and the substrate. In the previous research, a voltage sequence was optimized in order to reduce the excessive impact. The success rate of the particle deposition in the previous research was 44%, and is not sufficient for industrial applications. In this study, a technique to deposit the particle on the substrate by applying a single rectangular pulse is proposed, and the mechanism of the deposition by the proposed technique is described. In the mechanism, an electric discharge between the probe and the particle when the particle reaches the substrate plays a dominant role in the particle deposition. The current of the electric discharge generates the Joule heat due to the contact resistance between the particle and the substrate. The small part of the particle which contacts the substrate is melted by the Joule heat, and the melted part absorbs the impact of the collision between the particle and the substrate. Consequently, the particle is successfully deposited onto the substrate. Moreover, the mechanism of the proposed technique is verified by experiments of particle deposition, which are observed by using a high-speed camera (645,000 frames per second), a scanning electron microscope (SEM) and an oscilloscope. The success rate of the particle deposition has improved to 93% by the proposed technique. Furthermore, the Joule heat and the volume of the melted region are evaluated as indicators of the damage to the particle caused by the electric discharge using an RC circuit model, and the applicability of the proposed technique is discussed.

Nanomanufacturing Science and Technology Focus

Topic

Room: Central Hall - Session NM-TuP

Topics in Nanomanufacturing Poster Session

NM-TuP1 Fabrication and Characterization of Nanoscale Carbon Nanotube Patterns on Nanostructured Aluminum Surfaces, Y. Watanabe, H. Kato, S. Asami, S. Sato, S. Takemura, K. Shimada, T. Hiramatsu, Kanto Gakuin University, Japan

The aim of the present work is to develop the nanofabrication methods of highly-oriented patterns of carbon nanotubes on the various substrates and is to characterize the electronic and optical properties of the patterns. The authors proposed a nanoscale arrangement method using a nanostructured surfaces as a nanofabrication template. Single-walled carbon nanotubes (SWCNTs) were arranged in highly-oriented line pattern with nanoscale trenches fabricated on an aluminum surfaces by combined process of chemical treatments and anodization. SWCNTs dissolved in catechin containing solution. Then this solution were dropped on the nanostructures as a droplet utilizing micropipette and extended on the surface. SWCNTs were locally aligned along the line patterns. Dynamic force microscopy (DFM) observations and the cross section analysis were conducted on pre-aligned and aligned surfaces on the highly-oriented structures. Atomic force microscopy-current imaging tunneling spectroscopy (AFM-CITS) measurements were also conducted in order to investigate local conductive properties of CNTs. In the measurement of I-V characteristics by point contact, quantum conductivity of carbon nanotubes were observed. The proposed method can be applied for the CNT arrangement on different surfaces such as Si and glass substrates by nanoscale imprint which enables the prefabricated nanoscale pattern transcription. Nano-contact transcription was performed according to the following steps: CNTs dissolved in catechin containing solution were dropped with a micropipette on an aluminum line structure. The Al sample was placed on a silicon substrate and was pressed for 30 sec in order to transfer the CNTs pattern to the Si substrate. Then the Al template was removed and the Si substrate was dried naturally. In the case of the line pattern template, it was found that

SWCNTs line pattern could be transferred to a Si wafer. Transcription of double wall carbon nanotubes (DWCNTs) was also the same result. Arrangement of multi-walled carbon nanotube (MWCNT) and cup-stacking CNT was also performed. Raman characterization of the fabricated patterns of SWCNT, DWCNT, MWCNT and cup-stacking CNT was conducted in order to investigate the detailed structures on the surface. Two types of Raman peaks which were characteristic of CNT were observed by Raman measurements. Several RBM peaks appeared in the low frequency region (80–400 cm^{-1}). Asymmetric shaped G-band was confirmed (1500–1700 cm^{-1}). A shoulder peak was observed in the low wavenumber side of the G-band.

This work was aided by MEXT-supported Program for the Strategic Research Foundation at Private Universities.

NM-TuP2 Topographical and Raman Studies of Nano-graphite Patterns on Nanostructured Al and Si Surfaces by Carbon Drawing, Y. Takarai, T. Hirakawa, K. Doi, H. Kato, A. Ishii, Y. Watanabe, S. Takemura, T. Hiramatsu, Kanto Gakuin University, Japan

The authors performed carbon drawing and embossing methods in order to fabricate nanoscale structures on nanostructured Al surface and Si wafer. Carbon drawing is a nanofabrication method by gently pushing bulk graphite on the surface and drawing it. In the present study, the authors used HOPG and black carbon flakes for carbon drawing which performed on a nanostructured Al substrate. The surfaces were investigated by scanning probe microscopy (SPM) and Raman spectroscopy. The authors performed carbon drawing on the aluminum linked-crater structure. The AFM image demonstrated that each nanoscale crater was filled with carbon by the drawing and a unique carbon dots structure was created on the surface. A unique nanostructure was also fabricated by carbon drawing on the aluminum linked-crater structure. In the case of Si wafer, drawing with carbon flakes made stripe structure. The stripe separation was approximately 1 micrometer. Raman spectroscopy was used to characterize pre-drawing Si wafer and post-drawing Si wafer. Raman peaks due to Si were observed at around 500 cm^{-1} and 1000 cm^{-1} in the pre-drawing sample. Some characteristic peaks of carbon were observed in the post-drawing sample. A peak at 1360 cm^{-1} can be assigned to D band. A peak at 1600 cm^{-1} can be assigned to G band (Graphite band). Raman peaks due to glassy carbon appeared after carbon drawing on Si wafer. Furthermore, the authors performed embossing method with inserting carbon flakes between Si wafer and nanostructured Al. It was found that unique nanostructures were created on the Si surface by embossing method. In the case of aluminum highly-oriented line structure, the embossing made the nanoscale line pattern transfer to the Si wafer. The transferred line separation was estimated as several tens of nanometers. In the case of aluminum line structure, drawing a line perpendicular to the HOPG made arch-like structure. It was confirmed that the carbon was along the line in this structure. Raman spectroscopy was used to characterize pre-drawing and post-drawing nanostructured Al surfaces. A peak due to Al_2O_3 was observed at around 2900 cm^{-1} in the Pre-drawing. Some characteristic peaks were observed in the post-drawing sample. A peak at 1360 cm^{-1} can be assigned to D band due to defects in the crystal which is supposed to appear when crystallinity of thin graphene is distorted. A peak at 1600 cm^{-1} can be assigned to G band, which appears when the measured object is allotrope of carbon. This peak intensity depends on wavelength of incident light. This work was aided by MEXT-supported Program for the Strategic Research Foundation at Private Universities.

NM-TuP3 Photoluminescence Enhancement of Aluminum Surfaces with Various Shaped Nanostructures Filled with Metallophthalocyanines and Organic Dye Molecules, A. Ishii, T. Shimizu, H. Kato, T. Kamino, S. Takemura, T. Hiramatsu, Kanto Gakuin University, Japan

Nanostructures such as linked-crater and highly-oriented pillared structures made of anodized aluminum oxide were fabricated on an Al surface by combination process of chemical and electrochemical treatments. Crater-shaped structures were initially created on the aluminum surface by the chemical surface treatment. Successive anodization condition created the different sized linked-crater structures. A highly-oriented pillared structure was fabricated on an Al surface by chemical and electrochemical multi-process. Based on the initial structure fabricated by chemical surface treatments, successive anodization proceeded in the fabrication of well-ordered characteristic nanoscale patterns with highly-oriented aligned trenches on Al surface such as a groove-pattern structure. Successive surface treatment using Semi Clean assisted in fabrication of ordered finer nanoscale structures such as highly-oriented pillared structure. The present work also intended to make an organic nanoscale pattern using highly-oriented pillared structure as a template by filling of dye molecules, namely, rhodamine B (RB), brilliant green (BG) dissolved in acetonitrile, copper phthalocyanine (CuPc), iron phthalocyanine (FePc) and Cobalt phthalocyanine (CoPc) dissolved in toluene in order to functionalize the

surfaces. The cross section analysis demonstrated that the dye molecules were filling the trenches along the linked-crater structure and the highly-oriented pillared structure by dynamic force microscopy (DFM) measurement. Photoluminescence measurements showed that RB emission peaks appeared in the wavelength range of 600-640 nm. In the case of BG emission peaks appeared in the wavelength range of 450-500 nm. In the case of metal phthalocyanines, CuPc, FePc and CoPc, the emission peaks appeared in the wavelength range of 450-550 nm. The authors confirmed that the significant emission enhancement happened to dye molecules filling linked-crater and highly-oriented pillared structures fabricated on the aluminum surface. The structure of RB filling aluminum nano-structures were investigated by FT-IR measurements. It was found that the intensity of Al-O mode at 800-1000 cm^{-1} in the case of highly-oriented pillared structure was larger than that in the case of the linked-crater structure while the intensity of Al-O mode at 1000 cm^{-1} was comparable between two structures. It was also found that the emission peaks appeared in the wavelength range of 1200-1700 cm^{-1} in both cases of linked-crater and highly-oriented pillared structures. This work was aided by MEXT-supported Program for the Strategic Research Foundation at Private Universities.

Oxide Heterostructures-Interface Form & Function Focus Topic

Room: Central Hall - Session OX-TuP

Oxide Interfaces and Heterostructures Poster Session

OX-TuP1 A Kinetic Monte Carlo Study of Cu Cluster Formation on Cu and ZnO Surfaces using COMB Potentials. *Y.-T. Cheng, T. Liang, University of Florida, X.W. Nie, The Ohio State University, S.R. Phillpot, University of Florida, A. Asthagiri, The Ohio State University, S.B. Sinnott, University of Florida*

Heterogeneous systems of Cu clusters on ZnO surfaces are used as catalysts and it is a challenge to maintain the stability and activity of the catalyst under reaction conditions. Processes such as sintering, alloying, and encapsulation may play an important role in the activity of the catalyst but are difficult to model directly with electronic structure calculations. In this work, we will report on the development and use of charge-optimized many-body (COMB) potentials to model the Cu/ZnO system. In particular, the diffusion of Cu atoms and the ripening of Cu clusters on Cu and ZnO surfaces are modeled using kinetic Monte Carlo simulations, which is used in conjunction with the dimer method to find possible transition paths for Cu migration. Simulations allow for a comparison of transport mechanisms on the two different surfaces (Cu and ZnO) and the predictions are compared to the results of density functional theory calculations and published experimental data. This work was supported as part of the Center for Atomic Level Catalyst Design, an Energy Frontier Research Center funded by the U.S. Department of Energy, Office of Science, Office of Basic Energy Sciences under award number DE-SC0001058.

OX-TuP3 Molecular Dynamics Simulation Studies of The Toughening Mechanisms of Bio-inspired Hybrid Ceramic-based Materials. *K. Yao, T. Liang, D.E. Yilmaz, S.R. Phillpot, S.B. Sinnott, University of Florida*

Bio-inspired hybrid ceramic-based materials have attracted attention due to their high yield strength and fracture toughness. In this work, the mechanisms associated with the mechanical responses of composites of poly(methyl methacrylate), or PMMA, and Al_2O_3 in two hierarchical configurations, lamellar and brick-and-mortar, are considered. In particular, classical molecular dynamics simulations using charge optimized many-body (COMB) potentials are carried out to identify these mechanisms. The influence of such factors as the arrangement of the phases in the two different configurations, interfacial composition, nanometer-scale structure, and polymer thickness are considered. The nanometer-scale responses of the composites nanoindentation, shearing, and bending are compared with experimental data. This work is supported by DARPA.

OX-TuP4 A Variable Charge Reactive Potential for Nitrogen based Hydride and Oxide Molecules to Simulate Oxide Growth on AlN and TiN. *J. Martinez, S.R. Phillpot, S.B. Sinnott, University of Florida*

An empirical, variable charge potential for Nitrogen hydride and Nitrogen oxide molecular systems based on the charge optimized many body (COMB) potential framework is proposed. The potential is fitted to structure and energetic properties of certain key molecules such as NH_3 and NO_2 . This potential is used in conjunction with TiN/ TiO_2 and the AlN/ Al_2O_3 variable charge potentials based in the same COMB framework to study the structure, energetics, and mechanics of oxide growth on TiN and AlN under varying conditions.

OX-TuP5 Effects of Nonstoichiometry on the Structure and Electronic Properties of LaCrO_3 Thin Films on $\text{SrTiO}_3(001)$. *K.H.L. Zhang, Y.G. Du, L. Qiao, S.A. Chambers, Pacific Northwest National Laboratory*

The ability to precisely control the structure, stoichiometry and defect densities in epitaxial perovskite films is emerging as one of the major challenges for understanding the sometimes novel physical properties exhibited by interfaces and superlattices of these materials. Recently we have demonstrated that structurally excellent, stoichiometric LaCrO_3 thin films can be grown on $\text{SrTiO}_3(001)$ by molecular beam epitaxy. In this contribution, we further explore the effects of nonstoichiometry on the structure and electronic properties of $\text{La}_{1-x}\text{Cr}_x\text{O}_3$ thin films with $-0.13 < x < 0.05$. Interestingly, La-deficient films maintain high crystalline quality in spite of very large deviations from stoichiometry, while La-rich films exhibit significantly degraded crystalline quality. Ongoing studies of lattice parameters, film and interface microstructures, and electronic properties will be discussed in order to elucidate different mechanisms of accommodating A-site and B-site cation imbalances during the epitaxial growth of perovskites.

OX-TuP6 The Influence of Nano-Scale Interfaces and Co-Doping on the Oxygen Ionic Conductivity of Ceria and Zirconia Based Thin Film Electrolytes. *M.I. Nandasiri, Q. Langfitt, M. Quintero, T. Varga, A. Devaraj, S. Manandhar, P. Nachimuthu, V. Shutthanandan, S. Thevuthasan, EMSL, Pacific Northwest National Laboratory, A. Kayani, Western Michigan University*

The high temperature operation of solid oxide fuel cells (SOFC) is one of the main challenges we have to overcome, especially for commercializing SOFC for portable power generating applications. Solid state electrolytes with enhanced oxygen ionic conductivity at low and intermediate temperatures are needed to lower the operating temperature of SOFC. Thus, there is an ongoing need to develop new electrolytes or modify existing electrolytes to enhance the ionic conductivity. Co-doping can be used to modify existing ceria and zirconia based electrolytes. On the other hand, new electrolytes can be developed by utilizing the engineered interfaces in multi-layer thin films. Here, we investigate the influence of nano-scale interfaces and co-doping on the ionic conductivity of ceria and zirconia based electrolytes.

In this study, we have grown (i) multilayers of high quality samaria doped ceria (SDC) and scandia stabilized zirconia (ScSZ) epitaxial thin films, and (ii) samaria and gadolinia co-doped high quality ceria thin films using oxygen plasma-assisted molecular beam epitaxy and characterized using various capabilities. The number of layers in the SDC/ScSZ multi-layer thin films was varied from 2 to 20 by keeping the total film thickness constant at 140 nm to understand the effect of nano-scale interfaces on the ionic conductivity. To understand the effect of co-doping on the ionic conductivity of optimized SDC thin films, $\text{Ce}_{0.85}\text{Sm}_{0.15-x}\text{Gd}_x\text{O}_{2-\delta}$ (SGDC) thin films were deposited by varying the Gd concentration. The film growth was monitored using in-situ reflection high energy electron diffraction (RHEED). Structural properties of these films were studied using x-ray diffraction (XRD) and the XRD patterns confirmed the growth of epitaxial thin films. The film and layer thicknesses were determined by x-ray reflectivity. X-ray photoelectron spectroscopy was used to find the composition, depth profile and chemical state of elements of the films. The SDC/ScSZ multi-layer and SGDC thin films were carefully characterized using Rutherford backscattering spectrometry, coupled scanning transmission electron microscopy and atom probe tomography to study the oxygen vacancy and dopant distributions along with the inter-diffusion and dopant segregation at the interfaces. Oxygen ionic conductivity measurements were carried out as a function of temperature on well characterized samples using four probe surface impedance spectroscopy. Detailed analysis of oxygen ionic conductivity as a function of individual layer thickness, dopant concentration, and crystalline quality of the films will be discussed.

Advanced Surface Engineering

Room: Central Hall - Session SE-TuP

Advanced Surface Engineering Poster Session

SE-TuP1 Analysis of the Physical Damage during HBr/ O_2 /Ar Gate Etching using Various Pulsed Plasmas. *K.Y. Jeon, J.Y. Lee, G.J. Min, Samsung Electronics Co. Ltd., Republic of Korea*

Recent device has been rapidly scaled. The plasma oxidation and lattice damage by energetic ions cause the silicon oxidation in the channel and source/drain regions of the transistors. In addition, they generate the defects such as the Si/ SiO_2 interface trap sites, contaminations, Si bond breaking and interstitial atoms. Those damaged regions by energetic ions can no

longer be neglected. The continuous wave plasma is widely used in the conventional etch process, but it has some limitations to control the ion energy. It is difficult to reduce the damage layer in the atomic scaled device. This various plasma conditions in Gate etch process affect the physical damage on the substrate Si lattice and the gate oxide. In this work, the Si damage has been compared after etching by various plasma generation methods. Si etches has been performed in ICP chamber by using continuous wave HBr/O₂/Ar plasmas, bias pulsed HBr/O₂/Ar plasmas, synchronous pulsed HBr/O₂/Ar plasmas, and especially DC pulsed plasma. Ellipsometry and TEM were used to analyze the Si lattice damage. Plus some electrical tests such as time zero dielectric breakdown (TZDB), charge pumping current, C-V measurement respectively. As a result, the pulsed plasma etching method is promising alternatives in respect of the physical Si damage, including the charge build-up and etch uniformity, and the mask selectivity

SE-TuP2 Deposition of Hard SiOC(-H) Films by Atmospheric Pressure Plasma Enhanced CVD Method, M. Noborisaka, R. Horikoshi, A. Shirakura, T. Suzuki, Keio University, Japan

Atmospheric pressure-plasma enhanced CVD method is a cost-effective process which has been widely developed because we do not have to vacuum during the deposition of thin films. In this study, SiOC(-H) films were synthesized by atmospheric pressure-plasma enhanced CVD method from tetramethoxysilane (TMOS) and O₂ diluted with N₂. The deposited films were characterized by Fourier-transform infrared spectroscopy, nano-indentation technique, transmission electron microscopy and ellipsometry. The partially crystalline phase of silica was found in the deposited films. The nano-hardness of the films increased from 4.0 GPa to 6.9 GPa as the substrate temperature increased from 80°C to 300°C. The hardness slightly increased up to 4.5 GPa from 4.0 GPa by decreasing the TMOS flow rate at the substrate temperature of 80°C. The results suggested that increase in the relative ratio of Si-O-Si bonding in the network structure to Si-O-Si bonding in the cage structure led to increase in hardness.

SE-TuP3 Thermal Transport at Metal-Carbon Interfaces, J.J. Gengler, Spectral Engies LLC/Air Force Research Laboratory, S.V. Shenogin, UES Inc./Air Force Research Laboratory, A.A. Voevodin, A.K. Roy, C. Muratore, Air Force Research Laboratory

Carbon nanotubes are appealing for diverse thermal management applications due to their high thermal conductivity (as high as 3,000 W m⁻¹ K⁻¹) coupled with interesting mechanical properties (stiff and strong, but also exhibiting foam-like deformation in arrays). Unfortunately, CNT surfaces are generally non-reactive and demonstrate weak bonding to other materials, limiting thermal interfacial conductance. Functionalization with "linker molecules" has been shown to enhance interfacial conductance, but reduces thermal conductivity of the nanotubes themselves by altering carbon bond hybridization within the nanotube. Metal coatings provide a way to increase thermal interface conductance associated with carbon nanostructures, while maintaining their high thermal conductivity. We used Molecular Dynamics and vibrational modes analysis to study heat transfer through carbon nanotube - metal interfaces in highly nonequilibrium conditions (NEMD). The simulation results were compared to experimental measurements of conductance for metallized highly oriented pyrolytic graphite (HOPG) substrates. HOPG was selected as a practical 2-dimensional analog for nanotube sidewalls to facilitate experimentation by analysis of the two-color time domain thermoreflectance (TDTR) data from the samples. The TDTR analysis of the different metals on HOPG was made possible by employing an optical parametric oscillator on the probe beam which allows for tuning the probe beam wavelength to match absorption bands for each metal studied. Metal films were selected to identify effects of atomic mass (inversely proportional to Debye temperature), chemical interactions (i.e., interfacial carbide formation) and electron configuration. Measurements of chemically inert metals at the carbon interface, including Al, Cu and Au demonstrated a strong dependence on Debye temperature, with conductance values differing by a factor of 3. The effects of interfacial carbide layers with varied areal densities on HOPG surfaces on thermal conductance were also examined, in addition to the presence of molecular interlayers. These results were applied to 3D assemblages of carbon nanotubes, such as dry spun CNT yarn, where metallization yielded significant enhancements of thermal conductivity in addition to increased tensile strength.

SE-TuP4 Multilayer on a Staircase Substrate for Hard X-ray Gratings, C. Liu, Argonne National Laboratory, S. Lynch, E. Bennett, A. Gomella, National Institutes of Health, L. Assoufid, Argonne National Laboratory, H. Wen, National Institutes of Health

Traditional hard x-ray transmission gratings are fabricated using lithography processes. They are constrained by the maximal attainable aspect ratio of the vertical walls, which limits the smallest attainable grating periods. Advanced X-ray phase contrast imaging techniques require large-

area, high-density transmission gratings with smaller periods and higher aspect ratio to cover larger energy range for thicker samples. A new type of grating using multilayers grown on staircase substrates may meet this requirement. A thin Si substrate can be anisotropically etched to a staircase. With each stair surface supporting a multilayer as a micro grating and an X-ray beam shining through the layers at an oblique angle to the substrate and parallel to the layer surfaces, one has a large-area transmission grating with small grating periods. This method represents a new way to make gratings for hard x-rays. A [93 nm W / 93 nm Si] x 81 multilayer was grown on a 20 mm x 20 mm, 26°-blaze-angle Si staircase substrate using dc magnetron sputtering deposition. The multilayer thickness matches the stair height. A nitride layer was coated before multilayer deposition so that the Si substrate can be etched away to reduce x-ray absorption. Efforts have been made to grow the multilayer so that a major portion of layers is parallel to the stair surface with minimal amount on the sidewall. The sample was tilted during multilayer deposition to face the target. Deposition collimators were used to direct the coating flux. Uniform coatings were achieved using the profile-coating technique with specific masks made for each sputter gun. SEM images of sample cross sections and preliminary results of synchrotron x-ray diffraction and contact radiography at 25 keV are presented.

**Scanning Probe Microscopy Focus Topic
Room: Central Hall - Session SP-TuP**

Scanning Probe Microscopy Poster Session

SP-TuP1 Quantitative Barrier Height Measurements of Tryptanthrin Monolayers on HOPG, K. Sriraman, J. Novak, J. Baum, A. Olson, Florida Institute of Technology

Scanning tunneling spectroscopy (STS) was used to collect barrier height data on the molecule Indolo[2,1-b]quinazoline-6,12-dione (tryptanthrin) at the solution-graphite interface. Tryptanthrin and its analogues have shown good promise as potential therapeutic agents for a variety of pathogenic organisms. In this experiment, apparent barrier height ' Φ_{ap} ' (work function) values were collected at sub-molecular resolution. The STM topography and barrier height data are collected simultaneously so that the barrier height data can be compared with the topography of the molecule. Since a positive sample bias was used throughout the experiment, the topography corresponds to the lowest unoccupied molecular orbital (LUMO) of the molecule. These topography and barrier height image data are compared with the density functional theory (DFT) computed molecular orbital of tryptanthrin to ascertain the positions of various lobes of the molecule. These data from barrier height images correspond to the amount of energy required by electrons to enter or leave different parts of the molecule, which might be indicative of the likely locations of redox events.

**Surface Science
Room: Central Hall - Session SS-TuP**

Surface Science Poster Session

SS-TuP1 MORTON S. TRAUM AWARD FINALIST: Quantum Tunneling Driven Assembly and Diffusion of Hydrogen and Deuterium on Cu(111), A.D. Jewell*, Tufts University, G. Peng, University of Wisconsin Madison, G. Kyriakou, Tufts University, M. Mavrikakis, University of Wisconsin Madison, C.H. Sykes, Tufts University

Hydrogenation reactions are central to the petrochemical, fine chemical, pharmaceutical, and food industries and are of increasing interest in energy production and storage technologies. The processes of molecular adsorption, dissociation, diffusion, association, and desorption are important surface phenomena in heterogeneous catalysis. Typical heterogeneous catalysts often employ alloys based on platinum, palladium, rhodium and ruthenium. While these metals are active at modest temperature and pressure, they are not always 100% selective and are expensive. Given that molecular hydrogen (H₂) dissociation is often the rate limiting step, one strategy is to engineer the minimal catalytic ensemble that will activate H₂ but leave the other reactants untouched. We describe a system which offers low dissociation barriers at one location on the surface and weaker binding in other regions. The Pd/Cu surface alloy was prepared in the dilute limit in which 1% Pd resides as individual, isolated substitutional atoms in a 99% Cu(111) surface. In terms of adsorption, these Pd atoms significantly lower the barrier to H₂ dissociation and allow the spillover of H atoms onto the

* Morton S. Traum Award Finalist

Cu surface.[1] This system also offers the opportunity to study the diffusion, association, and assembly of large quantities of H and D on the Cu(111) surface. Through careful low-temperature scanning tunneling microscopy (STM) tracking experiments we show that quantum tunneling effects dominate the diffusion properties of H and D on the Cu surface.[2] With this direct visualization and quantification of quantum tunneling effects in adatom diffusion, we reveal two types of weak interactions between H adatoms, which lead to assembly into small clusters and larger assemblies of small clusters. We show that the self-assembly of H into large islands is, in fact, a tunneling effect resulting from inter-atom energy being much smaller than the diffusion barrier. We further demonstrate that these latter effects are not at play for D. Density Functional Theory (DFT) calculations provide estimates for both diffusion and interaction energies. Theory also provides quantum tunneling probabilities that agree well with experiment.[2] References: [1] G. Kyriakou, M.B. Boucher, A.D. Jewell, E.A. Lewis, T.J. Lawton, A.E. Baber, H.L. Tierney, M. Flytzani-Stephanopoulos, and E.C.H. Sykes, *Science* **335**, 1209 (2012). [2] A.D. Jewell, G. Peng, G. Kyriakou, M. Mavrikakis, E.C.H. Sykes, in preparation.

SS-TuP2 MORTON S. TRAUM AWARD FINALIST: Coverage-Dependent Interfacial Electronic Structures of Thiophenol and p-Fluorothiophenol on Cu(111), S.-Y. Hong*, P.-C. Yeh, J. Dadap, R.M. Osgood, Columbia University

Femtosecond two-photon photoemission spectroscopy is used to investigate and compare the interfacial electronic structures of thiophenol and p-fluorothiophenol films on Cu(111) as a function of molecular coverage. A new state is found to emerge as the coverage is increased; simultaneously, the Cu(111) Shockley surface state disappears for both molecular species. This similarity in behavior is shown to originate from spatial lateral confinement of the surface electron. In addition, the change in the workfunction vs. coverage shows that the two thiophenols exhibit almost identical behavior until an inflection point at $\sim 1/3$ ML coverage but then subsequently diverge. This divergent behavior is attributed to the changing orientation of the phenyl group with coverage. At a full monolayer, the net change in the workfunction for the two molecules have opposite signs, which can be explained using a quantitative model based on a surface and molecular dipole moments.

SS-TuP3 MORTON S. TRAUM AWARD FINALIST: Understanding Molecular Adsorption on Graphene-based Hybrid Nanostructures by In Situ Infrared Microspectroscopy, E. Mattson§§, S. Cui, K. Pande, H. Pu, M. Schofield, G. Lu, M. Weinert, M. Gajdardziska-Josifovska, J. Chen, C. Hirschmugl, University of Wisconsin Milwaukee

Graphene is an emerging platform for many applications, and being a strictly two-dimensional material, is particularly sensitive to atomic and molecular adsorption. These characteristics have made graphene-based materials a rising candidate for sensing applications targeting harmful chemicals which pollute our living environment. While under ideal ultra high vacuum (UHV) conditions, graphene monolayers have demonstrated single molecule detection sensitivity, such performance is not feasible under realistic operating conditions. To further improve sensitivity of graphene towards gas detection, we have performed controlled functionalization of graphene with oxygen and decoration with nanoparticles (NPs), where the graphene films act as a sensitive conduction channel, while oxygen functional groups, defects and NPs provide active adsorption sites. While these materials yield impressive performance, little is known about the chemical nature of the substrate/adsorbate interactions. To this end, we have performed *in situ* synchrotron-based infrared microspectroscopy (IRMS) on these atomically thin, micrometer-scale hybrid graphene materials during exposure to the environmentally significant gases NO₂ and NH₃ under *normal working conditions* (e.g., atmospheric pressure at low concentrations of target gases). Under such conditions, native functional groups are naturally present on the hybrid surfaces and may in fact contribute to the sensing processes. We have investigated hybrid sensing materials consisting of both chemically and thermally reduced graphene oxide (RGO) and chemically RGO decorated with tin dioxide NPs using transmission electron microscopy (TEM) and synchrotron-based IRMS. Experiments were performed at the synchrotron radiation center (SRC) in Stoughton, WI using the recently commissioned infrared environmental imaging (IRENI) beamline. Our studies of the as-produced materials have identified the native functional groups at the hybrid surfaces which are present under normal working conditions. As-produced chemically reduced GO contains functional groups due to residual carbonyl and epoxide species, while SnO₂-decorated RGO contains surface hydroxyl groups, adsorbed water and surface carbonyl groups. We then performed *in situ* IRMS upon exposure to gases to identify the chemical nature of the adsorbates and the resulting changes in the surface composition and

electronic properties of the substrate materials. *In situ* IRMS results for NH₃ and NO₂ adsorption on RGO and SnO₂-decorated RGO will be presented.

SS-TuP4 MORTON S. TRAUM AWARD FINALIST: Layer-by-Layer Assembly of Organic Molecular Donor-Acceptor Heterojunctions on Vicinal Gold Surfaces, J. Wang§§, J.-M. Tang, G.P. Miller, K. Pohl, University of New Hampshire

Molecular co-self-assembly of technological-relevant organic electron-donor and electron-acceptor molecules into ordered heterostructures on surfaces provides a fundamental molecular-level insight into how these two kinds of molecules would interact in a model organic photovoltaic cell with appropriate electrodes. I will present a study of the self-assembly of functionalized pentacenes (electron donors) and fullerenes (electron acceptors) into a layer-by-layer heterojunction on stepped gold surfaces by scanning tunneling microscopy (STM) characterization and density functional theory (DFT) calculations. The pentacene derivative -- 6,13-dichloropentacene (DCP) -- forms a striking long-range ordered brick-wall self-assembled monolayer (SAM) on a stepped Au(788) vicinal surface, with the long-axis parallel to the step edges [1]. Subsequently deposited fullerene (C60) molecules form parallel triple, double, and single long molecular chains on top of the intact DCP SAM on Au(788) [2]. The novel organic-metal and organic-organic interfacial interactions, as well as the adsorption geometry, have been explored by DFT. The adsorbed C60's form parallel commensurable (3:2) molecular chains on top of the DCP lattice -- three fullerenes line up with two DCP molecules along the long axis. The initial C60 chains grow along the upper step edges of the DCP/gold terraces. The observed adsorption position for the second C60 chain is the trough between two DCP molecular rows in accordance with the DFT calculations. The calculated C60-chain spacing of 1.1 nm agrees well with the experimental result. This subtle chain formation is attributed to the delicate balance of intermolecular interactions, interfacial dipolar interactions, and stepped-substrate interactions. The electronic properties for this model 3-component organic/metallic system, such as charge transfer between donors and acceptors, between the gold substrate and the molecular layers, will be discussed.

[1] J. Wang, I. Kaur, B. Diaconescu, J.-M. Tang, G. P. Miller, and K. Pohl, *ACS Nano* **5** (2011) 1792.

[2] J. Wang, J.-M. Tang, G. P. Miller, and K. Pohl, in preparation, (2012).

SS-TuP5 MORTON S. TRAUM AWARD FINALIST: Synthesis and Characterization of Yttrium Aluminum Garnet and Lanthanum Zirconate Particles, R.R. Harl§§, S.L. Gollub, G. Walker, B.R. Rogers, Vanderbilt University

Rare-earth doped yttrium aluminum garnet (YAG) and lanthanum zirconate (LZO) are luminescent ceramics that have been used in TV's, LED's, metal oxide transistors, and as laser sources. These materials are thermally and chemically stable. Recent work at Vanderbilt by the Walker and Rogers research groups has shown that the emitted spectrum of proton irradiated LZO particles differs from that of non-irradiated particles, suggesting these materials may be used as passive radiation exposure indicators.

We will discuss the combustion synthesis and characterization of YAG and LZO particles. Combustion synthesis involves heating a mixture of metal nitrates and a fuel until the mixture ignites. If the proper conditions are used, the energy released by the combustion is sufficient to form polycrystalline material. The type and amount of fuel used in the synthesis affect the amount of gaseous by-products produced and flame temperature achieved during a reaction, both of which affect the crystallite size formed. The organic fuels included in this study are urea and glycine with adiabatic flame temperatures 1780°C and 1210°C, respectively. Urea's higher flame temperature makes this fuel attractive for combustion syntheses. However, urea shows signs of degradation beginning around 120 °C, well below its ignition temperature. Glycine does not appear to degrade until approximately 230°C much closer to its ignition temperature. The trade-off between degradation and adiabatic flame temperature suggests the temperature ramp rate used will significantly affect the performance of combustion syntheses carried out with these fuels.

We will present results of detailed thermogravimetric analysis and differential scanning calorimetry (TGA/DSC) experiments used to study the effects of heating rate on the combustion process and on the characteristics of the material formed. TGA/DSC-determined heats of combustion and heat capacities of the reactants and products will also be presented.

* Morton S. Traum Award Finalist

Characterization results of powders made using conditions determined by the TGA/DSC experiments will also be presented. X-ray photoelectron spectroscopy (XPS) was used to determine chemical bonding information. Rutherford backscattering spectroscopy (RBS) was used to provide quantitative elemental composition of the material. X-ray diffraction (XRD) was used to determine the crystallinity of the material and to estimate crystallite sizes. Photoluminescence spectroscopy (PL) was used to characterize the materials' emission spectra.

SS-TuP6 The Influence of the Magnetic Field on the Photo-Functional Property of TiO₂/Ni/TiO₂ Thin Films Prepared by Sputtering. *A. Toyoda, I. Takano,* Kogakuin University, Japan

Since the photoinduced decomposition of water on TiO₂ electrodes were discovered, various characteristics based on photocatalyst have attracted extensive interest. TiO₂ is anticipated as one of materials which are alternative for an existing solar cell based on silicon. TiO₂ shows relatively high reactivity and chemical stability under UV light whose energy exceeds a band gap of 3.2 eV in the anatase crystalline phase. The sun can provide an abundant source of photons, however, UV light accounts for the only small fraction (5 %) of the sun's energy compared to the visible region (45 %). Many techniques have been examined to achieve this purpose.

In this study, the glass (Corning#1737) was used as the substrate. After the TiO₂ layer was prepared by reactive magnetron sputtering using a Ti target in an Ar/O₂ gas mixture, the Ni layer was deposited by using DC sputtering. Finally the TiO₂ layer was coated on the Ni layer. The TiO₂/Ni/TiO₂ multi-layer films were constituted with the first TiO₂ layer of 100 - 200 nm, second Ni layer of 25 nm and the third TiO₂ surface layer of 0 - 100 nm. Composition and microstructure of these films were investigated by X-ray photoelectron spectroscopy and X-ray diffraction, respectively. Chromatic change of a methylene blue solution was applied to photocatalytic evaluation. Light irradiation to TiO₂ films in a methylene blue solution was carried out using a commercial sterilizing lamp as ultraviolet light and an artificial sun lamp as visible light. Transmittance of a methylene blue solution was measured by a spectrophotometer. In this experiment the relationship between the photocatalytic effect and the magnetic field was investigated. Magnets with magnetic field intensity of 0.15 - 0.23 T were placed on the outside of a methylene blue cell. We anticipated that the magnetic field affected separation of an electron and a hole.

The XRD patterns of TiO₂ prepared by reactive magnetron sputtering showed anatase (101) and rutile (110) of TiO₂. The anatase content for the crystal structure of the TiO₂ was 82 %. When the magnetic field was applied in the parallel direction to the substrate surface, the TiO₂/Ni/TiO₂ thin film with the thinner TiO₂ surface layer, i.e. the third layer of 50 nm, showed the higher photocatalytic property. It was clear that the magnetic field affected a photocatalytic property.

SS-TuP7 Photo-function Property of TiO₂/Cu₂O Thin Films by Reactive Magnetron Sputtering. *T. Nakajima, I. Takano, S. Arahara,* Kogakuin University, Japan

Characteristics based on photo-inducement of TiO₂ have attracted various interests in many fields. One of those characteristics is a photocatalytic effect. The photocatalytic effect shows antifouling or antimicrobial activity and also has the ability to decompose environmental pollutants. The most important characteristic as a photocatalyst of TiO₂ is well known that photo-excited state is very stable and does not cause self-decomposition. Therefore, the electrolysis of water is performed under ultraviolet irradiation to TiO₂. However the light reaction region of TiO₂ is limited at ultraviolet region corresponded with only about 3 % of sunlight.

In this study, to improve the photo-function property of TiO₂ the double layer films were fabricated by the constitution of the TiO₂ layer with 3.0 - 3.2 eV and the Cu₂O layer with 2.2 eV in a band gap energy. Each constitution of the film with TiO₂/Cu₂O and Cu₂O/TiO₂ was also investigated about optical permeability. Furthermore, to prevent diffusion of Cu from the Cu₂O layer to the TiO₂ layer, the TiN layer was inserted between the TiO₂ layer and the Cu₂O layer. TiN has a high melting point, stability and the suitable electric property as a barrier layer. Those TiO₂/Cu₂O and TiN were fabricated by reactive magnetron sputtering. Composition and microstructure of these films were investigated by X-ray photoelectron spectroscopy and X-ray diffraction, respectively. Chromatic change of a methylene blue solution was applied for the photocatalytic evaluation. Light irradiation to the sample in a methylene blue solution was carried out using a commercial sterilizing lamp as ultraviolet light and an artificial sun lamp as visible light. Transmittance of a methylene blue solution was measured by a spectrophotometer after irradiation for 6 hours by each lamp.

The XRD pattern of the TiO₂/Cu₂O thin film showed the strong peak of the anatase-rutile TiO from an upper layer and the weak peak of Cu₂O from lower layer. The suitable photocatalytic effect was obtained by the constitution of TiO₂ with 300 nm and Cu₂O with 200 nm in thickness, when

the photocatalytic effect showed about 31 % under an artificial sun lamp and about 90 % under a sterilization lamp. In the case of the TiO₂/TiN/Cu₂O film it was estimated that the diffusion of Cu was prevented by inserting TiN from the XRD pattern, however, the high photocatalytic effect was not obtained. It was considered that the photocatalytic effect depended on thickness of the TiN layer.

SS-TuP8 Atomic Arrangements and Structural Stability of the Mn Adsorbed GaAs(001) Surfaces. *A. Hagiwara,* The University of Electro-Communications (UEC-Tokyo), Japan, *A. Ohtake,* National Institute for Materials Science (NIMS), Japan, *Y. Kanno, S. Yasumura, J. Nakamura,* The University of Electro-Communications (UEC-Tokyo), Japan

Epitaxial growth of MnAs on the zinc-blende (ZB) GaAs substrate has been extensively studied, because MnAs with ZB has been predicted to be half-metallic. In order to understand the growth mechanism of MnAs on GaAs, it is necessary to clarify the initial adsorption sites of Mn and to determine the well-defined structure of the Mn-adsorbed surface. It has been reported that a variety of (2x2) structures on the GaAs(001) surface appears depending on the coverage of Mn and on the pressure of incident As molecular beams [1]. The local structures which appear with the Mn coverage of 0.25 monolayer under the As-rich condition have been analyzed using electron diffraction and scanning tunneling microscopy (STM); this surface consists of the buckled Ga-As dimer and one Mn adatom in a (2x2) unit cell. However, the initial adsorption site for Mn has not been clarified yet. On the other hand, STM experiments have also shown that the configuration of buckled dimers is not well-ordered anywhere between neighboring unit cells: Local (4x2) or (2x4) arrangement is observed. In this study, first, we determine the position of the Mn atom in the (2x2) unit cell using first-principles calculations based on the spin density-functional theory. Next, in order to explore the onset of the local disordering of dimers, we employ (4x2), (2x4), and c(2x4) models as well as (2x2) and evaluate interactions between the Ga-As dimers.

We have revealed that the Mn atom prefers to adsorb at the site between Ga-As dimers along the dimer row of the (2x2) surface and the simulated STM images agree well with the experimental ones. Next, we have calculated the structure models which represent the different configurations of the dimers on the surface. It has been found that the (4x2) configuration, in which the Ga-As dimer and the As-Ga one align alternately along the dimer row, is most stable. In order to test what contributes to the stabilization of this configuration, we decompose the total energy into each constituent energy term. The Hartree and core-electron terms for (4x2) are lower than those for (2x2). The electronic charges transfer from Ga to As in the dimer structure, which results in the dipole formation at the dimer site. From this point of view, the (4x2) configuration, in which the adjacent dipoles are antiparallel with each other, has the energy gain because of the preferable dipole-dipole interactions. Therefore, the disordered configuration observed locally at the (2x2) surface can be attributed to the stabilization of the local (4x2) unit. This work was partially supported by Grant-in-Aid for Scientific Research (B) (No.22360020).

[1] A.Ohtake *et al.*, submitted.

SS-TuP9 Facets and Surfaces Observed on Si(5 5 12) Studied by using Ultra-High-Vacuum Scanning Tunneling Microscopy. *S.-G. Zhao, Y. Li, Y.-B. Song, Y.-Z. Zhu,* Yanbian University, China, *J.M. Seo,* Chonbuk National University, Republic of Korea, *S. Zhang, Z.-P. Guo,* Yanbian University, China

Si(5 5 12)-2x1 surface, which attracts much attention for one-dimensional (1-D) metal nanowire growth on the surface, usually appears wider area single domain with well ordered 1-D structure. In this work, phenomenon of the facets observed on the Si(5 5 12) surface is studied systematically by using ultra high vacuum scanning tunneling microscopy. On the well defined Si(5 5 12) surface, in addition to (1 1 3) facet and (6 9 17) facet, some components (and/or facets) can be observed on the surface as well, such as (7 7 17), (3 3 7), (1 1 2), (1 1 1)-5x5, (1 1 1)-7x7. It is considered that the surface orientations from Si(7 7 17) to (5 5 12), are stable and have almost the same surface free energy, i.e. it is weak anisotropic on the γ -plot. But the (3 3 7), (1 1 2), (1 1 1)-5x5, and (1 1 1)-7x7 facets are appeared to be confined delicately by the surface tensions and the driving force of the single domain growth of the stable surface and facet, which is accompanied by the process of the reconstruction of the surface. Acknowledgement: This work was supported by the National Natural Science Foundation of China (10964014 and 10864008).

References:

- [1] A. A. Baski, S. C. Erwin, L. J. Whitman, *Surf. Sci.*, 392, 69 (1997).
- [2] S. Jeong, H. Jeong, S. Cho, *et al. Surf. Sci.*, 557, 183 (2004).

- [3] H. Kim, H. Li, Y.-Z. Zhu, J. R. Hahn and J. M. Seo, *Surf. Sci.* 601, 1831 (2007).
- [4] C. Herring, *Phys. Rev.* 82, 87–93 (1951).
- [5] V. A. Shchukin and D. Bimberg, *Rev. Mod. Phys.* 71, 1125 (1999).
- [6] R. J. Phaneuf, N. C. Bartelt, and E. D. Williams, et al., *Phys. Rev. Lett.* 67, 2986–2989 (1991).
- [7] Y.-Z. Zhu, H. Kim, J.-M. Seo, *Phys. Rev. B.*, 73, 245319 (2006).

SS-TuP10 Photoelectron Spectroscopy and Valence Band Studies of Non-Stoichiometric Superconducting $\text{FeSe}_{1-x}\text{Te}_x$. *L. Huerta, V. Ortiz*, Universidad Nacional Autonoma de Mexico, *M. Flores*, Universidad de Guadalajara, Mexico, *R. Escamilla*, Universidad Nacional Autonoma de Mexico

Polycrystalline samples of $\text{Fe}(\text{Se}_{1-x}\text{Te}_x)$, with $x = 0.0, 0.25, 0.50, 0.75$ and 1.0 , were synthesized by solid state reaction. The samples were characterized by x-ray diffraction (XRD), measurements magnetization vs. temperature and photoelectron spectroscopy (XPS). Results of x-ray diffraction shows that the effect of the substitution of Se by Te is increase the lattice parameters. Curves of magnetization vs. temperature shows superconductivity for $x = 0.25, 0.5$ and 0.75 . Whereas, x-ray Photoelectron spectroscopy (XPS) identified the oxidation states of Fe 2p, Se 3d and Te 3d core levels associated with the chemical states $\text{Fe}(\text{Se}_{1-x}\text{Te}_x)$. Finally we compared the Valence Band obtained by XPS for each concentration of tellurium with the density of states electronic (DOS) reported.

SS-TuP11 Photovoltaic Property of $\text{Cu}_2\text{O}/\text{Cu}/\text{TiO}_2$ Thin Films Prepared by Reactive Magnetron Sputtering. *Y. Suzuki, I. Takano*, Kogakuin University, Japan

Recently, TiO_2 is considered as one of attractive materials. Since the photoinduced decomposition of water on the TiO_2 electrode was discovered, the photocatalysis based on semiconductor property has attracted extensive interest. TiO_2 is an n-type semiconductor with a band gap energy of 3.0 - 3.2 eV and is well known as a versatile material. From the view of solar cells TiO_2 is applied in development of dye-sensitized solar cells (DSSCs) or quasi-one-dimensional TiO_2 nanotube structure. On the other hand Cu_2O is a p-type semiconductor with a direct band gap of 2.0 eV and is a promising material on solar cell applications because of its nontoxicity, low cost and high absorption coefficient in the visible region. In this study, the photovoltaic property of p- $\text{Cu}_2\text{O}/\text{n-TiO}_2$ solar cells which was prepared by magnetron sputtering was investigated. Furthermore Cu buffer layer between TiO_2 and Cu_2O was used to obtain high efficiency.

$\text{Cu}_2\text{O}/\text{Cu}/\text{TiO}_2$ thin films with p-n heterojunction were fabricated by reactive magnetron sputtering. Firstly, glasses (Corning#1737) and ITO-film coated glasses as a substrate were ultrasonically cleaned by an acetone rinse. The TiO_2 thin film was deposited on glass substrates using pure metallic titanium (99.99%) as a sputtering target material in an oxygen gas atmosphere. The flow rates of a sputtering argon gas and an oxygen gas were 20 sccm and 1.5 sccm, respectively. Secondly, the Cu thin film was deposited on the TiO_2 thin film using pure metallic copper (99.99%) as a sputtering target material. Thirdly, the Cu_2O thin film was deposited on the Cu/TiO_2 thin film. The flow rates of a sputtering argon gas and an oxygen gas were 15 sccm and 10 sccm, respectively. Each thickness of the TiO_2 and Cu_2O layer was about 100 nm and 200 nm. Composition and microstructure of these films were investigated by the X-ray photoelectron spectroscopy and the X-ray diffraction. Transmittance of the TiO_2 and Cu_2O thin film was measured by a spectrophotometer. The photovoltaic property was evaluated by measuring the current-voltage curve.

The $\text{Cu}_2\text{O}/\text{Cu}/\text{TiO}_2$ thin films with p-n heterojunction were successfully fabricated by reactive magnetron sputtering. The XRD diffraction pattern of TiO_2 layers deposited at an oxygen flow rate of 1.5 sccm showed a mixture structure. The open voltage of $\text{Cu}_2\text{O}/\text{Cu}/\text{TiO}_2$ thin films showed a higher value under artificial sun light than $\text{Cu}_2\text{O}/\text{TiO}_2$ thin films. It was confirmed that the buffer layer of Cu improved the photovoltaic property of $\text{Cu}_2\text{O}/\text{TiO}_2$ thin films.

SS-TuP12 Measurement of pH Induced Transition in Redox Potential for Cerium Oxidation States in Nanoceria. *S. Saraf*, University of Central Florida, *A.S. Karakoti*, Pacific Northwest National Laboratory, *S. Barkam, S.S. Seal*, University of Central Florida

Cerium oxide is an important technological materials and widely used in catalytic converters in automobiles, solid oxide fuel cells, and fuel additives, etc. Recently, it has been discovered that Nanoceria has the ability to kill cancer cells. In addition, it is found that nanoceria can mimic superoxide dismutase (SOD) and catalase activities both of which are essentially the enzymes in the body that are responsible for disproportion of superoxide and peroxide respectively. All of the previously stated applications use the dynamic nature of valence states transition in Nanoceria and makes it electrochemically active. This study is specifically

designed to measure nanoceria's redox potential associated with its transition in biological media to fine-tune its further applications. In biological media, the pH also affects the transition characteristics in nanoceria. It is imperative to measure potential-pH diagram for nanoceria as well. In this study we propose to find redox potential of cerium oxide exposed to various pH by the use electrodes made up of nanoceria embedded onto platinum and nickel mesh substrates. Redox reactions are monitored by using cyclic voltammetry experiments. The redox potential of different ceria synthesis is compared at various pHs. Surfaces of Nanoceria are characterized using SEM, XPS and TEM. A complete picture of potential-pH diagram of Nanoceria is presented.

SS-TuP13 XPS and STM Studies of Metal Dopant-Ceria Mixed Oxide Interfaces. *J. Zhou, E. Ginting*, University of Wyoming, *Y.H. Zhou*, Xiamen University, China

Ceria has attracted great attentions in catalysis due to its unique redox properties and oxygen storage capacity. To improve the properties of ceria, suitable metal dopants such as Ti and Mn can be incorporated into it and form dopant-ceria mixed oxides. The additional metal component can modify the physical/chemical properties of ceria. To understand the intriguing chemistry at the metal dopant-ceria interfaces, we examined their structures at the nano-scale using X-ray photoelectron spectroscopy (XPS) and scanning tunneling microscopy (STM) techniques. Dopants including Ti and Mn were vapor-deposited onto well-ordered reducible $\text{CeO}_2(111)$ thin films grown on Ru(0001) under ultrahigh vacuum conditions. Both Mn and Ti are oxidized at the cost of ceria reduction upon deposition at 300 K. Ti is in the +4 formal oxidation state. However, +2 state of Mn is the predominate species on ceria. STM studies show the formation of two-dimensional structures on ceria which can further develop into chain structures or triangular domains upon heating. Our studies suggest a strong interaction between metal dopants and ceria. The nature of dopant-ceria interfaces greatly depends on the dopant type. The research is sponsored by the School of Energy Resources at University of Wyoming.

SS-TuP14 Phosphonic Acids for Surface Initiated Polymerization from Oxide Nanoparticles and Flat Surfaces: Towards Applications in Organic Electronics. *S.A. Paniagua, Y. Kim, N. Doubina*, Georgia Institute of Technology, *C.K. Luscombe*, University of Washington, *J.W. Perry, S.R. Marder*, Georgia Institute of Technology

In this work, tailor-made phosphonic acids are used as surface initiators for the growth of both dielectric and semiconductor polymers from barium titanate nanoparticles and transparent conductive electrodes respectively. For capacitor applications, grafting the polymer from the barium titanate surface gives a composite with high permittivity due to the inorganic inclusions as well as high breakdown strength, mechanical flexibility, and ease in processability due to the organic polymer. The polymer is grown using an atom transfer radical polymerization with catalyst in the ppm level and can be done with limited presence of air. The amount of polymer grown can be controlled in order to fabricate devices with varying polymer content to study its influence in device performance. Devices are created by simple blade casting without the need for any ball milling.

For transparent electrodes in solar cells, the growth of the donor phase directly from the substrate could lead to new morphologies, long term stability, and increased charge collection. We recently published a paper describing the growth of polymethylthiophene from ITO and some of its electrochemical properties.[1] Currently we are working on the optimization of the procedure to obtain smooth, thick polymer brushes that can be used to fabricate devices. Ongoing work involves X-ray photoelectron spectroscopy characterization of the starting monolayers and intermediate metallated species.

[1] Doubina, N.; Jenkins, J. L.; Paniagua, S. A.; Mazzio, K. A.; MacDonald, G. A.; Jen, A. K. Y.; Armstrong, N. R.; Marder, S. R.; Luscombe, C. K. *Langmuir* 2011, 28, 1900-1908.

SS-TuP15 Determination of Active Surface Region in Pure and Modified TiO_2 Photocatalysts. *T. Luttrell, J. Tao, M. Batzill*, University of South Florida

A novel approach for determining the photo catalytically active surface region is presented. In this method the photo activity of well-defined epitaxial anatase and rutile TiO_2 thin films is measured by methyl orange decomposition. The photo activity as a function of film thickness then enables to extract the active surface region, which is closely related to the bulk charge carrier diffusion length. Using this methodology we are able to compare differences in the photoactive region of anatase and rutile polymorphs of TiO_2 as well as to investigate the effect of dopants (nitrogen and tungsten) on the depth of the active surface layer. The latter highlights

the trade-off between enhanced (visible light) absorption and reduction of active volume of the photocatalyst. These studies are the first that quantifies the differences in rutile and anatase and the influence of dopants on charge carrier diffusion and thus photocatalytic activity.

SS-TuP16 Basic Regimes and Reaction Mechanisms of Chemi-current Generation during H₂ Oxidation on Catalytic MIM Nanostructures with Porous TiO₂ Support. *M. Hashemian, S. Dasari, E. Karpov,* University of Illinois at Chicago

Fundamental charge transfer processes and chemical reaction mechanisms at gas-solid interfaces require better understanding for catalysis, advanced sensing, and energy conversion and storage applications. Here, we report on distinct regimes of hydrogen oxidation reaction on catalytic Pt/TiO₂/Ti porous nanostructures with a potential barrier, identified via analysis of long term chemi-current kinetics recorded in the course of the surface reactions. Three regimes in total have been observed, where the reaction turnover rate, thermal effect and chemi-current production efficiency vary by orders of the magnitude. One the regimes is characterized with a nearly negligible thermal effect, but a surprisingly high yield of 0.1-0.4 electrons per water molecule produced, being highly encouraging for novel energy conversion applications of the present system. Correlations between occurrence of the distinct regimes and conditions in the gas phase are also established.

SS-TuP17 Photo-patternable Superhydrophobic Porous TiO₂ Films Prepared by Hydrothermal Treatment. *S. Nishimoto, M. Becchaku, Y. Kameshima, M. Miyake,* Okayama University, Japan

In recent years, highly porous TiO₂ surfaces prepared by hydrothermal treatment using aqueous alkaline solutions have attracted great interest due to their unique architectures, which include TiO₂ nanotubes and nanowires. These nanostructured surfaces can potentially be used as filtration membranes, high-surface-area electrodes, and photocatalysts for environmental purification. In addition to these applications, porous TiO₂ surfaces are considered to be suitable for use as functional surfaces that undergo photostimulated wettability conversion that changes them from being superhydrophobic to being superhydrophilic. However, to the best of our knowledge, no studies have been conducted on potential applications of such superhydrophobic-superhydrophilic surfaces. In this paper, we report the preparation of superhydrophobic TiO₂ surfaces by hydrothermally treating Ti plates with concentrated NaOH solution and then washing them in deionized water and HCl and subjecting them to heat treatment and surface modification with octadecylphosphonic acid (ODP). Rough nanostructured anatase TiO₂ surfaces with many pores were prepared by the hydrothermal treatment. Surface modification with self-assembled monolayers (SAMs) of ODP made the surface superhydrophobic with a static water contact angle (CA) of about 174°. This superhydrophobic surface could be converted into a superhydrophilic surface with a water CA of nearly 0° by irradiating it with ultraviolet light as the result of photocatalytic decomposition of the ODP SAM. Thus, the large wettability contrast of the surface, with a water CA difference of over 170°, would allow this photostimulated wettability conversion porous films to be used in many applications including offset printing, cell growth, spotting of biomolecules fluidic microchips, site-selective immobilization of functional materials, and so on.

SS-TuP18 High Hydrophobic Surface with Metabolic System using Organic Monolithic Structure. *M. Sakai,* Kanagawa Academy of Science and Technology, Japan, *T. Kato, A. Nakajima,* Tokyo Institute of Technology, Japan, *A. Fujishima,* Science University of Tokyo, Japan

Recently, the importance of controlling the wettability on the solid surface is recognized in various industries. Superhydrophobic surfaces with water contact angles exceeding 150° are currently the subject of great interest and intensive study. Superhydrophobic coatings that produce rough surfaces at the micro- and nanoscale level with low surface energies have been prepared by several methods. However, the practical applications have been limited, because the superhydrophobic coatings suffered from physical/chemical durability. In the current paper, the super hydrophobic coating with the high physical/chemical durability was designed using organic monolithic structure with TiO₂ photocatalyst and polytetrafluoroethylene particles. The structure was formed by nanoscale frames with 3-dimensional co-continuous, which was composed of epoxy resin. Therefore, the surface with micro structures newly appeared when the top surface was scratched by physical force. Moreover, the organic frame of top surface was slowly decomposed by TiO₂ photocatalyst. Then, the grimy surface could be removed by water fluid (ex. rain). The appearance of fresh micro structure might be similar to metabolic system in a plant. We evaluated the durability performance of the superhydrophobic coating in accelerated weathering test and wear resistance test. In these results, the superhydrophobic coating has kept outdoor durability for 6 years.

SS-TuP19 Adsorption of Water on a Hydrophobic Sb(111) Surface. *A. Chakradhar, J. Shan, Z. Yu, U. Burghaus,* North Dakota State University

The adsorption of water is studied on Sb(111) single crystals by using temperature programmed desorption (TPD) and molecular beam scattering. The surface of Sb(111) is characterized by auger electron spectroscopy (AES), low energy electron diffraction (LEED), and x-ray photoelectron spectroscopy (XPS). Interestingly, water TPD shows only a single peak at ~155 K while recording the parent mass of water obeying zeroth-order kinetics. The fact that the water monolayer peak is missing, suggests that the Sb(111) surface is hydrophobic. In addition, the results show that the antimony surface is inert towards the adsorption of small molecules such as CO, CO₂, and NO. Moreover, the co-adsorption of n-butane and water shows site blocking effects for n-butane adsorption only at very large pre-exposures of water, indicating the formation of a porous water film, as expected for a hydrophobic surface.

SS-TuP20 Insulating Si(111) Surfaces by Organic Fluorine Compound Molecular Monolayer. *F.Y. Tian, A.V. Teflyakov,* University of Delaware

Both trifluoroethylamine (TFEA) and p-fluoroaniline (pFA) were modified on Si(111) surfaces as insulators by forming Si-N bond through wet-chemistry. Fluorine functional groups are good chemical building block and tracking label for X-ray photon spectroscopy (XPS). Infrared spectroscopy (IR) was also employed to identify the surface Si-N bonding information. The experiment strategy is starting from native oxidized silicon (111) wafers, hydrogen-terminated Si(111) samples were obtained through modified RCA cleaning method and HF/NH₄F etching. Then, the H-Si(111) wafers were treated with PCl₅ to get Cl-terminated Si(111) surfaces. Finally, the samples were reacted in TFEA and pFA/THF solution, respectively, at inert atmosphere at room temperature for a variety reaction period. The formation of molecular monolayer of TFEA and pFA was confirmed by both XPS and IR. Density functional theory (DFT) was also applied to mimic both TFEA and pFA's behavior on Si(111) surfaces. In addition, due to various basicity and electron drawing capabilities, TFEA and pFA presented different reactivity towards Cl-terminated Si(111) surfaces.

SS-TuP21 Methanol Induced Nanopatterning of Si(111):H – Insights from Density Functional Calculations. *P. Thissen, T. Peixoto, K. Roodenko,* University of Texas at Dallas, *E. Fuchs,* Zyvex Labs LLC, *W.G. Schmidt,* University of Paderborn, Germany, *Y.J. Chabal,* University of Texas at Dallas

The reaction of methanol with hydrogen terminated Si(111) surfaces has been studied using density functional theory (DFT). Depending on the chemical potentials of hydrogen and methanol several surface configurations with various coverage are found to be stable. The temperature dependence of the chemical potentials as well as the entropy contributions to the surface free energy are found to result in only minor changes of the calculated surface phase diagram. In contrast, the calculated reaction barriers are found to be strongly dependent on the methoxy coverage of the surface. They strongly increase with increasing methoxy coverage. Our calculations thus suggest that the formation of a nanopatterned Si(111) surface, featuring 1/3 methoxy and 2/3 hydrogen termination as observed experimentally is related to the reaction kinetics rather than the surface thermodynamics. Consequently, we show that higher temperatures are the key parameter to prepare Si(111) surfaces with higher methoxy-group coverage than 1/3. Finally, a Kinetic Monte Carlo algorithm is applied to investigate the adsorption and the desorption rates until the surfaces reaction reaches the temperature-dependent equilibrium state. We find the reaction of methanol with hydrogen terminated Si(111) to be self-limited at temperatures over 400 K, since the methanol starts to react with itself.

SS-TuP22 Reactivity of Propane on Pd Oxide Phases Prepared by Surface Oxidation vs. Reduction. *C. Hakanoglu, J.F. Weaver,* University of Florida

We used temperature-programmed reaction spectroscopy (TPRS) to study the reactivity of propane on oxidized Pd(111) surfaces that were prepared by partially oxidizing Pd(111) as well as partially reducing a PdO(101) thin film in ultrahigh vacuum. These experiments were motivated in large part by recent observations of multiple phases co-existing during the autocatalytic thermal decomposition of a PdO(101) thin film, and the possibility that such phases exhibit distinct reactive properties. We find that the surface reactivity toward propane oxidation increases monotonically with increasing surface oxygen concentration, but that the reactivity exhibits a slight hysteresis as a function of oxygen coverage for surfaces prepared by Pd(111) oxidation vs. PdO(101) reduction. Based on the observation that propane desorbs in distinct features from different Pd-oxide phases, we determined that the hysteresis in reactivity arises from differences in the amount of PdO(101) domains present on partially oxidized vs. reduced surfaces and present evidence that propane reacts exclusively on PdO(101) domains even when a mixture of surface phases is

present. We show that deconvolution of the propane desorption traces also allows us to estimate the relative fractions of surface phases which develop during both oxide growth and reduction, and thus provides a means to quantify the phase evolution as a function of oxygen coverage. The analysis demonstrates that metallic domains as well as phases characteristic of monolayer oxides, so-called surface oxides, develop during the early stages of reduction of a multilayer PdO(101) film and appear to form on top of the multilayer oxide. This finding clarifies the nature of new structures that were observed in prior STM studies of PdO(101) film decomposition, and provides key insights for understanding the processes governing oxide decomposition.

SS-TuP23 Structural Properties of TbO_x Thin Films Grown on Cu(111). *W.S. Cartas*, University of Florida, *T.E. Milstrey, J.F. Weaver*, University of Florida

The oxides of the rare earth metals Tb, Pr and Ce are desirable for several catalytic applications due to their ability to store and release oxygen atoms. In contrast to ceria, terbium surfaces have not been widely investigated, and may exhibit interesting structural behavior since several bulk Tb oxide phases are known to exist. In this study, we investigated the growth of terbium oxide (TbO_x) thin films on Cu(111) in ultrahigh vacuum, using scanning tunneling microscopy (STM) and low energy electron diffraction (LEED) to characterize the surface structures. We used a stepwise procedure to prepare the TbO_x films, with each step involving Tb deposition onto Cu(111) held at 300 K in an O₂ background to produce an ~1 monolayer (ML) film, followed by annealing in O₂ at 750 K. The TbO_x films grow epitaxially on the Cu(111) substrate to generate TbO_x(111) with unit cell dimensions of about (1.4 x 1.4) relative to the Cu(111) lattice. STM images show that the TbO_x films (~2 - 5 ML) are comprised of large, flat terraces and reveal an atomic-structure consisting of hexagonal, close-packed arrangements of atoms that are separated by rows of oxygen vacancies at a spacing of about 2.2 nm. Estimates of the vacancy concentrations suggest that the oxide stoichiometry corresponds to an O:Tb ratio between 1.67 and 1.71, which agrees well with the composition of the stable iota phase of bulk terbium. The capability of preparing TbO_{1.7}(111) films with well-defined arrangements of vacancies may provide new opportunities for preparing model catalyst surfaces and studying the interactions of molecular reactants with ensembles of vacancies. Such studies are currently in progress.

SS-TuP24 Modeling of Chemical Reaction – Induced Thermal Currents in Metal Nanofilm – Semiconductor Schottky Diodes. *I. Nedrygailov*, University of Duisburg-Essen, Germany, *E. Karpov*, University of Illinois at Chicago, *E. Hasselbrink, D. Dising*, University of Duisburg-Essen, Germany

Chemically induced currents (chemicurrents) in metal nanofilm – semiconductor contacts attracted considerable attention of the surface physics and chemistry community since McFarland, Nienhaus *et al.* reported a direct detection of hot electrons and holes, excited by a surface chemical reaction, using Schottky diodes under zero-bias voltage conditions. This phenomenon is highly promising for studying the dynamics of elementary chemical processes on the interface between the gas phase and a solid surface. The use of the chemicurrents for ultrafast chemical sensing and direct conversion of energy of surface chemical reactions into electricity is also currently discussed. As a matter of fact, the mechanism underlying the chemicurrent generation and detection is a subject of ongoing discussions due to the presence of unavoidable thermal effects, accompanying surface chemical reactions, which hamper an unambiguous identification of the experimental data. In this contribution we report on a simple theoretical model for estimating the

magnitude of the chemical reaction - induced thermal currents in metal nanofilm – semiconductor Schottky diodes. As well, we present a comparison of our calculations with the experimental values of the chemicurrents reported earlier.

SS-TuP25 Synthesis, Characterization and Catalytic Activity of Pt Nanoparticles Supported on γ -Al₂O₃ and WC: Size and Support Effects. *M. Ahmadi, L. Merte, B. Roldan Cuenya*, University of Central Florida

Direct-methanol fuel cells (DMFC) are one of the promising candidates for alternative clean energy generation. Extensive efforts are going on to improve the efficiency of these cells using different Pt-based catalyst. Although tungsten carbide (WC) shows similar electronic structure as Pt and has promising catalytic properties, it is not extensively used due to its instability. However, it has been observed that one monolayer of Pt on the surface of WC displays a similar performance as bulk Pt and furthermore, it stabilizes the WC, which makes it a very cost-effective alternative for Pt electrodes. In this work we have synthesized size- and shape-selected Pt nanoparticles (NPs) via inverse micelle encapsulation methods. The NPs

were then supported on WC and γ -Al₂O₃ nanocrystalline powders as well as on WC/W thin films. We have investigated the size and morphology of our NPs by atomic force microscopy (AFM) and by transmission electron microscopy (TEM) and their chemical composition by X-ray photoelectron spectroscopy (XPS). Methanol oxidation was carried out in a packed-bed mass flow reactor and mass spectrometry was employed to quantify the catalyst's activity as a function of the NP size. The evolution of the structure of the Pt NPs during the oxidation of methanol was investigated under operando conditions using extended X-ray absorption fine-structure spectroscopy (EXAFS).

SS-TuP26 Ligand Functionalized Cerium Oxide Nanoparticles – Investigating the Mode and Energetics of Binding. *A.S. Karakoti, Z. Lu, W. Wang, P. Nachimuthu, H. Wang, P. Yang, S. Thevuthasan*, Pacific Northwest National Laboratory

Despite the significant amount of work done on functionalization of nanoparticles for various applications, studies on the determining the fundamental molecular level interaction between the various ligands and nanoparticle surfaces have been limited due to the inherent challenges associated with the characterization of highly reactive and dynamic nature of these particles. In order to obtain a fundamental understanding of nanoparticle-ligand interaction, cerium oxide nanoparticles (ceria) functionalized with simple ligands such as carboxylic acids were studied to characterize the nature of bonding, configuration of ligands and the energetics of the ligand-nanoparticle interactions. Mono-disperse ceria nanoparticles were synthesized by thermal hydrolysis process and functionalized with carboxylic acid groups from various organic ligands. The size distribution and morphology of the nanoparticles prior to and following functionalization were characterized by various imaging and spectroscopy tools to ascertain the integrity of nanoparticles. In-situ x-ray photoelectron spectroscopy (XPS) from aqueous solution of functionalized ceria nanoparticles frozen at liquid nitrogen temperature was performed to avoid any surface contamination and preserve the chemistry of the functionalized nanoparticles. XPS data suggests that the following functionalization the ceria nanoparticles predominantly exist in Ce⁴⁺ oxidation state. From XPS elemental quantification it was found that the oxygen from carboxylate molecules becomes a part of the ceria lattice to maintain the stoichiometry and bind to the ceria surface in bidentate orientation. Sum frequency generation vibration spectra (SFG-VS) showed the presence of OCO modes of vibration on the surface of cerium oxide confirming the bidentate mode of bonding between carboxylate and ceria nanoparticle surface. In addition isothermal titration calorimetry was used to determine energetics of ligand binding on the surface of nanoparticles. Results from these characterizations were combined with the periodic density functional theory (DFT) calculations to develop a complete visualization of the interaction of organic ligands with nanoparticle surfaces.

SS-TuP27 In Situ Coarsening Study of Micellar Pt Nanoparticles Supported on γ -Al₂O₃: Pretreatment and Environmental Effects. *J. Matos, L.K. Ono, F. Behafarid, J.R. Croy, S. Mostafa*, University of Central Florida, *A.T. DeLaRiva, A. Datye*, University of New Mexico, *A.I. Frenkel*, Yeshiva University, *B. Roldan Cuenya*, University of Central Florida

The thermal stability of micellar Pt nanoparticles (NPs) supported on nanocrystalline γ -Al₂O₃ was monitored in situ under different chemical environments (H₂, O₂, H₂O) via extended x-ray absorption fine-structure spectroscopy (EXAFS) and ex situ via scanning transmission electron microscopy (STEM). Drastic differences in the stability of identically synthesized NP samples were observed upon exposure to two different pre-treatments. In particular, exposure to O₂ at 400°C before high temperature annealing in H₂ (800°C) was found to result in the stabilization of the micellar Pt NPs, reaching a maximum overall size after coarsening of ~1 nm. Interestingly, when an analogous sample was pre-treated in H₂ at ~400°C, a final size of ~5 nm was reached at 800°C. The beneficial role of oxygen for the stabilization of small Pt NPs was also observed in situ during annealing treatments in O₂ at 450°C for several hours. In particular, while NPs of 0.5 ± 0.1 nm initial average size did not display any significant sintering (0.6 ± 0.2 nm final size), an analogous thermal treatment in hydrogen lead to NP coarsening (1.2 ± 0.3 nm). The same sample pre-dosed and annealed in an atmosphere containing water only displayed moderate sintering (0.8 ± 0.3 nm). Our data suggest that PtOx species, possibly modifying the NP/support interface, play a role in the stabilization of small Pt NPs. Our study reveals the enhanced thermal stability of micellar Pt NPs and the importance of the sample pre-treatment and annealing environment in the minimization of undesired sintering processes affecting the performance of nanosized catalysts.

SS-TuP28 Synthesis, Characterization and Reactivity of Cu-Zn and Cu-Pd Bimetallic Nanoparticles, H. Mistry, L. Merte, B. Roldan Cueyna, University of Central Florida

Bimetallic nanoparticles have become an important area of study because of their unique catalytic properties. We describe the synthesis and characterization of bimetallic copper-zinc and copper-palladium nanoparticles. The Cu-Zn and Cu-Pd bimetallics are synthesized using inverse micelle encapsulation in PS-P2VP diblock copolymers. The size and morphology of these nanoparticles supported on SiO₂/Si(111) and TiO₂(110) are characterized using atomic force microscopy (AFM), as well as scanning tunneling microscopy (STM) under ultra high vacuum. Characterization of electronic and chemical properties is carried out using x-ray photoelectron spectroscopy (XPS). Applications of these nanoparticles supported on γ -Al₂O₃ for the catalytic synthesis of methanol will be shown.

SS-TuP29 CO Oxidation over Au/TiO₂ Model Catalyst, T. Fujitani, I. Nakamura, AIST, Japan

In this work we have investigated the reaction mechanism and active sites for CO oxidation over the Au/TiO₂ model surface and Au single crystal surfaces, along with the role of moisture CO.

We examined the effect of moisture on the CO₂ formation rate at the reaction temperature of 300 and 400 K. The CO₂ formation rate at 300 K was increased significantly with increasing H₂O partial pressure up to 0.1 Torr, and then gradually decreased with H₂O pressure. In contrast, no promotional effect of H₂O was observed at the reaction temperature of 400 K. The moisture has an essential role to promote the CO oxidation reaction over Au/TiO₂ catalyst at low temperature, whereas the CO oxidation reaction proceeded without moisture with high reaction temperature. This important observation indicates that the CO oxidation mechanism over Au/TiO₂ is different between 300 and 400 K, considering that the activation process of oxygen molecules strongly depended on a reaction temperature. That is, molecular oxygen has been activated directly over the Au surface at the high temperature while the moisture takes part in the activation of the oxygen molecule at low reaction temperature.

Next, we examined the turnover frequencies (TOFs) for CO₂ formation at the two reaction temperatures as a function of mean gold particle diameter. To determine whether the active sites for CO oxidation were exposed gold atoms on the gold particles or perimeter sites at the interface between the gold particles and the TiO₂ support, we calculated the TOFs in two ways: (i) by normalizing the total number of exposed Au atoms at the gold particles (TOF-S) and (ii) by normalizing the the total number of gold atoms at the perimeter interfaces (TOF-P). The results clearly showed that the relationship between TOF and mean gold particle diameter depended strongly on reaction temperature. At 300 K, TOF-S decreased with increasing mean gold particle diameter, whereas TOF-P remained nearly constant regardless of particle diameter, suggesting that the active sites for CO oxidation were the gold atoms located at the periphery of the gold particles attached to TiO₂. In contrast, TOF-S at 400 K remained nearly constant regardless of the mean gold particle diameter, indicating that the active sites for CO oxidation were newly created on the gold metal surface at the high temperature. Thus, we can conclude that both the reaction mechanisms and the active sites differed between the low temperature region and the high temperature region.

SS-TuP30 Active Sites for H₂ Dissociation on Gold Model Catalyst, I. Nakamura, T. Fujitani, AIST, Japan

Au nanoparticles supported on metal oxides are highly active for various hydrogenation reactions. The dissociation of H₂ molecules is one of the most important elementary steps in hydrogenation reactions, and the nature of H₂ dissociation sites has been the subject of various studies. Recently, we demonstrated using Au/TiO₂(110) that the perimeter interface between Au and TiO₂ was the active sites for H₂ dissociation. However, the oxidation state of Ti and the structure of Ti oxide at the perimeter interface are not entirely clear. Here, we performed H₂-D₂ exchange reaction using TiO_x/Au(111) and TiO_x/Au(100) (x = 0-2), and clarified the influence of the oxidation state of Ti and the Au and TiO₂ structures on the creation of active sites for H₂ dissociation. We found that the presence of stoichiometric TiO₂ was essential for the creation of H₂ dissociation sites over the Au surfaces. The activation energies (E_a) for HD formation over TiO₂/Au(111) and TiO₂/Au(100) were consistent with each other, and these E_a agreed well with that for Au/TiO₂(110). This result shows that the active sites for H₂ dissociation created on TiO₂/Au(111) and TiO₂/Au(100) were identical to those formed on Au/TiO₂(110). Furthermore, we demonstrated that turnover frequencies (TOFs) for HD formation were close among these three surfaces, where TOFs were calculated by normalizing the number of HD molecules formed per second to the total number of Au atoms at the perimeter interfaces. These results clearly indicate that the active sites for H₂ dissociation over TiO₂/Au(111) and TiO₂/Au(100) were the perimeter

interface between TiO₂ and Au. Concerning the structure of TiO₂ on Au surfaces, LEED observations showed that the TiO₂ produced on Au(111) was the ordered structure, in contrast to disordered TiO₂ structure on Au(100). Thus, the creation of active sites for H₂ dissociation was independent of the Au and TiO₂ structures consisting perimeter interface. We concluded that local bonds between Au and O atoms of stoichiometric TiO₂ (Au-O-Ti) create the active sites for H₂ dissociation.

SS-TuP31 Image Potential State Mediated Excitation of Rubrene on Graphite, J. Park, Seoul National University, Republic of Korea, T. Ueba, L. Terawaki, T. Yamada, H. Kato, T. Munakata, Osaka University, Japan

Electronic excitation at the interface between an organic molecular film and a substrate is of general importance for the area of organic electronics and light conversion processes. We demonstrate rubrene/HOPG as a model system for an organic film/substrate interface. Many efforts have been devoted to improve the performance of a rubrene thin film transistor after high carrier mobility was achieved for rubrene single crystals. The reasons for the poor efficiency of the thin films are attributed to the molecular geometry on the surface. To understand the mechanisms of charge transportation for organic molecular devices, it is the primary step to unravel the molecular electronic structures of both occupied and unoccupied states at interfaces between the film and the substrate.

We have performed two-photon photoemission (2PPE) spectroscopy for rubrene films formed on HOPG substrate. It is revealed a prominently enhanced unoccupied molecular peak, which is resonantly excited from the highest occupied molecular orbital (HOMO). Interestingly, the enhancement of the peak becomes less significant at the coverage higher than 1 monolayer, where the image potential state (IPS) peak on the substrate disappears. The resonance enhancement is moderate with s-polarization, by which the transition to IPS is completely suppressed. We ascribe that the excitation of the level is mediated by the IPS on HOPG. Though the IPS wave function extends outside the molecules, it interacts with the unoccupied molecular orbital at the edges of molecular islands, causing the strong resonance enhancement of the unoccupied molecular level.

By clarifying the mechanism, the excitation process is expected to be useful to highly enhance the efficiency of organic molecular devices and light conversion processes. The energy of IPS is generally governed by the work function. It may be possible to tune the IPS level nearly resonant to an unoccupied level of organic films. This provides a way to tailor the electronic excitation efficiency.

SS-TuP32 Tribiological Properties in a Vacuum of DLC Thin Films Prepared by N₂⁺ Ion Beam Assisted Deposition, H. Nishi, K. Harada, I. Takano, Kogakuin University, Japan

DLC (Diamond-like carbon) classified in new materials is amorphous carbon including hydrogen and has the similar property to diamond. DLC films were formed by the ion beam evaporation method in the early 1970's and after that have been manufactured by various methods. Because the representative property of DLC shows the high hardness and low friction coefficient, DLC is applied in various fields such as motor parts or tools. The ion beam assisted deposition method has many parameters on the film formation condition in comparison with other dry process methods. Therefore this method was anticipated in production of new characteristics such as a high adhesion film.

From the result of our research, DLC thin films prepared by the ion beam assist method using an N₂ gas showed the excellent low friction coefficient in the atmosphere. In this study, the behavior on friction in a vacuum of those DLC films was investigated. The DLC films were formed using N₂⁺ ion beam assisted deposition in a toluene (C₇H₈) atmosphere. The formation conditions of DLC films were changed with an ion beam current density and an accelerating voltage. Stainless steels (304SS) were used for the sample substrate. The mechanical properties of hardness and friction coefficient were measured using the dynamic micro knoop hardness tester and the ball-on-disk tribotester respectively. Atomic concentration and structure of the films were investigated by X-ray photoelectron spectroscopy and Raman spectroscopy. The friction coefficient in a vacuum was measured under 5 x 10⁻⁴ Pa. The conditions of the ball-on-disk test were 0.98 N in a weight and 135 rpm in a sliding speed.

The suitable friction property of DLC films was obtained by the condition with an accelerating voltage of 5 kV at a current density of 10 μ A/cm². The minimum friction coefficient in a vacuum was 0.016 for an SUJ2 ball of the counter material, however, the DLC thin film started to cause partial peeling-off in a sliding distance of 52 m. It is anticipated that the property in a vacuum of these DLC films is applied in space technology.

SS-TuP34 Atomic Structure of the Bi-induced (1×3) Surface Reconstruction on GaAs(001). *A. Duzik, J.C. Thomas, A. Van der Ven,* University of Michigan, *N.A. Modine,* Sandia National Laboratories, *J.M. Millunchick,* University of Michigan

Bismuth (Bi) is a nearly ideal surfactant on GaAs owing to its large size relative to Ga and As, smoothing the surface morphology of the GaAs(001) surface. Surface modification in this manner is potentially useful in high-quality device growth, but corresponding atomic structure and its effects on subsequent device growth are unknown. Reflection high-energy electron diffraction indicates that the Bi surfactant induces a (1×3) surface reconstruction. Experimental scanning tunneling microscopy clearly shows a nm-length-scale step structure with a high density of alternating up/down steps and reconstruction rows of ×3 periodicity. From these observations, we propose a mechanism for the Bi surfactant surface smoothing. The alternating step heights on the nm length scale are likely a result of a Bi-induced surface energy change. However, compositional disorder obscures the atomic structure within the rows. Thus, the atomic structure of the (1×3) reconstruction cannot be revealed through experiment, but must be determined from simulation.

Ab-initio density functional theory and cluster expansion calculations were carried out to determine the relative stability of reconstruction in the Bi/GaAs(001) system. Differences in stability originate from two sources: structure, determined by surface bonding topology, and configuration, arising from the arrangement of Ga, As, and Bi species over the surface dimer sites. For the Bi/GaAs system, the (2×1), α2(2×4), β2(2×4), (4×3), and c(4×4) reconstructions and their species configurations were considered. Calculations show the observed (1×3) reconstruction explained by the (4×3) structure first proposed for AlSb and GaSb, which has a large number of stable configurations at 0K. At typical growth temperatures, the calculated Monte Carlo entropy approaches that of ideal mixing, indicating thermal excitations of these configurations produce the experimentally observed disorder.

SS-TuP35 Spectroscopic Study of the Chemical Reaction at the Ca/PMMA Interface. *H.X. Ju, J.F. Zhu,* University of Science and Technology of China

PMMA is an important thermoplastic material which has been utilized in a variety of engineering areas ranging from aeronautical applications to electronics industries, due to its attractive physical and optical properties. The physical and chemical interactions have been observed at the interfaces between metals and PMMA, which can play a crucial role in the device performance. As a result, significant attention has been paid to the interfaces in order to promote devices performance and stability.

In this work, we investigate in detail the chemical reaction during deposition of Ca on the PMMA surface by applying X-ray photoemission spectroscopy (XPS) and near-edge X-ray absorption fine structure spectroscopy (NEXAFS), which provide detailed information concerning surface chemical reaction. The changes of the O 1s and C 1s core level XPS spectra indicate a strong interaction between the Ca and the PMMA. The O K-edge NEXAFS spectra give a comprehensive insight into reaction sites. In this way, the pronounced decrease of the π^* (C=O) resonance intensities with deposition of Ca clearly demonstrates that Ca atoms attack carbonyl groups in PMMA. The experimental results confirm the previous work regarding the adsorption microcalorimetry measurements of metal particles adsorption on polymer surfaces, which provide a powerful approach for determining the adsorption energy and understanding interfacial interactions. There is a high heat of Ca adsorption on PMMA surfaces of 780 kJ/mol, attributed to the reaction of each Ca reacts with 2 esters to form the Ca carboxylate. Furthermore, we provide addition information regarding the details of specific chemical interactions at the interface. These will greatly contribute toward further understanding of the interfaces between metals and polymers.

SS-TuP36 Mass Ratio Effects in Hyperthermal Surface Scattering. *D. Kulkarni, C.E. Sosolik,* Clemson University

The forward scattering of heavy ionic projectiles from oriented crystal surfaces gives evidence of collective effects that are far more pronounced than those seen in scattering of light ionic projectiles. For example, molecules containing heavy atoms such as XeF₂ are known to initiate novel surface chemistry effects. To study these kinematic trends, MD and trajectory simulations were performed for hyperthermal energy ions. By sequentially increasing the mass of the projectile across the periodic table, we have observed energy and angle resolved trends that show a clear deviation from standard scattering events, which are typically interpreted as sequential binary collisions. The simulation results were compared to experimental data for alkali ions on metal surfaces, specifically for the cases of K⁺ and Cs⁺ scattered from Cu(001).

SS-TuP37 Ag Nanoparticles on Reducible CeO₂(111) Thin Films: Effect of Nanoscale Ceria. *S.W. Hu, X.F. Feng, D.D. Kong, D.L. Cheng, Y.F. Ye, J.F. Zhu,* University of Science and Technology of China

Ag/CeO₂ is of particular interests because of its importance in technical applications as catalysts for many chemical reactions such as CO and hydrocarbon oxidation. However, there are still some discrepancies remaining in the fundamental recognition of the Ag/CeO₂ catalysts such as the oxidation state of Ag species and the mechanism of Ag-induced the reduction of CeO₂. In order to obtain a detailed insight of the Ag/CeO₂ system, the growth and structures of Ag nanoparticles on CeO_x(111) thin films with different thicknesses, morphologies and reduction degrees have been systematically studied by scanning tunneling microscopy (STM), X-ray photoelectron spectroscopy (XPS) and low energy electron diffraction (LEED). These CeO_x(111) thin films were epitaxially grown on Cu(111). It is found that in most cases Ag exhibits the three-dimensional (3D) growth with constant particle densities on the CeO_x(111) surfaces. Ag only populates the sites at the ceria-ceria step edges, independent of the thicknesses and the reduction degree of the ceria films. Moreover, the particle density is directly proportional to the number of step edges of ceria, which is related to its thickness on Cu(111). On the reduced ceria films, Ag nanoparticles do not nucleate on point defects. Upon heating, the Ag nanoparticles undergo serious sintering before desorption at 800 K on the fully oxidized CeO₂ films. While on the reduced ceria films, the sintering and desorption process are slowed down at the same annealing temperatures as those on CeO₂. This result suggests that although the surface point defects have no influence on the growth behavior of Ag, they can enhance the thermal stability by inhibiting the diffusion of Ag on the ceria surface to form large particles during annealing.

Tribology Focus Topic

Room: Central Hall - Session TR-TuP

Tribology Poster Session

TR-TuP1 Nanomechanical and Nanotribological Responses of Si/SiO₂ Interfaces. *F.-Y. Lin, X. Sun, D.E. Yilmaz, S.R. Phillpot, S.B. Sinnott,* University of Florida

Nanomechanical and tribological responses of semiconductor/gate oxide interfaces have been demonstrated to significantly affect the performance of devices. Here, we use classical molecular dynamics (MD) simulations to investigate these responses at the atomic scale. The simulations utilize the variable charge, empirical charge optimized many-body (COMB) potential to describe the surface interactions and mechanical responses occurring within differing contacting interfaces. In particular, the mechanical response during nanoindentation and nanoscratching of a Si tip on SiO₂ and HfO₂ thin films is investigated to determine the influence of thin film structure and type on the measured properties as a function of normal load. In addition, the responses of crystalline and amorphous Si/SiO₂ sliding contacts are examined and the impact of operating environment and interfacial charge transfer on the tribological properties is explored.

This work is supported by the Office of Naval Research (N000141010165) and the National Science Foundation (DMR-1005779).

TR-TuP2 Origin of a Broad Band Emission in Triboluminescence during Friction between Diamond and Quartz in a Gas: Contribution of a Micro-discharge caused by Triboelectricity. *T. Miura,* National Institute of Occupational Safety and Health, Japan, *E. Imai, I. Arakawa,* Gakushuin University, Japan

The origin of triboluminescence of solid in air has been believed to be essentially photoluminescence excited by ultraviolet light from nitrogen discharge caused by triboelectricity (see Walton's review, *Adv. Phys.* Vol. 26 (1977) p.919.). In this study, we propose that electron-impact is a major and significant origin of the solid luminescence.

The experiment of friction between quartz and diamond was performed in rare gases or nitrogen by a pin-on-disk equipment in a vacuum chamber. A spatial distribution of the triboluminescence was observed by a microscope through the quartz disk and its spectrum was measured by a spectrometer.

Typical discrete lines due to the light emission of the gas discharge and a broad band (wavelengths of 300-600 nm) were observed in the triboluminescence spectrum. The microscopic measurement made it clear that the gas discharge occurred in a gap between quartz and diamond around the contact point and the broad band was emitted at the same place of the gas discharge.

By changing the gas pressure, however, we found that the discharge light almost vanished in the pressure range of 30-100 Pa of nitrogen, while the broad band emission intensely appeared in this range. The broad band

intensity became a maximum when a mean free path of electron in plasma was close to the gap distance of the discharge.

It has been known that the quartz was negatively electrified by friction with diamond. We have performed cathode-luminescence experiment for the same diamond sample. A broad band appeared in the spectrum of the cathode-luminescence was identical to the broad band of the triboluminescence.

In conclusion, gas discharge caused by triboelectricity induces cathode-luminescence of the solid. This is the main cause of the broad band in the triboluminescence. Contribution of the ultraviolet light of the nitrogen discharge to the solid luminescence, in contrast, is negligible.

TR-TuP3 Frictional Study of Carbon Nanotube Arrays Grown on Artificial Hip Joint Metal Surfaces, M. Yoshimura, K. Sumiya, Toyota Technological Institute, Japan

At present, a well-designed hip joint has a lifetime of 10-15 years. Since this is rather short compared with an increasing lifetime of human, there is great need to improve the durability and clinical lifetime of artificial joints. Reduction of wear debris through the coating of the material surface is one of methods to improve the durability. Here we grow carbon nanotube (CNT) array and composite film (CNT terminated with graphite layers) on the artificial bone surface (ASTM F75 (Co: 62 wt%, Cr: 30 wt%, Mo: 5 wt %)), and examine the tribological property by scratch measurement.

Alcohol chemical vapor deposition (ACVD) was employed to grow CNT arrays and composite films. Growth temperature, pressure and time were 800 C, 160 torr and 5 min. Ball-on-plate type tribo-test machine (Tribostation Type 32, Shinto Sci. Co., Ltd.) was employed. Normal loads were set at 50 g or 1 g. According to the recipe [1], CNT arrays standing perpendicular to the substrate and composite films were successfully grown on the ASTM surface. Tribological measurement with 50 g load reveals that both carbon film gives lower friction coefficient than a bare ASTM surface. In addition, CNT arrays showed a smaller friction than the composite films. SEM images of both surfaces after wear experiment under 1 g load show that CNT arrays fall flat to the substrate, and that cracks form in the graphite layers of the composite films. This study demonstrates possible use of CNTs as a solid lubrication for artificial hip joint metal materials.

[1] Y. Matsuoka et al., J. Vac. Sci. Technol. B29, 061801 (2011).

TR-TuP6 Comparative Study of Tribocorrosion Behavior of Biomedical Alloys Coated with Metal-Ceramic Multilayers, M. Flores, O. Jimenez, E. Rodriguez, Universidad de Guadalajara, Mexico, L. Huerta, Universidad Nacional Autonoma de Mexico

The tribocorrosion behavior of Ti6Al4V and CoCrMo alloys alone and coated with TiAlN/TiAl multilayers was investigated. The multilayers were deposited onto the alloys by magnetron sputtering. The structure and composition of multilayers were studied by means of XRD and RBS techniques respectively. The tribocorrosion was performed using a ball-on-flat reciprocating tribometer, the tests were conducted in a simulated body fluid at 36.5 ± 1 °C of temperature and 7.4 Ph. The loads used were between 1N and 5N, the oscillating frequency was 1Hz. The counterparts were Al₂O₃ balls 10 mm in diameter. The tribocorrosion and corrosion were studied using electrochemical techniques such as open circuit potential (OCP), electrochemical noise, potentiodynamic and potentiostatic polarizations in a simulated body fluid. The individual and synergistic effects of wear and corrosion on total wear loss were estimated. The worn surface was studied by means of profilometry. For the used conditions the CoCrMo alloys shows a high tribocorrosion resistance respect to the Ti6Al4V. The results indicate that multilayers improve the tribocorrosion resistance of both alloys.

Vacuum Technology

Room: Central Hall - Session VT-TuP

Vacuum Technology Poster Session and Student-built Vacuum System Poster Competition

VT-TuP2 Pressure Effects in Autoresonant Ion Trap Mass Spectrometers (ARTMS), P. Acomb, G.A. Brucker, J. Rathbone, Brooks Automation, Inc., Granville-Phillips Products

Autoresonant ion trap mass spectrometers (ARTMS) are gaining rapid acceptance in the vacuum market both as residual gas analyzers as well as process gas monitors. During the course of routine analysis, most ARTMS instruments are required to provide accurate analytical results over a wide range of total pressures and gas compositions. Since the performance of ion traps is pressure dependent, it is important to understand how total pressure impacts gas analysis results and to understand the methodologies available

to adjust operational parameters based on present pressure conditions. Important performance specifications that are affected by total pressure conditions include baseline offset, resolving power, sensitivity, dynamic range and fragmentation patterns. The pressure-related physical phenomena presently known to impact ion trap performance are identified and associated to the specific pressure ranges at which they are relevant. The ion trap operational parameters available to the user to optimize trap performance as a function of total pressure are explained. Vacuum practitioners presently using ARTMS instruments for gas analysis can quickly, easily and dynamically apply the concepts introduced in this poster to optimize the performance of their gas monitors as a function of total pressure conditions.

VT-TuP3 Investigation of a Method for Measurement of Water Vapor Coverage on Technical Surfaces, M. Sefa*, Laboratory Lotric d.o.o., Slovenia, J. Šetina, Institute of Metals and Technology, Slovenia

Coverage of a surface by a gas can be determined by desorption method where amount of gas is calculated by integrating the released flux. This can be measured fairly straight forward in a case when desorbed gas don't re-adsorb on surfaces of measurement chamber. Then mass conservation laws are applicable and flux can be determined by measurement of a pressure drop across the orifice of known conductance. In the case of adsorbing gas, like water vapor, the flux through the orifice is not equal to the flux coming from the sample, because significant amount can be re-adsorbed by the surfaces of measurement chamber. To determine surface coverage of water vapor on technical surfaces we have developed a special procedure where adsorption and desorption on the surfaces of measurement chamber can be taken into account. The sample is exposed to water vapor at known pressure (in the range from 0.1 kPa to 2.5 kPa) in a preparation chamber. After equilibration of surface coverage with the gas phase, the preparation chamber is opened to a measurement chamber which is continuously pumped through a known conductance. In the case of water vapor the shape of pressure burst is significantly influenced in the beginning by adsorption and later by desorption in the measurement chamber. However, the time integral of pressure burst over sufficiently long period represents the amount of water vapor coming from preparation chamber. This amount is sum of gas phase, desorbed amount from surfaces of preparation chamber and desorbed amount from the sample surface. In the presentation the measurement system will be described and examples of water coverage measurements on surfaces of Cu, Ni, Al and stainless steel will be given.

VT-TuP4 Flow of a Binary Gas Mixture Into Vacuum: Experiment, Models, Simulation, M. Vukovic, Tokyo Electron, US Holdings, R. Johnsen, University of Pittsburgh

The flow of gas through a small orifice into vacuum was experimentally analyzed by Fujimoto & Usami (1984). They developed a formula to describe the flow conductance as function of the orifice rarefaction parameter. R. Johnsen and B. K. Chatterjee (2011) measured the flow rate of a minority gas (H₂, O₂, CO₂) in a carrier gas (He, Ar) using the University of Pittsburgh ion drift tube experiment. Using the hard-sphere collision potential they also developed a heuristic formula to model the minority gas conductance rate as function of the carrier gas rarefaction parameter. In this work we generalize their formula to arbitrary intermolecular potentials. We also develop an alternative model and formula that successfully describes the data. We will describe the ion-drift tube experiment, discuss the two models and formulas. We will also present results of DSMC simulations using the Graem Bird's DS2V code (<http://www.gab.com.au>).

T. Fujimoto and M. Usami, ASME Trans. J. Fluids Eng. 106, 367 (1984).

R. Johnsen and B. K. Chatterjee J. Vac. Sci. Technol. A 29, 011002-1 (2011)

VT-TuP5 A Calibration System for Helium Leak Calibrator, Y.-W. Lin, C.-C. Hung, C.-P. Lin, C.-N. Hsiao, F.-Z. Chen, Instrument Technology Research Center, Taiwan

A calibration system for helium leak calibrator was developed, and the measurement uncertainty associated with the system. The design of the system took into consideration of influencing factors that include reference standard leak calibrator (ref.), leak calibrator under testing (dut.), vacuum chamber, He leak detector, I/O interface, and computer control. The system operates referring the standard test method for calibration of helium leak detectors by use of secondary standards (ASTM F78). This reference standard leak calibrator (ref.) was calibrated near 23°C by comparison with Flowmeter of the national institute standards and technology (NIST) primary Leak Standard, using a combination of direct flow and upper to lower chamber flow division technique. The present estimate of the total

* VT Student-Built Vacuum Systems Poster Competition

uncertainty in the measured leak rate of this artifact at 23°C at the time of test is 5.2%. This includes a systematic uncertainty of 2.0% in Flowmeter of the NIST primary Leak standard and 3.2% random errors in the measured leak rate of this artifact. The errors represent three standard deviations. In order to optimize the overall accuracy in the use of this artifact, it should be stored with any shutoff valve open (a dust cover can be used to protect the vacuum port). The leak artifact should be stored at the temperature at which it will be used for at least 24 hours and pumped for least 3 hours prior to use. Sufficient time should also be allowed for the system on which the leak artifact is to be used to come to equilibrium with the environment. The present research has demonstrated the high stability of the calibration system for helium leak calibrator, and its capabilities of conducting calibration for helium leak calibrator with great efficacy.

VT-TuP6 Status of the FRIB Vacuum System Design, P. Gibson, B. Durickovic, P. Guetschow, FRIB, R. Kersevan, CERN, M. Leitner, D. Leitner, L. Lingy, F. Marti, G. Morgan, FRIB, D. Sanderson, NSCL, M. Schein, M. Shupitar, FRIB

Facility for Rare Isotope Beams (FRIB), Michigan State University, East Lansing, MI 48824 USA

The Facility for Rare Isotope Beams (FRIB), a new national user facility for nuclear science funded by the U.S. Department of Energy - Office of Science and operated by Michigan State University (MSU), is currently being designed and established to provide intense beams of rare isotopes. It will enable scientists to make discoveries about the properties of these rare isotopes in order to better understand the physics of nuclei, nuclear astrophysics, fundamental interactions, and applications for society. The FRIB driver linac accelerates ions as heavy as 238U to energies beyond 200 MeV/u at beam powers up to 400 kW. Machine maintainability requires an average uncontrolled beam loss below 1 W/m. Baseline vacuum levels have been established to support this requirement and pumping systems have been defined. Vacuum levels in high loss regions such as beam stripping and collimation areas have also been evaluated and pumping systems defined. Value engineering has been applied to minimize the number of different vacuum pump and beam box types and sizes where possible. The pumpdown and operating vacuum of large, complex Target System chambers has been analyzed and pumping systems defined. This talk reports on the status of the FRIB vacuum system design.

This material is based upon work supported by the U.S. Department of Energy Office of Science under Cooperative Agreement DE-SC0000661

VT-TuP7 PLS-II Vacuum System Commissioning, C.D. Park, S. Chung, T. Ha, C.K. Kim, M.S. Hong, H.C. Kwon, Y.D. Joo, Pohang University of Science and Technology, Republic of Korea

è Pohang Light Source's upgraded machine (PLS-II) has been on commissioning stage since the installation completed in June 2011. PLS-II storage ring vacuum system is designed to maintain a base pressure in the low 10^{-9} Torr region for the beam-gas scattering lifetime in excess of 20 hours, and the vacuum components, especially photon absorbers, are designed to endure 3 GeV, 400 mA beam operation. Several issues regarding the vacuum system will be presented, such as BPM stability from mechanical or electrical point of view, vacuum chamber displacement, photon absorbers, and vacuum related events during the commissioning.

VT-TuP8 An Application of Electron Stimulated Desorption Technique to Measure the Isotherm and the Mean Residence Time of Hydrogen Physisorbed on a Metal Surface, H. Shimizu*, N. Inose, T. Miura, I. Arakawa, Gakushuin University, Japan

Physisorption characteristics of hydrogen on a cold metal surface were investigated in the range of a monolayer for the purpose of establishing a cryopumping technique in extremely high vacuum. Electron stimulated desorption (ESD) technique was applied to measure the adsorption density of hydrogen molecules. Hydrogen was adsorbed on a copper substrate at 3 - 4.2 K of temperature and was irradiated with a pulsed electron beam of a few hundreds nsec pulse width and 45 - 170 eV electron energy. ESD ions, H⁺, H₂⁺, and H₃⁺, were mass-separated by a time-of-flight measurement with the acceleration bias of 100 V. In submonolayer range, the signal intensity of ESD H⁺ was a useful measure for the amount of physisorbed H₂ and the monolayer completion of H₂, which was accompanied by two dimensional phase condensation, was detected by the rapid rise of H⁺ intensity followed by its saturation.

An adsorption isotherm was obtained as the ESD signal intensities of H⁺ as a function of the hydrogen pressure, which was gradually increased from 10⁻⁹ to 10⁻⁴ Pa so as to keep adsorption equilibrium. The observable lower end of the isotherm was 1x10⁻⁸ Pa of the equilibrium pressure and 0.001 of H₂ coverage, which was limited by back ground signal of H⁺ originated

from water or hydrocarbons adsorbed on the metal substrate. Though the validity of the assumption that the H⁺ desorption yields is proportional to the H₂ physisorption density should be further examined, the H⁺ yield curve between 1x10⁻⁸ and 2x10⁻⁶ Pa represents the adsorption isotherm between 1 and 0.001 of H₂ coverage.

Two transient methods were applied to measure the mean residence time, τ , of physisorbed H₂. A time development of ESD H⁺ intensity was monitored after either (1) a stepwise H₂ pressure rise to a certain fixed value or (2) YAG laser cleaning of the substrate under a constant H₂ pressure. In either case, the time constant of the increase of ESD H⁺ intensity is the direct measure of the mean residence time of H₂. Typical value of τ obtained by the method (1) at nearly monolayer and at 4.2 K was 62±3 sec, which corresponds to 1.19 kJ/mol of the adsorption energy on assumption of $\tau_0 = 10$ -13 sec.

The adsorption isotherms and the close examinations of the dependency of τ on the temperature and the coverage can reveal the fundamental properties of the hydrogen physisorption in low pressure and low coverage range.

VT-TuP9 Radiative Heating from a Magnetically Levitated Turbo Pump, H. Bull†††, CNSE, A. Antothe, SEMATECH, G. Kane, G. Denbeaux, CNSE

Thermal management within vacuum chambers is sometimes a concern for temperature dependent vacuum processes. We describe a phenomenon in which using a magnetically levitated turbo molecular pump causes internal heating of a chamber. We measured the heat load based on a thermocouple inside the vacuum chamber, exposed line of sight to the magnetically levitated turbo pump. The measurements showed a temperature change of more than 10C based on the heat load from the pump. We also measured the effect of any heating due to gas flows and found that the dominant effect was not related to gas flows and was likely simply radiative heat transfer from the pump. The source of the heating of the pump is likely Ohmic heating due to eddy currents in the turbo pump.

VT-TuP10 Novel Light Sputter Ion Pump with Neodymium Iron Boron Magnets and the Low Outgassing Body, T. Ha, S. Chung, C.D. Park, Pohang University of Science and Technology, Republic of Korea

A light sputter ion pump for ultra high vacuum was fabricated using 5-mm-thick neodymium iron boron (NdFeB) magnets. The weight of the pump was reduced by 30%, compared with conventional sputter ion pumps using ferrite magnets. For the sake of uniformity of magnetic field, three pieces of magnet were combined into a 100 mm x 150 mm magnet block for the 30 l/s pumping element. The authors coped with the low working temperature (below 150oC) of the NdFeB magnets by forming a pure and dense chromium oxide film on the inner surface of the stainless steel pump body. With this vacuum thermal oxidation, the outgassing rate of water and hydrogen was considerably reduced so that a high temperature bakeout was unnecessary. The ultimate pressure achieved by the developed pump was much lower than 10-10 mbar even with a low bakeout temperature at 100oC.

VT-TuP11 Expanded Capability of Measuring Pumping Speed of Dry Vacuum Pumps Using Calibrated Sonic Nozzles, W.S. Cheung, S.H. Nam, W.J. Kim, J.Y. Lim, KRISS, Korea

This paper addresses technical issues in expanding the capability of measuring the pumping speed of dry vacuum pumps using a built-up block of multiple calibrated sonic nozzles. The first challenging issue comes from the technical limit that their calibration results available from the flow measurement standard laboratories do not fully cover the low vacuum measurement range of 10 ~ 1000 mbar although the use of sonic nozzles for precision measurement of gas flow has been well established in national metrology institutes. In order to tackle the first technical issue, the constant volume flow measurement method dedicated for the vacuum range of 10 ~ 1000 mbar is exploited to calibrate the discharge coefficient multiplied by the cross-section area of each sonic nozzle used in the built-up block of sonic nozzles. On the other hand, the discharge coefficient multiplied by the cross-section area of each sonic nozzle in the upstream pressure range of 2 ~ 10 bar is calibrated in the gas flow standard laboratory. These combined calibration methods are illustrated to enable each sonic nozzle to cover the three decade measureable range 10 mbar ~ 10 bar. The second technical issue comes from a logical way of stacking multiple sonic nozzles to expand the capability of measuring the pumping speed of dry vacuum pumps. A target value of the upper limit of pumping speed in this work was selected to be 4,500 m³/h as the Korean flat display manufacturers requested to KRISS. On the onset of this work, sonic nozzles of 5 mm throat diameter were machined to fulfill the upper limit pumping speed by stacking three or four nozzles in the built-up block. Of course, small sized nozzles (0.1, 0.16, 0.5, and 1.0 mm throat diameter) were also machined in this work to cover the low and mid range of the throughput of 0.1 ~ 100 mbar-l/s. A prototype of the built-up block with the capacity of installing six sonic nozzles

* VT Student-Built Vacuum Systems Poster Competition

simultaneously is under test. Its design throughput was to be about 125,000 mbar-l/s. This prototype is expected to provide a possible 'on-line pumping speed tester' with the capability of 4,500 m³/h or more, applicable not only to the on-site flat display processes but also to the semiconductor processes.

VT-TuP12 Study on Improvement of Predictive Maintenance of Dry Vacuum Pumps Using an Adaptive Parametric Model of State Variables, S.H. Nam*, W.J. Kim, J.Y. Lim, W.S. Cheung, KRIS, Korea

This paper introduces unique statistical features extracted from the measured state variables of dry vacuum pumps in the semiconductor processes. They were found to have three distinctive means and overlapped distributions, not a single normal distribution. More specifically, two distinctive distributions near the upper and lower asymptotic bounds are obviously observed from the gas-loaded states of the vacuum pump and the third one from the idle states. These observations have provided new motivations of not only separating the pump operation state into the gas-loaded and idle states but also modeling the upper and lower bounds as a separated distribution. A linear adaptive parametric model (APM) is proposed such that their linear trends of each state variable are shown to be mapped onto their model parameters. Those estimated model parameters are used to construct the batch data obtained after each process. The APM-based batches are also exploited to construct the batches under the normal operating conditions (NOC) such that the major eigenvectors of the NOC batches are used to diagnose the current process batch data. It should be noted that the APM-based batch provides a dramatic reduction of memory usage and computation time (for example, 1~2 % memory usage and 10 times faster computation time) in comparison to the conventional dynamic-time wrapping methods. The feasibility of the proposed APM for the predictive maintenance of dry vacuum pumps is demonstrated to be successful by illustrating test results obtained from the six dry vacuum pumps.

This paper proposes the use of two statistics, the Hostelling's T² and the sum of squared residuals, in order to improve the reliability of the predictive maintenance and self-diagnostics of vacuum pumps. The first one is exploited to examine what amount of similarity the current process batch has in reference to the normal operation conditions and, furthermore, the second is to examine what contribution the current process batch provides to the noise space. The two proposed statistics are examined to quantitatively analyze the reliability and improvement of the predictive maintenance and self-diagnostics developed in this work.

VT-TuP13 Modeling of Energy Consumption Characteristics of Low Vacuum Dry Pumps, W.J. Kim, S.H. Nam, W.S. Cheung, KRIS, Republic of Korea, M.K. Ko, Konyang University, Republic of Korea, J.Y. Lim, KRIS, Republic of Korea

This presentation addresses measurements related to energy, utilities and materials usage on dry vacuum pumps. A particular course of action was taken into account with regard to the measurement into equivalent energy suggested by SEMI Document 4399.

Recent SEMATECH and SEMI studies showed that 50 ~ 60 % of equipment power is used for vacuum pumps. Currently vacuum pump suppliers have responded by reducing power consumption and cooling water flow requirement in energy consumption at the component level. Actual process studies showed that for some processes, the energy consumption level did not change significantly during idle and processing operation modes. However, specified studies in experimental scale to characterize the energy consumption pattern have not been reported yet.

We have performed a simulation study to characterize energy consumption pattern in the idle and process modes.

The pressure range of about 0.1 to 50 mbar for 7 minutes was assigned to the simulated process mode, meanwhile the pressure of <0.1 mbar for 3 minutes to the idle mode. The integrated characteristics evaluation system for dry vacuum pumps has been utilized to gather the dry pump characteristics data for the simulation. Roots, claw, classical screw, and multi-stage type vacuum pumps supplied from the manufacturers have been evaluated using the evaluation system in terms of ultimate pressure, pumping speed, power consumption, vibration, sound power as well as nitrogen purge, cooling water rate from the single pump monitoring system in time-synchronized mode. This study includes the application of the SEMI S23-0705 standards – A Guide for Conservation of Energy, Utilities and Materials Used by Semiconductor Manufacturing Equipment.

The estimated power consumption per pump per year was ranged from 10 to 30 MWh and 15 to 50 MWh for 600 ~ 1200 m³/h dry pumps in idle and processing modes, respectively. The utility energy consumption was also ranged from 5 to 10 MWh and 10 to 30 MWh, respectively. More specific energy consumption patterns with respect to the pressure are also presented.

In this work we suggest that the correlation mechanism dependant on the actual process lines should be carefully analyzed and furthermore understood, for example, the relationship between cooling water flow rate and temperature variation during processes. Simple characteristic modeling of energy consumption patterns dependent on dry and roots pump types are also discussed.

Acknowledgements: Results are partially attributed to two national projects (Contract Nos. 10031858 and 10031836) sponsored by the Korean Ministry of Knowledge Economy.

VT-TuP14 Dry Vacuum Pump, J.Y. Lim, W.J. Kim, S.H. Nam, KRIS, Republic of Korea, S.Y. In, Korea Atomic Energy Research Institute, Republic of Korea, D.Y. Koh, Korea Institute of Machinery and Materials, Republic of Korea, W.S. Cheung, KRIS, Republic of Korea

Advanced industrial processes such as semiconductor and display manufacturing continuously requires the precise measurement and control of the low mass flow of gases. The requirements include very low mass flows of less than 1sccm or 2×10^{-2} mbar-l/s. However, the lower limit of traceable mass flow ranges are not well defined even in the sophisticated NMIs (National Measurement Institute). Since the primary standard for mass flow (kg/s) must provide a method for deriving mass flow directly from its base units, almost all mass flow systems heavily rely on the gravimetric method. Current technical measurement limit of mass flow rate with the gravimetric method is 2×10^{-8} kg/s ($10^{-2} \sim 10^{-3}$ mbar-l/s).

Ensuring mass flow traceability ability in the range of greater than 10^2 mbar · l/s with the Korea Research Institute of Standards and Science (KRIS) standard system, an attempt to trace the lower mass flows down to 10^4 mbar · l/s has been undertaken with constant volume flow meters (CVFM), sonic nozzle systems, and orifice method. In this work we briefly demonstrate the systematic attempt for the completion of the traceability chain from 10^4 to 10^{-4} mbar · l/s.

Meanwhile the most effective way of ensuring completion of the traceability chain is, to say, characteristics monitoring of the mechanical rotary machines such as vacuum pumps used in advanced industry since these pumps have normally clean and smooth pumping capabilities during their stable operation.

Utilizing the combined mass flow systems mentioned above, the measurement of pumping speed has been performed with the throughput and orifice methods dependent on the mass flow regions. However, in the HV range of the molecular flow region, the high uncertainties of the gauges, mass flow rates, and conductance are too critical to precisely accumulate reliable data. In order to solve the uncertainty problems of pumping speeds in the HV range, we introduced an SRG with 1 % accuracy and CVFMs to measure the finite mass flow rates down to 10^{-3} mbar · l/s with 3 % uncertainty for the throughput method. In this way we have performed the measurement of pumping speed down to less than 10^{-6} mbar with an uncertainty of 6 %. In this article we suggest that the CVFM has an ability to measure the conductance of the orifice experimentally with flowing the known mass through the orifice chambers, so that we may overcome the discontinuity problem encountering during introducing two measurement methods in one pumping speed evaluation sequence.

VT-TuP16 An Evaluation of the Outgassing Rates of Stainless Steel Vacuum Chambers Subjected to Different Heat Treatments and Coatings, M.A. Mamun, Old Dominion University, P.A. Adderley, M.L. Stutzman, M. Poelker, Thomas Jefferson National Accelerator Facility

We present the results of an extensive study of the outgassing rates of four nominally identical stainless steel vacuum chambers. Chambers were either heat treated (semi-vacuum) at 400°C, coated with TiN, coated with SiO₂ (SilcoGuard™), or heat treated then coated with SiO₂. The outgassing rates were measured at a variety of room temperatures to determine the temperature dependence and compare to theoretical models of diffusion- or recombination-limited outgassing. In addition, outgassing rates were evaluated following venting to air and re-baking at 150°C and 250°C to simulate the impact of putting a chamber into service.

VT-TuP17 A Quantitate Examination of Venting Trapped Volumes Due to Fasteners, C. Bryson, Apparati Inc.

Why we care

The need addressed here is the problem of pumping out internal volumes in vacuum systems that may be blocked by construction methods. Vented screws are a common approach to reducing this problem. This discussion will focus on evaluating the magnitude of the problem and various solutions. Calculations on conductance for vented and unvented screws and some accessories will be given. These conductance values will be used to model different common configurations that have different amounts of trapped volumes.

* VT Student-Built Vacuum Systems Poster Competition

The conclusions are clear; vented screws and venting accessories are essential.

Summary

The direct measurements on un-vented screws were flawed because the screws tended to seal to varying degrees by the head of the screw. A use of a vented washer helped but the leak rate was hard to measure because of variability. Direct comparison to calculations is difficult because the tolerances in screw fasteners. There are large differences in conductance given the dimensions of the clearance between the screw and the mating fixtures. Calculating the ranges of conductance that can be expected for unvented screws, venting channels and internal volumes were done for different applications in vacuum systems. Ranges in excess of a factor >15 were encountered for a single divinition of a particular fastener. Some comparisons with data shed insight to the nature of the task.

The result is a "set of ground rules for design" based on the quantitative information derived. Examples are given for different designs with different parameters in terms of vacuum performance.

Wednesday Morning, October 31, 2012

Applied Surface Science
Room: 20 - Session AS-WeM

Surface Analysis of Biological Materials Using Vibrational & Non Linear Optical Spectroscopy Techniques (8:00-10:00 am) / 3D Imaging & Nanochemical Analysis - Part 1 (10:40 am-12:00 pm)

Moderator: R.P. Richter, CIC biomaGUNE & MPI for
Intelligent Systems, Spain, D. Roy, National Physical
Laboratory, UK, V.S. Smentkowski, General Electric Global
Research Center

8:00am AS-WeM1 Fibril Formation within the Extracellular Matrix, from Preventing Bacterial Infections to Artificial Tissue Generation, P. Koelsch, University of Washington **INVITED**

The ability to probe an interface beneath a layer of living cells *in vitro* without the need for labeling and fixation has the potential to unlock key questions in cell biology and biointerfacial phenomena. In particular fibril formation within the first steps of cell adhesion has been identified to play a key role for cell-implant interactions, for microbial biofilm formation on industrial surfaces, or for understanding basic phenomena in the context bacterial infections mediated through fibrillar assemblies. In this contribution we show how the technique of second-harmonic-generation microscopy and sum-frequency-generation spectroscopy can be utilized to detect ordered structures within tissue and at interphases between substrates and living, adherent cells. These were detected within the first steps of cell adhesion in real-time and *in vitro* with no labeling and/or fixation required.

References:

- [1] Diesner, M.-O.; Welle, A.; Kazanci, M.; Kaiser, P.; Spatz, J.; Koelsch, P., *In vitro* observation of dynamic ordering processes in the extracellular matrix of living, adherent cells. *Biointerphases* **2011**, 6, (4), 171-179.
- [2] Diesner, M. O.; Howell, C.; Kurz, V.; Verreault, D.; Koelsch, P., *In Vitro* Characterization of Surface Properties Through Living Cells. *J. Phys. Chem. Lett.* **2010**, 1, (15), 2339-2342.
- [3] Howell, C.; Diesner, M. O.; Grunze, M.; Koelsch, P., Probing the Extracellular Matrix with Sum-Frequency-Generation Spectroscopy. *Langmuir* **2008**, 24, (24), 13819-13821.

8:40am AS-WeM3 *In Situ* Monitoring of SDS Adsorption on Positively Charged Surfaces, S.-H. Song, P. Koelsch, T. Weidner, University of Washington, M.S. Wagner, The Procter & Gamble Company, D.G. Castner, University of Washington

Surfactants are important compounds used in many industrial applications, with sodium dodecyl sulfate (SDS) being one of the most widely used surfactant. This study uses vibrational sum-frequency-generation (SFG) spectroscopy and surface plasmon resonance (SPR) analysis to investigate molecular ordering and orientation within SDS films formed on positively charged surfaces. Substrates with different charge density and polarity include CaF₂ at different pH values and chemically modified CaF₂ and Au surfaces prepared by RF glow discharge plasma deposition of allylamine (AAm) films and heptylamine (HApp), respectively. SFG spectra were recorded in various spectral regions for SDS concentrations ranging from μ M to mM. At 0.2 mM SDS concentration, the intensity of CH and OH peaks decreased to background levels independently of the substrate. Previous studies have suggested that the SFG intensity minimum at 0.2 mM is due to neutralization effects of the positively charged (CaF₂) surface by the anionic charged head group of SDS.¹ In our studies, we found out that (i) the loss of SFG signal occurring at 0.2 mM is independent of surface charge density and (ii) SFG spectral intensities of lower concentrations vary significantly, whereas above 0.2 mM signals become reproducible. Therefore, in analogy to the behavior observed for alkane thiols on gold,² we interpret the loss of signal to a loss in order induced by a transition from a striped phase to a stand-up phase. As the number density of adsorbed SDS molecules increases above 0.2 mM, a second minimum in SFG intensity can be observed for all substrates, but at concentrations that are substrate dependent. Here we propose a model in which a monolayer is built up, but with opposing head group orientations (towards the substrate and the solution phase). This is supported by (i) SPR data showing a saturating number density towards SDS monolayer coverage at concentrations around the critical micelle concentration and above, (ii) a minimum for methyl vibrations related to an equal number in downward and upward orientations in the monolayer, and (iii) SFG spectral analysis for the polar SO₃⁻ band

revealed a band structure with two contributions of positive and negative phases. This can be associated to spectral shifts in close proximity to the substrate and opposing headgroup orientations (towards the substrate and the solution).

1. Becraft, K. A.; Moore, F. G.; Richmond, G. L., *Journal of Physical Chemistry B* **2003**, 107, (16), 3675-3678.
2. Schreiber, F., *Progress in Surface Science* **2000**, 65, (5-8), 151-256.

9:00am AS-WeM4 Enhanced Infrared Spectroscopy and Near-Field Microscopy with Infrared Antennas, T. Taubner, RWTH Aachen University, Germany **INVITED**

Infrared (IR) spectroscopy allows for the investigation of chemical, structural or electronic properties of a sample material by directly probing molecular, crystal lattice or charge carrier oscillations. Combined with scattering-type near-field optical microscopy (s-SNOM), which relies on the scattering of light at a sharp metallic tip, it is possible to obtain such spectroscopic information in images with strongly subwavelength spatial resolution [1-4] of typically about 20-30 nm. Currently, the main limitation of this technique comprises of the low signals that demand tunable laser sources and restrict the spectral range of operation.

Recently, new broadband IR light sources enabled s-SNOM near-field spectroscopy on different polar crystals [5], semiconductor nanostructures [6] as well as biominerals [7]. The majority of these experiments has been performed on samples which provide a resonant optical interaction between the sample and the probing tip, thus resulting in comparably strong signals. For the detection of weak molecular vibrations like polymers and proteins however, the SNOM signals either have to be enhanced or stronger IR light sources have to be developed.

Here we present a way to enhance the near-field probing process by suitable substrates [8], increasing both signals and contrasts in infrared s-SNOM when probing thin sample layers. In a next step, we investigate the use of resonant nanostructures ("infrared antennas", [9,10]) to enhance s-SNOM sensitivity even further. Additionally, we compare enhanced near-field spectra with the corresponding far-field spectra obtained by diffraction-limited FTIR-Microscopy. We will also present our latest results obtained with a new powerful broadband IR laser source that is currently developed at the Fraunhofer ILT.

References

- [1] T. Taubner, R. Hillenbrand, F. Keilmann, *APL* **85**, 5064 (2004).
- [2] R. Hillenbrand, T. Taubner, F. Keilmann, *Nature* **418**, 159 (2002).
- [3] A. Huber et al., *Nano Letters* **7**, 774 (2006).
- [4] B. Knoll, F. Keilmann, *Applied Physics Letters* **77**, 3980 (2000).
- [5] S. Amarie, T. Ganz & F. Keilmann, *Optics Express* **17**, 21794 (2009).
- [6] F. Huth et al., *Nature Materials* **10**, 352 (2011).
- [7] S. Amarie et al., *Beilstein J. Nanotechnol.* **3**, 312 (2012).
- [8] J. Aizpurua et al., *Optics Express* **16**, 1529 (2008).
- [9] F. Neubrech et al., *Physical Review Letters* **101**, 157403 (2008).
- [10] R. Adato et al., *PNAS* **106**, 19227 (2009).

9:40am AS-WeM6 FT-IR Spectrochemical Imaging: Applications with Focal Plane Array and Multiple Beam Synchrotron Radiation Source, M. Unger, E. Mattson, J. Sedlmaier, Z. Alavi, R. Dsouza, B. Manandar, C. Hirschmugl, University of Wisconsin Milwaukee

FT-IR spectrochemical imaging, which combines the chemical specificity of mid-infrared spectroscopy with spatial specificity, is an important demonstration of label-free molecular imaging. Mid-infrared optical frequencies are resonant with the vibrational frequencies of functional groups, thus an absorption spectrum is a "molecular fingerprint" of the material at every pixel. Each spectrum can be correlated with known material properties to extract chemical information. Synchrotron based FT-IR spectrochemical imaging, as recently implemented at the Synchrotron Radiation Center in Stoughton, WI, demonstrates the new capability to achieve diffraction limited chemical imaging across the entire mid-infrared region, simultaneously, with high signal to noise ratio.

IRENI [1] (Infrared Environmental Imaging) extracts a large swath of radiation ($320 \text{ hor.} \times 25 \text{ vert. mrad}^2$) to homogeneously illuminate a commercial IR microscope equipped with an infrared Focal Plane Array (FPA) detector. Wide field images are collected. IRENI rapidly generates high quality, high spatial resolution data. The relevant advantages (spatial oversampling, speed, sensitivity and signal to noise ratio) will be presented and demonstrated using examples from a variety of disciplines, including

formalin fixed [1] and flash frozen tissue samples [2], live cells, fixed cells, paint cross sections and polymer fibers will be presented.

* This work has been done with support from NSF (MRI-DMR-0619759 and CHE-1112433) and the Synchrotron Radiation Center, which is also supported by NSF (DMR-0537588) and UW-Milwaukee and UW-Madison.

[1] M.J. Nasse, et al. "High resolution Fourier-transform infrared chemical imaging with multiple synchrotron beams", *Nature Methods*, 8, (2011) 413-416

[2] M.Z. Kastyak-Ibrahim, et al. "Biochemical label-free tissue imaging with subcellular resolution synchrotron FTIR with Focal Plane Array Detector," *NeuroImage* 60, (2012) 376-383.

10:40am AS-WeM9 3D Analysis using X-ray Computed Tomography, S.R. Stock, Northwestern University **INVITED**

X-ray Computed Tomography (CT) can be performed on meter-sized objects or micrometer wide samples, and introduction of commercial x-ray tube-based instruments and dedicated synchrotron systems has produced an explosion of studies spanning the sciences and engineering disciplines. Using one of several numerical reconstruction methods, CT combines x-ray projections (radiographs) into a cross-sectional map, generally in 3D, of the x-ray absorption of the specimen. Other modalities (x-ray phase contrast, scattering, etc.) can also be used for reconstruction. The noninvasive interrogation allows the specimen to be studied multiple times during its evolution or to be returned undamaged to the museum collection.

This talk briefly introduces the fundamentals of x-ray CT and the different approaches to data acquisition and reconstruction. Most of the examples will focus on microCT, that is, reconstructions with isotropic volume elements (voxels) from 1-50 micrometers on edge. The first example is quantification of crack opening in a metal sample as a function of 3D position and applied load. In the second example, microCT data forms the basis of finite elements (FE) modeling of response of a spine of the sea urchin *Diadema setosum* to different applied loads. The third example illustrates local tomography, where data for high resolution reconstruction is only collected over a portion of the sample cross-section. Differences in x-ray phase contrast instead of x-ray absorption can be used as the basis for reconstruction; and the examples show how differences in polymers and soft tissues can be imaged using this approach. Intensity diffracted from the different phases within a specimen provide the basis for reconstructing the distribution of crystallographic phases; one example is SiC fibers in an Al matrix.

11:20am AS-WeM11 High Spatial Resolution 2D and 3D TOF-SIMS Analysis using Cluster Ion Beams, F. Kollmer, S. Kayser, ION-TOF GmbH, Germany, N. Havercroft, ION-TOF USA, Inc., D. Rading, R. Moellers, W. Paul, E. Niehuis, ION-TOF GmbH, Germany

Time-of-flight secondary ion mass spectrometry (TOF-SIMS) is a very sensitive surface analytical technique. It provides detailed elemental and molecular information about surfaces, thin layers, interfaces and full three-dimensional analysis of a sample. A major improvement especially for the analysis of molecular surfaces on a small scale has been the introduction of cluster ion beams that increases the sensitivity by orders of magnitude [1].

In recent years Bi clusters have become a standard primary ion species for all TOF-SIMS imaging applications providing a lateral resolution of down to 80 nm. Recent developments allow pushing the performance further towards the physical limits of the technique. Under optimized conditions we will present a lateral resolution of less than 20 nm by applying Bi₃ clusters on a certified reference material [2] and real world samples.

Usually for TOF-SIMS depth profiling and 3D-analysis, a dual beam approach is accomplished with dedicated analysis and sputter beams. However, the analysis of structures at greater depth (> 10 μm) needs long sputter times and the build-up of surface roughness at the crater bottom limits the achievable spatial resolution. In order to overcome these limitations we used a combined SIMS/FIB setup for the analysis of inorganic samples. Hereby, the Bi cluster beam is used to FIB mill a crater into a sample and the vertical crater wall is subsequently analysed by TOF-SIMS. We will present 2D and 3D data of reference samples, as well as, real world samples analysed by this approach.

The challenge of three dimensional analysis of molecular surfaces is to maintain the molecular structure of the exposed surface while removing the covering material. In this respect the development of new sputter ion sources using massive Ar clusters allows the preservation of molecular information under high dose sputtering [3]. This has enabled TOF-SIMS to do depth profiling and 3D analysis of organic materials. In our contribution we will present 3D analysis of an OLED display device using an Ar gas cluster ion beam for sputtering in combination with a Bi cluster beam for analysis.

[1] F. Kollmer, *Appl. Surf. Sci.* 231-232, 2004, 153-158

[2] M. Senoner, W. E. S. Unger, *Surf. Interface Anal.* 39, 2007, 16-25

[3] S. Ninomiya, K. Ichiki, H. Yamada, Y. Nakata, T. Seki, T. Aoki, J. Matsuo, *Rapid Communications in Mass Spectrometry* 2009, 23, 1601-1606

11:40am AS-WeM12 An Evolution of TOF-SIMS for Biological Analysis: From 2D Imaging to 3D FIB-TOF Tomography, G.L. Fisher, J.S. Hammond, S.R. Bryan, Physical Electronics

TOF-SIMS has become an important tool for 2D and 3D imaging mass spectrometry of biological and complex material specimens due to its unique capability to detect molecular and elemental ions at a spatial resolution of ≤ 300 nm, a mass resolution of ~ 15,000 m/Δm, and without the sample treatments or labeling required by e.g. MALDI or fluorescence microscopy. Among the advantages of TOF-SIMS are ~ 2 nm sampling depth, parallel detection and collection of the entire mass spectrum at every image pixel, and sensitivities in the ppm to ppb range. The ability to image surfaces having a large degree of topography while maintaining artifact-free chemical imaging is also highly desired; the resulting elemental and molecular images provide important information regarding the composition of biointerfaces, tissues and cells, and of materials such as oxide fuel cells and OLEDs.

Characterization of specimens to a depth of several microns below the sample surface has become somewhat routine with the use of a sputter ion beam to remove multiple layers of atoms and molecules between analysis (chemical imaging) cycles. Nevertheless, there are practical limitations to the use of ion beam sputtering for probing both organic and inorganic specimens beyond the surface region. Among the difficulties and limitations is the fact that the various matrix components sputter at different rates, called preferential or differential sputtering, which results in a distortion or complete loss of the true 3D chemical distribution as a function of depth. Many specimens also contain void spaces that are impossible to preserve in 3D images obtained by sputter depth profiling.

An alternative approach to achieve 3D chemical imaging of chemically complex specimens is to utilize *in situ* FIB milling and sectioning in conjunction with TOF-SIMS chemical imaging... what we have called FIB-TOF tomography. With FIB milling, the interior of a specimen is revealed to depths of more than 100 μm. 3D chemical imaging with a z-dimension of greater than 10 μm in tomographic increments of ≤ 0.5 μm may be achieved within a reasonable analysis time. The advantage of the FIB-TOF approach is that artifacts caused by sputter depth profiling such as differential sputtering and accumulated ion beam damage are avoided. 3D imaging by FIB-TOF tomography will be illustrated first with organic / inorganic composite materials. Applications in biological and clinical cancer research will also be presented with an emphasis on the conditions required to achieve FIB-TOF tomography.

Biomaterial Interfaces

Room: 23 - Session BI+SS+NS-WeM

Bio/Nano Interfaces with Applications in Biomedicine and Energy

Moderator: G.J. Leggett, University of Sheffield, UK

8:00am BI+SS+NS-WeM1 Combining Colloidal Lithography and Photolithography to Create Dual Length-Scale Topographical Features to Study Stem Cell Behavior, D.T. Bennetsen, D.C.E. Kraft, R. Ogaki, M. Foss, Aarhus University, Denmark

It is well known that topographical features influence cellular response. A novel combination of colloidal- and photolithography has been developed to create a dual length scale topographical platform. The presented approach permits rapid parallel fabrication of micro/nanoscale patterns. The aim is to study the response of primary human dental pulp stem cells (hDPSC) to such topographies in a systematic way.

Colloidal lithography is performed using the "lift-off" method, which is applicable to surfaces with a non-flat surface. This enables the combination of using photolithography pre-made wafers as substrates, resulting in a complex topographical structure, spanning two length scales (Figure 1). Topographical patterns are created using the colloidal mask with either evaporation or sputtering via physical vapor deposition (PVD). The principle combination of materials investigated is tantalum covered with tantalum features. These dual scale substrates are exposed to hDPSC and proliferation, attachment and differentiation are examined. Differentiation is examined using osteogenic markers and MyoD1 expression.

Initial cell proliferation data indicates that variations in the colloidal pattern heights do not seem to elicit a statistical significant response (Figure 2). A set of experiments to clarify the effect of the colloidal pattern on the

proliferation and cell cycle of the hDPSC is thus currently being performed. Furthermore, the effect of the dual scale topographical substrates on proliferation, differentiation and cell cycle is also being explored.

Concurrently we are investigating the combined effects of topographical/chemical patterns on cellular response. This can be achieved by depositing different materials site-specifically, followed by a material-specific self-assembly route. E.g. silanes and thiols with specific chemical moieties on oxides and gold, respectively. Characterization is performed using atomic force microscopy (AFM), scanning electron microscopy (SEM), X-ray photoelectron spectroscopy (XPS) and time-of-flight secondary ion mass spectrometry (ToF-SIMS).

Our fabrication approach enables the opportunity to increase the complexity of artificial 2D platforms thus by gaining a better understanding of cellular behavior for a range of biomedical and biotechnological applications.

8:20am BI+SS+NS-WeM2 Genetically Modified Tobacco Mosaic Virus (TMV)-based Electrochemical Detection of 2, 4, 6-trinitrotoluene (TNT), F. Zang, H. Ben-Yoav, X. Fan, A. Brown, J. Culver, R. Ghodssi, University of Maryland

Detection of chemical hazards and explosive compounds has received growing attention for applications in environmental monitoring, food science, and national security. Explosives, such as TNT, show low vapor pressure, molecular mass, and volume, which makes the detection of these molecules challenging for most mass and refractive index based sensors. Thanks to the redox reaction of nitro groups in TNT molecules, electrochemical methods may be used for detection of low concentrations of TNT in aqueous environments. Electrochemical sensors are suited for on-site explosive detection due to high sensitivity, low volume and convenient integration with miniaturized devices. However, to distinguish TNT from other electrochemically active compounds in complex environments, high selectivity is a more critical factor for development of TNT sensors.

The TMV has a high aspect ratio, rod-like nanostructure that can be genetically modified to express tailored chemical receptors. In this work, a 12-amino acid (WHWQRPLMPVSI) sequence peptide with multivalent recognition properties of TNT was expressed on the coat protein of TMV (TMV-p) which was utilized to develop a sensitive and selective electrochemical sensing mechanism for TNT detection. Selective binding of TMV-p with TNT molecules will decrease the free TNT concentration in solution, reducing the number of nitro groups available for redox reactions.

In preliminary studies, background signals generated from electrolytes were characterized and the signal-to-noise ratio was optimized by long term scans of square wave voltammetry. Three concentration dependent current peaks from the reduction of nitro groups in TNT were observed at the potentials of -0.53V, -0.72V and -0.86V vs. Ag/AgCl reference electrode, respectively, which agreed with the results in literatures. The initial results showed a stable and reliable electrochemical response by the TMV-p sensing system. By comparing the reduction currents in the mixtures of TMV-p and unmodified TMV with TNT solutions, we will demonstrate that TMV-p preserves the peptide binding affinity to TNT molecules while increasing the binding site density.

The approach described in this study is a sensitive and selective label-free method to detect TNT based on the binding of target molecules with peptide modified TMV. In addition to the highly selective peptide binding with analytes and a high binding site density, the genetically modified TMV is also capable of self-assembly, coating the active surfaces of a wide range of transducers. This work can potentially be implemented in the development of miniature sensors for selective TNT detection in complex environments.

8:40am BI+SS+NS-WeM3 Nanoparticles in Biology: Engineering the Interface for Sensing and Delivery, V. Rotello, University of Massachusetts

INVITED

A key issue in the use of nanomaterials is controlling how they interact with themselves and with the outer world. Our research program focuses on the tailoring of nanoparticles of surfaces for a variety of applications, coupling the atomic-level control provided by organic synthesis with the fundamental principles of supramolecular chemistry. Using these engineered nanoparticles, we are developing particles for biological applications, in particular delivery and sensing. This talk will focus on the interfacing of nanoparticles with biosystems, and will discuss our use of nanoparticles for delivery applications including our *in vitro* studies of small molecule, nucleic acid, and protein delivery. This presentation will also feature the use of nanoparticles for diagnostic applications, including the use of array-based sensing paradigms for the sensing and identification of proteins, bacteria and cell type and state.

9:20am BI+SS+NS-WeM5 Hydrophobic Forces, Electrostatic Steering, and Acid-Base Bridging between Atomically Smooth Self-Assembled Monolayers and End-Functionalized PEGolated Lipid Bilayers, M. Valtiner, Max-Planck-Institut für Eisenforschung, Germany, S.H. Donaldson, M.A. Gebbie, J.N. Israelachvili, University of California, Santa Barbara

A molecular-level understanding of interaction forces and dynamics between *asymmetric* apposing surfaces plays a key-role in utilizing molecular structures for functional surfaces in biological and materials applications. To quantify interaction forces and binding dynamics between apposing surfaces in terms of their molecular architecture we developed a novel surface-forces-apparatus experiment, using self-assembled monolayers (SAMs) on *atomically-smooth* gold. Varying the SAM head-group allowed to quantitatively identify and control which interaction forces dominated between the SAM surfaces and surfaces coated with short-chain, end-functionalized polyethylene-glycol (PEG) polymers extending from lipid-bilayers [1].

Three different SAM-terminations were studied: (a) carboxylic-acid, (b) alcohol, and (c) methyl head-group terminations. These functionalities allowed for the quantification of (a) specific acid-base bindings, (b) steric effects of PEG chains, and (c) adhesion of hydrophobic segments of the polymer-backbone, all as function of the solution pH. The pH-dependent acid-base binding appears to be a *specific, charge-mediated hydrogen bond* between oppositely-charged carboxylic-acid and amine functionalities, above the acid- pK_A and below the amine- pK_A . The long-range electrostatic "steering" of acid-base pairs leads to high binding probability even at distances close-to-full-extension of the PEG tethers, a result which has potentially important implications for protein-folding, enzymatic catalysis and biomaterial development.

[1] M. Valtiner et al., *JACS*, **2012**, 1746

9:40am BI+SS+NS-WeM6 Viral Encapsulation in Lecithin Liposomes to Enhance the Therapeutic Effect of Oncolytic Viral Therapy, N. Mendez, V. Herrera, A.C. Kummel, University of California San Diego

Oncolytic viruses have emerged as a novel platform for cancer therapeutics due to their tumor-selective replication in cancer cells. In particular, the oncolytic virus TAV-255 has shown viral replication attenuation in normal cells while retaining cytolytic activity in tumor cells by taking advantage of defects in the p53-tumor suppressor pathway. Extensive testing of oncolytic viruses has shown a limited therapeutic effect due to rapid clearance by the reticuloendothelial (RE) system and antibody neutralization. With the aim to overcome an immune response and to enhance localized delivery, an oncolytic virus-liposomal encapsulation method has been designed to increase tumor uptake and the therapeutic efficacy of oncolytic viruses in cancer cells. An inexpensive, non-toxic liposome has been prepared by self-assembly of Lecithin phospholipid bilayers around the Adenovirus capsid. Cholesterol and DSPE-PEG were incorporated into the lipid formulation to improve retention and stability. The developed method has shown that non-targeted encapsulated viral particles retain their ability to transfect cancer cells. In addition, surface functionalization of the liposomes may be applied to specifically target cancer cells and to compensate for decreased infectivity due to viral encapsulation.

10:40am BI+SS+NS-WeM9 Engineering Bio-Interfaces using Electric Field-Induced Nanolithography, S. Zauscher, R.J. Ferris, B. Yellen, Duke University

Field-Induced Nanolithography (FINL) offers a convenient tool to create physically or chemically distinct patterns for bio-interfacial sensing applications. For pattern transfer, FINL merely requires a conductively coated SPM tip or stamp, connected to a conductive substrate via a voltage source. The patterning electrode is placed in contact with the target surface and a bias voltage is applied. Few sub-diffraction limit surface patterning techniques offer FINL's versatility to function in both a serial and parallel fashion. Recently we demonstrated the use of FINL to pattern a range of polymer brushes: poly(acrylic acid) (PAA), poly(N-isopropylacrylamide) (PNIPAAm), poly(sulfobetaine methacrylate) (PSBMA), and poly(oligo(ethylene glycol) methyl methacrylate) (POEGMA). Our results show that FINL of non-fouling polymer brushes provides a novel patterning technique that results in the localized topographical and chemical modification of the polymer brush surface only. The resulting chemical modification allowed selective addressing of the brush surface with aldehyde reactive coupling chemistries. Our approach thus shows significant promise for fabricating large-scale sensing devices, as patterning can be accomplished in a step-and-repeat fashion. Using FINL, we also demonstrated patterning of surface charges onto ferroelectric thin films (FETFs). FETFs are materials that are able to maintain a bi-stable polarization state, and that once polarized, maintain a high surface charge density. Using FINL, it is possible to locally align unit-cell dipole moments within the film to produce nano-scale polarization patterns. Although to

date the use of FETFs is isolated to semiconductor and memory applications, we demonstrate that FETFs have great potential for biological and interfacial sensing applications. We show that FETF surface charge patterns can be used to control the lateral extent of electric double layer formation in dilute electrolyte solutions, with clear implications for field assisted particle deposition and programmed self assembly.

11:00am **BI+SS+NS-WeM10 Supramolecular Bioassemblies at Solid-Liquid Interfaces: Binding Control through Redox-Driven Multivalent Host-Guest Interactions**, *G.V. Dubacheva*, CIC biomaGUNE, Spain, *L. Guerente*, *D. Boturyn*, Joseph Fourier University, France, *R. Auzély*, CERMAV, France, *R.P. Richter*, CIC biomaGUNE, Spain; Joseph Fourier University, France; Max Planck Institute for Intelligent Systems, Germany, *P. Labbé*, Joseph Fourier University, France

The design of kinetically stable bioassemblies while keeping binding control is of high current interest for bioanalytical and biomedical sciences. The development of tunable biointerfaces is also a key issue in nanobiotechnology as they can be used for modeling cell surface-associated biological processes. In this context, supramolecular host-guest chemistry is particularly attractive as it allows controllable molecular recognition and structural modification at specific areas of a nanoassembly, i.e. purpose-designed molecules can be confined in time and space in a highly controlled manner.

Cyclodextrin (CD) is well-known to form host-guest complexes with hydrophobic molecules while being soluble at physiological conditions. Taking advantage of redox-driven β -CD-ferrocene (Fc) multivalent interactions, we designed stimuli-responsive biomaterials composed of linear polymers, their multilayer assemblies and biomolecules. For this aim, we developed a new method to create β -CD self-assembled monolayers (SAMs) allowing precise varying β -CD surface density.1 We showed that Fc-functionalized polymers can be reversibly attached to such β -CD SAMs.1 We also showed a possibility to build up multilayer host-guest polymer assemblies on β -CD surfaces.2 In addition, we applied these β -CD SAMs for the reversible attachment of biomolecules using orthogonal Fc/ β -CD- and specific bio-interactions under biological conditions.3 Finally, combined with guest-modified polysaccharide hyaluronan, the β -CD surfaces were explored as a model system to understand multivalent interactions at the cell-hyaluronan matrix interface associated to a variety of cellular functions and biological processes.

Physico-chemical properties of supramolecular assemblies were characterized by QCM-D, ellipsometry, cyclic voltammetry and contact angle goniometry. The redox-driven binding of polymers and biomolecules to β -CD surfaces was assessed by *in situ* combining electrochemistry/QCM-D and SPR ellipsometry/microfluidic systems. The developed tunable biointerfaces can be applied to investigate other topics in soft condensed matter physics, molecular physics and biophysics.

1Dubacheva et al., *Langmuir*, **2010**, 26:13976

2Dubacheva et al., *Soft Matter*, **2010**, 6:3747

3Dubacheva et al., *Chem Commun*, **2011**, 47:3565

11:20am **BI+SS+NS-WeM11 High-resolution In Situ Electrochemical STM Imaging of Phospholipid Model Cell Membrane**, *H. Shimizu*, *S. Matsunaga*, University of Tokyo, Japan, *T. Yamada*, *T. Kobayashi*, RIKEN, Japan, *M. Kawai*, University of Tokyo, Japan

We obtained molecular-scale images of phospholipid layers spread on a modified Au(111) immersed in a buffer solution, by means of *in situ* electrochemical scanning tunneling microscopy (EC-STM). Real cell membranes consist of a bilayer of phospholipids which continually gather and interact. There are various kinds of phospholipids in the real cell membranes. To understand the action of these molecules, a dynamic molecular-scale method of observation is necessary. Lipkowski [1] first visualized static monolayers of phospholipid on Au(111) by *in situ* EC-STM. Matsunaga *et al.* [2] revealed dynamic, microscopic motion of phospholipid monolayer on alkanethiol-modified Au(111) immersed in a buffer solution. We intended to compose a bilayer of phospholipid on a hydrophilic substrate in order to mimic the real cell membrane more truly. We used a hydrophilically modified Au(111), anticipating that the first lipid monolayer with the hydrophilic head group down to the surface, and the second lipid monolayer with the hydrophobic alkyl chains down, all spontaneously in aqueous buffer solution.

For this purpose, we used 3-mercaptopropionic acid (MPA) self-assembled monolayer (SAM) on Au(111), in which the COOH groups are expected to be exposed out of the surface. We first observed a ($\sqrt{3} \times \sqrt{3}$) type adlattice of MPA SAM by STM. Then the sample was immersed in 50 mM phosphate buffer containing minimal lipid particles of 200 μ M 1-palmitoyl-2-oleoyl-*sn*-glycero-3-phosphocholine (POPC) with or without 50 μ M cholesterol.

We uniquely observed a 2-dimensional adlattice with a parallelogram unit cell of 1.0 nm x 1.9 nm. Along the short segment, blight spots are aligned. The adlattice did not change with or without cholesterol, indicating that it was composed exclusively of pure POPC. The interval of 1.9 nm is apparently shorter than the full length of POPC molecule (≈ 2.5 nm). To interpret the adlattice structure, we considered a model structure composed of tilted POPC, with the head group attached to the MPA SAM. This model involves a strong affinity between the hydrophilic groups.

Although this frozen adlattice does not completely match our target structure of mobile lipid bilayer, we consider we could partly utilize the hydrophobicity/hydrophilicity of the phospholipid molecules to compose a uni-directional membrane. We will further develop this kind of methods by choosing the proper modifier on Au(111), aiming the bilayer structure. By this we expect to go closer to the nanometer-scale reality of cell membranes containing functional proteins.

[1] J. Lipkowski, *Phys. Chem. Chem. Phys.* **12**, 13874 (2010).

[2] S. Matsunaga *et al.*, *Electrochem. Commun.* **9**, 645 (2007).

11:40am **BI+SS+NS-WeM12 Characterization of Polymer/Drug Films as Model for Drug Eluting Coronary Stent Coating Layers**, *V. Ciarnelli*, *M.R. Alexander*, *M.C. Davies*, *C.J. Roberts*, University of Nottingham, UK

This work describes the characterization of a polymeric based drug eluting stent coating, used in coronary stenting to prevent restenosis [1]. The work examines thin films as models for drug eluting stent coatings. Complementary surface analysis techniques are used to investigate the drug polymer distribution on the surface and throughout the depth of the model films.

The first goal of this project is to establish the feasibility of certain surface analysis techniques in the characterisation of a drug eluting stent coating layer. Secondly, this study will act as a standard reference to determine the ideal operating conditions for characterizing the more complex stent device.

Thin film models were produced varying the substrate materials (silicon or glass), preparation procedures (spin casting or spray coating) and drying methods (oven or warm air). The different drug to polymer ratios used were: 1:3, 1:1 and 3:1 (w:w).

Complementary surface analysis techniques such as atomic force microscopy (AFM), time of flight secondary ion mass spectrometry (ToF-SIMS) and x-ray photoelectron spectroscopy (XPS) were employed for the characterization of the films. Depth profiling has also been performed using XPS and ToF-SIMS.

AFM imaging of the oven dried spun cast films shows domains of drug, characterized by a circular organization with features of 100 - 250 nm in diameter. These domains are not observed in other samples and appear to be related to phase separation during the drying step.

Surface characterization using XPS shows enrichment of the drug at the surface for all the model films with the exception of the spray coated films at the 1:3 drug-to-polymer weight ratio.

Depth profiling using both ToF-SIMS and XPS confirms that the drug is enriched at the surface, posing significant implications for drug loaded polymer delivery systems.

Complementary surface analysis techniques have proven extremely successful in characterizing the model films. Suitable techniques and their operative conditions have now been established for the characterization of a stent device.

[1] I. Iakovou *et al.*, Incidence, predictors, and outcome of thrombosis after successful implantation of drug-eluting stents. *JAMA.*, **293** (2005): p. 2126-2130.

Electronic Materials and Processing

Room: 9 - Session EM+TF-WeM

Hybrid Electronic Materials and Interfaces

Moderator: M.R. Linford, Brigham Young University, A.J. Muscat, University of Arizona

8:00am **EM+TF-WeM1 Versatile Electron Beam Chemical Lithography on the Basis of Monomolecular Films**, *M. Zharnikov*, University of Heidelberg, Germany **INVITED**

The talk reviews recent progress in Electron Beam Chemical Lithography (EBCL) on the basis of monomolecular templates provided by self-assembled monolayers (SAMs). Due to the monolayer thickness of SAMs and molecular size of their structural building blocks, patterning down to few nanometers is in principle possible. Depending on the architecture of

the SAM constituents, different EBCL strategies can be used [1]. In the case of aromatic backbone, selective modification of specific tail groups at the SAM-ambient interface can be exploited [1]. In the case of aliphatic backbone, irradiation-promoted exchange reaction between the molecules in the primary SAM and potential molecular substituents can be used [2]. A further promising technique within the EBCL framework is Electron Beam Activation Lithography which involves activation of the amino tail groups of the primary SAM template disabled by specific quencher moieties [3]. This method is especially useful for the fabrication of morphological patterns. EBCL can also be adapted for biological applications, based on protein-repelling templates [4]. One can either perform a direct writing in such a template, which can be both SAM-based and polymer-like, or apply irradiation-promoted exchange reaction with well-controlled parameters. Using the above techniques, chemical patterning and surface engineering on the length scale ranging from cm to nm can be performed. Not only simple dot or stripe structures, but complex gradient-like and biology-inspired patterns can be fabricated as will be demonstrated by representative examples.

[1] M. Zharnikov and M. Grunze, *J. Vac. Sci. Technol. B* **20**, 1793-1807 (2002).

[2] N. Ballav, S. Schilp, and M. Zharnikov, *Angew. Chem. Int. Ed.* **47**, 1421-1424 (2008).

[3] S. Schilp, N. Ballav, and M. Zharnikov, *Angew. Chem. Int. Ed.* **47**, 6786-6789 (2008).

[4] N. Ballav, H. Thomas, T. Winkler, A. Terfort, and M. Zharnikov, *Angew. Chem. Int. Ed.* **48**, 5833-5836 (2009); *Nature*, **460**, 308 (2009).

8:40am EM+TF-WeM3 Covalently Linked Organic Monolayers on Silicon Surfaces: Making Them Better, Stronger, Faster!, *H. Zuilhof*, Wageningen University, Netherlands

Covalently linked organic monolayers on silicon surfaces provide a prime example of hybrid electronic materials. Such systems are required on the one hand to passivate the Si surface, and on the other hand provide an optimal electrical link between the bulk of the Si semiconductor and the liquid with which it interacts.

To obtain an optimal passivation a highly dense monolayer is required, and we present novel agents and methods that yield a denser formation of the monolayers. At the same time monolayer formation can be made faster, which reduces the chance for competing silicon oxide formation. Finally, this combination of properties is desired for really thin monolayers, which drives research to allow attachment of small molecules. The paper will present a combination of such newly developed methods, properties of the resulting monolayers and an approach for further systematic improvements.

9:00am EM+TF-WeM4 Probing the Intrinsic Organic/Semiconductor Interface, *W. Peng, O. Seitz, R. Chapman*, University of Texas at Dallas, *E.M. Vogel*, Georgia Institute of Technology, *Y.J. Chabal*, University of Texas at Dallas

The electronic properties of organic/semiconductor interfaces are crucial for a variety of applications, such as organic dielectrics and organic/inorganic hybrid solar cells. However, the accurate characterization of these interfaces is prevented by the large tunneling current through the molecular layer. Moreover, standard fabrication methods, such as the formation of top metal contact via evaporation, cause damages during the processing even if applied directly with extreme caution. We present here a novel method to protect the interface with a layer of high- κ dielectric (Al_2O_3) gently deposited on top of the organic layer using atomic layer deposition. The metal precursor reacts with the carboxylic head group of the self-assembled monolayer (SAM) layer without affecting the underlying SAM/Si interface. Due to the increase of the dielectric layer thickness (SAM+ Al_2O_3), a large reduction in tunneling leakage current occurs, and conductance voltage measurements can be implemented with a mercury probe setup. Moreover, the gate stack shows enough robustness to survive the entire MOS capacitor fabrication. Capacitance voltage measurements show small frequency dispersion and a low D_{it} , on the order of $10^{11} \text{ cm}^{-2} \text{ eV}^{-1}$, for the intrinsic SAM/Si interface demonstrating inherent high quality when it is protected by the Al_2O_3 layer.

9:20am EM+TF-WeM5 Towards Organic Electronics: Methods for the Selective Deposition of Semiconductors and Metals, *J. Yang, Z. Shi, K. Borner, A.V. Walker*, University of Texas at Dallas

We describe recent progress in our laboratories to build robust complex two- and three-dimensional molecular constructs. This work has important applications in photovoltaics, molecular and organic electronics, sensing, photonics and other technologies. Several recent developments are discussed including the chemical bath deposition of PbS, the UV photoassisted chemical vapor deposition of Al, and the formation of Ni and Cu nanowires on micron-scale patterned surfaces. Optimization and further

development of these techniques requires a detailed understanding of the reaction pathways involved in the interaction of organic thin films with metals, organometallic compounds, ions, and other compounds.

9:40am EM+TF-WeM6 Electroless Deposition of Co on SiO_2 Surfaces Modified by an Aminosilane Self-Assembled Monolayer, *R. Jain, A. Ng, E. White, A.J. Muscat*, University of Arizona

As device interconnects continue to shrink in size, the formation of diffusion barriers between dielectric and metal surfaces becomes more difficult. Self-assembled monolayers (SAMs) can be used to chemically activate a variety of surfaces, and their potential for uniform and defect-free monolayer formation makes them attractive alternatives for barrier layers. SAMs can also serve as adhesion layers to promote the electroless deposition (ELD) of metals on some dielectric surfaces. A 3-aminopropyltrimethoxysilane (APTMS) SAM was formed on a well-hydroxylated SiO_2 surface and studied as a function of solvent (methanol, IPA, and toluene), APTMS concentration (5.72 mM and 57.2 mM), and post-deposition rinsing in methanol, IPA or chloroform depending on the solvent used. An aminopropylsilane monolayer with a thickness of $7.8 \pm 0.2 \text{ \AA}$ and roughness of $3 \pm 1 \text{ \AA}$ was formed at an APTMS concentration of 5.72 mM in methanol and IPA, but multilayers were formed in toluene, which were deposited at a rate of $0.4 \pm 0.06 \text{ \AA/min}$ and roughness of $31 \pm 18 \text{ \AA}$. The N 1s XPS peak at a binding energy (BE) of 398.8 eV verified that a primary amine group ($-\text{NH}_2$) was present together with an equal coverage of protonated amine ($-\text{NH}_3^+$). Based on N 1s XPS peak areas, the molecular density of the aminopropylsilane monolayer was $4.2 \pm 0.6 \text{ molecules/nm}^2$, which is about equal to the accepted value of the OH group density on the Si surface. ELD processes are known to be sensitive to surface termination and require a metal catalyst, such as palladium, to activate the surface. A layer of Pd atoms was deposited by immersing the APTMS SAM surfaces in an 80 mM $\text{PdCl}_2\text{-HCl}$ solution for 2 min, yielding one Pd atom bonded to two amine groups based on XPS peak areas. These results suggest that Pd atoms are bonded to primary amines rather than protonated amines resulting in a coverage of half of the N sites. Cobalt was plated by immersing the Pd-coated surface in a solution of 0.05 M CoSO_4 , 0.2 M dimethylaminoborane (DMAB), and 0.01 M diethylenetriamine (DETA). Cobalt replaced the Pd atoms on the surface depositing a seed layer that auto-catalytically yielded a thick cobalt film on the surface. The thickness of the Co increased with the deposition time as verified by both the Co 2p peak at a BE of 777.2 eV and attenuation of the Si 2p peak with time. These results demonstrate that an aminopropyl silane adhesion layer binds metals such as Co. The next step is to test the effectiveness as a diffusion barrier.

10:40am EM+TF-WeM9 Polymer-Colloidal Nanocrystal Hybrid Materials for Photovoltaic Applications, *J. Xue, R. Zhou, P.H. Holloway*, University of Florida

INVITED

Hybrid photovoltaic (PV) cells based on conjugated polymers and colloidal inorganic semiconductor nanoparticles have attracted significant attention as an alternative for all-organic solar cells. However, so far the highest efficiencies for hybrid PV cells have been limited to 2-3%, significantly lower than that of all-organic PV cells. One main reason for the lower performance is attributed to the complex interfaces and surfaces involving the inorganic nanocrystals.

Here we report our recent work that significantly improves the efficiency of hybrid PV cells to the 5% level. First, a 30-70% increase in the device efficiency was achieved by incorporating a solution-processed ZnO nanoparticle layer between the active layer and the cathode. This was attributed to a combination of electronic, optical, chemical, and morphological effects, including blocking leakage of photogenerated holes to the cathode, optimizing the optical intensity profile in the hybrid active layer, minimizing recombination or quenching of photogenerated excitons and charge carriers. Maximum power conversion efficiencies of 2.5% and 3.5% were achieved with a high-gap polymer P3HT and a low-gap polymer PCPDTBT, respectively. The incorporation of the ZnO nanoparticle layer also drastically improves the stability of the hybrid PV cells.

We further demonstrated another 30-50% improvement in the efficiencies of hybrid PV cells by treating the hybrid active layer in an acetonitrile solution with 1% ethanedithiol (EDT). This leads to a maximum efficiency of ~5.0% for the EDT-treated hybrid PV cell with a PCPDTBT:CdSe nanorod active layer. Detailed characterizations of the hybrid active layers before and after the EDT treatment revealed no appreciable differences in their morphology and absorption spectra; however the phosphonic acid organic ligands on CdSe nanocrystals are more completely removed, and an improved electron mobility was obtained upon EDT treatment. We attribute the enhanced efficiency to more complete removal of exciton/charge recombination centers and the subsequent atomic layer passivation of the CdSe nanorod surface.

11:20am **EM+TF-WeM11** **Obtention of Deterministic Patterns through Wrinkling Formation**, *J.L. Yague, J. Yin, D. Eggenziele, M.C. Boyce, K.K. Gleason*, Massachusetts Institute of Technology

Formation of wrinkles through buckling of a stiff coating on a compliant substrate can be found very commonly in nature. For instance, the epidermal ridges, which form our fingerprints, show a very unique pattern due to out-of-plane bending of the epidermis. The use of wrinkling to obtain patterned surfaces has become increasingly significant for a wide range of applications, such as: microfluidic, tunable wettability, stretchable electronics, photonics or anti-fouling surfaces. In this work, we demonstrate the ability to obtain labyrinth and herringbone patterns using a 2D stretching-releasing approach.

On top of a compliant substrate, an acrylate-based polymer is deposited by initiated chemical vapor deposition (iCVD). iCVD is a solvent-free method that yields a conformal thin coating on virtually any substrate, giving a controllable thickness and tunable structural, mechanical, thermal, wetting, and swelling properties. Monomer together with an initiator is introduced into a reactor chamber under vacuum, where the initiator is decomposed over resistively heated filaments to obtain radicals. Radicals and monomer are then adsorbed on a surface, which is kept at a controlled temperature to promote adsorption, to yield the polymer by the classical free-radical mechanism. Here, deterministic herringbone patterns are achieved through wrinkling of the polymer thin film. Furthermore, a simplified theoretical model is developed to predict the geometry of the ordered herringbone pattern. Depending on the experimental conditions is possible to control the features of such pattern. We report, for first time, the obtention of herringbone patterns with a jog angle lower than 90°. Finally, this method also provides a tool to determine the Young's modulus of the films based only on the characteristic wavelengths of the pattern.

11:40am **EM+TF-WeM12** **Surface Dynamics of Hybrid Silicon Interfaces Explored via Helium Atom Scattering**, *Z.M. Hund, R.D. Brown*, University of Chicago, *L.E. O'Leary*, California Institute of Technology, *D. Campi, M. Bernasconi, G. Benedek*, Università di Milano-Bicocca, Italy, *N.S. Lewis*, California Institute of Technology, *S.J. Sibener*, University of Chicago

Surface dynamical properties of methyl-terminated silicon(111) were investigated with energy and momentum resolved inelastic helium atom scattering measurements. The narrow energy distribution and nondestructive nature of neutral helium atom beams allow us to probe the vibrational dynamics of this hybrid organic-semiconductor interface. Time-of-flight experiments identify single phonon inelastic scattering events including, but not limited to, those attributed to Rayleigh wave excitations. We have mapped out the entire surface Brillouin zone along the nearest neighbor and next nearest neighbor azimuths, $\langle 011 \rangle$ and $\langle 121 \rangle$, respectively. Our experimental results are in excellent agreement with density functional perturbation theory calculations, which provide a detailed description of the dispersion curves. The combination of experimental measurements with theoretical calculations allows us to determine the interfacial Si-Si force constants, including coupling between the molecular adlayer and the substrate, displacement fields, and mode polarizations. Helium atom scattering complemented with DFPT calculations allow us to quantify these effects. Additionally, isotopic effects were probed by mapping the dispersion curves for the perdeutero-methylated silicon surface. Our results will be discussed with respect to hydrogen-terminated Si(111).

Energy Frontiers Focus Topic

Room: 15 - Session EN+PS-WeM

Plasmas for Photovoltaics and Energy Applications

Moderator: J.-P. Booth, LPP-CNRS, Ecole Polytechnique, France

8:00am **EN+PS-WeM1** **Electron Driven C₁-chemistry: Direct Conversion of Methane to Synthetic Fuels**, *T. Nozaki*, Tokyo Institute of Technology, Japan **INVITED**

Currently, industrial material and energy conversion technology platform consists of thermochemical processes including various catalytic reactions. Existing industry scale technology and related science has already been well established; nevertheless, further improvement in energy efficiency and material saving are demanded. Drastic reduction of CO₂ emission is also drawing keen attention with growing concern of energy and environmental issues. Green chemistry is a rapidly growing field of science and technology, and often highlights renewable bioenergy, bioprocesses, solar photocatalysis of water splitting, and CO₂ regeneration as synthetic fuels. Plasma catalysis of hydrocarbon feedstock is also highlighted as an

important part of the innovative next generation green technologies that meet the need for energy saving, environment protection, and material preservation [1-4]. Non-thermal plasma uniquely generates reactive species independently of reaction temperature, and these species are used to initiate chemical reactions at unexpectedly lower temperatures than normal thermochemical reactions. Non-thermal plasma thus broadens the operation window of existing chemical conversion processes, and ultimately allows modification of the process parameters to minimize energy and material consumption. We specifically focus on dielectric barrier discharge (DBD) as one of the viable non-thermal plasma sources for practical fuel reforming. In the presentation, room-temperature one-step conversion of methane to synthetic fuels such as methanol, hydrogen, and syngas (H₂+CO) using a microplasma reactor is highlighted. Not only practical background of the project, but also unique characteristics of plasma fuel reforming such as non-equilibrium product distribution is presented [5-7].

1. T Nozaki et al: *Journal of the Japan Petroleum Institute*, **54**(3) (2011) 146.

2. The special issues on " Non-thermal Plasma Assisted Fuel Conversion for Green Chemistry ", *J Phys D: Appl Phys.*, **44**(23), 2011

3. A Gutsol: *Handbook of Combustion*, Vol.5 New Technology, Wiley-VCH, 323 (2010)

4. H L Chen et al: *Appl. Catal. B: Environmental*, **85** (2008) 1.

5. T Nozaki et al: *Chemical Engineering Journal*, **166** (2011) 288– 293.

6. T Nozaki et al: *Energy & Fuels*, **22** (2008) 3600–3604.

7. T Nozaki et al: *Pure and Applied Chemistry*, **78**(6) (2006) 1147–1162.

8:40am **EN+PS-WeM3** **Plasma-assisted CO₂ Conversion as Candidate Element in Future Solar Fuel Economy**, *S. Welzel, S. Ponduri, F. Brehmer, M. Ma, M.C.M. van de Sanden, R. Engeln*, Eindhoven University of Technology, the Netherlands

Recently research in 'solar fuels' has been stimulated by the forthcoming depletion of fossil fuels along with a slowly increasing share of intermittently available renewable sources. New efficient methods of harvesting renewable (e.g. solar) energy and its storage in high energy density chemical fuels are therefore highly desirable. CO₂ and its recycling into 'solar fuels' will be an essential element in the future transport and energy infrastructure. Plasma-processing of CO₂ in the gas phase under low-temperature non-equilibrium conditions is thereby a promising alternative to specifically tackle the rate-limiting dissociation into CO. Two aspects of such a plasma-assisted CO₂ treatment have been studied and are detailed in this contribution.

Firstly, the direct hydrogenation of CO_x in a plasma-expansion created from mixtures of Ar and H₂ was investigated. Different (metallic) surface materials were employed to assess the influence of surface reactions on the molecule formation. Mass-spectrometry and infrared absorption spectroscopy were applied to quantify the gas phase composition of such argon-ion and hydrogen-radical enhanced plasmas. Although CO was a main product with up to 50 % conversion yield, the separation of CO₂ dissociation and subsequent hydrogenation was strongly suggested to optimise both processes individually. Furthermore it transpired that plasma-catalysis require new surface materials that are different from conventional catalysts: a copper surface typically reduced the CO and CH₄ yields by 50 %.

Secondly, to particularly account for the individual optimisation of the CO₂ dissociation and scrutinise the (energy) efficiency of the conversion process dielectric barrier discharges in CO₂ were studied. The focus was on establishing a consistent energy-balance of the proposed plasma-assisted route and involved the analysis of energy injected to the power supply, the transfer to the discharge and the correlation with the CO₂ conversion. Through reduction of loss channels in the resonance circuit operated in the kHz-range clearly more than 50 % of the input power were directly injected to the plasma. Plasma parameters such as electron and vibrational temperatures and the population distribution of excited species were determined to further characterise the excitation and dissociation channels in the CO₂ plasma.

9:00am **EN+PS-WeM4 Novel Processing Routes of Silicon Nanocrystals in a Remote Expanding Thermal Plasma for Photovoltaic Applications**, *I. Dogan**, Eindhoven University of Technology, Netherlands, *S.L. Weeks*, Colorado School of Mines, *K. Dohnalova, T. Gregorkiewicz*, University of Amsterdam, Netherlands, *S. Agarwal*, Colorado School of Mines, *M.C.M. van de Sanden*, Dutch Institute for Fundamental Energy Research, Netherlands

The interest in silicon nanocrystals (Si-NCs) has considerably increased since the observation of carrier multiplication and separation between adjacent Si-NCs. This mechanism might potentially enable a more efficient solar spectrum conversion. For successful integration of Si-NCs into solar cells, the key issues are size control, crystalline quality, surface preparation and cost efficient production of Si-NCs. Previous works have failed to address the latter point because they require multiple production steps yet with an insufficient amount of produced Si-NCs. Here, a novel synthesis method of Si-NCs by using a remote expanding thermal plasma (ETP) is presented, that allows a direct utilization for large scale production. One-step route synthesis of Si-NCs is realized in an argon/silane plasma with remarkable throughputs above 100mg/min of Si-NCs. Formation of Si-NCs is favoured by means of silane polymerization reactions. In contrast to the common belief of particle coagulation, all Si-NCs are found to be formed by nucleation as revealed from TEM analysis of the Si-NCs produced. TEM, Raman spectroscopy (RS) and photoluminescence spectroscopy (PL) consistently demonstrate that the Si-NCs have a size distribution in the range 2-140nm which is related to differences in residence times in the different zones of the reactor. To move towards a better control of the size distribution, a series of size separation experiments is discussed. Two approaches are proposed: spatial confinement of the plasma zones where the smaller Si-NCs are formed or a time modulation of the silane flow injected into the reactor. It will be shown that using these methods an average Si-NC size distribution of 5nm can be reached. Moreover, based on the results of time modulation, the role of different plasma species on the formation of small and large Si-NCs will be discussed. The observation of step-like enhancement of luminescence quantum yield with increased photon energy, which is a sign of carrier multiplication between Si-NCs will be discussed. It is expected that the ETP approach is capable to dramatically increase the production efficiency of Si-NCs to scalable throughputs without any loss of quality.

9:20am **EN+PS-WeM5 Growth of Microcrystalline Silicon using Tailored Voltage Waveform Driven Plasma Processes: From Materials to PV Devices**, *E.V. Johnson*, LPICM-CNRS, Ecole Polytechnique, France, *S. Pouliquen, P.A. Delatre, J.-P. Booth*, LPP-CNRS, Ecole Polytechnique, France **INVITED**

The use of non-sinusoidal, radio-frequency (RF) « tailored » voltage waveforms (TVW's) to drive plasma processes in a capacitively coupled plasma reactor allows one to decouple the injected power from the mean ion bombardment energy (IBE) at the substrate. Also known as the Electrical Asymmetry Effect (EAE), this decoupling stems from a controllable division of the sheath voltage between the two electrodes when an asymmetric voltage waveform is applied to one of the electrodes. In a symmetric reactor, this effect manifests itself through the presence of a self-bias voltage (V_{DC}), and as dramatic changes in this parameter in an asymmetric one. For example, the application of a “peaks” waveform to the RF electrode - consisting sharp pulses separated by plateaus - results in a large, negative V_{DC} , and thus a reduction in the IBE at a substrate on the grounded electrode. A “valleys” waveform results in the opposite, while both waveforms inject the same power into the plasma.

Such independent control over the sheath voltages is very useful when applied to the deposition by PECVD of thin-films of materials needing a high radical flux but low IBE, such as hydrogenated microcrystalline silicon ($\mu\text{-Si:H}$). By controlling the growth conditions of the $\mu\text{-Si:H}$ thin films through the shape of the waveform, one can control many aspects of the film properties (Raman crystallinity, density, hydrogen bonding, surface morphology, and electronic properties) without changing any other process conditions. In particular, the optical response of the films (and film surfaces) can be observed in-situ during growth using spectroscopic ellipsometry, thus linking the redistribution of the sheath voltages to the growth dynamics. Furthermore, we show that when TVW's are used to decrease the IBE during the growth of the absorber layer of thin-film solar cells, good device properties at acceptable deposition rates are obtained.

A promising aspect of this technique is the prospect of achieving process control without modifying the core of an existing reactor chamber. However, the counteracting challenge is that of efficiently coupling multiple harmonics to the reactor simultaneously, and these two facets will also be discussed.

10:40am **EN+PS-WeM9 Measurement and Control of Ion Energies in Dual Frequency Capacitive Hydrogen Discharges**, *E. Schuengel, S. Mohr, J. Schulze, U. Czarnetzki*, Ruhr-University Bochum, Germany

In plasma processing applications, capacitively coupled radio frequency (CCRF) discharges are widely used. A typical example is the manufacturing of silicon thin film solar cells using PECVD in a geometrically almost symmetric capacitive parallel plate discharge. For these applications, one of the major aims is the control of the fluxes and properties of radicals and ions at the substrate surface, thus controlling the surface chemistry and optimizing the (electrical) properties of the deposited film and/or the deposition rate. In particular, the shape of the ion velocity distribution function (IVDF) plays a crucial role [1]. The IVDF can be controlled to some extent in CCRF discharges driven by two substantially different frequencies, where the low frequency component is used to modify the ion energy while the total ion flux should be adjusted via the high frequency component. However, recent investigations have shown that this method is limited to a rather narrow window of discharge operating conditions [2]. As opposed to this concept, the Electrical Asymmetry Effect (EAE) uses the excitation via two consecutive harmonics to generate an asymmetric discharge even in geometrically symmetric discharge configurations [3]. Here, the symmetry of the discharge, the DC self bias, and the ion energy at the electrode surfaces are controlled via the phase angle between the two frequencies. In this study, the EAE is investigated in a discharge setup, which is similar to the ones described in the above example. A combination of 13.56 MHz and 27.12 MHz is applied to one electrode. The discharge is ignited in pure hydrogen at pressures of several hundred Pascals. Under these conditions, H_3^+ ions are the dominant ion species. A plasma process monitor is implemented into the center of the grounded electrode, allowing to measure the H_3^+ IVDF. The results show that the mean ion energy changes as a function of the phase angle, while the ion flux is kept almost constant. However, the control range of the ion energy via the EAE is limited and the shape of the IVDF shows a dependence on the phase angle. These experimental findings are understood in the frame of a simple model.

Funding by the German Federal Ministry for the Environment, Nature Conservation and Nuclear Safety (0325210B) is gratefully acknowledged.

[1] S. Nunomura and M. Kondo 2008 Appl. Phys. Lett. **93** 231502

[2] J. Schulze et al. 2009 Plasma Sources Sci. Technol. **18** 034011

[3] U. Czarnetzki et al. 2011 Plasma Sources Sci. Technol. **20** 024010

11:00am **EN+PS-WeM10 Raman Study of the Properties of Free Standing Silicon Nanocrystals Using Laser Induced Thermal Heating**, *L. Han, A.H.M. Smets, M. Zeman*, Delft University of Technology, Netherlands

Nanocrystals (NCs) exhibit unique physical properties which might open routes to new photovoltaic concepts conquering the Shockley-Queisser limit of single junction solar cell devices, such as multiple-exciton-generation (MEG) and down conversion using space-separated-quantum-cutting (SSQC). In addition, the strong dependence of the band gap of NCs on their sizes, allows the design of novel multi-junction solar cells. For these reasons, NCs made of variety of direct and indirect semiconductor materials, have been extensively studied in recent years. In this contribution we focus on silicon, the most dominant material in PV technology. Challenges in the processing of Si NCs are controlling their size distribution and passivation of surfaces to prevent unwanted Shockley-Read-Hall recombination of generated charge carriers.

The Si NCs studied in this paper are synthesized using the expanding thermal plasma chemical vapor deposition (ETP-CVD) technique with the advantage of incredible high yield, deposition rate, room temperature fabrication, low cost, high purity and post-surface passivation treatment based on plasma processing. Using the ETP-CVD technique free standing Si NCs with a wide variety of properties have been processed. The dependence of the processing conditions are studied using high resolution transmission electron microscopy. Furthermore, the surface oxidation kinetics of free standing Si NCs without any post-deposition surface-passivation-treatment is studied using IR absorption spectroscopy.

The main focus in this contribution is an unconventional Raman spectroscopy analysis on the free standing Si NCs. In this approach, Si NCs are additionally heated using a laser probe to study the quantum confinement effects of the Si NCs in more detail. An interesting huge red Raman peak shift for the transverse optic mode (520 cm^{-1}) of around 30 cm^{-1} and a width enhancement of 19.1 cm^{-1} are observed with the increasing power of the probe laser. We argue that the shift is due to the laser induced thermal heating of the Si NCs in line with analysis based on the ratio of the Anti-Stokes-to-Stokes peak of the free standing Si NCs [1]. As a reference, the Raman spectra of amorphous silicon and microcrystalline silicon thin films are studied using the same approach. This

* Coburn & Winters Student Award Finalist

experiment shows that thermal conduction between the free standing Si NCs is inefficient in contrast to the Si films, which allows the Si NCs to be heated up by laser light more efficiently.

[1] Khriachtchev et al., JAP 100, 053502 (2006)

11:20am **EN+PS-WeM11 Fabrication of 3D Array Si Quantum Dots Superlattice using Biotemplate and Neutral Beam Etching.** *M.E. Fauzi, M. Igarashi, W. Hu, S. Samukawa*, Tohoku University, Japan

Quantum dots have been used in many novel optoelectronic devices due to its quantum effect characteristics. To further improve quantum dots light absorption efficiency, it is vital to increase number of quantum dots while keeping straight alignment in vertical direction. However, in the conventional method using bottom-up approach, fabricated quantum dots structure is not uniform and well-aligned in vertical direction, while the conventional top-down etching has limitations in fabrication of nanometer size and leaves high-density defects. In previous study, we have fabricated well-ordered arrangement of high-density 2 dimensional (2D) array ($7 \times 10^{11} \text{ cm}^{-2}$) silicon nanodisk (Si-NDs) with a new process using bio-template and damage-free neutral beam etching (NBE). In this paper, we developed technology for fabricating 3D array of Si NDs with single step NBE technique and biotemplate technology, focusing on well-aligned structure in vertical direction.

Firstly, we deposited 4 layers of 4 nm-thick Si layer with 2 nm-thick silicon carbide (SiC) as its matrix using thin film deposition technique. Then, biotemplate was quasi-hexagonally arranged and used as mask during our etching process. These bio-templates provide 6 nm space between etching masks. After NBE process, high aspect ratio of 12 is achieved. The key technology in our approach is to utilize low-selectivity etching process to etch high aspect ratio structure in single step. Single step etching is made possible for three reasons. First, oxide layer on top of our Si/SiC structure was first removed by NF_3 gas/hydrogen radical treatment. Secondly, SiC that was used as matrix material has a comparable etching rate compare to Si. In our research, we make use of Si/SiC's low selectivity (1.3) to conduct a well-aligned vertical etching process. Thirdly, a high selectivity for Si/SiC structure to iron-core etching mask. After chlorine NBE process, iron-core mask pattern was precisely transferred, and anisotropic etching profile was achieved. Our SEM images of the top-view and cross-section view exhibits well-aligned, uniformity, high aspect ratio nano-columns. Lastly, we deposit SiC layer to complete Si/SiC matrix. As a result, we successfully fabricated 4 layers-stacked Si-NDs with sub-10 nm in diameter and 2 nm space between nanodisks.

We hope quantum dots superlattice fabricated by our technology could be used in quantum dot solar cell application for higher conversion efficiency.

11:40am **EN+PS-WeM12 Two-dimensional Simulations of Hydrogen and Hydrogen/Silane Capacitively Coupled Dual Frequency Discharges.** *S. Mohr, E. Schuengel, J. Schulze, U. Czarnetzki*, Ruhr University Bochum, Germany

Capacitively coupled radio-frequency (CCRF) discharges are commonly used in surface processing applications, for example the deposition of thin films. One of the most important challenges in optimizing CCRF discharges for this usage is achieving the ample and independent control of flux and energy of ions and reactive species at the surfaces, as these properties determine the quality and deposition rate of the films. This independent control can be attained by using electrically asymmetric discharges which use two consecutive harmonics to excite the plasma; the ion energy can be controlled by the phase between the two frequencies while the flux stays constant. The feasibility of this method has been demonstrated by both experiments and simulations in various gas mixtures [1-3], although limitations have been observed, for example in highly electronegative discharges.

Hydrogen is part of many gas mixtures used in industrial applications such as hydrogen/silane mixtures in the production of solar cells. Two traits, which distinguish hydrogen discharges from the already investigated gas mixtures, are the high ion mobility and the regular occurrence of field reversals during the sheath collapse. Additionally, deposition processes are usually carried out at quite high pressures of several 100 Pa. We conduct two-dimensional simulations of such discharges covering a wide range of discharge conditions (pressure: 20 Pa – 500 Pa, pure hydrogen discharges and hydrogen/silane mixtures) using the simulation tool Hybrid Plasma Equipment Model (HPEM) by Mark Kushner [4]. The focus of our investigations lies on the influence of high pressures, field reversals, and high ion mobilities on the separate control of ion energy and ion flux. For example, we observe a significant reduction of the ion energy control range, if field reversals are the main ionization source of the discharge. The physical mechanisms behind this effect and others occurring in hydrogen and hydrogen/silane - discharges will be discussed.

Funded by the German Federal Ministry for the Environment, Nature Conservation and Nuclear Safety (0325210B).

[1] U. Czarnetzki et al. 2011 *PSS* **20** 024010

[2] E. Schüngel et al. 2011 *J. Phys. D* **44** 285205

[3] J. Schulze et al. 2011 *PSS* **20** 045008

[4] M. Kushner 2009 *J. Phys. D* **42** 194013

Exhibitor Technology Spotlight

Room: West Hall - Session EW-WeM

Exhibitor Technology Spotlight

Moderator: D. Surman, Kratos Analytical Inc.

10:20am **EW-WeM8 Mass Spectrometer Now Supports Process Control.** *S. Lass*, Brooks Automation

With the introduction of the 835 Vacuum Quality Monitor and 835 Differential Pumping System, Granville-Phillips has added key control features and extended the operating pressure range to enable process monitoring and control. Driving outputs from user-defined equations which utilize the partial pressures from this gas analysis system provides the ability to start and stop a process based on specific conditions. And differential pumping allows operation at both process and base-out pressures. Process pressure operation together with the features required for process control will be covered.

Graphene and Related Materials Focus Topic

Room: 13 - Session GR+AS+BI+PS+SS-WeM

Graphene Surface Chemistry, Functionalization, Biological and Sensor Applications

Moderator: D.K. Gaskill, U.S. Naval Research Laboratory

8:00am **GR+AS+BI+PS+SS-WeM1 Structural Analysis of Chemically Functionalized Epitaxial Graphene with High-Resolution X-ray Reflectivity.** *J.D. Emery, Q.H. Wang, M. Zarrouati*, Northwestern University, *P. Fenter*, Argonne National Laboratory, *M.C. Hersam, M.J. Bedzyk*, Northwestern University

For graphene to realize its potential in next-generation electronics it must be incorporated with a variety of materials to form devices. Recently, the use of self-assembled organic monolayers deposited on epitaxial graphene (prepared by graphitization of the 6H-SiC(0001) surface) has been effective in the functionalization of the bare graphene sheet, enabling the additional chemistry necessary for device fabrication. In this work, we present high-resolution X-ray Reflectivity (XRR) studies of perylene-3,4,9,10-tetracarboxylic dianhydride (PTCDA) on epitaxial graphene. Initially, a model-independent vertical electron density profile of the graphene/silicon carbide interface is retrieved with the use of Feinup-based error correction algorithms in order to minimize ambiguities that can arise from model-based methods. This retrieved structure is then used as the foundation for model-based analysis, from which the final structures are extracted. A series of structures comprising 0, 1, and 2MLs of PTCDA deposited on 1-2ML graphene are discussed. The interlayer spacing between the PTCDA and top graphene layer are revealed to be approximately 0.35 nm, which supports the view that the PTCDA molecules are interacting only weakly (van der Waals) with the graphene layer. In addition to the characterization of PTCDA-functionalized graphene, we will also demonstrate the efficacy of these molecules to form a weakly-interacting seeding layer for subsequent growth of high-k dielectrics via atomic layer deposition.

8:20am **GR+AS+BI+PS+SS-WeM2 In Situ FT-IR Study of Graphene Fluorination using XeF₂.** *J.-F. Veyan, N. Shafiq*, University of Texas at Dallas, *K. Novoselov*, University of Manchester, UK, *Y.J. Chabal*, University of Texas at Dallas

Graphene fluorination to obtain fluorographene has been successfully realized by exposing graphene flakes to molecular Xenon-Difluoride¹⁻³. To gain a mechanistic understanding of XeF₂ reaction with the graphene flakes, an all-aluminum custom-made two-stage reaction cell has been designed to fit into the main sample compartment of an FTIR Nicolet 6700 interferometer, for *in situ* infrared absorption spectroscopy. The first stage is a clean expansion chamber to isolate the pure XeF₂ in its gas phase, from solid XeF₂ (powder) stored in a storage vessel. The XeF₂ vapor is extracted by opening the valve V1 to the storage chamber and its pressure (up to ~4

Torr) is controlled by the valve V2. The second stage is a reactor equipped with two KBr windows, allowing the IR beam to penetrate and exit the enclosure. A pneumatic valve allows the transfer of gaseous XeF₂ from stage 1 into stage 2. Pressures in both storage and reactor chambers are measured with Baratron gauges (Ga1, Ga2). To avoid any contamination of the reactor and sample holders during sample preparation and loading, a N₂-purged glove bag is placed over the reactor to maintain a controlled environment. The graphene flakes in suspension in a NMP (N-Methylpyrrolidone) solution, are transferred onto three mechanically polished Aluminum plates at a temperature of 70°C. The plates are then mounted on the specially designed 3-reflection sample holder flange designed to fit stage 2.

By varying the sample temperature from 20 to 200°C as well as the XeF₂ pressure in the reactor stage from 0.1 to 4 Torr, the chemical attachment of fluorine on graphene is identified from a comprehensive FT-IR study performed under industrial conditions. Fluorine attached out of plane can be easily differentiated from fluorine attached at edges (i.e. remaining within the basal plane) and terminating the edge atoms.

¹ R. R. Nair, et al., *Small* **6**, 2877 (2010).

² J. T. Robinson, et al., *Nano Letters* **10**, 3001 (2010).

³ K.-J. Jeon, et al., *Acs Nano* **5**, 1042 (2011).

8:40am **GR+AS+BI+PS+SS-WeM3 Molecularly Resolved Chemical Functionalization of Graphene, M.C. Hersam**, Northwestern University
INVITED

Graphene has emerged as one of the leading materials in condensed matter physics due to its superlative electrical and mechanical properties. With an eye towards expanding its functionality and applications, this talk will highlight our latest efforts to tailor the surface chemistry of graphene [1]. At the molecular scale, we employ ultra-high vacuum (UHV) scanning tunneling microscopy (STM) and conductive atomic force microscopy (cAFM) to characterize chemically modified epitaxial graphene on SiC(0001) [2,3]. For example, a suite of perylene-based molecules form highly ordered self-assembled monolayers (SAMs) on graphene via gas-phase deposition in UHV [4,5]. Due to their noncovalent bonding, these SAMs preserve the superlative electronic properties of the underlying graphene while providing uniform and tailorable chemical functionality [6]. In this manner, disparate materials (e.g., high-*k* gate dielectrics) can be seamlessly integrated with graphene, thus enabling the fabrication of capacitors, transistors, and related electronic/excitonic devices [7]. Alternatively, via aryl diazonium chemistry, functional polymers can be covalently grafted to graphene [8], while exposure to atomic oxygen in UHV enables chemically homogeneous and thermally reversible covalent epoxy functionalization [9]. Beyond UHV STM characterization, this talk will also delineate our most recent efforts to exploit chemically modified graphene in technologically significant applications including photovoltaics [10], transparent conductors [11-13], flexible GHz transistors [14], *in vivo* biomedical applications [15,16], and photocatalysts [17].

[1] Q. H. Wang and M. C. Hersam, *MRS Bull.*, **36**, 532 (2011).

[2] J. A. Kellar et al., *Appl. Phys. Lett.*, **96**, 143103 (2010).

[3] J. M. P. Alaboson et al., *Adv. Mater.*, **23**, 2181 (2011).

[4] Q. H. Wang and M. C. Hersam, *Nature Chemistry*, **1**, 206 (2009).

[5] Q. H. Wang and M. C. Hersam, *Nano Lett.*, **11**, 589 (2011).

[6] J. D. Emery et al., *Surf. Sci.*, **605**, 1685 (2011).

[7] J. M. P. Alaboson, et al., *ACS Nano*, **5**, 5223 (2011).

[8] Md. Z. Hossain et al., *J. Am. Chem. Soc.*, **132**, 15399 (2010).

[9] Md. Z. Hossain et al., *Nature Chemistry*, **4**, 305 (2012).

[10] I. P. Murray et al., *J. Phys. Chem. Lett.*, **2**, 3006 (2011).

[11] A. A. Green and M. C. Hersam, *J. Phys. Chem. Lett.*, **1**, 544 (2010).

[12] A. A. Green and M. C. Hersam, *Nano Lett.*, **9**, 4031 (2009).

[13] Y. T. Liang and M. C. Hersam, *J. Am. Chem. Soc.*, **132**, 17661 (2010).

[14] C. Sire et al., *Nano Lett.*, **12**, 1184 (2012).

[15] M. C. Duch et al., *Nano Lett.*, **11**, 5201 (2011).

[16] J.-W. T. Seo et al., *J. Phys. Chem. Lett.*, **2**, 1004 (2011).

[17] Y. T. Liang et al., *Nano Lett.*, **11**, 2865 (2011).

9:40am **GR+AS+BI+PS+SS-WeM6 Structure of a Peptide Adsorbed on Graphene and Graphite, J. Katoch**, University of Central Florida, S.N. Kim, Z. Kuang, B.L. Farmer, R.R. Naik, Air Force Research Laboratory, S.A. Tatulian, M. Ishigami, University of Central Florida

Non-covalent functionalization of graphene using peptides is a promising method for producing novel sensors with high sensitivity and selectivity. We have performed atomic force microscopy, Raman spectroscopy, infrared

spectroscopy and molecular dynamics simulations to investigate peptide-binding behavior to graphene and graphite. We studied a dodecamer peptide, GAMHLPWHMGTL, identified by phage display to possess affinity for graphite.

Optical spectroscopy reveals that the peptide forms secondary structures both in powder form and in an aqueous medium. The dominant structure in the powder form is α -helix, which undergoes a transition to a distorted helical structure in aqueous solution. The peptide forms a complex reticular structure upon adsorption on graphene and graphite, having a helical conformation different from α -helix due to its interaction with the surface. Our observation is consistent with our molecular dynamics calculations and our study paves way for rational functionalization of graphene using biomolecules with defined structures and, therefore, functionalities. Our results have recently been published [1].

[1] J. Katoch, S.N. Kim, Z. Kuang, B. L. Farmer, R. R. Naik, S. A. Tatulian, and M. Ishigami, dx.doi.org/10.1021/nl300286k, *Nano Letters* (2012).

10:40am **GR+AS+BI+PS+SS-WeM9 Controlling the Spatial Distribution of Graphene Chemistry, S.C. Hernández**, E.H. Lock, S.G. Walton, C.J. Bennett, R. Stine, P.E. Sheehan, F.J. Bezarez, L.O. Nyakiti, R.L. Myers-Ward, J.T. Robinson, J.D. Caldwell, C.R. Eddy, Jr., D.K. Gaskill, Naval Research Laboratory

Graphene has attracted a widespread of interest because of its unique structural and electronic properties however, manipulation of these properties is necessary before realizing its full potential as the next generation material in a broad range of applications. Precise control of the surface chemistry of graphene can allow for subsequent surface procedures both for device fabrication (i.e. atomic layer deposition) and sensor applications. Chemical composition strongly impacts the electronic properties as well as chemical reactivity, both globally and locally. Electron-beam generated plasmas are capable of imparting a variety of functional group types over a range of coverages with minimal damage to the carbon backbone because of their inherently low ion energies and as such offer a unique approach for large area uniform processing of graphene films with controlled surface chemistry. The ability to manipulate the surface chemistry of this atomically thin material coupled with the capability to regulate the spatial distribution of functional will be discussed. Plasma processing conditions and characteristics, as well as the resulting chemical, structural, and electrical properties of the functionalized graphene will be demonstrated. This work is supported by the Naval Research Laboratory base program.

11:00am **GR+AS+BI+PS+SS-WeM10 Coverage-dependent Ordering of Adsorbed Iron Phthalocyanine on Epitaxial Graphene Grown on SiC(0001)-Si, A.A. Sandin**, D.B. Dougherty, J.E. Rowe, North Carolina State University

The crystallographic and electronic structure of monolayer and sub-monolayer Iron-Phthalocyanine (FePc) films are experimentally studied on graphene grown on SiC(0001) using Scanning Tunneling Microscopy and Spectroscopy (STM and STS) as well as Low Energy Electron Diffraction (LEED). At full monolayer coverage of FePc the STM images show that a nearly square overlayer lattice forms with flat-lying molecules and a densely-packed structure oriented 10° relative to the graphene principle lattice directions. This close-packed structure appears to be the same as that previously reported for FePc on graphite surfaces. For sub-monolayer coverage at room temperature, our STM images suggest that FePc forms a unique 2D molecular gas with images that have the hexagonal symmetry of the graphene honeycomb lattice. This is interpreted as suggesting that only a small diffusion barrier exists for molecular motion between neighboring sites in the 3-fold symmetry of the sub-monolayer overlayer lattice. The sub-monolayer gas condenses into islands at liquid Nitrogen temperatures with bare graphene regions and this implies that a weak attractive interaction exists between FePc molecules causing the close-packed ordering. Near defects in the graphene lattice we observe ring-like structures at room temperature that suggest an increased residence time of the mobile 2-D gas of FePc molecules. Our results using Scanning Tunneling Spectroscopy suggest the possibility of a hybrid molecule-graphene state in the unoccupied density of both states near the Fermi level which could possibly be useful in modifying the charge injection into graphene in future devices.

11:20am **GR+AS+BI+PS+SS-WeM11 A Molecular Route to Carbon Nanomembranes, Graphene and Their Hybrids with Tailored Physical and Chemical Properties, A. Turchanin**, University of Bielefeld, Germany
INVITED

Bottom-up approaches via molecular self-assembly have high potential to facilitate the applications of two-dimensional (2D) carbon materials in nanotechnology. In this talk it will be demonstrated how self-assembled monolayers (SAMs) of aromatic molecules can be employed to this end.

These monolayers are converted into *carbon nanomembranes* (CNMs) with a thickness of one molecule by electron or photon irradiation. CNMs can be separated from their original substrates and transferred onto various other substrates, fabricated as suspended nanomembranes or stacked into multilayer films with precise control over their thickness and composition. They possess two chemically distinct faces, which can be used for their selective functionalization, opening broad avenues for the engineering of novel materials with tailored on demand properties. High temperature annealing induces the transformation of CNMs into *graphene*, which allows large-area fabrication of the homogenous sheets with tunable electrical, optical and chemical properties. Integration of graphene sheets with CNMs into novel hybrids presents a promising route to flexibly functionalize graphene for applications as optical, electrical, chemical and biofunctional coating in nanoelectronics and sensors. Various physical and chemical properties of these novel materials, their nanopatterning and functional applications will be presented.

- 1) A. Turchanin and A. Gözlhüser, *Prog. Surf. Sci.* (2012) in press.
- 2) A. Turchanin, D. Weber, M. Bünenfeld, C. Kisielowski, M. Fistul, K. Efetov, R. Stosch, T. Weimann, J. Mayer, A. Gözlhüser, *ACS Nano* 5 (2011) 3896-3904.
- 3) C.T. Nottbohm, A. Turchanin, A. Beyer, R. Stosch, A. Gözlhüser, *Small* 7 (2011) 874-883.
- 4) Z. Zheng, C.T. Nottbohm, A. Turchanin, H. Muzik, A. Beyer, M. Heilemann, M. Sauer, A. Gözlhüser, *Angew. Chem. Int. Ed.* 49 (2010) 8493-8497.
- 5) A. Turchanin, A. Beyer, C.T. Nottbohm, X. H. Zhang, R. Stosch, A. Sologubenko, J. Mayer, P. Hinze, T. Weimann, A. Gözlhüser, *Adv. Mater.* 21, 1233-1237 (2009).

In Situ Microscopy and Spectroscopy Focus Topic

Room: 7 - Session IS+AS+OX+ET-WeM

In Situ Characterization of Solids: Film Growth, Defects, and Interfaces

Moderator: P.W. Sutter, Brookhaven National Laboratory

8:00am **IS+AS+OX+ET-WeM1 Revealing Gas-Surface Radical Reaction Mechanisms of Self-Assembled Monolayers by Scanning Tunneling Microscopy**, *D.Y. Lee, M.M. Jobbins, S.A. Kandel*, University of Notre Dame

Scanning Tunneling Microscopy (STM) in ultra-high-vacuum is used *in situ* to investigate the surface changes of the octanethiolate self-assembled monolayer (SAM) on Au(111) upon reaction with atomic hydrogen and with atomic chlorine. For both reactions, the surface structure heavily influences the rate of monolayer degradation, but the effect of surface defects on reactivity is completely opposite when comparing the two systems. Monolayer reactivity increases with increasing hydrogen-atom exposure while decreases with further reaction with atomic chlorine. The monolayer-versus-exposure data are examined by kinetic Monte Carlo simulations and reveal that, for H-atom exposure, molecules located near surface defect sites are potentially over 500 times more reactive than close-packed areas. For Cl-atom interactions, however, the opposite occurs: close-packed regions are at least 100 times more reactive than defect sites. These observations result directly from the alkyl hydrogen abstraction and sulfur-gold bond cleavage mechanisms of SAM upon gas-phase radical bombardment.

8:20am **IS+AS+OX+ET-WeM2 In Situ Imaging of the Nucleation and Growth of Epitaxial Anatase TiO₂(001) Films on SrTiO₃(001)**, *Y.G. Du, D.J. Kim, T.C. Kaspar*, Pacific Northwest National Laboratory, *S.E. Chamberlin*, University of Wisconsin Milwaukee, *I. Lyubinsky, S.A. Chambers*, Pacific Northwest National Laboratory

TiO₂ has attracted much attention because of its potential utility in hydrogen production via water splitting, environmental remediation, and dye-sensitized solar cell fabrication. Heteroepitaxial growth of anatase is a powerful and unique way to fabricate model surfaces of the less stable anatase polymorph for fundamental surface science studies. In this work, the growth of TiO₂ anatase films on Nb doped SrTiO₃(001) by molecular beam epitaxy has been studied *in-situ* by scanning tunneling microscopy. We show that the initial growth follows the Stranski-Krastanov mode, where islands form on top of a wetting layer consisting of two monolayers (ML) of TiO₂. Well-defined (4x1) and (1x4) terraces are observed for film thicknesses in excess of 3 nm. At larger film thicknesses, large oriented crystallites form as a result of the coalescence of smaller islands. Within a given crystallite, either (4x1) or (1x4) reconstructed terraces account for

majority of the surface. The anatase grows in units of bilayers, resulting in a step height of 2 ML. This result explains the fact that the measured period of the RHEED specular-beam intensity oscillations corresponds to the time required for deposition of 2 ML. Ar ion sputtering and UHV annealing results in a transformation to coexisting (4x1) and (1x4) reconstructed terraces on individual crystallites, as commonly observed by *ex-situ* STM studies. In addition, we show that the nucleation and growth of anatase films are influenced by Nb doping in the SrTiO₃ substrates by comparing with similar growth occurring on pure SrTiO₃ substrates.

8:40am **IS+AS+OX+ET-WeM3 In Situ Synchrotron X-Ray Studies of Epitaxial Oxide Thin Film Synthesis Behavior**, *J.A. Eastman, M.J. Highland, P.H. Fuoss*, Argonne National Laboratory, *T.M. McCleskey*, Los Alamos National Laboratory, *D.D. Fong, C.M. Folkman, S.K. Keun, E. Perret, P.M. Baldo*, Argonne National Laboratory, *E. Bauer, Q. Jia*, Los Alamos National Laboratory

INVITED

Intense interest is focused on the growth science of epitaxial oxide thin films because of continuing discoveries of new interesting and important properties. The key to achieving desired maximum functionality of oxide heterostructures is the ability to synthesize high-quality films with full control of factors such as composition, crystallographic orientation, surface termination, and strain state. Many of the most promising thin film synthesis techniques involve non-vacuum, high-temperature environmental conditions that are difficult or impossible to probe using standard spectroscopic or structural probes. However, the use of high-energy x-rays available at synchrotron sources such as the Advanced Photon Source (APS) provides an opportunity to obtain real-time atomic-level structural and chemical information during synthesis. This talk will describe results from recent studies at APS Sector 12ID-D using an in-situ x-ray approach to understand and control the synthesis behavior of complex oxide epitaxial thin films prepared by two very different techniques: sputter deposition or polymer assisted deposition (PAD).

We recently built a new RF magnetron sputter deposition system at the APS, which brings to bear state-of-the-art real-time in-situ x-ray scattering and spectroscopy techniques to provide insight into the growth behavior of epitaxial oxide thin film heterostructures. Initial studies of the growth behavior of epitaxial films such as (001) LaGaO₃, SrZrO₄, and LaGaO₃/SrZrO₃ multilayer heterostructures during off-axis sputtering will be described, focusing on the effects of epitaxial strain and electrical compensation (e.g., surface polarity) on growth behavior.

PAD is a solution technique capable of synthesizing dense epitaxial thin films. Past work at Los Alamos has demonstrated that PAD can be used to prepare aligned epitaxial films of many different materials. We recently performed initial in-situ synchrotron x-ray experiments aimed at obtaining a fundamental understanding of the nucleation and growth processes associated with epitaxial film formation. Studies of the synthesis behavior of (001) BaTiO₃ epitaxial films will be described in this talk, focusing on the effects of thermal history and choice of substrate material on crystallization behavior and the development of epitaxy.

Argonne researchers were supported by the U. S. Department of Energy (DOE), Basic Energy Sciences (BES), Materials Sciences and Engineering Division. Los Alamos researchers were supported by the DOE through the LANL/LDRD Program. Use of the APS was supported by BES, under Contract DE-AC02-06CH11357 between UChicago Argonne LLC and the Department of Energy.

9:40am **IS+AS+OX+ET-WeM6 Understanding the Dynamic Electronic Properties of Electrode Materials by In Situ X-ray Absorption Spectroscopy**, *M. Bagge-Hansen, J.R.I. Lee, A. Wittstock, M.D. Merrill, M.A. Worsley, T. Ogitsu, B.C. Wood, T. Baumann, M. Stadermann, M. Biener, J. Biener, T. van Buuren*, Lawrence Livermore National Laboratory

In situ characterization of the evolution in electronic structure of electrode materials during repeated charge-discharge cycling is fundamentally important for more fully understanding the processes of charge storage and degradation, which, in turn, is essential for the development of new electrical energy storage (EES) materials with tailored properties and improved performance. X-ray spectroscopies provide ideal tools with which to obtain enhanced insight into the origins of electrode behavior in EES systems due to their capabilities for direct, element specific, characterization of the electronic densities of states. To date, in situ studies of EES materials have primarily focused on hard x-ray experiments due to the challenges associated with UHV compatibility and high photon attenuation of cells for soft x-ray measurements. Nonetheless, the use of soft x-ray spectroscopies to EES systems is vital since they provide complementary information that cannot be obtained via hard x-ray studies. We report the development of a cell for in situ soft x-ray emission spectroscopy and x-ray absorption spectroscopy studies of EES materials and will discuss experiments focused upon the x-ray spectroscopy

characterization of a series of novel electrode materials. Prepared by LLNL under Contract DE-AC52-07NA27344.

10:40am **IS+AS+OX+ET-WeM9 In Situ Studies of Al₂O₃ ALD Growth and Self-cleaning on III-V Surfaces by STM and XPS**, *L.N.J. Rodriguez, A. De Clercq*, IMEC, Belgium, *M. Tallarida*, BTU Cottbus, Germany, *D. Cuypers*, IMEC, Belgium, *J.P. Locquet*, KU Leuven, Belgium, *S. Van Elshocht*, *C. Adelmann*, *M. Caymax*, IMEC, Belgium

A custom built ALD UHV-compatible reactor has been used to study the growth of TMA on InP and InAlAs by STM in conjunction with additional studies performed in a reactor attached to a synchrotron XPS. The effects of selected ex-situ cleans has been measured along with the subsequent cycles of ALD growth from TMA and water. The STM data shows morphological differences between the ex-situ cleans on InP, with sulphuric acid cleans yielding plateaus but ammonium sulphide cleans yielding rough surfaces. In-situ measurements of these surfaces after TMA dosing shows the growth of islands which converge to film closure after ten cycles of ALD growth. In-situ measurements of the I-V curves by STS allowed the creation of bandgap maps of the III-V interfaces after TMA dosing. These bandgap maps showed a non-uniform distribution with regions of either higher or lower bandgap. The mean bandgap was seen to decrease with increasing numbers of ALD cycles. In-situ XPS data on similar systems showed a reduction in surface oxides for InAlAs but not for InP. The reduction of arsenic oxides with a creation of metallic arsenic, along partial reduction of indium oxides and a conversion of aluminium sub-oxides to aluminium oxide was seen in the former case. In the latter case, a formal oxidation of the phosphorus was seen with increased TMA dosing instead of a self-cleaning effect.

11:00am **IS+AS+OX+ET-WeM10 In Situ Transport Measurement of Kinetically Controlled Bi Atomic Layers**, *Y. Fujikawa, E. Saitoh*, Tohoku University, Japan

Thin film growth of Bi and related compounds has been attracted much attention because of their exotic properties originating in the large spin-orbit interaction of Bi. Growth of its simple substance is known to result in the formation of a thin-film phase in the initial stage, which is taken over by the bulk growth when the coverage exceeds several monolayers (ML). [1] With typical growth conditions, this transition takes place before the completion of the thin-film layer, which tends to agglomerate to form 4-ML thick islands, making it difficult to measure the intrinsic property of the thin-film phase. In this work, Bi growth on Si(111)-7x7 has been performed in a multi-probe VT-STM system, which provides wide-ranging opportunity of kinetic control and *in-situ* transport measurement during the thin film growth. By tuning the kinetic condition of the growth, it becomes possible to grow the thin-film phase uniformly covering the substrate. Its conductivity, monotonically increasing with the increase of the temperature, would suggest the variable-range hopping conduction rather than the carrier excitation of semiconductors. *In-situ* transport measurement has been performed during the layer-by-layer growth of the Bi thin-film phase, distinguishing the conductivity of each growth unit. It fluctuates with periods of 2 and 4 ML, which may reflect the atomic structure of the thin-film phase.

[1] Nagao *et al.*, Phys. Rev. Lett. **93**, 105501 (2004).

11:20am **IS+AS+OX+ET-WeM11 CAMECA IMS Series Advanced Ion Microscopy: High Throughput, Repeatability & Automation**, *P. Peres, F. Desse, F. Hillion, M. Schuhmacher*, Cameca, S.a., France, *A.N. Davis*, CAMECA Instruments, Inc.

The advantage of CAMECA IMS Series high performance secondary ion mass spectrometers are well established: extreme sensitivity, high mass resolution, and high dynamic range, providing low detection limits while keeping high analysis throughput. This instrument delivers high analytical performance for a wide range of applications: Si based devices, III-V and II-VI devices, both bulk materials and thin-film technology, as well as for different material science applications.

In order to meet the growing demand in terms of reproducibility and throughput performance as well as ease of use, CAMECA has developed a new IMS series, 7f-Auto.

The primary column has been redesigned in order to provide an easier and faster primary beam tuning. For high efficiency operation, automated routines for tuning the instrument are added for both primary and secondary columns, nominally: aperture adjustment, secondary ion beam centering, detector adjustment, among others. These routines not only increase the ease of use, but also enhance the reproducibility of the instruments by minimizing operator-related biases.

A motorized storage chamber has also been developed allowing to keep, under UHV environment, up to six sample holders. The holder exchange between the storage chamber and analysis chamber is fully motorized and

computer controlled, allowing a set of analyses to be performed in automated, unattended mode on multiple sample holders. This significantly improves the throughput of the tool, since up to 24 samples (assuming 4 samples per holder) can be analysed in chained mode, possibly overnight. These developments will be presented and discussed in detail.

Magnetic Interfaces and Nanostructures

Room: 6 - Session MI-WeM

Topological Insulators and Rashba

Moderator: M. Donath, Muenster University, Germany, E. Vescovo, Brookhaven National Laboratory

8:00am **MI-WeM1 UP or DOWN? Rashba-type Spin Structures in *sp*- and *d*-derived Surface States Below and Beyond the Fermi Level**, *M. Donath, S.D. Stolwijk, A. Zumbülle, S.N.P. Wissing, Ch. Langenkämper, A.B. Schmidt, P. Krüger*, Muenster University, Germany, *K. Miyamoto, K. Shimada, A. Kimura*, Hiroshima University, Japan, *K. Sakamoto*, Chiba University, Japan, *R.C. Hatch, P. Hofmann*, Aarhus University, Denmark

Rashba-type spin splittings in the surface electronic structure of heavy elements and topological insulators are a hot topic of today's research in condensed matter physics. The interest is guided by possible applications of these materials in spintronic devices, in which the electron spin is used as an information carrier.

In this talk, I will present several experimental studies of surface states of different origin and with distinct spin configurations. At W(110), a spin-polarized Dirac-cone-like surface state with *d* character was identified, which appears below the Fermi level in a spin-orbit-induced symmetry gap of the projected bulk-band structure [1]. At Ti/Si(111), an unoccupied surface state with a spin-dependent energy splitting of more the 0.5 eV exhibits a distinct spin structure around the K point, leading to almost complete spin polarization at the Fermi level. Furthermore, the spin-dependent unoccupied electron states of the topological insulator Bi₂Se₃(111) were studied as a function of different preparation conditions. Making combined use of direct and inverse photoemission, we were able to characterize the electronic states below and beyond the Fermi level.

[1] K. Miyamoto *et al.*, Phys. Rev. Lett. **108**, 066808 (2012).

8:20am **MI-WeM2 Scanning Tunneling Spectroscopy of Topological Insulators' Electrically Tunable Electronic Structure**, *N. Levy*, Center for Nanoscale Sci. and Tech. / NIST, *T. Zhang*, Center for Nanoscale Sci. and Tech. / NIST and Maryland NanoCenter / Univ. of Maryland, *J. Ha*, Center for Nanoscale Sci. and Tech. / NIST and Seoul National Univ., Korea, *Y. Kuk*, Seoul National Univ., Republic of Korea, *J.A. Stroscio*, Center for Nanoscale Sci. and Tech. / NIST

Three-dimensional (3D) topological insulators (TI) are a new state of matter with a bulk band gap but topologically protected gapless surface states. These protected surface states are massless helical Dirac fermions which are predicted to host many striking quantum phenomena [1]. Angle resolved photoemission spectroscopy (ARPES) and scanning tunneling microscopy (STM) measurements confirmed the existence of these surface states and their helical spin structure [1]. All the 3D TI materials to date have an initial doping level which places the Dirac point away from the Fermi level. Initial studies used chemical doping to align the surface states within the bulk band gap. A preferable method to realize the host of new phenomena in TI materials is to electrically tune the carrier density using the field effect from a gate electrode, as demonstrated in three terminal transport experiments [2]. However, the combination of local probe studies with samples containing low defect concentrations and a tunable carrier density remains a challenge, due to the chemical reactivity of the TI surfaces which precludes ex-situ fabrication and processing of the unprotected films.

In this talk we present new results on atomically flat Bi₂Se₃ and Sb₂Te₃ films grown on SrTiO₃ substrates using Molecular Beam Epitaxy (MBE). SrTiO₃ has a very large dielectric constant of ~10⁴ at 4 K [3], allowing tuning of the TI Dirac point and carrier density even with a relatively thick dielectric of 100 μm. The SrTiO₃ substrates were pre-patterned with platinum electrodes and mounted in specially designed sample holders, allowing us to *in-situ* control the carrier density with a back gate on *in-situ* grown films, avoiding any *ex-situ* post processing of the samples. As a result, we are able to continuously change the carrier density and observe the local electronic structure of pristine grown TI films. Initial measurements at 5 K are focused on very thin films of 2 to 10 quintuple layers. Scanning tunneling spectroscopy measurements of the thin film's surface electronic structure allow us to study the gate's efficiency vs. local film thickness in a single sample. We find that the efficiency of gating the top surface state's electronic structure depends on the film thickness, with a

decreasing efficiency for thicker films. In addition, we observe substantial differences in gating between Bi_2Se_3 and Sb_2Te_3 . We will discuss these results and models of the gating of carriers in the bottom and top surface states through the bulk films at different bulk carrier densities.

- [1] Rev. Mod. Phys. **82** 3045 (2010)
- [2] Nano Lett., **10** (12), 5032 (2010)
- [3] Phys. Rev. B **19**, 3593–3602 (1979)

11:20am **MI-WeM11 Scanning Tunneling Microscopy Observation of the Superconducting Gap in $\text{Cu}_x\text{Bi}_2\text{Se}_3$** , *J. Ha*, Center for Nanoscale Sci. and Tech. / NIST and Seoul National Univ., *N. Levy*, Center for Nanoscale Sci. and Tech. / NIST, *T. Zhang*, Center for Nanoscale Sci. and Tech. / NIST and Maryland NanoCenter / Univ. of Maryland, *R.L. Kallaher*, *F. Sharifi*, *A.A. Talin*, Center for Nanoscale Sci. and Tech. / NIST, *Y. Kuk*, Seoul National Univ., Republic of Korea, *J.A. Stroscio*, Center for Nanoscale Sci. and Tech. / NIST

The discovery of topological insulators has triggered the search for new topological states of matter. A topological superconductor is one such state, characterized by the existence of an unconventional superconducting gap in the bulk, and gapless Andreev bound states on the surface. Recently, Cu intercalated Bi_2Se_3 ($\text{Cu}_x\text{Bi}_2\text{Se}_3$) was found to be superconducting with $T_C \approx 3.8$ K [1], and is considered a prime candidate for topological superconductivity due to its peculiar band structure and strong spin-orbit coupling. A recent point contact measurement observed zero-bias conductance peaks, claiming these as evidence of surface Andreev bound states, and angle resolved photoemission spectroscopy has revealed the preservation of the topological surface states at the Fermi level [2, 3]. However, direct measurement of the superconducting gap in this material has not been reported.

In this work, we use an ultra-low temperature scanning tunneling microscope [4] to investigate the superconducting properties of a cleaved $\text{Cu}_x\text{Bi}_2\text{Se}_3$ bulk crystal. The crystal was synthesized by electrochemical intercalation of Cu atoms into a previously synthesized Bi_2Se_3 crystal. We observe a superconducting gap in scanning tunneling spectroscopy (STS) measurements. We estimate the size of the gap to be 0.35 meV from a preliminary BCS fit of the superconducting gap. STS measurements under a magnetic field show a complete suppression of the superconducting gap at a critical field of ≈ 1.5 T. Significant inhomogeneity is observed in the material with spatial variations of the superconducting gap. We will discuss these observations in the context of current theories of topological superconductors.

- [1] Y. S. Hor *et al.*, Phys. Rev. Lett. **104**, 057001 (2010)
- [2] L. A. Wray *et al.*, Nat. Phys. **6**, 855–859 (2010)
- [3] S. Sasaki *et al.*, Phys. Rev. Lett. **107**, 217001 (2011)
- [4] Y. J. Song *et al.*, Rev. Sci. Instrum. **81**, 121101 (2010)

Nanometer-scale Science and Technology Room: 12 - Session NS+AS+SS+SP-WeM

Nanoscale Catalysis and Surface Chemistry Moderator: U.D. Schwarz, Yale University

8:20am **NS+AS+SS+SP-WeM2 Preparation and Performance of Solid Rocket Propellant Containing *In Situ*-Synthesized Nanoparticle Catalysts and Fuels**, *D. Reid*, *R. Draper*, University of Central Florida, *M. Johnson*, *T. Allen*, *A. Demko*, *E. Petersen*, Texas A&M University, *S.S. Seal*, University of Central Florida

Energetic nanocomposites have the potential to substantially increase the performance of rocket propulsion systems, but adoption outside the laboratory has been slow, largely due to manufacturing difficulties, safety challenges, and performance that falls short of theoretical potentials. In this study, we explore some novel synthesis methods to significantly improve performance and alleviate the difficulties of incorporating nanoparticles into energetic materials. Solid rocket propellants containing *in-situ* synthesized catalytic TiO_2 and energetic aluminum nanoparticles were prepared. These propellants exhibited significant performance improvements over those containing conventionally prepared nanoparticles. The performance gains are attributed to the small particle sizes, high degree of dispersion, and surface property control afforded by the *in-situ* synthesis methods.

9:00am **NS+AS+SS+SP-WeM4 Synthesis and Catalytic Activity of WS_2 Nanotube Supported Cobalt and Nickel Catalysts Towards Thiophene Hydrodesulfurization**, *M. Komarneni*, *Z. Yu*, *A. Chakradhar*, *U. Burghaus*, North Dakota State University, *Y. Tsvetkov*, *R. Popovitz-Biro*, *Y. Feldman*, *R. Tenne*, Weizmann Institute of Science, Israel

Inorganic nanotubes (INT) including WS_2 INT are promising materials for heterogeneous catalysis due to their intriguing properties like enhanced surface area, defects, and confinement effects. The promotion effects of Co and Ni combined with novel nanomaterials such as INT- WS_2 may create the next generation hydrodesulfurization (HDS) catalysts. To verify this, M/INT- WS_2 (M = Co or Ni) catalysts were synthesized and their catalytic activity towards HDS of thiophene was characterized by gas chromatography/ambient pressure catalytic tests and ultra-high vacuum (UHV) thermal desorption spectroscopy (TDS) experiments. Synthesis of M/INT- WS_2 involved two steps: Surface activation of INT- WS_2 by palladium seeding process and electroless plating method to coat nanoparticles of M. The deposited nanoparticles of M formed non-uniform layer on the INT surface. Nanoparticles of size 10-20 nm for Co (*hcp* structure) and 10-20 nm for Ni (*fcc* structure) were coated on INT- WS_2 . Next, the catalytic activity of M/INT- WS_2 towards thiophene HDS was characterized using an atmospheric flow reactor. M/INT- WS_2 catalysts exhibited enhanced HDS activity when compared to pristine INT- WS_2 mainly due to the promotion effects of Co and Ni. Hydrogen sulfide and hydrocarbons such as 1,3-butadiene, butane, *cis*-2-butene, and *trans*-2-butene were formed as HDS products by both pristine and M/INT- WS_2 . Commercial HDS catalysts, CoMo and NiMo from Haldor Topsoe were found to show ~ 4 times higher activity than M/INT- WS_2 synthesized in this study. These results are promising and show that further optimization of the nanofabrication process yields better HDS nanocatalysts. Furthermore, the adsorption kinetics of thiophene on M/INT- WS_2 was studied by TDS at UHV conditions. Thiophene adsorbed on internal, external, and groove sites of the M/INT- WS_2 bundles. Binding energies of thiophene on Ni/INT- WS_2 are ~ 10 kJ/mol smaller than that of pristine INT- WS_2 . Thiophene also decomposed on M/ WS_2 NT at UHV conditions. In addition, catalytic screening of nanocatalysts such as Au and Co-Ni coated INT- WS_2 , pristine MoS_2 nanoparticles with fullerene-like structure (IF), and Re-doped IF- MoS_2 for HDS was also performed. Overall, M/INT- WS_2 catalysts were the best HDS catalysts among the new nanocatalysts studied. The results also reflected the promotion effects of Co and Ni on the M/INT- WS_2 catalysts for higher thiophene conversion rates.

11:20am **NS+AS+SS+SP-WeM11 Charge Exchange and Molecule/Metal Coupling in Fulvalene Surface Chemistry**, *G. Rojas*, *B.G. Sumpter*, Oak Ridge National Laboratory, *J.A. Schlueter*, Argonne National Laboratory, *P. Maksymovych*, Oak Ridge National Laboratory

Understanding the epitaxy of organic semiconductors on the surface, and the ensuing processes of charge transfer and band-alignment is vitally important for the deterministic design of energy harvesting and light-emitting devices based on molecular heterojunctions. While most of the attention so far has been directed to pi-conjugated aromatic compounds, little is known about the properties of the fulvalene family in contact with metal surface. Here we will present a spectroscopic study of bis(ethylenedithio)tetrathiafulvalene (ET) on Ag(111) in the sub-monolayer to monolayer coverage. Varying coverages of ET adsorption show the molecules dimerize in parallel, bonding to the Ag surface along the long-axis of the molecule. The dimers remain mobile after adsorption, resulting in the formation of a two-phase surface material: unidimensional loosely stacked nanoclusters and finely packed, two-dimensional domains of interlocked molecules. These structures are an intermediate kinetic state, as the molecules further chemically react with the underlying Ag surface following annealing to temperatures as low as 40 C. It is thought based on these data that the dimers form chemical bonds with a single, shared Ag adatom upon adsorption, as observed for other pi orbital dominated aromatic molecules such as PTCDA. Formation of a reactive layer has significant implications for the orbital alignment at the interface. We have therefore probed the properties of the 2D ordered layer and the reacted layers using a combination of current-distance and image-potential state spectroscopy. The interpretation of these results will be presented in conjunction with the first-principles calculations of the respective structures, and correlated with the induced density of interface states (IDIS) model for orbital alignment at metal-molecule interface.

This research was conducted at the Center for Nanophase Materials Sciences, sponsored at the Oak Ridge National Laboratory by the Division of User Facilities, U.S. Department of Energy.

11:40am **NS+AS+SS+SP-WeM12 Subpicosecond-pulse Photoinduced Chemistry on Nanoscale Palladium Model Catalyst Surfaces**, *A. Bhattacharya*, Brookhaven National Laboratory, *R. Palomino, J.C. Lofaro*, Stony Brook University, *H. Park, M.G. White, N. Camillone*, Brookhaven National Laboratory

To date, time-resolved investigations of surface chemical reaction dynamics have almost exclusively been conducted on metal single crystals. However, current and proposed catalysts and photocatalysts generally consist of nanometer-scale metal particles supported on metal oxides. To conduct time-resolved investigations of the surface chemical dynamics of such systems we have synthesized and characterized arrays of palladium nanoparticles (approximately 4 to 10 nm in diameter) supported on clean rutile TiO₂(110). We will present our synthetic approach and the results of chemical and morphological characterization and thermal chemistry experiments on these arrays. We will also discuss the results of subpicosecond-pulse photoinduced desorption of molecular oxygen and carbon monoxide, as well as the photoinduced bimolecular reaction between adsorbed atomic oxygen and carbon monoxide. Comparisons to the same reactions on single crystal Pd(111) surfaces will be made, and the unique features of the chemistry and dynamics at the nanoscale highlighted.

Plasma Science and Technology

Room: 24 - Session PS+TC-WeM

Atmospheric Plasma Processing for PV, Flexible Electronics (incl. R2R)

Moderator: S.A. Vitale, MIT Lincoln Laboratory

8:00am **PS+TC-WeM1 Formation Dynamics and Characterization of Organosilicon Powders in Microwave-Sustained Plasmas at Atmospheric-Pressure**, *V. Roy-Garofano, A. Kilicaslan, O. Levasseur, L. Stafford, M. Moisan*, Université de Montreal, Canada, *C. Côté, A. Sarkissian*, Plasmionique, Canada

An atmospheric-pressure plasma sustained by a propagating electromagnetic surface wave in the microwave regime combined with a bubbler/flash evaporator developed by Plasmionique for the injection of liquid precursors was used to generate organosilicon powders. Analysis of the plasma emission revealed the apparition of strong C₂ (Swan system) and CN emission bands along with Si emission lines following the addition of the hexamethyldisiloxane (HMDSO) precursors in the nominally pure argon plasma. Such features were not observed in atmospheric-pressure Ar/HMDSO discharges controlled dielectric barriers, indicating that microwave-sustained plasmas are characterized by much higher precursor fragmentation levels due to their much higher electron density. The emission spectra further showed a high-intensity continuum, the intensity of which decreased with time as powders started to form on the discharge tube walls. Analysis of the powder chemical composition by Fourier-Transform Infrared Spectroscopy showed very strong Si-(CH₃)_x and O-Si-(CH₃)_x bands, consistent with the formation of a silicon carbide. On the other hand, introduction of trace amount of O₂ in Ar/HMDSO produced white powders with strong Si-O-Si bands and no trace of carbon, consistent with the formation of SiO_x.

8:20am **PS+TC-WeM2 Infrared Gas Phase Studies in High-Current Dielectric Barrier Discharges Applied in Roll-to-Roll Deposition of Silica-Like Layers at Atmospheric Pressure**, *S. Wetzel*, Eindhoven University of Technology, Netherlands, *S.A. Starostin, H. de Vries*, FUJIFILM Manufacturing Europe B.V., Netherlands, *M.C.M. van de Sanden, R. Engeln*, Eindhoven University of Technology, Netherlands

Large-area plasma-enhanced roll-to-roll processing of polymeric substrates in diffusive dielectric barrier discharges (DBDs) have been shown to yield high-quality SiO₂-like barrier layers. This has been obtained through chemical vapour deposition at atmospheric pressure using organo-silicon precursors (HMDSO or TEOS) and industrially relevant air-like gas mixtures (N₂/O₂/Ar). Provided an electronic stabilisation circuit is applied, high currents in different diffusive discharge modes can be achieved without admixtures of Helium. Earlier, extensive surface analysis studies of the synthesised layers revealed a competition between deposition and etching regimes throughout the active plasma zone and led to the development of a deposition model.

This contribution is concerned with complementary studies of the gas phase composition using infrared absorption techniques. Given the challenging optical access to DBDs with gap distances smaller than 1 mm in industrial-like roll-to-roll configuration a gas sampling system was implemented to collect a fraction of the effluent into a multiple pass absorption cell. Main stable products were identified under various discharge conditions such as different O₂ admixtures and (average) power densities. Broadly speaking, a

typical H-N-O chemistry in the presence of traces of hydrocarbons is observed for such high-current DBDs. To establish a link to earlier model assumptions both dominant etching and deposition conditions were studied separately (i.e. precursor absent and added, respectively). Formic acid (HCOOH) was found to be a good marker molecule in the gas phase for strong etching of the polymeric substrate or incomplete precursor dissociation. Particularly, the appearance of precursor fragments in the infrared gas phase spectra can be correlated to the injected power and growth rate. Under conditions of complete precursor depletion the effluent zone of the reactor resembles an air-like plasma where NO₂, NO, N₂O and HNO₂ are observed whilst hydrocarbons or alcohols are absent.

8:40am **PS+TC-WeM3 Atmospheric Pressure Plasma Processes for Preparation of Si-Based Thin Films**, *K. Yasutake, H. Ohmi, T. Yamada, H. Kakiuchi*, Osaka University, Japan

INVITED

Thin-film deposition processes using atmospheric-pressure (AP) plasmas have attracted considerable attention as the low-cost deposition methods, because they can realize low-temperature and high-rate deposition without the necessity for ultrahigh vacuum. Recently, we have demonstrated that good-quality Si films with almost no ion damage can be prepared by using a 150-MHz very high-frequency AP plasma. Based on this result, we are studying applications of AP plasmas in semiconductor processing, e. g., i) atmospheric-pressure plasma chemical vapor deposition (AP-PCVD) of semiconductor and insulator thin films, ii) AP plasma oxidation of Si and Al, and iii) atmospheric-pressure plasma enhanced chemical transport (APECT) processes for Si purification and deposition. In this work, we will report the experimental results on the formation and characterization of Si-based thin films prepared by these AP plasma processes.

Firstly, we have studied the epitaxial Si growth by AP-PCVD. The purpose of the study is to develop a totally low-temperature semiconductor device fabrication process. Epitaxial Si films have been prepared on 4-inch-(001) Si wafers by AP-PCVD using a porous-carbon electrode. Defect-free growth of epitaxial Si is confirmed in the temperature range of 470–570°C by transmission electron microscopy and a selective etching method. A high carrier generation lifetime (≈ 2.0 ms) is observed in the Si film grown at 570°C with a reasonably high growth rate (≈ 0.4 $\mu\text{m}/\text{min}$). *In situ* H₂ plasma cleaning of the substrate surface is effective for eliminating O and C concentration peaks at the film/substrate interface. Heavy B doping with a carrier concentration of about 10^{20} cm⁻³ is achieved using B₂H₆ as a doping gas at 570°C. The relation between the mobility and carrier concentration in p- and n-doped Si films can be well fitted by the reported curves for bulk Si single crystals. These results demonstrate that the electrical quality of Si epitaxial films grown by AP-PCVD is sufficiently good for semiconductor device applications.

One of the other topics is on the AP plasma oxidation of Si. AP plasma oxidation is supposed to be most compatible for a chamber-less and open-air process, which is attractive as a high-throughput oxidation process for photovoltaic applications. SiO₂/Si structures have been prepared by AP plasma oxidation at 400°C using gas mixtures of O₂ and He. Various characterization results reveal that the properties of AP plasma oxides are similar to those of high-temperature thermal oxides, and that the SiO₂/Si structure has a low interface state density of the order of 10^{10} cm⁻²eV⁻¹.

9:20am **PS+TC-WeM5 Deposition of Organic-Inorganic Nanocomposite Coatings by Aerosol-Assisted Atmospheric Pressure DBDs**, *F. Fanelli*, Institute of Inorganic Methodologies and Plasmas (IMIP) - CNR, Bari, Italy, *A.M. Mastrangelo, F. Fracassi*, University of Bari Aldo Moro - IMIP CNR, Bari, Italy

Aerosol-assisted atmospheric pressure cold plasma processes have been recently addressed as an attractive route towards the deposition of multifunctional coatings. This approach seems to be particularly convenient, and can even offer the only possible solution, when non-volatile precursors, solutions or dispersions need to be injected directly in the atmospheric plasma. The aerosol of a dispersion of nanoparticles (NPs) in a liquid precursor can lead to the deposition of nanocomposite coatings in which the NPs are embedded in the matrix formed by the plasma polymerization of the precursor.

This contribution is focused on the study of the growth and structure of plasma-deposited polyethylene/zinc oxide (PE/ZnO) nanocomposite coatings with several potential applications due for instance to the UV-protection and photocatalytic properties of ZnO.

The coatings are deposited in a parallel plate dielectric barrier discharge (DBD) fed with He and the aerosol of a dispersion of oleate-stabilized ZnO NPs in octane or octane/1,7-octadiene mixtures. The characterization of the coatings is performed using X-ray photoelectron spectroscopy (XPS), Fourier transform infrared spectroscopy (FT-IR), scanning electron microscopy (SEM), water contact angle (WCA) goniometry.

A comprehensive study on the effect of different process parameters (e.g., atomization conditions, dispersion composition in terms of liquid precursor

and ZnO NPs concentration, deposition time) on the chemical composition and structure of the film will be presented.

Preliminary results show that, as expected, with increasing the concentration of ZnO NPs in the starting dispersion from 0.5 to 5% p/p, the ZnO content in the coating increases. Surprisingly, the addition of a small amount of 1,7-octadiene to octane (0.5% v/v) favors the inclusion of the NPs and hence results in an increase of the ZnO concentration of the coatings.

Advancing and receding WCAs steeply increase with the NPs content in the film and reach values higher than 165° with low hysteresis indicating the formation of slippery superhydrophobic surfaces. SEM images confirm that this superhydrophobic character is due to the hierarchical micro-/nano-structured surface morphology of the coatings. ZnO NPs generally aggregate in almost spherical clusters that can be incorporated to a different extent into the polyethylene-like matrix as a function of the deposition process conditions.

10:40am **PS+TC-WeM9 Modified Dielectric Barrier Discharges for Display Materials Processing**, *G.Y. Kim*, Sungkyunkwan University, Korea, *J.B. Park*, SKKU Advanced Institute of Nano Technology (SAINT), Korea, *G.Y. Yeom*, Sungkyunkwan University & SKKU Advanced Institute of Nano Technology (SAINT), Korea **INVITED**

Atmospheric pressure plasmas have been investigated tens of years for the application to semiconductor and display processing. Especially, due to the uniform discharge characteristics, dielectric barrier discharges (DBDs) composed of electrodes covered with dielectric material have been investigated intensively for those applications. In our study, the conventional DBDs have been modified to enhance the plasma density and also, the different types of DBDs such as remote-type DBD and hybrid-type DBDs (which is composed of direct-type DBD and remote-type DBD) have been used for the surface treatment, growth, deposition, and etching of material applied to flat panel displays and their effects on the material processing have been studied. In this presentation, I will present the plasma characteristics and materials characteristics obtained with those different types of modified DBDs and will suggest possible applications of the DBD-type atmospheric pressure plasmas for the next generation display processing such as in-line/roll-to-roll processing, flexible display substrate processing, inkjet processing, etc.

11:20am **PS+TC-WeM11 Etching of PTFE by Atmospheric Plasmas: Effect of the Gas Composition on the Reactions Processes and Hydrophobicity**, *J. Hubert**, *T. Dufour*, *N. Vandencastele*, Université Libre de Bruxelles, Belgium, *S. Desbief*, *R. Lazzaroni*, Matera Nova Research Center, Belgium, *F. Reniers*, Université Libre de Bruxelles, Belgium

Poly(tetrafluoroethylene) (PTFE) is a hydrophobic material due to its fully fluorinated backbone (-CF₂-CF₂-), with properties interesting for practical applications such as self-cleaning surfaces. It has been shown that superhydrophobic surfaces can be obtained by the treatment of PTFE in a helium-oxygen plasma at atmospheric pressure [1]. Contrary to oxygen-containing plasmas, the modification of PTFE by a pure helium plasma at atmospheric pressure usually leads to a strong decrease in water contact angle, in addition to an oxygen incorporation [2].

The treatment of PTFE by the atmospheric post-discharge of an RF plasma torch supplied in He and He-O₂ highlighted two totally different behaviors [3]. For this reason, the effect of the gas composition (ratio He/O₂) on the polymer modifications has been investigated. The treated surfaces have been characterized by WCA, XPS and AFM. Moreover, the species responsible for the modifications have been identified by optical spectroscopies (OES/OAS).

In pure helium plasmas, no significant change of the surfaces regarding chemical composition (XPS), wettability (WCA) and morphology (AFM) has been observed and this, despite an important mass loss measured. According to these observations, we presume a layer-by-layer physical etching without any preferential orientation, where the highly energetic helium metastables should be the main species responsible for the scission of -(CF₂)_n- chains. The XPS analysis of an aluminum foil (known to be an efficient fluorine trap) placed close to the PTFE tends to confirm this assumption as fluorine atom and -CF₂ fragments have been detected.

In He-O₂ plasmas, the helium metastables species being consumed by oxygen, fewer of them are then available to etch the PTFE, reducing the mass losses and fluorine detection on aluminum for higher O₂ flow rates. However, as it was previously shown [2], WCA and AFM measurements indicate an increase in hydrophobicity and roughness of the PTFE surface. The alveolar structures observed by AFM are then assumed to come from

the anisotropic etching where the atomic oxygen etches mainly the amorphous phase.

[1] T. Dufour, J. Hubert, P. Viville, C.Y. Duluard, S. Desbief, R. Lazzaroni, F. Reniers, PTFE surface etching in the post-discharge of a scanning RF plasma torch: evidence of ejected fluorinated species, *Plasma Process. Polym.*, 2012, DOI: 10.1002/ppap.201100209.

[2] N. Zettsu, H. Itoh, K. Yamamura, *Thin Solid Films*, 2008, 516,6683.

[3] J. Hubert, T. Dufour, N. Vandencastele, S. Desbief, R. Lazzaroni, F. Reniers, Etching processes operating on a PTFE surface exposed to He and He-O₂ atmospheric post-discharges. (Accepted : *Langmuir*).

11:40am **PS+TC-WeM12 Atmospheric Pressure Plasma Enhanced Chemical Vapor Deposition of Hydrophobic Thin Film Coatings Using Liquid Precursors**, *J. Yim*, *V. Rodriguez-Santiago*, *A. Williams*, *J. Hirvonen*, *D. Pappas*, U.S. Army Research Laboratory

Hydrophobic coatings are known to impart self-cleaning, anti-fouling, anti-fog and wicking properties on polymeric substrates and textiles. These coatings are largely derived from either wet chemical methods or low pressure plasma-based chemical vapor deposition techniques using gaseous precursors. In an effort to eliminate the use of large quantities of chemicals and solvents associated with wet chemistries and to deter the use of costly vacuum systems, we explored the practicality of an atmospheric pressure plasma jet (APPJ) as a comparable alternative to low pressure plasma systems. To obtain coatings typically achieved through wet chemistry, and often limited by commonly used fluorocarbon gases such as C₃F₆, liquid fluorinated precursors such as fluoroalkyl silanes (FAS) were explored. FAS with varying fluorocarbon chain lengths were studied and deposition conditions as a function of electrode-substrate gap distance, deposition time and power were investigated. Ultra high molecular weight polyethylene (UHMWPE) films served as the model polymer system in which the coatings were deposited owing to its simple molecular structure consisting of -CH₂-CH₂- chains. The characteristic properties of the coatings on UHMWPE such as hydrophobicity, chemical composition, uniformity and deposition rates were studied to establish a correlation between processing parameters and the coating properties. X-ray photoelectron spectroscopy (XPS) and attenuated total reflectance-Fourier transform infrared spectroscopy (ATR-FTIR) measurements confirmed the presence of CF, CF₂, and CF₃ functionalities in the coating composition and reveal that there is a strong dependence of these groups on the chain length of fluorocarbon groups in the FAS precursors. Water contact angle (WCA) measurements confirm hydrophobicity of the coating, where angles over 90° were recorded. Atomic force microscopy (AFM) and scanning electron microscopy (SEM) techniques were utilized to probe the morphological profiles of the coatings. Profilometry and ellipsometry show deposition rates of the coating ranging from nanometer to sub-micrometer thick coatings. Results show that the use of APPJ with liquid precursors is promising in achieving hydrophobic coatings under atmosphere without producing large volumes of hazardous waste.

Plasma Science and Technology
Room: 25 - Session PS-WeM

Advanced BEOL/Interconnect Etching
Moderator: A. Agarwal, Applied Materials Inc.

8:00am **PS-WeM1 The Role and Impact of Metal Hard Masks on BEOL Etch Processes**, *C. Labelle*, *R. Srivastava*, *R. Koshy*, *T.Q. Chen*, *F. Wu*, *A.P. Labonte*, GLOBALFOUNDRIES, *Y. Mignot*, STMicroelectronics, *M. Beard*, *B.G. Morris*, *Y. Yin*, IBM Systems and Technology Group **INVITED**

Back-End-of-Line (BEOL) etch processes have undergone a significant transition in recent years as the requirements of advanced technology nodes have shifted the advantage from via-first-trench-last (VFTL) to trench-first-metal-hard-mask (TFMHM) dual damascene patterning schemes throughout the industry. This shift has been primarily driven by the TFMHM scheme's ability to enable self-aligned vias (SAV), as well as inherently be more multi-patterning friendly through the use of a dissimilar hard mask material. However, typically key advances don't come without other complexities, and TFMHM is no exception. The role and impact that the metal hard mask material has on all of the etches where it is involved is significant and sometimes very subtle. At a high level, the metal hard mask influences can be split into two areas: patterning of the MHM itself, and etches where the material acts as the hard mask. The patterning of the MHM itself is where all of the challenges associated with multi-patterning come into play. The MHM profile largely determines the overall critical dimension behavior across all patterns, and so pattern control and fidelity in both x and y

* Coburn & Winters Student Award Finalist

dimensions are critical. The material properties of the MHM play a significant role in etch profile control and line edge/width roughness (LER/LWR). When considered as a hard mask in the etch, the MHM impacts are far-reaching. First, the selectivity of the MHM material vs. the underlying films must be considered. This is a key focus of etch process optimization when implementing an SAV patterning scheme and often drives all facets of the etch process. Second, the very properties that make it attractive as a hard mask (etch resistivity) can also make it the source of many other issues, typically due to the non-volatile nature of most MHM materials (Ti, TiN, TaN, etc.). Some examples include metal-containing sidewall and/or via hole residues, temperature sensitive profiles, ability to shape the MHM to help metallization, and chamber contamination effects (i.e., non-repeatability or slot-order effects). The MHM material properties have a large influence on these etches, as well, with tradeoffs between etch resistivity (good for SAV) and metal material stress (bad for pattern integrity --> can induce line wiggling). This talk will review some of the benefits of utilizing a metal hard mask, as well as some of the challenges that come hand-in-hand with it and how plasma etch process optimization is advancing in learning how to work with these materials.

This work was performed by the Research Alliance Teams at various IBM Research and Development Facilities.

8:40am PS-WeM3 Evaluation of Chemistry Effects of Fluorocarbon Molecules for High Aspect Ratio Silicon Oxide Etch, C.M. Anderson, R. Gupta, C. Dussarrat, Air Liquide

For semiconductor dry etch applications, the evolution of chemistry selection has shifted away from fully saturated fluorocarbons towards molecules that exhibit increased selectivity of silicon oxide over mask and underlayer materials. Recent studies show that the presence of both H atoms and C=C bonds can improve selectivity while maintaining reasonable silicon oxide etch rate. The reason for this is linked to the behavior of molecule fragments in a plasma etch environment, wherein higher C:F ratios are favored. The intent of this work is to systematically study the role of gas molecule structure as it affects etching behavior, with the goal of finding an ideal candidate molecule to enable current and future processing requirements. This study will provide an extensive survey of etch chemistries in order to uncover the specific effects of H, C=C double bonds, F:C ratio, and molecule structure as they relate to etching performance. The model chemistries for this work include both cyclic- and linear-type structures. Using a RIE plasma etch tool, the performance of each molecule is studied on blanket wafers, measuring silicon oxide etch rate as well as selectivity to photoresist, silicon nitride, and amorphous carbon hardmask films. For selected conditions of optimized etch rate and PR selectivity, patterned wafer stacks are also etched and examined in cross-section SEM. Corresponding optical emission spectroscopy (OES) data is collected at the same time, showing qualitatively the relative densities of active species in the plasma during the etch process. In order to develop predictive tools to correlate etch performance to the molecule structure, we perform mass spec measurements of the gases by direct injection of the fluorocarbon gas, measuring the electron-impact fragmentation of each gas. Electron energies from 10-100 eV are recorded, and the relative abundance of each fragment species is plotted against the electron energy. It is found that this method gives a strong indication of a molecule's propensity to deposit polymer films during an etch process. Further, the nature of the representative polymer film for each gas can be predicted from the fragmentation patterns, in terms of F:C ratio and C-F bonding as measured by XPS. As a result of this analytical work, several optimum etch molecules have been identified that exhibit excellent selectivity to both PR and a-C hardmask. These chemistries are currently being tested in commercial dielectric etch tools to validate performance.

9:00am PS-WeM4 Dielectric RIE Challenges Associated to Trench First Metal Hard Mask at 64 nm Pitch and Below, Y. Feurprier, L. Wang, Tokyo Electron Tech. Center, America, LLC, S. Nakamura, Tokyo Electron Miyagi Ltd., Japan, J. Stillahn, Y. Chiba, K. Kumar, Tokyo Electron Tech. Center, America, LLC, Y. Mignot, STMicroelectronics, E. Soda, Renesas Electronics, R. Koshy, R. Srivastava, GLOBALFOUNDRIES, Y.J. Park, Samsung Electronics Co. Ltd., J. Arnold, IBM Research Group

Over the last couple of technology nodes (from 45 nm node and beyond), Trench First Metal Hard Mask (TFMHM) integration scheme has gained traction and become the preferred integration of low-k materials for BEOL. This integration scheme also enables Self-Aligned Via (SAV) patterning which prevent via CD growth and confines via by line trenches to better control via to line spacing. Also for the 64 nm pitch technology and below, TFMHM is well suited for double patterning of the line definition required for the ever smaller line pitches of the most critical BEOL levels. In the SAV process, temperature, gas chemistry, power and pressure were shown to be key process parameters to meet the metal HM selectivity requirements. The flexible adjustment of the ion energy and control of the flux of ions and active neutrals was shown to be critical to meet the metal

HM selectivity requirements for both SAV and trench etching. The TFMHM integration at these dimensions requires careful and controlled metal HM selectivity. These tight technology requirements at these ever smaller pitches also challenge hardware to bring evolutionary improvements to enable wider process windows to meet tighter process specifications. In this paper, the RIE efforts on process controls of the via and trench profiles, the metal HM selectivity management and hardware solutions to address the dielectric RIE challenges associated to TFMHM scheme at 64 nm pitch and below will be discussed.

This work was performed by the Research and Development team at TEL Technology Center America in joint development with IBM Research Alliance Teams in Albany, NY 12203.

This work has also been supported by the independent Bulk CMOS and SOI technology development projects at the IBM Microelectronics Div. Semiconductor Research & Development Center, Hopewell Junction, NY 12533.

9:20am PS-WeM5 Interfacial Characterization of Patterned Porous Low-k Nanostructure using Infrared and X-ray Photoelectron Spectroscopy, S. Rimal, N. Ross, S. Koskey, T. Mukherjee, O. Chyan, University of North Texas

The advanced microelectronic architecture utilizes more conductive Cu interconnect insulated by porous low-k interlayer dielectrics (ILD) to minimize the overall RC delay. To decrease the dielectric constant, the porosity of organosilicate glass was increased by partial replacing Si-O with Si-C bonds during plasma-enhanced chemical vapor deposition. However, carbon stripping by subsequent plasma etching/patterning processes can make porous low-k interlayer dielectrics, with higher carbon content, more prone to water damage during subsequent wet cleans processes. In this presentation, we report the development of a new characterization approach that utilizes Multiple Internal Reflection Infrared Spectroscopy (MIR-IR) as a sensitive characterization tool to guide the development of cleans-friendly plasma etches with minimal ILD damages. Previously, we have successfully utilized MIR-IR to characterize chemical bonding of hydrogen termination, trace organic adsorption and plasma deposited polymer thin film on silicon wafer surface with sub-monolayer sensitivity. MIR-IR utilizes the silicon wafer (including patterned ILD wafer) itself as an IR waveguide to enable multiple total internal reflections which greatly enhances IR measuring sensitivity. Therefore, MIR-IR possesses a unique capacity of identifying specific functional groups of deposited thin films (sub 10 nm) and monitoring their corresponding reactivity evolution influenced by plasma process. We will discuss new characterization results of post-etch residues formation (fluoro-polymers), plasma etch induced water damage (silanol formation) and oxygen plasma etch of organic thin film on patterned porous low-k nanostructure using MIR-IR spectroscopy, x-ray photoelectron spectroscopy and other surface characterization techniques.

9:40am PS-WeM6 Separation of Radical and Photon Effects on Nanoporous Low-k Films, J. Lee*, D.B. Graves, University of California Berkeley

Porous low-k materials are highly susceptible to damage from plasma species during various stages of plasma processing. Oxygen plasma, possibly the most damaging, causes significant carbon loss throughout the film, making the material hydrophilic. Absorption of water results in an increase in the dielectric constant and degradation of dielectric properties. Various O₂ plasma species, such as oxygen radicals (O) and vacuum-ultraviolet (VUV) photons, can be shown to cause this carbon loss. Separation of these species to analyze individual effects can be achieved by covering the sample with a MgF₂ window to allow only VUV photons to pass or by placing the sample out of the line-of-sight of the plasma to obtain radical effects, since radicals are able to diffuse to, and into, the porous material. By doing this, we can analyze the carbon loss for each individual specie through bulk measurements using Fourier-transform infrared (FTIR) spectroscopy and compare them to uncovered, direct O₂ plasma exposures. Dilute HF dip etches only C-depleted SiO₂, allowing a measure of the depth of C removal by radicals or VUV photons. Oxygen radicals create a nearly C-free modified layer that deepens at a rate proportional to exposure time and that increases with pressure, presumably because of the increase in O density. By contrast, VUV photons travel fairly deep into the film due to relatively low absorption cross-sections, so photon effects gradually occur throughout this penetration depth at a slower rate. Yet, VUV photons alone do not directly result in carbon loss; molecular oxygen is also needed to form volatile species for permanent removal. The results clearly show that radicals and VUV photons generate the damaged layer in different ways and at different rates.

* Coburn & Winters Student Award Finalist

11:00am **PS-WeM10 Evaluation of Novel Etch Gas for BEOL Interconnect Pattern Transfer at 14nm and 22nm Technologies, R.L. Bruce**, IBM T.J. Watson Research Center, *T. Suzuki, M. Nakamura*, Zeon Chemicals L.P., *S. Engelmann, E.A. Joseph, E.M. Sikorski, N.C.M. Fuller*, IBM T.J. Watson Research Center, *A. Itou*, Zeon Corporation

As feature sizes continue to decrease, significant issues are found using high selectivity fluorocarbon gases to etch interconnect low-k dielectrics including low selectivity to organic masks, line wiggling and low-k damage. We have evaluated novel etch gases that enables the optimized fabrication of BEOL interconnects for 14nm and 22nm nodes. Compared to conventional fluorocarbon etch gases, experiments with a novel hydrofluorocarbon etch gas have shown a substantial increase in low-k dielectric etch selectivity to organic hard mask and improved selectivity to the capping layer. In addition, lower line-edge and line-width roughness values were observed. We investigate the etch behavior and selectivity between the low-k dielectric and organic hard mask, metal hard mask, and capping layer through optical emission spectroscopy and x-ray photoelectron spectroscopy. Etch performance is assessed for trench and via patterns and also full dual-damascene structures. Low-k damage is also investigated by post-etch HF treatment to measure critical dimension loss from dissolution of plasma-damaged dielectric. Finally, we propose a mechanism for high selectivity, low damage dielectric etch at sub-80nm pitch structures using rationally-designed novel etch gases.

11:20am **PS-WeM11 Dry Etching Characteristics Related to TiN Material Properties, A.P. Labonte, F. Wu, V. Arunachalam, S. Patil**, GLOBALFOUNDRIES, *C. Niu*, ST Microelectronics, France, *T.Q. Chen*, GLOBALFOUNDRIES, *E. Wornyo, B.G. Morris, Y. Yin*, IBM Microelectronics, *Y. Mignot*, ST Microelectronics, France

TiN is ubiquitous as a hard mask layer in semiconductor patterning applications. Deposition parameters such as DC power, N₂ flow, Ar flow, temperature, pressure, and target to wafer spacing influence the film properties: density, film stress, resistivity, roughness, grain size and uniformity. These changes in the TiN film properties can affect etch characteristics. For TiN hard mask etches, shifts in etch rate, sidewall angle, undercut/gouge, CD control and LER have been observed. For dielectric etches using the TiN layer as a hard mask, changes in selectivity, erosion rate, etch byproducts, CD control, profile angle and pattern loading have been observed. This presentation will show data on the etch behavior of TiN etch as well as the etch when TiN is used as a mask. In a TiN hard mask open application, a uniformly dense film is required. As part of an evaluation of different TiN films, both uniform and non-uniform density TiN films were generated. Changes in deposition conditions were used to adjust film density uniformity while maintaining average film density. The etch process used to pattern these films was a two step process consisting of an end-pointed main etch and a timed over-etch. The impact to the dry etch process of the film change, was to alter the behavior of the two etch steps in radically different ways. For the main etch, the sidewall angle and etch rate were impacted. For the over-etch chemistry, lateral etch-rate, CD control and profile were most impacted. In addition, the impact of pattern density on via CD definition has been studied for a via double patterning scheme employing TiN as a hard mask for part of the etch. The etch was found to behave differently as a function of pattern density in a fluorine-based plasma, which was theorized to be a consequence of redeposition of TiFx etch byproducts. This theory was supported by data showing a series of TiN films with different material properties resulted in different pattern density responses. The selectivity between the TiN and the underlying film being etched was changed by these TiN film changes, resulting in the different behavior. This work was performed by the Research Alliance Teams at various IBM Research and Development Facilities.

Scanning Probe Microscopy Focus Topic

Room: 16 - Session

SP+AS+BI+ET+MI+NM+NS+SS+TF-WeM

Probe-Sample Interactions, Nano-Manipulation and Fabrication

Moderator: S. Allen, The University of Nottingham, UK,
A.-P. Li, Oak Ridge National Laboratory

8:20am **SP+AS+BI+ET+MI+NM+NS+SS+TF-WeM2 Controlled Coupling of Silicon Atomic Quantum Dots at Room Temperature: A Basis for Atomic Electronics?, R.A. Wolkow**, University of Alberta and The National Institute for Nanotechnology, Canada, *J. Pitters*, The National Institute for Nanotechnology, Canada, *G. DiLabio, M. Taucer, P. Piva, L. Livadaru*, University of Alberta and The National Institute for Nanotechnology, Canada

INVITED

Quantum dots are small entities, typically consisting of just a few thousands atoms, that in some ways act like a single atom. The constituent atoms in a dot coalesce their electronic properties to exhibit fairly simple and potentially very useful properties. It turns out that collectives of dots exhibit joint electronic properties of yet more interest. Unfortunately, though extremely small, the finite size of typical quantum dots puts a limit on how close multiple dots can be placed, and that in turn limits how strong the coupling between dots can be. Because inter-dot coupling is weak, properties of interest are only manifest at very low temperatures (milliKelvin). In this work the ultimate small quantum dot is described – we replace an “artificial atom” with a true atom - with great benefit.

It is demonstrated that the zero-dimensional character of the silicon atom dangling bond (DB) state allows controlled formation and occupation of a new form of quantum dot assemblies - at room temperature. Coulomb repulsion causes DBs separated by less than ~2 nm to experience reduced localized charge. The unoccupied states so created allow a previously unobserved electron tunnel-coupling of DBs, evidenced by a pronounced change in the time-averaged view recorded by scanning tunneling microscopy. It is shown that fabrication geometry determines net electron occupation and tunnel-coupling strength within multi-DB ensembles and moreover that electrostatic separation of degenerate states allows controlled electron occupation within an ensemble.

Some speculation on the viability of a new “atomic electronics” based upon these results will be offered.

9:00am **SP+AS+BI+ET+MI+NM+NS+SS+TF-WeM4 Atomic Forces and Energy Dissipation of a Bi-Stable Molecular Junction, C. Lotze**, Freie Universität Berlin, Germany, *M. Corso, K.J. Franke, F.V. Oppen, J.I. Pascual*, Freie Universität Berlin, Germany

Tuning Fork based dynamic STM/AFM is a well established method combining the advantages of scanning tunneling and dynamic force microscopy. Using tuning forks with high stiffness, stable measurements with small amplitudes, below 1 Å can be performed. In this way, conductance and frequency shift measurements of molecular junction can be obtained simultaneously [1] with intramolecular resolution [2].

One of the most intriguing aspects of molecular junctions relates to the effect of structural bi-stabilities to the properties of the junction. These lead, for example, to conductance fluctuations, telegraph noise and the possibility to switch the electrical transport through the junction.

In this presentation, we characterize a model bi-stable molecular system using dynamic force spectroscopy. The effect of current-induced stochastic fluctuations of conductance are correlated with fluctuations in force. In our experiment we identified the last from both, frequency shifts and energy dissipation measurements, picturing a regime in which electrical transport and mechanical motion are coupled.

[1] N. Fournier *et. al*, PhysRevB 84, 035435 (2011),

[2] L. Gross *et. al*, Science 324, 1428 (2009)

9:20am **SP+AS+BI+ET+MI+NM+NS+SS+TF-WeM5 Acetylene on Cu(111): Imaging a Molecular Pattern with a Constantly Rearranging Tip, Y. Zhu, J. Wyrick, K.D. Cohen, K. Magnone, C. Holzke, D. Salib, Q. Ma, D.Z. Sun, L. Bartels**, University of California Riverside

Abstract: Using variable temperature STM and DFT simulation, we identify the phases of acetylene adsorbed on the Cu(111) surface. Depending on the coverage, a diffraction-derived surface pattern of acetylene on Cu(111) is validated by STM. The modification of the STM image transfer function

through the adsorption of an acetylene molecule onto the tip apex is taken into account. In this case, the images of acetylene patterns on Cu(111) also include direct evidence of the **rotational orientation and dynamics of the acetylene species attached to the tip apex**. DFT modeling of acetylene/Cu(111) reveals that the molecular orientation and separation is governed by a balance of repulsive interactions associated with stress induced in the top surface layer and attractive interactions mediated by the electronic structure of the substrate. Computationally modeling of the substrate with 3 layers obtains the periodicity of the intermolecular interaction that provides a theoretical underpinning for the experimentally observed molecular arrangement.

9:40am **SP+AS+BI+ET+MI+NM+NS+SS+TF-WeM6 Atomic Scale Imaging and Electronic Structure of Trimethylaluminum Deposition on III-V Semiconductor (110) Surfaces, T.J. Kent*, M. Edmonds, E. Chagarov, A.C. Kummel**, University of California San Diego

Silicon based metal oxide semiconductor field effect transistors (Si-MOSFETs) are quickly approaching their theoretical performance limits, as a result many semiconductors are being explored as an alternative channel material for use in MOSFETs. III-V semiconductors are an appealing alternative to Si because of their higher electron mobilities. The limiting factor in III-V based MOSFET performance is defect states which prevent effective modulation of the Fermi level. The InGaAs (001) As-rich (2x4) surface contains two types of unit cells: ideal unit cells with double As-dimers and defect unit cells with single As-Dimers. The missing As-dimer unit cells, which comprise ~50% of the surface, are believed to cause electronic defect states at the semiconductor-oxide interface, specifically at the conduction band edge of the semiconductor. *In-situ* scanning tunneling microscopy and spectroscopy (STM/STS) and density function theory (DFT) modeling show that TMA readily passivates the As-As dimers in the ideal unit cell but the missing InGaAs(001)-2x4 may not be fully passivated by TMA. To improve the electronic structure of the interface, the sidewalls of the finFETs on InGaAs(001) can be fabricated along the (110) direction. The (110) surface contains only buckled III-V heterodimers in which the lower group III atom is sp² hybridized with an empty dangling bond and the upper group V atom is sp³ hybridized with a full dangling bond. This results in an electrically unpinned surface.

To investigate the benefits of using a (110) surface as a channel material, the atomic and electronic structure of the ALD precursor trimethylaluminum (TMA) monolayer deposited on III-V (110) surfaces has been studied using *in-situ* STM and STS. Both GaAs and InGaAs samples were studied. GaAs wafers were obtained from Wafertech with a Si doping concentration of 4x10¹⁸/cm³. The (001) samples were cleaved *in-situ* to expose the (110) surface. Samples were transferred to the STM chamber (base pressure 1x10⁻¹¹ torr) where the atomic bonding structure of the precursor monolayer unit cell was determined. STS, which probes the local density of states (LDOS), was used to determine Fermi level pinning. A model of TMA chemisorption was developed in which TMA chemisorbs between adjacent As atoms on the surface, giving a highly ordered monolayer with a high nucleation density which could allow for aggressive effective oxide thickness (EOT) scaling.

10:40am **SP+AS+BI+ET+MI+NM+NS+SS+TF-WeM9 A New Experimental Method to Determine the Torsional Spring Constants of Microcantilevers, G. Haehner, J.D. Parkin**, University of St Andrews, UK
Cantilever based technologies have seen an ever increasing level of interest since the atomic force microscope (AFM) was introduced more than two decades ago. Recent developments employ microcantilevers as stand-alone sensors by exploiting the dependence of their oscillating properties on external parameters such as adsorbed mass [1], or the density and the viscosity of a liquid environment [2,3]. They are also a key part in many microelectromechanical systems (MEMS) [4]. In order to quantify measurements performed with microcantilevers their stiffness or spring constants have to be known. Following calibration of the spring constants a change in oscillation behavior can be quantitatively related to physical parameters that are probed. The torsional modes of oscillation have attracted significant attention due to their high sensitivity towards lateral and friction forces, and recent developments in torsional-tapping AFM technology [5]. However, the methods available to determine the torsional spring constants experimentally are in general not simple, not very reliable, or risk damage to the cantilever [6].

We demonstrate a new method to determine the spring constants of the torsional modes of microcantilevers experimentally with high accuracy and precision. The method is fast, non-destructive and non-invasive. It is based on measuring the change in the resonance frequencies of the torsional

modes as a function of the fluid flow escaping from a microchannel. Results for rectangular cantilevers will be presented and compared to results obtained with other methods [7].

- [1] J. D. Parkin and G. Hähner, Rev. Sci. Instrum. **82** (3), 035108 (2011).
- [2] N. McLoughlin, S. L. Lee, and G. Hähner, Appl. Phys. Lett. **89** (18), 184106 (2006).
- [3] N. McLoughlin, S. L. Lee, and G. Hähner, Lab Chip, 1057 (2007).
- [4] S. Beeby, G. Ensell, N. Kraft, and N. White, *MEMS Mechanical Sensors*. (Artech House London, 2004).
- [5] O. Sahin and N. Erina, Nanotechnology **19** (44), 445717 (2008).
- [6] M. Munz, Journal of Physics D-Applied Physics **43** (6), 063001 (2010).
- [7] C. P. Green, H. Lioe, J. P. Cleveland, R. Proksch, P. Mulvaney, and J. E. Sader, Rev. Sci. Instrum. **75** (6), 1988 (2004).

11:00am **SP+AS+BI+ET+MI+NM+NS+SS+TF-WeM10 A Torsional Device for Easy, Accurate and Traceable Force Calibration of AFM Cantilevers, J.F. Portoles, P.J. Cumpson**, Newcastle University, UK

Accurate measurement of biologically-relevant forces in the range of pN to µN is an important problem in nanoscience.

A number of force probe techniques have been applied in recent years. The most popular is the Atomic Force Microscope (AFM). Accuracy of force measurement relies on calibration of the probe stiffness which has led to the development of many calibration methods[1], particularly for AFM microcantilevers. However these methods typically exhibit uncertainties of at best 15% to 20% and are often very time consuming. Dependency on material properties and cantilever geometry further complicate their application and take extra operator time. In contrast, one rapid and straightforward method involves the use of reference cantilevers (the "cantilever-on-cantilever" method) or MEMS reference devices. This approach requires that a calibrated reference device is available, but it has been shown to be effective in providing measurement traceability[2].

The main remaining difficulty of this approach for typical users is the positional uncertainty of the tip on the reference device, which can introduce calibration uncertainties of up to around 6%. Here we present a new reference device based on a torsional spring of relatively large dimensions compared to the typical AFM cantilever and demonstrate how it is calibrated. This method has the potential to calibrate the reference device traceably[3] to the SI with a 1% accuracy by applying techniques typically used for the characterisation of micromechanical devices. The large dimensions of the device reduce the positional uncertainty below 1% and simultaneously allow the use of the device as an effective reference array with different reference stiffnesses at different positions ranging from 0.090 N/m to 4.5 N/m

- [1] P J Cumpson, C A Clifford, J F Portolés, J E Johnstone, M Munz Cantilever Spring-Constant Calibration in Atomic Force Microscopy, pp289-314 in Volume VIII of Applied Scanning Probe Methods, Ed. B Bhushan and H Fuchs (Springer, New York, 2009)
- [2] P J Cumpson PJ, J Hedley, Nanotechnology 14 (2003) pp. 1279-1288
- [3] J F Portolés, P J Cumpson, J Hedley, S Allen, P M Williams & S J B Tendler, Journal of Experimental Nanoscience 1 (2006) pp51-62.

11:20am **SP+AS+BI+ET+MI+NM+NS+SS+TF-WeM11 Nanoscale Surface Assembly by Single-Molecule Cut-and-Paste, H.E. Gaub**, Ludwig-Maximilians Universität, Germany

INVITED
Bottom up assembly of functional molecular ensembles with novel properties emerging from composition and arrangement of its constituents is a prime goal of nanotechnology. With the development of Single-Molecule Cut-and-Paste (SMC&P) we provided a platform technology for the assembly of biomolecules at surfaces. It combines the Å-positioning precision of the AFM with the selectivity of DNA hybridization to pick individual molecules from a depot chip and allows to arrange them on a construction site one by one. An overview on different applications of this technology will be given in this talk. One recent example demonstrates the functional of receptors for small molecules. By SMC&P we assembled binding sites for malachite green in a molecule-by-molecule assembly process from the two halves of a split aptamer. We show that only a perfectly joined binding site immobilizes the fluorophore and enhances the fluorescence quantum yield by several orders of magnitude. To corroborate the robustness of this approach we produced a micron-sized structure consisting of more than 500 reconstituted binding sites. To the best of our knowledge this is the first demonstration of a one by one bottom up functional bio-molecular assembly. Figure included in supplemental document. S. Kufer, Puchner E. M., Gump H., Liedel T. & H. E. Gaub *Science* (2008), Vol 319, p 594-S. Kufer, Strackham, M., Stahl S.W., Gump H., Puchner E. M. & H. E. Gaub *Nature Nanotechnology* (2009), Vol 4, p 45-M. Erdmann, R. David. A.N. Fornof, and H. E. Gaub, *Nature*

* ASSD Student Award Finalist

Surface Science

Room: 22 - Session SS+OX-WeM

Synthesis and Characterization of Oxides

Moderator: J.M. Millunchick, University of Michigan

8:00am SS+OX-WeM1 Structure and Dynamics of Oxide Surfaces and Interfaces, X. Pan, University of Michigan INVITED

Ferroelectric materials are characterized by a spontaneous electric polarization that can be reoriented between different orientations by an applied electric field. The ability to form and manipulate domains with different polarization orientations at the nanometer scale is key to the utility of ferroelectric materials for devices such as nonvolatile memories. The ferroelectric switching occurs through the nucleation and growth of favorably oriented domains and is strongly mediated by defects and interfaces. Thus, it is critical to understand how the ferroelectric domain forms, grows, and interacts with defects. In this talk I will present the nanoscale ferroelectric switching of BiFeO_3 and $\text{PbZr}_{0.2}\text{Ti}_{0.8}\text{O}_3$ thin films under an applied electric field using *in situ* transmission electron microscopy with atomic resolution. We follow the kinetics and dynamics of ferroelectric switching at millisecond temporal and subangstrom spatial resolution. We observed localized nucleation events at the electrode interface, domain wall pinning on point defects, the formation of ferroelectric domains localized to the ferroelectric/electrode interface, and domain wall pinning by dislocations. We also find that in writing nanosized domains the domain wall itself can drive backswitching. It was observed that the localized 180° polarization switching in $\text{PbZr}_{0.2}\text{Ti}_{0.8}\text{O}_3$ thin films initially forms domain walls along unstable planes. After removal of the external field, they tend to relax to low energy orientations. In sufficiently small domains this process results in complete backswitching. Our results suggest that even thermodynamically favored domain orientations are still subject to retention loss, which must be mitigated by overcoming a critical domain size.

8:40am SS+OX-WeM3 Capturing Ion-Solid Interactions with MOS Structures, R. Shyam, E.S. Srinadhu, S. Chambers, J.E. Harriss, W.R. Harrell, C.E. Sosolik, Clemson University

We have fabricated metal-oxide-semiconductor (MOS) devices for a study of implantation rates and damage resulting from low energy ion-solid impacts. Specifically, we seek to capture ion irradiation effects on oxides by exposing as-grown SiO_2 layers (50 nm to 200 nm) to incident beams of singly-charged alkali ions with energies in the range of 100 eV to 5 keV. The oxide is analyzed post exposure by encapsulating the irradiated region under a top metallic contact or within a finished MOS device. Characterization of the resulting ion-modified MOS device involves the standard techniques of room temperature and bias-temperature stress capacitance-voltage (C-V) measurements. The C-V results reveal alkali ion-induced changes in the flatband voltage and slope of C-V of irradiated devices which can be used to extract and delineate between implantation probabilities and irradiation effects of the ions. Biased C-V measurements are utilized to confirm the concentration or dosage of ions in the oxide. A triangular voltage sweep (TVS) measurement at elevated temperatures also reveals the total ionic space charge in the oxide and is used to extract mobility for the ions as they pass through the damaged oxide. Our C-V data show changes in flatband voltage which are greater than those expected for mobile charges present at the range calculated by SRIM which implies that stoichiometry, morphological and chemical changes in the SiO_2 layer are introduced by the ion impacts.

9:00am SS+OX-WeM4 Synthesis and Characterization of Yttrium Aluminum Garnet and Lanthanum Zirconate Particles, R.R. Hart*, S.L. Gollub, G. Walker, B.R. Rogers, Vanderbilt University

Rare-earth doped yttrium aluminum garnet (YAG) and lanthanum zirconate (LZO) are luminescent ceramics that have been used in TV's, LED's, metal oxide transistors, and as laser sources. These materials are thermally and chemically stable. Recent work at Vanderbilt by the Walker and Rogers research groups has shown that the emitted spectrum of proton irradiated LZO particles differs from that of non-irradiated particles, suggesting these materials may be used as passive radiation exposure indicators.

We will discuss the combustion synthesis and characterization of YAG and LZO particles. Combustion synthesis involves heating a mixture of metal

nitrate and a fuel until the mixture ignites. If the proper conditions are used, the energy released by the combustion is sufficient to form polycrystalline material. The type and amount of fuel used in the synthesis affect the amount of gaseous by-products produced and flame temperature achieved during a reaction, both of which affect the crystallite size formed. The organic fuels included in this study are urea and glycine with adiabatic flame temperatures 1780°C and 1210°C , respectively. Urea's higher flame temperature makes this fuel attractive for combustion syntheses. However, urea shows signs of degradation beginning around 120°C , well below its ignition temperature. Glycine does not appear to degrade until approximately 230°C much closer to its ignition temperature. The trade-off between degradation and adiabatic flame temperature suggests the temperature ramp rate used will significantly affect the performance of combustion syntheses carried out with these fuels.

We will present results of detailed thermogravimetric analysis and differential scanning calorimetry (TGA/DSC) experiments used to study the effects of heating rate on the combustion process and on the characteristics of the material formed. TGA/DSC-determined heats of combustion and heat capacities of the reactants and products will also be presented.

Characterization results of powders made using conditions determined by the TGA/DSC experiments will also be presented. X-ray photoelectron spectroscopy (XPS) was used to determine chemical bonding information. Rutherford backscattering spectroscopy (RBS) was used to provide quantitative elemental composition of the material. X-ray diffraction (XRD) was used to determine the crystallinity of the material and to estimate crystallite sizes. Photoluminescence spectroscopy (PL) was used to characterize the materials' emission spectra.

9:20am SS+OX-WeM5 X-ray Linear Dichroism of Epitaxial (Fe,N) Co-Doped Rutile TiO_2 Thin Films, T.C. Kaspar, Pacific Northwest National Lab, A. Ney, Univ. of Duisburg-Essen, Germany, A.N. Mangham, Pacific Northwest National Lab, S.M. Heald, Advanced Photon Source, Argonne National Lab, Y. Joly, Institut Néel, CNRS et Univ. Joseph Fourier, France, V. Ney, Univ. of Duisburg-Essen, Germany, F. Wilhelm, A. Rogalev, F. Yakou, European Synchrotron Radiation Facility, S.A. Chambers, Pacific Northwest National Lab

Efficient visible light photocatalysis could revolutionize hydrogen production, chemical synthesis, and pollution mitigation. Binary oxides such as TiO_2 have received much attention for these applications since they are stable under aqueous and oxidizing conditions, and show promise as ultraviolet-light photocatalysts. However, to operate in the visible portion of the solar spectrum, the wide bandgap of these oxides (~ 3 eV for rutile TiO_2) must be reduced. Anion doping of anatase TiO_2 has been widely explored, and shows some promise. However, in nanoparticles and fine powders, it can be difficult to determine the structural and electronic behavior of N dopants. Homoepitaxial $\text{Fe}:\text{TiO}_2$ and $(\text{Fe},\text{N}):\text{TiO}_2$ thin films deposited on rutile $\text{TiO}_2(110)$ were investigated by x-ray absorption spectroscopy (XAS) and associated theoretical simulations to elucidate the detailed structure of the doped materials. Co-doping with N was found to increase the extent of Fe incorporation into the rutile lattice. X-ray absorption near edge spectroscopy (XANES) spectra were collected at the Ti L-edge, Fe L-edge, O K-edge, N K-edge, and Ti K-edge. No evidence of structural disorder associated with a high concentration of oxygen vacancies was observed. Substitution of Fe for Ti could not be confirmed, although secondary phases such as Fe_2O_3 and metallic Fe could be ruled out. The similarity of the N K-edge spectra to O, and the presence of a strong x-ray linear dichroism (XLD) signal for the N K-edge, indicates that N is substitutional for O in the rutile lattice, and is not present as a secondary phase such as TiN . Simulations of the XANES spectra qualitatively confirm substitution, although N appears to be present in more than one local environment. Although optical absorption spectra confirm that substitutional N redshifts optical bandgap of Fe-doped rutile into the visible region, the film surfaces are photochemically inert with respect to hole-mediated decomposition of adsorbed trimethyl acetate.

9:40am SS+OX-WeM6 Unified Picture of the Excess Electron Distribution at the $\text{TiO}_2(110)$ Surface, P. Krueger, Institut Carnot de Bourgogne, France, J. Jupille, Institut des Nanosciences de Paris, France, S. Bourgeois, B. Domenichini, Institut Carnot de Bourgogne, France, A. Verdini, L. Floreano, A. Morgante, Laboratorio TASC, Italy

Titanium dioxide, an inert insulator in stoichiometric form, can be easily reduced into an n-type semiconductor TiO_{2-x} with the many electronic, photocatalytic and chemical properties that make the material of huge technological relevance. Formally associated with $\text{Ti}^{4+} + e^- \rightarrow \text{Ti}^{3+}$, the reduction of titania results in excess electrons (EE) that populate localized Ti 3d band gap states. Puzzling issues are the surface or subsurface distribution of EE and the lattice or interstitial nature (Ti_{int}) of the Ti^{3+} ions. Despite a number of experimental and theoretical studies, the reduced archetypal $\text{TiO}_2(110)$ has not been unambiguously pictured yet. Regarding the location of Ti^{3+} ions, density functional theory (DFT), DFT + U scheme

* Morton S. Traum Award Finalist

and DFT-Hartree-Fock hybrid functionals (the two latter including a better account of self interaction corrections) are far from consensus. EE that are suggested to be trapped either on sixfold (Ti1) and fivefold (Ti2) coordinated surface Ti, or on subsurface beneath Ti1 or beneath Ti2. In such context, the unique capability of resonant photoelectron diffraction (RPED) to map out the spatial distribution of Ti 3d gap states was previously demonstrated in the study of a TiO₂(110) surface involving vacancies in bridging oxygen rows (O_b-vac) [1]. However, our conclusion that EE mostly occupy subsurface Ti sites was later challenged by the suggestion that Ti_{int} atoms play a key role in the formation of EE [2,3]. This has prompted us to analyse the Na-covered TiO₂(110) surface on which Na adatoms are predicted to produce similar EE as by direct injection of electrons [4], while the formation of Ti_{int} is not expected.

The pivotal observation was that the Na/TiO₂ RPED pattern [4] was almost perfectly similar to the O_b-vac RPED pattern [1]. Data were fitted on the basis of the location of the Ti³⁺ ions on the Ti lattice sites. Indeed, attempts to model EE on Ti_{int} failed. A unified model of the reduced TiO₂(110) surface emerges, with EE located on subsurface beneath Ti2 > second subsurface beneath Ti1 > Ti1 [4] (See supplemental document). As shown by the qualitative agreement of the present findings with DFT approaches [5,6], the charge distribution of the Ti 3d states is dictated by electrostatics. It is essentially an intrinsic property of the titania surface that is independent on the way EE are created.

[1] Krueger et al. Phys. Rev. Lett. 100 (2008) 055501.

[2] Wendt et al., Science 320 (2008) 1755.

[3] Papageorgiou et al., Proc. Natl. Acad. Sci. U.S.A. 107 (2010) 2391.

[4] Krueger et al. Phys. Rev. Lett. 108 (2012) 126803.

[5] Albaret et al., Phys. Rev. B 65 (2001) 035402.

[6] Deskins et al., J. Phys. Chem. C 113 (2009) 14583.

10:40am **SS+OX-WeM9 XPS Satellite Structure and Covalent Bonding**, *P.S. Bagus*, University of North Texas, *E.S. Ilton*, Pacific Northwest National Laboratory, *C.J. Nelin*, Consultant

The satellites in X-Ray photoemission spectroscopy, XPS, especially for ionic compounds, are an important part of the spectra [1, 2] and may provide information about the electronic structure. For uranium oxides, they allow the oxidation state of the U cations to be determined. [2] It would be useful to establish and to understand how the satellite intensity may be related to the extent of covalent bonding in an oxide or other ionic material. It is often believed that the intensity lost from the main XPS peaks to satellites is directly related to the covalent bonding, with greater covalent bonding leading to greater losses to satellites. We show that this relationship is not rigorously correct. A more correct relationship is between satellite intensity and the difference of the degrees of covalency in the initial, unionized, state and the final, core-hole states with larger differences leading to larger losses to satellites. Furthermore, the final state covalency is less sensitive to the environment than is the initial state covalency since the bonding in the final state is more appropriate to that for an equivalent, Z+1, impurity atom representing the core-ionized atom. [3] We investigate the extent to which the effects of covalency can be tuned by comparing the Ni 2p XPS between NiO and Ni impurities in MgO.

1. P. S. Bagus, et al., Chem. Phys. Lett. **487**, 237 (2010).

2. E. S. Ilton and P. S. Bagus, Surf. Interface Anal. **43**, 1549 (2011).

3. W. L. Jolly and D. N. Hendrickson, J. Am. Chem. Soc. **92**, 1863 (1970).

11:00am **SS+OX-WeM10 Surface of BaTiO₃ (001): STM and STS Study**, *E. Morales*, *J. Martinez*, *A.M. Rappe*, *D.A. Bonnell*, University of Pennsylvania

BaTiO₃ is a versatile material that finds applications in sensors and electrooptical devices. Interactions start at the very surface, thus it is necessary to understand at a fundamental level its geometrical and electronic structure. Ferroelectricity is a key property that provides unique opportunities to explore molecular adsorption at a surface and allows investigation of chemical interactions as well. Interaction with gaseous species can be performed in-situ in "as-received" and poled crystals by controlling the poling voltage at the surface. Recent studies with macroscopic measurements show that polarization indeed affects molecular adsorption but mechanisms are not yet understood. Here we present scanning tunneling microscopy (STM) and scanning tunneling spectroscopy (STS) of atomically resolved reconstructions on BaTiO₃ (001) surfaces, ($\sqrt{5} \times \sqrt{5}$)R26.6°. A comparison of electronic structure determined by STS with theoretical calculations shows that the surface that is Ti terminated. In this and other reconstructions Ti-ad atoms create filled and empty states that are imaged in STM. The interactions of reconstructed surfaces with H₂O is examined with atomic resolution. This is the first atomic scale observation of molecular adsorption on a ferroelectric surface.

11:20am **SS+OX-WeM11 Synthesis and Characterization of White Light Emitting Ca_xSr_{1-x}Al₂O₄:Tb³⁺,Eu³⁺ Phosphor**, *S.K. Shaat*, *H.C. Swart*, *O.M. Ntwaeaborwa*, University of the Free State, South Africa

Today, many researchers are making efforts to develop white light emitting phosphors that can be used in solid state lighting applications such as phosphor lamps and light emitting diodes. Aluminates with a general formula MA₂O₄ (M = Ba, Ca, Mg, Sr) have emerged as preferred hosts for divalent (Mn²⁺ and Eu²⁺) and trivalent (Ce³⁺, Tb³⁺, Dy³⁺) ions to prepare such phosphors. We have prepared a potential white light emitting Ca_xSr_{1-x}Al₂O₄:Tb³⁺,Eu³⁺ (x = 0, 0.3, 0.7, 1) phosphor by combustion method and we are evaluating it for application in solid state lighting. Depending on the concentration of Ca²⁺ or Sr²⁺, the X-ray diffraction data showed that monoclinic structures of either CaAl₂O₄ or SrAl₂O₄ were crystallized and the stretching modes of Sr-Al-O and Ca-Al-O bonds were confirmed from the Fourier transform infrared spectroscopy data. The chemical compositions and electronic states of each element of the Ca_xSr_{1-x}Al₂O₄:Tb³⁺,Eu³⁺ phosphor were determined using X-ray photoelectron spectroscopy. White photoluminescent was observed when Ca_xSr_{1-x}Al₂O₄:Tb³⁺,Eu³⁺ was excited at 227 nm using a monochromatized xenon lamp. This was a result of the combination of blue and green emissions from Tb³⁺ and red emission from Eu³⁺. It is likely that Tb³⁺ and Eu³⁺ ions were simultaneously excited by a single photon of sufficiently high energy absorbed in Ca_xSr_{1-x}Al₂O₄ host.

11:40am **SS+OX-WeM12 A Novel 2-D Cu-Tungstate (CuWO₃) Phase on Cu(110)**, *F.P. Netzer*, *M. Denk*, *D. Kuhnness*, *M. Wagner*, *S. Surnev*, University of Graz, Austria, *F.R. Negreiros*, *L. Sementa*, *G. Barcaro*, *A. Fortunelli*, CNR-IPCF Pisa, Italy

We explore the feasibility to fabricate W-oxide nanostructures on metal surfaces via self-assembly and condensation of (WO₃)₃ clusters, deposited directly from the gas phase: here we report the formation of a novel two-dimensional Cu-tungstate CuWO_x phase on Cu(110). A beam of (WO₃)₃ cluster molecules, formed by sublimation of WO₃ powder at ~900-1000°C in a thermal evaporator, has been directed onto a Cu(110)2x1-O surface oxide at low temperature and the surface has been annealed subsequently at 600 K. At low temperature (< 15 K) the (WO₃)₃ clusters adsorb in intact molecular form, albeit in a somewhat distorted cluster geometry [1]. Upon heating to 600K, the (WO₃)₃ molecules dissociate and react with the Cu-O(2x1) surface oxide, forming a wetting monolayer with a well ordered incommensurate structure. The latter has been structurally characterized by high-resolution STM imaging and LEED. The chemical nature and electronic structure of this novel 2-D W-O-Cu layer has been investigated by high-resolution XPS core level spectroscopy, NEXAFS, and valence band spectra. The unusually sharp W 4f core level spectra, the specific NEXAFS fingerprint and the evolution of the valence band all suggest that this 2-D W surface oxide is of a Cu-tungstate CuWO_x type. Density functional calculations are in progress to help elucidating the physical and chemical nature of this unusual surface oxide phase.

Work supported by the ERC Advanced Grant SEPON

[1] M. Wagner, S. Surnev, M.G. Ramsey, G. Barcaro, L. Sementa, F.R. Negreiros, A. Fortunelli, Z. Dohnalek, F.P. Netzer, J. Phys. Chem. C **115** (2011) 23480

Surface Science

Room: 21 - Session SS-WeM

Chemisorption on Metallic Surfaces

Moderator: C.H. Sykes, Tufts University

8:00am **SS-WeM1 An Atomic-scale Study of the Adsorption, Assembly and Reactivity of Methanol with Model Cu, O/Cu and Pd/Cu Alloy Surfaces with STM, TPD and XPS**, *T. Lawton*, *M. Boucher*, *A. Baber*, *G. Kyriakou*, *C.H. Sykes*, Tufts University

Hydrogen is green fuel capable of producing electricity. Methanol is a promising hydrogen storage molecule with a high hydrogen-to-carbon ratio (4:1). My research examines methanol oxidation and decomposition on model catalysts via variable temperature scanning tunneling microscopy (VT-STM) and temperature-programmed reaction (TPR).

Methanol desorption on Cu(111) was studied from 130 K (multilayer desorption) to 165 K (monolayer desorption) with STM. Analysis of STM images reveals several structures that are governed by hydrogen-bonding interactions. From the STM images, hexamers are the most thermodynamically stable structure on Cu(111). Hydroxyl-proton localization on the hexamers leads to two enantiomers.

The Cu surface was chemically modified in two ways to alter methanol reactivity. First, the effect of oxygen at various temperatures on Cu(111)

was studied with STM. STM and XPS of a Cu(111) surface pre-adsorbed with oxygen after exposure to methanol show methoxy forms at the interface of the oxide-like domains and bare Cu.

The second avenue was a Cu-based bimetallic alloy containing small amounts of Pd. The TPD studies on model Pd/Cu catalysts interestingly reveal partial decomposition of methanol to formaldehyde and hydrogen. STM images acquired reveal that at temperatures above MeOH desorption, molecules only occupy sites near Pd atoms, suggesting these are the active sites.

8:20am **SS-WeM2 Imaging the Role of Ligand Groups in Surface Coordination Chemistry/Networks: Cyano- vs. Isocyano Groups**, *L. Bartels, M. Luo, S. Bobek, K.D. Cohen, C. Wang, R. Hooley*, University of California Riverside

We use STM to investigate the adsorption, self assembly and metal-coordination of isocyano- and cyano-based aromatic species on Cu (111). Despite their structural similarity, cyano and isocyano groups are chemically quite different. We investigate the effect of this distinction on the structures on the metal coordination structures they form and on the resultant geometric and electronic state of the metal coordination center. In particular we find very different structures for dicyano- and diisocyano-anthracene molecules. While the former generates a network consisting of trigonally coordinated metal centers, the latter generates molecular rows, i.e. more linear arrangement. Cyano- and Isocyano-naphthalene also generate different distributions of coordination compounds on Cu(111). The combination of these studies highlights the impact of the chemical structure of the ligand on the coordination center. Organic ligands are a common tool for affecting activity in homogeneous catalysis. Our study is aimed at exploring the capabilities of lateral coordination in controlling the activity of a surface.

8:40am **SS-WeM3 Chemisorption, Ordering, and Structural Transitions in the Terephthalic Acid Monolayer and Bilayer on Cu(100)**, *S.L. Tait*, Indiana University - Bloomington

The use of small organic molecules to control structure as well as electronic and chemical functionality of a surface is a critical field of surface chemistry. Interest in problems related to bonding, charge transfer and self-assembly of organic species at metal surfaces has grown, in correlation with stronger needs for inexpensive and highly functional organic technologies in energy conversion, sensors, electronics, and other applications. We have studied a prototypical system, terephthalic acid on Cu(100), using a set of complementary analysis tools to develop a complete picture of the chemisorption and structural transitions in this dynamic system, which is of key importance for structural control and organic-to-metal interface design. Scanning tunneling microscopy has been used to achieve molecular resolution structural characterization of the first layer structural transitions and of the second layer structures. High-resolution electron energy loss spectroscopy reveals orientation of the molecule in each layer and lends insight into the bonding interaction with the surface. X-ray standing wave spectroscopy and density functional theory calculations show a strong chemical bond to the surface and indicate that the apparent attractive interaction between molecules is likely due to a substrate mediated interaction, sufficient to overcome any electrostatic repulsion between the negatively charged carboxylate groups on the molecules. This system has also laid the ground work for related advances in using terephthalic acid layers and related molecules for coordination bonded structures, some of which show high levels of chemical selectivity, and for ionically bonded structures. These results provide general insight in the development of self-assembled organic thin films at surfaces, especially with regard to the nature of the metal/organic interface and growth transitions to obtain a second layer that bridges substrate commensurability and a more bulk-like structure, key issues in organic thin film design.

9:00am **SS-WeM4 Attachment and Nanoscale Patterning of Alkyne Groups on Gold via Non-thermal Pathways**, *Q. Li*, Oak Ridge National Laboratory, *C.B. Han*, North Carolina State University, *M. Fuentes-Cabrera, H. Terrones, B.G. Sumpter, W.C. Lu*, Oak Ridge National Laboratory, *J. Bernholc*, North Carolina State University, *Z. Gai, A.P. Baddorf, P. Maksymovych, M.H. Pan*, Oak Ridge National Laboratory

Self-assembled monolayers are the basis for molecular nanodevices, flexible surface functionalization and dip-pen nanolithography. Yet self-assembled monolayers are typically created by a rather inefficient process involving thermally driven tethering reactions of precursor molecules to a metal surface, followed by a slow and defect-prone molecular reorganization. Here we demonstrate a non-thermal control over the self-assembly of phenylacetylene on gold that produces previously unachievable well-ordered three-dimensional monolayers, where the molecules are attached directly through the alkyne group. While thermal excitation can only desorb the parent molecule due to prohibitively high activation barriers

for attachment, localized injection of hot electrons or holes not only overcomes this problem, but also enables an unprecedented control over subsequent ordering of attached molecules on the surface, including a nanoscale control over the size and shape of the self-assembly, defect structures and the reversible process between flatlying and upright molecular configuration from single molecular level to mesoscopic scale. This work thus demonstrates the feasibility of non-thermal reaction pathways that may lead to unique and controllable self-assembly in supported molecular layers.

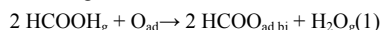
9:20am **SS-WeM5 Molecular Structure of a Mixed NH₃-O₂ Overlayer on Pt(111)**, *Z. Liang*, University of Illinois at Chicago, *H. Kim, Y. Kim*, RIKEN, Japan, *M. Trenary*, University of Illinois at Chicago

The interaction of NH₃ with chemisorbed molecular O₂ on a Pt(111) surface has been studied at the single-molecule level with low temperature scanning tunneling microscopy. Chemisorbed O₂ molecules are found to form an ordered network at high coverages for adsorption temperatures below 50 K. Sites unoccupied by O₂ molecules on Pt(111) appear as holes in the network. Various hole-hole distances among nearest neighbors are observed reflecting variations in the arrangement of O₂ molecules. A hole-hole distance of 0.74 nm is found to be predominant on the surface and is assigned to be the most favorable one as it maintains the 3-fold symmetry of underlying platinum lattice. Ammonia molecules are observed to adsorb in the holes within the ordered network of O₂ molecules, which is also the atop site with respect to the Pt(111) substrate. Further annealing of the ammonia-oxygen overlayer to 400 K results in the formation of a mixed p(2×2) overlayer of N, O and NH. This work provides new insights into the ammonia oxydehydrogenation reaction on platinum surface, which is an important catalytic reaction in the industrial production of nitric acid.

9:40am **SS-WeM6 Enthalpies of Formation of Formate Intermediates Adsorbed on Pt(111) by Microcalorimetry**, *T.L. Silbaugh, E.M. Karp, C.T. Campbell*, University of Washington

Knowing the heats of formation of adsorbed catalytic intermediates is an essential component in gaining the fundamental understanding of reaction mechanisms and the relationships between catalyst structure and activity necessary for rational design of heterogeneous catalysts. The current study utilizes the ultrahigh vacuum technique of single crystal adsorption calorimetry to determine the energetics of adsorbed formate species on Pt(111).

From previous literature, it is known that formic acid dosed on Pt(111) precovered with oxygen adatoms (O_{ad}) at 190K reacts completely to form adsorbed bidentate formate (HCOO_{ad,bi}) and gas phase water (H₂O_g) according to the reaction:



where HCOO_{ad,bi} bonds in a bridging configuration. The heat of Reaction (1) extrapolated to zero coverage was found to be -110 kJ/mol. A simple thermodynamic cycle that uses this and other known adsorption energies provides a heat of formation of HCOO_{ad,bi} of -418 kJ/mol.

Prior studies have shown that submonolayer coverages of formic acid on O-precovered Pt(111) at 130K first produce monodentate formate (HCOO_{ad,mon}) and adsorbed hydroxyl (OH_{ad}) via the reaction:



where HCOO_{ad,mon} forms a single Pt—O bond to the surface. The heat of Reaction (2) extrapolated to zero coverage was found to be -93 kJ/mol, which provides a heat of formation of HCOO_{ad,mon} of -354 kJ/mol. At this same temperature, this monodentate formate converts to bidentate bonding, but at a rate that is slow relative to the 100 ms heat measurement time, so this slower reaction does not complicate thermodynamic measurement of the formation of this monodentate species. Together with our earlier measurements of the heats of formation of -OCH_{3,ad} and -OH_{ad}, these allow us to estimate reaction energies for conversion pathways between formate and methoxy intermediates in Pt catalysis.

10:40am **SS-WeM9 Adsorption Energy of Oxygen on Pt(111): Errors in Calorimetry Values and Consequences for the Enthalpy of Related Hydroxyl Species**, *C.T. Campbell, E.M. Karp*, University of Washington

Beautiful calorimetric measurements of the adsorption enthalpy of O_{2,g} to make 2 O_{ad} on Pt(111) were performed by Fiorin et al. However, we show here that they used a calibration that relied upon a value for the optical reflectivity of Pt(111) that was incorrectly reported in the literature. This error in reflectivity led to a 40% error in the adsorption energies they originally reported. We use here our more accurate reflectivity of 76% to recalibrate their oxygen adsorption enthalpy data and show that it gives nearly identical results to the heats of adsorption below 0.15 ML determined from activation energies for desorption of oxygen from Pt(111) measured with temperature programmed desorption (TPD) by two separate groups (Campbell et al.2 and Parker et al.3). Differences arise above 0.15

ML, but we attribute these to the very low sticking probability of O₂ on Pt(111) (< 0.05) above 0.15ML, which we argue lead to large errors in the adsorption energies measured by calorimetry. Given this, we propose that the most reliable values for the adsorption enthalpy of oxygen on Pt(111) up to ¼ ML are those derived from those TPD experiments, rather than the more recent calorimetry data, except below 0.15 ML where they agree after this calibration correction. The best values are well described by (217-151θ) kJ/mol below ¼ ML, where θ is the O_{ad} coverage in ML (i.e., O_{ad} per Pt surface atom). We further use these corrected adsorption enthalpy data to revise the energetics of hydroxyl species on Pt(111) that we previously measured⁴. This gives revised values for the standard enthalpies of formation of the coadsorbed (DO-D₂O)_{ad} complex and of OD_{ad} on Pt(111) of -511 ± 7 and -210 ± 7 kJ/mol, respectively, and a revised O-Pt bond enthalpy in adsorbed hydroxyl of 248 ± 7 kJ/mol. These three corrected enthalpies are all 16 kJ/mol smaller in absolute value than originally reported.

- (1) Fiorin, V.; Borthwick, D.; King, D. A., *surf. sci.*, 2009, 603, 1360.
- (2) Campbell, C. T.; Ertl, G.; Kuipers, H.; Segner, J., *surf. sci.*, 1981, 107, 220.
- (3) Parker, D. H.; Bartram, M. E.; Koel, B. E., *surf. sci.*, 1989, 217, 489.
- (4) Lew, W.; Crowe, M. C.; Karp, E.; Lytken, O.; Farmer, J. A.; Arnadottir, L.; Schoenbaum, C.; Campbell, C. T., *J. Phys Chem. C.*, 115, 11586.

Work supported by the National Science Foundation.

11:00am **SS-WeM10 Mechanism of Halogenated Solvent Pre-Treatment of Polymeric Substrates to Significantly Improve Noble Metal Thin Film Adhesion**, *B.H. Augustine, W.C. Hughes, A.K. Mo, James Madison University, H.M. Meyer, Oak Ridge National Laboratory, T.C. DeVore, James Madison University*

Many emerging microfabrication technologies such as microfluidic devices rely on the deposition of metal features onto polymeric substrates. Au and Pt thin film metallization are particularly important for electrodes, IR reflectors, interconnects and catalytic surfaces in these devices. However, due to the inert nature of Au and Pt, adhesion to polymeric substrates is generally poor. We report on the use of halogenated organic solvents as a pre-treatment onto poly(methyl methacrylate) (PMMA) substrates to improve the adhesion of an array of 121 electron-beam or magnetron sputter deposited 1.5 mm diameter metal dots by up to a factor of five compared to deposition on cleaned PMMA substrates. We have observed improvement by both spin-casting and vapor phase pre-treatment of the PMMA surface. Nearly 90% of the Au dots remain after a standard tape pull-test for samples pre-treated with CHCl₃ compared with only 17% remaining on the untreated samples. The adhesion of CHCl₃, CH₂Cl₂ and CHBr₃ pre-treated samples are also significantly improved compared to remote O₂ plasma pre-treatment (26% adhesion). Atomic force microscopy roughness data shows that this is not due to surface roughening, and we have shown through X-ray photoelectron spectroscopy (XPS) and attenuated total reflection Fourier transform infrared spectroscopy (ATR-FTIR) studies that the halogenated solvent molecules form a Lewis acid-base adduct with the polymer chains leaving a halogen-rich surface. A covalent bond is then formed between the Cr metal adhesion layer and the surface terminated Cl which results in the strong metal adhesion. Molecular modeling has been performed to understand the origin of the enhanced adhesion. DFT calculations are consistent with the presence of adduct formation having a interaction enthalpy of ~35 kJ/mol. The mechanism of improved chemical metal bonding will be discussed.

11:20am **SS-WeM11 HREELS Investigation of Hydrocarbon Dehydrogenation on Oxide-Supported Platinum Nanoparticles**, *M.H.C. Van Spyk, K.A. Perrine, J.C. Hemminger, University of California Irvine*

Factors such as support type and nanoparticle morphology are known to impact catalytic activity, but detailed studies are required to elucidate the effect of nanoparticle size on the mechanism of dehydrogenation over nanoparticles supported on oxides. In this work, high resolution electron energy loss spectroscopy (HREELS) was used to characterize the dehydrogenation of hydrocarbons on platinum nanoparticles supported on an Al₂O₃ film grown by oxidation of a NiAl(110) single crystal. The alumina film is a good representation of the high surface area oxides used as catalyst supports in industry, and the flat surface enables investigation by electron inelastic scattering techniques. The platinum nanoparticles were deposited on a fresh alumina film at cryogenic temperatures, and platinum deposition was monitored by the reduction in elastic peak intensity in the HREEL spectra. Cyclohexane was used as a model hydrocarbon because the dehydrogenation on Pt(111) has been studied extensively and thus provides a good point of comparison for the nanoparticle studies. The HREELS spectra of cyclohexane on Pt(111) show a distinct low frequency peak at 2600 cm⁻¹ which can be monitored to determine the temperature at

which dehydrogenation begins.^{1,2} The HREELS annealing profile from an alumina film does not exhibit cyclohexane adsorption at 170 K, or upon successive annealing. In contrast, the HREEL spectra from platinum nanoparticles on alumina exhibit cyclohexane adsorption at 170 K with the ν_{C-H} stretch energy loss peak observed at 2930 cm⁻¹. Interestingly, HREEL spectra from cyclohexane on platinum nanoparticles do not resemble spectra from cyclohexane on Pt(111). Specifically, the additional ν_{C-H} energy loss peak observed at 2600 cm⁻¹ for cyclohexane adsorbed on Pt(111) is not seen in the case of platinum nanoparticles.^{1,2} In addition, the ν_{C-H} energy loss peak from cyclohexane on platinum nanoparticles does not shift or decrease in intensity upon annealing to room temperature. Our results indicate that cyclohexane dehydrogenates upon adsorption to platinum nanoparticles at 170 K. This dehydrogenation temperature is lower than that on Pt(111), indicating that platinum nanoparticles supported on an alumina film are more catalytically active for the initial stages of dehydrogenation than Pt(111).

1. Land, D. P.; Erley, W.; Ibach, H., HREELS Investigation of the Orientation and Dehydrogenation of Cyclohexane on Pt(111). *Surface Science* **1993**, 289 (3), 237-246.
2. Saeys, M.; Reyniers, M. F.; Neurock, M.; Marin, G. B., Adsorption of cyclohexadiene, cyclohexene and cyclohexane on Pt(111). *Surface Science* **2006**, 600 (16), 3121-3134.

11:40am **SS-WeM12 Scanning Tunneling Microscopy Investigation of the Conversion of Propylene and Butylene to Carbon Clusters on Pt(111)**, *G.F. Sun, S.S. Khan, A.B. De la Ree, J.C. Hemminger, University of California Irvine*

Thermal dehydrogenation of propylene and butylene adsorbed on Pt(111) has been studied under ultra-high vacuum (UHV) conditions

using scanning tunneling microscopy (STM). After heating to 700 K the alkenes dehydrogenated to form flat, uniform sized circular carbon clusters with less than a monolayer coverage. With cycles of continued adsorption and heating, particles grew in number but not in size. The catalytic activity stopped by the third saturation dose, leaving areas of bare Pt. Clusters of propylene and butylene were 12 ± 1.2 Å and 13 ± 1.0 Å in diameter, respectively. Propylene and butylene clusters contain an average of 44 and 51 carbons atoms per cluster, respectively.

Thin Film

Room: 11 - Session TF+SE+NS-WeM

Glancing Angle Deposition (GLAD)

Moderator: T. Karabacak, University of Arkansas at Little Rock

8:00am **TF+SE+NS-WeM1 Tunable-Refractive-Index Materials – A New Class of Optical Thin-Film Materials with Applications in Solid-State Lighting and Solar Photovoltaics**, *E.F. Schubert, Rensselaer Polytechnic Institute*

INVITED

Among the properties of optical materials, the refractive index is a most fundamental one. It determines many optical characteristics such as Fresnel reflection, Bragg reflection, Snell refraction, diffraction, and the phase and group velocity of light. The refractive index was introduced centuries ago by Isaac Newton who correlated the refractive index with the relative strength of refraction at the liquid-to-air interface. He realized that the degree of refraction is proportional to the mass density of the liquid, and therefore called the new optical quantity the “optical density.” Nowadays, this key quantity is known as the “refractive index.”

Among transparent dense materials, MgF₂ has the lowest refractive index: *n* = 1.39. Air and other gases have a refractive index very close to 1.0 but these materials are not viable for thin-film optoelectronic applications. Therefore, there are no dense materials with a refractive index in the range 1.0 < *n* < 1.39. That is, this range has remained unavailable and unexplored.

Over the last few years, a new class of materials, tunable-refractive-index materials, has been developed. Optical thin-film materials, with a refractive index as low as 1.05, have been demonstrated. The tunable-index materials are based on nano-porous materials, such as, for example, nano-porous SiO₂, nano-porous indium-tin oxide (ITO), and nano-porous TiO₂. The porosity can be precisely controlled by using oblique-angle deposition, a technique in which the substrate is at non-normal angle with respect to the deposition source. Whereas dense films form for normal-incidence deposition, porous films with a self-organizing nano-structure form for oblique-angle deposition.

In this presentation, we will present examples of novel structures and devices that exploit the newly gained controllability of the refractive index.

Devices to be discussed include distributed Bragg reflectors, light-emitting diodes, and solar cells, along with the performance enhancements enabled by the control of the refractive-index.

8:40am TF+SE+NS-WeM3 Nanostructured Homogenous CdSe/TiO₂ Composite Visible Light Photoanodes Fabricated by Oblique Angle Codeposition. *G.K. Larsen*, University of Georgia, *B.C. Fitzmorris*, University of California Santa Cruz, *C. Longo*, University of Campinas, Brazil, *J.Z. Zhang*, University of California Santa Cruz, *Y.-P. Zhao*, University of Georgia

A unique fabrication method, oblique angle codeposition, is used to deposit well-aligned nanorod arrays and thick films of homogeneously mixed CdSe/TiO₂ composites. The structural, optical, and photoelectrochemical properties of the films are investigated using a variety of experimental techniques. Ultrafast exciton dynamics are studied using femtosecond transient absorption (TA) spectroscopy. The CdSe/TiO₂ composites are compared with pure CdSe and TiO₂ films in order to determine their utility for photoelectrochemical (PEC) applications and to understand the mechanisms underlying the observed behaviors. The morphology of the deposited nanorods changes with film composition due to atomic collisions occurring in the vapor column, which can be modeled using a simplified Keller-Simmons expression. Furthermore, the two phase evaporation process of CdSe creates three different cluster types within the TiO₂ film structures: isolated Se, Se-deficient CdSe, and Se-rich CdSe. The prevalence of each cluster type is dependent on predicted film composition, and each is affected differently by open-air annealing. Isolated Se can be incorporated into the TiO₂ lattice, resulting in low energy rutile phase. Se-deficient CdSe clusters crystallize preferentially into cubic CdSe and are easily oxidized into CdO, while Se-rich CdSe clusters crystallize into hexagonal CdSe and are more stable. Furthermore, each of these cluster types interacts differently with the surrounding TiO₂ matrix, resulting in diverse optical and PEC behaviors. Interestingly, the stoichiometry of the CdSe domains is more important than overall CdSe content within the film in determining the structural, optical, and PEC properties of the films. The composite nanorod structure is a more efficient photoanode under visible light illumination than both the pure CdSe and TiO₂ nanorod array films. The higher efficiency of the composite films is attributed to efficient charge transfer and separation in the homogeneously mixed composite. This is confirmed by the extremely high electron injection rate from CdSe into TiO₂ observed in the ultrafast TA studies.

9:00am TF+SE+NS-WeM4 Control the Biaxial Texture of Vertically Aligned Nanostructures using Oblique Angle Sputtering Deposition with Substrate Flipping Rotation. *G.-C. Wang*, *L. Chen*, *T.-M. Lu*, Rensselaer Polytechnic Institute

It is known that oblique angle deposition can be used to grow 3D nanostructures with a variety of morphology such as nanorods and nanospirals. For a selective set of materials, the technique can also produce a preferred crystal orientation, particularly a biaxial texture where the texture selection occurs in both the out-of-plane and in-plane directions. Most frequently biaxial texture created using the oblique angle deposition is in the form of slanted nanorods. It is desirable to produce a biaxial structure in the form of vertically aligned nanostructures which may be useful as a buffer layer to grow functional films on top of it. In this talk we will discuss several strategies to grow vertically aligned nanostructures including nanorods with a biaxial texture by dynamically varying the incident flux angle with respect to the surface normal during deposition. A particularly robust technique to achieve this goal is a flipping rotation scheme where the substrate is rotated continuously at a fixed speed around an axis lying within and parallel to the substrate [1]. This is very different from the conventional substrate rotation mode where the rotational axis is perpendicular to the substrate surface. In the flipping rotational mode the incident flux is perpendicular to the rotational axis, and the incident flux angle changes continuously. Mo vertical nanorod films, grown on amorphous substrates under three orders of magnitude different rotation speeds, different flipping directions, and different ending deposition angles, were characterized using scanning electron microscopy. For texture characterization of these Mo nanostructures we used our newly developed reflection high energy electron diffraction surface pole figure technique [2]. Despite very different morphologies, such as 'C'-shaped, 'S'-shaped, and vertically aligned nanorods grown by the flipping rotation, the same (110)[1-10] biaxial texture with an average out-of-plane dispersion of ~15° was observed. In contrast, we showed that only a fiber-textured Mo film was obtained by using the conventional rotation mode with a fixed incident flux angle. These biaxial Mo vertical nanorod films have potential applications as buffer layers to grow near-single crystal semiconductor films through nanoheteroepitaxy. These films may find important applications in energy conversion and light emitting devices.

Work was supported by the NSF DMR-1104786.

[1] L. Chen, T.-M. Lu, and G.-C. Wang, *Nanotechnology* 22, 505701 (2011).

[2] F. Tang, T. Parker, G.-C. Wang, and T.-M. Lu, *J. of Physics D: Applied Physics* 40, R427 (2007).

9:20am TF+SE+NS-WeM5 Flux Engineering to Control In-Plane Crystal and Morphological Orientation. *J.M. LaForge*, *G. Ingram*, *M.T. Taschuk*, *M.J. Brett*, University of Alberta, Canada

Texture evolution during oblique angle deposition (OAD) and glancing angle deposition (GLAD) is of fundamental interest and important applications. As the distribution of size, shape and orientation of crystal grains impacts film electrical, optical, magnetic and mechanical properties control over texture evolution is important to optimizing performance. Morphology and crystal texture of OAD or GLAD nanostructured films is influenced by the orientation of the substrate relative to the collimated vapor flux, namely angle of incidence and the azimuthal angle, during deposition. Previous work has demonstrated control over the out-of-plane orientation through changes in the angle of incidence or azimuthal motion of substrate (e.g. stationary or continuous rotation).^{[1][2]} However, work on the development of in-plane orientation has focused on material kinetic effects, such as deposition temperature, residual gas concentration, and deposition rate rather than substrate motion.^{[3][4]}

We have deposited iron nanocolumns that have a tetrahedral apex and an out-of-plane texture (fiber texture) at a deposition angle of 88° under continuous substrate rotation. It is possible to induce in-plane crystal texture and morphological orientation by engineering the azimuthal distribution of the flux to match the symmetry of the nanocolumns (i.e. 3-fold rotational symmetry). Thus, biaxially textured nanocolumns with an in-plane alignment that is predominantly controlled by substrate motions (or flux configuration) can be created using this technique. In principle, this method could be generalized to nanocolumns with 4-fold and 6-fold azimuthal symmetry and therefore provides a mechanism to form biaxially textured, nanostructured films from a variety of materials deposited on amorphous or crystalline substrates.

[1] P. Morrow, F. Tang, T. Karabacak, P.-I. Wang, D.-X. Ye, G.-C. Wang, T.-M.T.-M. Lu, *Journal of Vacuum Science & Technology A: Vacuum, Surfaces, and Films* 2006, 24, 235.

[2] R. Krishnan, T. Parker, S. Lee, T.-M. Lu, *Nanotechnology* 2009, 20, 465609.

[3] K. Okamoto, T. Hashimoto, K. Hara, M. Kamiya, H. Fujiwara, *Thin Solid Films* 1985, 129, 299-307.

[4] K. Okamoto, T. Hashimoto, K. Hara, M. Kamiya, H. Fujiwara, *Thin Solid Films* 1987, 147, 299-311.

9:40am TF+SE+NS-WeM6 Bi-axial Texture Development in AlN Layers during Off-axis Sputter Deposition. *R. Deng*, *D. Gall*, Rensselaer Polytechnic Institute

Polycrystalline AlN layers were deposited by pulsed-DC reactive magnetron sputtering from a variable deposition angle $\alpha = 0-84^\circ$ in 5 mTorr pure N₂ at room temperature. X-ray diffraction pole figure analyses show that layers deposited from a normal angle ($\alpha = 0^\circ$) exhibit fiber texture, with a random in-plane grain orientation and the c-axis tilted by $42 \pm 2^\circ$ off the substrate normal, yielding wurtzite AlN grains with the {10-12} plane approximately parallel ($\pm 2^\circ$) to the substrate surface. However, as α is increased to 45° , two preferred in-plane grain orientations emerge, with populations I and II having the c-axis tilted towards and away from the deposition flux, by $53 \pm 2^\circ$ and $47 \pm 1^\circ$ off the substrate normal, respectively. Increasing α further to 65 and 84° , results in the development of a single population II with a $43 \pm 1^\circ$ tilt. This developing bi-axial texture is attributed to a competitive growth mode under conditions where the adatom mobility is sufficient to cause inter-grain mass transport but insufficient for the thermodynamically favored low energy {0001} planes to align parallel to the layer surface. Consequently, AlN nuclei are initially randomly oriented and form a kinetically determined crystal habit exposing {0001} and {11-20} facets. The expected direction of its highest growth rate is $49 \pm 5^\circ$ tilted relative to the c-axis, in good agreement with the $42-53^\circ$ measured tilt. The in-plane preferred orientation for $\alpha > 0^\circ$ is well explained by the orientation dependence in the cross-section of the asymmetric pyramidal nuclei to capture off-normal directional diffusion flux. The observed tilt is ideal for shear mode electromechanical coupling, which is maximized at 48° .

10:40am TF+SE+NS-WeM9 Engineered Indium Tin Oxide Nanowhiskers via Vapour Liquid Solid Glancing Angle Deposition. *A.L. Beaudry*, *R.T. Tucker*, *J.M. LaForge*, *M.T. Taschuk*, University of Alberta, Canada, *M.J. Brett*, University of Alberta, Canada and The National Institute for Nanotechnology

The vapour liquid solid (VLS) nanowire growth technique has been recently modified with spatially modulated vapour flux through glancing angle

deposition (GLAD).^{1,2} Using this new technique, named VLS-GLAD, our group has demonstrated improved morphological control over indium tin oxide (ITO) nanowhiskers.¹ Single crystal ITO nanowhiskers are grown via a self-catalyzed VLS growth mechanism, resulting in branched structures.³ VLS-GLAD exhibits improved control over the diameter, spacing, branching density and branching orientation of ITO nanowhiskers. As the angle of deposition is increased to glancing angles, there is a transition from a dense interconnected network to a porous film of individual ITO nanowhisker structures. In addition, branching was found to increase significantly with increasing deposition angle. This result is attributed to an increase in the proportion of vapour flux incident on the sides of the structures, resulting in an increase in self-catalytic VLS growth of branches. This effect has been used to engineer branch morphology and orientation. Vapour flux rate modulation at glancing angles results in further in-situ control over ITO nanowhisker features. HRTEM imaging revealed a continuation of crystal planes from the trunk into the branch. XRD results indicated single crystal cubic bixbyite structures with a $\langle 400 \rangle$ growth direction. Haacke's figure of merit was used to assess the suitability of ITO nanowhisker films as transparent electrodes.⁴

¹ Beaudry, A.L. et al. *Nanotechnology* **23**, 105608 (2012).

² Alagoz, A.S. and Karabacak, T. *MRS Proceedings* **1350**, (2011).

³ Castañeda, S.I. et al. *Journal of Applied Physics* **83**, 1995 (1998).

⁴ Haacke, G. *Journal of Applied Physics* **47**, 4086 (1976).

11:00am **TF+SE+NS-WeM10 CoPt Nanopillars for Advanced Media by Glancing Angle Deposition**, *H. Su, A. Natarajarithnam, S. Gupta*, The University of Alabama

We report for the first time the fabrication of CoPt+AlN "granular nanorods" utilizing glancing angle deposition (GLAD) on a multi-gun, planetary sputtering system. Initially, AlN was deposited by reactive sputtering from an Al target while CoPt multilayers were simultaneously sputtered using cobalt and platinum targets. Various ratios of Co and Pt, ranging from Co80Pt20 to Co50 Pt50, were used to deposit CoPt-AlN nanorods with different AlN volume percentages. X-ray diffraction (XRD), electron dispersive X-rays (EDX), scanning electron microscopy (SEM), and alternating gradient magnetometry (AGM) were employed to characterize the structural and magnetic properties, respectively. SEM micrographs indicated that the nanorods were approximately 16 nm in diameter, the angle between the substrate plane and the growth direction was about 78 degrees, while the lengths of the nanorods ranged from 30 to 50 nm, depending on deposition time. The angles between the substrate plane and incident flux ranged from 47 degrees to 82 degrees as the substrate presented itself at different angles to the target during the planetary deposition. The composition of CoPt-AlN has been studied by EDX for different ratios of AlN. M-H loops showed that the planetary GLAD sample had twice the coercivity of the flat sample.

We have also compared stationary vs. planetary GLAD, and sequential deposition of AlN/CoPt multilayers with true co-deposition, using an annular CoPt target with an Al insert. Simulations of the deposition have been carried out to gain a better understanding of where the AlN segregates with respect to the CoPt grains. These preliminary results indicate a novel and promising approach to nanopatterned graded media that is the subject of intense research in the data storage industry.

11:20am **TF+SE+NS-WeM11 Through-post Electrical Characterization of GLAD Thin Films**, *A. Lalany, R.T. Tucker, M.T. Taschuk*, University of Alberta, Canada, *M.D. Fleischer*, University of Alberta and The National Institute for Nanotechnology, Canada, *M.J. Brett*, University of Alberta, Canada

Glancing Angle Deposition (GLAD) [1] thin films are increasingly used in optoelectronic applications that benefit from their unique optical properties or ultra-high surface area. GLAD produces porous nanostructured thin films which have found applications as high surface area electrodes. Potential performance benefits of these nanostructured thin-films for optoelectronic devices include, but are not limited to, increased charge extraction [2]. Suitable electrical conductivity along the length of GLAD structures (normal to substrate plane) is necessary to exploit a GLAD film's high surface area for electronic devices. However, optimization of GLAD films for these devices has proven difficult without direct measurements of post resistivity.

In-plane resistivity measurements of metals and conductive oxide GLAD films have been performed [3-5], showing increasing in-plane resistivity with increasing oblique deposition angle (due to decreased film density resulting in fewer conductive pathways). Electrical anisotropy has also been observed, with differing in-plane resistivity for different nanocolumn orientations [3-5]. Through post conductivity measurements present additional challenges - it has been shown that as crystallite grain size

approaches the range of bulk electron mean free path, column-boundary scattering effects begin to dominate standard bulk-scattering mechanisms [6]. As such, the extensive boundaries present in GLAD structures can result in complex electrical behavior. While several attempts have been made to access through-post electrical properties, results have been limited to relative measures or are extremely low yield processes [7, 8].

We require a measurement technique that is both time and cost effective, statistically robust, and has high yield. This has been achieved with a Kelvin Cross-Bridge Resistor architecture specifically designed to measure through-post resistivity. Our devices can measure resistivities between 100 $\mu\Omega \text{ cm} < \rho < 11 \text{ G}\Omega \text{ cm}$, and we have successfully measured through-post conductivities for Indium-tin-oxide (ITO) and Cr GLAD films. Here, we will present device fabrication, validation and current experimental results.

[1] M.M. Hawkeye et al., *J. Vac. Sci. Technol. A* **25** (2007) 1317.

[2] D.A. Rider et al., *Nanotech.* **22** (2007) 0857060.

[3] J. Lintymer et al., *Surf. & Coat. Tech.* **174-175** (2003) 316.

[4] K.D. Harris et al., *Adv. Funct. Mater.* **18** (2008) 2147.

[5] D. Vick et al., *J. Vac. Sci. Technol. A* **24** (2006) 156.

[6] A. Besnard et al., *J. Phys. D: Appl. Phys.* **44** (2001) 215301.

[7] M.F. Canszozglu et al., *ACS Nano.* **4** (2010) 733.

[8] S.P. Chiu et al., *Nanotech.* **20** (2009) 105203.

11:40am **TF+SE+NS-WeM12 Direct Label-Free Detection of microRNA Using a Multi-well SERS Chip Fabricated By Oblique Angle Deposition**, *J.L. Abell*, University of Georgia, *J.M. Garren*, Georgia Health Science University, *J.D. Driskell*, Illinois State University, *R.A. Tripp*, *Y.-P. Zhao*, University of Georgia

Direct label-free nucleic acid detection is a desirable yet challenging task. The current mainstay detection and screening technologies, namely polymerase chain reaction (PCR) and DNA microarrays (i.e. DNA chips), rely heavily upon the use of extrinsic reporter molecules to detect the hybridization of a probe sequence to a target sequence. Removing the need for external labels reduces the cost and complexity of DNA detection assays. This, however, requires a sensing platform capable of highly sensitive, specific, direct chemical analysis. Surface-enhanced Raman spectroscopy (SERS) is an analytical technique capable of detecting highly resolved chemical signatures with superior sensitivity, and can be used to determine the relative quantities of a compound adsorbed on a nanostructured metal surface. The challenge for SERS detection is to produce a large area, uniform and highly sensitive substrate. Here, we report the use of Ag nanorod (AgNR) SERS substrates fabricated by oblique angle deposition (OAD) for microRNA (miRNA) detection. With such a large area (wafer size) and uniform response (signal intensity variation $\leq 10\%$) of the AgNR substrates, we have developed a simple molding technique to pattern the substrates into multi-well arrays. We demonstrate a 40-well 1" x 3" glass slide allowing for parallel screening of multiple specimens with uniform response. This multiwell substrate has been used in conjunction with a linear least squares (LS) analysis method by assuming that the SERS spectrum of miRNA is a convolution of the individual signals of each of the four A, C, G, and T components, where the contribution of each source signal to the total DNA signal is weighted by the relative quantities of A, C, G, and T present within the sequence. Experimentally we have demonstrated this method for detection and differentiation of four different DNA sequences. In addition, we show for the first time the subtle spectral changes observed after label-free hybridization can be quantified with LS to confirm the capture of the target sequence. This study reveals that the use of OAD SERS substrate could be a potential technique to replace to current microarray technique for DNA/RNA detection.

Thin Film

Room: 10 - Session TF-WeM

Thin Films for Encapsulation, Packaging, and Biomedical Devices

Moderator: L.W. Rieth, University of Utah

8:00am **TF-WeM1 Optimizing a Spatial Atomic Layer Deposition Cell for High Throughput, Low Temperature, Roll-to-Roll Applications**, *M.J. Dalberth*, *L. Lecordier*, *M.J. Sershen*, *M. Ruffo*, *R. Coutu*, *G. Sundaram*, *J.S. Becker*, Cambridge Nanotech, Inc.

Atomic layer deposition (ALD) has established itself as a technique capable of producing uniform, dense, pin-hole free films with extremely fine thickness control. The surface reactions involved in many ALD processes are thermally active at temperatures less than 200°C which makes it

attractive for emerging applications coating substrates with a limited thermal budget- for example, a barrier layer for organic photovoltaics on a flexible substrate. Many of these applications demand high throughput, however, and traditional ALD is too slow due to its temporally spaced pulses of reactant A and reactant B, and its need for a vacuum system requiring time consuming evacuation. Spatial ALD replaces the temporal separation of reactants with their spatial separation by confining them to separate gas channels in a deposition cell. Plus, it's a process that takes place at atmospheric pressure and can eliminate system evacuation times. In spatial ALD, the substrate and cell move relative to one another, and the number of A/B channels determines the thickness of material deposited. At speeds of 10m/min or more, equivalent throughput of 2000-4000 wafers can potentially be achieved with equivalent cycle time $\ll 0.1s/\text{\AA}$. As of today, Cambridge Nanotech has implemented two 150 mm x 150 mm cells based on two and six-cycle designs. 150mm Si wafer and PEN/PET substrates were processed using TMA and water at atmospheric pressure, 100-120°C, 10m/min speed and 0.1-0.5 mm gap size between cell and substrate. The impact of key process metrics on process performance such as GPC or uniformity was evaluated, including reactant dosage, temperature or stage velocity. Not surprisingly, the ability to maintain the spatial confinement of TMA and water in order to limit parasitic CVD-like reactions (which induces higher GPC and particle formation) is shown to be critically dependent on gap size and flow rate for the inert gas barriers. Data showing the impact of different cell designs (e.g., orifice distribution and size) on wafer- and process-scale metrics will also be discussed. While development on new cells is continuing, the data taken so far support the outlook that spatial ALD could be a key technology for rapid deposition of functional layers in high throughput applications.

8:20am TF-WeM2 Encapsulation of Implantable Devices by Atomic Layer Deposited Al_2O_3 and Parylene C Bi-layer, X. Xie, L.W. Rieth, F. Solzbacher, University of Utah

Encapsulation of 3-D electronic biomedical implants with complex geometries and tight gaps between components is one of the greatest challenges to achieve long-term functionality and stability. We have investigated a new encapsulation scheme that combines atomic layer deposited (ALD) Al_2O_3 and Parylene C for biomedical implantable system and will present results to quantify the performance of this system. Our approach combines the highly effective moisture barrier properties of ALD alumina, and Parylene as a barrier to many ions and for preventing contact of alumina with liquid water. 52 nm of Al_2O_3 was deposited by plasma-assisted (PA) ALD on interdigitated electrodes (IDEs). AFM micrographs show that as-deposited Al_2O_3 films on fused silica substrate have RMS surface roughness of 0.48 nm. XPS spectra determined that PA-ALD films had nearly stoichiometric O/Al ratio of 1.4. A 6- μm thick Parylene-C layer was deposited by CVD using Gorman process on top of Al_2O_3 and used A-174 (Momentive Performance Materials), an organosilane, as adhesion promoter. The IDEs coated with Al_2O_3 -Parylene C were soaked in phosphate buffered saline (PBS) solution for a period of about 9 months at both body temperature (37 °C) and elevated temperatures (57 to 80 °C) for accelerated lifetime testing. Electrochemical impedance spectroscopy (EIS) and chronoamperometry were used to evaluate the integrity and insulation performance of the soft encapsulation. The leakage current was ~ 20 pA by applying 5 V DC bias and impedance was ~ 3.5 M Ω at 1 kHz with phase of close to -87° by using EIS for samples under 67°C about 9 months (approximately equivalent to 72 months at 37°C), indicating no significant degradation. The encapsulation performance of combining alumina and Parylene C, Parylene C only and alumina only coatings were compared and the bi-layer coating shows its superiority of at least 5 times longer lifetime than the rest two coating approaches. The continuous 5 V bias voltage has no obvious effect on alumina and Parylene coated samples while it shortened the lifetime of Parylene coating by at least a factor of 4. Complex topography can shorten the lifetime of coating dramatically comparing with planar structures, especially with the existence of micromotion inside the body. The lifetime of alumina and Parylene coated devices with hand-wound coils and SMD capacitors was only about 50% or less of that of planar test structures. The long-term (more than 6 years of equivalent lifetime) insulation performance of the novel double-layer encapsulation shows its potential usefulness for chronic implantable electronic microsystems.

8:40am TF-WeM3 Ultra-barrier Technology for Moisture-Sensitive Electronics, P.F. Carcia, DuPont Central Research and Development INVITED

Organic materials are driving future electronic technologies in the direction of lighter weight, more robust, flexible, and lower cost manufacturing. Organic solar cells have reached 10% efficiency in the lab and are becoming an attractive low-cost option for generating electricity in isolated regions in the undeveloped world. Organic light emitting diodes (OLEDs) are poised to succeed LCDs as the next generation of more vibrant color

displays for TVs, computer tablets, and mobile phones. However, one obstacle to the broad utilization of organic electronic materials, and also some inorganic materials, is their sensitivity to atmospheric gases, especially moisture. In the case of OLED displays, hermetic packaging with glass or metal may be an interim solution for early product introduction, but this precludes advantages of lighter weight and flexibility, which could have cost penalties. But for organic photovoltaics (OPV), and for some thin-film inorganic PV technologies, e.g. CIGS, to be cost competitive, they will need to be fabricated with flexible polymer materials, which are permeable. These polymer materials will require low permeation coatings to exclude atmospheric gases that can readily degrade moisture sensitive electronic materials. For OLEDs, the barrier coating must uniformly reduce permeation through the polymer by $\sim 10^6$ times for the display to be defect-free. Solar cells will need a similar (10^4 - 10^5 times) reduction in permeation, if they are to have a reasonable outdoor lifetime. In our laboratory, we have discovered that single-layer, inorganic, barrier coatings grown by atomic layer deposition (ALD) can meet the demanding requirements of an ultra-barrier to protect sensitive electronic devices on a flexible polymer substrate. In this talk we will discuss many of the materials and processing insights we have learned about ALD barriers, their performance protecting sensitive electronic devices, and the outlook for practical, high-speed ALD manufacturing.

9:20am TF-WeM5 Multilayer Barrier Coatings for Organic Photovoltaics, A.M. Coclite, F. De Luca, K.K. Gleason, Massachusetts Institute of Technology

Encapsulant barrier coatings, which prevent the permeation of water through flexible plastic substrates, are an enabling technology for the commercialization of OPV devices. Such protective coatings are made of multilayer stacks where multiple dense, inorganic layers are alternated with soft, organic ones. The inorganic layer contains inevitably some pinholes and defects. The roles of the organic layer are creating a tortuous and longer path among the defects of two successive inorganic layers, filling the pores of the inorganic underlayer limiting the propagation of defects from one inorganic layer to the other and smoothing the substrate surface roughness.

We obtained good barrier properties (WVTR= 10^{-2} g/cm 2 /day at 25°C, RH=85%) with a bilayer obtained by coupling initiated-PECVD (iPECVD) and plasma enhanced CVD (PECVD) at very low thickness of inorganic layer (25 nm).

SiO_x layers were deposited through PECVD in MW plasma at high power and high oxygen dilution. The silanol and organic groups were not detectable by IR spectroscopy, resulting in dense film with high flexibility and high critical tensile strain. High critical tensile strain implies that the coating can be bent and stretched to a relatively big extent before cracking. Inorganic films obtained by other technologies (i.e. Al_2O_3 ALD coatings) showed smaller critical strain values.

Organic coatings were deposited through a new process named iPECVD with enhanced monomer structure retention compared to a conventional plasma deposition and faster deposition rate if compared to conventional iCVD processes from organosilicon monomer. The deposition conditions were tuned to obtained good planarizing properties. The deposition of planarizing organic layers was demonstrated by depositing the coating on the top of some microspheres (1 μm in diameter) which served as model defects on the surface. Increasing the thickness of the coating, the degree of planarization (DP), both local (DLP) and global (DGP), increases. The DLP increases much faster than the DGP: when the coating is 1 μm -thick the DLP is already 99%, for the global planarization instead a 1.8 μm -thick-coating is needed to reach DGP= 99%.

The great advantage of a similar approach is that we deposit the multilayer in a large-area reactor, maintaining the same organosilicon precursor and the same reactor configuration for both deposition of silica-like and organosilicon layers. A detailed investigation of the barrier and mechanical properties changing the number of layers in the stack and the measurements conditions will be presented in order to demonstrate the robustness of the following approach to create flexible ultra-high barrier layer.

9:40am TF-WeM6 Preparation of Hydrophobic Coatings on Si/SiO $_2$ by Incorporation of Nano- and Microdiamond in a Layer-By-Layer Deposition, A. Diwan, J. Wilcock, M.R. Linford, Brigham Young University

Hydrophobic coatings are required in a wide variety of applications. We are preparing robust hydrophobic coatings on silicon from nano-/microdiamond and polyallylamine (PAAm) deposited in a layer-by-layer fashion. After deposition of PAAm/diamond multilayers, two different approaches were considered for preparing hydrophobic surfaces. The first involved the reaction of the amine groups of PAAm with the epoxy groups of 2-(1H,1H-perfluoroundecyl)oxirane to yield hydrophobic surfaces. However, due to the formation of hydroxyl groups in this ring opening reaction, the roll off

of water drops, i.e., their receding contact angles, was poor although the surface showed high static and advancing water contact angles. The other approach, which appears to produce more robust coatings, used only nano-diamond and PAAm for the growth of electrostatically bound layers. The amine of the PAAm was reacted with (3-glycidylpropyl)trimethoxysilane (GPTMS) in a closed pressure vessel at 100°C, which should provide crosslinking to the film and also active sites for subsequent reaction. The final step involved the chemical vapor deposition of a fluorinated silane (F-13 silane) to give a hydrophobic surface. The static water contact angle of a flat PAAm/GPTMS/F-13 silane surface was 107°, which showed good roll off properties. The prepared coatings are evaluated and analyzed at every step using atomic force microscopy (AFM), x-ray photoelectron spectroscopy (XPS), time-of-flight secondary ion mass spectroscopy, ellipsometry for thickness measurements and water contact angles measurements.

Tribology Focus Topic

Room: 19 - Session TR+SE-WeM

Tribology and Wear of Low-Friction Coatings and Materials

Moderator: D.L. Burris, University of Delaware

8:00am **TR+SE-WeM1 Seeing Things as They Really are: *In Situ* Studies of Materials in Application Environments and the Development of Temperature-Adaptive Nanocomposites.** C. Muratore, Air Force Research Laboratory, J.J. Hu, J.E. Bultman, UDRI/Air Force Research Laboratory, A.A. Voevodin, Air Force Research Laboratory **INVITED**

In the early 1940s, military pilots and those who serviced their planes were surprised by serious problems with ignition systems and diverse electrical troubles in their state of the art aircraft. Further study revealed that the graphite commutator brushes used in the electrical generator on the airplane (similar to the alternator in our automobiles) were the source of these technical difficulties, because they wore out 100 to 1000 times faster than expected. Over 70 years later, sensitivity of materials at contact interfaces to the extreme ambient environments aircraft are subjected to is still limiting aerospace capability. One of the reasons materials scientists haven't overcome these problems sooner is because it is difficult to do materials science, at least the part where you correlate performance to structure and composition, when there is such a big difference between the operating environment and the environment in which analysis is conducted. All the materials tribologist can really do is *post mortem* forensics work on materials designed to get hot after they have cooled down to a convenient handling temperature. During that cooling down time, phase changes and grain growth occur, perhaps misleading the researcher on the compounds or phases yielding high or low friction at interfaces in relative motion. In this talk we will review innovative characterization techniques designed to provide the insight necessary to produce environmentally adaptive tribological coatings, especially materials designed to operate over broad ranges of humidity (i.e., earth to space) and temperature (i.e., ignition to supersonic flight). Characterization of temperature adaptive nanocomposite lubricant materials, such as MoN/Ag and VN/Ag via Raman spectroscopy will be reviewed in depth.

8:40am **TR+SE-WeM3 Tribological Surface Chemistry of Model Lubricant Additives Measured in Ultrahigh Vacuum.** W.T. Tysse, University of Wisconsin Milwaukee

Additives are generally added to lubricants, which react with the surfaces to form a boundary lubricating film that can lower friction and/or prevent wear. At the high interfacial temperatures that occur under so-called extreme-pressure conditions, the surface reaction and film growth kinetics are dominated by thermal processes. In contrast, it is postulated that, under mild conditions, where the surface temperature rise is low, a surface film can be formed by a shear-induced, surface-to-bulk transport mechanism. This effect is investigated by studying the tribologically induced surface reactions of model sulfur- and boron-containing additives on copper surfaces in ultrahigh vacuum (UHV) where the background pressure is $\sim 1 \times 10^{-10}$ Torr. The nature of the initial surface species that are formed by exposure of the copper surface to the model lubricant additive is investigated using a range of surface analytical techniques such as temperature-programmed desorption (TPD), reflection absorption infrared spectroscopy (RAIRS) and X-ray photoelectron spectroscopy (XPS). This enables the nature of the initial surface species to be identified, and their thermal stability to be measured in some detail. The effect of rubbing these adsorbate-covered surfaces is investigated, also in UHV, by measuring the friction coefficient and contact resistance during rubbing. The chemical composition of the wear track is followed using high-spatial-resolution

Auger spectroscopy to follow the fate of the surface species caused by rubbing and to test the above postulate.

In addition, the effect of low-coordination sites formed on the surface by rubbing on the reactivity of gas phase lubricants is explored and finally, this strategy is used to understand the tribochemistry of borate esters on copper under mild rubbing conditions.

9:00am **TR+SE-WeM4 Nanomechanical and Nanotribological Properties of ZnO Thin Films.** E. Broitman, L. Martinez de Olcoz Sainz, Linköping University, Sweden, C. Bojorge, Cinso, Citedef-Conicet, Argentina, J.B. Miller, Carnegie Mellon University, H. Canepa, Cinso, Citedef-Conicet, Argentina, L. Hultman, Linköping University, Sweden

During the last years, with the advances in nanotechnology, zinc oxide (ZnO) thin films have attracted an increased attention for applications as sensor devices in microelectromechanical systems. In these applications, where high mechanical stress could be imparted on the film in contact situations, the knowledge of the coating nanomechanical and nanotribological properties is critical since they will affect the functions and durability of the films. Sol-gel method is a simple and low cost process for the fabrication of ZnO thin films; interestingly, there are only two publications partially dealing with their mechanical and tribological properties.

In this work, we studied ZnO thin films grown on glass substrates by sol-gel process. Single and multilayered films were deposited by spin-coating technique onto glass substrates, and subsequently transformed into nanocrystalline films using different thermal treatments Tt.

The microstructural properties and morphology of the films have been studied by X-ray diffraction (XRD), scanning electron microscopy, and surface probe microscopy. XRD patterns of films dried at room temperature show features characteristic of layered basic zinc acetate, a lamellar ZnO precursor, consisting of zinc hydroxide hydrate sheets separated by intercalated acetate groups. At higher Tt, ZnO diffraction patterns are dominated by features corresponding to the (100), (002) and (101) reflections of the crystalline zinc oxide "wurtzite" structure. The higher relative (002) intensity in some films is evidence of preferential growth of the structure along the c-axis, the axis of symmetry in the wurtzite structure.

The nanomechanical and nanotribological properties were measured by a Triboindenter TI-950 from Hysitron. The hardness H and reduced Young's modulus Er of the ZnO thin films were investigated by nanoindentation measurements with a Berkovich indenter at peak loads of 150 μ N. The films with the lower Tt exhibit a wide dispersion in the values due to the inhomogeneities on the degree of coating crystallinity. At the higher temperatures, the dispersion vanishes and we obtained H = 5.6 GPa and Er = 99 GPa. We also observed at low temperatures the presence of pop-in events that can be associated to the presence of the multilayers. The friction coefficient was measured at ambient conditions using a conical diamond tip in a reciprocal test, applying a normal force of 10 μ N and a stroke distance of 10 μ m. The friction coefficient decreases from 0.37 to 0.30 when Tt is increased. The different mechanical and tribological properties can be correlated to the changes in the microstructure upon different heat treatments.

9:20am **TR+SE-WeM5 Tribological and Compositional Properties of Electroless Nickel-Boron Coatings Annealed at Various Temperatures.** K. Gilley, University of Florida, Y. Riddle, UCT Coatings Inc., S.S. Perry, University of Florida

In this study, the tribological and compositional properties of annealing temperatures on electrolessly deposited nickel boride coatings were investigated. All samples were coated in the same bath and had approximately the same starting composition: 31 atomic % Ni, 19 atomic % B, 42 atomic % O, and 8 atomic % C. Samples were annealed at temperatures of 250°C, 400°C, 550°C, and 700°C under a constant flow of oxygen. The tribological properties of the samples were tested using a novel pin-on-disc tribometer. The pin-on-disc tribometry was performed in air under ambient RH conditions, keeping conditions the same throughout all tests that were performed. The influence of the annealing temperature on surface composition was studied by X-ray photoelectron spectroscopy (XPS), used to identify and relatively quantify the elements present. Raman spectroscopy was used to differentiate between chemical species that were indistinguishable in XPS. Increasing annealing temperatures were seen to influence the tribological properties of the coatings to a large degree; with the samples with higher annealing temperatures having a significantly lower coefficient of friction, $\mu \approx 0.16$ for the sample annealed at 550°C and $\mu \approx 0.06$ for the sample annealed at 700°C, than the lower temperature annealed samples, $\mu \approx 0.5$ for samples annealed at 250°C and 400°C. Similarly, the chemical nature of the coatings were strongly affected by the differing

annealing temperatures; with the higher annealing temperature samples showing heavy oxidation and migration of boron to the surface, while the lower annealed samples remained largely unchanged. The lowering of the friction coefficient in the samples annealed at 550°C and 700°C was attributed to the migration and subsequent oxidation of boron forming low friction B₂O₃ at the surface.

10:40am **TR+SE-WeM9 First Contact: SPR and SERS Studies of the Initial Transfer Behavior of PTFE**, *K.L. Harris, B.A. Krick, D.W. Hahn, W.G. Sawyer*, University of Florida

Traditionally the tribological behavior of PTFE (polytetrafluoroethylene) has been studied in the steady state after many sliding cycles. Steady state studies neglect events that occur during the first contact and sliding cycles, as well as the early transient behavior of PTFE. In-situ surface plasmon resonance (SPR) tribology experiments allow for the observation of initial transfer after the first contact and first sliding cycle of PTFE. SPR showed transfer of PTFE after the first cycle of sliding, contrary to previous models of films formed by delamination wear debris. Surface enhanced raman spectroscopy (SERS) verified the chemical identity of the transfer film. Friction behavior of PTFE was shown to differ in the first cycle from the behavior seen after a transfer film was created and to depend on contact pressure and sliding speed.

11:00am **TR+SE-WeM10 Tribological Investigations of Octadecylphosphonic Acid (ODP) and Octadecyltrichlorosilane (OTS) Self-Assembled Monolayers: A Comparative Study of MEMS-type Interfaces**, *N. Ansari, Auburn University, S. Barkley, C. Bouxsein, M. Deram, N. Eigenfeld, St. Olaf College, O. Matthews, Luther College, A. Poda, W.R. Ashurst, Auburn University, B.P. Borovsky, St. Olaf College, E. Linn-Molin, E.E. Flater*, Luther College

Since microelectromechanical systems (MEMS) are critically-limited by interfacial phenomena such as friction and adhesion, strategies have been developed to reduce friction in these systems. One common strategy is to coat MEMS surfaces with molecularly-thin self-assembled monolayer (SAM) coatings. Silicon MEMS are most commonly coated with silane-based SAMs, such as octadecyltrichlorosilane (OTS). Continued development of MEMS technology may require new material systems to be employed. Therefore, in this study, we investigate the frictional properties of octadecylphosphonic acid (ODP) monolayers deposited on aluminum oxide surfaces. Measurements using an atomic force microscope (AFM) and separately using a nanoindenter-quartz crystal microbalance system were performed each with a microsphere-terminated probe, allowing for a comparative study between different velocity regimes using contacts with similar sizes, surface roughnesses, and interfacial chemistries. AFM colloidal probe friction measurements indicate that while the frictional properties of aluminum oxide can be reduced with the use of an ODP monolayer, a more dramatic rubbing-induced modification is clearly evident for both bare and SAM-coated aluminum oxide substrates. These modification effects depend on scanning duration and environmental conditions such as humidity. We hypothesize that a tribochemical reaction occurs between aluminum oxide and ambient water, which has also been observed in macroscopic tribological studies of aluminum oxide published in the literature.

11:20am **TR+SE-WeM11 Diffusion of Gold Islands on Graphene**, *B. Dawson, M. Lodge, M. Ishigami*, University of Central Florida

Recent theoretical work has suggested that gold nanoclusters on graphite can exhibit both diffusional friction and a novel ballistic friction behavior [1]. This ability to tune friction at nanoscale interfaces can be useful for developing nanoscale motors and machines in general. Furthermore, understanding this nanotribological behavior can be utilized for various nanomechanical devices fabricated from graphene, which is chemically identical to graphite.

We have measured the frictional energy dissipation of gold nanoclusters on graphene as a function of temperature and cluster size using the quartz crystal microbalance (QCM) ring-down technique. By measuring this dissipation, it is possible to quantitatively measure the island diffusion coefficient and precisely monitor how the diffusion and slip time change with temperature, and directly compare these results with the recent theoretical studies. In addition, our measurements give insight into the nanotribological properties of a two dimensional material studied at higher sliding speeds than typically accessible using atomic force microscopy.

[1] R. Guerra *et al.* Nature Materials **9**, 634 (2010).

11:40am **TR+SE-WeM12 Synthesis and Tribology of MoS₃ Nanoparticles**, *J.R. Lince*, The Aerospace Corporation, *A.M. Pluntze*, Colorado State University, *S.A. Jackson*, The Aerospace Corporation

There has been recent interest in the use of solid lubricant nanoparticles in coatings and as boundary additives in liquid lubricants. Examples include nanoparticles of MoS₂ and WS₂. The formation of these nanoparticles is nontrivial, requiring techniques such as gas phase syntheses and electric discharges. We are exploring simpler syntheses using wet chemical techniques. In particular, the synthesis of MoS₃ nanoparticles involves hydrothermal reaction between molybdate salts and sodium sulfide under controlled pH conditions.¹

The use of MoS₃ as a tribological material has not been explored beyond its use as an oil additive.² We are investigating its potential for use in solid lubricant coatings. Bonded MoS₂ coatings experience widespread usage for lubricating mechanisms on virtually every spacecraft (i.e., using micron-sized MoS₂ particles). We formulated resin-bonded coatings using MoS₃ nanoparticles as the lubricating pigment, and compared their tribological performance to commercial bonded MoS₂ coatings. Surprisingly, the MoS₃-formulated coatings performed similarly to the MoS₂-based coatings. Specifically, they showed similar coefficients of friction (i.e., 0.04 to 0.06) and durabilities in dry nitrogen (<0.1% RH). We will present results of surface analyses on worn coatings to reveal changes in composition and chemical state of the MoS₃ that might explain the measured low friction. In addition, results of tribological performance in humid air atmospheres will be presented.

We have also explored syntheses of MoS₂ nanoparticles using nanosize MoS₃ as a starting material. A recent study purported to create MoS₂ nanoparticles with the addition of an aqueous reducing agent during hydrothermal synthesis of MoS₃.³ However, X-ray fluorescence analysis of the product of our synthesis showed that the S:Mo remained at 3.0 after using the reducing agent. Other conversion methods including vacuum reduction of the MoS₃ nanoparticles will be discussed.

References:

1. P. Afanasiev, "Synthetic approaches to the molybdenum sulfide materials," *Comptes Rendus Chimie*, 11(1-2) (2008) 159-182.
2. O.P. Parenago, V.N. Bakunin, G.N. Kuz'mina, A.Yu. Suslov, and L.M. Vedeneva, "Molybdenum Sulfide Nanoparticles as New-Type Additives to Hydrocarbon Lubricants," *Doklady Chemistry*, 383(1-3) (2002) 86-88.
3. Y. Tian, X. Zhao, L. Shen, F. Meng, L. Tang, Y. Deng, "Synthesis of amorphous MoS₂ nanospheres by hydrothermal reaction," *Materials Letters* 60 (2006) 527-529.

This work was funded in part by The Aerospace Corporation's Sustained Experimentation and Research for Program Applications program.

© The Aerospace Corporation 2012

Vacuum Technology

Room: 14 - Session VT+AS+SS-WeM

Surface Analysis and Vacuum Manufacturing for Accelerators

Moderator: M.L. Stutzman, Thomas Jefferson National Accelerator Facility

8:00am **VT+AS+SS-WeM1 Manufacturing and Welding Processes for TPS Large Aluminum Bending-Chambers and 14 m Vacuum Cells**, *C.L. Chen, C.C. Chang, C.K. Chan, Y.C. Yang, T.Y. Lee, G.Y. Hsiung, J.R. Chen*, NSRRC, Taiwan, Republic of China

A unique manufacturing and welding technique has been developed for building the 3 GeV Taiwan Photon Source (TPS) large aluminum bending chambers and 14-meter vacuum cells. There are total 48 bending chambers, which are about 3.8 meters long each. Combined with an appropriate manufacturing processes, such as with a precise CNC machine, lubrication with pure alcohol and cleaning with ozonated water, the aluminum chambers have an oil-free interior surface finished for an ultra-high vacuum environment before aluminum welding. Ozonated water has a high oxidation potential and can remove most organic contaminations. It is used to effectively clean aluminum chambers' surfaces, and provides with the lowest outgassing yield. After the bending chambers are cleaned with ozonated water, the chambers are moved to a welding room for following welding processes. A novel automatic gas-tungsten arc-welding (GTAW) system has been established at NSRRC for welding the aluminum bending chambers. This welding system has a XY stage that is built and configured to provide high-performance positioning along multiple welding axes. The automatic welding system comprises six welding torches to implement

simultaneously two longitudinal side welds of a bending chamber, and is innovative in using computer-based software to control the welding movements and the welding parameters of the six-torch output. In traditional manual welding, the key success factors focus on elimination as much as possible the distortions of structural assemblies. The six-torch welding and a clamp-free approach together address the issue of reducing distortion and minimizing residual stresses with a novel one-step welding process. In addition, on-site welding sequence is introduced for assembling two straight and two bending chambers into one 14-meter vacuum cell. From the beginning of CNC machining to the end of vacuum cell assembly, deformations through all process sequences are measured and controlled under 300 μm . In this paper, both the manufacturing sequences, vacuum data and statistical analysis of deformation control are presented in detail.

8:20am **VT+AS+SS-WeM2 A High Power Electron Beam Stop for Cornell ERL Prototype Injector**, *X. Liu, Y. Li, K.W. Smolenski, I. Bazarov, B.M. Dunham*, Cornell University

The electron beam stop for Cornell University's Energy Recovery Linac (ERL) prototype injector was designed and manufactured for 600 kW electron beam power at beam energies between 5 and 15 MeV. To minimize neutron production from high energy electrons, aluminum was chosen over copper for the construction material. It consists of a 20 mm thick main body with machined outer cooling channels and a tight fit jacket, with the thickness mainly determined by the stopping power of the material. The stop body also serves as the vacuum envelope. The stop body is made of three sections, which are electron-beam welded together. It has a cylindrical shape with a cone at the end, about 0.5 m in diameter and 3 m in overall length. Flexibility is allowed at the body-jacket joint to minimize the thermal stress. The naturally small ERL electron beam is enlarged and rastered in a circular pattern using magnets at the entrance. The enlarged electron beam strikes the stop surface at an average angle of about 8 degrees. The electron scattering inside the stop body was simulated using GEANT4, and the inside profile of the body was optimized so that the thermal load is the most evenly distributed over the whole body. A quadrant detector is equipped at the entrance of the stop to monitor the electron beam centering and rastering. An array of thermocouples is installed on the outside surface of the jacket, providing a rough map of the heat load distribution. Gases generated in the close-circuit cooling water by radiolysis are vented and the concentration of hydrogen is monitored. The stop has been in operation since October 2008, and has been tested up to 250 kW to date.

8:40am **VT+AS+SS-WeM3 Ion Pump Starting Behaviour at High Pressures - Influence of Pump Design Diode / Triode and Power Supply**, *M. Thierley, C. Paolini*, Agilent Technologies, Italy

Today ion pumps are broadly seen as pumps for good high vacuum and ultra-high vacuum environments. Operated at these low pressures, the power consumption of ion pumps is also very low, making ion pumps one of the most energy efficient vacuum pump technologies. Power supplies, however, with several hundred Watts of power continue to be used, as in the past decades, often based on the fear of not being able to start the ion pump; historic issues associated with higher pressures. In this presentation/paper, the differences in starting behaviour of Diode and Triode pump elements are discussed, based on experimental data. Questions addressed will include; how does the pumping speed of these elements change while starting with voltage and current? What impact does the power and design of the pump control unit have on the start and the pump down time of the vacuum system? What is the impact of the power supply unit's technology (ie. classic transformer based design vs. more modern switching power supplies)? In addition to controller experimental data and discussion of the operation theory of the pump elements, pictures of the actual plasma development inside the pump will be featured.

9:00am **VT+AS+SS-WeM4 Superconducting Niobium for Accelerator Cavities: Status and Prospects**, *M.J. Kelley*, Jefferson Lab and College of William & Mary

INVITED

Radiofrequency accelerator cavities of superconducting niobium are the technology of choice for a number of recent and coming particle accelerators, largely because of their cost-for-performance. The principal aspects of performance are the amount accelerator needed to achieve a required final beam energy (accelerating gradient, E_{acc}) and energy consumption (cavity quality factor, Q_0). The former impacts chiefly initial cost; the latter both initial and operating costs. Research and development efforts are bearing fruit for both. Gaining the benefits need not await the construction of new accelerators or major upgrades, as accelerator modules are regularly cycled out of existing machines. A challenge that is underappreciated by physics researchers, but is well familiar to the AVS community, is the manufacturing excellence needed to translate research progress into hardware on the ground.

Authored by Jefferson Science Associates LLC under US DOE Contract De-AC05-06OR23177

9:40am **VT+AS+SS-WeM6 Niobium Nitride Thin Films and Multilayers for Superconducting Radio Frequency Cavities**, *W.M. Roach*, D.B. Beringer, Z. Li*, The College of William and Mary, *J.R. Skuza*, National Institute of Aerospace, *C. Clavero, R.A. Lukaszew*, The College of William and Mary

Niobium nitride in thin film form has been considered for a number of applications including multilayered coatings onto superconducting radio frequency (SRF) cavities which have been proposed to overcome the fundamental accelerating gradient limit of 50 MV/m in niobium based accelerators [1]. In order to fulfill the latter application, the selected superconductor's lower critical field, H_{c1} , must be larger than that of niobium and separated from the niobium surface by an insulating layer in order to shield the niobium cavity from field penetration, therefore allowing higher field gradients. Thus, for the successful implementation of such a multilayered stack it is important to consider not just the material's inherent properties, but also how these properties may be affected in thin film geometry and also by the specific deposition techniques used. Here, we present the results of our correlated study of structure and superconducting properties in niobium nitride thin films. Additionally, we explore how growth parameters can affect the surface morphology, since the quality of the surface has major implications on the ultimate performance of SRF cavities. Combining our findings on the surface morphology, microstructure, and superconducting properties in niobium nitride thin films, we discuss their potential application in multilayered coatings for accelerator cavities.

[1] A. Gurevich, Appl. Phys. Lett. **88**, 012511 (2006).

This work was funded by the Defense Threat Reduction Agency (HDTRA-10-1-0072).

10:40am **VT+AS+SS-WeM9 Characterization of Anisotropic Surface Morphology in Epitaxial Superconducting Thin Films by Wavelet Analysis**, *D.B. Beringer, J.B. Hackett, W.M. Roach, R.A. Lukaszew*, The College of William and Mary

Surface morphology and interface roughness are critical factors impacting the ultimate performance of many thin film materials and nano-scale devices. Next generation superconducting radio frequency (SRF) materials for particle accelerator cavities depend upon the ability to tailor and finely control the microstructure and morphology of superconducting / insulating /superconducting (SIS) multilayer thin film structures. The evolving surface of grown epitaxial thin films, influenced by nucleation and growth kinetics, may exhibit dendritic or fractal patterning where the resulting anisotropic features dominate a coarsening morphology. As such, a quantitative understanding of superconducting thin film morphology and the thin film deposition parameters leading to optimal SRF surfaces is desirable. Quantitative characterization of surface morphology is typically achieved with Fourier transform (FT) analysis and fractal characterization; however, this approach suffers intrinsic limitations as the FT is localized in the frequency domain and therefore cannot differentiate between specific features with isolated spatial coordinates. Wavelet analysis transcends these limitations by effectively isolating and quantifying surface features belonging to a designated length scale, thus enabling independent analysis of local surface features with varied spatial resolutions. Here we present our work with surface characterization by wavelet analysis of epitaxial superconducting Nb thin films.

11:00am **VT+AS+SS-WeM10 NbN-AlN-Nb Multilayer Thin Films for Superconducting Radio Frequency Cavities**, *Z. Li, W.M. Roach, D.B. Beringer, C. Clavero, R.A. Lukaszew*, College of William and Mary

Linear accelerators that are used in high-energy or nuclear physics experiments use superconducting radio frequency (SRF) cavities made with bulk Nb. However, as technology is improved for bulk Nb cavities, the accelerating gradient for these cavities is reaching the fundamental limit of 50 MV/m. Since the critical surface of Nb in SRF cavities is less than one micron, it is possible to use thin films and multilayers to overcome the accelerating gradient limit. It has been proposed to apply a superconductor-insulator-superconductor (SIS) multi-layer structure onto Nb based cavities in order to provide an improved lower critical field (H_{c1}) that will shield the Nb and therefore allow for an increase in the accelerating gradient [1]. NbN is one of the superconductors that may be implemented in this SIS structure. However, the choice of insulator is crucial in determining the performance of NbN thin films. Here, we present our study of epitaxial thin films

* ASSD Student Award Finalist

prepared on both MgO and AlN templates. The effect of substrate choice on microstructure and superconducting properties is explored in order to determine which insulator provides optimal performance of NbN thin films for SRF applications.

[1] A. Gurevich, Appl. Phys. Lett. **88**, 012511 (2006).

Wednesday Lunch, October 31, 2012

Exhibitor Technology Spotlight

Room: West Hall - Session EW-WeL

Exhibitor Technology Spotlight

Moderator: D. Surman, Kratos Analytical Inc.

12:00pm **EW-WeL1 Nanoparticle Coating Technology for Vacuum Deposition**, *A.H. Kean, S. Saranu, M. Green, L. Allers*, Mantis Deposition Ltd., UK

In-vacuum generation and deposition of nanoparticles can provide enhancement to traditional thin film deposition techniques. Traditional thin film deposition in vacuum utilizes an evaporation, or sputter process that forms a two dimensional thin film. The Mantis Deposition Nanogen provides three dimensional nanoparticle crystals that are formed via a high pressure sputtering process. Through the process, the nanoparticles are thermalized, charged, and deposited on the substrate via a controlled beam. The resulting coating is not a traditional thin film, but a three dimensional material consisting of deposited nanoparticles. Significant differences in the properties of these materials arise including greatly increased surface area and increased chemical reactivity. Because the nanoparticles are charged they can be measured and their kinetic energy may be controlled. This talk describes the technique as well as resulting material properties. Specific examples will be described as well as new nanoparticle structures such as core/shell materials enabled by this advanced technique.

12:20pm **EW-WeL2 Using the Ipad in PVD Applications**, *C. Malocsay*, Semicore

It has taken 30 years for computer control to become a main stay in the operational architecture of Thin Film deposition systems. Now with that hurdle gone, using some of today's new tablet devices in conjunction with the system PC can provide a complete array of documents, schematics, video including direct communication with the factory engineer. Inuring day to day process performance remains consistent and cost effective; the Apple iPad is just another example of Semicore leading the way.

12:40pm **EW-WeL3 Physics-based Simulation for Semiconductor Processing Optimization**, *K. Jain, N. Solanki*, ESI Group

ESI Group is a global supplier of end-to-end virtual prototyping software and solutions, incorporating the physics of materials for manufacturing industries. The presentation will focus on computation fluid dynamics (CFD) modeling in the semiconductor fabrication process. Semiconductor fabrication processes involve a complex interplay of physical and chemical phenomena at multiple time and length scales. The complexity of these processes is increasing with decreasing feature size. Understanding these processes is critical for achieving desirable feature characteristics. ACE Suite, from ESI Group, is a commercial CFD software that provides integrated simulation tools for analyzing a wide variety of semiconductor reactors, ranging from CVD to Electroplating reactors. The ACE Suite also includes a topological solver, CFD-TOPO, that allows designers to accurately predict the 3D shape evolution of the feature at micron level. Our presentation will include the key features and benefits of our software along with a few selected validation studies.

1:00pm **EW-WeL4 Passive Thermal Actuator**, *I. Miller*, MEWASA North America, Inc.

General Description: The PTA™ (Passive Thermal Actuator) developed and manufactured by MEWASA (A Swiss Manufacturing Company) is a self-operating device that changes its length according to temperature fluctuations and serves as a linear actuator in various applications. The metal Passive Thermal Actuator is designed for various specified temperature ranges and allows the user to design Mechanical, Cryogenic and Electro-optical systems with precise movement as required. The PTA™ unique sturdy construction design provides a maintenance free linear movement with an extremely high reliability. The PTA™ is designed for more than 1 million operational cycles. Principle Operation: The PTA™ is a stainless steel sealed welded metal construction is based on the precision Edge Welded Bellows that are designed and Manufactured by MEWASA. The sealed actuator is filled with thermal fluid which expands and retracts according to the fluid/environment temperature changes. Thus, generating precise repeatable linear movement; pushing and pulling the required mechanism under a specified load. The Expansion Rate (defined as the fractional change in length per degree change in temperature) is customized and tested at MEWASA's in-house laboratory per our rigid Q.A. standards prior to shipment. The PTA™ is designed to move within several microns (thousands of an inch) and will work in any temperature range between –

40°C and +80°C (-40°F to 176°F). This cost effective PTA™ is a leak tight actuator which maintains its repeatability in a wide range of temperatures and pressures. The PTA™ frictionless structure and compact design functions as the ultimate solution for systems where external power is undeliverable. The Passive Thermal Actuator designed and manufactured by MEWASA is capable to meet your parameters. Product Features: • Highly accurate linear movement in a wide range of temperatures and pressures. • Eliminates the need for external power. • Maintenance free operation – no elastomeric seals required. • Flexible design that can be installed in either horizontal or vertical orientation. • Hermetically sealed and environmentally protected. • Complete stainless steel construction to resist corrosion. • Frictionless operation. • Designed to customer specific functional needs • No calibration required – preset at factory (plug and play). • Designed to deliver extremely precise and highly repeatable linear activation. • Sizes: from Ø13mm (Ø ½") • Materials: St.St. 316, AM350, Titanium Gr. 2, Inconel, Hastelloy C-276. (Note: material selection should take into account the environment and application) • Available Lengths: From 12mm (½") according to design • End Piece Standards: Threads, flanges to fit customer design • Installation Position: Vertical or Horizontal • Thermal Expansion Coefficient: from 0.01mm/°C (0.0008"/°F) • Actuation Force: from 1kg (2.2 lb.)

1:20pm **EW-WeL5 Bipolar Technology for AZO Sputtering**, *P. Ozimek, W. Glazek, K. Ruda, A. Klimczak, A. Gieraltowski*, HUETTINGER Electronic Sp. z o.o., Poland

Bipolar technology is currently being implemented in progressing number of applications like sputtering and PECVD. Thanks to state of the art digital control platform, TruPlasma Bipolar NEW power supply has an ability to react to dynamically changing parameters of the process very fast in order to enhance process efficiency and repeatability. The new opportunities offered by such control electronics enables new features supporting reactive sputtering with Bipolar technology. Presented solutions enable to deposit coatings with enhanced quality and at high deposition rate. Moreover TruPlasma Bipolar series 4000 NEW in response to growing market demand is equipped with latest industrial communication protocols like EtherCat or internet IP. TruPlasma Bipolar NEW is a solution for PECVD and a wide range of sputtering applications. TruPlasma Bipolar can be used with materials like: AZO, Si, SiN, Zn also smooth operation with capacitive and inductive loads under both: symmetrical as well as non symmetrical load conditions.

1:40pm **EW-WeL6 Novel Dual Mode Air Photoemission and Kelvin Probe System for Work Function Analysis of Nanometer Films**, *I.D. Baikie*, KP Technology, UK

KP Technology have developed a novel surface characterization instrument – the Air Photoemission System (APS) – which yields information on both the absolute work function and the Density Of States (DOS) near the Fermi level of metals and semiconductors deposited as bulk, thin films, layers, devices etc. The new system uses low photon excitation energies (3.5 – 7.0eV)

and has been used to characterize thin films such as Cobalt-Phyllocyanine (CoPc) on Transparent Conducting Oxides (TCOs) used in electroluminescent displays. We have combined this technique with our ultra-high relative work function resolution (1 – 3meV) macroscopic scanning Kelvin Probe Systems and can build up 2D work function maps of surfaces with lateral resolution of 100 – 2000nm.

The work function is an extremely surface-sensitive property of a material, modified by thin or monomolecular adsorbed layers, surface charging and for semiconductors, illumination. Indeed, work function changes of 500 - 1000meV magnitude can be observed with nanometer thick films deposited on glass, TCOs, metals and semiconductors. Our Kelvin Probe systems are also extremely versatile, capable of automatic work function/Fermi-level monitoring operating in ambient, controlled atmosphere (nitrogen, humidity) and using a custom head unit, UHV over a wide temperature range (4 – 1000K). Using a 1.24 – 3.1eV monochromatic light source, SKP can be extended to provide Surface Photovoltage Spectroscopy (SPS) which is an ideal tool for surface characterization of organic semiconductors and solar cells, allowing clarification of the energy band diagram and adsorption phenomena. This presentation will provide illustrative data on materials such as wide bandgap semiconductors (ITO), TCOs (TiN, TiO₂), nanometer thickness films and OLEDs.

Wednesday Afternoon, October 31, 2012

Applied Surface Science

Room: 20 - Session AS+NS+SS+TF-WeA

3D Imaging & Nanochemical Analysis - Part 2 (2:00-3:20 pm)/ Advanced Data

Analysis and Instrument Control (4:00-6:00 pm)

Moderator: V.S. Smentkowski, General Electric Global Research Center, M.R. Linford, Brigham Young University, S.J. Pachuta, 3M Company

2:00pm AS+NS+SS+TF-WeA1 From Atomic Scale to Materials Behavior: Using Atom-Probe Tomography to Understand the Behavior of Alloys and Ceramics, *E.A. Marquis*, University of Michigan INVITED

The ability to improve the performance of functional materials is driven by how well microstructure can be understood and controlled. The three-dimensional distribution of solutes, dopants or impurities in particular, in relation to structural features determines such properties as fracture toughness, strength, ductility, as well as electrical and magnetic response. After a brief introduction to atom-probe tomography, I will illustrate how high resolution characterization approaches can be used systematically to understand the atomic scale processes controlling materials microstructures and their evolution, focusing on alloys and ceramic systems. Several topics will be presented: precipitation and coarsening behavior of Al-based alloys, grain boundary chemistry and role of impurities during irradiation in ferritic steels which may play an important role in fracture and corrosion resistance, the development of oxide-dispersion strengthened steels for structural applications in future nuclear reactors and the role of minor elements in controlling the oxidation behavior of Ni-base alloys for high temperature power generation applications.

2:40pm AS+NS+SS+TF-WeA3 Three Dimensional Atomic Scale Characterization of Binary and Complex Oxides using Atom Probe Tomography, *A. Devaraj, R. Colby, D.E. Perea, S. Thevuthasan*, EMSL, Pacific Northwest National Laboratory

The development of three dimensional, high spatial and mass resolution characterization techniques is important for several materials used in applications ranging from catalysis, sensors to optoelectronics. Laser assisted atom probe tomography (APT) technique offers such an opportunity to perform atomic scale three dimensional analysis of materials including metals, semiconductors and dielectrics, with subnanometer spatial resolution and sub-ppm level mass resolution. The Cameca LEAP 4000XHR Atom Probe equipped with 355nm UV pulsed laser is used to analyze technologically important binary bulk oxides like MgO, Al₂O₃, TiO₂ and CeO₂. A strong correlation between applied UV laser energy and measured stoichiometry was observed for all these binary oxides. Using those results the importance of laser energy optimization on obtaining accurate stoichiometric composition analysis for oxides will be highlighted. Extension of such laser parametric investigation to complex oxides including SrTiO₃, LaCrO₃ and LaSrMnO₃ will also be presented. In addition the impact of laser pulsing on atomic scale structure of the oxide APT sample surface was studied by a direct cross correlation with aberration corrected TEM. The information on the atomic scale structure of the field evaporated oxide APT samples will be utilized to postulate the laser-oxide material interaction occurring during APT analysis of such oxides leading to the dependency of applied laser energy on measured stoichiometry.

3:00pm AS+NS+SS+TF-WeA4 Atom Probe Tomography of Complex Heterogeneous Low Dimensional Materials, *S. Thevuthasan, A. Devaraj, R. Colby, D.E. Perea, V. Subramanian, V. Shutthanandan*, Pacific Northwest National Laboratory

EMSL, a national scientific user facility of the DOE, is developing a comprehensive chemical imaging capability combining atom probe tomography with high resolution (scanning) transmission electron microscopy (HR(S)TEM) and high resolution Rutherford back scattering spectrometry (HRRBS) to provide solutions to problems pertaining to energy and environmental applications. We will emphasize on a chemical imaging effort aimed at atomically-resolved composition and structural analysis of low dimensional materials such as nanowires and embedded metal nanoparticles highlighting the benefits and challenges for APT. A unique benefit of APT is the ability to characterize the ppm level concentration and distribution of dopants across semiconducting nanowire heterojunctions. The preferential incorporation of dopants at specific atomic facets at the heterojunction interface in Si-Ge nanowires can only be characterized by using APT. Another important class of low dimensional

materials includes embedded metal nanoparticles in oxides with applications in catalysis, sensors and optoelectronic applications. In order to extent APT analysis capability to such materials a cross correlative approach of combining APT with aberration corrected HRSTEM is employed. The results from the model system of ion beam synthesized Au and Ag nanoparticles embedded in MgO will be presented.

4:00pm AS+NS+SS+TF-WeA7 Upgrading a 25 Year Old ims-4f Magnetic Sector SIMS Instrument: Teaching an Old Dog New Tricks and Keeping Research in its Future, *A.J. Fahey, B.E. Naes, G. Hager*, Pacific Northwest National Laboratory

The CAMECA ims-4f at PNNL is nearly 25 years old. Although much of the vacuum system, electrostatic optics and associated apertures and slits have been maintained and remain operational the electronics that control the critical components of this machine has gone beyond the typical "mean-time-between failure" of nearly all components, which is typically 10 years.

The original electronics designs, many of which are no longer employed on the newer CAMECA models, incorporated multiple series of relays to control lens voltages that allowed isolation of low control and high voltage output. These relays, among other components, are failing.

Some components of the electrostatic optics and vacuum system are targeted to be replaced to upgrade the capabilities of the instrument and to use physical components from our "surplus" ims-4f system than would enhance the operation of the PNNL ims-4f giving in near-equivalence to the operation of an ims-7f.

The upgraded electronics and control systems are being designed in a modular way using as many commercial components as possible, such as modular high voltage power supplies and commercially available high-voltage operational amplifiers. The new system will allow for complete control of all subsystems on the instrument and will improve repeatability of settings and measurements. We will be able to perform measurements sets and sequences that are currently not possible on any existing SIMS instrument. In addition, the new computer controlled system should make operation of the SIMS instrument more accessible to other investigators as it should reduce the level of training needed to operate the instrument. Currently, the operator must adjust "knobs" to tune the instrument and reproduce prior operating conditions. With the upgraded system conditions will be recalled from saved files.

All modular components are being housed in ANSI-standard DIN modules and sub-racks. Control, monitoring and data acquisition will largely be performed via PXI subsystems. The Vacuum will be controlled and monitored via a commercial process control system. Also, several other individual instruments will be used in critical positions around the instrument.

Details of the upgrade will be discussed as well as improvements to the flexibility of measurements and the performance of the system. An outline of the types of measurements that should be available with all modern systems will be presented and discussed as well as the results of improvements implemented to the PNNL ims-4f SIMS instrument.

4:20pm AS+NS+SS+TF-WeA8 Automated Processing of X-ray Photo-Electron Spectra, *K. Macak, E. Macak, S.J. Coultas, S.J. Hutton, A.J. Roberts, R. Raso, S.J. Page, C.J. Blomfield*, Kratos Analytical Ltd, UK

Modern XPS instruments are capable of generating a large amount of data in a hands-off automated fashion. Many new material challenges are increasingly reliant upon XPS for sample screening and other high throughput, low operator intervention applications.

The interpretation of XPS data and reliable quantification from the acquired results presents an opportunity to improve the whole experimental automation still further. We present an algorithm for fully automated processing of X-ray photo-electron spectra. The analysis is split into three stages: background subtraction, peak identification and quantification of element composition.

Each step can be carried out separately and the user can provide prior knowledge of the sample by manually selecting regions, assigning their labels and/or explicitly include/exclude specific elements. This additional information then helps to improve the accuracy of the results.

The algorithm was tested on more than 1000 spectra, selected from a wide range of different materials; including steels, polymers, semiconductors and ceramics. These spectra were processed using the automated procedure and the outcomes were compared to those determined by expert users. The average element detection success rate was 87 %.

The influence of various experimental conditions (such as signal-to-noise ratio and operating conditions) on the identification procedure is also discussed.

4:40pm **AS+NS+SS+TF-WeA9 Correlating Structure and Chemistry – A Multitechnique Study using Light Microscopy (LM), SEM and XPS**, *M.L. Pacholski, P.Y. Eastman*, The Dow Chemical Company

Understanding the distribution of carbon-rich chemistries on organic substrates can be very difficult, particularly when the substrates are not uniform, such as cellulose fibers. Recently we have been challenged to measure the distribution of an olefin polymer on a fibrous cellulose sheet. In order to verify that measured chemical distributions were definitively from polymer, as well as to understand the morphology of the deposited polymer, it was highly desired to study identical areas using SEM and other imaging techniques. Although several chemical imaging methods were investigated, it became apparent that XPS imaging was the only chemical technique capable of obtaining distributions over the desired fields of view (1 mm-3 mm). Registry of the SEM images with XPS images proved to be difficult since many of the traditional registry methods, such as marking with ink or gluing markers to the surface are ill-suited to absorbent cellulose. The first step was to align relatively low magnification light microscope images from a stereoscope with optical images captured directly in the XPS instrument. These images were then used as a “bridge” to align the higher magnification SEM and XPS images. With this method, deposited polymer and chemical information were correlated with high spatial accuracy. Composite images showing the chemical information as colored overlays on the SEM images were generated to clearly display the correlation.

Biointerphases Focus Topic: Bioimaging

Room: 23 - Session BN+AS-WeA

Bioimaging

Moderator: M. Grunze, University of Heidelberg, Germany

2:00pm **BN+AS-WeA1 Label-free Non-Invasive Imaging of Live Cells by Raman Micro-Spectroscopy**, *I. Notinger*, University of Nottingham, UK **INVITED**

Stem cells have enormous potential for cell replacement therapies in curing age-related illnesses such as Alzheimer's and Parkinson's disease, as well as diabetes and cardiovascular disorders. In addition, they are a reliable cell source in tissue engineering and stem cell seeded scaffolds could provide an unlimited supply of grafts to replace and repair diseased tissues.

However, the current conditions to derive specific cell types remain suboptimal, generally producing only low yields of the desired differentiated lineages within highly heterogeneous populations that are not suitable for clinical use due to the presence of mainly unwanted cell types. This current limitation in the delivery of validated stem cells suitable for clinical applications, highlights the immediate need for non-invasive techniques capable of phenotypic identification of live cells within highly heterogeneous populations.

Raman micro-spectroscopy (RMS) is a label-free technique which can be used for imaging of live cells. This technique combines the high chemical specificity of Raman spectroscopy with the high spatial resolution of optical microscopy to provide detailed molecular information of complex biological samples. Since RMS has only a minimal background signal from water, it allows repeated observations of viable cells maintained under physiological conditions, which is difficult by other molecular vibrational techniques.

In the first part we will focus on using RMS to detect molecular markers for individual live cardiomyocytes (CMs) derived from human embryonic stem cells (hESCs). The ability to monitor and quantify these spectral markers during differentiation periods as long as 5 days is also demonstrated. The analysis of Raman spectra of hESC-derived CMs were characterised by increased signals associated to myofibrils and glycogen compared to the other differentiated cells present in the cultures. The prospects of label-free Raman activated cell sorting are also discussed.

The second part will present results on using RMS for imaging and quantifying spectral markers in neuronal stem cells (NSCs). Raman spectra of undifferentiated NSCs are compared to those of glial cells derived from NSCs, with the aim to identify molecular markers which can be used for assessing the differentiation status of the NSCs. High resolution spectral maps corresponding to nucleic acids show that NSCs are characterized by increased concentrations of cytoplasmic RNA.

These studies demonstrate that RMS represents a feasible approach for label-free non-invasive characterization of individual live cells and can be used to assess the differentiation status and the phenotypes of individual cells.

2:40pm **BN+AS-WeA3 Perfluoropentane Gas and Liquid Filled Hollow Silica Micro/Nano Spheres for Ultrasound Guided Surgery and HIFU Therapy**, *A. Liberman, H.P. Martinez, Z. Wu, C.V. Barback, S.L. Blair, Y. Kono, R.F. Mattrey, W.C. Trogler, A.C. Kummel*, University of California San Diego

The reported positive margin rate from wire localized excisions of breast cancers is approximately 20-50%; however, by preoperatively injecting a radio active seed into the tumor under CT guidance, the excision rate is halved because the surgeon can constantly reorient the dissection to place the seed in the center of the specimen. Unfortunately, radioactive seed localization has several safety challenges, only single foci can be localized, and incisions are required to implant the seeds, so it is rarely employed. As a safe alternative, gas-filled hollow Fe-doped silica particles have been developed, which can be used for ultrasound-guided surgery even for multiple foci. The function of the Fe doping is to render the silica shells biodegradable. The particles are synthesized through a sol-gel method on a polystyrene template, and subsequently calcined to create hollow, rigid microspheres. The Fe-doped silica shell is derived from tetramethoxy orthosilicate (TMOS) and iron (III) ethoxide, which forms a rigid, mesoporous shell upon calcination. The microspheres are filled with perfluoropentane (PFP) vapor or liquid. The flourous phase is contained within the porous shell due to its extremely low solubility in water. Considerable testing of particle functionality, signal persistence and acoustical properties have been performed in various phantoms including ultrasound gel, chicken breast, and excised human mastectomy tissue. *In vitro* studies have shown that continuous particle imaging time is up to approximately 45 minutes, and will persist for over five days. Furthermore, preliminary *in vivo* particle injection longevity studies have been performed in a rabbit model which are consistent with *in vitro* data showing signal presence even five days post injection. These silica spheres may be used as a sensitizing agent in high intensity focused ultrasound (HIFU). Traditional ultrasound agents pose several potential drawbacks such as poor *in vivo* persistence (minutes) and high risk (cardiac complications) during continuous perfusion. Preliminary *in vitro* results in HIFU ablation in an agar tissue phantom model suggest that very few particles are needed in order to develop a sensitizing effect to HIFU (approx. 1-10 µg/ml particles/agar varying by particle size). A novel technique has been developed to fill the particles with perfluorocarbon liquid which vaporizes upon exposure to HIFU thereby increasing the sensitivity compared to gas filled particles.

3:00pm **BN+AS-WeA4 Differentiation of Breast Cancer Cell Lines with ToF-SIMS**, *L.J. Gamble, M. Robinson*, University of Washington, F. Morrish, D. Hockenbery, Fred Hutchinson Cancer Research Center

Cancer is a heterogeneous malignancy that manifests itself in a variety of morphological types and clinical outcomes. Tumor metabolism plays a large role in cancer onset and progression, and its causes and effects are under intense scrutiny. Time-of-flight secondary ion mass spectrometry (ToF-SIMS) has been increasingly utilized for examining biological samples including biomaterials, cells, and tissues. The incorporation of cluster ion sources has allowed the detection of many high mass organic species that can be used to characterize biological surfaces. In combination with principal component analysis (PCA), we use ToF-SIMS to determine differences in the chemical makeup of eight different breast cancer cell lines. Four cell types are of the triple-negative (TN) phenotype, and four cell types are the luminal phenotype. Spectra have been acquired on an IONTOF TOF.SIMS V using Bi_3^+ before and after C_{60} etching. Using positively charged mass fragments, many of the cell lines can be separated from one another within a 95% confidence interval, with only two TN lines overlapping. Biological significance of the loadings peaks will be discussed with species such as diacylglycerols and cholesterol playing a role in the separation. This work is the foundation for future studies using human tumor biopsy samples that will help elucidate the link between fatty acid composition within a tumor and the potential drug resistance of that tumor.

4:00pm **BN+AS-WeA7 Biological Applications of Lipid Imaging with Cluster-TOF-SIMS and MALDI-TOF**, *A. Brunelle*, CNRS, Institut de Chimie des Substances Naturelles (ICSN), France **INVITED**

Time-of-Flight Secondary Ion Mass Spectrometry (ToF-SIMS) using keV energy metal cluster beams as primary ions is now recognized as a powerful method for *in situ* chemical, biological and medical applications [1,2]. It opens a new field of surface imaging, particularly for biological tissue sections. Compared to the more established MALDI (Matrix Assisted Laser Desorption Ionisation) imaging approach, TOF-SIMS imaging provides the incomparable advantages of a routine micrometre scale resolution and of an

easy sample preparation which does not require matrix coating of the surface. However TOF-SIMS suffers from some limitations, such as the narrow mass range, the lack of structural analysis of the species by tandem mass spectrometry, and the fact that mainly lipids are preferentially released from the biological samples.

This lecture intends to show the wealth of powerful information that can be obtained from the chemical analysis of biological surfaces, with several examples chosen among various applications such as the localization of xenobiotics, natural substances, lipid markers from genetic diseases and non-alcoholic fatty liver disease. The strengths and weaknesses of lipid imaging using TOF-SIMS and MALDI-TOF will also be compared, showing the complementarity between the two methods.

Tissue imaging using TOF-SIMS can also be associated with histology for medical diagnosis in order to correlate structural features with ion images. The possibility to use the same tissue section for both histology and mass spectrometry imaging has been tested. It is a major advantage in terms of sample preparation and precision on the histological structure localization, provided that none of the two methods disturbs the performances of the other [3].

Massive cluster ion sources of argon have recently been used for SIMS experiments [4]. These ion beams interact with surfaces with incomparable physical properties, and thus hold the promise for new opportunities such as organic depth profiling or large increases of sensitivity. Recent results will be presented showing the possibility of depth profiling in organic samples, but also the enhancement of the sensitivity, using both massive clusters and bismuth for dual beam depth profiling.

[1] F. Benabdellah, A. Seyer, L. Quinton, D. Touboul, A. Brunelle, O. Lapr votte, *Anal Bioanal Chem* 396 (2010) 151-162

[2] D. Touboul, O. Lapr votte, A. Brunelle, *Curr Opin Chem Biol* 15 (2011) 725-732

[3] C. Bich, S. Vianello, V. Gu rnieau, D. Touboul, S. De La Porte, A. Brunelle, *Surf Interface Anal* in press DOI:10.1002/sia.4846

[4] H. Gnaser, K. Ichiki, J. Matsuo, *Rapid Commun Mass Spectrom* 26 (2012) 1-8

4:40pm **BN+AS-WeA9 ToF-SIMS Image Analysis of Mouse Diaphragm Muscle Cross-Sections**, *D.J. Graham, N.P. Whitehead, S.C. Froehner, D.G. Castner*, University of Washington

Duchenne muscular dystrophy (DMD) is a common, X-linked, neuromuscular disease, caused by mutations in the dystrophin gene. The absence of dystrophin in DMD patients causes progressive muscle degeneration, characterized by inflammation, fibrosis and failure of muscle regeneration. Profound muscle weakness ensues, ultimately leading to respiratory or cardiac failure, and death around the age of 20 to 30. The *mdx* mouse is a dystrophin-deficient animal model of DMD. In addition to being a model for DMD, *mdx* mice have been found to be resistant to obesity when fed a high fat diet.

In this study we used ToF-SIMS imaging to study the differences in lipid composition of skeletal muscle cross-sections of *mdx* and wild type mice. Results show differences in both the morphology of the tissue and the distribution of lipids within the tissue. For example the *mdx* mouse tissue shows a more loosely organized muscle fiber structure with fibrotic tissue formation, whereas the fibers in the wild type mice show more tightly packed muscle fibers. Understanding differences in lipid composition between these mice can hopefully provide new insight into differences in muscle lipid metabolism and help understand the metabolic pathways that protect *mdx* mice from diet-induced obesity.

5:00pm **BN+AS-WeA10 ToF-SIMS Characterisation of the Distribution and Permeation of Topically Applied Pharmaceuticals**, *D.J. Scurr*, University of Nottingham, UK, *A. Judd*, Keele University, UK, *K. Wan*, University of Central Lancashire, UK, *J. Heylings*, Dermal Technology Laboratory Ltd., UK, *G. Moss*, Keele University, UK

Drug delivery through skin provides opportunities to reduce compliance challenges and is suited to use in environments in the developing world, e.g. micro needle patch delivery of vaccines. In this study, a widely applied chemical antiseptic, chlorhexidine is considered. This is utilised in low concentrations in topical skin treatments where permeation through the stratum corneum of the skin is of particular importance, as insufficient permeation leads to bacterial re-colonisation. Current standard practice for assessing the permeation of this, or any active pharmaceutical ingredient (API), through the upper skin layer is to firstly remove microscopic layers of pre-treated in vitro skin using adhesive tape ('tape stripping'). The removed material is then analysed using high performance liquid chromatography (HPLC) to evaluate the API penetration. The sensitivity of HPLC often requires several tape strips to quantify the API. [1] Using this protocol, the permeation of the API is difficult to confirm and no information regarding lateral distribution is gleaned. Here, we develop a

novel alternative method for assessing the permeation of this molecule within skin tissue and apply this protocol to assess the effectiveness of a permeation enhancing dendrimer pre-treatment.

In order to characterise permeation and lateral distribution of chlorhexidine through the skin, this study uses the high spatial resolution of time of flight mass secondary ion mass spectroscopy (ToF-SIMS) to analyse cross-sectioned skin. The samples are treated with chlorhexidine, cryomicrotomed and analysed by ToF-SIMS under cryo conditions. The results of these studies provide the specific localisation and real permeation depth of the chlorhexidine within the stratum corneum. Additionally, freeze dried tape stripped materials have also been analysed using ToF-SIMS as an independent cross-validation, the results from which support the observations made for the skin cross-sections. This ToF-SIMS methodology has also been applied to demonstrate the increased permeation of chlorhexidine following a dendrimer pre-treatment of the skin. In these samples the secondary ion fragments specific to the chlorhexidine structure are identified at higher intensities and are localised at increased depths within the skin tissue. This methodology which shows great promise in the development of transdermal delivery of pharmaceuticals. The high lateral resolution and molecular specificity complement label based approaches such as confocal microscopy and optical approaches that can function in vivo such as stimulated Raman scattering microscopy.

[1] Wagner et al, (2002) *J. Pharm. Sci.*, 91 (8)

5:20pm **BN+AS-WeA11 Coherent X-ray Microscopy of Vitrified Biological Samples**, *A. Rosenhahn*, Ruhr-University Bochum, Germany, *T. Gorniak, T. Senkbeil, A. Buck, M. Beckers, M.H. Grunze*, Karlsruhe Institute of Technology, Germany

Coherent X-ray microscopy of hydrated biological samples – especially in the 'water window' at photon energies of 284–540 eV – is of tremendous interest for life sciences due to the high contrast of organic matter with respect to the aqueous background. We present recent progress in imaging of biological samples with coherent X-ray microscopy (holography and ptychography) and scanning X-ray nano/microprobe imaging. The main goal is application of these emerging techniques to the in-situ analysis of vitrified biological specimen. Ptychography uses coherent diffraction patterns at different sample positions while maintaining a fixed spatial overlap between the fields of view. By introducing this spatial redundancy to the data an additional constraint for the iterative reconstruction algorithm is achieved. This enhances the convergence of phase retrieval drastically and allows imaging of extended samples. We supplement these results with resonant ptychographic imaging at the oxygen K-edge core level resonances of test particles where both, absorption and phase shifts, revealed information about the chemical composition of the samples. First results on imaging of frozen hydrated specimen and samples in the liquid environment will be shown and discussed.

5:40pm **BN+AS-WeA12 Characterization of Nanoparticles Implanted into Tissues for Enhancement of Ion-Mobility Mass Spectrometry Surface Imaging of Sagittal Brain Sections**, *E.K. Lewis*, Ionwerks, Inc., *J.F. Moore*, MassThink, *T.F. Egan*, Ionwerks, Inc., *B. Chen, B. Brinson*, Rice University, *V.M. Womack, D. Barbacci*, Ionwerks, Inc., *R. Hauge*, Rice University, *A.S. Woods*, National Institute on Drug Abuse / IRP, *J.A. Schultz*, Ionwerks, Inc.

Our research previously included the first demonstration of implanting nanoparticles nanometers below the surface of a biological tissue to provide a completely new method MALDI imaging. Now, we are working towards combining optical histology and molecular surface imaging. We are currently using x-ray photoelectron spectroscopy (XPS) to characterize the nanoparticle coverage, composition, and the depth nanoparticles are implanted into our biological tissue(s). Nanoparticles were implanted at energies from 2-6kV, initial XPS depth profiles demonstrated they are implanted into tissue at depths from 10-30nm. The use of nanoparticulate implantation provides a basis from which future surface imaging techniques can be developed and tested. This method is important in that not only are we preserving the optical histology, and location of lipids and peptides, but MALDI signals are increased on the order of 2-4 times over typical preparation with several orders of magnitude less matrix.

Electronic Materials and Processing

Room: 9 - Session EM+OX-WeA

Oxides and Dielectrics for Novel Devices and Ultra-dense Memory

Moderator: J.F. Conley, Oregon State University, J. Kim, The University of Texas at Dallas

2:00pm **EM+OX-WeA1 Dielectric Requirements for a Novel Tunnel-FET Based on Room-Temperature Superfluidity in Graphene Double Layers**, L.F. Register, X. Mau, D. Reddy, D. Basu, W. Jung, I. Sodeman, D. Pessin, A. Hassibi, A.H. MacDonald, S.K. Banerjee, University of Texas at Austin **INVITED**

The Bilayer pseudo-spin Field Effect Transistor (BiSFET) is a novel transistor concept based on possible room temperature superfluidity in two graphene layers separated by a thin dielectric. In principle, the switching energy per device could be on the scale of 10 zJ, over two orders of magnitude below estimates for "end-of the roadmap" CMOS transistors. However, at the time of writing, neither a BiSFET nor just such room temperature superfluidity have been demonstrated, and doing so poses substantial challenges both theoretical and experimental. Most significant among these challenge for this novel device concept now appear to be those associated with its novel dielectric requirements. In this presentation I will cover the basic concepts behind graphene superfluidity and BiSFET concepts, our current understanding—and limits to that understanding—of the requirements for condensate formation, and how these requirements could impact BiSFET design. In particular, I will compare and contrast the dielectric needs for the proposed BiSFET to those of conventional transistors.

2:40pm **EM+OX-WeA3 Interfaces and Surfaces in Tunnel Field-effect Transistors**, G. Xing, University of Notre Dame **INVITED**

Abstract: It is now recognized that compound semiconductor tunnel field-effect transistors (TFETs) can retain MOSFET-like speed at low supply voltages given that on-current and voltage can be lowered in proportion. To achieve high on-current at low V_{dd}, the staggered-gap and broken-gap AlGaSb/InAs heterojunctions and graphene are being developed. In this talk I will first outline the recent experimental progress in the development of interband tunnel transistors with sub-60 mV/decade subthreshold swing at Notre Dame. Subsequent discussions will be then focused on the impact of interfaces and surfaces of the transistor on the TFET performance, in particular, the interface between the gate dielectric and semiconductor as well as the semiconductor surface after transistor isolation etch.

4:00pm **EM+OX-WeA7 Resistive Switching Characteristics of Al₂O₃/TiO₂ Bilayer ReRAM dependent on Al₂O₃ Thickness**, H.Y. Jeon, J.S. Lee, J.G. Park, W.C. Jang, H.T. Jeon, Hanyang University, Korea

The next generation nonvolatile memory (NGNVM) devices should satisfy the device properties such as high density, fast operation speed, low power consumption, and high reliability. Recently, many type-NGNVM candidates are extensively considered to replace the conventional nonvolatile memory devices; polymer random access memory (PoRAM), phase change random access memory (PRAM), spin transfer torque random access memory (STT-RAM), and resistive switching random access memory (ReRAM). Among the many type-NGNVMs, ReRAM has attracted a great deal of attention in semiconductor industry mainly due to its high density integration, long retention time, small cell size, and fast switching speed. Also, the ReRAM has the simple structure like metal/insulator/metal (MIM) structure allowing the fabrication of 3 dimensional stack and nano cross-bar structure. There are two types of resistive switching for ReRAM. One is unipolar resistive switching (URS) and the other is bipolar resistive switching (BRS). The URS means the operation of set (program) and reset (erase) are under the same polarity of bias, whereas the polarity of bias for set operation is opposite to that of bias for reset operation in the BRS. The URS type ReRAM needs current compliance to prevent hard breakdown of transition metal oxide (TMO) when measuring the resistive switching. The URS is usually observed in ReRAM using binary transition metal oxides such as NiO, TiO₂, and Al₂O₃, while the BRS appeared in ReRAM using perovskite materials like Cr:SiZrO₃, Pr_{0.7}Ca_{0.3}MnO₃. Among many deposition methods for metal oxide, atomic layer deposition (ALD) has recently received a great interest for manufacture of ReRAM. Especially, remote plasma ALD is expected to enhance the reactivity between metal-organic precursor and reactant gas with minimal plasma damage on substrate, allowing the low impurity content and high density of the deposited films. In RPALD, plasma is generated remotely outside of chamber. And the radicals and ions generated in plasma region enter into the chamber by a downstream flow for chemical

reaction of deposition. In this study, we investigated URS switching behaviors of ReRAM using Al₂O₃/TiO₂ bilayer deposited by remote plasma atomic layer deposition (RPALD) method. The thickness of Al₂O₃ layers was varied to observe the discrepancy of set/reset voltage and operation current level. The deposited Al₂O₃ and TiO₂ films are perfectly amorphous structures and their binding states have nearly stoichiometric composition. When operating the ReRAM with different thickness ratio, the dependence of operation voltage and current level on the thickness of Al₂O₃ layers was observed.

4:20pm **EM+OX-WeA8 High- k SrTiO₃ Dielectric by Plasma-Assisted Atomic Layer Deposition**, N.Y. Garces, D.J. Meyer, B.P. Downey, V.D. Wheeler, D.W. Zapotok, C.R. Eddy, Jr., U.S. Naval Research Laboratory

Strontium titanate (STO) is a promising material that offers the possibility of achieving large dielectric permittivity (k) constants for gate dielectric and other applications. Thin (~28 nm) STO films were deposited by remote plasma-assisted atomic layer deposition on the native oxide of n-type Si substrates in an Oxford Instruments FlexAL reactor at ~250°C using Bis(Tris-IsopropylCyclopentadienyl) Strontium, Tetrakis(dimethylamido)titanium as metal precursors, and a remote oxygen plasma as oxidizer. The general approach to deposit the ternary perovskite SrTiO₃ is by alternating the ALD of the constituents TiO₂ and SrO in a specific ratio to control such properties as the stoichiometric composition and dielectric constant [1,2]. The deposition temperature was chosen to give optimum growth uniformity for both SrO and TiO₂ and to avoid decomposition of the precursors. The growth rate of the STO films was ~ 0.14 nm/cycle, which is slightly higher than the combined growth rate of the individual components. Also, the STO growth rate and stoichiometry are highly dependent on the temperature of the strontium precursor.

Initial capacitance-voltage (C-V) and current-voltage (I-V) results on 50-250 μm diameter circular capacitors patterned on ALD SrO:TiO₂ (1:1) films were obtained. These dielectrics exhibited a moderate (~ 20) dielectric constant with reduced reverse-biased leakage current of ~1.6x10⁻⁵ A/cm² but larger forward bias leakage current ~ 1.2x10⁻³ A/cm² at 1V. Hysteresis in forward and reverse C-V sweeps was not observed, suggesting that these films are high-quality with limited or no slow time-constant charge trapping. After annealing the STO films at 550°C in N₂ for 5 min, a reduction in the oxide thickness by ~ 9% was measured, as well as a small increase in the dielectric constant to ~ 28 as a result of crystallization [3].

During this study, the overall thickness of the dielectric was held relatively constant, while the relative ratio of SrO:TiO₂ was varied to tune the stoichiometry of the films and to monitor changes in the dielectric constant, optical band gap, E_g, and the electrical performance of the resulting oxides. The thickness, growth rates, and ALD mode behavior of STO, SrO, and TiO₂ oxides were evaluated by spectroscopic ellipsometry measurements. We will present electrical measurements of STO oxides of various compositions with optimized deposition conditions for the chosen precursors, as well as stoichiometry assessments by x-ray photoelectron spectroscopy.

1. Vehkamäki, et al. *Chem. Vap. Deposition*, **7**, 75 (2001)
2. Popovici, et al. *J. Electrochem. Soc.*, **157**, G1 (2009)
3. Langereis, et al. *J. Electrochem. Soc.*, **158**, G34-G38 (2011)

4:40pm **EM+OX-WeA9 Micro-Antenna Coupled Nano-MIM Diodes: Modeling, Design, Processing and Application**, N. Goldsman, Univ. of Maryland, CoolCAD Electronics LLC, F. Yesilkaya, Univ. of Maryland, S. Potbhare, CoolCAD Electronics, LLC, M. Peckerar, Univ. of Maryland, A. Akturk, CoolCAD Electronics, LLC, K. Choi, Univ. of Maryland, W. Churaman, U.S. Army Research Lab, N.K. Dhar, DARPA/MTO **INVITED**

An antenna coupled to a diode can convert electromagnetic power into DC power, which can be integrated over time and stored on a capacitor or used to charge a battery. The combination of the antenna and diode is typically called a "Rectenna". We are interested in developing a rectenna that operates in the infrared region of the electromagnetic spectrum. The applications of interest for IR rectennas include self-powering circuits and infrared imagers.

The rectenna structure we focus on consists of a micro-antenna and a rectifying metal-insulator-metal (MIM) diode for converting electromagnetic wave induced alternating current on the antenna to a direct current. The antenna couples to ambient or directed electromagnetic (EM) radiation, and the diode rectifies the AC signal for DC current and power generation. The frequency or the wavelength of the EM signal dictates the physical dimensions of the antenna, and the operating frequency of the diode. Here one of the main challenges in achieving DC output upon IR radiation is to fabricate a diode capable of operating in the infrared range of frequencies, and more specifically at 30 Terahertz corresponding to 10 micrometer infrared radiation or approximately 3000K. To meet this

challenge, we are fabricating metal-insulator-metal diode structures with oxide thicknesses of on the order a couple of nanometers or less.

An application of significant interest is a high resolution, high speed IR imager that can operate at room temperatures. Expanding from a single pixel to a complete large array is a challenge because the added complexity may give rise to electromagnetic coupling between adjacent elements, which needs to be accounted for. In addition, IR imaging, which corresponds to 30 terahertz region of operation, is special because it represents an 'in-between' region between radio and optical frequencies. At 10 micron wavelengths, the photons are typically too small in energy to economically convert their AC power into DC using semiconductor or quantum based photodetectors. At the same time, their frequency is too high to utilize standard PN or Schottky barrier diode based rectification. We thus explore the use of a micro-antenna coupled to a MIM diode for AC to DC conversion. A major difficulty here is to develop a diode that responds quickly enough to be forward biased during one part of the AC cycle and reverse biased to the other half of the cycle, without having the parasitic capacitance of the diode short out the signal. The rectenna we are developing uses a Nickel/Nickel-Oxide/Nickel (Ni-NiO-Ni) MIM structure, fabricated and designed using unique modeling and processing techniques.

5:20pm EM+OX-WeA11 High-Electron-Mobility SiGe on Sapphire Substrate for Next Generation Ultrafast Chipsets, H.J. Kim, Y. Park, National Institute of Aerospace (NIA), H.-B. Bae, Korea Advanced Institute of Science and Technology, S.H. Choi, NASA Langley Research Center (NASA LaRC)

In the conventional silicon-on-sapphire (SOS) technology with the epitaxy of Si on *r*-plane (1-102) sapphire, typical device region do not need reverse bias between the substrate and device area for electrical separation, because SOS wafer is separated by the sapphire itself, a best insulator. The advantage is that the sapphire insulator is very thick, which engenders an ultra-small capacitance and therefore it can reduce parasitic capacitance and leakage current at a high operating frequency. However, SOS wafer has a limitation in carrier mobilities due to the silicon material. The mobilities of SiGe can be a few times higher than those of silicon due to the high carrier mobilities of germanium (p-type Si: 430 cm²/V·s, p-type Ge: 2200 cm²/V·s, n-type Si: 1300 cm²/V·s, n-type Ge: 3000 cm²/V·s at 10¹⁶ per cm³ doping density). Therefore, RF devices which are made with rhombohedral SiGe on *c*-plane sapphire can potentially run a few times faster than RF devices on SOS wafers.

NASA Langley's rhombohedral epitaxy uses an atomic alignment of the [111] direction of cubic SiGe on top of the [0001] direction of the sapphire basal plane (*c*-plane). It shows a sample of rhombohedrally grown SiGe on *c*-plane sapphire with a single crystalline percentage of 95%. Twin defects exist only at the edge of the wafer. The electron mobilities of the tested samples are between those of single crystal Si and Ge. For instance, the electron mobility of 95% single crystal SiGe is 1538 cm²/V·s which is between 350 cm²/V·s (Si) and 1550 cm²/V·s (Ge) at 6x10¹⁷ /cm³ doping concentration. Typically, a rhombohedral single crystal SiGe has 2 or 3 times higher carrier mobility than monocrystalline silicon. If the defects in SiGe can be removed, transistors with higher operational frequencies can be fabricated for a new generation of ultrafast chipsets.

5:40pm EM+OX-WeA12 Fabrication and Characterization of Metal-Insulator-Insulator-Metal (MIIM) Tunnel Diodes, A.N. Nasir, J.F. Conley, Oregon State University

MIM tunnel diodes have been proposed for high speed applications such as hot electron transistors, IR detectors, and optical rectennas for IR energy harvesting as well as backplanes for LCDs. The majority of these applications require highly asymmetric and non-linear I-V behavior at low applied voltages. The standard approach to achieving asymmetric operation in MIM devices is through the use of metal electrodes with different workfunctions (Φ_M). However, the amount of asymmetry achievable using this method is limited by the Φ_M difference that can be obtained using practical metals. In this work, we use an alternative approach to achieving asymmetric and non-linear operation – engineering of the insulating tunnel barrier using nanolaminate pairs of insulators with different bandgaps and band-offsets to produce asymmetric tunnel barriers. Electrons tunneling from one metal electrode to the other will see a different shape barrier depending on the direction of tunneling and the bias applied.

Recently, we found that atomic scale roughness at the bottom metal-insulator interface can dominate the I-V characteristics of MIM diodes, even overwhelming the influence of Φ_M difference. By using the amorphous metal ZrCuAlNi (ZCAN) as an ultra-smooth bottom electrode in combination with high quality dielectrics deposited via ALD, we were able to fabricate MIM diodes dominated by FN tunneling. In this work, nanolaminate insulator stacks consisting of either HfO₂/Al₂O₃, Ta₂O₅/Al₂O₃, ZrO₂/Al₂O₃, or HfO₂/ZrO₂ are deposited on sputtered ZCAN bottom electrodes via ALD. Al dots form the top gate electrode.

MIIM I-V characteristics were found to be sensitive to the relative thickness as well as the arrangement of the individual dielectric layers. In the ZCAN / Al₂O₃ / HfO₂ / Al orientation, the asymmetric tunnel barrier opposes the effect of the asymmetric Φ_M , a larger current is measured at positive bias, and asymmetry is lower than for a neat Al₂O₃ insulator device. However, in the ZCAN / HfO₂ / Al₂O₃ / Al orientation, the asymmetric tunnel barrier enhances the asymmetric Φ_M , a larger current is measured at negative bias, and asymmetry is greater than for neat Al₂O₃ or HfO₂ insulator devices. High asymmetry is seen when conduction in both dielectric layers is dominated by FN tunneling rather than bulk limited mechanisms. Ta₂O₅/Al₂O₃, e.g., did not show an enhancement in asymmetry.

In conclusion, we have fabricated dual insulator MIIM diodes that exhibit improved asymmetry over single layer MIM diodes. These results represent an advancement of the understanding necessary to engineer thin film based MIM tunnel devices for microelectronics applications.

Energy Frontiers Focus Topic Room: 15 - Session EN+TF-WeA

Thin Films for Energy Applications

Moderator: M. Filler, Georgia Institute of Technology

2:00pm EN+TF-WeA1 Batteries and Battery Materials by Vapor Deposition, N. Dudney, Oak Ridge National Laboratory INVITED

Although most commercial rechargeable batteries are prepared by bulk and powder processing methods, vapor deposition of materials has led to important advances for fundamental research, for modification of battery materials and interfaces, and also for commercialization of thin film batteries. Each of these areas will be illustrated with our studies of thin film materials for the electrolyte, anode, and cathode components of rechargeable lithium and lithium-ion batteries with both planar and 3-dimensional architectures.

4:00pm EN+TF-WeA7 Efficient Radiative and Non-Radiative Energy Transfer from Quantum Dots to Silicon Nanomembrane. Evidence of Waveguiding Phenomena, O. Seitz, H.M. Nguyen, W. Peng, Yu.N. Gartstein, Y.J. Chabal, A.V. Malko, University of Texas at Dallas

Nanostructured materials attract a considerable attention as potential candidates for practical photovoltaic (PV) devices. The majority of current hybrid PV architectures are based on charge transfer schemes, which frequently suffer from bad interface quality and poor carrier transport, consequently lowering the light conversion efficiency. An alternative is offered by non-contact *energy transfer*-based hybrid nanostructures, which combine strongly absorbing components, such as inorganic nanocrystal quantum dots (NQDs), and high-mobility semiconductor (SC) layers. It is envisioned that in such hybrid systems, the excitonic energy would be transferred via non-radiative energy transfer (NRET) and radiative (RET) waveguide coupling across the interface with the subsequent separation and transport of charge carriers entirely within the SC-based component. In this talk, we demonstrate the efficient excitonic sensitization of crystalline Si nanomembranes via combined effects of radiative (RET) and non-radiative (NRET) energy transfer from a proximal monolayer of colloidal semiconductor nanocrystals. Ultrathin, 25–300 nm Si films are prepared on top of insulating SiO₂ substrates and grafted with a monolayer of CdSe/ZnS nanocrystals via carboxy-alkyl chain linkers. The wet chemical preparation ensures that Si surfaces are fully passivated with a negligible number of non-radiative surface state defects and that the separation between nanocrystals and Si is tightly controlled. Combining atomic force microscopy (AFM), ellipsometry, time-resolved photoluminescence measurements and theoretical modeling, we could identify and quantify the individual contributions from RET and NRET, which all combined exceed 85% efficiency of energy transferred into the Si substrate when the nanocrystals are at about 4 nm from the interface. This demonstration supports the feasibility of an advanced thin-film hybrid solar cell concept that relies on energy transfer between strong light absorbers and adjacent high-mobility Si layers.

4:40pm EN+TF-WeA9 Synthesis of a Thin-Film Ytria-Stabilized-Zirconia (Y₂O₃-ZrO₂) Thin Films by Radical Enhanced Atomic Layer Deposition for μ -Solid Oxide Fuel Cell Applications, J. Cho, D. Membreno, B. Dunn, J.P. Chang, University of California, Los Angeles

Solid Oxide Fuel Cells (SOFCs) is one outstanding alternative energy devices, owing to its significantly higher fuel conversion efficiency than that of fossil fuel based ones while being more environmentally benign. Despite its tremendous advantages and potentials, however, the commercial applications of this technology have been restrained due to its intrinsic problems such as the use of expensive interconnectors and long start-up

time, which are inevitably tied to its high operation temperatures (650-1000°C) to maintain high ionic conductivity of electrolytes. To fully utilize the revolutionary potentials of SOFCs in commercial applications, it is imperative to lower its operation temperatures to intermediate temperatures, below 700°C without sacrificing the efficiency of the cell.

Yttria-Stabilized-Zirconia (YSZ, $(Y_2O_3)_x-(ZrO_2)_{(1-x)}$) has been implemented as the electrolyte material of choice in SOFCs because of their high structural, chemical stability with along with high ionic conductivity at the operation temperatures of the cell. While the temperature of the cell could not be lowered as it compromises its conductivity, recent pioneering studies of YSZ in nanoscales have reported significantly enhanced ionic conductivities which could not only lower the working temperature of the cell much below 700°C, but will also allow an expansion in their potential applications even to power portable electronics, resulting in strong scientific and technological interests in investigating the feasibility of developing YSZ in nanoscale for electrolyte applications in next-generation SOFCs, including μ -SOFCs for portable electronics. A thin-film YSZ has been synthesized by Radical Enhanced Atomic Layer Deposition (REALD), with thickness and composition controllability. The metal precursors, Tris(2,2,6,6-tetramethyl-3,5-heptanedionato)yttrium(III) [Y(tmhd)3] and Bis(cyclopentadienyl)dimethylzirconium [Cp₂Zr(CH₃)₂] with Oxygen radicals as oxidant, were used to deposit Y₂O₃ and ZrO₂ with the deposition rates of 0.47 Å/cycle and 0.62 Å/cycle, respectively at ~250°C. The composition of each metal cations in YSZ thin films synthesized as a solid solution of Y₂O₃-ZrO₂ was found to correlate closely to the number of ALD cycles of each constituent oxide. The crystalline structures as well as the local environment of the deposited YSZ thin films were studied by X-ray diffraction (XRD) and Extended X-ray absorption fine structure (EXAFS). The conductivities of REALD YSZ films were found to be both a function of the thickness of YSZ film and the yttrium content in the film. The presence of conductivity enhancement effect on YSZ-SrTiO₃ nanoparticles are investigated as well.

5:00pm **EN+TF-WeA10 ALD-enabled Tunneling and Transparent Conductive Oxide Layers for Novel Silicon Nanowire Solar Cells**, *M. Toivola*, Picosun, Finland, *C.L. Dezelah*, Picosun USA, LLC

In order to enable more efficient harvesting of solar energy in the future, the recently ended (Dec 2011) EU 7th FP project ROD-SOL has successfully developed a novel, high efficiency solar cell based on Si nanostructures. The photoactive layer of this solar cell is a dense “forest” of adjacent Si nanowires (SiNW) deposited on metal or glass substrates. The 3D nanostructure of the NW forests offers various benefits over planar cell geometry, namely, more efficient light absorption due to light scattering in the NW forest, i.e. the NWs work as a light-trapping, antireflective layer.

The best solar cells in the project have already reached a promising value of near 10% efficiency and good long term stability. They were prepared with semiconductor-insulator-semiconductor concept, in which a 1-2 nm layer of ALD-deposited Al₂O₃ functions as a tunneling layer for the minority charge carriers between the SiNWs and the current collecting transparent conductive oxide (TCO) layer on the front side of the cell. Due to the high aspect ratio of the SiNWs ALD is the only method with which ultra-thin but highly uniform, conformal and pinhole-free tunneling layers can be coated on them. Also ALD-deposited, few hundreds of nm thick Al-doped ZnO (AZO) layer works as the TCO in SiNW solar cells, and we have investigated and optimized the electrical and optical properties of these layers.

AZO layers were prepared from trimethyl aluminum (TMA), diethyl zinc (DEZ) and deionized water (DIW). The varied parameters in AZO layers were deposition temperature (100 - 250 °C) and the percentage of Al in the ZnO matrix (0 - 11 %). The effects of post-ALD annealing and different TMA/DEZ/DIW pulsing orders were also tested.

The best conductivity ($1-2 \times 10^{-3} \Omega m$ specific resistance) was achieved at 200 °C with a pulsing ratio of 5 % TMA and 95 % DEZ, equaling ~2 % elemental Al in ZnO. Reverse pulse order, i.e. starting the process with oxidant pulse instead of metal precursor, didn't result in significant performance improvement, neither did the annealing.

Optically, the ALD AZO films had high transparency over the visible wavelengths (no significant dependence on deposition temperature and/or Al doping-%) and refractive index 1.8 - 2, so the films work efficiently as conformal antireflective coatings on Si.

In short, ALD-deposited TCO layers offer a potential alternative to indium-doped tin oxide (ITO) and other scarce element containing TCO materials in solar cells. In the novel nanostructured photovoltaic devices ALD is typically the only method with which thin enough coatings of high quality material (i.e. dense, uniform, conformal, crack- and pinhole-free) can be deposited.

5:20pm **EN+TF-WeA11 Effect of Top Electrodes on the Photovoltaic Properties of Ferroelectric PLZT Thin Film Capacitors**, *V. Nampoori*, *S. Kotru*, The University of Alabama

Ferroelectrics are emerging as potential candidate materials for energy harvesting and storage. A recent report suggesting the possibility of above band gap voltages from ferroelectric materials has attracted the interest of research community to study these materials for the applications towards non-conventional solar cells devices. Although these ferroelectric solar cells materials do not exhibit very high conversion efficiency compared to the conventional solar devices, but the control of the PV characteristics with controlled polarization in these materials, gives it an edge over the semi-conducting counterparts. It is now, widely agreed that the PV effect in a ferroelectric material is induced by internal polarization of the material which in turn separates the photo generated electron-hole pairs. However apart from controlling the polarization of the material, there are various other factors which could contribute to the PV output, choice of electrodes, is one among them.

In this work, PV response of ferroelectric PLZT thin film capacitors was investigated. The films were prepared using chemical solution deposition process. Capacitor type solar cells were fabricated from these films using various top electrodes. The IV curves were measured for each device. The ferroelectric/metal barrier as well as the bulk depolarizing field was shown to influence IV characteristics. Use of a metal top electrode with lower work function was found to increase the open circuit voltage (V_{oc}) from 0.17 V to 0.37 V. It was seen that use of a transparent conducting electrode could increase the V_{oc} further to ~ 1.3V. This in turn resulted in enhancement of PV efficiency of the devices. Such increase is attributed from the contribution of ferroelectric/metal barrier rather than from the bulk ferroelectric. These results indicate that choosing an appropriate top electrode can result in significant increase in the efficiency of the ferroelectric photovoltaic devices.

5:40pm **EN+TF-WeA12 Synthesis of Nano-structured Zn₃P₂ as a Solar Cell Absorber**, *P.S. Vasekar*, *S.P. Adusumilli*, *D. Vanhart*, *T. Dhakal*, Binghamton University

With rise in the prices and non-abundance of the materials like indium and gallium current research trends in thin film solar cells have been moving toward development of earth-abundant solar cell materials which can be synthesized using low-cost processes. Also zinc based hetero-junction partners are getting preference over toxic cadmium based compounds such as cadmium sulfide. Zn₃P₂ is also an important semiconductor from the II-V group and is used for optoelectronic applications. Zinc phosphide exhibits favorable optoelectronic properties such as direct bandgap of 1.5 eV which corresponds to the optimum solar energy conversion range. Also zinc phosphide has a large optical absorption coefficient of $>10^4 \text{ cm}^{-1}$, hence it can be positively used as a p-type absorber. Also due to its long minority diffusion length of ~10 μm , high current collection efficiency can be yielded. Zinc and phosphorus are quite abundant in earth's crust. It makes their cost-effective development quite feasible when it comes to large scale production. We have developed a very simple process using chemical reflux technique with Tri-octyl-phosphine (TOP) as a source of phosphorus. Zn₃P₂ has been synthesized in both nanowire and bulk form on zinc foil as well as glass substrates and initial results are quite encouraging. It has been observed that depending on the exposure method with TOP, either nanowire or bulk phase forms. Zinc metal when in contact with liquid TOP, develops nanowires in the range of 50-100 nm and the formation of nanowires exhibits a solution-liquid-solid (SLS) mechanism at the reaction temperature around 350 °C. To the best of our knowledge, zinc phosphide nanowire formation at this low temperature has been observed for the first time. Analysis has been carried out using SEM, XRD, TEM, XPS and PL.

Exhibitor Technology Spotlight

Room: West Hall - Session EW-WeA

Exhibitor Technology Spotlight

Moderator: D. Surman, Kratos Analytical Inc.

3:20pm **EW-WeA5 Heidelberg Instruments microPG501, A Direct Write Lithography Tool**, *N. Wijnaendts van Resandt*, Heidelberg Instruments

Heidelberg Instruments Presents the newest addition to its lineup of Direct Write Lithography tools. These tools are used for the production of photomasks as well as for direct write on substrates for MEMS, microfluidics, MicroTAS, micro optics and a wide variety of other applications where a lithographic process is required.

3:40pm **EW-WeA6 Dry Etching Enabling Surface Texturing for Thin Substrate Solar Cells**, *R. Mohondro*, Plasma-Therm LLC

Solar energy implementation continues to advance towards grid parity through efforts to reduce costs and increase efficiency. Higher cell efficiency can result from many approaches. This work looks at the method of surface texturing to enhance light capture and reduce losses due to unwanted reflection. Although surface texturing of crystalline silicon has traditionally been achieved with wet (alkaline) chemistry, it faces limitations with thin wafers. Significant work is being done to reduce silicon material costs by reducing wafer thickness. Recent work has demonstrated wafers 10-15 μm thick with 10x estimates of lower initial material costs. However, the desired efficiency improvements resulting from texturing are not possible with wet processing as the texturing thickness approaches or exceeds that of the wafer thickness. In this work we present enabling dry etching technology that offers efficiency enhancing texturing compatible with very thin wafers. Limiting the material removed to approximately 1 μm eliminates surface damage while maintaining the structural integrity of the thin wafer and generating the required anti-reflection morphology. Dry etching process data showing controlled adjustment of the textured surface and the impact on reflectivity will be discussed along with the challenges of handling these extremely thin substrates.

Graphene and Related Materials Focus Topic
Room: 13 - Session GR+AS+EM+NS+SS-WeA

Dopants and Defects in Graphene; Graphene Interfaces with Other Materials

Moderator: D. Gunlycke, Naval Research Laboratory

2:00pm **GR+AS+EM+NS+SS-WeA1 Increasing Interface Bonding and Tuning Doping Behavior at Metal-Graphene-Metal Sandwich Contact**, *C. Gong, R.M. Wallace, K.J. Cho, Y.J. Chabal*, The University of Texas at Dallas

Two types of interfaces can be formed between metals and graphene depending on the strength of the metal-graphene interaction: weak (metal physisorption) and strong (metal chemisorption) interfaces. "Physisorption" interfaces (e.g., with Al, Ag, Cu, Ir, Pt and Au) are characterized by a larger metal-carbon distance ($>3 \text{ \AA}$) with some charge transfer between metal and graphene (i.e. doping of graphene) that maintains its overall π -band dispersion. "Chemisorption" interfaces (e.g. with Ni, Co, Pd, and Ti) are characterized by a smaller metal-carbon distance ($<2.5 \text{ \AA}$) and strong orbital hybridization between metal- d and carbon- p_z orbitals, resulting in the destruction of the graphene's π -band dispersion around the Dirac point. Till now, only a small fraction of all available metals has been used as electrode materials for carbon-based devices due to metal-graphene interface debonding problems. The issue therefore is to keep graphene's intrinsic π bandstructure by using weakly interacting metals while enhancing the interface stability.

We report an enhancement of the bonding energy of weakly interacting metals by using a metal-graphene-metal sandwich geometry, without sacrificing the intrinsic π -electron dispersions of graphene that is usually undermined by strong metal-graphene interface hybridization. This sandwich structure further makes it possible to effectively tune the doping of graphene with an appropriate selection of metals. Density functional theory calculations reveal that the strengthening of the interface interaction is ascribed to an enhancement of interface dipole-dipole interactions. Raman scattering studies of metal-graphene-copper sandwiches are used to validate the theoretically predicted tuning of graphene doping through sandwich structures.

2:20pm **GR+AS+EM+NS+SS-WeA2 Defects in Two-Dimensional Materials and their Heterostructures**, *L. Adamska, I.I. Oleynik*, University of South Florida

Recent developments in graphene electronics have stimulated an interest in other two dimensional materials such as hexagonal boron nitride (BN) and molybdenum disulfide (MoS_2). In contrast to graphene, BN and MoS_2 possess appreciable band gap and may form good interfaces with graphene, which opens up exciting opportunities for development of novel nanoelectronic devices. For practical applications, it is important to understand the effect of defects, which appear during growth and processing, on resulting electronic properties. The defects in graphene, BN, MoS_2 and their heterostructures have been investigated by first-principles density functional theory. Their effect on electronic properties including density of states and simulated STM images will be discussed.

4:00pm **GR+AS+EM+NS+SS-WeA7 Metal Oxide Growth and Characterization on CVD Graphene**, *A. Matsubayashi*, College of Nanoscale Science and Engineering, University at Albany

Thin metal oxide layers deposited on graphene can be utilized as dielectric barriers between metals and graphene to help isolate a metal contact from the graphene channel. This is important for graphene based spintronic devices as dielectric layers between the ferromagnetic electrode and graphene have been shown to increase the spin relaxation time measured utilizing non-local detection and spin precession measurements^[1]. However, simply depositing metal oxide layers such as aluminum oxide on graphene results in non-uniform film lowering the quality of the interface barrier^[2]. In addition it is important to understand the stoichiometry of the resulting film. We will present a systematic study of aluminum oxide layers grown on CVD (chemical vapor deposition) graphene under ultra-high vacuum conditions with and without titanium seed layers. The aluminum oxide layers with the titanium seed layers showed reduced surface roughness. The chemical and structural composition determined by XPS (X-ray photoelectron spectroscopy) will be also presented that shows full oxidation of the aluminum and partial oxidation of the titanium.

References:

- (1) E. I. Rashba, Phys. Rev. B, **62**, 16267 (2000)
- (2) W. Han *et al*, Phys. Rev. Lett., **105**, 167202 (2010)

4:20pm **GR+AS+EM+NS+SS-WeA8 Bi-layer Graphene Growth on Ni(111): The Role of Monolayer Graphene Rotation**, *A. Dahal, A. Rafik*, University of South Florida, *P.W. Sutter*, Brookhaven National Laboratory, *M. Batzill*, University of South Florida

Bi-layer graphene synthesis by chemical vapor deposition is of importance for field effect devices because the band gap can be tuned in bi-layer graphene by an applied electric field. Here, we demonstrate that bi-layer graphene can be synthesized above 650 $^{\circ}\text{C}$ by chemical vapor deposition on thin Ni(111) films grown on YSZ(111) substrates in ultra high vacuum (UHV). We characterize the bi-layer graphene growth by low energy electron microscopy (LEEM), Auger electron spectroscopy (AES) and low energy electron diffraction (LEED). Below 600 $^{\circ}\text{C}$ graphene grows in registry with the Ni(111) lattice and no second layer graphene is formed upon cooling. At 650 $^{\circ}\text{C}$ rotationally misaligned graphene domains are formed on Ni(111) and we observe second layer graphene to grow by carbon-segregation under those rotated monolayer graphene domains. The difference in second layer graphene nucleation and growth is explained by the graphene-Ni interaction, which is much stronger for graphene in registry with the substrate than for rotated graphene. The segregated second layer graphene sheet is in registry with the Ni(111) substrate and this suppresses further carbon-segregation, effectively self limiting graphene formation to two layers.

4:40pm **GR+AS+EM+NS+SS-WeA9 Energetic and Kinetic Factors of Graphene Nucleation on Cu**, *N. Safran, M.S. Arnold*, University of Wisconsin-Madison

Chemical Vapor Deposition (CVD) of graphene on Cu substrates uniquely allows for growth of uniform monolayer graphene and is a promising route for its scalable production for many industrial applications due to low cost. The growth is a purely surface driven process, due to carbon's low solubility in the Cu substrate, and relies on the Cu surface catalytically decomposing a carbon precursor (methane). As the growth of graphene proceeds across the surface, the reactivity of the Cu is passivated by the graphene, making the growth self-limiting to monolayer coverage. Research interest on the control of nucleation is intensifying, as the polycrystalline character of the graphene films can limit mobility, thermal conduction, and mechanical strength via grain boundaries.

In this paper, we study the nucleation dependencies of graphene at ambient pressure CVD in the context of surface nucleation theory. At low methane partial pressures, the concentration of carbon on the surface on the copper is low and carbon clusters cannot grow to a critical size for nucleation. As the partial pressure is increased, the methane partial pressure reaches a critical value and nucleation occurs. Tracking the critical pressure as a function of temperature from 880 to 1075 $^{\circ}\text{C}$, we have determined the formation energy of the critical graphene nucleus to be $\sim 1.5 \text{ eV/carbon atom}$, via the relation $c_{\text{nuc}} \sim \exp(-E_{\text{form}}/k_{\text{B}}T)$. Additionally, we have found that the nucleation density of the graphene varies by 5 orders of magnitude over this temperature range at the critical methane concentration. The results are described under the desorption controlled regime of surface cluster nucleation.

Growths near the critical methane concentration yield hexagonal growing graphene domains characteristic of attachment limited kinetics, while at higher rates yield other growth shapes. Characterization by Raman Spectroscopy has been used to identify defects in the graphene layers. We find that the Raman defect band (D-Band) scales with the root of the

nucleation density, indicating the majority of defects are located at the domain boundaries and the D-band intensity scales with the distance between them. Electrical mobility measurements show nearly constant values in samples across the range of temperatures indicating other limiting factors besides internal defects. Growths at 900°C yield $\mu > 1000 \text{ cm}^2/\text{Vs}$, ON/OFF ratio ~ 10 , and Raman D/G ratio < 1 , demonstrating high quality of growth even at relatively low temperatures.

5:00pm **GR+AS+EM+NS+SS-WeA10 Magnetic Spin Reorientation Transition in Graphene Covered Cobalt on Iridium(111)**, *A.T. N'Diaye*

Lawrence Berkeley National Laboratory, *J. Coraux, N. Rougemaille, C. Vo-Van, O. Fruchart*, Institut NÉEL, CNRS & Université Joseph Fourier, France, *A.K. Schmid*, Lawrence Berkeley National Laboratory

One of graphene's promises is to be material for spintronic applications. While the influence of a magnet on graphene is under intense investigation by many groups little attention is given to the influence of graphene on a magnet.

With spin polarized low energy electron microscopy (SPLEEM) we studied thickness dependent spin reorientation transition on this system and compare with Co/Ir(111) without graphene. Monitoring the spin orientation in three dimensions while increasing the film thickness by one ML at a time, we find that the presence of graphene on the film at least doubles the thickness at which the spin reorientation from out-of-plane to in-plane occurs from 6ML Co to transition to 12ML-13ML at 300°C and to between 14ML and 20ML at room temperature.

We attribute the significant contribution of the graphene/Cobalt interface to the magnetic anisotropy energy to a strong hybridization of graphene with Cobalt in directional bonds.

This work was supported by the U.S. Department of Energy under Contract No. DE-AC02-05CH11231, by the French ANR contract ANR-2010-BLAN-1019-NMGEM and by the Alexander von Humboldt Foundation.

5:20pm **GR+AS+EM+NS+SS-WeA11 Nucleation and Growth of Rh and Au Clusters on Graphene Moiré/Ru(0001)**, *B. Habenicht*, Oak Ridge National Laboratory, *D. Teng*, Georgia Institute of Technology, *L. Semidey-Flecha*, Oak Ridge National Laboratory, *D. Sholl*, Georgia Institute of Technology, *Y. Xu*, Oak Ridge National Laboratory

Nanometer and sub-nanometer sized metal clusters may possess electronic and catalytic properties that differ greatly from those of the corresponding bulk metals. For potential applications, dense arrays of uniform metal clusters are desirable. However, the synthesis of such cluster materials remains a formidable challenge. Moiré superstructures that develop in graphene supported on certain metals have been shown to be viable templates for driving the formation of uniform metal clusters.[1] On graphene moiré (GM) on Ru(0001), dispersed clusters are obtained for Rh whereas Au coalesces into very large 2D islands.[2,3] We carry out a computational study to understand the disparate morphologies of Rh and Au clusters on GM/Ru(0001) via a multi-scale approach. DFT calculations are performed to study the adsorption and diffusion of the adatom and ad-clusters of Rh and Au on GM/Ru(0001) and the bonding mechanism between the metals, graphene, and Ru substrate. The potential energy landscape is then used to perform kinetic Monte Carlo simulations for the diffusion, nucleation, and growth of Rh and Au clusters. This approach allows us to predict the spatial and size distribution of the metal clusters and may be generally applicable to identifying the conditions necessary for obtaining desired cluster morphologies on GM.

(1) N'Diaye, A. T.; Bleikamp, S.; Feibelman, P. J.; Michely, T. *Phys. Rev. Lett.* **2006**, 97, 215501.

(2) Zhou, Z.; Gao, F.; Goodman, D. W. *Surf. Sci.* **2010**, 604, L31.

(3) Xu, Y.; Semidey-Flecha, L.; Liu, L.; Zhou, Z.; Goodman, D.W. *Faraday Discuss.*, **2011**, 152, 267.

5:40pm **GR+AS+EM+NS+SS-WeA12 Graphitic and Pyridinic N Species on N-doped HOPG Studied by STM, STS, PES and DFT**, *M. Sakurai*, *T. Shikano*, *D. Ushigome*, *T. Suzuki*, University of Tsukuba, Japan, *Y. Harada*, *M. Oshima*, University of Tokyo, Japan, *S. Casolo*, University of Milan, Italy, *M.I. Trioni*, ISTM, Italy, *G.F. Tantardini*, University of Milan, Italy, *T. Kondo*, *J. Nakamura*, University of Tsukuba, Japan

Nitrogen doped graphene and carbon nanotube have been reported to show superior catalytic activity or superior support effect in the fuel cell. However, effects of the dopant nitrogen on the modification of the electronic structure of such graphite-related materials have not been clarified because a wide variety of defects with different types of C-N bonding configurations can coexist in nitrogen doped graphite.

Here, we report comprehensive atomic-resolution characterization of the defects in a nitrogen-doped graphite surface by scanning tunneling microscopy (STM), scanning tunneling spectroscopy (STS), Photoemission spectroscopy (PES) and first-principles calculations based on the density functional theory (DFT). Nitrogen-doped graphite was produced by nitrogen ion bombardment of the HOPG (highly oriented pyrolytic graphite) followed by thermal annealing at about 900 K.

Two types of nitrogen species were identified at the atomic resolution. One is pyridinic N (N having two C nearest neighbors) with single-atom vacancy. The other is graphitic N (N having three C nearest neighbors). In the case of pyridinic N with single vacancy, the local electronic states of the non-bonding pz orbital of carbon are found to appear at occupied region near the Fermi level at the carbon atoms around pyridinic N. On the other hand, the local electronic states of the non-bonding pz orbital of carbon are found to appear at unoccupied region near the Fermi level at the carbon atoms around graphitic N.

These results indicate that in both cases more than 300 carbon atoms are found to be modified by the dopant N to show the non-bonding pz orbitals. Moreover, these results suggest that the graphitic-N and pyridinic-N as well as their surrounding carbon atoms may act as "acid" and "base", because their non-bonding pz orbitals appear at empty and occupied region, respectively.

Helium Ion Microscopy Focus Topic
Room: 19 - Session HI+AS+NS-WeA

Basics of Helium Ion Microscopy

Moderator: A. Götzhäuser, University of Bielefeld, Germany

2:00pm **HI+AS+NS-WeA1 Basics of Imaging with Ions**, *D. Joy*, University of Tennessee **INVITED**

Imaging with a helium ion microscope (HIM) offers numerous advantages, both fundamental and practical, as compared to a conventional scanning electron microscope (SEM). At the same time, however, many aspects of ion microscopy seem very different to those found in the SEM. In this presentation therefore we will examine ;

Why ions are a better choice for imaging than electrons and which ion (or ions) might be the best

In which areas of performance and operation the ion beam image is 'better'

The optimum beam energy for ion imaging for different materials; how typical imaging conditions compare to those for the SEM; and why they are different

The types of signals that are available for imaging in the ion microscope and how they compare with their electron beam counterparts

The problems of specimen charging and beam damage with the ion beams

The options available for microanalysis with the HIM

2:40pm **HI+AS+NS-WeA3 Surface Analysis using Channeling Contrast in NUHV Helium Ion Microscopy**, *B. Poelsema*, University of Twente, Netherlands **INVITED**

Helium Ion Microscopy, HIM, is a novel high-performance technique to image surfaces and with its high resolution, great surface sensitivity, enhanced material contrast, ability to investigate insulating material and large depth of field, it provides a viable alternative to classical scanning electron microscopy. A number of applications require improved vacuum conditions to achieve ultimate performance. The sharply focused He ion beam is, compared to an electron beam in SEM set-ups, very efficient in decomposing, e.g., hydrocarbons present in the chamber and thus on the sample surface, which may obscure a clear view of the sample. Where this phenomenon is beneficial for high resolution structuring, it may well negate the benefits of small spot size and reduce the acquisition time available for spectroscopy in material analysis. To substantially reduce this problem a Near UHV version of the HIM has been developed in close collaboration between the manufacturer, Carl Zeiss NTS, LLC and our group at the University of Twente [1].

We will report on a number of recent observations with special attention for a new contrast mechanism, i.e. dechanneling of ions that extends the high surface sensitivity – usually achieved in secondary electron images – to backscattered ions. We demonstrate [2-4] how monolayer "thick" organic

and inorganic films, as well as self assembled monolayers can be visualized, even when adsorbed on heavier substrates, by changes in the backscatter yield. Normally thin layers of a light element on a heavy substrate are “invisible” in backscattered ion yields. The results can be explained semi-quantitatively in terms of changes of the channelling probability. These results highlight the relevance of proper vacuum conditions for achieving monolayer sensitivity.

[1] R. van Gastel, L. Barriss, C. Sanford, G. Hlawacek, L. Scipioni, A.P. Merkle, D. Voci, C. Fenner, H.J.W. Zandvliet and B. Poelsema: *Microscopy and Microanalysis* **17(S2)**, 928-929 (2011)

[2] A. George, M. Knez, G. Hlawacek, D. Hagedoorn, H.H.J. Verputten, R. van Gastel and J.E. ten Elshof: *Langmuir* **28(5)**, 3045-3052 (2012)

[3] G. Hlawacek, V. Veligura, S. Lorbek, T.F. Mocking, A. George, R. van Gastel, H.J.W. Zandvliet, B. Poelsema: submitted

[4] V. Veligura, G. Hlawacek, R. van Gastel, H.J.W. Zandvliet, B. Poelsema: submitted

Acknowledgments: Gregor Hlawacek, Vasilisa Veligura, Raoul van Gastel, Harold J.W. Zandvliet.

4:00pm **HI+AS+NS-WeA7 Evaluation of W(111) Gas Field Ion Sources Based on Single Atom Tips, R. Urban**, University of Alberta and The National Institute for Nanotechnology, Canada, *J.L. Pitters*, National Institute for Nanotechnology, NRC Canada, *R.A. Wolkow*, University of Alberta and The National Institute for Nanotechnology, Canada

Atomically defined tips gained significant attention over the past decade because they serve as high brightness electron and ion sources. The success of the Scanning Helium Ion Microscope is dependent on the development of an appropriate Gas Field Ion Source (GFIS) to generate the helium ion beam. Single atom tips (SATs) represent a unique subgroup of atomically defined tips where emission only occurs from a single atom at the tip apex. Small virtual source size makes these tips attractive candidates for advanced scanning imaging applications such as SEM, TEM, and scanning ion microscopy (SIM) as well as for non-staining ion beam writing applications.

In this study SATs were fabricated from single crystal W(111) wire using a gas and field assisted etching process. By carefully controlling etching parameters SATs with extraction voltages between 5 and 17 kV were formed for various tips. During tip formation, we also used neon as an imaging gas to evaluate a W(111) tip shape during nitrogen-assisted etching. The neon image allows for the observation of atomic structure not available while imaging with helium and helps to elucidate the atomic structure of the tip during and after the etching to a single atom. The field ion microscopy (FIM) patterns (intensity maps) from SAT were fitted with 2D Gaussian curve to evaluate ion beam divergence and amplitude. The divergence of helium beam with respect to helium pressure and applied voltage will be discussed for various SATs.

Angular current density of various SATs was evaluated from their FIM patterns recorded by a microchannel plate and ion current measurements using a Faraday cup. The volume under the 2D Gaussian surface was found to be directly proportional to total ion current carried by an ion beam. The ion current was found to be linearly proportional to He pressure. However, comparing various tips it was found that the ion current increased faster than the extraction voltage. This suggests improved He capture by a broader tip base. The effect of the shape of the base of the tip was also evaluated and it was found that the beam opening angle varied with the size of the tip base leading to a forward focussing effect. The relative angular current densities from SATs supported on different tip curvatures were also evaluated and found to increase at a faster rate than current, also indicating that a forward focusing effect was in effect. This indicates that SATs on large bases would prove optimal for ion current generation in a scanning ion microscope.

4:20pm **HI+AS+NS-WeA8 Single-atom Tip as an Emitter of Gas Field Ion Sources, I.-S. Hwang, H.-S. Kuo**, Academia Sinica, Taiwan, Republic of China, *T.-Y. Fu*, National Taiwan Normal University, Taiwan, Republic of China, *J.-L. Hou, C.-Y. Lin, Y.-H. Lu, W.-T. Chang, T.T. Tsong*, Academia Sinica, Taiwan, Republic of China

Thermally and chemically stable single-atom tips (SAT) or nanotips are highly desirable for emission of high-brightness gas field ion beams. In 2001, Fu et al. demonstrated a Pd-covered W(111) SAT through vacuum deposition of an ultra-thin Pd film on a clean W tip surface followed by thermal annealing [1]. Later, Kuo et al. further simplified the preparation process by replacing the tip cleaning and the vacuum deposition with electrochemical processes and successfully prepared several different types of noble metal-covered W(111) SATs [2]. This type of SATs is thermally stable and chemically inert, and thus can be regenerated through a gentle annealing if the apex is contaminated.

We have successfully generated hydrogen, helium, argon, and oxygen ion beams using a Ir/W SAT and characterized these ion sources [3]. The first

two lightest ions provide the lowest sputtering rates, which is beneficial for scanning ion microscopy. The argon ion has a large mass and can provide a high sputtering rate, suitable for ion milling. Due to the high secondary ion yields, an oxygen ion beam may be applied to secondary ion mass spectrometry. The ion beam profiles indicate that the half opening angle is $\sim 0.5^\circ$. This single spot indicates that emission occurs only from the topmost atom. This small source size and the small opening angle are particularly favorable for achieving high angular intensity, high brightness, and low spherical aberration, which are important characteristics for a focused ion beam system. The ion current of these gas ion beams are very stable and the tip does not show any degradation under fields above 5 V/Å after a total operation time of 80 hours. Since the SAT can be regenerated for more than 50 times, therefore its lifetime is long enough for most practical applications.

In addition, we have also prepared a pure iridium SAT based on oxygen-induced crystal faceting of the Ir(210) [4]. We have shown that the Ir-SAT can be a good field ion emitter, capable of emitting a variety of gas ion beams, including He⁺, H₂⁺, N₂⁺, and O₂⁺, with high brightness and stability. In particular, nitrogen is a very corrosive gas for metal tips under strong positive electric fields. If we can achieve a stable emission of nitrogen ion, it also means many other gas field ion beams may also be emitted from this Ir-SAT. This may greatly broaden the application of focused ion beam technology.

[1] T.-Y. Fu et al., *Phys. Rev.B* **64** (2001), 113401.

[2] H.-S. Kuo et al., *Nano Lett.* **4** (2004), 2379.

[3] H.-S. Kuo et al., *Appl. Phys. Lett.* **92** (2008), 063106.

[4] H.-S. Kuo et al., *Nanotechnology* **20** (2009), 335701.

4:40pm **HI+AS+NS-WeA9 Helium Ions for Imaging and Nanofabrication on the nm Scale, E. Van Veldhoven, H.H.P.Th. Bekman, F.T. Molkenboer, N.B. Koster, D.J. Maas**, TNO Technical Sciences, The Netherlands

The Helium ion microscope (HIM, Zeiss Orion Plus™) has unique features. This microscope unravels a new application area for imaging sensitive and charging surfaces with (sub) nm resolution [1]. The beam-sample interaction generates secondary electrons with low energy and a low quantity of backscattering ions. These properties are very interesting for using the microscope not just for imaging only, but for nanofabrication too [2]. To explore all the capabilities for nanofabrication, the HIM is equipped with a pattern generator (Raith Elphy Multibeam™) and a gas injection system (Omniprobe Omnigis™) to explore direct write, lithography and gas induced applications.

In this contribution we would like to focus on imaging charging materials and our latest results for using the HIM for developing new applications for mainly the Semiconductor Industry. We consider a few HIM-based methods for TEM sample preparation. It is possible to use the HIM for making a thin wedge without significant artifacts like bubble formation and amorphization. With the gas injection system we develop new recipes for very local deposition and etching. These recipes are used for feasibility studies for mask repair and circuit editing. The helium ion microscope offers a novel way for nanofabrication and imaging on the nm scale.

5:00pm **HI+AS+NS-WeA10 Towards Secondary Ion Mass Spectrometry on the Helium Ion Microscope, T. Wirtz, N. Vanhove, L. Pillatsch, D. Dowsett**, Centre de Recherche Public – Gabriel Lippmann, Luxembourg, *S. Sijbrandij, J. Notte*, Carl Zeiss

The ORION Helium Ion Microscope (HIM) has become a well-established tool for high-resolution microscopy [1]. The high brightness ALIS gas field ion source can operate with helium and, after special prototype modifications, with neon [2]. However, the detection of backscattered atoms can provide only limited specimen composition information. By contrast, Secondary Ion Mass Spectrometry (SIMS) is an extremely powerful technique for analyzing surfaces due to its excellent sensitivity, high dynamic range, very high mass resolution and ability to differentiate between isotopes. In order to get chemical information with a higher sensitivity and a high lateral resolution, we have investigated the feasibility of performing SIMS on the HIM.

Therefore, the secondary ion formation process under He⁺ and Ne⁺ bombardment has to be investigated and optimized. To investigate secondary ion formation an experimental study was performed; to investigate sputtering effects on resolution and practical implementation aspects a simulation approach was taken.

First, secondary ion yields for different elements sputtered from different materials exposed to helium and neon ion beams were experimentally determined on a test set-up. The basic yields could be increased by several orders of magnitude by using reactive gas flooding (i.e. O₂ and Cs⁰ [3,4]). Afterwards, detection limits have been calculated taking into account the experimentally obtained useful yields. Depending on the dwell time, ppm

sensitivity can be obtained for Ne⁺ bombardment on silicon with oxygen flooding. Second, a detailed study of the sputtering phenomena using TRIM simulations was carried out in order to determine the effect of the collision cascade on the lateral resolution. The diameter (FW₅₀) of the area from which sputtered atoms originate has been determined for 10 keV He⁺ and Ne⁺ bombardment on different materials. While the obtained results are very encouraging, the practical instrumentation aspects have to be investigated as well in order to obtain a high secondary ion transmission and maintain the excellent primary beam characteristics. Therefore, the practical limitations imposed by adding an extraction system to the HIM have been studied in detail with respect to the extraction geometry.

In general, the combination of high-resolution microscopy and high-sensitivity chemical mapping on a single instrument will lead to a new level of correlative microscopy.

[1] L. Scipioni *et al.*, *J. Vac. Sci. Technol. B* **27**, 3250 (2009)

[2] F. Rahman *et al.*, *Scanning* **33**, 1 (2011)

[3] K. Franzreb *et al.*, *Surf. Sci.* **573**, 291 (2004)

[4] P. Philipp *et al.*, *Int. J. Mass Spectrom.* **253**, 71 (2006)

Late Breaking Session

Room: 14 - Session LB+EM+GR+MN+TR-WeA

Select Topics in Surface and Interface Science

Moderator: C.R. Eddy, Jr., U.S. Naval Research Laboratory, J.M. Fitz-Gerald, University of Virginia

2:00pm **LB+EM+GR+MN+TR-WeA1 Degradation Kinetics of Hard Gold Tribofilms**, *N. Argibay, M.T. Dugger, M.T. Brumbach, S.V. Prasad*, Sandia National Laboratories

Hard gold coatings are low alloy (> 98% Au) films exhibiting relatively low friction, electrical contact resistance (ECR) and chemical reactivity, making them uniquely suited for use in dynamic electrical connections. Hardness is primarily a result of grain refinement achieved through alloying. At relatively low temperature (approx < 0.5T_m) the diffusion of codeposited and underlayer species toward the free surface, dominated by grain boundary and pipe diffusion, has been identified as a principal degradation pathway. The consequent formation of metal oxides deteriorates ECR and often contributes to increased wear and friction. A clear antagonistic relationship exists between the hardening mechanism that improves tribological performance and the diffusion phenomena that reduce useful lifespan. This talk focuses on the role of diffusion and film morphology on the aging and degradation of the tribological and electrical characteristics of hard gold films.

2:20pm **LB+EM+GR+MN+TR-WeA2 Effect of Nitrogen Concentration on the Surface Properties of Plasma Nitrided Tool Steels**, *P. Abraha, J. Miyamoto*, Meijo University, Japan

The nitriding of tool steel was performed in electron beam excited plasma using neutral nitrogen species and nitrogen ions. The plasma apparatus is composed of three regions: the discharge region, the acceleration region and the processing region. This set up has the advantage of controlling the energy and number of electrons involved in producing the plasma independently.

In this study, the control of the nitrogen concentration on the formation of the hard but brittle compound layer and the effect on the tribology of the tool steel surface were investigated. Electron probe micro-analyzer (EPMA) results revealed that nitrogen concentration of samples nitrided by neutral nitrogen species had deep diffusion layer before reaching the threshold value of 6% nitrogen concentration that is necessary for the formation of the compound layer. Whereas in the samples nitrided by nitrogen ions, compound layer was confirmed right from the onset of the nitriding process.

The results of our experiments show that in nitriding the tool steel for 6h, below the threshold value, a mirror finish surface (Ra=14nm) with a deep diffusion layer of (up to 80 micrometers) and a surface hardness of more than two times (1300 Hv) that of the untreated sample (600 Hv) were produced. Our results demonstrate that neutral species based nitriding is effective for high performance and high precision mechanical components that require high hardness and wear resistance without altering the as finished dimensional accuracy, surface roughness and appearance.

2:40pm **LB+EM+GR+MN+TR-WeA3 High Strength Carbon Fiber Composite Wafers for Microfabrication**, *L. Pei, K. Zufelt, R. VanFleet, R.C. Davis, J. Lund, K. Jones, B.D. Jensen*, Brigham Young University, *J. Abbott, M. Harker, M. Zappe, S. Liddiard*, Moxtek

Carbon fiber composites are very high strength materials that could be enabling materials for micro and mesoscale applications. These materials have comparable strength to silicon but are much less brittle and can achieve four times higher strain. Several challenges must be overcome before carbon fiber composite devices can be fabricated on this scale. One challenge is the fabrication of ultra-thin wafers with low void density and low surface roughness. Another challenge is the ability to reliably machine the material into desired patterns. Here we present a method for curing carbon fiber wafers (~100 μm thick) with low surface roughness, low void density, a modulus of 50 GPa, and a yield strength of ~3.6 GPa. These wafers are suitable for laser machining into high fidelity micro and mesoscale structures. We will present laser micromachined devices made from these wafers including a series of high strength support structures for ultrathin membranes and a high-dynamic-range accelerometer.

4:00pm **LB+EM+GR+MN+TR-WeA7 Selective Graphitization using Multi-Ion Beam Lithography**, *J. Fridmann*, Raith USA Inc., *S. Tongay*, University of California, Berkeley, *M. Lemaire, A.F. Hebard, B. Gila*, University of Florida, *A. Nadzeyka*, Raith GmbH, Germany, *F. Ren, X. Wang*, University of Florida, *D.K. Venkatachalam, R.G. Elliman*, Australian National University, Australia, *B.R. Appleton*, University of Florida

Promising techniques for growing graphene on SiC single crystals for electronic device fabrication include heating in UHV above the graphitization temperature (T_G)¹; or processing them in vacuum using pulsed excimer laser².

We report recent findings on the graphitization of SiC using a patterned Ga implantation, in which the implanted regions exhibit reduced T_G and enhanced graphitization above T_G. Here we report an approach that combines ion implantation, thermal or pulsed laser annealing (PLA), and multi-ion beam lithography (MIBL) to both pattern and synthesize graphene nanostructures on SiC single crystals at low temperatures. This approach utilizes a MIBL system developed at the University of Florida in collaboration with Raith for implantation/nanofabrication, in combination with thermal annealing in vacuum or PLA with a 25 ns pulsed ArF laser in air. To investigate the mechanisms and the effects of the implanted species, ion damage, and annealing, samples were also subjected to broad-area ion-implantations using facilities at the Australian National University.

It has recently been shown that implantation of Si, Ge, Au, or Cu followed by thermal annealing in vacuum below the T_G of SiC can selectively grow graphene only where the ions are implanted, and that graphene nanoribbons a few nanometers to microns wide can be formed using MIBL³. Additionally, we will show that graphene can be formed on implanted and/or unimplanted SiC by ArF PLA in air, at fluences from 0.4-1.2 J/cm². AES, SEM, X-sectional TEM, micro-Raman analyses and heat flow simulations are presented to verify graphene growth and explain the effects and mechanisms involved.

1. C. Berger, Z. Song, T. Li, X. Li, A. Y. Ogbazghi, R. Feng, Z. Dai, A. N. Marchenkov, E. H. Conrad, P. N. First, and W. A. de Heer, *J. Phys. Chem.* **108**, 19912 (2004)

2. Sangwon Lee, Michael F. Toney, Wonhee Ko, Jason C. Randel, Hee Joon Jung, Ko Munakata, Jesse Lu, Theodore H. Geballe, Malcolm R. Beasley, Robert Sinclair, Hari C. Manoharan, and Alberto Salleo; *ACS Nano* Vol.4, No. 12, 7524-7530 (2010).

3. S. Tongay, M. Lemaire, J. Fridmann, A. F. Hebard, B. P. Gila, and B. R. Appleton, *Appl. Phys. Lett.* **100**, 073501 (2012).

4:20pm **LB+EM+GR+MN+TR-WeA8 Unrippling and Imaging of Extra-Large Free-Standing Graphene with Atomic Precision**, *W.W. Pai, R. Breitweiser, Y.C. Hu, Y.C. Chao*, National Taiwan University, Taiwan, Republic of China, *Y.R. Tzeng*, Institute of Nuclear Energy Research of Taiwan, Republic of China, *L.J. Li*, Academia Sinica, Taiwan, Republic of China, *K.C. Lin*, Catholic Fu Jen University, Taiwan, Republic of China

Nanoscale ripple is believed to be a common feature most manifested in free-standing graphene and is expected to play an important role in altering the coupling of graphene's electronic and geometric structures. Direct characterization of free-standing graphene ripple is challenging from atom-resolved transmission electron microscopy (TEM) due to its limited depth resolution. Recent scanning tunneling microscopy (STM) of free-standing graphene uses small suspended area (1 or 5 microns) samples and can introduce uncontrolled tension that alters the intrinsic graphene structure. Here we report an STM study of suspended extra-large (~4000 micron²) Cu CVD graphene that was prepared with a resist-free transfer and characterize its electromechanical response in details. In our study, a series of controlled "Z-V" spectroscopy were carefully conducted. In Z-V spectroscopy, the tip

displacement vs. sample bias in close-loop condition is recorded. This gives hints on the nature of interaction forces and the mechanical response of graphene. In contrast to a solid surface, the graphene membrane is very compliant and Z-V curves are characterized by a fast-rise regime and a plateau regime that follows. Graphene deformation up to 100 nm with simply a small ~ 1 V bias ramp was observed. We discovered that our graphene is in best analogy with a curved rubber band that maintains quasi-static in shape until it is either pulled or pushed to tensile stress regimes. The graphene can be manipulated by the STM tip through electrostatic and van der Waals forces, with the latter being significant when it is repulsive. In its transit to tensile-stressed state, the graphene exhibits a series of sudden speed jump; we interpret these events as unripping of graphene ripples and render support with molecular dynamics (MD) simulation. Atom-resolved graphene images provide direct evidence of nanoscale structure ripples in its intrinsic state and the smoothing out of such ripples in the tensile regimes. Surprisingly, on rippled monolayer graphene, coexistence of triangular and hexagonal graphene lattices without tip condition change were observed. Our study provides a foundation to understand and control the electromechanical response of graphene (or other flexural atomic crystals) in its pristine two-dimensional form when subjected to a local proximal probe, therefore paves way to further investigate its structure-property correlation with atomic precision.

4:40pm **LB+EM+GR+MN+TR-WeA9 Ultrafast Charge Transfer at Monolayer Graphene Surfaces with Varied Substrate Coupling.** S. Lizzit, ELETTRA Sincrotrone Trieste, Italy, R. Larciprete, CNR, Institute of Complex Systems, Italy, P. Lacovig, ELETTRA Sincrotrone Trieste, Italy, K. Kostov, Bulgarian Academy of Sciences, Bulgaria, D. Menzel, Technische Universität München and Fritz Haber Institute, Germany

The importance and scientific appeal of graphene monolayers (Gr) are out of question, and investigations of its electronic properties abound. Most of these center on the most spectacular region, that around the Dirac cone, which is also the most relevant region for possible devices. But regions outside of this region are also important, since their correct representation requires basic understanding, and since they may relate to applications in photonics, photochemistry, and contact formation. Also, static investigations are more frequent than those of dynamics.

We present here the first investigation of electron dynamics at energies above the Fermi (and Dirac) energy but below the vacuum level [1]. To this purpose we used the core hole clock (CHC) method with adsorbed argon and measured the transfer rate of a localized electron (the 4s electron on core-excited Ar) to the surface of Gr monolayers with variable substrate coupling: strong but graded coupling for Gr on Ru(0001) ("valleys" and "hills"), and decoupled Gr ML on SiO₂. We obtained the latter system by using the recently developed transfer-free approach [2] based on the synthesis of SiO₂ layers directly below Gr epitaxially grown on Ru(0001), through a stepwise reaction between intercalated silicon and oxygen. This method provides the optimal system to study the electronic properties of Gr using spectroscopic approaches, such as the CHC method.

We find strong variations of CT time between ~ 3 fs (Gr ML strongly coupled to substrate on Ru(0001) "valleys") and ~ 16 fs (decoupled Gr on SiO₂). A ratio of 1.7 is found between the "hills" and "valleys" of the corrugated Gr/Ru. The very fast CT on Gr/Ru valleys is interpreted as due to hybridized Ru orbitals "reaching through" the Gr layer which change with the relative Gr/Ru alignment and distance. On the decoupled Gr layers the intrinsic coupling to the Gr empty π^* states determines the CT time. The intermediate CT time for the Gr hills on Ru shows that these regions are far from the "decoupled" condition. The results contribute new information on the still controversial states of Gr/Ru, and shed light on the empty density of states above Gr surfaces and the coupling to them in an energy range possibly important for photonic applications of Gr, such as solar energy conversion.

[1] S. Lizzit, R. Larciprete, P. Lacovig, K.L.Kostov, D. Menzel, *in preparation*

[2] S. Lizzit *et al.* Nanoletters (2012) DOI: 10.1021/nl301614j

5:00pm **LB+EM+GR+MN+TR-WeA10 Fano Interference Effects in Hydrogen Intercalated Graphene.** A. Boosalis, T. Hofmann, University of Nebraska-Lincoln, R. Elmquist, M. Real, National Institute of Standards and Technology (NIST), M. Schubert, University of Nebraska-Lincoln

Graphene has been the focus of much recent research due to its unique electronic and optical properties, with potential for high performance electronics, tunable ultra-fast lasers, and transparent electrodes. Further development of graphene for commercial use requires effective large-area epitaxial production that maintains the desirable properties of exfoliated graphene. One such method of epitaxial graphene growth is thermal sublimation of Si from SiC. Sublimation of Si from the Si-face (0001) is the most controllable but produces a $(6\sqrt{3} \times 6\sqrt{3})R30^\circ$ surface reconstructed layer prior to graphene formation. This layer can be altered by subsequent

hydrogen intercalation, resulting in quasi-free-standing (QFS) epitaxial graphene.

In order to determine the effect of hydrogen intercalation on the optical properties of graphene we performed spectroscopic ellipsometry experiments in a spectral range of 3 to 9 eV before and after hydrogen intercalation of buffer layer only carbon growth on 6H SiC (0001). Spectroscopic ellipsometry is a widely used technique for determining the optical properties of thin films, and can provide sensitivity to film quality, morphology, and strain. In the case of graphene sensitivity is obtained through the critical-point (CP) located at 5.1 eV and modified by a Fano interference. Analysis of absorption near the CP is achieved through a parameterized model dielectric function (MDF) which is varied until a best-match between model and experimental data is obtained.

Best-match model results show drastic changes in the imaginary part of the MDF between previous measurements of buffer layer only growth on SiC, and buffer layer growth after hydrogen intercalation. Buffer layer only growth exhibits a far greater absorption throughout the spectrum, with an exciton produced maximum energy point that is shifted toward the infrared from the CP energy. After hydrogen intercalation, the QFS graphene layer exhibits a lowered absorption with a maximum closer to that of the CP energy; displaying an MDF closer to that of theoretical predictions for graphene.

In conclusion, hydrogen intercalation of buffer layer carbon growth on SiC (0001) has been shown to produce QFS graphene with optical properties closest to that of theoretical predictions for graphene, further proving its effectiveness as a tool for large-area epitaxial graphene production. In addition, buffer layer carbon growth shows optical properties sufficiently different from that of graphene to allow spectroscopic ellipsometry to become a viable in-situ monitor for commercial production of hydrogen intercalated graphene on SiC.

5:20pm **LB+EM+GR+MN+TR-WeA11 In Situ Dry-Cleaning of Ge(100) Surface using H₂O₂.** K. Kiantaj, T. Kaufman Osborn, T.J. Kent, A.C. Kummel, University of California San Diego

Since Ge has higher hole and electron mobility compared to silicon, it is a good candidate for development of a new channel material in CMOS semiconductor devices. One of the obstacles in using Ge as a channel material is the high interface trap density between Ge and Ge native oxide. Air exposed Ge surfaces have a high density of defects and contaminants, but, in order to make optimal semiconductor devices, nearly perfect bonding between each unit cell and the gate oxide layer is required. Although there are many methods available for cleaning the Ge surface, the effectiveness of each of these methods highly depends on the cleanliness of the processing chambers. After cleaning, the Ge surface is typically functionalized with OH groups via water (H₂O) or hydrogen peroxide (HOOH) during atomic layer deposition of the gate oxide. This OH functionalized surface ideally provides a high density of reactive sites for precursor nucleation. We have studied the effect of a very small amount of hydrocarbon in the processing chambers, and its effect on both the clean Ge surface and the OH functionalized surface since this may increase the density of interface traps and limit Equivalent Oxide Thickness (EOT) scaling. In-situ cleaned Ge surfaces as well as HOOH dosed surfaces have been studied after exposure to hydrocarbon contaminants with x-ray electron spectroscopy (XPS) and scanning tunneling microscopy (STM). An Argon ion source sputtering system was employed for in-situ cleaning of the Ge surface. After exposure to trace hydrocarbon contaminants, two different nanoscale features were observed by STM on the Ge and HOOH/Ge surfaces. One type of contamination denoted as carbon "nanoclusters" which are typically 0.3-0.5nm in height and 2-4nm in diameter. A distinctly different feature is observed on the Ge-OH terminated surface denoted as carbon "nanoflakes". In contrast to nanoclusters, nanoflakes were only observed on the Ge surfaces dosed with low concentration hydrogen peroxide. In the next step, a high concentration hydrogen peroxide source in combination with an ozone source was employed to study the removal of the contaminants from the Ge surface. Several dosing conditions and sample temperatures were studied and optimized. As the result, an atomically clean Ge surface were achieved by employing an all-dry in-situ process. The all-dry cleaning procedure does not involve any ion-milling or wet-cleaning procedures as both of these methods involve surface etching and result in surface roughness which is not desirable for semiconductor devices.

5:40pm **LB+EM+GR+MN+TR-WeA12 Hf-based High-k Dielectrics for Ge MOS Stacks.** S. Fadida, M. Eizenberg, Technion Israel Institute of Technology, Israel, L. Nyns, D. Lin, S. Van Elshocht, M. Caymax, IMEC, Belgium

Ge has drawn much attention recently, being a leading candidate to serve as the channel material of future metal oxide field effect transistors (MOSFETs) due to its high carrier mobility with respect to Si. The interest

in Ge is mostly because of its high hole mobility. Most of Ge related researches were focused so far on the challenge of Ge surface passivation. In this research we have moved on to the next challenge - finding a suitable high-k dielectric for a Ge-MOS stack. The high-k dielectric has to be chemically and thermally stable on top of the chosen passivation layer, have sufficiently high energy barriers with respect to Ge energy band edges, and have a large dielectric constant in order to obtain the required low effective oxide thickness (EOT). We have studied the chemical, structural and electrical properties of various HF-based high-k dielectrics: HfO_2 , $\text{Hf}_x\text{Zr}_{1-x}\text{O}_2$, $\text{Hf}_x\text{Al}_{1-x}\text{O}_2$ and $\text{Hf}_x\text{Gd}_{1-x}\text{O}_2$. All high-k dielectrics (4 nm thick) were deposited by atomic layer deposition (ALD) on top of a constant passivation stack composed of a thin GeO_2 layer (0.7 nm thick) followed by a thin (2 nm) ALD Al_2O_3 layer. The Al_2O_3 layer, which has high band offsets to Ge and GeO_2 , was added since HfO_2 , as many of the leading candidates for high-k dielectrics, are unstable on top of Ge or GeO_2 . A thorough and systematic electrical and chemical characterization of this complex gate stack was carried out. The interesting results show that this challenge of seeking for a superior high-k is not detached from the passivation challenge. Surprisingly, we have found that although the passivation stack was kept constant for all systems studied, the apparent D_{it} (density of interface states) changes when the top high-k material is modified. Another interesting phenomenon is revealed when different methods of D_{it} characterization are compared - each method points out a different high-k as the one with the lowest D_{it} . These observations imply that the C-V characteristics do not reflect only the role of Ge interface traps, but also of traps throughout the whole stack, at least to a distance of 2.7 nm (the total thickness of the passivation stack) from the Ge surface. These results emphasize even more the great challenges in integrating Ge as a new channel material. We have also analyzed the band alignment for all high-k dielectrics using XPS with respect to the underlying layers. All high-k dielectrics have similar band gaps at the range of 5.2-5.9 eV. The conductance and valence band offsets with respect to Ge are all larger than 1 eV, which make them all suitable for Ge-MOSFETs in terms of band alignment.

Magnetic Interfaces and Nanostructures

Room: 6 - Session MI+OX-WeA

Spintronics, Magnetolectrics, Multiferroics

Moderator: G.J. Mankey, University of Alabama

2:00pm **MI+OX-WeA1 Imaging of Temperature-Driven Nucleation of Ferromagnetic Domains in FeRh Thin Films**, *C. Baldasseroni, C. Bordel*, Univ. of California Berkeley, *A.X. Gray*, SLAC National Accelerator Lab, *A.M. Kaiser*, Peter-Grünberg-Institut, Germany, *F. Kronast*, Helmholtz-Zentrum Berlin für Materialien und Energie, Germany, *J. Herrero-Albillos*, Centro Univ. de la Defensa, Spain, *C.M. Schneider*, Peter-Grünberg-Institut, Germany, *C.S. Fadley*, Lawrence Berkeley National Lab, *F. Hellman*, Univ. of California Berkeley

Equiatomic FeRh is a unique material that undergoes a first order antiferromagnetic (AF) to ferromagnetic (FM) transition just above room temperature (near 350 K). This phase transition can be driven by temperature or magnetic field and is coupled to a lattice expansion. Current investigations of this unique transition range from the fundamental understanding of the origin and nature of the transition to applications associated with the transition such as a giant magnetocaloric effect.

FeRh has been studied in the bulk for over 50 years and most recently in thin film form, where the transition temperature has been shown to be sensitive to changes in composition and substrate-induced strain as well as structural and chemical order. FeRh thin films are also a promising candidate for heat-assisted magnetic recording in an exchange-spring system with a hard magnetic layer (for example FePt). Understanding the magnetic domain structure of FeRh and the mechanisms of the transition at the microscopic level involving nucleation and growth of magnetic domains as a function of temperature is vital for its further application to magnetic storage technology. Although many experimental studies of the transition have been recently performed on FeRh thin films, most of them focus on macroscopic measurements. Only a few studies have attempted at imaging domains through the transition but these have been limited to magnetic force microscopy (MFM) on bulk samples and were limited by lack of temperature control which prevented a study of the nucleation and growth across the full transition.

We used x-ray magnetic circular dichroism and photoemission electron microscopy to study the evolution of ferromagnetic domains across the temperature-driven AF to FM phase transition in uncapped and capped epitaxial FeRh thin films. The coexistence of the AF and FM phases was evidenced across the broad transition and the different stages of nucleation, growth and coalescence were observed. We also found that the FM phase

nucleates into single domain islands and the width of the transition of the individual nuclei is sharper than that of the macroscopic transition.

2:20pm **MI+OX-WeA2 Magnetic Properties of Cobalt and Permalloy Thin Films Grown on Self-Assembled Monolayers by Physical Vapor Deposition**, *G.J. Szulcowski, S. Schafer, B. Khodadadi, T. Mewes, J. Kreil, E. Ellingsworth, K. Anderson*, The University of Alabama

In this talk we will present results from a study to understand how terminal functional groups in self-assembled monolayers (SAMs) influence the growth and subsequent magnetic properties of Co and NiFe (permalloy) thin films. Self-assembled monolayers were made from both aryl and alkyl carboxylic acids adsorbed onto oxidized aluminum surfaces. The SAMs were characterized by contact angle measurements and x-ray photoelectron spectroscopy. The magnetic properties of the thin films were characterized by ferromagnetic resonance spectroscopy. In general we find that reactive functional groups, for example thiols, cause the metals to grow as continuous films. In contrast, deposition of the metals onto non-reactive functional groups, for example methyl, leads to penetration of metal atoms through the SAM and cluster formation. The permalloy films are superparamagnetic below ~ 4 nm, while Co films are ferromagnetic at room temperature. The coercivity of the films is also found to vary with functional group. In the case of halide substituents, for example, fluoro, chloro, bromo, and iodo on the aryl carboxylic SAMs, there is also a correlation between the magnetic properties of cobalt thin films and the strength of the carbon-halogen bond energy. Cobalt deposited onto SAMs with terminal C-F bonds tends to be non-reactive, while reactive toward C-I bonds. Not only do these reactivity patterns influence the magnetic properties of the thin film, but also they result in a measurable change in the resistance of tunnel junctions bearing these SAMs.

2:40pm **MI+OX-WeA3 Synthesis and Fundamental Properties of Fe16N2 Films - New Excitements of Fe16N2 Research and a 40-year Mystery**, *J.-P. Wang*, University of Minnesota **INVITED**

Pursuing magnetic materials with giant saturation magnetization (M_s) has huge impacts both scientifically and technologically. However, this effort has been fundamentally shadowed for decades by the classical itinerant magnetism theory. So far, the highest $4\pi M_s$ value that can be predicted by first principles calculation is 2.45 T for Fe65Co35 alloy.

In 1972, Kim and Takahashi firstly reported a material with a giant saturation magnetization ($4\pi M_s \sim 2.9$ T), Fe16N2, that surpasses Fe65Co35 alloy. Thereafter, various groups in the world have investigated the formation of Fe16N2 samples including films and particles by a variety of means. Unfortunately, experimentally reported $4\pi M_s$ values are largely inconsistent ranging from 2.2 T up to 2.9 T. Investigators, including theoreticians, weighted in on one side of this question or the other. In particular, at the annual conference on Magnetism and Magnetic Materials in 1996, a symposium was held on the topic Fe16N2. Key research teams on this topic presented apparently conflicting views on the synthesis and understanding of this material. No decisive conclusion was drawn on whether Fe16N2 has giant saturation magnetization at the moment. Since then, this research topic has been dropped by most of magnetic researchers since year 2000.

In 2010, Wang's group has reported the theory and fundamental experimental evidence of the origin of giant saturation magnetization and produced the Fe16N2 thin films with both giant M_s and high anisotropy. In this talk, Dr. Wang will review the history and analyze the previous inconsistencies and obstacles of the Fe16N2 topic in the past 40 years. Then he will present recent progress from his group and his collaborators on this topic. From X-ray magnetic circular Dichroism (XMCD) experiment, polarization-dependent x-ray absorption near edge spectroscopy (EXANE), polarized neutron reflectivity (PNR) and first-principle calculation, it has been both experimentally and theoretically justified that the origin of giant saturation magnetization and large magnetocrystalline anisotropy is correlated with the formation of highly localized 3d electron states in this Fe-N system. Thirdly, high magnetic anisotropy and high spin polarization ratio of Fe16N2 will be reported and discussed, which may lead to many new applications, such as in spintronic device and rare-earth free magnet. Finally remaining fundamental questions and possible approaches to address them will be reviewed and discussed.

This talk is a joint effort with five research teams at ORNL, Argonne National Lab, Brookhaven National Lab and one lab from Netherland.

4:00pm **MI+OX-WeA7 Spin Transfer Torque MRAM - Modeling, Experiments and Future Prospects**, *D. Apalkov, A. Khvalkovskiy, V. Nikitin, S. Watts, A. Driskill-Smith, D. Lottis, R. Chelupsky, V. Voznyuk, X. Tang, K. Moon, E. Chen, C.M. Park, M. Krounbi, Grandis, Inc.* **INVITED**
Spin transfer torque magnetic random access memory (STT-MRAM) is a new and promising memory technology that features fast read and write

times, small cell sizes of $< 6F_2$, nonvolatility, radiation hardness and low power consumption.

In this work, we will go over the fundamental physics of magnetoresistance and spin transfer torque effects – key scientific phenomena required for STT-MRAM memory operation. The precursor technology – conventional MRAM – is now successfully used in commercial applications; however it cannot be scaled down to compete with DRAM or Flash technologies. We will go over the *Write-Store-Read* (WSR) trilemma, which is the challenge to achieve fast and reliable writing, reading and storing information at the same time in STT-MRAM. For a successful product, the desired probability of a switching error at the current deliverable by the transistor should be less than 10^{-3} for storage-class memory and 10^{-9} - 10^{-18} for working-class memory. Depending on the switching time, two regimes of switching, thermal and precessional, can be identified, and the switching error can dramatically depend not only on the switching regime but also on the switching time within the regime. For the reading process, one critical parameter is read disturb – probability of inadvertent switching of the element during reading operation. For memory applications, this probability has to be smaller than $\sim 10^{-20}$ (with some dependence on particular design and array size). For storing the recorded information, the thermal stability parameter, defined as the ratio of energy barrier to $k_B T$ is important and typically has to be larger than 60-80 depending on specific application.

STT-MRAM can be implemented in two major realizations: in-plane and perpendicular. For each of them, single and dual MgO designs can be implemented, with the dual MgO design having up to 50% reduction of the switching current and providing much better switching symmetry than a single one. Special attention will be paid to our recent developments to of in-plane Dual MTJ design. By building special structure with modified reference layers, we were able to extract contributions from each barrier. Even though STT switching current is reduced in Dual design, the quality of the two barriers in currently built structures is deteriorated as compared to single MTJ. Respectively further improvement from Dual designs is expected if the quality of the two barriers is improved.

4:40pm MI+OX-WeA9 Epitaxial Growth of Multiferroic Heterostructures of Magnetic and Ferroelectric Oxides using the Dual-laser Ablation Technique, D. Mukherjee, M. Hordagoda, R.H. Hyde, N. Bingham, H. Srikanth, P. Mukherjee, S. Witanachchi, University of South Florida

Epitaxial multiferroic $PbZr_{0.52}Ti_{0.48}O_3$ (PZT)/ $CoFe_2O_4$ (CFO)/ $La_{0.7}Sr_{0.3}MnO_3$ (LSMO) composite thin films were fabricated on single-crystal $SrTiO_3$ substrates using the dual-laser ablation process. In this process, the target was initially heated by a pulsed CO_2 laser to produce a transient molten layer, from which a spatially-overlapped and slightly time-delayed pulsed KrF laser initiated the ablation. This not only resulted in a drastic reduction of particulates in the deposited films but also overcame the problem of non-congruent ablation of PZT, due to the high volatility of Pb, leading to stoichiometric PZT film deposition [1]. Moreover, the optimum coupling of the laser energies led to higher ionization of the ablated species particularly atomic oxygen (O) as seen in the optical emission spectra of the plumes. The higher excitation of O led to enhanced gas phase reaction and consequently reduced the oxygen vacancy-related point defects inherent in oxide films. X-ray diffraction (XRD) studies revealed the single crystalline nature and the cube-on-cube epitaxial relationship in the PZT/CFO/LSMO films. Atomic force microscopy revealed surface roughness values as low as 1.6 nm for the top PZT layers. Cross-sectional high resolution transmission electron microscope (HRTEM) images not only evidenced the epitaxial growth but also atomically sharp and flat interfaces with no structural defects (Suppl. PDF). The lattice parameters calculated from the HRTEM images matched well with the values obtained from XRD. Selected area electron diffraction (SAED) patterns showed linear square arrays confirming the single crystalline nature of the interfaces. Magnetization measurements exhibited perpendicular magnetic anisotropy with the easy axis along the film plane for the PZT/CFO/LSMO films, similar to PZT/LSMO bilayer thin films. PZT/CFO/LSMO films showed enhanced in-plane saturation magnetization (M_s) values of 360 emu/cm^3 as compared to 280 emu/cm^3 for PZT/LSMO and larger coercive field of 2.5 kOe as compared to 0.1 kOe for PZT/LSMO thin films. For ferroelectric measurements, top LSMO dot electrodes with 100 μm diameter were deposited using laser ablation to make LSMO/PZT/CFO/LSMO capacitors. Polarization measurements showed well saturated and square hysteresis loops at low nominal switching voltages of 5 V and with higher remnant polarization (P_r) values of $120 \mu\text{C/cm}^2$ as compared to $90 \mu\text{C/cm}^2$ for PZT/LSMO thin films.

[1]. D. Mukherjee et al, "Role of dual-laser ablation in controlling the Pb depletion in epitaxial growth of $Pb(Zr_{0.52}Ti_{0.48})O_3$ thin films with enhanced

surface quality and ferroelectric properties", *Journal of Applied Physics* 111, 064102 (2012).

5:00pm MI+OX-WeA10 The Highly Polarized Surface of Magnetolectric Antiferromagnet, N. Wu, X. He, J. Santana, J. Wang, University of Nebraska-Lincoln, *E. Vescovo,* Brookhaven National Laboratory, *C. Binek, P.A. Dowben,* University of Nebraska-Lincoln

Manipulation of magnetically ordered states by electrical means is among the most promising approaches towards novel spintronic devices. Electric control of the exchange bias can be realized when the passive antiferromagnetic pinning layer is replaced by a magneto-electric antiferromagnet, like the prototypical magneto-electric $Cr_2O_3(0001)$. Chromia works well in this case so long as there is also a finite remanent spin polarization at the surface or boundary, which can be achieved by cooling the thin film in the presence of both magnetic and electric fields. We have demonstrated that a very unusual high polarization can exist at the surface of the $Cr_2O_3(0001)$ from spin-polarized photoemission [1] and is robust against surface roughness. Both magnetic single domain and multidomains were imaged by magnetic force microscopy and X-ray magnetic circular dichroism – photoemission electron microscopy (XMCD-PEEM) [2] as achieved by field cooling in the presence of electric fields. The similar boundary magnetization has also been observed on the (110) surface of Fe_2TeO_6 by the XMCD-PEEM, which suggests this possible interface spin polarization to be a more universal phenomenon for magnetolectric antiferromagnets.

References:

[1] Xi He, Yi Wang, Ning Wu, Anthony N. Caruso, Elio Vescovo, Kirill D. Belashchenko, Peter A. Dowben and Christian Binek, *Nature Materials* 9, 579 (2010).

[2] Ning Wu, Xi He, Aleksander L. Wysocki, Uday Lanke, Takashi Komesu, Kirill D. Belashchenko, Christian Binek, and Peter A. Dowben, *Physical Review Letters* 106, 087202 (2011).

5:20pm MI+OX-WeA11 Sub-monolayer Spin Rotation of Photoelectrons from FePc on Fe(110), J.E. Rowe, D.B. Dougherty, A.A. Sandin, North Carolina State University, *E. Vescovo,* Brookhaven National Laboratory

Spin-resolved photoemission at the National Synchrotron Light Source, Brookhaven National Laboratory has been used to study the occupied electronic states of sub-monolayers to multi-layers of iron phthalocyanine (FePc) adsorbed on ~ 10 - 20 monolayer epitaxial films on Fe(110) on W(110). We find that the spin-resolved photoemission changes rapidly as a function of coverage and the initial (majority spin axis along [110]) rotates by ~ 30 degrees for sub-monolayer coverage and then becomes unpolarized at ~ 1 monolayer (ML). The coverage is determined by work function measurements which show that the initial work function of clean Fe(110) of 5.0 eV decreases monotonically to a value of ~ 3.8 eV at a coverage that we assign as ~ 1 monolayer of FePc. These values were determined from the measurements of the photoelectron spectrum using the low-energy vacuum-level cutoff of a biased sample. We used low intensity light at 41.4 eV photon energy to provide accurate intensity data and a well-defined vacuum-level threshold.

Our spin-resolved data for clean Fe(110) show highly spin-polarized photoelectrons from the Fermi energy to values about 3.5 eV below the Fermi energy for an applied B-field along [110] both for majority-spin and minority-spin electrons. The polarization is about 60% at -3.2 eV below E-Fermi. For 0.13 ML adsorbed FePc the spin polarization is somewhat reduced and is rotated from [110] towards [100] in the plane of the sample. We interpret this rotation as due to a strong coupling of the orbital moment of FePc with the conduction electrons of the Fe substrate. At a coverage of ~ 0.25 ML the polarization is reduced to ~ 0 and then at higher coverage (~ 1 ML) it increases to about 1/2 of the initial polarization. These data suggest that paramagnetic molecular species are useful for modifying the interfaces of spin-valve devices. A mechanism for this effect will be presented.

5:40pm MI+OX-WeA12 Magnetic Configurations of $Ni_{80}Fe_{20}/Ir$ Superlattices, G.J. Mankey, University of Alabama, *J. Hwang,* Lane College, *N. Pachauri, E.A. Manoharan, P.R. LeClair,* University of Alabama, *H. Ambaye, V. Lauter,* Oak Ridge National Laboratory

Antiferromagnetically coupled superlattices consisting of ferromagnetic (FM) layers separated by nonmagnetic (NM) spacer layers exhibit a wide range of magnetization behavior as a function of applied field. The magnetic configurations depend on the magnetization, thickness and anisotropy of the FM layers and the strength and type of magnetic coupling through the NM layers. The dependence of the magnetic configurations on applied magnetic field can be estimated with one-dimensional micromagnetic models that find the minimum energy configurations of the average magnetization vectors within the ferromagnetic layers. A set of

Ni80Fe20/Ir superlattice samples was designed to compare the measured magnetization curves as a function of applied field to magnetization curves generated by a micromagnetic model. The Ni80Fe20 layers were sputter deposited with an in-plane magnetic field, to induce uniaxial anisotropy within these layers. Both the FM layer thickness and number of superlattice periods were varied. FM layer thicknesses were verified by magnetometry and x-ray reflectivity analysis. The Ir NM layer thickness was tuned to the thickness for maximum antiferromagnetic coupling strength. It was chosen because the coupling strength has strong temperature dependence, increasing by about a factor of two as the temperature is reduced from 300 K to 5 K. A detailed comparison of the modeled and experimental magnetization curves enables a parameterization of the micromagnetic model that shows applying a magnetic field generates a complex magnetic structure in finite superlattices for multiple repeats. This complex structure, with twisted magnetic configuration is measured for a 16-repeat superlattice structure using polarized neutron reflectivity. Analysis of the polarized neutron reflectivity data for the applied magnetic field along the hard axis of the FM layers allows the determination of the detailed magnetic configuration.

1. U. K. Robler and A. N. Bogdanov, Phys. Rev. B 69, 184420 (2004).

The authors gratefully acknowledge financial support from DOE award DE-FG02-08ER46499. Research at Oak Ridge National Laboratory's Spallation Neutron Source was sponsored by the Scientific User Facilities Division, Office of Basic Energy Sciences, U.S. Department of Energy.

Nanometer-scale Science and Technology

Room: 12 - Session NS-WeA

Nanophotonics and Plasmonics

Moderator: D. Wei, University of Florida

2:00pm **NS-WeA1 Plasmon Induced Current In Hybrid Nanostructures**, *D.A. Bonnell, D. Conklin, S. Nanayakkara, X. Chen*, The University of Pennsylvania, *T.H. Park*, University of Michigan, *M. Therien*, Duke University

Interest in plasmon-exciton interactions is increasing owing to potential impact in light harvesting and optical signal manipulation. Recently a new mechanism of plasmon induced current generation was observed in porphyrin-Au nanoparticle hybrid nanostructures.[1] The plasmons associated with the gold nanoparticles enhanced photo conduction by many factors... even an order of magnitude. To understand this phenomena we have first developed an approach to the analysis of temperature dependent transport measurements that can lead to an unambiguous determination of mechanism in complex systems. [2] Then the temperature and wavelength dependent transport is examined as a function of nanoparticle size and distribution and molecule optical properties. [3] A Au-porphyrin combination is designed to distinguish the various potential mechanisms for plasmon induced current. We will show new evidence for a mechanism involving 'hot electron' generation. This has the potential to vastly increase efficiency of energy harvesting devices.

[1] Banerjee et al ACS Nano 4 (2010) 1019-1025

[2] Conklin et al NanoLetters 12 (2012) doi 10.1021/nl300400a

[3] Conklin et al Advanced Materials 21 (2011) 4712-4718.

2:20pm **NS-WeA2 Absorption from Plasmonic Antenna Arrays**, *K.E. O'Brien, P. Wang, P.H. Holloway, M.R. Davidson*, University of Florida

Photomixing over nano/micro scale plasmonic structures is a novel concept for generating narrow band radiation, specifically in the terahertz (THz) range. The plasmonic structures can serve as antennas for absorbing incoming photons and conversely emit radiation of a lower frequency if it is generated from mixing. In this experiment, antenna structures are excited by two tuned laser diodes to output THz radiation. Various designs for these antennas are have been considered, with presented results focusing on 2 dimensional arrays of elliptical antennas fabricated from Ag using electron-beam lithography and lift-off. The plasmonic antenna arrays exhibit polarization-dependent absorption when excited by visible light in agreement with results from simulations. The effect of varying antenna size on absorption will be discussed, as well as results from photomixing experiments.

2:40pm **NS-WeA3 New Directions in Plasmonics: Pushing the Sensitivity, Space, and Time Limits**, *R.P. Van Duyne*, Northwestern University **INVITED**

During the last few years, there has been an explosion of interest and activity in the field of plasmonics. The goal of plasmonics is to control and manipulate light on the nanometer length scale using the properties of the collective electronic excitations in noble metal films or nanoparticles, known as surface plasmons. An improved understanding of the interactions between adsorbed molecules and plasmonic nanostructures (i.e., molecular plasmonics) is having a significant impact in a number of research areas. These include surface-enhanced Raman spectroscopy (SERS), localized surface plasmon resonance (LSPR) spectroscopy, sub-wavelength optical microscopy, and nanolithography.

This talk will begin with some background material on the basic physical concepts underlying plasmonics with an emphasis on SERS and LSPR spectroscopy. Next, I will turn to two very recent developments. For the first time, the revolutionary techniques of surface enhanced Raman spectroscopy and femtosecond stimulated Raman spectroscopy (FSRS) have been combined. Thus, plasmonically enhanced broadband Raman spectra using an ultrafast four wave mixing process, which can simultaneously achieve spectral and temporal resolution below the time-energy uncertainty limit, has been achieved! Further we report substantial progress in tip-enhanced Raman spectroscopy (TERS). The isotopologue proof of single molecule specificity in ambient TERS has been demonstrated. We calculated the total TERS enhancement factor to be 1013, which includes a molecular resonance Raman contribution of 107. Further, an ultrahigh vacuum (UHV) TERS instrument has been constructed with atomic resolution of the surface and sub-molecular resolution of the adsorbate. For the first time, multiple vibrational modes for copper phthalocyanine (CuPc) adlayers on Ag (111) have been resolved in TER spectra obtained concurrently with molecular resolution UHV Scanning tunneling Microscopy (STM). All sample preparation and tip degassing are performed in-situ, maintaining atomically clean surfaces, greatly enhancing the stability of the tip-sample junction, and ensuring minimal contamination in the field enhancement region beneath the STM tip. We can now force the day when it will be possible to combine UHV-TERS and surface enhanced FSRS to enable single-molecule spectroscopy with simultaneous nanometer spatial resolution and femtosecond time resolution.

4:00pm **NS-WeA7 Near-Field Spatio-Temporal Control of Optical Fields for Spectroscopic Nano-imaging: Ultrafast Spectroscopy Reaching the Single Molecule Limit**, *M.B. Raschke*, University of Colorado **INVITED**

Combining plasmonic and optical antenna concepts with ultrafast and shaped laser pulses allows for the precise control of an optical excitation on femtosecond time and nanometer length scales. I will present several new concepts extending tip-enhanced spectroscopy into the nonlinear and ultrafast regime for nano-scale imaging and spectroscopy of surface molecules and nano-solids. Examples include the adiabatic nano-focusing on a tip for background free tip-enhanced Raman nano-spectroscopy, and spatio-temporal superfocusing with optical control at the 10 nm-10 fs level. Furthermore, the combination of ultrafast mid-IR femtosecond pulses with scattering-scanning near-field optical microscopy (s-SNOM) allows for the control of the ultrafast free-induction decay of infrared molecular vibrations with an increase in sensitivity of IR surface spectroscopy by 10⁹ compared to conventional IR micro-spectroscopy, reaching the single molecule limit.

4:40pm **NS-WeA9 Tuning the Optical Properties of Arrays of Pure and Doped Au Nano Chains**, *N. Nayyar, V. Turkowski, T.S. Rahman*, University of Central Florida

We apply time dependent density functional theory to study the absorption spectrum of arrays of nano-scale pure Au chains and those doped with transition metal (TM) atoms. We find that as the number of chains in the array increases the plasmon peak shifts to higher energies and appears in the visible range for an array of three gold chains, each consisting of 10 atoms. Doping with TM atoms also leads to the formation of additional plasmon peaks close in energy to the main one for the undoped case and is especially pronounced for Ni-doped chains. However, the response is very different when we have two chains in the array each doped with one TM atom in the middle. We trace the origin of the additional modes to the interplay between the collective and local plasmon oscillations of the chains. We compare the calculated optical absorption spectrum of the doped chains for several different types of TM atoms at different positions in the chains, and provide rationale for the trends. We also analyze the case of arrays consisting of chains of two different noble metal atoms (Au-Ag) and of arrays in which one chain is of noble metal atoms and the other of TM atoms. We find that the plasmon mode is suppressed when the second chain is composed of TM atoms. In addition we study the effect of plasmon-exciton interaction in arrays of infinite Au chains.

5:00pm **NS-WeA10 Synthesis, Characterization and Plasmonic Properties of Horizontally and Vertically Aligned Ag Nanorods and Nanowires**, *S. Vilayrganapathy, A. Pandey, A. Devaraj, D.E. Perea, S. Thevuthasan*, EMSL, Pacific Northwest National Laboratory, *A. Kayani*, Western Michigan University

One dimensional metal nanostructures such as nanorods and nanowires exhibit interesting linear and non-linear optical properties and find various applications as electronic, photonic and sensing devices. The optical properties of these composites are dominated by localized surface Plasmon resonance (LSPR) which results from the oscillations of conduction electrons in response to an external field. The resonant frequency of the electrons depends strongly on size, shape, distribution and the surrounding dielectric medium. By controlling the physical and chemical properties of the nanorods and nanowires the electronic and optical properties of the material can be tuned for appropriate applications. Nanorods and wires with well controlled aspect ratios can be grown by Electrodeposition and Polyol synthesis methods.

We have successfully employed the above two methods to grow both vertically and horizontally aligned Ag nanorods and wires. Vertically aligned and free standing Ag nanorods were grown by electrodepositing Ag onto an Anodized Aluminum oxide (AAO) template containing a sputtered layer of Ag on one side. The length of the nanorods varies linearly as a function of deposition time allowing us to obtain excellent control over the aspect ratio. The template was subsequently etched away using 6 wt. % Phosphoric acid/1.8 wt. % chromic acid solution leaving behind free standing vertically aligned nanorods. A Polyol process in which we reduce silver nitrate with ethylene glycol in the presence of a capping agent (PVP) was employed to grow nanorods in solution. A high yield of nanorods was obtained after centrifuging. The above grown nanorods were horizontally aligned onto a substrate by the Langmuir-Blodgett method. Scanning electron Microscope (SEM) was used to image the nanorods. The change in plasmonic response of both vertically and horizontally aligned nanorods as a function of aspect ratio as well as the influence of the surrounding dielectric medium on the plasmonic resonance of the nanorods embedded in a dielectric matrix will be discussed.

5:20pm **NS-WeA11 Localized Surface Plasmon Resonances in Silicon**, *L.-W. Chou, N. Shin, S. Sivaram, M. Filler*, Georgia Institute of Technology

Localized surface plasmon resonances (LSPRs) in semiconductors offer new opportunities to engineer the interaction of electromagnetic radiation with solid-state materials. Importantly, the carrier density of semiconductors, and thus LSPR frequency, can be modulated via doping and/or electric field. In addition to realizing novel plasmonic devices, the direct integration of plasmonic and excitonic behavior also promises fundamentally distinct functionality. Here, we demonstrate and systematically control LSPRs in nanoscale Si for the first time. More specifically, Si nanowires are synthesized via the vapor-liquid-solid (VLS) technique with a combination of Si_2H_6 and PCl_3 precursors. PCl_3 simultaneously introduces P atoms to the nanowire core and delivers Cl atoms to the sidewall so as to minimize radial dopant incorporation. This chemistry enables growth sufficiently far from equilibrium such that dopant concentrations can exceed thermodynamic limits. Electron microscopy reveals that these nanowires are single crystalline and $\langle 111 \rangle$ oriented with very few lattice defects. Polarization dependent *in-situ* infrared spectroscopy measurements show intense mid-IR absorption bands only for the P-doped nanowires, which we assign to longitudinal LSPRs. A significantly weaker transverse mode is occasionally observed as well. The LSPR frequency can be readily adjusted by varying nanowire length. Mie-Gans theory supports our experimental results and indicates that electrically active dopant concentrations exceed 10^{20} cm^{-3} .

Plasma Science and Technology

Room: 24 - Session PS1-WeA

Plasma Diagnostics, Sensors and Control 2

Moderator: R. Ramos, LTM, France

2:00pm **PS1-WeA1 ECR Plasma Etching Characterization using a Retarding Field Energy Analyzer**, *B. Dolinaj*, Dublin City University, Ireland, *V. Milosavljevic*, Dublin City University, *D. Gahan*, Impedans Ltd., *N. MacGearailt*, Intel Corporation, *M.B. Hopkins*, Impedans Ltd., *S. Daniels*, Dublin City University

Dry etching technology was introduced to integrated circuit manufacturing due to its unique ability to do anisotropic removal of material to create high

aspect ratio structures. Dry etching tools in the semiconductor industry use plasma to generate electrons, bombarding ions and free radicals. These radicals are chemically reactive and highly efficient at removing material from substrate surfaces, so the etch profiles depend on ion density and ion energy.

Electron cyclotron resonance (ECR) plasma etching reactors are widely used in wafer production. They use a low pressure, high density plasma source that has resonant magnetic field coils and two independently controlled microwave and radio frequency (RF) sources. ECR plasma etching is a very complex process and most of the progress with ECR etching tools up to this time has been accomplished empirically. Introducing new and adapted plasma diagnostic techniques is essential for further characterization and better understanding of plasma and etching processes.

In previous work we presented electrical measurements obtained using a retarding field energy analyzer (RFEA) installed in a commercial ECR etching reactor. RFEAs are generally used for charged particle flux and energy distribution measurements at electrically grounded surfaces. We demonstrated that an electrically isolated RFEA can be successfully used for measuring ion energy distribution functions (IEDFs) at the surface of RF driven electrodes in the presence of strong DC magnetic fields.

In this work we present further achievements in plasma diagnostics and ECR etching characterization. The original experimental setup is expanded for additional diagnostic tools. Phase resolved optical emission spectroscopy (PROES) measurements are taken at three different discharge locations simultaneously with RFEA measurements. Electrical and optical measurements show strong correlation in comparable aspects which proves their validity and together they provide more information about plasma in complementary aspects. The RFEA has also been used to measure the electron energy distribution function (EEDF) with the aim of electron temperature and density estimation in the bulk plasma. For validating EEDFs obtained with the RFEA, we performed similar measurements of EEDFs in a capacitively coupled plasma (CCP) reactor using the RFEA and the Langmuir probe. Results of this validation and estimations made from EEDFs are presented and discussed. Experimental and theoretical plasma etching characterization has been done through the analysis of spatially resolved data sets obtained from RFEA and spectroscopic ellipsometry at various radial locations.

2:20pm **PS1-WeA2 Time Resolved Ion Flux Measurement in Pulsed ICP Plasmas**, *G. Cunge, M. Darnon*, LTM-CNRS, France, *N.St. Braithwaite*, The Open University, UK, *E. Despiou-Pujo, P. Bodart, M. Brihoum, M. Haass, O. Joubert*, LTM-CNRS, France

Pulsed ICP plasmas are a promising solution to several technological issues related to IC circuit fabrication. Recent results are indicating that pulsing the inductively coupled power and/or the RF biasing power allows to increase the etch selectivity and to reduce plasma induced damages in ultrathin layer. However, the reasons for these improvements remain unclear. In particular, the impact of plasma pulsing on the ion flux (and ion energy) in electronegative gases used for IC circuit fabrication has not been studied in details. In this work, we have used a capacitively-coupled planar ion flux probe to monitor the time variations of the ions flux in various plasmas (CF_4 , SF_6 , Cl_2 , HBr ...etc) operated in an industrial etch reactor from AMAT. We will discuss in detail the experimental set-up that we have designed to carry out time resolved measurement and the issues associated with this measurement. Results will be presented from both electropositive (Ar, He) and electronegative (Cl_2 , BCl_3 , SiCl_4 , SF_6) plasmas. We will first present the impact of the ICP source pulsing frequency and duty cycle on the ion flux. These results will be compared to those obtained from a global model. We will then discuss the impact of the RF biasing power on the ion flux in pulsed plasmas. Both the ICP source power and the RF bias power can be independently or synchronously pulsed. In the latter case different duty cycles and a phase delay can be used. During synchronized pulsing with a delay between the ICP and the rf bias pulses, some interesting instabilities (ion flux oscillations) are observed. They are related to the generation of ion acoustic waves by the rapid expansion (or collapse) of the sheath in front of the wafer when the RF bias pulse is applied to the chuck. These results will be eventually compared to IEDF measurements in pulsed plasmas and the consequences on pulsed plasma etch process design will be discussed.

2:40pm **PS1-WeA3 In Situ Monitoring of Electron Density and Dielectric Layer on the Wall with Curling Probe**, *A. Pandey, Y. Liang, S. Ikezawa, K. Nakamura, H. Sugai*, Chubu University, Japan

A new type of microwave resonator probe, *curling probe*, has recently been proposed [1] which employs mono-pole excitation of spiral slot antenna. This probe enables direct measurement of electron density in reactive plasmas, based on a quarter-wavelength resonance at the frequency $f = b(c/4L)[2(\epsilon_{in} + \epsilon_{out})]^{1/2}$. Here, b is the finite-size correction factor, L is the antenna length, ϵ_{in} and ϵ_{out} are the relative permittivities of two dielectrics

inside and outside the slot antenna, respectively. When the probe is inserted into plasma, the outer dielectric constant ϵ_{out} is expressed as $\epsilon_p = 1 - (f_p/f)^2$ with the electron plasma frequency $f_p = (\epsilon^2 n / m e_0)^{1/2}$. Thus, measuring the resonance frequency of curling probe, one can determine f_p , and hence the electron density n . The finite-difference time-domain (FDTD) simulation of 11-mm-diam curling probe of 35-mm antenna length shows a sharp resonance at the frequency from 1 GHz to 6 GHz uniquely determined by the electron density. The sheath formed in front of the probe surface was modeled as a vacuum layer of $\sim 5\lambda_D$ in thickness. The resonance frequency was hardly influenced by the sheath at the density higher than 10^{11} cm^{-3} . Basic experiments of electron density measurement by the curling probe were performed in an argon (1–20 Pa) low-power (<2 kW) discharge in ICP device for 300-mm-wafer process. The power dependence of the resonance frequency observed by the curling probe was explained well by the FDTD simulation result as well as the analytical formula. The radial distribution of electron density was measured by a movable curling probe.

When a polymer layer (permittivity ϵ_d) is deposited on the probe surface, the resonance frequency decreases with the increasing layer thickness. Using this probe characteristic, one can *in situ* monitor the thickness of dielectric layer deposited onto a wall of plasma vessel, where the curling probe is positioned to just the same surface of inner wall. The FDTD simulation shows ~ 10 MHz shift in the resonance frequency for 15-mm-thick deposition of polymer ($\epsilon_d = 3.2$), in good agreement with the experimental observation. Thus, the wall deposition layer during chamber cleaning or CVD process can be monitored by the curling probe. In fact, amorphous carbon layer formed on the vessel wall was *in situ* monitored by the curling probe in a 1-kW surface-wave plasma in CH_4/Ar deposition discharge and in O_2/Ar cleaning discharge. This model experiment successfully demonstrated an applicability of curling probe to monitoring the dielectric layer deposited on the plasma vessel wall.

[1] I. Liang, K. Nakamura, and H. Sugai, *Appl. Phys. Express* 4, 066101 (2011).

4:00pm **PS1-WeA7 Time Resolved Laser Induced Fluorescence for Probing the Excitation Kinetics of a Low Temperature Argon Discharge.** *J.M. Palomares Linares, E.A.D. Carbone, S. Hübner, W.A.A.D. Graef, J.J.A.M. van der Mullen*, Eindhoven University of Technology, the Netherlands **INVITED**

In this contribution we report a series of experiments based on time resolved laser induced fluorescence (tr-LIF) on low temperature discharges. This technique is used, in combination with Thomson scattering (TS) measurements, to get insight in the excitation kinetics of the discharge.

This method is used to pump different levels within the 4p and 5p groups of the Ar excitation space, from the Ar metastable level $1s_5$. Measuring the tr-LIF decay times in combination with the TS measurements of electron density provides simultaneously total destruction rates by electron and heavy particle collision of the pumped levels. These effective excitation rates are of great importance for the development of models, and are scarce in the case of high excited argon levels.

Similarly, the time response of the collisional induced fluorescence signals (tr-LCIF) emitted by other excited levels is used to study the interaction between levels. In the particular case of Ar this method is used to obtain the “depopulation rates” of metastable $4s$ levels. When other gasses are introduced in the discharge tr-LCIF signals are obtained from the emission of different excited species of those gasses. These experiments enable us to probe in details the excitation exchange between different species. The use of a high rep-rate system is fundamental for the LCIF measurements, where the low intensity of the signals demands measurement times up to 30 minutes.

The experiments are done in a range of intermediate pressures (0.65 mbar – 40 mbar), on a surfatron microwave induced plasma, working with pure Ar, and mixtures of Ar with H_2 , O_2 , and N_2 . The tr-LIF diagnostic is performed with a 5KHz high rep-rate Nd:YAG laser in combination with a Dye laser system. This setup allows to record tr-LIF signals 500 times more intense than with the common 10 Hz systems. Two equivalent systems are used to pump different wavelengths, a tripled frequency Nd:YAG (@355 nm) in combination with a Coumarine-2 Dye laser (430 nm - 460 nm), and a doubled frequency Nd:YAG (@532 nm) with a Pyridine-1 Dye laser (670 nm – 720 nm). The Thomson scattering measurements are performed with an independent Nd:YAG (532 nm) system and a triple grating spectrograph for the detection of the scattered photons.

4:40pm **PS1-WeA9 Analysis of Run-to-Run Variability in the Bosch Process using rf Probe and Emission Spectroscopy Measurements.** *M. Fradet, L. Stafford*, Université de Montréal, Canada, *C. Coia*, Teledyne Dalsa, Canada

Deep silicon etching is a crucial step for several emerging and evolving technologies, including micro-electromechanical systems (MEMS) and CMOS image sensors. Among etching methods available, the Bosch

process is widely used because it allows fast etching rates together with high aspect ratios. This process relies on rapid switches between isotropic etching in SF_6 -containing plasmas and polymer deposition for sidewall passivation in C_4F_8 -containing plasmas. As a result of reactor wall conditioning, run-to-run variability in etching rates and uniformity is commonly observed. In order to understand the origin of such drifts and thus to develop new strategies to reduce these effects, we have started investigations of the temporal evolution of the properties of SF_6 and C_4F_8 plasmas in the Bosch process on an industrial, inductively-coupled plasma reactor (ICP) at Teledyne Dalsa. In this context, a rf probe was installed on the transmission line connecting the generator to the substrate holder. This system measures the amplitude of the current and voltage as well as the phase between them, allowing determination of the real and imaginary parts of the impedance. During one etch cycle in Ar/SF_6 (total duration of 10s), the absolute value of the reactance, $|X|$, decreased sharply within the first second and then reached a plateau. For one sample exposed to many etch and deposition cycles, the cycle-averaged value of $|X|$ slowly decreased between the first and the 70th cycle. For many samples etched in the same chamber with a 2 minutes O_2 plasma clean between each run, the run-averaged value of $|X|$ decreased with the sample number. Over this whole range of experimental conditions, the resistance remained fairly constant. From optical profilometry measurements, the etching rate was found to decrease from 340 to 300 nm/s between run #1 and #5. This decrease matched relatively well the observed decrease of $|X|$, suggesting that the reactance determined from rf probe measurements is a good parameter to examine in a non-intrusive way run-to-run variability in deep silicon etching. More recently, preliminary analysis of the plasma emission in the Ar/SF_6 plasma revealed that the F (703.7 nm)-to-Ar (750.4 nm) line-intensity ratio (related to the F density) remained constant within the first few seconds and then decreased mid-way in the etch cycle due to strong F uptake. Future experiments will attempt to determine whether the observed decrease of the Si etching rate due to wall conditioning can be attributed to a reduction of the fluorine concentration during the etch cycle or to a higher density of fluorocarbon radicals during the passivation cycle.

5:00pm **PS1-WeA10 Spatially-resolved Optical Emissions Spectroscopy of Capacitively Coupled Discharges.** *G. Franz, I. Krstev, F. Schamberger*, Hochschule München, Germany

Optical emission spectroscopy has evolved a mighty tool for evaluating the high-energy tail of the electron energy distribution function EEDF [1]. Since it is a non-evading technique, a spatially-resolved measurement cannot be performed, which limits its general applicability, especially for inhomogeneous plasmas, in particular capacitively-coupled discharges with their thick plasma sheaths and large rf electric fields, and microwave-driven plasmas which exhibit a very high plasma density in front of the microwave window which prevents the penetration of the microwave into deeper regions of the reactor. A spatially averaging technique therefore overdraws the region close to the window leading to erroneous results and conclusions.

To overcome these limitations, a cylindrical parallel-plate reactor was equipped with a magnifying double lens system with different focal lengths halfway between the two “electrodes” to resolve radially dependent spectroscopic data obtained with the two actinometric gases Kr and Xe [2]. From these data, the electron temperature of the high-energy tail of the EEDF of capacitively coupled discharges through argon and the weakly electronegative gas mixture CF_4/O_2 can be calculated [3].

These data are modeled with ray tracing programs to evaluate the degree of magnification. Compared with an experimental setup with a plane window instead of a converging lens and only one focusing lens for the glass fiber, we can enhance the S/N ratio by a factor of at least 100 yielding a radial resolution of about 1 – 2 mm which is in the same range of Langmuir probes.

Compared with measurements obtained with Langmuir probes in the plasma bulk, electron temperatures show in fact the expected behaviour of definitely hotter temperatures.

[1] V.M. Donnelly, *J. Phys. D: Appl. Phys.* 37, R217 (2004)

[2] G. Franz, I. Krstev, F. Schamberger, *Plasma Sci. Technol.* 14(8), to be published 2012

[3] M.V. Malyshev and V.M. Donnelly, *J. Vac. Sci. Technol.* A15, 550 (1997)

5:20pm **PS1-WeA11 Model-based Ion Energy Control in ICP Etcher.** *M. Klick*, Plasmatrex, Germany, *H.P. Maucher*, United Monolithic Semiconductors

In particular for III-V semiconductors, plasma processes close to active zones of surface-sensitive devices are critical, demanding low damage through ion bombardment and so an excellent process understanding and control. In order to get the ion energy into the right range, the bias power is switched off working then a downstream-like mode. A complete model of

the entire system with this special setup is presented and validated. It demonstrates that the bias matchbox capacitances are excellent control elements for the ion energy. We can also show that the Vp measurement is not representing the ion energy here. The ion energy is estimated by the sheath voltage from the model and shows a reasonable correlation to the etch rate observed.

This paper focuses on a general method to characterize equipment and plasma by a combination of off-line and real-time measurements. The first major goal of this paper is to show how reduced models of plasma equipment can be used to estimate important plasma parameters as to understand how the plasma process works. The equivalent circuit is only a tool to explain the overall plasma physical picture, it does mean that an equivalent circuit is always the right tool to describe a plasma. This resulting, reduced and so also not self-consistent model must be verified and then used for the ion energy control in an ICP etcher.

The model is based on a combined plasma and RF model in the special case of an existing bias matchbox but zero bias power. The control elements are the capacitance in the bias matchbox. We show the tune capacitance to be an excellent control element, but we can also demonstrate that – at least in this case – an RF peak voltage measurement is not representing the ion energy and alone not very useful.

Trikon/Aviza Omega 201 ICP etcher was used. A 100 mm electrode, a cylindrical coil around a ceramic chamber wall, and a Al chamber lid are main parts of the chamber.

Usually two generators are running at 13.56 MHz as master and slave with an adjustable phase shift between source and bias generator. In our case the bias generator is switched off in order to achieve a very low ion energy and thus almost no damage at the wafer. First investigations have shown that the position of load and tune capacitance in the bias matchbox to be very important for etch rate and wafer damage. Therefore a model was built to understand and finally to utilize these effects for process control.

5:40pm PS1-WeA12 High Energy IED Measurements with MEMS based Si Grid Technology Inside a 300mm Si Wafer. *M. Funk, B.G. Lane, L. Chen, J. Zhao, R. Sundararajan*, Tokyo Electron America, Y. Yamazawa, Tokyo Electron Limited, Japan

The measurement of ion energy at the wafer surface at conditions that are realistic for commercial equipment and process development without extensive modification of the reactor geometry has been an industry challenge. High energy, wide frequency range, process gases tolerant, minimally perturbing, contamination free and accurate ion energy measurements are the base requirements. In this work we will report on the complete system developed to achieve the base requirements, including the safe and easy use by engineers. The system includes: a reusable silicon ion energy analyzer (IEA) wafer, signal feed through, RF confinement, and high voltage measurement and control.

The commercial manufacturing of an IEA system at a reasonable cost involves many disciplines, but can be achieved through the use of commercial methods and suppliers. Design aspects will be presented, including MEMS silicon etch technology that enables features in the sensor design that overcomes challenges in high voltage RF potentials while minimizing ion neutralization. The IEA wafer detail design required careful understanding of the relationships between the plasma Debye length, the number of grids, intergrid charge exchange (spacing), capacitive coupling, materials, and dielectric flash over constraints. RF confinement with measurement transparency was addressed so as not to disturb the chamber plasma, wafer sheath and DC self-bias as well as to achieve spectral accuracy. For commercial plasma etch reactors the wafer is floating at several kV relative to the outside ground and often the plasma wetted DC ground area is small and not well defined. To overcome the difference between the wafer surface and the outside environment a non-perturbing measurement system was developed that can be isolated and floated by several thousands of volts, while making accurate ion energy current and voltage measurements. The experimental results reported were collected using a commercial parallel plate etcher powered by a dual frequency (VHF + LF) bottom electrode; with various power combinations. Various process gases were tested and variations by pressure were tested to confirm the robustness and sensitivity of the physical design and measurement circuit and methods.

Plasma Science and Technology **Room: 25 - Session PS2-WeA**

Plasma Surface Interactions during PECVD and Plasma Surface Modification

Moderator: C.A. Wolden, Colorado School of Mines

2:00pm PS2-WeA1 Surface Modifications Induced by Extreme Fluxes of Low-Energy Ions. *G. De Temmerman, K. Bystrov*, FOM Institute DIFFER, Netherlands, *M.J. Baldwin, R.P. Doerner*, University of California San Diego, *L. Marot*, University of Basel, Switzerland, *H.Y. Xu*, Tsinghua University, China, *M.C.M. van de Sanden*, FOM Institute DIFFER, Netherlands **INVITED**

The interaction of energetic particles with solid surfaces is at the core of numerous applications such as thin film deposition or materials processing. Ion-beam processing, for example, allows nanostructure formation on metal and semiconductor surfaces, while reactive ions can be used to chemically modify surfaces during nitriding for example. Those processes usually involve ions with energies above 100eV where ion-induced damage creation and physical sputtering are expected, and are relatively well documented. In a fusion reactor, at locations where the plasma intersects with the solid surfaces, plasma-facing surfaces are bombarded by extreme particle fluxes (up to $10^{24} \text{m}^{-2}\text{s}^{-1}$ or $1.6 \times 10^5 \text{A.m}^{-2}$), albeit with energies below 50eV. While the ion energy is below the damage threshold for the incoming ions, the particle flux is high enough to cause a local supersaturation of mobile gas particles within the implantation zone and strong surface morphology changes as a result of cluster/bubble growth.

Combining a high efficiency plasma source and a strong magnetic field, linear plasma devices (LPD) can generate such high ion fluxes and allow fundamental studies of plasma-induced surface modifications under high heat and particle fluxes. The effect of high fluxes of hydrogen, helium and neon ions on metal surfaces, such as tungsten, has been investigated over a wide range of surface temperatures (300-2000C) and ion energies (10-50eV). In all cases, the surface modifications depend strongly on these two parameters, which control the near-surface particle trapping and material properties (mechanical properties, self-diffusion).

Nanostructuring of the surface through formations of ripples or nanoscopic voids is observed for hydrogen irradiation. In the case of helium, a fibrous nanostructure is formed with a typical size in the range 20-1000nm depending on the surface temperature. For neon ions, both a fine-scale ripple structure and large blisters are observed on the surface.

An overview of these results will be given with an emphasis on the surface properties and the application of low-energy ion fluxes as a surface processing technique.

2:40pm PS2-WeA3 Investigation of Plasma-Surface Interactions Between Hydrogen Radical and Chemically Amplified Photoresist. *A. Malinowski*, Institute of Electron Technology, Poland, *M. Sekine, M. Hori, K. Ishikawa, H. Kondo, T. Takeuchi, T. Suzuki*, Nagoya University, Japan, *A. Jakubowski, L. Lukasiak*, Warsaw University of Technology, Poland, *D. Tomaszewski*, Institute of Electron Technology, Poland

As FinFET transistors become necessary, FEOL etch processes will become much more challenging, bringing new constraints to etch selectivity, anisotropy, and etch damage. System-on-a-chip RF and analog devices may have double and triple gates and can be subjected to 12 or more photoresist (PR) removals. Thus development damage-less PR removal is critical for reducing plasma induced transistor electrical parameters fluctuations. In addition to poor uniformity or heavy environmental burden, hydrogen radical-based PR removal is expected to overcome critical problem of damage to the device inborn to currently used PR removal based on oxygen plasmas. As double and "multi" ArF 193nm patterning solutions continue to be a significant vehicle for extending Moore's Law, it is imperative to investigate plasma-surface interactions between hydrogen radical and chemically amplified ArF 193nm PR. The key element from point of view of etch reaction process kinetics investigation is radical sticking coefficient (SC).

In our study we have developed novel technique for radical SC estimation based on processing of PAPE structure (PALlet for Plasma Evaluation) followed by numerical simulation. Our approach is based on normalized profiles matching of etched PR thickness on parallel plate after PAPE structure processing, using hydrogen high density radical source, with simulated profile of number of stuck radicals on the same plate.

Understanding of the interactions of atomic hydrogen with ArF 193nm PR surface is of both fundamental and technological interest thus recombination mechanism of hydrogen atom on PR surface must be considered. In our approach SC is a sum of etch probability (EP) and recombination probability (RP) and estimated values of EP (0.07) and RP

(0.1) reveal fact that recombination dominates during PR etching by hydrogen. Since recombination lowers the number of radicals that are bound to the surface, the reactive species coverage is reduced by this process. Dominance of recombination in conjunction with very low value of EP itself explains very low etch rate, which is on the order of a few nm per minute (it was 3.8 nm/min). In addition similarity of RP obtained in this study and Koleske et al. reveals that the recombination is the result of a gas phase atom abstracting an atom of the same type that has previously chemisorbed to the surface according to the Eley-Rideal mechanism.

Inefficiency of the kinetic energy loss by hydrogen radicals during the PR surface collision, by means of phonon excitation or momentum transfer explains very low value of EP (0.07). Increase of temperature (323 K) of the structure involved proportional increase of EP (0.09).

3:00pm **PS2-WeA4 Kinetic Theory of the Sheath near Electron Emitting Surfaces, J.P. Sheehan**, University of Wisconsin Madison, I.D. Kaganovich, Princeton Plasma Physics Laboratory, N. Hershkowitz, University of Wisconsin Madison, Y. Raitses, Princeton Plasma Physics Laboratory

It has long been known that electron emission from a surface significantly affects the sheath surrounding that surface. Typical fluid theory of a planar sheath with emitted electrons assumes that the plasma electrons follow the Boltzmann relation and the emitted electrons have zero energy at the surface and predicts a potential drop of $1.03 T_e$ across the sheath when the surface is allowed to float. By removing the assumption that all plasma electrons entering the sheath are reflected back into the bulk plasma (i.e. the Boltzmann relation) and considering those electrons lost to the wall, the predicted sheath potential is reduced to $0.91 T_e$. Analysis of this type has been published by various authors, but our work presents a more accurate model. We performed an analytical study of sheath and presheath structure making use of a kinetic description of the emitted and plasma electron densities in the self-consistent electric field. It is shown that kinetic theory predicts that the sheath potential depends on the ratio of temperatures of plasma and emitted electrons (Θ_e). For $\Theta_e = 5$ (for example, for 0.2 eV emitted electron temperature and 1.0 eV plasma electron temperature), theory predicts a sheath potential of half that predicted by fluid theory. The effects of a bi-Maxwellian Electron Energy Distribution Function (EEDF) were considered. These predictions were compared to measurements made in a non-magnetized plasma confined by a multidipole chamber which has a bi-Maxwellian EEDF. A barium-tungsten dispenser cathode was used as a planar emitted electron source. The inflection point in the limit of zero emission emissive probe technique was used to measure the plasma potential in the sheath and presheath near the emitting surface. These results were compared to the kinetic theory and the effects of the bi-Maxwellian EEDF were taken into account.

4:00pm **PS2-WeA7 Probing CF and CF₂ Surface Reactivities in Inductively-Coupled Fluorocarbon Plasmas, M.F. Cuddy***, E.R. Fisher, Colorado State University

Inductively-coupled fluorocarbon plasmas (FCPs) provide a wide range of potential applications from circuitry fabrication to preparation of optical coatings. In these systems, etching and deposition processes often occur simultaneously, with the net effect of surface processing dictated by the balance between the two phenomena. The behavior of CF_x (x=1,2) species in particular provide insight into these competing processes and allow for elucidation of the mechanisms of FCP processing. We have examined CF_x radical scatter coefficients (S) at the gas-surface interface for a range of FCPS during plasma-enhanced chemical vapor deposition (PECVD). Our imaging of radicals interacting with surfaces (IRIS) experiments reveal that CF and CF₂ species scatter from surfaces with a high probability in each of the systems investigated. These high scatter values are related to the ion energies of nascent plasma species, as measured by mass spectrometry. Highly energetic ions ablate fluorocarbon passivation layers to extricate CF_x units. The presence of vibrationally hot CF(²Δ) radicals correlates directly with increasing scatter values for CF(²Π), suggesting that internal energy transfer at surfaces is another important factor contributing to the observed S. The connection between interfacial interactions and the PECVD-deposited film is a critical component to consider for improved plasma applications and for designing specificity in fluorocarbon film properties. Ultimately, by controlling the parameters associated with our plasma systems, we can create tailored films with specific compositions and surface energies. The efforts recounted here offer additional insight into the fundamental plasma processes so crucial for advancement of plasma technology.

4:20pm **PS2-WeA8 Effects of Ar Ion Bombardment on Protection of Organosilicate Glass from O₂ Plasma Damage, H.Ur. Kazi, S. Gaddam, J.A. Kelber**, University of North Texas

In-situ XPS studies of Ar ion bombardment on organosilicate glass (OSG) films at ion kinetic energies between 500eV and 900eV demonstrate that such bombardment inhibits O₂ plasma-induced carbon loss by forming an SiO₂-like overlayer, and that the degree of protection correlates directly with increased ion energies, but not the thickness of SiO₂ overlayer. Bombardment at 500eV results in a ~3 Å thick SiO₂overlayer and subsequent O₂ plasma treatment results in a slower rate of carbon loss from the surface region than observed for a vicinal film, but complete carbon removal is observed after 3 min O₂plasma treatment under these conditions. In contrast, bombardment by a similar flux of 900eV ions results in a SiO₂-like overlayer of similar average thickness, but with greatly inhibited rate of carbon loss upon subsequent O₂ plasma exposure. Ar ion bombardment (900eV) in the presence of NH₃ (1 x 10⁻⁶ Torr) results exclusively in Si-N rather than C-N bond formation, and dramatically increases the average thickness of the Si-O-N overlayer to 22 Å. The formation of this overlayer further reduces the rate of subsequent O₂ plasma-induced carbon loss compared to 900eV Ar ions alone. These results indicate Ar ion bombardment causes Si-C bond scission. Subsequent NH₃ reaction results in Si-N bond formation and inhibits Si-Si and Si-O-Si formation, increasing the thickness of the ion-induced damage overlayer. The data indicate that ion kinetic energies are a critical parameter in protective noble gas plasma treatments to inhibit O₂ plasma damage, and also indicate that high energy ions alone can provide better protection against carbon loss when compared to plasmas or VUV photons.

Acknowledgement: This work was supported by the Semiconductor Research Corporation under Task ID 2071.002. The authors thank Novellus Systems Inc. for providing the low k samples. David Graves and Joe Lee are also acknowledged for stimulating discussions.

4:40pm **PS2-WeA9 Ion-Surface Interaction during Microcrystalline Silicon Thin Film Growth, J. Palmans, A.C. Bronneberg, X. Kang, M.C.M. van de Sanden, W.M.M. Kessels, M. Creatore**, Eindhoven University of Technology, the Netherlands

Thin-film silicon solar cells extensively use hydrogenated microcrystalline silicon (μc-Si:H) where large area and fast deposition processes are considered key issues. Both requirements can be fulfilled when operating in the so-called high pressure depletion (HPD) regime in a parallel plate capacitively coupled plasma (CCP). This latter involves high plasma powers (~0.5 W/cm²), enabling high growth rates through high silane (SiH₄) depletion, and high pressures (> 0.75 Torr) enhancing the material properties by suppressing the ion bombardment. In this work direct ion measurements obtained in a parallel plate CCP are presented for two collisional pressure regimes enabling a quantitative comparison of the role of ions during the plasma-surface interaction and its relation to the amorphous-to-microcrystalline silicon phase transition as determined in both the HPD (10.50 Torr) and a low pressure (0.45 Torr) regime by varying the SiH₄ flow rate, while preserving hydrogen (H₂) flow rate and power density. By relating Raman and infrared absorption spectroscopy data the absence of the narrow high stretching modes and oxidation processes for the solar-grade μc-Si:H thin films has been demonstrated. Next to material analysis, this contribution will address selected aspects of plasma-surface interaction during μc-Si:H deposition. A capacitive probe has been implemented to study the ion flux for a range of parameters, i.e. silane flow rate and plasma power, whereas ion energies are determined with a retarding field energy analyzer (limited to pressures < 0.75 Torr), both implemented in the substrate holder. In the HPD regime an increase of SiH₄ flow rate (0-10 sccm) is found to induce only a moderate increase in ion flux, accounting for 30% of the growth flux for solar-grade material [1]. With ion energies limited to below 19 eV (in collisionless H₂ plasma), less than 6 eV are estimated to be available per deposited Si atom, suggesting that we are either in a regime of Si surface atom displacement, or more likely that a thermal spike is induced at the surface by the arrival of ions, enhancing the radical surface diffusion. Since the ion energy measurements are compatible only with low pressure, this study supports the direct correlation between material quality and plasma-surface interaction in terms of ion energy. The novel insights obtained can lead to the further development of deposition techniques in order to meet the stringent requirements of solar cells in terms of efficiency and production costs.

[1] A.C. Bronneberg, X. Kang, J. Palmans, P.H.J. Janssen, T. Lorne, M.C.M. van de Sanden and M. Creatore,

Submitted to J. Appl. Phys. (2012)

5:00pm **PS2-WeA10 Time Resolved Characterization of Pulsed ICP CH₄ – H₂ Based Plasmas**, *S. Jacq, L. Le Brizoual, C. Cardinaud, A. Granier*, University of Nantes - CNRS, France

Pulsed rf plasmas are increasingly being employed for plasma etching or deposition. In the case of etching, as the semiconductor feature sizes decreases and feature density increases, the industry is facing the increasing challenge of finding new plasma processes for the requirement of the next devices generation. CH₄-H₂ based plasmas are widely used for dry etching of II-VI and III-V semiconductors. Pulsed plasmas combined to time resolved measurements are known to be powerful tools to study species kinetics. In this study, pulsed CH₄-H₂ plasmas created in a low pressure inductively coupled rf plasma (ICP) are analyzed by time resolved optical emission spectroscopy (TR-OES), mass spectrometry (TR-MS) and electrostatic probe measurements. Plasma conditions are the following: 800 or 1000 W RF power, 20 mTorr pressure, 5 to 50 ms period and 10 to 50 %duty cycle. A cylindrical Langmuir probe and a planar probe are used to measure the electron density (n_e), electron temperature (T_e) and ion flux density. The species creation kinetics is investigated by TR-OES. Since no emission occurs during the off time (n_e and T_e decreases drastically), the double pulse technique is used with a probing pulse time of 0.75 ms. This communication is focused on pseudo-actinometry for the kinetics of H atoms and radicals (CH_x). Mass spectrometry is carried out with a time resolved and energy-resolved mass spectrometer on CH₃. For TR-MS, the transit times in the apparatus are calculated for each ion.

During the post-discharge, the decay characteristic time is below 1 ms for H atom density. The time evolution of n_e over one period reveals that n_e needs 1 ms to reach a stationary state and decreases with a characteristic time of about 0.1 ms. However, the decrease time of T_e seems to be shorter than 0.1 ms. Although the H atom kinetics is very fast, and characterized by a decay time below 1 ms, it is slower than the time evolution of n_e and T_e. However, considering the diffusion coefficient of H atoms in the various gas mixtures, different rise and decrease characteristic times could indicate different reaction probabilities on the walls, in relation with the gas mixture. Characteristic times and associated reaction probabilities, using Chantray's formalism are determined to be equal to 0.52 ms (on time) 0.80 ms (off time) which corresponds to H loss probability $\gamma_{on}=0.3$ and $\gamma_{off}=0.1$. Similar mass spectrometry measurement on CH₃ plasma species will be presented. Influence of ion bombardment on the H loss rate at the chamber walls is discussed and this seems to be the key point for chamber conditioning in the pulsed mode.

5:20pm **PS2-WeA11 Plasma-Surface Interactions, Erosion, and Impact on Plasma Distribution Functions**, *N. Fox-Lyon*, University of Maryland, College Park, *D.B. Graves*, University of California Berkeley, *S.Y. Moon, V.M. Donnelly, D.J. Economou*, University of Houston, *G.S. Oehrlein*, University of Maryland, College Park

Plasma-surface interactions can play a large role in changing characteristic plasma distribution functions. To improve our fundamental understanding of these effects, we leverage several plasma characterization techniques (Langmuir probe, ion energy/mass analyzer, optical emission spectroscopy) with real-time characterization by *in situ* ellipsometry of the eroding plasma-facing surface. Using these methods, we qualitatively and quantitatively studied the time evolution of gaseous and surface derived plasma impurities. High-density inert plasmas (Ar) and low-density reactive plasmas (H₂, D₂) respond differently to molecular impurities in the plasma. When H₂/D₂ or surface/gaseous derived CH_x-related impurities are introduced into Ar plasma, large changes in plasma properties are observed. We report on changes to the ion energy/mass distributions, electron temperature/distribution functions, and plasma density for different conditions. CH_x effects on H₂ and D₂ plasmas, and H₂/D₂ plasma mixtures were also investigated. We also explore the effects of changing the relative C:H fluxes into the plasma from eroding surfaces using graphitic (high C:H ratio) and polymeric (lower C:H ratio) films. In steady-state contact with plasmas, hydrocarbons are eroded as C, H, and CH_x impurities into the plasma reflective of their initial C:H ratios. Along with these studies, we have compared how varying the gap distance between the plasma generation coil and hydrocarbon substrate electrode affects impurity fluxes and plasma properties. A comparison of plasma properties for two different inductively coupled plasma reactors has also been completed and sheds light on how plasma properties and observed trends change for different geometries and plasma sources.

5:40pm **PS2-WeA12 MD Simulations of Hydrogen Plasma Interaction with Graphene Surfaces**, *E. Despiou-Pujo, A. Davydova, G. Cunge*, CNRS/UJF-Grenoble1/CEA LTM, France, *L. Magaud*, CNRS/UJF Institut Neel, France, *D.B. Graves*, University of California Berkeley

Due to its unique 2D structure and its outstanding physical, chemical and mechanical properties, graphene is a promising candidate for a large number of novel applications in microelectronics, for transparent conducting electrodes, sensors or energy storage devices. The successful

development of graphene-based technologies relies on the capability to grow and integrate this new material into sophisticated devices but the nm-scale control of graphene processing overwhelms current based-plasma technology. Therefore, innovative technological steps have to be developed to allow the growth of graphene layers on large areas wafers and their patterning using conventional lithography and plasma etching schemes.

Due to high ion bombardment energies and significant fragmentation rates, conventional continuous-wave plasma processes are not able to selectively etch ultrathin films without damaging the active layers of nanoelectronic devices. In order to achieve uniform/smooth patterning, doping or chemical modification of graphene films without damaging the substrates, one possible alternative is to use pulsed-plasma discharges which exhibit lower average ion energies (thus minimizing surface damage) and are promising to achieve sub-nm thick layers etching. However, the interactions between reactive pulsed plasmas and surfaces are so complex that the efficient development of new processes requires numerical simulations. Therefore, we propose to develop Molecular Dynamics (MD) simulations to understand the role of ion energy in plasma-graphene interaction and to determine the relationship between the flux/energy of reactive species (ions, radicals) bombarding the surface and its structural/chemical modifications.

In this paper, we investigate the interaction between hydrogen plasma species and single/multilayer graphene samples via MD simulations. C-H interatomic potential curves and associated energy barriers are reported depending on the H impact position (top, bridge, hollow or edge sites of GNRs). The influence of graphene temperature and incident species energy on adsorption, reflection and penetration mechanisms is presented. Except for impacts at GNRs edges or at defects location, H species are shown to experience a repulsive force due to delocalized π -electrons which prevents any species with less than ~ 0.7 eV to adsorb on the graphene surface. It also appears that the chemical binding of H to sp²-C requires a local rehybridization from sp² to sp³ resulting in structural changes of the graphene sample. H⁺ bombardment of ABA- and ABC-stacked multilayer graphene sheets are compared and the possibility to store hydrogen between consecutive layers is discussed.

Scanning Probe Microscopy Focus Topic

Room: 16 - Session SP+AS+BI+ET+MI+TF-WeA

Emerging Instrument Formats

Moderator: A. Belu, Medtronic, Inc.

2:00pm **SP+AS+BI+ET+MI+TF-WeA1 Electrochemical Strain Microscopy: Nanoscale Imaging of Solid State Ionics**, *S. Jesse*, Oak Ridge National Laboratory **INVITED**

Electrochemical reactions in solids underpin multiple applications ranging from electroresistive non-volatile memory and neuromorphic logic devices memories, to chemical sensors and electrochemical gas pumps, to energy storage and conversion systems including metal-air batteries and fuel cells. Understanding the functionality in these systems requires probing reversible (oxygen reduction/evolution reaction) and irreversible (cathode degradation and activation, formation of conductive filaments) electrochemical processes. Traditionally, these effects are studied only on the macroscopically averaged level. In this talk, I summarize recent advances in probing and controlling these transformations locally on nanometer level using scanning probe microscopy. The localized tip concentrates an electric field in a nanometer scale volume of material, inducing local ion transport. Measured simultaneously, the electromechanical response (piezo response) or current (conductive AFM) provides the information on bias-induced changes in a material. Here, I illustrate how these methods can be extended to study local electrochemical transformations, including vacancy dynamics in oxides such as titanates, La_xSr_{1-x}CoO₃, BiFeO₃, and Y_xZr_{1-x}O₂. The formation of electromechanical hysteresis loops indistinguishable from those in ferroelectric materials illustrate the role ionic dynamics can play in piezoresponse force microscopy and similar measurements. In materials such as lanthanum-strontium cobaltite, mapping both reversible vacancy motion and vacancy ordering and static deformation is possible, and can be corroborated by post mortem STEM/EELS studies. The possible strategies for elucidation ionic motion at the electroactive interfaces in oxides using high-resolution electron microscopy and combined ex-situ and in-situ STEM-SPM studies are discussed. Finally, the future possibilities for probing electrochemical phenomena on in-situ grown surfaces with atomic resolution are discussed. This research was conducted at the Center for Nanophase Materials Sciences, which is sponsored at Oak Ridge National Laboratory by the Scientific User Facilities Division, Office of Basic Energy Sciences, U.S. Department of Energy.

2:40pm **SP+AS+BI+ET+MI+TF-WeA3 Probing Electrochemical Phenomena in Reactive Environments at High Temperature: *In Situ* Characterization of Interfaces in Fuel Cells**, *S.S. Nonnenmann, R. Kungas, J.M. Vohs, D.A. Bonnell*, University of Pennsylvania

Many strategies for advances in energy related processes involve high temperatures and reactive environments. Fuel cell operation, chemical catalysis, and certain approaches to energy harvesting are examples. Scanning probe microscopy provides a large toolbox of local and often atomic resolution measurements of phenomena at a scale that enables understanding of complex processes involved in many systems. Inherent challenges exist, however, in applying these techniques to the realistic conditions under which these processes operate. To overcome some of these challenges, we have designed a system that allows SPM at temperatures to 850° C in reactive gas environments. This is demonstrated with the characterization of an operating fuel cell. Solid oxide fuel cells (SOFCs) offer the highest conversion efficiencies with operating temperatures ranging from 400° C - 1000° C; and operate under variable gaseous fuel environments – H₂-based environments (anode side) and O₂-based environments (cathode side). Topography and the temperature dependence of surface potential are compared to impedance. While not (yet) at atomic levels of spatial resolution, these probes are at the scale to examine local interface properties.

3:00pm **SP+AS+BI+ET+MI+TF-WeA4 High-Resolution Scanning Local Capacitance Measurements**, *M. Brukman*, University of Pennsylvania, *S. Nanayakkara*, National Renewable Energy Laboratory, *D.A. Bonnell*, University of Pennsylvania

Spatial variation of dielectric properties often dictates the behavior of devices ranging from field effect transistors to memory devices to organic electronics, yet dielectric properties are rarely characterized locally. We present methods of analyzing 2nd harmonic-based local capacitance measurements achieved through non-contact atomic force microscopy. Unlike contact-based methods, this technique preserves tip shape and allows the same probe to realize high-resolution topographic imaging and scanning surface potential imaging. We present an improved analysis of the electrical fields between tip and sample, yielding high sensitivity to the capacitance-induced frequency shift.

The techniques are applied to thin-film ceramics (SrTiO₂ and HfO₂), metals (Pt and Ti), and mixed-phase self-

assembled monolayers to illustrate application over all orders of dielectric constant. Conversion from frequency shift signal to dielectric constant κ is demonstrated, with sub-5 nm spatial resolution and dielectric constant resolution between 0.25 and 1.

4:00pm **SP+AS+BI+ET+MI+TF-WeA7 Experimental Calibration of the Higher Flexural Modes of Microcantilever Sensors**, *J.D. Parkin, G. Hähner*, University of St Andrews, UK

Microcantilevers are widely employed as probes not only in atomic force microscopy [1], but also as sensors for mass [2], surface stress [3], chemical identification [3], or in measuring viscoelastic properties of cells [4].

Use of the higher flexural modes of microcantilever sensors is an area of current interest due to their higher Q-factors and greater sensitivity to some of the properties probed [2]. A pre-requirement for their exploitation, however, is knowledge of their spring constants [5]. None of the existing cantilever calibration techniques can calibrate the higher flexural modes easily.

We present a method that allows for the determination of the spring constants of all flexural modes. A flow of gas from a microchannel interacts with the microcantilever causing a measurable shift in the resonance frequencies of all flexural modes [6]. The method is non-invasive and does not risk damage to the microcantilever. From the magnitude of the frequency shifts the spring constants can be determined with high accuracy and precision. Experimental data for the response of the first four flexural modes of microcantilever beams used in AFM with spring constants in the range of ~0.03-90 N/m will be presented.

The spring constants of the first mode determined using our method are compared to those obtained with the Sader method [7]. Finite element analysis computational fluid dynamics (CFD) simulations of the experimental setup are used to provide an insight into the interaction of the flow with the microcantilever.

References

- [1] F.J. Giessibl, *Rev. Mod. Phys.* **75**, 949 (2003).
- [2] J.D. Parkin and G. Hähner, *Rev. Sci. Instrum.* **82**, 035108 (2011).
- [3] A. Boisen *et al.* *Rep. Prog. Phys.* **74**, 036101 (2011).
- [4] M. Radmacher *et al.* *Biophys. J.* **70**, 556 (1996).

[5] G. Hähner, *Ultramicroscopy* **110**, 801 (2010).

[6] G.V. Lubarsky and G. Hähner, *Rev. Sci. Instrum.* **78**, 095102 (2007).

[7] J.E. Sader, J.W.M. Chon, and P. Mulvaney, *Rev. Sci. Instrum.* **70**, 3967 (1999).

4:20pm **SP+AS+BI+ET+MI+TF-WeA8 Atomic Imaging with Peak Force Tapping**, *B. Pittenger, Y. Hu, C. Su, S.C. Minne*, Bruker AFM, *I. Armstrong*, Bruker Nano Surfaces Division

As its name implies, Atomic Force Microscopy (AFM) has long been used to acquire images at the atomic scale. However these images usually only show the lattice of atoms in the crystal and do not show individual atomic defects. In order to achieve atomic resolution, researchers have typically had to design their systems for the ultimate in noise performance, sacrificing ease of use, flexibility, and scan size. Recently we have demonstrated that, by using Peak Force Tapping, our large sample platforms (Dimension Icon, Dimension FastScan) are capable of obtaining atomic resolution imaging along with maps of the tip-sample interaction. Unlike standard TappingMode, or FM-AFM, Peak Force Tapping uses instantaneous force control, allowing the system to be insensitive to long range forces while maintaining piconewton level control of the force at the point in the tapping cycle that provides the highest resolution – the peak force. Since the modulation frequency is far from resonance, the technique is less sensitive to the cantilever thermal noise (Brownian motion). In addition to topography, this technique can provide maps of the interaction between the tip and the sample. This is possible since Peak Force Tapping has access to the instantaneous force between tip and sample at any point in the modulation cycle. To study the details of a tip-sample interaction, Atomic Peak Force Capture can acquire the entire force distance curve used to create the interaction maps. These curves can be exported for easy analysis with models of tip-sample interaction. In this talk we will discuss the latest atomic resolution results using Peak Force Tapping and the implications of this with regard to studies of dissolution, crystallization, ordered liquids, and corrosion.

4:40pm **SP+AS+BI+ET+MI+TF-WeA9 Nanoscale Chemical Composition Mapping with AFM-based Infrared Spectroscopy**, *C.B. Prater, M. Lo, Q. Hu*, Anasys Instruments, *C. Marcott*, Light Light Solutions, *B. Chase*, University of Delaware, *R. Shetty, K. Kjoller, E. Dillon*, Anasys Instruments

INVITED

The ability to identify material under an AFM tip has been identified as one of the "Holy Grails" of probe microscopy. While AFM can measure mechanical, electrical, magnetic and thermal properties of materials, until recently it has lacked the robust ability to chemically characterize unknown materials. Infrared spectroscopy can characterize and identify materials via vibrational resonances of chemical bonds and is a very widely used analytical technique. We have successfully integrated AFM with IR spectroscopy (AFM-IR) to obtain high quality infrared absorption spectra at arbitrary points in an AFM image, thus providing nanoscale chemical characterization on the sub-100 nm length scale. Employing the AFM-IR technique, we have mapped nanoscale chemical, structural and mechanical variations in multilayer thin films, nanocomposites, polymer blends, organic photovoltaics, and biological materials including hair, skin, and bacterial and mammalian cells. Light from a pulsed infrared laser is directed at a sample, causing rapid thermal expansion of the sample surface at absorbing wavelengths. The rapid thermal expansion creates an impulse force at the tip, resulting in resonant oscillations of the AFM cantilever. The amplitude of the cantilever oscillation is directly related to the infrared absorption properties of the samples, enabling measurements of IR absorption spectra far below the conventional diffraction limit. AFM-IR can be used both to obtain point spectra at arbitrary points and to spatially map IR absorption at selected wavelengths. Simultaneous measurement of the cantilever's contact resonance frequency as excited by the IR absorption provides a complimentary measurement of relative mechanical properties. We have used these techniques to chemically identify individual chemical components in polymer nanocomposites and multilayer films and performed subcellular spectroscopy and chemical imaging on biological cells. Using self-heating probes we have been able to locally modify the state of a semicrystalline polymer and observe the resulting change in absorption spectra on the nanoscale. Using polarization sensitive AFM-IR, we have mapped spatial variations in molecular orientation in electrospun fibers.

5:20pm **SP+AS+BI+ET+MI+TF-WeA11 Quantifying Nanomechanical Properties with Simultaneous AM-FM and $\tan\delta$ Imaging**, *T. Mehr, A. Moshar, R. Proksch, I. Revenko, N. Geisse, S. Hohlbauch, D. Walters, J. Cleveland, J. Bemis, C. Callahan, D. Beck*, Asylum Research

Frequency-Modulated (FM) is a powerful, quantitative technique for mapping interaction forces between an oscillating tip and sample. Since FM-AFM typically requires the use of three feedback loops, one ongoing

challenge has been stable and cross-talk free operation. Amplitude-modulated Atomic Force Microscopy (AM-AFM), also known as tapping mode, is a proven, reliable and gentle imaging method with wide spread applications. Recently, the phase signal of the first resonant mode has been recast in terms of the tip-sample loss tangent.[1] This allows quantitative imaging of a response term that includes both the dissipated and stored energy of the tip sample interaction. Combining AM and FM imaging allows reaping the benefits of both techniques.[2] Because the feedback loops are decoupled, operation is more robust and simple than conventional FM imaging. In this mode, the topographic feedback is based on the AM signal of the first cantilever resonance while the second resonance drive is frequency modulated. The FM image returns a quantitative value of the frequency shift that in turn depends on the sample stiffness and can be applied to a variety of physical models. We will present results on a wide variety of materials as well as discussing quantitative separation of the elastic and dissipative components of the tip-sample interactions.[3]

References

- [1] R. Proksch and D. Yablon, *Appl. Phys. Lett.* **100**, 073106 (2012) and R. Proksch, D. Yablon, and A. Tsou, ACS Rubber Division 180th Technical Meeting, 2011-24 (2011).
- [2] G. Chawla and S. Solares, *Appl. Phys. Lett.*, **99**, 074103 (2011) and R. Proksch and R. C. Callahan, US Patents 8,024,963 and 7,603,891.
- [3] R. Proksch and S. V. Kalinin, *Nanotechnology* **21**, 455705/1 (2010).

5:40pm SP+AS+BI+ET+MI+TF-WeA12 Simultaneous Scanning Tunneling and Atomic Force Microscopy with Subatomic Spatial Resolution, *F.J. Giessibl*, University of Regensburg, Germany

Frequency-modulation AFM can be combined with scanning tunneling microscopy, yielding a simultaneous data set for current and average force gradient. Ternes et al. [1] have shown that for some metallic contacts, force and current are proportional. The interaction of a tungsten tip with a CO molecule adsorbed on Cu(111), however, yields a much different symmetry and distance dependence of tunneling current and force [2]. The tunneling current yields a gaussian dip over the CO molecule, while the forces show a strong angular dependence with force fields that vary strongly by distance and angle within the extent of the single front atom, displaying subatomic variations. While the simultaneous acquisition of current and force can reveal new information about the atomic and electronic structure of matter, the tunneling current can modify the atomic forces. This "phantom force" [3,4], a modification of the electrostatic attraction between tip and sample, originates in an alteration of the effective potential difference between tip and sample caused by strongly localized voltage drop induced by the tunneling current. The talk discusses the potential of combined STM/AFM as well as the challenges, in particular with respect to tip preparation and characterization.

- [1] M. Ternes et al., *Phys. Rev. Lett.* **106**, 016802 (2011).
- [2] J. Welker, F. J. Giessibl, *Science* **326**, 444 (2012).
- [3] A.J. Weymouth et al. *Phys. Rev. Lett.* **106**, 226801 (2011).
- [4] T. Wutscher et al. *Phys. Rev. B* **85**, 195426 (2012).

Surface Science

Room: 22 - Session SS+EM-WeA

Semiconductor Surfaces

Moderator: M.A. Hines, Cornell University

2:00pm SS+EM-WeA1 Local Characterization of Laterally Patterned GaN Polar Surfaces, *J.D. Ferguson*, Virginia Commonwealth University, *J.K. Hite, M.A. Mastro, C.R. Eddy, Jr.*, U.S. Naval Research Laboratory, *A.A. Baski*, Virginia Commonwealth University

Using scanning probe microscopy techniques, we have investigated the topographic and electrical properties of lithographically defined Ga- and N-polar regions grown on the same surface of a GaN epilayer. These unique structures were created on N-polar substrates grown by either hydride vapor phase epitaxy (HVPE) or metalorganic chemical vapor deposition (MOCVD). A patented selective epitaxy process [1,2] was used to prepare the alternating polarity surfaces on the two separate substrate types. To produce adjacent stripes of alternating polarity on a single substrate, a thin inversion layer comprising AlN was selectively grown inside a nitride mask. After removing the mask, Ga- and N-polar GaN were simultaneously grown over the inversion layer and bare N polar substrate, respectively, using MOCVD. Atomic force microscope (AFM) topography images reveal that Ga-polar regions are smoother than N-polar ones by about two orders of magnitude (rms of ~0.5 nm and ~50 nm, respectively). Local current/voltage (I/V) spectra obtained by conductive AFM indicate a lower

turn-on voltage and higher conductivity for N polar regions, whereas Ga polar regions are insulating. Scanning Kelvin probe microscopy (SKPM) data show a surface potential drop of ~0.5 V across the interface domain boundary (< 200 nm lateral resolution) from the N- to the Ga polar regions on the HVPE substrate. A lower potential drop (~0.2 V) is seen across the N- to Ga- interface on the template, as well as inconsistent surface potential values (+/-0.1 V) for Ga-polar stripes. Using SKPM, the surface photovoltage (SPV), or the change in surface potential upon exposure to above-bandgap light, may also be measured for both surfaces simultaneously. Both samples show similar characteristics to previously studied polar GaN surfaces, where Ga-polar regions have higher initial SPV values (~0.3 V for HVPE, ~0.5 V for MOCVD) than N-polar regions (~0.2 V for HVPE, ~0.3 V for MOCVD). Restoration of the SPV signal after illumination is faster for Ga-polar regions, which is not consistent with previously studied bulk Ga-polar films. In summary, scanning probe methods can be used to distinguish Ga- versus N-polar GaN surface regions grown on the same GaN epilayer.

1. J.K. Hite, M.E. Twigg, M.A. Mastro, C.R. Eddy, Jr. and F.J. Kub, "Initiating Polarity Inversion in GaN Growth Using an AlN Interlayer", *Physica Status Solidi A* **208**, 1504-1506 (2011).
2. J.K. Hite, N.D. Bassim, M.E. Twigg, M.A. Mastro, F.J. Kub and C.R. Eddy, Jr., "GaN Vertical and Lateral Polarity Heterostructures on GaN Substrates", *Journal of Crystal Growth* **332**, 43-47 (2011).

2:20pm SS+EM-WeA2 Systematic Prediction of Entropic Surface Reconstruction Stabilization on GaAs(001) from First Principles, *J.C. Thomas, A. Van der Ven*, University of Michigan, *N.A. Modine*, Sandia National Laboratories, *J.M. Millunchick*, University of Michigan

Increasing evidence linking bulk material properties to surface structure has made critical the development of a comprehensive understanding of atomic-scale surface structure. This is particularly true in low-temperature-grown (LTG) GaAs, where As anti-site defects are incorporated at the As-rich growth surface. Unfortunately, GaAs(001) reconstruction stability is poorly characterized in this regime, where, in addition to the well-studied $\beta 2(2 \times 4)$ and $c(4 \times 4)$ reconstructions, a " $\times 3$ " reconstruction is also observed. This " $\times 3$ " reconstruction has been difficult to characterize experimentally, and theoretical calculations have failed to identify a stable " $\times 3$ " reconstruction on GaAs(001). We have developed a systematic, rigorous procedure for predicting equilibrium surface structure and ordering behavior at finite temperature. By combining new and established techniques, our method overcomes difficulties of studying multicomponent surfaces from first principles, which has traditionally followed a painstaking trial-and-error approach.

Using our approach of directed structural enumeration and density functional theory calculation, we can efficiently identify stable and near-stable reconstructions of the GaAs(001) surface in order to identify the structure of the missing " $\times 3$ " reconstruction. Accounting for lattice vibrations and configurational entropy from first principles, we predict finite-temperature stability of a (4×3) reconstruction over a range of As_4 partial pressure at low temperature. Our results reveal a competition between vibrational entropy of the (4×3) reconstruction and configurational entropy of the $c(4 \times 4)$ reconstruction, which becomes entropically stabilized at higher temperatures. We find that this same (4×3) reconstruction features prominently in calculated reconstruction phase diagrams for the wetting layer systems Bi/GaAs(001) and InAs/GaAs(001).

2:40pm SS+EM-WeA3 3D Atomic Scale Structure Analysis of Semiconductor Nanostructures by Atom Probe Tomography and Cross-Sectional STM, *P.M. Koenraad*, Eindhoven University of Technology, Netherlands

INVITED

Present day semiconductor science depends heavily on the construction of precise nanostructures in which atomic scale details are of key importance in the understanding and utilization of such nanostructured semiconductor materials. It is thus of key importance to have techniques that allow such details to be assessed by novel microscopy techniques that can obtain, preferable in 3D, atomic resolution. In this presentation I will present recent results that we have obtained by two exciting techniques that allow for an atomic scale resolution. We have used cross-sectional Scanning Tunneling Microscopy (X-STM) and Atom Probe Tomography (APT) on a range semiconductor nanostructures such as quantum dots and rings. The X-STM technique offers a superb 2D true atomic resolution in a single atomic plane intersecting the nanostructure. Atom Probe Tomography is a technique that has recently become available for the analysis of semiconductor nanostructures. Laser induced field emission is used to get a full atomically resolved 3D map of the composition of semiconductor nanostructure. In the presentation I will apply and compare these techniques on quantum dots and rings that have been obtained by various growth procedures such as the traditional Stransky-Krastonow process, droplet epitaxy or by applying Sb during the dot formation process.

4:20pm **SS+EM-WeA8 Coverage-dependent Adsorption of a Bifunctional Molecule with a Rigid Spacer on the Ge(100)-2 × 1 Surface**, *B. Shong, S.F. Bent*, Stanford University

Direct chemical functionalization of semiconductor surfaces with organic molecules has been gaining attention, in part due to its potential applications based on forming organic-inorganic interfaces with tailorable properties. Attachment of bifunctional molecule is important because of the possibility for manipulating the chemical properties of the surface to allow for successive reaction, for example by molecular layer deposition (MLD). Whether dual or single reaction occurs during adsorption of a bifunctional molecule is of critical interest. It is known that more singly-tethered adsorbates typically form at higher coverages, but most previous studies focused only on a few discrete coverages.

In this study, we investigate coverage-dependent adsorption behavior of resorcinol (1,3-benzenediol) on the Ge(100)-2 × 1 surface. *In situ* X-ray photoelectron spectroscopy and Fourier transform infrared spectroscopy experiments along with density functional theory calculations are combined to determine the products and reaction pathways. First, the results support our previous conclusion that molecular geometry is an important factor in the reactivity and stereoselectivity of rigid bifunctional adsorbates.¹ Resorcinol is found to dually and singly attach on Ge(100) through its two hydroxyl groups, and the dually reacted adsorbate assumes only one configuration due to geometrical restrictions. Moreover, a detailed study with respect to coverage shows that the product distribution is strongly dependent on coverage in a nonlinear fashion with two distinct adsorption regimes. In the low coverage regime, a constant fraction of singly-attached adsorbates is observed, independent of coverage. On the other hand, the fraction of singly-bound adsorbates increases with coverage in the high coverage regime. The increase in singly-bound species at higher coverages is explained by surface crowding, with existing adsorbates blocking reactive sites. This study provides fundamental knowledge about the reactivity of bifunctional molecules on semiconductor surfaces.

¹B. Shong, K. T. Wong, and S. F. Bent, *J. Phys. Chem. C* **116**, 4705 (2012).

4:40pm **SS+EM-WeA9 2012 AVS Medard Welch Award Lecture: Chemical Functionalization of H-terminated Silicon Surfaces**, *Y.J. Chabal**, The University of Texas at Dallas **INVITED**

Silicon is best known for its oxide because of its propensity to oxidize and the remarkable properties of the Si/SiO₂ interface. Yet, oxidation is ill-defined and hard to control. Moreover, modification of chemically stable oxide surfaces mostly involves silanization, typically characterized by disorder and poor chemical stability in solution. The ability to functionalize oxide-free Si surfaces opens new opportunities for a broader range of applications. Precise modification of clean Si surfaces in an ultra-high vacuum environment leads to interesting chemistry but is not widely applicable. In contrast, wet chemical preparation of well-defined H-terminated Si surfaces provides a platform for both fundamental science and further applications. Much work has been done to functionalize H/Si using well known chemical procedures, such as UV- or catalyst-induced hydrosilylation with alkene molecules or halogens followed by Grignard chemistry. Relatively little attention has been placed on the role of structure in H-terminated surfaces for selective modification. Yet, just as structure is important in etching, it also plays a role during chemical modification of surfaces, as illustrated by the reaction of ammonia on stepped Si(111) surfaces.¹ Understanding the role of structure during HF etching is also critical to devise new methods for expanding the functionality of H-terminated surfaces. This talk illustrates this concept and shows that thermal chemistry is well suited to explore such effects. It discusses, for instance, the use of methoxylation of H-terminated Si(111) surfaces to provide a well-defined template for interesting surface chemistry and a broader range of functionalization,² such as the grafting of phosphonates, amines, and metal complexes.

¹ Dai, M., Y. Wang, J. Kwon, M.D. Halls, and Y.J. Chabal, *Nitrogen interaction with hydrogen-terminated silicon surfaces at the atomic scale*. *Nature Materials* **8**, 825 (2009).

² Michalak, D.J., S.R. Amy, D. Aureau, M. Dai, A. Esteve, and Y.J. Chabal, *Nanopatterning Si(111) surfaces as a selective surface-chemistry route*. *Nature Materials* **9**, 266 (2010).

5:20pm **SS+EM-WeA11 Wet Chemical Approach for Amino Functionalization of Oxide-free Si(111) Surfaces**, *T. Peixoto, P. Thissen, Y.J. Chabal*, University of Texas at Dallas

The ability to functionalize H-terminated Si surfaces with NH₂ groups is crucial for a number of applications, such as biomedical (bio-sensors), solid diffusion barrier films, single electron devices, MOSFETs and MEMS. The Si-N bond provides a versatile functionality for chemical modification.

Although the creation of a well-defined and stable interface for the Si-N bonds has remained elusive, chlorosilanes have been shown to easily react with gas-phase or liquid ammonia and primary and secondary amines to achieve a stable silicon nitride bond¹.

For fluorosilane surfaces, we have performed DFT calculations indicating that the kinetic barrier for the NH₃ reaction with Si-F surfaces is only slightly higher than for Si-Cl surfaces, suggesting the reaction should occur at moderate temperatures (<70°C). The 1/3 ML Si-F and 2/3 ML Si-H nanopatterned model surface has a tailorable distance between Si-F groups (from 6.8 Å for 1/3ML to 3.9 Å at higher coverages) allowing the adsorption mechanism to be investigated in detail (and evaluated by DFT calculations) and the role of NH_x-NH_x interactions explored. We further show that the Si-F surface reacts with amino containing molecules (NH₂-R-NH₂), as evidenced by the reaction between Si-F and ethylenediamine at room temperature. Using these reactions we demonstrate that the amidation for the nanopatterned surface takes place for both small molecules (NH₃) and larger amino chains (NH₂-CH₂-CH₂-NH₂) with similar kinetics. The surfaces were characterized using Fourier-transform infrared spectroscopy (FTIR) and x-ray photoelectron spectroscopy (XPS) to verify reaction mechanisms.

These results provide a fundamental understanding of the amidation reaction mechanism for achieving stable Si-N bonds using fluorosilanes surfaces. Achieving a well-defined and stable Si-N interface is significant for a number of important technological applications.

References:

[1] Tian, F.; Taber, D.F.; Teplyakov, A.V. *J. Am. Chem. Soc.* **2011**, *133*, (20769)

[2] Michalak, D. J.; Amy, S. R.; Aureau, D.; Dai, M.; Esteve, A.; Chabal, Y. *J. Nat. Mater.* **2010**, *9*, (266).

5:40pm **SS+EM-WeA12 Ammonia- and Amine-based Chemical Modification of Silicon Surfaces**, *A.V. Teplyakov*, University of Delaware

Stable silicon-nitrogen bonds on surface of single crystalline silicon substrates can serve a variety of practical purposes. The main problem is that creating and controlling the formation of these bonds is done predominantly in the controlled ultra-high vacuum conditions. Here the formation of stable Si-N-based interfaces will be compared for vacuum procedures and for the wet chemistry-based methods. A number of compounds, including ammonia, amines, azides and nitro- and nitroso-compounds, dosed onto a clean silicon surface can yield stable Si-N bonds. However, designing surface reactions leading to contaminant-free interfaces that contain these bonds by wet chemistry methods has been a challenge. We will use multiple spectroscopy and microscopy techniques supplemented by density functional theory investigations to build interfacial systems based on Si-N bonds with ammonia and amines reacting with Cl-covered single crystalline silicon surfaces in a solvent at room temperature. Further transformations of the produced functionalized surfaces will also be discussed.

Surface Science

Room: 21 - Session SS-WeA

Catalysis on Metals and Alloys

Moderator: G. Fisher, University of Michigan

2:00pm **SS-WeA1 A Novel MoS_x Structure with High Affinity to Adsorbate Binding**, *D.Z. Sun, W.H. Lu*, University of California Riverside, *D. Le*, University of Central Florida, *Q. Ma*, University of California Riverside, *M. Amanpour*, University of Central Florida, *S. Bobek, J. Mann*, University of California Riverside, *T. Raman*, University of Central Florida, *L. Bartels*, University of California Riverside

MoS₂ is a semiconducting material consisting of sulfur-molybdenum-sulfur tripledecker layers loosely bound by van der Waals interactions. Single layer MoS₂ can be exfoliated mechanically similar to graphene. This presentation shows an alternative avenue for the fabrication of MoS₂ monolayers at comparatively low temperature and mild conditions through sulfur loading of a copper substrate using thiophenol followed by the evaporation of Mo atoms and annealing. Here we also demonstrate that another MoS_x structure can be formed in this fashion, which has a far higher affinity to adsorbate interaction. Using anthraquinone and formic acid as test molecules, we titrate the various MoS_x and copper-based structures presented on our substrate in order to determine the relative strength of adsorbate interaction.

* Medard W. Welch Award Winner

2:20pm **SS-WeA2 Atomic-Scale Determination of the Crystallographic Stacking at the Technologically-Important Cobalt-Copper Interface**, *E.A. Lewis, C.H. Sykes*, Tufts University

The deposition of Co on Cu has been studied extensively due to the use of layered Co/Cu systems in giantmagnetoresistance devices and the application of magnetic Co nanostructures in spintronics. Co deposited on Cu follows a Volmer-Weber type growth mechanism, forming bilayer-high, triangular islands. These islands grow in two orientations that are rotated 60° with respect to each other. The formation of triangular islands is dictated by the six-fold symmetry of the underlying Cu lattice, and triangular growth is preferred to hexagonal growth due to favored diffusion of Co from the (100) to the (111) facet of the islands during deposition. The consequence of this diffusion is that there must be a difference in the crystallographic packing between the two orientations of the islands. It is thought that one packing configuration of the Co islands is fcc, in which Co follows the stacking of the underlying Cu, but the second packing structure is still debated. Here we use low-temperature scanning tunneling microscopy to explore the stacking of these islands through adsorption of hydrogen on their surfaces.

Hydrogen adsorbs dissociatively on Co, and prefers to bind to fcc three-fold hollow sites, although it is calculated that there is only a 0.01 eV difference in the binding energy of hydrogen to fcc hollows vs. hcp hollows. We show that at 80 K, hydrogen is present on the Co surface in both adsorption sites, and that there is an electronic difference between the two states that is apparent in our STM images. Through high-resolution imaging of the hydrogen at the boundary between the two adsorption sites, we have been able to deduce the stacking of the underlying Co island lattice. We confirm that the majority orientation of the islands is indeed fcc stacking, and the minority of the islands follow Co's native hcp stacking. This has important ramifications in the development of Co/Cu/Co systems for GMR devices, as the interface between the two metals can significantly affect electron scattering.

2:40pm **SS-WeA3 Understanding the Growth and Surface Activity of Oxide-supported Bimetallic Clusters**, *R.P. Galhenage, H. Yan, A. Duke, K. Xie, D.A. Chen*, University of South Carolina **INVITED**

The nucleation, growth and surface composition of bimetallic clusters on titania have been investigated as model systems for understanding how surface chemistry can be controlled by bimetallic composition and interactions between the clusters and the oxide support. Specifically, we have focused on Au-based bimetallic systems (Au-Pt, Au-Ni, Au-Co) as well as Co-Pt systems. Scanning tunneling microscopy studies demonstrate that bimetallic clusters can be formed via sequential deposition when there is a difference in mobility between the two metals; the more mobile atoms (i.e. Au) can be nucleated at existing Ni, Pt and Co clusters. The surfaces of the Au-containing bimetallic clusters are almost pure Au at Au compositions greater than 50% due to the lower surface free energy of Au compared to other metals. In contrast, the Co-Pt clusters are rich in Pt despite the lower surface energy of Co. In the Au-containing bimetallic clusters, CO and methanol adsorbates induce diffusion of Pt and Ni to surface, whereas this effect is not observed for CO on Au-Co. The activity of these model surfaces have been studied in a prototype recirculating loop microreactor.

4:00pm **SS-WeA7 Synchrotrons, Catalysts and UOP: from Imaging to In Situ Spectroscopy**, *S.R. Bare*, UOP LLC, a Honeywell Company **INVITED**

The characterization methods available at today's synchrotron light sources are ideally suited to unravel the complexity of a practical working catalyst. This will be illustrated using examples from our work using a combination of synchrotron techniques including: (i) X-ray micro- and nano-tomography, (ii) X-Ray microprobe fluorescence and X-ray microprobe absorption fine structure (XAFS), and (iv) in situ XAFS combined with density functional theory (DFT) and DFT/MD calculations. Indeed, the use of in situ XAFS is now an integral catalyst characterization technique at UOP. The method provides detailed element-specific atomic-level structural and chemical information of the active catalyst. Often this information cannot be obtained by any other method. We have developed and implemented the appropriate equipment to allow these in situ studies to be performed. This equipment ranges from a plug flow reactor that operates at high pressure, to equipment that allows rapid collection of XAFS data from multiple samples simultaneously. These reactors are coupled to an automated gas manifold combined with on-line product analysis. Examples of our recent work will be presented. Each example will highlight a different aspect of the use of in situ XAFS in an industrial research environment. These examples will include in situ sulfidation of experimental hydroprocessing catalysts, and operando XAFS of rhenium-based catalysts. The talk will end with a look to the future.

4:40pm **SS-WeA9 Glycolaldehyde as a Probe Molecule for Biomass-derivatives**, *W. Yu, M. Barteau, J. Chen*, University of Delaware

Controlling the activity and selectivity of converting biomass-derivatives to syngas (H₂ and CO) is critical for the utilization of biomass feedstocks as renewable sources for chemicals and fuels. One key chemistry in the conversion is the selective bond scission of the C-OH and C=O functionalities, which are present in many biomass-derivatives. Because of the high molecular weight and low vapor pressure, it is relatively difficult to perform fundamental surface science studies of C6 sugars, such as glucose and fructose, using ultrahigh vacuum (UHV) techniques. Glycolaldehyde (HOCH₂CH=O) is the smallest molecule that contains both the C-OH and C=O functional groups, as well as the same C/O ratio as C6 sugars, and thus is selected as a probe molecule in the current study to determine how the presence of the C=O bond affects the reaction mechanism. Using a combination of density functional theory calculations and experimental measurements, our results indicate that the reaction pathway of glycolaldehyde to produce syngas can be enhanced by supporting monolayer Ni on a Pt substrate, which shows higher activity than either of the parent metals. Based on the comparison of the activity and reaction intermediates of ethylene glycol and glycolaldehyde, the presence of the C=O functionality enhances the activity on the Pt(111) surface. On the other hand, for surfaces with high activity toward the O-H bond scission, such as NiPtPt(111), the presence of C=O does not significantly affect the activity or reaction pathway of C2 oxygenates. Furthermore, the Pt substrate can be replaced by tungsten monocarbide (WC) to achieve similar activity and selectivity, indicating the possibility of using Ni/WC to replace Ni/Pt as active and selective catalysts with higher stability and lower cost.

5:00pm **SS-WeA10 Modifying Selectivity of Hydrocarbon Conversion Reactions by Alloying Sn and Pt: Benzene Formation from Acetylene**, *X. Yang*, Princeton University, *J. Gao, S. Podkolzin*, Stevens Institute of Technology, *B. Koel*, Princeton University

Bimetallic catalysts involving Sn and Pt have important applications in hydrocarbon conversion catalysis. We have performed experiments probing chemisorption and reaction kinetics on well-defined, ordered Pt-Sn surfaces in order to aid developments needed for improving catalyst selectivity and overall performance. One specific example from investigations of benzene formation from acetylene on Pt-Sn alloys with HREELS, TPD, and DFT calculations will be discussed. On Pt(111), $\mu_3\text{-}\eta^2$ -acetylene chemisorbed in a three-fold site is the most stable configuration, as indicated by DFT calculations, and has a C-C stretching frequency (ν_{CC}) of 1310 cm⁻¹. This configuration becomes less thermodynamically favorable in the presence of Sn compared to the bridge-bonded $\mu_2\text{-}\eta^2$ configuration ($\nu_{CC} = 1495$ cm⁻¹). The ν_{CC} peaks at ~1600 cm⁻¹ are assigned to π -bonded acetylene, which dominate the spectra collected at 90 K. Absence of three-fold Pt sites on the Pt₂Sn alloy inhibits the transformation of acetylene to CCH₂, and the ν_{CC} peak at 1412 cm⁻¹ assigned to CCH₂ appears only in the spectra of the Pt₃Sn alloy. DFT calculations show that the destabilizing effect of Sn alloying is more significant for CCH₂ and CCH + H than for acetylene. This change in relative stability increases the barrier for acetylene decomposition and makes associative reactions more likely. Results from DFT calculations indicate that benzene formation on the Pt-Sn alloys proceeds through the formation of an upright cyclic C₄H₄ intermediate, which is predicted to produce benzene by reacting with an additional surface acetylene. This closely integrated experimental-computational study has enabled us for the first time to characterize the adsorption modes of acetylene on Pt-Sn alloys. In addition, we developed a molecular level reaction mechanism for benzene formation by consolidating HREELS and TPD experimental results with DFT calculations. The presence of Sn changes the preferential adsorption sites for hydrocarbons, decreases the stability of adsorbed species to varying degrees, and favors associative reactions, thus, enabling benzene production by cyclotrimerization of acetylene.

B.E.K. acknowledges support by NSF Grant No. CHE-1129417.

5:20pm **SS-WeA11 Composition Spread Alloy Films for Study of Alloy Catalysis Across Composition Space**, *A.J. Gellman, B. Fleutot, P. Kondratyuk, J.B. Miller, G. Gumuslu*, Carnegie Mellon University

Composition spread alloy films (CSAFs) are alloy libraries that contain a continuous distribution of alloy compositions (A_xB_{3-x}C_{1-x-y}). Spatially resolved measurements of catalytic reactivity across CSAF libraries map catalytic reactivity as function of alloy composition. In many implementations CSAFs span continuous regions of ternary alloy composition space, but not the entire composition space. We describe the design and implementation of a method for deposition of a 1x1 cm² CSAF that contains all possible compositions of a ternary alloy (A_xB_{3-x}C_{1-x-y} with x = 0 → 1 and y = 0 → 1-x), all three binary alloys (A₂B_{1-x}, A₃C_{1-x}, and B_xC_{1-x} with x = 0 → 1) and all three pure component species. These CSAFs can be characterized using a number of methods including energy dispersive spectroscopy, electron back scatter diffraction, x-ray photoemission spectroscopy, and low energy ion scattering spectroscopy. The bulk

structure of $\text{Cu}_x\text{Pd}_{1-x}$ binary CSAFs matches that of the bulk phase diagram. XPS and LEISS show that the surface is enriched in Cu across the entire composition space. The catalytic reactivity of $\text{Cu}_x\text{Pd}_{1-x}$ binary CSAFs a $\text{Cu}_x\text{Au}_y\text{Pd}_{1-x-y}$ ternary CSAF have been mapped across composition space using a 100 channel microreactor array. The reactivity changes with bulk composition can be correlated to the electronic structure of the alloys. The suite of methods allows a comprehensive study and understanding of alloy catalysis across composition space.

5:40pm **SS-WeA12 Role of Dissociated Hydrogen in Stabilizing Catalytic Sites and Regulating Surface Reactions for Hydrogen Storage in Metal Hydrides**, *I. Chopra*, University of Texas at Dallas, *S. Chaudhuri*, Washington State University, *J.-F. Veyan*, *Y.J. Chabal*, University of Texas at Dallas

There has been an ongoing quest to find cheaper hydrogen activation routes based on aluminum. Recently it was shown that aluminum doped with very small amounts of Ti can activate molecular hydrogen at temperatures as low as 90K. The method is based on the ability to introduce a high flux of molecular hydrogen seeded with a guest molecule (CO) to probe the catalytic activity and H_2 dissociation. Once dissociated, hydrogen forms a complex with adsorbed CO (CO-H), characterized by a substantially and uniquely blue-shifted CO internal frequency.

We use this new method to determine that Titanium when present on the surface is catalytically more active (~30%) than subsurface Titanium. Dissociated hydrogen stabilizes Ti on the surface and as the surface becomes saturated with hydrogen it is possible for Ti atoms sitting in originally sub surface configurations to be pulled out of their original positions by the dissociated hydrogen into surface configurations. These "pulled" Ti atoms then contribute towards additional hydrogen activation when Ti is present in specific (nearest neighbor and next nearest neighbor) configurations.

Finally we show that this dissociated hydrogen protects the CO in the CO-H complex from additional reactions as is demonstrated by no isotopic exchange between CO16 and CO18. Dissociated hydrogen is present in the hollow sites around the Ti and protects the Ti-Al back-bond from further chemical activation. Similar experiments performed on surfaces with no hydrogen (Al/Ti, AlO/TiOx) show isotopic exchange reactions between CO16 (of the complex) and adsorbed CO18. The barrier for this isotopic exchange is the lowest for adsorbed CO on TiOx (desorption temperature ~140K) and highest for CO on Ti (desorption temperature ~300K).

These results provide critical information about the role of dissociated hydrogen in stabilizing Ti catalytic sites and the CO-H complex. A complete understanding of such mechanisms will help enhance material performance for hydrogen activation using cheap catalyst materials.

References:

[1] Chopra, I. S., Chaudhuri, S., Veyan, J.-F., and Chabal, Y. J., *Nature Materials*, 10, 884–889 (2011)

Transparent Conductors and Printable Electronics

Focus Topic

Room: 7 - Session TC+EM+AS-WeA

Printable and Flexible Electronics

Moderator: G.S. Herman, Oregon State University

2:00pm **TC+EM+AS-WeA1 Metal Oxides and Organic Materials for Printed Electronics**, *A. Facchetti*, Polyera Corp. and Northwestern U. **INVITED**

Printed electronics is a new technology envisioning the fabrication of electronic devices using printing methodologies instead of conventional photolithography employed in the silicon industry. Metal oxide- and organic-based materials will be key players for this technology. In this presentation I will discuss our latest results in developing new printable organic semiconductors. Furthermore, I will describe amorphous and polycrystalline metal oxide formulations in which the corresponding films can be annealed at temperatures < 250 °C. For instance, solution-processed amorphous tin-doped indium oxide (ITO) films for TFT fabrication at temperatures < 250 °C can be achieved by controlling film precursor solution In^{3+} vs. Sn^{4+} molar ratio resulting in electron mobilities $> 2 \text{ cm}^2 \text{ V}^{-1} \text{ s}^{-1}$ and $\sim 20 \text{ cm}^2 \text{ V}^{-1} \text{ s}^{-1}$ for TFTs using SiO_2 and a self-assembled nanodielectric (SAND) as the gate dielectrics, respectively. Finally, a new general strategy for

fabricating solution-processed metal oxide TFTs at dramatically lower temperatures (as low as 200 °C for all TFT electrical components) using self-energy generating combustion chemistry will be presented. Our results show that by tuning the gate dielectric-semiconductor interface dramatically enhances performance, yielding In_2O_3 , IZO, IZTO, and IGZO /amorphous alumina gate dielectric TFTs having electron mobilities of 40 cm^2/Vs and 13 cm^2/Vs at $T_{\text{anneal}} = 250 \text{ °C}$ and 200 °C, respectively.

2:40pm **TC+EM+AS-WeA3 Ion Dependence of Gate Dielectric Behavior of Beta-Aluminas in Transparent Oxide Field-Effect Transistors**, *Y. Liu*, *B. Zhang*, *H.E. Katz*, Johns Hopkins University

Sodium beta-alumina (SBA) is an excellent gate dielectric material which can be used in low-voltage (2 V), solution-processed transparent oxide field-effect transistors (FETs). Sodium ions have been experimentally proved to be the origin of the high capacitance observed in SBA gate dielectric. With this discovery, the investigation of dielectric properties of alumina with the incorporation of other alkali metal ions (for example K^+ , Li^+) becomes compelling.

High field-effect mobility (about 20 $\text{cm}^2 \text{ V}^{-1} \text{ s}^{-1}$), high saturation drain current (about 1 mA), and small subthreshold swing (about 200 mV/decade) were achieved in low-voltage (2 V), spin-coated zinc-tin-oxide (ZTO) FETs with potassium beta-alumina (PBA) and lithium beta-alumina (LBA) dielectrics. This proves that the incorporation of alkali metal ions in beta-aluminas is a general route to reduce operation voltage of transistors while achieve excellent electrical performance.

To investigate the effect of alkali metal ions on beta-alumina capacitance, beta-alumina Metal-Insulator-Metal (MIM) capacitors (PBA, LBA, and SBA) were analyzed in a frequency range from 100 Hz to 1 MHz. A tendency for beta-alumina capacitance to increase with increasing atomic number of alkali metal ions was observed. Besides, beta-alumina capacitance was found to decrease as temperature increases and LBA showed the strongest temperature dependence of capacitance. Moreover, capacitance of beta-aluminas with different thickness was measured and they were independent of thickness. With these results, electric double layer (EDL) structure was proposed as one way to explain the high capacitance of beta-alumina dielectrics. Ion exchange experiments showed significant diffusion of both lithium ion and potassium ion between PBA and LiNO_3 solution; however, a high concentration difference did not seem to cause obvious diffusion of either lithium ion or potassium ion between LBA and KNO_3 solution. This selective ion exchange behavior in beta-aluminas showed that the Al_2O_3 matrix structure would be affected by the alkali metal ions incorporated, and/or that Li ions are much more strongly bound. Thus, varying intercalated ion types and concentrations can be a means of tuning frequency-dependent capacitance of alumina films.

3:00pm **TC+EM+AS-WeA4 Selection Rule of Preferred Doping Site for N-Type Transparent Conducting Oxides**, *S.-H. Wei*, National Renewable Energy Laboratory, *C. Li*, *J.B. Li*, Institute of Semiconductor Physics, CAS, China

Traditionally, it is believed that the conduction band edges of d^0 or d^{10} oxides are derived mostly from cation s states, thus doping on anion sites is expected to cause less perturbation and produce shallow donor levels in these materials. Using first-principles calculations, we show that although this paradigm is applicable for more covalent oxides such as SnO_2 where F_0 is a better n-type dopant than Sb_{Sn} , for more ionic oxides such as ZnO , the conduction band edge actually contains a considerable amount of O s orbitals, thus F_0 in ZnO causes larger perturbation and consequently produces deeper donor levels than cation site doping such as Al_{Zn} . The rule that anion site doping is preferred for more covalent oxides and cation site doping is preferred for more ionic oxides for n-type metal oxides should be general and can be used to guide future study of and search for functional oxide materials.

4:00pm **TC+EM+AS-WeA7 Single-Walled Carbon Nanotube Aerogel Based Elastic Conductors**, *K.H. Kim*, *Y. Oh*, *I. Lee*, *M.F. Islam*, Carnegie Mellon University **INVITED**

Flexible conductors of various shapes and sizes with high electrical stability under large elastic stretching and bending are of significant importance in diverse fields ranging from microelectronics to biological implants. A major roadblock in the development of flexible conductors is the disparity between elastomers and stiff conducting materials used in microelectronics. We have developed a novel scheme to create flexible conductors by completely backfilling a prefabricated conducting porous single wall carbon nanotube (SWCNT) three-dimensional network, called SWCNT aerogel, with an elastic polymer polydimethylsiloxane (PDMS). Our approach allowed us to control SWCNT dispersion quality, and tune shapes, sizes and thicknesses of the SWCNT-aerogel/PDMS composite films to make them transparent. The resistance of our stretchable conductors remains nearly unchanged under repeated stretch-release cycles up to a tensile strain of

100% and high bending strain. We believe that the simple but unique fabrication method can be combined with different types of elastic polymers for different electrical, mechanical or biological demands.

4:40pm **TC+EM+AS-WeA9 Networked Metal Nanowire-Polymer Composites for Flexible, Transparent and Conducting Devices**, S. Narayanan, S. Fu, M.R. Bockstaller, L.M. Porter, Carnegie Mellon University

Transparent conductive metal oxides (TCOs) exhibit inherent disadvantages such as limited supply, brittle mechanical properties, expensive processing that present major barriers for the more widespread economic use in applications such as flexible transparent conductors. A promising alternative route towards flexible, transparent conductive materials is based on silver nanowire network structures, which can be easily processed from solution. We report a systematic analysis of the effect of nanowire geometry and solution processing on the network characteristics of nanowire deposits, and the associated electronic and optical properties of silver nanowire-based transparent electrodes. Ag nanowire (of average diameter ~100 nm) films drop-cast from solution were shown to exhibit bulk-like electrical conductivity (~2-50 Ω /sq) and high transparency (~70-75%). The electrical properties of nanowire networks were found to be sensitive to geometric parameters of the wire assembly that can be interpreted by use of percolation theory. At concentrations below the percolation threshold the sheet resistance increases dramatically, effecting a marked deviation from bulk-like behavior [1]. The dispersion of Ag nanowires in a conducting medium, like that of a conducting polymer was found to significantly reduce nanowire aggregation and thus decrease the percolation threshold. Preliminary results of spun-cast films of composites of these nanowire networks with PEDOT:PSS show higher transmittances (~79-82%) with similar conductivities (~10-170 Ω /sq) combined with better film forming properties. The use of composites was found to bring about a consistent improvement in electrical conductivity with very little change in the transmittance. Samples prepared on flexible PET substrates showed no degradation in conductivity on flexing thereby showing ample promise for incorporating flexibility in such structures. Through analysis of microstructural characteristics of these films, a quantitative correlation of the density of nanowires with conductivity and transmittance will be presented. The advantages of using such a composite structure in reducing the percolation threshold will be discussed.

[1] Sukanta De *et al.* ACS Nano 4 12 (2010) 7064-7072

Thin Film

Room: 11 - Session TF+AS-WeA

Thin Films: Growth and Characterization-I

Moderator: M.R. Davidson, University of Florida

2:00pm **TF+AS-WeA1 Studying the Microstructure of Cu₂ZnSn(S,Se)₄ Thin Film Solar Cells**, L. Zhang, Y. Cao, D.H. Rosenfeld, M. Lu, J. Caspar, C. Chan, DuPont Central Research and Development

To advance the next generation photovoltaic technology, the new ink-based Cu₂ZnSn(S,Se)₄ (CZTSSe) solar cells have attracted rapid growth attention in the thin film photovoltaic areas. As a potential alternative to CIGS, the CZTSSe technology offers a non-vacuum based and likely low manufacturing cost process with active area efficiency above 9%. In particular, the fact that CZTSSe utilizes only earth abundant elements enables the sustainability & renewability for future green energy demand.

The overall CZTSSe solar cell developed by DuPont scientists consists of multi-layer inorganic structures of ITO/ ZnO/ CdS / CZT(S,Se) / Mo on sodalime glass substrate. A novel synthetic method has been developed to produce the active CZTSSe layer. During the process, binary and ternary chalcogenide nanoparticles are first synthesized as starting materials, formulated into a precursor ink, applied onto a substrate, and then converted into CZTSSe upon a thermal annealing process. To aid product development for optimum efficiency, chemical and structural characterization of the active CZTSSe layer and interfaces between different layers are performed using multiple analytical techniques. For example, sputter depth profiling with XPS and Auger, and cross-section SEM/EDX helped us to visualize the structural chemistry at specific locations in the films which enabled the team to adjust ink formation as well as processing conditions for better and more efficient cell production. This presentation will cover the characterization of CZTSSe solar cells, including the study of film composition and morphology, inter-layer diffusion, and their correlation with device performance.

2:20pm **TF+AS-WeA2 Seed-Mediated Growth of 1D Pyrite (FeS₂) Structures**, Y.J. Kwon, N. Berry, M. Law, J.C. Hemminger, University of California Irvine

Iron pyrite is a promising semiconductor for use in solar cells due to its earth-abundance, suitable bandgap, and high absorption coefficient. Pyrite device efficiency is only about 3% due to a low open-circuit photovoltage and high dark current, possibly as a result of sulfur deficiency at the surface resulting in thermionic field emission. Although fabrication of pyrite thin films has been studied by various methods, specific details of the pyrite growth process in the presence of homogeneous nucleation sites has not been studied. In this project, the role of pyrite nucleation sites is investigated in the growth of pyrite thin films by atmospheric-pressure chemical vapor deposition (AP-CVD). The pyrite nanoparticle nucleation sites are fabricated by sulfurization of pre-deposited Fe₂O₃ grains on the step edges of highly oriented pyrolytic graphite (HOPG) using H₂S, elemental sulfur or a combination of the two annealing treatments and characterized by transmission electron microscopy (TEM), X-ray photoelectron spectroscopy (XPS), X-ray diffraction (XRD) and Raman spectroscopy. H₂S-sulfurized Fe₂O₃ nuclei coalesce to form FeS₂ nanowires containing both pyrite and marcasite phases. A subsequent elemental sulfur treatment on either H₂S-sulfurized samples or pre-deposited Fe₂O₃ samples yield pure pyrite; however, the nanowires convert to a less desirable morphology of randomly sized spherical grains as a result of this annealing treatment. Atmospheric Pressure-CVD of FeS₂ from iron-(III) acetylacetonate and *tert*-butyl disulfide was performed to grow pyrite on these seeded substrates. Initial deposition on the H₂S-annealed samples leads to only seed-mediated growth and the formation of linear arrays of polycrystalline FeS₂ nanowires. However, due to marcasite phase presence on pre-covered FeS₂ nanoparticle seeds, both marcasite and pyrite phases could be observed. Initial deposition on elemental sulfur treated samples with pure pyrite phase showed deposition occurring throughout the substrate. No preferential growth on seeded pyrite nucleation sites was observed. It is proposed that during elemental sulfur treatment, new nucleation sites form, leading to deposition covering the substrate. Further work is in process to clearly determine or identify the growth mechanism of pyrite. In this work, we will gain a greater understanding of early stages of pyrite growth process in the presence of homogeneous nucleation sites.

2:40pm **TF+AS-WeA3 Investigation of Recrystallization in Low-Temperature Grown CdTe Solar Cells in Substrate and Superstrate Configuration**, L. Kranz, C. Gretener, J. Perrenoud, S. Buecheler, A.N. Tiwari, EMPA, Switzerland **INVITED**

CdTe solar cells and modules on glass substrates have already shown high performance and low cost. Production costs and energy payback time can be further reduced by minimizing the thermal budget of the production process, increasing the throughput and by the use of low-cost substrates. We developed a process for the conventional superstrate configuration which involves substrate temperatures below 450°C. The low temperatures enable the growth on flexible polyimide foil. Efficiencies up to 15.6% and 13.8% on glass and polyimide were achieved, respectively.

In the conventional superstrate configuration sputtered ZnO:Al/ZnO was used as transparent front electrical contact. CdS and CdTe were evaporated at low temperatures of 160 and 350°C followed by an annealing treatment in the presence of CdCl₂ at 420°C and the cells were finished with a metallic electrical back contact. The annealing treatment is essential for highly efficient CdTe solar cells as it leads to grain growth of CdTe, improves electronic properties of CdTe and leads to an intermixing between CdTe and CdS.

For the growth on opaque substrates like flexible metal foils, we developed a growth process of CdTe solar cells in substrate configuration, where light does not need to pass the substrate. It enabled efficiencies of 11.3% and 8.7% on glass and flexible steel foil, respectively.

A combination of Mo, MoO₃ and Te was deposited as back contact and in some cases Cu was added. Evaporated MoO₃ grew with low crystallinity and recrystallized during subsequent processing. CdTe was deposited by vacuum evaporation while CdS was grown by chemical bath deposition. In substrate configuration, the CdTe and CdS layers were annealed separately as a combined annealing step would lead to excessive CdS-CdTe intermixing. The annealing treatment of the CdTe layer leads to similar grain growth as in superstrate configuration. The CdCl₂ treatment after deposition of CdS was optimized, resulting in increased grain size and wurtzite structure. CdS-CdTe intermixing, which is commonly observed in superstrate configuration was less pronounced in substrate configuration. The effects of the recrystallization treatments in substrate configuration are compared to the conventional superstrate configuration.

4:00pm **TF+AS-WeA7 High Quality ZnMgO Thin Films Grown on Sapphire and ZnO Substrates by Molecular Beam Epitaxy**, *M. Wei, R.C. Boutwell, W.V. Schoenfeld*, University of Central Florida

Zinc oxide (ZnO) based material is attractive for high efficiency ultraviolet (UV) optoelectronics devices. We will report growth of high quality ZnMgO on both sapphire and ZnO substrate by plasma-assisted molecular beam epitaxy (MBE). With relatively low growth rate and optimized growth condition, we were able to achieve step flow growth of ZnO thin films. ZnO thin films grown on sapphire showed high crystalline quality, low carrier concentration, high mobility and sub-nanometer surface roughness with terrace steps, indicating suitability for UV application. Homoepitaxial ZnO films were grown on both c-plane and miscut ZnO substrates with atomically flat surface, no threading dislocation and same crystallinity as the substrate. Ga doping was demonstrated for ZnMgO films on sapphire and ZnO substrates. This work may lead to the realization of high efficient UV emitters such as Laser diodes.

4:20pm **TF+AS-WeA8 Epitaxial Growth of Zirconium Dioxide Thin Film on Ge(111) Wafer**, *C. Hubault, A. Baba, A. Fleurence, Y. Yamada-Takamura*, Japan Advanced Institute of Science and Technology

GaN-based semiconductors are widely used in optoelectronic devices. To grow these films, substrates such as sapphire, SiC and Si are used. However, recently, Lieten *et al.* [1] have proposed to grow GaN on Ge(111) substrate to have a more closely matching thermal expansion coefficient and to decrease the lattice mismatch. Despite the good quality of the film, misoriented domain and voids can be found in it. While the domains can be suppressed, the voids cannot, as they come from a diffusion of Ge atoms in the film. This is a problem for the growth of p-type or semi-insulating GaN layers.

Using ZrB₂ as a buffer layer on Ge substrate could help by providing a diffusion barrier. Moreover, ZrB₂ substrate has already been used as a conductive growth template for GaN and has proven to be interesting thanks to the low lattice mismatch and close in-plane thermal expansion coefficient [2]. Therefore, ZrB₂ has been used as a buffer layer for the growth of GaN films on Si wafer [3] and those films were shown to be promising.

It was also demonstrated that on top of ZrB₂(0001) thin film on Si(111) substrate, silicene, which has a similar structure to graphene was present [4]. In the periodic table, C, Si and Ge are in the same column. Therefore, we can envisage the possibility of the formation of germanene in the same manner as silicene on top of the ZrB₂ layer grown on germanium substrate.

Here, we report on the epitaxial growth of ZrB₂ thin films on Ge(111) by thermal decomposition of Zr(BH₄)₄ in a dedicated UHV-chemical vapour deposition system. The growth was monitored *in situ* by RHEED, and the samples were further analysed by XRD and TEM. The film grows with epitaxial relationship of ZrB₂(0001)//Ge(111). Under slow growth conditions (substrate temperature, Ts=750°C), two types of in-plane orientations, which are rotated by 30° can be observed, while under faster growth condition (Ts=650°C), the layer is monocrystalline. The single-crystalline film has in-plane orientation of ZrB₂[11-20]//Ge[-110], similar to the case of single-crystalline ZrB₂ film on Si(111) [4], but with a different surface reconstruction of ($\sqrt{3}\times\sqrt{3}$) when cooled down under 450°C. There is a good epitaxy between the layer and the substrate with the presence of a second phase at the interface, which tends to disappear when the growth was carried out at 550°C.

[1] R.R. Lieten *et al.*, *J. Cryst. Growth*, 314, 71 (2011).

[2] H. Kinoshita *et al.*, *Jpn. J. Appl. Phys.*, 42, 2260 (2003).

[3] Y. Yamada-Takamura *et al.*, *Phys. Rev. Lett.*, 95, 266105 (2005).

[4] A. Fleurence *et al.*, *Phys. Rev. Lett.*, accepted for publication.

4:40pm **TF+AS-WeA9 Effect of Growth Conditions on Cubic ZnMgO films**, *C. Boutwell, M. Wei, W.V. Schoenfeld*, University of Central Florida

ZnMgO films were grown on MgO substrates by Plasma-Enhanced Molecular Beam Epitaxy. Epilayer morphology, stoichiometry, and crystalline orientation were investigated. Films were produced by varying cation source temperature/flux, substrate temperature, and oxygen plasma power and flow rate. Crystalline immiscibility was determined in the phase mixed cubic/wurtzite range. Growth rate varied from 30nm/hr to 175nm/hr while roughness varied from 4nm to 110nm in cubic to mixed-phase samples. Wurtzite ZnO peaks at (002) and (101) were apparent from θ -2 θ X-Ray Diffraction on phase separated films, indicating multiplanar ZnO crystalline growth on the (001) MgO substrate. Growth condition information will be useful for optimization of optoelectronic devices functional in the deep ultraviolet/solar-blind range.

5:00pm **TF+AS-WeA10 Properties of Ytterium Doped Zinc Oxide Thin Films Deposited by r.f. Magnetron Sputtering**, *K. VanSant, T. Barnes, J. Burst, J. Duenow, T.A. Gessert*, National Renewable Energy Laboratory

Transparent conducting oxides (TCOs) based on zinc oxide (ZnO) and aluminum (Al) doped ZnO (AZO) are important for many large-scale commercial applications because they exhibit good optical and electrical properties. Further, their constituent elements are non-toxic and abundant, and high-quality thin-films can be deposited at room temperature using a variety of deposition processes. These characteristics make AZO appealing for use as part of the top contact in copper indium gallium diselenide (CIGS) PV modules. Although the present generation of ZnO-based TCOs meet many of the technical requirements of present-generation technologies, it is known that the material could be much more widely applied if some of its properties were more consistent with another important TCO, In₂O₃:Sn (i.e., ITO). In this comparison, the main properties requiring improvement include increasing the mobility from ~20 to ~50 cm² V⁻¹ s⁻¹ while maintaining carrier concentrations > 5x10²⁰ cm⁻³ and improving the moisture-tolerance of the films. Earlier work has already shown that AZO with mobility approaching 50 cm² V⁻¹ s⁻¹ can be achieved by careful control of the sputtering ambient and the dopant concentration. This study investigates the use of the Group IIIA material yttrium (Y) as a dopant, as well as the impact it has on the optical properties of ZnO. The Y-doped ZnO films are deposited on glass by r.f. magnetron sputtering using pressed powder targets, and the Y concentration is varied by simultaneous co-sputtering from a ZnO:Y target. The films will be analyzed using a combination of Hall measurements, UV-Vis-NIR spectrophotometry, spectroscopic ellipsometry, and Auger/X-ray photoelectron spectroscopy (XPS) and Secondary Ion Mass Spectrometry (SIMS). Based on prior research related to the addition of zirconium (Zr) to ITO, it is suspected that the addition of Y in ZnO may lead to similar changes in the optical properties of this material. Understanding the functionality of these changes could have significant implications for device applications requiring greater control of the dielectric properties of ZnO.

5:20pm **TF+AS-WeA11 Effect of Process Parameters on Molybdenum Thin Films and Development of Single Layer Molybdenum Film for CIGS Thin Film Solar Cells**, *S. Pethe, A. Kaul, N. Dhere*, Florida Solar Energy Center, University of Central Florida

Molybdenum back contact in CuIn_{1-x}Ga_xSe_{2-y}S_y (CIGSeS) solar cells is usually deposited using DC magnetron sputtering. Properties of thin films are dependent on process parameters. Films deposited at high power and low pressure, tend to be more conductive. However, such films exhibit poor adhesion strength since the films are under compressive stress. Films deposited at low power and high pressure tend to be under tensile stress and exhibit higher roughness and resistivity, while the films adhere very well to the sodalime glass substrate. Therefore, it has been a practice to deposit multi-layered Mo back contact to achieve properties of good adhesion and higher conductivity. Deposition of multi-layered back contact results in either increase in deposition time if a single target is used or increase in footprint if multiple targets are used resulting in increase in the total cost of production. Experiments were carried out to understand effects of working pressure, sputtering power and working distance on molybdenum film properties with the final aim to develop a process recipe for deposition of a single molybdenum film with acceptable properties of both good adhesion and higher conductivity. Experiments were carried out at a fixed working distance by varying the working pressure and keeping the sputtering power constant and then varying the sputtering power keeping the working pressure constant. The same set of experiments were repeated with varying working distance. Moreover, the effect of the relative position of the substrate with respect to the sputtering target for a moving target was studied. Adhesive tape test was performed on each film to determine the adhesion strength of the films. Moreover, the sheet resistance and the average roughness for each film were measured using a four probe measurement setup and the Dektak Profilometer, respectively. All experiments were also carried out on narrow and long glass strips in order to estimate the residual stress in the film by using the bend test method. Based on the results obtained from the experiments carried out a process recipe was developed for depositing on a moving substrate, a single layer molybdenum film with acceptable properties of good adhesion and higher conductivity.

5:40pm **TF+AS-WeA12 Oxygen Reservoir Effect and its Impact on HfO₂**, *C. Vallee, C. Mannequin, P. Gonon, L. Latu-Romain*, LTM (CNRS / UJF-Grenoble1 / CEA), France, *A. Salatin, H. Grampeix, V. Jousseau*, CEA, LETI, MINATEC Campus, France

ReRAM device is a non-volatile memory based on resistive switching phenomena in a dielectric in a MIM (Metal Insulator Metal) structure. Depending on the nature of the oxide and the metallic electrode, the switching is based on a unipolar thermochemical mechanism (TCM), a

bipolar valence change mechanism (VCM), as well as a bipolar electrochemical metallization mechanism (ECM). For all these devices, the choice of the oxide (nature, crystallization, density, doping, vacancies), the metal (inert electrode, its free energy formation of the oxide) as well as the interfacial layer (role of the electrode, role of the process) are impacting the operation sets and reliability of the device. For example, it has been shown that electrode reaction is one of the major factors determining the functionality of ECM cells [1].

This work is focused on HfO₂ based ReRAMs which are good candidates for embedded non-volatile memories [2-4]. For this material, forming/set and reset processes are correlated with the respective generation of oxygen vacancies and recombination of Vo²⁺ positive charges with oxygen ions (O²⁻). It has been recently proposed that during the negative reset the passivation occurs by the back-diffusion of oxygen ions stored in the oxide portion near the conductive filaments and at the electrode, which serve as oxygen reservoir [5].

With this work we propose to discuss on the reservoir effect by studying HfO₂ memories obtained with top electrodes of different chemical compositions and morphologies. The HfO₂ dielectric (10 nm) is deposited by Atomic Layer Deposition on Pt and TiN. X-ray Photoelectron Spectroscopy and Transmission Electron Microscopy characterization have been used to investigate the chemical composition, morphology and crystalline structure of the oxide and metallic layers. It is hence demonstrated that devices with gold deposited by a PVD process give better results than those obtained with gold deposited by evaporation. This can be related to a modification of oxygen diffusion through the top electrode via a difference in the electrode morphology (roughness, thickness...) induced by the process. Moreover, it is shown that alloying the gold target of the PVD process with a suitable metal considerably helps to improve the reliability of the memory. This is discussed in terms of catalytic effect and modification of the electrode morphology and reservoir effect.

- [1] I. Valov *et al*, *Nanotech.* **22** (2011) 254003
- [2] P. Gonon *et al*, *J. Appl. Phys.* **107** (2010) 074507
- [3] J.J. Yang *et al*, *Appl. Phys.* **A102** (2011) 785
- [4] Ch. Walczyk *et al*, *J. Vac. Sci. Technol.* **B29** (2011) 01AD02-1
- [5] S. Yu *et al*, *IEDM* (2011) 17.3.1

Thin Film

Room: 10 - Session TF+MI-WeA

Thin Films for Memory and Data Storage

Moderator: S. Gupta, The University of Alabama

2:00pm **TF+MI-WeA1 Spin Transport Properties and Applications in Magnetic Multilayers**, *R.H. Victora, S.H. Hernandez, T. Qu*, University of Minnesota **INVITED**

Since the discovery of giant magnetoresistance (GMR) in 1988, spin transport has rapidly evolved as a research area examining effects such as Current Perpendicular to Plane (CPP) GMR and spin torque transfer (STT). Giant Magnetoresistance is caused by spin-dependent scattering. High electrical resistance (R_{AP}) is measured for antiparallel magnetizations of adjacent layers, while low resistance (R_P) is measured for parallel magnetizations. CPP GMR shows an advantage in MR ratio ($(R_{AP}-R_P)/R_P$), because all electrons must pass through all layers. This geometry is widely used as the reader in high areal magnetic recording, where it is likely that the current non-magnetic insulator will ultimately be replaced by a metallic layer in order to limit resistance. The reciprocal effect, STT, occurs when an electric current passes through a pinned ferromagnetic layer and the angular momentum (magnetic moment) is transferred to a neighboring free magnetic layer. The magnetization in the free layer may stably oscillate or may achieve a collinear state to the pinned layer. Magnetization switching with the help of a current has been proposed as potential magnetoresistive random access memory (MRAM). However, the mechanism of spin transport is not fully understood for these effects.

We consider multiple reflections between the interfaces of the adjacent magnetic layers. If the ferromagnetic material is not 100% polarized, electrons with different polarizations are not perfectly transmitted or reflected. We show that reflections, although typically neglected, strongly affect the spin transport properties. They explain the experimentally observed nonlinearity of GMR dependence on $\beta = \cos^2(\theta/2)$ (θ is the angle between the magnetizations of the fixed and free layers). Also the spin torque is decreased² by the reflection. The more orders of reflection we include in the spin torque, the more critical current is needed to switch the magnetization state. The spin torque oscillator (STO) is an attractive replacement for current microwave devices owing to its very small

(nanoscale) size. However, a single STO does not provide sufficient power for many applications. An array of oscillators in series or parallel has been proposed to generate more power. The problem is to phase lock the non-uniform oscillators. We calculate the power spectrum of serial oscillators. We show that the oscillators' could be closely synchronized by a feedback ac current, even at room temperature.

- 1. T. Qu and R.H. Victora, *J. Appl. Phys.* **111**, 07C516 (2012)
- 2. S. Hernandez and R.H. Victora, *Appl. Phys. Lett.* **97**, 062506 (2010)

2:40pm **TF+MI-WeA3 Ta Seeded Ultrathin Free Layer for Fully Perpendicular Magnetic Tunnel Junctions**, *A. Singh, A. Natarajarathinam, B.D. Clark, S. Gupta*, The University of Alabama

Studies of the effect of seed and capping layers on CoFeB free layers of magnetic tunnel junctions (MTJ's) originated from reports (1) of the crystallization of the CoFeB through diffusion of the B into the cap, as well as inducing an interfacial perpendicular magnetic anisotropy in the free layer (2, 3). We have also seen that CoFeB can be made perpendicular [3, 4] with seed layers of certain materials, such as Ta and Ru. We deposited Ta and Ru seed layers with the following stack structure: (Ta/Ru/Hf/Zr) 2/[CoFeBx]/MgO 0.9/TaN5 nm. The thickness of CoFeB, tCoFeB, was varied between 0.8 to 1.4 nm. Samples with the Ta seed layer showed higher perpendicular anisotropy than that of Ru, Hf and Zr because of the B diffusion into Ta after annealing. At tCoFeB = 1nm, high perpendicular anisotropy was seen, with anisotropy energy density $K_{ut} = 0.24$ erg/cm². The optimized Ta-seeded CoFeB was used as the free layer in a fully perpendicular MTJ stack with a Co/Pd multilayer synthetic antiferromagnet pinned layer [5]. These MTJ stacks were then patterned into devices with photolithography and planarized at each step of fabrication with a novel sputtered aluminum oxide passivation layer. After fabrication, these devices were subjected to a variety of annealing conditions: a) furnace annealed with a field of 0.5T applied in the plane of the sample at 1500C for 2 hours, b) rapid thermally annealed (RTA) at 3500C, 4000C and 5000C for various time periods. Magnetometry of the minor loops indicated that, as the RTA time was increased at each temperature, the free layer became fully perpendicular at 8 minutes and then went in-plane with longer annealing times of 12 minutes. These results matched closely with the transport measurements. Increase of annealing time improved the tunneling magnetoresistance (TMR) to a maximum of 50% at room temperature (nearly 60% at 4.2K). Further increase in annealing time degraded the TMR at all temperatures tested. Thus for the first time, we have found that magnetometry on the free layer of fully perpendicular magnetic tunnel junctions (pMTJ) can be used to optimize the annealing conditions.

References

- 1. E. Chen *et al.*, *IEEE Trans. Magn.* **46**, 1 (2010).
- 2. S. M. Watts *et al.*, Digest FV-11, 11th Joint MMM-Intermag Conference, Washington, DC(2010)
- 3. D. Worledge *et al.*, Digest HB-10, 11th Joint MMM-Intermag Conference, Washington, DC(2010)
- 4. D. C. Worledge, G. Hu, David W. Abraham, J. Z. Sun, P. L. Trouilloud, J. Nowak, S. Brown, M. C. Gaidis, E. J. O'Sullivan, and R. P. Robertazzi. *Appl. Phys. Lett.* **98**, 022501 (2011).
- 5. A. Natarajarathinam, R. Zhu, P.B. Visscher and S. Gupta, *J. Appl. Phys.* **111**, 07C918 (2012).

3:00pm **TF+MI-WeA4 Epitaxial Fe_{38.5}Pd_{61.5} Films Grown by Pulsed Laser Deposition: Structure and Properties**, *M.A. Steiner, R.B. Comes, J.A. Floro, W.A. Soffa, J.M. Fitz-Gerald*, University of Virginia

Thin films of 3d-4d/5d metallic alloys such as Fe-Pt, Co-Pt, and Fe-Pd are of technological interest due to their ordered L1₀ tetragonal phase which exhibits high magnetocrystalline anisotropy comparable to that of 3d-4f rare earth magnets. A combination of hard magnetic properties with ductility and corrosion resistance makes this family of alloys ideal for applications including micro-electro-mechanical systems and ultra-high-density magnetic storage. These alloys are known to develop unique microstructures, including a novel strain-induced chessboard eutectoid microstructure featuring exchange coupling effects that has been found between the hard L1₀ and soft L1₂ magnetic phases of the Co-Pt system. Within this class of materials, Fe-Pd alloys possess a somewhat lower magnetocrystalline anisotropy compared to Co-Pt and Fe-Pt, but the Fe-Pd phase diagram showing considerably lower order-disorder transition temperatures renders them well-suited for nanostructured magnetic applications and study.

Epitaxial films of Fe_{38.5}Pd_{61.5} at the L1₂-L1₀ eutectoid composition have been grown on MgO 001 oriented substrates by pulsed laser deposition. These films exhibit atomic ordering with increasing temperature, transitioning from the disordered A1 (FCC) phase to the ordered L1₂ phase. Fe_{38.5}Pd_{61.5} films grown at 550°C have been found to possess a two-phase

microstructure of prismatic 50-100 nm disordered Al secondary phases with 110 oriented facets embedded within an ordered $L1_2$ matrix. These secondary phases exhibit single domain magnetic axis rotation, while the easy magnetic axis of the ordered $L1_2$ matrix lies in plane due to strain induced by epitaxy. The growth these two-phase films has been studied as a function of deposition time. The films grown in this study were characterized by x-ray diffraction, vibrating sample magnetometry, atomic and magnetic force microscopy, and high resolution scanning electron microscopy.

Thursday Morning, November 1, 2012

Applied Surface Science
Room: 20 - Session AS-ThM

Applications of Large Cluster Ion Beams

Moderator: A.V. Walker, University of Texas at Dallas,
C.M. Mahoney, Pacific Northwest National Laboratory,
M.L. Pacholski, The Dow Chemical Company

8:00am AS-ThM1 Comparison of Primary Ion Beams for XPS Sputter Depth Profiling of Organic Samples, *S.J. Hutton, C.J. Blomfield, S.J. Page, W. Boxford*, Kratos Analytical Ltd., UK

Several types of cluster ion sources are available aimed at facilitating X-ray Photoelectron Spectroscopy (XPS) sputter depth profiling of organic materials. These ion sources may be categorised as either carbon based sources (e.g. Coronene) or Ar cluster ion sources. Both types of source may be fitted to modern XPS instruments. Experimental parameters such as primary ion voltage, primary ion incidence angle and cluster size may be optimised to improve profiling results. The sample environment may also be controlled to extend the range of polymers which are amenable to sputter profiling. Sample parameters which have been shown to be important include rotation with respect to the ion beam and sample temperature.

In this study we compare the performance of Carbon and Ar based cluster ion sources on a range of organic thin films, from fields as diverse as organic PV materials, OLED's, cross-linked plasma polymers and multilayers. Samples were analysed under a range of sample conditions with both sources. Direct comparison allows the efficacy of ion beams to be rated for a range of sample types.

8:20am AS-ThM2 Molecular SIMS - Revolutionized by Cluster Primary Ion Beams?, *J.C. Vickerman*, The University of Manchester, UK **INVITED**

The introduction of metal cluster and polyatomic primary ion beams had dramatically enhanced the capability of SIMS for the molecular analysis of complex, particularly organic materials. The metal cluster beams, based on gold and bismuth resulted in a very significant increase in ion yield of larger 'molecular' ions in the m/z range above 300. This has enabled significant advances in 2D imaging of bio-systems, although the analysis is still restricted to the static regime. Polyatomic ion beams such as SF₅⁺, C₆₀⁺ and Ar_n⁺ (n>50) have introduced a completely new analysis paradigm by enabling analysis and imaging far beyond the static limit such that molecular depth profiling and 3D imaging of organic and biological systems has become possible.

The paper will discuss some of the most recent advances and seek to assess the future opportunities for SIMS analysis using cluster ion beams.

9:00am AS-ThM4 New Organic Reference Materials for Cluster Ion Sputter Depth Profiling, *A.G. Shard, S. Spencer, S. Smith, I.S. Gilmore, R. Havelund*, National Physical Laboratory, UK

Over the past three years, the availability of multilayered organic reference materials has enabled rapid progress in cluster ion beam sputtering for organic depth profiling. These materials have provided manufacturers and practitioners with a common benchmark against which the performance of different experimental methods can be judged. Furthermore, such reference materials are invaluable in providing experimental evidence against which theory can be tested. Reference materials based on Irganox 1010 and Irganox 3114 [1] have been extensively used in this regard [2,3,4]. Results from a VAMAS interlaboratory study, completed in 2011, using argon cluster ion beams as the sputtering source are briefly presented to demonstrate the relevance and utility of these reference materials. These sources demonstrate a remarkable repeatability of better than 1% relative standard deviation in sputtering yield. Depth resolutions close to 5 nm at low impact energies can be achieved. The materials also demonstrate that electrons used for charge compensation can cause very significant molecular damage which affects profiles to a significant depth, often over many tens of nanometers. Whilst this reference material has been extremely valuable, it is not suitable for the full range of analytical methods used in conjunction with cluster ion beam sputtering and may not be representative of all molecular species of analytical interest. As examples, the Irganox 1010 and Irganox 3114 are difficult to distinguish using either XPS or positive SIMS analysis. Alternatives are being studied, such as those materials which are of great commercial importance to the organic electronic industry, e.g. aluminium tris(hydroxyquinolate). In this work, we describe the development of new reference materials including amino acids,

fluorinated compounds, specifically for XPS analysis, and compounds used in organic displays. The precision and accuracy of the layer thicknesses and the stability of the materials will be described along with their performance in cluster ion sputter depth profiling experiments. Additionally, research into a new class of reference material based upon binary mixtures of organic compounds with known compositions will be described.[1] A. G. Shard, F. M. Green, P. J. Brewer, M. P. Seah and I. S. Gilmore, *J. Phys. Chem. B* 2008; 112: 2596.[2] A. G. Shard, R. Foster, I. S. Gilmore, J. L. S. Lee, S. Ray and L. Yang, *Surf. Interface Anal.* 2011; 43: 510.[3] P. Sjovald, D. Rading, S. Ray, L. Yang, and A. G. Shard, *J. Phys. Chem. B* 2010; 114: 769.[4] D. Mao, A. Wucher, and N. Winograd, *Anal. Chem.* 2010; 82: 57.

9:20am AS-ThM5 Characterization of Nano-objects with Nanoprojectile-Secondary Ion Mass Spectrometry, *C.-K. Liang, J.D. DeBord, M. Eller, S. Verkhovurov, E. Schweikert*, Texas A&M University

The uniqueness of nano-objects due to functionalities not present in bulk size is well documented. Yet methods for molecular characterizations of isolated entities below micrometer dimensions are lacking. One reason is the minute amount of sample for analysis; another is that the characteristics of analytical signals from objects of nanoscale dimensions can be affected by their size, shape and environment. Our approach for the characterization of nano-objects is based on the method of event-by-event bombardment-detection. Bombardment is with a sequence of individual nanoprojectiles, specifically Au₄₀₀⁴⁺ accelerated to velocities of up to 30 km/s. The impacts cause abundant secondary ion emission. We will report on the modulation of the ejecta as a function of the nano-objects' size, shape and environment and describe the critical parameters for the accurate assay of their surface and core compositions.

9:40am AS-ThM6 Organic Solar Cell Composition Profiling by Large Clusters Ions: How can we Optimize the Information Retrieved?, *T. Conard, A. Franquet, E. Voroshazi, D. Cheyns, P. Favia, W. Vandervorst*, IMEC, Belgium

Organic material composition profiling has always been very challenging. Recently, it has been shown that using a Gas Clusters Ion Beam source (GCIB) with large Ar-clusters, organic information can be preserved while profiling. However, very little studies have been performed yet about the influence of beam parameters on the spectra/profiles obtained. We investigated systematically the influence of the sputter parameters in a dual beam TOFSIMS experiment (Bi_n⁺/Ar_m⁺) on organic solar cells composed of PCBM and P3HT. Environmental stability of organic solar cells prepared with oxide transport layers is considerably enhanced; hence the critical importance to be able to also investigate organic/inorganic interfaces with large ion clusters.

Qualitatively, it is known that the average energy per atom is an important parameter to keep organic information: For low eV/atom, no sputtering occurs and for high energy per atom, the molecular information is lost. We show for a layer of mixed P3HT:PCBM that the transition to the loss of molecular information occurs sharply at about 6eV/atom, independently of the primary cluster energy. However, we also observe a significant variation of the intensity of the molecular peaks within the energy-region where molecular information is kept. It occurs both towards the higher and the lower eV/atom limits. These are the consequence of the dual beam experiment. At the lower eV/atom limit, the molecular information is lost due to the damage induced by the analysis beam. Towards the higher eV/atom limit, we observed a decrease of the intensity of the molecular PCBM peak by a factor 2 between 2.8 and 4.0 eV/atom. This is interpreted as a partial degradation of the PCBM due to the sputtering.

Composition variations within the formed layers and/or polymer degradation are important for solar-cells devices performances. For a system like PCBM:P3HT mixed layer, one may follow the sulfur intensities throughout the layer as an indirect indication of segregation. This allows, for instance to use of energy-filtered TEM to analyze de-mixing of layers. By comparing TEM and molecular profiling, we show in this study that segregation within layers and degradation of solar cells can be analyzed by dual beam TOF-SIMS.

Finally, the interfaces between the organic and inorganic layers in a solar cell are also critical to the quality of the devices. However, the optimal analysis parameters of inorganic material using cluster ion source may significantly differ from the optimal parameters for organic layers (for instance sputtering rates). We will thus focus on the determination of the best trade-off parameters for heterogeneous systems.

10:40am **AS-ThM9 Molecular Imaging of Cells and Tissues with Ar Cluster Ion Beams**, J. Matsuo, S. Nakagawa, M. Py, T. Aoki, T. Seki, Kyoto University, Japan

Because molecular, structural and chemical state information is considered invaluable in life science, various mass spectroscopic techniques, such as secondary ion mass spectrometry (SIMS), matrix-assisted laser desorption ionization (MALDI) and desorption electrospray ionization (DESI), have been examined intensively during the last decade. The SIMS technique is considered to have the highest spatial resolution, but it is necessary to increase secondary ion yields of bio-molecules. It has been reported that cluster ion beams can enhance the secondary ion yields, because of the high-density energy deposition and multiple collisions near surfaces. Clusters such as SF₅, C₆₀, Au₃, and Bi₃ were found to be quite useful for SIMS of organic materials. Because these primary ion beams cause significant damage on organic surfaces, the primary ion dose is limited to a certain threshold value (known as "the static-limit", ~10¹² ions/cm²). Therefore, the intensity of bio-molecular ions (>500 Da) is too low to obtain high-resolution mass images.

Because Ar cluster ions provide much less damage on the surface than conventional ion beams, much attention is devoted to molecular depth profiling of organic multilayer and molecular imaging with Ar cluster-SIMS. We have developed a new SIMS imaging system with focused Ar cluster ion beam. An orthogonal acceleration time-of-flight (oa-TOF) mass spectrometer, which allows the use of a continuous beam, was employed in a new bio-imaging system. There was no need to use the ion-bunching technique in this system, and therefore there was no need for tradeoff between beam diameter and mass resolution, which is a problem in mass-imaging of biological samples with conventional SIMS. SIMS spectra of cells with Ar cluster ions are quite different from that with Bi₃ ions. Lipid molecular ions found in the mass range over 600 Da, are clearly observed with Ar cluster ions. Furthermore, background level of the spectra with Ar cluster ions is much lower than that with Bi₃ ions. This is attributed to the lower velocity of the primary ions.

The latest results of this system and its performance in molecular imaging of cells and tissues will be presented and discussed.

Acknowledgements

This work is supported by the Core Research of Evolutional Science and Technology (CREST) of Japan Science and Technology Agency (JST).

J. Matsuo, S. Ninomiya, H. Yamada, K. Ichiki, Y. Wakamatsu, M. Hada, T. Seki and T. Aoki, *Surf. Interface Anal.* (2011) 42, 1612

11:00am **AS-ThM10 Observation of High Ionization Probability for Desorption/Ionization Induced by Neutral Cluster Impact and its Application in Bioanalytics**, B.-J. Lee, M. Baur, University of Applied Sciences Esslingen, Germany, C.R. Gebhardt, Bruker Daltonik GmbH, Germany, M. Dürr, University of Applied Sciences Esslingen, Germany

Desorption and ionization induced by neutral cluster impact is a very soft method for transferring surface-adsorbed biomolecules into the gas phase [1]. The neutral clusters with a mean size of 10³ to 10⁴ molecules are seeded in a He beam which results in a narrow velocity distribution and an energy density of 0.5 to 0.8 eV/molecule. Using SO₂ clusters, the method furthermore makes use of the dipole moment of the cluster's constituents which allows both for solvation and charge transfer processes in the cluster. Thus the cluster provides not only the energy for the desorption process but also serves as a transient matrix. As a consequence, desorption and ionization of oligopeptides and proteins is observed at comparably low energies of the impacting clusters and without any fragmentation of the biomolecules.

In order to quantify the ionization probability during cluster-induced desorption and ionization, samples with well defined amount of substance, especially oligopeptides such as angiotensin II and bradykinin, were prepared by means of drop casting the respective solution on a SiO₂ surface. A biased grid in front of the target was used to transfer ions of one polarity into the time-of-flight mass spectrometer; simultaneously, the correlated ion current from the target was measured. In case of oligopeptides, the positive ion signal is dominant and both positive ion mass spectra and extracted charge per pulse were measured as a function of the number of cluster pulses applied. Comparison of the total charge desorbed from the respective sample with the amount of substance applied then yields the ionization efficiency which was found to be 3 to 4 % in the case of the investigated oligopeptides. The result is discussed with respect to the desorption and ionization mechanism during cluster-surface impact, taking into account the influence of functional groups and preparation conditions.

We furthermore show that desorption and ionization induced by neutral cluster impact can be successfully combined with ion trap mass spectrometry for applications in bioanalytics. Especially when the cluster beam is produced by a pulsed nozzle with pulse duration in the sub-millisecond regime, all ions generated during one pulse can be collected in

the ion trap. In combination with the high ionization efficiency of the process, femtomol sensitivity was achieved in the case of various oligopeptides; multiple sample arrays and low sampling time then allows for batch-type analysis of biosamples.

[1] C. R. Gebhardt, A. Tomsic, H. Schröder, M. Dürr, and K.L. Kompa, *Angew. Chem. Int. Ed.* **48**, 4162 (2009).

11:20am **AS-ThM11 Analysis of Molecular Surfaces Using a Pulsed Beam of Large Argon Clusters**, N. Havercroft, ION-TOF USA, Inc., D. Rading, S. Kayser, R. Moellers, F. Kollmer, E. Niehuis, ION-TOF GmbH, Germany

In the last few years it has been demonstrated that massive argon cluster ions can successfully be applied as primary ion projectiles in SIMS [1-7]. They can not only be applied to sputter organic surfaces without damaging the molecular information, it also has been shown that they desorb larger molecular ions effectively [4] with little fragmentation [2][7]. Although the secondary ion yield decreases with increasing cluster size [4][6], the ability of these projectiles to produce cleaner spectra emphasizing molecular ion signals makes them interesting for analysis purposes as well [5-7]. However, the generation of short primary ion pulses has been difficult due to the large cluster size distribution which typically ranges from hundred to several thousand atoms/cluster. The resulting flight time dispersion of the different cluster sizes determines the primary ion pulse lengths and thus limits the mass resolution.

We equipped a standard TOF.SIMS 5 instrument with a newly developed Ar cluster ion source. The 90° pulsing system of this primary ion gun enables the generation of long as well as short primary ion pulses. The long pulses are suited for sputtering purposes in a dual beam experiment whereas the short pulses are used for high mass resolution TOF-SIMS spectrometry. The pulsing system also allows the selection of a specific cluster size range out of the large distribution with a mass resolution of about 2 for long and 80 for short pulses.

In this study we will apply large Ar clusters ranging from several hundred to several thousand atoms/cluster at different beam energies to a variety of molecular surfaces. We will present and compare data about the influence of the cluster size and beam energy on the sputtering as well as analysis capabilities emphasizing on the spectra appearance and the fragmentation behavior.

[1] N. Toyoda, J. Matsuo, T. Aoki, I. Yamada, D.B. Fenner, *Nucl. Instr. and Meth. in Phys. Res.*, **B 190**, (2002) 860-864

[2] S. Ninomiya, Y. Nakata, K. Ichiki, T. Aoki, J. Matsuo, *Nucl. Instrum. Methods*, **B 256** (2007), 493

[3] S. Ninomiya, K. Ichiki, H. Yamada, Y. Nakata, T. Seki, T. Aoki, J. Matsuo,

Rapid Communications in Mass Spectrometry, **23**, (2009), 1601-1606

[4] K. Mochiji, M. Hahinokuchi, K. Moritani, and N. Toyoda, *Rapid Commun. Mass Spectrom.* **23** (2009) 648

[5] S. Ninomiya, Y. Nakata, Y. Honda, K. Ichiki, T. Seki, T. Aoki, J. Matsuo, *App. Surf. Sci.*, **255** (2008), 1588-1590

[6] S. Rabbani, A.M. Barber, J.S. Fletcher, N.P. Lockyer, J.C. Vickerman, *Anal. Chem.*, **83**, (2011), 3793-3800

[7] S. Kayser, R. Moellers, D. Rading, F. Kollmer, E. Niehuis,

to be published in *Surf. Interface Anal.* SIMS XVIII Proceedings

11:40am **AS-ThM12 Electropray Droplet Impact/SIMS: Some Insights into the Collisional Events**, K. Hiraoka, Y. Sakai, S. Ninomiya, R. Takaishi, University of Yamanashi, Japan

Electropray droplet impact (EDI) uses the water droplets with charge number of 60-300 and masses of 6.2X10⁵-1.6X10⁷ u. The charged droplets impact the sample surface with the velocity of about 12 km/s. Because this value is higher than sound velocities of solids, the supersonic collision takes place at the moment of collision. The supersonic collision is followed by the enormous pressure build-up at the interface and electronic excitation for the species near the colliding interface will follow. The observation of the ionic products by mass spectrometry and the surface analysis by XPS are regarded as the study of the ionization/desorption processes induced by the supersonic collision. For the sample of self-assembled monolayers, only the molecular ions of organic layer but no adducts with gold atoms were observed. In addition, no gold cluster ions but only Au⁺ was observed after Au surface was exposed. This indicates no ablation but atomic- or molecular-level etching takes place in EDI. For all the organic and inorganic samples investigated, no modification of components on the surface was observed after EDI irradiation as far as XPS measurements are concerned. Non-selective etching means that all the elements of the samples are desorbed with the same probabilities. These results suggest that the collisional events taking place in EDI is highly non-thermal. The water

clusters do not penetrate into the sample but they are reflected backward in very short time, maybe in ps. The high ionization efficiency for EDI (useful yield: ~10%) may be explained by the curve crossing mechanism. The sample of AgF was only one example found so far that suffered from surface modification. Due to the very reactive nature of F atoms, the surface was enriched by Ag during EDI irradiation. The CF_3^- and CF_3COO^- ions observed at the start of irradiation decreased and were taken over by $[AgF_3OH]$ and $[CH_3COOAg + CH_3COO^-]$. The enrichment of silver on the AgF sample (i.e., reactive loss of fluorine) is evident. The ions CF_3^- and CF_3COO^- originated from CH_3COOH used for the electrospray of 1 M aqueous CH_3COOH solution. Supersonic collision and followed chemical reactions are complicated and the mechanism of desorption/ionization in EDI remains to be elucidated.

Electronic Materials and Processing

Room: 14 - Session EM+SS+AS+NS-ThM

Nanoelectronic Interfaces, Materials, and Devices

Moderator: M. Filler, Georgia Institute of Technology

8:00am **EM+SS+AS+NS-ThM1 Tensilely Strained Ge Nanomembranes for Applications in Group-IV Infrared Photonics, R. Paiella, Boston University** **INVITED**

Single-crystal semiconductor nanomembranes have emerged as a new materials platform offering unique opportunities for strain engineering, by virtue of their ultrasmall thicknesses that result in extremely high thresholds for plastic deformation under stress. This talk will review our recent work aimed at exploiting this property for the development of CMOS-compatible group-IV semiconductor light sources for the technologically important short-wave infrared spectral region. It is well known that Si, Ge, and related alloys are very inefficient light emitters and generally unsuitable for laser action, due to the indirect nature of their fundamental energy bandgap. A possible solution to this important drawback is provided by the ability of biaxial tensile strain in Ge to lower the conduction-band edge at the direct (G) point relative to the L-valley minima, until at a strain of about 1.9% the fundamental bandgap becomes direct. In our work, mechanically stressed Ge nanomembranes capable of accommodating the required strain levels have been developed, and used to demonstrate strong strain-enhanced photoluminescence. A maximum biaxial tensile strain of over 2% in a 24-nm-thick nanomembrane has been measured, above the accepted threshold for the formation of direct-bandgap Ge. A detailed theoretical model of the light-emission and optical gain properties of tensilely strained Ge has also been developed and applied to the measured luminescence spectra, providing evidence of population inversion at strain levels as low as about 1.4%. More recent work is focused on integrating optical cavities on these strained nanomembranes for the development of infrared photonic active devices.

8:40am **EM+SS+AS+NS-ThM3 Self-activating and Self-limiting Features of the Thermally Assisted Growth Mechanisms of Thin Oxide-, Nitride- and Carbide Films on Si Surfaces at Low Gas or Plasma Pressures, P. Morgen, J. Drews, R. Dhiman, University of Southern Denmark, Z.S. Li, Aarhus University, Denmark**

The thermally assisted growth of oxide-, nitride-, and carbide films on Si surfaces, in direct reactions, carried out with neutral gases or remote plasmas under ultrahigh vacuum background conditions, are self-limiting processes, reaching different thicknesses. The mechanisms have been studied using photoelectron spectroscopies with synchrotron radiation or conventional x-ray induced photoelectron spectroscopy (XS). For the oxidation with neutral oxygen molecules, or microwave-excited remote oxygen plasmas, and for the nitride formation reaction with microwave-excited remote nitrogen plasmas, the "kinetics" (uptake versus exposure plots) is well described with a Hill-function. For the nitrogen reaction, the variation of the temperature causes the Hill parameters to vary because this reaction has more latitude than the oxidation, in temperature range and final thickness, as well as in the resulting structure of the nitride, going from amorphous to crystalline at higher temperatures. One known instance of the "Hill reaction" is a self-activating enzymatic-like reaction, and such a mechanism is believed to be relevant also in our systems. The carbide reaction is different, due to defects in the growing film, which allow a relatively unhindered transport of Si to the surface, where it reacts with carbon species arriving at the surface, from remote microwave-excited plasmas of methane. Thus the limiting thickness of SiC/Si (111) is around 100 nm, while the thickness of oxide is 0.8 nm, and the nitrides between 1 and 3 nm.

9:00am **EM+SS+AS+NS-ThM4 Functional Conductive Polymer to Inexpensive and Portable Chemiresistive Biosensor, D. Bhattacharyya, K.K. Gleason, Massachusetts Institute of Technology**

Extensive research has focused on developing different types of biosensors for detecting bio-threat risks and the occurrence of toxins in the food supplies. However, these food screening processes involve many steps, have high labor costs, reagent costs and time delays of at least 2-3 days to obtain reliable data. Despite the current availability of various types of sensors, limitations of the current state-of-the-art biosensors for molecular recognition of biomolecules are well known. Among these limitations are the unacceptably long process times required for detection and user non-compliance as a result of the excessive weight of the sensor modules coupled with the inflexibility of the sensor platforms for routine uses. Chemiresistive biosensors detect changes in resistance when analyte molecules specifically bind to the sensor surface. Chemiresistive biosensing technique is attractive because it is label-free and can be developed for faster detection of analytes. In this work, oxidative chemical vapor deposition (oCVD) technique is employed for deposition of functional conductive copolymer thin films on the electro-spun fiber mats. The dry oCVD process allowed us to deposit uniform and conformal conducting -OH functional copolymeric film on the electro-spun fiber mat in a single step. For the proof-of-concept of the biosensor application, avidin molecules were covalently immobilized to the -OH functional groups. Various concentrations of biotin solutions were employed as the analytes. The responses and the response times of the devices were significantly improved when the high surface area electro-spun mat were used as a substrate in contrast to a flat substrate.

9:20am **EM+SS+AS+NS-ThM5 Semiconductor Nanomembranes for Biomedical Applications, J.A. Rogers, University of Illinois at Urbana Champaign** **INVITED**

Biology is curved, soft and elastic; silicon wafers are not. Semiconductor technologies that can bridge this gap in form and mechanics will create new opportunities in devices that adopt biologically inspired designs or require intimate integration with the human body. This talk describes the development of ideas for electronics that offer the performance of state-of-the-art, wafer-based systems but with the mechanical properties of a rubber band. We explain the underlying materials science and mechanics of these approaches, and illustrate their use in bio-integrated, "tissue-like" electronics with unique capabilities for mapping cardiac electrophysiology, in both endocardial and epicardial modes, and for performing electrocorticography. Demonstrations in live animal models illustrate the functionality offered by these technologies, and suggest several clinically relevant applications.

10:40am **EM+SS+AS+NS-ThM9 Structure, Dynamics and Mechanism of a Single-Molecule Electric Motor, C.J. Murphy, C.H. Sykes, Tufts University**

Future nano-electronic devices, such as fluid pumps, sensors and switches, will rely on rotating molecules bound to surfaces as key components. To operate these devices, it is important to understand and direct molecular rotation at this interface. We utilized a Low Temperature Scanning Tunneling Microscope (LT-STM) to both drive and measure the rotation of a single asymmetric thioether molecule bound to a copper (111) surface. Due to the hexagonal arrangement of the underlying Cu atoms the rotor molecule has six favorable orientations, with an asymmetrical barrier to rotation around the Cu-S bond. The symmetry of this barrier is dependent on the surface bound chirality. Rotation of the molecule can be driven by either thermal or electrical means. In thermally driven systems, there is no preferred direction of rotation. In order to measure the rate of anisotropic rotation, the system is cooled to 5 K, and a tunneling current is applied to periodically excite the molecule, resulting in a flashing ratchet like mechanism of molecular rotation. The progression of molecular orientations relative to the tip can be determined by the exponential dependence of tunneling current on distance. This allows evaluation of the rate, direction and magnitude of rotation between these orientations in real time. We aim to further interrogate this novel mechanism for electrically-driven motion by quantifying the lifetime of the rotor in each stable orientation and the transitions between these states as a function of tunneling current and voltage.

11:00am **EM+SS+AS+NS-ThM10 Semiconductor Nanostructures for Efficient Thermoelectric Energy Conversion, Z. Aksamija, University of Wisconsin Madison**

Thermoelectric (TE) refrigeration using semiconductor-based nanostructures, such as nanowires, nanoribbons, and superlattices, is an attractive approach for targeted cooling of local hotspots inside integrated circuits due to inherently no moving parts, ease of miniaturization and on-chip integration, and the nanostructures' enhanced TE conversion efficiency. In addition, thermoelectric power generation enables the reuse of

waste heat in a variety of applications, from low-power and energy-efficient designs to internal combustion engines and solar cells. Thermoelectric efficiency, measured by the figure-of-merit ZT , is dictated by the ratio of electronic power factor $S^2\sigma$ over the total thermal conductivity. Consequently, largest gains in TE conversion efficiency have come from the ability to reduce thermal conductivity. This is especially true in nanostructures, where small physical dimensions lead to reduced thermal transport due to the scattering of lattice waves, or phonons, with the boundaries of the nanostructure. The design of efficient semiconductor thermocouples requires a thorough understanding of both charge and heat transport; therefore, thermoelectricity in semiconductor-based nanostructures requires that both electronic and thermal transport are treated on equal footing. SOI nano-membranes and membrane-based nanowires and ribbons show promise for application as efficient thermoelectrics, which requires both high electronic power factor and low thermal conductivity. I will present numerical simulation and modeling of both carrier and phonon transport in ultrathin silicon nanomembranes and gated nanoribbons. We show that the thermoelectric response of Si-membrane-based nanostructures can be improved by employing the anisotropy of the lattice thermal conductivity, revealed in ultrathin SOI nanostructures due to boundary scattering, or by using a gate to provide additional carrier confinement and enhance the thermoelectric power factor. Furthermore, we explore the consequences of nanostructuring on silicon/germanium and SiGe alloy superlattices, and show that the drastic reduction of thermal conductivity in these structures comes from the increased interaction of lattice waves with rough interfaces and boundaries. Finally we demonstrate reduced thermal conductivity in both suspended and supported graphene nanoribbons (GNRs), which exhibit strong anisotropy due to interaction of lattice waves with line edge roughness (LER) and the competition between LER and substrate scattering. The talk will conclude with an outlook for future nanostructured thermoelectric based on nanocrystalline and nanocomposite semiconductors, and nanopatterned graphene.

11:20am **EM+SS+AS+NS-ThM11 UV Ozone Irradiation Induced Defect Formation in Graphene/PZT Devices**, *C.X. Zhang, D.M. Fleetwood, M.L. Alles, R.D. Schrimpf*, Vanderbilt University, *E.B. Song, S. Kim, K. Galatsis, K.L. Wang*, University of California at Los Angeles, *E.X. Zhang*, Vanderbilt University

Graphene based materials are promising candidates for integration into future integrated circuit technologies. Initial studies of the effects of electron-beam and proton irradiation have been performed on graphene materials, but there remain significant questions about the nature of the conductivity and the defects that influence its material and electronic properties. We have found that low-energy x-ray irradiation can lead to significant shifts in the charge neutral point and increases in resistance of suspended graphene layers and graphene layers on SiO_2 . For graphene-on- SiO_2 structures, the reaction oxygen atoms may be supplied either by ozone in the ambient air, or by the adjacent SiO_2 substrate. Similar reactions may be observed for hydrogen, for devices exposed to x-ray and/or UV ozone (UVO) irradiation. Moreover, we also have found that graphene/PZT ferroelectric field-effect transistors (FFETs) are sensitive to UVO irradiation. The conducting channel in these devices is a single graphene layer. The device functions as a nonvolatile memory with reverse hysteresis, where charge trapping and detrapping in the PZT layer leads to a large memory window that is robust to x-ray irradiation and/or memory state cycling. When these devices are exposed to UVO irradiation, the memory window of the device decreases slightly with exposure time. In addition, an increase is observed in the slope of the I-V curves, along with a small positive shift in current-voltage characteristics. These results are consistent with the formation of negatively charged surface states on the graphene layer during the UVO exposure, which are most likely associated with adsorbed oxygen. The degradation in the I-V characteristics recovers somewhat with room temperature annealing. At the AVS meeting, the detailed electrical response will be described, and a physical model will be presented for the UVO degradation and recovery mechanisms.

11:40am **EM+SS+AS+NS-ThM12 Switching Molecular Kondo Effect by Chemical Reactions**, *H. Kim*, ISSP, University of Tokyo, Japan, *Y.H. Chang*, KAIST, Korea, *M.H. Chang*, Korea University, *Y.-H. Kim*, KAIST, Korea, *S.-J. Kahng*, Korea University

Motivated by spintronics applications, the methods to control Kondo effect have been actively studied in magnetic adsorbates on metal surfaces using scanning tunneling microscopy, but they were limited to the processes that required external energy supply from scanning tunneling microscope tip. We report new methods to control molecular Kondo effect by using bimolecular chemical reactions. A chemical binding between diatomic molecules and Co-porphyrin was exploited to switch off, or reset the molecular Kondo effect. The Kondo effect was switched back on using scanning tunneling microscope manipulation as well as thermal desorption. These methods rely on the hybridized pairing of unpaired spins in d_{z^2} and

π^* orbitals of Co-porphyrin and diatomic molecules, respectively, as supported by our density functional theory calculation results. Our study opens up ways to control the molecular Kondo effect using an enormous variety of bimolecular chemical reactions.

12:00pm **EM+SS+AS+NS-ThM13 Quantifying the Local Seebeck Coefficient using Scanning Thermoelectric Microscopy (SThEM)**, *J.C. Walrath, Y.H. Lin, K.P. Pipe, R.S. Goldman*, University of Michigan

Thermoelectric (TE) devices allow reliable solid-state conversion of heat to electricity. The efficiency of a TE device is determined by the figure of merit, ZT , which is sensitive to the Seebeck coefficient, S . Traditional S measurements are used to quantify thermally-induced electron transport on a macroscopic scale. A promising alternative method for nanoscale measurements of S is scanning thermoelectric microscopy (SThEM). In SThEM, an unheated scanning tunneling microscopy (STM) tip acts as a high-resolution voltmeter to measure the thermally-induced voltage, V , induced by a temperature gradient in a heated sample. SThEM has been utilized to measure V across a GaAs p - n junction [1], with the spatial profile of S determined through a comparison of the measured V with a simulation of a network of resistors and voltage sources, based upon a theoretical S -value [2]. Although this approach is useful for predicting the measured V , it does not provide a method for direct conversion of the measured V to a local S . We have developed a Fourier heat conduction model to calculate a temperature profile matrix, thereby enabling direct conversion between the measured V and the local S . According to our model, SThEM can be optimized by fine-tuning several parameters, including the cone angle of the STM tip and the relative thermal conductivity of the tip and sample. We applied our model to SThEM data across a GaAs p - n junction [1] and improved the agreement between the measured and theoretical S by 40%. Our progress towards SThEM measurements of CoSb_3 and InAs quantum dots will also be discussed. This material is based upon work supported by the Department of Energy under Award Number DE-PI0000012. Y.H. Lin and R.S. Goldman are supported in part by DOE under contract No. DE-FG02-06ER46339.

[1] H.K. Lyeo, A.A. Khajetoorians, L. Shi, K.P. Pipe, R.J. Ram, A. Shakouri, and C. K. Shih, *Science* **303**, 816 (2004).

[2] Z. Bian, A. Shakouri, L. Shi, H.K. Lyeo and C.K. Shih, *Appl. Phys. Lett.* **87**, 053115 (2005)

Electronic Materials and Processing Room: 9 - Session EM-ThM

Processing for Ultra Low Power Electronics + Semiconductor Heterostructures I

Moderator: S.A. Vitale, MIT Lincoln Laboratory, J.E. Ayers, University of Connecticut

8:00am **EM-ThM1 Advanced FinFET Process for 22nm and Beyond**, *M. Masahara, T. Matsukawa, Y. Liu, K. Endo, S. O'uchi*, National Institute of AIST, Japan **INVITED**

1. Introduction

One of the biggest challenges for the VLSI circuits with 22nm-node and beyond is to overcome the issue of a catastrophic increase in power dissipation of the circuit due to short channel effects (SCEs) and V_{th} variation. Fortunately, double-gate FinFETs have a promising potential to overcome this issue due to their superior SCE immunity even with an undoped channel thanks to the 3D structure. This paper presents novel FinFET process technologies for 22nm-node and beyond.

2. V_{th} Tuning

The V_{th} of the FinFET is determined by the gate workfunction (WF). A mid-gap metal gate (MG) such as TiN gives a relatively high V_{th} ($\approx 0.4V$) for both n- and pMOS FinFETs. In order to further reduce V_{th} , we have developed a novel dual MG FinFET integration process by using metal interdiffusion technology. In this work, we selected a Mo (4.95eV) and Ta (4.25eV) combination, and demonstrated the integration of a Ta/Mo gate nMOS and Mo gate pMOS FinFET. A Ta diffuses into the underlying Mo layer, piles up at the metal/dielectric interface. Thus, by depositing Mo on both n- and pMOS and by stacking Ta on only pMOS, dual MG CMOS FinFETs with low V_{th} ($\approx 0.2V$) were successfully realized without any MG removal process.

By separating the two gates in the FinFET and using one to control the V_{th} , we have succeeded in obtaining the great advantage of the post-fabrication flexible V_{th} controllability. The fabricated independent double-gate FinFET (called 4T-FinFET) enabled V_{th} to flexibly range from around 0.2V to 0.4V.

3. Vth Variation

So far we have investigated FinFET performance variability for undoped channels with TiN MG. By evaluating the influence of channel doping, fluctuation of gate length and that of fin thickness, we have also found that gate WF variation (WFV) is the dominant source of Vth variation for the undoped TiN FinFET. We speculated that the WFV originates from randomly aligned TiN on rough sidewall channels due to line edge roughness of the patterned resist mask. Then in order to reduce the WFV, we fabricated FinFETs having smooth sidewall channels formed by using orientation-dependent nanowet etching. It was found that σ_{Vth} 's for the wet-etched case is significantly lower than that for the dry-etched case. This means that the smooth sidewall channels formed by using the nanowet etching well contribute to the reduction of the WFV.

4. Summary

By introducing Ta/Mo dual metal gate technology, low Vth ($\pm 0.2V$) can be obtained for CMOS FinFETs. By separating the DG, Vth can be tuned from 0.2V to 0.4V flexibly. Flattening of Si-fin sidewall channel is very promising for reducing Vth variations.

9:00am EM-ThM4 Wideband Characterization for Optimized Performance in Low Voltage Low Power Applications, M. Emam, Incize, Belgium, J.-P. Raskin, Université Catholique de Louvain, Belgium

Portability and performance are becoming the main two keywords in any consumer or professional applications. Portable computers, mobile phones, handheld measurement instruments, and many other examples are all applications that need long battery lifetime while compromising the least at the performance level. Long battery lifetime is simply translated into less power consumption and hence operating at lower voltage schemes. This new approach requires solutions at all levels; including material, fabrication, device structure, circuit design, and system architecture. Wideband characterization is the bridge that links these levels together (especially material, fabrication and device structure levels) and provides the means to optimize this cycle of innovation for an optimized final product in the Low Voltage Low Power (LVLP) regime.

Wideband characterization is the process of measurement and extraction of many parameters of the Device-Under-Test (DUT) in order to fully understand its characteristics and be able to provide solutions for inconvenient performance aspects. Wideband characterization usually covers a wide range of frequency starting at a few Hz and going up to tens of GHz, depending on the characteristics to be studied. Recently, many high frequency techniques have been proposed to deeply understand and qualify new materials (especially wafers and substrates) and new devices (active devices such as transistors and passive devices such as inductors). These new techniques rapidly and efficiently define the advantages and the disadvantages of the material/device and precisely define the causes of malfunction or poor quality performance. The result is a shorter time-to-market thanks to less number of iterations between the different steps of final product fabrication.

This paper presents the importance of wideband characterization techniques for fabrication process. Examples are given for new substrate, new device structures and enhancement of existing and mature device structures. The objective is an optimized performance for a LVLP application.

9:20am EM-ThM5 Ultra Low-Power (ULP) Current Logic Gates for Subthreshold-Triode Operation, K. Lam, Chinese University of Hong Kong, Hong Kong Special Administrative Region of China, T. Mak, Newcastle University, UK

Most logic gates used today are based on voltage-mode ideas, where the two binary states for 0 and 1 are represented using inverted logic on voltages. In carrying out the basic operations for AND and OR on two levels of voltages for 0 and 1, NAND gates and NOR gates are often required by using inverted logic and inverters are commonly used to get the logical computations functionally correct. It is straightforward to construct a NAND gate with two tightly coupled common drain and source N-channel MOSFET transistors. A properly chosen resistor from the supply voltage to the common drain will then realize the NAND function to the two voltage levels with a reasonable margin. For subthreshold operation with a supply voltage close to the threshold voltage, the gate switching speed is determined by the subthreshold swing.

There are limitations for these voltage-mode logic gates due to the lack of accuracy and inability to work on very small voltage levels less than the threshold voltage for ultra-low power applications. We explore the idea of current logic by making use of small currents at the subthreshold-triode region to overcome some of these limitations. Using current for the binary inputs of 0 and 1, the 2-input current-mode minimum circuit and maximum circuit are investigated to realize the logical functions of OR and AND gates for subthreshold-triode operation. Our previous work reported that in subthreshold-triode operation it is possible to obtain a subthreshold swing

which can surpass the theoretical limit of 60 mV/dec at very small gate voltage less than 0.025V for the IMEC 90 nm process. Further simulation is focused on the evaluation of ULP current logic gates constructed using current-mode min-max circuits. A benchmark test on a dynamic programming network for solving transitive closure problem has been performed on using conventional voltage-mode NAND-NOR logic gates. The results will be compared with the proposed current-mode min-max circuits.

9:40am EM-ThM6 Impact of Threading Dislocation Density and Dielectric Layer on I-V Characteristics of Schottky Diodes Fabricated from Ti and Epitaxially Grown p-Type Ge on Si, S. Ghosh, S.M. Han, University of New Mexico

Epitaxially grown Ge and III-V on Si have emerged as a promising candidate for the next generation high performance devices, including high-mobility complementary metal-oxide-semiconductor field-effect transistors. For high-mobility transistors integrated on Si substrates, in particular, managing dislocations and metal-semiconductor contacts has become an important engineering challenge. Herein, we have investigated the impact of threading dislocations and metal-semiconductor interfacial states on Schottky diode characteristics made of Ti and wafer-scale Ge grown on Si. For the purpose of comparison, we have grown epitaxial Ge on Si with two threading dislocation densities: 2×10^8 and 5×10^7 cm⁻². The p-type carrier density in the Ge layer is approximately 5×10^{16} cm⁻³. To prevent Fermi-level pinning, we have also deposited a thin layer of SiO₂ and Al₂O₃ between Ti and Ge with varying thickness, ranging from 5 to 30 nm. With a thin dielectric layer (5 nm), Schottky diodes on two Ge epilayers resulted in an on/off current ratio of approximately 1. This result indicates that there is a significant amount of leakage current. When the dielectric thickness is optimized to 30 nm, we observe that the on/off ratio improves by a factor of 40 and 2000 for SiO₂ and Al₂O₃, respectively. In the case of Al₂O₃, we were able to achieve an ideality factor of 1.67 at 300 K and the reverse leakage current density of $\sim 4.3 \times 10^{-10}$ A/ μm^2 at 300 K. The ideality factor increases to 2.44 at 77 K. This result suggests that the thermionic emission might be the dominant current transport mechanism for Schottky diodes fabricated from Ti and epitaxially grown p-type Ge on Si. However, the slight increase in ideality factor at low temperatures implies a change in the dominant current transport mechanism. In summary, the use of 30-nm-thick Al₂O₃ between Ti and Ge provides improved I-V characteristics for the Schottky diodes. In this presentation, we will further discuss our latest approaches [1] to reduce the dislocations in the Ge epilayer to low 10^6 cm⁻² level and device characteristics of Schottky diodes fabricated on these low-dislocation-density Ge on Si substrates.

[1] Darin Leonhardt and Sang M. Han, *Appl. Phys. Lett.* 99, 111911 (2011).

10:40am EM-ThM9 Heteroepitaxial Lattice Mismatch Stress Relaxation in Nonpolar and Semipolar GaN by Dislocation Glide, J. Speck, University of California, Santa Barbara

INVITED
Light emitting devices, namely LEDs and laser diodes, grown on c-plane GaN suffer from large internal electric fields due to discontinuities in spontaneous and piezoelectric polarization effects which cause charge separation between holes and electrons in quantum wells and limits the radiative recombination efficiency. Nonpolar GaN devices, such as in the m-plane {1100}, are free from polarization related electric fields since the polar c-axis is parallel to any heterointerfaces. Semipolar GaN-based devices have reduced electric fields.

Nonpolar and semipolar nitride epitaxial layers have other striking differences from c-plane. Namely, in conventional c-plane GaN heteroepitaxy, there is no shear stress on the easiest slip plane – the (0001) or basal plane and the next easiest slip plane – the prismatic {1100} m-plane. Epitaxy of mismatched layers on nonpolar and semipolar GaN, there are significant shear stresses in the inclined m-planes and on the inclined c-plane. Significant lattice mismatch-related stresses can be relieved by misfit dislocation formation via threading dislocation glide.

In this talk, we present the progress in developing high quality relaxed semipolar templates. The predominant relaxation in semipolar InGaN on GaN or AlGaN on GaN, in orientations such as (1122) or (2021), proceeds via threading dislocation glide on the inclined basal plane, followed in many cases by prismatic slip [1]. Since semipolar GaN has only one (0001) plane, plastic relaxation results in crystallographic tilt which can easily be measured in on-axis x-ray rocking curves or reciprocal space maps and can be directly used to quantify the extent of plastic strain relaxation [2]. The initial misfit stress relaxation occurs by glide of pre-existing threading dislocations [3,4] at a thickness slightly greater than the Matthews-Blakeslee critical thickness; the development of pseudomorphic InGaN and AlGaN semipolar buffer layers via dislocation strain relaxation [5,6,7]; blue (1122) LDs in relaxed buffer layers [8]; green LEDs on relaxed buffer layers [9].

[1] F. Wu et al., *Appl. Phys. Lett.* 99, 251909 (2011).

- [2] E.C. Young et al. *Appl. Phys. Express* **3**, 011004 (2010).
 [3] E.C. Young et al. *Appl. Phys. Express* **3**, 111002 (2010).
 [4] P.S. Hsu et al., *Appl. Phys. Lett.* **99**, 081912 (2011).
 [5] F. Wu et al. *J. Appl. Phys.* **109**, 033505 (2011)
 [6] A.E. Romanov et al., *J. Appl. Phys.* **109**, 103522 (2011).
 [7] E.C. Young et al. *Appl. Phys. Express*, **4**, 061001 (2011).
 [8] P.S. Hsu et al. *Appl. Phys. Lett.* **100**, 021104 (2012).
 [9] I. Koslow et al. submitted for publication (2012).

11:20am **EM-ThM11 Electronically Unmixed State of a Statistical Two-Dimensional Ga-Si Semiconductor Alloy on Si(111)**, *P. Ebert, S. Landrock*, Forschungszentrum Jülich, Germany, *Y. Jiang*, Peking University, China, *K.H. Wu*, Chinese Academy of Sciences, China, *E.G. Wang*, Peking University, China, *R.E. Dunin-Borkowski*, Forschungszentrum Jülich, Germany

Alloying different semiconductor compounds attracted wide attention, since the materials properties of the resulting semiconductor alloy can be continuously tuned by varying the composition. Hence one can engineer semiconductor materials with, e.g., intentionally designed band gaps, lattice constants, and/or optical properties. This approach possesses a large technical and economical interest, as it is the basis for defining the wavelength of most optoelectronic devices.

For such applications, it is crucial that the newly formed semiconductor alloy has spatially homogeneous electronic properties, i.e., the original materials' properties of the individual alloyed compounds merge into the desired new properties. This is in general assumed to be the case for most three-dimensional compound semiconductor alloys. With the ever shrinking dimensions of semiconductor devices, the semiconductor alloy layers are becoming increasingly thinner. Ultimately only monolayer thin alloy layers may be needed and then the concept of a globally homogenous alloy band structure, different from that of its alloyed compounds, needs to be reassessed. The central question is if a two-dimensional semiconducting alloys would always exhibit a merged new band structure in analogy to three-dimensional semiconductor alloys, or if locally the different band structures of the constituent semiconductor compounds of the alloy persist.

In this paper, we present a two-dimensional Ga-Si $\sqrt{3}\times\sqrt{3}$ semiconductor alloy on Si(111) substrates as model system. Using atomically and momentum resolved STM and STS, we demonstrate that the electronic structure, i.e., density of states, band gap, and band structure, is atomically localized and different at Si and Ga atoms. No intermixing and formation of new alloy related electronic properties are observed, as if no alloying ever happened. This unmixed state is discussed in terms of the particular bonding structure of the two-dimensional alloy.

11:40am **EM-ThM12 Atomistic Analysis of Ge on a-SiO₂ using an Empirical Interatomic Potential to Describe Selective Epitaxial Growth**, *Y. Chuang*, University of Pennsylvania, *Q. Li, D. Leonhardt, S.M. Han*, University of New Mexico, *T. Sinno*, University of Pennsylvania

Integration of Ge and III-V compound semiconductors on Si has received significant recent attention for the next-generation, high-mobility transistors and III-V optoelectronic and photovoltaic devices.[1] However, managing dislocations and film stress due to lattice mismatch and thermal expansion coefficient mismatch remains a significant engineering challenge. One possible solution is selective epitaxial growth (SEG) where the epitaxial layer is grown in select areas to simultaneously manage dislocations and stress. For SEG, a dielectric layer (e.g., SiO₂ and Si₃N₄) with open windows that expose the underlying Si is typically employed to reduce the contact area between the deposited epitaxial layer and Si substrate, resulting in lower mismatch stress and defect density.[2] The selectively grown epitaxial islands can be further grown laterally over the dielectric layer and coalesced into a continuous film. The SEG technique squarely relies on weak interaction between growth precursors and the dielectric film, which prevents random nucleation. For instance, we have previously reported that desorption and surface diffusion barriers of Ge adspecies on SiO₂ are 0.44 ± 0.03 and 0.24 ± 0.05 eV, respectively.[3, 4] Herein, we present an atomistic analysis of Ge on SiO₂ in order to validate a Tersoff-based model for Si-Ge-O [5, 6]. We compare simulation predictions to detailed experimental data for a variety of properties. In particular, we consider bulk SiO₂ structural parameters as a function of temperature, Si-SiO₂ and Ge-SiO₂ interface energies, and the Ge-on-SiO₂ desorption energy and diffusion behavior. We show that with a single fitting parameter, the potential model provides a good overall description of the Si-Ge-O system, while retaining the highly efficient nature of the Tersoff potential, making it a good choice for larger-scale atomistic studies of Ge-on-Si SEG. We conclude by showing example calculations of stress distributions in epitaxial Ge islands in an SEG system.

[1] H. Lafontaine, D. C. Houghton, N. L. Rowell and G. C. Aers, *Appl. Phys. Lett.* **69**, 1444 (1996).

- [2] T. A. Langdo, C. W. Leitz, M. T. Currie, E. A. Fitzgerald, A. Lochtefeld and D. A. Antoniadis, *Appl. Phys. Lett.* **76**, 3700 (2000).
 [3] Q. Li, J. L. Krauss, S. Hersee, and S. M. Han, *J. Phys. Chem. C* **111**, 779 (2007).
 [4] D. Leonhardt and S. M. Han, *Surf. Sci.* **603**, 2624 (2009).
 [5] J. Tersoff, *Phys. Rev. B* **39**, 5566 (1989).
 [6] S. Munetoh, T. Motooka, K. Moriguchi and A. Shintani, *Comput. Mater. Sci* **39**, 334 (2007).

Energy Frontiers Focus Topic Room: 15 - Session EN+NS-ThM

Batteries and Fuel Cells

Moderator: Y. Wu, Purdue University

8:00am **EN+NS-ThM1 Advanced Polymer Electrolyte Materials for Fuel Cell Applications**, *A.M. Herring*, Colorado School of Mines
INVITED

Proton exchange membrane (PEM) fuel cells are still the most desirable component of future zero emission, high efficiency automobiles fueled with hydrogen. However, their unit cost, ease of operation, and reliability must be reduced which includes eliminating the humidifier from the fuel cell system. Currently the commercial PEM is fabricated from a perfluorosulfonic acid (PFSA) polymer such as Nafion[®]. Unfortunately PFSA ionomers must be fully hydrated to achieve practical levels of proton conductivity which can only be achieved in vehicles operating at an inlet RH of 85% which still necessitates the use of a humidifier and undesirable complex water management and recovery. To achieve the goal of a PEM that can operate at temperatures from freezing to 120°C using dry inlet gases it will be necessary to develop new PEMs that are based on new chemistries or dramatically improved morphologies of existing chemistries. The versatility of the polymer electrolyte fuel cell could be expanded to more complex fuels with the use of an anion exchange membrane (AEM). An AEM fuel cell could potentially utilize less expensive metal catalysts and have the ability to oxidatively cleave carbon-carbo bonds.

Ionomers are generally perceived as being phase separated materials. However, the optimal morphology that an ionomer should adopt and that would be practical is still being debated. This situation is not helped by the uncertainty of the morphology adopted under operating fuel cell conditions of the incumbent material. Here I will describe a study that contrasts fully amorphous materials with materials designed to have phase separated morphologies of known symmetries and dimensions. While the designed materials allow us to probe certain concepts of ion conduction with pore shape and size, they do not necessarily outperform the amorphous materials. Curiously we show that the role of water has more to do with morphological changes in flexible materials than enhancing ion conduction in non-sulfonic acid based materials. This has implications for the fabrication of thin robust films that will be needed for an operating fuel cell. In the case of AEMs while a cation has yet to be found that is stable under hot and dry operation, water may be a necessary evil rather than an enhancer of anion conduction.

8:40am **EN+NS-ThM3 Rational Design of Competitive Electrocatalysts for Hydrogen Fuel Cells**, *S. Stolbov, M. Alcántara Ortigoza*, University of Central Florida

The large-scale commercial application of hydrogen fuel cells requires efficient and cost-effective electrocatalysts for the oxygen reduction reaction (ORR), which occurs on the cathode. We demonstrate that rational design can render electrocatalysts possessing both virtues. In this work, by unifying the knowledge on surface morphology, composition, electronic structure and reactivity, we find that tri-metallic sandwich-like structures are an excellent choice for optimization. Their constituting species are designed to couple synergistically rendering reaction-environment stability, cost-effectiveness and high catalytic activity. This cooperative-action concept enabled us to predict two Pt-free ORR electrocatalysts: Pd/Fe/W(110) and Au/Ru/W(110) [1]. Density functional theory calculations of the reaction free-energy diagrams indicate that these materials are more active toward ORR than the so far best Pt-based catalysts.

1. S. Stolbov and M. Alcántara Ortigoza; *J. Phys. Chem. Letts.* **3**, 463 (2012)

9:00am **EN+NS-ThM4 Nanocomposite Materials for Lithium Ion Batteries**, *G. Yushin*, Georgia Institute of Technology **INVITED**

High power energy storage devices, such as supercapacitors and Li-ion batteries, are critical for the development of zero-emission electrical vehicles, large scale smart grid, and energy efficient cargo ships and locomotives. The energy storage characteristics of supercapacitors and Li-ion batteries are mostly determined by the specific capacities of their electrodes, while their power characteristics are influenced by the maximum rate of the ion transport. The talk will focus on the development of nanocomposite electrodes capable to improve both the energy and power storage characteristics of the state of the art devices. Carbon-polymer and carbon-metal oxide nanocomposites have been demonstrated to greatly exceed the specific capacitance of traditional electrodes for supercapacitors. Selected materials showed the unprecedented ultra-fast charging and discharging characteristics. Intelligently designed silicon-carbon-polymer composites showed up to 8 times higher specific capacity than graphite, the conventional anode material in Li-ion batteries, and stable performance for over 1000 cycles. In order to overcome the limitations of traditional composites precise control over the materials' structure and porosity at the nanoscale was required.

9:40am **EN+NS-ThM6 Engineering $\text{Li}_x\text{Al}_y\text{Si}_z\text{O}$ Ionic Conductive Thin Films by Atomic Layer Deposition for Lithium-ion Battery Applications**, *Y.-C. Perng, J. Cho, D. Membreno, N. Cirigliano, B. Dunn, J.P. Chang*, University of California, Los Angeles

Lithium (Li)-ion batteries have drawn much attention for their outstanding performance in portable electronics applications with the potentials to function as a power source for further miniaturized devices, including micro-systems through the utilization of 3-dimensional electrodes based on high aspect ratio pillars. To realize this potential, an ultra-thin and highly conformal electrolyte layer is needed to coat the 3D electrode array. The ionic conductor lithium aluminosilicate (LiAlSiO_4) synthesized by atomic layer deposition (ALD) is a promising electrolyte material for 3D battery applications not only due to its high ionic conductivity along its c-axis resulting from channels formed by the alternating tetrahedra of aluminum-oxygen (Al-O) and silicon-oxygen (Si-O), but also expected to provide similar improved cell cyclability, as reported in the preliminary studies of ultra-thin metal-oxide ALD coatings on electrodes.

The self-limiting characteristic of ALD allows for precise control of thickness and composition of complex oxides and results in a highly conformal and pinhole-free coating suitable in 3D micro-battery applications or electrolyte surface coatings. The metal precursors used in this work are tetraethyl orthosilicate (TEOS), trimethylaluminum (TMA) and lithium t-butoxide (LTB). These precursors, along with water vapor as the oxidant, were used to deposit SiO_2 , Al_2O_3 and Li_2O , with the deposition rates in the range of 0.8–2Å/cycle, respectively. The deposition rate of stoichiometric LiAlSiO_4 was ~20Å/cycle at a temperature of 290°C. The concentration of each metal element in $\text{Li}_x\text{Al}_y\text{Si}_z\text{O}$ (LASO) thin films was found to correlate closely to ALD cycles and the associated incubation times. The crystallinity of the films after post-deposition rapid thermal annealing (RTA) was a function of cation atomic percentage. Li-ionic conductivities and the activation energy of as-deposited LASO films with respect to lithium contents as well as their relation to the film thickness were studied. The LASO ALD coating on 3D features, such as NWs and nanoparticles (NPs), were confirmed to be conformal and uniform by transmission electron microscopy (TEM) imaging. The cell performance as well as cyclability enhancement from $\text{Li}_x\text{Al}_y\text{Si}_z\text{O}$ was investigated for a silicon-nanowire 3D microbattery, where SiNW was used as an anode, to explore the potentials of a solid-state SiNW battery with a solid-oxide electrolyte.

10:40am **EN+NS-ThM9 Titanium Oxide and Lithium Titanium Oxide Coated 3D Nanoelectrodes for Li-ion Microbatteries**, *G. Pattanaik, J. Haag, M.F. Durstock*, Air Force Research Laboratory

Titanium oxide based materials, including both Li-titanates and various TiO_2 polymorphs are promising alternatives to carbonaceous anode materials for Li-ion rechargeable batteries because of their higher voltage operation (enhanced safety), relatively small volume expansion upon lithiation, minimal electrode/electrolyte interface reactivity (nonexistent SEI layer), inexpensive and biocompatible non-toxic nature. Nanoscale three-dimensional (3D) architectures of current collectors for microbatteries would significantly increase the areal capacity over their planar counterparts, if the active Li-insertion electrode material could be coated conformally. The nanoscale thickness of the active electrode layer in combination with an electronically conducting 3D nanoarchitecture of the current collector should enable high areal capacity and fast charge-discharge rates.

Atomic layer deposition (ALD) is capable of growing conformal ultra thin films on complex 3D surface morphologies. We have used ALD to grow

conformal layers of titanium oxide and lithium titanium oxide on various 3D nanoarchitectures including high aspect ratio nanoporous Al_2O_3 templates, template-electrodeposited 3D metal nanowire arrays and carbon nanotube buckypapers. The precursors for ALD used in this study include lithium t-butoxide, tetrakis(dimethylamido)titanium (TDMAT) and water. We have been able to grow conformal layers with controllable thickness at nanometer scale uniformly coated around the high aspect ratio features.

A significant increase in areal capacity (up to two orders of magnitude) was obtained in anatase TiO_2 coated Ni nanowire arrays over 2D thin film electrodes of a similar footprint. ALD TiO_2 coated buckypapers showed specific capacities in excess of 200 mAh/g at C/10, with 70% of the capacity retained at 5C. At 1C, 95% of the initial capacity is retained after 500 charge/discharge cycles. ALD deposition of LiOx and TiOx and subsequent thermal annealing leads to a combination of TiO_2 and spinel lithium titanium oxide ($\text{Li}_4\text{Ti}_5\text{O}_{12}$) phases. The presence of these phases is reflected in XRD as well as electrochemical charge-discharge curves. This presentation will discuss a systematic study of the ALD growth of 3D titanium oxide and lithium titanium oxide nanostructures and their electrochemical characterization.

11:20am **EN+NS-ThM11 The Contribution of Auger Electron Spectroscopy to a Better Understanding of the Lithiation Process Occurring in Si-based Anodes Designed for Li-ion Batteries**, *E. Radvanyi, E. De Vito, W. Porcher, S. Jouanneau*, CEA Grenoble, France

With a specific capacity of almost 3580 mAh.g^{-1} at room temperature (corresponding to the $\text{Li}_{15}\text{Si}_4$ alloy), silicon is a promising element for designing new efficient anodes in Li-ion battery technology. However, because of huge material volumic expansion (around 300%) during the lithiation process¹, leading to a quick pulverization of the electrode², silicon has been used only as an additive to graphite in commercial cells so far³. In order to improve Si-based electrodes cyclability, a better understanding of the lithium insertion mechanisms is among the key issues⁴. The study of the lithiation process in silicon particles is particularly challenging. Indeed, a complete amorphization of the material during cycling⁴ makes difficult the use of surface characterization techniques based on beam diffraction (e.g. X-rays or electrons). In this study, we have used Auger Electron Spectroscopy (AES) to study these mechanisms. Poor attention has been focused on AES in the battery research field so far^{5,6}. In this work we emphasize its interest, notably for the study of the lithiation mechanisms in silicon particles. The first part of this work is dedicated to the study of Li-Si alloys by using AES. Several crystalline Li_xSi alloys (Li_7Si_3 , $\text{Li}_{13}\text{Si}_4$ and $\text{Li}_{22}\text{Si}_5$) have been synthesized and characterized by X-Ray diffraction and AES. It appears that the atomic relative concentrations obtained by AES for the elements Li and Si are accurate with a tolerance of approximately 10%. The effect of Ar^+ sputtering has also been investigated. After this initial work, six electrodes based on silicon particles have been analyzed by using AES for different "State Of Charge" (SOC) within the first electrochemical cycle.

For each SOC, several silicon particles have been investigated individually. Li and Si depth concentration profiles have been achieved by following Li (KLL) and Si (LVV) Auger transitions. Thanks to the good spatial resolution (17 nm at 10kV/1nA), it is possible to detect inhomogeneities of Li concentration at the particle surface. Based on the results obtained on different silicon particles at several SOC, a lithiation model is proposed and discussed.

- (1) Beaulieu, L. Y.; Hatchard, T. D.; Bonakdarpour, A.; Fleischer, M. D.; Dahn, J. R. *J. Electrochem. Soc.* **2003**, *150*(11), A1457-A1464
- (2) Kasavajula, U.; Wang, C.; Appleby, A. J. *J. Power Sources* **2007**, *163* (2), 1003-1039
- (3) www.hitachi.com
- (4) Zhang, W. *J. J. Power Sources* **2011**, *196* (1), 13-24
- (5) Morigaki, K. I.; Ohta, A. *J. Power Sources* **1998**, *76* (2), 159-166
- (6) Kim, Y. J.; Lee, H.; Sohn, H. *J. Electrochem. Comm.* **2009**, *11* (11), 2125-2128

11:40am **EN+NS-ThM12 Organic/Inorganic Composite Materials as Anodes for Lithium Ion Batteries**, *M. Thakur, R.B. Pernites*, Rice University, *M. Isaacson*, Lockheed Martin Space Systems, *M.S. Wong*, Rice University, *S.L. Sinsabaugh*, Lockheed Martin MS2, *S.L. Biswal*, Rice University

Silicon continues to draw great interest as an anode material for lithium ion batteries due to its large specific capacity for lithium. Electrochemical etching silicon is one of several anode materials of interest, but its energy density is oftentimes limited due to its attachment to an unreactive silicon substrate. Here, we present a novel "liftoff" method by which a freestanding macroporous silicon film (MPSF) is electrochemically detached from the underlying bulk silicon and combined with pyrolyzed polyacrylonitrile

(PAN), a conductive polymer. We report the performance of these silicon thin films with and without pyrolyzed PAN.

Electron Transport at the Nanoscale Focus Topic Room: 16 - Session ET+NS+EM-ThM

Electron Transport at the Nanoscale: Nanowires and Junctions

Moderator: K. Clark, Oak Ridge National Laboratory, A.-P. Li, Oak Ridge National Laboratory

8:00am ET+NS+EM-ThM1 Functional Imaging of Semiconductor Nanowires and Devices, L.J. Lauhon, Northwestern University INVITED

Microscopy has played a central role in the advancement of nanoscience and nanotechnology by enabling the direct visualization of nanoscale structure, and by extension predictive models of novel physical behaviors. Correlated imaging of nanoscale structure and properties is an important frontier that can provide a rational basis for engineering new materials and devices. I will describe our approach to correlated functional imaging with a focus on semiconductor nanowires. Nanocrystal growth modes such as the vapor-liquid-solid process provide the ability to tailor nanoscale structure and composition in three dimensions, creating new opportunities in a range of applications including light harvesting and solid state lighting. In this context, we have explored a number of important processing-structure-property relationships using atom probe tomography, scanning transmission electron microscopy, Raman microspectroscopy, and scanning photocurrent microscopy. From these studies, we develop a more comprehensive understanding of the influence of geometry, size, defects, dopants, and interfaces on carrier generation, recombination, and transport in nanostructured materials. This quantitative approach to characterization of model systems aims to identify applications that can derive significant benefits from the adoption of unconventional nanostructured materials.

8:40am ET+NS+EM-ThM3 Electronic Transport and Structure Relations in Self-Assembled GdSi₂ Quantum Wires, S.Y. Qin, T. Kim, Oak Ridge National Laboratory, Y. Zhang, W. Ouyang, University of California Irvine, H. Weitering, The University of Tennessee, C. Shih, The University of Texas at Austin, A.P. Baddorf, Oak Ridge National Laboratory, R. Wu, University of California Irvine, A.-P. Li, Oak Ridge National Laboratory

Quantum wires are extremely narrow one-dimensional (1D) materials where electron motion is allowed only along the wire direction, and is confined in the other two directions. Quantum wires, as a smallest electronic conductor, are expected to be a fundamental component in all quantum electronic architectures. The electronic conductance in quantum wires, however, is often dictated by structural instabilities and electron localization at the atomic scale. Adding interwire coupling can often lead to the formation of charge density waves. In both cases, the metallic state is not stable and a metal to insulator transition (MIT) occurs at low temperature. [1] Here we show that robust metallic conductance can be stabilized by interwire coupling, while the isolated single nanowires exhibit a MIT due to quantum localization.

We grow the quantum wires of GdSi₂ on Si(100) and study the evolution of electronic transport as a function of temperature and interwire coupling as the quantum wires are self-assembled *wire-by-wire*. As shown in Fig. 1, individual nanowires have a width of 16.7 Å, a height of 4 Å, and lengths of micrometers. These nanowires can be grown either in the form of isolated nanowires or bundles with a number of constituent wires separated by an atomic interwire spacing. We perform the correlated study of electronic properties by utilizing both scanning tunneling microscopy and nanotransport measurements on the same nanowire. [2] The approach takes advantage of our developments in fabricating nanocontacts using a field-induced atom emission process to bridge the atomic wires and the mesoscopic transport electrodes. [3] A MIT is revealed in isolated nanowires, while a robust metallic state is obtained in wire bundles at low temperature. The results provide a rare glimpse of the intrinsic structure-transport relations and the influence of local environments at the atomic scale. This research was conducted at the Center for Nanophase Materials Sciences, which is sponsored at Oak Ridge National Laboratory by the Office of Basic Energy Sciences, U.S. Department of Energy.

1. Changgan Zeng, P.R.C. Kent, Tae-Hwan Kim, An-Ping Li, Hanno H. Weitering, *Nature Materials*, **7**, 539 (2008).

2. Shengyong Qin, Tae-Hwan Kim, Wenjie Ouyang, Yanning Zhang, Hanno H. Weitering, Chih-Kang Shih, Arthur P. Baddorf, Ruqian Wu, and An-Ping Li, *Nano letters*, **12** (2), 938 (2012).

3. Shengyong Qin, Sondra Hellstrom, Zhenan Bao, Boyan Boyanov, and An-Ping Li, *Appl. Phys. Lett.* **100** (11), 022211 (2012).

9:00am ET+NS+EM-ThM4 Multi-Segment Nanowire Heterojunctions of AuGe and Ge: Fabrication and Electrical Transport, X.D. Li, G.W. Meng, Chinese Academy of Sciences, China, S.Y. Qin, A.-P. Li, Oak Ridge National Laboratory

One-dimensional (1D) multiple segment nanostructures that contain heterojunctions between various metals and semiconductors are of great interest due to their fascinating chemistry and size-, shape-, and material-dependent properties. Here we report on the synthesis and electronic characterization of multi-segment nanowire (NW) junctions of Au_{1-x}Gex and Ge. The 1D heterostructures are grown with a low-temperature chemical vapor deposition process, assisted by electrodeposited Au NWs inside nanochannels of anodic aluminum oxide template.[1,2] The Au-catalyzed vapor-liquid-solid growth process occurs simultaneously in multiple locations along the nanochannel, which leads to multi-segment Au_{1-x}Gex/Ge heterojunctions. The structures of the as-grown hybrid NWs, analyzed by using transmission electron microscopy and energy dispersive X-ray spectroscopy elemental mapping, show clear compositional modulation with variable modulation period and controllable junction numbers. Remarkably, both GeNW and Au_{1-x}GexNW segments are single crystalline with abrupt interfaces and good crystallographic coherences. The electronic and transport properties of individual NW junctions are measured by using a multi-probe scanning tunneling microscope (STM). The semiconducting nature of Ge segments and the metallic behavior of Au_{1-x}Gex segments are examined by scanning tunneling spectroscopy (STS). The transport current-voltage curves across the heterojunctions show a characteristic rectifying behavior, which is discussed in association with the potential barriers at the junction. The high yield of multiple segment NW junctions and the ability to control predictably the properties of a metal-semiconductor can facilitate the applications in nanoelectronics and optoelectronics that harness multiple functionalities of hetero-interfaces.

[1] Li, X. D.; Meng, G. W.; Xu, Q. L.; Kong, M. G.; Zhu, X. G.; Chu, Z. Q.; Li, A. P. Controlled Synthesis of Germanium Nanowires and Nanotubes with Variable Morphologies and Sizes. *Nano Lett.* **2011**, *11*, 1704–1709.

[2] Li, X. D.; Meng, G. W.; Qin, S. Y.; Xu, Q. L.; Chu, Z. Q.; Zhu, X. G.; Kong, M. G.; Li, A. P. Nanochannel-Directed Growth of Multi-Segment Nanowire Heterojunctions of Metallic Au_{1-x}Gex and Semiconducting Ge. *ACS Nano* **2012**, *6*, 831–836.

9:20am ET+NS+EM-ThM5 Single Charge Nano Memory using Nano Carbon Material, K. Matsumoto, T. Kamimura, Osaka University, Japan

Single charges nano memory which can shift the threshold voltage by the stored single charge and operated at room temperature was realized using the carbon nanotube as an ultra short channel of 10nm.

The double gate stack insulator layers of Al₂O₃(3nm) and SiN_x (27nm) are deposited using the atomic layer deposition to the suspended carbon nanotube with source and drain electrodes of 70nm separation. The carbon nanotube channel was then surrounded by this double gate stack insulator layers and the gap between the source drain electrodes with the insulator layers reduced down to as small as 10nm. The gate metal was then deposited through this gap to form the gate electrode of 10nm.

The dependence of the drain current on the top gate bias shows weak oscillation along the gate bias with the period of 220mV. The oscillation is attributed to the single charge injection from CNT channel to the Al₂O₃/SiN_x interface trap, which make the threshold voltage shift of 220mV. The injection of charge is regulated by the Coulomb blockade that stops the next charge to be injected to the trap. The around trip of the gate bias produces the hysteresis. The width of the hysteresis was also regulated by the single charge injection and shows the stepwise increase.

Thus, we have succeeded in fabricating the single charge memory operated at room temperature.

9:40am ET+NS+EM-ThM6 Combining Atomic Structure, Local Band Alignment, and Electron Transport through Individual Semiconductor Nanowires using Scanning Tunneling Microscopy, R. Timm, O. Persson, M. Hjort, M.T. Borgström, L. Samuelson, A. Mikkelsen, Lund University, Sweden

III-V semiconductor nanowires offer tremendous possibilities for device application in energy and information technology [1]. Due to their unique properties and extreme surface-to-volume ratio, it is both essential and challenging to investigate their atomic structure and to combine this information with electrical measurements on individual nanowires. Recently, we have managed to clean InAs nanowires from their native oxide and obtained first atomically resolved images of their side surfaces by using scanning tunneling microscopy (STM) [2]. Here, we present a

systematic STM study covering various nanowire surface structures emerging from different III-V material systems and different crystal structures. By combining STM imaging with scanning tunneling spectroscopy (STS) measurements we simultaneously study the surface structure and local electronic properties across the interfaces of nanowire heterostructures like polytypic nanowires, *p-n*-junctions, and material heterostructures.

In order to go further in combining local structural and electronic characterization as well as transport measurements of nanowire devices, we have developed a new method to perform STM/S on individual nanowires *in-situ* under device operation: For this, specific heterostructure nanowires, distributed on a SiO₂/Si substrate, are contacted with metal electrodes defined by electron beam lithography. Using a combined Atomic Force Microscopy (AFM) / STM setup, we can first locate an individual nanowire in AFM mode and then acquire STM images and STS spectra on the contacted nanowire. Thus, we obtain the LDOS spatially resolved along the nanowire, even while the nanowire is externally biased via the metal contacts, allowing simultaneous transport studies. We will show and discuss initial results for different heterostructure nanowire devices, demonstrating the large potential of this new method.

Finally, we can also use the STM to measure electron transport through individual upright standing nanowires still on their growth substrate: After imaging the nanowires from top by STM [3], a point contact between the STM tip and the Au particle on top of the nanowire can be established in ultrahigh vacuum, thereby overcoming the problems in contacting single nanowires known from conventional setups. A high accuracy and reproducibility of this method has been demonstrated for InP and InAs nanowires with different doping levels [4] as well as for Schottky barrier measurements on Au/GaAs nanowires.

[1] Y. Li *et al.*, Mater. Today **9** (10), 18 (2006).

[2] E. Hilner *et al.*, NanoLetters **8**, 3978 (2008).

[3] A. Fian *et al.*, Nano Letters **10**, 3893 (2010).

[4] R. Timm *et al.*, *submitted* (2012).

10:40am ET+NS+EM-ThM9 Point-Contact Spectroscopy Study of Topological Insulators and Superconductors, Z. Jiang, Georgia Institute of Technology

Recently, much attention has been given to an intriguing class of materials, the so-called topological insulators. This type of material exhibits a band gap in the bulk, but gapless states on the edge or surface, which are protected by topological order and cannot be analogized to previous conventional semiconductors or insulators. When topological insulators are in contact with a superconductor (e.g., Nb, a conventional *s*-wave superconductor), novel proximity effect occurs. Theory predicts that the proximity induced superconducting state is spinless and *p*-wave like, and Majorana bound states may appear at the edges. On the other hand, in a related research avenue topological superconductors are predicted to possess unconventional pairing symmetries and gapless surface Andreev bound states. Theoretically massless Majorana fermions could be realized in such materials and used as a building block for topological quantum computation.

Here we present our point-contact spectroscopy studies of topological insulators and superconductors. Specifically, we use a superconducting Nb tip to approach the surface of topological insulators and measure the interface conductance as a function of bias voltage, temperature and magnetic field. Indeed, we find that a superconducting state can be induced at the interface when the Nb tip is in good contact with the topological insulator, as evidenced by observation of a zero-bias conductance peak in the point-contact spectra at a temperature below the superconducting transition temperature of Nb. Such an induced superconducting state is robust even in a magnetic field up to 1T. In the study of topological superconductors, we use a normal-metal Au tip to approach the surface, and a zero-bias conductance peak is also observed. Owing to accurate control of the point-contact barrier strength (tip/sample) in our experiments, the obtained spectra are free of artificial background, and therefore can be quantitatively compared with existing theories; good agreement is achieved.

11:00am ET+NS+EM-ThM10 Identifying and Measuring the State Variables in TaOx Memristors, P.R. Mickel, M. Marinella, C.D. James, Sandia National Laboratories

We present evidence of the identification and characterization of a new state variable in TaOx memristors. Thus far, the state variable controlling the resistive switching has been believed to be the oxygen concentration in the conducting Ta filament. However, using voltage pulse measurements sensitive to small changes in resistance, we shown that the changing area of the conducting filament is in fact the dominant switching mechanism. The oxygen concentration in the Ta filament is shown to control the memristor resistance for low resistances, after which we observe a clear crossover to

the area state variable dominated resistance range. Voltage and temperature dependence are investigated for the switching time-scales, τ , and magnitudes of filament area change, providing insight into their driving mechanisms and the resolution limits of their modulation.

11:20am ET+NS+EM-ThM11 Terahertz Spectroscopy and Carrier Dynamics of Al Doped ZnO Nanowires, S. Balci, W. Baughman, D.S. Wilbert, G. Shen, N. Dawahre, P. Kung, S.M. Kim, The University of Alabama

Terahertz time domain spectroscopy (THz-TDS) has been widely investigated for many applications in sensing and imaging technologies over the past two decades. Terahertz wave, with a frequency between 300GHz to 10THz, is especially attractive for various applications including security monitoring, biomedical imaging, high speed electronics and communications, and chemical and biological sensing. There is also an increasing interest for nondestructive testing using the THz waves because they have unique properties of propagation through certain media and cover a number of important frequencies. For such applications, THz-TDS has become a powerful tool and measurement technique that can probe carrier dynamics at high frequencies, and thus may yield a better understanding of the characteristics of high frequency optoelectronics and many other fundamental properties of materials. Using THz-TDS, one can determine the frequency dependence of basic properties of materials, including their complex dielectric constant, refractive index and electrical conductivity. Unlike conventional Fourier-Transform spectroscopy, THz-TDS is sensitive to both the amplitude and the phase of the wave, thereby allowing for a direct approach to determining complex values of material parameters with the advantage of high signal to noise ratio and coherent detection. In addition, it is possible to carry out THz-TDS experiments without any electrical contact to the sample being probed, which significantly facilitates electrical measurements on nanostructures and nanomaterials.

In this work, we investigated the physical properties of ZnO:Al nanowires (NWs) in using THz-TDS both at room temperature and elevated temperatures for the first time. ZnO NWs were grown by thermal chemical vapor deposition and *in-situ* doped with Al, which increased their electrical conductivity by one order of magnitude compared to undoped nanowires. THz-TDS measurements yielded the relative change in the transmitted THz electric field magnitude and phase caused by the samples being probed, which was used to extract the nanowire material refractive indices through mathematical iterative calculations. These subsequently allowed a determination of the complex conductivity, refractive index, and absorption coefficient. To obtain the carrier dynamics parameters, we showed that the Drude-Smith model had to be applied to the frequency dependent complex conductivity in order to determine the plasma frequency and relaxation time. To gain a better understanding of the dependence on doping, the measurements were performed for both undoped ZnO NWs and Al-doped ZnO NWs, as well as a function of temperature in each case.

11:40am ET+NS+EM-ThM12 Probing Surface-Independent Minority Carrier Transport in Semiconductor Nanowires using Kelvin Probe Microscopy, A. Soudi, C. Hsu, Y. Gu, Washington State University

In advancing semiconductor nanowire-based device technologies, a quantitative knowledge of carrier transport properties is required for a rational design of devices with controlled performance. The one-dimensional confinement of charge carriers and phonons can lead to novel transport properties, and thus represents an advantage of semiconductor nanowires in electronic and opto-electronic applications. However, due to the high surface-to-volume ratio, surface effects are prevalent in nanowires, and the measured carrier transport properties are usually dominated by surface-related processes, such as carrier trapping and recombination processes facilitated by surface states. To evaluate the intrinsic transport properties, especially those related to the confinement effects, the capability to probe surface-independent carrier transport properties is desired. Here we present studies of bulk limited minority carrier transport properties in semiconductor nanowires using the scanning Kelvin probe microscopy technique. Specifically, by measuring and modeling the spatial variations of the nanowire surface potential close to a nanowire-metal Schottky junction, both under an above-bandgap illumination and in the dark, the surface-independent minority carrier diffusion length was obtained.

Graphene Nanostructures

Moderator: A. Kis, EPFL, Switzerland

8:00am **GR+AS+NS+SS-ThM1 Atomic and Electronic Structures of Graphene Nanoribbon made by MBE on Vicinal SiC Substrate.** *F. Komori, K. Nakatsuji, T. Yoshimura*, University of Tokyo, Japan, *T. Kajiwara, K. Takagi, S. Tanaka*, Kyushu University, Japan

Electronic states of graphene nanoribbon attract much interest because its intrinsic metallic band is modified to have a gap or a one-dimensional edge state at the Dirac energy E_D . Actually, microfabricated graphene [1] showed an energy gap at E_D , and the gap size increases with decreasing the width. Fabrication of well-controlled graphene nanoribbons on macroscopic area of a semiconductor substrate is, however, still one of the challenging issues in graphene research. Here, we report characterizations of graphene nanoribbon made by carbon molecular beam epitaxy (MBE) and a hydrogen treatment on a vicinal SiC(0001) substrate. Use of MBE is essential because graphene is made over the step edges of the SiC substrate in the case of graphene formation by widely-used thermal decomposition.

In the experiment, a $6\sqrt{3} \times 6\sqrt{3}$ structure was first made by MBE on the anisotropic terrace of the Si-terminated surface of a nitrogen-doped 6H-SiC(0001) substrate vicinal to the [1-100] direction. The tilting angle of the substrate was 4 degree, and a well-ordered step-and-terrace structure was made after cleaning the substrate by annealing in hydrogen as confirmed by atomic force microscopy. We optimized the substrate temperature and the carbon deposition rate to make a homogeneous $6\sqrt{3} \times 6\sqrt{3}$ structure on the terraces without thermal decomposition of the substrate. The surface structure was *in situ* monitored by reflection high energy electron diffraction, and the width of the $6\sqrt{3} \times 6\sqrt{3}$ area on the terrace was adjusted by monitoring the $6\sqrt{3} \times 6\sqrt{3}$ spots. After stopping the growth, the sample was exposed to hydrogen molecules at 600 °C to transform the surface $6\sqrt{3} \times 6\sqrt{3}$ layer to single-layer graphene by inserting hydrogen atoms at the interface. [2]

Graphene honeycomb lattice without the $6\sqrt{3} \times 6\sqrt{3}$ structure was confirmed by low energy electron diffraction and scanning tunneling microscopy (STM). Few point defects are seen at the graphene on the terrace in the STM images of atomic resolution. The width of graphene nanoribbon on the substrate terrace is 10-15 nm, depending on the growth condition. The electronic states of the graphene nanoribbon were studied using angle-resolved photoemission spectroscopy (ARPES) at 130 K as in the previous report. [3] The top of the π band of the graphene nanoribbon was 0.05 ~ 0.25 eV below the Fermi energy. No signal from the π^* band was detected by ARPES above the top of the π band, indicating the gap formation at E_D .

References

1. M. Y. Han *et al.*, Phys. Rev. Lett. **98**, 206805 (2007).
2. C. Riedl *et al.*, Phys. Rev. Lett. **103**, 246804 (2009).
3. K. Nakatsuji *et al.*, Phys. Rev. **B82** 045428 (2010).

8:20am **GR+AS+NS+SS-ThM2 Carrier Transport Behavior of Carbon Nanotube Transistors with Single Semiconducting and Metallic Tube.** *P. Sakalas, M. Schroter*, Technische Universität Dresden, Germany

The high interest in using carbon nanotube FETs in advanced electronics is based on their unique 1D transport properties such as quasi-ballistic transport. The high carrier velocity together with the quasi 1D tube geometry yield a very low intrinsic capacitance per tube of approximately 80 aF/mm in multitube structures. Those properties makes CNTFETs very interesting for high frequency and power applications.

CNTFETs with a single semiconducting tube yield too low current (25 μ A) for useful applications and thus the transistors with thousands tubes in parallel are being fabricated [1][2]. Unfortunately, following theory 1/3rd of all tubes are metallic. Carrier scattering is better understood for metallic tubes and it is believed that for semiconducting tubes, despite more complexity, the same scattering mechanisms are applicable: CNTs defect scattering, physical bends and phonon scattering are present. Investigation of CNTFETs with a single semiconducting (ST), single metallic (MT) and metallic+semiconducting (MST) tubes at different lattice temperature environment was never done before and enables a deeper insight of CNT transport properties to further improve the application-oriented device behavior. It was shown that multifinger CNTFETs exhibited a weak temperature dependence of IV, RF and NF indicating a very weak electron-phonon interaction and the absence of charge-carrier freeze-out known for conventional doped semiconductors [3],[4].

In this work transistors with single ST, single MT and double MST were selected. Transistors have 800 nm channel length and features n-type

behavior. IV characteristics were measured on wafer for manufacturable CNTFET process selected single CNTs at different lattice temperatures. The investigated structures have a fixed gate length of 0.35 μ m and gate width of 40 μ m. The source-drain spacing (channel length) is 800 nm. A 20 nm thick HfO₂ was used for the gate oxide. The devices were fabricated with the process technology described in [1][2]. The CNTFETs were embedded in DC pads for on-wafer measurements. Transfer characteristics of ST and MT transistor structures at ambient temperature $T_0 = 300$ K, are shown in Fig.1 and Fig.2, Fig.3, Fig.4. The drain current show saturation for ST device, typical for MOSFETs. Nevertheless the carrier transport is very different. The dependence of drain current over the temperature will enable the analysis of transport behavior of single ST and MT and coupled MST. As it is seen from Fig.3 and Fig.4 the MT transistor structure behaves as nonlinear resistor.

8:40am **GR+AS+NS+SS-ThM3 Fabrication of Chemically-isolated Graphene Nanoribbons (GNRs) by Scanning Probe Nanolithography using a Heated Probe.** *W.K. Lee, J.T. Robinson, R. Stine, C.R. Tamanaha, D. Gunlycke*, Naval Research Laboratory, *M. Haydell, E. Cimpoiasu*, U.S. Naval Academy, *W. King*, University of Illinois at Urbana Champaign, *P.E. Sheehan*, Naval Research Laboratory

One route to realizing graphene as a material for digital-type devices is through the lithographic patterning of graphene nanoribbons (GNRs). GNRs enable band gap engineering that is dependent on nanoribbon width and edge state. We employed two complementary AFM-based lithography techniques to pattern GNRs: (1) thermal dip-pen nanolithography (tDPN)¹ and (2) thermochemical nanolithography (TCNL)². Though inverse in approach, both techniques generate GNRs into a larger sheet of insulating chemically-modified graphene. Both lithographies were performed on CVD-grown single-layered graphene (SLG) on SiO₂/Si substrates using heated AFM probes. The first approach, tDPN, used the heated probe to deposit narrow polystyrene (PS) ribbons on pristine graphene. The areas of the graphene not protected by the polymer were then fluorinated, converting them to a highly insulating state, which leaves behind a chemically isolate GNR channel. We show that the PS protected ribbon was the only conductive pathway for active device. Secondly, we use the converse approach by using the heated AFM probe to locally reduce fluorographene back to graphene, leaving behind a conductive GNR channel. Both techniques can generate a wide range of nanoribbon widths while avoiding electron beams which can damage graphene. We discuss the relative merits of each strategy, as well as their impact on electrical properties (e.g., doping).

1. WK Lee *et al.*, *Nano Letters*, 11, 5461, 2011
2. Z Wei *et al.*, *Science*, 328, 1371, 2010

9:20am **GR+AS+NS+SS-ThM5 Growth of a Linear Topological Defect in Graphene as a Gate-tunable Valley Valve.** *A. Zettl, J.-H. Chen, N. Alem*, Univ. of California at Berkeley, Lawrence Berkeley Lab, *G. Autes, F. Gargiulo*, Ecole Polytechnique Fédérale de Lausanne (EPFL), Switzerland, *A. Gautam, M. Linck*, Lawrence Berkeley National Lab, *C. Kisielowski*, Lawrence Livermore National Lab, *O.V. Yazyev*, Ecole Polytechnique Fédérale de Lausanne (EPFL), Switzerland, *S.G. Louie*, Univ. of California at Berkeley, Lawrence Berkeley Lab

INVITED
The valleytronics, a zero-magnetic-field equivalent of spintronics, could be realized in graphene if a simple scheme can be conceived to generate and to detect valley polarization in the material. Here we provide the first direct experimental observation of the self-sustained, atomically controlled growth of a peculiar linear defect structure in suspended graphene. The structure consists in units of octagon and pentagon pairs (termed 5-5-8 defect) and can be grown from a single pentagon seed in graphene under electrical bias. First-principle simulations show that the 5-5-8 defect can act as a gate-tunable valley valve. The result represents a critical step towards realizing valleytronics in graphene.

10:40am **GR+AS+NS+SS-ThM9 Crystalline and Electrical Properties of Vertically-Laminated Carbon Nanowalls formed by Two-Step Growth Method.** *H. Kondo, T. Kanda*, Nagoya University, Japan, *M. Hiramatsu*, Meijo University, Japan, *K. Ishikawa, M. Sekine, M. Hori*, Nagoya University, Japan

Carbon nanowall (CNW) is one of carbon nanomaterials consisting of stacked graphene sheets, which are vertically standing on the substrate. Due to the unique properties of graphene sheets, such as high carrier mobility, large current carrying capability, and so forth, it is expected that the CNW also have such the excellent electrical and physical properties. On the other hand, in the CNWs, the bending and branching graphene sheets take a maze-like form. Therefore, due to their unique morphology and properties, the CNWs are promising as channel and electrode materials in the various types of the future nanoelectrics devices. At the construction of the CNW

devices, vertical lamination of different types of CNWs is one of the useful and important technique as basic elements of the devices.

In this study, we investigated sequential two-step growth of CNWs to form the vertically-laminated structures. In this experiment, two types of CNW growth processes with different conditions were sequentially performed on Si substrate by an electron beam excited plasma-enhanced chemical vapor deposition (EBEP-CVD) using CH₄/H₂ mixture gas. Firstly, the CNW was grown at 600°C and 2.67 Pa for 10 min. Then, the second-step growth process was performed at 480°C for 10 min. The CNW samples formed only by the single-step growth at 480°C or 600°C were also prepared for comparison. Morphology and crystalline structures of CNWs were analyzed by scanning electron microscopy and Raman spectroscopy.

In the case of the single-step growth, only after the growth at 600°C, about 600 nm-thick CNWs were formed, although CNWs hardly grew at 480°C. On the other hand, in the case of the step-growth, about 1200 nm-thick CNWs were formed after the second-step growth at 480°C, compared to the single-step growth at 600°C. No boundary was found between the lower and upper region. The stacks of graphene sheets formed seamless structures. According to the Raman spectra, the crystalline structures of the CNWs were hardly changed even after the first-step growth at 600°C and the second-step growth at 480°C. This result means that the nanographene can restart to grow easily and continuously at the edges of the previously-grown graphene even at 480°C without the nucleation. These results indicate the possibility to realize the vertical junction of different types of CNWs, such as a p-n junction. At the session, the interfacial structures and electrical properties of the vertically-laminated CNWs will also be discussed.

11:00am **GR+AS+NS+SS-ThM10 Surface Modification of Vertically Oriented Graphene Electrochemical Double-Layer Capacitors**, *R.A. Quinlan*, Naval Surface Warfare Center, Carderock Division, *M. Cai*, The College of William and Mary, *A.N. Mansour*, Naval Surface Warfare Center, Carderock Division, *R.A. Outlaw*, The College of William and Mary

Previously reported efforts have identified the potential of vertically oriented graphene nanosheets in electrochemical double-layer capacitors (Miller et al, Science 2010) for efficient AC line-filtering performance. Continued investigations to improve performance suggest that the availability of a high edge and surface defect density could be the dominant mechanism. Furthermore, charge/discharge profiles over time show that performance can actually increase as the device ages. In an effort to understand these findings, X-ray photoelectron spectroscopy, Auger electron spectroscopy and near edge absorption fine structure spectroscopy have been utilized to study the interaction of the electrolytes and solvents with the graphene-based electrode materials. The EDL capacitance of graphene nanosheets has been measured before and after Ar plasma bombardment for various times and after exposure to water, isopropanol, methanol, NaOH and KOH. Graphene nanosheet electrochemical capacitors have been disassembled and analyzed following short term and long term operation.

11:20am **GR+AS+NS+SS-ThM11 Electronic Properties and Device Applications of Wafer-Scale Graphene Nanoribbons**, *D. Jena*, University of Notre Dame **INVITED**

Graphene boasts unique physical, electronic, and optical properties. For conventional electronic device applications, the zero band gap of 2-dimensional graphene is an impediment. Opening of effective band gaps can be achieved by field-effect in bilayer graphene, or by using Klein-tunneling properties of graphene p-n junctions. However, these methods appear not to effectively scale to small dimensions. Another way to open band gaps in graphene is to make graphene nano ribbons (GNRs) and use size quantization. Though many of the properties of 2D graphene are lost in the process, GNRs become similar to semiconducting carbon nanotubes, but with planar structures and compatibility with conventional lithographic processes. In this talk, I will present our group's research progress in making such wafer-scale GNR transistors. Band gaps ~0.15 eV appear in ~10 nm wide single GNRs, and band gaps are preserved in parallel arrays of GNRs. Based on these GNRs, we measure current drives as high as 10mA/micron, which far exceeds all other semiconductor materials and seems attractive for both logic and interconnect applications. The effects of edge roughness on scattering and mobility, and the progress towards making GNR-based tunneling transistors will also be presented.

Helium Ion Microscopy Focus Topic

Room: 19 - Session HI+AS+BI+NS-ThM

Imaging and Lithography with the Helium Ion Microscope

Moderator: A. Götzhäuser, University of Bielefeld, Germany, V.S. Smentkowski, General Electric Global Research Center

8:40am **HI+AS+BI+NS-ThM3 Helium Ion Microscopy of Photonic Structures in Biological Systems**, *S.A. Boden*, *A. Asadollahbaik*, *H.N. Rutt*, *D.M. Bagnall*, University of Southampton, UK **INVITED**

The natural world is replete with examples of biological systems that have developed complex micro- and nano-scale structures to interact with light. Such structures, which include thin film multilayers, diffraction gratings, graded index layers and 2D and 3D photonic crystals, acting alone or in combination, allow the realization of a range of optical effects that would be impossible through the use of pigmentation alone. These effects range from the vivid iridescence observed on the skin of some species of bird, through the vibrant metallic sheen of some beetle species, to the dramatic interference patterns seen on the transparent wings of some species of fly. Lepidoptera (an order of insects that includes butterflies and moths) also provides a rich seam of examples of structural color ranging from the antireflective nipple arrays found on the eyes and wings of some species of moth to the photonic crystal structures producing vivid coloration on the wings of some butterfly species.

As these optical effects are a result of the scale of these structures being at or below that of visible light wavelengths, scanning electron microscopy (SEM) is often used to explore their form and to offer insights into their function. Recently, helium ion microscopy (HIM) has emerged as a surface imaging technique, similar to SEM but with the benefits of higher resolution and a larger depth of field. Here, HIM is used to probe the structures responsible for a number of optical effects observed in Lepidoptera. Images will be presented showing the fine details of the ribs and cross-ribs found on the highly-absorbing black ground wing scales of *Papilio ulysseus* (Blue Mountain Butterfly) and the complex gyroid 3D photonic crystal structure observed underneath the top lamina on vividly green wing scales from *Parides sesostris* (Emerald-patched Cattleheart). Other examples will include the antireflective close-packed nipple array on the wings of *Cephonodes hylas* (Pellucid Hawk Moth), and cross-sections of the multilayer structures that make up the various colored wing scales of *Chrysidia rhipheus* (Madagascar Sunset Moth).

The integrated electron flood gun on the helium ion microscope is employed to neutralize charge build-up, allowing samples to be imaged without the need of a conductive coating. This ensures that the natural surface itself is imaged at high resolution and details are not obscured by coating artefacts. In addition, by taking advantage of the large depth of field available with HIM, stereo pairs are generated to extract information on the three-dimensional nature of these structures.

9:20am **HI+AS+BI+NS-ThM5 Imaging of Carbon Nanomembranes (CNM) and Graphene with Helium Ion Microscopy**, *H. Vieker*, *A. Beyer*, *A. Polina*, *A. Willumat*, *N.-E. Weber*, *M. Bünenfeld*, *A. Winter*, *X. Zhang*, *M. Ai*, *A. Turchanin*, *A. Götzhäuser*, Bielefeld University, Germany

We present a Helium Ion Microscopy (HIM) study of carbon nanomembranes (CNMs). CNMs are extremely thin (~1 nm) nanolayers consisting only of surface. They are made via cross-linking of self-assembled monolayers (SAMs) with large-area exposures of electrons, photons or helium ions and a subsequent transfer to suitable substrates. Patterned radiation exposures allow the fabrication of perforated nanomembranes, e.g., nanosieves. After annealing at temperatures above 800K, CNMs become conductive and eventually transform into graphene. HIM images of CNMs with different precursor molecules are shown, and images of graphene from SAMs are compared with the CVD grown graphene. Capabilities of the HIM imaging of freestanding CNMs and graphene will be discussed.

10:40am **HI+AS+BI+NS-ThM9 Dopant Contrast in Helium Ion Microscopy**, *Y. Chen*, *H. Zhang*, *D. Fox*, *C.C. Faulkner*, *J. Wang*, *J. Boland*, *J. Donegan*, Trinity College, Ireland **INVITED**

Innovation in metrology is crucial to the future of semiconductor industry, since the miniaturization of transistors demands novel characterization technologies at and beyond the nanometre scale. Recent research has demonstrated that dopant contrast in the Helium-ion Microscope (HIM) is plausible and the HIM is a competitive platform for quantitative secondary-electron (SE) dopant mapping in terms of throughput, sensitivity, and

resolution. However, the contrast mechanism of SE imaging is still debatable and it hinders further development of the technique. In this research, quantitative HIM dopant contrast of gallium-doped silicon samples has been investigated and compared with the contrast observed in a scanning electron microscope (SEM). Beam-sample interaction, signal general, as well as detection configuration have been considered via using a range of detectors in the two microscopes. It has been found that the Everhart-Thornley (E-T) secondary electron detector attached to HIM provides similar contrast to the images acquired from the InLens detector attached to SEM, while contrast reversal is observed with the SEM E-T detector. The contrast reversal also depends on the Dwell time. We have confirmed that the HIM is more sensitive to type-I SEs and a capacitance model based on charging effect has been proposed to explain the contrast reversal. Our results indicate that quantitative dopant contrast in the HIM is promising, while charging effect and imaging conditions must be carefully considered.

11:20am **HI+AS+BI+NS-ThM11 High Resolution Patterning of Carbon Nanomembranes and Graphene via Extreme UV Interference Lithography: A Helium Ion Microscopy Study**, *A. Winter, A. Willunat, A. Beyer*, University of Bielefeld, Germany, *Y. Ekinici*, Paul Scherrer Institute, Switzerland, *A. Götzhäuser, A. Turchanin*, University of Bielefeld, Germany

Two-dimensional (2D) carbon materials like graphene, graphene oxide, carbon nanomembranes (CNMs) or ultrathin polymeric films have recently attracted enormous interest due to their potential use in electronics, chemical and biological sensors, nanofilters, hybrid materials, etc. Most of these applications require lithographic patterning of these 2D carbon materials with the nanoscale resolution. In this respect, Extreme UV Interference Lithography (EUV-IL) provides both large-scale patterning and high resolution with an ultimate limit in the sub-10 nm range. We employ EUV-IL to generate nanopatterns in ~1 nm thick CNMs and graphene. We characterize these nanopatterns with a Helium Ion Microscope (HIM). Its high surface sensitivity and lateral resolution provide excellent conditions for imaging of the topographic and chemical features in CNMs and graphene. The possibility to routinely fabricate and characterize the nanopatterns via EUV-IL and HIM on various technologically relevant insulating substrates (e.g., oxidized silicon wafers, glass, and quartz) and with the resolution below 20 nm shows high potential of both techniques for applications in carbon-based nanotechnology.

11:40am **HI+AS+BI+NS-ThM12 Application of Helium Ion Microscope on Processing and Characterization of Nano Wires**, *H.X. Guo, S. Nagano, K. Onishi, D. Fujita*, National Institute for Materials Science (NIMS), Japan

Scanning helium ion microscope (SHIM) is advanced in high resolution and high focal depth of secondary electron imaging and Rutherford backscattered ion imaging.[1] It also employed in the nano pattern or fabrication on surface and other various structures, such as 2D materials, graphene.[2] It is an excellent candidate for the nano processing of 1D nano structures, such as nanowires and nanotubes.

Rhenium trioxide (ReO₃) is an unusual transition metal oxide with high electrical conductivity close to that of metals. It is well investigated for the applications of photovoltaics[3], catalyst[4], and tip for scanning tunneling microscope[5]. Various ReO₃ nano structures such as nano particles[3,6], nano wires[7], and core-shell structures have been synthesized and characterized by different methods.

In this research, ReO₃ nanowires were synthesized by a physical vapor deposition method. Etched by the helium ion beam, the diameter of part of the nanowire was decreased. During this processing, the structure and transport properties of the ReO₃ nanowire were modified with a controllable method. In this presentation, we will show the structure and properties characterization of the etched nanowires by using scanning probe microscope (SPM), transmission electron microscope (TEM) and other methods. An *in-situ* transport properties measurement system with SHIM will also be introduced in the presentation.

[1] J. Morgan, J. Notte, R. Hill, and B. Ward, *Microsc. Today*, **14**, 24(2006)

[2] D. C. Bell, M. C. Lemme, L. A. Stern, J. R. Williams, and C. M. Marcus, *Nanotech.*, **20**, 455301(2009).

[3] S. V. Bhat, S. B. Krupanidhi, and C. N. R. Rao, *Appl. Phys. Express*, **3**, 115001(2010)

[4] E. Cazzanelli, M. Castriota, S. Marino, N. Scaramuzza, J. Purans, A. Kuzmin, R. Kalendarev, G. Mariotto, and G. Das, *J. Appl. Phys.*, **105**, 114904 (2009)

[5] S. I. Ikebe, D. Shimada, T. Akahane, and N. Tsuda, *Jpn. J. Appl. Phys.*, **30**, L405(1991)

[6] K. Biswas and C. N. R. Rao, *J. Phys. Chem. B*, **110**, 842, (2006).

[7] D. Myung, Y. Lee, J. Lee, H. K. Yu, J. L. Lee, J. M. Baik, W. Kim, M. H. Kim, *phys. status solidi-R*, **4**, 365 (2010)

Biofilms and Biofouling: Marine Medical Energy Focus Topic

Room: 23 - Session MB+BI-ThM

Biofilms and Biofouling in Medicine

Moderator: L. Hanley, University of Illinois at Chicago

8:20am **MB+BI-ThM2 Simple and Versatile Approaches to Design Oligoethylene Based Self-Assembled Monolayers using Thiolene Chemistry on Different Metal Oxide Surfaces: Impact on Protein Adsorption**, *A. Galtayries, A. Dellinger*, Chimie ParisTech (ENSCP), France, *V. Semetey*, Institut Curie, France

The control of biomolecules adsorption (such as proteins) and other microorganisms is of high interest for various fields of biotechnology, such as bioanalytics, cell biology, tissue engineering and biomaterials. An efficient method to control adsorption includes the use of well-defined oligo(ethylene glycol)-terminated self-assembled monolayer (SAM). However, multiple processing steps are often required to prepare SAM onto substrate. To address these problems of surface modification, we have developed a simple method using the powerful thiolene reaction to prepare self-assembled monolayer on different metal oxides to control bioadhesion on surfaces starting from commercially available building blocks, and taking the advantage of the photoreaction to easily create adhesive and anti-adhesive patterns.

Such well-controlled grafting strategy has been applied to different metal oxides: from silicon substrates for the methodology set-up to model metal oxides formed on biocompatible metals and alloys. The obtained films are robust; the process is low-cost, simple, and efficient.

Surface characterization as X-ray Photoelectron Spectroscopy (XPS), Time of Flight Secondary Ion Mass Spectrometry (ToF-SIMS) and Infra-Red Surface Spectroscopy (ATR-IRFT or PM-IRRAS) were used to check the surface composition at different steps of the reactions: the thiolene reaction, the PEG grafting, as well as after interaction with protein solutions: albumin for preliminary tests, and fibronectin, an adhesive protein present in the extra-cellular matrix. In addition to quantitative information, obtained by XPS, about the oxide composition and thickness at the different steps, and qualitative information, obtained by XPS and ToF-SIMS, surface patterning could be emphasized with ToF-SIMS chemical surface imaging.

8:40am **MB+BI-ThM3 Antibacterial Studies of Plasma Polymerised Cineole Thin Films**, *A. Pegalajar-Jurado*, Swinburne University of Technology, Australia, *C.D. Easton*, CSIRO Materials Science and Engineering, Australia, *S.L. McArthur*, Swinburne University of Technology, Australia

Essential oils such as tea tree oil are known for their antibacterial properties. They have been used extensively as effective topical antimicrobial agents and are active against a wide range of micro-organisms. Traditionally, the antimicrobial properties of tea tree oil has been linked to the constituents of the oil including terpinen-4-ol and 1,8-cineole. To translate these antimicrobial properties into medical devices, methods for incorporating or coating materials are required. Recently, thin polymer films from terpinen-4-ol have been fabricated using plasma polymerisation. Initial data suggests that some antimicrobial activity was maintained. While plasma polymer films of 1,8-cineole have been fabricated previously, little focus has been placed on the antibacterial activity of this constituent.

The activity of 1,8-cineole against *Staphylococcus aureus* (*S. aureus*) and *Escherichia coli* (*E. coli*) was evaluated based on the time-kill approach. Several concentrations of the oil (0.05 %, 0.2 %, 0.3 % and 0.5 % v/v) were added to broth media containing 3x10⁸ CFU/mL of each bacterium. The optical density of the resulting solutions was measured at intervals over 24-hrs to monitor bacterial growth rates. The results demonstrated that concentrations above 0.35% v/v gave a 90% kill rate in the gram-negative *E. coli* after 8-hrs. Interestingly, the oil was less effective against the gram-positive *S. aureus*, producing a lower kill rate and rapid growth recovery in a 24-hour period.

Plasma polymers thin films of 1,8-cineole and 1,7-octadiene (hydrophobic control) were prepared using a stainless steel plasma reactor as described previously, while uncoated glass slides were used as a hydrophilic, positive control. Samples were then exposed to broth media containing 3x10⁸ CFU/mL of each bacterium to determine the effects of the coatings on bacterial attachment and growth. In this work, bacterial studies of the

coating behaviour have focused on the attachment of *S.aureus* and *E. coli*, and biofilm formation of *E. coli*. Comparison of the plasma polymerised cineole (ppCineole) coating with the two controls demonstrated a reduction in bacterial attachments over 18-hrs. The reduction in bacterial attachment was more obvious in the case of *E.coli* in comparison with *S. aureus*. There were not significant differences between plasma polymerised cineole and octadiene in the inhibition of *E.coli* attachment and growth over a period of 18-hours. However, the biofilm studies indicated that only the 1,8-cineole film demonstrated antimicrobial behaviour over a period of time of 5 days.

Keywords: plasma polymerisation, antibacterial activity, cineole

9:00am **MB+BI-ThM4 Robustness Analysis of Biofilm Antibiotic Tolerance.** *R.P. Carlson*, Montana State University **INVITED**

Biofilms are ubiquitous and are thought to be involved in more than half of all medical infections. Even after decades of investigation, the *in vivo* efficacy of many antimicrobial strategies is still debated suggesting a need for better understanding of biofilm antimicrobial tolerances. The robustness of biofilm antibiotic tolerance to medically and industrially relevant culturing perturbations was characterized. By definition, robust systems return similar, predictable responses when perturbed while non-robust systems return very different and potentially unpredictable responses. Biofilm antibiotic tolerance was found to vary in unpredictable manners based on modest perturbations in culturing conditions. The predictability of an antibiotic tolerance response is essential to developing, testing, and employing antimicrobial strategies. The collective data represents both challenges and opportunities for the rational design of anti-biofilm strategies. The data demonstrates that biofilms can be countered effectively with some antibiotics if the appropriate environmental conditions are applied however, if inappropriate conditions are applied, the efficacy of the treatment can be negated. The results indicate it is essential to evaluate antimicrobial strategies over a range of perturbations relevant to the targeted application so accurate predictions regarding efficacy can be made. In addition, the highly dynamic antibiotic tolerance responses observed here may explain why some current antimicrobial strategies occasionally fail.

9:40am **MB+BI-ThM6 Analysis of Force Curves of *Pseudomonas Aeruginosa* obtained by Atomic Force Microscopy.** *E.V. Anderson, R.L. Gaddis, T.A. Camesano, N.A. Burnham*, Worcester Polytechnic Institute

Pseudomonas aeruginosa is extremely harmful to immune-compromised individuals. An atomic force microscope (AFM) can be used to measure the forces between the AFM tip and the bacterial exopolymers, with which the bacteria attach themselves to surfaces. These forces are characterized with a model that is a function of brush (exopolymer) layer thickness, probe radius, temperature, separation distance, and a molecular volume. Initial experiments with limited data sets are consistent with expected brush thicknesses of a few hundred nanometers. In order to progress – now with rigor – we have just developed a high throughput method for the analysis of force curves on the exopolymers of *P. aeruginosa* [1]. The above-described model is only valid for the region where the tip is in contact with the exopolymers, yet is not perturbing the bacterial membrane. MatLab code was written to determine the location of this region in each force curve, crop the curve to that region, and apply the force model in order to obtain parameters of the exopolymers. The standard deviation of the mean and Chauvenet's Criterion are then applied to the results of sets of one-hundred force curves to increase measurement precision and objectively remove outliers. This procedure removes user subjectivity in cropping, fitting, and outlier removal, decreases analysis time by two orders of magnitude, and increases the precision of fitted results by a factor of ten (for one-hundred curves), which is necessary for demonstrating the statistical significance of our data.

[1] Anderson et al., to be submitted May 2012.

10:40am **MB+BI-ThM9 Light and Dark Biocidal Activity of Conjugated Polyelectrolytes.** *K. Schanze*, University of Florida, *D.G. Whitten, T. Corbett, E. Ji, D. Daszier*, University of New Mexico, *A. Parthasarathy, S. Goswami*, University of Florida **INVITED**

Cationic conjugated polyelectrolytes (CPEs) are semiconducting organic polymers that contain ionic solubilizing groups. These polymers are soluble in water and they self-assemble into colloidal nanostructures in solution and layer-by-layer films at interfaces. CPEs interact strongly with bacteria in solution and on coated interfaces, and under short wavelength visible or near UV light irradiation they exhibit strong biocidal activity. Mechanistic studies using photophysics and cell live/dead assays find that the CPEs efficiently sensitize the production of singlet oxygen, and this is believed to be at least partially responsible for the light-activated biocidal activity. Structure-property studies find that specific hydrophobic CPEs exhibit strong dark biocidal activity. Studies with membrane models indicate that the dark active CPEs exhibit a strong tendency to interact with and disrupt the cell membrane structure.

11:20am **MB+BI-ThM11 Mechanisms of Antimicrobial Activity of Quaternary Ammonium Compounds in Solution and Immobilized on a Surface.** *H.C. Van der Mei*, University Medical Center Groningen, The Netherlands

Quaternary ammonium compounds (QAC) are potent cationic antimicrobials used in everyday consumer products like contact lens solutions and mouthrinses as well as in numerous industrial processes, like water purification. Unlike the case for many antibiotics, the development of bacterial resistance against QACs is considered unlikely, although *Pseudomonas aeruginosa* strains isolated from contact lens cases have been shown to possess resistance against QACs. The first step in the antimicrobial action of QACs is the approach of the QAC molecule towards the bacterial cell surface. This is mediated by hydrophobic and electrostatic attractions between positively charged QAC molecules and the negatively charged bacterial cell surface. Upon their subsequent adsorption, QAC molecules replace Ca^{2+} or Mg^{2+} ions from the cytoplasmic membrane in order to maintain charge neutrality in the membrane. The replacement of Ca^{2+} and Mg^{2+} ions by QACs destabilizes the intracellular matrix of a bacterium, as the hydrophobic tail interdigitates into the hydrophobic bacterial membrane causing leakage of intracellular fluid and loss of turgor pressure. Antimicrobial efficacy of QACs remains preserved when QAC molecules are immobilized on a substratum surface. It is difficult to envisage how immobilized QAC molecules can exert the same mechanism of antimicrobial activity as do QACs in solution. Immobilized QACs, especially after adsorption of a protein film as developing rapidly in the human body, are strongly hindered in their search for heterogeneously distributed negative charges on bacterial cell surfaces which is crucial for their efficacy in solution. Hence, it has been often hypothesized that QAC molecules immobilized to a substratum surface possess other generic mechanisms of action than QACs in solution, but these have never been elucidated. Immobilized QACs do not cause directly visual membrane damage. Instead, the strong adhesion forces arising from immobilized QACs enter bacterial adhesion forces into the lethal regime, i.e. where the stress exerted on the bacterial cell membrane is causing killing.

11:40am **MB+BI-ThM12 Combinatorial Discovery of Materials That Resist Bacterial Adhesion.** *A.L. Hook, C. Chang, J. Yang*, University of Nottingham, UK, *R. Langer, D.G. Anderson*, Massachusetts Institute of Technology, *S. Atkinson, P. Williams, M.C. Davies, M.R. Alexander*, University of Nottingham, UK

Biofilm formation leads to a 1000 times increase in antibiotic tolerance compared with planktonic bacteria and is associated with 80% of hospital acquired infections, resulting in \$3.0 billion in excess health-care costs each year in the U.S alone. Thus, new materials that prevent biofilm formation would offer enormous benefits to the health industry and improve patient welfare. However, the limited understanding of bacteria-material interactions restricts the rational design of such materials. Polymer microarrays are emerging as a key enabling technology for the discovery of new biomaterials[1] and have been utilised to identify novel polymers that resist bacterial attachment.

Polymer microarrays were formed as previously described.[2] This platform enabled a large combinatorial space to be rapidly screened by a biological assay to identify new materials that fulfil a given performance criterion.[3] In the present study a bacterial attachment assay was developed using green fluorescent protein (GFP) tagged bacterial strains (*Pseudomonas aeruginosa*, *Staphylococcus aureus* and *Escherichia coli*) where the attachment of bacteria to each material was quantified by measuring the fluorescence after incubation for 72 h.

Due to the large combinatorial chemical space available to the polymer microarray format a strategy was devised to rapidly identify the optimal polymer composition that resists bacterial adhesion. This utilised a multi-generation microarray approach where the 'hits' from one array feed into the design of a subsequent array. Initially, an array was formed from 22 monomers with varied chemistry that were mixed to form 488 unique material compositions. Hit compositions were chosen from this array to produce a focussed second generation array containing unique materials where the hit compositions were varied incrementally. The resulting hit compositions were all amphiphilic containing both hydrophobic and hydrophilic moieties.

A methodology has been developed to screen the vast combinatorial chemical space within polymer chemistry for optimised compositions that produce novel materials with inherent resistance to bacterial adhesion. Key to this approach was the use of multi-generation microarrays.

References

[1] Hook AL, Anderson DG, Langer R, Williams P, Davies MC, Alexander MR. Biomaterials 2010;31:187-198.

[2] Anderson DG, Levenberg S, Langer R. Nature Biotechnology 2004;22:863-866.

[3] Mei Y, Saha K, Bogatyrev SR, Yang J, Hook AL, Kalcioğlu ZI, Cho SW, Mitalipova M, Pyzocha N, Rojas F, Van Vliet KJ, Davies MC, Alexander MR, Langer R, Jaenisch R, Anderson DG. *Nature Materials* 2010;9:768-778.

Magnetic Interfaces and Nanostructures

Room: 6 - Session MI+SP+AS-ThM

Emerging Probes in Magnetic Imaging, Reflectometry and Characterization

Moderator: Z. Gai, Oak Ridge National Laboratory, V. Lauter, Oak Ridge National Laboratory

8:00am **MI+SP+AS-ThM1** **Toward Microscopy with Direct Chemical and Magnetic Contrast at the Atomic Level.** *V. Rose*, Argonne National Laboratory **INVITED**

In this talk we will discuss the development of a novel high-resolution microscopy technique for imaging of nanoscale materials with chemical, electronic, and magnetic contrast. It will combine the sub-nanometer spatial resolution of scanning tunneling microscopy (STM) with the chemical, electronic, and magnetic sensitivity of synchrotron radiation. [1] Drawing upon experience from a prototype that has been developed to demonstrate general feasibility, current work has the goal to drastically increase the spatial resolution of existing state-of-the-art x-ray microscopy from only tens of nanometers down to atomic resolution. The technique will enable fundamentally new methods of characterization, which will be applied to the study of energy materials and nanoscale magnetic systems. A better understanding of these phenomena at the nanoscale has great potential to improve the conversion efficiency of quantum energy devices and lead to advances in future data storage applications. The combination of the high spatial resolution of STM with the energy selectivity afforded by x-ray absorption spectroscopy provides a powerful analytical tool.

Work at the Advanced Photon Source, the Center for Nanoscale Materials, and the Electron Microscopy Center was supported by the U. S. Department of Energy, Office of Science, Office of Basic Energy Sciences, under contract DE-AC02-06CH11357.

[1] V. Rose, J.W. Freeland, S.K. Streiffer, "New Capabilities at the Interface of X-rays and Scanning Tunneling Microscopy", in *Scanning Probe Microscopy of Functional Materials: Nanoscale Imaging and Spectroscopy*, S.V. Kalinin, A. Gruverman, (Eds.), Springer, New York (2011), pg 405-432.

8:40am **MI+SP+AS-ThM3** **Effect of Sub-Micrometer Scale Magnetic Inhomogeneity on the Magnetoelectric Coupling in Manganites.** *A. Biswas*, University of Florida **INVITED**

The conventional magnetoelectric (ME) coupling in multiferroics is defined as the effect of a magnetic/electric field on the electric-polarization/magnetization. However, the strength of the ME coupling is usually small. Our recent results have revealed methods for significantly increasing the ME coupling in perovskite manganites and can be summarized in two broad categories: (1) in the phase separated manganite $(La_{1-x}Pr_x)_{1-x}Ca_xMnO_3$ (LPCMO), we have discovered that anisotropic strain leads to a fluid-like ferromagnetic material which can be manipulated using an electric field leading to an unconventional ME coupling [1,2] and (2) an ME coupling in $BiMnO_3$ (BMO) thin films which is about 30 times larger than previously observed in single phase multiferroics [3]. I will discuss the origin of the ME coupling in both multiferroic and phase-separated oxides and relate it to inhomogeneous magnetic properties of the thin films, measured using techniques such as low temperature scanning probe microscopy, spin-polarized neutron reflectometry, and strain dependent electric polarization. Acknowledgement: NSF DMR-0804452

1. Dhakal et. al., *Phys. Rev.* **B75**, 092404 (2007)

2. Jeen et. al., *Phys. Rev.* **B83**, 064408 (2011)

3. Jeen et. al., *J. Appl. Phys.* **109**, 074104 (2011)

9:20am **MI+SP+AS-ThM5** **Impact of Interfacial Magnetism on Magnetocaloric Properties of Thin Film Heterostructures.** *C.W. Miller*, University of South Florida **INVITED**

In an effort to understand the impact of nanostructuring on the magnetocaloric effect, we have grown and studied gadolinium in $W(5nm)/Gd(30nm)/W(5nm)_8$ heterostructures. The entropy change associated with the second-order magnetic phase transition was determined from the isothermal magnetization for numerous temperatures and the appropriate Maxwell relation. The entropy change peaks at a temperature of 284 K with a value of approximately 3.4 J/kg K for 30 kOe field change;

the full width at half max of the entropy change peak is about 70 K, significantly wider than that of bulk Gd under similar conditions. The relative cooling power of this nanoscale system is about 240 J/kg, somewhat lower than that of bulk Gd (410 J/kg). Polarized neutron reflectometry was used to determine the depth profile of the magnetic moment per Gd atom, m_{Gd} . Despite sharp interfaces observed by transmission electron microscopy, m_{Gd} is systematically suppressed near the Gd-W interfaces. Because the peak magnetic entropy change is proportional to m^2 , the maximum achievable magnetocaloric effect in Gd-W heterostructures is reduced. By extension, our results suggest that creating materials with Gd-ferromagnet interfaces may increase the m_{Gd} relative to the bulk, leading to enhanced magnetocaloric properties. Together, these observations suggest that nanostructuring may be a promising route to tailoring the magnetocaloric response of materials.

Supported by AFOSR and NSF.

10:40am **MI+SP+AS-ThM9** **Polarized Neutron Reflectometry on Exchange Biased Thin Films.** *K. Temst*, KU Leuven, Belgium **INVITED**

Polarized neutron reflectivity has established itself as an important tool in the study of magnetic thin film systems. It provides a high-resolution magnetic depth profile and it offers vectorial probing of the magnetization. In recent years polarized neutron reflectivity has played an influential role in elucidating the magnetic structure of exchange bias systems, i.e. structures in which a ferromagnetic layer is coupled to an antiferromagnetic layer. Exchange bias leads to a remarkable shift of the hysteresis loop, an increase in coercivity, and often a pronounced asymmetry of the hysteresis loop shape as well as a complex magnetic history. With this contribution we will take a closer look at two such exchange bias systems and highlight the role of polarized neutron reflectivity.

As a first model system, the archetypal exchange bias system Co/CoO will be highlighted. The antiferromagnetic CoO layer is prepared by oxidizing the surface of a Co thin film, by exposing it to a reduced oxygen atmosphere. We will review the properties of exchange bias in surface-oxidized Co thin films, with the emphasis on the asymmetry of the magnetization reversal mechanism and the training effect. We will also discuss how the training effect can be (partially) restored by applying a magnetic field perpendicular to the initial cooling field direction. Recently we explored an alternative way to establish exchange bias between Co and CoO: rather than creating the antiferromagnetic CoO layer by oxidizing a metallic Co layer, the antiferromagnetic CoO is produced by implantation of oxygen ions into a Co layer. Polarized neutron reflectivity (PNR) is used to determine the magnetic depth profile and to probe the magnetization reversal mechanism. Simultaneously with the PNR measurements, in situ anisotropic magnetoresistance measurements were carried out.

The second example is a ferromagnet/antiferromagnet FePt/FePt₃ bilayer in which complementary use is made of polarized neutron reflectivity (for studying the magnetic depth profile in the ferromagnetic layer) and nuclear resonant scattering of synchrotron x-rays (making use of the Mössbauer effect) to probe the antiferromagnetic FePt₃ layer. Below the Néel temperature, antiferromagnetic order appears in the FePt₃ layer with a spin wavevector pointing along the [100] axis. A net magnetization of the FePt₃, which increases towards the FePt/FePt₃ interface is found.

This work was supported by the Fund for Scientific Research-Flanders (FWO), the KU Leuven Concerted Research Action program (GOA/09/006), the Belgian Interuniversity Attraction Poles research programs (IAP P6/42), and the KU Leuven BOF (CREA/07/005) program.

11:20am **MI+SP+AS-ThM11** **Soft X-ray Microscopy to Study Complexity, Stochasticity and Functionality in Magnetic Nanostructures.** *P. Fischer, M.-Y. Im*, Lawrence Berkeley National Lab, *S.-K. Kim*, Seoul National University, Republic of Korea

Research in magnetism is motivated by the scientific curiosity to understand and control spins on a nanoscale and thus to meet future challenges in terms of speed, size and energy efficiency of spin driven technologies. Imaging magnetic structures and their fast dynamics down to fundamental magnetic length and time scales with elemental sensitivity in emerging multi-element and nanostructured materials is highly desirable. Magnetic soft X-ray microscopy is a unique analytical technique combining X-ray magnetic circular dichroism (X-MCD) as element specific magnetic contrast mechanism with high spatial and temporal resolution [1]. Our approach is to use Fresnel zone plates as X-ray optical elements providing a spatial resolution down to currently 10nm [2] thus reaching out into fundamental magnetic length scales such as magnetic exchange lengths. The large field of view allows to investigate both the complexity, but also the stochasticity of magnetic processes, such as nucleation or reversal. Utilizing the inherent time structure of current synchrotron sources fast magnetization dynamics such as current induced wall and vortex dynamics in ferromagnetic elements can be performed with a stroboscopic pump-probe scheme with 70ps time resolution, limited by the lengths of the electron bunches.

We will present studies of magnetic vortex structures, where we found a stochastic character in the nucleation process, which can be described within a symmetry breaking DM interaction [3]. We will also present time resolved studies of dipolar coupled magnetic vortices, where we find an efficient energy transfer mechanism, which can be used for novel magnetic logic elements [4].

This work was supported by the Director, Office of Science, Office of Basic Energy Sciences, Materials Sciences and Engineering Division, of the U.S. Department of Energy under Contract No. DE-AC02-05-CH11231.

[1] P. Fischer, *Exploring nanoscale magnetism in advanced materials with polarized X-rays*, Materials Science & Engineering R72 81-95 (2011)

[2] W. Chao, P. Fischer, T. Tyliczszak, S. Rekawa, E. Anderson, P. Naulleau, *Optics Express* **20(9)** 9777 (2012)

[3] M.-Y. Im, P. Fischer, Y. Keisuke, T. Sato, S. Kasai, Y. Nakatani, T. Ono, *Symmetry breaking in the formation of magnetic vortex states in a permalloy nanodisk*, (2012) submitted

[4] H. Jung, K.-S. Lee, D.-E. Jeong, Y.-S. Choi, Y.-S. Yu, D.-S. Han, A. Vogel, L. Bocklage, G. Meier, M.-Y. Im, P. Fischer, S.-K. Kim, *NPG - Scientific Reports* 1 59 (2011)

11:40am MI+SP+AS-ThM12 Elemental and Magnetic Contrast using X-ray Excited Luminescence Microscopy, R.A. Rosenberg, S. Zohar, D. Keavney, Argonne National Laboratory, A. Mascarenhas, M. Steiner, National Renewable Energy Laboratory, D. Rosenmann, R.S. Divan, Argonne National Laboratory

We have developed an imaging technique based on x-ray excited luminescence microscopy (XELM), that will enable elemental and magnetic specific imaging of a wide range of materials such as those used in solar cells, magnetic materials, spintronic devices, ferroelectrics, and solid-state lighting. This new scientific tool utilizes the benefits of pulsed, polarized, tunable synchrotron radiation excitation with microscopic detection of the resulting optical emission. A unique offshoot of the microscope is the ability to perform element specific magnetic microscopy of micron-sized features or domains in magnetic fields. X-rays transmitted through thin films are attenuated and the resultant absorption spectrum can be determined by changes in the substrate luminescence. Since many substrates, such as SrTiO₃ and GaAs, used in thin film growth have intense optical emission, this tool should impact many materials where photoelectron emission microscopy (PEEM) cannot be performed since it is not useable on insulating materials or if magnetic or electric fields are required. This approach will be especially useful at low temperatures where luminescence yields are highest, and PEEM has difficulties. In this presentation we will present some initial results from the microscope on some prototype solar cell materials and lithographically patterned Permalloy/GaAs and Permalloy/Cu/Co/GaAs samples. The results demonstrate the potential of XELM for elemental and magnetic specific imaging.

This work was performed at the Center for Nanoscale Materials and the Advanced Photon Source. It was supported by the U.S. Department of Energy, Office of Science and Office of Basic Energy Sciences under the contract number DE-AC02-06CH11357 and by the Department of Energy, Energy Efficiency and Renewable Energy, Solid State Lighting Program.

Nanometer-scale Science and Technology

Room: 12 - Session NS-ThM

Nanoscale Imaging and Microscopy

Moderator: N. Camillone, Brookhaven National Laboratory

8:00am NS-ThM1 Spin Friction Observed on the Atomic Scale, R. Wiesendanger, B. Wolter, A. Kubetzka, K. von Bergmann, Y. Yoshida, University of Hamburg, Germany, S.-W. Hla, Ohio University

With the advent of scanning probe microscopy techniques that involve a tip and a sample in relative motion in the contact or non-contact regime, the microscopic aspects of friction have become a major branch of research called nanotribology. A significant number of recent studies in this field have concentrated on the distinction between electronic and phononic contributions to friction. For the present study, we have used the combination of spin-polarized scanning tunneling microscopy [1] and single-atom manipulation in order to move individual magnetic atoms over a magnetic template [2]. By monitoring the spin-resolved manipulation traces and comparing them with results of Monte-Carlo simulations, we have been able to reveal the characteristic friction force variations resulting from the occurrence of spin friction on the atomic scale [3].

[1] R. Wiesendanger, *Rev. Mod. Phys.* **81**, 1495 (2009).

[2] D. Serrate, P. Ferriani, Y. Yoshida, S.-W. Hla, M. Menzel, K. von Bergmann, S. Heinze,

A. Kubetzka, and R. Wiesendanger, *Nature Nanotechnology* **5**, 350 (2010).

[3] B. Wolter, Y. Yoshida, A. Kubetzka, S.-W. Hla, K. von Bergmann, and R. Wiesendanger,

Phys. Rev. Lett. (2012), in press.

8:20am NS-ThM2 Observing Mineral Reactions in Supercritical Carbon Dioxide Utilizing High Pressure Atomic Force Microscopy, A.S. Lea, M. Xu, K.M. Rosso, Pacific Northwest National Laboratory

Geologic sequestration of CO₂ has become an emerging enterprise for reduction of greenhouse gas emissions. Because CO₂ will be injected and stored in host rock at depths >800m, lithostatic pressure will cause the CO₂ to remain in supercritical fluid state. Knowledge of mineral-fluid chemical transformation rates at geologically relevant temperatures and pressures is expected to be an important aspect of predicting reservoir stability. Many mechanisms of mineral transformation reactions where scCO₂ is the dominant phase and water availability is low have so far remained unstudied. We have developed an atomic force microscope capable of observing in-situ mineral transformations under supercritical conditions (i.e., >72.8 atm and >304K) in real time.

Observations of the disappearance of a 1.5nm layer on the surface calcite is evident in anhydrous scCO₂ are consistent with the dehydration of a hydrated calcium carbonate layer and is consistent with measurements from piezoelectric force microscopy. We have also followed the formation of a water film on the surface of geologically more relevant forsterite, which is deemed to be essential in the transformation of this silicate mineral into a carbonate, and have related film thickness to water content in the scCO₂.

8:40am NS-ThM3 Resolving Amorphous Solids - The Atomic Structure of Glass, M. Heyde, L. Lichtenstein, H.J. Freund, Fritz-Haber-Institute, Germany

INVITED

Vitreous silica is the basis of traditional glasses. Furthermore, it is the prototype oxide network former. Hence, it has been extensively investigated by diffraction methods, like X-ray and neutron scattering. Therefore, it is a great surprise how little is known about its atomic structure. It is impossible to directly extract ring statistics or local ring environments from diffraction. Theoretical structural models have been correlated to the diffraction data with reasonable agreement. Nevertheless, such agreement can never be unambiguously elucidate the structure of an amorphous material.

Modern imaging techniques render the investigation of two dimensional (2D) glass systems possible. Recently, we reported on the atomic structure of a thin metal-supported vitreous silica film on Ru(0001) using scanning tunneling microscopy (STM) [1]. For the first time, it was possible to verify Zachariasen's continuous random network [2] in real space. The existence of a 2D silica glass on a graphene support has been shown by scanning transmission electron microscopy [3] suggesting that further 2D glass systems may be prepared. The investigation of 2D glass models provides the unique possibility to study unexplored properties of amorphous materials.

Herein we report on the first non-contact atomic force microscopy (nc-AFM) images of a 2D silica glass grown on Ru(0001). We will present a thorough statistical analysis and a comparison to diffraction data of 3D silica glass as well as to theoretical models, hereby showing that a 2D thin film of vitreous silica can act as a model system for the amorphous 3D network.

[1] L. Lichtenstein, C. Büchner, B. Yang, S. Shaikhutdinov, M. Heyde, M. Sierka, R. Włodarczyk, J. Sauer, and H.-J. Freund, "The Atomic Structure of a Metal-Supported Vitreous Thin Silica Film", *Angew. Chem. Int. Ed.* **51**, 404 (2012).

[2] W. H. Zachariasen, "The Atomic Arrangement in Glass", *J. Am. Chem. Soc.* **54**, 3841 (1932).

[3] P. Y. Huang, S. Kurasch, A. Srivastava, V. Skakalova, J. Kotakoski, A. V. Krasheninnikov, R. Hovden, Q. Mao, J. C. Meyer, J. Smet, D. A. Muller, and U. Kaiser, "Direct Imaging of a Two-Dimensional Silica Glass on Graphene", *Nano Lett.* **12**, 1081 (2012).

9:20am NS-ThM5 Femtosecond Time-Resolved Scanning Tunneling Microscopy on Nanostructures, H. Shigekawa, University of Tsukuba, Japan

With the size reduction of structures in current electronic devices, differences in the electronic properties caused, for example, by the structural nonuniformity of each element have an ever-increasing effect on macroscopic functions. The study of nonequilibrium quantum dynamics in materials with small structures is of great importance not only from the fundamental viewpoint but also as a basis for the further development of functional devices. Real-space imaging of the transient carrier transport and

transitions in nanostructures is desired to obtain a deeper understanding of current semiconductor physics. Probing the effect of local electronic structures of nano-clusters on energy transfer is important for the analysis of chemical reactions in catalytic activities and also for the development of organic solar devices. To advance such studies, a method that enables the probing of local carrier dynamics with high spatial and temporal resolution is necessary.

Recently, femtosecond time-resolved scanning tunneling microscopy (STM), which enables ultrafast phenomena on a target material to be probed with the spatial resolution of STM, has been realized by the combination of STM with ultrashort-pulse laser technologies [1-4]. In time-resolved STM, the tunnel gap of STM is illuminated by a sequence of paired laser pulses, and the change in tunneling current ΔI is measured as a function of the delay time between the paired pulses (t_d). A high temporal resolution in the femtosecond range, which is limited only by the optical pulse width, is obtained simultaneously with the atomic spatial resolution of STM. This microscopy technique is applicable to systems in which the response of the tunneling current has a nonlinear dependence on the optical excitation intensity. In the case of semiconductors, for example, the magnitude of ΔI obtained for a certain delay time t_d reflects the density of photogenerated minority carriers at t_d after the first pulse excitation, and the carrier decay processes can be observed by analyzing the delay-time dependence of ΔI . Using polarized light, spin dynamics can be probed, and the detection of signals such as phonons is also possible.

In this talk, I would like to introduce this new microscopy technique with some new results.

References

[1] Y. Terada, S. Yoshida, O. Takeuchi and H. Shigekawa, *J. of Physics: Condensed Matter* 22, 264008 (2010). [2] Y. Terada, S. Yoshida, O. Takeuchi and H. Shigekawa, *Nature Photonics*, 4, 12, 869 (2010). [3] Y. Terada, S. Yoshida, O. Takeuchi and H. Shigekawa, *Advances in Optic.Tech.*, 2011, 510186 (2011). [4] S. Yoshida, Y. Terada, R. Oshima, O. Takeuchi and H. Shigekawa, *Nanoscale*, 2012, 4, 757 (2012).

9:40am **NS-ThM6 Unusual Island Formations of Iridium on Ge(111) Studied by STM**, *M. van Zijll, C. Mullet, B. Stenger, E. Huffman, D. Lovinger, W. Mann, S. Chiang*, University of California, Davis

We have used scanning tunneling microscopy (STM) to characterize the growth of iridium onto Ge(111). Iridium was deposited onto the Ge(111) c(2x8) surface at different coverages less than 1ML, and the samples were annealed to temperatures between 550K and 750K. A new form of growth was observed, consisting of pathways connecting larger iridium islands. As the annealing temperature increased, the iridium growth first formed unusual shapes with finger-like protrusions. Next, these shapes broke apart into smaller islands, which ultimately formed into larger islands at higher temperatures. High resolution images have been obtained, which allow insight into the atomic arrangements. We propose a model relating the activation energy of specific binding sites to the formation of various observed structures on the surface.

Funding from NSF CHE-0719504 and NSF PHY-1004848 (REU)

10:40am **NS-ThM9 Turning STM Images Into Chemical Understanding: Atomically Flat Si(100) Reveals the Mechanism of Silicon Oxidation**, *M.A. Hines, M.F. Faggin, K. Bao, A. Gupta, B.S. Aldinger*, Cornell University

Because of its technological importance, silicon oxidation has been studied intensely for decades; however, the disordered nature of the oxide makes these reactions notoriously difficult to understand. In this work, the oxidation reaction is coupled with a subsequent etching reaction, allowing oxidation to literally write an atomic-scale record of its reactivity into the etched surface — a record that can be read with scanning tunneling microscopy (STM) and decoded into site-specific reaction rates, and thus chemical understanding, with the aid of simulations and infrared spectroscopy. This record overturns the long-standing and much-applied mechanism for the aqueous oxidation of the technologically important face of silicon, Si(100), and shows that the unusually high reactivity of a previously unrecognized surface species leads to a self-propagating etching reaction that produces near-atomically flat Si(100) in a beaker at room-temperature — a long-standing technological goal. These findings show that, contrary to expectation, the low-temperature oxidation of Si(100) is a highly site-specific reaction and suggests strategies for functionalization by low-temperature, solution-based reactions.

11:00am **NS-ThM10 Spectroscopic Imaging of Silicon-Hafnia Interfaces**, *C. Guedj, H. Grampeix, C. Lictra, E. Martinez*, CEA, LETI, MINATEC Campus, France

New behavior and phenomena can emerge at oxide interfaces, and the nanocharacterization of these properties is a real challenge for the

semiconductor industry [i]. To replace the conventional SiO₂ insulator, hafnium-based oxides have been introduced [ii,iii] into advanced CMOS devices such as MOSFETs or memories [iv], but the nanometric control of their interfacial properties still remains a critical issue. For further industrial implementation of these oxides, it is necessary to obtain sufficiently high dielectric constants and bandgaps, good thermal stability on silicon, good scalability and sufficient reliability [v] at a reasonable cost. In this presentation, we have performed spectroscopic imaging of silicon-hafnia interfaces using energy filtered high-resolution transmission electron microscopy and valence electron energy loss spectroscopy (HRTEM-VEELS), coupled with X-Ray photoelectron spectroscopy (XPS), Reflection energy loss spectroscopy (REELS), UV photoelectron spectroscopy (UPS) and spectroscopic ellipsometry. Optical absorptions and bandgap profiles across the interface are obtained and novel ordering effects like axiotaxy are locally observed. An atomic-scale modelling is proposed, and the consequences in terms of device performances are detailed.

[i] <http://www.itrs.net/Links/2011ITRS/2011Chapters/2011Metrology.pdf>

[ii] R.M. Wallace and G.D. Wilk, *Crit. Rev. Solid State Mater. Sci.* 28, 213 (2003)

[iii] M.H. Cho et al., *Appl. Phys. Lett.* 81, 1071 (2002)

[iv] B.Govoreanu et al., *proc. IEEE IEDM*, p 729 (2011)

[v] J. Robertson, *Solid-state electron.*, Vol. 49, p 283-293 (2005)

11:20am **NS-ThM11 Atom Probe Tomography of AlInN/GaN based HEMT Structures**, *N. Dawahre, G. Shen, P. Tolmer, S.M. Kim, P. Kung*, University of Alabama, Tuscaloosa

Group III-Nitride semiconductors have been well known for their excellent optoelectronic properties associated with a wide direct bandgap, which has led to the emergence of blue and green lasers, ultraviolet-blue-green-amber and white light emitting diodes, and ultraviolet photodetectors. They are also rapidly becoming the material family of choice for next generation of RF-microwave devices, power amplifiers and high temperature electronics, thanks to high two-dimensional electron gas charge densities and high breakdown electric fields in these materials. GaN based materials are also more radiation resistant than conventional electronic materials, which makes them well suited for space electronics. Although less thoroughly investigated until now, lattice matched AlInN/GaN systems are promising to be a viable alternative to the current state-of-the-art strained AlGaIn/GaN devices and their reliability issues.

In this work, we present the nanoscale characterization of AlInN semiconductors and AlInN/GaN high electron mobility transistor (HEMT) structures using a combination of transmission electron microscopy (TEM) and laser assisted atom probe tomography (APT), and correlate these with the structures' electronic and optical properties, as well as the effects of irradiation. APT is an emerging technique based on the field ion emission from a needle-shaped region of interest and is capable of yielding 3D chemical mapping with atomic sensitivity and sub-nanometer spatial resolution. We report here a study of the field evaporation mechanisms from wide bandgap AlInN and GaN using a visible ps laser during APT experiments and correlate them with APT experiments (e.g. laser pulse energy, ...) in order to establish approaches for reliable chemical analysis at the nanoscale of AlInN compound alloys. We proceed to investigate the fundamental material characteristics of interest that can be extracted from a combined APT and TEM analysis, including indium segregation phenomena in AlInN, interdiffusion near the AlInN/GaN channel interfaces and interface roughness, as well as the effects of irradiation on the channel properties.

11:40am **NS-ThM12 Pit Initiation at MnS Nano-Inclusions in Carbon Steel under Exposure to Sulfate-Reducing Bacterium *D. alkanexedens***, *J.S. Hammond*, Physical Electronics, *B.H. Davis, Z. Suo*, Montana State University, *I. Beech*, University of Oklahoma, *D.F. Paul*, Physical Electronics, *R. Avci*, Montana State University

Cold rolled carbon steel (1018) is a commonly used structural material in various applications, including the construction of fuel storage tanks for naval ships. *Desulfoglaeba alkanexedens* (strain ALDCT) is a known fuel-degrading, anaerobic, sulfate-reducing bacterium (SRB) [1, 2] that thrives at fuel-water interfaces in marine environments and can influence the pitting corrosion of carbon steel. It has long been postulated that MnS inclusions in carbon steel can act as sites of pitting initiation [3]. The propagation of pitting corrosion is relatively well understood; however, the initiation of pits is still a subject of controversy [4, 5]. A careful study of pit initiation and propagation associated with sulfide inclusions, particularly as they relate to microbial influenced corrosion (MIC) under anaerobic conditions, has been lacking, partly because these inclusions are mostly submicron-sized and the evolution of their corrosion is difficult to monitor. The use of nanopores

instead of microprobes is required to determine the elemental and chemical composition and to map out the elemental distributions at the submicron scale. Quantitative surface sensitive techniques such as Auger electron spectroscopy [4, 5] are essential for monitoring the nanoscale changes associated with surface-related phenomena, including MIC. This presentation will review the results of comprehensive and systematic studies of nano-inclusions on carbon steel surfaces prior to and following exposure of the steel to a solution of a mature ALDCT culture and to abiotic sulfide as a control. The nano-inclusions were carefully characterized using a field emission Auger nanoprobe with a spatial resolution of approximately 10 nm for imaging and spectroscopy and compared with results obtained using X-ray microprobes, which typically have a spatial resolution of around 1000 nm for spectroscopy and 10 nm for imaging. The study elucidates biologically driven corrosion reactions taking place in and around nano-inclusions. The impact of this fundamental analysis on the understanding of MIC phenomenon will be discussed.

References:

1. Davidova, I.A., et al., *International Journal of Systematic and Evolutionary Microbiology*, 2006. **56**: p. 2737-2742.
2. Morris, B.E.L., J.M. Sufita, and H.H. Richnow, *Geochimica Et Cosmochimica Acta*, 2009. **73**(13): p. A907-A907.
3. G. Waglen. *Corrosion Science*, 1974. **14**: p. 331-349.
4. P. Schmuki, H. Hildebrand, A. Friedrich and S. Virtanen, *Corrosion Science*, 2005. **47**: p. 1239-1250.
5. J.E. Castle and Ruoru Ke, *Corrosion Science*, 1990. **30**(4/5): p. 409-428.
6. Support of ONR/MURI Grant No N00014-10-0946 is gratefully acknowledged.

Plasma Science and Technology

Room: 24 - Session PS1-ThM

Plasma Processing for Disruptive Technologies (NVM, TSV, etc.)

Moderator: S. Hamaguchi, Osaka University, Japan

8:20am **PS1-ThM2 Damage Free Cryogenic Etching of Porous Organosilica Ultralow-k Film**, L. Zhang, IMEC, Belgium, R. Ljazouli, T. Tillocher, P. Lefaucheu, R. Dussart, GREMI CNRS/Université d'Orléans, France, Y. Mankelevich, Moscow State University, Russia, J.-F. de Marneffe, S. de Gendt, M.R. Baklanov, IMEC, Belgium

Porous organosilicates (OSG) are popular candidates as low dielectric constant materials for interconnect application. However, the integration of this class of materials remains challenging, especially for $k \leq 2.3$ materials with a large open porosity. Due to carbon depletion and surface modification, porous low-k materials suffer from plasma induced damage (PID) that leads to k value degradation and high leakage current. In this paper, we report a cryogenic low-k etching approach that benefits from a sidewall surface protection effect. It is known that, at cryogenic temperature, an SiO_xF_y passivation layer forms more easily on the surface of the material being etched, providing efficient sidewall protection. In this work, cryogenic etching is applied to porous organosilicate ultralow-k materials with $k=2.3$ and $k=2.0$, which are prepared by Spin-coating and PECVD methods respectively. Influence of the chuck temperature and bias power with different plasma chemistries has been investigated in an ICP chamber. Plasma induced damage is evaluated by means of spectroscopic ellipsometry (SE), Fourier-transformed infra-red spectroscopy (FTIR) and time of flight secondary ion mass spectroscopy (TOF-SIMS). Blanket low-k films are exposed to pure SF_6 plasma with different chuck temperatures, ranging from 20°C to -120°C. Almost no carbon depletion is observed when the chuck temperature is below a threshold point (-70°C and -120°C for $k=2.3$ and $k=2.0$ materials respectively). By addition of SiF_4 and O_2 to the gas discharge, etching rate is reduced as a result of enhanced SiO_xF_y polymerization. In order to evaluate the damage depth, an equivalent damage layer (EDL) is calculated based on the measurement of FTIR methyl group loss. The EDL decreases by increasing the proportion of SiF_4/O_2 in gas discharge, which confirms the protection effect of the SiO_xF_y passivation layer. In addition, the formation of alkyl alcohol polymer during cryogenic etching is observed from ex-situ FTIR, which is a major etch by-product at cryogenic temperature due to the lack of activation energy for complete oxidation of the methyl groups into CO_2 and H_2O . Our experiments also show that this polymer can be easily removed by high temperature anneal without additional damage to low-k film. This incomplete oxidation of Carbon-based etch reaction products reveals the mechanism for reduced Carbon depletion during cryogenic etching. A protection model is proposed, for porous SOG etching at cryogenic

temperature, based on SiO_xF_y growth and incomplete oxidation. Although the etch by-products cannot plug the interconnected pores, they condense on their surface and retard the oxidation of methyl groups.

8:40am **PS1-ThM3 Deep GaN Etching : Role of SiCl_4 in Plasma Chemistry**, J. Ladroue, GREMI - STMicroelectronics, France, M. Boufnichel, STMicroelectronics, France, T. Tillocher, P. Lefaucheu, P. Ranson, R. Dussart, GREMI - Polytech Orleans/CNRS, France

Gallium nitride (GaN) is currently used for light emitter devices due to a large and direct bandgap. Otherwise, GaN physical properties open new prospects in microelectronics manufacturing. By combining a wide bandgap (3.4 eV), strong chemical bonds and a high electron mobility, GaN based devices should operate under higher temperature, higher power and higher frequency than typical silicon devices.

It was shown that wet etching is limited due to inert chemical nature of GaN [1], especially in the c-plan where the etching is generally needed [2]. Therefore, plasma etching is essentially used due to the combination of chemical and physical effects. Chlorine plasmas are used because GaCl_3 is the most volatile Ga etching product.

Due to the power density applied to the next generation of power devices, an etched depth as high as 6 to 10 μm is typically required. This could be qualified as deep GaN etching compared to the etched depth needed for light emitter devices which are of the order of few hundreds nanometers.

It was shown that bottom surface defects are linked with dislocations and nanopipes created during the epitaxial growth of GaN [3]. We will show that etched surface presents either pits or columnar defects closely linked with plasma conditions. Mass spectrometry data confirms the importance of ClO species in columnar regimes. We will show that SiCl_4 is able to scavenge ClO and allows to provide a smoother surface. SiCl_4 can be added in plasma gas or as the etching product of a silicon coverplate. We will also present data showing the influence of SiCl_x passivation layer on SiO_2 hard mask selectivity. Plasma diagnostics such as optical emission spectroscopy or mass spectrometry will allow us to propose mechanism of formation of this passivation layer.

[1] D. Zhuang and J.H. Edgar, *Mat. Sci. and Eng.*, 48 (2005) 1-46

[2] D. A. Stocker, E. F. Schubert, and J. M. Redwing. *Applied Physics Letters*, 73 (1998) 2654-2656

[3] J. Ladroue, A. Meritan, M. Boufnichel, P. Lefaucheu, P. Ranson, and R. Dussart, *J. Vac. Sci. Technol. A* 28, (2010) 1226

9:20am **PS1-ThM5 Etching Reaction Analysis of CoFeB by Carbon Monoxide / Methyl Alcohol Based Plasmas**, K. Karahashi, T. Ito, S. Hamaguchi, Osaka University, Japan

Magnetic random access memory (MRAM) devices, which are composed of magnetic-tunnel-junction (MTJ) stacks, have potential to replace static random access memory, dynamic access memory, and flash memory devices because they can provide high speed operation, low operating voltage, and nonvolatile storage. For the realization of high-density MRAM devices, dry etching of magnetic thin films must be developed. Argon ion milling seems to be almost the only etching technique available in the current manufacturing processes for MRAM devices. However, capabilities of Argon ion milling for anisotropic and selective etching of magnetic films are severely limited and therefore new technologies of reactive ion etching (RIE) for magnetic films are now seriously sought. RIE processes based on CO/NH_3 and CH_3OH are candidates for selective etching processes of magnetic thin films. In this study, we have focused on etching processes of CoFeB alloy thin films and examined etching reactions caused by energetic CO^+ or O^+ ions, which are considered to be the major etchants of CO/NH_3 or CH_3OH plasmas. We have determined the etching yields and analyzed surface reactions, using a mass-selected ion beam system. The ion beam system is designed to inject mono-energetic single-species ions into a sample surface in ultra-high vacuum conditions. The reaction chamber is equipped with an X-ray photoelectron spectroscopy (XPS) for in-situ chemical analyses of irradiated surfaces. The ion beam energy used in this study is in the range of 300-1000 eV. The etching rates are determined from measured depth profiles of irradiated surfaces and ion fluxes. It has been found that the etching rates of CoFeB by Ar^+ ions are smaller than those of CoFe. Therefore physical sputtering yields of such magnetic thin films are affected by boron atoms contained in them. The etching rates of CoFeB by CO^+ ions are found to be lower than those by Ar^+ and increase with the cobalt content. From XPS analysis of CO^+ irradiated CoFeB surfaces, it has been found that, although cobalt does not oxidize, iron of CoFeB oxidizes and inhibits the etching reactions. Therefore, the etching rates of CoFeB by CO^+ irradiation are dependent on the atomic compositions of CoFeB films. The results suggest that design of the atomic composition of CoFeB films is important also for the etching process development. This work was supported by the Semiconductor Technology Academic Research Center (STAR-C).

9:40am **PS1-ThM6 The Etching Characteristics of Flexible Substrate in Inductively Coupled Plasma System for Flexible Electronics**, *Y.S. Chun, Y.H. Joo, C.I. Kim*, Chung-Ang University, Republic of Korea

Recently, many attention was given to the flexible electronics due to its future applications, such as flexible display and e-paper, etc. In order to fabricate the devices on the flexible substrate, such as PES, PAR, and PI, the etching characteristics of the substrate should be studied respect to other deposited thin film layers because the surface roughness and etch by-products could affect the device performance. Also, the devices can be embedded in the flexible substrate, where the flexible substrate should be etched away.

In this study, polyarylate (PAR) and polyethersulfone (PES) flexible substrates were etched by using inductively coupled plasma (ICP) system at room temperature. BCl_3 , CF_4 , and Ar mixed chemistry gases were used to achieve a high etch rate and good selectivity respect to the other metal (Al) or oxide (ZnO) layers. The etching characteristics of the flexible substrate were studied by varying the process parameters, including process pressure, DC bias voltage, RF power, and gas mixing ratio. In addition to the etch rate and selectivity, the surface chemical bonding structure and roughness were studied because they are the important factors for the device fabrication and performance.

The etch rate and selectivity were measured by using a depth profiler (alpha-step 500, KLA tencor) and the surface roughness was measured by atomic force microscopy (AFM). The chemical states of etched surfaces were investigated with X-ray photoelectron spectroscopy (XPS). The elemental analysis of etched surfaces was investigated with the auger electron spectroscopy (AES) analysis.

10:40am **PS1-ThM9 Plasma Process Developments for Spintronics Devices**, *K. Kinoshita*, Tohoku University, Japan **INVITED**

Demands for zero-standby-power systems have increased in order to realize low-carbon society. For this purpose, non-volatile spintronics devices which use magnetic tunnel junction (MTJ) are receiving much attention due to its endurance and high speed. Another important advantage of the spintronics devices is their compatibility to CMOS process. Up to now, 16 Mb MRAM has been in the market. And, developments are ongoing on 300 nm wafer of 90 nm CMOS node or beyond targeting Gb class memory capacity. To combine with the BEOL process, low temperature (<350 degree C) processes are required for additional processes to fabricate the MTJ cell. Use of plasma which enables low temperature process matches the needs.

Whether the target is memory or logic, following three plasma processes are the key to realize the spintronics devices: (a) Damage-less PVD of thin-film multilayered-stack materials. (b) Dry etch for magnetic multilayer stack materials. (c) Protective film CVD over MTJ cell. Multi-target magnetron-PVD is the key equipment to deposit uniform, ultra-thin, multi-stacked MTJ. MgO barrier film quality determined the performances of the MTJ [1]. An Ar milling process has long been used to etch magnetic materials. C-O(X)-based chemistry is increasing attracting attention recently due to its high etch selectivity between hard mask Ta and magnetic materials [2]. Here, degradation of device performances by chemical modification of magnetic materials is one of the issues. Recovery treatment becomes important for the next step [3, 4]. Process chemistry of the protective film CVD should not degrade materials used in MTJ. In addition, high enough quality is needed to protect the MTJ cell during the following BEOL processes [5].

All the unit processes should be evaluated by the MTJ performances after fabricating MTJ in a BEOL structure. In addition, total coordination of BEOL process including these MTJ fabrication processes is required.

This work was supported by JSPS through its FIRST Program.

[1] K. Ono et al., Jpn. J. Appl. Phys. **50**, 023001 (2011). [2] I. Nakatani, IEEE Trans. Magn. **32**, 4448 (1996). [3] K. Kinoshita et al., Jpn. J. Appl. Phys. **49**, 08JB02 (2010). [4] K. Kinoshita et al., to be published on Jpn. J. Appl. Phys. **51**, (2012). [5] K. Suemitsu et al., Jpn. J. Appl. Phys. **47**, 2714 (2008).

11:20am **PS1-ThM11 Predictions of the Etch Behavior of Complex Oxide Films for High-k and Multiferroic Applications**, *N. Marchack, J. Chen, J.P. Chang*, University of California at Los Angeles

The ongoing quest to improve the performance of integrated circuit devices has led to a burgeoning body of research in synthesizing multifunctional materials. However, these materials are often intrinsically etch resistant and thus ensuring high-fidelity patterning via plasma etching faces significant challenges. This study aims to demonstrate predictive capability for the etch behavior of novel materials, e.g. complex oxides, by combining an established phenomenological model with thermodynamics-based volatility diagram analysis. The material systems studied were the potential high-k dielectric Hf_xLayO_z , and the multiferroic candidates Y_xMnyO_z and Bi_xFeyO_z .

Experiments to validate the theoretical analysis were conducted an inductively coupled plasma (ICP) reactor equipped with a quadrupole mass spectrometer (QMS) for analyzing etch products and a quartz crystal microbalance (QCM) for measuring the etch rate *in situ*. The use of the QCM eliminated the need to subject the samples to unwanted reactions in atmosphere prior to etch rate measurement, and also allowed for materials that were unable to be analyzed by other methods such as spectroscopic ellipsometry. The reactor was also connected to a UHV transfer tube which allowed the surface composition to be studied via x-ray photoelectron spectroscopy (XPS) without exposure to ambient conditions.

The calculated etch rates of the Hf_xLayO_z films in a 400W, 5 mT, Cl_2 plasma varied from 8.3 to 181.9 Å/min (for -25V to -200V bias voltage, respectively), generally lower than that of pure HfO_2 etched in comparable conditions by ~16 to 31%. The maximum etch rate observed for a 400W, 15mT BCl_3 condition was 61 Å/min (at -175V), with net deposition (1.34 – 4.71 Å/min) observed below -75V bias voltage. QMS was used to characterize the etch products, with LaCl , LaO_3 , LaOCl and LaO_2Cl (3.4 : 4.0 : 3.1 : 1.0) and LaB , LaB_2O , LaBOCl and LaO_2Cl (1.2 : 1.1 : 1.3 : 1.0) observed as the dominant La-containing species in Cl_2 and BCl_3 conditions, respectively. The surface compositions of the films post-etching revealed a decrease in the La and Hf fractions after Cl_2 and BCl_3 exposure, with a more significant reduction in La compared Hf (~50% v. ~19%) as determined via XPS. Similar analysis for the multiferroic oxides will be presented and comparative etch behavior analyzed through the aforementioned theoretical framework.

11:40am **PS1-ThM12 Sub-30nm Pitch Patterning of FEOL Materials for Aggressively Scaled CMOS Devices for 10 nm Node and Beyond**, *H. Miyazoe, S. Engelmann, H. Tsai, M. Brink, B.N. To, IBM T.J. Watson Research Center, J. Cheng, C. Liu, IBM Research - Almaden, W.S. Graham, E.M. Sikorski, M.A. Guillorn, N.C.M. Fuller, E.A. Joseph, IBM T.J. Watson Research Center*

As the feature size in CMOS technology continues to shrink, patterning below 40 nm pitch faces many challenges. Continued delays in production worthy EUV lithography has driven an interest in directed self-assembly (DSA) [1] and sidewall image transfer (SIT) [2] patterning. Both techniques can augment conventional lithographic patterning by providing sublithographic multiplication of feature pitch. In this work, we leverage the results of a parametric study of factors impacting fine feature patterning [3] to further optimize DSA and SIT based patterning in the sub 30 nm pitch regime. Recently, we successfully demonstrated the transfer of “fingerprint” DSA patterns to the materials typically used in front end of line (FEOL) processing. Patterning of Si, SiN_x and SiO_x at a ~28 nm feature pitch using poly(styrene-block-methyl methacrylate) (PS-b-PMMA) block copolymers was shown [4]. In this work, we discuss further optimization of the etch processes used to pattern the organic underlayer in the masking material stack as well as the substrate material. The use of templated DSA to generate line-space structures in the aforementioned materials was used to investigate the control of critical dimension (CD), line edge roughness and line width roughness throughout the patterning process. SIT-based patterning using metal oxide or nitride films as the side-wall hard mask was used to generate patterns in FEOL materials down to ~25 nm pitch. Typically, the CD of end lines are larger than the target CD of nested lines in structures generated by SIT. Dense/iso loading-like effects and other mechanisms to explain this phenomenon are explored. These initial patterning studies may play an important role in understanding feature formation and density limiting ground rules in future technology nodes. This work is sponsored by the DARPA GRATE (Gratings of Regular Arrays and Trim Exposures) program under Air Force Research Laboratory (AFRL) contract FA8650-10-C-7038.

[1] J. Cheng *et al.*, SPIE 2010. [2] H. Yaegashi *et al.*, SPIE 2012. [3] H. Miyazoe *et al.*, AVS2011. [4] S. Engelmann *et al.*, SPIE 2012.

Low Damage Processing

Moderator: E.A. Joseph, IBM T.J. Watson Research Center

8:00am PS2-ThM1 New Approaches for Overcoming Current Issues of Plasma Sputtering Process during Organic Based Micro-Electronic Device Fabrication : Room Temperature & Plasma Damage Free. M. Hong, Korea University

INVITED

While direct deposition of metal oxide thin films including transparent conductive oxide (TCO) and amorphous oxide semiconductor (AOS) on the organic layers, plasma damages against the organic materials are serious issues. These damages are believed to be mainly originated from highly energetic particles during the plasma sputtering process such as negative oxygen ions & reflecting neutrals from the target surface, etc. During the DC magnetron sputtering (DMS) process, most of energetic particles contribute in self-supplying of activation & crystallization energy and forming higher quality TCO thin film without an additional heating or post-annealing. However, the excessively accelerated negative oxygen ions can lead to fatal physical bombardment damages and defects in the oxide thin film, which are hardly recovered without post thermal annealing. To simply solve the inherent limitation of the DMS process, we are developing novel approaches for selectively filtering the negative ions by magnetic field arrays, named as Magnetic Field Shielded Sputtering (MFSS) process. The MFSS process effectively eliminates or suppresses the defect generation induced by the negative oxygen ion bombardments. The electro-optical properties of ITO thin films by the MFSS were superior to those by the conventional DMS at room temperature. While the DMS processed a-IGZO TFTs need a high temperature post annealing up to 400°C for healing the internal defects in the AOS thin film, the MFSS processed a-IGZO TFT scarcely requires the post thermal annealing and shows very comparable electrical performance to the DMS processed one with a high temperature post annealing. To completely overcome the plasma related damage issues, we are developing the Neutral Beam Assisted Sputtering (NBAS) process; electro-optical properties of the ITO thin film by the NBAS were achieved in lower resistivity ($< 4.0 \times 10^{-4} \Omega\text{-cm}$) and higher transmittance ($> 90\%$ at 550 nm) with nano-crystalline structure at room temperature process. Furthermore, for a TCO top anode on the inverted structure OLED cell, the NBAS TCO deposition process has induced almost no damages on the underlying organic layers. On the other hand, gas barrier coatings are essential to prevent the permeation of water and oxygen for a high efficiency flexible AMOLED device. Key factors for formation of the high quality inorganic gas barrier to satisfy the extremely lower water vapor transition rate (WVTR) requirement for OLED cells ($< 1 \times 10^{-6} \text{ g/m}^2/\text{day}$) are suppression of nano-sized defect sites and gas diffusion pathways among the grain boundaries. To achieve the nano-sized defect free inorganic gas barrier layer, new nano-structured Al₂O₃ single gas barrier layer is developing by using the NBAS technology; current WVTR of the NBAS processed Al₂O₃ gas barrier films was as low as $5 \times 10^{-6} \text{ g/m}^2/\text{day}$ by just single layer.

8:40am PS2-ThM3 Novel Inward Plasma Etching System for Failure Analysis in Nano-Scale Semiconductor Devices. T. Shimizu, T. Horie, Y. Naitoh, AIST, Japan, S. Takahashi, C. Iwase, Y. Shirayama, S. Yokosuka, K. Kashimura, S. Shimbori, H. Tokumoto, Sanyu Co. Ltd., Japan

In a plasma system with a capillary-discharge tube, Yoshiki has demonstrated that the plasma can expand even along an upper gas-stream side of the tube under proper conditions (gas pressure, electric power, etc), even if the plasma is excited in the tube center. By utilizing this fact, we have developed an "inward" plasma etching (IPE) system, where the etching sample is set close to the tube end, and successfully applied to expose the metal wires for failure analysis of nano-scale semiconductor devices. Insulating oxide layers in a multi-layered semiconductor device was etched locally, cleanly and well controlled with process gas CF₄. Thin metal wires about 90nm width embedded in the oxides were exposed without any damages (breaking, lifting off, etc) in much shorter time compared with the focused ion beam etching. Further, almost all etching products which flowed through the capillary tube were effectively analyzed with a quadrupole mass spectrometer. In a case of CF₄ gas etching of silicon wafer with thermal-oxides of about 600nm thick, mass peaks corresponding to SiF⁺, SiF₂⁺ and SiF₃⁺ were detected and the intensity of SiF₃⁺ was changed clearly at the boundary of silicon oxide and substrate silicon, indicating a good measure of the end-point detection. At the presentation, we shall present details of the system and its application.

9:00am PS2-ThM4 Effect of Open Area Ratio and Pattern Structure on Fluctuations in Critical Dimension and Si Recess. N. Kuboi, T. Tatsumi, M. Fukasawa, J. Komachi, T. Kinoshita, H. Ansaï, H. Miwa, Sony Corporation, Japan

The Si recess, which is caused after post-wet treatment in the Si gate etching process, can have a big effect on transistor properties such as threshold voltage (V_{th}) and off-state leakage current (I_{off}). We previously studied what caused the Si recess [1] and found through our analysis of a molecular dynamics (MD) calculation and a beam experiment that it could be the oxidation enhanced diffusion induced by incident hydrogen during HBr/O₂ gate etching [2]. The fluctuation in the Si recess depth (Δd_R) as well as in the critical dimension (ΔCD) is one of the key factors causing fluctuations in V_{th} (ΔV_{th}) and I_{off} (ΔI_{off}). The pattern dependence of the incident particle flux is related to Δd_R , therefore a prediction technology that considers this dependence is necessary in order to understand the effects on ΔV_{th} and ΔI_{off} .

To model the dependence, we assumed that three factors—mask open area ratio at the wafer level (global), chip level (semi-local), and local level (local)—affect ΔCD and Δd_R . We performed experiments using a dual frequency capacitively coupled plasma system. We used wafers ranging from 60 to 91% (the global range (R_G) and the semi-local (R_S)) with various patterns of the photo-resist mask on the Poly-Si film. These samples were treated by the HBr/O₂ process under a pressure of 30 mTorr.

We found that ΔCD had positive and linear correlations with the global, semi-local, and local levels, which was consistent with the trend of the by-product (SiBr_x) intensity and with that of the taper angles of the etched profiles. We also clarified that ΔCD was affected by the amount of SiBr_x generated within several times of the mean free path area for the semi-local dependence, and that it was the solid angle (S) viewing from a pattern, not the pattern space, that had a good correlation with variations in ΔCD as a control indicator. We used this experimental knowledge to model the SiBr_x flux and created a Si gate etching simulation that demonstrated the ΔCD value and etched profile trends. We also found that Δd_R depended on $(R_G + R_S)S$ as well as on the dosage of incident particles, considering the relationship between d_R and the ion energy reduced by the SiBr_x deposition depth [3]. Furthermore, when we used the analytical transistor model [3], we could predict ΔV_{th} and ΔI_{off} enhanced by the Si recess with $(R_G + R_S)S$.

These results show that it is crucial to control plasma processes such as ion energy, gas flux, and over-etch time considering the effect of pattern dependence of fluctuations in ΔCD and the Si recess.

[1] T. Ohchi et al., JJAP 47, 5324 (2008).

[2] T. Ito et al., JJAP 50, 08KD02 (2011).

[3] K. Eriguchi et al., JJAP 49, 08JC02 (2010).

9:20am PS2-ThM5 Control of Surface Properties on Plasma-Etched Gallium Nitride (GaN). R. Kometani, S. Chen, J. Park, J. Cao, Y. Lu, K. Ishikawa, K. Takeda, H. Kondo, H. Amano, M. Sekine, M. Hori, Nagoya University, Japan

Introduction - In plasma etching of gallium nitride (GaN), surface of GaN was etched by preferentially desorbed nitrogen [1] and roughened by bombardment by energetic ions at elevated temperature [2]. In this paper, we have studied about effects of temperature to form surface properties such as surface roughness.

Experimental - Samples were Si-doped GaN epitaxial layer with thickness of 1 μm grown by metal organic chemical vapor deposition (MOCVD) on sapphire substrates. After removed native oxides off chemically, the samples of GaN were partially etched off by using capacitively coupled plasma (CCP) reactor. Pure argon gas of 50 sccm was introduced and a pressure of 10 Pa was maintained. Plasmas were sustained by applying radio frequency (13.56 MHz or 100 MHz) power to a sample stage which temperature was maintained at 600°C. After the plasma processes for 10 min., morphology of the sample was measured by the atomic force microscopy (AFM), chemical composition was evaluated by the x-ray photoelectron spectroscopy (XPS).

AFM images of initial sample was shown smooth surface and also surface morphology was not significantly changed just after annealed at 600°C for 10 min. However, after exposed Ar plasma at elevated temperature of 600°C for 10min, surface roughness was observed in particular. This is considered that the observed roughness caused by forming metallic-Ga precipitates on the surface, which was supported by results increase of metallic Ga bonding by XPS analysis. Namely, this indicates that favorable volatilization of nitrogen created Ga-droplets and promoted to roughen the surface at 600°C.

On contrary, surface morphology after N₂ plasma was relatively smooth although the high temperature. The results in smoothness were possibly resulted by difference in Ga droplet formation because of suppression of metallic Ga formation by reacting of reactive N species.

In this study, we report a method to control surface properties on plasma etched GaN through experiments carried out with samples at elevated temperatures. Further detailed discussion will be conducted.

Acknowledgement - This work was partly supported by the Knowledge Cluster Initiative (Second Stage)-Tokai Region Nanotechnology Manufacturing Cluster.

- 1) R. Kawakami *et al.*, Thin Solid Film. **516**, 3478 (2008).
- 2) R. Kometani *et al.*, Jpn. Soc. Appl. Phys. Spring Meeting (2012), 30a-M-11.

10:40am **PS2-ThM9 Theoretical Calculation of Neutralization Efficiency of Positive and Negative Chlorine Ions with Consideration of Excited States**, *S. Ohtsuka, N. Watanabe*, Mizuho Information & Research Institute, Inc., Japan, *T. Kubota*, Tohoku University, Japan, *T. Iwasaki, Y. Iriye, K. Ono*, Mizuho Information & Research Institute, Inc., Japan, *S. Samukawa*, Tohoku University, Japan

We investigated the generation mechanism of neutral particles in high efficiency neutral beam source developed by Samukawa et al [1], by collision of positive and negative chlorine ions against graphite surface. It is already known experimentally that neutralization efficiency of negative ion (Cl-) is much higher than that of positive ion (Cl2+) [2] and that realized high efficiency and low energy neutral beam by usage of negative ions generated in pulse-time-modulated plasma. However, the mechanism has not been clarified. Recently we investigated the neutralization mechanism by using numerical simulations based on quantum mechanics [3-5] and succeeded in explaining higher neutralization efficiency of negative ions than positive ions. In this study, to obtain more reliable neutralization efficiency, we introduced consideration of excited states. A unit cell with a graphite surface and a chlorine particle (Cl, Cl+, Cl-, Cl2, or Cl2+) was used for the calculation. During a collision of the particle against the graphite, time evolution of wave functions of ion and graphite electrons was calculated by solving TD-Kohn-Sham equation [3, 4]. The probability of neutralization of an ion was estimated by calculating electron occupation numbers of each electron on each occupied and unoccupied molecular orbital. As a result, neutralization efficiencies of Cl- and Cl2+ ions were calculated as 87% and 77%, respectively. This result is consistent with our previous result that negative ions have higher neutralization efficiency due to resonant neutralization mechanism than that of positive ions with Auger neutralization mechanism. It was also found that electrons of the neutralized Cl2+ occupied some unoccupied orbitals of the grounded Cl2, namely Cl2+ became excited Cl2* by the collision. On the other hand, electrons of the neutralized Cl- did not occupy unoccupied orbitals of the grounded Cl, namely Cl- became grounded Cl by the collision. Since excited Cl2* are likely to be re-ionized to Cl2+ by the following collisions, so we consider the re-ionization process should be also an important factor to estimate the neutralization probability of Cl2+ ion. A part of this work was supported by the New Energy and Industrial Technology Development Organization (NEDO).[1] S. Samukawa et al, Jpn. J. Appl. Phys. **40**, L779 (2001).[2] S. Samukawa, Jpn. J. Appl. Phys. **45**, 2395 (2006).[3] N. Watanabe et al., Phys. Rev. E **65**, 036705 (2002).[4] <http://www.mizuho-ir.co.jp/solution/research/semiconductor/nano>[5] T. Kubota et al., J. Phys. D: Appl. Phys. **45**, 095202 (2012).

11:00am **PS2-ThM10 High-aspect Ratio and Diameter Controlled GaAs/AlGaAs Nano-Pillar Fabrication using Defect-free Neutral Beam Etching and Bio-template Process**, *Y. Tamura, M. Igarashi, M.E. Fauzi, W. Hu*, Tohoku University, Japan, *I. Yamashita*, Nara Institute of Science and Technology, Japan, *S. Samukawa*, Tohoku University, Japan

The III-V compound quantum dot (QD) has recently become extremely attractive when researching the quantum effect and developing novel opt/electronic devices such as high-efficiency intermediate-band solar cells. In the latter one, it is very important to precisely control the geometry size and alignment of QDs to form an intermediate-band. A high in-plane density is also necessary for photovoltaic devices in order to obtain a large optical gain. Molecular beam epitaxy have widely used and have been greatly researched for forming QDs. However, it is still a great challenge for realizing ideal nanostructures using self-organized bottom-up processes.

Our proposed top-down process of using bio-template [1] and neutral beam etching (NBE) [2] has great potential to fabricate defect-free, high-density (more than $7 \times 10^{11} \text{ cm}^{-2}$), sub-20-nm-in-diameter GaAs QDs structures [3]. This process uses 7-nm-in-diameter iron cores of ferritin (protein included iron core) as the etching mask and damage-free NB with eliminating UV photons and high-energy ions to etch GaAs without defects.

In this study, we successfully fabricated high aspect ratio nano-pillars etched the GaAs/AlGaAs stack-layered structure with 95 nm height and 15 nm the diameter by using a NBE. The diameter of the GaAs nanodisk could be precisely controlled from 12 to 18 nm by a combination of Hydrogen-radical treatment and Cl₂-NBE. This is because a taper profile of GaAs-NBO film could be controlled by Hydrogen-radical treatment time due to

the isotropic and slow etching rate. In addition, not only iron cores but also this tapered GaAs-NBO film can work as etching masks because of the high NBE selectivity of GaAs-NBO. Thus, the diameter of the GaAs nanodisk could be controlled using the surface GaAs-NBO film taper profile produced by the prior Hydrogen-radical treatment time before NBE. This result means that our fabricated nanodisk array structures have great potential for high performance III-V compound optical QDs devices.

- [1] I. Yamashita. Thin Solid Films. **393**, 12. (2001).
- [2] S. Samukawa. Jpn. J. Appl. Phys. **45**, 2395. (2006).
- [3] X. Y. Wang, et al., Nanotechnology, **22**, 365301. (2011).

11:20am **PS2-ThM11 3-Dimensional and Defect-free Neutral Beam Etching for MEMS Applications**, *Y. Yanagisawa*, Tohoku University, Japan, *T. Kubota*, Tohoku University and BEANS Project, Japan, *B. Altansukh*, Tohoku University, Japan, *K. Miwa*, BEANS Project, Japan, *S. Samukawa*, Tohoku University and BEANS Project, Japan

To fabricate MEMS devices, it is necessary to etch large-scale three-dimensional (3D) structures. Plasma etching is widely used for this purpose, but plasma irradiates charged particles and high energy UV photons and they may cause problems.

Ion sheath exists between bulk plasma and the etched sample. It accelerates and collimates ions in plasma and enables vertical etching. However, when the sample has large-scale 3D structure whose height is similar to or larger than the sheath thickness, the sheath is distorted along the surface. This causes distorted acceleration of ions and results in distorted etching shape. Also, high energy UV photons from plasma generates defects and deteriorates the mechanical property. It is reported that quality factor (*q* factor) and resonance frequency (*f*) were decreased by plasma irradiation [1]. In this study, we investigated 3D, damage-free, and high aspect ratio silicon etching for MEMS application using neutral beam (NB) to solve these problems. NB source developed by Samukawa et al. [2] can achieve high neutralization efficiency and elimination of UV irradiation damage.

First, large-scale 3D structure etching was investigated by using a sample with a vertical step of up to 725 μm high. In cases of plasma etchings (Cl₂ ICP etching and Bosch process), distortion of etching shape was observed. The etching shape distortion is concluded to be due to ion sheath distortion, based on the dependence on the step height and plasma parameters. On the other hands, no distortion was observed in the case of NB etching. This is because accelerated and collimated neutral particles without electric charge are used in NB etching.

Next, etching damage on mechanical property of silicon was investigated using microcantilever structure. Ar plasma and neutral beam were irradiated at the surface of the samples. Plasma irradiation degraded *q* factor and *f* of the cantilever, but neutral beam did not. This is due to crystalline defects generated by the UV irradiation from plasma. It is regarded that phonons are scattered by these defects, which causes loss of vibration energy and decrease of *q* factor and *f*.

In conclusion, MEMS process suffers both of sheath distortion and UV irradiation problems and neutral beam can solve these problems.

A part of this work was supported by the New Energy and Industrial Technology Development Organization (NEDO). This work is partly supported by Creation of Innovation Centers for Advanced Interdisciplinary Research Areas Program.

- [1] M. Tomura et al., Jpn. J. Appl. Phys. **40**, 04DL20 (2010).
- [2] S. Samukawa et al., Jpn. J. Appl. Phys. **40**, L779 (2001).

Surface Science

Room: 21 - Session SS+EN+OX-ThM

Catalysis and Photocatalysis on Oxides

Moderator: Z. Dohnalek, Pacific Northwest National Laboratory

8:00am **SS+EN+OX-ThM1 Photoelectrochemical Water Splitting under Sunlight Irradiation using Oxynitride Electrodes Fabricated by Particle Transfer Method**, *K. Domen, J. Kubota*, The University of Tokyo, Japan **INVITED**

Hydrogen production through the photoelectrochemical (PEC) water splitting is one of the attractive ways to convert solar energy to storable chemical energy. The availability of powder semiconductor materials through coating methods for preparing photoelectrodes is a one of strong point of PEC cells. Even if the surface is a rough particle layer, the electrolyte solution automatically forms the desirable solid-liquid interface

for whole semiconductor surfaces, where photoexcited carriers are separated by electric field.

Oxynitride and oxysulfide materials are promising candidates for photoelectrodes for water splitting. Among them, LaTiO₂N has a proper band structure from the view point of driving solar water splitting. The material shows photocatalytic hydrogen and oxygen evolutions in half reactions using sacrificial reagents, indicating that the material have a proper band structure to drive PEC water splitting. LaTiO₂N absorbs visible light up to 600 nm ($E_g = 2.1$ eV), so that they can capture more solar energy than oxide photocatalysts, which typically have absorption in the UV region. Photoelectrodes based on the material have been studied extensively, however, the photocurrent was low due to the lack of good preparation method of the electrode.

In the present study, we report a novel fabrication method of photoelectrodes for PEC water splitting using semiconductor powders. This method, which we have termed the particle transfer (PT) method, is shown to be applicable to a variety of semiconductor powders. LaTiO₂N was demonstrated to exceed those prepared by the conventional method of photoelectrode fabrication from powder materials.

8:40am **SS+EN+OX-ThM3 Multi-step Photooxidation of CO on TiO₂(110)**, G.A. Kimmel, N.G. Petrik, Pacific Northwest National Laboratory

TiO₂ is an important photocatalyst with many practical applications. However, a detailed understanding of the relevant physical and chemical processes for the photocatalysis remains elusive. We have studied the photooxidation of CO adsorbed on rutile TiO₂(110) during UV irradiation with ~1 ms time resolution. Previous investigations with ~0.1 s resolution found that the maximum CO₂ photon-stimulated desorption (PSD) signal occurred for the first data point and then decreased monotonically with increasing irradiation time. However our experiments with improved time resolution show that the initial rate of CO₂ production is zero, and then increases smoothly to a maximum before decreasing at longer irradiation times. Experiments varying the UV photon flux show that the CO₂ PSD kinetics are proportional to the photon fluence but are independent of the photon flux (for the range investigated). The photon fluence required to reach the maximum CO₂ PSD signal increases as the initial coverage of chemisorbed O₂ increases – an effect that we attribute to changes in the initial charge state of the chemisorbed O₂. These results demonstrate that the production of CO₂ proceeds through the formation of stable precursor. The angular distribution of the photodesorbing CO₂, which is peaked at ~40° with respect to the surface normal perpendicular to the BBO rows, is also consistent with the production of CO₂ from a precursor state. Previously, the photooxidation of CO on TiO₂(110) was believed to occur in a single non-thermal reaction step: CO + O₂ + hv → CO₂ + O_{ad}. However, our results show that the photooxidation of CO requires at least two non-thermal reaction steps – one to form the precursor and a second to produce the CO₂. We will compare the experimental results to DFT calculations and discuss the role of photo-generated electrons and holes in the photooxidation of CO. These results show that the photooxidation of CO on TiO₂ is more complicated than previously appreciated.

9:00am **SS+EN+OX-ThM4 Design of Band Engineered Photocatalysts using Titanium Dioxide**, S.W. Ong, D.E. Barlaz, E.G. Seebauer, University of Illinois at Urbana Champaign

Difficulties in achieving control over carrier concentration have impeded progress toward tailoring the electric fields in semiconducting oxide photocatalysts based upon principles of electronic band engineering drawn from classical optoelectronics. The present work demonstrates such principles using the model case of methylene blue photo-oxidation over thin-film anatase TiO₂ grown by atomic layer deposition. The carrier concentration in the polycrystalline semiconductor is controlled over a range of 2.5 orders of magnitude via an unconventional means - film thickness, which indirectly influences the concentration of electrically active donor defects at grain boundaries. Over this range, the reaction rate constant varies by more than a factor of 10, and is well described by a quantitative one-dimensional model for photocurrent. The model suggests that the changes in rate result fundamentally from variations in the width of the space charge layer near the surface. Electrical characterization of the films by capacitance-voltage measurements and ultraviolet photoelectron spectroscopy, together with detailed physical characterization by a variety of techniques, confirm this picture. Prospects for better control of grain boundary donor defects through film synthesis procedures are discussed.

9:20am **SS+EN+OX-ThM5 Adsorption of CO₂ on Oxygen Precovered TiO₂(110) Surfaces**, X. Lin, Y. Yoon, N.G. Petrik, G.A. Kimmel, Z. Li, Z.-T. Wang, B.D. Kay, I. Lyubinetsky, R. Rousseau, Z. Dohnalek, Pacific Northwest National Laboratory

Rutile TiO₂(110) was employed as a model oxide surface to investigate the adsorption behavior of CO₂ by means of scanning tunneling microscopy (STM) and density functional theory (DFT). STM images of partially reduced TiO₂(110) surfaces obtained before and after *in-situ* dosing of CO₂ molecules at 50 K show that CO₂ adsorbs preferentially on oxygen vacancy (V_O) sites. Since the reaction of CO₂ with oxygen adatoms (surface hydroxyl groups) may lead to the formation of carbonate (bicarbonate), O₂ (H₂O) was pre-dosed to form oxygen adatom (hydroxyl) covered TiO₂ surfaces. On the oxygen precovered surfaces, CO₂ molecules were found to preferentially bind on the Ti sites next to oxygen adatoms (O_a's) and form CO₂/O_a complexes, while on hydroxylated surfaces no interactions were observed between CO₂ and hydroxyl groups. CO₂ binding to O_a's is weak as revealed by the dissociation of the CO₂/O_a complexes at 50 K where CO₂ diffuses away along the Ti row. The weak binding indicates that CO₂ is bound to O_a only via dispersion forces. Temperature dependent studies (100 - 150 K) show that the CO₂ binding energy next to O_a's is smaller by ~20 mV than that on V_O's. At 50 K, however, the adsorption of CO₂ on V_O is partially hindered by the higher adsorption barrier. CO₂ molecules diffusing between two CO₂/O_a complexes are found to move fast compared to the STM sampling rate and are imaged as a time average of all CO₂ binding configurations on Ti sites. DFT studies reveal the rotation-tumbling mechanism for CO₂ diffusion with a very low diffusion barrier (~50 meV) in agreement with the experiment.

X.L. is grateful for the support of the Linus Pauling Distinguished Postdoctoral Fellowship Program at PNNL. This work was supported by the US Department of Energy, Office of Basic Energy Sciences, Division of Chemical Sciences, Geosciences & Biosciences. A portion of the research was performed using EMSL, a national scientific user facility sponsored by the Department of Energy's Office of Biological and Environmental Research and located at Pacific Northwest National Laboratory (PN NL). PNNL is a multiprogram national laboratory operated for DOE by Battelle.

9:40am **SS+EN+OX-ThM6 Probe of NH₃ and CO Adsorption on the Very Outermost Surface of a Porous TiO₂ Adsorbent Using Photoluminescence Spectroscopy**, A. Stevanovic, J.T. Yates, Jr., University of Virginia

The photoluminescence (PL) of powdered TiO₂ at 529.5 nm (2.34 eV) has been found to be a sensitive indicator of UV-induced band structure modification. As UV irradiation occurs, the positive surface potential changes and shifts the depth of the depletion layer. It was found that UV light (3.88 eV) induces a positive surface potential which diminishes band bending in n-type TiO₂ and enhances PL1. Also, adsorbates modify the PL intensity by exchanging charge with TiO₂, producing a change in the surface band bending structure.

In addition, we employ photoluminescence (PL) spectroscopy to probe the development of adsorbed layers on the very outermost surface sites of a porous solid adsorbent (TiO₂) in a depth of 20 nm where the meso-pores, separating 30-80 nm TiO₂ particles, join the gas phase. In parallel, we also employ transmission infrared (IR) spectroscopy to gain insight into the extent of adsorption averaged over the entire depth of the diffusion process. The combination of the two surface spectroscopies (PL and IR) allows one to observe the kinetics of transport of adsorbate molecules between the very outermost surface region (where adsorption first occurs) and the interior of the powdered substrate. The transport is governed by the surface mobility of the adsorbate molecules, and hysteresis effects in adsorption/desorption are observed.

References:

1. Stevanovic, A.; Buttner, M.; Zhang, Z.; Yates, J. T., Jr., Photoluminescence of TiO₂: effect of UV light and adsorbed molecules on surface band structure. *Journal of the American Chemical Society* **2012**, *134*, (1), 324-32.
2. Stevanovic, A.; Yates, J. T., Jr., Probe of NH₃ and CO Adsorption on the Very Outermost Surface of a Porous TiO₂ Adsorbent Using Photoluminescence Spectroscopy. *Langmuir: the ACS journal of surfaces and colloids* **2012**, *28*, (13), 5652-9.

Work supported by the Army Research Office.

10:40am **SS+EN+OX-ThM9 Site-Specific Photocatalytical Reactions of O₂ on TiO₂(110)**, *Z.-T. Wang*, Pacific Northwest National Laboratory, *N.A. Deskins*, Worcester Polytechnic Institute, *I. Lyubinetsky*, Pacific Northwest National Laboratory

Photo-stimulated reactions on TiO₂ have attracted much attention due to the variety of potential applications ranging from a hydrogen production by water splitting to environmental remediation through organic pollutant oxidation. In majority of these processes, the oxygen plays a crucial role. A better understanding of the fundamental aspects of oxygen on TiO₂ can potentially lead to improvements or developments of the TiO₂ applications. We present the direct observation at an atomic level with high-resolution scanning tunneling microscopy of photostimulated reactions of single O₂ molecules on reduced TiO₂(110) surfaces at 50 K. The critical relation between photoreactivity and adsorption sites on TiO₂ is demonstrated. Two distinct reactions of O₂ desorption and dissociation occur at different active sites of terminal Ti atoms and bridging O vacancies, respectively. These two reaction channels follow very different kinetics. While hole-mediated O₂ desorption is promptly and fully completed, electron-mediated O₂ dissociation is much slower and is quenched above some critical O₂ coverage. Density functional theory calculations indicate that both coordination and charge state of an O₂ molecule chemisorbed at specific site largely determine a particular reaction pathway.

11:00am **SS+EN+OX-ThM10 Bond Selectivity in the Activation of n-alkanes on PdO(101)**, *J.F. Weaver*, *A. Antony*, *C. Hakanoglu*, *F. Zhang*, University of Florida, *A. Asthagiri*, The Ohio State University

We have investigated initial C-H bond selectivity in the activation of propane and *n*-butane on PdO(101) both experimentally and computationally. Temperature-programmed experiments using different propane isotopologues reveal a strong preference toward primary C-H bond cleavage of propane on PdO(101); about 90% of the propane molecules which react do so by primary C-H bond activation. Direct measurements of the initial dissociation probability of various *n*-butane isotopologues also demonstrate a high selectivity for primary C-H bond activation of *n*-butane on PdO(101) at low coverages. Unlike propane, however, TPRS experiments show that the preference for primary C-H bond cleavage of *n*-butane diminishes with increasing molecular coverage. Calculations using dispersion-corrected DFT reproduce the selectivity toward primary C-H bond cleavage of propane and *n*-butane on PdO(101), and predict that alkane C-H bond scission occurs heterolytically on the oxide surface. The calculations suggest that greater substituent polarization in the 1-alkyl transition structures is responsible for the lower energy barriers for primary vs. secondary C-H bond activation of alkanes on PdO(101).

11:20am **SS+EN+OX-ThM11 Photoresponse, Electronic Transport and Magnetic Properties of Ti-doped (Cr,Fe_{1-x})₂O₃**, *S.E. Chamberlin*, *T.C. Kaspar*, *M.E. Bowden*, *V. Shuthanandan*, *S.A. Chambers*, *M.A. Henderson*, Pacific Northwest National Laboratory

There is widespread interest in discovering materials that can effectively harvest sunlight in the visible region of the electromagnetic spectrum in order to drive chemical processes on surfaces. Hematite (Fe₂O₃) has received renewed interest recently as the active photoanode in photoelectrochemical (PEC) water splitting to store solar energy as H₂. Hematite has three key advantages which make it appealing: it is very abundant, it has a bandgap of 2.2 eV, which is suitably narrow to harvest incident solar radiation, and it is sufficiently stable in the aqueous solutions required for PEC water splitting. However, hematite is a charge-transfer insulator with extremely poor electron and hole mobilities, which results in short hole diffusion lengths and ultrafast recombination of photogenerated electron/hole pairs before charge separation can occur. Substitutional Ti(IV) at an Fe(III) site should be a donor, and epitaxial Ti-doped α -Fe₂O₃ exhibits significantly enhanced conductivity relative to pure hematite when grown under certain conditions by oxygen-assisted molecular beam epitaxy (OAMBE) on α -Al₂O₃(0001) substrates.¹ In addition, Mashiko *et al.*² have shown that the bandgap of pure hematite can be reduced to 1.7 eV by alloying with Cr(III) in epitaxial films. Combining these approaches is expected to result in material with both a reduced bandgap and favorable electrical conductivity, which will facilitate visible-light photoactivity. Heteroepitaxial thin films of (Fe_{1-x}Cr_x)₂O₃ and (Fe_{1-x-y}Cr_xTi_y)₂O₃ were deposited on α -Al₂O₃(0001) substrates by OAMBE. Film quality was monitored *in situ* by reflection high energy electron diffraction (RHEED). *In situ* x-ray photoemission spectroscopy (XPS) was utilized to characterize the charge states of the cations. Film crystallinity and lattice parameters were determined *ex situ* by high resolution x-ray diffraction (HRXRD). Rutherford backscattering spectrometry (RBS) in both random and channeling geometries confirmed the film stoichiometry, and elucidated the degree of substitution of the cations in the lattice. Preliminary optical absorption measurements and photochemistry experiments will be presented.

1. B. Zhao, T. C. Kaspar, T. C. Droubay, J. McCloy, M. E. Bowden, V. Shuthanandan, S. M. Heald, and S. A. Chambers, *Phys. Rev. B* 84, 245325 (2011).

2. H. Mashiko, T. Oshima, and A. Ohtomo, *Appl. Phys. Lett.* 99, 241904 (2011).

11:40am **SS+EN+OX-ThM12 A Nonadiabatic Mechanisms of Inequilibrium Charge Carriers Production in Pd/n-GaP Schottky Nanodiode Exposed to Atomic Hydrogen**, *S.V. Simchenko*, *V. Styrov*, Azov State Technical University, Ukraine

Since the recent discovery of production of electronic flows in Schottky diodes with nanosized "top" metal layer due to ballistic metal-to-semiconductor transport of hot electrons formed by the surface exoergic chemical reaction, e.g. [1], this effect attracts attention of scientists owing to its fundamental and practical potential. Here we investigate a new system of that kind, namely Pd-(n)GaP planar Schottky diode (15 nm Pd-layer) placed in the atmosphere of atomic hydrogen. We found the steady-state current flow through the system under consideration in perpendicular direction to the metal surface on which the hydrogen atoms stationary recombine into molecules.

We elaborated a new approach to detect production of the inequilibrium charge carriers via nonadiabatic channel by observing the current-voltage characteristic of the Schottky diode in the presence and absence of the atomic flux incident on the structure. The nonequilibrium nature of the additional carriers is confirmed by kinetics measurements: the current drops to its initial value in the absence of atoms practically momentarily once the atoms are "switched off" and jumps immediately to its excited value when atoms are "switched on" (at the given temperature of the structure and the fixed forward voltage bias on the structures). We were able to draw some quantitative information about the processes of generation of nonequilibrium electron-hole pairs in the reaction of recombination of hydrogen atoms on Pd-surface and their transport in the metal film. The short circuit current is expressed in terms of yield of the chemoexcited carriers and probability of their survival while traveling through the Pd-film.

For a 1V forward bias the current drastically grows from 3 nA to 950 μ A; thus the bias allows gaining chemicurrent value as large as five orders of magnitude. This result can be of significant importance for the practical applications of the nonequilibrium chemiconductance and chemicurrents in Schottky nanostructures including sensing and chemical-to-electricity energy conversion.

[1] B. Georgen, H.Nienhaus, W.H. Weinberg, E. McFarland. *Science*, 294, 2521 (2003)

Surface Science

Room: 22 - Session SS-ThM

Molecular Films: Chirality & Electronic Features

Moderator: A.J. Gellman, Carnegie Mellon University, S.L. Tait, Indiana University - Bloomington

8:00am **SS-ThM1 Smooth and Transparent Organic Surfaces showing Exceptional Dynamic Dewetting Behavior Toward Nonpolar Liquids ~ Oleophobicity is Independent on Length of Perfluoroalkyl Groups ~**, *A. Hozumi*, *J. Park*, *D.F. Cheng*, *B. Masheder*, *C. Urata*, AIST, Japan

Perfluorinated compounds such as perfluoroalkylsilanes (FASs) and related materials have been widely employed in a wide variety of engineering fields by taking advantages of their excellent hydrophobic/oleophobic properties. However, their chemical and physical effects on human health and the environment have been lately viewed with suspicion. In particular, the use of long-chain perfluorinated chemicals (LCPFCs) is going to phase out by the end of 2015. An alternative hydrophobic/oleophobic treatment method not requiring LCPFCs has been strongly demanded.

In this study, we report smooth and transparent organic surfaces showing unusual dynamic dewetting behavior toward nonpolar liquids. We prepared two different surfaces on glass slides: one, organic surfaces consisting of self-assembled monolayers (SAMs) of FASs with different chain length [CF₃(CF₂)_nCH₂CH₂Si(OR)₃, n = 0, 3, 5, 7, R=CH₃ or C₂H₅], and the other, organic surfaces derived from a mixture of FASs and tetramethoxysilane (TMOS). Oleophobicity on the former surfaces was markedly depended on the length of perfluoroalkyl chains, but the latter exhibited excellent dynamic oleophobicity toward various kinds of nonpolar liquids, independent of the length of the perfluoroalkyl chains. Due to the addition of TMOS, condensed silica species most likely acted as spacer moieties such that an appropriate distance now separated the perfluoroalkyl

chains allowing them to rotate freely and confer liquid-like properties on the surface [1,2]. This leads to the exceptional dynamic dewetting behavior toward various nonpolar liquids.

[1] A. Hozumi and T. J. McCarthy, *Langmuir*, 26 (2010) 2567-2573.

[2] D. F. Cheng, C. Urata, M. Yagihashi and A. Hozumi, *Angew. Chem. Int. Ed.*, 51 (2012) 2956-2959.

8:20am **SS-ThM2 Enantioselective Separation on Chiral Au Nanoparticles**, *N. Shukla, N. Khosla, N. Ondeck, A.J. Gellman*, Carnegie Mellon University

Adsorption of chiral compounds on chiral surfaces is the initial step in enantioselective processes such as separations and catalysis. There has been a significant effort over the past decade aimed at the preparation of chiral nanoparticles based on metallic cores modified by chiral ligands. In principle, these can serve as the basis for enantioselective chemical processing. In this work we demonstrate a simple measurement of enantioselective adsorption on chiral metal nanoparticles using a method that can yield quantitative measures of the enantiospecific adsorption equilibrium constants [1].

The surfaces of chemically synthesized Au nanoparticles have been modified with D- or L-cysteine to render them chiral and enantioselective for adsorption of chiral molecules. Their enantioselective interaction with chiral compounds has been probed by optical rotation measurements when exposed to racemic propylene oxide. The ability of optical rotation to detect enantiospecific adsorption arises from the fact that the specific rotation of polarized light by R- and S-propylene oxide is enhanced by interaction Au nanoparticles. This effect is related to previous observations of enhanced circular dichroism by Au nanoparticles modified by chiral adsorbates. More importantly, chiral Au nanoparticles modified with either D- or L-cysteine selectively adsorb one enantiomer of propylene oxide from a solution of racemic propylene oxide, thus leaving an enantiomeric excess in the solution phase. Au nanoparticles modified with L-cysteine (D-cysteine) selectively adsorb the R-propylene oxide (S-propylene oxide). A simple model has been developed that allows extraction of the enantiospecific equilibrium constants for R- and S-PO adsorption on the chiral Au nanoparticles.

[1] N. Shukla, M.A. Bartel, A.J. Gellman "Enantioselective separation on chiral Au nanoparticles" *Journal of the American Chemical Society*, 132(25), (2010), 8575-8580

8:40am **SS-ThM3 2012 AVS Peter Mark Award Lecture: Effects of Chirality in Electron Tunneling, Molecular Excitation and Rotation**, *C.H. Sykes**, Tufts University **INVITED**

Industrially, the selective conversion of prochiral reagents to chiral products is a crucial step in the production of a variety of asymmetric pharmaceuticals. While this feat is accomplished using either chiral catalysts or crystallization, many external influences have been shown to be capable of inducing such symmetry breaking including circularly polarized light, spin-polarized electrons, and combinations of unpolarized light and magnetic fields. Pioneering studies have made great strides towards explaining these various interactions, however many of the fundamental mechanisms by which chirality is transferred at the molecular-level are not yet fully understood. It is also a great challenge to design experimental setups with which to study these phenomena in a quantitative and reproducible manner. We report a simple thioether system in which symmetry breaking can be both induced and measured *in situ* at the single-molecule level. We demonstrate that electrical excitation of a prochiral molecule on an achiral surface produces large enantiomeric excesses in the chiral adsorbed state of up to 40%, whereas thermal annealing produces racemic mixtures as expected. These effects arise from a previously unreported phenomenon that standard polycrystalline metal scanning probe tips can possess intrinsic chirality.

Thioethers also constitute a simple, robust system with which to study molecular rotation as a function of temperature, electron energy, applied fields, and proximity of neighboring molecules. In order for molecules to be used as components in molecular machines, methods are required to couple individual molecules to external energy sources and to selectively excite motion in a given direction. Studying the rotation of molecules bound to surfaces offers the advantage that a single layer can be assembled,

monitored and manipulated using the tools of surface science. We report that a butyl methyl sulfide (BuSMe) molecule adsorbed on a copper surface can be operated as a single-molecule electric motor. Electrons from a scanning tunneling microscope are used to drive directional motion of the BuSMe molecule in a two terminal setup. Moreover, the temperature and electron flux can be adjusted to allow each rotational event to be monitored at the molecular-scale in real time. The direction and rate of the rotation are related to the chiralities of the molecule and the tip of the microscope (which serves as the electrode), which again illustrates the importance of the symmetry of the metal contacts in atomic-scale electrical devices.

9:20am **SS-ThM5 Single-Site Studies of Chirality Transfer Complexes on Chirally Modified Pt(111)**, *J.-C. Lemay, P.H. McBreen, V. Demers-Carpentier, G. Goubert, Y. Dong, Université Laval, Canada, B. Hammer, A.M.H. Rasmussen, L. Ferrighi, Aarhus University, Denmark, F. Masini, Université Laval, Canada*

Stereoselective catalytic sites on achiral metallic surfaces may be prepared by adsorbing optically active compounds described as chiral modifiers. A fundamental understanding of the stereodirecting forces in such systems is necessary to develop more efficient enantioselective catalysts. We will present data for chirality transfer complexes formed by the chiral modifier (R)-(+)-1-(1-naphthyl)ethylamine ((R)-NEA) and pro-chiral α -phenylketone and α -ketoester substrates on Pt(111). Time-lapsed scanning tunneling microscopy allowed us to isolate individual chiral modifier/substrate complexes. The structure of the diastereomeric complexes were separately determined using DFT calculations. The extremely good convergence between the calculated structures and visual STM data, as well as supporting surface spectroscopy data, shows that prochiral steering on chirally modified Pt(111) can be followed with submolecular resolution at the reaction temperature (room temperature), thus enabling conformational, regiospecific and enantiospecific characterisation. The study reveals the contributions of steric repulsion, non-covalent attractive interactions and site-specific chemisorption to stereoinduction. We will conclude with a short description of the targeted design of new chiral modifiers.

9:40am **SS-ThM6 Chirality in Flatland: 2D Crystallization, Single-Molecule Dynamics and Unidirectional Rotors**, *K.-H. Ernst*, EMPA, Switzerland

A promising approach to study chiral molecular recognition is studying two-dimensional (2D) crystallization phenomena on well-defined surfaces via scanning tunneling microscopy (STM). We present studies on different two-dimensional chiral systems and discuss their tendency to undergo enantiomeric separation. A special surface enantiomorphism is observed via STM after adsorption of the enantiomers of a helical aromatic hydrocarbon on Cu(111). Instead of crystallization into homochiral 2D domains on the surface, racemic enantiomorphs are observed. In this situation, a small excess of one enantiomer is sufficient to create domains possessing single handedness throughout the entire surface layer. The induction of homochirality by chiral doping has also been observed for succinic acid and achiral (R,S)-tartaric acid. Our findings are explained by cooperative interactions between many chiral units, similar to the mechanism of chiral amplification observed in helical polymers and coined as "Sergeants-and-soldiers" principle. Another recently observed phenomenon is single enantiomorphism due to chiral conflict. Depending on the handedness of a chiral adduct to a racemic situation suppresses one enantiomorph during crystal growth, but supports the other by forming a quasisymmetric solid solution. Finally, we present chirality aspects in single molecule surface dynamics, including conversion of adsorbate handedness and linear, unidirectional propulsion of a molecular car with chiral "wheels".

10:40am **SS-ThM9 Functional Molecular Layers for Energy Applications**, *R.J. Hamers*, University of Wisconsin-Madison **INVITED**

Electrode materials for renewable energy applications are largely based on materials such as metal oxides and various forms of carbon because of their intrinsically high stability. However, the properties can be markedly enhanced through the integration of "smart" molecular functionalities. We have been investigating the development and application of new chemistry for fabricating novel types of electrochemically and photoelectrochemically active molecular structures on surfaces of metal oxides and on thin-film diamond. One area of interest has been the use of "click" chemistry as a versatile approach to functionalizing surfaces with redox-active molecules that can be used either as potential catalysts or as light-harvesting molecules. By using complementary functionalization on two different nanostructured oxides, it is also possible to make chemically-assembled oxide-oxide heterojunctions, such as TiO₂/SnO₂. In these cases the formation of a heterojunction can provide a built-in potential to enhance charge transfer at the interface.

A key question in these studies has been understanding how the presence of alkyl chain, ranging from ~4 atoms to ~12 atoms, impacts the electron

* Peter Mark Memorial Award Winner

transfer. While most previous work on molecular layers has been performed on densely packed layer on coinage metals such as gold and silver, when molecular layers are tethered to covalent materials such as diamond or metal oxides, the resulting layers have a high degree of disorder due to the mismatch between the native packing of the alkyl chains and the distribution of available surface sites. We have investigated the electron-transfer properties at these functionalized interfaces and find that the electron transfer rates are surprisingly high and only weakly dependent on the length of the alkyl chain, which we explain as a result of the increased conformational disorder. Our data suggest that the "best" molecular layers for electron-transfer applications are those that have a controlled degree of conformational disorder. We demonstrate these effects using recent measurements of electroactive Ru(bpy)-based complexes on diamond and on metal oxides.

11:20am **SS-ThM11 Atomic Study for P-type Doping Process of CuPc Molecules with STM**, *J.H. Park, K. Tyler, C.T. William, A.C. Kummel*, University of California San Diego

Metal phthalocyanines (MPc) have been widely employed as channel materials in organic thin film transistor (OTFT) for chemical vapor sensing, due to their novel gas adsorption properties. Theoretically, MPc molecules act electron donors during reaction with oxidative analytes and are the basis of their chemical sensing. However, this sensing reaction has not been understood fully. This study presents molecular scale observation of NO adsorption onto CuPc monolayers using ultra-high vacuum (UHV) scanning tunneling microscopy (STM). CuPc monolayers were deposited on Au (111) surfaces by organic molecular beam epitaxy in ultra-high vacuum (UHV) and subsequently dosed at 150 K substrate temperature with NO (5% : diluted by He of 95 %) via a supersonic molecular beam source (MBS). After dosing NO for 1 min, STM images reveal small NO chemisorption sites on the CuPc metal centers and ~4 % of CuPc molecules are reacted with NO. Un-reacted central Cu²⁺ ion of CuPc appears as dark hole in both of empty and filled states STM images. Conversely, after chemisorption of NO, the topographic appearance of core metal ion is modified into a bright spot, while the 4-leaf pattern of ring still remain. As dosing duration increases to 10 min, the coverage of NO chemisorption sites increases to ~7 %. However this coverage increase is sublinear and further dosing does not increase the coverage consistent with a chemisorption induced change in electronic structure. In order to study the electronic structure of NO chemisorption onto CuPc molecules, scanning tunneling spectroscopy (STS) data was also obtained. Unreacted CuPc has a Fermi level (E_F) almost in the middle of the band gap. However, after NO chemisorption, this central E_F shifts to the highest occupied molecular orbital (HOMO) and this transition indicates CuPc molecules is doped to 'p-type' by NO. This 'doping' process of NO is in good agreement with previously published theoretical predictions and is consistent with the high sensitivity of CuPc film to strong oxidants in CuPc OTFT chemical sensors.

11:40am **SS-ThM12 Formation of 2D Superstructure with Wide Band-gap n-type Behavior**, *T.K. Shimizu, J. Jung*, RIKEN, Japan, *T. Otani*, University of Tokyo, Japan, *Y.-K. Han*, Korea Basic Science Institute, *M. Kawai*, University of Tokyo, Japan, *Y. Kim*, RIKEN, Japan

A two-dimensional superstructure of molecules with high electron affinity was successfully formed on Au(111), and it indicated wide band-gap n-type behavior. The molecule used was fluorinated fullerene (C60F36). Although there exist three isomers (C3, C1, and T) in our molecular source, scanning tunneling microscopy (STM) images and density functional theory (DFT) calculations suggested that the molecules in the well-ordered region consisted of only the C3 isomer. Its LUMO distribution governs the adsorption orientation due to partial electron transfer from Au to the molecule. The intermolecular C-F...p electrostatic interactions determines the lateral orientation of C60F36 molecules.

[Ref] Shimizu et al., ACS Nano 6, 2679-2685 (2012).

Transparent Conductors and Printable Electronics Focus Topic

Room: 7 - Session TC+EM+AS+TF+EN-ThM

Transparent Conductors and Devices

Moderator: L.M. Porter, Carnegie Mellon University

8:20am **TC+EM+AS+TF+EN-ThM2 High Conductivity in Thin ZnO:Al Deposited by Means of the Expanding Thermal Plasma Chemical Vapor Deposition**, *K. Sharma, H.C.M. Knoops, M.V. Ponomarev*, Eindhoven University of Technology, The Netherlands, *R. Joy, M. Velden, D. Borsa, R. Bosch, Roth and Rau BV, Germany, W.M.M. Kessels, M. Creatore*, Eindhoven University of Technology, The Netherlands

Session: Transparent Conductors and Devices

The ever-increasing demand for transparent conducting oxides (TCO) for application in flat panel displays, light emitting diodes (LEDs), and thin film photovoltaics drives the present research in the field of TCOs. Aluminum-doped zinc oxide (ZnO:Al) is often referred to as a potential alternative to e.g. indium tin oxide. The ZnO:Al is considered appealing due to the relatively low cost, high abundance, non-toxicity, resistance to H₂ etching and, under specific conditions, surface texturing for light management/trapping. Thin ZnO:Al films (~100 nm) with low resistivity (2-5 · 10⁻⁴ ohm*cm) along with high transmission (> 85 %) are desirable in many devices. Furthermore, large area processing/ high throughput are essential pre-requisites for industrial applications.

ZnO:Al thin films (< 150 nm) have been deposited by using an in-line industrial expanding thermal plasma chemical vapor deposition (ETP-CVD) technique,^{1,2,3} by means of O₂/diethylzinc/trimethylaluminum mixtures. High diethyl zinc flow rate conditions² were applied, which enable the development of a conductive (5 · 10⁻⁴ Ω·cm), 300 nm-thick ZnO:Al layer by promoting the development of a densely packed structure at early stages of growth, as very recently reported.²

In the present contribution, the effect of the dopant, i.e. trimethylaluminum, is investigated to further improve the electrical quality of even thinner ZnO:Al layers. ZnO:Al films were analyzed with spectroscopic ellipsometry, four point probe, hall measurements, X-ray photon spectroscopy (XPS), Rutherford backscattering (RBS), elastic recoil backscattering (ERD), and X-ray diffraction (XRD).

A remarkable low resistivity of 5 · 10⁻⁴ Ω·cm was measured for a ZnO:Al film with thickness of only 120 nm, characterized by a carrier concentration of 1 · 10²¹ cm⁻³, with an electron mobility in the range of 10-25 cm²/V · s.^{2,3} The obtained mobility values are higher than previously reported value of 13 cm²/V · s for 300 nm thick ZnO:Al.² The improvement in terms of conductivity is attributed to the large hydrogen content (2-4 · 10²¹ at/cm³) promoting the chemical passivation of the grain boundaries.

A broad characterization of highly conductive thin ZnO:Al films along with insights on charge transport process will be presented.

Reference List

1. B. Hoex *et al.*, Progress in Photovoltaics **13**, 705 (2005).
2. M. V. Ponomarev *et al.* Journal of Applied Physics **112**, 043708 (2012).
3. M. V. Ponomarev, *et al.*, Journal of Applied Physics **111**, 063715 (2012).

8:40am **TC+EM+AS+TF+EN-ThM3 Recent Progress in Oxide Semiconductors and Oxide TFTs**, *H. Hosono*, Tokyo Institute of Technology, Japan

Transparent conductive oxides (TCOs) and transparent oxide semiconductors (TOSs) have a long history since 1950s. The material design concept for TCOs looks almost established, i.e., ionic oxides of p-block metals with an electronic configuration of (n-1)d¹⁰ns⁰ and a spatial spread of ns orbitals which is enough to have large overlap with neighboring metal ns orbitals irrespective of intervening oxygen ion¹. Concretely, most of the TCOs have been realized in the material systems of In₂O₃-SnO₂-CdO-Ga₂O₃-ZnO. Materials based on light metal oxides such as Al₂O₃ and SiO₂ have not been regarded as the candidates of TCOs. In 2002, we² reported high electronic conductivity in 12CaO·7Al₂O₃ (C12A7) which had been a typical insulator and this discovery was followed by transparent conductivity in cubic SrGeO₃ in 2011.³ These two materials are TCOs realized by a new material design concept.

As for TOS, the striking advances are seen in transparent amorphous oxide semiconductors (TAOS) in science and technology due to strong demand for active layer materials in thin film transistors (TFTs). Amorphous In-Ga-Zn-O (IGZO) TFTs, which was first reported in late 2004,⁴ has adopted to drive high resolution displays of new iPad.⁵ This is a first mass production of TOS

family. The major reasons for this adoption are high electron mobility (an order of larger than that of Si:H) and easy fabrication process. A major advance in TOS-TFTs is realization of p-channel TFTs and subsequent fabrication of C-MOS using ambipolar SnO.⁶⁾

In this talk, I review these progresses viewed from the electronic state of these materials.

- 1) H. Kawazoe, H. Yanagi, K. Ueda, and H. Hosono. *MRS Bull.*, 25, 28 (2000)
- 2) K. Hayashi, S. Mitsuishi, T. Kamiya, M. Hirano, H. Hosono, *Nature* 419, 462 (2002).
- 3) H. Mizoguchi, T. Kamiya, S. Mitsuishi, H. Hosono: *Nat. Commun.*, 2, 470 (2011).
- 4) K. Nomura, H. Ohta, A. Takagi, T. Kamiya, M. Hirano, H. Hosono, *Nature* 432, 488 (2004).
- 5) Sharp Press Release April 6, 2012
- 6) K. Nomura, T. Kamiya, and H. Hosono: *Adv. Mater.*, 23, 3431 (2011)

9:20am **TC+EM+AS+TF+EN-ThM5 Surface Functionalization of Amorphous Zinc Tin Oxide Thin Film Transistors**, G.S. Herman, M.S. Rajachidambaram, Oregon State University, A. Pandey, S. Vilayrganapathy, P. Nachimuthu, S. Thevuthasan, Pacific Northwest National Laboratory

Amorphous zinc tin oxide semiconductor materials have been studied primarily as the active semiconducting material for thin film transistors (TFT) for applications including transparent and flexible electronics. Due to the amorphous nature of these materials excellent uniformity can be obtained over large areas while still having reasonably high electron mobilities ($>10 \text{ cm}^2/\text{Vs}$). Considerable control over the electrical properties of ZTO can be maintained, where insulating, semiconducting, and conductive films can be obtained by varying the processing and post-annealing conditions. We have recently characterized sputter-deposited zinc tin oxide (ZTO) as the active material for TFTs and found that the switching properties of ZTO are closely related to deposition, post-annealing, and electrical test conditions. In this presentation we will discuss bias stress induced instabilities for ZTO TFTs. We have found that devices with a backchannel exposed to the atmosphere have a positive subthreshold shift under positive bias, which can be well explained by a stretched exponential model. Using this model the shifts may be related to either electron trapping at the dielectric semiconductor interface or due to metastabilities of the active material. We have found that the adsorption of a self-assembled monolayer (SAM) on the backchannel of the TFT effectively passivates the device and significantly reduces the bias stress induced instabilities. In this study we will present contact angle measurements and x-ray photoelectron spectroscopy to better understand the interaction of the SAM with the ZTO surface, and the improved stability of the ZTO TFTs will be discussed in regards to the interfacial chemistry of the backchannel.

9:40am **TC+EM+AS+TF+EN-ThM6 Work Function and Valence Band Structure of Oxide Semiconductors and Transparent Conducting Oxides Grown by Atomic Layer Deposition**, A. Yanguas-Gil, Argonne National Laboratory, R.T. Haasch, University of Illinois at Urbana Champaign, J.A. Libera, J.W. Elam, Argonne National Laboratory

Atomic Layer Deposition offers a low-temperature, scalable route to the synthesis of a wide range of oxide semiconductors and transparent conducting oxides both in flat and high aspect ratio surfaces. We have carried out studies on the influence of concentration and spatial distribution on the electrical properties within the ZnO-SnO₂-In₂O₃ compositional map, including standard TCO materials such as Al:ZnO and ITO. We will present results on the work function and valence band structure of transparent conducting oxides grown by ALD using ex-situ UPS measurements, including the influence of the surface termination on the interfacial properties of the materials. Finally, the ability of ALD to tailor the surface and interfacial properties of TCOs based on its layer-by-layer nature will be discussed.

10:40am **TC+EM+AS+TF+EN-ThM9 Low Temperature, High Performance Solution-Processed Metal Oxide Thin Film Transistors formed by a 'Sol-Gel on Chip' Process**, H. Sirringhaus, University of Cambridge, UK **INVITED**

N-type amorphous mixed metal oxide semiconductors, such as ternary oxides, where M¹ and M² are metals such as In, Ga, Sn, Zn, have recently gained momentum because of high carrier mobility and stability and good optical transparency, but they are mostly deposited by sputtering. To date only limited routes are available for forming high-performance mixed oxide materials from solution at low process temperature $< 250^\circ \text{C}$. Ionic mixed metal oxides should in principle be ideal candidates for solution processible materials because the conduction band states derived from metal s-orbitals are relatively insensitive to the presence of structural disorder and high

charge carrier mobilities are achievable in amorphous structures. Here we report the formation of amorphous metal oxide semiconducting thin films via a 'sol-gel on chip' hydrolysis approach from soluble metal alkoxide precursors, which affords unprecedented high field-effect mobilities of $10 \text{ cm}^2/\text{Vs}$, reproducible and stable turn-on voltages $V_{\text{on}} \gg 0 \text{V}$ and high operational stability at maximum process temperature as low as 230°C . We discuss the effect of film composition on device performance and stability.

11:20am **TC+EM+AS+TF+EN-ThM11 In Situ Measurements of Interface States and Junction Electrical Properties of Electrically Biased Metal / β -Ga₂O₃ Structures**, H. Pham, X. Zheng, B. Krueger, M.A. Olmstead, F.S. Ohuchi, University of Washington

A significant issue in application of wide-band-gap transparent conducting oxides is formation of reliable ohmic and rectifying metal contacts. The metal-oxide interface properties are dominated by chemical reactions during growth and the resultant interface state distribution once the interface is formed. We have investigated interface formation between the wide band gap TCO β -Ga₂O₃ ($E_g = 4.8 \text{ eV}$) and the metals Pd, Ni, Ti and Al with in-situ x-ray photoemission spectroscopy (XPS) both during growth and during sputter profiling. The two techniques give very similar results, demonstrating that in this case sputter profiling does not significantly alter the interface chemistry. Consistent with the relative compound heats of formation, Ni and Pd show very little interface reaction with either Ga or O, while Ti interacts strongly with both Ga and O and Al interacts primarily with oxygen. Electrically, Ni and Pd have similar Schottky barriers on the intrinsically n-type oxide (about 0.9 eV), Ti forms a symmetric, nearly ohmic contact, while Al exhibits a smaller barrier (about 0.6 eV). To probe the nanoscopic origins of the Schottky contact behavior through the interface state energy distribution, we combined *in-situ* deposition of thin metal layers and application of forward/reverse biases to the metal-oxide junction with XPS measurements of the relative positions of the Ga₂O₃ bands (via the Ga 3d or O 1s core level) and the metal Fermi level. The density of interface states determines the rate at which the Fermi level can be moved through the oxide band gap, so variation of the oxide core-level shift with respect to the bias voltage yields the interface state density. We find the metal and oxide bands maintain their relative alignment under forward bias (back-plane negative with respect to metal), while they separate at a rate about half that of the applied bias under reverse bias (positive bias with respect to metal).

11:40am **TC+EM+AS+TF+EN-ThM12 Atmospheric Pressure Dielectric Barrier Discharge (DBD) Post Annealing of Aluminium Doped Zinc Oxide (AZO) Films**, Y.L. Wu, E. Ritz, J. Hong, T.S. Cho, D.N. Ruzic, University of Illinois at Urbana Champaign

Aluminum-doped Zinc Oxide (AZO) is a material that has high electrical conductivity while being highly transparent at the same time. It could find many useful applications in our daily lives such as displays, mobile devices, solar cells, etc. Currently AZO films are considered as attractive alternatives to materials such as Indium Tin Oxide (ITO) due to its much cheaper cost and comparable high electrical conductivity. A process of depositing AZO film by dual DC magnetron system has been developed. Film thicknesses were measured to be about 300nm by stylus contact profilometer and transparency of greater than 90% in the visible range were measured with spectrophotometry methods. Film conductivities were in the order of 10^{-3} Ohm-cm with the four-point probe method. By using a Dielectric Barrier Discharge operating at atmospheric pressure, conductivity of film can be further lowered. A 500mm x 30mm line source operating at a Nitrogen flow of 250L/min was used and $\sim 0.4 \text{ L/min}$ Hydrogen gas was also introduced into the discharge system to create Hydrogen radicals. A 10%-15% decrease in electrical resistance was observed with no changes in the optical properties of the AZO films. The elemental composition of the film was measured by X-ray photoelectron spectroscopy (XPS) and the change of crystal structure after DBD post annealing was measured by X-ray diffraction (XRD).

Thin Film

Room: 10 - Session TF+EM+SE+NS-ThM

Nanostructuring Thin Films

Moderator: R.C. Davis, Brigham Young University

8:00am **TF+EM+SE+NS-ThM1 Plasma Effects in Nanostructuring Thin Films**, K. Ostrikov, CSIRO Materials Science and Engineering, Australia **INVITED**

In this presentation, several examples of uniquely plasma-enabled nanostructuring of thin film materials for applications in energy conversion and storage, environmental monitoring, and bio-sensing. Strong emphasis is

made on atom-, energy-efficiency, and environment-friendliness of plasma-based nanotechnologies.

1. Introduction: Atom- and energy-efficient nanotechnology is the ultimate Grand Challenge for basic energy sciences as has recently been road-mapped by the US Department of Energy. This ability will lead to the energy- and matter-efficient production of functional nanomaterials and devices for a vast range of applications in energy, environmental and health sectors that are critical for a sustainable future. Here we present examples related to atom- and energy-efficient nanoscale synthesis of advanced nanomaterials for energy conversion and storage, environmental sensing, and also discuss effective cancer cell treatment using low-temperature plasmas.

2. Atom- and energy-efficient nanostructure production for energy storage: Here we show an example of a recent achievement of a very low amount of energy per atom (~100 eV/atom) in the synthesis of MoO₃ nanostructures for energy storage (e.g., Li-ion battery) applications. This was achieved by using time-programmed nanosecond repetitive spark in open air between Mo electrodes. Highly-controlled dosing of Mo and O atoms was achieved through the controlled evaporation and dissociation reactions and maintaining reactive chemistry in air. These nanomaterials show excellent electrochemical and energy storage performance.

3. Environment-friendly, single-step solar cell production: Highly-efficient (conversion efficiency 11.9%, fill factor 70 %) solar cells based on the vertically-aligned single-crystalline nanostructures have been produced without any pre-fabricated p-n junctions in a very simple, single-step process of Si nanoarray formation by etching p-type Si wafers in low-temperature environment-friendly plasmas of argon and hydrogen mixtures. The details of this process and the role of the plasma are discussed.

4. Metal-nanotube/graphene environmental and bio-sensors: Plasma processing was successfully applied for the fabrication of hybrid nanomaterials based on metal-decorated carbon nanotubes and vertically aligned graphenes. The applications of these structures in environmental (gas) and bio-sensing (SERC/plasmonic) platforms are presented. The vertically-aligned graphene structures have been grown without catalyst and any external substrate heating, owing to the unique plasma properties.

8:40am **TF+EM+SE+NS-ThM3 Directed, Liquid Phase Assembly of Patterned Metallic Films by Pulsed Laser Dewetting.** *Y. Wu*, University of Tennessee, *J.D. Fowlkes, M. Fuentes-Cabrera*, Oak Ridge National Laboratory, *N.A. Roberts, P.D. Rack*, University of Tennessee

Self-assembly of materials offer the potential to synthesize complex systems by defining the *initial and bounding* conditions if the fundamental scientific principles guiding the assembly are known. Much work has been performed studying the assembly of continuous thin polymer and metal films which reveal interesting dewetting phenomenon. Less work has been devoted to the directed assembly and pattern formation of confined or patterned metallic thin films. Meanwhile, the synthesis of functional metallic nanomaterials via self-assembly has been an effective and low-cost approach to realize many critical applications of nanoscience and nanotechnology. In this study, the dewetting and nanopattern formation of nanolithographically pre-patterned thin films of various shapes via pulsed nanosecond laser melting were investigated to understand how initial boundary conditions facilitate precise assembly. Specifically we will show experimental and computational results (continuum and molecular dynamics) illustrating how so-called synthetic perturbations can vary the dispersion of the resultant nanoparticle size and shape distribution of pseudo-one-dimensional liquid metal wires. Furthermore, we will show how controlling the shape and size of bi-metallic nanostructures, the assembly of multifunctional nanoparticles can be assembled.

9:00am **TF+EM+SE+NS-ThM4 Nanosphere Lithography for Bit Patterned Media.** *A.G. Owen, H. Su, A.M. Montgomery, S.M. Kornegay, S. Gupta*, University of Alabama

Nanosphere lithography 1-4 has been used to pattern perpendicular magnetic anisotropy Co/Pd multilayers into nanopillars for the first time for bit-patterned media applications. A multilayer stack of Pd₁₀/[Co_{0.3}Pd_{1.9}]/Pt₅ nm nanolayers was deposited onto a bare silicon wafer. The nanospheres were spin-coated into a uniform monolayer and then reduced in size by plasma ashing in oxygen. The Co/Pd multilayer films were subsequently ion milled into nanopillars using the reduced nanospheres as masks. We tested two ranges of nanosphere sizes, one at about 100 nm, and the other at about 1000 nm. In order to optimize the ashing of the nanospheres, response surface methodology (RSM) was performed to optimize the ashing power and time. It was seen that ashing at low powers of less than 100 W for longer times was more effective than higher powers for short times in shrinking the nanosphere masks without damage. The subsequent ion milling of the Co/Pd films was performed at a near-perpendicular angle to minimize shadowing by the nanospheres. We will discuss some of the complex shapes the nanospheres were patterned into after ashing, and how

they translated into variously sized and shaped nanopillars of Co/Pd multilayers after ion milling. Magnetometry was used to characterize the films before and after patterning, showing an improvement in the coercivity and squareness of the media after patterning with nanospheres that were shrunk, but not damaged, by ashing. Micromagnetic simulations using Object Oriented Micromagnetic Framework (OOMF) have been carried out to produce a simulated hysteresis loop which is then compared with the experimental results.

Acknowledgements

The NSF ECCS 0901858 grant, entitled "GOALI: Nanopatterned graded media" is acknowledged for support. Alton Highsmith is acknowledged for support in the UA Microfabrication Facility.

References

1. Xiao Li, T. R. Tadisina, S. Gupta, J. Vac. Sci. Technol. A **27**, Jul/Aug 2009, 1062
2. Kosmas Ellinis, A. Smyrnakis, A. Malainou, A. Tseripi, E. Gogolides, Microelectronic Engineering, **88**, 2011, 2547-2551
3. C. L. Haynes, R. P. Van Duyne, J. Phys. Chem. B **105**, 5599, 2001
4. S. M. Weekes, F. Y. Ogrin, W. A. Murray, Langmuir **20**, 11208, 2004

9:20am **TF+EM+SE+NS-ThM5 Effects of Nanometer Scale Periodicity on the Self-Propagating Reaction Behaviors of Sputter-Deposited Multilayers.** *D. Adams, R. Reeves*, Sandia National Laboratories

Nanometer-scale, vapor-deposited multilayers are an ideal class of materials for systematic, detailed investigations of reactive properties. Created in a pristine vacuum environment by sputter deposition, these high-purity materials have well-defined reactant layer thicknesses between 1 and 1000 nm, minimal void density and intimate contact between layers. If designed appropriately, these energetic materials can be ignited at a single point and exhibit a subsequent, high-temperature, self-propagating formation reaction. The nanometer-scale periodicity set through design tailors the effective diffusion length of the subsequent self-propagating reaction.

With this presentation, we describe effects of the nanometer-scale, multilayer periodicity on i) the reactivity of multilayers in different surrounding gaseous environments and ii) the reaction front morphology as viewed in the plane of the multilayer. We show that nickel/titanium and titanium/boron multilayers are affected by the surrounding gaseous environment, and describe how the magnitude of average propagation speed depends on multilayer periodicity. Fine multilayer designs are characterized by fast reaction waves, and there is no difference in average propagation speed when reacted in air (atm. pressure) versus vacuum (1 mTorr). Coarse multilayer designs are generally slower and are affected by secondary oxidation reactions when conducted in air. These thick multilayer designs are affected by the pressure of the surrounding gaseous environment with enhanced propagation speeds owing to the highly exothermic reaction of Ti with O. Regarding the effects of nanometer-scale multilayer periodicity on reaction front morphology, we show that reactive multilayers often have a smooth reaction front when layer periodicity is small. However, multilayers having larger periodicity (and hence larger effective diffusion lengths) exhibit reaction front instabilities and complex reaction front morphologies.

In this talk, we also stress how the propensity to oxidize and the propensity to form reaction front instabilities (as affected through nanometer-scale design) impact final properties of the multilayers for applications such as localized joining.

Sandia is a multiprogram laboratory managed and operated by Sandia Corporation, a wholly owned subsidiary of Lockheed Martin Company, for the United States Department of Energy's National Nuclear Security Administration under Contract DE-AC04-94AL85000.

9:40am **TF+EM+SE+NS-ThM6 Ag Nanoparticles Supported by (111) Facets on Biaxial CaF₂ Nanoblades.** *M. Auer, D. Ye*, Virginia Commonwealth University

Silver nanoparticles of different diameters were grown in an effort to study methods of preferentially orienting the geometry of metal nanoparticles. Arrays of calcium fluoride nanorods were grown on silicon substrates using oblique angle deposition at 75° incident angle. A method was then developed to grow silver nanoparticles exclusively on the (111) facet of the calcium fluoride tips. Cross sectional scanning electron microscopy and transmission electron microscopy imaging was used to verify that the nanoparticles adhered exclusively to the desired facet of the tip. Using selected area diffraction and dark field in the TEM, it was shown that the nanoparticles did grow at a [111] orientation at the interface between them and the calcium fluoride rods. Different thicknesses and diameters of nanoparticles were then grown to determine what an ideal size was to achieve the most [111] orientation of the nanoparticles.

Thin Film

Room: 11 - Session TF+NS+EM-ThM

Thin Films: Growth and Characterization-II

Moderator: C. Vallee, LTM - MINATEC - CEA/LETI, France

8:00am **TF+NS+EM-ThM1 Plasma-enhanced Atomic Layer Epitaxy of AlN Films on GaN**, *N. Nepal, J.K. Hite, N. Mahadik, M.A. Mastro, C.R. Eddy, Jr.*, U.S. Naval Research Laboratory

AlN and its alloys with GaN and InN are of great interest for number of applications. In a device structure that employs an ultrathin layer of these materials, thickness control at the atomic scale is essential. Atomic layer epitaxy (ALE) is one of the most promising growth methods for control of epilayer thickness at the atomic scale. There are reports on atomic layer deposition of AlN on GaN and Si substrates [1]. In those reports, the AlN layers were either amorphous or composed of nm-sized crystallites. Since ALE is a low temperature growth process, there is significantly reduced thermal energy for adatoms to bond at preferred lattice sites and promote growth of crystalline material, therefore, surface preparation plays a very important role to ensure a crystalline layer.

In this work, we present recent efforts to improve the crystalline quality of ALE AlN layers on MOCVD grown GaN/sapphire templates, including the influence of *ex situ* and *in situ* surface pretreatments to promote uniform two-dimensional (2D) nucleation of AlN layers and ALE growth of crystalline AlN films thereupon. AlN layers were grown at 500°C by ALE simultaneously on Si(111) and GaN/sapphire templates and characterized using spectroscopic ellipsometry (SE), x-ray diffraction (XRD), and atomic force microscopy measurements. The SE measurements indicate that the AlN growth on Si(111) is self-limited for trimethylaluminum (TMA) pulse of length 0.04 to 0.06 sec. However, the AlN nucleation has a bimodal island size distribution for TMA pulses < 0.06 sec. The AlN nucleation becomes uniform and 2D for a pulse length of 0.06 sec, therefore, this pulse length was used to study the GaN surface pretreatment on the nucleation of AlN layer. GaN surfaces were pre-treated *ex situ* with HF and HCl wet chemical etches. Alternating pulses of trimethylgallium and hydrogen plasma followed by an hour of annealing at 500°C (emulating a Ga-flash-off process) were employed *in situ* before growing an AlN layer. For 3 cycles of Ga-flash-off the AlN nucleation is uniform and replicates the GaN surface morphology on both HF and HCl pretreated GaN. XRD measurements on 36 nm thick AlN films reveal that the ALE AlN on GaN/sapphire is crystalline with only a wurtzite structure and a (0002) peak rocking curve FWHM of 630 arc-sec, which is close to the typical value for AlN grown by MBE and MOCVD [2,3]. Electrical characterization of 2D electron gas at the AlN/GaN interface will also be presented.

References:

1. M. Alevli et al., Phys. Status SolidiA **209**, 266 (2012), and references therein.
2. T. Koyama et al., Phys. Stat. Sol. (a) **203**, 1603 (2006).
3. K. Balakrishnan et al., Phys. Stat. Sol. (c) **3**, 1392 (2006).

8:20am **TF+NS+EM-ThM2 In Situ Infrared Spectroscopy Study of Cobalt Silicide Thin Film Growth by Atomic Layer Deposition**, *K. Bernall Ramos*, University of Texas at Dallas, *M.J. Saly*, SAFC Hitech, *J. Kwon*, University of Texas at Dallas, *M.D. Halls*, Materials Design Inc., *R.K. Kanjolia*, SAFC Hitech, *Y.J. Chabal*, University of Texas at Dallas

Cobalt silicide has potential applications in microelectronics. For instance, the drive to scale down integrated circuitry (IC) has led to the consideration of cobalt silicide (CoSi₂) as an alternative contact material for titanium silicide (TiSi₂) in future self-aligned silicide technology due to its wider silicidation window and superior thermal and chemical stability. Studies of the growth mechanisms during film deposition are critical to better understand and control thin film formation.

This work focuses on the atomic layer deposition (ALD) of cobalt silicide (CoSi₂), using (tertiarybutylalyl)cobalttricarboxyl ((tBuAllyl)Co(CO)₃) and trisilane on H-terminated silicon to uncover the film growth mechanisms. The first pulse of (tBuAllyl)Co(CO)₃ reacts completely with the H-terminated Si surface forming one monolayer of metallic silicide through the reduction of the allyl ligand by transfer of the surface hydrogen and the formation of Co-Si bonds. In situ infrared absorption spectra show the complete loss of H-Si bonds, and the appearance of surface-bound carbonyl and CH_x ligands after the first (tBuAllyl)Co(CO)₃ pulse on H/Si(111). Further deposition of CoSi₂ is possible only after the linear carbonyl groups (initially observed, on the surface after the first (tBuAllyl)Co(CO)₃) are removed by subsequent ALD cycles. Further ALD cycles give rise to cobalt silicide growth through ligand exchange after a

nucleation period of 2–4 cycles. The resultant CoSi₂ films are characterized by a low concentration of carbon impurities in the bulk according to X-ray photoemission spectroscopy (XPS).

1 Kwon et al. Chem. Mater. 2012, 24, 1025–1030

8:40am **TF+NS+EM-ThM3 Thin Film Growth: From Gas Phase to Solid Phase – Links and Control**, *P. Raynaud*, CNRS and University Paul Sabatier – Toulouse – France

INVITED

PECVD, PVD, ALD, sputtering processes, are widely used for thin film growth. Nevertheless, the growth mechanisms need to be controlled and understood to be able to propose stable, adaptable and reproducible processes. Gas, plasma or “volume” phase is one parameter; interaction with surfaces to be treated is the second one, the last one being the final property (ies) to be reached. The Gas phase is controlled by external parameters (pressure, power, polarization, temperature, gas mixture, type of power supply in plasma processes, type of target, duty cycle,). Moreover, these external parameters are linked to internal parameters such as: density and energy of species, type of species (neutrals, ions, electrons, radicals, photons ...), temperature, bombardment energy... Thus, interaction with surfaces and growth process (growth mode, growth rate...) are obviously controlled by these internal parameters and the couple “Gas phase/surface (nature of substrate)”. The purpose of this talk is to explain through examples (In situ Infrared spectroscopy of gas phase, OES, MS, Growth modes characterization by in situ ellipsometry, RBS, ARXPS...) how to characterize (in or ex situ) the gas phase et solid phase to find links between these two phases and give some explanation of the processes “from power supply to final properties of the layer”.

9:20am **TF+NS+EM-ThM5 Investigation of Precursor Infiltration and ALD Growth on Polymers and Effect on Fiber Mechanical Properties**, *R.P. Padbury, J.S. Jur*, North Carolina State University

Atomic layer deposition (ALD) provides the opportunity to unite the properties of organic fiber forming polymers and nanoscale inorganic films creating a hybrid material interface. Prior research has shown that ALD materials nucleation on polymers varies in composition and structure based on how the precursor interacts with the polymer chemistry and the process conditions. The purpose of this work is to explore the effect of this processing on the mechanical behavior of fibrous materials. To study this in more detail, *in-situ* quartz crystal microgravimetry (QCM) is employed to understand the material growth mechanisms of ALD TiO₂, ZnO, and Al₂O₃ on poly (acrylic acid), polyamide-6, and polyethylene terephthalate. Particular emphasis is placed on controlling the ALD precursor diffusion into the sub-surface region of these polymers. *In-situ* QCM data was complemented by *ex-situ* characterization methods such as FT-IR and TEM to examine the interaction between the precursor and polymer and the compositions of the inorganic films. Finally, these results are correlated to the mechanical performance of the ALD treated fabrics. This work has important implications on sustainable textiles processes as well as the introduction of hybrid material properties to textile systems.

9:40am **TF+NS+EM-ThM6 Atomic Layer Deposition Enabled Synthesis of Nanostructured Composite BiFeO₃/CoFe₂O₄ Thin Films for Multiferroic Applications**, *C.D. Pham, J.P. Chang*, University of California at Los Angeles

Multiferroic materials, that can either exist as single-phase materials or multi-phase composites, exhibit two or more forms of ferroic order such as (anti)ferroelectricity, (anti)ferromagnetism, or ferroelasticity and have been proposed for use in future non-volatile memory technology. Atomic layer deposition (ALD) is proposed as a scalable approach to synthesize multiferroic thin films and to enable the synthesis of multiferroic composites which utilize conformal deposition onto 3-D nanostructures. Challenges that must be overcome in the ALD of multiferroic materials is the amorphous nature of as-deposited films and the difficulty in attaining the desired crystallinity and structure that would enable multiferroic properties to emerge from these materials.

In this work, multiferroic BiFeO₃ was deposited by ALD as a single-phase multiferroic thin film as well as the ferroelectric component in a composite multiferroic using a ferrimagnetic CoFe₂O₄ mesoporous template that was synthesized using an evaporation induced di-block copolymer self-assembly technique. The ALD process used the metallorganic precursors Bi(tmhd)₃ (tmhd = 2,2,6,6-tetramethylheptane-3,5 dione) and Fe(tmhd)₃ alongside oxygen atoms produced from a coaxial waveguide microwave powered atomic beam source. A variety of ALD process conditions were studied, such as the effects of process temperature, precursor pulsing time, and precursor pulsing ratio on film composition, growth rate, and crystallization. The ALD films were able to be grown with a composition ratio Bi:Fe close to unity and with a controlled nanostructure and growth rate of ~0.7 Å/cycle. In order to achieve the desired crystalline material

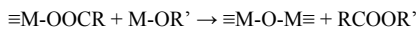
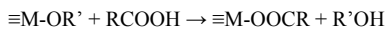
after rapid thermal processing, the composition and nanostructure of the as-deposited films must first be controlled via the ALD process to fit within narrow windows.

To compare the performance of the multiferroic ALD films to more well established synthesis methods, measurements of magnetic and ferro/piezoelectric properties were accomplished using SQUID magnetometry and piezoresponse force microscopy, respectively. Magnetic measurements showed that the out-of-plane remnant magnetization of a composite film at room temperature was approximately 66.4 emu/cm³ while the coercive field was approximately 1950 Oe which was comparable to epitaxial films grown by other methods such as PLD. The magnetoelectric coupling effects in the composite films were studied to assess the effectiveness of the nanostructured material approach.

10:40am **TF+NS+EM-ThM9 In Situ Infrared Spectroscopic Study of Atomic Layer Deposited TiO₂ Thin Film Formation Using Non-Aqueous Routes**, *K. Bernal Ramos*, University of Texas at Dallas, *G. Clavel*, Université Montpellier 2, France, *C. Marichy*, Universidade de Aveiro / CICECO, Portugal, *W. Cabrera*, The University of Texas at Dallas, *N. Pinna*, Universidade de Aveiro / CICECO, Portugal, *Y.J. Chabal*, University of Texas at Dallas

Atomic layer deposition (ALD) is a unique technique for the deposition of conformal and homogenous thin films, by the use of successive self-limited surface reactions. Non-aqueous sol-gel routes are elegant approaches for the synthesis of metal oxide nanomaterials.¹ High quality inorganic nanocrystals,¹ ordered hybrid materials² or ALD thin films³ can be obtained.

Our ALD approach makes use of metal alkoxides and carboxylic acids as metal and oxygen source, respectively.⁴ It is expected that the reaction of carboxylic acids with the surface alkoxide species leads to surface carboxylate species (eq. 1), in a second step an aprotic condensation reaction between surface carboxylate species and metal alkoxides leads to metal-oxide bond formation (eq. 2).



Characterization of interface properties by in situ investigation of surface reaction mechanisms during deposition of high-*k* materials provides critical information for the development of semiconductor devices, where sharp interfaces and impurity free films are sought after.

In this work, in-situ IR spectroscopy is used to investigate the mechanisms for TiO₂ growth using either acetic acid or O₃ as oxygen source and titanium isopropoxide as metal source. It is believed to avoid intermediate OH group and to lead to sharp Si-high-*k* interfaces.

The IR results of the acetic acid process show clearly a ligand exchange leading to formation of acetates at the surface (vibrational bands at 1527 and 1440 cm⁻¹) during the acetic acid pulse and then to their removal during the metal alkoxide pulse. These findings confirm the expected mechanism and demonstrate the absence of OH intermediate. However, the ligand exchange does not seem to be complete leading to accumulation of C impurities.

The in-situ study of O₃ based ALD demonstrates similarities with the above process. Indeed, formation of formate, carboxylate or carbonate species are observed function of the O₃ flow.⁵ The formation of surface carboxylic species upon reaction with O₃ leads then to similar surface states as in the case of the reaction with carboxylic acids.⁴ The mechanism of both approaches and their similarities and differences will be discussed.

1. N. Pinna and M. Niederberger, *Angew. Chem.-Int. Edit.*, 2008, **47**, 5292-5304
2. N. Pinna, *J. Mater. Chem.*, 2007, **17**, 2769-2774
3. G. Clavel, E. Rauwel, M. G. Willinger and N. Pinna, *J. Mater. Chem.*, 2009, **19**, 454-462
4. E. Rauwel, G. Clavel, M. G. Willinger, P. Rauwel and N. Pinna, *Angew. Chem.-Int. Edit.*, 2008, **47**, 3592-3595
5. J. Kwon, M. Dai, M. D. Halls, E. Langereis, Y. J. Chabal and R. G. Gordon, *J. Phys. Chem. C*, 2009, **113**, 654-660

11:00am **TF+NS+EM-ThM10 Nanomechanical Shaft-Loading Blister Testing of Thin Films**, *M. Berdova*, A. Baby, J. Lyytinen, Aalto University, Finland, *K. Grigorias*, L. Kilpi, H. Ronkainen, VTT Technical Research Center, Finland, *J. Koskinen*, S. Franssila, Aalto University, Finland

Atomic Layer Deposition (ALD) is important in micro- and nanoelectromechanical systems, since it provides smooth, uniform, pin-hole free, and conformal layers. In particular, ALD aluminum oxide has excellent properties such as high mechanical strength and hardness, and chemical inertness.

We propose a new technique to measure the mechanical properties of ALD thin films. In the present work, a MEMS version shaft-loading blister test

used to evaluate the adhesion between ALD alumina and Cu, Cr/Cu, SiN_x, SiC_x, and Pt thin films. The test structure consists of microcylinders with diameters 1000 μm and 2000 μm, surrounded by etched annular rings making 50 μm, 100 μm and 200 μm gaps (Figure 1). The test structures are examined by applying the load along the microcylinder with a help of CSM Microindenter, inducing displacement which then causes the delamination between thin films and therefore, contributing to obtain the work of adhesion (Figure 2).

The fabrication of the test structure begins from the cleaning of double-side polished silicon wafer in hydrogen-peroxide-based (RCA) wet cleans. The following step is Atomic Layer Deposition of alumina on both sides of the wafer using trimethyl aluminium and water as precursors at 220 °C. 20 nm of Al₂O₃ is grown on one side as the etch mask, and 200 nm of Al₂O₃ is grown on another side to act both as an etch-stop mask and a testing layer. Next, the top layer is patterned to create alumina etch mask; and the rings are etched through silicon wafer by dry anisotropic Bosch process, forming this way a microcylinders supported only by 200 nm of Al₂O₃ layer. Then, thin films (300 nm thick) are deposited by sputtering, or by PECVD techniques. The silicon nitride and silicon carbide were deposited at 300 °C. Magnetron sputtering was used for deposition of Pt, Cu, and Cr/Cu thin films at room temperature. Finally, those films are released by wet etching supporting alumina layer around the microcylinder.

As a result, we have not observed the delamination for nitride and carbide films: after certain reached displacement point (7 μm for nitride, 12 μm for carbide) the films start to break. For soft films as Pt and Cu, at similar displacement values we observed the starting of delamination. Comparing copper and copper with chromium layer underneath, the delamination of the film with adhesive layer starts at higher displacement and load values, proving the adhesive action of chromium. In the case of metal films large displacement and delamination can be achieved without breaking of the film (Table 1). The proposed MEMS shaft-loading blister test might become a valuable tool for all thin film adhesion testing.

11:20am **TF+NS+EM-ThM11 Phase Formation and Thermal Stability of Arc-Evaporated ZrAlN Thin Films**, *L. Rogström*, Linköping University, Sweden, *M.P. Johansson*, SECO Tools AB, Sweden, *M. Ahlgren*, Sandvik Tooling AB, Sweden, *N. Ghafoor*, Linköping University, Sweden, *J. Almer*, Advanced Photon Source, Argonne National Lab, *L. Hultman*, *M. Odén*, Linköping University, Sweden

Transition metal nitrides are widely used as wear protective coatings due to their high hardness also at elevated temperatures. Hence, TiAlN is one of the most common materials for coating of cutting tools. Its attractive mechanical properties are connected with the phase separation of the cubic TiAlN phase when the coating is exposed to high temperatures. The related ZrAlN system is less studied while its large miscibility gap with possibility for phase separation at elevated temperatures makes this material interesting for high temperature applications. Here, we present a comprehensive study of the phase formation in arc-evaporated ZrAlN thin films and their mechanical properties and thermal stability. Zr_{1-x}Al_xN thin films with a wide range of compositions (0.12 < x < 0.73) were grown by cathodic arc-evaporation. The structure of as-deposited and annealed films was characterized by x-ray diffraction and transmission electron microscopy and the mechanical properties were determined by nanoindentation.

The structure of the as-deposited ZrAlN thin films was found to depend on the Al-content. A low Al-content (x < 0.38) results in cubic (*c*) structure films while for high Al-content (x > 0.70) a hexagonal (*h*) ZrAlN phase is obtained [1]. In the compositional range between x = 0.38 and x = 0.70, the films exhibit a nanocomposite structure with a mixture of cubic, hexagonal, and amorphous phases [1, 2]. In all films, separation of ZrN and AlN takes place during annealing. In films with a nanocomposite structure, the phase transformation is initiated by nucleation and growth of *c*-ZrN in the ZrN-rich domains while the AlN-rich domains remain largely amorphous at 1100 °C [3]. Nucleation and growth of *h*-AlN is hindered by a high nitrogen content in the film and takes place at annealing above 1300 °C, simultaneously to loss of the excess nitrogen. The depletion of amorphous phase during annealing results in an improved hardness of the film. In the *h*-ZrAlN films, ZrN- and AlN-rich domains form within the hexagonal lattice during annealing above 900 °C. The formation of domains with different composition results in an increased hardness, from 24 GPa of the as-deposited film to 31 GPa of the annealed film. The *c*-ZrAlN phase is found to be stable to annealing temperatures of 1000 °C, while at higher temperatures, *h*-AlN nucleates and grows. This is different from the *c*-TiAlN system where spinodal decomposition occurs resulting in age hardening of the films.

[1] L. Rogström et al., *J. Vac. Sci. Technol. A* 30 (2012) 031504.

[2] L. Rogström et al., *Scr. Mater.* 62 (2010) 739.

[3] L. Rogström et al., *J. Mater. Res.*, In press (2012)

11:40am **TF+NS+EM-ThM12 Ion-assisted Epitaxial Sputter-Deposition and Properties of Metastable $Zr_{1-x}Al_xN(001)$ (0.05 x 0.25) Alloys**, *AR.B. Mei, B.M. Howe*, University of Illinois at Urbana Champaign, *N. Ghafoor, E. Broitman*, Linköping University, Sweden, *M. Sardela*, University of Illinois at Urbana Champaign, *L. Hultman*, Linköping University, Sweden, *A. Rockett, J.E. Greene, I. Petrov*, University of Illinois at Urbana Champaign, *M. Oden, H. Fager*, Linköping University, Sweden

Single-phase epitaxial metastable $Zr_{1-x}Al_xN/MgO(001)$ (0.05 x 0.25) thin films were deposited by ultra-high vacuum magnetically-unbalanced reactive magnetron sputtering from a single $Zr_{0.75}Al_{0.25}$ target at a substrate temperature of 650°C. We control the AlN content, x , in the films by varying the ion energy ($5 < E_i < 55$ eV) incident at the film growth surface with a constant ion to metal flux ratio of 8. The net atomic flux was decreased from 3.16 to 2.45×10^{15} atoms $cm^{-2}s^{-1}$, due to efficient resputtering of deposited Al atoms (27 amu) by Ar^+ ions (40 amu) neutralized and backscattered from heavy Zr atoms (91.2 amu). Consequentially, films varied in thickness from 400 nm to 290 nm during 20 min depositions. HfN buffer layers were deposited on the $MgO(001)$ substrates to reduce the lattice mismatch from ~8 to ~0.5%. High resolution x-ray diffraction ω -2 θ scans and reciprocal lattice mapping revealed single-phase NaCl structure with a cube-on-cube orientation relative to the substrate, $(001)_{Zr_{1-x}Al_xN} \parallel (001)_{MgO}$, and relaxed lattice parameters varying from 4.546 with $x = 0.25$ to 4.598 Å with $x = 0.05$. Film nanoindentation measurements showed that hardness decreases from 28.6 to 23.3 Gpa and Young's modulus increases from 263 Gpa to 296.8 GP as x is varied from 0.25 to 0.05. For the same range in x , electronic transport measurements established the films to have electron mobilities increasing from 2.67 to 462 $cm^2V^{-1}s^{-1}$, resistivities decreasing from 162.4 to 25.4 $\mu\Omega$ -cm, and positive temperature coefficients of resistivity spanning from 0.3164 to 1.307 Ω -cm K^{-1} . Films deposited with incident ion energy above 35 eV ($x < 0.08$) exhibited superconductivity with T_c of 8.26 K.

Thursday Lunch, November 1, 2012

Exhibitor Technology Spotlight

Room: West Hall - Session EW-ThL

Exhibitor Technology Spotlight

Moderator: D. Surman, Kratos Analytical Inc.

12:00pm EW-ThL1 EW Multi Vendor Presentation:
Kratos/PHI/Thermo/Omicron

Thursday Afternoon, November 1, 2012

Applied Surface Science
Room: 20 - Session AS-ThA

Applications of Large Cluster Ion Beams - Part 2 (2:00-3:20 pm)/ Surface

Analysis using Synchrotron Techniques (3:40-5:40 pm)

Moderator: A.V. Walker, University of Texas at Dallas, C.M. Mahoney, Pacific Northwest National Laboratory, M.L. Pacholski, The Dow Chemical Company, A. Herrera-Gomez, UAM-Azcapotzalco and CINVESTAV-Queretaro, Mexico

2:00pm AS-ThA1 Applications of a C60 Ion Source for Surface Chemical Analysis: It's Not Just for Polymers, *W.F. Stickle, M.D. Johnson, D. Bilich*, HP

While C60⁺ ion sources are becoming one of the routinely used tools in the surface chemical analysis laboratory its primary value has been for the study of organic systems. Commonly used for ToF SIMS, the C60⁺ ion source is also a standard option for photoelectron spectroscopy tools. But many surface analysis laboratories study a wide variety of materials, not just organic thin films, which raises the question as to using this novel ion source for 'routine' analyses. Being able to use of this ion source in a 'routine' fashion requires characterization and understanding of the surface that is being created during the ion milling process. It is important to understand the sputter induced chemistry that may be created by the C60⁺ source as well as understanding the physical changes that occur to a sample surface during the ion milling. The effects of preferential sputtering, chemical changes or reactions and the nature of surface roughening than can occur will be presented. Several different material systems are examined and discussed with regard to using a C60⁺ ion gun for enhancing and clarifying 'routine' analyses. The different types of samples to be discussed will include inorganic oxides, multilayer structures as well as metal-metal oxide layered structures and polymers.

2:20pm AS-ThA2 Towards Ultimate Organic Depth Profiling using Argon Cluster Beams – Recommendations for Dual Beam Profiling and Sample Charge Compensation, *R. Havelund, A.G. Shard, M.P. Seah, I.S. Gilmore*, National Physical Laboratory, UK

The recent innovation of large argon cluster ion sources has revolutionised the ability of SIMS to give 3D chemical images of important classes of organic materials, such as organic electronic materials. Furthermore, sputtering with argon clusters gives the best depth resolution currently achievable of 5 nm [1], constant sputtering yields [2] and minimal chemical degradation [3]. It is clear that this important capability will have major impact in the innovation and manufacture of many advanced technologies. Consequently, there is an urgent need to develop the underpinning metrology. An essential first phase has been the VAMAS interlaboratory study [4] which has highlighted two key issues which we now study in detail. Firstly, the improved depth resolution using argon cluster sputtering and reduced chemical damage reveals effects of the primary beam in a dual beam depth profiling experiment become increasingly important. In this study, we use the Irganox organic multilayer reference material [5] and show that the apparent position of a delta-layer depends on which secondary ion signal is used. It is observed that the delta-layer profiles for small fragment ions appear before the molecular ion profile. The position shift increases with primary beam energy and can be more than 4 nm when a 50 keV Bi₃ ion beam is used. We understand this in terms of a simple sputtering model and provide recommended analytical conditions to reduce this effect. Secondly, it has been widely reported that an initial increase in intensity is observed when depth profiling some organic materials with argon clusters. This is observed for the Irganox reference material and we show this is due electron beam damage from the charge compensation system. Since, typically, lower sputtering yields are used for argon cluster sputtering (owing to the choice of low energy per atom to reduce the sputtering damage) the emitted flux of positive ions is reduced and more electron beam current is required than typically needed using C₆₀ sputtering. Previously, we have shown that a maximum limit of 6·10¹⁸ electrons per m² should be used to spectroscopy [6]. Here, we show that electron damage extends up to 100 nm into the profile. We conduct a systematic study of the electron beam damage as a function of electron dose and energy and give a recommend dose limit.

[1] A.G. Shard et al., This conference

[2] J.L.S. Lee et al., Anal. Chem. (2010), 82, 105

[3] S. Ninomiya et al., Rapid Commun. Mass Spectrom. (2009), 23, 1601

[4] A.G. Shard et al., Surf. Interface Anal. (2011), 43, 1240v

[5] A.G. Shard et al., J. Phys. Chem. B (2008), 112, 2596

[6] I.S. Gilmore and M.P. Seah, Appl. Surf. Sci. (2002), 187, 89

2:40pm AS-ThA3 Comparative Study of C₆₀ and Gas Cluster Ion Sputtering in XPS Depth Profiling for Thin Film Analysis, *S.S. Alnabulsi, J.F. Moulder, S.N. Raman, S.R. Bryan, J.S. Hammond*, Physical Electronics

The objective of successful XPS sputter depth profiling is to accurately identify the layer thicknesses and chemical composition of materials within thin film structures. Cluster ion beam sputtering has been widely used in recent years with the intent to address this essential analytical goal for a broader range of materials, including organic materials. C₆₀ cluster ion beam sputtering provided the first access to quantitative chemical state information below the surface for many polymers, organic and inorganic oxide materials [1].

The recent introduction of argon gas cluster ion beam sputtering to the XPS community has further expanded the capability of successful depth profiling with an emphasis on preserving the chemical structure of challenging polymer and organic materials that exhibit rapid radiation induced damage due to the mobility and reactivity of free radicals that are formed during the sputtering process when other ion sources are used [2].

The purpose of this study is to present a comparative evaluation to quantify the benefits of using either C₆₀ or argon gas cluster ion beam sputtering for XPS compositional depth profiling by characterizing several standard organic and inorganic thin film structures.

N. Sanada, A. Yamamoto, R. Oiwa, and Y. Ohashi, *Surf. Interface Anal.* 36, 280 (2004).

T. Miyayama, N. Sanada, M. Suzuki, J. S. Hammond, S.-Q. D. Si and A. Takahara, *J. Vac. Sci. Technol. A*, 28, No. 2, L1 (Mar/Apr 2010)

3:00pm AS-ThA4 Damage Profiles of Si (001) Surfaces Bombarded by Ar Gas Cluster Ion Beam, *J.G. Chung, D.J. Yun, Y.K. Kyoung, H.I. Lee, J.C. Lee*, Samsung Advanced Institute of Technology, Republic of Korea, *H.J. Kang*, Chungbuk National University (CBNU), Republic of Korea

The damage profiles of Si (001) surface bombarded by argon gas cluster ion beam (GCIB) and mono-atomic argon ion beam bombardment were investigated using X-ray photoelectron spectroscopy (XPS) and medium energy ion scattering (MEIS). The Ar-GCIB beam was 2 mm in diameter and scanned in an area of 3 mm × 4 mm and the beam current was about 60 nA. The incident angle of the GCIB was fixed at 55° from the surface normal and the mean cluster size was approximately 2500 argon atoms/cluster. The damage profiles of Si (001) bombarded by the Ar GCIB and the mono-atomic Ar ion beam sputtering were measured *ex-situ* MEIS system and *in-situ* MEIS system, respectively. The MEIS results showed that the thickness of the damaged layers on Si(100) is approximately 10 nm for 20 keV, 6.4 nm for 10 keV, and 4.2 nm for 5 keV after the Ar cluster ion dose of 2.3 × 10¹⁵ clusters/cm² and the maximum concentration of the implanted Ar atoms is 0.2 at% for 20 keV and 0.1 at% for both 10 keV and 5 keV. The MEIS spectra taken from the Si (001) surface before and after the Ar ion bombardment with the ion dose of 5 × 10¹⁶ ions/cm² showed that the maximum Ar atom concentration was 5.5, 5.8, and 7.8 at% and the damage depth was 5.3 nm, 8.5 nm and 12 nm at 1.0, 2.0, and 3.0 keV, respectively. The depth of the damaged layer is proportional to the in-depth distribution of the implanted primary ions which can be explained in terms of the collision cascade model. Our results showed that the damage did not result from the linear collision cascade for the sample bombarded by Ar GCIB sputtering since the primary cluster Ar atoms were not implanted into the subsurface. The mechanism for the damage generation via the Ar GCIB bombardment is not clear yet, but it should be understood to make it useful for practical applications in solid surface analysis such as SIMS, XPS and AES.

3:40pm AS-ThA6 Non-Destructive Depth Profiling using VKE-XPS and Maximum Entropy Regularization, *C. Weiland, J.C. Woicik*, National Institute of Standards and Technology

X-ray photoelectron spectroscopy (XPS) is an excellent tool for semi-quantitative analysis of the chemical structure of solid material systems. However, the in-depth distribution of elements in a solid is known to affect the intensity of the measured photoelectron peaks and can thus lead to errors in quantification. The depth distribution itself can be interesting for deposited thin-film systems and buried interfaces. Typically, depth

dependent measurements are made by sputtering layers of the material off the surface, but complications can arise due to knock-on effects, differential sputtering rates and implantation of the sputtering ions. Angle-resolved XPS (ARXPS) coupled with maximum entropy regularization can provide non-destructive depth sensitive information, but analysis is typically performed using a lab-based X-ray source, limiting the ultimate probe depth to tens of Angstroms. Here, we adapt the maximum entropy analysis method used for ARXPS to variable kinetic energy XPS (VKE-XPS) using hard X-rays. Using VKE-XPS with beam energies ranging between 2.1 and 6 keV, we can vary the photoelectron inelastic mean free path to adjust the effective analysis depth to technologically relevant thicknesses. Conversion from intensity vs. beam energy to depth profile can be accomplished using a regularization routine. Development of the routines will be discussed, followed by results of VKE-XPS analysis of plasma-enhanced chemical vapor deposited TiO₂ films on Si performed at NIST beamline X24A at the National Synchrotron Light Source.

4:00pm **AS-ThA7 The Early Stage of Corrosion of Cu₃Au Alloy, P. Rajput**, ESRF, France, *A. Gupta*, UGC-DAE Consortium for Scientific Research, India, *C. Meneghini*, Università di "Roma Tre", Italy, *G. Sharma*, UGC-DAE Consortium for Scientific Research, India, *J. Zegenhagen*, ESRF, France

Metallic alloys are important in our daily life and in industry, but unfortunately highly susceptible to corrosion in wet environment. De-alloying is a particular type of corrosion, attacking alloys which are composed of metals of different "nobility". When coming into contact with an electrolyte, the less noble metal may go into solution, typically causing crack formation and subsequent material failure upon stress. Potential controlled corrosion of a well ordered Cu₃Au crystal in sulfuric acid had been investigated *in situ* [1] showing that, far below the critical potential E_c , at which the alloy is massively dissolved, Cu goes into solution, leaving a \approx 1 nm thick film of small, Au-rich clusters. Just below E_c , the surface is eventually covered with about 10-20 nm large gold islands with a thickness of 2-3 nm. The Au-rich surface protects the bulk of the alloy against further corrosion (unless E_c is exceeded).

We used, hard x-ray photoelectron spectroscopy (HAXPES), x-ray standing waves (XSW) and depth-selective x-ray absorption fine structure (XAFS) to investigate the very early stages of the corrosion of a more 'realistic', disordered CuAu binary alloy. Ultra-thin Cu_xAu films (2.5 nm, $x \approx 3$) were deposited on a Ru/B₄C multilayer to produce the XSW field. The XSW study provides detailed information about the concentration profile of Cu and Au upon de-alloying. HAXPES provides the binding energies (oxidation states) of Au and Cu and XAFS reveals the local atomic structure around Cu and Au.

The pristine Cu_xAu film appeared partially oxidized (CuO and Cu₂O). After dealloying at 245 mV for 2 min in 0.1 M H₂SO₄, the partial Cu dissolution leads to the formation of a Au-rich film with CuAu₃-like composition. Quantitative XRF analysis showed that, surprisingly, even below E_c dealloying leads to the loss of some Au as well.

[1] F. U. Renner, A. Stierle, H. Dosch, T. L. Lee, D. M. Kolb, J. Zegenhagen, Nature 439, 707 (2006).

4:20pm **AS-ThA8 Hard X-ray Photoelectron Spectroscopy (HAXPES) Investigations of Electronic Materials and Interfaces, J.C. Woicik**, National Institute of Standards and Technology **INVITED**

Photoelectron spectroscopy can uniquely measure the chemical and electronic structure of solids and films; however, owing to the generally limiting electron inelastic mean-free path of lab based instruments, the technique is extremely surface sensitive, probing only the first several atomic layers of a given structure. For this reason, synchrotron based hard x-ray photoelectron spectroscopy (HAXPES) in which the photon energy can be varied between 2.1 and 6 keV has emerged as a technique that is ideally suited for studying the electronic and chemical structures of advanced materials systems. In this talk, we will discuss developments of the HAXPES technique at the NIST beamline X24A at the National Synchrotron Light Source for the study of electronic materials. Examples will include nitrogen treatment of HfO₂ gate stacks on Si, depth profiling of the HfO₂/SiO₂ interface, Ga and As "out-diffusion" at semiconductor/oxide interfaces, band offsets and Schottky barrier heights at semiconductor/oxide and diamond/metal interfaces, and oxygen vacancies in N doped TiO₂ and solid-oxide fuel cells. In all cases, the increased probing depth of HAXPES over traditional lab based XPS is crucial to study the electronic structure of entire overlayers and/or buried interfaces with thicknesses of industrial significance.

5:00pm **AS-ThA10 Hard X-ray Photoemission Spectroscopy used to Investigate the Resistive Switching Behavior of Manganite Heterostructures: The Case of Ti/PrCaTiO₃ Interface, F. Offi**, CNISM and Dipartimento di Fisica, Università Roma Tre, Italy, *F. Borgatti*, CNR-ISMN, Bologna, Italy, *Y. Yamashita*, *A. Yang*, *M. Kobata*, *K. Kobayashi*, Synchrotron X-ray Station at SPring-8, NIMS, Japan, *C. Park*, *A. Herpers*, *R. Dittmann*, Peter Grünberg Institut, Research Center Jülich, Germany, *G. Panaccione*, CNR-IOM, Basovizza-Trieste, Italy

Electrical pulse induced resistance change has been observed at several oxides interfaces but its microscopic origin is still an open issue. In order to shed light on this problem we investigated with hard x-ray photoemission spectroscopy (HAXPES) the interface electronic structure of Ti covered 40 nm PrCaMnO₃ (PCMO) film within SrRuO₃/PrCaMnO₃/Ti/Pt devices exhibiting resistive switching behaviour. In particular, we searched for differences arising among the spectra of the virgin (not formed) and the high-resistivity states (HRS). The electronic structure of the Ti top electrode has been probed by measuring the Ti 2*p* spectra. The identification of the Ti 2*p* chemical states on the basis of literature binding energy (BE) values, indicate that the dominant Ti peak at lower BE corresponds to metallic state. Evidence is also found for the presence of Ti(IV) chemical state, due to the formation of TiO₂, and of other intermediate oxide species. Interestingly, the peak corresponding to Ti(IV) is more intense for the HRS than for the virgin state of the samples, suggesting that formation of Ti oxide is induced in the HRS through redox reactions related to the migration of oxygen ions from the PCMO inside the Ti layer. Moreover, the core-level spectra of all the elements of the PCMO layer, when compared to the spectra of the reference (uncovered) thick films of these materials, show BE shift and a change of the spectral lineshape that strongly resembles the BE shift dependence of the photoemission spectra on the amount of hole doping, which is related to the change of the chemical potential. Therefore the HAXPES results show changes of the PCMO and Ti electronic structure for this manganite heterostructure, indicating the increment of Ti oxide in the high-resistivity state and pinning of the PCMO chemical potential.

Electronic Materials and Processing

Room: 9 - Session EM+MI-ThA

Semiconductor Heterostructures II + Heusler Alloys

Moderator: J.E. Ayers, University of Connecticut, B.D. Schultz, University of California, Santa Barbara

2:00pm **EM+MI-ThA1 Dislocation Compensation in Ungraded ZnS_ySe_{1-y}/GaAs (001) Heterostructures, T.M. Kujofsa, J.E. Ayers**, University of Connecticut

Control of strain and dislocation dynamics are important in determining the performance and reliability of semiconductor devices such as light-emitting diodes and photo-detectors. Experimental studies of ZnS_ySe_{1-y}/GaAs (001) heterostructures show that a dislocation compensation mechanism is active in structures involving abrupt interfaces. This mechanism involves the bending over of threading dislocations associated with misfit segments of one sense by misfit dislocations having the opposite sense, and it allows removal of threading dislocations from device structures.

Semiconductor device structures may be designed to take advantage of the dislocation compensation with the aid of a dislocation dynamics model accounting for misfit-threading interactions. To develop such a model we studied strain relaxation in ZnSe/GaAs (001) and ZnS_ySe_{1-y}/GaAs (001) heterostructures to determine the kinetic material parameters associated with dislocation glide and multiplication. Based on these results and by including misfit-threading interactions we developed a dislocation dynamics model which predicts dislocation compensation in arbitrary ZnS_ySe_{1-y}/GaAs (001) heterostructures.

Whereas our previous experimental work involved graded structures, this work focuses on the study of theoretical heterostructures comprising a device layer (DL) of ZnS_ySe_{1-y} on a ungraded buffer layer (BL) of ZnS_ySe_{1-y} deposited on a GaAs (001) substrate. We show that for a given device layer thickness and compositional change at the buffer-device layer interface there exists an optimum thickness of the ungraded buffer layer where the mobile threading dislocation density can be removed entirely. The optimum buffer layer thickness decreases monotonically with the compositional difference between buffer and device layer.

2:20pm **EM+MI-ThA2 Dynamical X-ray Diffraction from Semiconductor Heterostructures with Asymmetrical Dislocation Densities, P.B. Rago, J.E. Ayers**, University of Connecticut

We extend the dynamical theory of Bragg x-ray diffraction to include asymmetrical dislocation densities on the two types of active slip systems in

zinc blende semiconductor heterostructures with (001) orientation. In such structures the dislocations exist in eight active slip systems of two basic types distinguished by the orientation of their misfit segments, which are oriented along either the [1-10] or [110] direction. Variation of the incident x-ray beam azimuth results in a change in the shape of the diffraction profile if the two types of slip systems exhibit an asymmetry in dislocation densities. Our work allows simulation of the x-ray diffraction profile of an arbitrary zinc blende semiconductor heterostructure, and through comparison to experimentally measured data, the two dislocation densities of an experimentally measured sample can be extracted. In this work we have demonstrated use of the model by applying it to the ZnSe/GaAs (001) and HgCdTe/CdTe (001) material systems.

3:40pm **EM+MI-ThA6 Epitaxial Growth and Electronic Bandstructure of the Semiconducting Half Heusler Compound CoTiSb**, *J. Kawasaki*, University of California Santa Barbara, *L. Johansson*, *M. Hjort*, *R. Timm*, Lund University, Sweden, *B. Shojai*, University of California Santa Barbara, *A. Mikkelsen*, Lund University, Sweden, *B.D. Schultz*, *C. Palmstrom*, University of California Santa Barbara **INVITED**

The Heusler compounds are an exciting class of intermetallics due to their ability to adopt a wide range of tuneable electrical and magnetic properties. These properties include ferromagnetism, paramagnetism, half-metallic ferromagnetism, large thermoelectric figures of merit, and both semiconducting and metallic behaviour. Additionally, some of the semiconducting Half Heuslers have been theoretically proposed to be topological insulators, making the Heusler compounds a promising system for multifunctional heterostructure devices. However, due to challenges in controlling defects and stoichiometry, little is known about the experimental band structure of the semiconducting Half Heuslers. We demonstrate the epitaxial growth of the Half Heusler compound CoTiSb by molecular beam epitaxy. Samples consist of an InP (001) substrate, lattice matched In_xAl_{1-x}As buffer layer, and CoTiSb layer. The films are single crystalline and of high structural quality, as measured *in situ* by reflection high energy electron diffraction (RHEED) and scanning tunnelling microscopy (STM) and *ex situ* by X-ray diffraction (XRD), with an out of plane lattice mismatch of less than 0.5%. For growth temperatures of less than 400°C the films grow in a layer-by-layer mode as demonstrated by RHEED intensity oscillations. Under stoichiometric growth conditions the films have a (2x1) surface reconstruction and for Sb-rich conditions the films have a (1x1) reconstruction. Electrical transport measurements show the resistivity of the films decreases as a function of temperature down to 10K, consistent with semiconducting behaviour, and using tunnelling differential conductance spectroscopy (dI/dV) we measure a band gap on the order of 160 meV. However, this band gap is much smaller than the value of 1.0 eV predicted by density functional theory. Angle resolved photoemission spectroscopy (ARPES) measurements were also performed at the MAX-Lab synchrotron facility in Lund, Sweden. A protective Sb capping and decapping scheme was developed to maintain the surface quality of the films as the samples are transported to the characterization facility and exposed to air. The structural, chemical, and electrical properties of the single crystal CoTiSb films will be presented to provide insights into the band structure of the semiconducting Half Heuslers. This work was supported in part by the Office of Naval Research and the National Science Foundation.

4:20pm **EM+MI-ThA8 Application of Magnetic Heusler Alloys to All-Metal Sensors for Ultrahigh-Density Magnetic Recording**, *J.R. Childress*, HGST San Jose Research Center **INVITED**

Magnetic Heusler alloys are attractive materials for a number of applications in spintronics due to their potential high spin-polarization at the Fermi level, advantageous for spin-injection experiments and magnetoresistive devices. In the magnetic recording heads used in today's hard-disk drives (HDD's), the magnetoresistive thin-film sensors are multilayer spin-valves which operate in the current-perpendicular-to-film-plane (CPP) geometry, and rely on the spin-filtering properties of ultrathin MgO tunnel barriers (junction resistance < 1 Ohm-micron²) to achieve large tunnel-magnetoresistance (TMR) values using standard CoFe and CoFeB magnetic alloys as electrodes. Sensors with lower resistance (and thus lower-noise) are continuously required as sensor dimensions are reduced to keep up with the increased areal density of recorded data (approaching 1 Tb/in²). Intrinsically, an all-metal sensor can operate similarly to TMR sensors and will be able to achieve much lower resistances (~ 0.05 Ohm-micron²) and lower noise, but also requires a relatively large giant magnetoresistance (GMR) ratio to achieve sufficiently large signal to noise ratios (SNR). A number of Co-based full-Heusler alloys have the required magnetization, high T_{Curie} and a predicted half-metallic behavior at low temperatures, and are therefore of interest for this application. But while the high spin-polarization in these Heusler alloys can significantly increase the GMR signal, integrating these materials in recording head sensors is a challenge due to their complex crystalline structure which typically requires high-temperature processing, and strong sensitivity to compositional

disorder. In addition, the high polarization and low magnetic damping observed in these materials results in a high sensitivity to spin-torque excitations which limits the maximum allowable bias voltage, and is also a source of noise which limits the signal to noise (SNR) ratio. The geometrical, thermal, and magnetic constraints which influence the integration of Heusler alloys in magnetic recording head sensors will be presented, along with some examples of materials characterization and multilayer stack optimization required to improve the properties and robustness of the devices. It is found that practical spin-valves with Heusler alloy-based magnetic layers can be fabricated with CPP-GMR ratios which can be increased to >10%, more than 2x larger than for conventional ferromagnetic alloys. The outlook for applicability of such sensors to magnetic recording at high densities > 1 Tb/in² will be discussed.

5:00pm **EM+MI-ThA10 Growth of Epitaxial Co₂MnSi/MgO/Co₂MnSi Magnetic Tunnel Junctions by Molecular Beam Epitaxy**, *S. Patel*, *A. Kozhanov*, *B.D. Schultz*, *C. Palmstrom*, University of California, Santa Barbara

Epitaxial magnetic tunnel junctions (MTJs) have the potential to be used as low-energy non-volatile random access memory. The use of half metallic ferromagnets as electrodes has drawn great interest due to the predicted 100% spin polarization at the Fermi level. Co₂MnSi is predicted to be half-metallic[1], with a Curie temperature of 985K [2], and is a strong candidate for use in magnetic random access memory devices. These devices, however, are highly sensitive to interfacial and bulk disorder, which may result in the loss of a minority spin gap [3]. Therefore it is critical to understand the fundamental properties of the Heusler alloy films and correlate these properties with device performance. We have successfully grown highly-ordered, epitaxial Co₂MnSi(001) films by molecular beam epitaxy (MBE) using a "seeded growth" technique to form a crystalline seed layer on various substrates, including MgO (001) and a Sc_{0.3}Er_{0.7}As lattice-matched diffusion barrier layer on GaAs (001). The lattice mismatch between GaAs and Co₂MnSi is only -0.06% and x-ray diffraction of the MBE grown thin films show the two are nearly lattice matched. These films also have relatively smooth surfaces and coercivities down to 4 oersteds for stoichiometric films. Composition is also found to play a large role in the magnetic properties of the films. Off-stoichiometry films display lower saturation magnetization as well as higher coercivities. We have subsequently been able to grow epitaxial MTJ heterostructures of Co₂MnSi/MgO/Co₂MnSi with different switching fields for the top and bottom electrodes. We have characterized the structure of each layer and interfaces with reflection high-energy electron diffraction (RHEED), low-energy electron diffraction (LEED), scanning tunneling microscopy (STM) and cross-sectional transmission electron microscopy (XTEM) and the corresponding magnetic properties using vibrating sample magnetometry (VSM) and a superconducting quantum interference device (SQUID) to better understand the fundamental properties of these epitaxial heterostructures. This work was supported in part by the Semiconductor Research Corporation under award number 2011-IN-2153.

References

- [1] S. Picozzi, A. Continenza, and A. J. Freeman. Phys. Rev. B 69 (9), 094423 (2004)
- [2] P.J. Webster and K.R. Ziebeck. J. Phys. Chem. Solids 32, 1221 (1971)
- [3] B. Hülsen, M. Scheffler, and P. Kratzer. Physical Review B 79 (9), 094407 (2000)

5:20pm **EM+MI-ThA11 Fabrication of Highly Ordered Co₂FeAl Thin Films by Reactive Ion Beam Deposition for Spintronic Devices**, *Y.S. Cui*, University of Virginia, *S. Schäfer*, *T. Mewes*, University of Alabama, *M. Osofsky*, Naval Research Laboratory, *J.W. Lu*, *S.A. Wolf*, University of Virginia

Co₂FeAl (CFA) is a full Heusler alloy that has potentially very low damping parameter and high spin polarization, highly desired for spintronic devices such as magnetic tunnel junctions and spin valves. CFA with B2-type chemical ordering has shown an extremely low Gilbert damping parameter among the Heusler alloys, which facilitates spin dynamics such as spin current driven magnetization switching. A large tunnel magnetoresistance (TMR) has been reported in B2-CFA based magnetic tunnel junctions, which is ascribed to its intrinsic high spin polarization efficiency. The high spin polarization efficiency originates from the half-metal gap in some of its energy bands with certain symmetry. It was predicted by theory that both low damping parameter and high spin polarization can only be achieved with a high chemical ordering existing in the CFA crystal structure. We will present the synthesis of high quality CFA thin films, prepared by a novel deposition technology, Reactive Biased Target Ion Beam Deposition (RBTIBD). The surface roughness (RMS) was observed as low as 0.14 nm. It was determined that CFA thin films grew on MgO(001) epitaxially along both in-plane and out-of-plane directions with a B2-type chemical ordering, according to the results obtained in XRD and TEM. The chemical ordering

can be significantly improved by properly choosing the post annealing parameters. The ferromagnetic resonance (FMR) measurements suggested an extremely small damping parameter (~ 0.002). The damping parameter was strongly correlated with the chemical ordering of B2 structure. In addition, the impact of chemical ordering on the spin polarization efficiency of CFA films based on PCAR measurements will be discussed.

Electronic Materials and Processing Room: 14 - Session EM+TF+AS-ThA

Growth and Characterization of Group III-Nitride Materials

Moderator: N. Dietz, Georgia State University

2:00pm **EM+TF+AS-ThA1 AlN-based Technology for Deep UV and High-power Applications**, Z. Sitar, HexaTech, Inc. & North Carolina State University, B. Moody, S. Craft, R. Schlessler, R. Dalmau, J. Xie, S. Mita, HexaTech, Inc., T. Rice, J. Tweedy, J. LeBeau, L. Hussey, R. Collazo, B. Gaddy, D. Irving, North Carolina State University **INVITED**

For the first time in history of III-nitrides, the availability of low defect density ($<10^3 \text{ cm}^{-2}$) native AlN substrates offers an opportunity for growth of AlGaIn alloys and device layers that exhibit million-fold lower defect densities than the incumbent technologies and enable one to assess and control optical end electrical properties in absence of extended defects. Epitaxial AlN wafers are fabricated from AlN boules grown by physical vapor transport at temperatures between 2200 and 2300°C. Gradual crystal expansion is achieved through a scalable, iterative re-growth process in which the high crystal quality is maintained over many generations of boules. Despite the excellent crystal quality, below bandgap optical absorption bands in the blue/UV range affect the UV transparency of wafers. We use density functional theory (DFT) to develop a model to understand the interplay of point defects responsible for this absorption. We show a direct dependence of the mid-gap absorption band with the carbon concentration within the AlN. Low defect density AlN and AlGaIn epitaxial films are grown upon these wafers that exhibit superior optical properties in terms of emission efficiency and line width and can be doped with an efficiency that is several orders of magnitude higher than possible in technologies using non-native substrates. UV LED structures and Schottky diodes were fabricated on these materials that exhibit low turn-on voltages and breakdown fields greater than 10 MV/cm. This presentation will review state-of-the-art of AlN-based technology and give examples of potential applications in future devices and contrast these with other wide bandgap technologies.

2:40pm **EM+TF+AS-ThA3 Atomic Layer Deposition of AlN Thin Films as Gate Dielectrics for Wide Bandgap Semiconductors**, Y.-C. Perng, J.P. Chang, D. Chien, University of California at Los Angeles

Aluminum nitride (AlN) is a potential dielectric layer for wide bandgap semiconductor based power electronic devices, such as those demanded in radio frequency, high-speed and high-temperature communication, because of its wide bandgap and high dielectric constant. In particular, for 4H-SiC, AlN is also a promising interfacial layer due to their similar atomic arrangement, small lattice mismatch (1.3%) and comparable thermal expansion coefficients. Although various deposition techniques have been investigated to synthesize AlN thin films with atomic controllability over a large substrate remains a challenge. Atomic layer deposition (ALD) was thus used in this work to grow AlN thin films.

AlN deposition was performed in an ultra-high vacuum chamber with base pressure of 10^{-7} Torr using trimethylaluminum (TMA) and ammonia (NH₃) as precursors. It was discovered that ALD of AlN is possible only when the minute amount of moisture in NH₃, which competed with and inhibited the nitride growth, was completely eliminated. The ALD window was found to be 500-570°C with a growth rate of 1.5 Å/cycle. The deposited film composition was evaluated via *in-situ* x-ray photoelectron spectroscopy (XPS) with Al/N determined to be 1.2. *In-situ* reflective high-energy electron diffraction (RHEED) measurements showed as-deposited AlN films were crystalline, which was confirmed by x-ray diffraction (XRD). AlN/4H-SiC MIS capacitors were fabricated to examine the electrical properties with the dielectric constant of AlN determined to be 8.3 and a leakage current density of 10^{-3} A/cm^2 at 4.3 MV/cm. The 150 Å ALD AlN passivated AlGaIn/GaN hetero-structure demonstrated 11% increase in the carrier density and 3% decrease in mobility compared to those of non-passivated hetero-structure as $8.3 \times 10^{12} \text{ cm}^{-2}$ and $1100 \text{ cm}^2/\text{V}\cdot\text{s}$. While with amorphous 150 Å Al₂O₃ surface passivation, the mobility decrease by 22% with carrier density increase by 12%, showing that the crystalline AlN providing a superior property on passivating the hetero-structure.

3:00pm **EM+TF+AS-ThA4 Low-Temperature Behavior of the Surface Photovoltage in p-type GaN**, J.D. McNamara, M. Foussekis, A.A. Baski, M.A. Reshchikov, Virginia Commonwealth University

The effect of low temperature on the surface photovoltage (SPV) in semiconductors is rarely studied and not well understood. We studied the SPV behavior for Mg-doped, p-type GaN using a Kelvin probe at temperatures from 80 to 300 K. Under band-to-band UV illumination at room temperature, the measured SPV signal in p-type GaN becomes negative as electrons are swept to the surface. However, we observed that at low temperatures, the SPV signal becomes positive under UV illumination, contrary to the SPV behavior of p-type GaN at room temperature. This positive SPV resembles the behavior of an n-type semiconductor. We assume that under UV illumination and at low temperatures, the conductivity of Mg-doped GaN does indeed convert from p- to n-type. This conversion was predicted from photoluminescence studies on Zn-doped GaN.^[1] At low temperatures, photo-generated electrons may accumulate in the conduction band which causes an upward shift in the bulk Fermi level towards the conduction band. This results in a positive SPV signal, since the Kelvin probe uses the bulk Fermi level as a reference for the measured SPV signal. Interestingly, the characteristic temperature at which we observe this transition from p- to n-type behavior depends on illumination intensity. As the excitation intensity increases from 10^{15} to $10^{17} \text{ cm}^{-2} \text{ s}^{-1}$, the characteristic temperature increases from 130 to 170 K. This result also agrees with previously reported photoluminescence data and further authenticates the above assumption.^[1]

[1] M. A. Reshchikov, A. Kvasov, T. McMullen, M. F. Bishop, A. Usikov, V. Soukhovuev, and V. A. Dmitriev, Phys. Rev. B **84**, 075212 (2011).

3:40pm **EM+TF+AS-ThA6 Controlling GaN Polarity on GaN Substrates**, J.K. Hite, M.E. Twigg, J.A. Freitas, Jr., M.A. Mastro, J.R. Meyer, I. Vurgaftman, S. O'Connor, N.J. Condon, F.J. Kub, S.R. Bowman, C.R. Eddy, Jr., U.S. Naval Research Laboratory

Gallium nitride is a high quality semiconductor widely used in both optical and electronic devices. The polarity of GaN (+/- c-direction) influences many properties of the resultant material, including chemical reactivity and electric field in these 'piezoelectric' materials. Control over the polarity of GaN grown on sapphire and SiC substrates has been previously demonstrated by controlling the growth conditions, doping levels, and buffer or nucleation layer properties. Further, in the case of heavily doped p-type layers, spontaneous polarity inversion has been demonstrated in GaN homoepitaxial layers, switching the doped layer from Ga-polar to N-polar. However, this approach leads to uncontrolled inversion domain boundaries and often results in dopant clustering within the film, impacting film quality and resultant device performance.

In this work we investigate the fabrication of Mg-free inversion layers (ILs) to control the polarity of MOCVD-grown GaN on GaN substrates. By changing the IL material, we demonstrate conversion of GaN polarity in both directions (N-polar to Ga-polar and Ga-polar to N-polar). By employing a patented selective growth method to deposit the IL, the lateral polarity of the GaN can also be alternated, allowing control of the polarity in both vertical and lateral directions. A one-dimensional grating of periodically oriented (PO) GaN stripes was achieved over square-centimeter (or large) areas. The boundaries between polarities are found to be both sharp and vertical, and the growth conditions have been adjusted to result in equal growth rates of both polarities. Chemical etching of the material verifies the polarity of the material. Transmission electron microscopy (TEM) rules out the presence of alternating polar inclusions in the inverted material while showing a strong inversion domain boundary at the vertical interfaces. Dislocation density and grain size are determined through the use of electron channeling contrast imaging. The MOCVD-grown PO GaN structures have been extended in thickness by further HVPE growth. TEM and photoluminescence imaging confirms that the PO GaN structure is maintained throughout the extended growth (up to 80 μm in thickness). This method of GaN polarity inversion offers the promise of engineering both lateral and vertical polarity heterostructures and the potential of novel engineered polarity-based devices.

4:00pm **EM+TF+AS-ThA7 Direct Green and Yellow Light Emitting Diodes – Polarization Control and Epitaxy**, C. Wetzel, T. Detchprohm, Rensselaer Polytechnic Institute **INVITED**

Solid state lighting by means of GaInN/GaN light emitting diodes (LEDs) is rapidly progressing to a major factor in energy savings technology. By convergence of lighting and lighting control, however, smart lighting is an opportunity to elevate lighting to a holistic experience of human wellbeing beyond the obvious economic benefits. Full epitaxial control of the GaInN/GaN active region is prime to fulfill the promise of an optical bandgap tunable across the entire visible spectrum. As such it will serve both, as tunable absorption layer for multijunction solar cells and emitter for direct emitting LEDs. The later aspect is of particular promise to

outperform the traditional phosphor conversion approach known from historic fluorescence lamps and current white light LEDs.

Rigorous defect reduction approaches have enabled us to continuously improve the emission efficiency in ever longer wavelength emission reaching beyond green, deep green to yellow and orange (590 nm). In contrast to conventional phosphor or AlGaInP-based LED, such emitters show a superior temperature stability of their light output performance. A further leap in defect reduction has been demonstrated by the implementation of heteroepitaxy on nanotextured templates. Unlike widely explored lateral epitaxial overgrowth, growth zones primarily coalesce without the generation of threading dislocations. Implemented at the sapphire substrate level in green LEDs, the texturing substantially boosts both, internal quantum efficiency and light extraction. Furthermore, by control of the crystallographic orientation of growth we achieve a modulation of the piezoelectric polarization within the active region. This for once results in the emission of highly linear polarized light but on the other hand holds the promise to move the actual sweet spot of LED performance from the blue into the green and yellow spectral region. We discuss our approaches in light of our latest achievements.

This work was supported by a DOE/NETL Solid-State Lighting Contract of Directed Research under DE-EE0000627. This work was supported in part by the Engineering Research Centers Program of the National Science Foundation under NSF Cooperative Agreement No. EEC-0812056.

4:40pm EM+TF+AS-ThA9 The Influence of Substrate and Gas Phase Temperatures on the Properties of InN Epilayers, M.K.I. Senevirathna, S.D. Gamage, R. Atalay, R.L. Samaraweera, A.G.U. Perera, Georgia State University, B. Kucukgok, A.G. Melton, I. Ferguson, University of North Carolina at Charlotte, N. Dietz, Georgia State University

The influence of the substrate growth temperature on the structural and optoelectronic properties of group III-nitride layers grown by various growth techniques has been extensively studied and reported on, due to the close relationship of substrate temperature with crystalline quality and the point defect chemistry of the alloy. Most thin film growth systems only control the substrate temperature and have limited control to adjust the gas phase decomposition dynamic independent to influence to growth surface chemistry.

In this contribution, we present results on the growth of InN epilayers grown the high-pressure chemical vapor deposition (HPCVD), studying in influence of and independent from the substrate temperature controlled gas phase temperature above the substrate reactor zone. The HPCVD reactor system has two heater elements: one that controls the substrate temperature and a second radiative heat source above, which allows the control of the gas phase temperature. While the substrate temperature dominantly controls the growth process and the crystalline layer properties, the heater above the substrate surface influences strongly the precursor decomposition processes and the diffusion and concentrations of the precursor fragments in the boundary layer and at the growth surface. InN epilayers grown with different gas phase heating settings were grown and analyzed with the respect to their short- and long-range crystalline ordering and their optoelectronic properties as function of the gas phase temperature. The long-range and the short-range crystalline order of the layers have been analyzed by x-ray diffraction $2\theta-\omega$ scans FWHM and the Raman E_2 (high) FWHM, respectively. The optoelectronic properties have been studied by reflectance spectroscopy and are related to the structural properties and the additional gas phase heating.

The figure depicts the FWHM values of Raman- E_2 (high) peak of the InN epilayers as a function of reactor pressure for higher (red line) and lower (blue line) gas phase temperature. The results indicate that there is an improvement of the short-range crystalline order of the layers with lower gas phase temperature. However, the FWHM values of XRD $2\theta-\omega$ scans, which are not shown here, are indicating that there is an improvement of long-range crystalline order of the layers with increasing gas phase heating.

5:00pm EM+TF+AS-ThA10 Absence of Electron Accumulation at InN(11-20) Cleavage Surfaces, H. Eisele, Technische Universität Berlin, Germany, S. Schaafhausen, Forschungszentrum Jülich, Germany, A. Lenz, Technische Universität Berlin, Germany, A. Sabitova, Forschungszentrum Jülich, Germany, L. Ivanova, M. Dähne, Technische Universität Berlin, Germany, Y.-L. Hong, S. Gwo, National Tsing-Hua University, Taiwan, P. Ebert, Forschungszentrum Jülich, Germany

InN in principle opens up the possibility of using only one ternary III-V semiconductor alloy (InGaN) in optoelectronic devices to cover the whole visible spectral range. Despite this, key material properties of InN are still under debate. The intrinsic energetic position of the Fermi level is unclear, i.e., whether the Fermi level is located within the fundamental band gap or shifted slightly into the conduction band. The latter case induces electron accumulation at the surfaces of the crystal. Such an electron accumulation is

typically observed at InN surfaces upon air contact, raising the question whether it is an intrinsic material property or not?

In order to probe intrinsic bulk properties by STM and not only contamination or surface effects, a clean and stoichiometric surface is necessary. This can be achieved by cleaving InN along non-polar planes. To analyze the origin of the different electronic states in detail, we investigated the clean non-polar (11-20) cleavage surface using cross-sectional scanning tunneling microscopy (XSTM) and spectroscopy (XSTS).

Using combined XSTM and XSTS we were able to locate an InN layer grown on an AlN buffer layer on top of a Si(111) substrate [1]. XSTS spectroscopy on the InN(11-20) cleavage surface yield normalized conductivity spectra, where three contributions to the tunneling current can be observed: (i) the contribution from the conduction band density of states for biases above the conduction band minimum at +0.3 V, (ii) a defect induced current, dominating the spectra between biases of 0 and -0.4 V, and (iii) a valence band related tunneling current rising at a bias of about -0.4 V and dominating the spectrum for biases below. The defect induced current arises from semi-filled defect states being present at the surface steps, and probably also from other (point) defects at the surface. Within the bulk band gap of $E_G = 0.7$ eV no intrinsic surface states could be observed. Furthermore, the Fermi level pinning at about 0.3 eV below the conduction band minimum indicates the absence of an electron accumulation layer.

The results illustrate that electron accumulation at InN surfaces is not a universal property on InN. For clean stoichiometric cleavage surfaces no electron accumulation is observed. Thus, electron accumulation results primarily from the details of the surface structure and is hence not an intrinsic property of the bulk InN material.

[1] Ph. Ebert, S. Schaffhausen, A. Lenz, A. Sabitova, L. Ivanova, M. Dähne, Y.-L. Hong, S. Gwo, and H. Eisele, Appl. Phys. Lett. **98**, in press (2011).

5:20pm EM+TF+AS-ThA11 Dependence of Gallium Incorporation and Structural Properties of Indium-rich In_xGa_{1-x}N Epilayers on Ammonia - MO Precursor Pulse Separation, S.D. Gamage, R. Atalay, M.K.I. Senevirathna, R.L. Samaraweera, Georgia State University, A.G. Melton, I. Ferguson, University of North Carolina at Charlotte, N. Dietz, Georgia State University

The large band gap tunability of ternary In_xGa_{1-x}N alloys has opened new avenues in the field of advanced optoelectronics devices fabrication. However, the growth process of the epilayers of these materials is yet to be well explored. In this contribution, the growth of In_xGa_{1-x}N epilayers under super atmospheric pressure is studied. In order to mitigate the gas phase reactions and the gap of dissociation temperatures between the binary alloys GaN and InN, and to improve the phase stability, high growth chamber pressure has been used together with a pulsed precursor injection system. This pulsed precursor injection scheme introduces two important process parameters; the precursor separation times between the metal organic (MO) sources (TMI and TMG) and ammonia (S₁), and ammonia and MO (S₂).

With the aim to find the optimum S₂ separation for high quality indium-rich InGaN epilayers, a set of In_xGa_{1-x}N samples with nominal x=0.9 has been grown with different S₂ timings. It will be shown that the S₂ separation is critical for the incorporation of gallium into the epilayers. In order to maintain single-phase epilayers, the S₂ separation has to be increased from S₂=400 ms for InN to over 1200 ms for In_xGa_{1-x}N. Raman spectroscopy and X-ray diffraction (XRD) spectroscopy are used to study the structural properties while the Fourier Transform Infra-red (FTIR) and transmission spectroscopy are utilized to investigate the electrical and optical properties of the epilayers.

5:40pm EM+TF+AS-ThA12 MBE-Growth of Coherent-Structure InN/GaN Short-Period Superlattices as Ordered InGaN Ternary Alloys for III-N Solar Cell Application, A. Yoshikawa, K. Kusakabe, N. Hashimoto, T. Okuda, T. Itoi, Chiba University, Japan

We have recently proposed "SMART" III-N tandem solar cells in which all sub-cells could be coherent-structure high-quality pn junctions with low leakage current, resulting in high performance solar cells. SMART means "Superstructure Magic Alloys fabricated at Raised Temperature". The most important feature in the proposed SMART solar cell is a novel idea for realizing ordered and/or quasi InGaN-ternary alloys with InN/GaN Short-Period Superlattices (SPS) enabling coherent-structure band engineering for the (InN)_n/(GaN)_m SPSs with simple integer pairs of (n, m) ≤ 4. In this symposium, detailed epitaxy processes, structural and physical properties of SPSs, and also the idea and features of proposed "SMART" III-N tandem solar cells are reported.

We have ever reported successful growth of fine and coherent-structure 1-ML InN/GaN matrix QWs, and they can be fabricated so under self-limiting and self-ordering growth processes at remarkably higher and/or "raised" temperatures (~650 °C) than the critical one (~500 °C) for growing thick

InN layer under +c growth regime in MBE. We are now underway to extend this understanding and the corresponding epitaxy technology to realize the proposed $(\text{InN})_n/(\text{GaN})_m$ SPSs, and we have started to achieve $(\text{InN})_1/(\text{GaN})_m$ ($m=1-20$) SPSs. When fabricating high structural quality those SPSs, very careful surface stoichiometry control such as $(\text{In}+\text{Ga})/\text{N}$ and In/Ga composition in adlayers, and also periodical complete surface dry-up of In and Ga for each one-cycle growth of SPSs are necessary and quite important.

In brief, 50-100 periods of $(\text{InN})_1/(\text{GaN})_m$ SPSs were grown on MOCVD-grown +c-GaN template at 650 °C by a conventional plasma-assisted MBE. Surface stoichiometry and surface dry up were quite carefully monitored and controlled by in-situ Spectroscopic-Ellipsometry. First, structural properties of 50 periods of $(\text{InN})_1/(\text{GaN})_m$ SPSs were characterized with XRD diffraction patterns taking the m as a parameter. It was found that coherent structure SPSs could be fairly easily fabricated even when the m was decreased down to 4. Generally, much more careful surface stoichiometry control was necessary with decreasing the m , though it was confirmed coherent structure $(\text{InN})_1/(\text{GaN})_4$ SPSs could be grown finally after quite careful control, such as selective re-evaporation between In and Ga consuming a long time. This leads to complete In re-evaporation leaving only some Ga metals on the surface. Of course those Ga metals must be completely dried up with irradiating plasma-excited nitrogen just before the following deposition of 1ML InN on it. It is still difficult at present, however, to grow fine structure InN/GaN SPSs with the m below 3.

Energy Frontiers Focus Topic

Room: 15 - Session EN+AS-ThA

Characterization of Energy Materials and Systems

Moderator: L. Lohstreter, Medtronic, Inc.

2:00pm EN+AS-ThA1 Growth Temperature and Stoichiometry Effects on the Inherent Stability of CdS/CdTe Solar Cells, D.S. Albin, T.A. Gessert, R. Dhere, S.-H. Wei, J. Ma, D. Kuciauskas, A. Kanevce, R. Noufi, National Renewable Energy Laboratory

INVITED

Capacitance-voltage (CV) measurements are commonly used to characterize semiconductor junctions. A common observation when performing such measurements on polycrystalline CdTe solar cells is that the measured capacitance is a strong function of the voltage scan direction. These results in a noticeable hysteresis in the C-V profile when capacitance data is collected using both forward (fwd) and reverse (rev) voltage scan directions. Similarly, hysteresis curves for the usual derived quantities such as net carrier density, N_a , and depletion width, W , naturally follows. We have recently observed that in particular, the hysteresis in calculated carrier acceptor density, $N_{a,hys}$, arbitrarily defined as $N_{a,fwd} - N_{a,rev}$ decreases as the CdTe growth temperature is reduced. At higher CdTe growth temperatures, this value is positive and shifts to negative values at lower growth temperatures. This behavior is believed to reflect a transition of the CdTe stoichiometry in CdS/CdTe solar cells from Cd-poor at higher temperatures to Cd-rich at lower temperatures based upon recently published CdTe binary phase diagrams.

The impact of Cd/Te stoichiometry on cell performance is suspected. Cd-poor stoichiometry favors the formation of Cd-vacancies (V_{Cd}), a beneficial acceptor, but it also simultaneously increases the formation of the Te antisite (Te_{Cd}), an important recombination center in CdTe. Recent theoretical calculations using the hybrid Heyd-Scuseria-Ernzerhof (HSE) functional also suggests that Te interstitials (Te_i) may be an important recombination center under Cd-poor conditions. Increased Cd chemical potential will reduce the formation of these recombination centers, but also reduce hole carrier density. Thus, an optimal growth condition, which could include extrinsic p-type doping, may be needed for leading to higher performance CdTe solar cells.

Not discussed to date however is whether stoichiometry has an inherent impact on the stability of CdTe solar cells. In this talk, we contrast accelerated lifetime study results for CdTe cells grown at different growth temperatures. Open-circuit voltage (V_{oc}) stability in cells grown at lower temperatures was noticeably improved. $N_{a,hys}$ in the latter cells was considerably smaller. Both V_{oc} and FF were well correlated with this capacitance-derived parameter. $N_{a,hys}$ was observed to be relatively unchanged in devices where V_{oc} did not degrade. Finally, time-resolved photoluminescence lifetimes of nearly 10 ns were measured in these cells made at lower temperatures relative to values of around 2 ns measured in higher temperature devices.

3:00pm EN+AS-ThA4 XPS Characterization of Organic Gradients in Organic Photovoltaic and Organic Light Emitting Devices Using Ar GCIB Depth Profiling, S.N. Raman, J.S. Hammond, J.F. Moulder, Physical Electronics

The use of organic materials for electronic applications such as Organic Photovoltaics (OPV's) and Organic Light Emitting Diodes (OLED's) is rapidly growing. The efficiencies of these devices are widely recognized to depend on the molecular gradients fabricated into the devices. Conversely, the degradation of these devices is suspected to depend on several factors including chemical degradation and chemical migration as a function of use. It is therefore very desirable to develop analytical techniques which can quantify chemical gradients as well as identify degradation products in these films.

Gas Cluster Ion Beam (GCIB) sources with low energy per atom $Ar_{2,000}^+$ ions have recently been demonstrated to provide a depth profiling technique for molecular species (1,2). GCIB depth profiling in an interleaved mode with the surface analysis spectroscopy of X-ray Photoelectron Spectroscopy (XPS) has been applied to model OPV and OLED devices. The 2 to 5 nm information depth of XPS, combined with the demonstrated "non-destructive" chemical information revealed after each GCIB sputter interval, facilitates the chemical gradient analysis of a series of model samples up to several 100 nm in depth with molecular depth resolution < 10 nm.

Selected model OPV and OLED samples were exposed to annealing and environmental degradation testing. The XPS depth profiles measured the migration of organic components and dopants as a function of fabrication processes. This presentation will provide an overview of GCIB depth profiling with XPS as well as discuss the insights into efficiencies and degradation processes elucidated by this chemical gradient analysis technique.

1. T. Miyayama, et al. *Surf. Interface. Anal.* 42 (2010) 1453-1457.

2. T. Miyayama, et al. *J. Vac. Sci. Technology A*, 28 (2) (2010) L1-L4.

3:40pm EN+AS-ThA6 Characterization of Degradation Mechanisms of Membrane Electrode Assemblies by XPS and SEM Imaging, A. Patel, K. Artyushkova, P. Atanassov, University of New Mexico, S. Wessel, V. Colbow, M. Dutta, Ballard Power Systems, Canada

Durability of catalyst layer (CL) is of key importance in the deployment of PEMFCs. Catalyst layer (CL) degradation is linked to several failure mechanisms including Pt dissolution and agglomeration and support corrosion. X-ray photoelectron spectroscopy (XPS), a powerful technique to study chemical changes, has been applied to quantitatively analyze catalyst layer degradation in PEM fuel cells. More specifically, ionomer degradation was characterized by a decrease of CF_3 and CF_2 species and an increase in oxidized forms of carbon (e.g. C-O and C=O). Chemical speciation as determined by XPS for catalysts powders was correlated with electrochemical performance losses. MEAs using catalyst coated membranes that are composed of Pt catalyst supported on differing carbon supports were subjected to aging protocols to accelerate the degradation mechanisms of the cathode CL. In-situ and ex-situ diagnostics were used to quantify performance losses and structural changes of the CL.

Large area XPS was used for analysis of fresh, conditioned and aged cathode catalyst layers. Spectroscopic analysis, which provides an integral spectrum from approximately 1mm^2 area, may have a contribution from the GDL sublayer that was not fully removed from the catalyst layer side during separation of the MEA components. The GDL sublayer exhibits a peak in the same BE range as fully fluorinated carbons that are detected in the catalyst layer. Changes that have been detected in CL may not be due to the changes within the ionomer, but rather due to physical intermixing of layers caused by the testing protocols. XPS imaging enabled separation of the differing component contributions. Using Pt 4f imaging, regions are clearly identified where no Pt is present, indicating that GDL pieces adhere to the CL. Fluorine images at two different binding energies (one for the ionomer, and another for the GDL) confirm this. High resolution C 1s spectrum extracted from the area where catalyst is present does not show a high BE component in the C 1s spectrum of the area where GDL is present, confirming that the high BE component detected by large area spectroscopy are contributions from the GDL. High-resolution spectra acquired from the area where only catalysts layer is present shows higher amounts of oxidized forms of carbons. In addition, morphological changes of aged cathode catalyst layers have been evaluated by Digital Image Processing of SEM images for roughness, porosity and texture parameters.

4:00pm **EN+AS-ThA7 Selective Adsorption Behavior of CO₂ and C₂ Hydrocarbon Isomers over N₂ and Methane in a Flexible Metal Organic Frameworks**, *N. Nijem, P. Thissen*, University of Texas at Dallas, *P. Canepa*, Wake Forest University, *H. Wu, J. Li*, Rutgers University, *T. Thonhauser*, Wake Forest University, *Y.J. Chabal*, University of Texas at Dallas

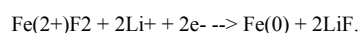
Post combustion carbon capture is a complementary approach to research in renewable energy to combat the exponential increase of CO₂ emission and global warming. An important outcome of enhancing gas separation in materials, for example, is the decrease in energy needed for separation of hydrocarbons. Metal-organic Frameworks (MOFs) have shown promise in this area because their high surface area, porosity and chemical/structural tailorability contribute to the preferential selective adsorption of gases. This work explores the incorporation of CO₂ and hydrocarbons into a flexible framework, Zn₂(bpdC)₂(bpee), (bpdC= 4,4'-biphenyl dicarboxylate, bpee=1,2-bis(4-pyridyl)ethylene) using infrared (IR), Raman spectroscopy and van der Waals density Functional (vdW-DF) calculations. We present evidence for "gate opening" phenomenon, where the structure of the framework changes only upon adsorption of CO₂ and C₂ hydrocarbon isomers but not for N₂ or methane. Understanding the specifics of CO₂ interaction with the framework was explored to identify parameters affecting its selectivity. We find that the high quadrupole moment of CO₂ and its interaction through its carbon with the bpdC linker induces the transformations. The flexibility of the framework was found to be primarily due to the specific connectivity of the Zn metal center to the ligands, at one end in a monodentate mode and at the other in a bidentate mode. The unexpected gate opening behavior in this same framework upon the adsorption of C₂ hydrocarbon isomers was also studied. We find that the specific hydrogen bonding between the CH of the hydrocarbon and the C=O bond of the bpdC linker is responsible for this interesting behavior. Furthermore, the strength of the hydrogen bond was found to affect the gate opening pressure point. This effect points towards the potential of this framework for uses such as pressure swing adsorption based separation. In conclusion, we have identified specific interactions of CO₂ and hydrocarbons in a flexible framework that lead to their selective adsorption properties. This knowledge allows the design of frameworks with optimized properties.

4:20pm **EN+AS-ThA8 Fabrication and Characterization of a PCBM-Terminated Organic Monolayer on a Si(111) Surface**, *T.J. Miller, A.V. Teplyakov*, University of Delaware

The energy sector is a large, growing field in research and technology. A growing subset of the solar field is organic photovoltaics (OPV). Two areas that have long challenged researchers are efficiency and stability of the OPV devices. An area that is in need of fundamental understanding that may increase efficiency of these devices is the charge transfer. However, a precise nature of the bulk-heterojunction OPV donor/acceptor interface is difficult to pinpoint. Thus, model systems can be used initially to mimic these interactions. In the system presented here, the donor/acceptor interface is well-defined. Phenyl-C61-butiric acid methyl ester (PCBM) was reacted with an amino-terminated organic monolayer on a single crystalline Si(111) surface. Poly 3-hexylthiophene (P3HT) was then deposited onto this complex substrate, and the produced interface can be observed and investigated. Fourier transform infrared spectroscopy was used to identify the functional groups on the surface. The chemical and electronic states of the coating and the substrate were investigated by X-ray photoelectron spectroscopy, and the morphology was determined through atomic force microscopy. Preliminary charge carrier lifetime measurements will also be reported.

4:40pm **EN+AS-ThA9 Conversion Reaction of Thin Film Metal Fluorides and Metal Oxides Exposed to Atomic Lithium**, *R. Thorpe, S. Rangan, R.A. Bartynski*, Rutgers University

Modern Li-ion intercalation batteries use electrode materials that accommodate Li intercalation, enabling the exchange of Li ions during battery cycling without extensive alteration of the electrode's crystalline structure. Despite the stability of these materials to the intercalation process, the ability of such batteries to store energy is limited by the number of host sites in the electrodes to approximately one electron per formula unit. Conversion reaction materials could potentially store several times more energy than current generation batteries by utilizing the full range of charge states available to their constituent metal ions. For example, the following reaction occurs in a FeF₂ cathode:



Although conversion reaction materials have shown the promise of high energy storage density in electrochemical cells, their cycling stability is poor, and relatively little is known about the phase evolution and structural changes that occur during charge and discharge.

In order to study the fundamental properties of these materials, we have grown high purity thin films of conversion materials FeF₂, FeF₃, FeOF, FeOx, and CoO. By exposing these films to atomic Li in vacuum, can follow the evolution of these materials as they approach the reaction products reached in the discharge of a conversion battery. We have used UV and inverse photoemission to measure the electronic structure of the valence and conduction bands respectively. Using these techniques in tandem, we are able to measure the band gap of these materials, which can then be related to their electronic conductivity. Using x-ray photoemission, we have measured the stoichiometry and valence states of the compounds involved in these reactions. In addition, we have examined the structure of these nano-scale materials using TEM and LEED.

For FeF₂, our XPS results show immediate reaction upon exposure to Li, fully reducing the Fe to the metallic state and forming LiF, with no evidence of intermediary phases in the film due to the high mobility of lithium. TEM of the initial and final films indicates a drastic morphology alteration, leading to a local precipitation of Fe⁰ and LiF formation, with an overall particle size reduction from 10nm to 2nm, consistent with what is found in electrochemical studies.

However, the Li-CoO and Li-FeOx reactions appear to diverge from the results of Li⁺ electrochemical reactions, leading to the simultaneous formation of both Li₂O and Li₂O₂, the latter of which hinders further reduction of the Fe and Co. These observations will be contrasted with results obtained from the related conversion reaction compounds FeOx_y and FeF₃.

Energy Frontiers Focus Topic Room: 7 - Session EN+NS-ThA

Thermophotovoltaics, Thermoelectrics and Plasmonics
Moderator: R.A. Quinlan, Naval Surface Warfare Center, Cardercock Division

2:00pm **EN+NS-ThA1 Structuring of the Radiative Thermal Emission in Tungsten Inverse Opals for Thermophotovoltaic Applications**, *M.D. Losego*, North Carolina State University, *K.A. Arpin*, University of Illinois at Urbana Champaign, *B. Kalanyan*, North Carolina State University, *P.V. Braun*, University of Illinois at Urbana Champaign, *G.N. Parsons*, North Carolina State University

Materials with photonic bandgaps are generated by periodic mesostructuring at length-scales comparable to visible wavelengths. While photonic bandgaps are often used to control the interaction of incident light with a material (e.g. reflect incident light over a narrow bandwidth), these structures can also be used to tune the thermal emission of light. Consequently, a heated metallic photonic crystal could be used in a thermophotovoltaic (TPV) device scheme. Such a TPV would (1) absorb broadband incident solar radiation, (2) heat up, and (3) re-emits the radiation over a narrow band of energies. This narrow-band radiation could then be converted to electricity with high efficiencies using a simple single-junction solar cell. However, demonstrating narrow-band thermal emission from a multidimensional architecture remains elusive. The central challenge is finding a materials set that demonstrates the required combination of thermal stability and dielectric function in a nanostructured architecture capable of high-temperature radiant emission.

This talk will examine our development of refractory tungsten inverse-opal structures designed for thermal emission in the visible spectrum. The first generation of these structures were constructed from silica opals infiltrated with electrodeposited tungsten. While ultrathin (<20 nm) oxide ALD layers were found to improve high temperature stability (>1000°C, 12 hours) by restricting surface diffusion and limiting sintering, difficulties with massive structural cracking during the molten-salt electrodeposition process could not be overcome. Second generation devices are now being developed using a lower temperature tungsten atomic layer deposition (ALD) process. Besides the avoidance of massive structural cracking, these ALD materials appear to be denser than electrodeposited materials, further reducing the unwanted sintering effects at high temperatures. Room temperature spectra collected from these structures indicate photonic effects not seen in planar tungsten films and suggest enhanced thermal emission at visible wavelengths.

2:40pm **EN+NS-ThA3 Nanowires and Nanowire Heterostructures for Thermoelectric Energy Harvesting**, *Y. Wu*, Purdue University **INVITED**
Substantial efforts have been devoted to use nanostructured materials for thermoelectric energy harvesting and solid-state cooling in the past decade. However, the majority of the research is still limited in lab scale due to the incapability to mass-produce well-defined nanostructured materials with

low yet industrial-compatible process. In addition, a lot of widely used thermoelectric materials contain toxic and expensive elements that prevent the large-scale deployment of the thermoelectric devices. In this presentation, we will discuss our research on the development of mass production of molecular scale nanostructures of chalcogenides and metal oxides, as well as their heterostructures, for the manufacture of thermoelectric generators operating at different temperature ranges. Particularly, we will talk about our approach to discover and investigate the non-toxic and abundant nanostructured materials to achieve an environmentally friendly process. Our preliminary research indicated that thermoelectric figure of merit (ZT) close to 2 can be achieved in the molecular scale nanowires of certain chalcogenide due to significantly enhanced power factor and reduced thermal conductivity as a result of quantum confinement.

3:40pm EN+NS-ThA6 Plasmonic Polymer Solar Cells with Spectrally Tuned Au/SiO₂ Core/Shell Nanorods incorporated in Active Layers, V. Jankovic, J.P. Chang, UCLA

Octadecyl tri-methoxysilane (OTMS) functionalized Au/SiO₂core/shell nanorods were incorporated into the active layers of two different polymer bulk heterojunction (BHJ) systems: a broad band gap polymer (poly(3-hexylthiophene)(P3HT):[6,6]-phenyl-C61-butyrac acid methyl ester (PCB60M)) and a low band gap polymer poly{2,6-4,8-di(5-ethylhexylthiophenyl)benzo[1,2-b;3,4-b']dithiophene-alt-5-dibutyl-3,6-bis(5-bromothiophen-2-yl) pyrrolo[3,4-c]pyrrole-1,4-dione} (PBDTT-DPP):PC60BM. The extinction peaks of the Au nanorod scattering centers was tuned to match the band edge of the two polymers by controlling their aspect ratio. For the P3HT:PC60BM system with a band edge around 700 nm, the addition of the core/shell nanorods of an aspect ratio 1:2.5 (resonant frequency peak is at around $\lambda=650\text{nm}$), resulted in 8% improvement in short circuit current (J_{sc}); for the low band gap polymer system PBDTT-DPP:PC60BM with band edge around 850 nm, we tuned the resonant frequency to near-infrared region by increasing the aspect ratio to 1:4 (resonant frequency peak is at around $\lambda=800\text{nm}$), the addition of the core/shell nanorods resulted in 18% improvement in short circuit current (J_{sc}). The J_{sc} enhancement was consistent with external quantum efficiency (EQE) measurements and the EQE improvement factor matched the absorption resonance spectrum of Au/SiO₂ nanorods in both systems. This work will instruct us on how to utilize and manipulate plasmon resonance of metallic nanoparticles to improve device efficiency in different polymer solar cell systems.

4:00pm EN+NS-ThA7 Optics and Photonics Research Priorities and Grand Challenges as Relating to Today's Energy Frontiers, E.B. Svedberg, The National Academies

A new report from the National Research Council of the National Academies identifies research priorities and grand challenges to fill gaps in optics and photonics, a field that has the potential to advance not only the energy field but also the economy of the United States and the world, the report provides visionary directions for future technology applications, and ensure progress in energy related research. As one of its recommendations the report recommends that the federal government develop a "National Photonics Initiative" to bring together academia, industry, and government to steer federal research and development funding and activities.

Eight particular areas of technological application are discussed in separate chapters: communications, information processing, and data storage; defense and national security; energy; health and medicine; advanced manufacturing; advanced photonic measurements and applications; strategic materials for optics; and displays. Each chapter reviews updates that have occurred since the 1998 National Research Council report *Harnessing Light: Optical Science and Engineering for the 21st Century*, as well as the technological opportunities that have risen from recent advances in optical science and engineering. This presentation will focus on the energy section of the report that deals not only with energy generation but also how to reduce excessive usage of energy. The report additionally recommends actions for the development and maintenance of the photonics-driven sector of the energy industry, including both near-term and long-range goals, likely participants, and responsible agents of change.

The recommended National Photonics Initiative will help manage the breadth of rapidly expanding applications of photonics technologies, allowing both governments and industry to develop coherent strategies for technology development and deployment in the energy sector. The initiative should also spearhead a collaborative effort to improve the collection and reporting of research, development, and economic data on this sector.

**Electron Transport at the Nanoscale Focus Topic
Room: 16 - Session ET+SS+GR+SP-ThA**

Electron Transport at the Nanoscale: Molecules and Defects

Moderator: S. Allen, The University of Nottingham, UK, J. Wendelken, Oak Ridge National Laboratory

2:00pm ET+SS+GR+SP-ThA1 Molecule Substrate Interactions Probed by Scanning Tunneling Microscopy, H.-J. Gao, Chinese Academy of Sciences INVITED

Molecule substrate interactions play an important role in constructing nanostructures of functionalities and controlling of the physical properties and thus have stimulated a great interest in the past decades. One of the challenges in this top is to make a single molecule or small quantum systems stably connected to a single metal atom on metal surfaces, and further to make the nanostructure create electric energy and optical/electro radiation. In the talk, I will present that by using Au adatoms of the Au(111) surface we have successfully formed a single molecule rotor array, isolated tetra-*tert*-butyl Zinc Phthalocyanine ((*t*-Bu)₄-ZnPc) molecules sticking to the Au adatoms of the Au(111) and rotating on the surface at 78 K. This kind of single molecular rotor was also found to be controlled by the different sites of the Au(111) surface using low temperature scanning tunneling microscopy (STM). Furthermore, by changing the molecular structure the same molecular family of the P_c, ZnP_c and FeP_c can also modulate the rotation behavior of the molecular rotors. Given that the lateral structure of a molecule/substrate interface can be modified by the attachment of ligands, our results will be helpful for opening up the possibility to tailor physical properties of a single molecule or complex aggregates to the desired specifications.

2:40pm ET+SS+GR+SP-ThA3 Electron Localization in Single Mixed-Valence Molecules, R.C. Quardokus, N.A. Wasio, Y. Lu, S.A. Kandel, University of Notre Dame

Scanning tunneling microscopy (STM) is used to study two dinuclear organometallic molecules, meta-Fe₂ and para-Fe₂. These molecules share identical molecular formulas but differ in their positions of connectivity to the central phenyl ring. STM images of neutral meta-Fe₂ and para-Fe₂ show symmetrical distribution of electron density across the two metal centers. Chemical oxidation of these molecules leads to mixed-valence species. STM images of mixed-valence meta-Fe₂ show an asymmetric distribution of the electron density between the two metal centers. Despite the greater distance between the two metal centers, the electron density remains symmetric in mixed-valence para-Fe₂. Comparison with constrained density functional (CDFT) calculations leads to the conclusion that through-bond coupling of the two metal centers is more prevalent than through-space coupling. Further investigation of mixed-valence dinuclear organometallic molecules with asymmetric electron state density may open up the possibility for their use in molecularly based electronic devices.

3:00pm ET+SS+GR+SP-ThA4 Rectification by a Single Molecular Diode, L. Adamska, University of South Florida, M. Kozhushner, Institute of Chemical Physics, Russian Academy of Sciences, I.I. Oleynik, University of South Florida

Single-molecule rectification has been recently observed using the STM modulated break-junction technique in non-symmetric diblock dipyrimidinyl-diphenyl molecule covalently bound to metallic electrodes. To provide an insight to the nature of the rectification, first-principles calculations of atomic, electronic and transport properties of gold/molecule/gold junctions have been performed for both symmetrical tetraphenyl and asymmetrical dipyrimidinyl-diphenyl diblock molecules. The charge transport was found to occur by hole resonant tunneling mechanism via positively-charged hole states of the molecule, which are very susceptible to the external electric field and dispersive interactions with the metallic electrodes. It was found that the rectification effect in chemically-asymmetric dipyrimidinyl-diphenyl molecule is due to strong localization of the hole wave function at one end of the diblock under applied electric field. Such behavior is contrasted by symmetric I-V curves exhibited by symmetric tetraphenyl molecule.

3:40pm ET+SS+GR+SP-ThA6 Electron Transport Study of Graphene Grain Boundaries Using Scanning Tunneling Potentiometry, K. Clark, X.-G. Zhang, I. Vlasiouk, A.-P. Li, Oak Ridge National Laboratory

Graphene, due to its unique electronic structures, has quickly become one of the most notable "super-materials" poised to transform the electronics and nanotechnology landscape. The symmetry of the graphene honeycomb lattice is a key element for determining many of graphene's unique

electronic properties, such as the linear energy-momentum dispersion and the reduced backscattering (i.e., high carrier mobility). However, topological lattice defects, such as grain boundaries and step edges, break the sublattice symmetry and can affect the electronic properties, especially in transport of graphene in unexpected ways. To utilize the full potential of graphene a complete understanding of the physical and electronic properties of defects in this system is needed. By using a scanning tunneling potentiometry method with a low temperature four-probe scanning tunneling microscope, two-dimensional maps of electrochemical potentials have been measured across individual grain boundaries on the graphene films grown on copper foil and transferred to SiO₂. An Atomic Force Microscope (AFM) is implemented to image the grain boundary that forms between individual graphene flakes that grow on the surface. The AFM imaging along with scanning tunneling potentiometry characterize the grain boundaries formed between coalesced grains on the SiO₂ surface. Results of the influence of the grain boundary on the electronic transport across this potentially revolutionary new electronic system will be presented. This research was conducted at the Center for Nanophase Materials Sciences, which is sponsored at Oak Ridge National Laboratory by the Office of Basic Energy Sciences, U.S. Department of Energy.

4:00pm **ET+SS+GR+SP-ThA7 Static and Dynamic Conductance in Topological Defects in Ferroelectrics, S.V. Kalinin**, Oak Ridge National Laboratory **INVITED**

Topological defects in ferroic materials are attracting much attention both as a playground of unique transport, magnetic, and ferroic phenomena and due potential applications in reconfigurable electronic devices. In this presentation, I will summarize recent studies of transport phenomena in 2D (domain walls) and 1D (vortexes and antivortexes) in ferroelectric materials by combination of piezoresponse force microscopy, phase-field modelling, and density functional theory. In particular, the observations such as memory effects and hysteresis in domain wall conductance, metallic conductivity of ferroelectric walls, and conductivity in vortex cores will be discussed. For domain walls, these observations are consistent with carrier accumulation due to presence of charged wall segments. We further demonstrate that a continuum of non-volatile metallic states across decades of conductance can be encoded in the size of ferroelectric nanodomains using electric field. For vortexes, modelling predicts that the core structure can undergo a reversible transformation into a metastable twist structure, extending charged domain walls segments through the film thickness. The vortex core is therefore a dynamic conductor controlled by the coupled response of polarization and electron/mobile vacancy subsystems with external bias. This controlled creation of conductive 1D channels opens a pathway for design and implementation of integrated oxide electronic devices based on domain patterning. Finally, recent insight on domain walls structure from combination of aberration corrected scanning transmission electron microscopy and phase-field theory will be discussed. Research supported (SVK) by the U.S. Department of Energy, Basic Energy Sciences, Materials Sciences and Engineering Division and partially performed at the Center for Nanophase Materials Sciences, a DOE-BES user facility.

4:40pm **ET+SS+GR+SP-ThA9 Transport and Mechanical Properties of Molecular Junctions formed by Acetophenone Deposited on Si (100) Surface, M. Setvin, Z. Majzik, O. Krejci, P. Hapala, P. Jelinek**, Institute of Physics of ASCR, Czech Republic

One of the main challenges of Molecular electronics is to understand and control charge transfer through a reproducible single molecule contact between electrodes. Most investigations of electron transport through molecules have been performed in “blind” junction experiments, where the molecular conformation and contact geometry cannot be probed. Therefore large gaps in our knowledge remains since in molecular electronics the atomic-scale structure of the entire junction including the leads is important for its conductance properties.

Our goal is to study electrical transport through well-defined molecular junction on semiconductor surfaces. Formation of molecular junctions using organic molecules on semiconductor surfaces might lead to interesting phenomena. For example, the presence of the band gap in electrodes can lead to the negative differential resistance observed in transport through molecules bonded to dangling-bond sites[1].

In this contribution, we investigate formation of molecular junction consisting of a single acetophenone molecule deposited on Si(100) surface in upright position by means of simultaneous AFM/STM measurements and DFT calculations. We used a modified UHV VT STM/AFM Omicron machine allowing simultaneous acquisition of the current and forces with atomic resolution using a tuning fork sensor[2]. The simultaneous acquisition of the tunneling current and force during tip approach allows precise control of contact formation and its consequence on the charge transport through molecular junction[3]. On other hand, DFT simulations provide more insight into interaction mechanism between probe and

molecule. It also helps to understand induced structural and electronic relaxations during tip approach.

References

- [1] T. Rakshit et al. Nanoletters 4, 1803–1807 (2004).
- [2] Z. Majzik et al, Beilstein J. Of Nanotech. 3, 249 (2012).
- [3] N. Fournier et al Phys. Rev. B 84, 035435 (2011).

5:00pm **ET+SS+GR+SP-ThA10 Experimental Determination of the Charge Neutrality Level (CNL) of Conjugated Polymers, W. Wang, R. Schlaf**, University of South Florida

The charge neutrality levels (CNL) of poly-(3-hexylthiophene) (P3HT) and poly-[2-methoxy-5-(2'-ethylhexyloxy)-p-phenylene vinylene] (MEH-PPV) were determined. This was achieved by investigating a number of interfaces between these conjugated polymers and metals with varying work function. The interfaces were fabricated using the electrospray deposition technique, which allows the direct deposition of polymers from solution into vacuum environment without interference of significant surface contamination. This enabled the measurement of the charge injection barriers at clean polymer interfaces without contamination interlayer with photoemission spectroscopy. The results of these measurements enabled the establishment of the correlation between barrier heights and substrate. The results indicate that conjugated polymer interfaces form in a similar fashion as small molecular materials interfaces to metals as described by the ‘induced density of states’ (IDIS) model. In contrast, the presented results also suggest that the ‘integer charge transfer’ (ICT) model, which was developed for polymer/metal interfaces, only describes interfaces prepared under atmosphere or inert environment, where the presence of contamination weakens the interaction between the materials in contact.

5:20pm **ET+SS+GR+SP-ThA11 Investigation on the Electronic Structure of Arylthio (ArS)-functionalized CdSe Nanoparticle Hybrid Materials, Z. Li, University of South Florida, K. Mazzi, University of Washington, S. Gutmann, University of South Florida, C.K. Luscombe, University of Washington, R. Schlaf, University of South Florida**

CdSe nanoparticles are a promising material for 3D heterojunction solar cells due to their tunable electronic and optical properties through size control. By covalently bonding these nanoparticles to organic ligands, a novel light absorption, charge separation and transportation system can be formed. This presentation will discuss efforts to measure the hybrid-internal orbital line-up at the nanoparticle/ligand junction. Photoemission spectroscopy was used to characterize a prototypical arylthio (ArS)-functionalized CdSe molecule nanoparticle/ligand hybrid. Generally, in such hybrid molecules, the highest occupied molecular orbital (HOMO) emission is a superposition of the emissions of the nanoparticles and that of the organic ligands. This superposition makes the direct study of the orbital line-up through PES measurements impossible. Hence, a new technique needed to be developed to delineate the orbital line-up at such inner-molecular contacts. This was achieved through the additional investigation of the isolated components, which yielded detailed information of their electronic structure. Combination of this data with measurements on the assembled hybrid molecules enabled the determination of the orbital line-up at the interface. The influence of the covalent bond on the orbital line-up was investigated by comparing the hybrid line-up with the electronic structure of a physisorbed interface formed between the hybrid components. This interface was prepared through in-vacuum electrospray deposition of a thin film sandwich of CdSe and ArSH films, while measuring the transition from the CdSe to the ArSH electronic structure.

**Graphene and Related Materials Focus Topic
Room: 13 - Session GR+EM+NS+SS+TF-ThA**

Beyond Graphene: BN and Other 2D Electronic Materials; 2D Heterostructures

Moderator: I.I. Oleynik, University of South Florida

2:00pm **GR+EM+NS+SS+TF-ThA1 X-ray Photoelectron Spectroscopy Investigation of the Valence and Conduction Band Offset at Hexagonal a-BN:H/Si Interfaces, S. King, M. French, J. Bielefeld, Intel Corporation, M. Jaehnig, Intel Corporation, M. Kuhn, B. French, Intel Corporation**

Due to a wide band gap (~ 6 eV) and close lattice matching, hexagonal boron nitride (h-BN) is of interest as a potential gate dielectric in graphene channel transistor devices. A key property for the success of h-BN as a gate dielectric in such devices is the valence and conduction band offsets at the

h-BN/graphene and h-BN/gate electrode interfaces. In many graphene channel devices, amorphous or poly-Si is a desirable gate electrode material for compatibility in standard CMOS processing. In this regard, we have utilized x-ray photoelectron spectroscopy (XPS) to determine the valence band offset present at the interface between plasma enhanced chemically vapor deposited hexagonal a-BN:H and a (100) Si substrate. Combined with Reflection Electron Energy Loss Spectroscopy measurements of the a-BN:H band gap, we have also been able to determine the conduction band offset at this interface. The combined measurements indicate a type I alignment with valence and conduction band offsets of 1.95 ± 0.1 and 2.15 ± 0.17 eV respectively.

2:20pm GR+EM+NS+SS+TF-ThA2 Monolayer Graphene-Boron Nitride 2D Heterostructures, R. Cortes, J. Lahiri, E. Sutter, P.W. Sutter, Brookhaven National Laboratory

Unusual electronic properties have been predicted for monolayer graphene-boron nitride heterostructures, but access to these properties depends on methods for controlling the formation of graphene-boron nitride interfaces [1]. Here we report on the growth and interface formation of monolayer graphene (MLG)-hexagonal boron nitride (h-BN) 2D heterostructures on Ru(0001), investigated by a combination of real-time low-energy electron microscopy (LEEM) and scanning tunneling microscopy (STM).

LEEM observations of sequential chemical vapor deposition growth show that h-BN attaches preferentially to the edges of existing MLG domains, while nucleation of h-BN on the Ru surface away from MLG is not observed at the conditions considered here. With increasing coverage, h-BN expands anisotropically and, ultimately, the substrate is covered by a continuous 2D membrane of MLG domains embedded in h-BN. The study of the 1D interface between MLG and h-BN in these membranes by STM demonstrates that, following sequential growth at high temperatures, the interface is not abrupt, but contains an intermixed zone consisting of h-BN with embedded carbon atoms. Using quantitative LEEM, we have identified processes that eliminate this intermixing and pave the way to atomically sharp graphene-boron nitride boundaries, as confirmed by STM. The application of a similar growth procedure to terminate the edges of atomically controlled graphene nanoribbons with h-BN, embedding them in a h-BN membrane, will be considered.

[1] P. Sutter, R. Cortes, J. Lahiri, and E. Sutter. *Submitted* (2012).

2:40pm GR+EM+NS+SS+TF-ThA3 Large Area Vapor Phase Growth and Characterization of MoS₂ Atomic Layers, J. Lou, S. Najmaei, Z. Liu, Y. Zhan, P. Ajayan, Rice University INVITED

Monolayer Molybdenum disulfide (MoS₂), a two-dimensional crystal with a direct bandgap, is a promising candidate for 2D nanoelectronic devices complementing graphene. Unlike conductive graphene and insulating h-BN, atomic layered MoS₂ is a semiconductor material with a direct bandgap, offering possibilities of fabricating high performance devices with low power consumption in a more straight-forward manner.

In this talk, we will discuss our recent efforts on the large area growth of MoS₂ atomic layers by a scalable chemical vapor deposition (CVD) method. The as-prepared samples can either be readily utilized for further device fabrication or be easily released from the growth substrate and transferred to arbitrary substrates. High resolution transmission electron microscopy and Raman spectroscopy on the as grown films of MoS₂ indicate that the number of layers range from single layer to a few layers. Our results on the direct growth of MoS₂ layers on dielectric leading to facile device fabrication possibilities show the expanding set of useful 2D atomic layers, on the heels of graphene, which can be controllably synthesized and manipulated for many applications.

3:40pm GR+EM+NS+SS+TF-ThA6 Formation of Silicene and 2D Si Sheets on Ag(111): Growth Mode, Structural and Electronic Properties, P. Vogt, Technical University of Berlin, Germany, T. Bruhn, A. Resta, B. Ealet, CNRS CiNaM, Marseille, France, P. De Padova, CNR-ISM, Rome, Italy, G. Le Lay, CNRS CiNaM, Marseille, France

Since the discovery of graphene enormous efforts have been invested to discover other similar 2-dimensional materials, like e.g. silicene. These 2D materials share similar structural, electronic and optical properties as graphene but are expected to differ in terms of their respective chemical reactivity and thus their applicability for electronic devices. In particular silicene could more easily be integrated into current Si-based electronics

than graphene. Silicene has been predicted theoretically [1,2] but does not seem to exist in nature.

Recently, we could synthesize silicone layers grown epitaxially by depositing Si on Ag(111) surfaces. The electronic properties of these silicone layers were shown to behave as theoretically predicted [3] and the structural and electronic properties are very similar to graphene. In STM images the hexagonal 2D silicone sheet gives rise to triangular structures situated in a honeycomb arrangement with (4x4) symmetry with respect to the Ag(111) surface. A structural model derived from the STM measurements showed a very good agreement with DFT results and exhibited a downward conical electronic dispersion resembling that of relativistic Dirac fermions at the Si K-points [3]. Depending on the growth conditions the formation of different 2D silicon arrangements can be observed: 1) Si-clusters at low deposition temperatures, 2) the formation of less ordered 2D hexagonal Si-based structures at temperatures up to 180°C, 3) the formation of the (4x4) silicene sheet around 220°C and 4) a 2D Si structure with a ($\sqrt{13}\times\sqrt{13}$)-like periodicity at higher growth temperatures exhibiting a very regular, wide range ordered Moiré-like surface pattern in STM.

Here, we will discuss the formation and epitaxial growth mode of these different 2D Si structures and the dependence on the growth parameters. We will also investigate whether these different 2D Si layers all refer to similar silicene sheets which give rise to different appearances in STM due to a varying rotation with respect to each other.

Keywords: silicene, 2D materials, graphene, Dirac fermions

References:

- [1] S. Cahangirov et al., *Phys. Rev. Lett.* **102**, 236804 (2009)
- [2] G. G. Guzman-Verri and L. C. Lew Yan Voon, *Phys. Rev. B* **76**, 75131 (2007)
- [3] P. Vogt et al., *Phys. Rev. Lett.* **108**, 155501 (2012)

4:00pm GR+EM+NS+SS+TF-ThA7 Yttria-monolayer on Pt(111) Supported Graphene: A Novel Two Dimensional Heterostructure and its Affect on Charge Doping of Graphene, R. Addou, A. Dahal, M. Batzill, University of South Florida

Yttrium oxide (Y₂O₃) is a high-k dielectric material, with promising wetting behavior of graphene [1]. In our study we grew yttria by reactive MBE on Pt(111) supported graphene to investigate the structural and electronic properties of the graphene/yttria interface. Photoemission measurements indicate that the graphene layer is covered by yttria. Scanning tunneling microscopy (STM) and low energy electron diffraction reveal that at annealing temperatures higher than 600 °C yttria forms an ordered monolayer on top of graphene. In STM, a moiré pattern is observed that is a consequence of super-positioning of a hexagonal yttria monolayer lattice with that of graphene. X-ray photoemission indicates a shift of the C1s peak by 1 eV to higher binding energy upon depositing of the yttria film. This peak shift is explained by charge doping of graphene by the underlying Pt substrate due to the change in the work function of the yttria coated graphene.

[1] Z. Wang et al. *Nano Lett.* **2010**, *10*, 2024–2030; L. Ding et al. *Nano Lett.* **2009**, *9*, 4209–4214.

4:20pm GR+EM+NS+SS+TF-ThA8 Probing the BCN-triangle by Computations—Outside the Carbon Corner, Jakobson, Rice University INVITED

We will discuss recent work on modeling 2D-materials “beyond graphene” [1-2]: two dimensional hexagonal h-BN, pure B polymorphs, MoS₂, etc. Lessons from graphene studies remain invaluable as they offer general approach and views on the edges [3] and interface structures and energies, and especially organization of the grain boundaries [4,5]. New dislocation cores in BN (both 5/7 and 4/8 types) lead to accordingly new physical properties of emerging polar GB [6]. Similarly, we identify the dislocation cores and the grain boundary structure for more complex polar layer-material, MoS₂ (X. Zou, unpublished). Our analysis of edge and cleavage energies helps to explain fracture patterns emerging in the course of synthesis. In principle, computations suggest possibility of metastable 2D-layers of GaN or ZnO or even their hybrids. Finally, it is important to mention clear opportunities of designing 2D-circuits by combining 2D-materials in specific functional patterns like proposed nanoroads and quantum dots [7-8] which now become a subject of experimental laboratory work.

- [1] Y. Liu et al. *Nano Lett.* **11**, 3113 (2011). [2] E. Penev, et al, *Nano Lett.* **12**, 2441 (2012). [3] Y. Liu et al. *Phys. Rev. Lett.* **105**, 235502 (2010). [4] BIY and F. Ding, *ACS Nano* **5**, 1569 (2011). [5] Ajayan and BIY, *Nature Mater.* **10**, 415 (2011). [6] Y. Liu et al. *ACS Nano* (2012). [7] A. Singh and

5:00pm **GR+EM+NS+SS+TF-ThA10 Single-layer MoS₂ Devices and Circuits, A. Kis, EPFL, Switzerland** **INVITED**

Single layer MoS₂ is a recent addition to the family of 2D materials and is reminiscent of graphene except that it is an intrinsic direct band gap semiconductor with a 1.8 eV gap. We have exfoliated single layers 6.5 Angstrom thick from bulk crystals of semiconducting MoS₂, using the micromechanical cleavage technique commonly used for the production of graphene. Our nanolayers are mechanically and chemically stable under ambient conditions. We have fabricated transistors based on single-layer MoS₂ which demonstrate that this material has several advantages over silicon for potential applications in electronics. Our transistors have room-temperature current on/off ratios higher than 10⁸, mobility higher than 780 cm²/Vs and leakage currents in the fA range. Integrated circuits based on MoS₂ have the capability to amplify signals and perform logic operations. Finally, I will show our work on suspended MoS₂ membranes that show ripples similar to those observed in graphene. MoS₂ also has superior mechanical properties: higher stiffness than steel and 30 times its breaking strength which makes it suitable for integration in flexible electronics.

References

1. B. Radisavljevic, A. Radenovic, J. Brivio, V. Giacometti, and A. Kis. Single-layer MoS₂ transistors. Nature Nanotechnology 6, 147, 2011. doi: 10.1038/nnano.2010.279
2. M.M. Benameur, B. Radisavljevic, J.S. Heron, S. Sahoo, H. Berger, and A. Kis. Visibility of dichalcogenide nanolayers. Nanotechnology 22, 125706, 2011. doi: 10.1088/0957-4484/22/12/125706
3. B. Radisavljevic, M.B. Whitwick, and A. Kis. Integrated circuits and logic operations based on single-layer MoS₂. ACS Nano 5, 9934, 2011. doi: 10.1021/nn203715c
4. J. Brivio, D.T.L. Alexander, and A. Kis. Ripples and Layers in Ultrathin MoS₂ Membranes. Nano Letters 11, 5148, 2011. doi: 10.1021/nl2022288
5. S. Bertolazzi, J. Brivio, and A. Kis. Stretching and Breaking of Ultrathin MoS₂. ACS Nano 5, 9703, 2011. doi: 10.1021/nn203879f

Biofilms and Biofouling: Marine Medical Energy Focus Topic

Room: 23 - Session MB+BI-ThA

Marine Biofouling

Moderator: D.E. Barlow, Naval Research Laboratory

2:00pm **MB+BI-ThA1 The Role of Oxygen in Microbiologically Influenced Marine Corrosion, B.J. Little, J.S. Lee, R.I. Ray, Naval Research Laboratory** **INVITED**

Two microbiologically mediated processes dominate the literature on microbiologically influenced corrosion (MIC) in natural marine environments – ennoblement and sulfate reduction that leads to sulfide derivitization. Both are global phenomena and both depend on the presence of oxygen for aggressive attack. Marine biofilms cause a noble shift, or ennoblement, in corrosion potential (E_{corr}) for most passive alloys. E_{corr} ennoblement increases the probability for pitting and crevice corrosion initiation and propagation for those passive alloys where E_{corr} is within a few hundred millivolts of the pitting potential (E_{pit}) (e.g. 304L and 316L stainless steels). Numerous researchers have shown that increased cathodic oxygen reduction reaction (ORR) rates accompany ennoblement of E_{corr} , but do not agree on a universal mechanism for acceleration of ORR by biofilms. The role of oxygen in accelerating marine sulfide influenced corrosion has not been precisely defined. Past experiments have demonstrated that dissolved oxygen (DO) in stagnant natural seawater (8 ppm) exposed to corroding carbon steel will be depleted to the detection limits of an electrochemical probe (100 ppb) within 48 h due to aerobic microbial respiration and corrosion reactions. Furthermore, most solid surfaces in contact with seawater are anaerobic because the rate of microbial respiration within a biofilm is greater than the rate of oxygen diffusion. Even in an oxygenated bulk environment, sulfate-reducing bacteria (SRB) dominate anaerobic niches in marine biofilms and produce aqueous sulfides that can derivitize some metals and alloys (e.g., carbon steel and copper-based alloys). In the absence of oxygen, corrosion will slow or cease as bare metal, surface oxides and metal ions are derivitized forming protective surface metal sulfides. Whereas in the presence of oxygen, the protective surface-bound sulfides are oxidized thus allowing more corrosion reactions can take place. In addition, introduction of oxygen (e.g., flow after stagnation) dramatically increases instantaneous corrosion rates owing to

metal sulfides being more efficient oxygen reduction cathodes compared to metal oxides. The end result is deeper metal penetration when compared to strictly anaerobic environments. More recent experiments have demonstrated that even transient DO in the bulk medium can influence the microflora and corrosion rates of carbon steel. Using optical DO probes (detection limits 4 ppb) bulk concentrations of DO in the bulk medium are being correlated with corrosion rates and pit depths in carbon steel. Persistence of aerobic bacteria at ppb DO is being followed.

2:40pm **MB+BI-ThA3 3D-Tracking of Biofouling Microorganisms with Digital In-Line Holographic Microscopy, S.M. Stuppy, University of Heidelberg, Germany, A. Rosenhahn, T. Schwartz, Karlsruhe Institute of Technology, Germany, T. Ederth, Linköping University, Sweden, J.A. Callow, M.E. Callow, University of Birmingham, UK, B. Liedberg, Linköping University, Sweden, G.W. Swain, Florida Institute of Technology, M.H. Grunze, Karlsruhe Institute of Technology, Germany**

Digital in-line holographic microscopy, based on Gabor's initial idea of a lensless microscope¹, is an imaging technique which allows to track microorganisms in three dimensions. A so-called "source wave" interferes with the wave scattered off the swimming objects and forms an interference pattern (Hologram) on the detector which contains three-dimensional information of the objects investigated. To obtain real space information from the Hologram, a reconstruction algorithm is applied². The reconstructed data provides 3D trajectories of single spores with a 10 Hz time resolution and thus allows a qualitative and quantitative analysis of swimming behavior and settlement kinetics of microorganisms such as marine biofoulers or pathogen bacteria down to a length of 1-2 μm .

In our recent work the swimming and settlement behavior of *Ulva linza* zoospores as a common motile biofouling organism was investigated in the vicinity of surfaces with different chemistry^{3,5}. We analyzed the effect of fast and abnormal settlement of *Ulva* spores on a charged Arginin containing oligopeptide surface⁶ by digital holography to study the exploration behavior and kinetics of the colonization of the surfaces. As step towards application of holography at ocean test sites in the field, we constructed a compact holographic setup and tested it at the FIT test site and studied the swimming behavior of small marine organisms in their native environment.

We also applied holography to study motile biofilm forming bacteria. Using a large CMOS sensor, we were able to resolve and track rod shaped bacteria with a length of 2 μm , namely the pathogen *Pseudomonas aeruginosa*. We will show the first three-dimensional trajectories for a free swimming *Pseudomonas aeruginosa*.

1 Gabor, D. *Nature***161**, 777 (1948).

2 Xu, W. B., Jericho, M. H., Meinertzhagen, I. A. & Kreuzer, H. J.. *Proceedings of the National Academy of Sciences of the United States of America***98**, 11301-11305 (2001).

3 Heydt, M., Divós, P., Grunze, M. & Rosenhahn, A. *The European Physical Journal E***30**, 141-148, doi:DOI 10.1140/epje/i2009-10459-9 (2009).

4 Heydt, M. *et al. Journal of Adhesion***83**, 417-430 (2007).

5 M. Heydt, M. E. Pettitt, X. Cao, M. E. Callow, J. A. Callow, M. Grunze, A. Rosenhahn, *Biointerphases***2012**, in press

6 Ederth, T. *et al. Biofouling***24**, 303-312, doi:Doi 10.1080/08927010802192650 (2008).

3:00pm **MB+BI-ThA4 A Multidisciplinary Approach to Tackling Microbiologically Influenced Corrosion, S.A. Wade, P.R. Stoddart, E. Palombo, M.M. Hlaing, M.A. Javed, D. Marić, D. Eldridge, S.L. McArthur, Swinburne University of Technology, Australia**

Microbiologically influenced corrosion (MIC) can lead to localized material degradation rates that are orders of magnitude higher than would normally be expected from standard, abiotic corrosion. This can lead to the premature failure of a wide range of important structures that can not only be costly to repair, but in some cases can have fatal consequences.

Studies of MIC require expertise from a wide range of fields such as material science, microbiology, chemistry and engineering. However, much of the past work that has been undertaken on MIC has been performed with a discipline-specific focus. This is somewhat understandable in a historical research context and may help to explain some of the observed discrepancies between MIC studies undertaken in the laboratory and field observations. In order to overcome some of these issues and develop solutions to the problems caused by MIC a multidisciplinary approach is required.

We have assembled a multidisciplinary team to investigate two specific aspects of MIC, namely the composition of bacterial consortia implicated in MIC and the associated physicochemical processes that drive MIC.

With respect to bacterial identification work is being carried out using a variety of techniques, including the relatively novel application of MALDI-TOF and Raman spectroscopy to MIC. The latter technique is particularly attractive as it potentially allows single bacteria to be identified at different stages of their life cycle, as well as in biofilm. Initial work in this area has required the development of data analysis techniques in order to remove background fluorescence signals in a consistent manner. MALDI-TOF potentially allows rapid routine identification from large numbers of samples. Initial results obtained with this technique will be presented.

The second area of interest includes work undertaken to look at how changes in field conditions can affect the likelihood of MIC. Metal coupon corrosion tests using seawater samples obtained from different field locations have been performed. A range of metallurgical, chemical and microbiological measurements were made to investigate differences observed for samples tested in two different seawater solutions and also for replicate samples tested using seawater from the same location.

Although progress remains challenging, the multidisciplinary approach reported here is showing great promise, with chemists, metallurgists and physical scientists working closely with microbiologists to understand the full complexity of the underlying biological processes.

3:40pm **MB+BI-ThA6 Bioinspired Surfaces with Dynamic Topography for Active Control of Biofouling**, *X.H. Zhao, G.P. Lopez, D. Rittschof*, Duke University

Biofouling of ship hulls and propellers increases drag and power usage and decreases fuel efficiency. Biofouling costs the US Navy alone approximately one billion dollars per year, and the decreases in fuel efficiency further increase green-house gas emissions. Traditional antifouling coatings, relying primarily on biocidal organics and metals, have negative environmental impacts, while newer polymer-based coatings are easily damaged and ineffective in long-term applications.

On the other hand, nature has created an enormous number of biological surfaces that can effectively clean themselves via active deformation and motion. For example, tiny hairs called cilia on the surfaces of respiratory tracts constantly move back and forth, pushing inhaled foreign particles out of our lungs. The ciliary cleaning has also been used by molluscs, corals and many other marine organisms for active antifouling.

Inspired by active biological surfaces found in nature, we have developed a novel active-antifouling technology by harnessing dynamic deformation of polymer coatings in response to external stimuli. We discover that the surfaces of silicone-based coatings can be significantly deformed by applying a direct-current voltage across the coatings. The deformation is on-demand, dynamically switching the coating surfaces between patterned and flat states as the applied voltage is on and off. The on-demand deformation can actively and effectively detach various biofouling organisms such as bacterial films and barnacles adhered to the polymer coatings. The new technology can be readily integrated with existing or newly-developed polymer coatings, combining the advantages of various state-of-the-art antifouling technologies. This new active-antifouling system is environmentally friendly, autonomous, highly effective, and potentially durable over long-term applications. Next, we will further discuss the fundamental effect of active surface deformation on marine organism-surface interactions. A new theory for biofouling detachment caused by substrate deformation, instead of external forces, will be presented.

4:00pm **MB+BI-ThA7 Seasonal Study of Cathodic Current and Elucidation of Oxygen Reduction Enhancement Mechanism in Marine Biofilms**, *M.J. Strom*, Naval Research Laboratory, *S.C. Dexter*, University of Delaware

The ability of a biofilm to influence the corrosion rates through the enhancement of cathodic currents is well known but what mechanisms cause this enhancement and how sustainable is it during seasonal variation? Enhancement of the oxygen reduction reaction has been shown to occur in Delaware Bay waters. Historically, enhancement of the oxygen reduction reaction by biofilms has been attributed to the presence of catalase in biofilms. However, recent work has indicated that manganese oxides may also provide a means for oxygen reduction enhancement in. The following investigation looks at the effect of seasonal variation of the sustainability of oxygen reduction enhancement and distinguishes between manganese and catalase based mechanisms

The following work used sacrificial anodes to provide a long-term cathodic current to biofilm-coated cathodes in Delaware Bay waters, in order to monitor seasonal variation of biofilm-coated cathodes under varying polarization intensities over a year. Manganese and catalase based oxygen reduction enhancement mechanisms were evaluated through the addition of glutaraldehyde or formaldoxime (FAD) treatments to the bulk solution of immersed galvanic couples.

Varying the polarization intensities of 6XN cathodes in a galvanic couple with a sacrificial anode has provided further evidence that the sustainable cathodic current enhancement found by biofilms of Delaware Bay is a result of oxygen reduction enhancement. Glutaraldehyde treatment experiments indicate that a catalase mechanism of oxygen reduction enhancement is not likely in at this location. FAD treatment experiments support the hypothesis that manganese oxides are the dominant catalysts in oxygen reduction enhancement in these waters. Seasonal studies of cathodic current enhancement show that cathodic current enhancement in Delaware Bay is seasonally dependent, with higher cathodic currents in the late spring to early fall. It is suggested that this variation is the result of the biological activity of the surrounding sediments providing a manganese resource into the water column during the warmer seasons.

4:20pm **MB+BI-ThA8 Tailoring Anode and Cathode Biofilms for Higher Current Production in Bioelectrochemical Systems**, *J. Regan*, Penn State University **INVITED**

Bioelectrochemical systems (BESs) exploit the ability of some microbes to reduce an anode (exoelectrogenesis) or oxidize a cathode (exoelectrotrophy) for the generation of electrical current coupled with some biotransformation. There has been a lot of research in the past decade on improving the performance of BESs, primarily by addressing system features that allow reduced internal resistance. These design advancements have led to more than a six order of magnitude increase in power densities in that short time period. Moreover, a growing number of potential BES applications are being developed, including electricity production from wastes and sediments in microbial fuel cells for remote or centralized power, the production of fuels such as hydrogen and methane in microbial electrolysis cells, the recovery of value-added chemical products such as caustic and hydrogen peroxide, water desalination in microbial desalination cells, and microbial electrosynthesis for the production of organic products. Some design and operation parameters can have significant effects on anode and cathode biofilm architecture, composition, and functionality. For a given system configuration (e.g., electrode material, electrode spacing, membrane), there are only a few parameters that can be manipulated during operation. One of these operational variables is the external load or the applied potential in a potentiostatically operated system, which can significantly affect the microbial ecology of BESs as it influences the availability of the anode to serve as an electron acceptor for exoelectrogens and thereby controls the cooperation and competition among various community members in mixed-culture systems. This directly translates into performance effects, not only with respect to the time required to achieve a desired electron donor removal efficiency, but also with electron losses to competing metabolisms such as methanogenesis and aerobic respiration in an air-cathode system. This presentation will cover the mechanics of BESs, including some of the emerging designs and applications, as well as some of the parameters that can be manipulated to include microbial function, density, and productivity.

Plasma Science and Technology

Room: 25 - Session PS-ThA

Plasma Sources

Moderator: M. Funk, Tokyo Electron America

2:00pm **PS-ThA1 Study on Microwave ECR Plasma Source for 450-mm Wafer Etching**, *K. Maeda*, Hitachi, Ltd., Japan, *H. Tamura, S. Obama, M. Izawa*, Hitachi High-Technologies Corp., Japan, *G. Miya*, Hitachi, Ltd., Japan **INVITED**

In semiconductor industries, a high level of productivity to reduce the cost of ULSI fabrication has always been required for plasma etching tools, as well as the other tools. According to the International Technology Roadmap for Semiconductors (ITRS) 2010, increasing the size of the wafer improves the productivity, and the diameter of the Si wafer will be 450 mm in 2014. One of the most significant problems for achieving an extremely uniform process for the 450-mm wafer area is precise control of the plasma distribution over a large area. We have developed a newly designed microwave electron cyclotron resonance (M-ECR) plasma reactor for next-generation 450-mm wafer processing. The reactor configuration is based on the previous M-ECR etching reactor for 300-mm wafers. A microwave power of 2.45-GHz in a circular TE₁₁ mode (principal mode) is supplied to the chamber via the circular waveguide, microwave circuit (cavity), and quartz window. The chamber is surrounded by solenoid coils and a yoke, and the position of the ECR plane (87.5 mT magnetic field strength) is controlled by the currents supplied to the coils.

We present the measurement of two-dimensional (radial and vertical) distribution of ion saturation currents in the reactor, which was measured by

a movable single probe system in halogen gas mixture at 0.4 Pa for poly-Si etching. The ring-shaped high density region was observed at the ECR plane in the optimized microwave circuit type, in which we could obtain uniform plasma distribution just above the wafer. This plasma distribution could be controlled by changing the position of the ECR plane. On the other hand, strongly convex-shaped plasma distribution was observed in an inappropriately designed microwave circuit. A plasma generating distribution is also estimated by comparing the result of plasma-diffusion analysis in magnetized plasma to that of a probe experiment. We confirmed that the plasma seemed to be generated in a very thin (1-2 cm) region at the ECR position. In addition to the result of plasma characteristics, the etching results, i.e., radial distribution of poly-Si etching rate, with a uniformity of 1.5%, and critical dimension control of the line and space pattern by controlling the temperature of the wafer are also presented.

2:40pm PS-ThA3 A Grid Reactor with Low Ion Energy Bombardment for Large Area PECVD of Thin Film Silicon Solar Cells, M. Chesaux, A.A. Howling, Ecole Polytechnique Fédérale de Lausanne (EPFL), Switzerland, U. Kroll, D. Dominé, Oerlikon Solar-Lab SA, Switzerland, Ch. Hollenstein, Ecole Polytechnique Fédérale de Lausanne (EPFL), Switzerland

This study presents a PECVD reactor using localized remote plasma in a grid electrode. The aim is to reduce the ion energy bombardment inherent in RF capacitively-coupled parallel plate reactors conventionally used to deposit large area thin film silicon solar cells. This bombardment could cause defects in silicon layers and deteriorate electrical interfaces. Here, low ion bombardment energy is obtained by inserting a grounded grid close to the RF electrode of a parallel plate reactor. The plasma is then localized in the grid holes and remote from the substrate. This grid also increases the negative self-bias by increasing the effective area of grounded electrode in contact with the plasma while retaining the lateral uniformity required for large area deposition. The self-bias reduces the ion energy bombardment, but retarding field energy analyzer measurements show that the ion energy is even lower than expected from the self-bias effect alone. This reduced ion energy could be caused by a non sinusoidal RF cycle of the plasma potential as was measured with a capacitive probe and supported by phase resolved optical emission spectroscopy. Measurements were done in hydrogen at 0.5 mbar and 13.56 MHz.

3:00pm PS-ThA4 Plasma Generation and Delivery from a VHF Remote Source, D. Carter, D. Hoffman, K. Peterson, R. Grilley, Advanced Energy Industries Inc.

A new remote plasma source (RPS) driven by capacitively coupled VHF power has been defined for use in chamber cleaning or other processes where ex-situ plasma generation is desired. The combination of VHF drive, compact size and unique geometry results in a plasma source capable of very high plasma densities and a resulting field structure offering some interesting characteristics. The device is shown to allow operation in a conventional "remote" mode where the plasma is largely confined within the primary volume of the source or alternatively in a "projecting" mode where the plasma extends well beyond the output of the device reaching to and even filling a downstream chamber with active plasma. This study evaluates behaviors of the VHF RPS in both remote and projected modes as well as in a hybrid mix of both modes. We report on operating characteristics and plasma parameters including density, potential and electron temperatures at the source and downstream and additionally look at ion energy distributions at various points in the system. Results are compared with alternative remote source technologies to illustrate the differences and potential advantages offered by this new RPS topology.

3:40pm PS-ThA6 Mechanical Optimization of a Plasma Source Device, S. Polak, M. Thornton, D. Hoffman, D. Carter, Advanced Energy Industries Inc.

A new, remote plasma source device (RPS) is being developed. From a mechanical standpoint, there are a number of unique challenges and areas for optimization. The RPS features high plasma density in a compact, mechanical envelope, resulting in high heat-flux and therefore requiring robust cooling solutions. Also, because the RPS has the ability to confine plasma within the chamber or project the plasma downstream, the locations and magnitudes of heat flux are dynamic, depending on the process. High and variable-density heat fluxes result in high temperatures and high thermal gradients, both of which lead to thermal-mechanical strain and stress within the components. Numerical models and finite-element simulations have been developed to predict the thermal and structural responses within the critical components in the RPS assembly and to mitigate structural failure of these components. Furthermore, because the RPS features high gas flow rates through a relatively small-volume chamber, optimization of the fluid flow becomes paramount to the ignition, stability, and efficiency of the plasma. Finite-volume, computational fluid dynamics (CFD) models were developed to characterize and optimize the

gas flow into the chamber. We report on the development of these thermal-mechanical and fluid dynamics analysis tools, including correlation of the analytical models to empirical data. Also, we will discuss the parameters and techniques of optimization.

4:20pm PS-ThA8 Impact of Reactor Design on Plasma Polymerization Processes - An International Round-Robin Study, J.D. Whittle, A. Michelmore, D.A. Steele, R.D. Short, University of South Australia

Plasma polymerization is capable of producing adherent pinhole-free thin films with a diverse range of chemical functional groups and physical properties. These materials are used widely in applications ranging from composites, electronics, solar cells and biomaterials. Although a number of plasma processes have been scaled up very successfully and have used sophisticated diagnostics, the majority of researchers utilize lab-built reactor systems with very little in the way of plasma diagnostics, relying on control of external parameters to achieve reproducibility and to guide materials design. Often the focus is on retaining chemical function from the precursor compounds, and these processes are typically described by a limited number of variables, for example, rf power, reactor pressure, monomer flow rate. While these parameters often give reasonable control within a given system, it is not clear to what extent these parameters correlate between systems. This becomes a problem when comparing plasma polymerisation experiments with those in the literature - generally the only practical way to repeat a treatment is to re-engineer the process on ones own system by a trial and error process.

In this paper we report the results of an international round-robin exercise which sought to explore the differences resulting from plasma polymerization using 14 different reactor designs spread across seven countries.

We have explored two separate processes; argon plasma treatment of spin-cast polystyrene films and deposition of plasma polymerized acrylic acid at different discharge powers. In all experiments the monomer or gas flow rate was kept the same, and treatments were carried out at the same nominal power. Surfaces were characterized using atomic force microscopy (AFM) and X-ray photoelectron spectroscopy (XPS), and the effect of reactor geometry, and other uncontrolled variables on the resulting surface properties was examined.

Whilst we did expect significant differences between these systems, the magnitude of these variations was surprising - for many of the surface properties, the coefficient of variation was in excess of 100%. We speculate on the key factors which influence the observed differences in the resulting surface treatment, and how these differences could be reduced in the future.

4:40pm PS-ThA9 A Mini Plasma Source for In Situ Sample Cleaning, N.B. Koster, F.T. Molkenboer, R.J. Bolt, T.J. Versloot, J.P.B. Janssen, TNO Technical Sciences, The Netherlands

Energetic photons, ions and electrons can induce carbon growth on surfaces due to residual hydrocarbons present on the sample surface or in the vacuum system. This effect is well known and has been a major obstacle for the successful introduction of EUV Lithography. This has been overcome by introducing a very clean vacuum system in combination with surface cleaning technologies. For EUVL we have developed a plasma cleaning process for the mirrors that has a relatively high efficiency for carbon removal and causes no surface damage[1]. In high resolution imaging applications like SEM, TEM or Helium Ion Microscopy (HIM) this problem is also present and more difficult to counteract due to the delicate nature of samples or that the sample itself is the source of contaminants. We have applied our cleaning process and successfully and non-intrusively cleaned samples for electron microscopes. As a result, and on request of several microscopy users, we have developed a miniature microwave-induced plasma source to be used on various types of imaging systems for sample and chamber cleaning. The miniature source is to be mounted on the load lock of the imaging system or on the microscope chamber by means of a standardized vacuum flange.

We will report on the design, manufacturing and realization of such a miniature source and discuss the results that were obtained on our own HIM as well as other microscopes. This plasma process has already successfully been used to clean samples with graphene, EUV reticle materials or asbestos. Part of the experiments presented include characterization of the plasma with Langmuir probes and Optical Emission Spectroscopy (OES).

[1] N.B. Koster et al, Towards defect free EUVL reticles: carbon and particle removal by single dry cleaning process, and pattern repair by HIM, Proc. of SPIE Vol. 7969 79690X-1, 2011

5:00pm **PS-ThA10 Magnetic Neutral Loop Discharge Reactor for Low-k Dielectric Plasma Processing**, *W.Y. Li, Z. Ling, H.-Z. Zhang, J.A. Bray, T.M. Griffin, M.T. Nichols*, University of Wisconsin-Madison, *B.N. Moon, Y.M. Sung*, Kyungsoong University, Korea, *S. Banna*, Applied Materials, Inc., *Y. Nishi*, Stanford University, *J.L. Shohet*, University of Wisconsin-Madison

Since the magnetic Neutral-Loop Discharge (NLD) plasma was first proposed by Uchida *et al.* [1], its properties and usage have been investigated by a number of researchers. In this work, we design an NLD reactor to investigate the response of low-k dielectric materials to plasma exposure. Moreover, the NLD reactor will be used to compare the properties of its plasma to that of conventional inductively and capacitively coupled plasma reactors. The NLD reactor is located inside of a set of cylindrical magnet coils which at first glance appears to be a simple solenoid. However, the magnet current in the center of the solenoid is reversed from that near the ends of the solenoid which causes the field in the central solenoid to reverse from that in the outer solenoids. By carefully adjusting the coil currents, a circular region of zero magnetic field can be generated underneath the center solenoid—the neutral loop. The shape of the NLD magnetic fields was numerically evaluated and experimentally confirmed. Numerical calculations of particle orbits show the effect of the neutral-loop zero-field region. A region of electron cyclotron resonance appears around the neutral loop. By adjusting the currents, the radius of the neutral loop can be controlled to move closer or farther from the central axis of the reactor.

This work has been supported by Semiconductor Research Corporation under Contract No. 2008-KJ-1781 and by the National Science Foundation under Grant CBET-1066231.

[1] T. Uchida, "Application of radio-frequency discharged plasma produced in closed magnetic neutral line for plasma processing," 33, L43-L44 (1994).

5:20pm **PS-ThA11 High Efficiency ICP Source for Plasma Dry Clean Processing**, *V. Nagorny, O. Todor, V. Surla, A. Kadavanich*, Mattson Technology, Inc.

Inductively coupled plasma (ICP) sources are widely used in the semiconductor industry for plasma processing. They can easily produce high density plasma and provide good plasma control. For photoresist strip (dry clean) processes, direct plasma interaction with a wafer is undesirable and plasma is used as an intermediate for modification of a gas composition and creating chemically active radicals for processing the wafers. As strip rate directly relates to the flux of radicals to the surface of the wafer this process usually uses high gas flows (5-20slm), high RF power (3-5kW) and high gas pressure (~1000mTorr). Obviously, when the gas and energy consumption is that high, the efficiency of the source becomes very important, since it affects both capital and operational costs, and with newer and more restrictive regulations, efficiency may become determining characteristic of the source.

There are a few factors that strongly affect source efficiency, as well as the process, the most important of which are the gas flow and electron heating efficiency. If only small fraction of gas molecules participate in collisions with hot electrons then most of the gas simply flows through the system without dissociation. In this case most of the gas is simply wasted. So it is important to make the gas flow in such a way that most (if not all) gas molecules have a high probability of collision with hot electrons. To increase efficiency of generating hot electrons one has to improve electron confinement in the region where the induced electric field is high.

We accomplished both goals by modifying Mattson Technology Inc.'s production-proven ICP strip source. By modifying the gas injection system into the plasma generating volume and optimizing the vessel, we simultaneously achieved significantly increased photoresist removal rate at reduced input of process gas and a much larger operational window for the source, with concomitant process benefits.

Our implementation is scalable for processing 450mm wafer sizes and the underlying concepts are generalizable for optimizing other types of ICP sources, as will be discussed in the presentation.

Surface Science

Room: 21 - Session SS+NS-ThA

Surface Science of Nanostructures

Moderator: J.M. Millunchick, University of Michigan

2:00pm **SS+NS-ThA1 Direct Atomic Scale Imaging and Spectroscopy of III-V Semiconductor Nanowire Surfaces**, *A. Mikkelsen*, Lund University, Sweden **INVITED**

Free-standing III-V nanowires have the potential to become central components in future electronics and photonics with applications in IT, life-science and energy[1]. The atomic scale structure and morphology of semiconductor nanowire surfaces are central in determining both growth and function of the wires. Surface diffusion and nucleation will directly influence the final appearance of the wires, and transport and optical properties of semiconductor nanowires is often governed by their surfaces.

We develop and use scanning probe and synchrotron based microscopy/spectroscopy to completely determine structure, chemistry and physical properties of III-V nanowire surfaces with extreme precision. We use our novel methods to directly image both interior and exterior surfaces of the nanowires down to the single atom level, revealing geometric structure as well as both electrical and mechanical properties[2-4]. With our rather diverse toolbox we can obtain a real understanding of the connections between nanowire structure, growth and function.

We present recent Scanning Tunneling Microscopy/spectroscopy (STM/S) results, on nanowires consisting of various III-V materials and of polytypic heterostructures with wurtzite (WZ) and zincblende (ZB) crystal segments - only possible in nanowires. We have obtained images of the atomic scale structure for all common WZ and ZB facets as well as information about the electronic structure using STS. We are now developing these methods to perform STM/S on individual nanowires under device operation. Further, we show that STM, can be used for direct top view imaging of the micrometer high free-standing nanowires. We then determine mechanical resonances up to hundreds of MHz with sub Ångström precision[4].

Finally, using synchrotron based Photo Emission / Low Energy Electron Microscopy/Spectroscopy (PEEM/LEEM/XPS) we have characterized III-V nanowire surface chemistry and electronic properties and investigated the influence of various ultra-thin dielectrics to reduce surface band-bending effects[5-8]. A complete picture of oxide thicknesses, effects on bandbending and information on axial and radial doping is obtained.

1. C.M. Lieber and Z.L. Wang, *MRS Bull.***32**, 99 (2007), and other papers in this issue.
2. A. Mikkelsen *et al*, *Nature Mater.***3**, 519 (2004) ; L. Ouattara *et al*, *Nano Lett.***7**, 2859 (2007)
3. E. Hilner, *et al*, *Nano Lett.*, **8**, 3978 (2008)
4. A. Fian, *et al*, *Nano Lett.*, **10**, 3893 (2010)
5. R. Timm *et al.*, *Appl. Phys. Lett.***99**, 222907 (2011).
6. B. Mandl *et al.*, *Nano Lett.*, **10**, 4443 (2012)
7. R. Timm *et al.*, *Microelectron. Eng.*, **88**, 1091 (2011).
8. M. Hjort *et al*, *Appl. Phys. Lett.***99**, 233113 (2011)

2:40pm **SS+NS-ThA3 Spontaneous Assembly of Ordered Atomic Wires with a Long Interwire Distance on a Stepped Nanotemplate**, *B.G. Shin, M.K. Kim, D.-H. Oh, C.-Y. Park, J.R. Ahn*, Sungkyunkwan University, Republic of Korea

Atomic wires do not interact directly with each other and are therefore ordered by an indirect substrate mediated interaction, whereas molecular structures can be assembled spontaneously by a direct interaction with each other. Such interwire interactions were very short and subsequently an interwire distance of ordered atomic wires were a few Å. Because of the interwire interaction, atomic wires have been described as a quasi 1D system rather than an ideal 1D system. Therefore, an atomic wire with a long interwire distance needs to study an ideal 1D system but, as mentioned before, atomic wires were not ordered with a long interwire distance. Assembly of a long interwire distance atomic wire is thus very challenging and demanded to widen experimental scope of studies on one-dimensional physics. In this study, indium atomic wires with a long interwire distance of 5.7 nm were ordered spontaneously at room temperature on a stepwise nanotemplate, a Si(557) surface. In general, interwire interactions are required to produce ordered nanowires so that other ordered atomic wires have a short interwire distance of a few Å, as described above. The long interwire distance of the ordered indium atomic wires is therefore very unique. Indium atoms were mobile at room temperature and were adsorbed on a only specific step among four steps, one (111) and three (112) steps of the reconstructed Si(557) surface, maintaining the stepwise nanotemplate

structure, as observed by scanning tunneling microscopy (STM), despite the fact that the triple steps have similar local atomic structures. The energetic stability of the indium atomic wires was calculated by first-principles calculations. The reconstructed Si(557) structure model was based on the dimer-adatom-stacking fault (DAS) model and adatom-parallel dimer (AD) model of (111) and (112) facets, respectively.[1, 2] Total energy differences between indium atomic wires on the three (112) steps was very small and the most stable atomic structure was located at the second (112) step, which was consistent with STM images. STM simulations also reproduced the x2 periodicity of the In-induced atomic wires along the wire direction.

[1] K. Takayanagi, Y. Tanishiro, M. Takahashi, and S. Takahashi, *J. Vac. Sci. Technol. A* 3, 1502 (1985)

[2] D. Oh, M. Kim, J. Nam, I. Song, C. Park, S. Woo, H. Hwang, C. Hwang, J. Ahn, *Phys. Rev. B*, 77, 155430 (2008)

3:00pm **SS+NS-ThA4 Influence of Surface Steps on the Initial Oxidation of TiN (100)**, *M. Hong, S.R. Phillpot, S.B. Sinnott*, University of Florida

Titanium nitride (TiN) film has extreme hardness, high chemical reactivity and high electrical conductivity and thus is widely used for wear and corrosion resistant coatings as well as diffusion barriers and gate electrodes in microelectronic devices. They are thus routinely subjected to extreme conditions such as high pressure and temperature, corrosive environments, and consequently undergo oxidation. Here, density functional theory calculations are used to determine the mechanisms associated with step-related oxidation process and the formation of TiO_x induced by both the dissociation of O₂ and Ti surface diffusion on TiN (100). Preliminary calculations reveal stable adsorption sites near surface steps for O₂ molecules and single O adatoms, both of which have adsorption energies larger than on terraces. This indicates that the dissipated energy during O₂ dissociation near the surface step is larger than that on (100) terraces so that consequent oxidation reactions can occur more easily. The calculations reveal potential O₂ dissociation paths with activation energies in the range of 1-2 eV. This work is supported by the National Science Foundation (DMR-1005779).

3:40pm **SS+NS-ThA6 Growth of Ag/Ge(111) Phases Studied with LEEM and LEED**, *S. Chiang, C. Mullet*, UC Davis

Low energy electron microscopy (LEEM) and low energy electron diffraction (LEED) were used to study the growth of structural phases of Ag deposited on Ge(111) above and below the Ag desorption temperature. Ag deposited on Ge(111) formed three main surface phases above 100°C: (4x4), ($\sqrt{3}\times\sqrt{3}$)R30°, and (3x1). At a given coverage, (4x4) island size increased with deposition temperature and decreased with deposition rate. The (4x4) structure nucleated at steps edges and grew only at steps for samples with very high step density. While the $\sqrt{3}$ structure did not show a preference for nucleating at steps, its growth was bounded by substrate step bunches. The (3x1) was the only Ag phase on the surface for deposition at 370°C and coverage $\Theta < 0.1$ ML, forming domains large enough to be resolved in LEEM images. The (3x1) and (4x4) phases coexisted for $T < 350^\circ\text{C}$ and $0.1 < \Theta < 0.38$ ML, while the (3x1) and $\sqrt{3}$ phases coexisted for $T > 400^\circ\text{C}$ and $\Theta > 0.4$ ML. LEEM images of Ag desorption from Ge(111) at $T > 575^\circ\text{C}$ showed that Ag (4x4) and $\sqrt{3}$ phases reversibly transform to a disordered (1x1) phase, with desorption proceeding from the edges of disordered (1x1) domains and the (1x1) phase being slightly less dense than the (4x4) phase. For sufficiently high deposition rates, Ag was observed to accumulate on Ge(111) above the 575°C desorption temperature. For deposition between 580 and 640°C, a silver layer formed with a (3x1) LEED pattern; upon completion of that layer, a $\sqrt{3}$ layer formed. For deposition at 660°C, only the (3x1) layer formed. Desorption proceeded by the reverse sequence of phases.

Funded by NSF CHE-0719504 and NSF PHY-1004848

4:00pm **SS+NS-ThA7 A Synchrotron XPS Study of the Radio-Frequency SF₆ Plasma Fluorination of Single-Walled Carbon Nanotubes**, *A.J. Barlow*, NEXUS XPS Facility, Newcastle University UK, *A.J. Blanch, A.D. Slattery, J.S. Quinton*, Flinders University, Australia

With the ever increasing utilisation of carbon nanostructures across many fields, researchers are continuously looking for new and more efficient methods for the reliable and controllable functionalisation of these materials, in a way that is easily scalable. This is particularly true for the one dimensional carbon nanotube (CNT). While plasma science is not a new field, its application towards the covalent attachment of chemically reactive species to the sidewalls of the initially somewhat inert CNT structure has only more recently been investigated. Furthermore, in-depth studies of the plasma functionalisation of CNTs using fluorine-rich species

such as sulphur hexafluoride (SF₆) are limited for a process that is capable of not only providing reactive sites for further chemical attachment but also the modification of the electronic structure of the nanotube [1, 2].

In this presentation research efforts into the fluorination of single-walled CNTs (SWCNTs) in a controlled manner using SF₆ plasma will be discussed. Control over the amount of fluorine attached to the CNT surfaces is demonstrated through variation in experimental conditions such as plasma power. Furthermore, the *type* of fluorine bonding present on the surface (covalent or semi-ionic) is shown to be controllable through the addition of oxygen containing species into the fluorination mechanism. This can be achieved through either the doping of the plasma itself with oxygen or water vapour, or by an oxidative surface pretreatment of the CNTs through wet-chemical or plasma methods. With this level of control, greatly enhanced C-F covalency can be achieved over a pure SF₆ plasma treatment alone. Results will be presented from lab-based XPS analysis of SWCNT surfaces performed at Flinders University, South Australia, as well as synchrotron-based XPS analysis performed at the Australian Synchrotron.

1. Park, K.A., Y.S. Choi, and Y.H. Lee, *Atomic and electronic structures of fluorinated single-walled carbon nanotubes*. *Phys. Rev. B*, 2003. **68**: p. 045429.

2. Plank, N.O.V., et al., *Electronic properties of n-type carbon nanotubes prepared by CF₄ plasma fluorination and amino functionalisation*. *J. Phys. Chem. Lett.* **2005**, **109**: p. 22096-22101.

4:20pm **SS+NS-ThA8 Solving the Shape of Micellar Pt Nanoparticles Supported on TiO₂(110) and γ -Al₂O₃: A STM, TEM and EXAFS Study**, *F. Behafarid, B. Roldan Cuenya*, University of Central Florida

Nanoparticles (NPs) with well-defined sizes and shapes were synthesized via inverse micelle encapsulation methods. For 2-4 nm Pt and Au NPs supported on TiO₂(110), the shape was resolved by scanning tunneling microscopy (STM). Geometrical information on smaller Pt NPs supported on nanocrystalline γ -Al₂O₃ was extracted by a combination of transmission electron microscopy (TEM) and extended x-ray absorption fine-structure spectroscopy (EXAFS) measurements. It will be shown that the size, interparticle distance, and the geometry (2D vs 3D) of the NPs can be tuned via our micellar synthesis.

Pt NPs in the size range of 2-4 nm supported on TiO₂(110) were studied by STM after heating in UHV at high temperature (>1000°C). This thermal treatment facilitates the melting of the NPs and the formation of NP-support epitaxial interfaces. High resolution STM images allowed us to determine the shape of the NPs as well as facet orientations. Three different shape types were observed, and each category of shapes was found to appear within a particular NP size regime. In addition, the epitaxial relationship between the NPs and the TiO₂(110) surface was investigated in order to explain the specific orientation of the NPs observed in our study. It was also found that due to interface-induced strain, the NP shapes obtained do not follow the Wulff theorem, namely $\{100\}/\{111\}$ facet area ratios deviating from the value obtained for support-free clusters.

Pt NPs in the size range of 0.8-1.5 nm supported on γ -Al₂O₃ were studied by EXAFS, and the nearest neighbor coordination numbers up to the 4th shell were obtained following multiple scattering analysis. These coordination numbers, together with the NP diameter obtained by TEM were examined against a theoretically generated database of possible NP shapes to determine the most representative shape of Pt NPs in each of the samples. Correlations between the reactivity and the shape of the Pt NPs were established.

4:40pm **SS+NS-ThA9 Geometrical, Electronic, and Vibrational Properties of Bare and H-covered Pt_n(n=22, 33, 44, 55, and 85) Nanoparticles**, *G. Shaifai, S. Hong, M. Alcantara, T.S. Rahman*, University of Central Florida

We have performed systematic density functional theory (DFT) calculations of the geometrical, electronic, and vibrational properties of small Pt_n nanoparticles (n=22, 33, 44, 55, and 85) and their changes with NP size and adsorbate (H₂) coverage. We find our calculated H adsorption energy to be in range of -0.42 eV and -0.62 eV, and with increasing hydrogen coverage the H adsorption energy decreases due to adsorbate-adsorbate interactions. We find increase of Pt-Pt bond length upon hydrogen adsorption and, strikingly, the red shift of the center of the *unoccupied* d-bands of the bare Pt clusters turns to a blue shift upon hydrogen adsorption in good agreement with experiment [1]. We also find that there is a net charge transfer from all Pt atoms within the NPs to all hydrogen atoms of 0.55 (Pt₂₂H₂₂) and 1.37 electrons (Pt₄₄H₄₄). Thus, the remarkable hydrogen effect on the electronic structure of Pt NPs can be attributed to charge transfer from the Pt NPs to hydrogen. Regarding the optimal H coverage on Pt NPs, our calculated free-energy phase diagram shows non-zero H coverage even at beyond 600K under ambient H₂ pressure. This work is supported in part by US-DOE under Grant No. DE-FG02-07ER46354.

[1] F. Behafarid, L.K. Ono, S. Mostafa, J. R. Croy, G. Shafai, S. Hong, T. S. Rahman, Simon R. Bare, and B. Roldan Cuenya, submitted.

5:00pm **SS+NS-ThA10 The Effect of S to Se Substitution in SAMs: Odd-Even Polymorphism of Biphenyl-Substituted Alkaneselenolate on Au(111)**, *M. Dendzik*, Jagiellonian University, Poland, *A. Terfort*, Goethe University, Germany, *P. Cyganik*, Jagiellonian University, Poland

To fabricate aromatic self-assembled monolayers (SAMs) of practical importance for molecular electronics and other applications, high level of control over the SAMs properties should be achieved. In particular, besides monitoring the electronic properties, the control of structure and stability, is an issue of equal importance. As demonstrated previously one way to improve structure and stability of these systems can be achieved by the substitution of the headgroup atom (S versus Se, which binds SAMs constituent to the substrate) [1-3]. In the present study [4], to elucidate how the S to Se substitution influences SAMs structure and stability, we investigate influence of the BPnSe/Au(111) (BPnSe, $\text{CH}_3\text{-(C}_6\text{H}_4)_2\text{-(CH}_2)_n\text{-Se-}$, $n=2-6$) formation temperature and compare obtained results with the corresponding data obtained for their thiol analogues i.e. for BPnS/Au(111) SAMs. Obtained STM data are discussed and analysed in view of the spectroscopic [2] and spectrometric [3] results reported by us recently for these systems, as well as compared to the previously reported STM data [1]. Observed odd-even effect in polymorphism for BPnSe/Au(111) indicates that bonding configuration at the molecule-substrate interface contributes significantly to the energetics of the SAM. We conclude that S to Se substitution increases strength of the molecule-substrate bonding at the expense of reducing strength of the $\text{Au}_{\text{surface}}\text{-Au}_{\text{bulk}}$ and Se-C bonding.

References

- (1) P. Cyganik, K. Szelagowska-Kunstman, et al. *J. Phys. Chem. C* **2008**, *112*, 15466.
- (2) K. Szelagowska-Kunstman, P. Cyganik, et al. *Phys. Chem. Chem. Phys.* **2010**, *12*, 4400.
- (3) S. Wyczawska, P. Cyganik, A. Terfort, P. Lievens, *ChemPhysChem* **2011**, *12*, 2554.
- (4) M. Dendzik, A. Terfort, and P. Cyganik *in preparation*

5:20pm **SS+NS-ThA11 Molecular Self-Assembly by Ionic Bonding in a Series of Carboxylate Species on the Cu(100) Surface**, *D. Skomski*, *S.L. Tait*, Indiana University - Bloomington

To expand the catalogue of available interactions for the efficient self-assembly of highly-ordered nanoscale structures, we have investigated the formation of high-stability supramolecular networks constructed with anionic carboxylate species and sodium cations. Our experiments demonstrate that these two-component approaches can steer organic molecules towards efficient self-assembly, even with molecules that do not show a strong tendency towards long-range, two-dimensional ordering when deposited alone. Biphenyl-3,3',5,5'-tetracarboxylic acid (BTA) on Cu(100) serves as a model system to illustrate this effect. Ionic structures have been resolved with molecular and atomic resolution using scanning tunneling microscopy (STM). Chemical shifts in the Na 1s, C 1s, and O 1s core level binding energies, measured by X-ray photoelectron spectroscopy, confirm the active chemical interactions inferred from the STM results.

Ionic self-assembly has been achieved on the Cu(100) surface with terephthalic acid, trimesic acid, as well as BTA. We have shown that the carboxylate and sodium chloride undergo a replacement reaction producing a new salt with long range periodic structure. Chemical shifts in the sodium 1s photoelectron peak have been observed upon addition of the organic species to the surface, confirming a direct interaction. Resulting extended network structures demonstrate very high stability, maintaining their supramolecular structure up to at least 165 °C. The formation of new structures illustrates the interplay between adsorbate-substrate and ionic interactions and opens new possibilities for ionic self-assemblies at surfaces with highly-ordered structure and specific chemical function.

Surface Science

Room: 22 - Session SS-ThA

Liquid/Surface Interactions

Moderator: G.A. Kimmel, Pacific Northwest National Laboratory

2:00pm **SS-ThA1 Interface Properties of Aqueous Nitrile Solutions**, *K.A. Perrine*, *A. Margarella*, *M.H.C. Van Spyk*, University of California Irvine, *B. Winter*, Helmholtz-Zentrum Berlin für Materialien und Energie, Germany, *H. Bluhm*, Lawrence Berkeley National Laboratory, *J.C. Hemminger*, University of California Irvine

It is important to understand the molecular-level properties of aqueous organic mixtures that can affect the environment as well as a variety of chemical systems. Mixtures of acetonitrile and water solutions have been shown to have different properties at the surface and in the bulk at different bulk acetonitrile concentrations. According to surface sensitive studies and molecular dynamic simulations, at 0.07 mole fraction, hydrogen bonding is lost at the interface with increasing acetonitrile concentration, leading to a reorientation of the acetonitrile at the surface. In addition, water and acetonitrile clusters have been shown to coexist and interact by dipole interactions between 0.2 and 0.8 mole fraction of acetonitrile. The reorientation of another nitrile at the surface, propionitrile, by hydrogen bonding has also been observed, but for this molecule, there is a lack of bulk studies of water-nitrile solutions.

In our studies, liquid-jet X-ray photoelectron spectroscopy was used to determine the nature of aqueous solutions of these two nitriles. The C1s, N1s and O1s regions suggest that clustering of the nitrile and water is apparent at the surface as well as the bulk. A full range of nitrile concentrations was studied. In addition, we made comparisons between experiments in which the liquid jet is in contact with a few torr of vapor and experiments in which the jet is exposed to high vacuum. The surface and bulk properties, as determined by XPS, are the same under these two experimental conditions. Our results also allow us to compare the differences between solubility of the two nitrile aqueous solutions and their hydrogen bonding properties at the surface and in the bulk.

2:20pm **SS-ThA2 Photoelectron Spectroscopy of Sulfuric Acid Aqueous Solutions**, *A. Margarella*, *K.A. Perrine*, University of California Irvine, *T. Lewis*, Lawrence Livermore National Laboratory, *M. Faubel*, Max-Planck-Institut für Dynamik und Selbstorganisation, Germany, *B. Winter*, Helmholtz-Zentrum Berlin für Materialien und Energie and BESSY, Germany, *J.C. Hemminger*, University of California Irvine

The air-liquid interface of aerosols is an important site for heterogeneous chemistry in the atmosphere, associated, for instance, with the formation of reaction products relevant for ozone depletion. Concentrated (5-14 M) super-cooled aqueous solutions of sulfuric acid are known as sulfate aerosols and are one of the most abundant types of atmospheric aerosols. Fully understanding the dissociation of sulfuric acid, on the molecular level, is important because heterogeneous chemistry occurring on the surface of sulfate aerosols depends on the availability, speciation, location, and solvation structure of the species in solution. Aqueous solutions of sulfuric acid and the subsequent acid dissociation are useful models for sulfate aerosols. As a strong acid, the bulk of an aqueous solution of sulfuric acid will have H_3O^+ , HSO_4^- and SO_4^{2-} , and at high concentrations when the water concentration is very low, un-dissociated H_2SO_4 may be present. The bulk species composition is a function of the initial solution concentration, as well as temperature, and this composition as been well characterized by a variety of methods, such as sum frequency generation and Raman spectroscopy. Here, the chemistry of sulfuric acid aqueous solutions is explored by photoelectron spectroscopy on a liquid micro-jet. Experiments were performed at Beamline U41-PGM at the BESSY II synchrotron facility. A series of sulfuric acid aqueous solutions is measured at a low temperature of 6°C. Deconvolution of the photoelectron spectra yields electronic information on the ionization species of sulfuric acid.

2:40pm **SS-ThA3 Using Nanoscale Amorphous Solid Water Films to Create and Study Deeply Supercooled Liquid Water**, *S.R. Smith*, *B.D. Kay*, Pacific Northwest National Laboratory **INVITED**

Vapor deposition of water on cryogenic substrates is known to produce amorphous solid films. When heated above their glass transition (136 K) these films transform into deeply supercooled liquid water which subsequently crystallizes around 160 K. These nanoscale liquid films can be used to study processes such as diffusion, isotope exchange, and crystallization at cryogenic temperatures not attainable by conventional supercooling of the bulk liquid. Molecular beam scattering, programmed desorption (both TPD and isothermal), and vibrational spectroscopy are

used to study the thermodynamics and chemical kinetics of these processes in unprecedented detail. This talk will highlight our recent advances in this area. This work was supported by the U.S. Department of Energy (DOE), Office of Basic Energy Sciences, Division of Chemical Sciences, Geosciences, and Biosciences. The research was performed using EMSL, a national scientific user facility sponsored by DOE's Office of Biological and Environmental Research and located at Pacific Northwest National Laboratory, which is operated by Battelle, operated for the U.S. DOE under Contract DE-AC05-76RL01830.

3:40pm SS-ThA6 DFT Study of Water Dissociation and Diffusion on Metal Surfaces, Kinks and Step. *L. Arnadottir*, Oregon State University

Surface defects play a critical role in many surface processes, for example in the formation of a water layer on Pt(111). In this DFT study, we describe water adsorption, diffusion, dissociation and early cluster formation on terrace, steps and kinks on Pt(111). The adsorption energy of a single water molecule increase as it moves from the flat terrace up to the step edge and then atop a kink atom. The highest activation barrier along this path is only 0.22 eV. The stronger binding on the step and kinks makes the reverse barriers much larger and, therefore, the diffusion from the step or kink back to the flat terrace less likely. This suggests that at approximately 100 K, water will diffuse to lower energy adsorption sites on the steps and kinks and form chains on step edges before wetting the lower terrace, in agreement with STM measurements by Morgenstern, M. et al. [1].

Surface defects also play an important role in the dissociation of water molecules. The calculated reaction energy for water dissociation, $\text{H}_2\text{Oads} \rightarrow \text{OHads} + \text{Hads}$, on flat terrace, step and kink shows an interesting trend where the reaction energy on the flat terrace is almost twice the energy at a kink and three times the energy on a step. Water molecule dissociation on flat Pt(111) terrace is therefore less likely than at defects. The reaction energy is 0.21 eV on the (221) step and 0.37 eV on the (854) kink, making the defect sites significantly more promising for water dissociation.

The activation energy for dissociation is also lowest at a step site, 0.80 eV. An oxygen assisted dissociation on the step ($\text{H}_2\text{Oads} + \text{Oads} \rightarrow 2 \text{OHads}$) has even lower reaction energy but the activation barrier is similar. Although the reaction energy at the kink was not so high, the activation barrier for dissociation is very high, 1.4 eV. The energy landscape is quite complicated around the kink but we consistently get this high barrier for the various dissociative pathways that have been tried. The high barrier may be the result of the strong adsorption at the kink sites.

1. Morgenstern, M., Michely, T. and Comsa, G., *Phys. Rev. Lett.* **77** 703 (1996).

4:20pm SS-ThA8 Adsorption and One-Dimensional Chain Formation of Water on $\text{TiO}_2(110)$. *J. Lee, D.C. Sorescu, X. Deng*, National Energy Technology Laboratory, *K.D. Jordan*, University of Pittsburgh

The adsorption of water molecule on a reduced rutile $\text{TiO}_2(110)-(1 \times 1)$ surface has been investigated using scanning tunneling microscopy (STM) and density functional theory (DFT) calculations. STM results indicate that water monomer adsorbs on top of Ti(5f) atom on the Ti row. The DFT calculations show that the most stable configuration of adsorbed water on $\text{TiO}_2(110)$ has the binding energy of 23.6 kcal/mol. In this configuration, the oxygen atom is positioned on top of a Ti(5f) atom with one of the O-H bonds pointing toward a bridging oxygen via H-bonding and the other pointing along the Ti row direction. The water monomer can be dissociated by the electron injection from the STM tip into an oxygen adatom on Ti row. As the coverage increases, water molecules start to form one-dimensional chains via H-bonding along the Ti row direction. Thermal annealing after the adsorption of water at low temperature on $\text{TiO}_2(110)$ is also found to be effective in the formation of the one-dimensional water chain. The effects of other coadsorbates such as CO_2 and O_2 in the formation of water chain will also be discussed.

4:40pm SS-ThA9 Characterization of Surface and Adsorbate Chemistry on TiO_2 ; Particle Ensembles and Atmospherically Prepared TiO_2 ; Single Crystalline Surfaces. *C. Kunze, B. Torun, G. Grundmeier*, University of Paderborn, Germany

Titanium dioxide (TiO_2) plays a crucial role for modern technical applications such as the design of new catalysts or biomaterials. TiO_2 particles in the modifications of rutile or anatase are a widely used material as an inorganic white pigment. In particle processing the force interactions within particle collectives are of outmost interest in terms of bulk flow properties and agglomerate dispersibility. As the adhesion between small particles is mostly driven by capillarity- and van der Waals forces, the investigation of surface chemistry plays a crucial role to understand interactions at TiO_2 particle surfaces. For studies of particle ensembles a new experimental setup was developed to investigate particle parameters under both control of relative humidity (capillary forces) and UV light exposure (hydrophobic to hydrophilic transition). By combined Fourier

Transform Infrared Spectroscopy (FTIR) and quartz crystal microbalance (QCM) we studied the influence of surface hydroxyl densities and molecular adsorbates on the formation of surface water adsorbate films in environments of defined relative humidity.

To study the formation of adsorbates on a model surface, $\text{TiO}_2(100)$ and $\text{TiO}_2(110)$ single crystalline surfaces were prepared by a wet chemical etching procedure followed by an annealing step. The crystal surface and the native adsorbate layer were studied by means of angle resolved photoelectron spectroscopy (XPS), low energy electron diffraction (LEED) and atomic force microscopy (AFM).

The surface analysis by AFM and LEED revealed a single crystalline TiO_2 surface for both crystal orientations. An ad-layer of surface-hydroxides and specifically adsorbed water additionally to the native contamination layer of low-weight (hydro)carbon species formed under ambient conditions could be proven by angle resolved XPS experiments.

As a model of the carboxy-functional, (hydro)carbon contamination film the adsorption of nonadecylcarboxylic acid (NDCA) on the crystal surface was studied by AFM and angle resolved XPS experiments. Here a significantly different mechanism of adsorption was found comparing the $\text{TiO}_2(100)$ and $\text{TiO}_2(110)$ surfaces. AFM investigations showed a micellar adsorption of NDCA on the (100) surface forming a dense layer of NDCA micelles which could be removed from the surface by AFM based "nanoshaving"-experiments. In comparison the (110) surface showed very weak interactions with NDCA leading to a coverage of less than one monolayer as a result of different surface termination in comparison to the (100) crystal.

5:00pm SS-ThA10 The Critical Marangoni Number Dependence with Different Aspect Ratio Comparing Microgravity Experiments and Numerical Simulation. *S. Yoda*, ISAS, Japan, *S. Matsumoto*, IASA, Japan, *H. Kawasaki, I. Ueno*, Tokyo University of Science, Japan

Marangoni experiments with a large diameter, 50 mm, were carried out under microgravity condition in Japanese Experiment Module to make clear critical Marangoni number dependence in liquid bridge configuration such as liquid bridge aspect ratios(length/diameter of liquid bridge). The experiments with the different aspect ratios (length/diameter of liquid bridge) were changed from 0.25 to 1.2 which determined each critical Marangoni numbers. The critical Marangoni numbers decreased up to around 0.4, and after that the number increased monotonically up to 1.2. The most smallest number is observed at critical $\text{Mac}(20000)$ at 0.4 and the maximum is $\text{Mac}(50000)$ at 1.2. The large liquid bridge was vibrated by crew activity, so that all experiments were done during crew sleeping. This behavior can be qualitatively explained by considering thermal boundary layers which form at both heating and cooling desks of the liquid bridge. The experimental data were good agreement with the numerical results.

Thin Film

Room: 11 - Session TF+AS+SS-ThA

Thin Films: Growth and Characterization-III

Moderator: M.R. Davidson, University of Florida

2:00pm TF+AS+SS-ThA1 Atomic Force Microscopy (AFM)-Based Nanografting for the Study of Self-Assembled Monolayer Formation of Organophosphonic Acids on Al_2O_3 Single Crystal Surfaces. *B. Torun, B. Oezkaya, G. Grundmeier*, University of Paderborn, Germany

The surface chemistry of aluminum oxides plays a crucial role in the field of catalysis, corrosion and adhesion. Alumina (Al_2O_3) covered aluminum alloys are employed in the construction of lightweight automotive and aerospace parts. In order to protect these materials from environmental factors organic coatings are commonly used. In this context the adhesion between polymer and oxide surfaces is of outmost importance to improve the longevity of industrial parts. Using self-assembled adhesion promoting monolayers the complexity of surface pretreatment processes could be reduced tremendously. Long aliphatic phosphonic acids, such as octadecylphosphonic acid (ODPA), were found to be suitable for forming dense self-assembled monolayers on native oxide covered aluminum substrates. However in contrast to amorphous oxide films, single crystal surfaces provide a much more well-defined experimental and theoretical platform for studies on the adsorption mechanisms and the stability of organophosphonic acids.

In the presented study^[1], adsorption, stability, and organization kinetics of organophosphonic acids on single-crystalline alumina surfaces were investigated by means of atomic force microscopy (AFM)-based imaging, nanoshaving, and nanografting. The latter, nano-shaving and -grafting, are rather new techniques to study self-assembly processes. Since they were

first reported^[2] in 1997, atomic force microscopy based nanografting has been used as a tool to investigate the adsorption of organic monolayers mostly on noble metals, such as gold.^[3] Moreover recent studies focused on influences of the confinement between AFM-tip and background monolayer on the adsorption of molecules during the grafting process. [about:blank#_ENREF_1]

AFM friction and phase imaging have shown that chemical etching and subsequent annealing led to heterogeneities on single-crystalline surfaces with (0001) orientation indicating differences in the local surface termination. These findings were supported by angle resolved X-Ray photoelectron spectroscopy (AR-XPS) measurements suggesting a partially hydroxide terminated surface. Self-assembly and stability of ODPA were shown to be strictly dependent upon the observed heterogeneities of the surface termination, where it was locally shown that ODPA can loosely or strongly bind on different terminations of the crystal surface. Furthermore, organization kinetics of ODPA was monitored with nanografting on (0001) surfaces. Supported by measurements of surface wettability and diffuse reflectance infrared Fourier transform spectroscopy (DRIFTS), it was demonstrated that the lack of organization within the protective adsorbed hexylphosphonic acid (HPA) monolayer on alumina surfaces facilitated the reduced confinement effect during nanografting, such that kinetics information on the organization process of ODPA could be obtained.

[1] Torun, B. et al., *Langmuir* **2012**, 28, (17), 6919-6927.

[2] Xu, S. et al., *Langmuir* **1997**, 13, (2), 127-129.

[3] Yu, J. et al., *Langmuir* **2008**, 24, (20), 11661-11668.

[4] Xu, S. et al., *J. Amer. Chem. Society* **1998**, 120, (36), 9356-9361.

2:20pm TF+AS+SS-ThA2 SIMS as a Method for Probing Stability of the Molecule-Substrate Interface in SAMs, J. Ossowski, J. Rysz, Jagiellonian University, Poland, A. Terfort, Goethe University, Germany, P. Cyganik, Jagiellonian University, Poland

Despite the numerous structural studies of Self-Assembled Monolayers (SAMs) available nowadays, the structure and stability of the SAM-substrate interface is still poorly understood and controversial even for the most simple SAM system. As a consequence, the experimental and theoretical analysis of the bonding geometry and the stability of the molecule-substrate interface for technologically relevant, and therefore more complicated SAMs, is extremely difficult.

In this presentation we report extensive static secondary ion mass spectrometry (SIMS) studies¹ on homologous series of thiols (BPnS, $\text{CH}_3\text{-C}_6\text{H}_4\text{-C}_6\text{H}_4\text{-(CH}_2\text{)}_n\text{-S-Au(111)}$, $n = 2-6$) and selenols (BPnSe, $\text{CH}_3\text{-C}_6\text{H}_4\text{-C}_6\text{H}_4\text{-(CH}_2\text{)}_n\text{-Se-Au(111)}$, $n = 2-6$) where structure and stability of molecule-substrate interface was systematically modified as verified by our previous experiments²⁻⁵. Correlating SIMS data with previous microscopic², spectroscopic³ and very recent neutral mass spectrometry studies^{4,5} we show that SIMS can be successfully applied to monitor fine changes in the molecule-substrate interface stability of these model SAMs. Further, to demonstrate general applicability of SIMS for such analysis, we report use of this method for monitoring influence of S versus Se substitution in purely aliphatic (heksadecanethiol/selenol) and aromatic (anthracenethiol/selenol) SAMs on Au(111). In summary our experiments show that a new approach for probing the stability of molecule-substrate interface in SAMs can be proposed by using SIMS. Importantly, this technique is relatively fast and can be applied for virtually all complicated and technologically relevant SAMs.

References

(1) J. Ossowski, P. J. Rysz, A. Terfort and P. Cyganik *in preparation*.

(2) P. Cyganik, K. Szlagowska-Kunstman, et al. *J. Phys. Chem. C* **2008**, *112*, 15466.

(3) K. Szlagowska-Kunstman, P. Cyganik, et al. *Phys. Chem. Chem. Phys.* **2010**, *12*, 4400.

(4) S. Wyczawska, P. Cyganik, A. Terfort, P. Lievens, *ChemPhysChem* (communication) **2011**, *12*, 2554.

(5) F. Vervaecke, S. Wyczawska, P. Cyganik, et al. *ChemPhysChem* (communication) **2011**, *12*, 140.

2:40pm TF+AS+SS-ThA3 Wet Chemical Surface Modification of Silicon Oxide and Oxide Free Silicon by Aluminum Oxide, P. Thissen, A. Vega, T. Peixoto, Y.J. Chabal, University of Texas at Dallas

Wet chemical surface modification is a powerful method to change the chemical properties of surfaces. Although it has been used extensively, there are still many issues that limit the applicability of these reactions. Substrate dip coating in aqueous solutions is particularly useful to facilitate both organic and inorganic layer functionalization. For instance, the bonding of phosphonic acid to silicon oxide is weak in water because the Si-O-P bond is easily hydrolyzed. We demonstrate here that this problem is

alleviated by the addition of an ultra-thin aluminum oxide layer to the silicon oxide surface via dip-coating a silicon substrate in an aqueous solution of aluminum chloride. The growth kinetics of the aluminum oxide layer are characterized by several surface sensitive techniques and found to follow a Stranski-Krastanov mechanism. Once the aluminum oxide layer is in place, a self assembled monolayer (SAM) of octadecylphosphonic acid (ODPA) is attached by the "tethering by aggregation and growth" (T-BAG) method performed in a controlled environment. We demonstrate that this ODPA layer grafted on the aluminum oxide interlayer remains stable in water. We also show that, following the same wet chemical approach, we are able to attach aluminum hydroxyl directly on oxide-free silicon surfaces previously functionalized with 1/3 monolayer OH. [1] Finally, we show that our approach can easily be transferred to other metal oxides and discuss the most influencing parameters.

[1] Michalak, D. J.; Amy, S. R.; Aureau, D.; Dai, M.; Esteve, A.; Chabal, Y. J. *Nat. Mater.* **2010**, *9*, 266-271.

3:00pm TF+AS+SS-ThA4 Static and Dynamic Depth Profiling of Thin Films with Low Energy Ion Scattering (LEIS), H.R.J. ter Veen, M. Fartmann, Tascon GmbH, Germany, T. Grehl, ION-TOF GmbH, Germany, B. Hagenhoff, Tascon GmbH, Germany

With the ever increasing demand of thinner and better defined thin layer structures, good depth resolution becomes more and more critical in depth profiling techniques. Low Energy Ion Scattering (LEIS) is known as the most surface sensitive chemical analysis technique (see [1] for a review of LEIS technique). It is considerably less known that LEIS can also be applied for so called "static depth profiling" by interpreting the backgrounds on the low energy side of the LEIS peaks. The energy that the particles lose while travelling through the sample is a measure for the depth of the scattering atom, in a way similar to Rutherford Back Scattering (RBS) but for a much smaller depth range. New models have been developed to understand the process that gives rise to these backgrounds and that contains the information from layers below the surface up to depths of 10 nm. These models will be presented.

The models for this static depth profiling can be verified by dynamic (sputter) depth profiling. After each sputter step a full LEIS spectrum is recorded, which contains the surface information as well as the static depth profile at that point in the dynamic depth profile. In this way, the static depth profile can forecast the dynamic depth profile. This technique will be demonstrated for an Si/SiO₂/W/Al₂O₃ system.

LEIS is particularly suited for dynamic depth profiling. Since LEIS is so surface specific, the depth resolution is excellent, as long as the sputter conditions are chosen with care. Furthermore, LEIS can be quantified easily, in many cases - such as in depth profiles - without the use of references. However, any dynamic depth profile suffers from artifacts, such as preferential sputtering and ion beam mixing. By combining the dynamic depth profiling with static depth profiling there is an independent check on these artifacts. Furthermore, it will be shown how static depth profiling can give relevant information also at shallow depths where in a dynamic depth profile sputter equilibrium will not have been reached yet.

[1] H.H. Brongersma et al, *Surf. Sci. Rep.* **62** (2007)63

3:40pm TF+AS+SS-ThA6 Paul Holloway Award Talk: Surface Chemistry and Structure of Alloy Thin Films under Reaction Conditions and their Correlations to Catalytic Performances of CO₂ Conversion and Methane Partial Oxidation, F. Tao*, University of Notre Dame

Formation of alloys is one of the important approaches to design of new catalysts with high activity and selectivity as a second metal could tune electronic structure of the first metal or/and create thermodynamically favorable sites for an ideal reaction channel. Co-Ru alloys are active catalysts for conversion of CO₂ into fuel molecules CH₄. Pd-based alloys are important catalysts for methanol partial oxidation to produce hydrogen. Thin films of model catalysts of alloys Co-Ru and Pd-Co were prepared through e-beam evaporation in UHV. In-house ambient pressure X-ray photoelectron spectroscopy using monochromatic Al K α were used to examine the evolution of surface compositions of alloy catalysts and the oxidation states of the constituting elements under reaction conditions and during catalysis in contrast to those before or after a reaction; Surface chemistry (composition and oxidation state) of active phases of Co-Ru and Pd-Co was revealed. High pressure STM provided visible information of surface structure at nano and atomic scale under reaction conditions. These studies clearly suggest a modification of Co electron state through coordinating Ru atoms and thus tuning the adsorption energy of intermediates on Co in CO₂ conversion, which enhances the selectivity to production of CH₄. The formed Co_{0.85}Ru_{0.15} alloy exhibits 100% selectivity

* Paul Holloway Award Winner

to the production of CH₄ and a conversion of 40% which is higher than both pure Co and pure Ru. The promotion effect of the alloy film for CO₂ conversion was rationalized by electronic effects of Ru to Co in the alloy thin films under reaction conditions. In terms of Pd-Co alloy catalysts, segregation of Co to surface under reaction conditions was observed. Through the measurement of surface composition using AP-XPS and the coordination of Pd on surface visualized with STM, a correlation between surface chemistry and structure of Pd-Co alloy surface under reaction conditions and the corresponding catalytic performances were built. The modification of Co to the catalytic behaviors of Pd was identified.

4:20pm **TF+AS+SS-ThA8 Time-resolved and Surface Plasmon Resonance Studies in Metal-Insulator Phase Transition in VO₂ Thin Films**, *L. Wang, C. Clavero, K. Yang, E. Radue, M.T. Simons, I. Novikova, R.A. Lukaszew*, College of William and Mary

Vanadium dioxide (VO₂) is a prominent example for a material exhibiting a metal-insulator transition (MIT) as a function of temperature with a phase transformation around 340 K from a low-temperature insulator state to a high-temperature conducting state. During the MIT the lattice structure of VO₂ transforms from a monoclinic (insulator) to a tetragonal structure (conductor). Whether these structural changes are solely responsible for the nature of the transition or whether correlation effects also play a role, has been a subject of much debate. Two mechanisms have been generally considered to explain the origin of the MIT in VO₂. The Mott-Hubbard mechanism suggests that electron-electron correlation drives the first-order MIT whereas the Peierls mechanism proposes that a strong electron-lattice interaction leads to the MIT. In order to have a better understanding of the phase transition mechanism and the optical properties of this material across the MIT, we present our research studies on epitaxial VO₂ thin films. We have investigated the optical transmission of a VO₂ thin film during the thermally induced MIT in two different optical spectral regions, with cw THz light and low power (1 mW) IR light (1520 nm HeNe), to identify different mechanisms at play. We have found that the transmission of the THz light starts to decrease at higher temperature than that of the IR light thus probing different stages during the thermally induced MIT. We also investigated surface plasmon polariton excitation in VO₂ thin films in the IR region, and observed a clear trend from non-absorption in the insulator phase to a high absorption in the metallic phase while changing the VO₂ temperature. Our studies are aimed at helping to understand the evolution of the metallic phase in VO₂ thin films after the MIT and relaxation back to the insulator phase upon the MIT which is of paramount importance for ultra-fast switch applications. Finally, we note that Cavalleri *et al.* [1] reported that the light-induced phase transition happens in less than half a pico-second thus hinting at electronic processes, although they also found that it strongly depended on pump-laser power which is suggestive of lattice interactions. We will compare our time-resolved measurements also using pump-probe techniques but with the sample held at low-temperature vs. room-temperature to illustrate the role of the pump-power on the photo-induced MIT.

[1] A. Cavalleri, Cs. Tóth, C.W. Siders, J. A. Squier, F. Ráksi, P. Forget and J. C. Kieffer, Phys. Rev. Lett. **87** (23), 237401 (2001).

4:40pm **TF+AS+SS-ThA9 Growth, Microstructure and Optical Properties of Sputter-Deposited Gallium Oxide Thin Films**, *S.K. Samala, C.V. Ramana*, The University of Texas at El Paso

Gallium oxide (β -Ga₂O₃), which is a stable oxide of gallium, is a wide band gap material. The high melting point coupled with stable structure makes of β -Ga₂O₃ the best candidate for high temperature sensing. β -Ga₂O₃ thin films can be used for developing oxygen sensors operating at higher temperatures (≥ 900 °C). This feature opens the possibility of developing the integrated of β -Ga₂O₃ based oxygen sensors for power generation systems. The present work was performed on the analysis of growth behavior, microstructure, and optical properties of β -Ga₂O₃ films grown by sputter deposition. Ga₂O₃ thin film were deposited on Si(100) and quartz substrate by varying the growth temperature from room temperature to 800 °C. The characteristic analysis of the samples was performed employing grazing incidence X-ray diffraction (GIXRD), scanning electron microscopy (SEM), and spectrophotometry measurements. GIXRD analyses indicate that the samples grown at lower temperatures were amorphous while those grown at ≥ 400 °C. SEM results indicate that the morphology evolution is dependent on the temperature. The characteristic shape of the grains changed from triangular to square and finally to spherical morphology with increasing temperature. Optical characterization indicates that the band gap varies from 4.1 to 5.1 eV as a function of increasing temperature. The correlation between growth conditions, microstructure and band gap is established.

5:00pm **TF+AS+SS-ThA10 Optical and Structural Properties of Hafnium Oxide Thin Films Prepared Using Different Deposition Techniques**, *L. Sun, N.R. Murphy, J.T. Grant, J.G. Jones, R. Jakubiak*, Air Force Research Laboratory

The high dielectric constant and optical transparency of hafnium oxide makes it a useful component in leading-edge integrated circuitry and optical coatings. The optical and structural properties of stoichiometric HfO₂ films vary significantly depending on the deposition mechanism. We prepared 200 nm thick films of HfO₂ on silicon (100) substrates derived from DC magnetron sputtering (DCMS), high power impulse magnetron sputtering (HiPIMS) and pulsed laser deposition (PLD). Analysis of x-ray diffraction data revealed that films deposited via PLD are amorphous, while those deposited using the magnetron sputtering methods had peaks at 2θ of 28.3°, 31.3°, 34.3° and 50.0° indicative of polycrystalline monoclinic HfO₂. This is further supported by the FT-IR data collected in the far-IR regime where absorption bands at 258, 341, 410 and 514 cm⁻¹ were present. AFM and SEM images indicate that the sputtered samples had rougher surface morphology and larger grain sizes than the PLD films where the surface was uniform and smooth (RMS surface roughness less than 0.1nm). The degree of surface roughness and grain size is inversely proportional to the refractive index. At 632 nm PLD films had an index of refraction of 2.10 while the index of the sputter coated films was 1.98, presumably due to presence of voids. The high refractive index and homogeneity of the PLD films indicate that they were highly packed without voids during growth. Additionally, the influence of the O₂/Ar ratio, working pressure, HiPIMS pulse profile and duty cycle on optical properties, surface roughness, particle size and structural properties of the HfO₂ thin films were characterized and evaluated.

5:20pm **TF+AS+SS-ThA11 Nitrogen Induced Changes in the Structure and Electronic Properties of WO₃ Thin Films**, *C.V. Ramana, R.S. Vemuri*, The University of Texas at El Paso, *M. Engelhard, S. Thevuthasan*, Pacific Northwest National Laboratory

Tungsten oxide (WO₃) is a wide band gap semiconductor (~ 3.2 eV), which exhibits excellent physical, chemical and electronic properties. WO₃ thin films have been widely used in electrochromics and chemical sensors. Recently, the band gap modification with anionic and cationic doping of WO₃ was gained importance to utilize these materials in photo-catalysis for energy production and utilization. The present work was performed on nitrogen incorporated WO₃ (N-WO₃) films to explore the options to engineer the microstructure and electronic properties. Specifically, the effect of nitrogen incorporation and processing parameters on the microstructure evolution and band gap of WO₃ thin films is investigated. The samples were grown using reactive RF magnetron sputtering where the nitrogen concentration in the films is varied by varying partial pressure of nitrogen during deposition while keeping all other process parameters constant. Quantitative measurements employing X-ray photoemission spectroscopy indicate the nitrogen content increases with increasing nitrogen partial pressure. Structural analysis employing grazing incidence X-ray diffraction demonstrated that the nitrogen atoms embedded in WO₃ crystal matrix changes the crystal-texturing and thus induce changes in the physical properties. Optical spectrophotometry analysis on the N-WO₃ films revealed a shift in the fundamental absorption edge which is in linear relation with the corresponding nitrogen concentration. The correlation between microstructure, dopant profile, dielectric constant and band gap in WO₃ films will be presented and discussed.

Thin Film

Room: 10 - Session TF+EM+SS-ThA

Applications of Self-Assembled Monolayers and Layer-by-Layer Assemblies

Moderator: M.R. Linford, Brigham Young University

2:00pm **TF+EM+SS-ThA1 Light-Directed Nanosynthesis: Near-Field Optical Approaches to Integration of the Top-Down and Bottom-Up Fabrication Paradigms**, *G.J. Leggett*, University of Sheffield, UK
INVITED

The integration of top-down (lithographic) and bottom-up (synthetic chemical) methodologies remains a major goal in nanoscience. At larger length scales, light-directed chemical synthesis, first reported two decades ago, provides a model for this integration, by combining the spatial selectivity of photolithography with the synthetic utility of photochemistry. Work in our laboratory has sought to realise a similar integration at the nanoscale, by employing near-field optical probes to initiate selective chemical transformations in regions a few tens of nm in size. A combination of near-field exposure and an ultra-thin resist yields exceptional

performance: in self-assembled monolayers, an ultimate resolution of 9 nm (ca. $\lambda/30$) has been achieved. A wide range of methodologies, based on monolayers of thiols, silanes and phosphonic acids, and thin films of nanoparticles and polymers, have been developed for use on metal and oxide surfaces, enabling the fabrication of metal nanowires, nanostructured polymers and nanopatterned oligonucleotides and proteins. Strategies based upon the use of nitrophenyl-based photocleavable protecting groups have enabled the introduction of synthetic chemical methodology into nanofabrication. Nanoscale control of chemistry over macroscopic areas remains an important challenge. Recently parallel near-field lithography approaches have demonstrated the capacity to pattern macroscopic areas at high resolution, yielding feature sizes of ca. 100 nm over an area four orders of magnitude larger; they have also demonstrated the ability to function under fluid, yielding feature sizes of ca. 70 nm in photoresist under water and suggesting exciting possibilities for surface chemistry at the nanoscale. Finally, the monolayer patterning methods we have developed are by no means restricted to near-field lithography; all that is required is a suitable means of confining the optical excitation. For example, SAM photochemistry has been combined with interferometric exposure to facilitate the fabrication of periodic nanostructures over macroscopic areas in fast, simple, inexpensive processes, underlining the versatility of photochemistry as a nanofabrication tool.

2:40pm **TF+EM+SS-ThA3 Molecular Layer Deposition (MLD) of Polymer Multiple Quantum Dots on TiO₂**, *T. Yoshimura, S. Ishii*, Tokyo University of Technology, Japan

[Introduction] We previously proposed oxide-semiconductor-based sensitized solar cells, in which polymer multiple quantum dots (MQDs) are utilized for sensitizing layers, and fabricated the polymer MQDs on glass substrates by Molecular Layer Deposition (MLD) [1]. In the present study, we grew polymer MQDs on TiO₂ by MLD. The polymer MQD growth on TiO₂ was confirmed by photoluminescence (PL) spectra.

[Proposed Solar Cells Sensitized by Polymer MQDs] The proposed sensitized solar cell consists of an oxide semiconductor layer and polymer MQDs on the surface. The polymer MQD contains different-length quantum dots (QDs) in the backbone wire, and consequently, a wide absorption band is obtained by superposition of narrow absorption bands of the individual QDs. This spectral division with the narrow bands can reduce the energy loss arising from the heat generation due to excess photon energy in light absorption processes.

[Absorption/Photoluminescence Spectra of Polymer MQDs] Reference samples of poly-azomethine (AM) and polymer MQDs: OTPTPT, OTPT, and OT were grown on glass substrates by connecting terephthalaldehyde (TPA), *p*-phenylenediamine (PPDA), and oxalic dihydrazide (ODH) with designated orders using MLD. The QD lengths in OTPTPT, OTPT and OT are respectively ~ 3 , ~ 2 and ~ 0.8 nm. With decreasing the QD length, while the absorption peak shifts to high-energy side due to the quantum confinement, the PL peak shifts to low-energy side due to the Stokes shift. Namely, in the order of poly-AM to OT, the electrons become highly localized to increase the surrounding atoms' displacement caused by the electron transitions, resulting in the Stokes shift enhancement.

[Growth of Polymer MQDs on TiO₂] We performed MLD to grow poly-AM on ZnO and TiO₂ powder layers. A yellow film of poly-AM was observed on TiO₂. For ZnO, however, no film growth was observed because of weak hydrophilic characteristics of ZnO surfaces. We grew poly-AM and polymer MQDs of TO on the TiO₂ powder layers by MLD, and measured their PL spectra. The PL spectrum of TO was located at lower-energy side than that of poly-AM, which is parallel to the tendency observed in the PL spectra of the reference samples. From this result, it is concluded that polymer MQDs can be grown on TiO₂ by MLD as the sensitizing layers for solar cells.

[1] T. Yoshimura, R. Ebihara, A. Oshima, "Polymer Wires with Quantum Dots Grown by Molecular Layer Deposition of Three Source Molecules for Sensitized Photovoltaics," *J. Vac. Sci. Technol. A*, **29**: 051510-1-6 (2011).

3:00pm **TF+EM+SS-ThA4 Thiol-yne Click Chemistry: Old Concept & New Applications in Surface Science**, *N.S. Bhairamadgi, H. Zuilhof*, Wageningen University, Netherlands

Click chemistry reactions have opened new horizons in the field of surface chemistry, as these reactions are easy to perform on surfaces. A nice example is the addition of thiol moieties onto C=C bonds, which have been shown to be highly efficient, orthogonal to many other reactions, highly selective, etc. Recently we and others have shown that thiol-ene click reactions can be used efficiently for the modification of semiconductor surfaces and nanoparticles with a wide range of materials. In the current presentation we show an improved procedure involving C=C bonds, i.e. thiol-yne click reactions.

We modified oxide-free Si(111) surfaces with alkene-terminated and alkyne-terminated monolayers, and these surfaces were further modified

with various thiols such as thioglycolic acid, thioacetic acid, thioglycerol, thio- β -D-glucose tetraacetate lactose and 9-fluorenylmethoxy-carbonyl cysteine by using thiol-ene and thiol-yne click reactions. Upon detailed surface analysis it was found that after some optimization the thiol-yne click reaction yielded 20 – 80 % more surface coverage compared to thiol-ene click reactions. Thus surface modification with thiol-yne click reactions promise to be the next step in surface-bound thiol click chemistry.

References:

1. Campos, M. A. C.; Paulusse, J. M. J.; Zuilhof, H., Functional monolayers on oxide-free silicon surfaces via thiol-ene click chemistry. *Chem. Commun.* 2010, 46 (30), 5512-5514.
2. Lowe, A. B.; Hoyle, C. E.; Bowman, C. N., Thiol-yne click chemistry: A powerful and versatile methodology for materials synthesis. *J. Mater. Chem.* 2010, 20 (23), 4745-4750.
3. Ruizendaal, L.; Pujari, S. P.; Gevaerts, V.; Paulusse, J. M. J.; Zuilhof, H., Biofunctional Silicon Nanoparticles by Means of Thiol-Ene Click Chemistry. *Chem. Asian J.* 2011, 6 (10), 2776-2786.
4. Wendeln, C.; Ravoo, B. J., Surface Patterning by Microcontact Chemistry. *Langmuir* 2012, 28 (13), 5527-5538.
5. Wendeln, C.; Rinnen, S.; Schulz, C.; Arlinghaus, H. F.; Ravoo, B. J., Photochemical Microcontact Printing by Thiol-Ene and Thiol-Yne Click Chemistry. *Langmuir* 2010, 26 (20), 15966-15971.

3:40pm **TF+EM+SS-ThA6 Attachment of Conjugated Diruthenium Alkynyl Compounds by Click Chemistry**, *S. Pookpanratana*, National Institute of Standards and Technology, *S.P. Cummings, T. Ren*, Purdue University, *C.A. Richter, C.A. Hacker*, National Institute of Standards and Technology

Attaching electrochemically-active molecules to a variety of different surfaces is of particular interest for applications in photovoltaic devices, catalysis, and molecular electronics. The family of diruthenium 2-anilino-pyridinate (ap) molecules is redox active [1], which makes it an ideal candidate to incorporate on surfaces for molecular catalysis, photoelectrochemical cells for water splitting, and as an active component in molecular electronic devices. Often times, the attachment of a tailored-molecule requires the additional design challenge to incorporate a specific anchoring group (e.g., thiol). Click chemistry has been demonstrated as an effective method to incorporate bulky and complex molecules to a variety of surfaces [2-6]. This route has introduced numerous possibilities of tailoring molecular surfaces.

Here, we have employed a Cu-catalyzed azide-alkyne cycloaddition (CuAAC) click reaction to attach Ru₂(ap)₄-(C=C-C₆H₄-C≡CH), (henceforth referred to as Ru₂-alkynyl) to Au and SiO₂ surfaces. First, we form an azide-terminated monolayer on Au and SiO₂ by using azidoundecanethiol and azidoundecyl trimethoxysilane, respectively. Next, the Ru₂-alkynyl is linked to the azide-containing monolayers via a CuAAC reaction (adapted from Ref. 4). The clicked-on Ru₂-alkynyl molecule was physically characterized by X-ray photoelectron spectroscopy (XPS) and infrared (IR) spectroscopy. The formation of the azide monolayer on Au and SiO₂ surfaces is confirmed by IR measurements. After the CuAAC click reaction of the Ru₂-alkynyl to the azide-treated surfaces, there is a reduction of the azide stretch in the IR which indirectly confirms the progress of the click reaction. The incorporation of Ru₂-alkynyl is confirmed by XPS, where we estimate the Ru₂-alkynyl covers about 10% of the azide sites.

The formation of molecular electronic junctions (Au/Ru₂-alkynyl/Si structures) by flip-chip lamination [7] for electrical and backside IR [8] characterizations is currently ongoing. With these results, we are able to obtain a thorough picture linking electrical properties with physical and chemical structure of the diruthenium molecular junctions.

S. P. Cummings et al., *Organometallics* **29**, (2010) 2783 – 2788.

R. Chelmoski et al., *Langmuir* **25**, (2009) 11480-11485.

G. Qin et al., *J. Am. Chem. Soc.* **132**, (2010) 16432-16441.

R. E. Ruther et al., *J. Am. Chem. Soc.* **133**, (2011) 5692 – 5694.

A. C. Cardiel et al., *ACS Nano* **6**, (2012) 310-318.

P. K. B. Palomaki and P. H. Dinolfo, *Langmuir* **26**, (2010) 9677 – 9685.

M. Coll et al., *J. Am. Chem. Soc.* **131**, (2009) 12451-12457.

C. A. Richter et al., *J. Phys. Chem. B* **109**, (2005) 21836 - 21841.

4:00pm **TF+EM+SS-ThA7 Vapor Phase Surface Functionalization using Hybrid SAMs / ALD Heterostructures**, *L. Lecordier, M.J. Dalberth, G. Sundaram, J.S. Becker*, Cambridge Nanotech, Inc.

Self-assembled monolayers and atomic layer deposition are two methodologies commonly used to tailor surface properties at the atomic scale and achieve thin films with excellent electrical, chemical, mechanical

or optical performances thus leading to a broad portfolio of applications from thin films for flexible electronics to biological surface functionalization.

While ALD film growth is the result of a discretized process where inorganic monolayers are built upon one another through a sequence of reactant exposure/purge cycles until the desired film thickness is achieved (typically 1-100nm), SAMs on the other hand allow the deposition of a single ordered organic monolayer. Both processes are driven by self-limited chemisorbed surface reactions and can be deposited under vacuum conditions at relatively low temperatures, facilitating the integration of these two processes on a single platform.

The current work was implemented on a commercial Cambridge Nanotech hybrid ALD/SAMs platform. The tool is based on a Savannah S200 ALD reactor and integrates a SAMs kit for the accurate delivery of a variety of SAMs reactants. Stable SAMs monolayers are deposited under vacuum conditions using exposure mode (EXPO) characteristic of Cambridge Nanotech ALD tools. Key process metrics such as precursor pulse and exposure times, source and reactor temperatures were investigated for a variety of precursors including non-polar hydrophobic alkylsilanes (DTS), oleophobic fluorinated silanes (FOTS), hydrophilic polyethylene glycol (PEG) and thiols. In all cases, the self-limited surface saturation was achieved within 1 to 15 min minute exposures to the precursor at temperature ranging from 50 to 110°C.

In some instances, oxide ALD films were used to deposit a very thin seed layers (<5Å) to promote the adhesion of a SAM without prior surface cleaning/conditioning. Heterostructures based on oxide ALD (Al₂O₃, ZrO₂, SiO₂) and SAMs were also obtained to develop efficient water moisture barriers to be used for encapsulation. Overall the integration of these processes in a single platform provides a versatile and scalable method to surface functionalization where surface properties such as wettability can be tuned by controlling at the atomic level the structures of these hybrid coatings.

4:20pm **TF+EM+SS-ThA8 Chemically and Mechanically Stable Hydrophobic Thin Films Prepared by Combination of Layer-By-Layer Approach and Thiolene Chemistry, N. Madaan, J.A. Tuscano, N.R. Romriell, M.R. Linford**, Brigham Young University

The current aim of our research is to create robust hydrophobic thin films, for glass/silicon substrates, which can withstand extreme pH conditions and temperatures, have good release properties, and at the same time are mechanically durable. This approach consists of deposition of 3-aminopropyltriethoxy silane (APTES) on a silicon substrate followed by layer-by-layer deposition and cross-linking of alternating layers of poly(acrylic acid) (PAA) and poly(allylamine hydrochloride) (PAH). These nylon-like cross-linked layers have already been demonstrated to possess stability in extreme pH conditions. Their permeability can be controlled by the extent of crosslinking, which depends on the time and temperature of crosslinking. A careful study using X-ray photoelectron spectroscopy in our lab showed 71% cross-linking when these assemblies were heated at 250 °C for 2 h. We also found that the ratio of ammonium to amine groups in these bilayers is 2:1, and that there is a potential to impart additional properties to the films by utilizing these residual amine groups. This was part of an experimental design over a series of times and temperatures. These substrates can further be modified using a variety of chemistries. One approach is to expose these substrates to basic NaOH solution (pH ~ 10) in order to deprotonate the ammonium groups of the terminal PAH layer followed by treatment with Traut's reagent to convert amine groups into thiol groups. The thiol groups are then reacted with 1,2-polybutadiene and a perfluoroalkanethiol using thiol-ene chemistry. Another approach is to use hydrolyzed poly(maleic anhydride alt 1-octadecene) as a terminal electrostatic anionic layer. A chemical and tribological stability comparison will be performed between the above prepared films and a perfluoroalkane silane film on Si substrates. The effect of the total thickness of cross-linked PAH-PAA bilayers on the stability of prepared films will be studied. The substrates are thoroughly analyzed at each surface modification step using X-ray photoelectron spectroscopy, time-of-flight secondary ion mass spectrometry, ellipsometry, water contact angles, and atomic force microscopy.

4:40pm **TF+EM+SS-ThA9 A Detailed Investigation of the Conditions for Monolayer Deposition from Silane Precursors, J. Knauf**, Advanced Molecular Films GmbH / RWTH Aachen University, Germany, L. Reddemann, Advanced Molecular Films GmbH / Universität zu Köln, Germany, A. Böker, RWTH Aachen University, Germany, K. Reihls, Advanced Molecular Films GmbH, Germany

We have systematically investigated the process parameters for the vapor-phase deposition of monolayers from fluoroalkylated silane precursors. Our study reveals the influence of many process parameters on the molecular structure of the monolayers. Of particular interest to us are wetting and

frictional properties of the monolayer obtained from the variation of process conditions. For reproducibly preparing high quality films particular parameters have to be meticulously controlled in a very narrow range which is not achievable without advanced deposition equipment.

Although the deposition of monolayers from silane precursors has been accomplished by various methods and has been subject to numerous studies, the properties and reproducibility of the resulting films remain unsatisfying for many applications. As an example, fluid wall slippage strongly depends on small changes in monolayer processing conditions which sensitively influence the structure of the monolayer deposited on structured surfaces [1].

Self-assembled monolayers (SAMs) were prepared by controlling a variety of process parameters, such as processing sequence and partial pressures of reactive compounds, deposition temperatures, adsorption/desorption times. These conditions were investigated for linear fluoroalkylated silane precursors of different chain lengths.

SAMs were deposited from fluoroalkylated silane precursors on pre-treated Si-wafers. Samples were examined by dynamic contact angle measurements, x-ray photoelectron spectroscopy (XPS), and static secondary ion mass spectrometry (sSIMS). The precursors applied were linear 1H,1H,2H,2H-Perfluoroalkyltrichlorosilanes and varying chain lengths of the fluoroalkyl part were used for comparative studies based on detailed investigations using 1H,1H,2H,2H-Perfluorodecyltrichlorosilane. Short-chain precursors were commercially available in ready-to-use quality whereas longer-chain compounds starting from 1H,1H,2H,2H-Perfluorododecyltrichlorosilane were synthesized in our labs. While the short-chain compounds could be processed by routine measures special precautions had to be applied for storage and handling of longer-chain compounds due to their higher reactivity.

Results of the study of deposition conditions will be presented and discussed and may serve as a guideline for the reproducible preparation of well-defined monolayers from silane precursors.

[1] L. Reddemann, J. Knauf, A. Böker, K. Reihls, 14th International Conference on Organized Molecular Films (ICOMF14) - LB14, Abstract 146 (2012)

5:00pm **TF+EM+SS-ThA10 Self Limiting Behavior in the Directed Self-Assembly of Mounds on Patterned GaAs(001), C.-F. Lin**, University of Maryland, C.J.K. Richardson, Laboratory for Physical Science, H.-C. Kan, University of Maryland, N.C. Bartelt, Sandia National Laboratories, R.J. Phaneuf, University of Maryland

We present results demonstrating directed self assembly of nm scale mounds during molecular beam epitaxial growth on patterned GaAs(001) surfaces. In the initial stages of growth, a lithographically-defined pattern directs the spontaneous formation of multilayer islands at the centers of bridges between near-neighbor nanospots along [110] crystal orientation, seemingly due to the presence of an Ehrlich-Schwoebel barrier. As growth continues, the heights of mounds at these 2-fold bridge sites "self-limit". Beyond this point mounds at other, 4-fold bridge sites dominate the topography, but these self-limit as well. This behavior suggests the existence of a minimum, 'critical terrace width' for nucleation of islands during growth, and provides a physical mechanism for understanding the transient nature of the observed instability during growth on these patterned surfaces

5:20pm **TF+EM+SS-ThA11 Characterization of Fully Functional Spray-on Antibody Thin Film, J.J. Figueroa, S. Magana, D. Lim, R. Schlaf**, University of South Florida

Physical adsorption (solid-liquid interface) is known as a simple and rapid option to immobilize biomolecules on various surfaces. Proteins, receptors and antibodies are attached via physisorption to different surfaces by various attachment protocols. However, physical adsorption has been often labeled in the past with disadvantages like variability, reversibility and low surface density of immobilized biomolecules. In contrast, the presented research demonstrates that spray deposition with a pneumatic nebulizer can be used to immobilize fully functional and stable physisorbed antibody coatings on glass surfaces with high reproducibility.

The experiments were performed using a low flow concentric nebulizer (commonly used on mass spectrometry), regular glass slides as a substrate and *E. coli* O157:H7 antibody as prototypical test system. The antibody films were examined for functionality, specificity and shelf life. A series of films with varying thickness and deposition conditions was characterized

with respect to functionality, mechanical stability, surface morphology and antibody density. The results demonstrate that the films are comparable to films prepared with the standard covalent attachment protocol (avidin-biotin). They show low denaturation or conformational changes, minimal loss during the rinsing process suggesting good attachment to the surface, and they perform as well with regard to sensitivity, specificity and shelf-life. The morphology studies suggest that the non-oriented attachment of the spray deposited antibodies (compared to the oriented attachment achieved with the covalent attachment scheme) is compensated by a higher antibody density enabled by the non-equilibrium spray deposition process.

Thursday Afternoon Poster Sessions

Electronic Materials and Processing Room: Central Hall - Session EM-ThP

Electronic Materials and Processing Poster Session

EM-ThP1 Proton Irradiation of Lattice Matched InAlN/GaN High Electron Mobility Transistors. C.-F. Lo, L. Liu, T.S. Kang, F. Ren, University of Florida, C. Schwartz, E. Flitsyan, L. Chernyak, University of Central Florida, H.-Y. Kim, J. Kim, Korea University, Republic of Korea, O. Laboutin, Y. Cao, J.W. Johnson, Kopin Corporation, P. Frenzer, S.J. Pearton, University of Florida

The DC characteristics of InAlN/GaN High Electron Mobility Transistors (HEMTs) were measured before and after irradiation with 5, 10 or 15 MeV protons at doses up to 2×10^{15} cm⁻². At 5 MeV, the on/off ratio degraded by two orders of magnitude for the highest dose, while the sub-threshold slope increased from 77 to 122 mV/decade. There was little change in transconductance or gate or drain currents for doses up to 2×10^{13} cm⁻², but for the highest dose the drain current and transconductance decreased by ~40% while the reverse gate current increased by a factor of ~6. The minority carrier diffusion length was around 1 μm independent of proton dose. The InAlN/GaN heterostructure is at least as radiation hard as its AlGaIn/GaN counterpart.

EM-ThP2 Effects of 2MeV Ge⁺ Irradiation on AlGaIn/GaN HEMTs. E.A. Douglas, P. Frenzer, S.J. Pearton, C.-F. Lo, L. Liu, T.S. Kang, F. Ren, University of Florida, E. Bielejec, Sandia National Laboratories

The DC characteristics of AlGaIn/GaN High Electron Mobility Transistors (HEMTs) were measured before and after irradiation with 2 MeV Ge⁺ ions at doses from 5×10^{10} to 5×10^{12} cm⁻². The drain current, gate leakage current and transconductance decreased monotonically with dose, while the drain-source resistance increased to a much greater extent than observed previously for proton irradiation of similar devices. The gate leakage current decreased with dose, as shown above. To understand the mechanism, we probed on-chip transmission line method (TLM) patterns receiving the same dose. Those irradiated with 5×10^{10} cm⁻² showed in a ~4x increase in sheet resistance and a 75% decrease in specific contact resistance. TLM patterns irradiated at 5×10^{11} cm⁻² and 5×10^{12} cm⁻² showed nA current (100mA prior to irradiation). Threshold voltage shifted to more positive values for increasing dose. There was no systematic effect of gate width or length (gate length from 0.1 to 1 micron and width from 100-200 micron) on the degree of degradation in device parameters. Reverse recovery switching times in the HEMTs were unaffected by the Ge⁺ fluences we investigated. In contrast to proton implantation with moderate doses, which does not lead to high sheet resistivities of the implanted layers, the use of heavier ions like Ge⁺ causes the sheet resistivity to be greatly increased. The basic degradation mechanism is still carrier loss from the channel as a result of trap formation in the AlGaIn layer and in the GaN buffer.

EM-ThP3 Influence of AlInN Buffer Layer Thickness on the Properties of GaN Films on Si(111) Substrate using RF Metal-Organic Molecular Beam Epitaxy. W.C. Chen, C.T. Lee, C.-N. Hsiao, Instrument Technology Research Center, National Applied Research Laboratories, Taiwan

Hexagonal structure GaN films were grown on silicon (111) substrate by radio-frequency metal-organic molecular beam epitaxy with Al_xIn_{1-x}N buffer layers. We discussed the influence of AlInN buffer layer thickness on properties of GaN films. The thickness of the AlInN buffer layer can effectively counteract the tensile stress usually observed in the GaN layer deposited on Si(111). For a 10-nm-thick AlInN, crack density of 2.4×10^5 /mm and a crystalline quality of 150 arcmin are obtained. Also, the average layer thicknesses measured about 300 nm, and the growth rate about 0.2 μm/hr. Also, Strong band-edge emission from GaN on Si(111) is observed at 3.39 eV with 70 nm-thick AlInN interlayer. The reduced lattice mismatch between the GaN film and Si(111) is responsible for improvement of GaN quality using the buffer-layer technique.

EM-ThP4 Morphological Study of GaN Films Grown Under ALD Process Conditions as Well as Both Over- and Under- Saturated Growth Conditions. J.C. Revelli, T.J. Anderson, University of Florida

Gallium Nitride films were grown by pulsed deposition of GaCl₃ and NH₃ using nitrogen as both carrier and purge gas. The pulse and purge times leading to self-limiting, ALD-mode growth were investigated at 585°C. ALD growth conditions led to a constant thickness increment per cycle. The ALD conditions were determined to be a 3-6 second GaCl₃ pulse, a 30

second NH₃ pulse, and 30 second nitrogen purge times in between. The surface morphology of all films were examined by AFM. ALD films showed RMS surface roughness of 0.3nm, similar to that of the underlying (0002) sapphire substrate, while films that had a GaCl₃ pulse below 3 seconds had an RMS roughness of 0.5nm and films oversaturated with GaCl₃ had an RMS roughness of 1.2nm. This result suggests that ALD can be used as a rapid and non-destructive method to identify ALD growth conditions.

EM-ThP5 Structural, Compositional, and Thermal Stability Studies on In_{1-x}GaN Epilayers. A. Acharya, Georgia State University, M. Buegler, Technical University of Berlin, Germany, S.D. Gamage, N. Dietz, B. Thoms, Georgia State University

The structural and compositional properties of indium gallium nitride (InGaN) epilayers grown by high-pressure chemical vapor deposition have been studied using x-ray diffraction (XRD), Auger electron spectroscopy (AES) and high-resolution electron energy loss spectroscopy (HREELS). In addition, the thermal stability of the epilayers have been studied using temperature programmed desorption (TPD). The XRD pattern shows the InGaN (0002) Bragg reflex at 31.38 deg, indicating single-phase InGaN epilayers. Both XRD and AES measurements indicate a composition x of 4% gallium. The HREELS spectra of atomic hydrogen-exposed surfaces exhibit modes assigned to a surface N-H species, which were confirmed by observation of isotopic shifts following exposure to atomic deuterium. No In-H or Ga-H vibrations were observed suggesting the epilayer is N-polar. The thermal desorption study indicated that nitrogen desorption from the sample starts at 625 °C and peaks at 740 °C. No significant desorption of NH₃/NH₂⁺ fragments have been observed. From an Arrhenius plot, an activation energy for the desorption of nitrogen of 1.14 ± 0.06 eV was found.

EM-ThP6 The Influence of the Group V/III Molar Precursor Ratio on the Structural and Optoelectrical Properties of InN Epilayers Grown by High-Pressure CVD. R. Atalay, Georgia State University, M. Buegler, Technische Universität Berlin, Germany, S.D. Gamage, M.K.I. Senevirathna, Georgia State University, G. Durkaya, University of California Irvine, L. Su, UNC Charlotte, A.G.U. Perera, Georgia State University, I. Ferguson, UNC Charlotte, N. Dietz, Georgia State University

Over the last two decades, significant research efforts have been devoted to understand and improve the physical properties of InN epilayers. However, even today, there is still a significant lack of understanding how the different partial pressures of the precursor fragments of trimethylindium and ammonia affect the InN surface and growth chemistry and influence the materials properties.

In this study, high-pressure chemical vapor deposition (HPCVD) is used to control and suppress the disassociation of InN alloys at higher growth temperatures, together with a pulsed precursor injection approach to reduce gas phase reactions and to control the surface chemistry. In this contribution, we will present results on the influence of the group V/III molar precursor ratio on the structural and optoelectronic properties of InN epilayers grown on sapphire substrate with a reactor pressure of 8 bar. The group V/III molar precursor ratio was studied in molar V/III-ratio range of 900 to 3600. The structural analysis show for molar V/III-ratio of 2400 an optimum with, Raman and XRD having the lowest FWHM of 7.53 cm⁻¹ and 210 arcsec, respectively. The XRD results indicate improved grain size and reduced strain effect. Optical FTIR reflectance analysis of this epilayer found a free carrier concentration of 1.7×10^{18} cm⁻³, a mobility of 1020 cm² V⁻¹ s⁻¹ and a growth rate of 120 nm/h. The Raman analysis for these epilayers indicate that the non-polar phonon frequency with symmetry of E₂ is changes little within the studied molar V/III precursor ratio range; however, the polar phonon modes of both transverse optical (TO) and longitudinal optical (LO) are affected significantly. The studies showed also reveal that LO-phonon is influenced from the free carrier concentration (n_e) and TO-phonon is influenced from the free carrier mobility (μ). In addition, surface morphology studies by AFM show an improved average grain size of 8.51×10^{-2} μm² for the molar V/III-ratio of 2400.

EM-ThP7 Prototype of Junctionless Transistor on SOI Wafers using Focused Ion Beam Milling. L. Petersen Barbosa Lima, J. Alexandre Diniz, I. Doi, J. Godoy Filho, State University of Campinas, Brazil, H. Ivanov Boudinov, University of Rio Grande Do Sul, Brazil

Nowadays, Junctionless devices (JL) have gained much attention of microelectronics industry, because it is compatible with CMOS technology and can be useful for 3D devices. In this context, nMOS JL devices were fabricated on SOI substrates using Ga⁺ Focused Ion Beam (FIB) milling and for depositions of SiO₂ (gate dielectric) and Pt layers (as gate, drain and source electrodes) of JL transistor. In this work, two methods to fabricate

the JL devices were used. One method is using on FIB system to milling the Si substrate and the other method used Reactive Ion Etching (RIE) and FIB system to etch the Si substrate. The samples with only FIB system were called JLFIB and samples with RIE plasma etch and FIB system were called JLRFB. First of all, the wafers JLFIB and JLRFB were doped with phosphorus, dose 10^{19} cm⁻³ and energy of 30 KeV, using ion implantation system. After that, Rapid Thermal Annealing (RTA) were used to anneal the SOI samples after the ion implantation procedure. 0.6- μ m-thick SiO₂ were obtained using a wet oxidation on conventional furnace to get thinner height of Si substrate on SOI wafer. So, lithography to define MESA structures and RIE Si etching were carried out only on JLRFB samples. Then JLFIB and JLRFB samples were insert on FIB system to get the JL fabrication. First of all, using a Ga⁺ ion beam the Si substrates were milled to obtain the Si nanowire to define the gate, drain and source regions of JL transistor. Width, length and height dimensions of Si nanowire were about 100 nm, 4 μ m and 50-80 nm, respectively. Then, 10-nm-thick SiO₂ was deposited to be gate dielectric and finally, Pt were deposited to be gate, drain and source electrodes. Energy Dispersive X-Ray Spectroscopy (EDS) measurements were carried out to confirm the surface composition of Si nanowire, SiO₂ gate dielectric deposition and Pt electrodes deposition. In addition, EDS results show some Ga incorporation on Si nanowire surface, however, this incorporation was derived from Ga⁺ FIB and no significant damage on Si nanowire was occurred. Finally, these devices were sintered in a conventional furnace in forming gas at 450°C for 10 and 20 minutes. Drain-source current (I_d) x drain-source voltage (V_{ds}) measurements of JLFIB and JLRFB devices were carried out, and indicate that the devices are working, like a gated resistor or JL device, with high Pt source and drain contact resistances, which lead to the distortions of I_d x V_{ds} curves. However, these distortions can be reduced using a longer time of contact sintering process and a Si nanowire height lower than 50 nm. Finally, our fabrication method using FIB process steps can be used to obtain JL devices.

EM-ThP8 Simulation of Millisecond Laser Anneal on SOI: A Study of Dopant Activation and Mobility and its Application to Scaled FinFET Thermal Processing. *T. Michalak, J. Herman, M. Rodgers, D. Franca, C. Borst*, University at Albany-SUNY

Next generation CMOS requires high activation and hyper-abrupt junction formation for low sheet resistance and device performance. The primary method of doping, ion implantation, provides excellent spatial control of dose. A high temperature anneal (>1000° C) is required to remove defects introduced from ion implantation and to electrically activate the implanted specie. A “diffusionless anneal” by which dopant is activated without significantly diffusing, would be ideal for ultra-shallow junction (USJ) formation. This work investigates one such technique, laser annealing, which uses a scanning laser to locally heat the wafer surface. We investigate the laser system via simulation to determine the peak temperature achieved in the active area during processing. We employed the Sentaurus TCAD software by Synopsys to perform a 2D simulation of a laser scanning across the active area of the device, solving the heat equation in both time and space (Fig 1). An absorber layer is deposited on the wafer surface to encourage the absorption of optical power and consequent heating of the wafer surface. An effective absorption coefficient of $\alpha=8861$ cm⁻¹ was calculated for the absorber layer, calibrated with the experimental laser intensity of 52526 W/cm² required to melt silicon at a scan speed of 150 mm/s which lies within the range for amorphous carbon stated in literature (Fig 2). This absorption coefficient correctly predicts the silicon temperature as a function of power with any arbitrarily defined scan speed (Fig 3). To investigate the role of dopant activation, an SOI wafer was implanted at 25 keV, dose $3e15$ cm⁻² and laser annealed in stripes of target temperatures ranging from 1100-1300 °C. The sheet resistance was measured on wafer showing Rs improvement with increasing laser temperature (Fig 4). The extracted temperature cycle from the 2D heat simulation was used as an equivalent millisecond RTA in a full 3D finFET process simulation to study dopant distribution and activation using Sentaurus Process Kinetic Monte Carlo (KMC), considering the effect of dopant clusters and point defects. The results of this simulation, supplemented with Hall mobility measurement and secondary ion mass spectroscopy (SIMS), show that there is no further activation of arsenic with increasing laser temperature (~ 25%) which suggests healing of the implant crystal damage may be reducing sheet resistance. As well, an electrical device simulation of the finFET was performed to compare device performance between RTA and laser annealing (schematic Fig 5). Simulation results show a theoretical improvement in drive current with the laser process over standard RTA.

EM-ThP9 Equivalent-Circuit Model for Vacuum Ultraviolet Irradiation of Dielectric Films. *H. Sinha, J.L. Shohet*, University of Wisconsin-Madison

VUV irradiation causes electron photoemission from dielectrics. Photoemission occurs from defect states in the dielectric band gap and results in trapped positive charges. We propose an equivalent-circuit model using which, once the circuit parameters are determined, charging of dielectric materials under VUV irradiation can be predicted. The circuit includes a dielectric capacitor, the intrinsic and photo conductivities of the dielectric and substrate, and the processes of photoemission and photoinjection. The model has the back of the substrate grounded through an ammeter to the vacuum chamber. The ammeter reads the substrate current. To simulate the circuit between the dielectric sample and the vacuum chamber that collects photoemitted electrons, a photodiode is used. The sample itself, *i.e.* the dielectric deposited on a Si substrate, is represented by a combination of capacitors, resistors and dependent voltage sources. An ideal dielectric can be expressed as a parallel-plate capacitor. However in a real dielectric leakage currents are present due to defect states. Thus, we include a resistor in parallel to the capacitor that represents the intrinsic conductivity. In addition, photoconductivity is introduced in the dielectric during VUV radiation, which is shown by another resistor in parallel to the capacitance. A dependent voltage source models the electron depopulation from the defect states. We represent the substrate, which is a semiconductor, by a resistor. This resistor signifies the intrinsic resistance. As VUV photons also cause electron-hole pair generation in substrate, a resistor as a photoconductivity component is added in parallel to the intrinsic resistor. The circuit components were determined using experimental photoemission/substrate current data for SiCOH. The prediction of photoemission/substrate current using the model was found to match experimental results over different thickness of SiCOH. To conclude, an equivalent circuit can model the effect of VUV radiation on charging and currents in dielectrics.

This work has been supported by Semiconductor Research Corporation under Contact No. 2008-KJ-1871 and the National Science Foundation under Grant CBET-1066231. The UW-Madison Synchrotron is funded by NSF under Grant DMR- 0537588.

EM-ThP10 Surface Photoconductivity of SiO₂ and SiCOH Induced by Vacuum Ultraviolet Radiation. *H. Zheng, M.T. Nichols, D. Pei*, University of Wisconsin-Madison, *G.A. Antonelli*, Novellus Systems, Inc., *Y. Nishi*, Stanford University, *J.L. Shohet*, University of Wisconsin-Madison

The change in the electrical surface conductivity of SiO₂ and SiCOH during exposure to vacuum ultraviolet radiation is investigated¹. To measure the change in conductivity, special fabricated patterned titanium finger “comb structures” are deposited on dielectric films and exposed to synchrotron radiation in the range of 50–300 nm, which is in the energy range of most plasma vacuum-ultraviolet radiation. For the measurements of the VUV-induced currents along the surface of the layer in between the titanium fingers, electrical connections are made from the test structure to outside circuitry through vacuum feedthroughs. A numerical simulation shows that the bulk current is too small to account for the measured values and most of the current indeed flows across the surface of the dielectric film in the test structure. By measuring the I-V curve of the comb test structures under controlled fluxes of VUV light, we determine that the measured current per unit photon-flux density is linear with applied electric field up to a saturation value that is VUV flux limited. This permits the surface conductivity to be calculated based on a simple photoconductor model. The increase in surface conductivity induced by VUV radiation can be beneficial in limiting charging damage of dielectrics by depleting the plasma-deposited charge.

This work is supported by the National Science Foundation under Grant CBET-1066231 and the Semiconductor Research Corporation under contract 2008-KY-1781. We also thank M. Severson for helping set up the VUV exposure.

¹ C.Cismaru, J.L. Shohet and J.P. McVittie, *Applied Physics Letters*, **71** 2191 (2000).

EM-ThP11 Spatial Volume Charge Distribution Measurement in Thin Dielectric Films: Electro-Acoustic Method. *D. Pei, M.T. Nichols*, University of Wisconsin-Madison, *Y. Shkel*, Commet LLC, *Y. Nishi*, Stanford University, *J.L. Shohet*, University of Wisconsin-Madison

Trapped volume charge inside dielectric films can lead to breakdown permanently damaging the dielectric film. Measurement of the spatial volume charge distribution is critical to estimate the electric field and the change in properties of dielectric films. A pulsed electro-acoustic (PEA)[1-2] method is applied to measure the volume charge distribution throughout the thickness of the thin film dielectric. In this method, a high voltage pulse signal (1 kV, 10 ns) or a sinusoidally varying high-voltage signal (4 kV, 5

kHz) is applied across a thin film of low-density polyethylene. An acoustic wave is generated by the volume charge inside the film and transmitted to each side of the film. A piezoelectric transducer on one side of the dielectric film is used as a sensor to detect and measure the arrival times of the acoustic waves in the case of pulsed excitation or the shift in phase of the detected signal in the case of sinusoidal excitation. This allows spatial resolution of both the location and magnitude of the charge distribution.

This work was supported by the Semiconductor Research Corporation under Contract No. 2008-KJ-1871 and by the National Science Foundation under Grant No. CBET-1066231.

[1] T. Maeno, T. Futami, H. Kushibe, T. Takada and C. M. Cooke "Measurement of Spatial Charge Distribution in Thick Dielectrics Using the Pulsed Electroacoustic Method" IEEE Transactions on Electrical Insulation Vol. 23 No. 3, June 1988

[2] M. Abou-Dakka, S.S. Bamji and A.T. Bulinski, "Space Charge Distribution in XLPE by TSM, Using the Inverse Matrix Technique", *IEEE Trans. Dielect. And Electr. Insul.*, vol. 4, pp. 314-320, 199

EM-ThP12 Investigation of Photoluminescent Characteristics and Structural Properties of Thin Film Zinc Silicate Doped with Manganese, K.H. Yoon, J.H. Kim, Chungbuk National University (CBNU), Republic of Korea

The photoluminescent characteristics and structural properties of manganese-doped zinc silicate ($Zn_2SiO_4:Mn$) thin films were investigated. The $Zn_2SiO_4:Mn$ films were deposited by radio frequency magnetron sputtering, followed by post-deposition annealing at temperatures of 600 - 1200 °C. The $Zn_2SiO_4:Mn$ films exhibited a pronounced optical absorption edge in the near ultraviolet wavelength region and the maximum transmittance reached approximately 0.922. The refractive index of the $Zn_2SiO_4:Mn$ films showed normal dispersion behavior. X-ray diffraction and atomic force microscopy measurements revealed that the as-deposited $Zn_2SiO_4:Mn$ films had an amorphous structure with a smooth surface morphology. The $Zn_2SiO_4:Mn$ films became crystalline after annealing at 800 °C and the crystallinity of the films was continuously improved up to 1200 °C. The annealed $Zn_2SiO_4:Mn$ films had a polycrystalline rhombohedral structure with no preferred crystallographic orientation of the crystallites. The photoluminescence spectra of the annealed $Zn_2SiO_4:Mn$ films showed broad-band emissions with a peak maximum at about 523 nm. The PL emission intensity was enhanced as the annealing temperature increased, resulting from the improvement of the crystallinity of the $Zn_2SiO_4:Mn$ films. The excitation band exhibited a peak maximum at around 243 nm in the near ultraviolet region, which was considered to be associated with the charge transfer transition of divalent manganese ion in the Zn_2SiO_4 system.

EM-ThP13 The Electrical and Thermal Properties of Nanoscale Multilayered Bi_2Te_3/Sb_2Te_3 and $Bi_2Te_3/Bi_2Te_{3-x}Se_x$ Thin Films, M. Hines, Z. Xiao, Alabama A&M University

Nanoscale multilayered Bi_2Te_3/Sb_2Te_3 and $Bi_2Te_3/Bi_2Te_{3-x}Se_x$ thin films were grown using the e-beam evaporation. The in-plane and cross-plane micro thermoelectric devices were fabricated using the clean room-based microfabrication techniques such as UV lithography. The e-beam-grown multilayered thin films and the fabricated thermoelectric devices were measured and characterized. The nanoscale multilayered Bi_2Te_3/Sb_2Te_3 and $Bi_2Te_3/Bi_2Te_{3-x}Se_x$ thin films can have much higher thermoelectric figure of merit than their bulk materials. The measurement results on the electrical and thermal properties of the nanoscale multilayered Bi_2Te_3/Sb_2Te_3 and $Bi_2Te_3/Bi_2Te_{3-x}Se_x$ thin films will be reported in the conference.

EM-ThP14 Mapping the Magnetic Detection Properties of Chip-Scale Optically Pumped Magnetometers, N. Ptschelintzew, P.H. Holloway, M.R. Davidson, University of Florida

Magnetometers have a wide range of utilization from Nuclear Magnetic Resonance (NMR), to medical applications such as the Magneto-Encephalogram (MEG), Magnetocardiography (MCG), and Magnetic Resonance Imaging (MRI). However, these techniques often depend on superconducting quantum interference detection magnetometers or the detection of a radio frequency magnetic resonance in a paramagnetic target induced while in a large field. Chip-scale, low-power optical magnetometers can improve the cost and size as well as reduce the complexity of these devices. The directional variation of sensitivity of these detectors can be exploited to make devices that can form images. We have designed and instrument that will be the functional equivalent of a portable MRI that will be capable of near real-time imaging. The inverse algorithm of mapping a series of detector responses to a magnetic "image" has been calculated and an algorithm for rapidly calculating images from sparse optical magnetometer data sets has been developed. Experimental measurement of the directional sensitivity of Rb-based optical

magnetometers will be presented. A prototype imaging system for magnetic tomography is being constructed.

EM-ThP15 Characterization of ZnO/CuO Nanolaminate Materials, S.T. King, L. Bilke, B. Oleson, J. Krueger, E. Tennyson, University of Wisconsin - La Crosse

ZnO and its alloys have shown much promise to replace ITO as the transparent conducting layer in many electrical devices. However, ZnO typically does not exhibit a low enough resistivity for such applications. Beyond doping ZnO, much work has focused on developing heterostructures in which ZnO is layered with a metal on the nanometer scale [1]. A recent study has suggested that bilayers of ZnO and Cu exhibit properties which may allow such laminate materials to be employed in photovoltaic applications [2]. However, it is apparent that these Cu interlayers will oxidize over time resulting in the formation of CuO interlayers. Therefore, the properties of ZnO/CuO laminates must be understood to determine the effects of interlayer oxidation on these materials.

The current study has employed x-ray diffraction, spectroscopic ellipsometry, UV-Vis spectroscopy, and four-point resistivity measurements to examine the effects that CuO interlayer thickness has on the structural, optical, and electrical properties of ZnO/CuO nanolaminate films deposited by reactive DC sputter deposition. Results suggest that CuO interlayers may afford similar transmittance and resistivity results as Cu interlayers thus alleviating possible difficulties incurred from interlayer oxidation in nanolaminate materials.

[1] J.S. Cho, S. Baek, and J.C. Lee; SOLAR ENERGY MATERIALS AND SOLAR CELLS, **95**, 7, 1852-1858 (2011)

[2] J.G. Lu, X. Bie, Y.P. Wang, L. Gong, and Z.Z. Ye; JOURNAL OF VACUUM SCIENCE & TECHNOLOGY A, **29**, 3, 03A115 (2011)

EM-ThP16 Small-Molecule Scaffolds for Directed Self-Assembly, P.L. Mancheno-Posso, A.J. Muscat, University of Arizona

Functionalization of oxide surfaces with vinyltrichlorosilane (VTCS, $CH_2=CH-SiCl_3$) was studied using water contact angle, ex situ ellipsometry, X-ray photoelectron spectroscopy (XPS), and atomic force microscopy (AFM). VTCS monolayers can be used as scaffolds for the deposition of a subsequent layer and keep it in close proximity to the surface due to its short length and terminal vinyl group. In this work, Si(100) samples were ultrasonically cleaned in acetone, methanol, and DI water for 5 min each. Native oxide was removed using a 1:100 (v/v) solution of 49% HF in water for 1 min. Subsequently, samples were hydroxylated with a 3:1 (v/v) solution of H_2SO_4 and H_2O_2 for 10 min at 60 °C. VTCS was adsorbed from 1:1000 (v/v) solutions in toluene, chloroform, and acetone. The layer thickness after 30 min in toluene was 47.5 ± 6.4 Å, in chloroform 7.1 ± 0.9 Å, and in acetone 4.0 ± 1.9 Å. These results suggest acetone as the most appropriate solvent to produce a monolayer. The contact angle was near 0° on the piranha-treated surface and increased to $25.3 \pm 0.5^\circ$ after VTCS adsorption. Addition of bromine atoms to the vinyl group was performed by immersing the samples in a 2% (v/v) solution of elemental bromine in dichloromethane for 2 hr. The contact angle was $63.2 \pm 3.9^\circ$ after bromination. A Br 3d XPS peak at 70.0 eV (C-Br) demonstrated the chemical modification of the unsaturated bond of the VTCS molecule. AFM roughness analysis yielded an RMS value of 0.11 nm for the VTCS monolayer. The reaction of VTCS with hydroxyl groups at the surface was demonstrated on a thick hafnia layer by the presence of XPS peaks at 102.6 eV for Si 2p and 532.3 eV for O 1s, which correspond to Si-O bonds formed by VTCS and the substrate. Oxidation of the vinyl group with potassium permanganate (5 mM) and sodium periodate (195 mM) yielded a peak at 286.6 eV for C 1s, suggesting the formation of C-OH moieties.

Energy Frontiers Focus Topic

Room: Central Hall - Session EN-ThP

Energy Frontiers Poster Session

EN-ThP1 Tungsten Carbide: Synthesis and Reactivity with Oxygen on the Nanoscale, J.B. McClimon, P. Reinke, University of Virginia

Transition metal carbides have shown considerable promise as catalysts, which is often attributed the similarities in electronic structure between noble metals and transition metal carbides. The addition of tungsten carbide to microbial fuel cells, and their use as an anode material has proven to be quite advantageous. However, the bottleneck in the use of tungsten carbide lies in the loss of function due to partial or complete oxidation of the surface. We study the reactivity of tungsten, and carbon-rich tungsten carbide clusters with oxygen to investigate the progression of oxidation. We

suggest that carbon-rich carbide surfaces are less susceptible to oxidation and can be regenerated by annealing.

The tungsten and tungsten carbide clusters are made by the co-deposition of W and C₆₀ which enables us to fine-tune composition in a wide range. The morphology and electronic structure of the surface is probed with STM in-situ, which is supplemented by chemical analysis with XPS, and structural analysis with TEM. The progression of oxidation is observed with bandgap maps with spatial resolution in the nm-range. The experiments were performed on graphite substrates, where the metal clusters remain highly mobile and do not react in the temperature regime of our work (< 650 K).

We begin with a discussion of the synthesis of clusters with compositions ranging from pure W-clusters, to carbon-rich surfaces. The cluster sizes are between 5-30 nm, and the carbon is introduced either by co-deposition of W and C₆₀ or by the deposition of fullerenes on pure W-clusters (and vice-versa). The C₆₀ aggregates to large islands and a reaction with the W-clusters is only initiated by annealing, and leads to carbon-terminated metallic clusters. The motion of fullerene molecules is reflected in the sawtooth signature of tip induced displacement, which is also a probe for the surface chemistry. The co-deposition of W and C₆₀ (and W deposition on C₆₀) leads to the formation of spherical structures whose granularity reflects the dimensions of the C₆₀ cage. We assume that the C₆₀ cage reacts with surface W but the low temperature prevents collapse. The oxidation of tungsten clusters has been observed as a function of oxygen partial pressure, and shows the progression of the reaction as a function of cluster size and surface morphology. We will present a complete set of bandgap maps, which are recorded during the oxidation at room temperature and elevated temperature for the different carbide structures. A model describing the oxidation as a function of carbide structure and composition will be presented.

EN-ThP2 F-doped ZnO Thin Films Deposited by Pulse DC Magnetron Sputtering of Zinc Target, B.-H. Liao, Instrument Technology Research Center, Taiwan, Republic of China

In this study, Fluorine doped ZnO (FZO) films were deposited on glass substrate by pulse DC magnetron sputtering of zinc targets with Ar, H₂, O₂ and CF₄ containing gas mixtures at room temperature. Increasing CF₄ gas in ZnO films can increase the carrier concentrations but slightly decrease the mobility. After introducing 1 sccm CF₄ gas in ZnO films we can get the lowest resistivity 7.6×10⁻⁴ (Ω-cm) with mobility 12.4 cm²/V-s and carrier concentrations 6.6×10²⁰cm⁻³. Besides, its average transmittance in the visible region was over 82.95%. All of the results indicate that we have found a cost effective and mass production process suitable for the application of manufacture in the real-world industry.

EN-ThP3 Photoresponse of PbS Nanoparticle - Quaterthiophene Films Prepared by Gaseous Deposition as Probed by XPS, M. Majeski, D. Pleticha, I. Bolotin, L. Hanley, University of Illinois at Chicago, E. Yilmaz, S. Suzer, Bilkent University, Turkey

Semiconducting lead sulfide (PbS) nanoparticles were cluster beam deposited into evaporated quaterthiophene (4T) organic films, which in some cases were additionally modified by simultaneous 50 eV acetylene ion bombardment. Surface chemistry of these nanocomposite films was first examined using standard X-ray photoelectron spectroscopy (XPS) and laser desorption positionization mass spectrometry. XPS was also used to probe photoinduced shifts in peak binding energies upon illumination with a CW green laser and the magnitudes of these peak shifts were interpreted as changes in relative photoconductivity. The four types of films examined all displayed photoconductivity: 4T only, 4T with acetylene ions, 4T with PbS nanoparticles, and 4T with both PbS nanoparticles and acetylene ions. Furthermore, the ion-modified films displayed higher photoconductivity, which was consistent with enhanced bonding within the 4T organic matrix and between 4T and PbS nanoparticles. PbS nanoparticles displayed higher photoconductivity than the 4T component, regardless of ion-modification. Finally, development of a new instrument is discussed that will allow analysis of films without prior exposure to air.

EN-ThP4 The Investigation of the Shunt Resistance using Conductive AFM and EL Measurements in Si Based Thin Film Solar Cells, M.H. Joo, J.M. Lee, K.H. Park, LG Electronics Advanced Research Institute, Republic of Korea

Silicon (Si)-based solar cells are of great interest for photovoltaic applications, such as bulk type, thin film type, and heterojunction type. Recently amorphous silicon based thin film solar cells have attracted much attention from researchers and engineers because of low consumption of raw materials and low temperature deposition. However, the conversion efficiency of these solar cells is still very poor compared to other types of solar cells. An improved understanding on defects in Si based thin film solar cells is required to further enhance cell performance. Due to the short exposure time and high spatial resolution, camera-based techniques, such as

photoluminescence (PL), electroluminescence (EL) and dark lock-in thermography (DLIT), have recently emerged as powerful characterization tools for the investigation of different loss mechanisms in solar cells and modules. And the combination of these techniques with high resolution electrical and structural analysis such as conductive atomic force microscopy (c-AFM) and transmission microscopy (TEM) allow for advanced studies on shunt and for determination of recombination current.

In this report, we studied the evolution of the shunt resistance in Si based thin film solar cells. The solar cell (1x1 cm²) structures have a configuration of glass/Al-doped ZnO (AZO)/ a-Si/ a-SiGe/Al. AZO and Al are top and bottom electrodes respectively, deposited with DC magnetron sputter. A-Si and a-SiGe are used for absorption layers prepared by plasma enhanced chemical vapor deposition (PE-CVD). AZO was textured for the light management before the deposition of absorption layers. For defect investigation of solar cells, we measured the samples with both EL and c-AFM. Electroluminescence is driven by injecting a constant current from a power source into the cell. After EL measurements, current distributions in the local area of the cells were evaluated with c-AFM. EL results show the recombination loss of defect area, which is correlated with high leakage current area of c-AFM results. In the result of TEM analysis, low shunt area in the cells evolved from the crack defects in absorption layers. The surface structures of AZO such as high angle textures and pinhole defects make an important role of crack evolution in the absorption layers. When the sample was controlled with low angle AZO texture and no pinhole defects, there was no recombination loss and leakage current in the cells.

EN-ThP5 Growth Methods and Applications of SiC Nanopowder and Nanowhiskers, R. Dhiman, University of Southern Denmark, E. Johnson, University of Copenhagen, Denmark, P.K. Kristensen, Aalborg University, Denmark, P. Morgen, University of Southern Denmark

Nanomaterials have in a number of cases shown physical and chemical properties differing from their macroscopic counterparts. These differences can be tailored through form and size of the nanostructured materials, related to the restriction of the electronic degrees of freedom in one-, two-, or three dimensions. In this study, nanoporous SiC has been produced through reactions at high temperatures between carbon nanoparticles and SiO gas, while SiC nanowhiskers are made from saw dust impregnated with TEOS, reacting at high temperatures in a complex set of reactions to produce SiC clusters with a high concentration of SiC nanowhiskers sticking out perpendicularly from planar areas on the clusters. After suitable separation and extraction procedures individual crystals or whiskers may be handled and studied, with SEM and TEM methods. The SiC nanopowders successfully applied as support material for Pt nanoparticles in the fuel cell technology, while the individual whiskers show very interesting mechanical properties and one-dimensional semiconductor properties. They are also currently used, in agglomerate form, as a very stable and inert type of binder material for new water-electrolysis active membrane systems.

EN-ThP6 Epitaxial Growth of ZnInON Films for Piezo-Electric-Field Effect MQW Solar Cells, K. Matsushima, Kyushu University, Japan

Multi-quantum well (MQW) solar cells belong to the most promising "third generation photovoltaics" with ultra-high conversion efficiencies at low cost. In order to approach their theoretical maximum efficiency (>50%), a significant improvement in the extraction efficiency of photo-generated carriers is important. We have recently proposed piezo-electric-field effect (PEF) MQW solar cells that utilize novel oxynitride semiconductor ZnInON (ZION) films [1,2]. Our simulation predicts that the electron-hole recombination rate in ZION-QWs is noticeably low compared to those in conventional QWs with III-V materials such as GaAs and InGaN. Here we fabricate epitaxial ZION films on GaN and ZnO templates aiming at realization of PEF-MQW solar cells. Furthermore, we also demonstrate coherent growth of ZION films in order to study the piezo-electric field in ZION-QWs which can prevent the recombination and thus enhance the extraction efficiency of photo-generated carriers.

Epitaxial ZION films were fabricated by RF magnetron sputtering, which is suitable for large-area and low-cost fabrication. Commercial GaN templates that were fabricated by metal-organic chemical vapor deposition (MOCVD) and sputtered ZnO templates were used as epitaxial substrates. The ZnO templates were fabricated by RF magnetron sputtering at 700°C in Ar-O₂ atmosphere on ZnO buffer layers that were fabricated via nitrogen mediated crystallization (NMC) in N₂-Ar atmosphere at 700°C [3,4]. On GaN and ZnO templates, ZION films were deposited in N₂-Ar atmosphere at the total pressure of 0.2-0.5 Pa. The applied RF power was 10-90 W and the deposition temperature was 400°C. The film thickness was 30-700 nm.

X-ray diffraction measurements show that the ZION films have wurtzite crystal structure and the full width at half maximum (FWHM) of rocking curve from (002) plane for the films is noticeably small of 0.115°, indicating small fluctuation of the crystalline orientation. Furthermore, measurements of reciprocal lattice map of (105) plane suggest that the

ZION films are grown coherently on GaN templates, indicating that a piezo-electric field can be generated. From these results, we conclude that ZION films are full of promise for Piezo-Electric-Field effect MQW solar cells that can be fabricated at low cost.

- [1] N. Itagaki, *et al.*, Jpn. Patent Application No. 2012-49805 (2012) (in Japanese).
- [2] N. Itagaki, *et al.*, U.S. Patent Publication No. 2010/0109002 (2010).
- [3] N. Itagaki, *et al.*, Appl. Phys. Express 4 (2011) 011101.
- [4] K. Kuwahara, *et al.*, Thin Solid Films 520 (2012) 4674.

EN-ThP7 Texture-Etched Surface Structure Control of Transparent Conductive Impurity-Doped ZnO Films Deposited by r.f. Power Superimposed d.c. Magnetron Sputtering. T. Minami, T. Fujita, T. Miyata, J. Nomoto, Kanazawa Institute of Technology, Japan

This paper describes the influence of the supplied r.f. power on the light scattering characteristics and the surface texture formation obtainable by wet-chemical etching transparent conducting impurity-doped ZnO thin films prepared by an r.f. power superimposed d.c. magnetron sputtering deposition (rf+dc-MSD) using a high-density-sintered rectangular Al- or Ga-doped ZnO (AZO or GZO) target (127 mm×275 mm) : prepared with an Al₂O₃ content of 1 or 2 wt.% or Ga₂O₃ content of 5.7 wt.%, respectively. Both AZO and GZO thin films were prepared with a film thickness of either 1000 or 2000 nm on OA-10 glass substrates at a temperature of 200°C by varying both the supplied d.c. and r.f. power used in the rf+dc-MSD: d.c. power in the range of 0-800 W and r.f. power in the range of 0-1000 W. The surface texture formation was carried out by wet-chemical etching (in a 0.1% HCl solution at 25°C) conducted after heat-treatment with rapid thermal annealing (RTA) at 500 or 550°C for 5 min in air. It was found that the light scattering characteristics and surface texture formation obtainable for texture-etched AZO (or GZO) thin films were considerably dependent on both the ratio of supplied r.f. to d.c. power as well as the Al (or Ga) content doped into the films. In particular, the haze value was significantly improved at wavelengths up to about 1200 nm in the near-infrared region in surface-textured AZO films prepared with an increased ratio of supplied r.f. power to d.c. power and etched after being heat treated with RTA, whereas the film deposition rate was found to decrease with the increased power ratio. The obtained haze value improvement is attributable to an increase of etch pit size as well as a decrease of carrier concentration. In addition, the obtainable improvement in texture-etched AZO thin films was also found to be considerably dependent on the Al content doped into the films. In particular, texture-etched AZO thin films that are appropriate for transparent electrode applications in thin-film solar cells were obtained with the following preparation conditions: rf+dc-MSD using an AZO target with an Al₂O₃ content of 2 rather than 1 wt.%, r.f. power superimposed at an appropriate value and wet-chemical etching after heat-treatment with RTA. A high haze value above 80% at wavelengths up to 1100 nm in the near-infrared region was attained in texture-etched AZO thin films prepared by rf+dc-MSD (700 W r.f. component added to a constant d.c. power of 570 W) using an AZO target with an Al₂O₃ content of 2 wt.%.

EN-ThP8 Thermoelectric Properties of SbI₃ Doped Bi₂Te₃+Bi₂Se₃ Alloys by Mechanical Alloying and Spark Plasma Sintering. M. Babu, S.J. Hong, Kongju National University, Republic of Korea

Thermoelectric (TE) materials and its devices provide attractive increasing attention because of their potential applications in the field of energy conversion, cooling for electronic devices and thermal sensors. For enhancing the thermoelectric performance, we fabricated the micro-sized n-type Bi₂Te₃+Bi₂Se₃ (Bismuth-Tellurium-Selenium) with different compositions doped with 0.05 wt%SbI₃ alloys via high energy mechanical alloying which is associated with vacuum atmosphere. The milled powder was consolidated by Spark Plasma Sintering (SPS) technique at the temperature range of 400°C with a holding time of 10 minutes at 50 MPa pressure. The effects of milling time and temperatures were investigated. In order to investigate microstructural analysis of the samples, both Optical microscope (OM) and Scanning Electron Microscope (SEM) were used. The phase of different compounds was characterized by X-ray Diffraction (XRD). Mechanical properties were calculated by measuring the density and micro Vickers hardness of the samples. The temperature dependence of the Seebeck coefficient, electrical resistivity and hall coefficient were determined for the alloys samples with different compositions. From the experimental results, the thermoelectric properties are mainly influenced by the milling time, vacuum condition and temperature. The maximum values of Figure-of-merit (ZT) for the different compounds of samples were calculated using the thermoelectric properties.

EN-ThP9 Structure-to-Function Relationship in Porous Pt/TiO₂/Ti Planar Nanostructures with a Potential Barrier for Chemicurrent Related Applications. S. Dasari, M. Ariyan, M. Hashemian, E. Karpov, University of Illinois at Chicago

Recent observations of enhanced chemicurrent effects of heterogeneous reactions on porous MIM structures with an intrinsic potential barrier make them promising for novel sensing and energy conversion applications. This presentation describes relationships between morphological features of Pt/TiO₂/Ti nanostructures, derived from XRD and SEM studied, and chemicurrent production capabilities of this material system. In particular, samples containing anatase phase in the oxide film layer show significantly greater chemicurrent effect of catalytic hydrogen oxidation on the nanostructure surface and chemical to electrical energy conversion efficiency than those with a dominant rutile phase. Strategies of thin oxide film growth by plasma electrolytic oxidation method leading to porous anatase TiO₂ thin films are also presented.

EN-ThP10 Investigation of the Molecular Interaction between CdSe Quantum Dots and P3HT for Hybrid Solar Cell Applications. A.S. Karakoti, P. Nachimuthu, S. Thevuthasan, Pacific Northwest National Laboratory

We took a systematic approach to study the interaction between CdSe quantum dots (QDs) and regioregular P3HT polymer using spectroscopic and imaging tools. Photoluminescence (PL) measurements following the titration of CdSe quantum dots with P3HT showed evidence of charge transfer between the CdSe QDs and the P3HT matrix. The titration led to an immediate quenching of main PL emission from both CdSe and P3HT and a new emission in low energy region of the electromagnetic spectrum starts appearing from the recombination of electrons in CdSe with holes in P3HT. The effect of the size of QDs on charge transfer as a function of reaction time following the addition of CdSe quantum dots in to a fixed concentration of P3HT was monitored. The time course PL measurements show the quenching of main PL emission from P3HT follow the order 6.6 nm<3.3 nm<2.1 nm while no significant changes was observed in the absorbance spectrum. These results suggest that the size-dependent interaction between QDs and P3HT. However, dynamic light scattering measurements (DLS) from the ligand capped CdSe QDs indicate a strong tendency for agglomeration of smaller QDs in the presence of P3HT. Addition of P3HT to a known concentration of CdSe QDs increases their average diameter for 2.1nm and 3.3nm QDs in toluene while the average diameter of QDs with 6.6nm in toluene remains unchanged at the same concentrations. This suggests that the interaction between CdSe QDs and P3HT is controlled by the agglomeration of QDs and not by the size of the dots. Findings from these results and the effect of changing the capping ligands of CdSe QDs on the charge transfer will be discussed.

EN-ThP11 Low-Damage Deposition of Thin Silicon Films for Solar Panel Production using Surface-Wave Plasma Source. J. Peck, University of Illinois at Urbana Champaign, P. Zonooz, Starfire Industries LLC and University of Illinois at Urbana Champaign, D. Curreli, University of Illinois at Urbana Champaign, M. Reilly, R. Stubbers, B. Jurczyk, Starfire Industries, LLC, D.N. Ruzic, University of Illinois at Urbana Champaign

An innovative kind of plasma source for the deposition of thin silicon films used in semiconductor manufacturing is currently under development at Starfire Industries LLC and CPMI Center for Plasma Material Interaction, University of Illinois Urbana Champaign. The source, operating in the microwave range, is able to efficiently generate high-density and low-electron-temperature SiH₄-H₂ plasmas, and can easily be scaled upward to the deposition of thin films on large-area surfaces. The silicon films deposited at low RF power on glass substrates have been characterized using multiple techniques, comprising SEM, Ellipsometry and Raman Spectroscopy. Spectroscopic data in the UV-VIS-NIR range have been acquired during the discharge operations for plasma characterization. By using Raman spectroscopy, the crystalline volume fraction of the deposited films has been obtained for several input mass-flows of silane, as a function of the substrate temperature and for several pressures of the Hydrogen gas. The averaged film growth rate has been obtained from both ellipsometry measurements and SEM imaging. From the results of the preliminary characterization, the possibility to obtain low-damage growth of a-Si:H and nc-Si:H thin films has been assessed. The trend of the crystallinity as a function of the electron temperature has also been presented, and its relationship with the low potential-drop allowed by this source at plasma-substrate interface has been discussed.

EN-ThP12 Relationship Between Interface Microstructures and Obtainable Photovoltaic Properties in ZnO/Cu₂O Heterojunction Solar Cells, Y. Nishi, S. Abe, T. Miyata, T. Minami, N. Ikenaga, O. Ueda, Kanazawa Institute of Technology, Japan

In this paper, we present our investigation into the relationship between the observable microstructure at heterojunction interfaces and the obtainable photovoltaic properties in ZnO/Cu₂O heterojunction solar cells fabricated with various structures on thermally oxidized Cu₂O sheets. Recently, we reported that high efficiencies of 2.19 and 4.12% as well as open circuit voltages of 0.5 and 0.72 V were obtained in heterojunction solar cells fabricated with an Al-doped ZnO (AZO)/Cu₂O or AZO/non-doped ZnO/Cu₂O structure, respectively: solar cells fabricated by depositing thin films on thermally oxidized Cu₂O sheets at room temperature using a pulsed laser deposition (PLD) method [1,2]. The improvement in obtained photovoltaic properties suggests that it is necessary to stabilize the surface of Cu₂O sheets as well as develop low-damage and low-temperature deposition techniques for forming and applying heterojunctions. In addition to improvements in the surface condition of Cu₂O sheets, the significant improvement of obtained photovoltaic properties exhibited in AZO/non-doped ZnO/Cu₂O heterojunction solar cells is attributable to enhanced potential barrier height and carrier lifetimes near the interface, resulting from the inserted buffer layer functioning as an n-type ZnO layer as well as an active layer in the n-p heterojunction. Cross-sectional views of ZnO/Cu₂O heterojunctions obtained by transmission electron microscopy revealed interface microstructures that differed significantly between high-efficiency and low-efficiency solar cells, fabricated with different deposition conditions, irrespective of the device structure used. For example, in AZO/non-doped ZnO/Cu₂O heterojunction solar cells fabricated with both the AZO and non-doped ZnO thin films prepared by PLD at the same deposition temperatures, either RT or 200°C, the solar cells formed at RT exhibited higher efficiency than those formed at 200°C. A smooth heterojunction was observed near both the interfaces within AZO/non-doped ZnO/Cu₂O heterojunction solar cells fabricated at RT; this contrasts with many dislocations observable near both of these interfaces of solar cells fabricated at 200°C, *i.e.*, between the non-doped ZnO layer and the Cu₂O and between the AZO and non-doped ZnO layers. Thus, the TEM observations of the heterojunction solar cells fabricated by forming both thin films at RT indicate that the higher efficiency results from an increase of carrier lifetimes, a consequence of suppressing carrier recombination and trapping near the interfaces of the heterojunctions.

[1] Y. Nishi et al., *Thin Solid Films*, 520 (2012) 3819.

[2] Y. Nishi et al., *J. Vac. Sci. Technol. A* 30 (2012) 04D103.

**Electron Transport at the Nanoscale Focus Topic
Room: Central Hall - Session ET-ThP**

Electron Transport at the Nanoscale Poster Session

ET-ThP1 The Performance of Organic Light-Emitting Diodes with Rb₂CO₃-doped Alq₃ Layer for Improving Carrier-Injecting Probability, J.W. Park, J.T. Lim, J.S. Oh, G.Y. Yeom, Sungkyunkwan University, Republic of Korea

Organic light-emitting diodes (OLEDs) is strongly influenced by both the injection barrier height and the number of carriers in the metal/organic contact formed between the Fermi levels (EF) of the electrodes and the relevant levels for conduction in the OLED.

In this study, this study elucidates the enhancement of the optoelectronic properties of OLEDs by n-doping effect of rubidium carbonate (Rb₂CO₃)-doped tris(8-quinolinolato)aluminum (III) (Alq₃). The device performance strongly depends on both doping concentrations of the Rb₂CO₃-doped Alq₃ layer and the thickness. As the doping concentration is increased from 2.5% to 50%, the electron ohmic properties of the electron-only device with the glass/ITO/ Rb₂CO₃-doped Alq₃ (10 nm)/Al structure were improved at doping concentration of 10%, due to the increase in the n-type doping effect. However, the Alq₃ molecules were decomposed above the doping concentration of 10%. Also, the photoemission spectra revealed that the n-type doping effect cause the lowering of the electron-injecting barrier height, as well as the improvement of the electron conductivity. The OLED with the glass/ITO/MOXX-doped NPB (25%, 5 nm)/NPB (63 nm)/Alq₃ (32 nm)/ Rb₂CO₃-doped Alq₃ (10%, 10 nm)/Al (100 nm) structure showed both a high maximum luminance of 114,400 cd/m² at 9.8 V and a high power efficiency of 2.7 lm/W at about a luminance of 1000 cd/m².

**Graphene and Related Materials Focus Topic
Room: Central Hall - Session GR-ThP**

Graphene and Related Materials Poster Session

GR-ThP1 Using Raman Spectroscopy and X-ray Photoelectron Spectroscopy to Guide the Development of Graphene-Based Materials, T.S. Nunney, M.H. Wall, Thermo Fisher Scientific, UK

The potential uses of graphene are currently being explored by the materials science community. Its immediate potential as a transparent conductive electrode for the microelectronics industry is already being exploited; the unique combination of electronic, chemical and structural properties exhibited by graphene are already having a significant impact on the development of thin film transistors and touch-screen devices. Further applications for the development of graphene-based catalytic systems and molecular sensors are also underway. Good materials characterization is required at all steps in the creation of new graphene devices, from guiding the initial graphene synthesis and transfer to the desired substrate, to chemical modification and analysis of the finished device. In this presentation we will show how a multi-technique approach using both Raman spectroscopy and XPS can address the challenges posed at these steps. Raman microscopy is an analytical technique that is well suited for the characterization of graphene. It is a vibrational spectroscopy that is very sensitive to small changes in the geometric structure of a molecule and its environment. This sensitivity allows Raman to be used as a probe for a number of properties important to a specific graphene samples, such as layer thickness. X-ray photoelectron spectroscopy (XPS) is ideally suited to the determination of the surface chemistry and the way in which that chemistry changes in the surface and near-surface region. The technique provides quantitative elemental and chemical information with extremely high surface specificity and is ideal for comprehensively and quantitatively characterising the elemental composition and chemical bonding states at surfaces and interfaces. This approach will be illustrated by examples from graphene samples created by mechanical exfoliation, chemical reduction and CVD methods.

GR-ThP2 Ionic Strength Effects on Graphene Oxide Nanosheets and Fluorescence Quenching of ssDNA Aptamers, M.Y. Lin, Y.P. Lu, National Applied Research Laboratories, Taiwan, Republic of China

Recently, graphene has attracted considerable attention because of its remarkable electronics, its mechanical and optical properties, and its unique single-atom thickness and two-dimensional sp² carbon networking material [1]. Graphene oxide (GO) presents excellent properties in high water dispersibility, capabilities of bridging biomolecules on the surface, and acts as a highly efficient fluorescent quencher material [2]. Single-stranded DNA (ssDNA) has been reported to bind on a graphene surface through non-covalent π - π interactions, whereas double-stranded DNA (dsDNA) cannot bind on graphene surfaces. Aptamers are synthetic, single-stranded DNA or RNA molecules that fold into unique 3D structures, and bind specifically to a wide range of molecules such as chemicals, proteins, and drugs. Therefore, aptamer-based GO biosensors have been developed for detecting various targets [3-5]. Ionic strength and pH are closely related to biochemical reactions and interactions between aptamer and targets. However, less studies have been reported to the ionic strength and pH effects on GO and interaction between GO and DNA [6]. Phosphate buffer saline (PBS) was commonly used as isotonic reagent for protein solution. In this study, the fluorescence intensity of GO significantly decreasing with increasing concentration of PBS. In addition, increasing quenching effect was found in the group with PBS as solvent for GO-aptamer interaction. The reported report are of importance in further applications of GO in biosensors and biochemical reactions.

GR-ThP3 Isotope Effect in the Graphene Deuteration Kinetics, A. Nefedov, Karlsruhe Institute of Technology, Germany, A. Paris, Interdisciplinary Laboratory for Computational Science, FBK-CMM, Italy, N. Verbitsky, Moscow State University, Russia, Y. Wang, Nagoya University, Japan, A. Fedorov, D. Haberer, IFW Dresden, Germany, M. Oehzelt, Helmholtz-Zentrum Berlin für Materialien und Energie, Germany, L. Petaccia, ELETTRA Synchrotron Light Laboratory, Italy, D. Usachov, St. Petersburg State University, Russia, D. Vyalikh, Technical University Dresden, Germany, H. Sachdev, Max-Planck-Institute for Polymer Research, Germany, Ch. Wöll, Karlsruhe Institute of Technology, Germany, M. Knupfer, B. Buechner, IFW Dresden, Germany, L. Calliari, Interdisciplinary Laboratory for Computational Science, FBK-CMM, Italy, L. Yashina, Moscow State University, Russia, S. Irle, Nagoya University, Japan, A. Grueneis, University of Vienna, Austria

Kinetic isotope effects (KIE) are important phenomena in physical chemistry and have been investigated for a long time in relation to

activation and rate of chemical reactions. KIE are easily observable for the hydrogen isotopes due to the large relative mass difference and have been studied for example in hydrogen transfer in organic chemistry such as acid and base catalysis, enzyme reactions and catalytic decomposition.

Here we present results of time-dependent x-ray photoemission spectroscopy (XPS) in order to investigate the kinetics of the hydrogenation/deuteration reaction of graphene. A pristine monolayer graphene was prepared under ultrahigh vacuum conditions by chemical vapor deposition on Ni(111) thin films epitaxial grown on W(110). Then a monolayer of Au was intercalated into the interface between Ni and graphene, making the latter quasi free-standing. The graphene layer was then exposed to hydrogen or deuterium atomic gas beams, obtained by thermal cracking in a tungsten capillary at T=3000 K. The maximum surface coverage was obtained after several hydrogenation or deuteration steps of different time. After each step XPS of the C1s line was performed in order to measure H/C and D/C ratios. After reaching saturation, the electronic structure of the hydrogenated and deuterated layer was analyzed by near-edge X-ray adsorption fine structure (NEXAFS) spectroscopy at the carbon K-edge.

We have observed a strong inverse KIE for the hydrogenation/deuteration reaction leading to substantially faster adsorption and higher maximum D/C ratios as compared to H/C (D/C~35% vs. H/C~25%). These results can be understood by the fact that atomic D has a lower chemisorption barrier and a higher desorption barrier. Quantum chemical calculations and molecular dynamics simulations can reproduce the experimental trends and reveal the contribution of the constituent chemisorption, reaction and associative desorption processes of H(D) atoms onto graphene. The reported case of a strong inverse KIE is an extremely unusual case and is important for isotope specific chemical reactivity in organic molecules and functionalized graphene.

GR-ThP4 Graphene Nanoribbons Electronic Structure Modulations, N.B. Le, L.M. Woods, University of South Florida

Graphene nanoribbons are studied using density functional theory methods. Various factors are considered as different ways to tailor their electronic structure properties. These include folding, types of edges, and extended defects. Of particular importance is the van der Waals interaction in the folded structures with closed edges. These are taken into account via a DFT-D2 method, which is a pragmatic approach based on a semi-empirical pairwise correction to the conventional Kohn-Sham energy. Equilibrium distances, stacking patterns, and geometry configurations upon folding are determined. The energy gaps, band structure changes, and characteristic energies are also obtained for nanoribbons with armchair and zigzag edges when folded and/or extended defects present. Our results attest to the many possible methods that can be explored to modify the properties of these graphitic nanostructures.

GR-ThP5 Effects of an Interfacial Water Layer on Protein Adsorption to Graphene Sheets on Solid Substrates, K. Yamazaki, T. Ogino, Yokohama National University, Japan

Graphene is two-dimensional honeycomb lattice of carbon atoms. It is well known that the graphene sheets are strongly affected by their environment because of its extremely small thickness and large specific surface area. There are many reports about the chemical doping into graphene films induced by the support substrate and charge transfer. In this paper, we studied control of chemical doping to graphene flakes through the substrate engineering and using raman spectroscopy. We also demonstrate the selective adsorption of biomolecules toward the unique sensors.

We used sapphire surfaces for support substrates of graphene. After the acid treatment, the sapphire surfaces are terminated with hydroxyl groups, which work as adsorption sites of water molecules. We deposited graphene flakes on sapphire (0001) and (1-102) surfaces by mechanical exfoliation method. To reveal influence of a water layer at the interface between the sapphire surface and graphene, we annealed the sapphire surfaces at 700°C for 1h just before graphene deposition and compared the G-peak and 2D-peak positions on Raman spectra.

We observed shift of G-peak and 2D-peak positions to wave numbers lower than those on the hydrophilic sapphire (0001) substrate. But, in the case of (1-102) surfaces, the G-peak and 2D-peak positions did not shift upon annealing. The peak positions are almost same among the annealed (0001), the annealed (1-102), and the on-annealed (1-102) surfaces. It is well known that formation of water layers on sapphire surfaces depends on plane directions¹. A (0001) surface has more bound water molecules than the other faces. Therefore, the peak shifts were induced by the amount of water layer that existed at the interfaces between the sapphire surfaces and the graphene flakes. We demonstrated the adsorption of protein molecules on these surfaces. We used ferritin molecules, which are negatively charged for adsorption on the graphene flakes. We observed well-correlated adsorption pattern with the G-peak and the 2D-peak positions of Raman spectra.

Ferritin molecules were preferentially adsorbed to the graphene flakes that were supported by hydrophilic (0001) surfaces. Amount of adsorbed ferritin molecules to the other surfaces were dramatically small. These different adsorption behaviors directly show the effect of chemical doping from the interfacial water molecules to the graphene flakes.

In summary, we demonstrated control of protein adsorption to the graphene surfaces by using the suitable support substrates for graphene towards the biosensors without any labeling to substrates and targets.

1) T. Tsukamoto et al. *J. Phys. Chem. C* (2012) 116, 4732-4737.

GR-ThP6 Layer Dependent Growth of Pentacene on Epitaxial Graphene, W. Jung, D.-H. Oh, J. Lee, B.G. Shin, C.-Y. Park, J.R. Ahn, Sungkyunkwan University, Republic of Korea

Graphene have showed promising performance as electrodes of organic devices such as organic transistors, light-emitting diodes, and photovoltaic solar cells. In particular, among various organic materials of graphene-based organic devices, pentacene has been regarded as one of promising organic materials because of its high mobility, chemical stability, and compatibility with a low-temperature silicon processing. In the development of graphene-based organic devices, it is thus important to understand an interaction of pentacene with graphene. In this study, we focused on how the growth of pentacene depends on an interaction between graphene and a substrate. Epitaxial graphene grown on a 6H-SiC(0001) surface was used as a pristine graphene because zeroth-layer graphene, called a buffer layer, and monolayer graphene have the same graphene structure but zeroth-layer graphene, which bonds strongly to a SiC substrate, has different electronic properties from monolayer graphene. We have studied how graphene grows differently at room temperature on monolayer graphene in comparison to zeroth-layer graphene using scanning tunneling microscopy and first principles calculations. On the zeroth-layer graphene, pentacene was adsorbed on specific sites with three different orientations but did not show a long-range order. In contrast to zeroth-layer graphene, pentacene forms a two dimensional ordered structure on monolayer graphene. The orientation of pentacene in the ordered structure was determined by the zigzag direction of the edge structure of monolayer graphene. The short-range and long-range ordering on zeroth-layer and monolayer graphene, respectively, was understood by different energetics of pentacene on zeroth-layer from monolayer graphene, where a total energy of pentacene on graphene was calculated by first principles calculations.

GR-ThP7 Optical Properties and Surface Radicals Content of Graphene Decorated with Metal Nanoparticles, M.A. Bratescu, T. Ueno, O. Takai, N. Saito, Nagoya University, Japan

Recently the increased interest of carbon-based materials decorated with metal nanoparticles (NPs) for sensors and energy applications has generated a huge development of the research in this field. Unfortunately, the immediate use of graphene in sensors or fuel cells applications is not yet possible since more effort must be performed to understand how NPs decorated graphene affect the selectivity and the sensitivity of the sensor and how surface radicals content influences the fuel cell performance.

In the present research, we developed a simple synthesis method of metal NPs on graphene layer and we investigated the optical properties and the surface radicals content of this system. Graphene layer have been produced on Cu foils by CVD method and transferred on different substrates to be characterized.¹ The metal NPs were synthesized on the graphene layer using a well-established method used in our laboratory, based on a solution plasma process (SPP) system^{2,3}, directly on the Cu foil covered with the graphene layer. The metal NPs were synthesized on the graphene surface through the reduction of the metal ion from the salt to the neutral form, or by the erosion of the electrode material. The graphene layer decorated with metal NPs was transferred on glass, Si/SiO₂ substrate, Kapton scotch and carbon/Cu(Mo) grid surfaces to be analyzed by UV-vis spectroscopy, micro-Raman mapping spectroscopy, electron spin resonance (ESR), and transmission electron microscope (TEM) techniques, respectively. Micro-Raman mapping of 2D band at 2700 cm⁻¹ (two photon double resonance band) which has higher intensity than G band at 1583 cm⁻¹ (interlayer vibrations band of sp²-hybridized carbon) shows the quality and the uniformity of graphene layer on substrates. An enhanced Raman spectrum of graphene was detected when gold or silver NPs were adsorbed on the surface. The UV-vis spectra of graphene layer decorated with gold NPs which was transferred on a glass substrate, shows a weak absorption band of surface plasmon resonance, at 520 nm, due to the thin layer of NPs on surface. The adsorbed metal NPs on graphene layers was observed by high resolution TEM analysis. The surface radicals content will be examined using ESR through calibration with stable free radicals compounds. The dependence of the surface radicals content of the graphene decorated with NPs on the size and shape of NPs will be discussed.

1 Xuesong Li, et al., *Science* **2009**, 324, 1312.

2 Takai, O. *Pure Appl. Chem.* **2008**, 80, 2003 – 2011.

GR-ThP8 Electronic Structure of MoS₂ Monolayers on Copper. *Q. Ma, D.Z. Sun, W.H. Lu*, University of California Riverside, *D. Le, M. Amanpour*, University of Central Florida, *J. Mann, S. Bobek*, University of California Riverside, *T. Raman*, University of Central Florida, *L. Bartels*, University of California Riverside

MoS₂ is a very promising material for photocatalysis and it has many current applications in catalytic hydrodesulfurization. Similar to graphene, it is a layered material. Recently, it has been shown that it transitions from an 1.6 eV indirect bandgap to a 1.9 eV direct bandgap semiconductor when reduced to a monolayer. Important for its usefulness e.g. in catalytic hydrogen splitting, is not only its bandgap but also its band alignment when deposited on different substrates. Using CVD grown MoS₂ on a copper surface, we use XPS to ascertain the identity of the material and the nature of its internal bonding when on this metallic substrate. Spectroscopy also shows a metal induced reduction of the bandgap to 1.5 eV and a strong signature of n-type doping through the underlayer. Density Functional Theory calculation corroborate this finding and provide a microscopic understanding of the bandgap and alignment depending on the number of MoS₂ layers and the presence of any substrate.

GR-ThP9 Dry Transfer of Graphene to Organic and Inorganic Substrates. *E.H. Lock, S. Hernandez, S.G. Walton, M. Laskoski, S.P. Mulvaney, P.E. Sheehan, W.K. Lee, T.J. Anderson, F.J. Bearez, V.D. Wheeler, F.J. Kub, J.D. Caldwell, K.D. Hobart, B.N. Feygelson, L.O. Nyakiti, R.L. Myers-Ward, C.R. Eddy, Jr., D.K. Gaskill*, Naval Research Laboratory

High quality graphene transfer is critical for preserving the extraordinary graphene properties. In this paper we report our progress on transferring graphene from different growth substrates. Our method is a dry transfer approach which exploits an azide linker molecule to establish a covalent bond to graphene. Successful transfer is observed when the adhesion between the graphene and the transfer substrate is higher than the graphene/growth substrate adhesion. Thus, this transfer technique provides a novel alternative route of graphene transfer. This work was supported by the Naval Research Laboratory Base Program.

GR-ThP10 Controllable Assembly of Aromatic Molecules on a Surface via Diels-Alder Reaction: A Carbon Source for Graphene. *C.L. Henderson, J. Baltazar, H. Sojoudi, J. Kowalik, S. Graham, L. Tolbert*, Georgia Institute of Technology

Graphene is of tremendous interest based on its electronic properties, such as mobilities $\geq 200,000$ cm²/V-s, as well as a very high thermal conductivity. Furthermore, graphene is one atom thick, making it a perfect substitute for silicon in small high performance devices. Graphene formation by directed chemical synthesis, utilizing intelligently designed precursors that can be converted thermally or chemically to graphene and graphene nanostructures with interesting electronic properties are of great interest. We successfully synthesized a silyl derivative of a maleimide that allows: (1) self-assembly to produce a controllable aromatic monolayer on a CMOS compatible surface, and (2) the ability to perform a reverse Diels-Alder reaction that allows us to obtain the carbonaceous starting material of interest in the surface for further thermal or chemical consolidation. Graphene so produced was analyzed and identified by Raman spectroscopy and other methods.

GR-ThP11 Unique Electronic Mixing between Iron Phthalocyanine and Graphene*, *D.B. Dougherty, A.A. Sandin*, North Carolina State University, *A. Calzolari*, CNR-NANO, Istituto Nanoscienze, Italy, *M. Buongiorno-Nardelli*, North Carolina State University, *A. Al-Mahboob, J.T. Sadowski*, Brookhaven National Laboratory, *J.E. Rowe*, North Carolina State University

Graphene is an ideal material for long-range spin transport due to its very high carrier mobilities and long spin lifetimes due to minimal spin-orbit scattering effects [1]. Direct spin injection into graphene has been demonstrated, but is inefficient due to the well-known bulk conductivity mismatch between graphene and a magnetic metal electrode. The standard approach to overcome this effect is to engineer a tunneling barrier at the interface to provide an effectively large spin-dependent interface resistance. However, for insulating tunnel barrier growth on graphene, great care must be taken to avoid 3D islanding due to the typically weak interactions between the substrate and deposited species [1].

An alternate approach is to consider the use of planar organic materials as interfacial layers to enhance spin injection into graphene. Since weak intermolecular interactions can be comparable in size to molecule-substrate interactions for planar aromatics on graphene, high quality film growth is more likely. We have studied the growth of iron phthalocyanine (FePc), a chemically-robust paramagnet, on epitaxial graphene on SiC(0001) by a

combination of STM, STS, LEED, UPS, and density functional theory calculations. Our calculations predict an energetically weak interaction between graphene and FePc that nevertheless leads to a unique spin-dependent electronic mixing. A non-dispersive hybrid interface state is created along with a small gap in one spin sub-band while the graphene band structure is essentially unchanged in the other sub-band. STM and LEED indicate a highly-ordered, flat-lying monolayer film of FePc on epitaxial graphene and UPS measurements compare favorably with the calculated occupied density of states. STS studies of the ordered monolayer show an unoccupied state for FePc on graphene that is *not present* for FePc on graphite. We interpret this unique state as evidence for the predicted spin-polarized interface state.

*This work was funded by the NSF Phase I Center for Chemical Innovation: Center for Molecular Spintronics (CHE-0943975).

[1] Han et al., *J. Magn. Mag. Mat.* 324, 369 (2012).

GR-ThP13 Raman Spectroscopy of Double Layer Graphene FETs: Mapping the Misorientation Angle. *Z. Razavi Hesabi, C. Joiner, T. Roy, E.M. Vogel*, Georgia Institute of Technology

Double layer graphene, a stacked two dimensional honeycomb lattice of carbon atoms, is a very promising candidate for nanoelectronic applications. The electrical properties, such as high carrier mobility and tunable band gap, have been theoretically predicted to be highly dependent on the misorientation angle between the two layers. For industrial applications, the ability to map and control the misorientation angle between layers will be necessary to achieve the desirable electrical properties of the graphene devices. This work presents a method for systematically determining the misorientation between two layers on a wafer scale through the use of Raman spectroscopy.

Helium Ion Microscopy Focus Topic Room: Central Hall - Session HI-ThP

Aspects of Helium Ion Microscopy Poster Session

HI-ThP1 Fabrication of Carbon Nanomembranes by Helium Ion Lithography. *X. Zhang, H. Vieker, A. Beyer, A. Götzhäuser*, University of Bielefeld, Germany

A helium-ion microscope (HIM) is capable of creating nanoscale patterns and its beam can perform ion milling as commonly done in focused ion beam (FIB) systems. Here we use a helium ion beam as direct writing tool to cross-link 4'-nitro-1,1'-biphenyl-4-thiol (NBPT) SAMs with arbitrary patterns. The cross-linked SAMs were transferred to either silicon substrates with an oxide layer for optical characterization or transmission electron microscopy (TEM) grids for preparing free-standing carbon nanomembranes (CNMs). The required dose for the complete cross-linking with helium ions is quite similar to the dose earlier established with electrons. To determine the feature resolution limit, we prepared dot arrays of CNMs at various doses and 5 nm feature sizes have been achieved. Proximity effect and sample damage on the nanoscale patterns were also investigated. Furthermore, we use the ion beam to form nanopores in the CNM with an attainable feature size of 5 nm.

HI-ThP2 Site Specific He Ion Irradiation Damage Studies in Nanolayered Thin Films. *V. Shutthanandan, A. Devaraj, R.S. Vemuri, C.M. Wang, T. Varga, C.H. Henager Jr, S. Thevuthasan*, Pacific Northwest National Laboratory

Over recent years materials with a high density of nanoscale interfaces are finding increasing attention due to their improved radiation tolerance in comparison to their bulk form. The efficient trapping and recombination of radiation induced point defects such as vacancies and interstitials at such interfaces are proposed to be the fundamental reason for their increased radiation tolerance. Several different ODS steels, nanostructured ceramic materials and nanolayered thin films have been recently investigated to understand the fundamental mechanism of radiation damage. In many of these investigations high energy He ion irradiations were carried out in a large area over the entire specimen followed up with characterization of radiation damage. The spot size of ion irradiation beams from conventional sources was in the order of 100s of microns or larger preventing a site specific irradiation damage investigation of individual microstructural features. In such cases often the overall irradiation damage evolution in the material would be a cumulative response of the entire material microstructure (grain boundaries, interphase-interfaces, second phase precipitates and other preexisting defects) to the ion beam irradiation. A nanoscale site specific He ion irradiation method, if made possible can aid in decoupling and individually analyzing the He ion irradiation response of different microstructural features in a mutually exclusive manner. He ion

microscopy (HIM) developed in recent years offer such a capability for obtaining coherent He ion beams that can be precisely controlled and directed to areas as small as few nanometers. In EMSL, a DOE national user facility in PNNL, efforts are underway to look at irradiation response of nanoscale microstructural features in nanolayered metallic thin films by cross coupling site specific He ion irradiations with site specific TEM and Atom probe tomography (APT) sample preparation methods made possible by Focused ion beam system. Proof of principle experiments are being conducted in nanoscale PVD synthesized Ti/Al nanolayer thin films using He ion irradiation doses ranging from $1E14$ to $1E17$ ions/cm² and subsequent analysis by TEM and APT. Recent results from this study will be presented in this paper.

HI-ThP3 Helium and Neon Ion Beams Induced Platinum Deposition. *H. Wu, D. Ferranti, D. Xia, W. Thompson, L.A. Stern, Carl Zeiss, P.D. Rack, C.M. Gonzalez, The University of Tennessee, M.W. Phaneuf, Fibics Incorporated*

Gallium focused ion beams (Ga-FIB) have been used by the semiconductor industry to provide nanoscale deposition or milling. However, Ga ion implantation and limited spatial resolution capability encourage people to explore other ion sources for nanofabrication. Helium and Neon ion beams have been studied for many years as good alternative ion sources to replace Ga ion beams. The GFIS (gas field ion source) microscope is able to provide both He and Ne ion beams. Because of the mass difference of He and Ne ions, the interactions of ions with precursor molecules result in different sputtering rates, implantation and deposition yields. In this study, we use methylcyclopentadienyl trimethyl platinum (PtC₅H₁₆) as the precursor, and the metal deposition is induced by He and Ne ion beams respectively. To optimize the deposition process, beam current and dwell time have been studied. Compared with Ga ions, both He and Ne ion beams have smaller probe sizes, cause less surface damage and results in deposited material with superior properties without gallium contamination. The Pt nanowires using Ne ion beam exhibit lower resistivities, as low as 600 $\mu\Omega$ -cm, than those nanowires using He ion beam. Composition analysis by EDX shows the higher Pt: C ratio of Pt deposition by Ne ion beam than that by He ion beam, which is consistent with the resistivity results.

Magnetic Interfaces and Nanostructures

Room: Central Hall - Session MI-ThP

Magnetic Interfaces and Nanostructures Poster Session

MI-ThP1 Magnetic Properties of Ferromagnetic-Antiferromagnetic Bi-Layers with Different Spin Configuration. *W. Kim, Korea Research Institute of Standards and Science (KRISS), G.-E. Yang, Chungnam National University, Korea, C. Hwang, Korea Research Institute of Standards and Science (KRISS), E. Cho, Chungnam National University, Korea*

We investigated the effect of different spin direction of anti-ferromagnetic (AFM) layer on the magnetic properties of ferromagnetic (FM) layer in Fe-NiO and Fe-CoO bi-layer systems. For Fe-NiO system, we prepared successfully Fe/NiO/Ag(001) and Fe/NiO/MgO(001) systems on a single MgO(001) substrate. We examined magnetic properties of the bi-layer system using the surface magnetic optical Kerr effect (SMOKE) and X-ray magnetic linear dichroism (XMLD). From SMOKE measurement we observed the coercivity enhancement due to the set-up of AFM order of NiO films in both of the Fe/NiO/MgO(001) and Fe/NiO/Ag/MgO(001) system. The most remarkable results in our observation is that the coercivity enhancement of Fe/NiO/Ag/MgO(001) is much larger than that of Fe/NiO/MgO(001). XMLD experiments confirmed the out-of-plane spin direction of NiO layers in Fe/NiO/MgO(001) and in-plane spin-direction of NiO layers in Fe/NiO/Ag/MgO(001), and we concluded that the origin of large enhancement of coercivity is due to the strong parallel coupling between Fe layers and NiO layers. We also confirmed that this strong parallel coupling maintained across the thin Ag layer inserted between Fe and NiO layers. With this Ag inserted Fe/NiO system, we could estimate the Neel temperature of the NiO layers. We also realized different spin configuration in Fe-CoO systems by growing CoO films on the Ag(001) and MnO(001) surfaces. We observed much larger coercivity enhancement in Fe/CoO/Ag(001) than in Fe/CoO/MnO(001) below the Neel temperature of CoO films.

MI-ThP2 Spin Dynamics and Exchange Bias in Core-Shell Fe γ -Fe₂O₃ Nanoparticles. *S. Chandra, H. Khurshid, University of South Florida, W. Li, G.C. Hadjipanayis, University of Delaware, M.H. Phan, H. Srikanth, University of South Florida*

Exchange bias in core-shell nanoparticles has been an area of intense research. While several research efforts have been devoted in understanding the role of interfacial spins in the nanoparticles that exhibit exchange bias, a clear understanding of the spin dynamics of the core and the shell remains to be investigated. A detailed study has been carried out on the magnetic properties of Fe γ -Fe₂O₃ core-shell structured nanoparticles synthesized by thermal decomposition method. Our focus is to understand the spin dynamics of the core and shell independently and their role in triggering exchange bias (EB) phenomenon. The nanoparticles exhibit memory effect and aging associated with a superspin glass state (SSG). We show that the energy barrier distribution shows two maxima that marks the freezing temperatures of the core and shell. Lastly, hysteresis measurements after field cooling reveal a strong EB indicated by a loop shift. The onset of EB is at 35 K when the ferromagnetic core is frozen and the moments in the ferrimagnetic shell begin to block resulting in enhanced exchange coupling.

MI-ThP4 Modeling-assisted Synthesis and Characterization of Epitaxial NiTiO₃ Films as New Multiferroics. *T. Varga, T.C. Droubay, M.E. Bowden, S.A. Chambers, B.C. Kabius, E. Apra, W.A. Shelton, V. Shutthanandan, Pacific Northwest National Laboratory*

In a search for new multiferroic materials where the direction of magnetization can be switched by an applied electric field, we have looked for materials in which polarization and magnetization are strongly coupled. Recent theory calculations predicted that the family of compounds MTiO₃ (M = Mn, Fe, Ni), in a certain polymorphic structure (acentric R3c), are promising candidates where a polar lattice distortion can induce weak ferromagnetism. Guided by these insights, a rhombohedral phase of NiTiO₃ has been prepared in epitaxial thin film form, whose structure is of the predicted multiferroic. Preliminary physical property measurements suggest a Neel transition also consistent with the R3c structure and SHG imaging shows a polarized lattice. The synthesis of epitaxial NiTiO₃ films, their full structural characterization and physical property measurements along with our first-principles DFT calculations to predict the desired NiTiO₃ structure, its stability, and the effect of lattice strain on the growth are reported.

MI-ThP5 Nanomechanical Manipulation of the Anomalous Hall Effect in GaMnAs. *J.H. Lee, M.L. Cho, Y.D. Park, Seoul National University, Republic of Korea*

We show an explicit dependence of the anomalous Hall effect (AHE) as well as magnetic anisotropy (MA) on locally induced mechanical strains in low-temperature molecular beam epitaxy (LT-MBE) prepared GaMnAs. LT-MBE GaMnAs (001) epilayers were prepared on AlGaAs layer, which serves (1) to enhance compressive strain in GaMnAs during growth as well as (2) to act as a sacrificial layer. By selective nanopatterning and removal of the AlGaAs layer, we realise free-standing GaMnAs microbeams (along (110), (1 $\bar{1}$ 0), and (100) directions) with multiple lateral probes along the length of the microbeam. Due to the relaxation of the the compressive strain when released, GaMnAs microbeam mechanically buckles. By simultaneous measurements of ρ_{xx} and ρ_{xy} along the length of the buckled GaMnAs microbeam ($1.4 \text{ K} < T < 300 \text{ K}$), we probe both AHE and MA as functions of local strain. We find relatively small changes in MA while large suppression of AHE for regions along the microbeam experience the highest mechanical strain. We demonstrate the novelty of such interplay between mechanical strain and AHE by realising simple Hall crosses which mechanical state can be robustly read by the AHE signal - which correspondence between mechanical state and transport properties are well suited for a low-power, non-volatile memory elements. Furthermore, we demonstrate the applicability of above methods beyond GaMnAs to other material systems which are sensitive to small mechanical strains via strong spin-orbit interactions, namely topological insulator Bi₂Se₃.

Nanometer-scale Science and Technology

Room: Central Hall - Session NS-ThP

Nanometer-scale Science and Technology Poster Session

NS-ThP1 Composites of Silicene Nanofilaments and TiO₂ Nanoparticles for Photocatalysis. *G.R. Meseck, R. Kotic, G.R. Patzke, S. Seeger, University of Zurich, Switzerland*

Secured access to clean water resources is a fundamental need of human society and nanoparticulate TiO₂ is amongst the most important materials for the photocatalytic degradation of organic pollutants. While TiO₂-

nanoparticles (NPs) thus offer photocatalytically effective routes to wastewater treatment, separation of NPs from reaction media is difficult and catalyst recycling often impossible. Immobilization of TiO₂-NPs is therefore indispensable to facilitate handling as well as to control potential health and environmental hazards. We present silicone nanofilaments as a new flexible carrier type for TiO₂-NPs, because they can be deposited as thin carpets on a variety of substrates and their silicone nature renders them chemically and environmentally stable. We deposited TiO₂-NPs on thin carpets of silicone nanofilaments on glass slides in a convenient one-step reaction in ethanol/water mixtures from TiF₄ as precursor under mild conditions. The resulting nanocomposite material is characterized with a wide range of electron microscopy and other analytical techniques. The photocatalytic activity in the decomposition of methylene blue (MB) is proved and superior to TiO₂-NPs immobilized on bare glass supports. Furthermore, the substrates are reusable for several cycles without significant loss in activity.

NS-ThP2 Organic Vapor Adsorption on In Situ Grown Carbon Nanotube Films, K. Bosnick, S. Ban, W.K. Hiebert, Z. Shi, C. Huang, R. Lister, M. Mleczko, National Research Council of Canada

Organic vapor adsorption isotherms are measured on in situ grown carbon nanotube (CNT) films using piezoelectric GaPO₄ crystal microbalances as mass sensing substrates. The isotherms are Type IV and show adsorption / desorption hysteresis, consistent with a porous material. The measured porosity is 2%, a value surprisingly low given an over 90% void volume in the film estimated from density considerations. At low pressures ($p/p_0 < 0.25$) the isotherm is well fit by the Freundlich model and at intermediate pressures ($p/p_0 = 0.1-0.4$) by the Brunauer, Emmett, Teller (BET) model. Monte Carlo simulations show three consecutive adsorption processes: filling of the intratube micropores at low pressures, monolayer coverage of the CNT external surface at intermediate pressures, and capillary condensation in the intertube mesopores at high pressures. The simulation results validate the use of the BET model for surface area analysis in the experimental system. The average total accessible surface area is found to be $180 \pm 100 \text{ mm}^2$ and the specific surface area is estimated to be $45 \pm 25 \text{ m}^2/\text{g}$. Further engineering of the CNT film microstructure should lead to much higher surface areas. [Carbon 49 (2011) 3639]

NS-ThP3 Integrated Ultra-High Vacuum Tip-Enhanced Raman Spectroscopy with Molecular-Resolution Microscopy of Large Polyatomic Molecular Adsorbates on Single Crystal Surfaces, N. Jiang, E.T. Foley, J.M. Klingsporn, M.D. Sonntag, M.C. Hersam, R.P. Van Duyne, Northwestern University

Multiple vibrational modes have been observed for copper phthalocyanine (CuPc) adlayers on Ag(111) using ultrahigh vacuum (UHV) tip-enhanced Raman spectroscopy (TERS). Several important new experimental features are introduced in this work that significantly advance the state-of-the-art in UHV-TERS. These include (1) concurrent sub-nm molecular resolution STM imaging using Ag tips with laser illumination of the tip-sample junction, (2) laser focusing and Raman collection optics that are external to the UHV-STM that has two cryoshrouds for future low temperature experiments, and (3) all sample preparation steps are carried out in UHV to minimize contamination and maximize spatial resolution. Further, density-functional theory calculations have been carried out that allow quantitative identification of eight different vibrational modes in the TER spectra. The combination of molecular-resolution UHV-STM imaging with the detailed chemical information content of UHV-TERS allows the interactions between large polyatomic molecular adsorbates and specific binding sites on solid surfaces to be probed with unprecedented spatial and spectroscopic resolution.

NS-ThP4 An New One-step Synthesis Method for Generating Nanocarbon-supported Metal Nanoparticle, J. Kang, L. Li, N. Zetsu, O. Takai, N. Saito, Nagoya University, Japan

Introduction

Metal nanoparticles attract sustained attention due to their application in electrocatalysis for cell. Recently, many loading methods of nanoparticles on carbon material such as chemical reductions, electrochemical reductions, sol-gel polymerization and ultrasonic vibration have been reported for the generation of cell electrode. However, these methods generally require either reducing agent to reduce metal ions or removal of residues from the solution dispersed nanoparticles and its dispersibility and loading amount is poor. To supplement these weaknesses, in this study, the Au, Ag, Pt, Au-Pt bimetallic alloyed nanoparticles were synthesized simultaneously with carbon nanoball (Au, Ag, Pt, Au-Pt/CNB) by our progressive method, Solution Plasma Process (SPP).

Experimental Procedures

Highly porous CNBs were synthesized from 200 ml of organic. The glow discharge in solution was produced by using a bipolar pulsed power supply

operated at 1.6 kV of voltage, 15 kHz of pulse frequency, 0.7ms of pulse width, and 0.3 mm electrode distance, respectively and then NPs/CNB were annealed for improvement conductivity of CNB. The nanoparticle/carbon nanoball (NPs/CNB) were characterized by X-ray diffraction (XRD), transmission electron microscopy (TEM), scanning electron microscope (SEM) Brunauer-Emmett-Teller (BET) method and cyclic voltammetry (CV)

Results and Discussion

Approximately 500mg of CNB were generated by SPP of 200ml of organic solution in 15 minute process time. As evaluated by SEM, the diameters of CNB were in a range of 20 nm to 30nm and it showed that these carbon spheres have a ball-like and chain-like morphology, accompanied with a quite uniform diameter. The Scanning Transmission Electron Microscopy (STEM) image showed that the 1~2 nm diameter of Au, Pt, Au-Pt bimetallic alloyed nanoparticles were deposited on all of CNB with high loading and dispersion. The BET surface area and the pore volume of as obtained CNB were respectively, 120~130 m²/g and 0.8~0.9 cm³/g. The average pore size could be estimated approximately as 20~25nm. Subsequent heating of the CNB at 850°C for 30 minutes under an Ar environment encouraged the increase of the BET surface area and pore volume of CNB to 250~300 m²/g and 1.1~1.3 cm³/g respectively. The average pore size was calculated around 15~16nm. These results strongly suggested that our newly developed process of NPs/CNB synthesis might be a potential method for a single-step production of nanocarbon-supported metal nanoparticle.

NS-ThP5 The Role of an Amorphous Carbon Layer on a Multi-Wall Carbon Nanotube Attached Atomic Force Microscope Tip in Making Good Electrical Contact to a Gold Electrode, S.J. Ahn, KRISS, Republic of Korea

Multi-wall carbon nanotube (MWNT) attached atomic force microscope (AFM) tips (MWNT tips) have good potential for use in AFM lithography. Good conducting MWNT tips are needed in such applications. However, characterizing the conductance of MWNT tips is nontrivial: making a good electrical contact between the MWNT and electrode is difficult. We observed that MWNT tips produced by hydrocarbon-deposition attachment usually do not make good electrical contacts to gold electrodes because of the thin and rough amorphous carbon layer on the MWNT that was unintentionally deposited during the attachment. We found that good contacts can be made if a more amorphous carbon layer is deposited to form a thick and smooth amorphous carbon layer on MWNTs. Good contact was made either by transformation of the amorphous carbon layer into a conducting or peel-off layer, exposing the bare MWNT surface. MWNT tips with an exposed MWNT surface showed the well-known high-current-flowing capacity and the stepped-cutting behavior of bare MWNTs. The peeling-off behavior of a thick amorphous carbon layer may be utilized in producing bare-surfaced MWNT tips that have good conductance and therefore are useful for applications.

NS-ThP6 Passivation Effects on Electrical Properties of SnO₂ Nanowires FET Treated by Nitrogen Plasma, Y.H. Choi, P.S. Kang, J.H. Na, J.S. Kim, Korea University, Republic of Korea, S.-H. Choi, Korea Institute of Science and Technology, Republic of Korea, M.Y. You, G.T. Kim, Korea University, Republic of Korea

SnO₂ (tin oxide) are used in various research fields such as thin film transistors (TFTs), flexible and transparent nanowire transistors, and gas sensors, because of large band gap of 3.6 eV, high electron mobility and a high surface-to-volume ratio. However, the electrical characteristics of SnO₂ nanowires FETs are not so stable in ambient conditions due to the chemical reactions between oxygen molecules in air and oxygen vacancies in SnO₂ nanowires. To improve the device reliabilities of SnO₂ nanowires FETs, the N₂ plasma were treated. The N₂ plasma treatments on SnO₂ nanowires FETs led to the reduction of the hysteresis width in the transfer characteristics. Also the threshold voltage shifted to the positive direction. Even though the reliability of SnO₂ nanowires FETs is improved after the N₂ plasma treatment, unnecessary degradations can be induced with time in an ambient environment, requiring the passivation process. The PMMA and the carbon polymers deposited by CF₄ plasma treatments were used for the passivation of the SnO₂ nanowire FET devices. To investigate the effect of the passivation, the unpassivated and the passivated devices have been compared. The changes of the mobility and the carrier concentration were separately analyzed, indicating the different behaviors with or without the passivation.

NS-ThP7 Application of Rolling Circle Amplification and Thermal Dynamic Principle for Manipulating the Interparticle Spacing of Gold Nanoparticle Chains. *Y.P. Lu, M.Y. Lin, Y.-C. Ou*, National Applied Research Laboratories, Taiwan, Republic of China

Biomolecular nanotechnology draws a lot of attention in organizing DNA sequence, which can architecturally build up a nano-sized scaffold, because of their potential utility in nano-machines and biosensing. According to the DNA complementary base-pairing interactions and aptamer design, DNA backbone has further been used for the construction of a variety of geometric objects and anchoring sites for functionalized proteins or metals. A simple and applicable procedure to miniature nanostructures is expected to enhance the detection sensitivity of devices. It is important to construct the metallic nanoparticle chain with different interparticle spacing because the organized metallic nanoparticles self-assembled from DNA nanostructure may affect the photoelectric properties. We successfully generate well-controlled formation of long, flexible, one dimensional gold nanoparticle (AuNP) chains by employed DNA template for self-assembly AuNP based on rolling circle amplification (RCA) technique. For the purpose of controlling the interparticle spacing of AuNP, we report the construction of long chain DNA-AuNP with or without secondary structure of DNA scaffold by using of base-pairing strategy and thermal dynamic reaction. The heating process under appropriate temperature broke the intramolecular Watson-Crick interactions to form the hairpin structure. This ultimately allowed no AuNP modified primers to hybridize with the open region of single strand DNA backbone, hence increased the interparticle spacing between each AuNP. The effect of AuNP distance in optical and electronic properties can be designed by controlling the DNA sequence and thermal dynamic reaction, and thus changed the optical and electronically characters of AuNP-based nanostructures for many applications in optoelectronics and biosensing devices fabrication.

NS-ThP8 Synthesis of Gold Nanofluids for Improved Heat Transfer using Solution Plasma. *Y.K. Heo, M.A. Bratescu, N. Saito*, Nagoya University, Japan

In recent years, the development of high speed devices and their integrated circuits has facing some obstacles owing to localized heat generation in terms of safety and efficiency of devices. Nanofluids which were defined fluids containing nanometer-size particles, have been researched for their high and efficient heat transfer. It was reported that heat transfer enhancement was due to the Brownian motion of the nanoparticles contained in the fluids. Therefore, the diameter of nanoparticles in nanofluids is a key-factor in order to develop new heat transfer systems with higher energy-efficiency.

Recently our research group has developed a new synthesis method for well-defined nanoparticles in an aqueous solution, by solution plasma process (SPP). This process allows us to fabricate solutions containing high quantity of small monodispersed nanoparticles in order to obtain a heat transfer system with improved efficiency.

In this research, we aimed to reveal the heat transfer of nanofluids. The solution containing monodispersed gold nanoparticles was synthesized by SPP using a DC bipolar pulsed power supply. Gold nanofluids were synthesized with various concentrations of 0.1, 0.3, 0.6, 0.9 mM HAuCl₄ and 4 times KOH of each HAuCl₄ concentration in distilled water. The reaction time is 15 minutes. The solution plasma optical and electrical conditions were measured by OES and oscilloscope. The evaluation of the synthesized nanoparticles was performed by TEM analysis and UV vis spectroscopy. The dispersion stability was evaluated using zeta potential. In addition, KD2 pro & viscometer were used for heat transfer analysis of the synthesized nanofluids.

The decrease of the nanoparticles diameter from 13.8 ± 4.3 nm to 5.6 ± 1.4 nm was measured in dependence with the precursor concentration. The viscosity of the nanofluid increased with precursor concentration from 1.95 mPa·s to 2.05 mPa·s at 283 K (Viscosity of Di Water is 1.51 mPa·s.). A precursor concentration of 0.9 mM produced the smallest nanoparticles diameter of 5.6 ± 1.4 nm, and the highest increase of the thermal conductivity of 29.4 %.

NS-ThP9 Post Ion-Implant Growth of Epitaxial Graphene on 6H-SiC. *J. Seo, H. Shin, J.-H. Park, J.R. Ahn*, Sungkyunkwan University, Republic of Korea

Graphene, a two-dimensional sheet of sp²-bonded carbon arranged in a honeycomb lattice has attracted significant attention due to its interesting characteristics such as high carrier mobility, optical transparency, mechanical strength, and possible applications in various fields. Among the techniques developed for producing graphene, epitaxial growth on silicon carbide (SiC) is a promising method for large-scale production. Ion implantation is also a mature technology in large-scale electronic industry, which can take the epitaxial graphene into the semiconductor foundries.

Here we studied post ion-implant growth of epitaxial graphene on 6H-SiC substrates according to ion fluences, acceleration voltages, and substrate temperatures. N⁺ ions at 40-145keV were implanted with fluences of 1×10^{17} N⁺/cm² and 3×10^{17} N⁺/cm² into 6H-SiC substrates under room temperature (RT) and 650°C. The ion distributions and structural variations in the implanted samples have been studied using secondary ion mass spectrometry (SIMS) and transmission electron microscopy (TEM) both before and after the graphene growth. This study revealed that the implanted N⁺ ion distributions in 6H-SiC are robust up to ~1330°C at which the epitaxial graphene begins to grow on Si-face of 6H-SiC and the graphene is formed only when the substrates are maintained at 650°C during ion implantation. This is believed to be due to the prominent damage recovery of 6H-SiC in high temperature implantations. The high crystallinity of the epitaxial graphene grown on the damage-recovered 6H-SiC was confirmed by photoelectron spectroscopy and low-energy electron diffraction.

NS-ThP11 Preparation of Metal Nanoparticles within Mesoporous Silica via Solution Plasma Process (SPP). *W. Yaowarat, N. Saito*, Nagoya University, Japan

Recently, nanoparticles within mesoporous silica have been extensively studied due to their significant physicochemical characteristic. It is widely used in various applications such as instant microbial inhibition, sensor, catalyst, and electronic devices. As previously reported that nanoparticles within mesoporous silica could be synthesized by chemical treatment and calcination. However, high temperature and long time treatment must be required.

Solution plasma process (SPP) is a new plasma system which could be used to synthesis metal nanoparticles. SPP is superior to other conventional methods, in term of ease of handling, low temperature, and short time treatment. It is therefore of our interest to apply the solution plasma process to prepare metal nanoparticles within mesoporous silica. The voltage, frequency and pulse width of solution plasma conditions were fixed at 1.6 kV, 15 KHz, and 2 μs, respectively. 1 mM of AgNO₃ solution with 0.2 g mesoporous silica was treated with solution plasma for 15 minutes. The plasma-treated sample was filtrated prior to air dry for overnight. The dried sample was characterized by transmission electron microscopy (TEM). The TEM results showed that the silver nanoparticles could be performed during solution plasma treatment and filled within nanoscale channels of mesoporous silica matrix. This suggested that the solution plasma process could be a potential method for prepare metal nanoparticles within mesoporous silica.

NS-ThP12 The Electrical Property of the Interface Between Dielectrophoresis (DEP)-Aligned Single-Walled Carbon Nanotubes and Semiconductors. *M. Hines, Z. Xiao*, Alabama A&M University

The dielectrophoresis (DEP) method was used to align and deposit single-walled carbon nanotubes for the fabrication of high-performance single-walled carbon nanotube field-effect transistors (CNTFETs). Semiconducting materials such as silicon and germanium were used as the source/drain contact material in the fabrication of CNTFETs for improving the device electrical performance. The DEP-aligned carbon nanotubes were mesh networks interconnecting with metallic nanotubes and semiconducting nanotubes. The vacuum-based deposition such as e-beam evaporation and sputtering deposition was used to grow the silicon and germanium thin films, and clean room-based microfabrication techniques such as UV lithography was used to fabricate the CNTFETs. The electrical property of fabricated CNTFETs were measured and characterized. The semiconductors can significantly increase the ratio of the switch-on/off electrical currents in the fabricated CNTFETs. The electrical property of the interface between the single-walled carbon nanotubes and the semiconductors and the fabricated CNTFETs will be reported in the conference.

NS-ThP14 Field Emission Based Hydrogen Sensing Characteristics from Carbon Nanotubes Synthesized on Catalytical Substrates. *C. Dong*, Wenzhou University, Republic of China

A new hydrogen sensing concept is demonstrated based on the field emission form multi-walled carbon nanotubes. The low emission currents rise in proportional to hydrogen partial pressures above from 10⁻⁹ to 10⁻⁵ Torr. Catalytic Ni participated C-H reactions in low emission regime are considered the key factor of the sensing behavior. Simple setup, tiny structure, high sensitivity, and fast recovery make this innovative technique attractive to build miniature low cost hydrogen sensors for low pressure applications.

Plasma Science and Technology Poster Session

PS-ThP1 Plasma Etch Challenges to Produce Metallization-Friendly Profiles at 20nm and Beyond Technology Nodes in the BEOL. *Y. Mignot*, STMicroelectronics, *R. Koshy*, GLOBALFOUNDRIES, *Y. Park*, Samsung Electronics Co. Ltd., *R. Srivastava*, GLOBALFOUNDRIES, *E. Soda*, Renesas Electronics, *Y. Yin*, *M. Beard*, *B.G. Morris*, IBM Microelectronics, *K. Trevino*, GLOBALFOUNDRIES, *J. Arnold*, *S. Allen*, IBM Microelectronics, *C. Labelle*, GLOBALFOUNDRIES, *M. Sankarapandian*, IBM Microelectronics, *Y. Loquet*, STMicroelectronics, *Y. Feuprier*, *L. Wang*, *J. Stillahn*, *Y. Chiba*, *V. Gizzo*, *K. Kumar*, Tokyo Electron Technology Center, America, LLC, *C.A. Wang*, *Q. Zhang*, GLOBALFOUNDRIES, *A. Inada*, Renesas Electronics, *S. Mignot*, STMicroelectronics

As feature critical dimension (CD) shrinks towards and beyond the 14nm node, new patterning techniques within the context of a trench-first-metal-hard-mask (TFMHM) patterning scheme have been developed to generate trenches and vias below 100nm pitch. One of the main challenges at advanced nodes is to create structures (i.e., trenches & vias) that can be robustly metalized. This requires several elements of focus for the etches: first, there must be zero dielectric etch damage that results in undercut of any hard masks in the film stack; second, the aspect ratio of the final etch structure must be minimized; and third, the shape of the trench or via profile must be tailored to be metallization-friendly (i.e., slight angle better than vertical). These requirements often conflict with each other, especially within a patterning scheme that requires self-aligned vias, where the desired high selectivity to the hard mask conflicts with the need to minimize the amount of hard mask left in order to decrease aspect ratio. In this paper, we will discuss some of the approaches that we have investigated to achieve the best profile for metallization. This includes plasma etch all-in-one (AIO) dielectric etch optimization as well as multi-step solutions that potentially can use techniques including wet chemistries, ion beam metal etching, and dry metal etching. In addition, data will be presented on efforts to minimize overall metal-related residues observed as a function of the pattern density and thus, metal exposure. Metal-containing etch byproducts have also been observed and the material characteristics and/or morphology of these etch byproducts can vary across the wafer, producing non-uniform residue patterns and affecting the plasma etch erosion of the metal hard mask itself. Understanding the underlying mechanisms of observed metal-induced defects (i.e., residues, etch byproducts, etc.) is key to applying the correct plasma etch optimization to eliminate or minimize the effects. Some data will be presented showing the progress that has been made on these issues.

PS-ThP2 A Comparative Study of Plasma-Treated Fluoropolymers at Atmospheric Pressure. *T. Dufour*, *J. Hubert*, *N. Vandencastele*, *F. Reniers*, Université Libre de Bruxelles, Belgium

Due to their extraordinary range of properties, polymeric materials play an essential and ubiquitous role in everyday life. Plasma-modifications of polymeric surfaces further extend the range of their applications, especially with fluoropolymers due to their widespread in biocompatibility and self-cleaning coatings applications.

The aim of our work is to compare the treatments carried out with two distinct plasma sources on a selection of fluoropolymers: PVF, PVDF, TrFE, PTFE, Nafion®, FEP and PFA. The first treatment is performed with a post-discharge generated by an RF plasma torch, supplied with a helium-oxygen mixture and operating at atmospheric pressure. The second treatment is achieved in the plasma phase of a DBD and operates at atmospheric pressure, also in the same gases. In both cases, we discuss the influence of the treatment time and of the O₂ flow rate on the surface properties. A comprehensive study of the plasma/polymer interface has also been performed by mass spectrometry and optical emission spectroscopy to identify the species responsible of the surface texturization, i.e. the species breaking the atomic bindings on the surface top atomic layers.

The surface properties are characterized by determining the advancing and receding WCA so as to show if the treated polymers can be classified into the Wenzel or Cassie-Baxter models. The super-hydrophobicity of PTFE has already been achieved. Moreover, two liquid probes have been used: milliQ water (H₂O) and diiodomethane (CH₂I₂) to discuss the validity of the Fowkes theory.

Finally, the XPS analyses give information on the surface composition which remains unchanged for the majority of the studied fluoropolymers. We will also explain how it is possible to identify the fragments ejected from the polymeric surfaces during the etching process by using the XPS instrument. CF₂ fragments have already been evidenced in the case of the PTFE and different ones in the case of Nafion®.

PS-ThP3 Advances in 2D/3D Feature Profile Simulations. *P. Moroz*, Tokyo Electron US Holdings Ltd

Plasma etching, deposition, and implantation are widely used in semiconductor industry, with application of complex chemistries and plasmas to obtain desirable profiles and material properties. However, in practice, etched profiles might show undesirable effects such as bowing, or necking, or micro-trenching, among others, as well as might demonstrate the so-called loading effect. Those effects become more concerning or even dangerous for features of smaller sizes, especially for high aspect ratio etching of trenches and contact holes where they could lead to defects of the device. Selecting proper gas mixtures as well as the regimes of plasma operation to obtain proper profiles is a very tedious process, and numerical simulation could become a highly needed and useful tool. Here we discuss new capabilities and unique characteristics of the 2D/3D feature profile simulator FPS-3D [1-2]. The FPS-3D simulator was developed as a general type simulator, in principle, applicable to any materials, reactive gases, plasmas, or beams, for which the user could provide proper reaction mechanisms. FPS-3D can simulate etching, deposition, or implantation processes going on at the same time. Among new developments to be presented is the capability of considering multi-step (or multi-recipe) processes, when each step could have different fluxes to the surface and different chemistry. Another new development in FPS-3D is the possibility of simulating the pulse-plasma effects. Examples presented are mainly based around a particular case of HARC etching of SiO₂ by the fluorocarbon-argon-oxygen plasma in a capacitive-type plasma system. [1] P. Moroz, ECS Transactions, 35 (20) 25 (2011).[2] P. Moroz, IEEE Transactions of Plasma Science, 39 (11) 2804 (2011).

PS-ThP4 Laser Thomson Scattering Measurements of Plasma Parameters in the Low Temperature Plasmas. *J.-H. Kim*, Korea Research Institute of Standards and Science, Republic of Korea, *B.H. Seo*, Korea Advanced Institute of Science and Technology, Republic of Korea, *S.-J. You*, *D.J. Seong*, Korea Research Institute of Standards and Science, Republic of Korea

Diagnostics of electron density and temperature play an important role for characterization of processing plasmas and basic plasma researches. Laser Thomson scattering is a one of the most accurate diagnostic technique for measuring electron density and temperature because of none-perturbation to plasma among various diagnostic techniques invented to measure plasma density and temperature. I will briefly review the method of Laser Thomson Scattering to measure the electron temperature and density. Electron energy probability functions (EPPFs) having a fine resolution of electron energy were measured in low-pressure inductively coupled plasma with laser Thomson scattering method (LTS) at various plasma conditions (rf powers and gas pressures) and compared with the EPPFs measured by a single Langmuir probe (SLP) at the same experimental conditions. The result of LTS showed that the measured electron density normally increases with the rf power and the gas pressure, and the electron temperature decreased with the rf power and the gas pressure. The results have a good agreement not only with the previous reports qualitatively but also with our SLP measurement result quantitatively. We have a plan to establish a standard of plasma measurement with this LTS, which will be discussed.

PS-ThP5 Development of a New Plasma Treatment Followed by a Bake for Photoresist Linewidth Roughness Smoothing. *M. Fouchier*, *E. Pargon*, CNRS/UJF-Grenoble1/CEA LTM, France, *L. Azarnouche*, ST Microelectronics, France, *K. Mengueli*, *M. Brihoum*, CNRS/UJF-Grenoble1/CEA LTM, France

As the dimensions of microelectronic circuits scale down, the gate linewidth roughness (LWR) increasingly impacts the electrical performances of transistors. It has previously been shown that the significant photoresist (PR) sidewall roughness after lithography is transferred into the gate during the subsequent plasma etching process, resulting in a final gate LWR far above the ITRS requirements. The key to reduce the gate LWR is to minimize the photoresist LWR before plasma transfer. Plasma treatments are commonly used for that purpose. In previous studies, we have shown that photoetching mechanisms occurring during plasma exposure plays a key role in PR smoothing. We have also demonstrated that the carbon species outgassed during the treatment can redeposit on the PR pattern sidewalls and degrade the LWR. Moreover, we have shown the benefit of applying a bake after plasma treatment in order to further decrease the LWR. From this knowledge, we develop a new treatment based on HBr/O₂ plasma exposure followed by a bake. The plasma conditions are optimized in order to emit strongly in the vacuum ultra violet (VUV) range (below 200 nm) and to prevent carbon redeposition on the resist sidewalls. We show that by controlling the VUV dose (mainly by tuning source power or plasma exposure time), the PR bulk can be either softened (photolysis) or strengthened (crosslinking). Moreover, the formation of the carbon deposit on the resist surface can be controlled by the O₂ content of the plasma. The surface and bulk properties

of the PR line after plasma treatment will determine the LWR behavior during the subsequent thermal cure treatment. A soft resist bulk combined with a thin surface carbon layer is the ideal case to get the best LWR smoothening during the bake without reflowing. By optimizing both the plasma oxygen content and VUV dose, we obtain a 60% LWR decrease after bake reducing the LWR from 7.3 nm to 2.9 nm.

PS-ThP6 Analysis of Target Oxidation in Reactive Sputter Deposition Processes of Silicon Dioxide. *K. Hoshino, K. Demura, S. Tamaya, M. Okamoto, Y. Murakami, Canon Inc, Japan, M. Isobe, T. Ito, K. Karahashi, S. Hamaguchi, Osaka University, Japan*

Reactive sputtering is widely used for thin film deposition of various compounds such as oxides and nitrides of metal and non-metal elements. In reactive sputtering processes, reactive gases such as oxygen are added to discharge of a sputtering system and chemical reactions between gaseous species and sputtered materials from the target form chemical compounds that are deposited on the substrate. In reactive sputtering processes, chemical compounds are also formed on the target surface and the thickness of the compound layer affects the sputtering rate of the target, which in turn can affect the film deposition rates and even film qualities. Therefore, for deposition of high quality thin films, control of compound formation on the sputter target is considered to be of significant importance.

Compound-layer formation on a target must be caused by influx of reactive ions and free radicals from the plasma despite the constant sputtering of the target surface. Details of such surface reaction processes have not been well understood to the extent that such knowledge could be readily used for the control of reactive sputter deposition processes.

In this work, we have focused on reactive sputtering deposition processes of SiO_2 thin films and examined the oxide layer formation on a Si target, using multi-beam injection experiments with beams of radicals and mass-analyzed energetic ions as well as molecular dynamics (MD) simulations of surface reactions. It has been found that oxygen ions, which penetrate the substrate more deeply than argon ions at the same incident energy, cause constant oxidation of the surface whereas the flux ratio of low-energy charge-neutral oxygen radicals to argon ions can also significantly affect the thickness of surface oxide. These results can be used to facilitate the control of plasma conditions for reactive sputter deposition processes.

PS-ThP7 On the Origin of the Line Width Roughness of Photoresist Patterns after Plasma Exposure. *R. Ramos, M. Brihoum, K. Menguelti, L. Azarnouche, M. Fouchier, E. Pargon, G. Cunge, O. Joubert, LTM (CNRS / UJF-Grenoble1 / CEA), France*

The control and minimization of the roughness on the sidewalls of transistor gates is a major aspect of the plasma patterning technology in microelectronics. The line width roughness (LWR) in the active layers is known to originate mostly from the transfer of the initial LWR of the photoresist patterns defined by 193 nm lithography. As a consequence, numerous plasma pre-treatments of the photoresist have been developed and applied to decrease the mask LWR prior to the plasma etching of the gate stack. However, the final LWR is still higher than the requirements for the next technological nodes. It is therefore necessary to develop a clear understanding of the physical mechanisms responsible for the modifications of the photoresist LWR during plasma exposure to further reduce the gate width roughness. In this work, we will show that plasma treatments of photoresist patterns result in the formation of a shell surrounding the pattern, i.e. including on surfaces not exposed to ion bombardment. The redeposition of by-products from the (photo)etching of the resist polymer plays a major role in the formation of this shell. We will highlight the influence of the mechanical properties of both the shell and the underlying modified photoresist on the LWR of plasma-exposed resist patterns. Based on the proposed mechanism, we will discuss the potential of pulsed plasmas for LWR reduction processes.

PS-ThP8 Effect of Film Properties on Nitride Etching. *T. Wanifuchi, G. Takaba, H. Ohtake, M. Sasaki, Tokyo Electron Technology Development Institute, INC., Japan*

Silicon nitride has been widely used for dielectrics of CMOS logic devices, especially, for spacers or stopper layers. However, the mechanism of etching was not known well. In addition, several kinds of nitride film have been used in the devices and we have to know the effect of film properties on the etching characteristics. In this paper, the effect of film properties on nitride etching characteristics was investigated. 5 kinds of nitride wafers were prepared by changing the deposition temperature. The film density was lower at the lower deposition temperature, which contains more hydrogen in the film. As etching tools, RLSA™ Etch, ICP and CCP were used. RLSA™ Etch has high Ne of more than $1 \times 10^{11} \text{ cm}^{-3}$ and low Te of less than 1 eV around the stage because RLSA™ Etch tool uses the surface wave plasma and diffusion chamber. $\text{CH}_3\text{F}/\text{CF}_4/\text{O}_2$ gas chemistry was used

in all etchers. CCP showed ion-dominated etching because the etching rate was almost constant at various nitride films. On the other hand, RLSA™ Etch and ICP showed the dependence of etching rate on film property. The etching rate decreases by increasing the film density. However the RLSA™ Etch showed stronger dependency as compared with ICP. It is considered that radical-surface reaction dominated etching was realized at RLSA™ Etch because ICP generates fluorocarbon polymers more than RLSA™ Etch. Moreover, the dependency on film property was strongly related to the etching recipes. Film dependency was enhanced at the radical (chemical) etching condition as compared with ion dominated etching condition. In addition, we also observed the surface of nitride after oxygen plasma exposure because we used this plasma for surface cleaning. The results showed the dense and shallow oxidation layer was generated at the dense nitride film. Based on these result, we found that the etch characteristics was drastically changed by the film property and we have to use the appropriate plasma for precise nitride etching, corresponding to the film property.

PS-ThP9 A DC-RF Magnetized Plasma Source. *Y. Raitses, I.D. Kaganovich, Princeton Plasma Physics Laboratory*

We report results for a new plasma source which uses a low pressure ($\sim 10^{-4}$ Torr) discharge with applied electric and magnetic fields. A dc voltage of 20-100 V is applied between the RF plasma cathode and the anode-chamber. The magnetic field is varied between 50-500 G. Under such conditions this cross-field discharge is shown to sustain an efficient ionization of xenon and argon gases ($n_e^{\text{max}} \sim 10^{11}-10^{12} \text{ cm}^{-3}$, $T_e \sim 1-10 \text{ eV}$). Probe measurements revealed that the magnetized plasma of the DC-RF discharge has a non-Maxwellian EEDF with a depleted high-energy tail. It is also shown that spatial variations of the EEDF are governed by a non-local electron heating and anomalous electron transport across the magnetic field. An important implication of the above results is that the anomalous electron transport may degrade the magnetic filter effect, which supposes to separate "hot" and "cold" groups of plasma electrons.

This work was supported by the US DOE.

PS-ThP10 Quick Estimation of Deposition Rate for a Sputter System. *G. Ding, Y. Wang, J. Cheng, D. Schweigert, Z. Sun, M. Le, Intermolecular Inc.*

Here we present a practical estimation on deposition rate for a sputter system. The sputter system consists of four sputter sources in a high vacuum chamber, with an independent power supply for each sputter source. Quick estimation of deposition rate could be helpful for efficient experimental planning and reducing the number of experiments and time.

First, theory: Our early JAP paper* disclosed an energy balance model and derived a sputter rate $= k(P - P_0)$. The physical meaning is that the sputter rate has a linear relationship with plasma source power P , with a nearly constant offset P_0 , and constant slope k . Here we present several different materials results which illustrate the good fit between deposition rate and power within the working range of 100W to 550W.

Second, P_0 estimation: The physical meaning of P_0 is the power consumed to sustain plasma, which is dependent on the plasma boundary condition (chamber/plasma source geometry), ion diffusion co-efficient, electron temperature etc. In this situation, since the plasma ion is primarily Argon ion with fixed chamber geometry, P_0 is nearly constant within the range of 25 to 52 W. With a simple estimation of 39W, an error of only 13W could be introduced. For a typical 200-400W experimental condition, the error from this estimation is small (2-5% error).

Third, slope k estimation: The different materials trends with slope k are calculated $M/D * Y * V$ and plotted. (M : is the atomic weight, D : is the density, Y : is the sputter yield at 300V for Argon ion, and V is the DC voltage of the sputter source). The model assumes that the slope k is proportional to the sputter yield at the DC voltage, and converts the mass to volume for thin film thickness based on the deposition rate calculation. In our case, DC voltage V is close to 300V, so that sputter yields at 300V were used. However, further investigation showed that the simple sputter yield might not be accurate enough, and the correction for the sputter DC voltage could provide a better fit. The slope k trend agreed well with model estimation $M/D * Y * V$. Thus, results here implied that the slope k could be estimated for different materials.

Thus, a quick deposition rate estimation method was derived in comparison with experiments, which is expressed as: $\text{dep rate} = M/D * Y * V * k' * (P - P_0)$, and k' and P_0 are chamber specific that need to be experimentally determined. Once calibrated from one experiment, the deposition rates of other materials can be estimated from this formula.

In addition, this study could be helpful in applying to other chambers and sputter sources for a quick deposition rate estimation, even for alloy target or reactive sputtering.

PS-ThP12 Application of E-beam Curing Technique to EUV Resist Utilizing DC Superimposed Capacitively-Coupled Plasma, M. Honda, T. Katsunuma, K. Narishige, Tokyo Electron Miyagi Ltd., Japan, K. Yatsuda, Tokyo Electron Limited, Japan

EUV lithography provides much bigger dry etch challenges than 193-nm lithography did. Its depth of focus (DOF) is

so small that the thickness of EUV resist is much thinner than that of 193-nm resist. Although EUV resist requires

higher etch selectivity than 193-nm resist does, UV/VUV cure, which has been used in 193-nm resist, is not an

effective technique to enhance etch selectivity and physical strength. This is because UV/VUV light is essentially

transparent in EUV resist. Etch selectivity normally attributes to polymer which prevents material from being etched.

In the case of EUV resist, line width roughness (LWR) is easily enhanced by polymer because its physical strength

is so low, and the resist width is so small that the resist cannot tolerate the stress of polymer. This is quite contrary

to the ideal reactive ion etch (RIE) which diminishes LWR. Therefore, an alternative curing technique for EUV resist

is required to improve the etch selectivity without increasing LWR.

We introduced the e-beam curing technique for 193-nm resist utilizing a direct current superimposed (DCS) capacitively-coupled plasma (CCP) at the 55th AVS in 2008. Negative high DC voltage is applied in DCS CCP,

and positive ions collide with the upper electrode. Thus, secondary electrons are emitted from the upper electrode.

The applied negative high DC voltage also accelerates the emitted secondary electrons, which turn into ballistic

electrons. The curing mechanism of 193-nm resist is scission and cross-linking of polymer by e-beam which is a

consequence of ballistic electrons. Considering its mechanism, the e-beam curing should be available to any

polymer. Thus, we applied this technique to EUV resist, and investigated the effect of e-beam in EUV resist. In order

to identify the cured thickness and chemical structure change, the surface was analyzed with cross-sectional SEM

and ToF-SIMS, respectively. As a result, the curing effect was confirmed. In addition to the curing technique, we

also invented a coating technique with a silicon compound material by sputtering the upper electrode utilizing the

DCS technology. This coating technique increases the etch selectivity to EUV resist. In this technique, silane type

gases are not required, making it easily applicable to manufacturing.

PS-ThP13 SiH₄/H₂ and CH₄ Multi-Hollow Discharge Plasma CVD of SiC Nano-Composite Anode for High Charge-Discharge Capacity Lithium Ion Batteries, Y. Morita, Kyushu University, Japan

Although most lithium ion batteries employ carbon in various forms such as graphite, hard carbon and microspheres, as an anode material; carbon has the low charge-discharge capacity up to 372 mAh/g. Silicon is one of the most attractive material to replace the carbon anode because it is abundant and has the high charge-discharge capacity up to 4200 mAh/g. Fully lithiated silicon is 4 times larger in volume than Si and such significant increase in volume causes fracture and pulverization of the electrode, thereby leading to capacity degradation and failure of battery cells. Recent studies showed that carbon-silicon composite material is effective to solve the silicon related problems. Here we employ SiC nanoparticles as an anode material [1]. Surface carbonization of silicon nanoparticles was performed using double multi-hollow discharges, where nanoparticle generation and the surface carbonization were independently controlled with the double multi-hollow discharges. Silicon nanoparticles were produced by the multi-hollow discharges of H₂ + SiH₄ multi-hollow discharge plasma. CH_x radicals for carbonization, which was produced by the CH₄ multi-hollow discharge plasma, were irradiated to nanoparticles during their transportation to the downstream region. The electrolyte was 1M LiPF₆ in ethylene carbonate (EC)/ dimethylene carbonate (DMC) (1:2). For measurements of anode properties, a Li metal sheet of 1 mm in thickness was used as a cathode [2]. Li intercalation capacity was measured with a constant current of 0.1 mA/mg. Charge-discharge capacity of the SiC nano-composite anode of the first cycle was 3000 mAh/g, which is 9 times higher than the capacity of graphite anode. SiC nano-particle-composite anode produced by plasma CVD is promising for lithium ion batteries. Lithium-ion batteries will play the most important role in the future of electric

energy storage applications, including hybrid and electric vehicles over the next five years.

Work partly supported by Regional Innovation Strategy Support Program, MEXT.

[1] G. Uchida, et al., Jpn. J. Appl. Phys. 51 (2011) 01AD01-1.

[2] T. Ishihara, et al., Electrochem. Solid-State Lett., 10 (2007) A74.

PS-ThP14 Interface Trap Generation by VUV/UV Radiation from Fluorocarbon Plasma, M. Fukasawa, Sony Corporation, Japan, Y. Miyawaki, Y. Kondo, K. Takeda, H. Kondo, K. Ishikawa, M. Sekine, Nagoya University, Japan, H. Matsugai, T. Honda, M. Minami, F. Uesawa, Sony Corporation, Japan, M. Hori, Nagoya University, Japan, T. Tatsumi, Sony Corporation, Japan

Incident species from plasma needs to be strictly controlled to fabricate advanced devices. We found that simultaneous injection of VUV/UV radiation and radicals caused the marked etch rate enhancement of SiN_x:H films [1]. This indicates that not only ions, but also VUV/UV radiation affects the surface reaction of radicals with SiN_x:H. In this study, we investigated the effect of transmitted VUV/UV radiation on underlying interface traps of SiN_x:H/Si substrate by using the pallet for plasma evaluation (PAPE) [2].

A dual frequency (60/2 MHz) CCP reactor was used. SiN_x:H films were deposited on Si substrates by PECVD and those were exposed to CF₄/O₂ plasma. The thicknesses of SiN_x:H films were 200 nm. To investigate the effect of radiation, MgF₂ (> 115 nm), quartz (> 170 nm), and borosilicate crown glass BK7 (> 300 nm) windows were put directly on the SiN_x:H film. The capacitance-voltage (*C-V*) characteristics of SiN_x:H on Si substrate were analyzed to study the interface-trap density (*D_{it}*).

The penetration depths of photons strongly depend on the wavelength of the VUV/UV radiation and the absorption coefficient of materials. The wavelengths of photons were classified into three major ranges by their interaction with the material:

- 1) Photons are absorbed in the material and damage the film and/or enhance the surface reaction [1].
- 2) Photons are transmitted through the material and absorbed in the underlying interfaces, resulting in the increase in *D_{it}*.
- 3) Photons are transmitted through both the material and interface, and there is no impact on the damage generation.

The *D_{it}* increase is the most serious issue for advanced device fabrication since the *D_{it}* directly degrades electrical performance. Thus, the damage of SiN_x:H/Si substrate interface was investigated by *C-V* measurement. The *D_{it}* of SiN_x:H/Si substrate was unaffected by the VUV radiation (< 170 nm) since all the high-energy photons were absorbed in the SiN_x:H film (case 1). When the photons in the UV region (> 170 nm) were irradiated, the *D_{it}* increased and a negative charge was generated in the interface (case 2). This indicates that the VUV/UV radiation transmitting through the upper dielectrics causes the electrical characteristics of underlying devices to fluctuate. The UV radiation (> 300 nm) had almost no effect on the increase in *D_{it}* (case 3) due to the lack of absorption in both the material and interface.

Thus, the wavelength dependence of increases in *D_{it}* needs to be investigated for possible interfaces in advanced devices.

[1] M. Fukasawa *et al.*, Jpn. J. Appl. Phys., 51 (2012) 026201.

[2] S. Uchida *et al.*, J. Appl. Phys., 103 (2008) 073303.

PS-ThP15 Design of a Standalone Plasma Diagnostics Box, F.T. Molkenboer, H.H.P.Th. Bekman, F.H. Elferink, T.J. Versloot, E. Te Sligte, N.B. Koster, TNO Technical Sciences, The Netherlands

In setups for plasma research there are in most cases several sensors available to monitor the plasma conditions. However there are also numerous plasma systems for non-research applications that have limited or no plasma diagnostics available at all.

To solve this problem we have designed, a so called plasma diagnostics box. The plasma diagnostics box is made out of two units, a sensor head and the data logger box containing the data logger, batteries and electronics, connected by a flexible tube.

The sensor head contains multiple stand-alone sensors. The prototype device contains five basic plasma monitoring sensors, a PT100 temperature sensor, a heat flux sensor, silicon photodiode, a double Langmuir probe and a Faraday cup for measuring several key plasma parameters

The two unique features of the plasma diagnostics box is that it is a complete standalone unit and that it can be placed within the vacuum/plasma system. This means that there is no need for a feedthrough flange on the plasma/ vacuum system. However, if a feedthrough is available, the data logger box can be placed outside the vacuum, and the sensor head alone can be inserted in the system.

Because of the flexible connection the sensor head can be placed anywhere within the plasma. This makes it possible to characterise the plasma at different positions.

In this contribution we will discuss the design and manufacturing of the plasma diagnostics box. Besides the design we also will present the data we have measured with the plasma diagnostics box in one of our research plasma setups that we have available at TNO. The results obtained with these measurements will be benchmarked against the commercially available diagnostics on our research plasma setup.

PS-ThP18 A New Compact ICP Source for Neutral and Ion Beam Extraction, E. Karakas, V.M. Donnelly, D.J. Economou, University of Houston

A new compact inductively-coupled plasma (ICP) source will be presented. The source is designed to extract either a monochromatic ion beam or a neutral beam out of the plasma, to achieve highly selective etching of silicon, silicon nitride, or silicon dioxide. Two identical plasma sources were fabricated and installed on a processing chamber, with their axes perpendicular to one another. This setup offers flexibility in bombarding a substrate with neutrals and energetic ions either simultaneously, at a 450 angle of incidence, or sequentially at 900. Ion and neutral beams can be extracted in continuous or pulsed plasma modes. The sources can be characterized with line-of-sight mass spectroscopy, while etched surfaces can be examined by vacuum-transferred x-ray photon spectroscopy (XPS). A Langmuir probe was employed to measure spatially- and temporally-resolved plasma parameters as a function of pressure and power. At the center of the plasma, an electron density of $9.5 \times 10^{11} \text{ cm}^{-3}$ was reached for 500 W input power at a pressure of 50 mTorr Ar. A retarding field ion energy analyzer was employed to measure the ion energy distributions (IEDs) on a grounded substrate. In a pulsed mode, when the electron temperature decreased to a low value late in the afterglow, a synchronous pulsed DC bias was applied to a boundary electrode, creating a monoenergetic ion beam at a peak energy that was nearly equal to the bias voltage. The IEDs showed a single peak with or without bias. Initial characterization of the neutral beam composition and etching of silicon will also be presented.

*Work supported by Lam Research Corp.

PS-ThP19 The Role of Ions in the Gas-Surface Interactions of Nitrogen Oxide Plasma Systems, J.M. Blechle, M.F. Cuddy, E.R. Fisher, Colorado State University

Improving upon the effectiveness of substrates that are used in vehicular emissions abatement hinges on the ability to elucidate the contributions of various gas-phase species in surface reactions. Utilizing inductively coupled plasmas, the role of ions on surface reactivity is investigated to improve and tailor surfaces for the reduction of nitrogen oxide (N_xO_y) species. Here, nascent ions are monitored via mass spectrometry and energy analysis for NO, N_2O , NO_2 , and a 50/50 mixture of N_2 and O_2 precursor gases. The mean ion energy ($\langle E_i \rangle_{\text{total}}$) determined for all ions within each respective plasma system shows a strong positive correlation with applied rf power and a negative correlation with system pressure for all precursors studied. Ions also play varying roles in the surface scatter of NO radicals as demonstrated by the imaging of radicals interacting with surfaces (IRIS) technique. The net effect of ions on surface processing is dependent upon plasma parameters including the choice of precursor gas. Scatter coefficients (S), determined for ion-limited plasma systems are compared to ion-rich systems to correlate $\langle E_i \rangle_{\text{total}}$ and scatter, which suggests a need for precise control of the chemistry occurring between the gas-phase and surface. Such information lends itself not only to the evaluation of plasma processing as a method of N_xO_y emission control, but also to improve current substrates and techniques.

PS-ThP21 Diagnosing Toroidally Confined Pure Electron Plasma using Electrostatic Waves, S.A. Exarhos, M.R. Stoneking, J.W. Darrell, Lawrence University

Non-neutral plasma, or plasma made up of particles of a single sign of charge can be isolated and confined for long periods of time, permitting detailed examination. Non-neutral plasma possesses characteristics that are unique (such as a dynamic equilibrium state), while exhibiting some phenomena that are similar to neutral plasma (such as supporting the propagation of electrostatic waves). Previous work on non-neutral plasma

has been conducted largely in cylindrical traps, but our toroidal trap offers the opportunity to test theoretical predictions that are not observable in cylindrical geometry. One such effect is the transport and mode damping due to a phenomenon called magnetic pumping. We report on experiments in which we excite toroidal analogs of two different so-called 'diocotron' (or flute-like) modes in the plasma in order to diagnose its characteristics and behavior. The frequency of the $m=1$ diocotron mode is proportional to the total trapped charge in the plasma. The damping of this mode has a strong dependence on magnetic field that is not presently understood, though theory suggests there is a dependence on, as yet unmeasured, plasma temperature. The frequency of the $m=2$ diocotron mode provides information about the average density of the plasma and its time variation, as well as its dependence on magnetic field, and other experimental control parameters. The combination of total charge and average plasma density provides a measure of plasma transport. This work is supported by National Science Foundation Grant No. PHY-0812893.

PS-ThP22 Diagnostic Studies of Ar/C-C₄F₈ Plasmas: The Effect of N₂ addition on Gas Phase and Surface Kinetics, P.K. Kao, Y.J. Yang, National Taiwan University, Taiwan, Republic of China, P.W. Chiou, C.C. Chou, Tokyo Electron Taiwan Limited, Taiwan, Republic of China, C.C. Hsu, National Taiwan University, Taiwan, Republic of China

The effects of N_2 addition on gas phase and surface kinetics in C-C₄F₈ and Ar-containing capacitively coupled plasmas are studied. The plasma is sustained using a 13.56-MHz rf power supply with an L-type matching network. Two systems with different geometries are utilized in this study. The first system consists of a cylindrical glass chamber with an annular ring-shaped powered electrode and a planar sample stage that serves as the grounding electrode. The second system is a parallel-plate discharge chamber with the electrode diameter 25.4 cm and the gap distance 60 mm. Optical emission spectroscopy is used to identify key species and to quantify gas temperature. The surface deposition is analyzed using XPS, FTIR, and SEM. Various solvents are used to test the chemical resistance of the deposited fluorocarbon film. Preliminary optical emission spectroscopic studies identified CN emission, which strongly suggests nitrogen incorporation into the gas phase reaction. The gas temperature is found to be between 1200 and 1350 K under 97 mT with 50 W power, and is found to be insensitive to N_2 addition. XPS analysis clearly shows the existence of the N peak, which clearly shows that nitrogen is involved in the surface kinetics. FTIR clearly shows the existence of stretching vibrations of CF_2 bond. Under 57 mT and 50 W power with Ar:C₄F₈=12:4 sccm, the surface fluorocarbon film deposition rate is approximately 25 nm/min. No major effect in this deposition rate is seen with up to 4 sccm of N_2 addition. The chemical resistance test shows that this deposited film is not resistant to acetone. This clearly demonstrates that the film is rather different from polytetrafluoroethylene film, which is resistant to various solvents including acetone. Finally, the implication of N_2 addition on the etching processes will be discussed.

PS-ThP23 Advanced Etch Profile Control and the Impact of Sidewall Angle at SiC Etch for Metal Filling Process, H.K. Sung, W.S. Lim, K.W. Lee, S.K. Kim, J.W. Choi, B.O. Lee, H.M. Yoon, Y.S. Lee, M.L. Park, E.A. Cho, J.K. Kim, H.K. Kang, C.G. Ko, Korea Advanced Nano Fab Center, Republic of Korea

This study relates generally to etching processes and in particular to method for controlling the profile of an opening etched in a SiC wafer. In the fabrication of high power device via hole is formed in an insulating layer prior to metallization to provide contacts to underlying regions. It is preferable that these openings have a low slope etch profile in order to minimize the possibility of defects in the overlying metal layer. One problem is a step-coverage defect, which sometimes occurs when a metal layer is formed over an opening having a steep profile and causes a discontinuity in the conductor formed by the metal layer. Such steep openings, that is, openings having nearly vertical sidewalls, typically occur when an SiC wafer is anisotropically etched, for example by a etch mask of high selectivity metal.

In this study, the SiC etching characteristics and the dry etch mechanism of SiC as function of etch mask material (metal masks) and etch mask edge shape were investigated. The etched step height was measured using step profilometer. And Scanning Electron Microscope (SEM) was used to measure the etch profile. Also, X-ray Photoelectron spectroscopy (XPS) was utilized to analyze the SiC etch mechanism.

PS-ThP24 Etching Characteristics of Magnetic Tunnel Junction Layer by using Non-Corrosive Gas Mixtures in ICP System, M.H. Jeon, K.N. Kim, H.J. Kim, G.Y. Yeom, Sungkyunkwan University, Republic of Korea

Magnetic random access memory (MRAM) has made a prominent progress in memory performance and has brought a bright prospect for the next generation nonvolatile memory technologies due to its several advantages.

Dry etching process of magnetic thin film is one of the important issues for the magnetic devices such as magnetic tunneling junctions (MTJs) based MRAM. MTJs which are the basic elements of MRAM can be used as bits for information storage. CoFeB is a well-known soft ferromagnetic material, of particular interest for magnetic tunnel junctions (MTJs) and other devices based on tunneling magneto-resistance (TMR), such as spintransfer-torque MRAM. Recently, transferring the pattern by using an Ar⁺ ion milling is a commonly used, although the redeposition of sputter etch products on the sidewalls and the low etch rate are main disadvantages of this method. Other method, which reported the etch rates higher than 50 Å/s for magnetic multilayer structures using Cl₂/Ar plasmas, is also proposed. However, the chlorinated etch residues on the sidewalls of the etched features tend to severely corrode the magnetic material. To remove this problem, the etching of MTJ layer by using organic-based gases such as CO/NH₃, CH₃OH, etc. are actively investigated currently.

In this study, MTJ materials such as CoFeB, MgO, etc. were etched using various gas ratios which can be expected to form volatile metal-organic compounds and the results were compared with those etched using Cl₂-based gas mixture. As one of the gas mixtures, gas mixtures of carbon monoxide (CO) and ammonia (NH₃) were used as etching gases to form carbonyl volatiles. The etch results showed the enhanced etch rates higher than 3 times by using a gas mixture of CO/NH₃ compared to that etched by pure CO or NH₃ possibly indicating the formation of products composed of carbonyl volatiles. The composition of etched surface was less damaged compared with that etched with Cl₂-based gas.

PS-ThP25 Evaluation of Surface Chemical Bonding State and Surface Roughness of Chemical Dry Etched Si using NO and F₂ Gas Mixture, S. Tajima, T. Hayashi, K. Ishikawa, M. Sekine, M. Hori, Nagoya University, Japan

Economical Si etching is required to fabricate through silicon via (TSV) integration architecture for multi-layered packaging, micro-electro-mechanical system (MEMS), and surface patterning of solar panels. Chemical dry etching techniques by highly reactive ClF₃ gas [Ibbotson et al. J. Appl. Phys. 56 (1984) 2939] has been reported but the contamination by Cl is problematic. In this study, we have been investigating a new and economical Si chemical dry etching technique using nitric oxide (NO) and molecular fluorine (F₂) gas mixture. Atomic fluorine (F) is generated by mixing these gases at room temperature by the reaction of F₂ + NO → FNO + F. Kinetic energy of F at 0.8 eV and the change in post-reaction bonding energies of Si, SiF_x (x = 1-4), Si-NO, Si-NOF, and HF were calculated by B3LYP/6-311+G(d) in Gaussian 09. Si etch rate, etch directionality, etch selectivity, surface chemical bonding states, and surface roughness were evaluated by scanning electron microscopy (SEM), X-ray photoelectron spectroscopy, and Fourier transform infrared spectroscopy, and atomic force microscopy to elucidate the Si etch dynamics in molecular level.

A prototype etching reactor was fabricated using the quartz tube with the inner diameter of 7.5 mm and the length of 150 mm. Flow rate of gases introduced into this chamber was Ar/5%F₂ ~ 38.5 sccm, F₂ ~ 1.9 sccm and NO ~ 1.5-5 sccm while maintaining the constant pressure at 620 Pa. The corresponding flow rate ratio, NO/NO + F₂, was 0.44 ~ 0.72. Etching was performed for 15 ~ 600 s. Single crystal and poly-Si samples were prepared to determine the etch rate, which is calculated from the cross-sectional SEM images. Preliminary results show that the etch rate was increased from 0.2 ~ 1.8 m m/min at NO/NO + F₂ = 0.44 ~ 0.72. This measured etch rate was more than 100 times faster than the estimated value by F atom reaction with H terminated Si. The etch rate sharply increased with NO up to NO/NO + F₂ ~ 0.57 and became almost constant when NO/NO + F₂ > 0.57. The etched surface after the exposure to the atmosphere mainly consisted of SiO₂, indicating that the reaction between Si-F_x, Si-NO, Si-NOF and H₂O in the air may occur rapidly. The detail analysis of the change in surface chemical bonding state during and after etching is in progress. The etched surface became rough and scalloped Si was formed when NO flow rate was increased. The surface roughening may be due to the presence of Si-NO and/or Si-NOF bond prior to the formation of Si-F_x that would eventually form SiF₄. From these results, Si etching is initiated not only the presence of F but also the existence of F₂, NO, and FNO.

PS-ThP26 High K Metal Gate Etching towards sub 14 nm Features, S. Barnola, L. Desvoires, C. Vizioz, CEA, LETI, MINATEC Campus, France, C. Arvet, ST Microelectronics, Crolles, France

To progress towards the 11nm node, sub 14nm HK metal gates need to be patterned with a good CD control. Two lithography techniques were used at the same time on the wafer to achieve the same CD target for different goals : electron-Beam lithography with 30nm dense litho features for the circuit development and optical lithography with 80nm isolated features for single device optimization. A gate etching process has been developed at LETI starting from these two lithography options using different trimming strategies to achieve this aggressive CD target For this study, wafers were patterned with hybrid lithography. In the same die, E-beam and optical

fields were realized separately using a common stack made of trilayer / hard masks/ HKMG. The optical side was first printed and patterned down to the Poly-si, then the ebeam side was printed with positive photoresist and etched to the Poly-Si as well. Finally the HKMG parts were etched at the same time on both fields. Metal Gate patterning has been performed in a 300mm industrial platform etcher: LAM VERSYS, Kiyo CX. Several conditions were tested to minimize added LWR for such small dimensions. We focused on several trimming conditions at different location on the stack to achieve our CD target : resist, ARC, SOC and hard mask. After optimization sub 14nm CD have been successfully achieved for FDSOI technology. Best results were achieved with hard mask trimming strategies for ebeam part and resist + hard mask trimming for optical part.

PS-ThP27 The SiO_x Thin Film Deposition by using a Double Discharge System with a HMDS/Ar/He/O₂ Gas Composition, G.Y. Kim, J.B. Park, G.Y. Yeom, Sungkyunkwan University, Republic of Korea

Silicon oxide thin films have been extensively investigated due to the outstanding characteristics such as hardness, specific chemical structure, and high scratch resistance. In most of cases, SiO_x thin films are deposited by the plasma enhanced chemical vapor deposition processes because the high quality materials can be obtained. However, the PECVD has some drawbacks that are related to vacuum system. Therefore, plasma deposition at atmospheric pressure has received attention as promising technology. Among the many kinds of AP-plasma sources, Dielectric Barrier Discharge (DBD) source which consists of two parallel electrodes can get the uniform and large-area glow discharge. Especially, double discharge system which composed of direct-type DBD and remote-type DBD was improved the various mechanical characteristics of SiO_x thin film and increased the process efficiency. In this paper, SiO_x thin films with a low content of impurities were deposited by using a double discharge system with a gas mixture of hexamethyldisilazane (HMDS)/ O₂/ He/ Ar. The use of the double discharge system increased not only the SiO_x thin film deposition rates, but also precess efficiency. When AC voltage was applied to the remote-type DBD from 4 to 7 kV, the deposition rate of SiO_x was increased from 7 to 36.1 nm/scan. Also as using double discharge system (5 kV, 20 kHz AC voltage was applied to the direct-type DBD), the deposition rate of the SiO_x thin films was further increased from 20 to 58.3 nm/scan with the increase of the AC biasing to the remote-type DBD from 4 to 7 kV. The improvement in the properties of SiO_x films was partially related to the increased gas dissociation by the additional AC biasing of substrate.

PS-ThP28 The Effect of a Low Plasma-Induced Damage Etching on sub-32nm Metal Gate/High-k Dielectric CMOSFETs Characteristics, K.S. Min, S.H. Kang, G.Y. Yeom, Sungkyunkwan University, Republic of Korea

According to international technology roadmap for semiconductors (ITRS), as the critical dimension (CD) of metal-oxide-semiconductor field effect transistor (MOSFET) is scaled down to 45nm node and below, the present gate (poly-Si) with a high-k dielectric is intrinsically limited. Therefore, a metal gate compatible with a high-k dielectric, which is physically thicker with the same equivalent oxide thickness (EOT) has been investigated. For the etching of metal gate/high-k dielectric, reactive ion etching technique is currently applied to maintain accurate CD by etching the gate structure anisotropically with minimal damage on substrate. However, it can introduce plasma induced damages (PIDs) and was found to degrade the electric characteristics of metal gate/high-k dielectric CMOSFETs, particularly in the short channel devices. For low standby power (LSTP) application, an etch technique with low plasma-induced damage composed of neutral beam etching and atomic layer etching has been applied to metal gate and high-k dielectric etching of complementary metal-oxide-semiconductor field effect transistors (CMOSFETs), respectively, and their electrical characteristics were compared with those etched by conventional wet and dry etching techniques. It has been found that, after the etching using the low plasma-induced damaged etching technique, device performances have been improved compared to those etched by conventional wet and dry etching techniques. Especially, gate induced drain leakage and I_{off} which are key factors for LSTP have been reduced significantly.

PS-ThP29 Catalytic Activities of Metal/Carbon Compound used by Vacuum and Solution Plasma Processes, H.S. Lee, M.A. Bratescu, N. Saito, Nagoya University, Japan

Fuel cells have been recognized as a potential clean energy-converting device due to their high efficiency and low emissions. However, two major technical gaps limit their commercializations: cost and reliability. Currently, platinum (Pt)-based catalysts and their corresponding cathode catalyst layers are among the major causes which limit their performance and cost for proton exchange membrane (PEM) fuel cells, although these are the most promising and practical fuel cell catalysts. Some approaches have

been studied to reduce the cost and to improve the performance over twenty years, but there has been no real breakthrough yet. Recently, most researchers focused on the use of carbon catalyst and non-rare metal catalyst for replacement of Pt-based catalysts. The former groups are divided in organic dope methods and inorganic dope methods on carbon material such as nanotubes or graphene sheets. The major drawback of organic and inorganic dope method are, respectively, low thermal stability and limited controlling of the process. Meanwhile, non-rare metal catalysts show low catalytic activities.

In this study, we synthesized nickel/carbon nano-particles produced by solution plasma process.

SPP is a useful and simple method for the metal NPs synthesis because this non-equilibrium plasma can provide extremely rapid reactions due to the reactive chemical species, radicals and UV radiation produced in atmospheric pressure plasma operating in glow discharge limits and offering a suitable medium to control the chemical reactions inside the solutions.

The SPP was generated by the electrical discharge between opposite nickel electrodes. The glow discharge in 0.1 M KCl solution was produced by using bipolar pulsed power supply operated at 1~2 kV of voltage, 15 kHz of pulse frequency and 2 μ s of pulse width. The diameter of the electrode was 0.6 mm and the interelectrode gap was 0.5 mm. In addition, 0.1 g of dispersion treated carbon (CNT, CNB) was inserted in 100 ml solution.

M/C NPs morphology was investigated by transmission electron microscopy, energy dispersive X-ray microanalysis, X-ray Diffraction, Fourier transform infrared spectroscopy. Cyclic voltammetry was demonstrated for evaluating catalytic activities.

In conclusion, as applied voltage increased, diameter of synthesized NPs decreased. The smallest synthesized NPs with 3 nm showed the higher oxygen reduction rate in catalytic activities according to decrease diameter.

PS-ThP31 Plasma Etching of PTFE: Differences between Low and Atmospheric Pressure Treatments, N. Vandecasteele, J. Hubert, T. Dufour, S. Collette, C. De Vos, F. Reniers, Université Libre de Bruxelles, Belgium

PTFE samples were treated by O₂/He plasma at various pressures, from low (6.67 Pa) to atmospheric pressure. Treatments were carried out using different mixtures of He and O₂. The first results highlight two completely different etching mechanisms depending on the gas mixture used and working pressure.

The etching was studied by mass loss measurements, weighing the sample before and after plasma exposure.

At low pressure the strongest etching occurs for pure oxygen plasma while no etching is detected for helium plasma. The opposite is observed at atmospheric pressure, the strongest etching takes place with pure helium.

X-ray photoelectron spectroscopy (XPS) analysis was used to study the chemistry of the PTFE surfaces as well as the etching products. High resolution F1s and C1s peak show different etching products as the pressure and/or the gas composition are changed. In all cases both carbon and fluorine are detected. Depending on the plasma parameters (pressure and gas composition) either CF₂ fragments (BE C1s = 292 eV) or CC (BE C1s = 285 eV) are detected.

Optical emission spectroscopy (OES) measurements were used to study the plasma phase and the etching products. A change in the He plasma emission was observed above a certain pressure (around 13.3 Pa). The plasma color changes from greenish to pink. This change could be related to the increase of the He metastable emission line at 389 nm. OES measurements also allowed us to detect etching products in the gas phase during the plasma exposure of the PTFE samples. Fluorine, CO and CO₂ lines were detected.

Those various results allow us to suggest two different mechanisms of PTFE etching.

In the case of low pressure O₂ plasma, the surface composition after the treatment and the etching products (detected by XPS and OES) suggest an etching mechanism where the C-F bonds are broken by charged particles (probably e⁻). Oxygen then reacts with the carbon backbone to produce CO₂. The role of the charged particles was evidenced using different sample positioning and magnets.

In the case of atmospheric pressure treatments the etching occurs via the removal of CF₂ fragments. The main active specie responsible for the etching seems to be metastable He atoms.

PS-ThP32 Surface Modification of Polyethylene Terephthalate using Water Containing He/O₂ and Ar/O₂ Plasma, P. Leroy, S. Abou Rich, S. Colette, F. Reniers, ULB, Belgium

Like many polymers, Polyethylene Terephthalate (PET) has excellent bulk physical and chemical properties but exhibit poor adhesion abilities.

Therefore, in order to improve the deposition of a subsequent layer onto such compounds, a pretreatment of the surface is usually performed. Plasma treatments have a lot of advantages compared with other methods used to treat and modify such polymers like chemical, thermal or mechanical processes. Indeed the modifications only affect the top layer of the material without changing the bulk properties and it is environmental friendly (solvent free). *It is well known that plasma treatment improves the wettability and the hydrophilicity of polymers by surface oxydation*, creating at the interface new oxygen-based functionalities such as hydroxyl or carboxylic acid groups.

In this work, plasma treatment was performed on Polyethylene terephthalate (PET) using a Dielectric Barrier Discharge in Helium/ Oxygen and Argon/Oxygen mixtures at atmospheric pressure, and containing various concentration of water vapour. The experimental set up uses a roll-to-roll system, the film passing through electrodes at varying speeds (0.01m/min and 0.1m/min which correspond to film exposure times of 0.1 and 10 seconds respectively).

The goal of this work is to evaluate the influence of water vapour injection into the discharge on the polymer functionalisation. It is shown that water changes the plasma characteristics, and strongly modifies the oxidative properties of the plasma. The influence of the water vapour partial pressure, the gap between electrodes and the power of the discharges are emphasized in order to optimize the surface wettability.

Chemical and physical changes on the polymer surface plasma treated are observed using X-ray Photoelectron Spectroscopy (XPS), Water Contact Angle and Atomic Force Microscopy (AFM) measurements.

PS-ThP33 Numerical Investigation of Optimum Conditions for Magnetic Neutral Loop Discharge Plasma Production, S.H. Kim, D. Akbar, J.L. Shohet, University of Wisconsin-Madison, B.N. Moon, W.J. Choi, Y.M. Sung, Kyungsoong University, Korea

In processing plasma sources for semiconductor device fabrication, both uniformity over a large area and controllability to obtain desirable plasma parameters are required. A magnetic neutral loop discharge (NLD) plasma¹⁾ has been proposed as a new plasma source which satisfies these requirements. The position and the diameter of the plasma can be easily controlled by changing the position and the diameter of a neutral loop (NL). It has been theoretically shown that the electron motion becomes nonlinear around the NL when the radio frequency (RF) electric field is applied along the NL perpendicular to the magnetic field lines²⁾. The electron makes meandering motions and acquires kinetic energy of several tens of electron-volts from the RF electric field where the meandering range contains the region between the NL and the electron cyclotron resonance (ECR) region, the length of which is designated by L^{3,4)}. Through such a process, the electrons are heated efficiently without collisions. The electron behavior near the NL determines the uniqueness of this plasma production technique and therefore details of its motion are needed. In this work, in order to accurately understand the characteristics of an NLD plasma, a numerical analysis of electron behavior around the NL was performed based on a 2-dimensional model in which three-dimensional effects were taken into account. For obtaining the optimum conditions for plasma production, the relationship between the normalized electric field and the average electron energy were also investigated.

This Work was supported by Kyungsoong University Research Program (2011) and by the Semiconductor Research Corporation under Contact No. 2008-KJ-1871 and the National Science Foundation under Grant CBET-1066231.

[1] Z. Yoshida and T. Uchida, Jpn. J. Appl. Phys. **34** (1995) 4213.

[2] Z. Yoshida et al., Phys. Rev. Lett. **81** (1998) 2458.

[3] Y. M. Sung et al., J. Vac. Sci. Technol. **A18** (2000) 2149.

[4] Y. M. Sung et al., J. Vac. Sci. Technol. **B20** (2002) 1457.

PS-ThP34 No- Residue and High- Rate Etching of InGaAs by High Density Plasma, Y. Ohsawa, Tokyo Electron Technology Center, America, LLC, H. Nakajima, T. Nishizuka, M. Takahashi, Tokyo Electron America, Y. Trickett, G. Nakamura, A. Ko, Tokyo Electron Technology Center, America, LLC, H. Ohtake, Tokyo Electron Technology Development Institute, INC., Japan, C. Huffman, R. Hill, SEMATECH

III-V materials are promising candidates for the channel materials beyond 10 nm generation of CMOS-logic devices. Among them, InGaAs was one of the best materials for NFET channel because of the high electron mobility. However, there are few reports of InGaAs etching. Previous reports showed that the problems were the residue of Indium and low etching rate. Because these issues came from the low reaction between the InGaAs surface and radicals, we have to enhance the surface reaction. In this paper, the precise InGaAs etching was investigated by high electron density (high Ne)/ low electron temperature (low Te) plasma with hot stage operation to improve the issue of residue and low rate. We used RLSATM

Etch tool as an InGaAs etcher. This tool has high Ne of more than $1 \times 10^{11} \text{ cm}^{-3}$ and low Te of less than 1 eV around the stage because RLSA™ Etch tool uses the surface wave plasma and diffusion chamber. A selection of gas chemistry and temperature was optimized to enable the proper plasma reactivity with Indium without creating residues. High rate of more than 100nm/min was obtained without Indium residue. Since the reaction of Indium-methyl radical are enhanced by more than 150 °C, it was considered that the etching reaction was enhanced by hot stage. In addition, the re-deposition of by-products was reduced because of low electron temperature. Based on additional analytical investigations, we found that the combination of high Ne- low Te plasma and hot stage is one of the best solution for no-residue and high rate etching of InGaAs.

PS-ThP35 Using Capillary Array Windows to Minimize Ion Bombardment Effects during Plasma Processing of Dielectrics, K.W. Hsu, F.A. Choudhury, H. Ren, University of Wisconsin-Madison, B.N. Moon, Kyungsoo University, Korea, A.G. Olson, University of Wisconsin-Madison, Y.M. Sung, Kyungsoo University, Korea, Y. Nishi, Stanford University, J.L. Shohet, University of Wisconsin-Madison

Microelectronic devices are often exposed to radiation and charged-particle bombardment from processing plasmas during their fabrication stages often resulting in damage to the dielectric materials. This work investigates the effectiveness of capillary-array windows to partially block charged particles in order to distinguish the effects of photons and charged particle bombardment during plasma exposure. A capillary-array window is placed over a $1 \times 1 \text{ cm}^2$ exposed area of an aluminum wafer chuck [i] in an ECR reactor and the substrate current during plasma exposure is measured at different bias voltages with and without the capillary window in order to determine the effectiveness of the window to partially block charged particles. Additionally, using an Object-Oriented-Particle-in-cell (OOPIC) code [ii], the ion and electron fluxes passing through the window can be estimated. The experimental measurements and the simulation results confirm that the capillary-array window can be arranged to block almost all ions during plasma exposure.

This work has been supported by Semiconductor Research Corporation under Contact No. 2008-KJ-1871 and the National Science Foundation under Grant CBET-1066231.

[i] T. Lucatorto, T. J. McIlrath, and J. R. Roberts, *Appl. Opt.* **18**, 2505 (1979)

[ii] Y. M. Sung, M. Wada, M. Otsubo, C. Honda, Y. K. Kim, and C. H., *J. Appl. Phys.* **43** 800 (2004)

PS-ThP36 Deposition of YSZ Thin Films by Laser-Assisted Plasma Coating at Atmospheric Pressure (LAPCAP), Z. Ouyang, Y.L. Wu, P. Raman, L. Meng, T.S. Cho, D.N. Ruzic, University of Illinois at Urbana Champaign

A laser-assisted plasma-coating technique at atmospheric pressure (LAPCAP) for depositing thin yttria-stabilized-zirconia (YSZ) films has been developed. This technique allows columnar-structured YSZ films with a thickness of 1–5 μm to be prepared on a Ni-based superalloy substrate at atmospheric pressure. The atmospheric pressure plasma is generated in a microwave-induced plasma torch system with a gas temperature T_g of more than 2,000 °C. Optical emission spectroscopy (OES) technique has been used to spatially analyze some critical characteristics of plasma, such as electron density ($n_e > 10^{15} \text{ cm}^{-3}$), electron temperature ($T_e \sim 1 \text{ eV}$), and plasma gas temperature ($T_g \sim 800\text{--}1200 \text{ }^\circ\text{C}$). The thermally grown oxide (TGO) layer is found to affect the film morphology significantly, and characteristics of TGO grown by pre-heating the substrate to 800–1200 °C are investigated. TGO in the form of $\alpha\text{-Al}_2\text{O}_3$ with a thickness of $\sim 1 \mu\text{m}$ is found to provide a means to deposit high quality, adhesive thin YSZ films on substrates with columnar microstructure, same as seen in films by high-vacuum electron-beam PVD method. The morphology and characteristics of the films have been compared at various deposition temperatures (100–1200 °C) and laser energy density (1–10 J/cm^2), using microanalysis techniques such as scanning electron microscope (SEM), focused ion beam (FIB), X-ray photoelectron spectroscopy (XPS), and X-ray diffraction (XRD).

PS-ThP38 Plasma Propagation Speed and Electron Temperature in Atmospheric Pressure Non-thermal Bioplasma Jet, P. Suanpoot, Maejo University Phrae Campus, Thailand, Y.G. Han, W.Y. Lee, G.S. Cho, E.H. Choi, Kwangwoon University, Republic of Korea

Space and time resolved discharge images from an atmospheric pressure non-thermal bioplasma jet have been observed by a high-speed single-frame

camera to investigate the electron temperatures. The plasma propagation speed on the cathode has been shown to be about 5 km/s at input voltage of 4.7 kV and driving frequency of 40 kHz. Particularly, the electron temperature in atmospheric pressure non-thermal bioplasma jet were found to be about 1.5 eV at input voltage of 4.7 kV and driving frequency of 40 kHz, respectively. Implications of the results and directions for further studies are discussed. **Key words** : Non-thermal plasma jet, Plasma propagation speed, Electron temperature _____ # This project is supported by Kwangwoon University Research Fund, Korea .

PS-ThP39 Increase Film Quality and Campaign Length in Reactive Sputtering Applications With Pulsed-DC Power, D. Pelleymounter, Advanced Energy Industries Inc.

In reactive sputtering applications, arcs can contribute to costly film defects and process interruptions. Charge buildups on small areas of the target cause these electrical breakdowns, or arcs, which manifest as particles on the substrate—leading to defects, pinholes, rate reduction, short circuits, or other undesirable process disturbances and loss of film quality. Entire lots are oftentimes scrapped due to poor quality thin film layers, and severe arcing can damage equipment and shut down entire lines for maintenance. While there are several types of process power technologies available to help manage arcs, pulsed-DC technology offers a marked performance advantage over AC or straight DC power. The addition of low frequency pulsing lowers the effective electronic voltage of the whole plasma while maintaining the actual delivered voltage of individual electrons for high deposition rate and film flatness. Improved packing density also results. Adding reverse voltage while pulsing momentarily stops the energized electrons in the plasma and creates a haphazard path to the substrate, preventing hills and valleys from forming. This paper discusses how pulsed DC power conversion technologies can do much more than supply power but effectively manage arcs for greater surface control, film quality, and overall process control.

PS-ThP40 Control of Radical/Ion Ratios in Electron Beam-Generated Plasmas and their Effect on Polymer Surface Modification, S.G. Walton, E.H. Lock, R. Fernsler, Naval Research Laboratory

Electron beam-generated plasmas are unique type of plasmas generated when high electron energy beam is injected into the gas. The beam preferentially ionizes the gas molecules, thereby producing daughter electrons with energies up to half of the initial beam energy. The daughter electrons, however, quickly lose energy as they collide with gas molecules. Thus, without an external electric field to heat them, the daughter electrons cool and they soon outnumber the beam electrons and the energetic daughter electrons responsible for ionization. The low-energy “plasma” electrons are not only far more populous, but also largely determine the plasma characteristics – i.e. the plasma density n_e , plasma potential ϕ_p , and electron temperature T_e . Typically T_e is 1 eV or less in beam-produced plasmas and thus the kinetic energy of the ions bombarding the surface is below the polymer bond energies. In this talk we estimate the charged, excited and resonant species concentrations and the fluxes bombarding the polymer surface. We correlate the ion to radical ratios in different gas environments with observed morphological and chemical modifications in polystyrene, poly(methyl methacrylate) and polyethylene. This work was supported by Naval Research Laboratory Base Program.

PS-ThP43 Atomic Layer Etching of Ultra-thin High-k Dielectric Film for Gate Oxide in MOSFET Devices, C.K. Kim, Sungkyunkwan University, Republic of Korea, J.K. Kim, Samsung Electronics Co. Ltd., Republic of Korea, G.Y. Yeom, Sungkyunkwan University, Republic of Korea

As the dimensions of integrated circuit devices, such as metal-oxide-semiconductor field effect transistors (MOSFETs), etc., continue to be scaled down, the thickness of gate dielectrics, such as SiO_2 , etc., also continues to be scaled down to nanosize. Tunneling currents through the gate dielectric, however, limit the scaling of SiO_2 to approximately a few nanometers. Therefore, for further scaling down of devices, alternate gate dielectric materials with higher dielectric constants need to be used to reduce the gate leakage current while maintaining the gate dielectric capacitance with a thicker material. Considerable research attention has focused on the potential of HfO_2 as a next generation gate dielectric material due to many advantages in comparison with SiO_2 , such as a high dielectric constant (15–25), good thermal stability, wide band gap (5.6 eV) and large band offsets (1.5 eV). However, conventional RIE of ultra-thin HfO_2 film tends to cause electrical and physical damage to the surface of the devices due to use of energetic reactive ions and the difficulty in the precise etch rate (depth) control at an atomic scale. Precise etch depth control of ultra-thin HfO_2 (3.5 nm) films applied as a gate oxide material was investigated by using atomic layer etching (ALET) with an energetic Ar neutral beam and BCl_3 gas to minimize etch damage. A monolayer etching condition of 1.2 Å/cycle with a low surface roughness and an

unchanged surface composition was observed for ultra-thin, ALET-etched HfO_2 by supplying BCl_3 gas and an Ar neutral beam at higher levels than the critical pressure and dose, respectively. When HfO_2 -nMOSFET devices were fabricated by ALET, a 70% increase in the drain current and a lower leakage current were observed compared with the device fabricated by conventional reactive ion etching, which was attributed to the decreased structural and electrical damage.

PS-ThP44 Study on the Plasma Damage on the Interface between the Titanium Nitride and Hafnium Oxide during Etching Carbon Mask on the Titanium Nitride, K.H. Bai, Y. Jeon, M.C. Kim, S. Choi, Samsung Electronics Co. Ltd., Republic of Korea

We investigated the etch damage on the interface between the titanium nitride (TiN) and hafnium oxide (HfO_2) during etching the carbon layer on the TiN. HfO_2 is widely used as a high-k gate dielectric material to reduce the gate leakage current and improve the reliability in the semiconductor device. TiN and amorphous carbon layer (ACL) are deposited on the HfO_2 as a gate electrode and mask material, respectively. We fabricated complementary metal oxide semiconductor (CMOS) devices with patterning ACL on the TiN by dry etching and removing the TiN layer by wet chemical. We realized that an interlayer between the TiN and HfO_2 layer was generated due to the plasma damage during the ACL etching and the interlayer was not removed clearly by the wet chemical, which resulted in device degradations. We studied the properties of the interlayer with changing the ACL etching recipe to find the key factor of generating the interlayer. The properties changed significantly with the ion energy and the gas composition of the ACL etch recipe.

PS-ThP45 Experimental and Simulation Studies of Capacitively Coupled Silan-Hydrogen Plasmas for Deposition of m-C Si Film, C.-H. Fan, S.-E. Lien, K.-C. Leou, National Tsing Hua University, Taiwan, Republic of China, **C.-H. Hsieh, M.-C. Wang, C.-F. Ai,** Institute of Nuclear Energy Research, Taiwan, Republic of China

Capacitively coupled SiH_4/H_2 plasmas (CCP) have been widely employed for deposition of Si film for applications such as thin film transistors and thin film solar cells. For Si thin film solar cells, requirements for yielding higher conversion efficiency at a lower cost calls for a high rate and high uniformity plasma process for deposition of microcrystalline Si film. A better understanding of the plasma discharge is needed. In this study, a VHF SiH_4/H_2 CCP discharge has been investigated by both numerical simulation, based on fluid model, and experimental study employing plasma optical emission spectroscopy analysis. Simulation was performed for VHF SiH_4/H_2 CCP operated at 27.12 MHz with 27 species and 47 reactions. Simulation results show that, for a power density of 0.4 W/cm^2 , a gas pressure of 600 Pa and a SiH_4/H_2 flow rate ratio, or hydrogen dilution ratio, of 2.5/200, electron density profile is quite uniform in the discharge region with a plasma density up to $1.8 \times 10^{16} \text{ m}^{-3}$. For the key species related to the film growth, i.e., SiH_3 and H, the densities of their fluxes arriving on the grounded substrate surface are uniform. Their ratio, which controls the crystalline fraction of the Si film, is strongly dependent on plasma parameters, such as rf power, hydrogen dilution ratio and gas pressure. Results from experimental OES analysis show similar trends as predicted by the simulation as rf power and hydrogen dilution ratio were varied but little correlation was found as gas pressure was changed. The discrepancy, however, can be explained by analyzing the reactions responsible for the production and loss of SiH_3 and SiH_2 . The detailed results from simulation and OES analysis of the parametric analysis of varying, rf power, gas flow rates and gas pressures will be presented.

*Work supported by the National Science Council of ROC.

PS-ThP46 Diagnostic Study of Plasmas in Solution Driven by Pulsed Power - Study of History Effect and Observation of S_2 Emission, C.Y. Sie, C.C. Hsu, National Taiwan University, Taiwan, Republic of China

Diagnostic studies of plasmas in salt solutions are performed. The plasma is sustained by a pulse power source with the pulse voltage up to 600 V, T_{on} (voltage on duration) between 10 μs to 1 s, and T_{off} (voltage off duration) between 30 μs to 3 s. The driving electrode is made of a platinum wire with a diameter of 0.5 mm covered by a glass tube to precisely define the area in contact with the solution. The grounding electrode is a bare platinum wire with the same diameter with a length of approximately 1 cm. The power electrode is set upward and both electrodes are immersed in salt solution. Current and voltage probes are used to monitor the current and voltage waveforms, respectively. An optical emission spectrometer is used to monitor the emission spectra generated by the plasma. In the first part, we demonstrate the observation of the history effect. With a sufficiently short T_{off} (less than 100 ms), the history effect, i.e. the plasma generated in one power cycle is consistently affected by that generated in the previously cycle, is observed when NaNO_3 solution is used. With the history effect, the maximum current within a power cycle increases with cycles, from the

first cycle upon Ton. With a sufficiently long T_{off} (~2 s), good cycle to cycle reproducibility is observed, and the current waveform in each cycle is nearly identical. The history effect is therefore fully eliminated. The transition characteristic time is 0.1 to 1 s, which suggests heating of the electrode is the major mechanism for the history effect. In the second part, we show the detection of S_2 emission when the plasma is ignited in low concentration Na_2SO_4 . The intensity of S_2 emission gradually drops to the noise level with a long operating time. This observation suggests that the optical emission emanating from the plasma involves a more complex pathway than those suggested in the literature.

Transparent Conductors and Printable Electronics

Focus Topic

Room: Central Hall - Session TC-ThP

Transparent Conductors and Printable Electronics

Poster Session

TC-ThP2 Ellipsometry Characterization of Thin Organic Films for Flexible Electronics, C. Eypert, M. Stchakovsky, L. Yan, Horiba Scientific

In recent years, there has been an enormous research effort on both materials and processes for the production of electronic devices on flexible polymeric substrates. Flexible electronics encompass a broad set of technologies applicable across a range of products, from flexible solar cells, printed solid state lighting, to medical devices, etc. Precise control of film thickness and optical constants is vital for optimization of the device performance (efficiency, reliability, cost, etc.) In this work, we demonstrate the use of ellipsometry as a non-destructive, powerful and sensitive optical means of studying organic electronic devices. Examples in two specific areas of applications are included: OLED, and organic solar cell based on the blend of P3HT and PCBM.

TC-ThP4 Toward Active-Matrix Lab-On-Chip: Programmable Electrofluidic Device Integrated with the Arrayed IGZO Oxide Thin Film Transistors, J.H. Noh, J. Noh, P.D. Rack, University of Tennessee Knoxville

Agile micro- and nano-fluidic control is critical to numerous life science and chemical science synthesis as well as kinetic and thermodynamic studies. Electrical addressability of lab-on-chip devices currently requires external switching devices for each individual electrode for droplet transport, merging, and splitting. Thus for complex arrays, many switching devices and interconnections are needed and scale directly with the number of elements (increased size or resolution). Therefore fabrication processes and cost can be complicated and expensive as the number of input-output connections becomes unwieldy. The active matrix (AM) addressing method integrated with an electrofluidic platform is a significant breakthrough for complex electrofluidic arrays (increased size or resolution) with enhanced function, agility and programmability because the AM method can minimize the number of control lines necessary ($m + n$ lines for the $m \times n$ elements array) as is used in liquid crystal display technologies.

We have previously demonstrated arrayed amorphous indium gallium zinc oxide (a-IGZO) thin film transistors as a platform and the control of an electrofluidic array by AM addressing method. An a-IGZO semiconductor active layer is used because of its high mobility, low-temperature processing and transparency for spectroscopy and imaging. However, the a-IGZO transistors and an electrofluidic array were connected by external wires because the electrical properties of the a-IGZO thin film transistors were degraded after passivation. The degradation is likely due to reaction of hydrogen with a-IGZO active layer during PECVD SiO_2 passivation and post-annealing process, and this can be mitigated by changing deposition temperature and annealing ambient. In this study, the effects of hydrogen and oxygen on the PECVD passivated a-IGZO thin film transistors is investigated as a function of deposition temperature and post annealing ambient. The change of hydrogen and oxygen concentration in both the IGZO active layer and SiO_2 passivation layers are discussed. Finally, we review the process flow for fully integrated electrofluidic arrays on an a-IGZO transistor array and the programmable addressability of electrofluidic devices by AM addressing method. The requisite material and device parameters will be discussed for optimal active matrix addressing from device measurements in context with a VGA scale active matrix addressed electrofluidic platform.

Thin Film

Room: Central Hall - Session TF-ThP

Thin Film Poster Session

TF-ThP1 Vanadium Oxide Thin Films Grown by ALD using TEMAV and O₃ or H₂O Precursors, A. Premkumar, IMEC, Belgium, M. Toeller, Tokyo Electron Limited, Japan, I. Radu, Katholieke Universiteit, Leuven, Belgium, C. Adelman, M. Schaeckers, J. Meersschaut, T. Conard, J. Malgorzata, S. Van Elshocht, IMEC, Belgium

Vanadium dioxide (VO₂) is a smart material and offers interesting optical and electrical switching applications because of the reversible semiconductor-metal transition (SMT) that is observed at a temperature of about 68°C. Thin film growth of VO₂ has been extensively studied by CVD, PVD and sol-gel techniques. Aggressive scaling and increasing integration complexity have placed greater importance on atomic layer deposition (ALD) for depositing oxides in microelectronics. In this work we have developed an ALD process for VO₂ on 300 mm Si substrates using TEMAV precursor comparing different reactants (O₃ and H₂O) and starting surfaces (SiO₂ or Al₂O₃). We studied the ALD process in a 100-210°C temperature window. The as deposited films (100-150°C) were found to be XRD amorphous. Annealing in N₂/O₂ ambient (425-500°C) resulted in crystalline films. For the O₃ based process, the VO₂ formation conditions were found to be strongly dependent on the substrate investigated with a narrow process window for the preparation of phase pure and continuous VO₂ films. In contrast, highly uniform layers with consistent phase formation pathways were observed for the water based ALD process on all the substrates investigated. Films resulting from the water based process were smoother. Growth/anneal conditions were optimized to yield a resistivity change at the SMT of two orders of magnitude for 8 nm VO_x films.

TF-ThP2 Roles of MoO₃ Layer for Charge Injection and Charge Generation in an Organic Light Emitting Diode, M. Kawamura, S. Yoshida, Y. Abe, Kitami Institute of Technology, Japan

It has been reported that MoO₃ inserted between ITO anode and hole transport layer is useful as a hole injection layer to improve properties of organic light emitting diodes (OLEDs). However, its optimum thickness in the devices varies from sub-nanometer to 30 nm, depending on reports. In addition, as the mechanism of hole injection at the MoO₃ layer and α -NPD layer, it is argued that either charge injection mechanism or charge generation mechanism is dominant. As a fundamental study to investigate the main mechanism, we investigate the influence of MoO₃ thickness on properties of normal OLED device and also a device with a charge generation layer in the present work. First of all, we investigated properties of an OLED consists of ITO/MoO₃/ α -NPD/Alq₃/LiF/Al prepared by vacuum evaporation. As a results, the best device properties were obtained when 1.0 nm thick MoO₃ was inserted. Using atomic force microscopy, we found that the best device properties were obtained when the ITO surface was not completely covered with MoO₃. It is considered that the incomplete coverage was preferable in the view point of energy alignment because HOMO of α -NPD (5.4 eV) is intermediate between work functions of ITO (5.0 eV) and MoO₃ (5.7 eV). Then we confirmed charge generation phenomenon using device consists of ITO/Alq₃/MoO₃/ α -NPD/Al. Current did not flow without MoO₃ layer. When thickness of the MoO₃ layer was above 1.0 nm, a large current flowed and the current-voltage curves were the same even the MoO₃ thickness was increased to 10 nm. As the reason, it is considered that a high charge generation ratio was obtained from continuous MoO₃ layer. Consequently, we propose that MoO₃ work mainly for charge injection when the thickness is thin discontinuous film, and for charge generation when thick continuous film.

TF-ThP4 Effects of Preparation Conditions on the Magnetocaloric Effect of Gd Thin Films, H.F. Kirby, D.D. Belyea, J.T. Willman, University of South Florida, C.G. Hendryx, Newsome High School, C.W. Miller, University of South Florida

The effects of deposition temperature, post-deposition annealing, and chamber gettering were investigated on the magnetocaloric properties in Ta(5nm)/Gd(30nm)/Ta(5nm) grown by magnetron sputtering. The magnetocaloric effect (MCE) in these thin films, as indicated by the magnetic entropy change around the ordering temperature, increases with both growth temperature and post-deposition annealing of samples grown under ambient conditions. The full width at half max of the entropy change peak generally decreased toward the value for bulk Gd with increasing deposition and annealing temperature. Similarly, the temperature of the maximum entropy change increased toward the bulk Gd ordering

temperature. Overall the relative cooling power increased as deposition and annealing temperatures were increased. Gettering proved useful in limiting oxidation of the Gd especially for high temperature growth: ungettered samples grown at 600°C were purely diamagnetic GdO (111), while gettered samples, though still containing some GdO, were ferromagnetic.

TF-ThP5 Advanced Analytical Characterization of Multilayered Thin Films for Corrosion Inhibition, G. Zorn, M. Karadge, GE Global Research, C.C. Pierce, J.I. Melzer, GE Power & Water, M.M. Morra, GE Global Research

Advanced corrosion inhibitors developed by General Electric Power and Water can have complex multilayered structures that incorporate metal, ceramic and polymeric structures. For optimal performance it is important to understand the structure, morphology and composition of different layers. However, characterizing these nano scale films is very challenging, as they can be sensitive to preparation technique and damage. Moreover, surface roughness and homogeneity of the layers should be considered. The challenges in characterizing these multilayered structures will be discussed as an example for thin film characterization in the industrial R&D world. A multi technique approach that provides a detailed view of complex structures and compositions will be presented. Transmission Electron Microscopy (TEM) equipped with EDS was used to define local morphologies, crystalline structures and chemical composition; and Time-of-Flight Secondary Ion Mass Spectrometry (ToF-SIMS) depth profiles were used to determine the molecular distribution within the different layers. TEM provides local information in the range of a few nanometers over Focused Ion Beam (FIB) cross sections while ToF SIMS allows the analysis of larger areas, in the range of hundreds of nanometers, and provides top down views of the layers. The talk will emphasize how these two methods complement each other to achieve a detailed picture of complex structures within thin films.

TF-ThP6 Sputter Deposition of Atomically Smooth ZnO Films with Buffer Layers Crystallized via Nitrogen Mediation, K. Kuwahara, Kyushu University, Japan

Zinc oxide (ZnO) is a promising oxide semiconductor for optoelectronic devices because of its attractive properties such as wide direct band gap (3.3 eV), high exciton binding energy (58 meV), and material abundance. For realizing optoelectronic devices utilizing such attractive properties, a fabrication method of high quality crystalline ZnO films is essential. We have recently demonstrated a novel fabrication method of ZnO films utilizing nitrogen mediated crystallization (NMC), where the crystal nuclei density can be controlled because the nitrogen atoms suppress crystallization of ZnO films [1]. By using NMC-ZnO films as buffer layers, we have succeeded in high-quality epitaxial growth of ZnO films on sapphire substrates by RF magnetron sputtering [2]. However, for device applications such as light emitting diodes (LED), there still remains a need for improvement of properties of ZnO films. Here we apply off-axis sputtering to epitaxial growth of ZnO films on NMC-ZnO buffer layers aiming at reduction of negative-ion bombardment that causes serious damage during oxide deposition. NMC-ZnO buffer layers were fabricated by RF magnetron sputtering. The used gas was N₂-Ar and the total pressure was 0.3 Pa. ZnO ceramic targets were used. The applied RF power was 100 W and the deposition temperature was 700°C. The thickness of the buffer layers was 10 nm. On NMC-ZnO buffer layers, ZnO films were deposited by off-axis RF magnetron sputtering at 700°C. Ar-O₂ was used and the total pressure was 0.67 Pa. The applied RF power was 60 W. The film thickness was 1 μ m. After deposition, the films were annealed in a furnace at 1000°C for 3h in air. The surface of as-deposited ZnO films fabricated by off-axis sputtering on NMC-ZnO buffer layers has subnm scale corrugation and the RMS roughness is 0.28 nm, being significantly small compared with 1.02 nm for the films fabricated by conventional on-axis sputtering. Moreover, the annealed surface has 0.26-nm-high steps corresponding to one molecular layer of ZnO. We have demonstrated fabrication of atomically flat ZnO films by using NMC-ZnO buffer layers together with the off-axis sputtering.

[1] N. Itagaki, K. Kuwahara, K. Nakahara, D. Yamashita, G. Uchida, K. Koga, and M. Shiratani, Appl. Phys. Express 4 (2011) 011101.

[2] K. Kuwahara, N. Itagaki, K. Nakahara, D. Yamashita, G. Uchida, K. Kamataki, K. Koga, and M. Shiratani, Thin Solid Films 520 (2012) 4674.

TF-ThP7 Influence of Substrate Temperature on the Microstructure and Surface Morphology of Pulsed DC Magnetron Sputtered ZrB₂ Films, C.T. Lee, W.C. Chen, Instrument Technology Research Center, Taiwan, Republic of China

The ZrB₂ films were prepared on Si(100) substrate by pulsed DC magnetron sputtering with ZrB₂ target. Effects of substrate temperature (from 400 °C to 550 °C) on the microstructure and surface roughness of ZrB₂ films were investigated by X-ray diffraction, field emission scanning electron

microscopy and atomic force microscopy. X-ray diffraction analysis reveals that ZrB₂ film was polycrystalline with (001) and (101) orientation when substrate temperature was 450 °C. However, the ZrB₂ film has preferred orientation along (001) when substrate temperature was above 500 °C. An increase in average grain size with increase of substrate temperature was observed. The average grain size of ZrB₂ film was increased from 6.2 nm to 15 nm as substrate temperature increased from 400 °C to 550 °C. In this study, the preferred orientation along (001) of ZrB₂ films on Si(100) substrate can be obtained at substrate temperature above 500 °C by pulsed DC magnetron sputtering.

TF-ThP8 Effect of Fluorine Doping on the Structural, Optical and Electrical Properties of CdS Films Deposited by Chemical Bath Deposition. *K.E. Nieto-Zepeda*, Cinvestav-IPN, Mexico, *E. Mota-Pineda*, ESIME-IPN, Mexico, *M.A. Zapata-Torres*, CICATA-Legaria, IPN, Mexico, *M.A. Melendez-Lira*, Cinvestav-IPN, Mexico

The efficiency of photovoltaic structures based on the CdS/CdTe heterojunction is far from that predicted theoretically. Within the various problems that affect negatively the efficiency of this system is the lack of a methodology to get a controlled doping of the n-type window layer of CdS. The chemical bath deposition methodology generally produces uncontrolled n-type CdS films. This paper proposes the use of fluoride as an electron donor to substituting the atoms of S in CdS. With this objective we deposited CdS films using different molar compositions of thiourea doped with fluorine. The molar compositions used are between 0.025 and 0.25 M with variations of 0.025 M. The samples obtained were characterized by UV-Vis transmission spectroscopy, X-ray diffraction and the electric transport by I vs V measurements. Representative samples were characterized by using Atomic Force Microscopy, Scanning Electron Microscopy, Raman, photoluminescence and photoconductivity spectroscopies. The results are discussed considering the presence of defects associated with the molar concentration of thiourea. The crystallographic quality of the samples increases with fluorine doping. There is a growing trend in the band gap values with thiourea concentrations. Raman spectroscopy results suggest that fluorine is substitutionally incorporated in sulphur sites and photoluminescence spectroscopy indicates that chemical bath deposited samples have a low density of radiative defects. I vs V curves indicated that transport is carried out through a percolation process. Our results indicated that the samples with the best characteristics are those fluorine doped grown with thiourea concentrations between 0.075 y 0.125 M showing that fluorine substitutionally replaces to sulphur and passivates interfacial states.

* This work has been partially supported by CONACYT-Mexico and Instituto de Ciencia y Tecnología-DF

TF-ThP9 Interfacial Properties of Atomic Layer Deposited TiO₂ Films on InAs (100) Surfaces. *L. Ye, T. Gougousi*, UMBC

TiO₂ has been deposited on both native oxide and etched InAs (100) surfaces by thermal atomic layer deposition (ALD) from tetrakis dimethyl amido titanium (TDMAT) and H₂O. X-ray photoelectron spectroscopy (XPS) and high resolution transmission electron microscopy (HRTEM) were utilized to study the interface between the TiO₂ films and the InAs substrate. For depositions at 200°C, the native oxide was thinned and part of the native oxide bubbled to the top of the TiO₂ surface. HRTEM data for a ~4 nm film of TiO₂ on InAs confirmed that the native oxide was completely removed from the interface. When TiO₂ was deposited on HF and NH₄OH etched InAs surfaces, practically sharp interfaces were maintained. To investigate the effect of temperature on the native oxide consumption, two sets of samples with film thickness of 2 and 3 nm were prepared at deposition temperatures ranging from 100 to 325°C. XPS showed that the native oxides were consumed most effectively at 250°C. Deviation of the deposition temperature from 250°C in either direction resulted in a reduction of the native oxide consumption rates.

TF-ThP10 AES and XPS Characterizations in ALD ZnO Films Doped with Al and P. *H. Yuan*, Northwestern Polytechnical University, China, *B. Luo, W.L. Gladfelter, S.A. Campbell*, University of Minnesota

Zinc oxide based films are transparent conductive oxide materials. As part of our research in solar cells, Al- and P-doped ZnO films were prepared at 250 °C in a hot-wall atomic layer deposition (ALD) system. Ozone, diethylzinc, trimethylaluminum or trimethylphosphite were used as the precursors. We obtained films with different Al or P concentrations by varying the precursor vapor pressures, and characterized their physical, chemical and electrical properties. The Al-doped films were n-type with the lowest resistivity occurring at an Al concentration of 1-2%. The as-deposited P-doped films were n-type, but upon rapid thermal annealing in oxygen, the films changed to p-type. The temperature of the n- to p-type transition decreased as the phosphorus concentration increased.

In this presentation, we will describe details of the Auger electron spectroscopic (AES) and X-ray photoelectron spectroscopic (XPS) measurements. AES depth profiling was used to determine the compositions of all of the films, which confirmed that a layered microstructure for the films prepared by introducing the Zn precursor and Al precursor alternatively, and a homogeneous distribution of the Al in the films prepared by co-injecting the Al and Zn precursors. XPS determined the compositional change of the oxygen species upon sputtering. The oxidation state of the P dopant was determined to be +5 for both the as-deposited and annealed films.

TF-ThP12 Photoluminescence and Life-Time Characterization of Polythiophene Incorporated with Dye Molecules. *H. Kobe, H. Kato, A. Yamada, S. Takemura, T. Hiramatsu, K. Shimada, K. Matsui*, Kanto Gakuin University, Japan

Conducting polymer polythiophene (PT) films incorporated with highly-functional molecules such as copper phthalocyanine (CuPc), fullerene (C60) and rhodamine B (RB), further, tetrathiafulvalene (TTF) which is a donor and tetracyanoquinodimethane (TCNQ) which is an acceptor were synthesized and characterized by photoluminescence measurements (PL), time correlated single photon counting (TCSPC) life time measurements and fourier transform infrared spectroscopy (FTIR) in order to obtain fundamental photoluminescence properties of the polymer complexes. Those molecules were doped in the polymer film by the diffusion method. The solvents used in the doping process were acetonitrile or toluene. In the FTIR measurement, the molecular vibration mode of each molecule was observed in each polymer, and it was observed that each molecule had been doped in PT film. A photoluminescence single emission peak was observed at 610 nm in the case of PT doped sample with CuPc by diffusion method. Adding TCNQ molecules to the CuPc diffused PT sample by the diffusion method made the emission peak position varied and the photoluminescence intensity varied. A photoluminescence double emission peak was observed at 590nm and 738nm in the case of PT doped sample with C60 by diffusion method. Double emission peak was observed at 610nm and 663nm when TTF was added after CuPc doping. When TCNQ was added after CuPc doping, emission peak became a 480nm single peak. A photoluminescence double emission peak was observed at 590-660 nm in the case of PT doped sample with RB by diffusion method. In the case of using acetonitrile as a solvent, emission peaks were 610nm and 660nm. In the case of using toluene as a solvent, emission peaks were 590nm and 660nm. As for intensity, the low wavelength side became stronger. Adding TTF and TCNQ molecules to the RB diffused PT sample by the diffusion method made the emission peak position varied and the photoluminescence intensity varied. In the case of PT doped RB and TTF using toluene as a solvent, emission peak was a 590nm single peak. In the TCSPC measurements, 2 or 3 life time components with several tens of nsec to several hundreds of nsec existed in the case of highly-functional molecules doped PT. Adding TTF or TCNQ caused the life time change in the components. It suggests that the change of the emission states in the polymer complexes causes the shift of the emission peaks and the change in intensity.

This work was aided by MEXT-supported Program for the Strategic Research Foundation at Private Universities.

TF-ThP13 Production of Miniaturized Optical Interference Filters Array for CMOS Sensor. *C.-N. Hsiao, P.-K. Chiou, H.-P. Chen, B.-H. Liao, Y.-W. Lin, F.-Z. Chen*, Instrument Technology Research Center, Taiwan

Optical interference filters designed for use in a space-grade multispectral assembly in a complementary metal-oxide-semiconductor sensor were deposited on fused silica by ion-beam-assisted deposition. The optical parameters of optical interference coatings were optimized using admittance loci analysis. The patterned multispectral assembly containing blue, green, red, near infrared, and panchromatic multilayer high/low alternated dielectric band-pass filter arrays in a single chip was fabricated by photolithography process. The corresponding properties of the films were investigated by *in situ* optical monitoring, ellipsometry, spectrometry, scanning electron microscopy and high resolution scanning transmittance microscopy. It was found that the optical properties were significantly improved by employing ion-beam-assisted deposition. The average transmittances were above 90 % for the multispectral assembly, with a rejection transmittance of less than 1% in the spectral range 350–1100 nm. To estimate the optical stability of optical coatings for aerospace applications, a space environment assuming a satellite orbiting the Earth at an altitude of near 780 kilometers was simulated by a Co⁶⁰ gamma (γ) radiation test.

TF-ThP14 Analysis of Thin Layers with Low Energy Ion Scattering (LEIS). *B. Hagenhoff, M. Fartmann, D. Breitenstein*, Tascon GmbH, Germany, *T. Grehl*, ION-TOF GmbH, Germany, *H.R.J. ter Veen*, Tascon GmbH, Germany

When growing thin layers – through ALD or other processes – it is important to know how the layer is growing. Low Energy Ion Scattering (LEIS) can play a pivotal role in the study of film growth. It can be used for a quantitative analysis of the outermost atomic layer. This feature is used to determine layer closure or the existence of pinholes.

At the same time, LEIS gives information about the composition below the surface (similar to RBS). This so called "static depth profiling" can be used to monitor and study the evolution of layer thickness.

Examples will be shown for ALD Ta layers on Si, demonstrating the capabilities of LEIS to determine layer closure and the development of the layer thickness in the ALD process, also at low cycle numbers.

A Diamond Like Carbon (DLC) on Si system will be shown to demonstrate the possibilities to combine static depth profiling with dynamic (sputter) depth profiling, combining the advantages of both techniques and overcoming their drawbacks.

TF-ThP15 Reaction Mechanism for the Atomic Layer Deposition of Titanium Dioxide using Titanium Tetrachloride and Titanium Tetraisopropoxide as Precursors, *R.P. Chaukulkar, S. Agarwal*, Colorado School of Mines

Atomic layer deposition (ALD) is a thin film deposition technique widely used to deposit highly conformal thin films of a wide range of materials including metal oxides and nitrides, metals and more recently, polymers. Most ALD processes for the deposition of metal oxides require the use of H_2O , O_2 plasma, O_3 , or H_2O_2 as the oxygen source. ALD processes for depositing metal oxides using metal halides and metal alkoxides as the oxygen source were first reported by Ritala (Science **288**, 319 (2000)) to mitigate the problem of an interfacial oxide formation during deposition on semiconductor surfaces such as Si and Ge. Herein, we report an ALD process to deposit titanium dioxide using $TiCl_4$ and titanium tetraisopropoxide ($Ti[(OC_3H_7)_4]$, TTIP) as the oxygen source. We have used *in situ* attenuated total reflection Fourier transform infrared spectroscopy to probe the corresponding surface reactions during film growth over a temperature range of 150-250 °C. Depending on the surface temperature, alkyl-transfer and β -hydride elimination have been proposed as two possible reaction pathways for TTIP on a $TiCl_4$ -terminated surface. However, our infrared data show that alkyl-transfer is the only reaction pathway for this ALD process even at temperatures of up to 250 °C, which is close to the decomposition temperature of TTIP. We also report the growth per cycle, stoichiometry, and the band gap for these TiO_2 films grown over the above temperature range. Finally, we discuss the growth of these TiO_2 films on Cl-terminated Ge nanoparticle surfaces.

TF-ThP16 Nitrogen Doped Zinc Oxide Thin Films Prepared by Reactive RF Magnetron Sputtering of Zinc in Nitrous Oxide Atmosphere and Post-deposition Annealing Structural and Optical Properties, *L.A. Hernández-Hernández*, ESFM-IPN, Mexico, *A. Hernández-Hernández, F. De Moure-Flores, J.G. Quiñones-Galván*, CINVESTAV-IPN, Mexico, *J.J. Araiza-Ibarra*, UAF-UAZ, Mexico, *M. Meléndez-Lira*, CINVESTAV-IPN, Mexico

Nitrogen doped zinc oxide thin films were deposited on glass and silicon substrates by reactive magnetron RF sputtering of zinc in a N_2O -Ar ambient. The deposition conditions were optimized varying the substrate temperature and the N_2O /Ar sputtering gas ratio. Representative films were studied employing structural, optical and spectroscopic techniques. A correlation between the nitrous oxide partial pressure, the chemical composition and the crystalline structure of the films was obtained. Stoichiometric and highly oriented ZnO thin films along the (0 0 2) crystallographic direction were obtained for a nitrous oxide partial pressure of ~33%. Lower temperatures produced samples with higher nitrogen content and slightly higher band-gap energy. Post-deposition annealing treatments in nitrous oxide atmosphere at 500 °C significantly improved the crystallinity of the samples as confirmed by x-ray diffraction.

† : partially funded by CONACyT-Mexico and ICYT-DF.

TF-ThP17 Physical and Electrical Characteristic of Atomic Layer Deposition of $Al_xHf_yO_z$ on Silicon, *Y. Lin, W. Li, S. Fanz, R. Candler*, UCLA

In order to meet the increasing demand for high frequency electronic devices, the physical dimensions of MOSFETs have been continuously scaled down into nanoscale. However, one of the bottlenecks we encounter during the scaling-down process is the tunneling current leakage at the gates. SiO_2 , the most commonly used traditional gate dielectric experiences an appreciable amount of tunneling current when the gate thickness is

below 1-1.2 nm. And leakage greatly degrades the performance of nanoelectronics. Therefore, we propose using high-k dielectrics to replace SiO_2 , which can effectively limit the tunneling leakage without losing the current control at gates. Our research has mainly focus on $Al_xHf_yO_z$ deposited on silicon via Atomic Layer Deposition (ALD). The Aluminum to Hafnium ratio in the oxide is tuned to maximize the electrical and physical properties of the film. The electrical properties of each oxide will be characterized by fabricating transistors with gate oxide thicknesses of 5, 10, and 15 nm. Other than taking C-V and I-V measurements for capacitors and transistors, the films will be characterized by XPS, AFM, and spectroscopic ellipsometry. Finally, the effects of various annealing and deposition temperatures at the silicon-oxide interface will be studied using TEM.

TF-ThP18 Wetting Properties of Silicon Incorporated DLC Films, *T.G. Kim*, Pusan National University, Korea

Recently, Diamond-like carbon (DLC) films have come to the center stage of developing coatings for moisture resistant lubricant, water repellent and cathode for lithium batteries. Hydrophilic nature of DLC films played an important role in the above applications.

In this study, Silicon incorporated diamond-like carbon films were deposited on aluminum substrate by a radio frequency plasma-enhanced chemical vapor deposition method. The control of hydrophilic of Silicon incorporated diamond-like carbon surfaces has been studied by the use of O_2 plasma etching and heat treatment. The characteristic of DLC films was evaluated by various techniques such as Contact angle, Micro Raman spectroscopy and Nano indentation. Contact angle of Si-DLC film was about 60°. The contact angle was decreased into about 2° by not only by oxygen plasma treatment for 10min but by heat treatment at 700°C, respectively. In addition, increase of heat treatment temperature makes the contact angle of Si-DLC film decrease.

Friday Morning, November 2, 2012

Applied Surface Science

Room: 20 - Session AS+TF+VT-FrM

Surface Analysis using Synchrotron Techniques

Moderator: A. Herrera-Gomez, UAM-Azacapozalco and CINVESTAV-Queretaro, Mexico, J.C. Woicik, National Institute of Standards and Technology

8:20am **AS+TF+VT-FrM1 Surface and Interface Analyses by X-ray Absorption and Hard X-ray Photoemission Spectroscopies**, *Q. Xiao, X. Cui*, Canadian Light Source, Canada, *H. Piao*, General Electric Global Research Center, *Y.F. Hu*, Canadian Light Source, Canada, *T.K. Sham*, The University of Western Ontario, Canada

Synchrotron-based techniques, such as X-ray absorption spectroscopy (XAS) and variable energy X-ray photoemission spectroscopy (XPS) are increasingly applied to the characterization of surfaces and interfaces of advanced materials. This presentation will introduce the XAS and variable energy XPS capabilities in the study of thin films and nanomaterials at the Canadian Light Source—the third generation synchrotron in Canada. Advantages of these techniques over the conventional techniques (such as lab-based XPS) will be demonstrated using examples in studies of two types of materials: (1) Gate oxide development on SiC and (2) heterogeneous nanocatalysts. In particular, examples using the recently commissioned high energy XPS at the SXRMB beamline (up to 10 KeV) will be highlighted.

8:40am **AS+TF+VT-FrM2 Differences in the Electronic Structure Highly-Oriented Films of H₂, Fe-, Co-, and Cu-Phthalocyanines Revealed by NEXAFS Spectroscopy**, *T.M. Willey, M. Bagge-Hansen, J.R.I. Lee, R. Call, L. Landt, T. van Buuren*, Lawrence Livermore National Laboratory, *C. Colesniuc, C.M. Monton, I. Schuller*, University of California, San Diego

Phthalocyanines are extensively studied as molecular semiconductor materials for chemical sensors, dye-sensitized solar cells, and other applications. Phthalocyanines offer high tunability through the choice of metal center atom; nearly all transition metals and many other heavier elements can reside at the relatively stable square planar center of the phthalocyanines. H₂, Fe-, Co-, and Cu-phthalocyanine molecules in films deposited on gold substrates show prostrate orientation, as opposed sapphire substrates, where phthalocyanines stand in a more upright conformation under deposition conditions used. Angular dependence in NEXAFS, commonly attributable to π^* and σ^* resonances, in both carbon and nitrogen K-edges, quantify the orientational order. H₂-phthalocyanine shows the cleanest angular dependence, with nearly no intensity in the π^* regime with normal beam incidence. Metal L-edges in prostrate films, on the other hand, have dramatic variation in angular dependence of resonances into empty states. Fe- and Co- resemble the K-edges; StoBe DFT shows that the lowest-energy allowed resonances are indeed molecular π^* states, with a high degree of mixing with the d_{xz} and d_{yz} orbitals of the metals. In contrast, the intense, in-plane resonance of the Cu-PC L-edge LUMO resembles a molecular σ^* state. Confirmed by StoBe, the $d_{x^2-y^2}$ character at the Cu center is responsible for this intense in-plane resonance. NEXAFS thus directly probes the electronic structure, illuminating the uniqueness of Cu-compared to H₂, Fe-, and Co- phthalocyanines.

9:00am **AS+TF+VT-FrM3 Hard X-ray Photoelectron Study of Graphene/ h-BN Layer Structures Grown on Polycrystalline Cu Substrates**, *L. Kövér*, MTA ATOMKI, Hungary, *L. Tapasztó*, Inst. Tech. Physics and Materials Sci. & Korea-Hungary Joint Lab for Nanosciences, Hungary, *C. Hwang*, KRISS & Korea-Hungary Joint Lab for Nanosciences, Republic of Korea, *L.P. Biró*, Inst. Tech. Physics and Materials Sci. & Korea-Hungary Joint Lab for Nanosciences, Hungary, *I. Cserny, J. Tóth, A. Csik*, MTA ATOMKI, Hungary, *W. Drube, S. Thiess*, Deutsches Elektronen-Synchrotron DESY, Germany

INVITED

Graphene-hexagonal BN layer structures are recently in the focus of interest having a great potential importance as promising candidates to be utilized in many electronic and spintronic ultrathin device applications. Hard X-ray photoelectron spectroscopy (HAXPES) based on application of synchrotron radiation for excitation is a useful tool for revealing multilayer structures nondestructively providing information on the chemical state of the components at the surface and (even in the case of deeply embedded) interface layers. The aim of the present study is to test the applicability of the HAXPES method for characterizing graphene-hexagonal BN layer systems. h-BN and single layer graphene/multilayer h-BN structures were grown on polycrystalline Cu substrates using the Chemical Vapor Deposition technique [1]. HAXPES measurements were performed at the

BW2 beamline of the DORIS III synchrotron at DESY using the Tunable High Energy XPS facility [2] and monochromatic photons of 3000 eV energy. The surface layer structure of the same samples were also studied with conventional XPS in ATOMKI using non-monochromated Al K α radiation [3]. For obtaining information on the order and relative depth of the particular layers the dependence of the XPS and HAXPES spectra on the angle of emission of photoelectrons was also studied. Our results demonstrate the advantage of the combination of XPS and HAXPES measurements, the use of the Auger parameter for identifying the chemical state of the components at the interface between the layer structure and the substrate, the removal of the overlap between the Auger spectra from the substrate and the photoelectron spectra of the overlayer structure in the HAXPES spectra. In addition, HAXPES, due to the high energy resolution and sensitivity applied, makes possible the separation and identification of the contributions from atoms in different chemical states to photoelectron peaks of the components of the layer structure, and the quantitative estimation of their relative intensity, even at near grazing photon beam incidence (high surface sensitivity).

The research leading to these results has received funding from the European Community's Seventh Framework Programme (FP7/2007-2013) under grant agreement n° 312284, by OTKA grants PD 84244, K 101599 and in the framework of the Korea- Hungary Joint Laboratory for Nanosciences.

[1] C. Hwang, K. Yoo, S.J. Kim, E.K. Seo, H. Yu, L.P. Biro, J. Phys. Chem. C 115, 22369 (2011)

[2] W. Drube, T. M. Grehk, R. Treusch and G. Materlik, J. Electron Spectrosc. Relat. Phenom. **88-91**, 683 (1998).

[3] L. Kövér, D. Varga, I. Cserny, J. Tóth, K. Tökési, Surf. Interface Anal. **19**, 9 (1992).

9:40am **AS+TF+VT-FrM5 Beyond Hard X-ray Photoelectron Spectroscopy: Simultaneous Combination with X-ray Diffraction**, *G.R. Castro, J. Rubio-Zuazo*, SpLine at the European Synchrotron Radiation Facility, France

Nowadays, the great challenge in materials science is the incorporation of complex systems in the area of the nano-technologies. A fundamental aspect is the production of materials with specific and controlled properties. Many of these materials are aggregates of different components, frequently multilayer thin films where the interface and the surface play a key role. Therefore, it is very important to develop an experimental set-up capable to investigate different aspects under identical experimental conditions, in particular to differentiate between surface and bulk properties.

*Hard X-ray photoelectron spectroscopy (HAXPES) is a powerful novel emerging technique for bulk compositional, chemical and electronic properties determination in a non-destructive way. It benefits from the exceptionally large escape depth of high kinetic energy photoelectrons enabling the study of bulk and buried interfaces up to several tens of nanometres depth. At SpLine, the Spanish CRG beamline at the European Synchrotron Radiation Facility (ESRF), we have developed a novel and exceptional set-up that combine HAXPES and X-ray diffraction (X-ray Reflectivity, Surface X-ray Diffraction, Grazing Incidence X-ray Diffraction and reciprocal space maps). Both techniques can be operated simultaneously on the same sample and using the same excitation source. The set-up includes a robust 2S+3D diffractometer with its main axis vertical hosting an UHV chamber equipped with a unique photoelectron spectrometer (few eV < E_{kin} < 15keV), X-ray tube (Mg/Ti), 15 keV electron gun and auxiliary standard surface facilities: MBE, ion gun, LEED, sample heating/cooling system, leak valves, load-lock port, etc.. The photon energy ranges between 7 and 45 keV. The HAXPES analyzer is an electrostatic cylinder-sector (FOCUS HV CSA), with a compact geometry and high transmission due to second order focusing. The analyzer is capable to handle kinetic energies both up to 15 keV and down to a few eV with the same analyzer setup and power supply. The SpLine station offers a unique opportunity to obtain, on a same sample and under identical experimental conditions, simultaneous information about the electronic properties, chemical composition and geometric/crystalline structure of bulk, buried interfaces and surfaces. This *novel tool* for non-destructive characterization of bulk and buried interfaces is available to the *scientific community*.*

In this contribution, we will present a general view of HAXPES-XRD station available at SpLine. Three aspects will be specially addressed: physical background, experimental set-up and selected examples.

10:00am **AS+TF+VT-FrM6 Spectroscopic Imaging using Vector Potential Photoelectron Microscopy**, *R. Browning*, R. Browning Consultants

A new class of electron microscope, vector potential photoelectron microscopy (VPPEM) has been developed. This microscope will enable the chemical microanalysis of a wide range of samples using photoelectron spectroscopy (PES). The microscope is a full field spectroscopic imaging technique with a very large equivalent depth of focus. The unique imaging properties of this method opens up many experimental opportunities including the chemical microanalysis of a wide range of real world samples. Highly structured, three dimensional samples, such as fiber mats and fracture surfaces can be imaged, as well as insulators, and magnetic materials. The new microscope uses the vector potential field from a solenoid magnet as a spatial reference for imaging. A prototype instrument has demonstrated imaging of Au grids, uncoated silk, magnetic steel wool, and micron sized single strand tungsten wires.

10:20am **AS+TF+VT-FrM7 Trends in Synchrotron-based Photoemission; High Energy and High Pressure**, *H.J. Bergersen, J. Åhlund, R. Moberg*, VG Scienta, Sweden

The fields of Hard X-ray Photoelectron Spectroscopy (HAXPES) and High Pressure Photoemission (HiPP) are growing fast. In this contribution we present instrument development and results within HAXPES and HiPP as well as the merged field of HiPP-HAXPES.

Photoelectron spectroscopy (PES) is an excellent tool in surface science due to the possibility to probe electronic and geometric structure. During the past decade Angle Resolved Photoelectron Spectroscopy (ARPES) has had a remarkable upswing, due to the development of parallel angular detector analyzers, and is today used routinely for band mapping, depth profiling and X-ray diffraction (XPD) in the Ultra Violet (UV) and soft X-ray regime. With higher energies (hard X-rays), in combination with improvements in PES detection techniques, this tool can be extended to the HAXPES regime, enabling studies of bulk materials. Here we demonstrate new development of analysers capable of measuring angular resolved spectra in the High Energy regime as well as results obtained using such analyzers.

Experiments done under normal surface science conditions (Ultra High Vacuum) are of limited use in some applications, e.g catalysis, due to the pressure gap problem. This motivates the study of systems at ambient pressures. Here we present a HiPP instrument developed in collaboration with Advanced Light Source (ALS). This instrument allows standard PES measurements as well as spatial and angle resolved spectra at HiPP conditions. Some recent results include spatially resolved investigations of solid oxide electrochemical cells (SOC:s) and electrochemical properties of junctions.

Finally, we report on recent advances in constructing a new generation of instrumentation combining HiPP and HAXPES. A novel electron analyser, designed for optimal transmission in combination with very efficient differential pumping, will be presented together with preliminary results.

Electronic Materials and Processing **Room: 14 - Session EM+NS-FrM**

Low-Resistance Contacts to Nanoelectronics **Moderator: S. Zollner, New Mexico State University**

8:20am **EM+NS-FrM1 Electrical Transport on Chemically Modified Silicon-on-Insulator Substrates**, *G.P. Lopinski*, National Research Council of Canada **INVITED**

Electrical transport of semiconductor surfaces and nanostructures are strongly influenced by interfacial processes. Adsorption and reaction events which result in charge re-distribution can modulate conductivity through long-range electric field effects. These effects are being exploited to tailor electronic properties of nanomaterials and devices as well as in the development of electrically-based chemical and biological sensors. Silicon-on-insulator(SOI) substrates, in which the top layer is thinner than the depletion length, are particularly well-suited for demonstrating and investigating the effects of surface processes on electrical transport. Measurements on hydrogen terminated H-SOI substrates (with both (100) and (111) orientations) have demonstrated that adsorption of certain polar molecules (water, pyridine and ammonia) results in large reversible increases in conductivity, attributed to charge transfer effects which induce accumulation of majority carriers on n-type and minority carrier channels (inversion) on p doped substrates. Adsorption of the prototypical electron acceptor tetracyanoethylene (TCNE) results in a strong decrease in conductivity on n-type substrates due to depletion of majority carriers. This effect is not fully reversible due to reactions of TCNE with the H-

terminated surface. Use of SOI substrates also facilitates formation of point contact pseudo-MOSFETs, allowing transistor characteristics to be obtained without the need for device fabrication. This approach has been shown to be a simple and straightforward way to monitor the effect of adsorption and reaction events on the electronic properties of the silicon substrate. Pseudo-MOSFET measurements have been used to monitor surface reactions such as ambient oxidation of the H-terminated surface. Gas phase photochemical reaction of alkenes has been used to chemically passivate these surfaces while maintaining a low density of electrically active defects ($<1 \times 10^{11} \text{ cm}^{-2}$). These alkyl monolayer passivated SOI surfaces show a large reversible response to TCNE, suggesting they can function as good ultrathin gate dielectrics for sensing applications.

9:00am **EM+NS-FrM3 Evidence for Single Electron Tunnel Junction using Gold Nanoparticles on Oxide-Free Si(111)**, *L. Caillard, O. Seitz, P. Campbell*, University of Texas at Dallas, *O. Pluchery*, Université Pierre et Marie Curie, France, *Y.J. Chabal*, University of Texas at Dallas

It has been suggested that the phenomenon of Coulomb blockade could be achieved by placing a metallic nanoparticle between two tunnel junctions. While the Coulomb blockade has been well established theoretically and demonstrated on metal substrates¹, it is more challenging to observe on semiconductor surfaces due in part to the defective nature of the interfaces and to the depletion layer. We present an experimental study of two ultra small-capacitance normal tunnel junctions connected in series between the Si substrate and a STM tip. To achieve such a structure, we use an amine-terminated self-assembled monolayer (SAM) grafted on silicon (111) as the insulator layer, acting as a linker to attach gold nanoparticles on the surface. The SAM layer is grafted directly on oxide-free silicon through a Si-C bond formation using hydrosilylation reactions and is characterized by a low interface state density². Moreover, this SAM layer provides a long-term passivation (weeks) of the interface that prevents oxidation of the substrate during Au nanoparticle deposition. The SAM quality is characterized using an extensive range of techniques, including in-situ IR spectroscopy, spectroscopic ellipsometry, X-ray photoelectron spectroscopy (XPS) and Atomic force microscopy (AFM). The second capacitance is formed by the gap between the gold nanoparticle and the tip of the Scanning tunneling microscope/spectroscopy (STM/S). The current-voltage measurements have been performed in ultra high vacuum. Several parameters have been investigated: silicon doping level, sample temperature, and size of the gold nanoparticles (AuNPs), ranging from 1 to 15 nm. The junction is achieved by either grafting synthesized AuNPs or depositing evaporated gold directly on the SAM. Preliminary data confirm that coulomb staircases are observed under different conditions, mostly clearly for highly doped substrates at low temperature (10K). The steps width and height of these Coulomb staircases depend on particle size. These results are an important step toward future control for single electron transistor and flash memory applications.

[1] Zhang, H.; Yasutake, Y.; Shichibu, Y.; Teranishi, T.; Majima, Y., Tunneling resistance of double-barrier tunneling structures with an alkanethiol-protected Au nanoparticle. *Phys. Rev. B*, 72, (20) (2005)

[2] D. Aureau, Y. Varin, K. Roodenko, O. Seitz, O. Pluchery and Y. J. Chabal, Controlled Deposition of Gold Nanoparticles on Well-Defined Organic Monolayer Grafted on Silicon Surfaces. *Phys. Chem. C*, 114 (33), pp 14180–14186 (2010)

9:20am **EM+NS-FrM4 A Distribution of Variable Size Sn-islands on 0.8 nm Oxide/ Si (111): Local MOS Properties and Tunneling Studied with Synchrotron Radiation**, *A. Silva*, Universidade Nova de Lisboa, Portugal, *K. Pedersen*, Aalborg University, Denmark, *Z.S. Li*, Aarhus University, Denmark, *P. Morgen*, University of Southern Denmark

The thinnest possible uniform and stable oxide layer grown thermally on Si (111) is 0.8 nm thick. This oxide is grown at around 500°C, in a self-limiting process, which has earlier been fully characterized with surface sensitive, high-resolution core level photoemission at the ASTRID storage ring facility at Aarhus, Denmark. Such oxides are too thin for use in current generations of CMOS-devices, yet they have potential applications in devices, where controlled tunneling could be of importance, or as diffusion barriers. To study the tunneling properties of this oxide covering the Si (111) surface isolated nanometer-sized Sn islands in different diameters and concentrations were deposited at 500°C and became negatively charged, with different charges depending on their size. The deposition was done from a Knudsen source in a way programmed to produce a systematic variation of the Sn coverage across about 2 cm of the surface. This is done to allow locally resolved photoemission characterization of the system, at a resolution (with a photon beam width) of around 150 micron. The resulting shifts of Si 2p and Sn 4d core levels at, and across the surface, with varying amounts of Sn, and charge on the Sn islands, are used to determine the local changes in band bending and fields in the oxide. This method thus offers a unique possibility to evaluate MOS properties of nano-systems in-situ without direct electrical contacts.

9:40am **EM+NS-FrM5 Signatures of Interface Band Structure and Parallel Momentum Conservation of Hot Electrons across Metal-Semiconductor Schottky Diodes**, *J. Garramone*, Northwestern University, *J. Abel*, *R. Balsano*, University at Albany-SUNY, *S. Barraza-Lopez*, University of Arkansas at Fayetteville, *V.P. LaBella*, University at Albany-SUNY

Understanding hot electron transport and scattering through materials and interfaces is important for conventional integrated circuit technologies and futuristic applications such as hot carrier photovoltaics and hydrogen sensing. In this presentation, the hot electron attenuation length of Ag is measured utilizing ballistic electron emission microscopy (BEEM) on nanoscale Schottky diodes for Si(001) and Si(111) substrates. Marked differences in the attenuation length are observed at biases near the Schottky barrier depending upon the substrate orientation, increasing by an order of magnitude only for Si(001), while remaining unchanged for Si(111). These results provide clear evidence that the crystallographic orientation of the semiconductor substrate and parallel momentum conservation affect the hot electron transport across these interfaces. A theoretical model reproduces the effect that combines a free-electron description within the metal with an ab-initio description of the electronic structure of the semiconductor.

10:00am **EM+NS-FrM6 Metal-Fullerene Interfaces: A Dynamic System**, *P. Reinke*, *J.B. McClimon*, *H. Sahalov*, University of Virginia

Fullerenes and other small organic molecules are used in organic solar cells, organic LEDs and molecular electronics system, and the interface between the organic layer and the metal electrode is critical to achieve the desired functionality. The majority of studies focusses on the interaction of molecules with metal surface, and the interaction of metals with organic surfaces has garnered much less attention. However, the addition of metal to an organic layer surface has been one of the bottlenecks in the fabrication of molecular electronics devices. We therefore present here a comprehensive study of the metal interaction with fullerene surfaces. Our past research has investigated the deposition of Au and Si on fullerene surfaces, and our presentation here focuses on the interface to transition metals Vanadium and Tungsten. All of these systems show a dynamic behavior: the metal atoms are highly mobile and thus perturb the C₆₀ matrix substantially.

The fullerene and metal atoms/films are deposited by electron beam and thermal evaporation, and the interface formation is observed with STM under UHV conditions in a sequential manner. V immediately diffuses into the fullerene matrix, and surface clusters are sparse. The STM images reflect the change in the local electronic structure of the molecules through the interaction with sub-surface V: the apparent height of molecules in contact with V is reduced, and their rotation ceases and the molecular orbitals can be identified by the characteristic C₆₀ substructure within the molecule.

We suggest that the subsurface V forms complexes with C₆₀ where charge donation to the fullerene cage occurs, and preferential bonding to the hexagonal face determines the molecule orientation. The increase of V concentration leads to agglomeration of V-clusters and consequently the extension of regions with a smaller apparent height in the filled state images. The charge exchange between metal clusters and fullerene matrix allows to observe the V-cluster growth within the matrix. The empty state images are essentially flat, and show small variations in topography and cracks in the fullerene layer for large V-concentrations (~0.6 to 1 ML). We will present a comprehensive model for the diffusion of V through the matrix, the complex formation and cluster growth. The behavior of W is distinguished by a larger percentage of surface clusters, and the dynamics of cluster formation within the matrix will be compared to V. However, both transition metals do not destroy the C₆₀ matrix, but only react to form carbides at elevated temperatures.

10:20am **EM+NS-FrM7 Scaling Silicide Contacts in Microelectronics: At What Size will Material Characteristics affect Device Properties?**, *C. Lavoie*, IBM T.J. Watson Research Center

With the continued scaling of CMOS technology, the typical contact area to the source and drain of a CMOS device can now reach below 1000 nm². At these nano-dimensions, typical intrinsic contact resistivities of 1x10⁻⁸ Ω-cm², easily lead to resistances exceeding the KΩ solely for crossing the interface silicide-silicon. Such resistances are unacceptable as they dominate the overall resistance of a device. In an attempt to mitigate this increase in interfacial resistance with contact area reduction, much research has been performed concentrating on the tailoring of material properties of both the silicide and the semiconductor substrate as well as on the optimization of contact geometries and the advanced engineering of interfaces. As the size of the contact reaches dimensions that are similar or smaller than the typical microstructure of the expected poly crystalline material, some dramatic effects are to be anticipated. First, the presence of a single grain during the silicidation eliminates the typical dominant diffusion

path: grain boundaries. As a result, phase nucleation and kinetics of growth can only proceed through the silicide bulk or the available interfaces. This will likely retard formation of the desired phases in the narrowest dimensions. Another expected disadvantage of very small contacts resides in the variability of the intrinsic contact resistance discussed above. It is accepted that the Schottky barrier height of a given silicide to a silicon substrate varies with substrate orientation. As a result, variation of crystal orientation from contact to contact may lead to dramatic effects on contact resistance. This orientation variation can originate from either a variation in silicide texture from contact to contact or a variation in device geometry (i.e. silicidation on Si(100), Si(110) or Si nanowire device depending on geometry). In this presentation, we will first explain how the importance of contact resistivity has caused a shift in contact engineering from yield and defect control towards the optimization of device performance. We will then describe some of the challenges involved in building arrays of nanostructures and characterizing them.

11:00am **EM+NS-FrM9 Compositional Dependence of the Dielectric Function and Optical Conductivity of NiPt Alloy Thin Films**, *L.S. Abdallah*, *T. Tawalbeh*, *I.V. Vasiliev*, *S. Zollner*, New Mexico State University, *C. Lavoie*, IBM T.J. Watson Research Center, *A. Ozcan*, IBM Systems and Technology Group, *M. Raymond*, GLOBALFOUNDRIES

Optical properties of metals are less well known than those of insulators and semiconductors, because it is hard to achieve similar purity and crystallinity in metals. Many metals are reactive and easily form oxides, or they exhibit significant surface roughness. We report the dielectric function and optical conductivity of Ni-Pt alloys as a function of composition (10 to 25 atomic % Pt) from 0.8 to 6.5 eV. Our films are 10 nm thick and were prepared by physical vapor deposition (co-sputtering from pure Ni and Pt targets). To avoid reaction between Si and the metal alloy, films were deposited on thick thermal oxides (220 nm). Some films were annealed at 500°C for 30 s. Similar Ni-Pt alloys are used as Ohmic contacts in CMOS device processing, to achieve highly stable low-resistance contacts between copper back-end metallization and front-end silicon transistors. Our results will enable in-line process control of Ni-Pt alloy deposition using spectroscopic ellipsometry.

Since our metal thickness is below the penetration depth, the interference from the thick SiO₂ layers creates artifacts when extracting the optical conductivity. We minimize this issue by acquiring the ellipsometric angles over a broad range of incidence angles (20° to 80°), which varies the optical path length and thus shifts the interference problems to different energies. Our resulting dielectric functions are similar to those tabulated by Palik for pure Ni. The data are dominated by a Drude divergence due to free carriers at low photon energies. We can remove this divergence by multiplying with the photon energy. We find several trends: (1) The optical conductivity of the annealed films is always greater than that of the as-deposited films, due to improvements in crystallinity and reduced grain boundary scattering after annealing. (2) All four alloys show conductivity peaks near 1.5 and 4 eV due to transitions from the d-like valence bands to the s-like conduction bands. (3) These peaks are significantly broader and weaker than those in pure Ni, but at the same energy. The broadenings increase with increasing Pt content. However, the amplitude of the 4 eV conductivity peak remains constant near 3500/Ωcm, independent of Pt content.

From electronic structure calculations for pure Ni and Pt and a Ni₃Pt ordered compound, we find that Ni, Pt, and Ni-Pt d-bands have similar energy, which explains why the 4 eV peak in the conductivity does not shift with Pt addition. Furthermore, the bandwidth of the Ni 3d bands is smaller than that of the Pt 5d bands, consistent with the increase in the broadening of the optical transitions.

This work was supported by NSF (DMR-11104934).

11:20am **EM+NS-FrM10 Ultra-Shallow Junction Formation for sub-22nm CMOS Technology and Characterization using High-resolution SIMS**, *M.J.P. Hopstaken*, *H. Wildman*, *D. Pfeiffer*, IBM T.J. Watson Research Center, *Z. Zhu*, *P. Ronsheim*, IBM Systems and Technology Group, *K.K. Chan*, *I. Lauer*, *J.S. Newbury*, *D.-G. Park*, IBM T.J. Watson Research Center

Secondary Ion Mass Spectrometry (SIMS) has shown great resilience over the last decades in keeping up with the aggressive downscaling of advanced CMOS technology. Major improvements contributing to the staying power of SIMS are lower primary ion beam energies to meet the ever more stringent depth resolution demands [1] and application of novel external standard-free calibration methods for quantification in the near-surface region [2]. Here we demonstrate state-of-the-art applications of SIMS to Ultra-Shallow Junction (USJ) formation and in-situ doped thin epitaxial layers.

We present As-USJ extension formation for nFET with junction depths below 120 Å, obtained using low energy ion implantation and micro-second flash (μ-flash) annealing. SIMS depth profiling employing a 200 eV Cs⁺

beam provides detailed information on diffusion and segregation of As at the sub-nm scale for different annealing conditions. Low energy implantation of P has been proposed as an alternative to As for the formation of Source/Drain (S/D) regions to reduce crystalline damage. This is crucially important for advanced CMOS technology based on Extremely Thin SOI or FinFET. Here, we present different analytical approaches to determine the most accurate quantification for shallow P concentration profiles in Si. Also, we have employed 3D atom probe tomography to independently determine in-depth [P] profiles for SIMS calibration purposes [3].

For pFET processes, nm-scale control of B-diffusion is instrumental to obtain highly activated and abrupt B-USJ. Here we present a novel doping strategy employing ultra-thin solid source Si:B diffusion sources—in combination with μ -flash annealing—to form the B-USJ extensions. Presence of high [B] and minimal diffusion length necessitates use of ultra low O_2^+ impact energy for accurate determination of junction depth and abruptness. Regarding S/D formation, In-Situ Boron Doped (ISBD) SiGe is an important technology element for pFET strain enhancement. Quantitative analysis of [B] in SiGe using reactive low energy O_2^+ ion sputtering is complicated due to large yield variations as a function of [Ge] [4]. We present a calibration protocol based on multiple B-implanted epitaxial $Si_{1-x}Ge_x$ standards on Si(100) with constant [Ge] ranging from 20 to 50 at.%. This approach allows for explicit correction of both SiGe sputter yield and B^+ and Ge^+ yield variations as function of [Ge], enabling quantitative analysis of ISBD SiGe.

- [1] A. Merkulov et al., JVST B **28**(1) (2010) C1C48.
- [2] W. Vandervorst et al., AIP Conf. Proc. **931**(1) (2007) 233-245.
- [3] M.J.P. Hopstaken et al., SIA, DOI 10.1002/sia.4916 (2012).
- [4] Z. Zhu et al., SIA **43**(1-2) (2011) 657-660.

11:40am **EM+NS-FrM11 A Deep Dive into the Liquid Fermi Sea.** *R.K. Schulze, J.C. Lashley, B. Mihaila, D.C. Wallace*, Los Alamos National Laboratory

We reexamine high resolution photoemission in some of the liquid metals accessible in a UHV environment. These include Ga, In, and Bi, and at a basic level, involves comparison of the DOS EDCs between the crystalline solid and liquid metal. The motivation is to gain an understanding of the fundamental differences between normal and anomalous melters. This includes a search for an understanding of the electronic contribution to the melt phase transformation. Normal melters, such as In, show a difference in liquid and crystal solid entropy at constant volume, $\Delta S^* = 0.8 \pm 0.1$ k_B/atom, and exhibit a volume expansion upon melting, while anomalous melters, such as Ga and Bi, have $\Delta S^* \gg 0.8$ k_B/atom, and show a volume collapse upon melting. Observed changes to the electronic structure near the Fermi energy upon crossing the solid-liquid phase boundary will be discussed.

Energy Frontiers Focus Topic Room: 15 - Session EN+SS-FrM

Photocatalysis and Solar Fuels

Moderator: N.G. Petrik, Pacific Northwest National Laboratory

8:20am **EN+SS-FrM1 Atomic Layer Deposition for Electronic Band Engineering of Silicon Photoelectrochemical Cells.** *B. Kalanyan, M.D. Losego, D.H. Kim, G.N. Parsons*, North Carolina State University

Nanostructured semiconductor materials are generating considerable interest for application in photoelectrochemical cells (PEC) for solar water splitting. A key challenge is improving the long-term chemical and operational stability of semiconductor electrodes. Our research in PEC devices focuses on utilizing atomic layer deposition (ALD) as a means to engineer the semiconductor-liquid interface of photoelectrodes. ALD modification can both impart chemical stability and tune the electronic band structure at the semiconductor's surface. P-type silicon photocathodes are a model PEC system capable of high photocurrents (>10 mA/cm²) in aqueous electrolytes under AM 1.5 illumination. Here we will detail our efforts to improve the reproducibility of silicon photocathode fabrication and to use TiO₂ ALD coatings for band engineering that permits planar catalyst integration.

This talk will discuss silicon photocathodes fabricated from p-type Si (100) wafers with ~1 cm² functional area. Electrodes were tested in a three-electrode electrochemical cell containing sulfuric acid electrolyte (0.5M, pH ~0), a Pt mesh (>5 cm²) counter electrode, and a Ag/AgCl reference electrode. To ensure similar dopant profiles, experiments were run using a range of silicon samples from the same wafer. We will first discuss the

effects of varying the processing schemes for forming an ohmic back contact. We find a large and distinct effect on both the photocurrent saturation value and the photocurrent onset potential with the size and composition of this back contact. Through contact optimization, series resistance of the back contact can be reduced by 5x, as measured by impedance spectroscopy.

The second portion of our talk will describe our results using ALD TiO₂ thin films to engineer the electronic band structure at the photocathode/electrolyte interface. Deposition of a coalesced Pt thin film catalyst layer directly on p-type silicon is well known to form an Ohmic contact that pins the silicon's Fermi level in a nearly flat band state. Without the internal bias caused by surface carrier depletion, photoelectrode activity is eliminated. However, by inserting an interfacial TiO₂ layer with sub-nanometer thickness control, a p-n junction can be formed which generates the necessary electric field for photoelectrode operation. Here, we will demonstrate how uniform ALD layers are capable of providing the necessary electronic band engineering to form completely planar p-Si/TiO₂/Pt structures with photocurrents exceeding 10 mA/cm² with no applied bias.

8:40am **EN+SS-FrM2 Photochemical Hole Scavenging Reactions of Methanol on TiO₂: Identification of Active Species and Water Coadsorption Study.** *M. Shen, M.A. Henderson*, Pacific Northwest National Laboratory

Molecular and dissociative forms of adsorbed methanol were prepared on the rutile TiO₂(110) surface to study their relative photocatalytic activity for hole-mediated oxidation. Molecular methanol is the dominant surface species on the vacuum-annealed TiO₂(110) surface in ultrahigh vacuum (UHV). Coadsorption of methanol with oxygen results in ~20% of the adsorbed methanol decomposing to methoxy and OH. Subsequent heating of the surface to 350 K leaves a surface with only adsorbed methoxy groups. Using temperature-programmed desorption, we show that adsorbed methoxy is at least an order of magnitude more reactive than molecularly adsorbed methanol for hole-mediated photooxidation. Methoxy photodecomposes through cleavage of a C-H bond forming adsorbed formaldehyde and a surface OH group. These results suggest that methoxy, and not molecular methanol, is the effective hole scavenger in photochemical reactions of methanol on TiO₂. Same reactions were also studied with water coadsorption.

9:00am **EN+SS-FrM3 Nanostructured Antimony Doped Tin Oxide Enhances Photoelectrochemical Water Splitting by Supported TiO₂.** *Q. Peng*, Duke University, *B. Kalanyan*, North Carolina State University, *M. Andrew, P. Hoertz*, Research Triangle Institute, *L. Alibabaei*, University of North Carolina at Chapel Hill, *J. Liu*, Duke University, *T.J. Meyer*, University of North Carolina at Chapel Hill, *G.N. Parsons*, North Carolina State University, *J.T. Glass*, Duke University

Photoelectrochemical (PEC) water splitting devices hold great promise for harvesting solar energy, however, existing electrodes suffer from either stability or efficiency limitations. Owing to its low production cost, environmental compatibility, and remarkable stability, TiO₂ has been widely investigated as a PEC electrode since 1972. However, the solar-to-fuel conversion efficiency of TiO₂ PEC electrodes is still much lower than the theoretical value. This is partially due to the dilemma of short minority carrier diffusion length and long optical absorption length, as well as the low electron mobility. Nanostructured conductive scaffolds show promise to solve this challenge by decoupling light absorption and charge carrier diffusion while enhancing conductivity. In this research, we synthesized TiO₂ PEC electrodes on a conductive scaffold comprised of antimony doped tin oxide particles (ATO-particle film). These structures, which are a cost effective alternative to semiconductor supported TiO₂ electrodes, yielded a photocurrent density of 0.58 mA/cm². This is approximately 3× the corresponding current density for planar TiO₂ PEC electrodes on FTO glass. Our results have shown that the porosity of ATO-particle film has limited the further efficiency improvement, which can be addressed by optimizing particle size, thickness, and assembly strategy for ATO-particle films. Owing to its transparency in a wide range of wavelengths, the ATO-particle scaffold also has great potential to boost the efficiency of devices using other narrow bandgap PEC materials, e. g. Fe₂O₃.

9:20am **EN+SS-FrM4 Plasmon-Mediated Charge Transfer in Au-TiO₂ Heterostructures for Visible Light Water-Splitting.** *J. DuChene, B. Sweeny*, University of Florida, *A. Johnston-Peck, D. Su*, Brookhaven National Laboratory, *W.D. Wei*, University of Florida

Solar water splitting to produce hydrogen represents a potential approach to satisfy the global energy demand in a sustainable manner. Recently it has been reported that the incorporation of plasmonic nanoparticles into semiconductor architectures offers a potential route to increase the efficiency of photoelectrochemical water splitting due to the unique optical

properties of plasmonic nanomaterials. We investigated the energetics and dynamics of electron flow in Au-TiO₂ heterostructures following excitation of the Au nanoparticles surface plasmon resonance with visible light. Our results show that the incorporation of Au nanoparticles into wide band gap semiconductors has promise for use as visible light sensitizers. Moreover, we have studied the role of the hole scavenger methanol in the plasmon-mediated charge transfer process in order to ascertain the nature of possible thermodynamic or kinetic limitations involved in this process. These results demonstrate that the excited-state lifetime of these hot electrons in the TiO₂ conduction band is dramatically extended relative to direct band gap excitation within the semiconductor itself, suggesting a possible strategy for improving the efficiency of photocatalytic reactions.

9:40am **EN+SS-FrM5 Narrowing of Band Gap in 1D Arrays of TiO₂ Nanoparticles for Photocatalysis: Studies using X-ray Spectroscopies with *In Situ* Water Exposure and Heating.** *Y. Liu, J. Taing*, University of California Irvine, *C.C. Chen*, SLAC National Accelerator Lab, *A. Sorini*, Lawrence Livermore National Lab, *M.H. Cheng*, University of California Irvine, *H. Bluhm, Z. Liu*, Lawrence Berkeley National Lab, *T. Devereaux*, SLAC National Accelerator Lab, *J.C. Hemminger*, University of California Irvine

Titanium(IV) oxide (TiO₂) has a wide range of applications in energy science and acts as a stable support for photocatalysts and sensitizers. Utilizing ambient pressure synchrotron x-ray photoelectron and absorption spectroscopies, we explore the properties of TiO₂ thin films and ordered linear arrays of TiO₂ nanoparticles under *in situ* water vapor exposure and heating. Our nondestructive depth profiles (obtained by varying the photoelectron kinetic energy) of electronic and surface structures, combined with density-functional theory calculations, indicate an enhancement of the density of states (DOS) near the Fermi level due to surface Ti³⁺ and oxygen vacancies. Introducing water on the interface suppresses this DOS enhancement. The Ti L-edge and O K-edge absorption spectra, in combination with atomic multiplet calculations, provide information on crystal field effects and multiplet interactions, helping to determine the phases of the TiO₂ particles. Our *in situ* studies suggest that isolated TiO₂ nanoparticles may enhance solar absorption efficiency, and the TiO₂ band gap can be tuned reversibly under water exposure and heating.

10:00am **EN+SS-FrM6 A Theoretical Study of Carbon Dioxide Reduction on Catalysts.** *T. Liang, Y.-T. Cheng, S.R. Phillpot, S.B. Sinnott*, University of Florida

Catalytic reduction of carbon dioxide into fuels would provide an ideal storage medium for intermittent renewable energy sources. Copper and copper oxides electro-catalysts have been found to be capable of producing significant quantities of hydrocarbons or alcohols from CO₂ in aqueous solutions. Selectivity to methanol is speculated to be due to Cu(I) species in electrochemical systems; however, these pathways have not been experimentally verified. Here, the third-generation charge optimized many body (COMB3) potentials, which are proven to be successful to characterize different types of bonding in the heterogeneous systems, are employed to investigate the atomic scale mechanisms associated with catalytic reactions on Cu surfaces and clusters supported on metal oxide surfaces. In particular, the reaction free energies of selected CHO molecules on the Cu (211) surface are investigated and validated with density functional theory calculations. The electrochemical systems are simulated with room temperature, low-energy (5 or 10 eV) deposition of CO₂ or CO₂+H₂O on the Cu (211) surface and Cu cluster interface with the ZnO (101-1) surface. The results suggest that the higher incident energy and the presence of water molecules facilitate CO₂ dissociation. The charge state of the Cu cluster and the charge transfer process are predicted to play significant roles in the selectivity of the catalysts. In particular, the Cu(I) species at the Cu/ZnO interface are predicted to be preferable sites for CO₂ reduction and dissociation, which is consistent with experimental observations. This work was supported as part of the Center for Atomic Level Catalyst Design, an Energy Frontier Research Center funded by the U.S. Department of Energy, Office of Science, Office of Basic Energy Sciences under award number DE-SC0001058.

10:20am **EN+SS-FrM7 Doping Effects on the Electronic Structure of Graphitic C₃N₄ Photocatalysts: Insights from First Principles.** *S. Zuluaga, S. Stolbov*, University of Central Florida

Band gap engineering and facilitating charge separation in the graphitic C₃N₄ semiconductors are promising means for improving the photocatalytic activity of these materials. A number of experiments suggest that doping of C₃N₄ is an efficient way to increase the rate of hydrogen production from water using this photocatalyst. In this work we apply a first principles computational approach to reveal the main factors controlling the S and P doping effects on the properties of C₃N₄. Our density-functional-theory-based calculations show that these dopants are bound to the edges of the triazine elements rather than substituting N or C. Valence charge density

analysis provides detailed description of the charge transfer upon doping. We show, for example, that S does not work as an anion in these materials: it does not accept, but donates electronic charge to the C-N system. Using the GW method we calculate with high accuracy the electronic structure, including the band gap, of the pristine and doped C₃N₄. We show that sufficiently large S doping make the system a conductor. The obtained results shed light on how doping affect the catalytic properties of C₃N₄.

Electron Transport at the Nanoscale Focus Topic

Room: 16 - Session ET+SS+GR+SP-FrM

Electron Transport at the Nanoscale: Development of Theories and Techniques

Moderator: C. Su, Bruker Nano

8:20am **ET+SS+GR+SP-FrM1 What is Missing in the Space Charge Limited Current Theory?**, *X.-G. Zhang*, Oak Ridge National Laboratory, *S.T. Pantelides*, Vanderbilt University

INVITED

Space-charge-limited currents are important in energy devices such as solar cells and light-emitting diodes, but the available theory from the 1950's finds it necessary to postulate defect states that are distributed in energy in order to match data. This has prevented the theory to be used in extracting reliable defect information such as energy level and trap density from measurements. Here we revisit the theory and show that this postulate is not warranted. Instead, we demonstrate that dopants and the concomitant Frenkel effect, which have been neglected, control the shape of measured current-voltage characteristics. For highly disordered material, there is a significant inter-trap tunnelling current in the Ohmic regime, which accounts for the observed peak in the noise power. The new theory can anchor efforts to develop experimental techniques to measure deep-trap levels.

This research was conducted at the Center for Nanophase Materials Sciences, sponsored at ORNL by the Division of Scientific User Facilities (XGZ), and by Division of Material Science and Engineering, Basic Energy Sciences, U.S. Department of Energy (STP), and the McMinn Endowment at Vanderbilt University (STP).

9:00am **ET+SS+GR+SP-FrM3 Mapping Solar Cell Internal Fields and Band Offsets.** *H. Cohen, Y. Itzhaik, G. Hodes*, Weizmann Institute of Science, Israel

The internal fields and band offsets across device interfaces are key features in various applications and, yet, this information is generally inaccessible by standard electrical tools. A systematic approach addressing this problem is demonstrated here, based on chemically resolved electrical measurements (CREM). Studying nanoporous photovoltaic cells, we resolve the internal details layer-by-layer and, thus, extract a realistic band diagram for the multi-interfacial structure. We show the spontaneous evolution of two p-n-like junctions and quantify the associated band bending at corresponding domains. An account for the 'real' working conditions of the device is attempted by exposing the cell to optical and electrical stimuli, revealing the charge trapping at each specific layer and showing how certain sample treatments affect the trapping mechanisms. Our methodology overcomes a critical missing link in device characterization and in fundamental studies of nanoscale solid-state devices.

9:20am **ET+SS+GR+SP-FrM4 Quantum Degeneracy Revealed by the Relation between the Tunneling Current and the Chemical Force.** *P. Jelinek, M. Ondracek*, Institute of Physics of ASCR, Czech Republic, *F. Flores*, Universidad Autonoma de Madrid, Spain

Recent progress has allowed merging AFM and STM into a new experimental setup where tunneling current and atomic forces are recorded simultaneously. The possibility to collect both quantities simultaneously opens new horizons not only in advanced characterization at the atomic scale but also in understanding fundamental relations between the electron transfer and formation of the chemical bond between two bodies.

Actually, there is a long-standing debate in the scientific community about the relation between the chemical force and the tunneling current (see e.g. [1]) on the atomic scale. Both the tunneling current and the short-range component of the force, induced by the formation of the chemical bond, exhibit in atomic contacts an exponential decay with increasing distance in the range of several angstroms. As the quantities depend directly on the wave-function overlap between outermost atoms of tip and surface, the corresponding exponential functions should have similar characteristic decay length. In particular, the relation between the chemical force F and the tunneling current I follows the law $F^n \sim I$, where n is an integer number. Over the last 10 years, several different scaling factors n , varying from 1 to

4, have been proposed by different groups based on both theoretical analysis and experimental measurements (see reference in [2]); still there is no consensus on the relation between the chemical force and the tunneling current.

In this contribution, we explain the relation between the tunneling current and the interaction force at the atomic scale using a simple analytical model [2]. The model unveils the existence of two characteristic scaling regimes, where the tunneling current is either proportional to the chemical force $I \sim F$ or to the square of the chemical force, i.e. $I \sim F^2$. We show that the existence of a given regime is basically controlled by two parameters: (i) the electronic level degeneracy and (ii) the hopping between electronic levels involved in the interaction process. Finally, we will collate our theoretical prediction with experimental AFM/STM measurements of single-atom point contacts and complex DFT simulations [3] to confirm the existence of these two characteristic regimes.

[1] W. Hofer and A.J. Fisher, *Phys. Rev. Lett.* 91, 036803 (2003) and the reply in by C.J. Chen

[2] P. Jelinek et al, *J. Cond. Mat. Phys.* 24, 084001 (2012).

[3] M. Ternes et al *Phys. Rev. Lett.* 106, 016802 (2011).

9:40am **ET+SS+GR+SP-FrM5 Understanding the Influence of the Tunneling Current and the Chemical Force on the Contrast Formation in KPFM**, **Z. Majzik, M. Ondráček, M. Švec, J. Berger, P. Jelinek**, Institute of Physics of ASCR, Czech Republic

Kelvin Probe Force Microscopy (KPFM) [1] senses the variation in the electrostatic force. The electrostatic force is $F_{el} = -dCTS/dz(V_{bias} - V_{lcpd})^2$, where V_{lcpd} denotes to the local contact potential difference (LCPD). Atomic scale resolution was achieved by KPFM on the prototypical Si(111)- 7×7 surface [2]. It was shown that the formation of a chemical bond between the closest tip-surface atoms induces significant variation in the LCPD [2]. Lately it was observed that the tunneling current leads to the raise of an additional electrostatic (phantom) force [3]. Consequently, the total electrostatic force must be the combination of several components where the contribution of each component is defined by the tip-sample separation.

Recent progress in Scanning Probe Microscopy opens the possibility of simultaneous acquisition of the tunneling current, atomic forces and local potential difference with atomic resolution [4]. The aim of this contribution is to discuss the origin of electrostatic force contribution at different tip-sample separations. In particular, we performed simultaneous site-specific AFM/STM measurements on Si(111)- 7×7 using a modified Omicron qPlus (tuning fork based) system [5]. We found that along the tip approach three characteristic regions can be well distinguished. At large tip-sample separations, the capacitance is a function of tip geometry and the tip-sample distance. Approaching the tip closer towards the surface, quantum effects become to play important role. The overlap between the tip and sample wave functions produces electron tunneling, which induces additional electrostatic force. Formation of the chemical interaction between the tip apex atom and the adatoms of the 7×7 surface induces changes in the electron charge distribution reflected in variation of the LCPD [2] and the permittivity in the tunneling gap. Hence the capacitance is modified accordingly. In order to have better understanding of the impact of the chemical interaction, atomic hydrogen was deposited to saturate the dangling bonds of adatoms. Over the hydrogenated adatoms, nor strong shift in the LCPD or sudden change in the capacitance was observed. Further to gain more insight into ongoing processes we carried out DFT calculations for tip-sample interaction to understand affect of the formation of covalent bond between tip apex and surface adatoms on the Si 7×7 surface.

References

[1] M. Nonnenmacher et. al, *App. Phys. Lett.* 58, 2921 (1991)

[2] S. Sadewasser et. al, *Phys. Rev. Lett.* 103, 266103 (2009)

[3] A. J. Weymouth et. al, *Phys. Rev. Lett.* 106, 226801 (2011)

[4] F.J. Giessibl, *Appl. Phys. Lett.* 73, 3956 (1998)

[5] Z. Majzik et. al. *B. J. Nano* 249, 3 (2012)

10:00am **ET+SS+GR+SP-FrM6 An In Situ Technique for Using Ballistic Electron Emission Microscopy to Measure Hot Electron Transport at Metal-Semiconductor Interfaces**, **R. Ralsano, V.P. LaBella**, University at Albany-SUNY

Ballistic electron emission microscopy (BEEM) is a scanning tunneling microscopy (STM) technique that can measure transport of hot electrons through materials and interfaces with high spatial and energetic resolution. BEEM requires an additional contact to ground the metal base layer of a metal semiconductor junction. Performing BEEM *in situ* with the sample fabrication requires a custom built STM or modifying a commercial one to facilitate the extra contact, which leaves the technique to highly trained

experts. This presentation will describe our work to develop a special silicon substrate that has the extra contact and oxide hard mask built in to enable *in situ* BEEM without modifications to the STM. Electrically isolated contact traces are lithographically patterned *ex situ* onto the silicon substrate. Then a hard mask is grown and lithographically patterned and connected to the BEEM sample plate which is then inserted into the ultra-high vacuum chamber. The metal is then deposited on top of the hard mask and then mounted *in situ* onto the STM for BEEM measurements. BEEM measurements comparing both *in situ* and *ex situ* deposited films will be presented.

10:20am **ET+SS+GR+SP-FrM7 Electronic Transport on the Nanoscale**, **R. Moeller**, University of Duisburg-Essen, Germany **INVITED**

To study the transport through objects at the nanoscale a scanning tunneling microscope with several tips is used. Two different configurations will be discussed. The lateral transport of electrons may be studied by using two tips to drive a current parallel to the surface. A third tip enables to map the corresponding electrochemical potential. Measurements for a 2D conducting layer will be discussed. To analyze the transport perpendicular to the surface, a thin metallic layer is placed on a semiconducting surface. At the interface a Schottky barrier is formed, which can only be overcome by electrons of sufficient energy. This may be used to split the current of electrons coming from the tip of the microscope into two parts, the ballistic electrons and the electrons which have been scattered. This technique has been applied to study the ballistic transport of electrons through individual molecules. On the other hand inelastic processes may be revealed by analyzing the fluctuations in the tunneling current observed at different positions of the tunneling tip above an adsorbed molecule.

Graphene and Related Materials Focus Topic Room: 13 - Session GR+EM+ET+MS+NS-FrM

Graphene Device Physics and Applications

Moderator: A. Turchanin, University of Bielefeld, Germany

8:20am **GR+EM+ET+MS+NS-FrM1 Heterointegration of Graphene with Nano and Molecular Scale Structures for High Performance Devices**, **X. Duan**, University of California, Los Angeles **INVITED**

Nanoscale integration of dissimilar materials with distinct compositions, structures and properties has the potential to create a new generation of integrated systems with unique functions and/or unprecedented performance to break the boundaries of traditional technologies. In this talk, I will focus my discussion on the heterointegration of graphene with a variety of nano and molecular scale structures of designed architectures to open up exciting opportunities for nanoscale device engineering. In particular, I will discuss our recent effort in integrating graphene with a self-aligned nanowire gate to create the highest speed graphene transistors, integrating graphene with plasmonic nanostructures to create multi-color high speed photodetectors, integrating graphene with nanoscale templates for the creation of graphene nanostructures, and integrating graphene with various π -conjugating molecular systems for band gap engineering and molecular sensing.

9:00am **GR+EM+ET+MS+NS-FrM3 Graphene RF: From Fundamentals to Opportunities**, **J.S. Moon, H.-C. Seo, M. Antcliffe, S. Lin, A. Schmitz, D. Le, C. McGuire, D. Zehnder**, HRL Laboratories LLC, L.O. Nyakiti, V.D. Wheeler, R.L. Myers-Ward, C.R. Eddy, Jr., D.K. Gaskill, P.M. Campbell, Naval Research Laboratory, K.-M. Lee, P. Asbeck, UC San Diego **INVITED**

Graphene is a topic of very active research from basic science to potential applications. Various RF circuit applications are under evaluation, which include low-noise amplifiers, frequency multipliers, mixers and high-speed radiometers. Potential integration of graphene on Silicon substrates with CMOS compatibility would also benefit future RF systems. The future success of the RF circuit applications depends on vertical and lateral scaling of graphene MOSFETs to minimize parasitics and improve gate modulation efficiency in the channel. In this presentation, we highlight recent progress in graphene materials and devices. For example, with hydrogen intercalation, a graphene wafer showed an electron mobility of 2500 cm^2/Vs at $6.8 \times 10^{12} / \text{cm}^2$ carrier density, and sheet resistance of 230 ohm/square . The Ti-based ohmic contact resistance is below 100 $\text{ohm} \cdot \mu\text{m}$ and hysteresis in $\text{HfO}_2/\text{Graphene}$ MOSFET transfer curves are no longer concerns in RF applications. We will show graphene MOSFETs in mixer and detector applications with performances comparable to and better than the current state-of-the-art technologies. Also, we will present recent process in graphene heterostructure based diodes with on/off ratio greater than 10^6 . In

summary, while graphene is relatively new material, it shows a strong potential to become disruptive in RF applications.

This work was partially supported by DARPA, monitored by Dr. J. Albrecht, under SPAWAR contract number N66001-08-C-2048.

The views, opinions, and/or findings contained in this article/presentation are those of the author/presenter and should not be interpreted as representing the official views or policies, either expressed or implied, of the Defense Advanced Research Projects Agency or the Department of Defense.

[1] J. S. Moon and D. K. Gaskill, IEEE Trans. Microwave Theory and Techniques, p. 2702, 2011

9:40am **GR+EM+ET+MS+NS-FrM5 Graphene and Dielectric Integration: A Sticky Situation?, V.D. Wheeler, N.Y. Garces, L.O. Nyakiti, R.L. Myers-Ward, D.J. Meyer, U.S. Naval Research Laboratory, A. Nath, George Mason University, C.R. Eddy, Jr., D.K. Gaskill, U.S. Naval Research Laboratory**

INVITED

Scalable high- κ dielectric integration is needed to realize graphene-based THz transistors. Yet, the inert nature of graphene inhibits direct application of high-quality uniform atomic layer deposition (ALD) dielectrics. While several methods have rendered the surface more susceptible to ALD[1], they often degrade mobility and/or shift the Dirac voltage due to charges within the gate stack. Recently, we developed a dry chemical functionalization approach using XeF₂ that results in conformal, thin high- κ ALD oxide films with a 10-25% improvement in graphene mobility[2], high dielectric constants (HfO₂=18.5, Al₂O₃=8.9), and small Dirac voltage shifts (HFO₂=2V, Al₂O₃=0.1V), indicating the effectiveness of F functionalization. We will present in-depth details of our fluorination process, discuss its advantages and limitations with respect to other methods used to enhance ALD reactivity with graphene, and provide future directions for this field of study.

Fluorination of EG surfaces was performed in a Xactix X3 XeF₂ etcher operating in pulse mode. Results show that 15 nm pinhole-free Al₂O₃ and HfO₂ films are obtained with an optimized XeF₂ surface treatment prior to ALD consisting of six, 20s pulses (XeF₂=1 torr, N₂=35 torr). This optimal treatment resulted in ~6% fluorine surface coverage, as semi-ionic C-F bonds (F1s ~687eV) only, which provided additional ALD reaction sites needed to obtain uniform oxide films. This unique semi-ionic nature of the C-F bond allows the graphene lattice to maintain planarity and minimize degradation to transport properties.

Theoretical studies suggest that the semi-ionic nature of the C-F bond is related to the graphene electron sheet carrier density (n_e), requiring at least 10¹³ cm⁻² to form[3]. To test this, EG samples with similar thickness but varying n_e (2x10¹²-1.3x10¹³ cm⁻²) were fluorinated simultaneously using the optimal conditions above. Samples with $n_e > 1x10^{13}$ cm⁻² had only semi-ionic C-F bonding, but those with $n_e < 1x10^{13}$ cm⁻² had both covalent and semi-ionic bonding – verifying the theoretical calculations. The amount of covalent bonding increased as n_e decreased, and an increased pinhole density was seen in subsequent Al₂O₃ films. This implies that the underlying EG properties can impact the effectiveness of this fluorination method. Yet, by adjusting the pulse conditions one can tailor this method to still obtain uniform ALD oxides on low carrier density and even p-type EG. To this end, results of our XeF₂ approach on p-type H₂ intercalated EG samples will be shown.

1. Garces, et.al. *JVST B* **30(3)** 03D104 (2012)
2. Wheeler, et.al. *Carbon* **50** 2307 (2012)
3. Sofo, et.al. *Phys Rev B* **83(8)** 081411(R) (2011)

10:20am **GR+EM+ET+MS+NS-FrM7 Achieving Scaled Dielectrics on Graphene Using Atomic Layer Deposition, S. Jandhyala, G. Mordi, R.M. Wallace, J. Kim, University of Texas at Dallas**

In order to realize high-performance graphene-based field-effect-devices, local gating of graphene channel is one of the foremost requirements [1]. Therefore, deposition of high-quality, scalable dielectrics on graphene is required. The ability to precisely control thickness and conformally deposit materials makes atomic layer deposition (ALD) an ideal technique for achieving such dielectrics [2]. However, ALD is a surface-reaction limited process [2] and graphene, being sp² bonded, has no *out-of-plane* covalent functional groups [3] and this can cause difficulties in initiating the ALD reaction [4]. In previous studies we have shown that using a reversibly physisorbed ozone (O₃) functionalization approach, we can deposit high quality ALD oxides (such as Al₂O₃) on graphene with thicknesses below 5 nm [5]. Further understanding regarding the interaction of O₃ and metal precursors with graphene is required for successfully applying the ozone process to deposit different oxides.

In this study, we will use *in-situ* electrical measurements of graphene devices inside an ALD chamber as a characterization technique in order to understand the adhesion mechanisms of oxidants (such as O₃ and H₂O) and metal precursors (such as trimethylaluminum-TMA, titanium tetrachloride-TiCl₄) on graphene surfaces. The characterization scheme used is packaged back-gated graphene-FETs which can detect the molecules adsorbed on the graphene surface. We will compare exfoliated graphene and chemical vapor deposited (CVD) graphene (which tends to have a higher number of defect sites). Using such *real-time* electrical measurements, the observed charge scattering mechanisms and the effect on mobility and doping due to the interaction of these molecules with graphene will be presented.

Acknowledgement

This work was funded through the South West Academy of Nanoelectronics (SWAN) program of NRI under SRC.

References

- [1] S. K. Banerjee, et al., Pro. of the IEEE **98** (12), pp. 2032-2046 (2010).
- [2] R. L. Puurunen, J. Appl. Phys. **97** (12), pp. 121301-121352, (2005)
- [3] A. H. Castro Neto, et al., Rev. Mod. Phys. **81** (1), pp. 109-162 (2009)
- [4] L. Liao, X. Duan, Mat. Sci. Eng. R **70** (3-6), pp. 354-370, (2010)
- [5] S. Jandhyala, et al., ACS Nano, **6** (3), pp. 2722-2730 (2012)

10:40am **GR+EM+ET+MS+NS-FrM8 Atomically-Smooth MgO Films Grown on Epitaxial Graphene by Pulsed Laser Deposition, S.C. Stuart, A.A. Sandin, North Carolina State University, O. Nayfeh, M.D. Dubey, Army Research Laboratory, J.E. Rowe, D.B. Dougherty, North Carolina State University, M.D. Ulrich, Army Research Office**

The growth of high quality insulating films on graphene is a crucial materials science task for the development of graphene-based spintronics because graphene is a potentially revolutionary material for electronic and spintronic applications. For efficient spin-injection, graphene is expected to suffer from the well known “conductivity mismatch” problem at metal-semiconductor spin electrode interfaces. The standard approach to mitigating this problem has been to grow thin, insulating tunnel barriers between the graphene and the magnetic metallic electrode to provide a spin-dependent resistance via the tunneling magnetoresistance effect. It has been demonstrated by several experiments that direct spin injection from a magnetic electrode to graphene is possible but using aluminum oxide or MgO tunnel barriers to assist injection in graphene spin-valve devices is more efficient if suitable oxide-graphene interfaces can be formed. To address this problem we have used pulsed laser deposition (PLD) to grow thin (1-1000 nm) magnesium oxide films directly on epitaxial graphene on SiC(0001). We observe very smooth film morphologies (typical rms roughness of ~0.4 nm) that are nearly independent of film thickness and conform to the substrate surface which had ~0.2 nm rms roughness. Surface roughness is less than 0.5 nm for thicknesses up to 1000 nm and is independent of deposition laser pulse energy within the range 300-700 mJ/pulse at rates of 1-50 Hz. X-ray diffraction shows predominant (111) and (100) orientations, indicating the possibility of doping the graphene by the polar (111) interface. Raman spectroscopy indicates that the graphene is not measurably damaged by magnesium oxide growth. This work shows that PLD is a good technique to produce graphene-oxide interfaces without pre-deposition of an adhesion layer. The films are free of defects or pinholes (that can be observed by atomic force microscopy) and can be grown at arbitrary thicknesses without increasing the roughness or damaging the graphene. The details and kinetics of the deposition process will be described with comparisons being made to other dielectric-on-graphene deposition approaches.

11:00am **GR+EM+ET+MS+NS-FrM9 Facile, Controllable Graphene-based P-N Junctions Using Self-Assembled Monolayers, J. Baltazar, H. Sojoudi, J. Kowalik, L. Tolbert, S. Graham, C.L. Henderson, Georgia Institute of Technology**

In this study we investigate the use of a self-assembled monolayer (SAM) to create a p-n junction in graphene films. Previous techniques rely on charge transfer from adsorbants or electrostatic gate/potentials. Here we demonstrate that, by successfully modifying the SiO₂ surface with an aminopropyltriethoxysilane (APTES) layer, and using intrinsically p-doped transferred CVD graphene films, a well-defined junction can be achieved. Field-effect transistors and p-n junction regions are fabricated prior to graphene film transfer, in order to preserve the pristine properties of the graphene. The I-V characteristic curve indicates the presence of two thermally-controllable neutrality points. This method allows a facile, controllable and low temperature fabrication of graphene p-n junctions.

11:20am **GR+EM+ET+MS+NS-FrM10** **Impact of Cleaning Procedures on the Performance of Graphene-Based Field Effect Transistors**, *M. Lodge, M. Ishigami*, University of Central Florida

It is now widely accepted that surface contaminants have large effects on the performance of graphene-based field effect transistors. Various techniques are now available to clean processing residues from graphene, yet some of these techniques are chemically aggressive leaving concerns that they may damage graphene and affect the device performance. In addition, there are no consensus on the best method to produce the cleanest and, therefore, the best graphene devices.

Here, we have performed a study on the impact of various chemical treatments on the performance of field effect transistors fabricated from graphene grown using chemical vapor deposition. By measuring the impact of hydrogen-annealing, oxygen-annealing, and various solvent-based cleaning on 50 graphene field effect transistors, we generate a statistically-significant conclusion on the best cleaning technique for producing the highest performance. We will present our results along with our scanning tunneling microscopy images and Raman spectra to shed a light on the mechanism involved in each cleaning technique.

11:40am **GR+EM+ET+MS+NS-FrM11** **High Efficiency Graphene Solar Cells by Chemical Doping**, *X. Miao, S. Tongay, M.K. Petterson, K. Berke, A.G. Rinzler, B.R. Appleton, A.F. Hebard*, University of Florida

We demonstrate single layer graphene/n-Si Schottky junction solar cells that under AM1.5 illumination exhibit a power conversion efficiency (PCE) of 8.6%. This performance, achieved by doping the graphene with bis(trifluoromethanesulfonyl)amide, exceeds the native (undoped) device performance by a factor of 4.5 and is the **highest PCE** reported for graphene-based solar cells to date. Current-voltage, capacitance-voltage, and external quantum efficiency measurements show the enhancement to be due to the doping-induced shift in the graphene chemical potential that increases the graphene carrier density (decreasing the cell series resistance) and increases the cell's built-in potential (increasing the open circuit voltage) both of which improve the solar cell fill factor.

Authors Index

Bold page numbers indicate the presenter

— A —

Abbott, J.: LB+EM+GR+MN+TR-WeA3, 173
Abdallah, J.: PS2-TuM9, 73
Abdallah, L.S.: EL+TF+AS+EM+SS-TuP2, 118;
EL+TF+BI+AS+EM+SS-MoA9, 33; EM+NS-
FrM9, **268**
Abdulagatov, A.: TF+EN-MoA3, 53
Abe, M.: SP+AS+BI+ET+MI+NS-TuA11, 102
Abe, S.: EN-ThP12, 249
Abe, Y.: TF-ThP2, 263
Abel, J.: EM+NS-FrM5, 268;
GR+AS+NS+SP+SS-TuA11, 91
Abel, M.-L.: AS-TuP4, 111
Abell, J.L.: TF+SE+NS-WeM12, **157**
Abou Rich, S.: PS-ThP32, 260
Abraha, P.: LB+EM+GR+MN+TR-WeA2, **173**
Abrasonis, G.: SE+NS-MoM2, **21**
Acharya, A.: EM-ThP5, **244**
Acomb, P.: VT-TuP2, **131**
Adam, T.N.: EL+TF+AS+EM+SS+PS+EN+NM-
MoM9, 7
Adamiv, V.T.: AC+TF+SS+MI-MoA7, 29
Adams, D.: TF+EM+SE+NS-ThM5, **217**
Adamska, L.: ET+SS+GR+SP-ThA4, **229**;
GR+AS+EM+NS+SS-WeA2, 170
Adderley, P.A.: VT-MoM5, 26; VT-TuP16, 133
Addou, R.: GR+EM+NS+SS+TF-ThA7, **231**
Adelmann, C.: IS+AS+OX+ET-WeM9, 145; TF-
ThP1, 263
Adesanya, K.: MN+AS-MoM10, 14
Adib, K.: SS-TuM4, **76**
Adiga, V.P.: MN-MoA1, 38; MN-TuM10, **68**;
MN-TuM11, 68
Adusumilli, S.P.: EN+TF-WeA12, 169
Agarwal, A.: PS2-MoA3, **48**; PS2-TuM11, 74
Agarwal, S.: EN+PS-WeM4, 141; NS-MoM6, 16;
TF-ThP15, 265
Ahanotu, O.N.: NS+SP-MoA11, 44
Ahlgren, M.: TF+NS+EM-ThM11, 219
Åhlund, J.: AS+TF+VT-FrM7, 267
Ahmadi, M.: SS-TuP25, **128**
Ahn, J.R.: GR+EM+NS+PS+SS+TF-MoM11, 12;
GR+EM+NS+PS+SS+TF-MoM4, 11; GR-
ThP6, 250; NS+EN-TuM1, 69; NS-ThP9, 254;
SS+NS-ThA3, 235
Ahn, S.J.: NS-ThP5, **253**
Ai, C.-F.: PS-ThP45, 262
Ai, M.: HI+AS+BI+NS-ThM5, 202
Aihara, T.: EN+TF-TuA11, **89**; EN+TF-TuA12, 89
Ajayan, P.: GR+EM+NS+SS+TF-ThA3, 231
Ajayi, O.: TF-MoM8, **25**
Akarvardar, K.: PS2-TuM9, 73
Akarvardar, S.: PS2-TuM9, 73
Akbar, D.: PS-ThP33, 260
Akhmetov, A.: BI+AS-TuA8, 85
Aksamija, Z.: EM+SS+AS+NS-ThM10, **194**
Akturk, A.: EM+OX-WeA9, 167
Akyildiz, H.: TF2-TuA10, **107**
Alaboson, J.M.P.: GR+AS+NS+SP+SS-TuA9, 90
Alavi, Z.: AS-WeM6, 135
Al-Bataineh, S.A.: PS+BI-MoA7, **47**
Albert, M.: NM+AS+MS-MoM4, 14
Albin, D.S.: EN+AS-ThA1, **227**
Albrecht, P.M.: SS-TuM11, **76**
Alcantara Ortigoza, M.: AS+BI-TuA1, **83**;
EN+NS-ThM3, 197; NS-MoM10, 16
Alcántara Ortigoza, M.: AS+BI-TuA3, 83
Alcantara, M.: SS+NS-ThA9, 236
Aldinger, B.S.: NS-ThM9, 207
Aldred, N.: BI-TuP16, 118
Alem, N.: GR+AS+NS+SS-ThM5, 201
Alexander, M.R.: BI+SS+NS-WeM12, 138; BI-
MoA10, 32; BI-MoA4, 31; BI-MoA8, 31;
MB+BI-ThM12, 204
Alexander, W.A.: SS-MoA1, 51

Alexander-katz, A.: MN-MoA11, 40
Alexandre Diniz, J.: EM-ThP7, 244
Alian, A.: EM+TF+OX+GR-MoA1, 34
Alibabaei, L.: EN+SS-FrM3, 269
Allard, L.F.: IS-TuP3, 119
Allen, M.S.: MN-MoA6, 39; MN-TuM6, 67
Allen, S.: BI+SS+AS-TuM5, **60**; PS-ThP1, 255;
SP+AS+BI+ET+MI+NS-TuA9, 102
Allen, T.: NS+AS+SS+SP-WeM2, 146
Allers, L.: EW-WeL1, 163
Alles, M.L.: EM+SS+AS+NS-ThM11, 195
Allred, D.D.: MN+AS-MoM4, 13
Al-Mahboob, A.: GR-ThP11, 251;
IS+AS+BI+ET+GR+NS-TuA8, **92**
Almer, J.: TF+NS+EM-ThM11, 219
Alnabulsi, S.S.: AS-ThA3, **222**
Altansukh, B.: PS2-ThM11, 211
Altfeder, I.: TR-TuA12, 108
Altman, E.I.: OX+SS+TF+MI-MoA2, **44**;
SP+AS+BI+ET+MI+NS-TuA10, 102
Alvarez, C.: IS+AS+BI+ET+GR+NS-TuA7, 92
Alves, E.: AC+TF+SS+MI-MoA9, 29
Amano, H.: PS2-ThM5, 210
Amanpour, M.: GR-ThP8, 251; SS-WeA1, 185
Ambaye, H.: MI+OX-WeA12, 176
Aminpour, M.: AS+BI-TuA1, 83; AS+BI-TuA3,
83
Ancona, M.G.: TF+AS-TuA3, 104
Anders, A.: SE+PS-TuM1, **74**; SE+PS-TuM10, 75
Andersen, J.N.: GR+AS+NS+SP+SS-TuA7, 90;
IS+AS+SS+EN-TuM12, 67
Andersen, O.Z.: BI-MoM11, **6**; BI-TuP1, 115
Anderson, C.M.: PS-WeM3, **149**
Anderson, D.G.: BI-MoA10, 32; BI-MoA4, 31; BI-
MoA8, 31; MB+BI-ThM12, 204
Anderson, E.V.: MB+BI-ThM6, 204
Anderson, K.: MI+OX-WeA2, 175
Anderson, T.J.: EM-ThP4, 244; EN+TF-TuM10,
63; GR+EM+ET+NS+TF-MoA1, 37; GR-
ThP9, 251
Ando, T.: EM+TF+OX+GR-MoA7, **35**
Andrew, M.: EN+SS-FrM3, 269
Ansai, H.: PS2-ThM4, 210
Ansari, N.: TR+SE-WeM10, 160
Antcliffe, M.: GR+EM+ET+MS+NS-FrM3, 271
Antohe, A.: VT-TuP9, 132
Antonelli, G.A.: EM-ThP10, 245
Antony, A.: SS+EN+OX-ThM10, 213
Anuniwat, N.: MI+EN+BI-TuA7, **93**
Anwar, S.R.M.: EM+TF+OX+GR-MoA4, **34**
Aoki, T.: AS-ThM9, 193
Aoki, Y.: SS-MoA8, **52**
Aouadi, S.: SE+NS-MoA1, **49**
Apalkov, D.: MI+OX-WeA7, **175**
Apkarian, V.A.: SP+AS+BI+ET+MI+NS-TuA3,
101
Appleton, B.R.: GR+EM+ET+MS+NS-FrM11,
273; LB+EM+GR+MN+TR-WeA7, 173
Apra, E.: MI-ThP4, 252
Arahara, S.: SS-TuP7, 125
Arai, K.: VT-MoA1, 54; VT-MoA4, 55
Araiza-Ibarra, J.J.: TF-ThP16, 265
Arakawa, I.: TR-TuP2, **130**; VT-TuP8, 132
Arcot, A.R.: BI+AS-TuA3, 84
Areias, A.C.: AS-TuP11, 113; BI+AS-TuA7, 84
Arenholz, E.: GR+AS+EM+MI+MN-TuM9, 65
Argibay, N.: LB+EM+GR+MN+TR-WeA1, **173**
Ariyan, M.: EN-ThP9, **248**
Arlinghaus, H.F.: AS-TuP1, **111**; BI-TuP12, 118
Arman, M.A.: GR+AS+NS+SP+SS-TuA7, 90;
IS+AS+SS+EN-TuM12, 67
Armstrong, I.: SP+AS+BI+ET+MI+TF-WeA8,
183
Armstrong, S.: EW-TuA6, **89**
Arnadottir, L.: SS-ThA6, **238**
Arnebrant, T.: BI+SS+AS-TuM3, **60**

Arnold, J.: PS2-TuM9, 73; PS-ThP1, 255; PS-
WeM4, 149
Arnold, M.S.: EN+TF-TuA3, **88**;
GR+AS+EM+NS+SS-WeA9, 170
Arnold, P.C.: VT-MoA11, **56**
Arpa, R.: VT-TuM9, 80
Arpa-Sancet, M.P.: BI-TuP16, 118
Arpin, K.A.: EN+NS-ThA1, 228
Arregi, J.A.: MI+EN+BI-TuA12, **94**
Artyushkova, K.: EN+AS-ThA6, 227;
IS+AS+SS+EN-TuM6, **66**
Arunachalam, V.: PS-WeM11, 150
Arvet, C.: PS-ThP26, 259
Aryal, P.: EL+TF+AS+EM+SS+PS+EN+NM-
MoM1, 6
Asadollahbaik, A.: HI+AS+BI+NS-ThM3, 202
Asami, S.: NM-TuP1, 121
Asbeck, P.: GR+EM+ET+MS+NS-FrM3, 271
Ashurst, W.R.: TR+SE-WeM10, 160
Assoufidi, L.: SE-TuP4, 123
Asthagiri, A.: OX-TuP1, 122; SS+EN+OX-
ThM10, 213
Ataç, D.: NS+SP-MoA9, 43
Atalay, R.: EM+TF+AS-ThA11, 226;
EM+TF+AS-ThA9, 226; EM-ThP6, **244**
Atanassov, P.: EN+AS-ThA6, 227;
IS+AS+SS+EN-TuM6, 66
Atkinson, S.: MB+BI-ThM12, 204
Attili, S.: BI+AS-TuA9, 85
Attygalle, D.: EL+TF+AS+EM+SS+PS+EN+NM-
MoM1, 6
Atwater, H.A.: EN+TF-TuA1, **87**
Aubry, O.: PS+EM-MoM3, 18
Auer, M.: TF+EM+SE+NS-ThM6, 217
Auerbach, D.J.: SS-MoM4, **23**
Augustine, B.H.: SS-WeM10, **155**
Autes, G.: GR+AS+NS+SS-ThM5, 201
Auzély, R.: BI+SS+NS-WeM10, 138
Avci, R.: NS-ThM12, 207
Axnanda, S.: IS+AS+SS+EN-TuM4, **66**
Aydil, E.S.: EN+TF-MoA8, 36; EN+TF-MoA9,
36; EN+TF-TuM9, 63
Ayers, J.E.: EM+MI-ThA1, 223; EM+MI-ThA2,
223
Azamouche, L.: PS2-TuM2, 72; PS-ThP5, 255;
PS-ThP7, 256

— B —

Baba, A.: TF+AS-WeA8, 189
Baber, A.: SS-WeM1, 153
Babu, M.: EN-ThP8, 248
Baby, A.: TF+NS+EM-ThM10, 219
Baddorf, A.P.: ET+NS+EM-ThM3, 199; SS-
WeM4, 154
Bader, S.D.: MI+EN+BI-TuA1, **93**
Bae, H.-B.: EM+OX-WeA11, 168
Baetz, C.: SE+NS-MoM2, 21
Baek, H.-J.: EN+NS-MoM1, 9
Baer, D.R.: AS+BI-TuA12, **84**; BI-TuP9, 117
Bagge-Hansen, M.: AS+TF+VT-FrM2, **266**;
IS+AS+OX+ET-WeM6, **144**
Bagnall, D.M.: HI+AS+BI+NS-ThM3, 202
Bagus, P.S.: SS+OX-WeM9, **153**
Bahng, W.: EM-TuM10, 62
Bai, K.H.: PS-ThP44, 262
Baikie, I.D.: EW-WeL6, **163**
Bakhru, H.: EM+TF+OX+GR-MoM3, 8
Baklanov, M.R.: PS1-ThM2, 208
Balci, S.: ET+NS+EM-ThM11, 200
Baldasseroni, C.: MI+OX-WeA1, **175**
Baldo, P.M.: IS+AS+OX+ET-WeM3, 144
Baldwin, M.J.: PS2-WeA1, 180
Balog, J.: IS+AS+BI+ET+GR+NS-TuA3, 92
Balsano, R.: EM+NS-FrM5, 268
Baltazar, J.: GR+EM+ET+MS+NS-FrM9, **272**;
GR-ThP10, 251

- Ban, S.: NS-ThP2, 253
Banerjee, S.K.: EM+OX-WeA1, 167
Banik, A.: PS2-TuM1, 72; PS2-TuM6, 73
Banna, S.: PS-ThA10, 235
Banquy, X.: TR-TuA4, 107
Bao, K.: NS-ThM9, 207
Bao, Y.: MI+EN+BI-TuA9, **94**
Baran, N.: BI-TuP14, 118
Barankova, H.: SE+PS-TuA7, **100**
Barbacci, D.: BN+AS-WeA12, 166
Barback, C.V.: BN+AS-WeA3, 165
Barcaro, G.: SS+OX-WeM12, 153
Bardos, L.: SE+PS-TuA7, 100
Bare, S.R.: SS-WeA7, **186**
Barkam, S.: BI-TuP7, **117**; BI-TuP8, 117; SS-TuP12, 126
Barker, P.M.: SE+PS-TuM5, 75
Barkett, L.A.: MN-MoA6, 39
Barkley, S.: TR+SE-WeM10, 160
Barlam, D.: OX+EM+MI+NS+TF-MoM11, 18
Barlow, D.E.: SS+EN+OX-ThM4, **212**
Barlow, A.J.: SS+NS-ThA7, **236**
Barmak, K.: EM-TuA2, 86; EM-TuA7, 86
Barnes, T.: TF+AS-WeA10, 189
Barnola, S.: MN-TuP3, 120; PS2-TuM5, **73**; PS-ThP26, 259
Barraud, S.: PS2-TuM5, 73
Barraza-Lopez, S.: EM+NS-FrM5, 268
Barrett, D.A.: BI-MoA8, 31
Barrett, L.: MN+AS-MoM4, 13
Barrett, N.: GR+AS+NS+SP+SS-TuA1, 89
Barteau, M.: SS-WeA9, 186
Bartels, C.: SS-MoM4, 23
Bartels, L.: GR-ThP8, 251;
SP+AS+BI+ET+MI+NM+NS+SS+TF-WeM5, 150; SS-WeA1, 185; SS-WeM2, **154**
Bartelt, N.C.: TF+EM+SS-ThA10, 242
Bartha, J.W.: NM+AS+MS-MoM4, 14
Bartis, E.: PS+BI-MoA2, 46; PS+BI-MoA6, **46**
Barton, D.: EL+TF+AS+EM+SS+PS+EN+NM-MoM10, 8
Barton, R.A.: MN-MoA1, 38; MN-TuM10, 68; MN-TuM11, **68**
Bartynski, R.A.: AS-MoA10, 30; EN+AS-ThA9, 228; OX+SS+TF+MI-MoA6, 45
Baruth, A.: EN+TF-MoA9, 36
Baski, A.A.: EM+TF+AS-ThA4, 225; SS+EM-WeA1, 184
Basu, D.: EM+OX-WeA1, 167
Batan, A.: SE+PS-TuA9, 100
Batzill, M.: GR+AS+EM+NS+SS-WeA8, 170; GR+EM+NS+SS+TF-ThA7, 231; SS-TuP15, 126
Bauer, E.: IS+AS+OX+ET-WeM3, 144
Bauer, S.: BI-TuP16, **118**
Baughman, W.: ET+NS+EM-ThM11, 200
Baum, J.: SP-TuP1, 123
Baumann, T.: IS+AS+OX+ET-WeM6, 144
Baur, M.: AS-ThM10, 193
Baykara, M.Z.: SP+AS+BI+ET+MI+NS-TuA10, 102
Bazarov, I.: VT+AS+SS-WeM2, 161; VT-TuA11, 109
Be, C.L.: BI-MoM5, 5
Beard, M.: PS2-TuM9, 73; PS-ThP1, 255; PS-WeM1, 148
Beard, M.C.: EN+NS-MoM3, 9
Beaudry, A.L.: TF+SE+NS-WeM9, **156**
Becchaku, M.: SS-TuP17, 127
Beck, D.: SP+AS+BI+ET+MI+TF-WeA11, 183
Becker, J.S.: PS1-TuA11, 97; TF+EM+SS-ThA7, 241; TF-WeM1, 157
Becker, U.: VT-MoA1, 54
Beckers, M.: BN+AS-WeA11, 166
Bedzyk, M.J.: GR+AS+BI+PS+SS-WeM1, **142**; GR+AS+NS+SP+SS-TuA9, 90
Beech, I.: NS-ThM12, 207
Beechem, T.E.: GR+AS+NS+SP+SS-TuA8, 90
Behafarid, F.: SS+NS-ThA8, **236**; SS-TuP27, 128
Behkam, B.: BI-TuP10, 117
Bekman, H.H.P.Th.: HI+AS+NS-WeA9, 172; PS-ThP15, 257
Belu, A.: AS+BI-TuM4, 58
Belyansky, M.P.: NM+NS+MS+EM-MoA4, **41**
Belyea, D.D.: TF-ThP4, 263
Bemis, J.: EW-TuM8, 64;
SP+AS+BI+ET+MI+TF-WeA11, 183
Benavidez, T.: EL+TF+BI+AS+EM+SS-MoA3, 33
Benedek, G.: EM+TF-WeM12, 140
Bennetsen, D.T.: BI+SS+NS-WeM1, **136**
Bennett, B.: EM+TF+OX+GR-MoA10, 35
Bennett, C.J.: GR+AS+BI+PS+SS-WeM9, 143
Bennett, E.: SE-TuP4, 123
Bent, S.F.: EM-TuA1, 85; SS+EM-WeA8, 185
Ben-Yoav, H.: BI+SS+NS-WeM2, 137
Bera, K.: TF+AS-TuA11, **105**
Berdova, M.: TF+NS+EM-ThM10, **219**
Berger, A.: MI+EN+BI-TuA12, 94
Berger, J.: ET+SS+GR+SP-FrM5, 271
Bergersen, H.J.: AS+TF+VT-FrM7, **267**
Beringer, D.B.: VT+AS+SS-WeM10, 161;
VT+AS+SS-WeM6, 161; VT+AS+SS-WeM9, **161**
Berke, K.: GR+EM+ET+MS+NS-FrM11, 273
Berkh, O.: MN+AS-MoM10, 14
Bernal Ramos, K.: TF+NS+EM-ThM2, **218**; TF+NS+EM-ThM9, 219
Bernasconi, M.: EM+TF-WeM12, 140
Bernholz, J.: SS-WeM4, 154
Bernson, E.: BI-MoA3, 30
Berry, N.: TF+AS-WeA2, 188
Besenbacher, F.: BI-MoM11, 6; BI-TuP1, 115
Besnier, J.-F.: EL+TF+AS+EM+SS+PS+EN+NM-MoM3, 6
Beugin, V.: NM+NS+MS+EM-MoA6, 41
Beyer, A.: HI+AS+BI+NS-ThM11, 203;
HI+AS+BI+NS-ThM5, 202; HI-ThP1, 251
Bezares, F.J.: GR+AS+BI+PS+SS-WeM9, 143;
GR+EM+ET+NS+TF-MoA1, 37
Bezarez, F.J.: GR-ThP9, 251
Bhairamadgi, N.S.: TF+EM+SS-ThA4, **241**
Bhardwaj, C.: BI+AS-TuA8, 85
Bhat, N.: AS-TuP23, 115
Bhattacharya, A.: NS+AS+SS+SP-WeM12, 147
Bhattacharyya, D.: EM+SS+AS+NS-ThM4, **194**
Biegalski, M.D.: IS+AS+SS+EN-TuM5, 66
Bielefeld, J.: EM-TuA1, **85**; GR+EM+NS+SS+TF-ThA1, 230
Bielejec, E.: EM-ThP2, 244
Biener, J.: IS+AS+OX+ET-WeM6, 144
Biener, M.: IS+AS+OX+ET-WeM6, 144
Bilich, D.: AS-ThA1, 222
Bilke, L.: EM-ThP15, 246
Bindl, D.J.: EN+TF-TuA3, 88
Binek, C.: MI+OX-WeA10, 176
Bingaman, D.: EW-TuA6, 89
Bingham, N.: MI+OX-WeA9, 176;
OX+EM+MI+NS+TF-MoM1, 17
Biolsi, P.: PS2-TuM1, 72; PS-MoM5, 20
Biró, L.P.: AS+TF+VT-FrM3, 266
Biswal, S.L.: EN+NS-ThM12, **198**
Biswas, A.: MI+SP+AS-ThM3, **205**
Blair, S.L.: BN+AS-WeA3, 165
Blanch, A.J.: SS+NS-ThA7, 236
Blanchet, P.: PS+BI-MoA11, 47
Blaze, M.: BI+AS-TuA8, 85
Blechle, J.M.: PS-ThP19, **258**
Blomfield, C.: EW-TuL4, **82**
Blomfield, C.J.: AS+BI-TuM10, 59; AS+BI-TuM3, 58; AS+NS+SS+TF-WeA8, 164; AS-ThM1, 192; AS-TuP13, 113; AS-TuP14, **113**
Bluhm, H.: EN+SS-FrM5, 270; IS+AS+SS+EN-TuM1, **65**; IS+AS+SS+EN-TuM5, 66; SS-ThA1, 237
Bobek, S.: GR-ThP8, 251; SS-WeA1, 185; SS-WeM2, 154
Bockowski, M.: AC+TF+SS+MI-MoA9, 29
Bockstaller, M.R.: TC+EM+AS-WeA9, 188
Bodart, P.: PS1-WeA2, 178
Boden, S.A.: HI+AS+BI+NS-ThM3, **202**
Bodnar, O.: VT-MoA1, 54
Boineau, F.: VT-MoA1, 54
Bojorge, C.: TR+SE-WeM4, 159
Böker, A.: TF+EM+SS-ThA9, 242
Bol, A.: TF+EN-MoA4, 53
Boland, J.: HI+AS+BI+NS-ThM9, 202
Bolotin, I.: EN-ThP3, 247
Bolotin, K.I.: GR+EM+ET+NS+TF-MoA3, **37**
Bolt, R.J.: PS-ThA9, 234
Bolvardi, H.: SE+NS-MoM8, 22
Bonnell, D.A.: NS-WeA1, 177;
SP+AS+BI+ET+MI+TF-WeA3, 183;
SP+AS+BI+ET+MI+TF-WeA4, 183; SS+OX-WeM10, 153
Bonucci, A.: VT-TuM12, 81
Boos, J.B.: EM+TF+OX+GR-MoA10, 35
Boosalis, A.: LB+EM+GR+MN+TR-WeA10, **174**
Booth, J.-P.: EN+PS-WeM5, 141
Bootman, M.: IS-TuP3, 119
Bora, D.: IS+AS+SS+EN-TuM3, 65
Borchers, J.: OX+EM+MI+NS+TF-MoM10, 18
Bordel, C.: MI+OX-WeA1, 175
Borgatti, F.: AS-ThA10, 223
Borgström, M.T.: ET+NS+EM-ThM6, 199
Boris, D.R.: PS1-TuM12, **72**
Borisov, V.: BI+AS-TuA9, 85
Borkowski, M.: AC+EN-TuM9, **57**
Borner, K.: EM+TF-WeM5, 139
Bornschein, L.: VT-TuM11, 81
Borovsky, B.P.: TR+SE-WeM10, 160; TR-TuA10, **108**
Borsa, D.: TC+EM+AS+TF+EN-ThM2, 215
Borst, C.: EM-ThP8, 245
Bosch, R.: TC+EM+AS+TF+EN-ThM2, 215
Bose, S.: OX+EM+MI+NS+TF-MoM10, 18
Bosnick, K.: NS-ThP2, **253**
Bostwick, A.: GR+EM+ET+NS+TF-MoA8, 38
Böttiger, J.: BI-MoM11, 6
Boturyn, D.: BI+SS+NS-WeM10, 138
Bouarouri, A.: PS+BI-MoA10, **47**
Boucher, M.: SS-WeM1, 153
Bouchoule, S.: AS-MoM4, 3
Boufnichel, M.: MN+AS-MoM6, 13; PS1-ThM3, 208
Bourgeois, S.: SS+OX-WeM6, 152
Boutwell, C.: TF+AS-WeA9, **189**
Boutwell, R.C.: TF+AS-WeA7, 189
Bouxsein, C.: TR+SE-WeM10, 160
Bowden, M.E.: MI-ThP4, 252; SS+EN+OX-ThM11, 213
Bowman, S.R.: EM+TF+AS-ThA6, 225
Boxford, W.: AS-ThM1, 192; AS-TuP13, 113; AS-TuP14, 113
Boyce, M.C.: EM+TF-WeM11, 140
Braithwaite, N.St.: PS1-WeA2, 178
Brant, A.T.: AC+TF+SS+MI-MoA7, 29
Bratescu, M.A.: GR-ThP7, **250**; NS-ThP8, 254; PS-ThP29, 259
Braun, A.: IS+AS+SS+EN-TuM3, 65
Braun, P.V.: EN+NS-ThA1, 228; SE+NS-MoA10, **51**
Braunstein, P.: GR+EM+ET+NS+TF-MoA7, 37
Bravo-Sanchez, M.: AS-TuP15, **113**
Bray, J.A.: PS-ThA10, 235
Brehmer, F.: EN+PS-WeM3, 140
Breitenstein, D.: TF-ThP14, 265
Breitung, E.: TF-MoM3, 24
Breitweiser, R.: LB+EM+GR+MN+TR-WeA8, 173
Brennan, B.: EM+TF+OX+GR-MoM5, 8; EM-TuM3, 61
Brenner, D.W.: TF+AS-TuA12, 105; TF+AS-TuA7, **105**
Brett, M.J.: TF+SE+NS-WeM11, 157;
TF+SE+NS-WeM5, 156; TF+SE+NS-WeM9, 156
Brewer, J.R.: EL+TF+AS+EM+SS-TuP1, 118

- Brigg, W.: PS2-MoA6, 48
 Brihoum, M.: PS1-WeA2, 178; PS-ThP5, 255; PS-ThP7, 256
 Brink, M.: PS1-ThM12, 209
 Brinson, B.: BN+AS-WeA12, 166
 Brocklesby, W.S.: SE+NS-MoA3, 50
 Broitman, E.: TF+NS+EM-ThM12, 220; TR+SE-WeM4, 159
 Bronneberg, A.C.: PS2-WeA9, 181
 Brown, A.: BI+SS+NS-WeM2, 137; MN-MoA10, 39
 Brown, R.D.: EM+TF-WeM12, 140
 Browning, R.: AS+TF+VT-FrM6, 267
 Bruce, R.L.: PS-MoM6, 20; PS-WeM10, 150
 Bruchez, M.: IS-TuP3, 119
 Brucker, G.A.: VT-MoA10, 56; VT-TuP2, 131
 Bruhn, T.: GR+EM+NS+SS+TF-ThA6, 231
 Brukman, M.: SP+AS+BI+ET+MI+TF-WeA4, 183
 Brumbach, M.T.: LB+EM+GR+MN+TR-WeA1, 173; OX+SS+TF+MI-MoA9, 45
 Brunelle, A.: BN+AS-WeA7, 165
 Bryan, S.R.: AS-ThA3, 222; AS-WeM12, 136
 Bryson, C.: VT-TuP17, 133
 Buchanan, D.A.: AC+TF+SS+MI-MoA7, 29
 Buchholz, M.: OX+SS+TF+MI-MoA10, 45
 Bucholz, E.W.: TR+BI-TuM10, 79
 Buck, A.: BN+AS-WeA11, 166; IS-TuP4, 119
 Buecheler, S.: TF+AS-WeA3, 188
 Buechner, B.: GR-ThP3, 249
 Buegler, M.: EM-ThP5, 244; EM-ThP6, 244
 Büenfeld, M.: HI+AS+BI+NS-ThM5, 202
 Buie, C.: EM+TF+OX+GR-MoA4, 34
 Bull, H.: VT-TuP9, 132
 Bultman, J.E.: TR+SE-WeM1, 159
 Buongiorno-Nardelli, M.: GR-ThP11, 251
 Burak, Ya.V.: AC+TF+SS+MI-MoA7, 29
 Burden, D.: BI+AS-TuA4, 84
 Burghaus, U.: NS+AS+SS+SP-WeM4, 146; SS-TuP19, 127
 Burkett, S.L.: MN+AS-MoM5, 13
 Burnham, N.A.: MB+BI-ThM6, 204
 Burris, D.L.: TR+BI-TuM4, 79
 Burst, J.: TF+AS-WeA10, 189
 Bürstel, D.: SS-MoM2, 23
 Bushell, A.: AS-MoM10, 4; AS-TuP10, 112; EW-TuL3, 82
 Busse, C.: GR+AS+NS+SP+SS-TuA7, 90
 Butler, W.H.: MI+EN+BI-TuA3, 93
 Butorin, S.M.: AC+MI+SS+TF-MoM5, 2
 Butz, T.: GR+AS+EM+MI+MN-TuM9, 65
 Büyükköse, S.: NS+SP-MoA9, 43
 Byrns, B.: SE+PS-TuA3, 100; SE+PS-TuA4, 100
 Bystrov, K.: PS2-WeA1, 180
- C —
- Cabrera, W.: EM+TF+OX+GR-MoA6, 34; TF+NS+EM-ThM9, 219
 Cahill, D.G.: SE+NS-MoA10, 51
 Cai, M.: GR+AS+NS+SS-ThM10, 202
 Caillard, L.: EL+TF+BI+AS+EM+SS-MoA2, 32; EM+NS-FrM3, 267
 Caldwell, J.D.: GR+AS+BI+PS+SS-WeM9, 143; GR+EM+ET+NS+TF-MoA1, 37; GR-ThP9, 251
 Call, R.: AS+TF+VT-FrM2, 266
 Callahan, C.: EW-TuM8, 64; SP+AS+BI+ET+MI+TF-WeA11, 183
 Calliari, L.: GR-ThP3, 249
 Callow, J.A.: BI-TuP16, 118; MB+BI-ThA3, 232
 Callow, M.E.: BI-TuP16, 118; MB+BI-ThA3, 232
 Calzolari, L.: BI+SS+AS-TuM12, 60
 Calzolari, A.: GR-ThP11, 251
 Camesano, T.A.: MB+BI-ThM6, 204
 Camillone, N.: NS+AS+SS+SP-WeM12, 147
 Campbell, C.: EN+TF-TuM10, 63
 Campbell, C.T.: SS-TuM12, 77; SS-WeM6, 154; SS-WeM9, 154
 Campbell, P.: EM+NS-FrM3, 267
 Campbell, P.M.: GR+EM+ET+MS+NS-FrM3, 271
 Campbell, S.A.: EN+TF-TuM9, 63; TF-ThP10, 264
 Campi, D.: EM+TF-WeM12, 140
 Canavan, H.E.: BI-TuP2, 116
 Candler, R.: MN-TuP7, 120; TF-ThP17, 265
 Canepa, H.: TR+SE-WeM4, 159
 Canepa, P.: EN+AS-ThA7, 228; IS-TuP2, 119
 Cantoro, M.: EM+TF+OX+GR-MoA1, 34
 Cao, J.: PS2-ThM5, 210
 Cao, Y.: EM-ThP1, 244; TF+AS-WeA1, 188
 Carbone, E.A.D.: PS1-WeA7, 179
 Carcia, P.F.: TF-MoM10, 25; TF-WeM3, 158
 Cardinaud, C.: AS-MoM4, 3; PS2-WeA10, 182
 Carlson, R.P.: MB+BI-ThM4, 204
 Cartas, W.S.: SS-TuP23, 128
 Carter, D.: PS-ThA4, 234; PS-ThA6, 234
 Cartier, E.A.: EM+TF+OX+GR-MoA7, 35
 Caruso, F.: BI-MoM1, 4
 Caruso, L.: VT-TuM12, 81
 Casolo, S.: GR+AS+EM+NS+SS-WeA12, 171
 Caspar, J.: TF+AS-WeA1, 188
 Castner, D.G.: AS+BI-TuA11, 83; AS-WeM3, 135; BI+SS+AS-TuM6, 60; BN+AS-WeA9, 166; IS+AS+BI+ET+GR+NS-TuA1, 91
 Castro, G.R.: AS+TF+VT-FrM5, 266
 Caubet, P.: NM+NS+MS+EM-MoA6, 41
 Cavanagh, A.: TF+EN-MoA3, 53
 Caymax, M.: EM+TF+OX+GR-MoA1, 34; IS+AS+OX+ET-WeM9, 145; LB+EM+GR+MN+TR-WeA12, 174
 Ceballos-Sanchez, O.: EM+TF+OX+GR-MoA9, 35
 Ceccone, G.: BI+SS+AS-TuM12, 60; NS+EN+GR-TuA2, 94
 Celiz, A.D.: BI-MoA8, 31
 Chabal, Y.J.: EL+TF+BI+AS+EM+SS-MoA2, 32; EM+NS-FrM3, 267; EM+TF+OX+GR-MoA6, 34; EM+TF-WeM4, 139; EN+AS-ThA7, 228; EN+TF-WeA7, 168; GR+AS+BI+PS+SS-WeM2, 142; GR+AS+EM+NS+SS-WeA1, 170; IS-TuP2, 119; NS+SP-MoA7, 43; SS+EM-WeA11, 185; SS+EM-WeA9, 185; SS-TuP21, 127; SS-WeA12, 187; TF+AS+SS-ThA3, 239; TF+NS+EM-ThM2, 218; TF+NS+EM-ThM9, 219
 Chae, J.: GR+EM+ET+NS+TF-MoA10, 38
 Chagarov, E.: SP+AS+BI+ET+MI+NM+NS+SS+TF-WeM6, 151
 Chakradhar, A.: NS+AS+SS+SP-WeM4, 146; SS-TuP19, 127
 Chamberlin, S.E.: IS+AS+OX+ET-WeM2, 144; SS+EN+OX-ThM11, 213
 Chambers, S.: SS+OX-WeM3, 152
 Chambers, S.A.: IS+AS+OX+ET-WeM2, 144; MI-ThP4, 252; OX-TuP5, 122; SS+EN+OX-ThM11, 213; SS+OX-WeM5, 152
 Champlain, J.: EM+TF+OX+GR-MoA10, 35
 Chan, C.: TF+AS-WeA1, 188
 Chan, C.K.: VT+AS+SS-WeM1, 160; VT-TuA12, 109
 Chan, K.K.: EM+NS-FrM10, 268
 Chandra, S.: MI-ThP2, 252; NS-MoM9, 16
 Chang, C.: MB+BI-ThM12, 204
 Chang, C.C.: VT+AS+SS-WeM1, 160; VT-TuA12, 109
 Chang, C.S.: GR+EM+ET+NS+TF-MoA6, 37
 Chang, C.Y.: MN-MoA9, 39
 Chang, H.W.: PS+BI-MoA1, 46
 Chang, J.: PS2-TuM6, 73
 Chang, J.P.: EM+TF+AS-ThA3, 225; EN+NS-ThA6, 229; EN+NS-ThM6, 198; EN+TF-WeA9, 168; PS1-ThM11, 209; PS-MoM3, 20; TF+NS+EM-ThM6, 218
 Chang, M.H.: EM+SS+AS+NS-ThM12, 195
 Chang, W.-T.: HI+AS+NS-WeA8, 172
 Chang, Y.H.: EM+SS+AS+NS-ThM12, 195
 Chanson, R.: AS-MoM4, 3
 Chao, Y.C.: LB+EM+GR+MN+TR-WeA8, 173
 Chapman, R.: EM+TF-WeM4, 139
 Charraut, E.: TR-TuA4, 107
 Chase, B.: SP+AS+BI+ET+MI+TF-WeA9, 183
 Chaudhuri, S.: SS-WeA12, 187
 Chauhan, L.: AS-TuP23, 115
 Chaukulkar, R.P.: TF-ThP15, 265
 Chebiam, R.: EM-TuA12, 87
 Chen, B.: BN+AS-WeA12, 166
 Chen, C.: VT-TuA12, 109
 Chen, C.C.: EN+SS-FrM5, 270
 Chen, C.L.: VT+AS+SS-WeM1, 160; VT-TuA12, 109
 Chen, D.A.: SS-WeA3, 186
 Chen, E.: MI+OX-WeA7, 175
 Chen, F.-Z.: TF-ThP13, 264; VT-TuP5, 131
 Chen, H.: PS2-TuM9, 73
 Chen, H.-P.: TF-ThP13, 264
 Chen, J.: EL+TF+AS+EM+SS+PS+EN+NM-MoM4, 7; GR+AS+NS+SP+SS-TuA2, 90; PS1-ThM11, 209; SS-TuP3, 124; SS-WeA9, 186
 Chen, J.-H.: GR+AS+NS+SS-ThM5, 201
 Chen, J.R.: VT+AS+SS-WeM1, 160; VT-TuA12, 109
 Chen, L.: NS+SP-MoA8, 43; PS1-TuM11, 72; PS1-WeA12, 180; PS2-MoA10, 49; PS2-MoA11, 49; PS2-MoA9, 49; TF+SE+NS-WeM4, 156
 Chen, Q.: PS+BI-MoA8, 47
 Chen, R.: BI-MoM1, 4
 Chen, S.: GR+AS+NS+SP+SS-TuA11, 91; PS2-ThM5, 210
 Chen, T.Q.: PS-WeM1, 148; PS-WeM11, 150
 Chen, W.C.: EM-ThP3, 244; TF-ThP7, 263
 Chen, X.: NS-WeA1, 177; TF+EN-MoA6, 54
 Chen, Y.: HI+AS+BI+NS-ThM9, 202
 Chen, Y.C.: MN-MoA9, 39
 Chen, Z.: PS1-TuA10, 96
 Cheng, D.F.: SS-ThM1, 213
 Cheng, D.L.: SS-TuP37, 130
 Cheng, J.: PS1-ThM12, 209; PS-ThP10, 256
 Cheng, M.H.: EN+SS-FrM5, 270
 Cheng, S.-F.: GR+AS+EM+MI+MN-TuM1, 64
 Cheng, Y.-T.: EN+SS-FrM6, 270; OX-TuP1, 122
 Chepulskey, R.: MI+OX-WeA7, 175
 Chernyak, L.: EM-ThP1, 244
 Chesaux, M.: PS-ThA3, 234
 Cheung, W.S.: VT-TuP11, 132; VT-TuP12, 133; VT-TuP13, 133; VT-TuP14, 133
 Cheyns, D.: AS-ThM6, 192
 Chhowalla, M.: NS+EN+GR-TuA8, 95
 Chiang, S.: NS-ThM6, 207; SS+NS-ThA6, 236
 Chiba, Y.: PS-ThP1, 255; PS-WeM4, 149
 Chichester, H.J.M.: AC+EN-TuM1, 57
 Chien, D.: EM+TF+AS-ThA3, 225
 Childress, J.R.: EM+MI-ThA8, 224
 Chiou, P.-K.: TF-ThP13, 264
 Chiou, P.W.: PS-ThP22, 258
 Chirita, V.: TF+AS-TuA4, 104; TF+AS-TuA9, 105
 Chitre, K.: OX+SS+TF+MI-MoA6, 45
 Cho, E.: MI-ThP1, 252
 Cho, E.A.: PS-ThP23, 258
 Cho, G.S.: PS+BI-MoA3, 46; PS-ThP38, 261
 Cho, H.J.: MN-TuP6, 120
 Cho, H.K.: NS+EN+GR-TuA11, 95; OX+EM+MI+NS+TF-MoM2, 17
 Cho, J.: EN+NS-ThM6, 198; EN+TF-WeA9, 168
 Cho, K.J.: GR+AS+EM+NS+SS-WeA1, 170
 Cho, M.L.: MI-ThP5, 252
 Cho, T.S.: PS-ThP36, 261; SE+PS-TuM3, 74; SE+PS-TuM4, 74; TC+EM+AS+TF+EN-ThM12, 216
 Choi, D.: EM-TuA7, 86
 Choi, D.H.: PS2-TuM6, 73
 Choi, E.H.: PS+BI-MoA3, 46; PS-ThP38, 261
 Choi, G.J.: BI-TuP5, 116
 Choi, J.: GR+EM+ET+NS+TF-MoA7, 37; PS2-TuM11, 74
 Choi, J.W.: EN+NS-MoM5, 10; PS-ThP23, 258

- Choi, J.Y.: GR+EM+NS+PS+SS+TF-MoM11, 12
Choi, K.: EM+OX-WeA9, 167; EM+TF+OX+GR-MoA7, 35
Choi, S.: PS-ThP44, 262
Choi, S.H.: EM+OX-WeA11, 168
Choi, S.-H.: NS-ThP6, 253
Choi, W.J.: PS-ThP33, 260
Choi, Y.H.: NS-ThP6, 253
Choi, Y.J.: EM-TuM4, 61
Chopra, I.: SS-WeA12, 187
Chou, C.C.: PS-ThP22, 258
Chou, L.-W.: NS-WeA11, 178
Choudhury, F.A.: PS-ThP35, 261
Coraux, H.M.: IS+AS+SS+EN-TuM5, 66
Christiani, G.: TF+AS-TuA10, 105
Christophis, C.: BI-TuP14, 118
Chu, D.: NM+NS+MS+EM-MoA2, 40
Chu, J.-W.: PS+BI-MoA2, 46; PS+BI-MoA6, 46
Chuang, Y.: EM-ThM12, 197
Chumbuni-Torres, K.: EL+TF+BI+AS+EM+SS-MoA3, 33
Chun, S.H.: OX+EM+MI+NS+TF-MoM2, 17
Chun, Y.S.: PS1-ThM6, 209
Chung, B.W.: AC+MI+SS+TF-MoM9, 2
Chung, J.G.: AS-ThA4, 222; AS-TuP22, 114
Chung, S.: VT-TuP10, 132; VT-TuP7, 132
Chung, T.-Y.: PS+BI-MoA2, 46; PS+BI-MoA6, 46
Chupas, P.: IS+AS+SS+EN-TuM9, 66
Churaman, W.: EM+OX-WeA9, 167
Chyan, O.: PS-WeM5, 149
Ciarnelli, V.: BI+SS+NS-WeM12, 138
Cimpoiasu, E.: GR+AS+NS+SS-ThM3, 201
Cipriany, B.R.: MN-TuM11, 68
Cirigliano, N.: EN+NS-ThM6, 198
Clare, A.S.: BI-TuP16, 118
Clark, B.D.: TF+MI-WeA3, 190
Clark, K.: ET+SS+GR+SP-ThA6, 229; GR+EM+NS+PS+SS+TF-MoM2, 11
Clark, M.D.: EN+TF-TuA7, 88
Clark, T.: BI+AS-TuA4, 84
Clarke, J.: EM-TuA12, 87
Clavel, G.: TF+NS+EM-ThM9, 219
Clavero, C.: TF+AS+SS-ThA8, 240; VT+AS+SS-WeM10, 161; VT+AS+SS-WeM6, 161
Clayton, A.: BI-MoM6, 5
Clendenning, S.: EM-TuA1, 85
Clergereaux, R.: PS+BI-MoA10, 47
Cleveland, E.: EM+TF+OX+GR-MoA10, 35; NS+EN-TuM2, 69
Cleveland, J.: EW-TuM8, 64; SP+AS+BI+ET+MI+TF-WeA11, 183
Clifton, P.H.: AS-TuP18, 113
Coad, B.R.: BI-MoA9, 31
Coclite, A.M.: TF-WeM5, 158
Coffey, K.R.: EM-TuA2, 86; EM-TuA7, 86
Coh, S.: OX+SS+TF+MI-MoA6, 45
Cohen, H.: ET+SS+GR+SP-FrM3, 270
Cohen, K.D.: SP+AS+BI+ET+MI+NM+NS+SS+TF-WeM5, 150; SS-WeM2, 154
Cohen, S.A.: EM-TuA8, 86
Cohen, S.R.: OX+EM+MI+NS+TF-MoM11, 18
Coia, C.: PS1-WeA9, 179
Colbow, V.: EN+AS-ThA6, 227
Colburn, M.: PS2-TuM9, 73
Colby, R.: AS+NS+SS+TF-WeA3, 164; AS+NS+SS+TF-WeA4, 164
Colesniuc, C.: AS+TF+VT-FrM2, 266
Colette, S.: PS-ThP32, 260
Collazo, R.: EM+TF+AS-ThA1, 225
Collette, S.: PS-ThP31, 260
Collins, K.: PS2-MoA3, 48
Collins, R.W.: EL+TF+AS+EM+SS+PS+EN+NM-MoM1, 6; EL+TF+AS+EM+SS+PS+EN+NM-MoM4, 7
Colón Santana, J.: GR+EM+ET+NS+TF-MoA7, 37
Colpo, P.: NS+EN+GR-TuA2, 94
Comes, R.B.: TF+MI-WeA4, 190
Conard, T.: AS-ThM6, 192; TF-ThP1, 263
Condon, N.J.: EM+TF+AS-ThA6, 225
Conklin, D.: NS-WeA1, 177
Conley, J.F.: EM+OX-WeA12, 168
Conrad, E.: GR+AS+NS+SP+SS-TuA1, 89
Constable, E.C.: IS+AS+SS+EN-TuM3, 65
Conte, A.: VT-TuM12, 81
Cook, K.: EL+TF+BI+AS+EM+SS-MoA10, 33
Cooper, R.: SS-MoM4, 23
Cooperstein, M.A.: BI-TuP2, 116
Copel, M.W.: GR+EM+NS+PS+SS+TF-MoM8, 11
Coppée, S.: SE+NS-MoA4, 50
Coraux, J.: GR+AS+EM+NS+SS-WeA10, 171
Corbitt, T.: MB+BI-ThM9, 204
Corso, M.: SP+AS+BI+ET+MI+NM+NS+SS+TF-WeM4, 150
Cortes, J.P.: MN-MoA6, 39; MN-TuM6, 67
Cortes, R.: GR+EM+NS+SS+TF-ThA2, 231
Cossement, D.: PS1-TuA8, 96
Côté, C.: PS+TC-WeM1, 147
Coultras, S.J.: AS+BI-TuM10, 59; AS+BI-TuM3, 58; AS+NS+SS+TF-WeA8, 164
Counsell, J.D.P.: AS+BI-TuM10, 59; AS+BI-TuM3, 58
Coutu, R.: TF-WeM1, 157
Cowin, J.: IS+AS+BI+ET+GR+NS-TuA12, 93
Cozza, I.F.: VT-TuM9, 80
Craft, S.: EM+TF+AS-ThA1, 225
Craighead, H.G.: MN-MoA1, 38; MN-TuM10, 68; MN-TuM11, 68
Creatore, M.: EL+TF+AS+EM+SS+PS+EN+NM-MoM6, 7; PS1-TuA1, 95; PS2-WeA9, 181; TC+EM+AS+TF+EN-ThM2, 215
Croad, O.: BI+SS+AS-TuM5, 60
Croy, J.R.: SS-TuP27, 128
Crumlin, E.: IS+AS+SS+EN-TuM5, 66
Cserny, I.: AS+TF+VT-FrM3, 266
Csik, A.: AS+TF+VT-FrM3, 266
Cuddy, M.F.: PS2-WeA7, 181; PS-ThP19, 258
Cui, J.B.: PS1-TuA12, 97
Cui, S.: GR+AS+NS+SP+SS-TuA2, 90; SS-TuP3, 124
Cui, X.: AS+TF+VT-FrM1, 266
Cui, Y.S.: EM+MI-ThA11, 224
Culbertson, J.C.: GR+EM+NS+PS+SS+TF-MoM3, 11
Culver, J.: BI+SS+NS-WeM2, 137; MN-MoA10, 39
Cummings, P.T.: TF+AS-TuA1, 104
Cummings, S.P.: TF+EM+SS-ThA6, 241
Cumpson, P.J.: AS-MoA1, 29; SP+AS+BI+ET+MI+NM+NS+SS+TF-WeM10, 151
Cunge, G.: PS1-WeA2, 178; PS2-WeA12, 182; PS-ThP7, 256
Cunningham, G.B.: EN+NS-MoM11, 10
Cuomo, J.: SE+PS-TuA3, 100
Curreli, D.: EN-ThP11, 248
Curtiss, L.: TF+EN-MoA1, 53
Cuypers, D.: IS+AS+OX+ET-WeM9, 145
Cyganik, P.: SS+NS-ThA10, 237; TF+AS+SS-ThA2, 239
Czaplewski, D.A.: MN+AS-MoM3, 12; NS+SP-MoA10, 44
Czarnetzki, U.: EN+PS-WeM12, 142; EN+PS-WeM9, 141
— D —
Dadap, J.: SS-TuP2, 124
Dadson, A.E.: TF2-TuA2, 106
Dahal, A.: GR+AS+EM+NS+SS-WeA8, 170; GR+EM+NS+SS+TF-ThA7, 231
Dähne, M.: EM+TF+AS-ThA10, 226
Dalberth, M.J.: TF+EM+SS-ThA7, 241; TF-WeM1, 157
Dalmiau, R.: EM+TF+AS-ThA1, 225
Daniels, S.: PS1-TuM3, 71; PS1-TuM9, 72; PS1-WeA1, 178
Darachieva, V.: AC+TF+SS+MI-MoA9, 29
Darbal, A.: EM-TuA7, 86
Darnon, M.: PS1-WeA2, 178
Darrell, J.W.: PS-ThP21, 258
Das, S.: BI-TuP11, 117; BI-TuP13, 118; BI-TuP3, 116; BI-TuP7, 117; BI-TuP8, 117; MN-TuP6, 120
Dasari, S.: EN-ThP9, 248; SS-MoM10, 24; SS-MoM11, 24; SS-TuP16, 127
Dascier, D.: MB+BI-ThM9, 204
Datye, A.: SS-TuP27, 128
Davidson, M.R.: EM-ThP14, 246; NS-WeA2, 177
Davies, M.C.: BI+SS+NS-WeM12, 138; BI-MoA10, 32; BI-MoA4, 31; BI-MoA8, 31; MB+BI-ThM12, 204
Davis, A.N.: IS+AS+OX+ET-WeM11, 145
Davis, B.H.: NS-ThM12, 207
Davis, K.O.: NM+NS+MS+EM-MoA9, 41
Davis, R.C.: LB+EM+GR+MN+TR-WeA3, 173; MN+AS-MoM4, 13; TF2-TuA2, 106
Davis, R.F.: IS-TuP3, 119
Davydova, A.: PS2-WeA12, 182
Dawahre, N.: ET+NS+EM-ThM11, 200; NS+EN-TuM3, 69; NS-ThM11, 207
Dawson, B.: TR+SE-WeM11, 160
Day, Chr.: VT-TuM4, 80
Day, D.: BI+AS-TuA4, 84
De Alba, R.: MN-MoA1, 38
De Clercq, A.: IS+AS+OX+ET-WeM9, 145
de Gendt, S.: PS1-ThM2, 208
De Graeve, I.: SE+PS-TuA9, 100
De Jesus, J.C.: AS-TuP28, 115
De la Ree, A.B.: SS-WeM12, 155
De Luca, F.: TF-WeM5, 158
de Marneffe, J.-F.: PS1-ThM2, 208
De Moure-Flores, F.: NS-MoM2, 15; TF-ThP16, 265
De Padova, P.: GR+EM+NS+SS+TF-ThA6, 231
de Rooij, M.R.: TR+BI-TuM5, 79
De Temmerman, G.: PS2-WeA1, 180
De Vito, E.: EN+NS-ThM11, 198
De Vos, C.: PS-ThP31, 260
de Vries, H.: PS+TC-WeM2, 147
Dean, C.: GR+EM+ET+NS+TF-MoA10, 38
DeBord, J.D.: AS-ThM5, 192
Dedkov, Y.: EW-TuL6, 82
Dekoster, J.: EM+TF+OX+GR-MoA1, 34
DeLaRiva, A.T.: SS-TuP27, 128
Delattre, P.A.: EN+PS-WeM5, 141
Dellinger, A.: MB+BI-ThM2, 203
Demberger, C.: NM+NS+MS+EM-MoA9, 41
Demers-Carpentier, V.: SS-ThM5, 214
Demko, A.: NS+AS+SS+SP-WeM2, 146
Demura, K.: PS-ThP6, 256
Denbeaux, G.: VT-TuP9, 132
Dendzik, M.: SS+NS-ThA10, 237
Deng, R.: TF+SE+NS-WeM6, 156
Deng, X.: SS-ThA8, 238
Denis, L.: PS1-TuA8, 96
Denk, M.: SS+OX-WeM12, 153
Denning, C.: BI-MoA4, 31; BI-MoA8, 31
Denny, Y.R.: AS-TuP22, 114
Deram, M.: TR+SE-WeM10, 160
Desai, T.V.: IS+AS+BI+ET+GR+NS-TuA2, 92
Desbief, S.: PS+TC-WeM11, 148
Deskins, N.A.: SS+EN+OX-ThM9, 213; SS-TuM5, 76
Despiau-Pujo, E.: PS1-WeA2, 178; PS2-WeA12, 182
Desplats, O.: EM+TF+OX+GR-MoA9, 35
Despont, M.: NS+SP-MoA2, 42
Desse, F.: IS+AS+OX+ET-WeM11, 145
Desvoivres, L.: PS2-TuM5, 73; PS-ThP26, 259
Detchprohm, T.: EM+TF+AS-ThA7, 225
Detslefs, B.: GR+AS+NS+SP+SS-TuA9, 90
Devaraj, A.: AS+NS+SS+TF-WeA3, 164; AS+NS+SS+TF-WeA4, 164; HI-ThP2, 251; NS-WeA10, 178; OX-TuP6, 122
Devereaux, T.: EN+SS-FrM5, 270
DeVore, T.C.: SS-WeM10, 155

- Dewdney, J.: NS-MoM9, 16
Dexter, S.C.: MB+BI-ThA7, 233
Dezelah, C.L.: EN+TF-WeA10, **169**
Dhakal, T.: EN+TF-WeA12, 169
Dhar, N.K.: EM+OX-WeA9, 167
Dhayal, M.: NS-MoM11, 17
Dhere, N.: EN+TF-TuM11, 63; TF+AS-WeA11, **189**
Dhere, R.: EN+AS-ThA1, 227
D'hers, S.: MN-MoA11, 40
Dhiman, R.: EM+SS+AS+NS-ThM3, 194; EN-ThP5, **247**
Diao, L.: PS2-TuM10, **73**
Diao, Z.: MN+AS-MoM9, 13; MN-TuM5, 67; MN-TuM9, **68**
Dick, D.: NS+SP-MoA7, **43**
Dickinson, J.E.: SS-TuM4, 76
Diebold, A.C.:
EL+TF+AS+EM+SS+PS+EN+NM-MoM9, 7;
GR+AS+NS+SP+SS-TuA11, 91;
NM+AS+MS-MoM3, 14
Diesing, D.: SS-MoM2, **23**; SS-MoM3, 23; SS-TuP24, 128
Dietz, N.: EM+TF+AS-ThA11, 226; EM+TF+AS-ThA9, 226; EM-ThP5, 244; EM-ThP6, 244
DiLabio, G.:
SP+AS+BI+ET+MI+NM+NS+SS+TF-WeM2, 150
Dillon, E.: SP+AS+BI+ET+MI+TF-WeA9, **183**
Dimitrakopoulos, C.: GR+AS+NS+SP+SS-TuA11, 91
Ding, G.: PS-ThP10, **256**
Ding, M.: MI+EN+BI-TuA7, 93
Diomede, P.: PS2-MoA1, **48**
Dittmann, R.: AS-ThA10, 223
Divan, R.S.: MI+SP+AS-ThM12, 206; MN+AS-MoM5, 13; NS+SP-MoA11, 44
Diwan, A.: TF-WeM6, **158**
Doerner, R.P.: PS2-WeA1, 180
Dogan, I.: EN+PS-WeM4, **141**
Dohnalek, Z.: SS+EN+OX-ThM5, 212; SS-TuM1, **75**
Dohnalova, K.: EN+PS-WeM4, 141
Doi, I.: EM-ThP7, 244
Doi, K.: NM-TuP2, 121
Dolinaj, B.: PS1-WeA1, **178**
Domen, K.: SS+EN+OX-ThM1, 211
Domenichini, B.: SS+OX-WeM6, 152
Dominé, D.: PS-ThA3, 234
Donaldson, S.H.: BI+SS+NS-WeM5, 137
Donath, M.: MI-WeM1, **145**
Donegan, J.: HI+AS+BI+NS-ThM9, 202
Dong, C.: NS-ThP14, **254**
Dong, H.: EM+TF+OX+GR-MoM5, 8; EM-TuM3, 61
Dong, Y.: SS-ThM5, 214
Dongare, A.D.: TF+AS-TuA7, 105
Donnelly, V.M.: PS1-TuA10, 96; PS2-MoA1, 48; PS2-TuA3, 98; PS2-WeA11, 182; PS-MoM8, 21; PS-ThP18, 258
Doris, B.: EL+TF+AS+EM+SS+PS+EN+NM-MoM9, 7
Dornstetter, J.-C.:
EL+TF+AS+EM+SS+PS+EN+NM-MoM3, **6**
Doubina, N.: SS-TuP14, 126
Doudin, B.: GR+EM+ET+NS+TF-MoA7, 37
Dougherty, D.B.: GR+AS+BI+PS+SS-WeM10, 143; GR+AS+NS+SP+SS-TuA11, 91; GR+EM+ET+MS+NS-FrM8, 272; GR-ThP11, **251**; MI+OX-WeA11, 176
Douglas, E.A.: EM-ThP2, 244
Dowben, P.A.: AC+TF+SS+MI-MoA1, 28; AC+TF+SS+MI-MoA7, 29; GR+EM+ET+NS+TF-MoA7, 37; MI+OX-WeA10, 176
Downey, B.P.: EM+OX-WeA8, 167
Dowsett, D.: HI+AS+NS-WeA10, 172
Draper, R.: BI-TuP13, **118**; NS+AS+SS+SP-WeM2, 146
Draude, F.: AS-TuP1, 111; BI-TuP12, 118
Drayman-Weisser, T.: TF-MoM3, 24
Drews, J.: EM+SS+AS+NS-ThM3, 194
Driskell, J.D.: TF+SE+NS-WeM12, 157
Driskill-Smith, A.: MI+OX-WeA7, 175
Droubay, T.C.: MI-ThP4, 252
Drube, W.: AS+TF+VT-FrM3, 266
Dsouza, R.: AS-WeM6, 135
Du, Y.G.: IS+AS+OX+ET-WeM2, **144**; OX-TuP5, **122**; SS-TuM5, 76
Duan, X.: GR+EM+ET+MS+NS-FrM1, **271**
Dubacheva, G.V.: BI+SS+NS-WeM10, **138**
Dubey, M.D.: GR+EM+ET+MS+NS-FrM8, 272
Dubois, P.: PS1-TuA8, 96
Dubruel, P.: MN+AS-MoM10, 14
DuChene, J.: EN+SS-FrM4, **269**
Dudis, D.: SE+NS-MoA11, 51
Dudney, N.: EN+TF-WeA1, **168**
Duenow, J.: TF+AS-WeA10, 189
Duerig, U.: NS+SP-MoA2, 42
Dufour, T.: PS+TC-WeM11, 148; PS-ThP2, **255**; PS-ThP31, 260
Dugger, M.T.: LB+EM+GR+MN+TR-WeA1, 173
Duke, A.: SS-WeA3, 186
Dumont, G.: MN-TuP3, 120
Dunham, B.M.: VT+AS+SS-WeM2, 161; VT-TuA11, 109
Dunin-Borkowski, R.E.: EM-ThM11, 197
Dunn, B.: EN+NS-ThM6, 198; EN+TF-WeA9, 168
Durakiewicz, T.: AC+MI+SS+TF-MoM8, **2**
Durickovic, B.: VT-TuA3, **108**; VT-TuP6, 132
Durkaya, G.: EM-ThP6, 244
Dürr, M.: AS-ThM10, **193**
Durstock, M.F.: EN+NS-ThM9, 198
Dussarrat, C.: PS-WeM3, 149
Dussart, R.: MN+AS-MoM6, 13; PS+EM-MoM3, **18**; PS1-ThM2, 208; PS1-ThM3, 208
Dussault, L.: NM+NS+MS+EM-MoA6, 41
Dutta, M.: EN+AS-ThA6, 227
Dutta, P.: EN+TF-TuA8, 88
Duzik, A.: SS-TuP34, **130**
— **E** —
Ealet, B.: GR+EM+NS+SS+TF-ThA6, 231
Eastman, J.A.: IS+AS+OX+ET-WeM3, **144**
Eastman, P.Y.: AS+NS+SS+TF-WeA9, 165
Easton, C.D.: MB+BI-ThM3, 203
Ebert, P.: EM+TF+AS-ThA10, 226; EM-ThM11, **197**
Economou, D.J.: PS1-TuA10, 96; PS2-MoA1, 48; PS2-WeA11, 182; PS-MoM8, 21; PS-ThP18, 258
Eddy, Jr., C.R.: EM+OX-WeA8, 167; EM+TF+AS-ThA6, 225; EM+TF+OX+GR-MoM9, 9; GR+AS+BI+PS+SS-WeM9, 143; GR+AS+EM+MI+MN-TuM1, 64; GR+AS+NS+SP+SS-TuA9, 90; GR+EM+ET+MS+NS-FrM3, 271; GR+EM+ET+MS+NS-FrM5, 272; GR+EM+ET+NS+TF-MoA1, 37; GR+EM+NS+PS+SS+TF-MoM1, 10; GR+EM+NS+PS+SS+TF-MoM3, 11; GR-ThP9, 251; SS+EM-WeA1, 184; TF+NS+EM-ThM1, 218
Eden, J.G.: PS+EM-MoM1, **18**
Ederth, T.: MB+BI-ThA3, 232
Edgar, J.H.: EM+TF+OX+GR-MoM9, 9
Edlmayr, V.: SE+NS-MoM9, 22
Edmonds, M.: AS-TuP21, **114**; SP+AS+BI+ET+MI+NM+NS+SS+TF-WeM6, 151
Edwards, P.R.: AC+TF+SS+MI-MoA9, 29
Egan, T.F.: BN+AS-WeA12, 166
Eggenspiele, D.: EM+TF-WeM11, 140
Eigenfeld, N.: TR+SE-WeM10, 160
Eisele, H.: EM+TF+AS-ThA10, **226**
Eizenberg, M.: LB+EM+GR+MN+TR-WeA12, **174**
Ek, S.: SE+NS-MoM10, **22**
Ekinci, Y.: HI+AS+BI+NS-ThM11, 203
Eklund, P.: VT-TuM5, **80**
Elam, J.W.: IS+AS+SS+EN-TuM9, 66; TC+EM+AS+TF+EN-ThM6, 216; TF+EN-MoA1, **53**
Eldridge, D.: MB+BI-ThA4, 232
Elferink, F.H.: PS-ThP15, 257
El-Khatib, S.: OX+EM+MI+NS+TF-MoM10, 18
El-Khoury, P.Z.: SP+AS+BI+ET+MI+NS-TuA3, 101
Ellefson, R.: VT-MoA7, **55**
Eller, M.: AS-ThM5, 192
Elliman, R.G.: LB+EM+GR+MN+TR-WeA7, 173
Ellingsworth, E.: MI+OX-WeA2, 175
Elliott, S.: TF-TuM3, **77**
Elliston, R.: PS2-TuM10, 73
Elman, N.M.: MN-MoA11, **40**
Elmqvist, R.: LB+EM+GR+MN+TR-WeA10, 174
Elswick, D.: EW-TuM7, **64**
Emam, M.: EM-ThM4, **196**
Emery, J.D.: GR+AS+BI+PS+SS-WeM1, 142; GR+AS+NS+SP+SS-TuA9, **90**
Endo, K.: EM-ThM1, 195
Engel, L.: MN+AS-MoM10, **14**; MN-MoA8, **39**
Engelhard, M.: TF+AS+SS-ThA11, 240
Engelmann, S.: PS1-ThM12, 209; PS-MoM2, **20**; PS-WeM10, 150
Engeln, R.: EN+PS-WeM3, **140**; PS+TC-WeM2, 147
Engstrom, J.R.: IS+AS+BI+ET+GR+NS-TuA2, **92**
Enta, Y.: GR+EM+NS+PS+SS+TF-MoM10, 12
Erdemir, A.: TR+BI-TuM9, **79**
Eriguchi, K.: PS2-TuA10, 98; PS2-TuA12, 99; PS-MoM10, **21**
Erkens, I.J.M.: TF-TuM11, **78**
Ernst, K.-H.: SS-ThM6, **214**; SS-TuM9, 76
Ershov, M.V.: SE+NS-MoA7, 50
Eryilmaz, O.L.: TR+BI-TuM9, 79
Escamilla, R.: SS-TuP10, 126
Espinosa-Magaña, F.: AS-TuP15, 113
Esquinazi, P.: GR+AS+EM+MI+MN-TuM9, 65
Evans, R.A.: BI-MoM1, 4; BI-MoM5, 5
Everitt, H.O.: TF2-TuA1, 106
Ewin, J.J.: TR-TuA9, 107
Exarhos, A.L.: GR+AS+EM+MI+MN-TuM2, **64**
Exarhos, S.A.: PS-ThP21, **258**
Eypert, C.: TC-ThP2, 262
— **F** —
Facchetti, A.: TC+EM+AS-WeA1, **187**
Facsko, S.: SE+NS-MoM2, 21
Fadida, S.: LB+EM+GR+MN+TR-WeA12, 174
Fadley, C.S.: MI+OX-WeA1, 175
Fager, H.: TF+NS+EM-ThM12, 220
Faggin, M.F.: NS-ThM9, 207
Fahey, A.J.: AS+NS+SS+TF-WeA7, **164**
Fairley, N.: AS+BI-TuM12, 59
Fan, C.-H.: PS-ThP45, **262**
Fan, X.: BI+EM+NS-WeM2, 137; MN-MoA10, **39**
Fanelli, F.: PS+TC-WeM5, **147**
Fanz, S.: TF-ThP17, 265
Faradzhev, N.S.: SS-TuM3, **75**
Farmer, B.L.: GR+AS+BI+PS+SS-WeM6, 143
Fartmann, M.: TF+AS+SS-ThA4, 239; TF-ThP14, 265
Faubel, M.: SS-ThA2, 237
Faulkner, C.C.: HI+AS+BI+NS-ThM9, 202
Fauzi, M.E.: EN+PS-WeM11, **142**; PS2-ThM10, 211
Favia, P.: AS-ThM6, 192
Fazel, K.: AS-TuP27, **115**
Fears, K.: BI+AS-TuA4, **84**
Fedchak, J.A.: VT-MoA1, 54; VT-MoM9, **26**
Fedorov, A.: GR-ThP3, 249
Feenstra, R.: GR+AS+NS+SP+SS-TuA10, 91
Feigelson, B.: GR+AS+EM+MI+MN-TuM1, 64
Feldman, Y.: NS+AS+SS+SP-WeM4, 146
Felhofer, J.L.: EL+TF+BI+AS+EM+SS-MoA3, 33
Feliciano, D.M.: EN+NS-MoM6, 10
Felix, V.: PS+EM-MoM3, 18

- Feng, G.: TF+AS-TuA1, 104
 Feng, X.F.: SS-TuP37, 130
 Feng, X.-L.: MN+AS-MoM1, 12
 Fenter, P.: GR+AS+BI+PS+SS-WeM1, 142
 Ferekides, C.S.: EN+TF-TuM1, 62
 Ferguson, G.S.: EL+TF+BI+AS+EM+SS-MoA10, 33
 Ferguson, I.: EM+TF+AS-ThA11, 226; EM+TF+AS-ThA9, 226; EM-ThP6, 244
 Ferguson, J.D.: SS+EM-WeA1, 184
 Fernandez, M.-C.: AS-MoM4, 3
 Fernandez-Torre, D.: SP+AS+BI+ET+MI+NS-TuA11, 102
 Fernsler, R.: PS1-TuM12, 72; PS-ThP40, 261
 Ferranti, D.: HI-ThP3, 252
 Ferreira, P.: EM-TuA7, 86
 Ferrighi, L.: SS-ThM5, 214
 Ferris, R.J.: BI+SS+NS-WeM9, 137
 Feurprier, Y.: PS-ThP1, 255; PS-WeM4, 149
 Feygelson, B.N.: GR-ThP9, 251
 Figueroa, J.J.: TF+EM+SS-ThA11, 242
 Filippov, S.V.: SE+NS-MoA7, 50
 Filler, M.: NS+EN-TuM4, 69; NS-WeA11, 178
 Finlay, J.: BI-TuP16, 118
 Firrincelli, A.: EM+TF+OX+GR-MoA1, 34
 First, P.N.: GR+AS+NS+SP+SS-TuA3, 90
 Fischer, P.: MI+SP+AS-ThM11, 205
 Fisher, E.R.: PS2-WeA7, 181; PS-ThP19, 258; SE+NS-MoA6, 50
 Fisher, G.L.: AS-WeM12, 136
 Fitz-Gerald, J.M.: TF+MI-WeA4, 190
 Fitzmorris, B.C.: TF+SE+NS-WeM3, 156
 Flater, E.E.: TR+SE-WeM10, 160
 Fleetwood, D.M.: EM+SS+AS+NS-ThM11, 195
 Fleischauer, M.D.: TF+SE+NS-WeM11, 157
 Fleurence, A.: TF+AS-WeA8, 189
 Fleutot, B.: SS-WeA11, 186
 Flitsyan, E.: EM-ThP1, 244
 Flood, A.: SS-MoA3, 51
 Floreano, L.: SS+OX-WeM6, 152
 Flores, F.: ET+SS+GR+SP-FrM4, 270
 Flores, M.: SS-TuP10, 126; TR-TuP6, 131
 Floro, J.A.: TF+MI-WeA4, 190
 Foley, E.T.: NS-ThP3, 253
 Folkman, C.M.: IS+AS+OX+ET-WeM3, 144
 Fong, D.D.: IS+AS+OX+ET-WeM3, 144
 Fortunelli, A.: SS+OX-WeM12, 153
 Foss, M.: BI+SS+NS-WeM1, 136; BI-MoM11, 6; BI-MoM2, 5; BI-TuP1, 115
 Fouchier, M.: PS-ThP5, 255; PS-ThP7, 256
 Foussekis, M.: EM+TF+AS-ThA4, 225
 Fowlkes, J.D.: NS+SP-MoA4, 43; TF+EM+SE+NS-ThM3, 217
 Fox, D.: HI+AS+BI+NS-ThM9, 202
 Fox, J.R.: MN-MoA6, 39; MN-TuM6, 67
 Fox-Lyon, N.: PS2-WeA11, 182
 Fracassi, F.: PS+TC-WeM5, 147
 Fradet, M.: PS1-WeA9, 179
 França, D.: EM-ThP8, 245
 Frank, M.M.: EM+TF+OX+GR-MoA7, 35
 Franke, E.: PS-MoM1, 20
 Franke, K.J.: SP+AS+BI+ET+MI+NM+NS+SS+TF-WeM4, 150
 Franquet, A.: AS-ThM6, 192
 Franssila, S.: TF+NS+EM-ThM10, 219
 Franz, G.: PS1-WeA10, 179
 Franz, R.: SE+PS-TuM10, 75
 Franz, S.: MN-TuP7, 120
 Freeman, M.R.: MN+AS-MoM9, 13; MN-TuM5, 67; MN-TuM9, 68
 Freitas, Jr., J.A.: EM+TF+AS-ThA6, 225
 French, B.: EM-TuA9, 87; GR+EM+NS+SS+TF-ThA1, 230
 French, M.: GR+EM+NS+SS+TF-ThA1, 230
 Frenkel, A.I.: SS-TuP27, 128
 Frenzer, P.: EM-ThP1, 244; EM-ThP2, 244
 Freund, H.J.: NS-ThM3, 206
 Friddle, P.: PS-MoM1, 20
 Fridmann, J.: LB+EM+GR+MN+TR-WeA7, 173
 Fritz, E.C.: VT-TuA9, 109
 Froehner, S.C.: BN+AS-WeA9, 166
 Fromm, F.: GR+EM+NS+PS+SS+TF-MoM10, 12
 Fruchart, O.: GR+AS+EM+NS+SS-WeA10, 171
 Fu, J.: NS+SP-MoA8, 43
 Fu, S.: TC+EM+AS-WeA9, 188
 Fu, T.-Y.: HI+AS+NS-WeA8, 172
 Fuchs, E.: SS-TuP21, 127
 Fuentes-Cabrera, M.: SS-WeM4, 154; TF+EM+SE+NS-ThM3, 217
 Fujikawa, Y.: IS+AS+OX+ET-WeM10, 145
 Fujishima, A.: SS-TuP18, 127
 Fujita, D.: HI+AS+BI+NS-ThM12, 203
 Fujita, T.: EN-ThP7, 248
 Fujitani, T.: SS-TuP29, 129; SS-TuP30, 129
 Fukasawa, M.: PS2-ThM4, 210; PS2-TuA9, 98; PS-MoM10, 21; PS-ThP14, 257
 Fukidome, H.: GR+EM+NS+PS+SS+TF-MoM10, 12
 Fukutani, K.: SS-MoA9, 52
 Fukuyama, A.: EN+TF-TuA12, 89
 Fuller, N.C.M.: PS1-ThM12, 209; PS-MoM2, 20; PS-MoM6, 20; PS-WeM10, 150
 Funk, M.: PS1-TuM11, 72; PS1-WeA12, 180
 Fuoss, P.H.: IS+AS+OX+ET-WeM3, 144
- G —
 Gaddam, S.: PS2-WeA8, 181
 Gaddis, R.L.: MB+BI-ThM6, 204
 Gaddy, B.: EM+TF+AS-ThA1, 225
 Gahan, D.: PS1-WeA1, 178
 Gai, Z.: SS-WeM4, 154
 Gajdardziska-Josifovska, M.: GR+AS+NS+SP+SS-TuA2, 90; SS-TuP3, 124
 Galatage, R.V.: EM-TuM3, 61
 Galatsis, K.: EM+SS+AS+NS-ThM11, 195
 Galhenage, R.P.: SS-WeA3, 186
 Gall, D.: TF+SE+NS-WeM6, 156
 Galla, S.: AS-TuP1, 111
 Galoppini, E.: OX+SS+TF+MI-MoA6, 45
 Galtayries, A.: MB+BI-ThM2, 203
 Galtsyan, E.: EN+TF-TuA8, 88
 Gamage, S.D.: EM+TF+AS-ThA11, 226; EM+TF+AS-ThA9, 226; EM-ThP5, 244; EM-ThP6, 244
 Gaman, C.: PS1-TuM9, 72
 Gamble, L.J.: BN+AS-WeA4, 165
 Ganesh, K.: EM-TuA7, 86
 Gao, H.-J.: ET+SS+GR+SP-ThA1, 229
 Gao, J.: SS-WeA10, 186
 Gao, Y.: EN+TF-TuA8, 88; GR+EM+ET+NS+TF-MoA10, 38
 Garces, N.Y.: EM+OX-WeA8, 167; EM+TF+OX+GR-MoM9, 9; GR+AS+EM+MI+MN-TuM1, 64; GR+EM+ET+MS+NS-FrM5, 272; GR+EM+NS+PS+SS+TF-MoM1, 10; GR+EM+NS+PS+SS+TF-MoM3, 11
 Garcia, B.: EW-TuA5, 89
 Garcia, C.D.: EL+TF+BI+AS+EM+SS-MoA3, 33
 Garcia, S.: TR+BI-TuM5, 79
 Gardiner, J.: BI-MoM6, 5
 Gargiulo, F.: GR+AS+NS+SS-ThM5, 201
 Garino, T.J.: AS-TuP5, 111
 Garramone, J.: EM+NS-FrM5, 268
 Garren, J.M.: TF+SE+NS-WeM12, 157
 Gartstein, Yu.N.: EL+TF+BI+AS+EM+SS-MoA2, 32; EN+TF-WeA7, 168
 Gaskill, D.K.: GR+AS+BI+PS+SS-WeM9, 143; GR+AS+NS+SP+SS-TuA9, 90; GR+EM+ET+MS+NS-FrM3, 271; GR+EM+ET+MS+NS-FrM5, 272; GR+EM+ET+NS+TF-MoA1, 37; GR+EM+NS+PS+SS+TF-MoM1, 10; GR+EM+NS+PS+SS+TF-MoM3, 11; GR-ThP9, 251
 Gassilloud, R.: NM+NS+MS+EM-MoA6, 41
 Gates, G.: TF-MoM3, 24
 Gates, S.M.: EM-TuA8, 86
 Gaub, H.E.: SP+AS+BI+ET+MI+NM+NS+SS+TF-WeM11, 151
 Gautam, A.: GR+AS+NS+SS-ThM5, 201
 Gazquez, J.: OX+EM+MI+NS+TF-MoM10, 18
 Ge, Q.: SS-TuM10, 76
 Gebbie, M.A.: BI+SS+NS-WeM5, 137
 Gebhardt, C.R.: AS-ThM10, 193
 Geidel, M.: NM+AS+MS-MoM4, 14
 Geidobler, R.: AS+BI-TuM3, 58
 Geisler, H.: EM-TuA11, 87
 Geisse, N.: EW-TuM8, 64; SP+AS+BI+ET+MI+TF-WeA11, 183
 Gellman, A.J.: SS-MoA6, 52; SS-ThM2, 214; SS-WeA11, 186
 Gembocki, O.J.: NS+EN-TuM2, 69
 Gemming, S.: SE+NS-MoM2, 21
 Gengler, J.J.: SE-TuP3, 123
 George, S.M.: TF+EN-MoA3, 53; TF2-TuA8, 106; TF-MoM10, 25
 Gerber, T.: GR+AS+NS+SP+SS-TuA7, 90
 Gessert, T.A.: EN+AS-ThA1, 227; EN+TF-MoA1, 35; TF+AS-WeA10, 189
 Ghafoor, N.: TF+NS+EM-ThM11, 219; TF+NS+EM-ThM12, 220
 Gherardi, N.: PS+BI-MoA10, 47; PS+BI-MoA11, 47
 Ghodssi, R.: BI+SS+NS-WeM2, 137; MN-MoA10, 39; TR-TuA11, 108
 Ghorai, S.: IS+AS+BI+ET+GR+NS-TuA9, 93
 Ghosh, S.: EM-ThM6, 196
 Giannuzzi, L.A.: AS+BI-TuA10, 83
 Giasson, S.: TR-TuA4, 107
 Gibson, P.: VT-TuA3, 108; VT-TuP6, 132
 Giesen, W.L.M.: VT-TuA9, 109
 Gieraltowski, A.: EW-WeL5, 163
 Giessibl, F.J.: SP+AS+BI+ET+MI+TF-WeA12, 184
 Giewekemeyer, K.: IS-TuP4, 119
 Gil, W.: VT-TuM11, 81
 Gila, B.: LB+EM+GR+MN+TR-WeA7, 173
 Gilles, M.K.: IS+AS+BI+ET+GR+NS-TuA9, 93
 Gilley, K.: TR+SE-WeM5, 159
 Gilliland, D.: BI+SS+AS-TuM12, 60
 Gilmore, I.S.: AS-MoA9, 30; AS-ThA2, 222; AS-ThM4, 192
 Giner, I.: OX+SS+TF+MI-MoA11, 45
 Ginting, E.: SS-TuP13, 126
 Girard-Lauriault, P.-L.: AS+BI-TuM5, 58
 Girshevitz, O.: OX+EM+MI+NS+TF-MoM11, 18
 Gizzo, V.: PS-ThP1, 255
 Gladfelter, W.L.: TF-ThP10, 264
 Glass, J.T.: EN+SS-FrM3, 269
 Glattauer, V.: BI-MoM5, 5; BI-MoM6, 5
 Glazek, W.: EW-WeL5, 163
 Gleason, K.K.: EM+SS+AS+NS-ThM4, 194; EM+TF-WeM11, 140; TF-WeM5, 158
 Glück, B.: MN-TuP3, 120
 Go, D.B.: PS+EM-MoM11, 19
 Godoy Filho, J.: EM-ThP7, 244
 Goeke, R.S.: VT-MoM10, 26
 Goertz, M.P.: TF-TuM9, 78
 Gold, J.: BI-MoA3, 30
 Goldman, R.S.: EM+SS+AS+NS-ThM13, 195
 Goldoni, A.: AC+TF+SS+MI-MoA3, 28
 Goldsman, N.: EM+OX-WeA9, 167
 Goldstein, C.: TF+AS-TuA12, 105
 Golibrzuch, K.: SS-MoM4, 23
 Gollub, S.L.: SS+OX-WeM4, 152; SS-TuP5, 124
 Götzhäuser, A.: HI+AS+BI+NS-ThM11, 203; HI+AS+BI+NS-ThM5, 202; HI-ThP1, 251
 Gomella, A.: SE-TuP4, 123
 Gonçalves, A.: AC+TF+SS+MI-MoA6, 28
 Gong, C.: GR+AS+EM+NS+SS-WeA1, 170
 Gong, Q.: IS-TuP2, 119
 Gonon, P.: TF+AS-WeA12, 189
 Gonzalez, C.M.: HI-ThP3, 252
 Gonzalez, I.J.: AS-TuP28, 115
 González-Díaz, J.B.: MI+EN+BI-TuA12, 94

- Gonzalez-Mancera, A.: BI-TuP6, 116
 Gorman, B.P.: AS+BI-TuA10, 83
 Gorniak, T.: BN+AS-WeA11, 166; IS-TuP4, 119
 Gorobey, V.: VT-MoA1, 54
 Gorovikov, S.: AC+TF+SS+MI-MoA3, 28
 Goswami, S.: MB+BI-ThM9, 204
 Gotlib-Vainshtein, K.: OX+EM+MI+NS+TF-MoM11, 18
 Goto, M.: MN-TuP5, 120
 Gottscho, R.: PS2-TuM3, 73
 Götzen, J.: SP+AS+BI+ET+MI+NS-TuA10, 102
 Goubert, G.: SS-ThM5, 214
 Gougousi, T.: TF-ThP9, 264
 Govorkov, A.V.: EM-TuM9, 62
 Gowda, M.H.: GR+AS+EM+MI+MN-TuM1, 64
 Grabowski, K.: AS-TuP27, 115
 Grady, M.: SE+NS-MoA10, 51
 Graef, W.A.A.D.: PS1-WeA7, 179
 Graham, D.J.: BN+AS-WeA9, 166
 Graham, S.: GR+EM+ET+MS+NS-FrM9, 272; GR-ThP10, 251
 Graham, W.S.: PS1-ThM12, 209; PS-MoM2, 20
 Grampeix, H.: EM+TF+OX+GR-MoA9, 35; NS-ThM10, 207; TF+AS-WeA12, 189
 Granados, B.: TF-TuM6, 77
 Gránäs, E.: GR+AS+NS+SP+SS-TuA7, 90; IS+AS+SS+EN-TuM12, 67
 Granier, A.: PS2-WeA10, 182
 Grant, J.T.: SE+PS-TuM9, 75; TF+AS+SS-ThA10, 240
 Grant-Jacob, J.A.: SE+NS-MoA3, 50
 Grassian, V.: NM+AS+MS-MoM10, 15
 Grätzel, M.: IS+AS+SS+EN-TuM3, 65
 Graur, I.: MN-TuP1, 119
 Graves, D.B.: PS+BI-MoA2, 46; PS+BI-MoA6, 46; PS2-WeA11, 182; PS2-WeA12, 182; PS-WeM6, 149
 Gray, A.X.: MI+OX-WeA1, 175
 Greeley, J.: IS+AS+SS+EN-TuM9, 66; TF+EN-MoA1, 53
 Green, M.: EW-WeL1, 163
 Greene, A.: EM+TF+OX+GR-MoM3, 8
 Greene, J.E.: TF+AS-TuA4, 104; TF+NS+EM-ThM12, 220
 Greer, F.: TF-MoM5, 24
 Gregorkiewicz, T.: EN+PS-WeM4, 141
 Gregory, C.W.: EN+NS-MoM11, 10
 Grehl, T.: TF+AS+SS-ThA4, 239; TF-ThP14, 265
 Greiner, M.T.: OX+SS+TF+MI-MoA7, 45
 Gretener, C.: TF+AS-WeA3, 188
 Griesser, H.J.: PS+BI-MoA7, 47; PS1-TuA3, 95
 Griffin, T.M.: PS-ThA10, 235
 Grigoras, K.: TF+NS+EM-ThM10, 219
 Grill, A.: EM-TuA8, 86; GR+AS+NS+SP+SS-TuA11, 91
 Grilley, R.: PS-ThA4, 234
 Gross, L.: SP+AS+BI+ET+MI+NS-TuA1, 101
 Grueneis, A.: GR-ThP3, 249
 Grundmeier, G.: OX+SS+TF+MI-MoA11, 45; SS-ThA9, 238; TF+AS+SS-ThA1, 238
 Grunze, M.H.: BI+SS+AS-TuM2, 59; BN+AS-WeA11, 166; MB+BI-ThA3, 232
 Gu, Y.: ET+NS+EM-ThM12, 200
 Guallar-Hoyas, C.: IS+AS+BI+ET+GR+NS-TuA3, 92
 Gudimenko, E.: PS1-TuM3, 71
 Guedj, C.: NS-ThM10, 207
 Guerente, L.: BI+SS+NS-WeM10, 138
 Guerrero, J.: EM+TF+OX+GR-MoA9, 35
 Guetschow, P.: VT-TuA3, 108; VT-TuP6, 132
 Guillorn, M.A.: PS1-ThM12, 209
 Gumuslu, G.: SS-WeA11, 186
 Gunlycke, D.: GR+AS+NS+SS-ThM3, 201
 Guo, H.X.: HI+AS+BI+NS-ThM12, 203
 Guo, J.H.: GR+EM+ET+NS+TF-MoA11, 38; IS+AS+SS+EN-TuM3, 65
 Guo, X.: NS+EN-TuM11, 70
 Guo, Z.-P.: SS-TuP9, 125
 Gupta, A.: AS-ThA7, 223; NS-ThM9, 207
 Gupta, R.: PS-WeM3, 149
 Gupta, S.: AS-TuP23, 115; BI-MoM10, 5; TF+EM+SE+NS-ThM4, 217; TF+MI-WeA3, 190; TF+SE+NS-WeM10, 157
 Gupta, V.: TF-MoM4, 210
 Gutmann, S.: ET+SS+GR+SP-ThA11, 230
 Guttman, P.: BP+AS-SuA3, 1
 Gwo, S.: EM+TF+AS-ThA10, 226
- H —
 Ha, J.: MI-WeM11, 146; MI-WeM2, 145
 Ha, T.: VT-TuP10, 132; VT-TuP7, 132
 Haag, J.: EN+NS-ThM9, 198
 Haas, H.: VT-TuM4, 80
 Haasch, R.T.: TC+EM+AS+TF+EN-ThM6, 216
 Haase, A.: AS-TuP1, 111
 Haass, M.: PS1-WeA2, 178; PS-MoM6, 20
 Habenicht, B.: GR+AS+EM+NS+SS-WeA11, 171
 Haberer, D.: GR-ThP3, 249
 Habermann, D.: NM+NS+MS+EM-MoA9, 41
 Hacker, C.A.: TF+EM+SS-ThA6, 241
 Hackett, J.B.: VT+AS+SS-WeM9, 161
 Hadj Nacer, M.: MN-TuP1, 119
 Hadjipanayis, G.C.: MI-ThP2, 252
 Hachner, G.: SP+AS+BI+ET+MI+NM+NS+SS+TF-WeM9, 151
 Hagenhoff, B.: TF+AS+SS-ThA4, 239; TF-ThP14, 265
 Hager, G.: AS+NS+SS+TF-WeA7, 164
 Hagiwara, A.: SS-TuP8, 125
 Hahn, D.W.: TR+SE-WeM9, 160
 Hahn, J.H.: BI-TuP5, 116
 Hähner, G.: SP+AS+BI+ET+MI+TF-WeA7, 183
 Hakanoglu, C.: SS+EN+OX-ThM10, 213; SS-TuP22, 127
 Halbur, J.C.: TF2-TuA1, 106; TF-MoM9, 25
 Halevi, B.: IS+AS+SS+EN-TuM6, 66
 Hall, C.J.: PS1-TuA3, 95
 Hall, S.: EN+NS-MoM11, 10
 Halls, M.D.: TF+NS+EM-ThM2, 218
 Hamaguchi, S.: PS1-ThM5, 208; PS2-TuA2, 97; PS2-TuA4, 98; PS2-TuA9, 98; PS-ThP6, 256
 Hamers, R.J.: SS-ThM9, 214
 Hammad, M.: BI-MoA10, 32
 Hammer, B.: SS-ThM5, 214
 Hammond, J.S.: AS-ThA3, 222; AS-WeM12, 136; EN+AS-ThA4, 227; NS-ThM12, 207
 Han, C.B.: SS-WeM4, 154
 Han, L.: EN+PS-WeM10, 141
 Han, S.M.: EM-ThM12, 197; EM-ThM6, 196
 Han, Y.: SS+NS-TuA11, 104
 Han, Y.G.: PS-ThP38, 261
 Han, Y.-K.: SS-ThM12, 215
 Handa, H.: GR+EM+NS+PS+SS+TF-MoM10, 12
 Hanke, M.: BI-TuP14, 118
 Hänke, T.: EW-TuL6, 82
 Hanley, L.: BI+AS-TuA8, 85; EN-ThP3, 247
 Hannon, J.B.: GR+EM+NS+PS+SS+TF-MoM8, 11
 Hanrahan, B.: TR-TuA11, 108
 Hanrath, T.: EN+NS-MoM5, 10
 Hansen, R.: MN+AS-MoM4, 13
 Hanus, J.: NS+EN+GR-TuA2, 94
 Hao, Y.: GR+AS+NS+SP+SS-TuA11, 91
 Hapala, P.: ET+SS+GR+SP-ThA9, 230; NS-MoM5, 15
 Harada, K.: SS-TuP32, 129
 Harada, Y.: GR+AS+EM+NS+SS-WeA12, 171
 Harari, I.: MN+AS-MoM10, 14
 Harker, M.: LB+EM+GR+MN+TR-WeA3, 173
 Harl, R.R.: SS+OX-WeM4, 152; SS-TuP5, 124
 Harrell, W.R.: SS+OX-WeM3, 152
 Harris, K.L.: TR+SE-WeM9, 160
 Harriss, J.E.: SS+OX-WeM3, 152
 Hartig, M.: PS2-TuM9, 73
 Hasegawa, H.: EM-TuM1, 61
 Hashemian, M.: EN-ThP9, 248; SS-MoM10, 24; SS-MoM11, 24; SS-TuP16, 127
 Hashimoto, N.: EM+TF+AS-ThA12, 226
 Hasselbrink, E.: SS-MoM3, 23; SS-TuP24, 128
 Hassibi, A.: EM+OX-WeA1, 167
 Hatakeyama, R.: PS+BI-MoA8, 47
 Hatch, R.C.: MI-WeM1, 145
 Hauge, R.: BN+AS-WeA12, 166
 Havela, L.: AC+TF+SS+MI-MoA6, 28
 Havelund, R.: AS-ThA2, 222; AS-ThM4, 192
 Havercroft, N.: AS-MoA4, 29; AS-ThM11, 193; AS-WeM11, 136
 Haverkamp, H.: NM+NS+MS+EM-MoA9, 41
 Hawley, C.J.: NS+EN-TuM6, 70
 Hayashi, T.: PS2-MoA7, 49; PS-ThP25, 259
 Haydell, M.: GR+AS+NS+SS-ThM3, 201
 Hayden, B.E.: SS+NS-TuA9, 103
 Hayes, S.L.: AC+EN-TuM1, 57
 Haylock, D.: BI-MoM5, 5
 He, C.: OX+EM+MI+NS+TF-MoM10, 18
 He, G.: GR+AS+NS+SP+SS-TuA10, 91
 He, J.: PS2-TuM11, 74
 He, X.: MI+OX-WeA10, 176
 Heald, S.M.: SS+OX-WeM5, 152
 Hebard, A.F.: GR+EM+ET+MS+NS-FrM11, 273; LB+EM+GR+MN+TR-WeA7, 173
 Hedrick, J.L.: NS+SP-MoA2, 42
 Hell, S.W.: BP+AS-SuA5, 1
 Hellman, F.: MI+OX-WeA1, 175
 Hemminger, J.C.: EN+SS-FrM5, 270; SS+NS-TuA3, 103; SS-ThA1, 237; SS-ThA2, 237; SS-WeM11, 155; SS-WeM12, 155; TF+AS-WeA2, 188
 Hemthavy, P.: MN-TuP9, 121
 Henager Jr, C.H.: HI-ThP2, 251
 Henderson, C.: EL+TF+BI+AS+EM+SS-MoA6, 33
 Henderson, C.L.: GR+EM+ET+MS+NS-FrM9, 272; GR-ThP10, 251
 Henderson, M.A.: EN+SS-FrM2, 269; SS+EN+OX-ThM11, 213; SS-TuM5, 76
 Hendricks, J.H.: VT-MoM6, 26
 Hendryx, C.G.: TF-ThP4, 263
 Henry, F.: SE+NS-MoA4, 50
 Henzler, K.: BP+AS-SuA3, 1
 Heo, D.: PS2-TuM11, 74
 Heo, S.: AS-TuP22, 114
 Heo, Y.K.: NS-ThP8, 254
 Herdiech, M.W.: OX+SS+TF+MI-MoA2, 44
 Herman, G.S.: TC+EM+AS+TF+EN-ThM5, 216
 Herman, J.: EM-ThP8, 245
 Hermkens, P.M.: TF-TuM5, 77
 Hernandez, S.: GR-ThP9, 251
 Hernández, S.C.: GR+AS+BI+PS+SS-WeM9, 143; GR+EM+NS+PS+SS+TF-MoM1, 10
 Hernandez, S.H.: TF+MI-WeA1, 190
 Hernández-Hernández, A.: NS-MoM2, 15; TF-ThP16, 265
 Hernández-Hernández, L.A.: NS-MoM2, 15; TF-ThP16, 265
 Herpers, A.: AS-ThA10, 223
 Herrera, V.: BI+SS+NS-WeM6, 137
 Herrera-Gomez, A.: AS-MoM5, 3; AS-TuP15, 113; AS-TuP16, 113; EM+TF+OX+GR-MoA9, 35
 Herrero-Albillos, J.: MI+OX-WeA1, 175
 Herring, A.M.: EN+NS-ThM1, 197
 Hersam, M.C.: GR+AS+BI+PS+SS-WeM1, 142; GR+AS+BI+PS+SS-WeM3, 143; GR+AS+NS+SP+SS-TuA9, 90; NS-ThP3, 253
 Hershkowitz, N.: PS2-WeA4, 181
 Herzog, A.: AS+BI-TuA9, 83
 Hettiarachchi, C.: EN+NS-MoM6, 10
 Heyde, M.: NS-ThM3, 206
 Heylings, J.: BN+AS-WeA10, 166
 Heyns, M.: EM+TF+OX+GR-MoA1, 34
 Hicks, R.F.: PS+EM-MoM9, 19
 Hiebert, W.K.: MN+AS-MoM9, 13; MN-MoA7, 39; MN-TuM5, 67; MN-TuM9, 68; NS-ThP2, 253
 Highland, M.J.: IS+AS+OX+ET-WeM3, 144
 Hikita, Y.: OX+EM+MI+NS+TF-MoM3, 17

- Hill, R.: PS-ThP34, 260
Hill, S.B.: SS-TuM3, 75
Hillhouse, H.W.: EN+TF-MoA3, **36**
Hillion, F.: IS+AS+OX+ET-WeM11, 145
Hilpert, F.: PS2-TuA1, 97
Hines, M.: EM-ThP13, 246; NS-ThP12, **254**
Hines, M.A.: NS-ThM9, **207**
Hinkle, C.L.: EM+TF+OX+GR-MoA4, 34; EM-TuM3, 61
Hinkov, V.: TF+AS-TuA10, 105
Hirakawa, T.: NM-TuP2, 121
Hiramatsu, M.: GR+AS+NS+SS-ThM9, 201
Hiramatsu, T.: NM-TuP1, 121; NM-TuP2, 121; NM-TuP3, 121; TF-ThP12, 264
Hirano, A.: SE+PS-TuA8, 100
Hiraoka, K.: AS-ThM12, **193**; AS-TuP3, 111; AS-TuP6, 112
Hirayama, H.: SS-MoA8, 52
Hirsch, B.: SS-MoA3, **51**
Hirschmugl, C.: AS-WeM6, 135; GR+AS+NS+SP+SS-TuA2, **90**; SS-TuP3, 124
Hirvonon, J.: PS+TC-WeM12, 148
Hisamatsu, H.: VT-TuA1, 108
Hite, J.K.: EM+TF+AS-ThA6, **225**; SS+EM-WeA1, 184; TF+NS+EM-ThM1, 218
Hjort, M.: EM+MI-ThA6, 224; ET+NS+EM-ThM6, 199
Hla, S.-W.: NS-ThM1, 206
Hlaing, M.M.: MB+BI-ThA4, 232
Ho, A.: BI-TuP14, 118
Hobart, K.D.: GR-ThP9, 251
Hobbs, J.K.: SP+AS+BI+ET+MI+NS-TuA7, **101**
Hockenbery, D.: BN+AS-WeA4, 165
Hodes, G.: ET+SS+GR+SP-FrM3, 270
Hoehne, R.: GR+AS+EM+MI+MN-TuM9, 65
Hoertz, P.: EN+SS-FrM3, 269
Hoffman, D.: PS-ThA4, 234; PS-ThA6, 234
Hoffman, R.S.: EN+NS-MoM5, 10
Hofman, G.L.: AC+EN-TuM1, 57
Hofmann, P.: MI-WeM1, 145
Hofmann, T.: LB+EM+GR+MN+TR-WeA10, 174
Hohlbauch, S.: EW-TuM8, 64; SP+AS+BI+ET+MI+TF-WeA11, 183
Holbrook, R.D.: AS+BI-TuA9, 83
Holland, J.: PS-MoM11, 21
Hollenstein, Ch.: PS-ThA3, 234
Hollerweger, R.: SE+NS-MoM6, 22
Holliday, K.S.: AC+EN-TuM10, **57**
Holloway, P.H.: EM+TF-WeM9, 139; EM-ThP14, 246; NS-WeA2, 177
Holohan, A.: PS1-TuM9, 72
Holzke, C.: SP+AS+BI+ET+MI+NM+NS+SS+TF-WeM5, 150
Holzner, F.: NS+SP-MoA2, 42
Honda, M.: PS-ThP12, **257**
Honda, T.: PS-ThP14, 257
Hone, J.C.: GR+EM+ET+NS+TF-MoA10, 38; NS+EN-TuM11, 70
Hong, J.: TC+EM+AS+TF+EN-ThM12, 216
Hong, M.: PS2-ThM1, **210**; SS+NS-ThA4, **236**
Hong, M.S.: VT-TuP7, 132
Hong, S.: SS+NS-ThA9, **236**
Hong, S.J.: EN-ThP8, **248**
Hong, S.-Y.: SS-TuP2, **124**
Hong, W.T.: IS+AS+SS+EN-TuM5, 66
Hong, Y.-L.: EM+TF+AS-ThA10, 226
Hook, A.L.: BI-MoA8, 31; MB+BI-ThM12, **204**
Hook, D.J.: AS-TuP19, 114
Hooley, R.: SS-WeM2, 154
Hopkins, M.B.: PS1-WeA1, 178
Hopstaken, M.J.P.: EM+NS-FrM10, **268**
Hopwood, J.: PS+EM-MoM5, **19**
Hordagoda, M.: MI+OX-WeA9, 176; OX+EM+MI+NS+TF-MoM1, **17**
Hori, M.: GR+AS+NS+SS-ThM9, 201; PS1-TuM5, 71; PS2-MoA7, 49; PS2-ThM5, 210; PS2-TuA7, 98; PS2-WeA3, 180; PS-ThP14, 257; PS-ThP25, 259
Horibe, H.: PS2-TuA7, 98
Horie, T.: PS2-ThM3, 210
Horikoshi, R.: SE-TuP2, 123
Horn, K.: GR+EM+ET+NS+TF-MoA8, 38
Horowitz, S.B.: MN-MoA6, 39; MN-TuM6, 67
Horsfall, A.B.: GR+EM+NS+PS+SS+TF-MoM1, 10
Horvath, B.: VT-MoA10, 56
Hosadurga, S.: EM-TuA8, 86
Hosemann, P.: SE+NS-MoM6, 22
Hoshino, K.: PS-ThP6, **256**
Hoskinson, A.: PS+EM-MoM5, 19
Hosono, H.: TC+EM+AS+TF+EN-ThM3, **215**
Hossain, M.Z.: NS+SP-MoA6, **43**
Hossain, T.: EM+TF+OX+GR-MoM9, 9
Hou, J.B.: SS+NS-TuA11, 104
Hou, J.-L.: HI+AS+NS-WeA8, 172
Houssiau, L.: AS-MoA2, 29
Howe, B.M.: SE+NS-MoA11, **51**; TF+NS+EM-ThM12, 220
Howe, J.: GR+EM+NS+PS+SS+TF-MoM3, 11
Howling, A.A.: PS-ThA3, 234
Hozumi, A.: SS-ThM1, **213**
Hsiao, C.-N.: EM-ThP3, 244; TF-ThP13, **264**; VT-TuP5, 131
Hsieh, C.-H.: PS-ThP45, 262
Hsieh, C.J.: MN+AS-MoM11, 14
Hsiung, G.Y.: VT+AS+SS-WeM1, 160; VT-TuA12, 109
Hsu, C.: ET+NS+EM-ThM12, 200
Hsu, C.C.: PS+BI-MoA1, 46; PS+EM-MoM4, 18; PS-ThP22, 258; PS-ThP46, 262
Hsu, K.H.: VT-TuA12, 109
Hsu, K.W.: PS-ThP35, **261**
Hsu, S.N.: VT-TuA12, 109
Hsueh, H.P.: VT-TuA12, 109
Hu, J.J.: TR+SE-WeM1, 159
Hu, L.: TF+EN-MoA6, 54
Hu, Q.: SP+AS+BI+ET+MI+TF-WeA9, 183
Hu, S.W.: SS+NS-TuA11, 104; SS-TuP37, **130**
Hu, W.: EN+PS-WeM11, 142; PS2-ThM10, 211
Hu, X.: TF+EN-MoA7, 54
Hu, Y.: SP+AS+BI+ET+MI+TF-WeA8, 183
Hu, Y.C.: LB+EM+GR+MN+TR-WeA8, 173
Hu, Y.F.: AS+TF+VT-FrM1, **266**
Hua, X.: PS2-TuM11, 74
Huang, C.: NS-ThP2, 253
Huang, E.: EM-TuA8, 86
Huang, J.: TF2-TuA9, **106**
Huang, L.W.: GR+EM+ET+NS+TF-MoA6, **37**
Huang, Y.T.: VT-TuA12, 109
Hubault, C.: TF+AS-WeA8, **189**
Hubert, J.: PS+TC-WeM11, **148**; PS-ThP2, 255; PS-ThP31, 260
Hubler, G.: AS-TuP27, 115
Hübner, S.: PS1-WeA7, 179
Hudak, S.: SE+PS-TuA3, 100
Huerta, L.: SS-TuP10, **126**; TR-TuP6, 131
Huffman, C.: PS-ThP34, 260
Huffman, E.: NS-ThM6, 207
Hughes, G.J.: AS-TuP23, 115; AS-TuP7, 112; EM-TuM5, **62**
Hughes, T.P.: VT-MoM10, 26
Hughes, W.C.: SS-WeM10, 155
Hultman, L.: TF+AS-TuA4, 104; TF+AS-TuA9, 105; TF+NS+EM-ThM11, 219; TF+NS+EM-ThM12, 220; TR+SE-WeM4, 159
Hund, Z.M.: EM+TF-WeM12, **140**
Hung, C.-C.: VT-TuP5, 131
Hunter, C.: NM+MS-TuM9, **68**
Hunter, M.: NM+MS-TuM4, **68**
Huo, S.: TR+BI-TuM2, 78
Huo, Y.J.: BI+AS-TuA10, **85**
Hurley, P.K.: AS-TuP7, 112; EM-TuM5, 62
Hussein, R.: BI+SS+AS-TuM12, 60
Hussey, L.: EM+TF+AS-ThA1, 225
Hutton, S.: EW-TuL4, 82
Hutton, S.J.: AS+BI-TuM10, 59; AS+BI-TuM3, 58; AS+NS+SS+TF-WeA8, 164; AS-ThM1, **192**; AS-TuP13, 113; AS-TuP14, 113
Hwang, C.: AS+TF+VT-FrM3, 266; MI-ThP1, 252
Hwang, H.H.: AS-TuP2, **111**; EN+NS-MoM1, 9
Hwang, I.-S.: HI+AS+NS-WeA8, **172**
Hwang, J.: MI+OX-WeA12, 176
Hyde, R.H.: MI+OX-WeA9, 176; OX+EM+MI+NS+TF-MoM1, 17
— I —
Iacobucci, S.: AC+TF+SS+MI-MoA3, 28
Ianno, N.J.: EL+TF+AS+EM+SS-TuP1, 118
Ide, T.: GR+EM+NS+PS+SS+TF-MoM10, 12
Idigoras, O.: MI+EN+BI-TuA12, 94
Igarashi, M.: EN+PS-WeM11, 142; PS2-ThM10, 211
Iida, S.: AS+BI-TuM9, 59
Ikari, T.: EN+TF-TuA12, **89**
Ikenaga, N.: EN-ThP12, 249
Ikezawa, S.: PS1-WeA3, 178
Ilic, B.: MN-MoA1, 38
Ilic, B.R.: MN-TuM10, 68; MN-TuM11, 68
Iliev, M.N.: PS1-TuA10, 96
Ilton, E.S.: SS+OX-WeM9, 153
Im, M.-Y.: MI+SP+AS-ThM11, 205
Imai, E.: TR-TuP2, 130
In, S.Y.: VT-TuP14, 133
Inada, A.: PS-MoM5, 20; PS-ThP1, 255
Ingram, G.: TF+SE+NS-WeM5, 156
Inose, N.: VT-TuP8, 132
Iriye, Y.: PS2-ThM9, 211
Irle, S.: GR-ThP3, 249
Irving, D.: EM+TF+AS-ThA1, 225; TF+AS-TuA12, 105
Isaacson, M.: EN+NS-ThM12, 198
Ishibashi, K.: PS2-MoA11, 49
Ishibashi, T.: VT-TuA1, 108
Ishigami, M.: GR+AS+BI+PS+SS-WeM6, **143**; GR+EM+ET+MS+NS-FrM10, 273; GR+EM+ET+NS+TF-MoA2, 37; NS+EN-TuM11, 70; TR+SE-WeM11, 160
Ishihara, T.: VT-MoM1, **25**
Ishii, A.: NM-TuP2, 121; NM-TuP3, **121**
Ishii, S.: TF+EM+SS-ThA3, 241
Ishikawa, K.: GR+AS+NS+SS-ThM9, 201; PS1-TuM5, 71; PS2-MoA7, 49; PS2-ThM5, 210; PS2-TuA7, **98**; PS2-WeA3, 180; PS-ThP14, 257; PS-ThP25, 259
Ishikawa, T.: NS+EN-TuM5, 70
Islam, M.F.: TC+EM+AS-WeA7, **187**
Ismail-Beigi, S.: OX+SS+TF+MI-MoA2, 44
Isobe, M.: PS2-TuA4, 98; PS2-TuA9, 98; PS-ThP6, 256
Israelachvili, J.N.: BI+SS+NS-WeM5, 137; TR-TuA4, 107
Itagaki, N.: EN+NS-MoM2, 9
Ito, M.: PS2-TuA7, 98
Ito, T.: PS1-ThM5, 208; PS2-TuA2, **97**; PS2-TuA9, 98; PS-ThP6, 256
Itoi, T.: EM+TF+AS-ThA12, 226
Itou, A.: PS-MoM2, 20; PS-WeM10, 150
Itzhaik, Y.: ET+SS+GR+SP-FrM3, 270
Ivanov Boudinov, H.: EM-ThP7, 244
Ivanova, L.: EM+TF+AS-ThA10, 226
Iwao, T.: PS2-MoA11, 49
Iwasaki, T.: PS2-ThM9, 211
Iwase, C.: PS2-ThM3, 210
Izawa, M.: PS-ThA1, 233
— J —
Jackson, S.A.: TR+SE-WeM12, 160
Jacq, S.: PS2-WeA10, 182
Jaehrig, M.: GR+EM+NS+SS+TF-ThA1, 230
Jain, K.: EW-WeL3, 163
Jain, R.: EM+TF-WeM6, 139
Jaiswal, P.: AS-TuP23, 115
Jakubiak, R.: SE+PS-TuM9, 75; TF+AS+SS-ThA10, 240
Jakubowski, A.: PS2-WeA3, 180
James, C.D.: ET+NS+EM-ThM10, 200
Jandhyala, S.: GR+EM+ET+MS+NS-FrM7, **272**
Jang, J.S.: AS-TuP2, 111; EN+NS-MoM1, 9

- Jang, L.: PS2-TuM9, 73
 Jang, W.C.: EM+OX-WeA7, 167
 Jankovic, V.: EN+NS-ThA6, **229**
 Jansen, A.: VT-TuM10, 80
 Janssen, J.P.B.: PS-ThA9, 234
 Javed, M.A.: MB+BI-ThA4, 232
 Jelinek, P.: ET+SS+GR+SP-FrM4, **270**;
 ET+SS+GR+SP-ThA9, 230; NS-MoM5, 15;
 SP+AS+BI+ET+MI+NS-TuA4, 101
 Jelinek, P.: ET+SS+GR+SP-FrM5, 271
 Jen, S.H.: TF-MoM10, 25
 Jena, D.: GR+AS+NS+SS-ThM11, **202**
 Jennings, W.D.: AS-MoA6, **30**
 Jensen, B.D.: LB+EM+GR+MN+TR-WeA3, 173;
 MN+AS-MoM4, 13
 Jensen, D.S.: TF2-TuA2, 106
 Jeon, H.T.: EM+OX-WeA7, 167
 Jeon, H.Y.: EM+OX-WeA7, **167**
 Jeon, K.Y.: SE-TuP1, **122**
 Jeon, M.H.: PS-ThP24, **258**
 Jeon, Y.: PS-ThP44, **262**
 Jernigan, G.G.: TF+AS-TuA3, **104**
 Jespersen, M.L.: EN+TF-TuA7, 88
 Jesse, S.: SP+AS+BI+ET+MI+NS-TuA12, 102;
 SP+AS+BI+ET+MI+TF-WeA1, **182**
 Jewell, A.D.: SS-MoA7, **52**; SS-TuP1, **123**
 Jezewski, C.: EM-TuA12, 87
 Ji, E.: MB+BI-ThM9, 204
 Ji, S.-H.: GR+EM+NS+PS+SS+TF-MoM8, 11
 Ji, X.: PS2-TuM11, 74
 Jia, Q.: IS+AS+OX+ET-WeM3, 144
 Jian, W.: VT-MoA1, 54
 Jiang, K.: NM+NS+MS+EM-MoA9, 41
 Jiang, N.: NS-ThP3, **253**
 Jiang, S.: EM+TF+OX+GR-MoA1, 34
 Jiang, Y.: EM-ThM11, 197
 Jiang, Z.: ET+NS+EM-ThM9, **200**
 Jimenez, O.: TR-TuP6, 131
 Jobbins, M.M.: IS+AS+OX+ET-WeM1, 144
 Johansson, L.: EM+MI-ThA6, 224
 Johansson, M.P.: TF+NS+EM-ThM11, 219
 Johnsen, R.: VT-TuP4, 131
 Johnson, C.E.: IS+AS+BI+ET+GR+NS-TuA7, 92
 Johnson, C.W.: PS1-TuM4, 71
 Johnson, D.J.: PS1-TuM4, 71
 Johnson, E.: EN-ThP5, 247
 Johnson, E.V.: EN+PS-WeM5, **141**
 Johnson, J.A.: IS+AS+BI+ET+GR+NS-TuA7, **92**
 Johnson, J.W.: EM-ThP1, 244
 Johnson, M.: EN+TF-MoA8, **36**; EN+TF-MoA9,
 36; NS+AS+SS+SP-WeM2, 146
 Johnson, M.D.: AS-ThA1, 222
 Johnson, S.D.: GR+AS+EM+MI+MN-TuM1, **64**
 Johnston-Peck, A.: EN+SS-FrM4, 269
 Joiner, C.: GR-ThP13, 251
 Joly, Y.: SS+OX-WeM5, 152
 Jones, J.G.: SE+PS-TuM9, 75; TF+AS+SS-ThA10,
 240
 Jones, K.: EW-TuM8, **64**; LB+EM+GR+MN+TR-
 WeA3, 173
 Joo, M.H.: EN-ThP4, **247**
 Joo, Y.D.: VT-TuP7, 132
 Joo, Y.H.: PS1-ThM6, 209
 Jordan, K.D.: SS-ThA8, 238
 Jordan, M.B.: MN+AS-MoM5, **13**
 Joseph, E.A.: PS1-ThM12, 209; PS-MoM2, 20;
 PS-WeM10, 150
 Jouanneau, S.: EN+NS-ThM11, 198
 Joubert, O.: PS1-WeA2, 178; PS-ThP7, 256
 Jousseau, V.: TF+AS-WeA12, 189
 Jousten, K.: VT-MoA1, **54**; VT-MoA7, 55
 Joy, D.: HI+AS+NS-WeA1, **171**
 Joy, R.: TC+EM+AS+TF+EN-ThM2, 215
 Ju, H.X.: SS-TuP35, **130**
 Judd, A.: BN+AS-WeA10, 166
 Jung, I.W.: MN-TuM3, **67**
 Jung, J.: SS-ThM12, 215
 Jung, R.: PS+BI-MoA3, 46; PS2-TuM1, 72; PS2-
 TuM6, 73; PS2-TuM9, 73; PS-MoM5, 20
- Jung, S.: GR+EM+ET+NS+TF-MoA10, 38
 Jung, W.: EM+OX-WeA1, 167; GR-ThP6, **250**
 Jungnickel, H.: AS-TuP1, 111
 Junige, M.: NM+AS+MS-MoM4, **14**
 Jupille, J.: SS+OX-WeM6, **152**
 Jur, J.S.: TF+NS+EM-ThM5, 218; TF2-TuA1,
106; TF2-TuA10, 107; TF-MoM9, 25; TF-
 TuM9, 78
 Jurczyk, B.: EN-ThP11, 248
- **K** —
 Kabir, A.K.: MI+EN+BI-TuA8, **94**
 Kabius, B.C.: MI-ThP4, 252
 Kadavanich, A.: PS2-TuM10, 73; PS-ThA11, 235
 Kaganovich, I.D.: PS2-MoA10, 49; PS2-MoA9,
 49; PS2-WeA4, 181; PS-ThP9, 256
 Kahng, S.-J.: EM+SS+AS+NS-ThM12, 195
 Kaiser, A.M.: MI+OX-WeA1, 175
 Kajiwara, T.: GR+AS+NS+SS-ThM1, 201
 Kakaroglou, A.: SE+PS-TuA9, 100
 Kakekkhani, A.: OX+SS+TF+MI-MoA2, 44
 Kakiuchi, H.: PS+TC-WeM3, 147; SE+PS-TuA8,
100
 Kalanyan, B.: EN+NS-ThA1, 228; EN+SS-FrM1,
269; EN+SS-FrM3, 269; TF+EN-MoA8, 54
 Kalfon-Cohen, E.: OX+EM+MI+NS+TF-MoM11,
 18
 Kalinin, S.V.: ET+SS+GR+SP-ThA7, **230**;
 SP+AS+BI+ET+MI+NS-TuA12, 102
 Kallaher, R.L.: MI-WeM11, 146
 Kalyanaraman, R.: MN-TuP6, 120
 Kamarthy, G.: PS-MoM1, 20; PS-MoM11, 21
 Kamataki, K.: EN+NS-MoM2, 9
 Kambhampati, R.: PS2-TuM6, 73
 Kameshima, Y.: SS-TuP17, 127
 Kamimura, T.: ET+NS+EM-ThM5, 199
 Kamineni, V.: EM-TuA11, 87
 Kamino, T.: NM-TuP3, 121
 Kampen, T.: EW-TuL6, 82
 Kan, H.-C.: TF+EM+SS-ThA10, 242
 Kan, M.R.: MN+AS-MoM9, **13**; MN-TuM9, 68
 Kanakasapathy, S.: PS2-TuM1, 72; PS2-TuM6,
 73; PS2-TuM9, 73; PS-MoM1, 20; PS-MoM5,
 20
 Kanazawa, K.: VT-TuA1, 108
 Kanda, T.: GR+AS+NS+SS-ThM9, 201
 Kandel, S.A.: AS-TuP26, 115; ET+SS+GR+SP-
 ThA3, 229; IS+AS+OX+ET-WeM1, 144
 Kandratsenka, A.: SS-MoM4, 23
 Kane, G.: VT-TuP9, 132
 Kaneko, T.: PS+BI-MoA8, **47**
 Kanevce, A.: EN+AS-ThA1, 227
 Kang, H.J.: AS-ThA4, 222; AS-TuP2, 111; AS-
 TuP22, 114
 Kang, H.K.: PS-ThP23, 258
 Kang, J.: NS-ThP4, **253**
 Kang, P.S.: NS-ThP6, 253
 Kang, S.H.: PS-ThP28, 259
 Kang, T.S.: EM-ThP1, 244; EM-ThP2, 244
 Kang, X.: PS2-WeA9, 181
 Kanjolia, R.K.: TF+NS+EM-ThM2, 218
 Kanno, Y.: SS-TuP8, 125
 Kant, C.: NS-MoM11, 17
 Kanyal, S.: TF2-TuA2, 106
 Kao, P.K.: PS-ThP22, **258**
 Karadze, M.: TF-ThP5, 263
 Karahashi, K.: PS1-ThM5, **208**; PS2-TuA2, 97;
 PS2-TuA9, 98; PS-ThP6, 256
 Karakas, E.: PS-ThP18, **258**
 Karakoti, A.S.: AS+BI-TuA12, 84; BI-TuP11, 117;
 EN-ThP10, 248; SS-TuP12, 126; SS-TuP26,
128
 Kargar, M.: BI-TuP10, **117**
 Karim, A.M.: IS+AS+SS+EN-TuM10, **66**
 Karmel, H.J.: GR+AS+NS+SP+SS-TuA9, 90
 Karp, E.M.: SS-WeM6, 154; SS-WeM9, 154
 Karpov, E.: EN-ThP9, 248; SS-MoM10, 24; SS-
 MoM11, **24**; SS-TuP16, 127; SS-TuP24, 128
 Karpov, S.Y.: EM-TuM9, 62
 Kasahara, A.: MN-TuP5, **120**
- Kashimura, K.: PS2-ThM3, 210
 Kasouit, S.: EL+TF+AS+EM+SS+PS+EN+NM-
 MoM3, 6
 Kaspar, T.C.: IS+AS+OX+ET-WeM2, 144;
 SS+EN+OX-ThM11, 213; SS+OX-WeM5, **152**
 Kasuya, A.: SS-MoA10, 53
 Kato, H.: NM-TuP1, 121; NM-TuP2, 121; NM-
 TuP3, 121; NS+SP-MoA6, 43; SS-MoA10, 53;
 SS-TuP31, 129; TF-ThP12, 264
 Kato, T.: SS-TuP18, 127
 Katoch, J.: GR+AS+BI+PS+SS-WeM6, 143;
 GR+EM+ET+NS+TF-MoA2, **37**
 Katsunuma, T.: PS-ThP12, 257
 Katz, H.E.: TC+EM+AS-WeA3, 187
 Kaufman Osborn, T.: LB+EM+GR+MN+TR-
 WeA11, 174
 Kaufman-Osborn, T.: EM+TF+OX+GR-MoA3, **34**
 Kaul, A.: EN+TF-TuM11, **63**; TF+AS-WeA11,
 189
 Kawai, M.: BI+SS+NS-WeM11, 138; NS+SP-
 MoA6, 43; SS-ThM12, 215
 Kawai, Y.: GR+EM+NS+PS+SS+TF-MoM10, 12
 Kawakami, R.: GR+AS+EM+MI+MN-TuM3, **64**
 Kawamura, M.: TF-ThP2, **263**
 Kawasaki, H.: SS-ThA10, 238
 Kawasaki, J.: EM+MI-ThA6, **224**
 Kay, B.D.: SS+EN+OX-ThM5, 212; SS-ThA3,
237
 Kayani, A.: NS-WeA10, 178; OX-TuP6, 122
 Kayser, S.: AS-MoA4, **29**; AS-ThM11, 193; AS-
 WeM11, 136
 Kazi, H.Ur.: PS2-WeA8, **181**
 Kean, A.H.: EW-WeL1, 163
 Keavney, D.: MI+SP+AS-ThM12, 206
 Keckes, J.: SE+NS-MoM5, 22
 Keimer, B.: TF+AS-TuA10, 105
 Kelber, J.A.: PS2-WeA8, 181
 Kelkar, U.: TF+AS-TuA11, 105
 Keller, A.: BI-TuP1, 115
 Kelley, M.J.: VT+AS+SS-WeM4, **161**
 Kellogg, G.L.: GR+AS+NS+SP+SS-TuA8, 90
 Kelly, S.T.: IS+AS+BI+ET+GR+NS-TuA9, **93**
 Kelly, T.D.: AC+TF+SS+MI-MoA7, **29**
 Kelly, T.F.: AS-TuP18, 113
 Kennedy, J.R.: AC+EN-TuM1, **57**
 Kenney, J.: PS2-MoA3, 48
 Kent, T.J.: AS-TuP21, 114;
 LB+EM+GR+MN+TR-WeA11, 174;
 SP+AS+BI+ET+MI+NM+NS+SS+TF-WeM6,
151
 Kernert, N.: VT-TuM10, 80
 Kersevan, R.: VT-TuA3, 108; VT-TuP6, 132
 Kershner, R.: EW-TuL2, **82**
 Kessels, W.M.M.:
 EL+TF+AS+EM+SS+PS+EN+NM-MoM6, 7;
 PS2-WeA9, 181; TC+EM+AS+TF+EN-ThM2,
 215; TF+EN-MoA4, 53; TF-TuM10, 78; TF-
 TuM11, 78; TF-TuM5, 77
 Keun, S.K.: IS+AS+OX+ET-WeM3, 144
 Keville, B.J.: PS1-TuM10, **72**; PS1-TuM9, 72
 Khan, A.: PS2-TuM11, 74
 Khan, S.S.: SS-WeM12, 155
 Khare, R.: PS2-TuA3, 98
 Khodadadi, B.: MI+OX-WeA2, 175
 Khosla, N.: SS-ThM2, 214
 Khrabrov, A.V.: PS2-MoA10, **49**; PS2-MoA9, 49
 Khurshid, H.: MI-ThP2, 252; NS-MoM8, 16; NS-
 MoM9, 16
 Khvalkovskiy, A.: MI+OX-WeA7, 175
 Kiantaj, K.: EM+TF+OX+GR-MoA3, 34;
 LB+EM+GR+MN+TR-WeA11, **174**
 Kiefer, B.: IS+AS+SS+EN-TuM6, 66
 Kikkawa, J.M.: GR+AS+EM+MI+MN-TuM2, 64
 Kikuchi, Y.: PS1-TuA9, **96**
 Kilicaslan, A.: PS+TC-WeM1, **147**
 Kilpi, L.: TF+NS+EM-ThM10, 219
 Kim, B.: EM-TuA8, 86
 Kim, C.I.: PS1-ThM6, 209
 Kim, C.K.: PS-ThP43, **261**; VT-TuP7, 132

- Kim, D.H.: EN+SS-FrM1, 269;
NM+NS+MS+EM-MoA8, 41; NS+EN+GR-
TuA10, 95; TF+EN-MoA8, 54
- Kim, D.J.: IS+AS+OX+ET-WeM2, 144
- Kim, G.T.: NS-ThP6, 253
- Kim, G.Y.: PS+TC-WeM9, 148; PS-ThP27, 259
- Kim, H.: EM+SS+AS+NS-ThM12, 195; SS-
WeM5, 154
- Kim, H.J.: EM+OX-WeA11, 168; EM-TuM4, 61;
PS-ThP24, 258
- Kim, H.-Y.: EM-ThP1, 244; EM-TuM10, 62
- Kim, J.: EM+TF+OX+GR-MoM6, 8; EM-ThP1,
244; EM-TuM10, 62; GR+EM+ET+MS+NS-
FrM7, 272; TF2-TuA9, 106
- Kim, J.H.: EM-ThP12, 246; NS+EN+GR-TuA11,
95
- Kim, J.-H.: PS-ThP4, 255
- Kim, J.K.: EM-TuA8, 86; PS-ThP23, 258; PS-
ThP43, 261
- Kim, J.S.: NS-ThP6, 253
- Kim, K.H.: TC+EM+AS-WeA7, 187
- Kim, K.J.: AS-TuP2, 111; EN+NS-MoM1, 9
- Kim, K.N.: PS-ThP24, 258
- Kim, M.C.: PS-ThP44, 262
- Kim, M.J.: EM+TF+OX+GR-MoA4, 34
- Kim, M.K.: SS+NS-ThA3, 235
- Kim, P.: GR+EM+ET+NS+TF-MoA10, 38
- Kim, S.: EM+SS+AS+NS-ThM11, 195
- Kim, S.H.: BI-TuP5, 116; EN+TF-TuM12, 63; PS-
ThP33, 260; TR+BI-TuM11, 79
- Kim, S.K.: PS-ThP23, 258
- Kim, S.-K.: MI+SP+AS-ThM11, 205
- Kim, S.M.: ET+NS+EM-ThM11, 200; NS+EN-
TuM3, 69; NS-ThM11, 207
- Kim, S.N.: GR+AS+BI+PS+SS-WeM6, 143
- Kim, T.: ET+NS+EM-ThM3, 199
- Kim, T.G.: TF-ThP18, 265
- Kim, W.: MI-ThP1, 252
- Kim, W.J.: VT-TuP11, 132; VT-TuP12, 133; VT-
TuP13, 133; VT-TuP14, 133
- Kim, W.K.: EN+TF-TuM10, 63
- Kim, Y.: PS+BI-MoA3, 46; SS-ThM12, 215; SS-
TuP14, 126; SS-WeM5, 154
- Kim, Y.-H.: EM+SS+AS+NS-ThM12, 195
- Kim, Y.S.: AC+EN-TuM1, 57
- Kimmel, G.A.: SS+EN+OX-ThM3, 212;
SS+EN+OX-ThM5, 212; SS-TuM5, 76; SS-
TuM6, 76
- Kim-Ngan, N.-T.: AC+TF+SS+MI-MoA6, 28
- Kimura, A.: MI-WeM1, 145
- King, S.: EM-TuA9, 87; GR+EM+NS+SS+TF-
ThA1, 230
- King, S.T.: EM-ThP15, 246
- King, W.: GR+AS+NS+SS-ThM3, 201
- Kingshott, P.: BI+AS-TuA3, 84; BI-MoM6, 5
- Kinoshita, K.: PS1-ThM9, 209
- Kinoshita, T.: GR+EM+NS+PS+SS+TF-MoM10,
12; PS2-ThM4, 210
- Kinross, J.: IS+AS+BI+ET+GR+NS-TuA3, 92
- Kintaka, H.: PS2-TuM1, 72; PS-MoM5, 20
- Kioussis, D.R.: EM-TuA8, 86
- Kirby, H.F.: TF-ThP4, 263
- Kirchlechner, C.: SE+NS-MoM5, 22
- Kis, A.: GR+EM+NS+SS+TF-ThA10, 232
- Kisielowski, C.: GR+AS+NS+SS-ThM5, 201
- Kjoller, K.: SP+AS+BI+ET+MI+TF-WeA9, 183
- Klem, E.J.D.: EN+NS-MoM11, 10
- Klick, M.: PS1-WeA11, 179
- Klimczak, A.: EW-WeL5, 163
- Klingsporn, J.M.: NS-ThP3, 253
- Kloss, F.: BI-MoM11, 6
- Klymko, N.: EM-TuA8, 86
- Knappe, D.: SE+PS-TuA4, 100
- Knauf, J.: TF+EM+SS-ThA9, 242
- Knaut, M.: NM+AS+MS-MoM4, 14
- Knies, D.: AS-TuP27, 115
- Knoll, A.W.: NS+SP-MoA2, 42
- Knoops, H.C.M.:
EL+TF+AS+EM+SS+PS+EN+NM-MoM6, 7;
- TC+EM+AS+TF+EN-ThM2, 215; TF-TuM5,
77
- Knudsen, J.: GR+AS+NS+SP+SS-TuA7, 90;
IS+AS+SS+EN-TuM12, 67
- Knupfer, M.: GR-ThP3, 249
- Ko, A.: PS-ThP34, 260
- Ko, C.G.: PS-ThP23, 258
- Ko, M.K.: VT-TuP13, 133
- Koay, C.: PS2-TuM9, 73
- Kobata, M.: AS-ThA10, 223
- Kobata, T.: VT-MoA4, 55
- Kobayashi, K.: AS-ThA10, 223
- Kobayashi, M.: PS2-TuM6, 73
- Kobayashi, T.: BI+SS+NS-WeM11, 138
- Kobe, H.: TF-ThP12, 264
- Koegler, P.: BI-MoM6, 5
- Koel, B.: SS-WeA10, 186
- Koelsch, P.: AS-WeM1, 135; AS-WeM3, 135
- Koenraad, P.M.: SS+EM-WeA3, 184
- Koga, K.: EN+NS-MoM2, 9
- Koh, D.Y.: VT-TuP14, 133
- Koirala, P.: EL+TF+AS+EM+SS+PS+EN+NM-
MoM4, 7
- Kolind, K.: BI-MoM2, 5
- Kollmer, F.: AS-MoA4, 29; AS-ThM11, 193; AS-
WeM11, 136
- Kolosko, A.G.: SE+NS-MoA7, 50
- Komachi, J.: PS2-ThM4, 210
- Komarneni, M.: NS+AS+SS+SP-WeM4, 146
- Kometani, R.: PS2-ThM5, 210
- Komori, F.: GR+AS+NS+SS-ThM1, 201
- Kondo, H.: GR+AS+NS+SS-ThM9, 201; PS1-
TuM5, 71; PS2-MoA7, 49; PS2-ThM5, 210;
PS2-WeA3, 180; PS-ThP14, 257
- Kondo, T.: GR+AS+EM+NS+SS-WeA12, 171
- Kondo, Y.: PS2-MoA7, 49; PS-ThP14, 257
- Kondoh, H.: IS+AS+SS+EN-TuM12, 67
- Kondratyuk, P.: SS-WeA11, 186
- Kong, C.S.: TR+BI-TuM10, 79
- Kong, D.D.: SS-TuM9, 76; SS-TuP37, 130
- Kong, L.: GR+EM+ET+NS+TF-MoA7, 37
- Konicek, A.R.: AS+BI-TuA9, 83
- Konneker, A.: MN+AS-MoM4, 13
- Kono, Y.: BN+AS-WeA3, 165
- Kontic, R.: NS-ThP1, 252
- Kornegay, S.M.: TF+EM+SE+NS-ThM4, 217
- Korolkov, V.: SP+AS+BI+ET+MI+NS-TuA9, 102
- Körsgen, M.: AS-TuP1, 111
- Koshihara, S.: NS+EN-TuM5, 70
- Koshy, R.: PS-ThP1, 255; PS-WeM1, 148; PS-
WeM4, 149
- Koskey, S.: PS-WeM5, 149
- Koskinen, J.: TF+NS+EM-ThM10, 219
- Koster, N.B.: HI+AS+NS-WeA9, 172; PS-ThA9,
234; PS-ThP15, 257; VT-TuA7, 109
- Kostov, K.: LB+EM+GR+MN+TR-WeA9, 174
- Kotru, S.: EN+TF-WeA11, 169
- Kotsugi, M.: GR+EM+NS+PS+SS+TF-MoM10,
12
- Kotula, P.G.: AS-TuP5, 111
- Kövér, L.: AS+TF+VT-FrM3, 266
- Kowalik, J.: GR+EM+ET+MS+NS-FrM9, 272;
GR-ThP10, 251
- Kozhanov, A.: EM+MI-ThA10, 224
- Kozhushkova, E.A.: EM-TuM9, 62
- Kozhushner, M.: ET+SS+GR+SP-ThA4, 229
- Krafcik, J.: NS+EN-TuM3, 69
- Kraft, D.C.E.: BI+SS+NS-WeM1, 136; BI-
MoM11, 6; BI-MoM2, 5; BI-TuP1, 115
- Kranz, L.: TF+AS-WeA3, 188
- Krause, M.: SE+NS-MoM2, 21
- Kravchenko, I.I.: EM-TuA2, 86
- Kreil, J.: MI+OX-WeA2, 175
- Krejci, O.: ET+SS+GR+SP-ThA9, 230
- Krick, B.A.: TR+SE-WeM9, 160; TR-TuA3, 107;
TR-TuA9, 107
- Krim, J.: TR-TuA12, 108
- Krishnan, R.: EN+TF-TuM10, 63
- Krist, B.: EM-TuA12, 87
- Kristensen, P.K.: EN-ThP5, 247
- Kristiansen, K.: TR-TuA4, 107
- Kroemker, B.: GR+AS+NS+SP+SS-TuA1, 89
- Kroll, U.: PS-ThA3, 234
- Krommenhoek, P.J.: TF2-TuA1, 106
- Kronast, F.: MI+OX-WeA1, 175
- Krounbi, M.: MI+OX-WeA7, 175
- Krstev, I.: PS1-WeA10, 179
- Krueger, B.: TC+EM+AS+TF+EN-ThM11, 216
- Krueger, J.: EM-ThP15, 246
- Krueger, P.: SS+OX-WeM6, 152
- Krüger, P.: MI-WeM1, 145
- Krylov, S.: MN+AS-MoM10, 14; MN-MoA8, 39
- Ku, J.H.: EM-TuM4, 61
- Kuang, Z.: GR+AS+BI+PS+SS-WeM6, 143
- Kub, F.J.: EM+TF+AS-ThA6, 225;
GR+AS+EM+MI+MN-TuM1, 64; GR-ThP9,
251
- Kubetzka, A.: NS-ThM1, 206
- Kuboi, N.: PS2-ThM4, 210
- Kubota, J.: SS+EN+OX-ThM1, 211
- Kubota, T.: MN-TuP4, 120; PS2-ThM11, 211;
PS2-ThM9, 211; PS-MoM6, 20
- Kuchibhatla, S.V.N.T.: AS+BI-TuA12, 84
- Kuciauskas, D.: EN+AS-ThA1, 227
- Kucukgok, B.: EM+TF+AS-ThA9, 226
- Kuemin, C.: NS+SP-MoA2, 42
- Kuhn, M.: GR+EM+NS+SS+TF-ThA1, 230
- Kuhness, D.: SS+OX-WeM12, 153
- Kujofsa, T.M.: EM+MI-ThA1, 223
- Kuk, Y.: MI-WeM11, 146; MI-WeM2, 145
- Kulkarni, D.: SS-TuP36, 130
- Kulkarni, P.: BI-TuP7, 117
- Kulsreshath, M.: PS+EM-MoM3, 18
- Kumar, A.: BI-TuP11, 117; BI-TuP3, 116;
EL+TF+BI+AS+EM+SS-MoA8, 33; MN-
TuP6, 120; PS+EM-MoM8, 19
- Kumar, K.: PS2-TuM1, 72; PS-MoM5, 20; PS-
ThP1, 255; PS-WeM4, 149
- Kumar, S.: EL+TF+BI+AS+EM+SS-MoA8, 33
- Kummel, A.C.: AS-TuP21, 114; BI+SS+NS-
WeM6, 137; BN+AS-WeA3, 165;
EM+TF+OX+GR-MoA3, 34;
LB+EM+GR+MN+TR-WeA11, 174;
SP+AS+BI+ET+MI+NM+NS+SS+TF-WeM6,
151; SS-ThM11, 215
- Kung, M.: TF+EN-MoA1, 53
- Kung, P.: ET+NS+EM-ThM11, 200; NS+EN-
TuM3, 69; NS-ThM11, 207
- Kungas, R.: SP+AS+BI+ET+MI+TF-WeA3, 183
- Kunze, C.: SS-ThA9, 238
- Kuo, H.-S.: HI+AS+NS-WeA8, 172
- Kusakabe, K.: EM+TF+AS-ThA12, 226
- Kushner, M.J.: PS2-TuA11, 99
- Kusova, K.: NS-MoM5, 15
- Kuwahara, K.: TF-ThP6, 263
- Kwan, J.K.: MN-MoA7, 39
- Kwon, G.: PS+BI-MoA3, 46
- Kwon, H.C.: VT-TuP7, 132
- Kwon, J.: TF+NS+EM-ThM2, 218
- Kwon, T.: PS2-TuM6, 73
- Kwon, Y.H.: OX+EM+MI+NS+TF-MoM2, 17
- Kwon, Y.J.: TF+AS-WeA2, 188
- Kyoung, Y.K.: AS+BI-TuM9, 59; AS-ThA4, 222
- Kyriakou, G.: SS-MoA7, 52; SS-TuP1, 123; SS-
WeM1, 153
- Kysar, J.W.: MN-MoA3, 38
- L —
- Labbé, P.: BI+SS+NS-WeM10, 138
- LaBella, V.P.: EM+NS-FrM5, 268;
ET+SS+GR+SP-FrM6, 271;
GR+AS+NS+SP+SS-TuA11, 91
- Labelle, C.: PS-ThP1, 255; PS-WeM1, 148
- Labonte, A.P.: PS-WeM1, 148; PS-WeM11, 150
- Laboutin, O.: EM-ThP1, 244
- Lacovig, P.: LB+EM+GR+MN+TR-WeA9, 174
- Ladroue, J.: MN+AS-MoM6, 13; PS1-ThM3, 208
- Laera, S.: BI+SS+AS-TuM12, 60

- LaForge, J.M.: TF+SE+NS-WeM5, **156**;
TF+SE+NS-WeM9, 156
- LaGoo, L.: AS+BI-TuM4, 58
- Lahiri, J.: GR+EM+NS+SS+TF-ThA2, 231
- Lalany, A.: TF+SE+NS-WeM11, **157**
- Lam, K.: EM-ThM5, **196**
- Lampen, P.: NS-MoM8, **16**
- Lanceros-Méndez, S.: BI+AS-TuA7, 84
- Landrock, S.: EM-ThM11, 197
- Landt, L.: AS+TF+VT-FrM2, 266
- Lane, B.G.: PS1-TuM11, **72**; PS1-WeA12, 180
- Langenkämper, Ch.: MI-WeM1, 145
- Langer, R.: BI-MoA10, 32; BI-MoA4, 31; BI-MoA8, 31; MB+BI-ThM12, 204
- Langfitt, Q.: OX-TuP6, 122
- Larciprete, R.: LB+EM+GR+MN+TR-WeA9, 174
- Laroussi, M.: SE+PS-TuA1, **99**
- Larsen, G.K.: TF+SE+NS-WeM3, **156**
- Larson, D.J.: AS-TuP18, 113
- Lashley, J.C.: EM+NS-FrM11, 269
- Laskin, A.: IS+AS+BI+ET+GR+NS-TuA9, 93
- Laskoski, M.: GR-ThP9, 251
- Lass, S.: EW-WeM8, **142**
- Latu-Romain, L.: TF+AS-WeA12, 189
- Lauer, I.: EM+NS-FrM10, 268
- Lauhon, L.J.: ET+NS+EM-ThM1, **199**
- Lauter, V.: MI+OX-WeA12, 176
- Laver, M.: OX+EM+MI+NS+TF-MoM10, 18
- Lavoie, C.: EM+NS-FrM7, **268**; EM+NS-FrM9, 268
- Law, M.: EN+TF-MoA6, **36**; TF+AS-WeA2, 188
- Lawrence, D.: AS-TuP18, 113
- Lawton, T.: SS-WeM1, **153**
- Lazovsky, D.: NM+MS-TuM9, 68
- Lazzaroni, R.: PS+TC-WeM11, 148; SE+NS-MoA4, 50
- Le Brizoual, L.: PS2-WeA10, **182**
- Le Lay, G.: GR+EM+NS+SS+TF-ThA6, 231
- Le, D.: GR+EM+ET+MS+NS-FrM3, 271;
GR+EM+ET+NS+TF-MoA2, 37; GR-ThP8, 251; NS+EN+GR-TuA7, **94**; SS-WeA1, 185
- Le, M.: PS-ThP10, 256
- Le, N.B.: GR-ThP4, **250**
- Lea, A.S.: NS-ThM2, **206**
- LeBeau, J.: EM+TF+AS-ThA1, 225
- LeClair, P.R.: MI+OX-WeA12, 176
- Lecondier, L.: TF+EM+SS-ThA7, **241**; TF-WeM1, 157
- Lee, A.J.: NS+SP-MoA1, 42
- Lee, B.H.: TF-MoM10, 253
- Lee, B.-J.: AS-ThM10, 193
- Lee, B.O.: PS-ThP23, 258
- Lee, C.: PS2-TuM10, 73
- Lee, C.-M.: GR+EM+ET+NS+TF-MoA7, 37
- Lee, C.T.: EM-ThP3, 244; TF-ThP7, **263**
- Lee, D.Y.: IS+AS+OX+ET-WeM1, **144**
- Lee, G.: PS+BI-MoA3, 46
- Lee, H.I.: AS-ThA4, 222
- Lee, H.S.: PS-ThP29, **259**
- Lee, I.: TC+EM+AS-WeA7, 187
- Lee, J.: GR-ThP6, 250; PS-WeM6, **149**;
SP+AS+BI+ET+MI+NS-TuA3, **101**; SS-ThA8, **238**
- Lee, J.C.: AS+BI-TuM9, **59**; AS-ThA4, 222; AS-TuP22, 114
- Lee, J.H.: EN+TF-TuM12, **63**; MI-ThP5, 252;
OX+EM+MI+NS+TF-MoM2, 17
- Lee, J.M.: EN-ThP4, 247
- Lee, J.R.I.: AS+TF+VT-FrM2, 266;
IS+AS+OX+ET-WeM6, 144
- Lee, J.S.: EM+OX-WeA7, 167; EM+TF+OX+GR-MoA3, 34; MB+BI-ThA1, 232
- Lee, J.Y.: OX+EM+MI+NS+TF-MoM2, 17; SE-TuP1, 122
- Lee, K.I.: AS-TuP22, 114
- Lee, K.M.: NS+EN+GR-TuA10, **95**; TF+EN-MoA8, 54
- Lee, K.-M.: GR+EM+ET+MS+NS-FrM3, 271
- Lee, K.W.: PS-ThP23, 258
- Lee, M.: TF2-TuA9, 106
- Lee, N.I.: EM-TuM4, 61
- Lee, S.H.: EM-TuM4, 61
- Lee, S.Y.: AS-TuP22, 114
- Lee, T.G.: BI-TuP5, 116
- Lee, T.H.: EM-TuA8, 86
- Lee, T.Y.: VT+AS+SS-WeM1, 160
- Lee, W.J.: BI-TuP5, 116
- Lee, W.K.: GR+AS+NS+SS-ThM3, **201**; GR-ThP9, 251
- Lee, W.Y.: PS-ThP38, 261
- Lee, Y.: TF2-TuA8, **106**
- Lee, Y.H.: EN+TF-TuM12, 63
- Lee, Y.K.: SS-MoM1, 23
- Lee, Y.S.: PS-ThP23, 258
- Leever, B.J.: EN+TF-TuA7, **88**
- Lefauchaux, P.: MN+AS-MoM6, 13; PS+EM-MoM3, 18; PS1-ThM2, 208; PS1-ThM3, 208
- Legget, G.J.: NS+SP-MoA1, 42
- Leggett, G.J.: TF+EM+SS-ThA1, **240**
- Lei, Y.: IS+AS+SS+EN-TuM9, **66**
- Leick, N.: EL+TF+AS+EM+SS+PS+EN+NM-MoM6, 7; TF-TuM10, 78
- Leick-Marius, N.: TF+EN-MoA4, 53
- Leidy, C.: BI-TuP6, 116
- Leighton, C.: EN+TF-MoA8, 36; EN+TF-MoA9, 36; OX+EM+MI+NS+TF-MoM10, **18**
- Leinweber, C.: BI-TuP14, 118
- Leitner, D.: VT-TuA3, 108; VT-TuP6, 132
- Leitner, M.: VT-TuA3, 108; VT-TuP6, 132
- Lemaitre, M.: LB+EM+GR+MN+TR-WeA7, 173
- Lemay, J.-C.: SS-ThM5, **214**
- Lenahan, P.: EM-TuM11, **62**
- Lenox, C.: PS-MoM8, 21
- Lenz, A.: EM+TF+AS-ThA10, 226
- Leonhardt, D.: EM-ThM12, 197
- Leou, K.-C.: PS-ThP45, 262
- Leroux, C.: NM+NS+MS+EM-MoA6, 41
- Leroy, P.: PS-ThP32, **260**
- Letofsky-Papst, I.: SE+NS-MoM9, 22
- Levasseur, O.: PS+BI-MoA10, 47; PS+BI-MoA11, 47; PS+TC-WeM1, 147
- Levy, N.: MI-WeM11, 146; MI-WeM2, 145
- Lewin, E.: SE+PS-TuM5, 75
- Lewis, E.A.: SS-WeA2, **186**
- Lewis, E.K.: BN+AS-WeA12, 166
- Lewis, J.: EN+NS-MoM11, **10**
- Lewis, N.S.: EM+TF-WeM12, 140
- Lewis, T.: SS-ThA2, 237
- Li, A.-P.: ET+NS+EM-ThM3, 199; ET+NS+EM-ThM4, **199**; ET+SS+GR+SP-ThA6, 229;
GR+EM+NS+PS+SS+TF-MoM2, 11
- Li, C.: TC+EM+AS-WeA4, 187
- Li, J.: EN+AS-ThA7, 228; IS-TuP2, 119
- Li, J.B.: TC+EM+AS-WeA4, 187
- Li, K.: NS+SP-MoA8, 43
- Li, L.: NS-ThP4, 253
- Li, L.J.: LB+EM+GR+MN+TR-WeA8, 173
- Li, Q.: EM-ThM12, 197; SP+AS+BI+ET+MI+NS-TuA12, 102; SS-WeM4, **154**
- Li, S.: TF+AS-TuA1, 104
- Li, W.: MI-ThP2, 252; TF-ThP17, 265
- Li, W.Y.: PS-ThA10, **235**
- Li, X.D.: ET+NS+EM-ThM4, 199
- Li, Y.: SS-TuP9, 125; VT+AS+SS-WeM2, 161; VT-TuA11, **109**
- Li, Z.: ET+SS+GR+SP-ThA11, **230**; SS+EN+OX-ThM5, 212; SS+NS-TuA4, 103; VT+AS+SS-WeM10, **161**; VT+AS+SS-WeM6, 161
- Li, Z.S.: EM+NS-FrM4, 267; EM+SS+AS+NS-ThM3, 194
- Lian, T.: EN+NS-MoM8, **10**
- Liang, C.-K.: AS-ThM5, 192
- Liang, T.: EN+SS-FrM6, **270**; OX+SS+TF+MI-MoA1, 44; OX-TuP1, 122; OX-TuP3, 122
- Liang, Y.: PS1-WeA3, 178
- Liang, Z.: SS-WeM5, **154**
- Liao, B.-H.: EN-ThP2, **247**; TF-ThP13, 264
- Liao, Y.C.: PS+EM-MoM4, 18
- Libera, J.A.: TC+EM+AS+TF+EN-ThM6, 216
- Lieberman, A.: BN+AS-WeA3, **165**
- LiCausi, N.: EM-TuA11, **87**
- Lichtenstein, L.: NS-ThM3, 206
- Licitra, C.: NS-ThM10, 207
- Liddiard, S.: LB+EM+GR+MN+TR-WeA3, 173
- Liddle, J.A.: NM+AS+MS-MoM1, **14**
- Lie, F.: PS2-TuM9, 73
- Liedberg, B.: MB+BI-ThA3, 232
- Lien, S.-E.: PS-ThP45, 262
- Ligot, S.: PS1-TuA8, **96**
- Lii, T.: PS-MoM8, 21
- Lim, D.: TF+EM+SS-ThA11, 242
- Lim, H.J.: EM-TuM4, **61**
- Lim, J.T.: ET-ThP1, 249
- Lim, J.Y.: VT-TuP11, 132; VT-TuP12, 133; VT-TuP13, 133; VT-TuP14, **133**
- Lim, W.: EM-TuM9, 62
- Lim, W.S.: PS-ThP23, 258
- Lin, C.-F.: TF+EM+SS-ThA10, **242**
- Lin, C.-P.: VT-TuP5, 131
- Lin, C.-Y.: HI+AS+NS-WeA8, 172
- Lin, D.: LB+EM+GR+MN+TR-WeA12, 174
- Lin, F.-Y.: TR+BI-TuM10, 79; TR-TuP1, **130**
- Lin, J.H.: AS-TuP7, 112; EM-TuM5, 62
- Lin, J.M.: AS-TuP20, **114**
- Lin, K.C.: LB+EM+GR+MN+TR-WeA8, 173
- Lin, M.Y.: BI-TuP4, 116; GR-ThP2, **249**; NS-ThP7, 254
- Lin, P.A.: PS+EM-MoM8, 19
- Lin, Q.: EM-TuA10, 87; PS2-TuM6, 73
- Lin, S.: GR+EM+ET+MS+NS-FrM3, 271
- Lin, W.Z.: SP+AS+BI+ET+MI+NS-TuA12, 102
- Lin, X.: SS+EN+OX-ThM5, **212**
- lin, Y.: TF-ThP17, **265**
- Lin, Y.: EM-TuA8, 86
- Lin, Y.C.: MN+AS-MoM11, 14
- Lin, Y.H.: EM+SS+AS+NS-ThM13, 195
- Lin, Y.-W.: TF-ThP13, 264; VT-TuP5, **131**
- Lince, J.R.: TR+SE-WeM12, **160**
- Linck, M.: GR+AS+NS+SS-ThM5, 201
- Linder, B.P.: EM+TF+OX+GR-MoA7, 35
- Lindh, L.: BI+SS+AS-TuM3, 60
- Lindsay, A.: SE+PS-TuA3, 100; SE+PS-TuA4, **100**
- Linford, M.R.: TF+EM+SS-ThA8, 242; TF2-TuA2, **106**; TF-MoM4, 24; TF-WeM6, 158
- Ling, Z.: PS-ThA10, 235
- Lingy, L.: VT-TuA3, 108; VT-TuP6, 132
- Linn-Molin, E.: TR+SE-WeM10, 160
- Liou, J.C.: MN+AS-MoM11, 14
- Lippitz, A.: AS+BI-TuM5, 58
- Lister, R.: NS-ThP2, 253
- Little, B.J.: MB+BI-ThA1, **232**
- Liu, B.: IS+AS+SS+EN-TuM9, 66
- Liu, C.: PS1-ThM12, 209; SE-TuP4, **123**
- Liu, J.: EN+SS-FrM3, 269
- Liu, L.: EM-ThP1, 244; EM-ThP2, **244**; PS-MoM8, 21
- Liu, X.: EM-TuA7, 86; VT+AS+SS-WeM2, **161**; VT-TuA11, 109
- Liu, Y.: EM-ThM1, 195; EN+SS-FrM5, **270**;
SS+NS-TuA3, 103; TC+EM+AS-WeA3, **187**
- Liu, Y.H.: VT-TuA12, 109
- Liu, Z.: EN+SS-FrM5, 270; GR+EM+NS+SS+TF-ThA3, 231; IS+AS+SS+EN-TuM4, 66;
IS+AS+SS+EN-TuM5, 66
- Livadaru, L.:
SP+AS+BI+ET+MI+NM+NS+SS+TF-WeM2, 150
- Lizzit, S.: LB+EM+GR+MN+TR-WeA9, **174**
- Ljazouli, R.: PS1-ThM2, 208
- Lo, C.-F.: EM-ThP1, 244; EM-ThP2, 244
- Lo, E.: IS+AS+BI+ET+GR+NS-TuA1, 91
- Lo, M.: SP+AS+BI+ET+MI+TF-WeA9, 183
- Lock, E.H.: GR+AS+BI+PS+SS-WeM9, 143; GR-ThP9, **251**; PS-ThP40, 261
- Locquet, J.P.: IS+AS+OX+ET-WeM9, 145

- Lodge, M.: GR+EM+ET+MS+NS-FrM10, **273**;
TR+SE-WeM11, 160
- Lofaro, J.C.: NS+AS+SS+SP-WeM12, 147
- Logvenov, G.: TF+AS-TuA10, 105
- Lohstreter, L.: AS+BI-TuM4, 58; AS-MoA8, **30**
- Longo, C.: TF+SE+NS-WeM3, 156
- Lopez, G.P.: MB+BI-ThA6, 233
- Lopez-Lopez, S.: PS2-MoA6, 48
- Lopinski, G.P.: EM+NS-FrM1, **267**
- Loquet, Y.: PS-ThP1, 255
- Lorenz, K.: AC+TF+SS+MI-MoA9, 29
- Losby, J.E.: MN-TuM9, 68
- Loscutoff, P.: EM-TuA1, 85
- Losago, M.D.: EN+NS-ThA1, **228**; EN+SS-FrM1,
269; SE+NS-MoA10, 51
- Losovyj, Ya.B.: AC+TF+SS+MI-MoA1, 28;
AC+TF+SS+MI-MoA7, 29
- Lottis, D.: MI+OX-WeA7, 175
- Lotze, C.: SP+AS+BI+ET+MI+NM+NS+SS+TF-
WeM4, **150**
- Lou, J.: GR+EM+NS+SS+TF-ThA3, **231**
- Lou, Y.: SS+NS-TuA4, 103
- Louette, P.: AS-MoA2, 29
- Louie, S.G.: GR+AS+NS+SS-ThM5, 201
- Love, C.: BI+AS-TuA4, 84
- Lovinger, D.: NS-ThM6, 207
- Lu, C.-J.: MN-MoA9, 39
- Lu, G.: GR+AS+NS+SP+SS-TuA2, 90; SS-TuP3,
124
- Lu, H.L.: MN-MoA9, 39
- Lu, J.: IS+AS+SS+EN-TuM9, 66
- Lu, J.W.: EM+MI-ThA11, 224; MI+EN+BI-TuA7,
93
- Lu, L.: EM-TuM9, 62
- Lu, M.: TF+AS-WeA1, 188
- Lu, N.: EM+TF+OX+GR-MoA4, 34
- Lu, T.-M.: TF+SE+NS-WeM4, 156
- Lu, W.C.: SS-WeM4, 154
- Lu, W.H.: GR-ThP8, 251; SS-WeA1, 185
- Lu, Y.: AS-TuP26, 115; ET+SS+GR+SP-ThA3,
229; PS2-ThM5, 210
- Lu, Y.-H.: HI+AS+NS-WeA8, 172
- Lu, Y.P.: BI-TuP4, **116**; GR-ThP2, 249; NS-ThP7,
254
- Lu, Y.W.: PS+EM-MoM4, 18
- Lu, Z.: SS-TuP26, 128
- Lu, Z.-H.: OX+SS+TF+MI-MoA7, **45**
- Lucartoto, T.B.: SS-TuM3, 75
- Lucchini, J.-F.: AC+EN-TuM9, 57
- Lucero, A.T.: EM+TF+OX+GR-MoM6, **8**; TF2-
TuA9, 106
- Luch, A.: AS-TuP1, 111
- Lui, Y.: IS+AS+BI+ET+GR+NS-TuA7, 92
- Lukasiak, L.: PS2-WeA3, 180
- Lukaszew, R.A.: TF+AS+SS-ThA8, 240;
VT+AS+SS-WeM10, 161; VT+AS+SS-
WeM6, 161; VT+AS+SS-WeM9, 161
- Lund, J.: LB+EM+GR+MN+TR-WeA3, 173
- Luo, B.: TF-ThP10, **264**
- Luo, H.: EL+TF+BI+AS+EM+SS-MoA9, 33
- Luo, M.: SS-WeM2, 154
- Luo, X.: VT-TuM4, 80
- Luscombe, C.K.: ET+SS+GR+SP-ThA11, 230;
SS-TuP14, 126
- Luther, J.M.: EN+NS-MoM3, **9**
- Lutolf, M.: BI-MoA1, **30**
- Luttrell, T.: SS-TuP15, **126**
- Lynch, S.: SE-TuP4, 123
- Lyubinitzky, I.: IS+AS+OX+ET-WeM2, 144;
SS+EN+OX-ThM5, 212; SS+EN+OX-ThM9,
213; SS-TuM5, **76**
- Lyytinen, J.: TF+NS+EM-ThM10, 219
- **M** —
- Ma, J.: EN+AS-ThA1, 227
- Ma, M.: EN+PS-WeM3, 140
- Ma, Q.: GR-ThP8, **251**;
SP+AS+BI+ET+MI+NM+NS+SS+TF-WeM5,
150; SS-WeA1, 185
- Maas, D.J.: HI+AS+NS-WeA9, 172
- Macak, E.: AS+NS+SS+TF-WeA8, 164
- Macak, K.: AS+NS+SS+TF-WeA8, **164**
- Maccallini, E.: EW-TuA5, 89
- Macco, B.: NS-MoM6, 16
- MacDonald, A.H.: EM+OX-WeA1, 167
- MacGearailt, N.: PS1-WeA1, 178
- Mack, P.: AS+BI-TuM11, 59; AS-MoA2, **29**; AS-
MoM10, 4; BI+AS-TuA7, 84; EW-TuL3, 82
- Macke, S.: TF+AS-TuA10, **105**
- Mackenzie, K.D.: PS1-TuM4, **71**
- Mackus, A.J.M.: TF+EN-MoA4, 53; TF-TuM10,
78
- Madaan, N.: TF+EM+SS-ThA8, **242**
- Madan, A.: EM-TuA8, 86
- Madiseti, S.: EM+TF+OX+GR-MoM3, **8**
- Maeda, K.: PS-ThA1, **233**
- Maerkl, S.: BI+AS-TuA11, **85**
- Magana, S.: TF+EM+SS-ThA11, 242
- Magaud, L.: PS2-WeA12, 182
- Magel, G.A.: NS+SP-MoA4, 43
- Magnone, K.:
SP+AS+BI+ET+MI+NM+NS+SS+TF-WeM5,
150
- Magnuson, C.W.: GR+AS+NS+SP+SS-TuA11, 91
- Mahadevan, S.: PS2-MoA11, 49
- Mahadik, N.: TF+NS+EM-ThM1, 218
- Mahlstedt, M.: BI-MoA8, 31
- Mahoney, C.M.: AS+BI-TuM6, **58**
- Maidecchi, G.: EL+TF+BI+AS+EM+SS-MoA8,
33
- Majer, M.: EM-TuA11, 87
- Majeski, M.: EN-ThP3, **247**
- Majkic, G.: EN+TF-TuA8, 88
- Majzik, Z.: ET+SS+GR+SP-FrM5, **271**;
ET+SS+GR+SP-ThA9, 230;
SP+AS+BI+ET+MI+NS-TuA4, 101
- Mak, T.: EM-ThM5, 196
- Makabe, T.: PS+EM-MoM10, 19
- Maksymovych, P.: NS+AS+SS+SP-WeM11, 146;
SS-WeM4, 154
- Malgorzata, J.: TF-ThP1, 263
- Malinowski, A.: PS1-TuM5, 71; PS2-WeA3, **180**
- Malko, A.V.: EL+TF+BI+AS+EM+SS-MoA2, 32;
EN+TF-WeA7, 168
- Mallik, S.: BI-TuP7, 117
- Malocsay, C.: EW-WeL2, **163**
- Malyshev, O.B.: VT-TuM1, **79**
- Mamun, M.A.: VT-MoM5, 26; VT-TuP16, **133**
- Manandar, B.: AS-WeM6, 135
- Manandhar, S.: OX-TuP6, 122
- Mancheno-Posso, P.L.: EM-ThP16, **246**
- Mancini, D.C.: NS+SP-MoA11, 44
- Mangham, A.N.: SS+OX-WeM5, 152
- Manini, P.: EW-TuA5, 89; VT-TuM12, 81
- Mankelevich, Y.: PS1-ThM2, 208
- Mankey, G.J.: MI+OX-WeA12, **176**
- Mann, H.S.: TF+EN-MoA7, 54
- Mann, J.: GR-ThP8, 251; SS-WeA1, 185
- Mann, W.: NS-ThM6, 207
- Mannequin, C.: TF+AS-WeA12, 189
- Manno, M.: EN+TF-MoA8, 36; EN+TF-MoA9, 36
- Manoharan, E.A.: MI+OX-WeA12, 176
- Mansour, A.N.: GR+AS+NS+SS-ThM10, 202
- Mao, B.: IS+AS+SS+EN-TuM4, 66
- Marchack, N.: PS1-ThM11, **209**
- Marchman, K.R.: TR+BI-TuM10, 79; TR-TuA3,
107
- Marcott, C.: SP+AS+BI+ET+MI+TF-WeA9, 183
- Marder, S.R.: SS-TuP14, 126
- Margarella, A.: SS+NS-TuA3, 103; SS-ThA1, 237;
SS-ThA2, **237**
- Mari, D.: VT-MoA1, 54
- Maria, J.-P.: TF+AS-TuA12, 105
- Mariani, R.D.: AC+EN-TuM1, 57
- Marić, D.: MB+BI-ThA4, 232
- Marichy, C.: TF+NS+EM-ThM9, **219**
- Marinella, M.: ET+NS+EM-ThM10, 200
- Marot, L.: PS2-WeA1, 180
- Marquardt, A.E.: TF-MoM3, **24**
- Marquis, E.A.: AS+NS+SS+TF-WeA1, **164**
- Marshall, C.: TF+EN-MoA1, 53
- Marsillac, S.: EL+TF+AS+EM+SS+PS+EN+NM-
MoM1, 6; EL+TF+AS+EM+SS+PS+EN+NM-
MoM4, 7
- Marti, F.: VT-TuA3, 108; VT-TuP6, 132
- Martin, F.: EM+TF+OX+GR-MoA9, 35
- Martin, R.L.: AC+MI+SS+TF-MoM3, **2**
- Martin, R.M.: PS2-TuM6, **73**; PS-MoM6, 20
- Martin, R.W.: AC+TF+SS+MI-MoA9, 29
- Martinez de Olcoz Sainz, L.: TR+SE-WeM4, 159
- Martinez, E.: EM+TF+OX+GR-MoA9, **35**; NS-
ThM10, 207
- Martinez, H.P.: BN+AS-WeA3, 165
- Martinez, J.: OX-TuP4, **122**
- Martinez, L.: PS1-TuM4, 71
- Martini, A.: SE+NS-MoA1, 49
- Martirez, J.: SS+OX-WeM10, 153
- Masahara, M.: EM-ThM1, **195**
- Mascarenhas, A.: MI+SP+AS-ThM12, 206
- Mashedor, B.: SS-ThM1, 213
- Masini, F.: SS-ThM5, 214
- Masters, A.E.: TF+EN-MoA7, 54
- Mastrangelo, A.M.: PS+TC-WeM5, 147
- Mastro, M.A.: EM+TF+AS-ThA6, 225; SS+EM-
WeA1, 184; TF+NS+EM-ThM1, 218
- Mathias, A.D.: MN-MoA6, 39; MN-TuM6, 67
- Mathieu, P.: NS+SP-MoA7, 43
- Matos, J.: SS-TuP27, **128**
- Matsubayashi, A.: GR+AS+EM+NS+SS-WeA7,
170
- Matsuda, A.: PS-MoM10, 21
- Matsugai, H.: PS-ThP14, 257
- Matsui, K.: TF-ThP12, 264
- Matsukawa, T.: EM-ThM1, 195
- Matsumoto, H.: PS-MoM2, 20
- Matsumoto, K.: ET+NS+EM-ThM5, **199**
- Matsumoto, S.: SS-ThA10, 238
- Matsunaga, S.: BI+SS+NS-WeM11, 138
- Matsuo, J.: AS-ThM9, **193**
- Matsushima, K.: EN-ThP6, **247**
- Matsushita, S.Y.: SS-MoA10, 53
- Matsuura, G.: PS-MoM2, 20
- Matthews, O.: TR+SE-WeM10, 160
- Mattrey, R.F.: BN+AS-WeA3, 165
- Mattson, E.: AS-WeM6, 135;
GR+AS+NS+SP+SS-TuA2, 90; SS-TuP3, **124**
- Mau, X.: EM+OX-WeA1, 167
- Maucher, H.P.: PS1-WeA11, 179
- Mavrikakis, K.: EM-TuA10, 87
- Mavrikakis, M.: SS-MoA7, 52; SS-TuP1, 123
- Maxisch, M.: OX+SS+TF+MI-MoA11, 45
- Mayer, B.: SE+NS-MoM5, 22
- Mayrhofer, P.H.: SE+NS-MoM5, **22**; SE+NS-
MoM6, 22
- Maziarz, E.P.: AS-TuP19, 114
- Mazzio, K.: ET+SS+GR+SP-ThA11, 230
- McArthur, S.L.: MB+BI-ThA4, 232; MB+BI-
ThM3, 203
- McBreen, P.H.: SS-ThM5, 214
- McCleskey, T.M.: IS+AS+OX+ET-WeM3, 144
- McClimon, J.B.: EM+NS-FrM6, 268; EN-ThP1,
246
- McClory, J.W.: AC+TF+SS+MI-MoA1, **28**;
AC+TF+SS+MI-MoA7, 29
- McCormack, R.N.: MN-TuP6, **120**
- McDonald, K.: SS-MoA3, 51
- McEuen, P.L.: MN-TuM10, 68; MN-TuM11, 68
- McGuckin, T.: NS+EN-TuM6, 70
- McGuire, C.: GR+EM+ET+MS+NS-FrM3, 271
- McHale, S.R.: AC+TF+SS+MI-MoA1, 28
- McLean, K.M.: BI-MoM1, 4
- McLean, R.S.: TF-MoM10, 25
- McNamara, J.D.: EM+TF+AS-ThA4, **225**
- McNeilan, J.D.: GR+AS+NS+SP+SS-TuA11, 91
- McWilliams, A.: SE+PS-TuA3, 100
- Meagher, L.: BI-MoM5, **5**
- Medikonda, M.:
EL+TF+AS+EM+SS+PS+EN+NM-MoM9, 7

- Medina, A.A.: EL+TF+AS+EM+SS-TuP2, **118**
 Meererschaut, J.: TF-ThP1, 263
 Mehr, T.: SP+AS+BI+ET+MI+TF-WeA11, 183
 Mei, AR.B.: TF+NS+EM-ThM12, **220**
 Mei, W.N.: AC+TF+SS+MI-MoA1, 28
 Mei, Y.: BI-MoA11, **32**
 Meléndez-Lira, M.: NS-MoM2, 15; TF-ThP16, 265
 Meléndez-Lira, M.A.: TF-ThP8, **264**
 Melese, Y.G.: EL+TF+AS+EM+SS+PS+EN+NM-MoM6, 7
 Melitz, W.: AS-TuP21, 114
 Melton, A.G.: EM+TF+AS-ThA11, 226;
 EM+TF+AS-ThA9, 226
 Melvin, T.: SE+NS-MoA3, 50
 Melzer, J.I.: TF-ThP5, 263
 Membreno, D.: EN+NS-ThM6, 198; EN+TF-WeA9, 168
 Mendes, G.P.: AS-TuP11, 113; BI+AS-TuA7, 84
 Mendez, N.: BI+SS+NS-WeM6, **137**
 Mendez, P.: BI-TuP3, **116**
 Meneghini, C.: AS-ThA7, 223
 Meng, G.W.: ET+NS+EM-ThM4, 199
 Meng, L.: PS-ThP36, 261; SE+PS-TuM3, 74;
 SE+PS-TuM4, **74**
 Menguelti, K.: PS-ThP5, 255; PS-ThP7, 256
 Menzel, D.: LB+EM+GR+MN+TR-WeA9, 174;
 SS+NS-TuA1, **102**
 Méolans, J.G.: MN-TuP1, 119
 Merchea, M.: AS-TuP19, 114
 Merckling, C.: EM+TF+OX+GR-MoA1, **34**
 Merrill, M.D.: IS+AS+OX+ET-WeM6, 144
 Merte, L.: SS-TuP25, 128; SS-TuP28, 129
 Meseck, G.R.: NS-ThP1, **252**
 Messer, B.: PS-MoM5, 20
 Metzler, D.: PS2-TuA1, **97**
 Mewes, K.A.: MI+EN+BI-TuA3, **93**
 Mewes, T.: EM+MI-ThA11, 224; MI+EN+BI-TuA3, 93; MI+OX-WeA2, 175
 Meyer III, H.M.: AS-TuP12, **113**;
 EM+TF+OX+GR-MoM9, 9
 Meyer, D.J.: EM+OX-WeA8, 167;
 GR+EM+ET+MS+NS-FrM5, 272
 Meyer, G.: SP+AS+BI+ET+MI+NS-TuA1, 101
 Meyer, H.M.: SS-WeM10, 155
 Meyer, J.R.: EM+TF+AS-ThA6, 225
 Meyer, R.L.: BI+AS-TuA3, 84
 Meyer, T.J.: EN+SS-FrM3, 269
 Mhatre, B.S.: SS-MoA6, **52**
 Miao, X.: GR+EM+ET+MS+NS-FrM11, **273**
 Michael, J.R.: AS-TuP5, 111
 Michalak, T.: EM-ThP8, **245**
 Michallon, P.: NM+NS+MS+EM-MoA6, 41
 Michelmore, A.: PS1-TuA4, **96**; PS-ThA8, 234
 Michely, T.W.: GR+AS+NS+SP+SS-TuA7, 90;
 GR+EM+NS+PS+SS+TF-MoM5, **11**
 Mickel, P.R.: ET+NS+EM-ThM10, **200**
 Mignot, S.: PS-ThP1, 255
 Mignot, Y.: PS2-TuM9, 73; PS-ThP1, **255**; PS-WeM1, 148; PS-WeM11, 150; PS-WeM4, 149
 Mihaila, B.: EM+NS-FrM11, 269
 Mikkelsen, A.: EM+MI-ThA6, 224; ET+NS+EM-ThM6, 199; SS+NS-ThA1, **235**
 Miller, C.W.: MI+SP+AS-ThM5, **205**; TF-ThP4, 263
 Miller, G.P.: SS-TuP4, 124
 Miller, I.: EW-WeL4, **163**
 Miller, J.: IS+AS+SS+EN-TuM9, 66
 Miller, J.B.: SS-WeA11, 186; TR+SE-WeM4, 159
 Miller, T.J.: EN+AS-ThA8, **228**
 Millunchick, J.M.: SS+EM-WeA2, 184; SS-TuP34, 130
 Milosavljevic, V.: PS1-TuM3, 71; PS1-WeA1, 178
 Milstrey, T.E.: SS-TuP23, 128
 Mily, E.: TF+AS-TuA12, 105
 Min, B.K.: PS+BI-MoA3, 46
 Min, G.J.: SE-TuP1, 122
 Min, H.: AS+BI-TuM5, 58
 Min, K.S.: PS-ThP28, **259**
 Minami, M.: PS-ThP14, 257
 Minami, T.: EN-ThP12, 249; EN-ThP7, **248**
 Minne, S.C.: SP+AS+BI+ET+MI+TF-WeA8, 183
 Minton, T.K.: SS-MoA1, 51
 Mirmelstein, A.: AC+MI+SS+TF-MoM9, 2
 Misra, S.: TR-TuA11, **108**
 Mistry, H.: SS-TuP28, **129**
 Mita, S.: EM+TF+AS-ThA1, 225
 Mitterer, C.: SE+NS-MoM6, 22; SE+NS-MoM9, **22**
 Miura, N.: PS+EM-MoM5, 19
 Miura, T.: TR-TuP2, 130; VT-TuP8, 132
 Miwa, H.: PS2-ThM4, 210
 Miwa, K.: MN-TuP4, **120**; PS2-ThM11, 211
 Miya, G.: PS-ThA1, 233
 Miyake, K.: PS2-TuA9, 98
 Miyake, M.: SS-TuP17, 127
 Miyamoto, J.: LB+EM+GR+MN+TR-WeA2, 173
 Miyamoto, K.: MI-WeM1, 145
 Miyashita, H.: GR+EM+NS+PS+SS+TF-MoM10, 12
 Miyata, T.: EN-ThP12, 249; EN-ThP7, 248
 Miyawaki, Y.: PS2-MoA7, 49; PS-ThP14, 257
 Miyazoe, H.: PS1-ThM12, **209**
 Mizotani, K.: PS2-TuA4, **98**; PS2-TuA9, 98
 Mleczko, M.: NS-ThP2, 253
 Mo, A.K.: SS-WeM10, 155
 Moberg, R.: AS+TF+VT-FrM7, 267
 Modine, N.A.: SS+EM-WeA2, 184; SS-TuP34, 130
 Moeller, R.: ET+SS+GR+SP-FrM7, **271**
 Moellers, R.: AS-MoA4, 29; AS-ThM11, 193; AS-WeM11, 136
 Mohan, P.: VT-MoA1, 54
 Mohn, F.: SP+AS+BI+ET+MI+NS-TuA1, 101
 Mohondro, R.: EW-WeA6, **170**
 Mohr, S.: EN+PS-WeM12, **142**; EN+PS-WeM9, 141
 Moisan, M.: PS+TC-WeM1, 147
 Molis, S.: EM-TuA8, 86
 Molkenboer, F.T.: HI+AS+NS-WeA9, 172; PS-ThA9, 234; PS-ThP15, **257**
 Moll, N.: SP+AS+BI+ET+MI+NS-TuA1, 101
 Mönig, H.: SP+AS+BI+ET+MI+NS-TuA10, 102
 Montgomery, A.M.: TF+EM+SE+NS-ThM4, 217
 Monton, C.M.: AS+TF+VT-FrM2, 266
 Monya, Y.: IS+AS+SS+EN-TuM12, 67
 Moody, B.: EM+TF+AS-ThA1, 225
 Moon, B.N.: PS-ThA10, 235; PS-ThP33, 260; PS-ThP35, 261
 Moon, D.W.: BI-TuP5, 116; BP+AS-SuA1, **1**
 Moon, J.S.: GR+EM+ET+MS+NS-FrM3, **271**;
 GR+EM+NS+PS+SS+TF-MoM1, 10
 Moon, K.: MI+OX-WeA7, 175
 Moon, S.Y.: PS2-WeA11, 182
 Moore, J.F.: BN+AS-WeA12, 166
 Moore, R.: EM+TF+OX+GR-MoM3, 8;
 GR+AS+NS+SP+SS-TuA11, 91
 Moore, T.M.: NS+SP-MoA4, 43
 Morales, C.: NS-MoM9, 16
 Morales, E.: SS+OX-WeM10, **153**
 Mordi, G.: GR+EM+ET+MS+NS-FrM7, 272
 Morgan, G.: VT-TuA3, 108; VT-TuP6, 132
 Morgante, A.: SS+OX-WeM6, 152
 Morgen, P.: EM+NS-FrM4, 267; EM+SS+AS+NS-ThM3, **194**; EN-ThP5, 247
 Mori, T.: PS-MoM5, 20
 Morita, S.: SP+AS+BI+ET+MI+NS-TuA11, 102
 Morita, Y.: PS-ThP13, **257**
 Moroz, P.: PS-ThP3, **255**
 Morra, M.M.: TF-ThP5, 263
 Morris, B.G.: PS2-TuM6, 73; PS2-TuM9, 73; PS-ThP1, 255; PS-WeM1, 148; PS-WeM11, 150
 Morrish, F.: BN+AS-WeA4, 165
 Morrish, R.: EN+TF-MoA10, 36
 Moshar, A.: EW-TuM8, 64;
 SP+AS+BI+ET+MI+TF-WeA11, **183**
 Moss, G.: BN+AS-WeA10, 166
 Mostafa, S.: SS-TuP27, 128
 Mota-Pineda, E.: TF-ThP8, 264
 Moulder, J.F.: AS-ThA3, 222; EN+AS-ThA4, 227;
 EW-TuL5, **82**
 Mousa, M.B.: NM+NS+MS+EM-MoA8, **41**
 Mowll, T.: GR+EM+NS+PS+SS+TF-MoM2, 11
 Mráz, S.: SE+NS-MoM8, 22
 Mucha, J.A.: PS1-TuA10, 96
 Mücklich, A.: SE+NS-MoM2, 21
 Muir, B.W.: BI-MoM1, **4**
 Muirhead, L.: IS+AS+BI+ET+GR+NS-TuA3, 92
 Mukherjee, D.: EN+NS-MoM6, 10; MI+OX-WeA9, **176**; OX+EM+MI+NS+TF-MoM1, 17
 Mukherjee, P.: EN+NS-MoM6, 10; MI+OX-WeA9, 176; OX+EM+MI+NS+TF-MoM1, 17
 Mukherjee, T.: PS-WeM5, 149
 Mulhollan, G.A.: VT-MoM3, **25**
 Mullet, C.: NS-ThM6, 207; SS+NS-ThA6, 236
 Mullins, D.R.: SS-TuM11, 76
 Mulvaney, S.P.: GR-ThP9, 251
 Mumcu, G.: TF-MoM8, 25
 Munakata, T.: SS-TuP31, 129
 Muñoz-Flores, J.: AS-TuP16, **113**
 Munson, A.: GR+AS+NS+SP+SS-TuA11, 91
 Munusamy, P.: AS+BI-TuA12, 84; BI-TuP9, **117**
 Murakami, Y.: PS-ThP6, 256
 Muratore, C.: SE+NS-MoA1, 49; SE-TuP3, 123;
 TR+SE-WeM1, **159**
 Murphy, C.J.: EM+SS+AS+NS-ThM9, **194**
 Murphy, N.R.: SE+PS-TuM9, **75**; TF+AS+SS-ThA10, 240
 Murphy, P.J.: PS1-TuA3, 95
 Muscat, A.J.: EM+TF-WeM6, **139**; EM-ThP16, 246; TF-TuM6, 77
 Music, D.: SE+NS-MoM8, 22
 Müthing, J.: AS-TuP1, 111
 Muthinti, G.R.:
 EL+TF+AS+EM+SS+PS+EN+NM-MoM9, 7;
 NM+AS+MS-MoM3, **14**
 Mutombo, P.: SP+AS+BI+ET+MI+NS-TuA4, 101
 Mutoro, E.: IS+AS+SS+EN-TuM5, 66
 Muzzillo, C.: EN+TF-TuM10, **63**
 Myers-Ward, R.L.: GR+AS+BI+PS+SS-WeM9, 143; GR+AS+NS+SP+SS-TuA9, 90;
 GR+EM+ET+MS+NS-FrM3, 271;
 GR+EM+ET+MS+NS-FrM5, 272;
 GR+EM+ET+NS+TF-MoA1, **37**;
 GR+EM+NS+PS+SS+TF-MoM1, 10;
 GR+EM+NS+PS+SS+TF-MoM3, 11; GR-ThP9, 251
 — N —
 Na, J.H.: NS-ThP6, 253
 Nabok, A.V.: NS+SP-MoA1, 42
 Nachimuthu, P.: EN-ThP10, 248; OX-TuP6, 122;
 SS-TuP26, 128; TC+EM+AS+TF+EN-ThM5, 216
 Nadzeyka, A.: LB+EM+GR+MN+TR-WeA7, 173
 Naes, B.E.: AS+NS+SS+TF-WeA7, 164
 Nagaiah, P.: EM+TF+OX+GR-MoM3, 8
 Nagano, S.: HI+AS+BI+NS-ThM12, 203
 Nagareddy, V.K.: GR+EM+NS+PS+SS+TF-MoM1, 10
 Nagata, M.: VT-MoM1, 25
 Nagorny, V.: PS2-TuM10, 73; PS-ThA11, **235**
 Nahif, F.: SE+NS-MoM8, 22
 Naik, R.R.: GR+AS+BI+PS+SS-WeM6, 143
 Nain, A.S.: BI-TuP10, 117
 Naitoh, Y.: PS2-ThM3, 210
 Najmaei, S.: GR+EM+NS+SS+TF-ThA3, 231
 Nakabayashi, D.: MN-TuP9, **121**
 Nakagawa, S.: AS-ThM9, 193
 Nakajima, A.: SS-TuP18, 127
 Nakajima, H.: PS-ThP34, 260
 Nakajima, S.: SS-MoA8, 52
 Nakajima, T.: SS-TuP7, **125**
 Nakakubo, Y.: PS-MoM10, 21
 Nakamura, G.: PS-ThP34, 260
 Nakamura, I.: SS-TuP29, 129; SS-TuP30, **129**
 Nakamura, J.: GR+AS+EM+NS+SS-WeA12, 171;
 SS-TuP8, 125
 Nakamura, K.: PS1-WeA3, 178

- Nakamura, M.: PS-MoM2, 20; PS-WeM10, 150
 Nakamura, S.: PS-WeM4, 149
 Nakano, Y.: EN+TF-TuA12, 89
 Nakatsujii, K.: GR+AS+NS+SS-ThM1, 201
 Nakayama, D.: PS-MoM6, 20
 Nakazaki, N.: PS2-TuA10, 98
 Nam, S.H.: VT-TuP11, 132; VT-TuP12, 133; VT-TuP13, 133; VT-TuP14, 133
 Nampoori, V.: EN+TF-WeA11, 169
 Nanayakkara, S.: NS-WeA1, 177;
 SP+AS+BI+ET+MI+TF-WeA4, 183
 Nandasiri, M.L.: OX-TuP6, 122
 Narayanan, S.: TC+EM+AS-WeA9, 188
 Narayanan, V.: EM+TF+OX+GR-MoA7, 35
 Narishige, K.: PS-ThP12, 257
 Nasir, A.N.: EM+OX-WeA12, 168
 Nasse, M.: GR+AS+NS+SP+SS-TuA2, 90
 Natarajarathinam, A.: TF+MI-WeA3, 190;
 TF+SE+NS-WeM10, 157
 Nath, A.: GR+EM+ET+MS+NS-FrM5, 272;
 GR+EM+ET+NS+TF-MoA1, 37;
 GR+EM+NS+PS+SS+TF-MoM1, 10;
 GR+EM+NS+PS+SS+TF-MoM3, 11
 Nathanson, G.M.: SS-MoA1, 51
 Naudé, N.: PS+BI-MoA10, 47; PS+BI-MoA11, 47
 Nayfeh, O.: GR+EM+ET+MS+NS-FrM8, 272
 Nayyar, N.: NS-WeA9, 177
 N'Diaye, A.T.: GR+AS+EM+NS+SS-WeA10, 171
 Neal, C.: BI-TuP11, 117
 Nedrygailov, I.: SS-MoM2, 23; SS-MoM3, 23; SS-TuP24, 128
 Nefedov, A.: GR-ThP3, 249; OX+SS+TF+MI-MoA10, 45
 Negreiros, F.R.: SS+OX-WeM12, 153
 Nelin, C.J.: SS+OX-WeM9, 153
 Nelson, A.J.: AC+EN-TuM10, 57; AC+EN-TuM3, 57
 Nelson, C.M.: EL+TF+BI+AS+EM+SS-MoA9, 33
 Nelson, F.J.: GR+AS+NS+SP+SS-TuA11, 91
 Nemani, S.D.: PS2-TuM2, 72
 Nepal, N.: EM+TF+OX+GR-MoM9, 9;
 GR+EM+ET+NS+TF-MoA1, 37; TF+NS+EM-ThM1, 218
 Netzer, F.P.: SS+OX-WeM12, 153
 Neunzehn, J.: BI-TuP12, 118
 Newbury, J.S.: EM+NS-FrM10, 268
 Ney, A.: SS+OX-WeM5, 152
 Ney, V.: SS+OX-WeM5, 152
 Ng, A.: EM+TF-WeM6, 139
 Nguyen, H.M.: EL+TF+BI+AS+EM+SS-MoA2, 32; EN+TF-WeA7, 168
 Nguyen, S.: TF+EN-MoA1, 53
 Nichols, M.T.: EM-ThP10, 245; EM-ThP11, 245;
 EM-TuA10, 87; PS-ThA10, 235
 Nie, X.W.: OX-TuP1, 122
 Niehuis, E.: AS-MoA4, 29; AS-ThM11, 193; AS-WeM11, 136
 Nienhaus, H.: SS-MoM5, 23
 Nieto-Zepeda, K.E.: TF-ThP8, 264
 Nigge, P.: IS+AS+BI+ET+GR+NS-TuA9, 93
 Nijem, N.: EN+AS-ThA7, 228; IS-TuP2, 119
 Nikitin, V.: MI+OX-WeA7, 175
 Ninomiya, S.: AS-ThM12, 193; AS-TuP6, 112
 Nishi, H.: SS-TuP32, 129
 Nishi, Y.: EM-ThP10, 245; EM-ThP11, 245; EN-ThP12, 249; PS-ThA10, 235; PS-ThP35, 261
 Nishimori, Y.: MN-TuP4, 120
 Nishimoto, S.: SS-TuP17, 127
 Nishizuka, T.: PS-ThP34, 260
 Nisol, B.: SE+PS-TuA9, 100
 Niu, C.: PS-WeM11, 150
 Noborisaka, M.: SE-TuP2, 123
 Noei, H.: OX+SS+TF+MI-MoA10, 45
 Noh, J.: TC-ThP4, 262
 Noh, J.H.: TC-ThP4, 262
 Nomoto, J.: EN-ThP7, 248
 Nonnenmann, S.S.: SP+AS+BI+ET+MI+TF-WeA3, 183
 Notestein, J.: TF+EN-MoA1, 53
 Notingher, I.: BN+AS-WeA1, 165
 Notte, J.: HI+AS+NS-WeA10, 172
 Noufi, R.: EN+AS-ThA1, 227
 Novak, J.: SP-TuP1, 123
 Novak, S.: EM+TF+OX+GR-MoM3, 8
 Novikova, I.: TF+AS+SS-ThA8, 240
 Novoselov, K.: GR+AS+BI+PS+SS-WeM2, 142
 Nozaki, T.: EN+PS-WeM1, 140
 Nozawa, T.: PS2-MoA11, 49
 Nozik, A.J.: EN+NS-MoM3, 9
 Ntwaeaborwa, O.M.: SS+OX-WeM11, 153
 Nunney, T.: EW-TuL2, 82
 Nunney, T.S.: AS+BI-TuM11, 59; AS-MoA2, 29;
 EW-TuL3, 82; GR-ThP1, 249
 Nyakiti, L.O.: GR+AS+BI+PS+SS-WeM9, 143;
 GR+AS+NS+SP+SS-TuA9, 90;
 GR+EM+ET+MS+NS-FrM3, 271;
 GR+EM+ET+MS+NS-FrM5, 272;
 GR+EM+ET+NS+TF-MoA1, 37;
 GR+EM+NS+PS+SS+TF-MoM1, 10;
 GR+EM+NS+PS+SS+TF-MoM3, 11; GR-ThP9, 251
 Nyns, L.: LB+EM+GR+MN+TR-WeA12, 174
 — O —
 Oates, T.W.H.: SE+NS-MoM2, 21
 Obama, S.: PS-ThA1, 233
 Obare, S.: NM+AS+MS-MoM8, 15
 O'Brien, C.J.: TF+AS-TuA7, 105
 O'Brien, K.E.: NS-WeA2, 177
 Ocola, L.E.: NS+SP-MoA10, 44
 O'Connor, S.: EM+TF+AS-ThA6, 225
 Oda, S.: NS+EN-TuM5, 70
 Oden, M.: TF+NS+EM-ThM12, 220
 Odén, M.: TF+NS+EM-ThM11, 219
 O'Donnell, K.P.: AC+TF+SS+MI-MoA9, 29
 Oehrling, G.S.: PS+BI-MoA2, 46; PS+BI-MoA6, 46; PS2-TuA1, 97; PS2-WeA11, 182
 Oehzelt, M.: GR-ThP3, 249
 Oezkaya, B.: TF+AS+SS-ThA1, 238
 Offermanns, V.: BI-MoM11, 6
 Offi, F.: AC+TF+SS+MI-MoA3, 28; AS-ThA10, 223
 Ogaki, R.: BI+AS-TuA3, 84; BI+SS+NS-WeM1, 136; BI-MoM2, 5
 Ogino, T.: GR-ThP5, 250
 Ogitsu, T.: IS+AS+OX+ET-WeM6, 144
 Oh, D.-H.: GR-ThP6, 250; NS+EN-TuM1, 69;
 SS+NS-ThA3, 235
 Oh, J.S.: ET-ThP1, 249
 Oh, Y.: TC+EM+AS-WeA7, 187
 Ohkouchi, T.: GR+EM+NS+PS+SS+TF-MoM10, 12
 Ohldag, H.: GR+AS+EM+MI+MN-TuM9, 65
 Ohlhausen, J.A.: AS-TuP5, 111
 Ohmi, H.: PS+TC-WeM3, 147; SE+PS-TuA8, 100
 Ohno, S.: SS-MoA9, 52
 Ohsawa, Y.: PS-ThP34, 260
 Ohsiek, S.: EM-TuA11, 87
 Ohta, T.: GR+AS+NS+SP+SS-TuA8, 90
 Ohtake, A.: SS-TuP8, 125
 Ohtake, H.: PS-ThP34, 260; PS-ThP8, 256
 Ohtsuka, S.: PS2-ThM9, 211
 Ohuchi, F.S.: TC+EM+AS+TF+EN-ThM11, 216
 Okamoto, M.: PS-ThP6, 256
 Oktyabrysky, S.: EM+TF+OX+GR-MoM3, 8
 Okuda, T.: EM+TF+AS-ThA12, 226
 Oldham, C.J.: NM+NS+MS+EM-MoA8, 41; TF2-TuA7, 106
 O'Leary, L.E.: EM+TF-WeM12, 140
 Oleson, B.: EM-ThP15, 246
 Oleynik, I.I.: ET+SS+GR+SP-ThA4, 229;
 GR+AS+EM+MI+MN-TuM10, 65;
 GR+AS+EM+NS+SS-WeA2, 170
 Olmstead, M.A.: TC+EM+AS+TF+EN-ThM11, 216
 Olson, A.: SP-TuP1, 123
 Olson, A.G.: PS-ThP35, 261
 Olson, D.: AS-TuP18, 113
 Olson, D.A.: VT-MoM6, 26
 Omberg, R.P.: AC+EN-TuM1, 57
 Ondeck, N.: SS-ThM2, 214
 Ondracek, M.: ET+SS+GR+SP-FrM4, 270;
 SP+AS+BI+ET+MI+NS-TuA4, 101
 Ondráček, M.: ET+SS+GR+SP-FrM5, 271
 Ong, P.: MN-TuM11, 68
 Ong, S.W.: SS+EN+OX-ThM4, 212
 Onishi, K.: HI+AS+BI+NS-ThM12, 203
 Ono, K.: PS2-ThM9, 211; PS2-TuA10, 98; PS2-TuA12, 99; PS-MoM10, 21
 Ono, L.K.: SS-TuP27, 128
 Oppen, F.V.:
 SP+AS+BI+ET+MI+NM+NS+SS+TF-WeM4, 150
 Ortiz, V.: SS-TuP10, 126
 Osgood, R.M.: SS+NS-TuA4, 103; SS-TuP2, 124
 Oshima, M.: GR+AS+EM+NS+SS-WeA12, 171
 Osma, J.F.: BI-TuP6, 116
 Osofsky, M.: EM+MI-ThA11, 224
 Ossowski, J.: TF+AS+SS-ThA2, 239
 Ostrikov, K.: TF+EM+SE+NS-ThM1, 216
 Otani, T.: SS-ThM12, 215
 Ou, Y.-C.: NS-ThP7, 254
 O'uchi, S.: EM-ThM1, 195
 Outlaw, R.A.: GR+AS+NS+SS-ThM10, 202
 Ouyang, W.: ET+NS+EM-ThM3, 199
 Ouyang, Z.: PS-ThP36, 261
 Overzet, L.J.: PS+EM-MoM3, 18
 Owen, A.G.: TF+EM+SE+NS-ThM4, 217
 Ozcan, A.: EM+NS-FrM9, 268
 Ozimek, P.: EW-WeL5, 163
 — P —
 Pachauri, N.: MI+OX-WeA12, 176
 Pacholski, M.L.: AS+NS+SS+TF-WeA9, 165
 Paddy, R.P.: TF+NS+EM-ThM5, 218; TF2-TuA10, 107; TF-TuM9, 78
 Page, S.J.: AS+NS+SS+TF-WeA8, 164; AS-ThM1, 192
 Pai, W.W.: LB+EM+GR+MN+TR-WeA8, 173
 Paiella, R.: EM+SS+AS+NS-ThM1, 194
 Pal, S.: NS-MoM9, 16
 Palai, R.: AC+TF+SS+MI-MoA1, 28
 Palmans, J.: PS2-WeA9, 181
 Palmer, J.A.: TF-TuM9, 78
 Palmstrom, C.: EM+MI-ThA6, 224
 Palmström, C.: EM+MI-ThA10, 224
 Palomares Linares, J.M.: PS1-WeA7, 179
 Palombo, E.: MB+BI-ThA4, 232
 Palomino, R.: NS+AS+SS+SP-WeM12, 147
 Pan, H.B.: SS+NS-TuA11, 104
 Pan, M.H.: SP+AS+BI+ET+MI+NS-TuA12, 102;
 SS-WeM4, 154
 Pan, X.: SS+OX-WeM1, 152
 Pan, Y.H.: SS+NS-TuA11, 104
 Panaccione, G.: AC+TF+SS+MI-MoA3, 28; AS-ThA10, 223
 Pande, K.: SS-TuP3, 124
 Pandey, A.: NS-WeA10, 178; PS1-WeA3, 178;
 TC+EM+AS+TF+EN-ThM5, 216
 Pandey, R.R.: NS-MoM11, 17
 Paniagua, S.A.: SS-TuP14, 126
 Pantelides, S.T.: ET+SS+GR+SP-FrM1, 270
 Paolini, C.: VT+AS+SS-WeM3, 161
 Pappas, D.: PS+TC-WeM12, 148
 Pargon, E.: PS2-TuM2, 72; PS-ThP5, 255; PS-ThP7, 256
 Paris, A.: GR-ThP3, 249
 Park, B.: PS+BI-MoA3, 46
 Park, C.: AS-ThA10, 223
 Park, C.D.: VT-TuP10, 132; VT-TuP7, 132
 Park, C.M.: MI+OX-WeA7, 175
 Park, C.-Y.: GR+EM+NS+PS+SS+TF-MoM4, 11;
 GR-ThP6, 250; NS+EN-TuM1, 69; SS+NS-ThA3, 235
 Park, D.-G.: EM+NS-FrM10, 268
 Park, H.: NS+AS+SS+SP-WeM12, 147
 Park, J.: PS2-ThM5, 210; SS-ThM1, 213; SS-TuP31, 129
 Park, J.B.: PS+TC-WeM9, 148; PS-ThP27, 259

- Park, J.G.: EM+OX-WeA7, 167
 Park, J.H.: EN+NS-MoM1, 9; SS-ThM11, **215**
 Park, J.-H.: GR+EM+NS+PS+SS+TF-MoM11, **12**
 Park, J.-H.: NS-ThP9, 254
 Park, J.W.: ET-ThP1, **249**
 Park, J.Y.: SS-MoM1, **23**
 Park, K.H.: EN-ThP4, 247
 Park, M.L.: PS-ThP23, 258
 Park, T.H.: NS-WeA1, 177
 Park, Y.: EM+OX-WeA11, 168; PS-ThP1, 255
 Park, Y.D.: MI-ThP5, **252**
 Park, Y.J.: BI-TuP5, **116**; PS-WeM4, 149
 Parkin, J.D.:
 SP+AS+BI+ET+MI+NM+NS+SS+TF-WeM9, 151; SP+AS+BI+ET+MI+TF-WeA7, **183**
 Parks, C.: EM-TuA8, 86
 Parpia, J.M.: MN-MoA1, **38**; MN-TuM10, 68; MN-TuM11, 68
 Parracino, M.A.: NS+EN+GR-TuA2, **94**
 Parsons, G.N.: EN+NS-ThA1, 228; EN+SS-FrM1, 269; EN+SS-FrM3, 269; NM+NS+MS+EM-MoA8, 41; NS+EN+GR-TuA10, 95; TF+EN-MoA8, 54; TF2-TuA1, 106; TF2-TuA7, 106
 Parthasarathy, A.: MB+BI-ThM9, 204
 Pascual, J.L.:
 SP+AS+BI+ET+MI+NM+NS+SS+TF-WeM4, 150
 Pasic, P.: BI-MoM5, 5; BI-MoM6, 5
 Pastewka, L.: TR-TuA1, 107
 Patel, A.: EN+AS-ThA6, **227**
 Patel, A.K.: BI-MoA4, **31**
 Patel, R.: PS1-TuA7, **96**
 Patel, S.: EM+MI-ThA10, **224**
 Paterson, A.: PS-MoM11, 21
 Patil, S.: PS-WeM11, 150
 Patscheider, J.: SE+PS-TuM5, **75**
 Pattanaik, G.: EN+NS-ThM9, **198**
 Patzke, G.R.: NS-ThP1, 252
 Paul, D.F.: NS-ThM12, 207
 Paul, P.: NS+SP-MoA2, 42
 Paul, W.: AS-WeM11, 136
 Paulitsch, J.: SE+NS-MoM5, 22
 Payzant, E.A.: EN+TF-TuM10, 63
 Pearton, S.J.: EM-ThP1, 244; EM-ThP2, 244; EM-TuM9, 62
 Peck, J.: EN-ThP11, **248**
 Peckerar, M.: EM+OX-WeA9, 167
 Pedersen, K.: EM+NS-FrM4, 267
 Pegalajar-Jurado, A.: MB+BI-ThM3, **203**
 Pei, D.: EM-ThP10, 245; EM-ThP11, **245**
 Pei, L.: LB+EM+GR+MN+TR-WeA3, **173**
 Peixoto, T.: SS+EM-WeA11, **185**; SS-TuP21, 127; TF+AS+SS-ThA3, 239
 Pelant, I.: NS-MoM5, 15
 Pelissier, B.: NM+NS+MS+EM-MoA6, 41
 Pellemounter, D.: PS-ThP39, **261**
 Pelster, A.: AS-TuP1, 111
 Peng, G.: SS-MoA7, 52; SS-TuP1, 123
 Peng, Q.: EN+SS-FrM3, **269**
 Peng, W.: EM+TF-WeM4, **139**; EN+TF-WeA7, 168
 Perdue, S.M.: SP+AS+BI+ET+MI+NS-TuA3, 101
 Perea, D.E.: AS+NS+SS+TF-WeA3, 164; AS+NS+SS+TF-WeA4, 164; NS-WeA10, 178
 Pereira, L.: AC+TF+SS+MI-MoA6, 28
 Pereira, S.: BI-MoM5, 5
 Perera, A.G.U.: EM+TF+AS-ThA9, 226; EM-ThP6, 244
 Peres, P.: IS+AS+OX+ET-WeM11, 145
 Perez Medina, G.J.: GR+EM+ET+NS+TF-MoA7, 37
 Pérez Quintero, K.J.: MN+AS-MoM3, 12
 Perez Roldan, M.J.: NS+EN+GR-TuA2, 94
 Perez, R.: SP+AS+BI+ET+MI+NS-TuA10, 102; SP+AS+BI+ET+MI+NS-TuA11, **102**
 Perez, V.P.: BI-TuP8, 117
 Perkins, F.K.: TF+AS-TuA3, 104
 Perng, Y.-C.: EM+TF+AS-ThA3, 225; EN+NS-ThM6, **198**
 Pernites, R.B.: EN+NS-ThM12, 198
 Perrenoud, J.: TF+AS-WeA3, 188
 Perret, E.: IS+AS+OX+ET-WeM3, 144
 Perrier, P.: MN-TuP1, 119
 Perrine, K.A.: AS-TuP20, 114; SS-ThA1, **237**; SS-ThA2, 237; SS-WeM11, 155
 Perriot, R.: GR+AS+EM+MI+MN-TuM10, 65
 Perry, J.W.: SS-TuP14, 126
 Perry, S.S.: BI+AS-TuA10, 85; TR+BI-TuM2, **78**; TR+SE-WeM5, 159; TR-TuA7, 107
 Persson, O.: ET+NS+EM-ThM6, 199
 Pertsin, A.J.: BI+SS+AS-TuM2, 59
 Pesin, D.: EM+OX-WeA1, 167
 Petaccia, L.: AC+TF+SS+MI-MoA3, 28; GR-ThP3, 249
 Petersen Barbosa Lima, L.: EM-ThP7, **244**
 Petersen, E.: NS+AS+SS+SP-WeM2, 146
 Peterson, B.: NM+AS+MS-MoM3, 14
 Peterson, K.: PS-ThA4, 234
 Petford-Long, A.: IS+AS+BI+ET+GR+NS-TuA7, 92
 Pethe, S.: EN+TF-TuM11, 63; TF+AS-WeA11, 189
 Petrik, N.G.: SS+EN+OX-ThM3, 212; SS+EN+OX-ThM5, 212; SS-TuM5, 76; SS-TuM6, **76**
 Petrosky, J.C.: AC+TF+SS+MI-MoA1, 28; AC+TF+SS+MI-MoA7, 29
 Petrov, I.: TF+AS-TuA4, 104; TF+NS+EM-ThM12, 220
 Petrovykh, D.Y.: AS-TuP11, 113; BI+AS-TuA7, **84**
 Petterson, M.K.: GR+EM+ET+MS+NS-FrM11, 273
 Pettit, C.: EN+TF-TuM9, 63
 Pfeiffer, D.: EM+NS-FrM10, 268
 Pham, C.D.: TF+NS+EM-ThM6, **218**
 Pham, H.: TC+EM+AS+TF+EN-ThM11, **216**
 Pham, T.: PS2-TuM2, 72
 Phan, M.H.: MI-ThP2, 252; NS-MoM8, 16; NS-MoM9, 16
 Phaneuf, M.W.: HI-ThP3, 252
 Phaneuf, R.J.: TF+EM+SS-ThA10, 242; TF-MoM3, 24
 PhanVu, H.: PS2-TuM10, 73
 Phillpot, S.R.: EN+SS-FrM6, 270; OX+SS+TF+MI-MoA1, 44; OX-TuP1, 122; OX-TuP3, 122; OX-TuP4, 122; SS+NS-ThA4, 236; TR+BI-TuM10, 79; TR-TuP1, 130
 Piallat, F.: NM+NS+MS+EM-MoA6, **41**
 Piao, H.: AS+BI-TuM12, **59**; AS+TF+VT-FrM1, 266
 Pierce, C.C.: TF-ThP5, 263
 Pillatsch, L.: HI+AS+NS-WeA10, 172
 Pimenta-Barros, P.: PS2-TuM5, 73
 Pinna, N.: TF+NS+EM-ThM9, 219
 Pioda, A.: EW-TuL6, 82
 Pipe, K.P.: EM+SS+AS+NS-ThM13, 195
 Pireaux, J.J.: AS-MoA2, 29
 Pitenis, A.A.: TR-TuA9, **107**
 Pittenger, B.: SP+AS+BI+ET+MI+TF-WeA8, 183
 Pitters, J.: SP+AS+BI+ET+MI+NM+NS+SS+TF-WeM2, 150
 Pitters, J.L.: HI+AS+NS-WeA7, 172
 Piva, P.: SP+AS+BI+ET+MI+NM+NS+SS+TF-WeM2, 150
 Plaeue, J.: AC+EN-TuM10, 57
 Pleticha, D.: EN-ThP3, 247
 Pluchery, O.: EM+NS-FrM3, 267
 Pluntze, A.M.: TR+SE-WeM12, 160
 Poda, A.: TR+SE-WeM10, 160
 Podkolzin, S.: SS-WeA10, 186
 Podraza, N.J.: EL+TF+AS+EM+SS+PS+EN+NM-MoM1, 6; EL+TF+AS+EM+SS+PS+EN+NM-MoM4, 7
 Poelker, M.: VT-MoM5, 26; VT-TuP16, 133
 Poelsema, B.: HI+AS+NS-WeA3, **171**
 Poepplmeier, K.: TF+EN-MoA1, 53
 Pohl, K.: SS-TuP4, 124
 Pohler, M.: SE+NS-MoM9, 22
 Polak, S.: PS-ThA6, **234**
 Polcik, P.: SE+PS-TuM10, 75
 Polina, A.: HI+AS+BI+NS-ThM5, 202
 Polyakov, A.Y.: EM-TuM9, **62**
 Ponduri, S.: EN+PS-WeM3, 140
 Ponomarev, M.V.:
 EL+TF+AS+EM+SS+PS+EN+NM-MoM6, 7; TC+EM+AS+TF+EN-ThM2, 215
 Pookpanratana, S.: TF+EM+SS-ThA6, **241**
 Poon, J.: MI+EN+BI-TuA7, 93
 Popov, E.O.: SE+NS-MoA7, 50
 Popovitz-Biro, R.: NS+AS+SS+SP-WeM4, 146
 Porcher, W.: EN+NS-ThM11, 198
 Porter, D.L.: AC+EN-TuM1, 57
 Porter, L.M.: TC+EM+AS-WeA9, **188**
 Portoles, J.F.:
 SP+AS+BI+ET+MI+NM+NS+SS+TF-WeM10, **151**
 Posseme, N.: PS2-TuM2, 72
 Postma, A.: BI-MoM1, 4
 Potapenko, D.V.: SS+NS-TuA4, **103**
 Potbhare, S.: EM+OX-WeA9, 167
 Pou, P.: SP+AS+BI+ET+MI+NS-TuA11, 102
 Poulighen, S.: EN+PS-WeM5, 141
 Povey, I.M.: EM+TF+OX+GR-MoA6, 34
 Powell, C.J.: AS-MoM3, 3; AS-MoM6, **3**
 Powell, L.J.: IS-TuP3, **119**
 Pradeep, N.: NS+SP-MoA8, 43
 Pradelles, J.: PS2-TuM5, 73
 Pradhan, P.: EL+TF+AS+EM+SS+PS+EN+NM-MoM1, 6
 Prasad, S.V.: LB+EM+GR+MN+TR-WeA1, 173
 Prater, C.B.: SP+AS+BI+ET+MI+TF-WeA9, 183
 Premkumar, A.: TF-ThP1, **263**
 Prokes, S.M.: EM+TF+OX+GR-MoA10, 35; NS+EN-TuM2, **69**
 Proksch, R.: EW-TuM8, 64; SP+AS+BI+ET+MI+TF-WeA11, 183
 Prosa, T.J.: AS-TuP18, 113
 Provo, J.L.: AC+TF+SS+MI-MoA4, **28**
 Ptschelinzew, N.: EM-ThP14, **246**
 Pu, H.: GR+AS+NS+SP+SS-TuA2, 90; SS-TuP3, 124
 Pu, Y.K.: PS1-TuA10, 96
 Putkonen, M.: NM+NS+MS+EM-MoA1, **40**
 Py, M.: AS-ThM9, 193
 — Q —
 Qiao, L.: OX-TuP5, 122
 Qin, S.Y.: ET+NS+EM-ThM3, **199**; ET+NS+EM-ThM4, 199
 Qin, X.: EM+TF+OX+GR-MoM5, **8**
 Qu, L.: IS-TuP3, 119
 Qu, T.: TF+MI-WeA1, 190
 Quardokus, R.C.: AS-TuP26, 115; ET+SS+GR+SP-ThA3, **229**
 Quinlan, R.A.: GR+AS+NS+SS-ThM10, **202**
 Quiñones-Galván, J.G.: NS-MoM2, 15; TF-ThP16, 265
 Quintero, M.: OX-TuP6, 122
 Quinton, J.S.: SS+NS-ThA7, 236
 — R —
 Rack, P.D.: HI-ThP3, 252; NS+SP-MoA4, **43**; TC-ThP4, 262; TF+EM+SE+NS-ThM3, 217
 Radi, A.: TF+AS-TuA10, 105
 Rading, D.: AS-ThM11, 193; AS-WeM11, 136
 Radja, A.: EL+TF+BI+AS+EM+SS-MoA2, 32
 Radu, I.: TF-ThP1, 263
 Radue, E.: TF+AS+SS-ThA8, 240
 Radvanyi, E.: EN+NS-ThM11, 198
 Rafaja, D.: SE+NS-MoM3, **21**
 Rafati, A.: AS+BI-TuA11, **83**
 Rafik, A.: GR+AS+EM+NS+SS-WeA8, 170
 Rago, P.B.: EM+MI-ThA2, **223**
 Rahinov, I.: SS-MoM4, 23
 Rahman, T.S.: AS+BI-TuA1, 83; AS+BI-TuA3, 83; GR+EM+ET+NS+TF-MoA2, 37; MI+EN+BI-TuA8, 94; NS+EN+GR-TuA7, 94;

- NS-MoM10, 16; NS-WeA9, 177; SS+NS-ThA9, 236
- Raigoza, A.: BI-TuP18, **118**
- Raitses, Y.: PS2-WeA4, 181; PS-ThP9, **256**
- Raj, R.: TF+EN-MoA3, 53
- Raja, L.: PS2-MoA11, 49
- Rajachidambaram, M.S.: TC+EM+AS+TF+EN-ThM5, 216
- Rajan, K.: TR+BI-TuM10, 79
- Rajput, P.: AS-ThA7, **223**
- Raley, A.: PS-MoM5, **20**
- Ralsano, R.: ET+SS+GR+SP-FrM6, **271**
- Raman, P.: PS-ThP36, 261; SE+PS-TuM3, 74
- Raman, S.N.: AS-ThA3, 222; EN+AS-ThA4, **227**
- Raman, T.: GR-ThP8, 251; SS-WeA1, 185
- Ramana, C.V.: TF+AS+SS-ThA11, **240**; TF+AS+SS-ThA9, 240
- Ramos, R.: PS-ThP7, **256**
- Randall, J.N.: NS+SP-MoA7, 43
- Ranga, A.: BI-MoA1, 30
- Rangan, S.: EN+AS-ThA9, 228; OX+SS+TF+MI-MoA6, **45**
- Ranish, J.: TF+AS-TuA11, 105
- Ranjan, A.: PS2-TuM1, **72**; PS-MoM5, 20
- Ranjana, V.: EL+TF+AS+EM+SS+PS+EN+NM-MoM1, 6
- Ranson, P.: MN+AS-MoM6, 13; PS1-ThM3, 208
- Rao, M.: MN+AS-MoM5, 13
- Rao, M.V.: GR+EM+NS+PS+SS+TF-MoM1, 10
- Rappe, A.M.: SS+OX-WeM10, 153
- Raschke, M.B.: NS-WeA7, **177**
- Raskin, J.-P.: EM-ThM4, 196
- Rasmussen, A.M.H.: SS-ThM5, 214
- Raso, R.: AS+NS+SS+TF-WeA8, 164
- Rathbone, J.: VT-MoA10, 56; VT-TuP2, 131
- Ratner, B.D.: BI+AS-TuA1, **84**; IS+AS+BI+ET+GR+NS-TuA1, 91
- Rauf, S.: PS2-MoA3, 48; PS2-TuM11, 74
- Ray, R.I.: MB+BI-ThA1, 232
- Raymond, M.: EM+NS-FrM9, 268
- Raynaud, P.: TF+NS+EM-ThM3, **218**
- Razavi Hesabi, Z.: GR-ThP13, **251**
- Real, M.: LB+EM+GR+MN+TR-WeA10, 174
- Rebello de Figueiredo, M.: SE+NS-MoM6, **22**
- Reddemann, L.: TF+EM+SS-ThA9, 242
- Reddy, D.: EM+OX-WeA1, 167
- Reed, D.T.: AC+EN-TuM9, 57
- Reeves, R.: TF+EM+SE+NS-ThM5, 217
- Regan, J.: MB+BI-ThA8, **233**
- Register, L.F.: EM+OX-WeA1, **167**
- Rehbein, S.: BP+AS-SuA3, 1
- Reid, D.: NS+AS+SS+SP-WeM2, **146**
- Reihls, K.: TF+EM+SS-ThA9, 242
- Reilly, M.: EN-ThP11, 248
- Reinhard, D.A.: AS-TuP18, 113
- Reinke, P.: EM+NS-FrM6, **268**; EN-ThP1, 246
- Ren, F.: BI-TuP6, 116; EM-ThP1, 244; EM-ThP2, 244; EM-TuM9, 62; LB+EM+GR+MN+TR-WeA7, 173
- Ren, H.: PS-ThP35, 261
- Ren, T.: TF+EM+SS-ThA6, 241
- Renaux, F.: PS1-TuA8, 96; SE+NS-MoA4, 50
- Rendon, E.A.: AS-TuP28, 115
- Reniers, F.: PS+TC-WeM11, 148; PS-ThP2, 255; PS-ThP31, 260; PS-ThP32, 260; SE+NS-MoA4, 50; SE+PS-TuA9, **100**
- Reshchikov, M.A.: EM+TF+AS-ThA4, 225
- Resta, A.: GR+EM+NS+SS+TF-ThA6, 231
- Restaino, D.: EM-TuA8, 86
- Reuveny, A.: MN-MoA8, 39
- Revelli, J.C.: EM-ThP4, **244**
- Revenko, I.: EW-TuM8, 64; SP+AS+BI+ET+MI+TF-WeA11, 183
- Reviakine, I.: BI-MoM10, **5**
- Reznicek, A.: EL+TF+AS+EM+SS+PS+EN+NM-MoM9, 7
- Rhallabi, A.: AS-MoM4, 3
- Rhim, S.: GR+AS+NS+SP+SS-TuA2, 90
- Ribeiro, F.: TF+EN-MoA1, 53
- Rice, T.: EM+TF+AS-ThA1, 225
- Richardson, C.J.K.: TF+EM+SS-ThA10, 242
- Richmann, M.K.: AC+EN-TuM9, 57
- Richter, C.A.: TF+EM+SS-ThA6, 241
- Richter, R.P.: BI+AS-TuA9, **85**; BI+SS+NS-WeM10, 138
- Ricker, J.E.: VT-MoM6, 26
- Riddle, Y.: TR+SE-WeM5, 159
- Riedl, B.: PS+BI-MoA11, 47
- Rieth, L.W.: TF-WeM2, **158**
- Rigby-Singleton, S.: BI+SS+AS-TuM5, 60
- Rimal, S.: PS-WeM5, 149
- Rinzler, A.G.: GR+EM+ET+MS+NS-FrM11, 273
- Rittschof, D.: MB+BI-ThA6, 233
- Ritz, E.: TC+EM+AS+TF+EN-ThM12, 216
- Rizzo, A.: AC+TF+SS+MI-MoA3, 28
- Roach, W.M.: VT+AS+SS-WeM10, 161; VT+AS+SS-WeM6, **161**; VT+AS+SS-WeM9, 161
- Robbins, M.O.: TR-TuA1, **107**
- Roberts, A.J.: AS+BI-TuM10, 59; AS+BI-TuM3, 58; AS+NS+SS+TF-WeA8, 164; AS-TuP13, **113**
- Roberts, C.J.: BI+SS+AS-TuM5, 60; BI+SS+NS-WeM12, 138; SP+AS+BI+ET+MI+NS-TuA9, 102
- Roberts, N.A.: NS+SP-MoA4, 43; TF+EM+SE+NS-ThM3, 217
- Robertson, J.: EM+TF+OX+GR-MoM10, **9**
- Robinson, J.T.: GR+AS+BI+PS+SS-WeM9, 143; GR+AS+NS+SP+SS-TuA8, 90; GR+AS+NS+SS-ThM3, 201
- Robinson, M.: BN+AS-WeA4, 165
- Robinson, Z.R.: GR+AS+NS+SP+SS-TuA11, 91; GR+EM+NS+PS+SS+TF-MoM2, **11**
- Robson, M.: PS-MoM1, 20
- Roca i Cabarrocas, P.: EL+TF+AS+EM+SS+PS+EN+NM-MoM3, 6
- Rockett, A.: TF+NS+EM-ThM12, 220
- Rodenhausen, K.B.: EL+TF+BI+AS+EM+SS-MoA1, 32
- Rodgers, M.: EM-ThP8, 245
- Rodriguez Perez, A.: SP+AS+BI+ET+MI+NS-TuA3, 101
- Rodriguez, E.: TR-TuP6, 131
- Rodriguez, G.: MN-TuP3, 120
- Rodriguez, L.N.J.: IS+AS+OX+ET-WeM9, **145**
- Rodriguez-Santiago, V.: PS+TC-WeM12, 148
- Rogalev, A.: SS+OX-WeM5, 152
- Rogers, B.R.: SS+OX-WeM4, 152; SS-TuP5, 124
- Rogers, J.A.: EM+SS+AS+NS-ThM5, **194**
- Rogström, L.: TF+NS+EM-ThM11, **219**
- Rohrer, G.: EM-TuA7, 86
- Rojas, G.: NS+AS+SS+SP-WeM11, **146**
- Roldan Cuenya, B.: SS+NS-ThA8, 236; SS+NS-TuA7, **103**; SS-TuP25, 128; SS-TuP27, 128
- Roldan Cuenya, B.: SS-TuP28, 129
- Romriell, N.R.: TF+EM+SS-ThA8, 242
- Ronkainen, H.: TF+NS+EM-ThM10, 219
- Ronsheim, P.: EM+NS-FrM10, 268
- Roodenko, K.: EL+TF+BI+AS+EM+SS-MoA2, **32**; SS-TuP21, 127
- Roozeboom, F.: TF-TuM11, 78; TF-TuM5, 77
- Rosa, L.: GR+EM+ET+NS+TF-MoA7, 37
- Rose, M.: VT-TuM9, 80
- Rose, V.: MI+SP+AS-ThM1, **205**
- Rosenberg, R.A.: MI+SP+AS-ThM12, **206**
- Rosenfeld, D.H.: TF+AS-WeA1, 188
- Rosenhahn, A.: BI-TuP14, 118; BI-TuP16, 118; BN+AS-WeA11, **166**; IS-TuP4, 119; MB+BI-ThA3, 232
- Rosenmann, D.: MI+SP+AS-ThM12, 206
- Ross, F.M.: GR+EM+NS+PS+SS+TF-MoM8, 11
- Ross, N.: PS-WeM5, 149
- Rossi, F.: BI+SS+AS-TuM12, 60; NS+EN+GR-TuA2, 94
- Rosslee, C.: PS2-TuM2, 72
- Rosso, K.M.: NS-ThM2, 206
- Rotello, V.: BI+SS+NS-WeM3, **137**
- Rotenberg, E.: GR+EM+ET+NS+TF-MoA8, **38**
- Rougemaille, N.: GR+AS+EM+NS+SS-WeA10, 171
- Rousseau, R.: SS+EN+OX-ThM5, 212
- Roussel, P.: AC+EN-TuM3, **57**
- Routaboul, L.: GR+EM+ET+NS+TF-MoA7, 37
- Rowe, J.E.: GR+AS+BI+PS+SS-WeM10, 143; GR+AS+NS+SP+SS-TuA11, 91; GR+EM+ET+MS+NS-FrM8, 272; GR-ThP11, 251; MI+OX-WeA11, **176**
- Roy, A.K.: SE-TuP3, 123
- Roy, T.: GR-ThP13, 251
- Roy-Garofano, V.: PS+TC-WeM1, 147
- Rozen, J.: EM+TF+OX+GR-MoA7, 35
- Rubio-Zuazo, J.: AS+TF+VT-FrM5, 266
- Rubloff, G.W.: TF+EN-MoA6, 54; TF-MoM3, 24
- Ruda, K.: EW-WeL5, 163
- Rudy, A.: TR+BI-TuM2, 78
- Ruffo, M.: TF-WeM1, 157
- Ruggieri, C.: OX+SS+TF+MI-MoA6, 45
- Rumbach, P.: PS+EM-MoM11, 19
- Ruocco, A.: AC+TF+SS+MI-MoA3, 28
- Ruoff, R.S.: GR+AS+NS+SP+SS-TuA11, 91; GR+AS+NS+SP+SS-TuA2, 90
- Ruppalt, L.: EM+TF+OX+GR-MoA10, 35
- Rusu, C.: PS-MoM11, 21
- Rutt, H.N.: HI+AS+BI+NS-ThM3, 202
- Ruzic, D.N.: EN-ThP11, 248; PS-ThP36, 261; SE+PS-TuM3, 74; SE+PS-TuM4, 74; TC+EM+AS+TF+EN-ThM12, 216
- Ryadnov, M.G.: BI+SS+AS-TuM11, **60**
- Ryan, E.T.: EM-TuA11, 87; EM-TuA8, 86
- Rye, M.J.: AS-TuP5, 111
- Rysz, J.: TF+AS+SS-ThA2, 239
- Ryzhkov, M.V.: AC+MI+SS+TF-MoM9, 2
- S —**
- Sabitova, A.: EM+TF+AS-ThA10, 226
- Sabnis, V.A.: EN+TF-TuA9, **88**
- Sachdev, H.: GR-ThP3, 249
- Sadowski, J.T.: GR-ThP11, 251; IS+AS+BI+ET+GR+NS-TuA8, 92
- Safron, N.: GR+AS+EM+NS+SS-WeA9, **170**
- Sahalov, H.: EM+NS-FrM6, 268
- Saini, K.K.: NS-MoM11, **17**
- Saito, N.: GR-ThP7, 250; NS-ThP11, 254; NS-ThP4, 253; NS-ThP8, 254; PS-ThP29, 259
- Saito, S.: MN-TuP9, 121
- Saito, Y.: VT-TuA10, 109
- Saitoh, E.: IS+AS+OX+ET-WeM10, 145
- Sakai, M.: SS-TuP18, **127**
- Sakai, Y.: AS-ThM12, 193; AS-TuP6, **112**
- Sakakibara, R.: MN-TuM11, 68
- Sakalas, P.: GR+AS+NS+SS-ThM2, 201
- Sakamoto, K.: MI-WeM1, 145
- Sakurai, M.: GR+AS+EM+NS+SS-WeA12, **171**
- Salaün, A.: TF+AS-WeA12, 189
- Salditt, T.: IS-TuP4, 119
- Sales, B.C.: SP+AS+BI+ET+MI+NS-TuA12, 102
- Salib, D.: SP+AS+BI+ET+MI+NM+NS+SS+TF-WeM5, 150
- Salter, T.L.: AS-MoA9, 30
- Saly, M.J.: TF+NS+EM-ThM2, 218
- Samala, S.K.: TF+AS+SS-ThA9, **240**
- Samaraweera, R.L.: EM+TF+AS-ThA11, 226; EM+TF+AS-ThA9, 226
- Samuelson, L.: ET+NS+EM-ThM6, 199
- Samukawa, S.: EN+PS-WeM11, 142; MN-TuP4, 120; PS1-TuA9, 96; PS2-ThM10, 211; PS2-ThM11, 211; PS2-ThM9, 211; PS-MoM6, 20
- Sanderson, D.: VT-TuP6, 132
- Sandin, A.A.: GR+AS+BI+PS+SS-WeM10, **143**; GR+AS+NS+SP+SS-TuA11, 91; GR+EM+ET+MS+NS-FrM8, 272; GR-ThP11, 251; MI+OX-WeA11, 176
- Sanghadasa, M.: MN-MoA6, 39; MN-TuM6, 67
- Sangiiovanni, D.G.: TF+AS-TuA4, 104; TF+AS-TuA9, **105**
- Sankaran, R.M.: PS+EM-MoM11, **19**; PS+EM-MoM8, 19

- Sankarapandian, M.: PS-ThP1, 255
Sano, N.: AS-MoA1, 29; AS-TuP4, **111**
Santana, J.: MI+OX-WeA10, 176
Santeufemio, C.: AS+BI-TuA10, 83
Santos, P.V.: NS+SP-MoA9, 43
Santoyo-Salazar, J.: NS-MoM2, 15
Saraf, S.: SS-TuP12, **126**
Saranu, S.: EW-WeL1, 163
Sardela, M.: TF+NS+EM-ThM12, 220
Sarkar, A.: EL+TF+AS+EM+SS-TuP1, **118**
Sarkissian, A.: PS+BI-MoA11, 47
Sarkissian, A.: PS+TC-WeM1, 147
Sasaki, M.: MN-TuP5, 120; PS-ThP8, 256
Sasi-Szabo, L.A.: IS+AS+BI+ET+GR+NS-TuA3, 92
Sato, S.: NM-TuP1, 121
Sauer, V.T.K.: MN+AS-MoM9, 13; MN-MoA7, 39; MN-TuM5, **67**; MN-TuM9, 68
Saulnier, N.: PS2-TuM9, 73
Saurabh, S.: IS-TuP3, 119
Sawai, K.: MN-TuP9, 121
Sawatzky, G.: TF+AS-TuA10, 105
Sawyer, W.G.: TR+BI-TuM10, 79; TR+SE-WeM9, 160; TR-TuA3, 107; TR-TuA9, 107
Scarel, G.: TF+EN-MoA7, **54**
Schaaflhausen, S.: EM+TF+AS-ThA10, 226
Schaeckers, M.: TF-ThP1, 263
Schafer, K.C.: IS+AS+BI+ET+GR+NS-TuA3, 92
Schafer, S.: MI+OX-WeA2, 175
Schäfer, S.: EM+MI-ThA11, 224
Schamberger, F.: PS1-WeA10, 179
Schanze, K.: MB+BI-ThM9, **204**
Scheele, M.: SS-MoM2, 23
Schein, M.: VT-TuA3, 108; VT-TuP6, 132
Scheltjens, G.: SE+PS-TuA9, 100
Schlaf, R.: ET+SS+GR+SP-ThA10, 230; ET+SS+GR+SP-ThA11, 230; TF+EM+SS-ThA11, 242
Schlesser, R.: EM+TF+AS-ThA1, 225
Schlögl, M.: SE+NS-MoM5, 22; SE+NS-MoM6, 22
Schlueter, J.A.: NS+AS+SS+SP-WeM11, 146
Schmid, A.K.: GR+AS+EM+NS+SS-WeA10, 171
Schmidt, A.B.: MI-WeM1, 145
Schmidt, D.: EL+TF+BI+AS+EM+SS-MoA1, **32**
Schmidt, W.G.: SS-TuP21, 127
Schmitt, J.: OX+EM+MI+NS+TF-MoM10, 18
Schmitz, A.: GR+EM+ET+MS+NS-FrM3, 271
Schnadt, J.: IS+AS+SS+EN-TuM12, **67**
Schneider, C.M.: MI+OX-WeA1, 175
Schneider, G.: BP+AS-SuA3, **1**
Schneider, J.M.: SE+NS-MoM8, **22**
Schneckenburger, J.: AS+BI-TuM1, **57**
Schneller, E.: EN+TF-TuM11, 63
Schoenfeld, W.V.: NM+NS+MS+EM-MoA9, 41; TF+AS-WeA7, 189; TF+AS-WeA9, 189
Schofield, M.: GR+AS+NS+SP+SS-TuA2, 90; SS-TuP3, 124
Schreiber, D.: MN-MoA8, 39
Schrimpf, R.D.: EM+SS+AS+NS-ThM11, 195
Schröder, U.: GR+AS+NS+SP+SS-TuA7, 90
Schroter, M.: GR+AS+NS+SS-ThM2, **201**
Schubert, E.: EL+TF+BI+AS+EM+SS-MoA1, 32
Schubert, E.F.: TF+SE+NS-WeM1, **155**
Schubert, M.: EL+TF+BI+AS+EM+SS-MoA1, 32; LB+EM+GR+MN+TR-WeA10, 174
Schuengel, E.: EN+PS-WeM12, 142; EN+PS-WeM9, **141**
Schuhmacher, M.: IS+AS+OX+ET-WeM11, 145
Schuller, I.: AS+TF+VT-FrM2, 266
Schulte, K.: GR+AS+NS+SP+SS-TuA7, 90
Schultz, B.D.: EM+MI-ThA10, 224; EM+MI-ThA6, 224
Schultz, J.A.: BN+AS-WeA12, **166**
Schulze, J.: EN+PS-WeM12, 142; EN+PS-WeM9, 141
Schulze, R.K.: EM+NS-FrM11, **269**
Schwab, Y.: TF+EN-MoA7, 54
Schwaederle, L.: PS+EM-MoM3, 18
Schwartz, C.: EM-ThP1, 244
Schwartz, T.: MB+BI-ThA3, 232
Schwarz, U.D.: SP+AS+BI+ET+MI+NS-TuA10, **102**
Schweigert, D.: PS-ThP10, 256
Schweikert, E.: AS-ThM5, **192**
Schwendemann, T.C.: SP+AS+BI+ET+MI+NS-TuA10, 102
Schwerdtle, T.: AS-TuP1, 111
Scott, D.J.: BI+SS+AS-TuM5, 60
Scott, T.B.: AC+TF+SS+MI-MoA6, 28
Scurr, D.J.: BI-MoA8, 31; BN+AS-WeA10, **166**
Seah, M.P.: AS-ThA2, 222
Seal, S.S.: AS+BI-TuA12, 84; BI-TuP11, 117; BI-TuP13, 118; BI-TuP7, 117; BI-TuP8, **117**; MN-TuP6, 120; NS+AS+SS+SP-WeM2, 146; SS-TuP12, 126
Sedlmaier, J.: AS-WeM6, 135
Seebauer, E.G.: SS+EN+OX-ThM4, 212
Seeger, S.: NS-ThP1, 252
Sefa, M.: VT-TuP3, **131**
Sefat, A.S.: SP+AS+BI+ET+MI+NS-TuA12, 102
Seitz, O.: EL+TF+BI+AS+EM+SS-MoA2, 32; EM+NS-FrM3, 267; EM+TF-WeM4, 139; EN+TF-WeA7, **168**
Seki, T.: AS-ThM9, 193
Sekiguchi, A.: NM+MS-TuM1, **68**
Sekine, M.: GR+AS+NS+SS-ThM9, 201; PS1-TuM5, 71; PS2-MoA7, 49; PS2-ThM5, **210**; PS2-TuA7, 98; PS2-WeA3, 180; PS-ThP14, 257; PS-ThP25, 259
Sellers, J.R.V.: SS-TuM12, **77**
Selvamanickam, V.: EN+TF-TuA8, **88**
Sementa, L.: SS+OX-WeM12, 153
Semetey, V.: MB+BI-ThM2, 203
Semidey-Flecha, L.: GR+AS+EM+NS+SS-WeA11, 171
Semonin, O.E.: EN+NS-MoM3, 9
Senevirathna, M.K.I.: EM+TF+AS-ThA11, 226; EM+TF+AS-ThA9, **226**; EM-ThP6, 244
Senkbeil, T.: BN+AS-WeA11, 166; IS-TuP4, **119**
Senor, D.J.: AC+EN-TuM1, 57
Seo, B.H.: PS-ThP4, 255
Seo, H.: EN+NS-MoM2, 9
Seo, H.-C.: GR+EM+ET+MS+NS-FrM3, 271
Seo, J.: NS-ThP9, **254**
Seo, J.M.: SS-TuP9, 125
Seo, J.-W.T.: NS+EN-TuM12, **70**
Seo, S.C.: PS2-TuM6, 73
Seo, S.J.: AS-TuP22, 114
Seog, J.: PS+BI-MoA2, 46; PS+BI-MoA6, 46
Seong, D.J.: PS-ThP4, 255
Serov, A.: IS+AS+SS+EN-TuM6, 66
Sershen, M.J.: PS1-TuA11, 97; TF-WeM1, 157
Setina, J.: VT-MoM8, **26**
Šetina, J.: VT-MoA1, 54; VT-MoA7, 55; VT-TuP3, 131
Setsuhara, Y.: PS1-TuM5, 71
Setvin, M.: ET+SS+GR+SP-ThA9, 230; SP+AS+BI+ET+MI+NS-TuA4, 101
Seyhan, A.: NS+EN-TuM5, **70**
Seyller, Th.: GR+EM+ET+NS+TF-MoA8, 38; GR+EM+NS+PS+SS+TF-MoM10, 12
Sgammatto, B.: AS-TuP10, **112**
Shaaf, S.K.: SS+OX-WeM11, 153
Shacham-Diamand, Y.: MN+AS-MoM10, 14; MN-MoA8, 39
Shafai, G.: NS-MoM10, **16**
Shafarman, W.N.: EN+TF-TuM3, **63**
Shafiq, N.: GR+AS+BI+PS+SS-WeM2, 142
Shaifai, G.: SS+NS-ThA9, 236
Shakouri, A.: SE+NS-MoA8, **51**
Shalimov, A.: SE+NS-MoM2, 21
Sham, T.K.: AS+TF+VT-FrM1, 266
Shan, J.: SS-TuP19, 127
Shannon, S.: SE+PS-TuA3, 100; SE+PS-TuA4, 100
Shao-Horn, Y.: IS+AS+SS+EN-TuM5, 66
Shard, A.G.: AS-ThA2, 222; AS-ThM4, **192**
Sharifi, F.: MI-WeM11, 146
Sharipov, F.: VT-TuM3, **80**; VT-TuM4, 80
Sharma, G.: AS-ThA7, 223
Sharma, K.: TC+EM+AS+TF+EN-ThM2, **215**
Sharma, M.: OX+EM+MI+NS+TF-MoM10, 18
Sharp, T.: TR-TuA1, 107
Shea, M.J.: EN+TF-TuA3, 88
Shearer, J.C.: SE+NS-MoA6, **50**
Sheehan, J.P.: PS2-WeA4, **181**
Sheehan, P.E.: GR+EM+BI+PS+SS-WeM9, 143; GR+AS+NS+SS-ThM3, 201; GR-ThP9, 251
Shelton, W.A.: MI-ThP4, 252
Shen, G.: ET+NS+EM-ThM11, 200; NS+EN-TuM3, **69**; NS-ThM11, 207
Shen, J.: EN+TF-TuM10, 63
Shen, M.: EN+SS-FrM2, **269**
Shenogin, S.V.: SE-TuP3, 123
Shepard, K.L.: GR+EM+ET+NS+TF-MoA10, 38
Sherwood, P.M.A.: AS-MoM8, **4**
Shetty, R.: SP+AS+BI+ET+MI+TF-WeA9, 183
Shi, Z.: EM+TF-WeM5, 139; NS-ThP2, 253
Shibata, K.: VT-TuA1, 108
Shigekawa, H.: NS-ThM5, **206**
Shih, C.: ET+NS+EM-ThM3, 199
Shikano, T.: GR+AS+EM+NS+SS-WeA12, 171
Shimada, K.: MI-WeM1, 145; NM-TuP1, 121; TF-ThP12, 264
Shimbori, S.: PS2-ThM3, 210
Shimizu, H.: BI+SS+NS-WeM11, **138**; VT-TuP8, **132**
Shimizu, T.: NM-TuP3, 121; PS2-ThM3, **210**
Shimizu, T.K.: SS-ThM12, **215**
Shin, B.G.: GR-ThP6, 250; SS+NS-ThA3, **235**
Shin, H.: GR+EM+NS+PS+SS+TF-MoM4, **11**; NS-ThP9, 254; PS-MoM8, 21
Shin, H.-J.: GR+EM+NS+PS+SS+TF-MoM11, 12
Shin, N.: NS+EN-TuM4, 69; NS-WeA11, 178
Shin, Y.J.: EN-TuM10, 62
Shiradkar, N.: EN+TF-TuM11, 63
Shirai, M.: VT-TuA1, 108
Shirakura, A.: SE-TuP2, 123
Shiratani, M.: EN+NS-MoM2, 9; PS1-TuM5, 71
Shirato, N.: MN-TuP6, 120
Shirayama, Y.: PS2-ThM3, 210
Shirazi, M.: TF-TuM3, 77
Shivashankar, S.A.: AS-TuP23, 115
Shkel, Y.: EM-ThP11, 245
Shklovsky, J.: MN+AS-MoM10, 14
Shkovsky, J.: MN-MoA8, 39
Shohet, J.L.: EM-ThP10, 245; EM-ThP11, 245; EM-ThP9, **245**; EM-TuA10, 87; PS-ThA10, 235; PS-ThP3, 260; PS-ThP35, 261
Shojaei, B.: EM+MI-ThA6, 224
Sholl, D.: GR+AS+EM+NS+SS-WeA11, 171
Shong, B.: SS+EM-WeA8, **185**
Short, R.D.: PS+BI-MoA7, 47; PS-ThA8, 234
Short, R.T.: VT-MoA8, **55**
Shukla, N.: SS-ThM2, **214**
Shuptar, M.: VT-TuA3, 108; VT-TuP6, 132
Shutthanandan, V.: AS+NS+SS+TF-WeA4, 164; HI-ThP2, **251**; MI-ThP4, 252; OX-TuP6, 122; SS+EN+OX-ThM11, 213
Shyam, R.: SS+OX-WeM3, **152**
Sibener, S.J.: EM+TF-WeM12, 140
Sie, C.Y.: PS-ThP46, **262**
Siebentritt, S.: EN+TF-TuM5, **63**
Siekhaus, W.J.: AC+EN-TuM10, 57; AC+EN-TuM6, **57**
Sijbrandij, S.: HI+AS+NS-WeA10, 172
Sikorski, E.M.: PS1-ThM12, 209; PS-MoM2, 20; PS-WeM10, 150
Silbaugh, T.L.: SS-WeM6, **154**
Siligardi, G.: BI+SS+AS-TuM12, 60
Sillassen, M.: BI-MoM11, 6
Silva, A.: EM+NS-FrM4, **267**
Silva, S.: BI-TuP6, 116
Silver, R.: NS+SP-MoA8, 43
Silverstein, R.: EN+TF-MoA10, 36
Simanullang, M.: NS+EN-TuM5, 70

- Simchenko, S.V.: SS+EN+OX-ThM12, **213**
 Simmons, M.Y.: NS-MoM3, **15**
 Simons, D.S.: AS+BI-TuA9, **83**
 Simons, M.T.: TF+AS+SS-ThA8, **240**
 Singh, A.: TF+MI-WeA3, **190**
 Singh, U.: MN-TuP6, **120**
 Sinha, H.: EM-ThP9, **245**
 Sinno, T.: EM-ThM12, **197**
 Sinnott, S.B.: EN+SS-FrM6, **270**;
 OX+SS+TF+MI-MoA1, **44**; OX-TuP1, **122**;
 OX-TuP3, **122**; OX-TuP4, **122**; SS+NS-ThA4,
236; TR+BI-TuM10, **79**; TR-TuA3, **107**; TR-
 TuP1, **130**
 Sinsabaugh, S.L.: EN+NS-ThM12, **198**
 Siringhaus, H.: TC+EM+AS+TF+EN-ThM9, **216**
 Sit, J.C.: MN-MoA7, **39**
 Sitar, Z.: EM+TF+AS-ThA1, **225**
 Sivaram, S.: NS-WeA11, **178**
 Siviero, F.: VT-TuM12, **81**
 Sivula, K.: IS+AS+SS+EN-TuM3, **65**
 Siwak, N.: MN-MoA10, **39**
 Skomski, D.: SS+NS-ThA11, **237**
 Skuza, J.R.: VT+AS+SS-WeM6, **161**
 Slattery, A.D.: SS+NS-ThA7, **236**
 Smart, L.: VT-MoM11, **27**
 Smekal, W.: AS-MoM3, **3**; AS-MoM6, **3**
 Smentkowski, V.S.: AS-TuP18, **113**
 Smets, A.H.M.: EN+PS-WeM10, **141**
 Smirnov, N.B.: EM-TuM9, **62**
 Smith, S.: AS-ThM4, **192**
 Smith, S.R.: SS-ThA3, **237**
 Smolenski, K.W.: VT+AS+SS-WeM2, **161**; VT-
 TuA11, **109**
 Snow, A.W.: TF+AS-TuA3, **104**
 Snyders, R.: PS1-TuA8, **96**; SE+NS-MoA4, **50**
 Sobolewski, M.A.: PS1-TuM1, **70**
 Soda, E.: PS-ThP1, **255**; PS-WeM4, **149**
 Sodeman, I.: EM+OX-WeA1, **167**
 Soffa, W.A.: TF+MI-WeA4, **190**
 Sohn, Y.H.: EN+TF-TuM10, **63**
 Sojoudi, H.: GR+EM+ET+MS+NS-FrM9, **272**;
 GR-ThP10, **251**
 Sokolov, I.: MN+AS-MoM10, **14**
 Solanki, N.: EW-WeL3, **163**
 Solzbacher, F.: TF-WeM2, **158**
 Song, E.B.: EM+SS+AS+NS-ThM11, **195**
 Song, I.: GR+EM+NS+PS+SS+TF-MoM4, **11**;
 NS+EN-TuM1, **69**
 Song, I.Y.: AS+BI-TuM9, **59**
 Song, S.-H.: AS-WeM3, **135**
 Song, Y.-B.: SS-TuP9, **125**
 Sonntag, M.D.: NS-ThP3, **253**
 Sorescu, D.C.: SS-ThA8, **238**
 Sorini, A.: EN+SS-FrM5, **270**
 Sosolik, C.E.: SS+OX-WeM3, **152**; SS-TuP36, **130**
 Sotres, J.: BI+SS+AS-TuM3, **60**
 Sottos, N.R.: SE+NS-MoA10, **51**
 Soudi, A.: ET+NS+EM-ThM12, **200**
 Sousa, C.: AS-TuP11, **113**; BI+AS-TuA7, **84**
 Sowa, M.J.: PS1-TuA11, **97**
 Sozias, S.: PS+EM-MoM3, **18**
 Spampinato, V.: NS+EN+GR-TuA2, **94**
 Spanier, J.E.: NS+EN-TuM6, **70**
 Spatz, J.P.: BI-MoM3, **5**
 Speck, J.: EM-ThM9, **196**
 Spemann, D.: GR+AS+EM+MI+MN-TuM9, **65**
 Spencer, N.D.: NS+SP-MoA2, **42**
 Spencer, S.: AS-ThM4, **192**
 Spies, M.: EL+TF+BI+AS+EM+SS-MoA9, **33**
 Spooner, T.: PS2-TuM9, **73**
 Sreenivasan, R.: PS2-TuM6, **73**
 Sridhar, S.: PS-MoM8, **21**
 Srikanth, H.: MI+OX-WeA9, **176**; MI-ThP2, **252**;
 NS-MoM8, **16**; NS-MoM9, **16**;
 OX+EM+MI+NS+TF-MoM1, **17**
 Srinadhu, E.S.: SS+OX-WeM3, **152**
 Srinivasan, S.: PS2-TuM11, **74**
 Sriraman, K.: SP-TuP1, **123**
 Sriraman, S.: PS2-TuM3, **73**; PS-MoM11, **21**
 Srivastava, A.K.: PS2-TuA3, **98**
 Srivastava, N.: GR+AS+NS+SP+SS-TuA10, **91**
 Srivastava, R.: PS-ThP1, **255**; PS-WeM1, **148**; PS-
 WeM4, **149**
 Stach, E.: TF+EN-MoA1, **53**
 Stadermann, M.: IS+AS+OX+ET-WeM6, **144**
 Stafford, L.: PS+BI-MoA10, **47**; PS+BI-MoA11,
47; PS+TC-WeM1, **147**; PS1-WeA9, **179**
 Stair, P.C.: OX+SS+TF+MI-MoA3, **44**; TF+EN-
 MoA1, **53**
 Standaert, T.: PS2-TuM6, **73**
 Starostin, S.A.: PS+TC-WeM2, **147**
 Startsev, E.A.: PS2-MoA10, **49**; PS2-MoA9, **49**
 Stchakovsky, M.: TC-ThP2, **262**
 Steele, B.: GR+AS+EM+MI+MN-TuM10, **65**
 Steele, D.A.: PS+BI-MoA7, **47**; PS-ThA8, **234**
 Stefani, G.: AC+TF+SS+MI-MoA3, **28**
 Stein, K.: PS2-TuM6, **73**
 Stein, M.J.: IS+AS+BI+ET+GR+NS-TuA1, **91**
 Steiner, M.: MI+SP+AS-ThM12, **206**
 Steiner, M.A.: TF+MI-WeA4, **190**
 Steiner, M.B.: NS+EN-TuM9, **70**
 Stenger, B.: NS-ThM6, **207**
 Stern, L.A.: HI-ThP3, **252**
 Stevanovic, A.: SS+EN+OX-ThM6, **212**
 Stevie, F.A.: AS+BI-TuA10, **83**
 Stickle, W.F.: AS-ThA1, **222**
 Stillahn, J.: PS-ThP1, **255**; PS-WeM4, **149**
 Stine, R.: GR+AS+BI+PS+SS-WeM9, **143**;
 GR+AS+NS+SS-ThM3, **201**
 Stock, S.R.: AS-WeM9, **136**
 Stoddart, P.R.: MB+BI-ThA4, **232**
 Stojak, K.: NS-MoM9, **16**
 Stolbov, S.: EN+NS-ThM3, **197**; EN+SS-FrM7,
270
 Stolwijk, S.D.: MI-WeM1, **145**
 Stone, D.: SE+NS-MoA1, **49**
 Stone, J.A.: VT-MoM6, **26**
 Stoneking, M.R.: PS-ThP21, **258**
 Storch, I.R.: MN-TuM10, **68**; MN-TuM11, **68**
 Storm, A.J.: VT-TuA7, **109**
 Stout, P.: PS2-MoA4, **48**
 Strietzel, C.: VT-MoM2, **25**
 Strohmeier, B.: AS+BI-TuM11, **59**
 Strom, M.J.: MB+BI-ThA7, **233**
 Stroschio, J.A.: GR+EM+ET+NS+TF-MoA10, **38**;
 MI-WeM11, **146**; MI-WeM2, **145**
 Strouse, G.F.: VT-MoM6, **26**
 Stuart, S.C.: GR+EM+ET+MS+NS-FrM8, **272**
 Stubbers, R.: EN-ThP11, **248**
 Stuppy, S.M.: MB+BI-ThA3, **232**
 Stutzman, M.L.: VT-MoM5, **26**; VT-TuP16, **133**
 Styan, K.: BI-MoM5, **5**
 Styrov, V.: SS+EN+OX-ThM12, **213**
 Su, C.: SP+AS+BI+ET+MI+TF-WeA8, **183**
 Su, D.: EN+SS-FrM4, **269**
 Su, H.: TF+EM+SE+NS-ThM4, **217**; TF+SE+NS-
 WeM10, **157**
 Su, L.: EM-ThP6, **244**
 Suanpoot, P.: PS+BI-MoA3, **46**; PS-ThP38, **261**
 Subramanian, V.: AS+NS+SS+TF-WeA4, **164**
 Such, G.K.: BI-MoM1, **4**
 Sudipta, S.: BI-TuP3, **116**
 Suemitsu, M.: GR+EM+NS+PS+SS+TF-MoM10,
12
 Suetsugu, Y.: VT-TuA1, **108**
 Sugai, H.: PS1-WeA3, **178**
 Sugimoto, Y.: SP+AS+BI+ET+MI+NS-TuA11,
102
 Sugiyama, M.: EN+TF-TuA12, **89**; MN-TuP4, **120**
 Sukenik, C.N.: OX+EM+MI+NS+TF-MoM11, **18**
 Sumant, A.V.: AS-TuP12, **113**; MN+AS-MoM3,
12; MN+AS-MoM5, **13**
 Sumiya, K.: TR-TuP3, **131**
 Sumpter, B.G.: NS+AS+SS+SP-WeM11, **146**; SS-
 WeM4, **154**
 Sun, D.Z.: GR-ThP8, **251**;
 SP+AS+BI+ET+MI+NM+NS+SS+TF-WeM5,
150; SS-WeA1, **185**
 Sun, G.F.: SS-WeM12, **155**
 Sun, L.: SE+PS-TuM9, **75**; TF+AS+SS-ThA10,
240
 Sun, T.: EM-TuA7, **86**
 Sun, X.: TR-TuP1, **130**
 Sun, Y.: TF-TuM9, **78**
 Sun, Z.: EM-TuA8, **86**; PS-ThP10, **256**
 Sundaram, G.: PS1-TuA11, **97**; TF+EM+SS-ThA7,
241; TF-WeM1, **157**
 Sundararajan, R.: PS1-TuM11, **72**; PS1-WeA12,
180; PS2-MoA10, **49**; PS2-MoA11, **49**; PS2-
 MoA9, **49**
 Sung, C.Y.: GR+AS+NS+SP+SS-TuA11, **91**
 Sung, H.K.: PS-ThP23, **258**
 Sung, Y.M.: PS-ThA10, **235**; PS-ThP33, **260**; PS-
 ThP35, **261**
 Suntharampillai, T.: BI-TuP9, **117**
 Suo, Z.: NS-ThM12, **207**
 Surla, V.: PS-ThA11, **235**
 Surman, D.: EW-TuL4, **82**
 Surnev, S.: SS+OX-WeM12, **153**
 Sutarto, R.: TF+AS-TuA10, **105**
 Suthar, K.J.: NS+SP-MoA11, **44**
 Suto, S.: SS-MoA10, **53**
 Sutter, E.: GR+EM+NS+SS+TF-ThA2, **231**
 Sutter, P.W.: GR+AS+EM+NS+SS-WeA8, **170**;
 GR+EM+NS+SS+TF-ThA2, **231**
 Suzer, S.: AS-MoM11, **4**; EN-ThP3, **247**
 Suzuki, H.: MN-TuP5, **120**
 Suzuki, T.: GR+AS+EM+NS+SS-WeA12, **171**;
 PS1-TuM5, **71**; PS2-WeA3, **180**; PS-MoM2,
20; PS-WeM10, **150**; SE-TuP2, **123**
 Suzuki, Y.: SS-TuP11, **126**
 Švec, M.: ET+SS+GR+SP-FrM5, **271**
 Svedberg, E.B.: EN+NS-ThA7, **229**
 Sverdllov, Y.: MN-MoA8, **39**
 Swain, G.W.: MB+BI-ThA3, **232**
 Swaraj, S.: AS+BI-TuM5, **58**
 Swart, H.C.: SS+OX-WeM11, **153**
 Sweeny, B.: EN+SS-FrM4, **269**
 Sweet, W.J.: TF2-TuA7, **106**
 Swinney, T.C.: VT-MoA11, **56**
 Sydorenko, D.: PS2-MoA10, **49**; PS2-MoA9, **49**
 Sykes, C.H.: EM+SS+AS+NS-ThM9, **194**; SS-
 MoA7, **52**; SS-ThM3, **214**; SS-TuP1, **123**; SS-
 WeA2, **186**; SS-WeM1, **153**
 Synowicki, R.A.:
 EL+TF+AS+EM+SS+PS+EN+NM-MoM5, **7**
 Szakal, C.: AS+BI-TuA9, **83**
 Szili, E.J.: PS+BI-MoA7, **47**
 Szulczewski, G.J.: MI+OX-WeA2, **175**
 — T —
 Tagami, M.: PS2-TuM9, **73**
 Taing, J.: EN+SS-FrM5, **270**; SS+NS-TuA3, **103**
 Tait, S.L.: SS+NS-ThA11, **237**; SS-MoA3, **51**; SS-
 WeM3, **154**
 Tajima, S.: PS-ThP25, **259**
 Takaba, G.: PS-ThP8, **256**
 Takagi, K.: GR+AS+NS+SS-ThM1, **201**
 Takahashi, K.: MN-TuP9, **121**
 Takahashi, M.: PS-ThP34, **260**
 Takahashi, N.: VT-MoA3, **54**
 Takahashi, R.: VT-TuA10, **109**
 Takahashi, S.: PS2-ThM3, **210**
 Takai, O.: GR-ThP7, **250**; NS-ThP4, **253**
 Takaishi, R.: AS-ThM12, **193**; AS-TuP3, **111**; AS-
 TuP6, **112**
 Takano, I.: SS-TuP11, **126**; SS-TuP32, **129**; SS-
 TuP6, **125**; SS-TuP7, **125**
 Takao, Y.: PS2-TuA10, **98**; PS2-TuA12, **99**; PS-
 MoM10, **21**
 Takarai, Y.: NM-TuP2, **121**
 Takats, Z.: IS+AS+BI+ET+GR+NS-TuA3, **92**
 Takeda, K.: PS1-TuM5, **71**; PS2-MoA7, **49**; PS2-
 ThM5, **210**; PS-ThP14, **257**
 Takemura, S.: NM-TuP1, **121**; NM-TuP2, **121**;
 NM-TuP3, **121**; TF-ThP12, **264**
 Takeuchi, T.: PS2-WeA3, **180**
 Talin, A.A.: MI-WeM11, **146**

- Tallarida, M.: IS+AS+OX+ET-WeM9, 145
Tamanaha, C.R.: GR+AS+NS+SS-ThM3, 201
Tamaya, S.: PS-ThP6, 256
Tamura, H.: PS-ThA1, 233
Tamura, Y.: PS2-ThM10, **211**
Tan, K.: IS-TuP2, **119**
Tan, X.: EL+TF+AS+EM+SS+PS+EN+NM-MoM4, 7
Tanaka, S.: GR+AS+NS+SS-ThM1, 201
Tang, J.-M.: SS-TuP4, 124
Tang, X.: MI+OX-WeA7, 175
Tanski, J.A.: VT-MoA6, 55
Tantardini, G.F.: GR+AS+EM+NS+SS-WeA12, 171
Tao, F.: TF+AS+SS-ThA6, **239**
Tao, J.: SS-TuP15, 126
Tapasztó, L.: AS+TF+VT-FrM3, 266
Taschuk, M.T.: TF+SE+NS-WeM11, 157; TF+SE+NS-WeM5, 156; TF+SE+NS-WeM9, 156
Tasneem, G.: AS-MoM6, 3
Tatsumi, T.: PS2-ThM4, 210; PS2-TuA9, 98; PS-MoM10, 21; PS-ThP14, 257
Tatulian, S.A.: GR+AS+BI+PS+SS-WeM6, 143
Taubert, I.: BI-TuP14, 118
Taubner, T.: AS-WeM4, **135**
Taucer, M.: SP+AS+BI+ET+MI+NM+NS+SS+TF-WeM2, 150
Tawalbeh, T.: EM+NS-FrM9, 268
Te Slight, E.: PS-ThP15, 257
Telib, H.: VT-TuM9, 80
Temmen, M.G.: MN-TuM6, 67
Temple, D.S.: EN+NS-MoM11, 10
Temst, K.: MI+SP+AS-ThM9, **205**
ten Elshof, A.: EL+TF+BI+AS+EM+SS-MoA8, 33
Tendler, S.J.B.: SP+AS+BI+ET+MI+NS-TuA9, 102
Teng, D.: GR+AS+EM+NS+SS-WeA11, 171
Tenne, R.: NS+AS+SS+SP-WeM4, 146
Tennyson, E.: EM-ThP15, 246
Tennyson, J.: PS2-MoA6, 48
Tentschert, J.: AS-TuP1, 111
Teplyakov, A.V.: AS-TuP20, 114; EN+AS-ThA8, 228; SS+EM-WeA12, **185**; SS-TuP20, 127
ter Veen, H.R.J.: TF+AS+SS-ThA4, **239**; TF-ThP14, 265
Terauds, K.: TF+EN-MoA3, 53
Terawaki, L.: SS-TuP31, 129
Terfort, A.: SS+NS-ThA10, 237; TF+AS+SS-ThA2, 239
Terrones, H.: SS-WeM4, 154
Terry, H.: SE+PS-TuA9, 100
Terui, S.: VT-TuA1, 108
Teslich, N.E.: AC+EN-TuM6, 57
Thakur, M.: EN+NS-ThM12, 198
Theilacker, W.: AS+BI-TuM4, **58**
Therien, M.: NS-WeA1, 177
Thevuthasan, S.: AS+BI-TuA12, 84; AS+NS+SS+TF-WeA3, 164; AS+NS+SS+TF-WeA4, **164**; EN-ThP10, **248**; HI-ThP2, 251; IS+AS+BI+ET+GR+NS-TuA12, 93; NS-WeA10, 178; OX-TuP6, 122; SS-TuP26, 128; TC+EM+AS+TF+EN-ThM5, 216; TF+AS+SS-ThA11, 240
Thierley, M.: VT+AS+SS-WeM3, **161**
Thiess, S.: AS+TF+VT-FrM3, 266
Thissen, A.: EW-TuL6, **82**
Thissen, H.: BI-MoM5, 5; BI-MoM6, 5
Thissen, P.: EN+AS-ThA7, 228; SS+EM-WeA11, 185; SS-TuP21, **127**; TF+AS+SS-ThA3, 239
Thomas, E.: SE+NS-MoA11, 51
Thomas, J.C.: SS+EM-WeA2, **184**; SS-TuP34, 130
Thomas, M.A.: PS1-TuA12, **97**
Thomas, W.: BI+SS+AS-TuM6, 60
Thompson, W.: HI-ThP3, 252
Thoms, B.: EM-ThP5, 244
Thonhauser, T.: EN+AS-ThA7, 228; IS-TuP2, 119
Thornton, M.: PS-ThA6, 234
Thorpe, R.: EN+AS-ThA9, **228**
Tian, F.Y.: SS-TuP20, **127**
Tian, P.: PS2-TuA11, 99
Tian, W.-C.: MN+AS-MoM11, 14; MN-MoA9, 39
Tillocher, T.: MN+AS-MoM6, **13**; PS+EM-MoM3, 18; PS1-ThM2, 208; PS1-ThM3, 208
Timm, R.: EM+MI-ThA6, 224; ET+NS+EM-ThM6, **199**
Titus, M.: PS-MoM1, 20
Tivanski, A.: IS+AS+BI+ET+GR+NS-TuA9, 93
Tiwald, T.E.: EL+TF+BI+AS+EM+SS-MoA1, 32
Tiwari, A.N.: TF+AS-WeA3, **188**
Tkach, I.: AC+TF+SS+MI-MoA6, 28
Tkadletz, M.: SE+NS-MoM6, 22
To, B.N.: PS1-ThM12, 209
Tobin, J.G.: AC+MI+SS+TF-MoM9, **2**
Tochigi, H.: VT-MoM1, 25
Todor, O.: PS2-TuM10, 73; PS-ThA11, 235
Todorovic, M.: SP+AS+BI+ET+MI+NS-TuA10, 102
Toeller, M.: TF-ThP1, 263
Toivola, M.: EN+TF-WeA10, 169
Tokei, Z.: EM-TuA3, **86**
Tokluoglu, E.: PS2-MoA10, 49; PS2-MoA9, 49
Tokranov, V.: EM+TF+OX+GR-MoM3, 8
Tokumoto, H.: PS2-ThM3, 210
Tolbert, L.: GR+EM+ET+MS+NS-FrM9, 272; GR-ThP10, 251
Tolmer, P.: NS-ThM11, 207
Toman, B.: VT-MoA1, 54
Tomaszewski, D.: PS2-WeA3, 180
Tompkins, H.G.: EL+TF+AS+EM+SS+PS+EN+NM-MoM8, 7
Toney, M.F.: EM-TuA2, 86; EM-TuA7, 86
Tongay, S.: GR+EM+ET+MS+NS-FrM11, 273; LB+EM+GR+MN+TR-WeA7, 173
Torija, M.: OX+EM+MI+NS+TF-MoM10, 18
Torun, B.: SS-ThA9, 238; TF+AS+SS-ThA1, **238**
Tosa, M.: MN-TuP5, 120
Tosun, B.S.: EN+TF-TuM9, **63**
Tóth, J.: AS+TF+VT-FrM3, 266
Tougaard, S.: AS-MoM1, **3**
Toyoda, A.: SS-TuP6, **125**
Tracy, J.B.: TF2-TuA1, 106
Travis, J.: TF+EN-MoA3, **53**
Trenary, M.: SS-WeM5, 154
Trevino, K.: PS-ThP1, 255
Trickett, Y.: PS-ThP34, 260
Trioni, M.I.: AC+TF+SS+MI-MoA3, 28; GR+AS+EM+NS+SS-WeA12, 171
Tripp, R.A.: TF+SE+NS-WeM12, 157
Trogler, W.C.: BN+AS-WeA3, 165
Tromp, R.M.: GR+EM+NS+PS+SS+TF-MoM8, **11**
Tronic, E.: BI+SS+AS-TuM6, 60
Tsai, H.: PS1-ThM12, 209
Tsai, J.H.: PS+EM-MoM4, 18
Tsang, K.: BI-MoM5, 5
Tsargorodska, A.B.: NS+SP-MoA1, **42**
Tsong, T.T.: HI+AS+NS-WeA8, 172
Tsuchikawa, R.: NS+EN-TuM11, **70**
Tsuda, H.: PS2-TuA10, 98; PS2-TuA12, **99**
Tsushima, T.: SE+PS-TuA8, 100
Tsverin, Y.: NS+AS+SS+SP-WeM4, 146
Tucker, R.T.: TF+SE+NS-WeM11, 157; TF+SE+NS-WeM9, 156
Turchanin, A.: GR+AS+BI+PS+SS-WeM11, **143**; HI+AS+BI+NS-ThM11, 203; HI+AS+BI+NS-ThM5, 202
Turk, M.E.: GR+AS+EM+MI+MN-TuM2, 64
Turkowski, V.: MI+EN+BI-TuA8, 94; NS-WeA9, 177
Turner, M.: PS1-TuM10, 72; PS1-TuM9, 72
Tusciano, J.A.: TF+EM+SS-ThA8, 242
Tweedy, J.: EM+TF+AS-ThA1, 225
Twigg, M.E.: EM+TF+AS-ThA6, 225
Tyagi, P.: GR+AS+NS+SP+SS-TuA11, **91**; GR+EM+NS+PS+SS+TF-MoM2, 11
Tyler, K.: SS-ThM11, 215
Tyliszczak, T.: GR+AS+EM+MI+MN-TuM9, 65; IS+AS+BI+ET+GR+NS-TuA9, 93
Tysoe, W.T.: TR+SE-WeM3, **159**
Tzeng, Y.R.: LB+EM+GR+MN+TR-WeA8, 173
- U —**
- Uchida, G.: EN+NS-MoM2, **9**
Ueba, T.: SS-TuP31, 129
Ueda, O.: EN-ThP12, 249
Ueki, S.: MN-TuP4, 120
Ueno, I.: SS-ThA10, 238
Ueno, T.: GR-ThP7, 250
Uesawa, F.: PS-ThP14, 257
Ugelow, M.: AS+BI-TuA9, 83
Uhm, H.: PS+BI-MoA3, 46
Ulfig, R.M.: AS-TuP18, 113
Uljin, R.: BI+SS+AS-TuM9, **60**
Ulrich, M.D.: GR+EM+ET+MS+NS-FrM8, 272
Unger, M.: AS-WeM6, **135**
Unger, W.E.S.: AS+BI-TuM5, **58**
Ungureneanu, M.: GR+AS+EM+MI+MN-TuM9, 65
Ünverdi, Ö.: SP+AS+BI+ET+MI+NS-TuA10, 102
Upadhyay, R.: PS2-MoA11, 49
Upadhyaya, G.: PS-MoM1, **20**
Urata, C.: SS-ThM1, 213
Urban, F.K.: EL+TF+AS+EM+SS+PS+EN+NM-MoM10, **8**
Urban, R.: HI+AS+NS-WeA7, **172**
Usachov, D.: GR-ThP3, 249
Usami, K.: NS+EN-TuM5, 70
Ushigome, D.: GR+AS+EM+NS+SS-WeA12, 171
Utz, A.L.: SS-MoA4, **52**
- V —**
- Vahedi, V.: PS-MoM11, 21
Vail, M.A.: TF2-TuA2, 106
Valefi, M.: TR+BI-TuM5, 79
Vallee, C.: TF+AS-WeA12, **189**
Vallée, C.: NM+NS+MS+EM-MoA6, 41
Vallier, L.: PS2-TuM2, **72**
Valtiner, M.: BI+SS+NS-WeM5, **137**
Van Assche, G.: SE+PS-TuA9, 100
van Buuren, T.: AS+TF+VT-FrM2, 266; IS+AS+OX+ET-WeM6, 144
van de Loo, B.W.H.: EL+TF+AS+EM+SS+PS+EN+NM-MoM6, 7; TF-TuM5, 77
van de Sanden, M.C.M.: EN+PS-WeM3, 140; EN+PS-WeM4, 141; PS+TC-WeM2, 147; PS2-WeA1, 180; PS2-WeA9, 181
van der Donck, J.C.J.: VT-TuA7, 109
Van der Mei, H.C.: MB+BI-ThM11, **204**
van der Mullen, J.J.A.M.: PS1-WeA7, 179
van der Veen, J.: NS+SP-MoA9, 43
Van der Ven, A.: SS+EM-WeA2, 184; SS-TuP34, 130
van der Wiel, W.G.: NS+SP-MoA9, 43
van der Zwaag, S.: TR+BI-TuM5, **79**
Van Duyne, R.P.: NS-ThP3, 253; NS-WeA3, **177**
Van Elshocht, S.: IS+AS+OX+ET-WeM9, 145; LB+EM+GR+MN+TR-WeA12, 174; TF-ThP1, 263
Van Mele, B.: SE+PS-TuA9, 100
Van Spyk, M.H.C.: SS-ThA1, 237; SS-WeM11, **155**
Van Veldhoven, E.: HI+AS+NS-WeA9, **172**
van Zijll, M.: NS-ThM6, **207**
Vandencastele, N.: PS+TC-WeM11, 148; PS-ThP2, 255; PS-ThP31, **260**; SE+NS-MoA4, 50
Vanderleyden, E.: MN+AS-MoM10, 14
VanDerslice, J.: EL+TF+BI+AS+EM+SS-MoA1, 32
Vandervorst, W.: AS-ThM6, 192
VanFleet, R.: LB+EM+GR+MN+TR-WeA3, 173; MN+AS-MoM4, 13
Vanhart, D.: EN+TF-WeA12, 169
Vanhove, N.: HI+AS+NS-WeA10, **172**
Vaniapura, V.: PS2-TuM10, 73
VanSant, K.: TF+AS-WeA10, 189
Varela, M.: OX+EM+MI+NS+TF-MoM10, 18

- Varga, T.: HI-ThP2, 251; MI-ThP4, **252**; OX-TuP6, 122
- Varoutis, S.: VT-TuM4, **80**
- Vasekar, P.S.: EN+TF-WeA12, **169**
- Vasiliev, I.V.: EM+NS-FrM9, 268
- Vega, A.: TF+AS+SS-ThA3, **239**
- Velden, M.: TC+EM+AS+TF+EN-ThM2, 215
- Vélez, C.: BI-TuP6, **116**
- Vemuri, R.S.: HI-ThP2, 251; TF+AS+SS-ThA11, 240
- Venkatachalam, D.K.: LB+EM+GR+MN+TR-WeA7, 173
- Ventrice, Jr., C.A.: GR+AS+NS+SP+SS-TuA11, 91; GR+EM+NS+PS+SS+TF-MoM2, 11
- Ventzek, P.: PS2-MoA10, 49; PS2-MoA11, **49**; PS2-MoA9, 49
- Verberk, R.: VT-TuA7, 109; VT-TuA9, 109
- Verbitsky, N.: GR-ThP3, 249
- Verdini, A.: SS+OX-WeM6, 152
- Verheijen, M.A.: TF+EN-MoA4, 53; TF-TuM10, 78; TF-TuM11, 78
- Verkhuturov, S.: AS-ThM5, 192
- Versloot, T.J.: PS-ThA9, 234; PS-ThP15, 257
- Versluis, R.: VT-TuA7, 109; VT-TuA9, **109**
- Vescovo, E.: MI+OX-WeA10, 176; MI+OX-WeA11, 176
- Veyan, J.-F.: GR+AS+BI+PS+SS-WeM2, **142**; NS+SP-MoA7, 43; SS-WeA12, 187
- Viale, L.: VT-TuM12, 81
- Vicar, M.: VT-MoA1, 54
- Vickerman, J.C.: AS-ThM2, **192**
- Victoria, R.H.: TF+MI-WeA1, **190**
- Vieker, H.: HI+AS+BI+NS-ThM5, **202**; HI-ThP1, 251
- Vilayrganapathy, S.: NS-WeA10, **178**; TC+EM+AS+TF+EN-ThM5, 216
- Vilmercati, P.: AC+TF+SS+MI-MoA3, 28
- Vincent-Johnson, A.J.: TF+EN-MoA7, 54
- Virwani, K.: EM-TuA8, 86
- Vizioz, C.: PS-ThP26, 259
- Vlassiok, I.: AS-TuP12, 113; ET+SS+GR+SP-ThA6, 229
- Voelcker, N.H.: PS+BI-MoA7, 47
- Voevodin, A.A.: SE+NS-MoA1, 49; SE-TuP3, **123**; TR+SE-WeM1, 159
- Vogel, E.M.: EM+TF-WeM4, 139; EM-TuM3, 61; GR-ThP13, 251
- Vogli, E.: PS2-TuA1, 97
- Vogt, P.: GR+EM+NS+SS+TF-ThA6, **231**
- Vohs, J.M.: SP+AS+BI+ET+MI+TF-WeA3, 183
- von Bergmann, K.: NS-ThM1, 206
- Vora, P.M.: GR+AS+EM+MI+MN-TuM2, 64
- Voronin, S.: PS2-TuM1, 72
- Voroshazi, E.: AS-ThM6, 192
- Vo-Yan, C.: GR+AS+EM+NS+SS-WeA10, 171
- Voznyuk, V.: MI+OX-WeA7, 175
- Vratzov, B.: NS+SP-MoA9, 43
- Vukovic, M.: VT-TuP4, **131**
- Vurgafman, I.: EM+TF+AS-ThA6, 225
- Vyalikh, D.: GR-ThP3, 249
- **W** —
- Wada, A.: PS1-TuA9, 96; PS-MoM6, 20
- Wade, S.A.: MB+BI-ThA4, **232**
- Wadikar, M.: SE+PS-TuA9, 100
- Waerenbogh, J.-C.: AC+TF+SS+MI-MoA6, 28
- Wagner, M.: SS+OX-WeM12, 153
- Wagner, M.S.: AS-WeM3, 135
- Walker, A.V.: EM+TF-WeM5, **139**
- Walker, G.: SS+OX-WeM4, 152; SS-TuP5, 124
- Walker, R.: AS-TuP9, **112**
- Wall, M.H.: GR-ThP1, 249
- Wallace, D.C.: EM+NS-FrM11, 269
- Wallace, R.M.: EM+TF+OX+GR-MoM1, **8**; EM+TF+OX+GR-MoM5, 8; EM-TuM3, 61; GR+AS+EM+NS+SS-WeA1, 170; GR+EM+ET+MS+NS-FrM7, 272
- Wallig, J.: SE+PS-TuM10, 75
- Wallin, C.B.: MN-TuM10, 68
- Wallin, P.: BI-MoA3, 30
- Walrath, J.C.: EM+SS+AS+NS-ThM13, **195**
- Walsh, L.A.: AS-TuP7, **112**; EM-TuM5, 62
- Walter, A.: GR+EM+ET+NS+TF-MoA8, 38
- Walters, D.: SP+AS+BI+ET+MI+TF-WeA11, 183
- Walton, J.: AS+BI-TuM12, 59
- Walton, S.G.: GR+AS+BI+PS+SS-WeM9, 143; GR+EM+NS+PS+SS+TF-MoM1, 10; GR-ThP9, 251; PS1-TuM12, 72; PS-ThP40, **261**
- Wan, K.: BN+AS-WeA10, 166
- Wang, B.: IS+AS+BI+ET+GR+NS-TuA9, 93
- Wang, C.: SS-WeM2, 154
- Wang, C.A.: PS-ThP1, 255
- Wang, C.M.: HI-ThP2, 251
- Wang, E.G.: EM-ThM11, 197
- Wang, G.-C.: TF+SE+NS-WeM4, **156**
- Wang, H.: PS2-TuM6, 73; SS-TuP26, 128
- Wang, J.: HI+AS+BI+NS-ThM9, 202; MI+OX-WeA10, 176; NS-MoM9, 16; SS-TuP4, **124**; TF-MoM8, 25
- Wang, J.-P.: MI+OX-WeA3, **175**
- Wang, K.L.: EM+SS+AS+NS-ThM11, 195
- Wang, L.: AC+TF+SS+MI-MoA1, 28; GR+EM+ET+NS+TF-MoA10, 38; PS-ThP1, 255; PS-WeM4, 149; TF+AS+SS-ThA8, **240**; VT-MoA6, **55**
- Wang, L.B.: MN+AS-MoM11, **14**
- Wang, M.-C.: PS-ThP45, 262
- Wang, P.: NS-WeA2, 177
- Wang, Q.H.: GR+AS+BI+PS+SS-WeM1, 142
- Wang, R.: EN+TF-TuA8, 88
- Wang, S.: MN-TuM11, 68
- Wang, W.: ET+SS+GR+SP-ThA10, **230**; SS-TuP26, 128
- Wang, X.: BI-TuP6, 116; LB+EM+GR+MN+TR-WeA7, 173
- Wang, Y.: EN+NS-MoM2, 9; EN+TF-TuA12, 89; GR-ThP3, 249; OX+SS+TF+MI-MoA10, 45; PS-ThP10, 256
- Wang, Z.: AS-MoA3, 29
- Wang, Z.-T.: SS+EN+OX-ThM5, 212; SS+EN+OX-ThM9, **213**; SS-TuM5, 76
- Wanifuchi, T.: PS-ThP8, **256**
- Warren, A.P.: EM-TuA2, **86**; EM-TuA7, 86
- Wasio, N.A.: AS-TuP26, **115**; ET+SS+GR+SP-ThA3, 229
- Watanabe, N.: PS2-ThM9, 211
- Watanabe, Y.: NM-TuP1, **121**; NM-TuP2, 121
- Waters, J.: NS+EN-TuM3, 69
- Waterton, C.: IS+AS+BI+ET+GR+NS-TuA1, 91
- Watkins, J.: NM+NS+MS+EM-MoA10, **42**
- Watts, J.F.: AS-TuP4, 111
- Watts, S.: MI+OX-WeA7, 175
- Weaver, J.F.: SS+EN+OX-ThM10, **213**; SS-TuP22, 127; SS-TuP23, 128
- Webb, L.: BI-TuP18, 118
- Weber, J.W.: EL+TF+AS+EM+SS+PS+EN+NM-MoM6, 7
- Weber, M.J.: TF+EN-MoA4, **53**
- Weber, N.-E.: HI+AS+BI+NS-ThM5, 202
- Weber, P.K.: AC+EN-TuM6, 57
- Weeks, S.L.: EN+PS-WeM4, 141; NS-MoM6, **16**
- Wehbe, N.: AS-MoA2, 29
- Wei, D.: EM+TF+OX+GR-MoM9, **9**
- Wei, M.: TF+AS-WeA7, **189**; TF+AS-WeA9, 189
- Wei, S.-H.: EN+AS-ThA1, 227; TC+EM+AS-WeA4, **187**
- Wei, W.D.: EN+SS-FrM4, 269
- Weidner, T.: AS-WeM3, 135
- Weiland, C.: AS-ThA6, **222**
- Weinberg, R.Y.: VT-MoA6, 55
- Weinert, M.: GR+AS+NS+SP+SS-TuA2, 90; SS-TuP3, 124
- Weisheit, M.: EM-TuA11, 87
- Weitering, H.: ET+NS+EM-ThM3, 199
- Weller, T.: NS-MoM9, 16
- Welzel, S.: EN+PS-WeM3, 140; PS+TC-WeM2, **147**
- Wen, H.: SE-TuP4, 123
- Wenger, W.N.: EN+NS-MoM5, 10
- Werij, H.G.C.: VT-TuA7, **109**
- Werner, S.: BP+AS-SuA3, 1
- Werner, W.S.M.: AS-MoM3, **3**; AS-MoM6, 3
- Wessel, S.: EN+AS-ThA6, 227
- Westwood, J.N.: MN-MoA7, **39**
- Wetzel, C.: EM+TF+AS-ThA7, **225**
- Wheeler, V.D.: EM+OX-WeA8, 167; GR+AS+NS+SP+SS-TuA9, 90; GR+EM+ET+MS+NS-FrM3, 271; GR+EM+ET+MS+NS-FrM5, **272**; GR+EM+ET+NS+TF-MoA1, 37; GR+EM+NS+PS+SS+TF-MoM1, 10; GR+EM+NS+PS+SS+TF-MoM3, 11; GR-ThP9, 251
- White, E.: EM+TF-WeM6, 139
- White, M.G.: NS+AS+SS+SP-WeM12, 147
- White, R.G.: AS-MoA2, 29; AS-MoM10, 4; AS-TuP11, **113**; EW-TuL3, 82
- Whitehead, N.P.: BN+AS-WeA9, 166
- Whitten, D.G.: MB+BI-ThM9, 204
- Whittle, J.D.: PS-ThA8, **234**
- Wielunski, L.S.: AS-MoA10, **30**
- Wiemer, M.: EN+TF-TuA9, 88
- Wiens, J.P.: SS-MoA1, 51
- Wiesendanger, R.: NS-ThM1, **206**
- Wiesmann, H.P.: BI-TuP12, **118**
- Wijnaendts van Resandt, N.: EW-WeA5, **169**
- Wilbert, D.S.: ET+NS+EM-ThM11, 200
- Wilcock, J.: TF-WeM6, 158
- Wilde, M.: SS-MoA9, 52
- Wildman, H.: EM+NS-FrM10, 268
- Wilhelm, F.: SS+OX-WeM5, 152
- Willey, T.M.: AS+TF+VT-FrM2, 266
- William, C.T.: SS-ThM11, 215
- Williams, A.: PS+TC-WeM12, 148
- Williams, A.I.: PS2-MoA6, **48**
- Williams, P.: MB+BI-ThM12, 204
- Williams, P.M.: BI+SS+AS-TuM5, 60
- Williams, T.S.: PS+EM-MoM9, **19**
- Willman, J.T.: TF-ThP4, 263
- Willunat, A.: HI+AS+BI+NS-ThM11, 203; HI+AS+BI+NS-ThM5, 202
- Wilson-Rae, I.: MN-MoA1, 38
- Winans, L.: TF+EN-MoA1, 53
- Windisch, Jr., C.F.: AS+BI-TuA12, 84
- Winkler, K.: GR+AS+NS+SP+SS-TuA1, **89**
- Winter, A.: HI+AS+BI+NS-ThM11, **203**; HI+AS+BI+NS-ThM5, 202
- Winter, B.: SS-ThA1, 237; SS-ThA2, 237
- Winter, G.: AS+BI-TuM3, 58
- Wirtz, T.: HI+AS+NS-WeA10, 172
- Wissing, S.N.P.: MI-WeM1, 145
- Witanachchi, S.: EN+NS-MoM6, 10; MI+OX-WeA9, 176; OX+EM+MI+NS+TF-MoM1, 17
- Wittstock, A.: IS+AS+OX+ET-WeM6, 144
- Witzke, M.: PS+EM-MoM11, 19
- Wodtke, A.M.: SS-MoM4, 23
- Woicik, J.C.: AS-ThA6, 222; AS-ThA8, **223**; AS-TuP7, 112; EM-TuM5, 62; OX+SS+TF+MI-MoA9, 45
- Wolden, C.A.: EN+TF-MoA10, **36**; PS1-TuA7, 96
- Wolf, H.: NS+SP-MoA2, 42
- Wolf, J.: VT-TuM10, **80**; VT-TuM11, 81
- Wolf, S.A.: EM+MI-ThA11, 224; MI+EN+BI-TuA7, 93
- Wolkow, R.A.: HI+AS+NS-WeA7, 172; SP+AS+BI+ET+MI+NM+NS+SS+TF-WeM2, **150**
- Woll, A.R.: IS+AS+BI+ET+GR+NS-TuA2, 92
- Wöll, Ch.: GR-ThP3, 249; OX+SS+TF+MI-MoA10, 45
- Wolstenholme, J.: AS+BI-TuM11, 59
- Wolter, B.: NS-ThM1, 206
- Womack, V.M.: BN+AS-WeA12, 166
- Won, S.-O.: EN+TF-TuM12, 63
- Wong, B.: MN-TuP7, 120
- Wong, M.S.: EN+NS-ThM12, 198
- Wood, B.C.: IS+AS+OX+ET-WeM6, 144
- Woodroof, M.: TF+EN-MoA8, 54

- Woods, A.S.: BN+AS-WeA12, 166
Woods, L.M.: GR-ThP4, 250
Wormeester, H.: EL+TF+BI+AS+EM+SS-MoA8, **33**
Wornyo, E.: PS-WeM11, 150
Worsley, M.A.: IS+AS+OX+ET-WeM6, 144
Wright, A.E.: AC+EN-TuM1, 57; AS-MoM10, 4; AS-TuP10, 112; EW-TuL3, 82
Wu, C.: PS+EM-MoM5, 19
Wu, F.: PS-WeM1, 148; PS-WeM11, 150
Wu, H.: EN+AS-ThA7, 228; HI-ThP3, **252**
Wu, J.: AC+TF+SS+MI-MoA1, 28
Wu, K.H.: EM-ThM11, 197
Wu, M.-F.: PS2-MoA3, 48
Wu, M.-Y.: EN+TF-TuA3, 88
Wu, N.: MI+OX-WeA10, **176**
Wu, R.: ET+NS+EM-ThM3, 199
Wu, S.: GR+AS+NS+SP+SS-TuA12, 91
Wu, Y.: EN+NS-ThA3, **228**; PS-MoM11, 21; TF+EM+SE+NS-ThM3, **217**; TF-TuM5, **77**
Wu, Y.L.: PS-ThP36, 261; TC+EM+AS+TF+EN-ThM12, **216**
Wu, Z.: BN+AS-WeA3, 165
Wuchter, P.: BI-TuP14, 118
Wüest, M.: MN-TuP1, **119**; VT-MoM2, 25
Wygladacz, K.A.: AS-TuP19, **114**
Wyrick, J.: SP+AS+BI+ET+MI+NM+NS+SS+TF-WeM5, 150
- **X** —
Xia, D.: HI-ThP3, 252
Xia, Y.: SS-TuM10, 76
Xiao, Q.: AS+TF+VT-FrM1, 266
Xiao, Z.: EM-ThP13, **246**; NS-ThP12, 254
Xie, J.: EM+TF+AS-ThA1, 225
Xie, K.: SS-WeA3, 186
Xie, X.: TF-WeM2, 158
Xing, G.: EM+OX-WeA3, **167**
Xu, H.Y.: PS2-WeA1, 180
Xu, M.: NS-ThM2, 206
Xu, Y.: EL+TF+BI+AS+EM+SS-MoA9, 33; GR+AS+EM+NS+SS-WeA11, 171; PS2-TuM9, 73
Xue, A.: PS+EM-MoM8, 19
Xue, J.: EM+TF-WeM9, **139**
- **Y** —
Yacout, A.M.: AC+EN-TuM1, 57
Yagisawa, T.: PS+EM-MoM10, **19**
Yague, J.L.: EM+TF-WeM11, **140**
Yakimov, M.: EM+TF+OX+GR-MoM3, 8
Yakobson: GR+EM+NS+SS+TF-ThA8, **231**
Yakou, F.: SS+OX-WeM5, 152
Yamada, A.: TF-ThP12, 264
Yamada, T.: BI+SS+NS-WeM11, 138; PS+TC-WeM3, 147; SE+PS-TuA8, 100; SS-MoA10, **53**; SS-TuP31, 129
Yamada-Takamura, Y.: TF+AS-WeA8, 189
Yamashita, I.: PS2-ThM10, 211
Yamashita, Y.: AS-ThA10, 223
Yamazaki, K.: GR-ThP5, **250**
Yamazawa, Y.: PS1-WeA12, 180
Yan, H.: SS-WeA3, 186
Yan, L.: TC-ThP2, **262**
Yan, Y.H.: VT-MoA1, 54
Yanagisawa, Y.: PS2-ThM11, **211**
Yang, A.: AS-ThA10, 223
Yang, C.S.: VT-TuA12, 109
Yang, G.-E.: MI-ThP1, 252
Yang, J.: EM+TF-WeM5, 139; MB+BI-ThM12, 204; PS+EM-MoM9, 19
Yang, K.: TF+AS+SS-ThA8, 240
Yang, L.: IS+AS+BI+ET+GR+NS-TuA12, **93**
Yang, M.: EN+TF-TuA8, 88; PS2-TuM6, 73
Yang, P.: SS-TuP26, 128
Yang, Q.: PS2-TuM6, 73
Yang, X.: SS-WeA10, 186
Yang, Y.C.: VT+AS+SS-WeM1, 160
Yang, Y.J.: PS+EM-MoM4, **18**; PS-ThP22, 258
- Yanguas-Gil, A.: TC+EM+AS+TF+EN-ThM6, **216**
Yao, B.: EM-TuA7, 86; EN+TF-TuM10, 63
Yao, K.: OX-TuP3, **122**
Yaowarat, W.: NS-ThP11, **254**
Yashina, L.: GR-ThP3, 249
Yasumura, S.: SS-TuP8, 125
Yasutake, K.: PS+TC-WeM3, **147**; SE+PS-TuA8, 100
Yates, Jr., J.T.: SS+EN+OX-ThM6, 212; SS-TuM3, 75
Yatsuda, K.: PS-ThP12, 257
Yazawa, K.: SE+NS-MoA8, 51
Yazyev, O.V.: GR+AS+NS+SS-ThM5, 201
Yckache, K.: EM+TF+OX+GR-MoA9, 35
Ye, D.: TF+EM+SE+NS-ThM6, **217**
Ye, J.: SS-TuM10, 76
Ye, L.: TF-ThP9, **264**
Ye, Y.F.: SS-TuP37, 130
Yeh, P.: PS+EM-MoM9, 19
Yeh, P.-C.: SS-TuP2, 124
Yellen, B.: BI+SS+NS-WeM9, 137
Yeom, G.Y.: ET-ThP1, 249; PS+TC-WeM9, **148**; PS-ThP24, 258; PS-ThP27, 259; PS-ThP28, 259; PS-ThP43, 261
Yesilkoya, F.: EM+OX-WeA9, 167
Yilmaz, D.E.: OX+SS+TF+MI-MoA1, **44**; OX-TuP3, 122; TR-TuP1, 130
Yilmaz, E.: EN-ThP3, 247
Yilmaz, M.: MN-MoA3, **38**
Yim, J.: PS+TC-WeM12, **148**
Yin, J.: EM+TF-WeM11, 140
Yin, Y.: PS2-TuM6, 73; PS2-TuM9, **73**; PS-ThP1, 255; PS-WeM1, 148; PS-WeM11, 150
Yoda, S.: SS-ThA10, **238**
Yokosuka, S.: PS2-ThM3, 210
Yokus, M.: TF2-TuA10, 107
Yoo, H.: EM-TuA12, 87
Yoon, H.M.: PS-ThP23, 258
Yoon, J.-H.: EN+TF-TuM12, 63
Yoon, K.H.: EM-ThP12, 246
Yoon, Y.: SS+EN+OX-ThM5, 212
Yoshida, H.: VT-MoA3, 54; VT-MoA4, **55**
Yoshida, S.: TF-ThP2, 263
Yoshida, Y.: NS-ThM1, 206
Yoshikawa, A.: EM+TF+AS-ThA12, **226**
Yoshikawa, J.: PS2-MoA11, 49
Yoshimura, M.: TR-TuP3, **131**
Yoshimura, T.: GR+AS+NS+SS-ThM1, 201; TF+EM+SS-ThA3, **241**
Yoshinaga, J.: VT-MoM1, 25
You, M.Y.: NS-ThP6, 253
You, S.-J.: PS-ThP4, 255
Young, A.: GR+EM+ET+NS+TF-MoA10, 38
Young, L.: BI-MoA8, 31
Yu, H.: PS+EM-MoM9, 19; SE+PS-TuM3, **74**; SE+PS-TuM4, 74
Yu, J.: GR+AS+NS+SP+SS-TuA12, **91**
Yu, S.W.: AC+MI+SS+TF-MoM9, 2
Yu, W.: SS-WeA9, **186**
Yu, X.-Y.: IS+AS+BI+ET+GR+NS-TuA12, 93
Yu, Z.: NS+AS+SS+SP-WeM4, 146; SS-TuP19, 127
Yuan, H.: TF-ThP10, 264
Yuen, H.B.: EN+TF-TuA9, 88
Yun, D.J.: AS-ThA4, 222
Yurtsever, A.: SP+AS+BI+ET+MI+NS-TuA11, 102
Yushin, G.: EN+NS-ThM4, **198**
- **Z** —
Zandvliet, H.J.W.: EL+TF+BI+AS+EM+SS-MoA8, 33
Zang, F.: BI+SS+NS-WeM2, **137**
Zapata-Torres, M.A.: TF-ThP8, 264
Zapotok, D.W.: EM+OX-WeA8, 167
Zappe, M.: LB+EM+GR+MN+TR-WeA3, 173
Zarrouati, M.: GR+AS+BI+PS+SS-WeM1, 142
Zauscher, S.: BI+SS+NS-WeM9, **137**
- Zegenhagen, J.: AS-ThA7, 223; GR+AS+NS+SP+SS-TuA9, 90
Zehnder, D.: GR+EM+ET+MS+NS-FrM3, 271
Zeman, M.: EN+PS-WeM10, 141
Zendejas, J.: MN-TuP7, **120**
Zeng, H.: TR-TuA4, 107
Zettl, A.: GR+AS+NS+SS-ThM5, **201**
Zettsu, N.: NS-ThP4, 253
Zhakhovskiy, V.: GR+AS+EM+MI+MN-TuM10, 65
Zhan, Y.: GR+EM+NS+SS+TF-ThA3, 231
Zhang, B.: SS-TuM10, 76; TC+EM+AS-WeA3, 187
Zhang, C.X.: EM+SS+AS+NS-ThM11, 195
Zhang, E.X.: EM+SS+AS+NS-ThM11, **195**
Zhang, F.: SS+EN+OX-ThM10, 213
Zhang, H.: HI+AS+BI+NS-ThM9, 202
Zhang, H.-Z.: PS-ThA10, 235
Zhang, J.Z.: TF+SE+NS-WeM3, 156
Zhang, K.H.L.: OX-TuP5, 122
Zhang, L.: GR+EM+ET+NS+TF-MoA11, **38**; IS+AS+SS+EN-TuM3, 65; PS1-ThM2, **208**; TF+AS-WeA1, **188**
Zhang, Q.: PS-ThP1, 255
Zhang, S.: BI+AS-TuA3, 84; SS-TuP9, 125
Zhang, T.: MI-WeM11, 146; MI-WeM2, 145
Zhang, X.: EN+TF-MoA8, 36; EN+TF-MoA9, **36**; HI+AS+BI+NS-ThM5, 202; HI-ThP1, 251
Zhang, X.-G.: ET+SS+GR+SP-FrM1, **270**; ET+SS+GR+SP-ThA6, 229
Zhang, Y.: ET+NS+EM-ThM3, 199; PS1-TuM10, 72; PS1-TuM9, **72**
Zhang, Z.: NS+EN-TuM11, 70; SS-TuM10, **76**
Zhao, H.: IS+AS+SS+EN-TuM9, 66
Zhao, J.: PS1-TuM11, 72; PS1-WeA12, 180; PS2-MoA11, 49
Zhao, S.-G.: SS-TuP9, 125
Zhao, X.: TR-TuA7, **107**
Zhao, X.H.: MB+BI-ThA6, **233**
Zhao, Y.: GR+EM+ET+NS+TF-MoA10, 38
Zhao, Y.-P.: TF+SE+NS-WeM12, 157; TF+SE+NS-WeM3, 156
Zharnikov, M.: EM+TF-WeM1, **138**
Zheng, H.: EM-ThP10, **245**
Zheng, X.: TC+EM+AS+TF+EN-ThM11, 216
Zhernokletov, D.M.: EM-TuM3, 61
Zhitenev, N.B.: GR+EM+ET+NS+TF-MoA10, 38
Zhou, B.: PS-MoM1, 20
Zhou, C.: AS+BI-TuA10, 83
Zhou, H.: EM-TuA1, 85; PS2-TuM11, **74**
Zhou, J.: SS+NS-TuA12, **104**; SS-TuP13, 126
Zhou, R.: EM+TF-WeM9, 139
Zhou, Y.H.: SS+NS-TuA12, 104; SS-TuP13, 126
Zhu, H.: TF+EN-MoA6, 54
Zhu, J.F.: GR+EM+ET+NS+TF-MoA11, 38; IS+AS+SS+EN-TuM3, 65; SS+NS-TuA11, **104**; SS-TuM9, 76; SS-TuP35, 130; SS-TuP37, 130
Zhu, W.: PS-MoM8, **21**
Zhu, Y.: SP+AS+BI+ET+MI+NM+NS+SS+TF-WeM5, **150**
Zhu, Y.-Z.: SS-TuP9, **125**
Zhu, Z.: AS-MoA3, **29**; EM+NS-FrM10, 268; IS+AS+BI+ET+GR+NS-TuA12, 93
Zoffmann Andersen, O.: BI-MoM2, 5
Zohar, S.: MI+SP+AS-ThM12, 206
Zollner, S.: EL+TF+AS+EM+SS-TuP2, 118; EL+TF+BI+AS+EM+SS-MoA9, **33**; EM+NS-FrM9, 268
Zonooz, P.: EN-ThP11, 248
Zorn, G.: TF-ThP5, **263**
Zufelt, K.: LB+EM+GR+MN+TR-WeA3, 173
Zuilhof, H.: EM+TF-WeM3, **139**; TF+EM+SS-ThA4, 241
Zuluaga, S.: EN+SS-FrM7, **270**
Zumbülte, A.: MI-WeM1, 145
Zunft, H.: NM+NS+MS+EM-MoA9, 41

